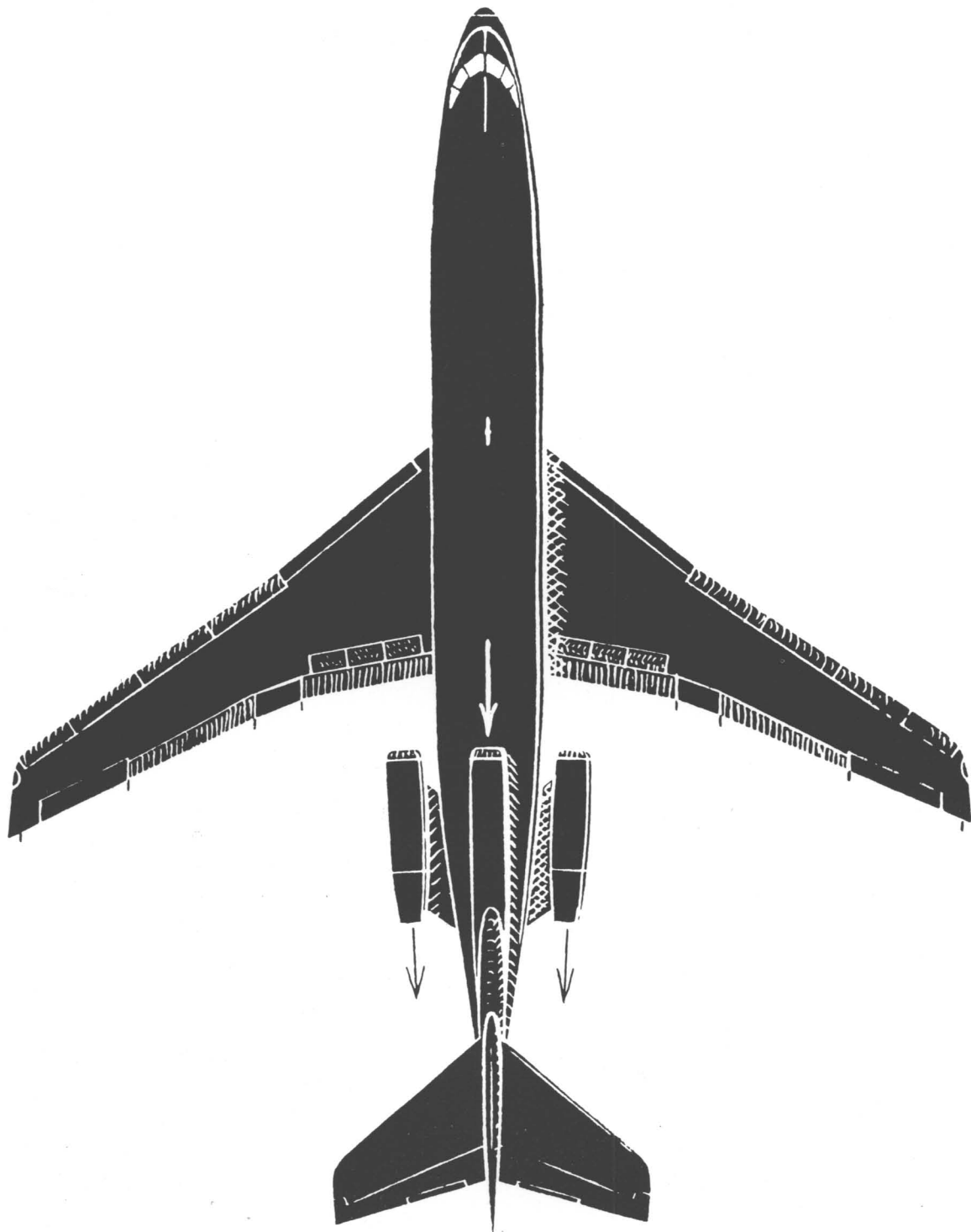


FLUID-DYNAMIC DRAG

theoretical, experimental and statistical information

presented by Dr.-Ing. S. F. HOERNER

1965



FLUID-DYNAMIC DRAG

Practical Information on
AERODYNAMIC DRAG and HYDRODYNAMIC RESISTANCE

by

SIGHARD F. HOERNER

Dr.-Ing.

Published by the Author

1965

COPYRIGHT 1992 BY LISELOTTE A. HOERNER

COPYRIGHT IN GREAT BRITAIN

Text and/or illustrations of this publication may not be reproduced, neither as a whole nor in part, without the specific permission of the copyright holder and publisher.

PRODUCED IN THE UNITED STATES OF AMERICA

Library on Congress Catalog Card Number 64-19666

The book is only for sale by mail order, directly from

HOERNER FLUID DYNAMICS

P.O. Box 21992

Bakersfield, CA 93390

Phone/Fax: (661) 665-1065

Should this address expire, the new location may be found in listings such as the Membership Roster of the American Institute of Aeronautics and Astronautics (AIAA, in New York City, with offices in Los Angeles and Brussels) or in copies of the book recently purchased.

FOREWORD

In the second edition of his book, Dr. Hoerner has added two chapters on hydrodynamics; the title has been changed accordingly. It is certain that this expansion of scope will meet with approval from all who are working in the field of "fluid dynamics".

I see no reason for any material change in the foreword given in the first edition ("Aerodynamic Drag", May 1951). What is said there, applies to the second edition with obvious minor modifications. I have, therefore, suggested that it be so revised and included as follows.

When Dr. Hoerner asked me to read his manuscript and write this foreword, I consented to do so, but with some misgivings regarding the nature of a book carrying the title AERODYNAMIC DRAG. Although Dr. Hoerner is known as a highly competent aerodynamicist, it did not seem possible within the scope of the title to do much more than prepare another compilation of drag data.

My first impression on reading the text was one of great surprise at the magnitude of the author's achievement. He had succeeded in producing an outstanding treatment of the subject; so that we now have an entire book concerned with but one of the six components of the total aerodynamic force. And it is not just another book. It is an exceptionally well written, systematic treatise showing a splendid balance between the theoretical and the experimental approach. The presentations are always made with great clarity, even in those cases where the author has had some obvious difficulties working in a new language.

It is safe to predict that this volume will be well received, not only by aeronautical engineers but also by all who have any concern whatever with aerodynamic or hydrodynamic drag. The whole field of transportation is involved, and many will find here for the first time a readily usable compilation of basic data.

I take great pleasure in being the first to congratulate Dr. Hoerner on his contribution to aeronautical progress.

Only those who have tried to evaluate, to compile, and to correlate data in the form as it has been done in this book, can fully appreciate Dr. Hoerner's effort.

WASHINGTON, D. C. — August 1957

WALTER S. DIEHL

ACKNOWLEDGEMENTS. During the years of his work in applied aerodynamic and hydrodynamic research, the author had the opportunity of doing himself, and of directing others in performing aerodynamic investigations of a more general nature. This book is the result of such original work as well as that of the author's analysis and evaluation of material from other sources. The author is particularly indebted in this respect to the National Advisory Committee for Aeronautics (now NASA, Washington, D. C.) for the large volume of information made available in their publications, and to the American Institute of Aeronautics and Astronautics (New York City) for their assistance in obtaining information from publications of every type. The author acknowledges also his indebtedness to Walter S. Diehl (Captain U.S.N. Ret., formerly Chief of Research and Development, Bureau of Aeronautics) author of "Engineering Aerodynamics", for his encouragement when first publishing this book.

AUTHOR'S PREFACE

In 1951, the author introduced the first edition of his book, entitled "Aerodynamic Drag", in part as follows:

It is the author's objective in this book, to present information on drag or fluid-dynamic resistance in a comprehensive, generally-valid and intelligible manner to students, engineers and researchers. The text is not always a "handbook", however, giving ready results. The reader is expected to work out the desired information himself, considering cause and effect involved in the problem he wants to solve.

It is primarily the aeronautical engineer who is interested in aerodynamic drag problems, so that he can predict and possibly improve the performance of airplanes. The principles of aerodynamic drag, many detailed data, and some special sections in this book should, however, find interested readers in several other fields of engineering as well — in the design of automobiles, in shipbuilding, in the construction of chimneys (wind loads), in the design of high-speed railroad trains, in machines applying aerodynamic or hydrodynamic forces, and finally in the design of ventilation systems.

"Aerodynamic Drag" was originally written in 1945 and 1946, as a result of the author's experience in German research- and industrial organizations (such as Junkers and Messerschmitt). Many additional and more recent data have been added, however, during the translation in the following years. Subsequently, the technical publishing houses in New York City were not found to be confident enough to bring out a book as specialized as this one. The author, therefore, decided to do the publishing himself.

The following information is now added on "Fluid-Dynamic Drag":

Progress in aerodynamics is rapid in these years. The volume of information published during the last five years is very large. A second edition of "Aerodynamic Drag" could, therefore, not very well be a reprint. Instead, every section of the text has been worked over and numerous improvements and additions have been made, in an effort to keep the publication up to date. This is particularly true in compressive and supersonic aerodynamics, which are now presented in three chapters.

Besides air, the medium of water is most predominant in practical applications of fluid dynamics. The author was happy, therefore, to have the opportunity during the last years in New York City, to participate in research and design of ships and hydrofoil boats — and to acquire in this way personal experience in water flow too. As a result, two chapters on hydrodynamic resistance have been added to the essentially aerodynamic content of the first edition. The title of the second edition has been adapted accordingly.

Another chapter has also been added, presenting wind loads on various types of structures, especially buildings.

After acquiring some experience as his own publisher, the author could not resist repeating the procedure in the second edition. Appearance of the text and readability of the illustrations have been improved. The author feels much indebted to the typesetter, the printer and the book-binder — for having produced the book very skilfully.

The 1965 edition differs from the preceding one, as follows: A number of misprints and some mistakes have been eliminated. "Drag in cavitating flow", in Chapter X, has been rewritten. Hypersonic characteristics such as in missiles and re-entering vehicles, are presented in an added chapter. The "atmospheric properties" in Chapter XIX, have completely been rewritten. A section has been added, dealing with the aerodynamic drag of satellites. Chapter XX is also new. Information on various subjects of drag, ranging from base-vented hydrofoils to characteristics at supersonic speeds, has been collected in this chapter.

NEW YORK CITY — AUGUST 1964 SIGHARD F. HOERNER

THE AUTHOR studied mechanical engineering at the Institute of Technology in München (Dipl.Ing.), he earned a degree as Dr.-Ing. in aerodynamics at the Institute of Technology in Braunschweig, and he obtained a degree as Dr.-Ing.habil. from the TH Berlin. He served at one time as research assistant at the Deutsche Versuchsanstalt für Luftfahrt (DVL, near Berlin), as aerodynamicist in the Fieseler Corporation (working on the first STOL airplane, the "Stork") and later for a time as head of design aerodynamics in the Junkers A.G. He was then research aerodynamicist at the Messerschmitt A.G. After World War II, the author was invited to come to the United States, where he worked in aerodynamics at Wright Field, Ohio. For some years he has been acting as specialist for aerodynamics and hydrodynamics in the field of naval architecture at Gibbs & Cox, Inc., New York City.

TABLE OF CONTENTS

(pages are numbered by chapters)

CHAPTER I — GENERAL INFORMATION

1. NOTATION — ABBREVIATIONS

bibliographical references, abbreviations	1-1
equations and graphs, angles, subscripts	1-2

2. GLOSSARY OF TERMS AND NAMES

boundary layer, cavitation, circulation	1-3
compressibility, induced, laminar	1-4
pressure rotation, schlieren, separation	1-5
streamlines, turbulence, vorticity, wind	1-6
tunnel, personalities in fluid dynamics	1-6

3. DRAG AND THEORETICAL ANALYSIS

action and reaction, momentum transfer	1-7
statistical methods, approach in this book	1-8

4. NON-DIMENSIONAL COEFFICIENTS

dynamic pressure, drag area	1-8
force coefficients, pressure coefficient	1-9

5. PHYSICAL SIMILARITY LAWS

Reynolds number, compressibility, rarefied	1-9
gases, cavitation, free water surface	1-10

6. PROPERTIES OF AIR AND WATER

dynamic pressure, viscosity, speed of sound	1-11
dynamic pressure and viscosity in water	1-12

CHAPTER II — SKIN-FRICTION DRAG

1. AT VERY SMALL REYNOLDS NUMBERS

in two-dimensional flow, past disk, B'layer	2-1
---	-----

2. GENERAL BOUNDARY-LAYER DATA

velocity distribution in, total thickness of	2-2
sub-layer, displacement, momentum thickness ..	2-3

3. FRICTION WITH LAMINAR B'LAYER

laminar skin-friction drag coefficient	2-4
--	-----

4. WITH TURBULENT BOUNDARY LAYER

theoretical functions, practical equations	2-5
local coefficient, transitional coefficient	2-6

5. FRICTION OF 3-DIMENSIONAL BODIES

pressure gradient, B'layer displacement	2-7
cylinder in axial flow, longitudinal edges	2-8

6. TRANSITION OF B'LAYER FLOW

turbulence, stability limit, transition	2-8
turbulence, surface roughness, protuberances	2-9
single elements, forced transition	2-10

7. LAMINAR-FLOW FOIL SECTIONS

possibilities, pressure gradient, transition	2-11
location of thickness, influence of lift	2-12
stream turbulence, surface roughness	2-13
permissible roughness, boundary-layer suction ..	2-14
suction volume, surface-roughness, stimulation ..	2-15

CHAPTER III — PRESSURE DRAG

1. AT VERY SMALL REYNOLDS NUMBERS

sphere and disk, pressure due to friction	3-1
stagnation pressure (Barker), floating dust	3-1
two-dimensional, intermediate R'numbers	3-3

2. MECHANISM OF FLOW SEPARATION

boundary-layer theory, pressure distribution	3-3
mechanism, separation, drag due to separation ..	3-4

3. VARIOUS VORTEX SYSTEMS

vortex types, sphere, vortex street, frequency	3-5
general street characteristics, splitter plate	3-6

4. CRITICAL REYNOLDS NUMBER

spheres, laminar separation, turbulent B'layer ..	3-7
surface-roughness, stream turbulence, cylinder ..	3-8

5. DRAG OF ROUND BODIES

separation, rear-side pressure, cylindrical	3-9
shapes, elliptical sections, cross-flow principle ..	3-10
R'number, ellipsoidal bodies, half bodies	3-11
parallel-sided shapes, rounding radius	3-12
rotating bodies, "how fast a man falls"	3-13

6. DRAG OF VARIOUS TYPES OF PLATES	
at small R'numbers, turbulence, "aspect ratio"	3-15
rear-side pressure, at an angle, with hole, caps	3-16
7. DRAG OF WEDGES AND CONES	
angle of flow, free-streamline, brake, wedges	3-18
8. BASE-DRAG CHARACTERISTICS	
(a) Base Drag of 3-Dimensional Bodies	
jet-pump mechanism, "insulating" B'layer	3-19
base drag of bodies, effect of boat-tailing	3-20
(b) Base Drag in 2-Dimensional Shapes	
sheet-metal joints, blunt trailing edges	3-21
laminar mixing, cut-off trailing edge	3-22
optimum T'edge thickness, thick sections	3-22
9. DRAG OF NON-SOLID BODIES	
loss coefficient, free-flow principle	3-23
streamline grids, fine fabrics, compressibility	3-24
drag in free stream, parachutes, drag of flags	3-25
10. REDUCTION OF PRESSURE DRAG	
(a) Mechanical Devices	
moving skin, turbulence generators, ring, vanes	3-26
(b) Boundary-Layer Control	
discharging fluid, suction method, sphere with	3-26
suction, cylinder suction, thick foil section	3-27
11. SUPPLEMENTARY NOTES	
forebody drag, about Leonardo da Vinci	3-28

CHAP IV—WIND FORCES ON STRUCTURES

1. WIND CHARACTERISTICS	
speed distribution, boundary layer on ground	4-1
2. VARIOUS BUILDINGS	
houses, hangars, tall buildings	4-3
3. CYLINDRICAL STRUCTURES	
storage tank, chimneys, oscillations, smoke	4-4
stacks, pipe line, cables, galloping lines	4-5
4. STEEL STRUCTURES	
beams, girders, bridge structure, radio masts	4-6
5. OTHER STRUCTURES	
open roofs, spherical shapes, Statue of Liberty	4-7

CHAPTER V — SURFACE IRREGULARITIES

1. DRAG DUE TO SURFACE ROUGHNESS	
(a) Permissible Grain Size, Reynolds number	5-1
critical roughness size, physical grain size	5-2
(b) Skin-Drag Coefficients; terminal drag	5-3
sand roughness, concentration, grain shape	5-4
permissible size, C_f slope, polytropic roughness	5-5
2. DRAG OF SURFACE IMPERFECTIONS	
(a) General; independent drag coefficient	5-6
(b) Spanwise Protuberances; sheet-metal joints	5-7
(c) Spotlike Protuberances; rivet heads	5-8
critical Reynolds number, longitudinal elements	5-9
(d) Drag of Holes and Gaps; transverse gaps	5-10
3. IMPERFECTIONS, STREAMLINE SHAPES	
(a) Imperfections and Protuberances	
sheet metal wing, dirt and ice formation	5-11
(b) Drag of Control Gaps; gap definition	5-13
edges, flow through gap, B'layer interference	5-14

CHAP VI — DRAG OF STREAMLINE SHAPES

A. DRAG OF WING- AND STRUT SECTIONS	
1. Drag as a Function of Reynolds Number	
turbulence, Reynolds number phases	6-2
2. As a Function of Thickness Ratio	
wing tips, lateral edges, optimum wire, critical	6-4
Reynolds number, laminar airfoils, roughness	6-6
3. Applications of Streamline Sections	
airfoil-section families, fairings, struts	6-9
B. SECTION DRAG AS A FUNCTION OF LIFT	
insects, birds, optimum lift coefficient, camber	6-10
sharp leading edge, wing flap, slats and slots	6-13
C. DRAG OF STREAMLINE SHAPES	
various shapes, low Reynolds numbers, thickness	6-16
laminar boundary layer, optimum shape	6-18
D. SUPPLEMENTARY INFORMATION	
stimulation, wing-tip drag, reversed 0012	6-20

CHAPTER VII — DRAG DUE TO LIFT

1. INDUCED DRAG AND ASPECT RATIO	
lifting line, downwash, induced angle, A'ratio ..	7-2
2. INFLUENCE OF SHAPE ON DRAG	
(a) Plan Form and Tip Shape	
lift distribution, cut-outs, tip vortex flow	7-4
plan form, sweep, optimum shape, tip tanks	7-7
(b) Twist and Related Characteristics	
wing twist, wing flaps, taking-off, climbing	7-8
(c) Form of Lifting Line	
angle of sweep, negative sweep, dihedral angle	7-9
(d) Characteristics of End Plates	
height ratio, area ratio, inboard plates	7-10
single end plates, viscous drag of E'plates	7-10
(e) Rotating Cylinders	
drag due to lift, Flettner rotor	7-10
3. IN VARIOUS WING ARRANGEMENTS	
(a) Biplanes and Similar Configurations	
biplane, multiplanes, ring foil, ground effect	7-12
(b) Wings in Tandem and Similar Arrangements	
tandem configuration, horizontal tail	7-14
(c) Airplanes Flying in Formation	
wing gap, flying side by side, stagger	7-15
4. DRAG IN SMALL ASPECT RATIOS	
(a) First Drag Component	
circulation in small aspect ratios	7-16
first drag term, flat plates	7-17
(b) Second Drag Component	
zero aspect ratio, momentum, lateral vortex	7-18
second component, flat plates, delta wings	7-19
(c) Lift of Streamline Bodies	
second lift component, due to lift, rotation	7-20
(d) Parasitic Wing-Tip Drag	
second lift term, influence of wing-tip shape	7-21
5. SUPPLEMENTARY NOTES	
characteristics of birds, blade rotors	7-22

CHAPTER VIII — INTERFERENCE DRAG

1. BETWEEN PAIRS OF BODIES	
shielding effect, tandem struts, side by side	8-2
2. DRAG OF HALF BODIES ON WALLS	
dynamic pressure, plates, flow pattern	8-3
half bodies, optimum, fairings, trailing edge	8-4
3. ON THREE-DIMENSIONAL BODIES	
added body, B'layer thickness, buoyancy effect	8-5
pressure gradient, thickness, turbulence	8-6
fuselage with canopy, fuel tank of Me-109	8-7
gun turret, interference method, long bodies	8-9
4. WINGS (STRUTS) AND WALLS	
in corners, boundary layer, influence of lift	8-10
inclined struts, strut junctions, tail	8-11
configurations, fairings, junction angle	8-12
5. INTERFERENCE DRAG ON WINGS	
protuberances, induced interference drag	8-13
horizontal tail drag, glide-path control	8-14
6. DRAG OF WING-BODY CONFIGURATIONS	
wing-fuselage junctions, engine nacelles	8-15
tail surfaces, propeller blades, "α" flow	8-16
wing-fuselage angle, induced drag due to body	8-17
engine nacelles, interference method	8-19

CHAPTER IX — INTERNAL-FLOW SYSTEMS

A. MECHANICS OF DUCTED SYSTEMS	
loss coefficient, diffuser, rate of flow	9-1
intake flow, internal losses, outlet pressure	9-2
B. DRAG OF RADIATOR INSTALLATIONS	
1. Considerations for the System	
surface cooling, ducted systems, radiator size	9-3
2. Internal Radiator Drag	
radiator cores, diffuser, boundary-layer control	9-4
momentum, outlet pressure, drag due to leaks	9-4
3. External Radiator Drag	
drag near $w/V = 0$, belly-type radiator	9-6
ring radiators, wing radiators, lift effect	9-6

C. DRAG OF ENGINE INSTALLATIONS

1. Engine Cowlings	
internal characteristics, conductivity	9-7
external drag, streamline cowling	9-8
2. Jet-Engine Installations	
nose inlet, internal characteristics, scoop intake	9-9
wing-root inlet, lift due to, flush intake	9-10

D. HEAT AND COMPRESSIBILITY EFFECTS

1. Influence of Cooling Heat	
radiator core, propulsion, air-cooling	9-11
2. Influence of Compressibility	
temperature, radiators, air-cooled engines	9-12

E. DRAG OF IN- AND OUTLET OPENINGS

1. Drag of Air Scoops	
momentum drag, external drag, internal losses	9-13
2. Drag of Ventilation Systems	
(a) Inlet Openings	
scoop intakes, flush inlets, internal flow	9-14
(b) Outlet Openings	
streamline openings, thrust due to exhaust, vents	9-16

CHAPTER X—HYDRODYNAMIC DRAG**A. FULLY SUBMERGED BODIES**

drag of fish, critical R'number, foils in water	10-1
surface roughness, guide vanes, torpedo	10-2

B. DRAG IN CAVITATING FLOW

1. Fundamentals of Cavitation	
mechanism of cavitation, cavitation number	10-4
critical speed due to cavitation, erosion	10-5
2. Onset of Cavitation	
cavitation number, in 3-dimensional shapes	10-5
vortex cavitation, past disk, round bodies	10-6
in streamline sections, "delay" of cavitation	10-7
3. Drag Coefficient in Cavitating Flow	
sharp-edged bodies, circular cylinder	10-7
spheres, missile, size of cavity	10-8
4. Cavitating Hydrofoils	
inception of cavitation, cavitating flat plate	10-9
cambered foil sections, finite-span foils	10-11
in small aspect ratios, at zero aspect ratio	10-12

C. DRAG OF SURFACE-PIERCING SOLIDS

1. Wave and Spray Drag	
Froude number effect, wave drag, spray drag	10-13
2. Drag Due to Ventilation	
mechanism of ventilation (cavitation), half-body	10-14
depth of pocket, cylinder, surface-piercing	10-15
ventilated strut, ventilation plate	10-16
inclined shaft characteristics, angle of yaw	10-16

CHAPTER XI—WATER-BORNE CRAFT**A. RESISTANCE OF DISPLACEMENT VESSELS**

1. General Principles	
general notation, "resistance", wetted surface	11-1
turbulence stimulation, Froude number	11-2
2. Drag Caused by Friction	
extrapolation method, skin-friction law	11-3
influence of thickness, roughness, fouling	11-4
3. Model-Full-Scale Correlation	
drag of barges, appendages, shafting	11-6
influence of condenser water, wind resistance	11-7
skin-friction belt, surface roughness	11-9
full-scale correlation, extrapolation method	11-10
4. Wave Resistance	
nature of wave-drag, humps + hollows, Froude number	11-11
volumetric and prismatic coefficient	11-12
maximum hull section, bulbous bow	11-12
Maier form, in shallow water, drag in seaway	11-13
5. Types of Displacement Vessels	
ship statistics, motorboats, submarine resistance	11-16
submerged submarines, streamlining	11-17
submerged bodies, sailboat, induced drag	11-18

B. CHARACTERISTICS OF PLANING CRAFT

1. Theory of Planing	
two-dimensional theory, buoyancy lift	11-19
start of planing, small-aspect-ratio planing	11-20
higher aspect ratios, planing plates, camber	11-22
2. Characteristics of Planing Craft	
"V" bottoms, motorboats, power and speed	11-23
seaplanes, floats, planing skis, racing boats	11-24

C. HYDROFOIL BOATS

basic wave drag, induced drag, end struts	11-26
drag in finite aspect ratios, tandem foils	11-28
surface-piercing hydrofoils, V-shaped foils	11-29
ventilation, hydrofoil boats, power and speed	11-30
small aspect ratios, ventilated hydrofoils	11-31

CHAPTER XII — LAND-BORNE VEHICLES**A. DRAG OF MOTOR VEHICLES**

1. Experimental Methods	
road tests, wind-tunnel testing, ground plate	12-1
image method, moving ground, R'number	12-2
2. Drag of Basic Shapes	
friction drag, separation, aerodynamic lift	12-3
induced drag, wind shield, blunt rear end	12-4
3. Drag Due to Operational Parts	
headlights, underside, wheel openings	12-5
open windows, cooling air, streamlining	12-6
4. Efficiency of Passenger Cars	
rolling resistance, power required, optimum	12-7
5. Drag of Other Motor Vehicles	
trucks, omnibuses, racing cars, motorcycles	12-9

B. DRAG OF RAILROAD VEHICLES

1. Locomotives and Self-Powered Cars	
rail cars, steam locomotives, power cars	12-10
2. Drag of Railroad Trains	
aerodynamic drag law, drag of railroad cars	12-12
base drag, protuberances, complete train drag	12-13
3. Efficiency of Railroad Trains	
traction, freight train, wheel ventilation	12-14
SUPPLEMENTARY; interference, sports car	12-16

INDEX — EIGHT PAGES OF SUBJECT INDEX

→ see at the end of the book

CHAPTER XIII — AIRCRAFT COMPONENTS**1. DRAG OF FUSELAGES**

fineness ratio, open cockpits, canopy drag	13-1
due to windshields, roughness, armament, tail	13-2
turrets, guns, radiators, engines, leakage	13-4

2. DRAG OF ENGINE NACELLES

(a) Drag of Solid Nacelle Bodies	
induced drag, length ratio, high-wing nacelle	13-5
(b) Ducted Nacelles	
cowlings, wing interference, inlet and outlet	13-7
jet-engine nacelles, influence of lift	13-8

3. DRAG OF FLOATS AND BOAT HULLS

chines, fineness ratio, steps, step fairing	13-9
---	------

4. DRAG OF LIFTING SURFACES

interference drag, dive brake flaps	13-10
pervious flaps, due to spoiler control	13-12
tail surfaces, due to asymmetric engine power	13-13

5. DRAG OF LANDING GEARS

wheels, fixed and retractable, tail wheels, skis	13-14
--	-------

6. DRAG OF EXTERNAL LOADS

belly tanks, wing-tip tanks, range, bombs	13-16
bomb racks, neck suspension, interference	13-18

7. DRAG OF MISCELLANEOUS PARTS

(a) Drag of Cylindrical Parts	
fairings, cables, towing, refuelling hose	13-20
(b) Drag of Stopped Propellers	
blade angle, induced, tilted, windmilling	13-21
(c) Ejection Seats; drag and trajectory	13-22

8. CHARACTERISTICS OF PARACHUTES

basic shapes, flow pattern, gliding parachutes	13-23
permeability, oscillations, Reynolds number	13-24
fabric elasticity, size, rigging, ribbon type	13-25
"shaped" parachutes, guide-surface type	13-26

9. DRAG OF TOW TARGETS

wind socks, "flag" type, streamlining	13-28
---	-------

CHAPTER XIV — COMPLETE AIRCRAFT

1. DRAG OF AIRSHIPS

hull, fins, car, engine nacelles, full scale 14-1

2. DRAG ANALYSIS OF FIGHTER AIRPLANE

(a) full-Scale Performance
dimensions, exhaust thrust, induced drag 14-3

(b) Drag of the Wing
skin friction, imperfections, additional drag 14-4

(c) Drag of the Fuselage
due to appendages, interference, slip stream 14-5

(d) Drag of Appendages
of engine installation, due to tail surfaces 14-5

(e) Results of Me-109 Analysis
compressibility, imperfections, efficiency 14-6

3. PERFORMANCE OF OTHER AIRPLANES

(a) Maximum Speed Performance
cleanliness, Reynolds number, Ju-88 and Me-262 14-8
wetted-area drag coefficient, maximum speed 14-10

(b) Drag as a function of Lift
“e” method, Me-109, effective aspect ratio 14-12
sailplane, optimum lift, sinking speed 14-13

(c) Influence of Thrust
lift due to thrust, climbing, slipstream drag 14-14
jet thrust, pusher propeller, climb performance 14-15

(d) The First Powered Aircraft
airships, the Wright Brothers 11-16

XV — INFLUENCE OF COMPRESSIBILITY

1. ELEMENTS OF COMPRESSIBILITY

sonic speed, Mach number, stagnation pressure 15-1
the Prandtl rule, stagnation temperature 15-2

2. CHARACTERISTICS OF BLUFF BODIES

plates, cylinders, wedges, 0012 reversed 15-4
struts, drag divergence, cylinder, sphere 15-5
R'number, critical Mach number, up-down-up 15-6
half-streamline shapes, canopies, antenna rods 15-7

3. SKIN FRICTION IN COMPRESSIVE FLOW

on plane wall, boundary-layer stability 15-9
BL transition, laminarization, roughness 15-10

4. DRAG OF FOIL AND STRUT SECTIONS

friction, pressure drag, roughness, struts 15-10
optimum section thickness ratio, laminar flow ..15-12

5. CRITICAL MACH NUMBER OF WINGS

Prandtl factor, airfoil sections15-15
thickness location, blunt trailing edge15-16
finite wings, function of lift, recompression15-17
drag dip, pressure peaks, nose shape, foil camber 15-18

6. CHARACTERISTICS OF SWEPT WINGS

cosine component of speed, sweep definition15-20
drag of inclined struts, critical M'number15-21
wing center part, sheared and “delta” wings15-23

7. STREAMLINE BODY CHARACTERISTICS

friction, supersonicities, compressibility rule15-24
pressure drag, streamline bodies15-25
surface roughness, critical Mach number15-27

8. DRAG OF AIRCRAFT COMPONENTS

wing-fuselage configurations, wall interference 15-28
drag of crossed wings, plotting against $(P)^3$ 15-29
engine nacelles, slipstream, canopies, stores15-31
bombs, cowlings, radiators, dive brakes15-32

9. DRAG OF AIRPLANE CONFIGURATIONS

(a) Induced Drag of Wings
drag due to wing twist, induced interference15-33

(b) Parasitic Drag of Airplanes
drag of “Meteor”, twin-engine configurations ..15-34

(c) Statistical Compressibility Method
interference, airplane configurations15-35
importance of interference, on wetted area15-36

(d) Swept Wing Configurations
fuselage interference, contouring, “F-86” fighter 15-38

10. DRAG ABOVE DRAG DIVERGENCE

critical M'number, separation, growth of drag 15-39
influence of aspect ratio, angle of sweep15-40

CHAPTER XVI — AT TRANSONIC SPEEDS**1. ELEMENTS OF TRANSONIC FLOW**

cross section, Laval nozzle, free-air testing	16-1
transonic wind tunnel, normal shock, stagnation pressure, static and minimum pressure	16-2
..... static and minimum pressure	16-3

2. BASE DRAG AT TRANSONIC SPEEDS

function of M , flow pattern, "subsonic" phase	16-4
transonic phase, forebody drag, terminating	16-5
M' -number, "supersonic" phase, forebody shape	16-6
length ratio, wetted area, sting effect	16-8
rocket nozzle, boat tail, fin interference	16-10
blunt trailing edge, maximum base drag	16-11
"transonic" base-drag phase, forebody drag	16-12

3. BLUFF BODIES AT TRANSONIC SPEEDS

(a) Drag of Blunt Bodies

cylinder, bluff heads, rotating cubes, plates	16-14
---	-------

(b) Drag of Rounded Shapes

spheres, spheroidal heads, circular cylinder	16-16
fairing shapes, elliptical cylinders	16-17

4. TRANSONIC DRAG OF SLENDER BODIES

conical flow, at $M = 1$, supersonic cone flow	16-18
similarity, cone-cylinders, fineness ratio	16-20
ogival noses, projectiles, surface roughness	16-21
boat tail, boat-tail angle, parabolic bodies	16-22
double cones, drag of streamline bodies	16-24
"critical" Mach number, thickness location	16-25
transonic drag of fin-stabilized missiles	16-25
drag of RM-10 missile, bombs, rounded noses	16-26

5. DRAG OF SWEPT AND POINTED WINGS

(A) Characteristics of Swept Wings

transonic drag rise, M (max), "supersonic" drag	16-28
transonic hump, drag due to lift, "lift angle"	16-29

(B) Pointed and/or Triangular Wings

"critical" Mach numbers, thickness line	16-30
no peaks, reversal theorem, trailing edge	16-31
maximum drag coefficient, drag due to lift	16-32

6. DRAG OF AIRCRAFT CONFIGURATIONS

(A) Transonic Area Rule

drag rise, indentation, wing similarity	16-34
---	-------

(B) Interaction at Supersonic Speeds

supersonic biplane, shrouded body principle	16-35
---	-------

(C) Drag of Component Parts

canopy, external stores, wing-tip tanks	16-36
---	-------

(D) Internal Flow at Transonic Speeds

open-nose inlets, additive drag, oblique	16-38
--	-------

shock, controlled inlets, optimum shape	16-39
---	-------

internal momentum, protruding spike	16-40
---	-------

CHAPTER XVII — AT SUPERSONIC SPEEDS**1. ELEMENTS OF SUPERSONIC FLOW**

Mach angle, compression, "silent" space	17-1
expansion, stagnation pressure, entropy	17-2

2. FRICTION DRAG IN COMPRESSIVE FLOW

B'layer temperature, turbulent, BL stability	17-4
cone flow, pressure gradient, surface roughness	17-5
size and drag due to roughness, lap joints	17-6

3. TRANSONIC DRAG OF STRAIGHT WINGS

basic flow pattern, transonic similarity rule	17-7
wedge sections, theory, fairing at $M = 1$	17-9
10% double wedge, biconvex, round-nosed	17-10
foil sections, finite-span wings, aspect ratio	17-11

4. STRAIGHT WINGS IN SUPERSONIC FLOW

flow pattern, thin airfoil linear theory	17-13
second-order theory, afterbody, biconvex and	17-14
round-nosed sections, optimum fairing	17-14
blunt trailing edge, influence of aspect ratio	17-16

5. DRAG OF WINGS DUE TO LIFT

(A) Drag at "Supersonic" Speeds	
induced drag, 2-dimensional drag, total drag	17-17
lift (aspect ratio), slender wings, ring wing	17-18

(B) Drag Due to Lift at Transonic Speeds

leading edge flow, at $M = 1$, flow pattern	17-19
drag and lift, influence of aspect ratio	17-19
section camber, practical approach	17-20

6. DRAG OF ROCKET VEHICLE

the Atlas launch vehicle	17-20
--------------------------------	-------

XVIII — DRAG AT HYPERSONIC SPEEDS

(A) DRAG OF AIRFOIL SECTIONS

similarity parameter, drag due to thickness	18-1
double wedges, afterbody drag, single wedge	18-1
narrow wedge, double-arc, friction, " H " — ∞	18-2

(B) CONES AND SIMILAR BODIES

cones, optimum shapes (theory)	18-4
ogives, blunted cones	18-5

(C) FREE-FLYING CONFIGURATIONS

skin friction, drag at $M = 10$	18-6
ballistic missile, missile models	18-7

(D) VISCOSITY EFFECTS IN SLENDER SHAPES	
(a) Characteristics of Two-Dimensional Shapes	
BL displacement, B'layer-induced pressure	18-7
B'layer viscosity, heat transfer, blunt	18-8
leading edges, wedge pressure, drag of wing	18-8
wedge section, flat-plate lift, wing drag	18-9
(b) Characteristics of "Conical" Bodies	
conical probes, spiked conical body, drag	18-10
brakes, blunt cylinders, skin friction	18-11
delta wings, total drag of cones, boundary—	18-12
layer transition, turbulent friction	18-13
(E) BLUFF BODIES AT HYPERSONIC SPEEDS	
(1) Two-Dimensional Shapes	
blunt shapes, Newtonian flow, circular	18-13
cylinder, shoulder pressure, centrifugal	18-14
effect, leading edges, double arc, leading-	18-15
edge sweep, inclined cylinder, spoiler	18-16
(2) Three-Dimensional Bodies	
bluff cones, blunted cone, rounded cone,	18-17
parabolic nose, Newtonian analysis, at angle	18-18
of attack, towed cones, inflated shapes,	18-19
spheres, flat disk, blunt cylinder, face	18-20
pressure, conical skirt, function of	18-21
Mach number, satellite capsule	18-22
pressure distribution, short nose shape	18-23
(F) TEMPERATURE AND HEAT TRANSFER	
high temperatures, radiation, hypersonic	18-24
tests, heat transfer, molecular changes	18-24
dissociation, stagnation pressure, hypersonic	18-25
vehicle, Stanton number, blunt bodies	18-25
re-entry, meteorites, drag of a meteorite	18-26

CHAPTER XIX — DRAG AT HIGH SPEEDS AFFECTED BY VISCOSITY & RAREFACTION

(A) REALMS OF FLUID DYNAMICS

mean free path, Knudsen number, rarefaction	19-1
BL thickness, fluid-dynamic phases, interaction	19-2

(B) VISCOSITY EFFECTS AT HIGH SPEEDS

(1) Bluff Bodies at Supersonic Speeds	
stagnation pressure, spheres as a function of	19-4
R'number, at low R'numbers, cylinders	19-5
base pressure, zero B'pressure, at low R'numbers	19-6
(2) Viscous Effects in Slender Shapes	
skin friction, turbulent B'layer, cone drag	19-7

(C) CONDITIONS IN UPPER ATMOSPHERE

dimensions of the earth, atmospheric layers	19-10
thermosphere, number density, upper layers	19-9
radiation belts, interplanetary space	19-9
stratosphere temperature, atmospheric	19-10
density, molecular speed, mean-free path	19-11

(D) DRAG IN FREE MOLECULE FLOW	
(1) Principles of Free Molecule Flow	
molecular speed ratio, Newton's theory,	19-16
reflection, impinging momentum, re-emission	19-17
(2) Drag of Various Body Shapes	
bluff cone, sphere, cylinder, slip flow	19-18
shear force, slender cones, optimum nose	19-19
magnitude of lift, drag due to lift	19-17
decay of satellite, energy, reduction of period	19-18

CHAP XX — VARIOUS PRACTICAL RESULTS

A. EXAMPLES OF PRESSURE DRAG

flat plates, lattice beams, afterbody	20-1
boat-tailing, radar antennas, trailer truck	20-2
gun openings, cooling duct, engine nacelle	20-3

B. HYDRODYNAMIC INFORMATION

base-vented hydrofoils, cavitation number	20-4
parabolic sections, optimum strut	20-5
parabolic bodies, approximation, short bodies	20-6

C. RESULTS AT TRANSONIC SPEEDS

single wedge, ejection seat, parachutes	20-7
windshield, blunt canopy	20-8
on fuselage, location on airplane	20-9

D. NOSE DRAG AT SUPERSONIC SPEEDS

nose shape, spikes, projectile with	20-10
blunt "probe", retro-rocket	20-10

E. NACELLES, LOADS, EXTERNAL STORES

jet engines, fuel tank, pylon, chordwise	20-11
position, buoyancy, transonic drag	20-12

F. SURFACE IMPERFECTIONS

body with rings, surface steps	20-13
lap joints, rivet heads, projectile	20-14

G. CHARACTERISTICS OF BASE DRAG

length of body, tail surfaces, rocket	20-15
nozzles, trailing edge, step pressure	20-16
flared base, boattail, pointed tail	20-18

INDEX — EIGHT PAGES OF SUBJECT INDEX

—————> see at the end of the book

CHAPTER I — GENERAL INFORMATION

This first chapter is intended to be a general introduction to FLUID-DYNAMIC DRAG, pointing out approach and philosophy in treating the subject. The chapter also presents necessary and/or useful information of a general nature, such as a notation and the physical properties of the fluids concerned.

1. NOTATION — ABBREVIATIONS

Most of the abbreviations and symbols used throughout the book are listed as follows.

BIBLIOGRAPHICAL REFERENCES indicating the sources of theoretical methods or experimental results used or quoted throughout the text and in the illustrations, are presented in the form of "footnotes", placed at the bottom, usually of the odd-numbered pages. Within the text, the references are usually referred to in parentheses.

Documents. Technical reports (or memorandums) have been quoted extensively in the text, particularly those issued by NACA and NASA. Although the documents used are not classified, they may not readily be available to the public in general. The referenced German documents may be accessible through the Armed Services Information Agency in Dayton, Ohio. A source for more recent technical information is the Defense Documentation Center, Cameron Station, Alexandria, Virginia 22314.

There are two methods available in order to find information on a particular subject in this book. The first is by the Table of CONTENTS, beginning on page 0-7. The other way is through the use of the INDEX at the end of the book.

Abbreviations, listed as follows, are employed within the footnotes quoting bibliographical references:

N A S A	Nat'l Aeronautics Space Administration
N A C A	Nat'l Advisory Committe for Aeronautics
T.Rpt	Technical Report of the NACA
T.Note	Technical Note of the NACA
W.Rpt	Wartime Report of the NACA
T.Memo	Technical Memorandum = Translation
Transl	Translation (into English)
R M	Declassified Document by the NACA
A R C	British Aeronautical Research Council
R M	Reports and Memorandums of the ARC
C.Paper	Current Paper of the ARC
A V A	Aerodynamische Versuchsanstalt Göttingen
D V L	Deutsche Versuchsanstalt für Luftfahrt
Z W B	Zentrale Tech.-Wi'schaftl. Berichtswesen
F B	Forschungs Bericht of the ZWB
U M	Untersuchungen-Mitteilungen of the ZWB
D.Lufo	Deutsche Luftfahrtforschung (Yearbook)
Lufo	Luftfahrtforschung (German periodical)
Ing.Arch.	Igenieur Archiv (German)
ZAMM	Zeitschr. Angewandte Math. Mechanik
J.A.Sci.	Journal of the Aeronautical Sciences
I A S	Institute of the Aeronautical Sciences
A I A A	Am Inst of Aeronautics and Astronautics
ASME	Am. Society of Mechanical Engineers
CAHI	Central Aero-Hydrodynamic Inst. (Moscow)
Ref	Reference = Footnote
Rpt(s)	Report and Reports, respectively
Trans	Transactions of a Society
Proc.	Proceedings of a Society
Soc.	Society (Engineering)
T M B	David Taylor Model Basin
NAME	Naval Architects and Marine Engineers
Inst.	Institute (or Institution)
I N A	Institution of Naval Architects (England)
S T G	Schiffbauteschnische Gesellschaft
AGARD	NATO Adv. Group Aeron'l Res. Devel.
W G L	Wissenschaftl. Gesellschaft f.Luftfahrt

Fluid-Dynamic Coefficients

SYMBOLS IN EQUATIONS AND GRAPHS. With some exceptions, the symbols employed throughout this book are those accepted or recommended by the NACA and the American Standards Association (1).

"Fluid-Dynamic" Dimensions

b	wing span (or width of a body)
c	chord of airfoil section
d	diameter of a body of revolution
δ	total boundary-layer thickness
h	height of a body; also TE thickness
k	diameter of sand grain (also other meanings)
l	length of a body (in x-direction)
S	area ("wing" area if without subscript)
t	maximum foil-section thickness
θ	momentum thickness of boundary layer
x	length of forebody (to max. thickness)
x	dimension in direction of flow
y	dimension transverse to flow direction
z	altitude above sea level

"Fluid-Dynamic" Ratios and Factors

A	$= b^2/S =$ aspect ratio of wings
λ	$= l/A =$ length ratio $= "c"/b$
e	indicating effective aspect ratio
f/c	camber ratio of foil sections
k	specific heat ratio in gasdynamics
k	constant or factor (used in many definitions)
K	constant or factor (used in many definitions)
l/d	fineness ratio of body of revolution
σ	indicating solidity ratio
t/c	thickness ratio of sections

Terms Associated With Speed

V	flow- or flight speed (between body and fluid)
w	local velocity at specified point of a body
w	downwash velocity (behind wings)
w	internal velocity (in ducts)
M	$= V/a'$ = Mach number, with 'a' = sonic speed
R	Reynolds number (always with subscript)
ρ	$= \gamma/g =$ mass density of the fluid
q	dynamic pressure (see Chapter I)
"q"	impact pressure (see Chapters XV and XVI)
"P"	Prandtl factor (see chapter XV)
P	engine power (usually in HP)
T	absolute temperature (in degrees "Kelvin")
T	thrust of propeller or jet engine
p	absolute static pressure in lb/ft ²
f	vortex frequency (per second)
"S"	Strouhal number $= f l/V$

D	drag (or resistance), in "x" direction
"f"	$= D/q$ in ft ² = drag area
c _d	on effective dynamic pressure (Chap. V)
C _{Di}	for induced drag (of wings)
C _{Ds}	for profile or section drag (of wings)
C _{D0}	based on frontal area of body
C _{Da}	on circumscribed area
C _{Dwet}	on wetted surface area of a solid
C _f	skin friction drag (on wetted area)
L	lift (in "y" or "z" direction)
C _L	lift coefficient $= L/q S$
C _{DL}	for drag associated with lift
C _p	$= \Delta p/q =$ pressure coefficient
Γ	$= 0.5 C_L V c =$ circulation about foil section
ξ	pressure-loss coefficient

Geometrical and Other Angles

α	angle of attack, especially of wings
β	angle of yaw or sideslip
Γ	angle of dihedral (of wings)
Λ	angle of sweep (of wings)
δ	angle of deflection of flaps
ε	half vertex angle of cone or wedge shapes
μ	Mach angle (see chapter on "supersonics")

In Shipbuilding and Vehicles

l	water-line length of a ship
l	average wetted length of planing surface
b	beam of the hull
h	draft or submergence
D	resistance = drag
W	weight (in lb)
Δ	displacement in long tons (2240 lb each)
C _{pris}	prismatic coefficient
F	Froude number (in the "hydrodynamics" chap.)
σ	cavitation number (see "hydrodynamics")
∇	displacement (volume) in ft ³

General Subscripts and Exponents

amb	indicating ambient condition
av	indicating mean "average"
crit	critical (Reynolds or Mach number)
eff	or "e" = "effective"
min	indicating "minimum"
n	a general exponent
o	original condition
opt	= optimum, as defined in text
x	or "max" for "maximum"
x	for distance from L'edge or nose

Specific Subscripts

a	indicating "added" or "attached"
b	indicating reference area b^2
B	for "base" (also propeller blade)
c	indicating reference area c^2
comp	= compressible or compressive
Δ	indicating displacement
f	for "frictional" (also for "fuselage")
H	for horizontal tail
i	indicating "induced" (also "effective")
inc	indicating "incompressible"
lam	= laminar (boundary layer)
lat	for "lateral" forces
m	indicating main body (also as exponent)
M	for momentum (internal flow)
N	indicating "normal" force
O	on "developed" parachute area
p	for pressure, also indicated by "P"
t	indicating reference area t^2
turb	= turbulent (boundary layer)
w	pertaining to speed "w"
W	indicating "weight" or "wave"
wet	= wetted area (in contact with fluid)
x	or "ext" for external
•	indicating frontal area of body
□	on circumscribed area

The Reynolds number "R" and the Froude number "F" usually carry a subscript, indicating the dimension upon which they are based. Angles are usually presented in degrees, and marked correspondingly. Without such notation, they are usually meant to indicate a ratio. Some other symbols and subscripts are used and defined within the text, or they are understandable without explanation.

Abbreviations. The author has taken the liberty of using some abbreviations throughout the text and/or in the illustrations, respectively:

BL	= boundary layer
LE	= leading edge
TE	= trailing edge
Ref	= reference (footnote)
Equ	= equation

Also "Reynolds number" is sometimes abbreviated to "R'number", Mach number to "M'number", "boundary layer" to "B'layer" and "aspect ratio" to "A'ratio". Instead of the laborious phrase "approximately equal to", the author has very often substituted the symbol " \approx ".

2. GLOSSARY OF TERMS AND NAMES

There are many specific terms partly developed during the last 50 or more years, used and understood by every specialist in the field of fluid dynamics. For the benefit of readers from other fields of science or engineering, the more important ones of these terms are briefly explained as follows.

"Airfoil" is a lifting surface, either a wing or one of the tail surfaces of an airplane or any other, usually profiled surface producing lift or a force in any other direction normal to the direction of flow. In water, the same type of surface is called a hydrofoil; and the common short word is "foil". In contradistinction, "wing" is that airfoil which essentially carries the weight of an airplane.

Boundary Layer is a comparatively thin sheet of decelerated fluid originating through friction along the surface of solids. The "B'layer" can have either a *laminar* flow pattern (at small Reynolds numbers); or it may be turbulent (at higher R'numbers). Presence of the boundary layer can cause flow separation (see under that heading). Proper consideration of the boundary layer (4) has opened the way to theoretical treatment of certain flow patterns.

Cavitation. Voids or cavities are formed in water (or in other liquids) when and where the static pressure is reduced below the vapor pressure. The water then vaporizes thus forming bubbles as in boiling water. Cavities comparable to those in water are also formed in air; namely at hypersonic speeds where a vacuum can be obtained behind bluff obstacles. It seems that lightning is an example of this sort; the thunder being the result of the collapsing cavity. — Cavitation must not be confused with "separation" (see later). A phenomenon similar to cavitation is "ventilation" (see in the "hydrodynamic" chapter).

Circulation (7) is the motion of a fluid "circulating" around a certain axis; it is the motion representing a vortex in non-viscous flow; its dimension is (ft^2/sec). Every fluid particle moves about the vortex center basically in the same manner as the cars of a *Ferris Wheel*. Each of these cars remains in horizontal position, while circling around the wheel's axis. In other words, the non-viscous motion within a vortex is "irrotational"; see under "rotation".

Compressibility is the quality of a fluid, and of gases in particular, of reducing in volume when the static pressure is increased. In place of "compressible", the word "compressive" has recently been proposed to indicate the *active* property of velocity or pressure in distinction from the *passive* quality of the fluid as such. Both of these terms are applied in this book (making the distinction as defined above, as far as possible). — Water does not have compressibility worthwhile to speak of.

Downwash is (strictly speaking) the *permanent* downward component of the velocity behind lifting wings. This type of downwash is the resultant of the velocities "induced" by the trailing vortex system of such wings. There are other downward and upward components around a wing which are also called "downwash" or "upwash", respectively. A downwash of this type (caused by the "bound vortex") is found at the trailing edge of a wing; and a corresponding upwash exists ahead of the leading edge.

Fluid Dynamics, also called "fluid mechanics", is the all-encompassing term denoting the field of fluid motion. Subheadings are as follows: *Hydrodynamics* (meaning not only the subject of water flow but also fluid-dynamics of incompressible flow). *Aerodynamics*, describing characteristics in air (and in other gaseous fluids) from incompressible through hypersonic conditions. *Gas dynamics*, dealing with compressible gases from subsonic to supersonic speeds. With respect to compressibility, we have the field of *subsonic* flow, of *transonic* Mach numbers (roughly between $M = 0.9$ and 1.5), *supersonic* conditions and finally *hypersonic* flow, meaning comparatively high Mach numbers in connection with slender body shapes. The field of aerodynamics in *rarefied gases* is encountered in very high altitudes (by rockets and satellites). The extreme of this type of fluid dynamics is the *free-molecular* flow, in which the gas molecules strike an obstacle individually, without interfering with each other.

"*Induced*" is a word taken from the field of electricity. Magnetic forces are "*induced*" around a conductor carrying an electric current (8). In fluid dynamics, the velocity at any point within the field of a vortex is called the induced velocity due to its circulation. The word "*induced*" also is applied, however, to indicate velocity components and pressures caused by displacement.

Lift is not directly a subject of this book. Drag is a function of lift, however, in several respects; so that lift must be considered too. One of the important characteristics of a lifting wing is the so-called lift-curve slope ($dC_L/d\alpha$), indicating the rate at which lift increases as a function of the angle of attack " α ". However, a parameter sometimes more convenient than ($dC_L/d\alpha$), is the reversed value " $d\alpha/dC_L$ "; and this value is called in this book the "lift angle".

"*Laminar*", derived from the latin word for "layer", indicates a state of flow where the various fluid "sheets" do not mix with each other, where all stream tubes keep essentially parallel to each other and where their velocities are steady (although the velocity may very well have a gradient both in the direction of motion and between different stream tubes).

Parasite Drag. If accepting the induced drag as something necessarily connected with the useful generation of lift, the rest of the drag of an airplane can be called to be parasitic (because it represents a waste of fuel). Another terminology (10) denotes the parasite drag as "*viscous*", thus stressing the fact that frictional drag as well as pressure drag (due to boundary-layer deceleration or flow separation) are basically caused by viscosity.

Pressure — Static. Usually, "pressure" is meant to be the ambient "static" pressure " p " (for example in lb/ft^2) within a certain space or container. However, in applied aerodynamics, pressure differentials $\Delta p = (p_{\text{local}} - p_{\text{amb}})$ are very often considered, rather than the absolute static pressure. The variation of the pressure along a surface is of importance for the development of the boundary-layer. A positive gradient, corresponding to a distribution in which the pressure increases in the direction of flow can lead to flow separation. Therefore, such a gradient is also called "*adverse*". Changes of the static pressure near, at and behind obstacles are the primary subject of supersonic aerodynamics.

Pressure — Dynamic. A pressure differential of particular definition is the so-called dynamic pressure $q = 0.5 \rho V^2$. This quantity is thus a property of a fluid flow; it corresponds to the momentum of the fluid particles. In non-compressive fluid flow, this quantity appears in the form of a static-pressure *increment* that can directly be measured (for instance in lb/ft^2) after the flow has been brought to rest (when and where $V \rightarrow 0$, without having lost momentum). The dynamic pressure is then the differential between the "total" pressure as tested in the open end of a so-called Pitot tube and the ambient static pressure. There are instruments (the Pitot-static tube or the "Prandtl Rohr") directly indicating the dynamic pressure differential. In many or most practical applications, fluid-dynamic forces are (at least approximately) proportional to the dynamic pressure.

Pressure — Total. The most important principle governing non-compressive fluid flow, is the fact that under undisturbed and non-viscous conditions, the sum of static and dynamic pressure is always constant. This so-called Bernoulli law (13) can be utilized to explain basically the generation of drag (other than frictional). Speed and dynamic pressure of the fluid particles reduce upon approaching an obstacle; the static pressure at the front of a solid is increased accordingly. In theoretical non-viscous flow, a corresponding exchange between dynamic and static pressure would take place at the rear of the obstacle; and there would not be any drag (as found by d'Alambert in the 18th century). Actually, of course, there is viscous friction, boundary layer and separation. As a consequence, the flow pattern is changed as stated in Prandtl's BL theory. The deceleration of the fluid particles upon approaching the "rear stagnation point", and the corresponding pressure recovery do not completely take place. The resultant of increased pressure at the front end and a more or less deficient pressure at the rear side of the obstacle, is pressure drag. The total pressure (and/or momentum) of the stream tubes involved is reduced, accordingly.

Ratios. There are many dimensional ratios, describing the shape of solid bodies exposed to fluid flow. We have, for example, the thickness ratio " t/c " of wing sections, the fineness ratio of rotationally-symmetric bodies, the aspect ratio of wings $A = b^2/S = b/c$, the length ratio $\lambda = 1/A = c/b$. Ratios of secondary order are, for example, that of the location of maximum thickness with respect to chord or length, respectively. Related geometrical ratios are particularly used in the field of ship hydrodynamics (Chapter XI) describing, among others, magnitude and distribution of a hull's displacement.

Rotation means the motion of fluid particles around their own "center" or some other center in a manner similar to any part of a "rotating" solid wheel. Insofar as each particle changes its angular position while going around, more or less facing the center of motion, this type of motion is basically different from the "Ferris-Wheel" motion mentioned under "circulation". Every real vortex has a rotating core; while beyond a certain distance from the center, the circulation-type of flow pattern is found as indicated by theory (7). Rotation is also called "vorticity".

"Schlieren" is not the name of a man; it is the German word for "streaks" as they appear as a consequence of density differentials in the "shadow" of compressive and in particular of supersonic patterns of fluid flow.

Separation. Because of the frictional losses within the boundary layer, separation of BL as well as of the adjoining external flow takes place, for example, from the rear of many "bluff" bodies. The region of flow following separation is sometimes called "dead space". However, a "wake" is not necessarily the product of separation. Any loss of momentum (for example by friction) appears as a deficiency of dynamic pressure within the wake behind every obstacle. Separation and "detached" flow pattern can also be found along the sides and even in front of obstacles, wherever boundary-layer thickness and "adverse" pressure gradient are large enough to produce this phenomenon. The opposite of "separated" is "attached". Under certain conditions, a separated pattern may also become "re-attached". Separation from sharp edges can also be understood and treated without considering viscosity.

Streamlines. When replacing a small cross-sectional part of a fluid flow, for example by smoke — a single "line" becomes visible, called streamline. Upon giving the line a finite cross-sectional area (as indeed that smoke line has) we obtain a *stream tube*. A so-called streamline body or shape, is not a very logical application of that word. We have the word, however, not only in English (see Webster) but also in other languages. The best explanation we can give for the application is the fact that most of the stream tubes continue past such a shape without crossing each other and without being disrupted and/or dissolved as they are in the flow field past a bluff obstacle.

-
- (1) See Aeronautical Engineering Review 1953 p.41.
 - (4) Prandtl, Boundary-Layer Theory, established 1904.
 - (7) See in books such as Prandtl's "Fluid Dynamics", (German 1941) New York 1952; also in Lamb or Milne-Thomson.
 - (8) Glauert, "Aerofoil and Airscrew Theory", 1926.
 - (10) Weinblum, in his papers listed in Chapter XI.
 - (13) Daniel Bernoulli, in "Hydrodynamica", 1738.
 - (15) "Turbulence" as stated in TMB Rpt 670 (1948).

Turbulence is a more or less irregular "eddying" motion, a "state of commotion and agitation" (15), consisting of velocity fluctuations superimposed to the main flow, within boundary layers (at higher R'numbers) and within the wake behind solid bodies. Turbulence should not be confused with separation. In fact, separation can be reduced and possibly avoided by forcing turbulence. Such "stimulation" of turbulence can be obtained through some disturbance of the laminar B'layer flow, such as surface roughness, stream turbulence (in wind tunnels), sound and/or mechanical vibrations (from aircraft engines, for example). The intensity of turbulent motion (expressed by the root-mean-square $\sqrt{w^2}$ of its components) decreases as $\sim 1/x$, where x = distance behind the object producing turbulence. Besides their amplitude (in the order of 1% of main velocity in ordinary wind tunnels, for example) frequency is also of importance.

Vortex. The flow pattern of a vortex in non-viscous fluid is mentioned under "circulation". An important example is the "bound" vortex or "lifting line" (7) which is the fluid-dynamic equivalent of a physical wing. Other examples are the "rolled-up" vortexes originating from the lateral ends of every wing or other lifting body, and the well organized rows of vortices found in alternating vortex "streets". In free-surface hydrodynamics (as in ships) "trailing vortexes" appear in the form of waves; the motion of the fluid particles is called "orbital".

Vorticity. The words "vortex" and "vorticity" are also used in connection with the shear flow in boundary layers and in wakes (behind obstacles), where rotation is produced by viscous friction. The word "vorticity" is thus used to indicate the amount of rotation present in a flow pattern. Vorticity has the same dimension as "circulation" (ft^2/sec).

Wind Tunnel. Possibly a thousand wind tunnels have been built and used during the last 50 years, for the purpose of finding the aerodynamic characteristics not only of airplane wings, component parts of aircraft and of airships, but also of automobiles and stationary structures (bridges and buildings). The test section of such tunnels may be "closed" or "open-jet" type. Corrections (due to "blockage" or due to the finite size of the jet of air) are sometimes cumbersome. Because of their excessive power requirements, most of the tunnels designed for *supersonic* speeds are comparatively small in size, down to a few centimeters squared. Very large installations have, on the other hand, been built in order to test aircraft "full-scale". — A number of water tunnels are also existing, primarily used for hydrodynamic purposes, as a supplement to towing tanks.

Personalities In Fluid Dynamics. Among the many names found as authors of, and found quoted in fluid-dynamic publications, a few are particularly outstanding; and they are often referred to in the text of this book. We therefore present the list as follows:

Froude, William (1810 to 1879 in England) not to be confused with his also famous son, is the "father" of modern ship hydrodynamics (17). The free-surface similarity law (see Chapter XI) is named after him.

Von Kármán, Theodore; was a very prominent aerodynamicist (18). Born in Hungary (1881), he was associated for a time with the Göttingen circle, was later Director of the Guggenheim Aeronautical Laboratory in Pasadena (California), and last Chairman of NATO aerodynamic activities. He died in 1962. See *Astronautics and Aerospace Engineering*, July 1963.

Pitot, Henry; French physicist 1695 to 1771, introduced an open-ended tube used to measure "total" or Pitot pressure (equal to $p + q$ in non-compressive fluid flow).

Prandtl, Ludwig (1875 to 1953) Professor and Director of the K.Wilhelm Institute in Göttingen (20). Together with Albert Betz, he was for some 50 years the spirit of aerodynamic research at the AVA. Among his numerous publications, "Essentials of Fluid Dynamics" is available in English (London 1952).

Reynolds, Osborne (1842 to 1912), Professor at the University of Manchester (England), published results of experimental investigations, "Whether Motion of Water shall be Direct or Sinuous and of the Law of Resistance in Parallel Channels", in *Philos.Trans.Royal Society* (London) 1883 p.935. Also: "On the Dynamic Theory of Viscous Fluids and the Determination of the Criterion . . . ", in *Philos.Trans.Royal Society* 1895. The basic similarity law of fluid dynamics indicating the ratio between viscous and dynamic forces, is named after Reynolds; thus the "Reynolds number".

Others. There are many others worth-while mentioning. A few of them are listed in the footnotes of this Chapter. The names of still others appear as authors of papers and articles in the balance of this book.

3. DRAG AND THEORETICAL ANALYSIS

"Resistance" was evidently the first fluid-dynamic force, arising from an obstacle placed against a stream of air or water, to become obvious to man. Lilienthal (22) named every force caused by flow "Widerstand"; and Eiffel (23) entitled the publications on his aerodynamic research "la résistance de l'air"— although there is more information presented on lift than on drag in his books. Today, using the word "drag", one thinks only of that component of any fluid-dynamic force, the direction of which coincides with that of the undisturbed flow (against an obstacle). In English-language terminology, "drag" is preferred in aviation; while "resistance" is common notation in marine engineering (and possibly in other fields of transportation too).

Action and Reaction. It is known that a wind-tunnel experiment, where a wind stream is blown against the stationary model, is equivalent to actual conditions, where for example, an airplane is propelled against more or less resting air. Upon discussing aerodynamic flow patterns, the stationary wind-tunnel system is usually preferred. One speaks, for example, of streamlines passing some object, protuberances exposed to the flow, boundary layer originating along a surface, the dead space behind a blunt body — and so on. Analyzing drag problems, it seems to be useful, however, to consider both systems and to observe the action of the air as well as the reaction of the body — or vice versa. As far as the body is concerned, a drag of certain magnitude is thus produced by the fluid flow. On the other hand, a disturbance is caused by, and left behind the moving body within the fluid space. This disturbance is the equivalent of the resistance; the energy involved in the disturbance is equal to that expended in propelling the body or craft considered.

Momentum. A concept very useful in fluid dynamics is that of "momentum". The momentum of a body (with respect to a suitable system of reference)

mass times speed, in (slugs ft/sec) or in (lb sec)

is an indication for the impact that it can produce when stopped. Momentum is transferred from a moving body upon the surrounding fluid; thus (momentum transferred per unit time) equal to (drag). By measuring the momentum deficiency within the wake of an obstacle, its drag can be determined, accordingly. This method is called "momentum-deficiency," or "wake-survey", or "Pitot-traverse" technique (see also Chapter II). To keep an airplane flying at constant speed, its momentum has continuously to be replenished (by means of the propelling engine or by "paying" altitude).

Momentum Transfer. There are several forms in which momentum is transferred from a moving body onto the fluid. (a) A certain volume of fluid is accelerated either in the direction of the moving body, or (b) in a direction transverse to that of the motion, as in the case of the induced wing drag for instance. (c) The fluid can also be put into irregular, turbulent motion; or the momentum equivalent to the drag may (d) be contained in a regulated system of vortices (vortex street). (e) At supersonic speeds, momentum (and heat) are carried sideways by means of compression waves. Finally, (f) in the presence of a free water surface, momentum is dissipated in a system of gravity waves (and/or in the form of spray). Usually several of the listed ways are combined with each other. All the "dynamic" types are consumed after some time by the viscous friction between the fluid particles, and they are finally transformed into heat. A simple proof of this transformation is the fact that the temperature in a wind tunnel increases appreciably with time during operation.

Theoretical Sources. A long time ago, somebody has said that induced drag was the only type of resistance on which theory could really give an answer. This is no longer true; we have more or less explicit results on growth and characteristics of the boundary layer; we can predict flow separation; knowledge on wave drag in supersonic conditions has emerged from elementary concepts; theories are available indicating the wave-making resistance of ships and other bodies in water; characteristics in cavitating water flow are known from theoretical sources; theories are also available, describing fluid-dynamic conditions in free-molecular flow. Most of the existing solutions are partial, however, or rather complex; some of them are so involved that their mathematical evaluation has not yet been accomplished.

-
- (17) Papers of W. Froude, a Memoir by INA (London) 1955.
 - (18) VonKármán, see special issue of the J. Aeronautical Sciences May 1956, commemorating his 75th birthday.
 - (20) Prandtl, Necrology, see J. Aeron. Sci. 1953 p.779.
 - (22) Lilienthal (1848 to 1896), Der Vogelflug als Grundlage der Fliegekunst, Berlin 1889.
 - (23) Eiffel (1832 to 1923), Récherches de l'air et l'aviation, Paris 1910; Nouvelles recherches, Paris 1914.
 - (24) Lanchester, "Aerodynamics", London 1907.
 - (25) Engineering-type presentations of aerodynamics are:
 - a) Diehl, "Engineering Aerodynamics", since 1928.
 - b) Wood, "Technical Aerodynamics", by Author, 1955.

Statistical Methods. Very often, a considerable lack of understanding is apparent between "mathematicians" and "engineers". Their abilities and their assignments are basically different (26); and there are only a few who can master both, theoretical research and practical design. Also, many technical devices, such as indeed the airplane, have been invented and originally developed without much of a theoretical foundation. The engineer is usually forced to proceed without the help of theory, wherever a solution is not available, or where it is too complicated for practical application. This is particularly true in the field of fluid dynamics where detailed analysis of the boundary layer, for example, serves more basic purposes while the engineer only needs to know the consequences as far as they affect the resultant forces of aircraft (or other devices). Therefore, the way many questions are handled in *applied* fluid dynamics, is by testing models in wind tunnels or water tanks, and by statistic knowledge derived from such experience.

Approach In This Book. The primary thesis of this book is to supply educated engineering information. Written by an "engineer", and primarily for engineers, the text is not "theoretical", accordingly. However, there is "nothing" more practical than a good theory. The results of theoretical calculations are, therefore, used as a basis and as a framework, within which the various problems concerning the resistance of bodies in air or in any other medium are presented. Wherever possible, experimental data are checked against and correlated with theoretical predictions. Practical conclusions are drawn from more academic functions. Limiting cases, which may not have any practical significance by themselves, are also presented, from time to time. They often confirm the trend of a function within that range in which one is really interested. On the other hand, where theoretical information is not available, efforts are made to

obtain a physical understanding of the flow mechanism from experimental observations. Applying statistical methods, certain "rules" may then be derived from experimental results. For example, the interference drag is treated in this book on a statistical basis. Such semiempirical methods usually enable the engineer to perform his calculations with an accuracy which is *consistent* with other phases of design work. Some information of this type may naturally grow obsolete, after more complete test results have become available. As an excuse for possible errors in the presentations in this text, psychology may be called upon as a witness; "even a wrong answer is closer to the truth than an apathetic 'I don't know'; a wrong answer can be proved to be wrong, and the correct answer can be sought" (J. A. Winter). Another important element in the presentation is the selection of suitable parameters to be considered in a problem. "Without computing relative importance, a class of facts leads to the most cluttered confusion" (Hubbard). We may say, in this respect, that successful theories and/or rules do just that; they are usually simplifications (disregarding secondary terms). — At the end of this somewhat philosophical section, a number of statements are quoted from personalities engaged in scientific and/or engineering work (28).

4. NON-DIMENSIONAL COEFFICIENTS

Dynamic Pressure. In one or possibly in more than one particular point on the front of every solid exposed to a flow of air or water, the "impinging" fluid particles come to rest; that is, their velocity approaches zero in these points. During their deceleration, the momentum of the particles is transformed into static pressure. The pressure increment

$$q = 0.5 \rho V^2 \quad (\text{lb}/\text{ft}^2) \quad (2)$$

is called "dynamic" pressure, because it is the equivalent of a dynamic quantity.

Drag Area. Disregarding the range of very small Reynolds numbers, aero- or hydrodynamic pressures and forces are in many conditions and at least predominantly proportional to the dynamic pressure. It is, therefore, convenient to refer the flow forces to this pressure. Regarding drag, the so-called drag area

$$D/q = C_d S \quad (\text{ft}^2) \quad (3)$$

is useful in cases where an area of reference is not obvious (such as, for instance, in the case of a motorcycle) or where several component parts are combined in some system.

-
- (26) The British physiologist Grey has discovered that the two types differ in the frequency pattern of their electric brain impulses; see Grey "Living Brain" N. York 1953. Other pairs of terms describing the two, are "logical" and "geometrical", or "abstract" and "visual-imaginative".
 - (28) Quotations in regard to science and engineering:
 - a) Appleton: "I have watched with admiration the engineer's ability to do things — while I've only been able to think about them in a theoretical way." (Partnership of Science and Engineering, Trans NE Coast Inst'n of Engineers and Shipbuilders Vol. 71, 1954 p.89).
 - b) Geyer: "Mathematics is tautology" (in "Die Dummheit", Göttingen 1954). He also makes the statement that "computing machines are perfect idiots".
 - d) VonKármán: "to remind persons engaged in the professional use of aerodynamic science, how much mental effort was necessary to arrive at an understanding of the fundamental phenomena" (in "Selected Topics", Cornell Univ. Press 1954).
 - e) Lewis: "The model test may be considered as an analogue type of computer" (Trans SNAME 1954 p.431).
 - f) Munk: "Wind tunnelling (can) degenerate into fruitless weighing and air blowing" (J. Aeron'l Sci. 1938 p.241).

Force Coefficients. Naturally, fluid-dynamic forces also increase with the size of the body involved. Usually, the forces are proportional to a suitable area; such as for instance, the projected plan-form area of a wing (S), or the frontal area of an obstacle (S_0). Referring the "drag area" (equation 3) to such an area, a nondimensional fluid-dynamic drag coefficient is thus obtained:

$$C_D = D/q S = D/0.5 q V^2 S \quad (4)$$

Readers who are not familiar with fluid-dynamic coefficients, may take notice here, that they will usually find information in the form of the drag coefficient (equation 4). The drag in lbs (or in any other weight unit) is then

$$D = C_D q S = 0.5 q V^2 C_D S \quad (5)$$

with all quantities in a consistent system of dimensions (as the foot-pound-second system). In compressed or in sonic or supersonic flow, the impact pressure at the stagnation point is higher than ($0.5 q V^2$). The coefficients are still based upon the dynamic pressure (equation 2) however, which in this case merely represents the momentum of the fluid flow.

Pressure Coefficient. Another coefficient which is very useful in the analysis of resistance is that indicating certain differentials of the static pressure

$$C_p = \Delta p/q = (p_{local} - p_{amb})/q \quad (6)$$

where p_{amb} = undisturbed static pressure (at some distance away from the body which is under observation). At the stagnation point in uncompressed fluids, this coefficient is obviously equal to "one".

5. PHYSICAL SIMILARITY LAWS

The drag- or pressure coefficients and the similarly defined lift coefficients are primarily a function of shape and attitude of the body which is under consideration. Under certain conditions, the flow pattern in the vicinity of a body and the non-dimensional coefficients — are identical in air, water, or in other liquid or gaseous fluids. On this basis, the fluid-dynamic characteristics of a body exposed to a flow in one medium, can be predicted from experiments in a different medium. So, for example, submarine models have been investigated in wind tunnels; and airplane wings in water tanks or -tunnels. The coefficients may also depend upon certain physical characteristics present in one medium but not in a different one. There are certain more or less defined

regions, however, within which such specific properties (as for example, compressibility) only have a negligibly small effect upon flow pattern and flow forces. In ranges which are still further restricted, the coefficients are eventually constants. — A system of these coefficients, within a framework of equally non-dimensional classifying "numbers", has been accepted as an international fluid-dynamic language, so to speak.

Reynolds Number. According to Reynolds' similarity law (see section 2) flow pattern (including boundary layer) and force coefficients of two similar bodies (identical in shape, but different in size), or those of one and the same body in different mediums — are similar if their Reynolds numbers are identical. This number

$$R_l = V l q / \mu = V l / \nu \quad (7)$$

represents the ratio of the dynamic forces (represented by the velocity V , the body dimension l , and the density of the medium q) to the friction forces (represented by the viscosity μ of the medium). Unfortunately, the principle of identical Reynolds numbers cannot generally be realized in model testing because of the necessary economy in size and operation of wind-tunnel or towing-tank installations. The fluid-dynamic research of the last 40 or 50 years was, therefore, confronted again and again with the problem of how to transfer model results to the real conditions of flying aircraft, or of ships in full-scale operation. It is (among others) for this reason that the variation of drag coefficients against Reynolds number is so often presented in this book.

Compressibility. Under certain conditions, certain fluids can be considered to be incompressible. This is particularly true for water (where the speed of sound, a measure of non-compressibility, is almost 5000 ft/sec). In air, compressibility may be neglected within the range of small and moderate speeds. Disregarding the effects near the blade tips of propellers, the practical design of airplanes, therefore, did not seriously take into account compressibility during the first 20 or 30 years of its history (since 1903). Dealing with today's flying speeds close to and exceeding the speed of sound, theoretical and experimental research on compressibility have been highly advanced, especially in recent years. Since, however, most airplanes in practical service are still flying, and may continue to fly, at moderately high speeds, simply by reasons of economy, the field of non-compressive aerodynamics remains the basic subject in a book such as this one. The Mach number

$$M = V/a \quad (8)$$

(named after Ernst Mach, 1838 to 1916) is commonly used to classify flow conditions with respect to compressibility.

Rarefied Fluid Flow. The forceful development of rockets as a launching device for satellites, leads into the upper atmosphere and "out" of it. At such altitudes, density is so small, that air or gas cannot be considered any longer as a continuous medium. Instead, the gas molecules strike against a flying object singly; and they are reflected or rebound, possibly like balls. A chapter is added in this book, to present principles and available results "at high altitudes".

after William Froude 1810 to 1879)

$$F_f = V / \sqrt{g l} \quad (10)$$

Basically, this number indicates the ratio of dynamic forces (represented by $V^2 \rho / g$) to static forces (displaced water Weight ρl^3). The particular problems of resistance in water are presented in two chapters of this book.

Cavitation. Water changes its physical status radically, after reaching a certain temperature (boiling) or after the pressure has been reduced below a certain value (cavitation). Cavitation; that is, the appearance of voids which are filled with vapor instead of water — is, therefore, encountered in water (and in other liquids) at higher velocities. The tendency (preparedness of a flow of water to cavitate), is indicated by the cavitation number

$$\sigma = (p_{min} - p_{amb}) / q \quad (9)$$

which is believed to have been introduced by Thoma (in München).

Free Water Surface. Flow characteristics of bodies in water, in proximity of or penetrating through the free surface, display considerable interaction with this surface. The pressure field of the obstacle causes a deformation of the surface. As a consequence, a wave system originates, trailing behind the moving body — particularly known in connection with ships. Such wave systems and the characteristics of spray and ventilation are functions of the Froude number (named

6. PROPERTIES OF AIR AND WATER.

(A) Characteristics of Atmospheric Air

Practical information on density, viscosity, speed of sound, vapor pressure, and other characteristics of many fluids and gases, are found in physical text books and/or engineering handbooks. The properties of the two most important fluids, air and water, are briefly presented as follows — as a function of pressure and temperature.

Dynamic Pressure in Air. The mass density of air is essentially

$$\begin{aligned} q (\text{lb sec}^2 / \text{ft}^4) &= 0.000324 p (\text{lb}/\text{ft}^2) / T (\text{°K}) \\ &= 0.0229 p (\text{inch Hg}) / T (\text{°K}) \end{aligned} \quad (15)$$

with $T_{\text{°K}} = 273 + t_{\text{°C}}$ indicating the absolute temperature in degrees "Kelvin" (which is the equivalent of centigrades). Many examples of air flow take place at the ground or flying near sea level. For such cases, a "normal" temperature of $t = 15 \text{ °C} = 59 \text{ °F}$ and a pressure corresponding to 29.9 inches (= 760 mm) of mercury — has been adopted by international convention, averaging conditions in the temperate zones of the earth. The corresponding mass density of the air is $q = 0.00238 \text{ lb sec}^2 / \text{ft}^4$; and the "standard" dynamic pressure in sea-level air is

$$\begin{aligned} q (\text{lb}/\text{ft}^2) &= 0.5 q V^2 \approx (V, \text{ft/sec})^2 / 840 \\ &\approx (V, \text{mph})^2 / 391 \approx (V, \text{kts})^2 / 295 \end{aligned} \quad (16)$$

as plotted in figure 1. Aviation is not all confined to sea level altitudes, however. Figure 2 presents the internationally (34) normalized average decrease of density against altitude above sea level. Replacing in equation 16, the normal mass density of q_0 by $(q/q_0)q_0$, the dynamic pressure can be determined as a function of altitude.

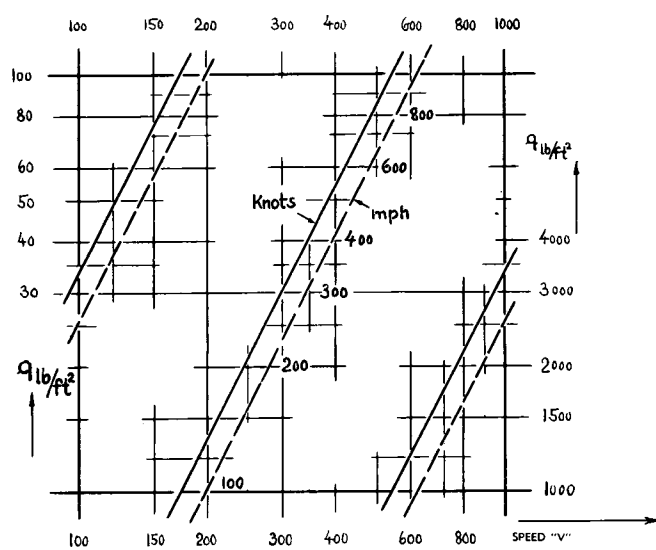


Figure 1. Dynamic pressure (equation 16)
in standard sea-level air.

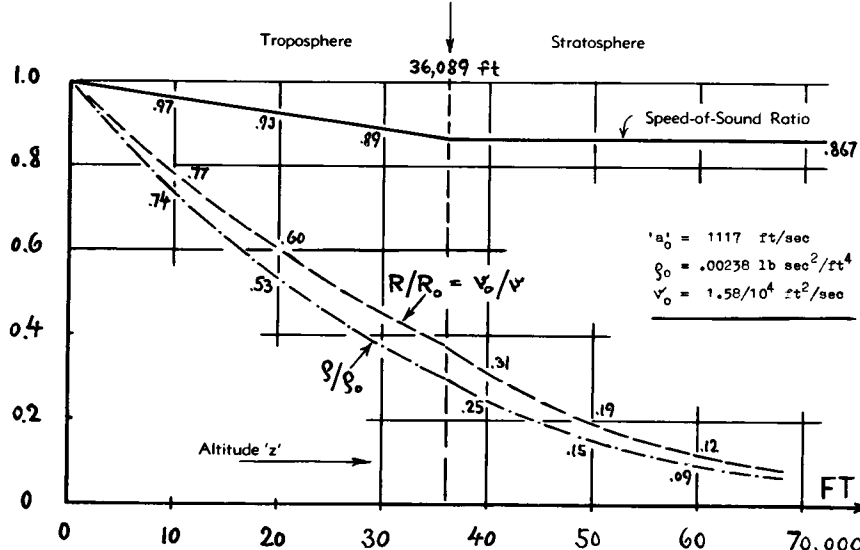


Figure 2. Variation of physical air properties with altitude as indicated by the ICAO standard atmosphere (34).

Viscosity of the Air. The dynamic viscosity of air (μ in $\text{lb sec}/\text{ft}^2$) is a function of temperature (is for most practical purposes independent of pressure), as plotted in figure 3. Within the range of engineering applications (between $T = 170$ and 500°K) the "absolute" viscosity varies as

$$\mu \sim T^{0.76} \quad (17)$$

By combination with the density, the *kinematic* viscosity $\nu = \mu/\rho$ in ft^2/sec is obtained. Under "normal" sea-level conditions, this type of viscosity is approximately

$$\nu = 1.56/10^4 \quad (\text{ft}^2/\text{sec}) \quad (18)$$

Since density and temperature decrease as the altitude is increased, the value of ν increases considerably with altitude. The Reynolds number (for constant speed) decreases accordingly, as shown in figure 2.

Speed of Sound. Sound travels at the natural velocity with which a vanishingly small pressure variation is propagated through the air. This speed is generally

$$'a' = \sqrt{dp/d\rho} = \sqrt{k g R T} \quad (20)$$

with $k = 1.4$ (in the air up to 300,000 ft of altitude), g = acceleration of gravity, ' R ' = gas constant and T = absolute temperature. In air (throughout the troposphere):

$$'a' (\text{ft/sec}) = 66 \sqrt{T (\text{°K})} \quad (22)$$

For standard sea-level temperature, the sonic velocity is (34), $'a' = 1117 \text{ ft/sec} = 760 \text{ mph} = 660 \text{ knots}$. — Since temperature decreases as altitude is increased, the speed of sound decreases accordingly; and the Mach number (equation 8) increases at the same time for a given speed, as illustrated in figure 2. In regard to compressibility, it is thus seen to be favorable to conduct subsonic airplane speed records in locations which are as low as possible and as hot as available, to keep away from the critical Mach number.

- (30) Properties of air as a function of altitude:
 - a) Burgess, Altitude, The Engineer 1952 p.338 & 370.
 - b) NACA, Tentative Tables for the Properties of the Upper Atmosphere, Technical Note 1200 (1947).
 - c) Additional presentation in Chapter XVIII.
- (31) Influence of Compressibility, NACA T.Rpt 837 (1946).
- (32) Physical properties of the atmosphere are presented at length in Wood's "Technical Aerodynamics" (25,b).
- (34) The presented physical values have tentatively been agreed upon by the ICAO (International Civil Aviation Organization) in 1952; see Manual of ICAO Standard Atmosphere, NACA T. Note 3182 (1954) which is now T. Rpt 1235.
- (36) Information on air viscosity is found in:
 - a) J. Aeron. Sci. 1951 p.156 and 1952 p.236 & 510.
 - b) Basilescu, Experimental, Publ. Scientifiques et Techniques French Ministère de l'Air, Rpt 111 (1937).
 - c) Fortier, Experimental, Ann. de Physique 1945 p.292.
 - d) Also in NACA T. Rpt 1135, on "Compressibility".
 - e) To $p = 200$ at, Tokyo Univ. Rpt (A)3, 1951 p.247.
 - f) Keyes, Viscosity, Trans ASME 1951 p.589.
- (38) Roberts, Atmosphere, Aeron. Engg. Review Oct. 1949.
- (39) Chapman, Gas Mixtures, NACA T. Rpt 1259 (1956).
- (40) Fano and Others, Compressibility Density Viscosity and Properties of Steam, NACA T. Note 3273 (1956).
- (42) Physical properties of water (sea and fresh):
 - a) See for example Trans INA 1953 p.358.
 - b) See in any modern Engineering Handbook.

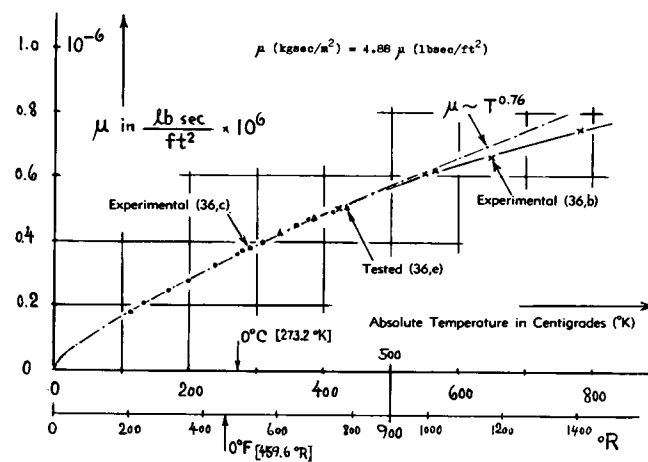


Figure 3. Variation of the physical viscosity of air as a function of temperature.

High Altitudes, above some 60,000 ft, have been explored by various direct (balloons and rockets) and indirect (physical) methods. A survey of the known atmospheric properties at high altitudes (as of 1949) is given in (38). The density decreases steadily with altitude to vanishingly small values. The average temperature shows heavy up-and-down variations, however, which correspond to the atmospheric zones illustrated in the last chapter of this book.

Humidity. The amount of water vapor "solved" in atmospheric air, is usually small (less than 1% by weight). The influence of humidity upon mass density is small, accordingly. For example, in "normal" sea level condition, 100% humidity (indicating saturation) reduces density by less than 1%. The influence of humidity on other characteristics is well explained in (32).

Steam. Properties of steam are presented in (40). Its density is very roughly 2/3 of that of air under the same conditions as to temperature and pressure.

Gases. Physical and thermodynamic properties of a number of gases other than air are reported and discussed in (39).

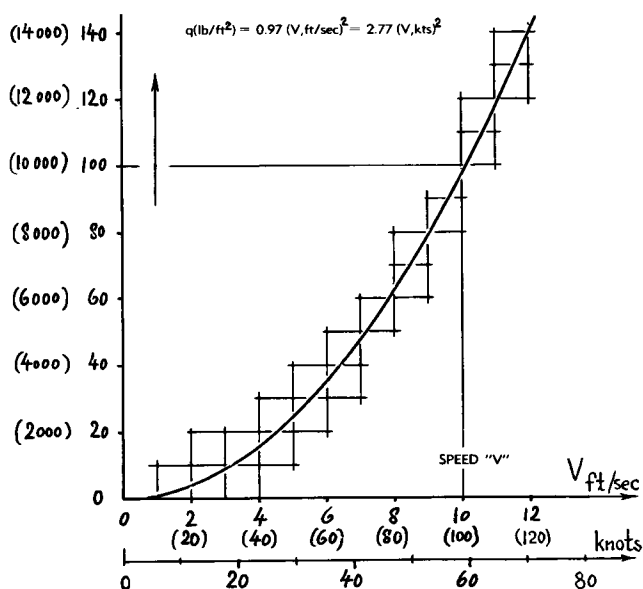


Figure 4. Dynamic pressure in fresh water (equation 28).

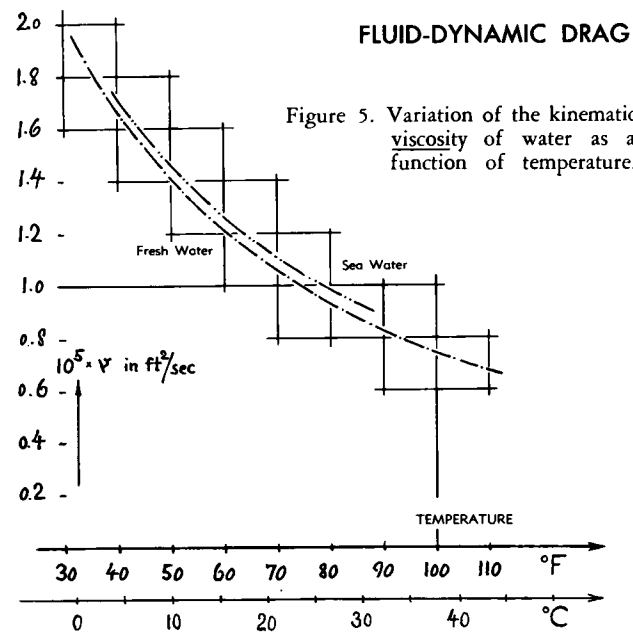


Figure 5. Variation of the kinematic viscosity of water as a function of temperature.

(B) Physical Properties of Water

Dynamic Pressure in Water. For all practical applications (to date), the density of water can be considered to be constant (being independent of temperature and pressure):

$$\rho_{\text{fresh water}} = 62.3/32.2 = 1.94 \text{ lb sec}^2/\text{ft}^4 \quad (24)$$

In average (Atlantic) sea water, with a salinity in the order of 3.5%, the density is 2.7% higher than in distilled or "fresh" water:

$$\rho_{\text{sea water}} = 64/32.2 = 1.99 \text{ lb sec}^2/\text{ft}^4 \quad (25)$$

Corresponding to these densities, the dynamic pressure is

$$q = 0.5 \rho V^2 = 0.97 (V, \text{ft/sec})^2 \quad (26)$$

in fresh water, as plotted in figure 4. In sea water, the dynamic pressure is

$$q = 0.995 (V, \text{ft/sec})^2 = 2.85 (V, \text{kts})^2 \quad (28)$$

The Viscosity in Water, needed for the computation of the Reynolds number, is a function of temperature as plotted in figure 5 in the form of the so-called kinematic viscosity $\nu = \mu/\rho$. At the "normal" temperature of 15 °C (59 °F) the viscosity of water is in the order of $\nu = 1.25/10^5$ (ft²/sec). Average sea water has a kinematic viscosity some 4.6% higher than that of fresh water. — In water, viscosity decreases appreciably as the temperature is increased. For example, at 120 °F, the viscosity is only half of that at "normal" temperature. Heating the water in a towing tank or in a water tunnel, is therefore a means of possibly doubling the Reynolds number in model testing.

CHAPTER II — SKIN-FRICTION DRAG

Viscosity is a molecular "resistance" which fluid particles exhibit against displacement in relation to each other and with respect to the surface of solid obstacles. Most directly, this type of resistance presents itself in the form of frictional drag. This means that in a manner roughly comparable to that of solid surfaces sliding along each other, a tangential force originates where air or any other fluid moves past the surface of a body. This force is the skin-friction drag.

to determine the resistance of two-dimensional plates in tangential flow. Referred to the area (b times l), the drag coefficient is

$$C_D = \frac{8\pi/R_\lambda}{3.2 - 2.3 \log R_\lambda} = \frac{10.9/R_\lambda}{1.4 - \log R_\lambda}$$

This equation is plotted in figure 1 in the form of $C_f = 0.5 C_D$. The graph gives a certain perspective as to the "viscous" regime in comparison to the "dynamic" functions of laminar and turbulent skin-friction drag at higher Reynolds numbers.

1. VERY SMALL REYNOLDS NUMBERS

At very low speeds, and/or in fluids with high viscosity, and/or in very small dimensions, that is roughly below $R_\lambda = 1$, viscosity is the predominant parameter determining the drag of a body.

Two-Dimensional. As a solution of equation 6 in the "pressure drag" chapter, for $h = 0$, it is possible

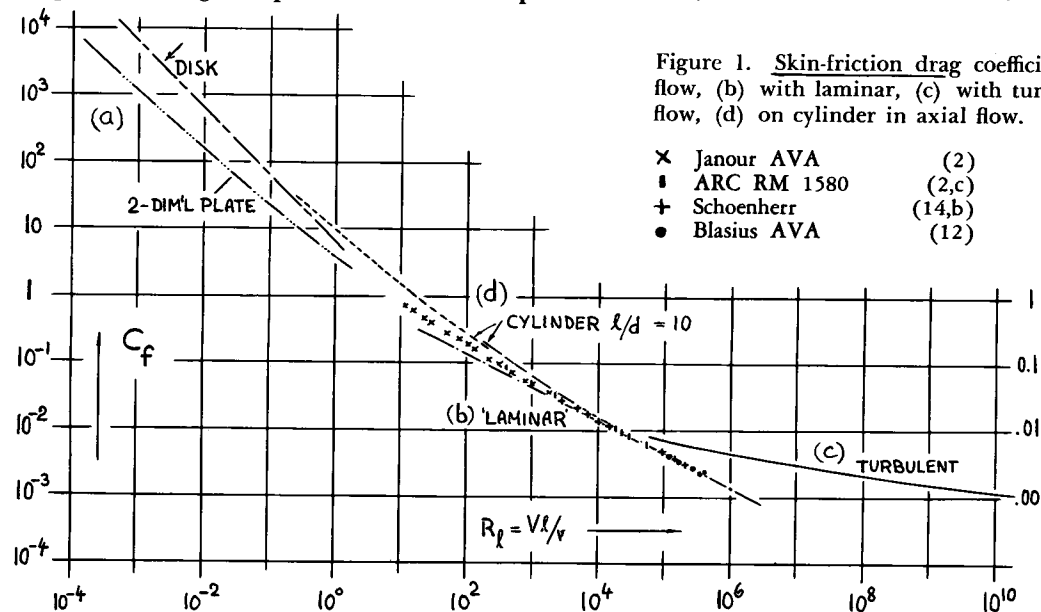
Disk. The drag of a thin disk, exposed on both sides to a tangential flow, is indicated (1) by the theoretical non-dimensional coefficient

$$D/\mu dV = 5.34; \quad D = 5.34 \mu dV \quad (\text{lb}) \quad (2)$$

with the viscosity "μ" in (lb sec/ft²) and the diameter "d" of the disk in ft. This type of drag is thus proportional to the velocity V (in ft/sec); we have here a typical example where the "quadratic" drag law, which is the basis of the standard fluid-dynamic

Figure 1. Skin-friction drag coefficient; (a) in "viscous" flow, (b) with laminar, (c) with turbulent boundary-layer flow, (d) on cylinder in axial flow.

- | | |
|---------------|--------|
| ✖ Janour AVA | (2) |
| ■ ARC RM 1580 | (2,c) |
| ✚ Schoenherr | (14,b) |
| ● Blasius AVA | (12) |



drag coefficients, does not apply. In the form of such a coefficient, based upon wetted disk area $S_{\text{wet}} = d^2\pi/2$, the skin-frictional resistance in this type of viscous flow is

$$C_f = \frac{D}{q S_{\text{wet}}} = \frac{4 \cdot 5.34}{\pi R_d} = \frac{6.8}{R_d} \quad (3)$$

This coefficient (plotted in figure 1) is appreciably higher than the two-dimensional function. The physical reason will be discussed later.

Applications. The region of very small Reynolds numbers has a limited practical meaning. Numbers below $R = 1$, are only found in oil-lubricated bearings (3), or in the case of water draining through the ground, or in tight fabrics (4). Theoretically and actually, there is a very small region near the nose or leading edge of every solid body where locally, frictional drag coefficients apply, similar in magnitude to those indicated in figure 1. Very low Reynolds numbers are also encountered at very high altitudes (as treated in the chapter on "rarefied gases").

Boundary Layer. Within the described range of smallest Reynolds numbers, "all" of the fluid space is affected by a moving body by means of viscous forces. To make such flow pattern better understood, one may assume the fluid medium to be replaced by a "plastic" material. A solid body (for instance a knife) pushed into this type of "fluid" encounters a resistance which is more or less directly transferred onto the "total" of the material. Testing the drag of bodies at such small Reynolds numbers in a towing channel is accordingly difficult (as reported in 5), because of the great influence of the tank walls upon the measured forces. This "remote-control" influence of viscosity decreases steadily, however, within a range of the Reynolds number which may be said to be between 1 and 100. Above this range, the influence of viscosity becomes limited to a comparatively thin layer closely adjacent to the surface of the moving body — generally called the "boundary layer".

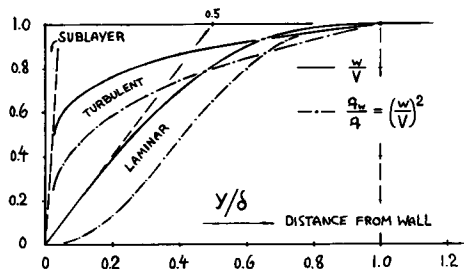


Figure 2. Non-dimensional distribution of velocity and dynamic pressure across the boundary layer, for turbulent and for laminar flow. The area between " w/V " and " q_w/q " is a measure for the frictional drag.

2. BOUNDARY-LAYER DATA

In the flow past a solid obstacle, certain fluid particles cling to the surface; their relative velocity is $w \rightarrow 0$. Particles at some small distance from the wall loose only part of their original velocity; they are kept balanced by viscous shearing stresses between the wall and the undisturbed flow. Beyond a certain distance, defined as the total boundary-layer thickness, the outer flow is found, with a total pressure which fully corresponds to Bernoulli's law (see in Chapter I).

Velocity Distribution. Figure 2 shows the velocity distribution across the boundary layer. Starting from zero, directly at the surface, the shape of the distribution curve is very much a function of the type of flow. For *laminar* boundary-layer flow (6) :

$$w/V = 2(y/\delta) - 2(y/\delta)^3 + (y/\delta)^4 \quad (4)$$

This function means that near the wall, the local velocity "w" increases in linear proportion to the distance y ; thus

$$(w/V)_o = 2(y/\delta) \quad (5)$$

The distribution across *turbulent* boundary layers can be interpolated by

$$w/V = (y/\delta)^{1/n} \quad (6)$$

The intersection of this function with $w/V = 1$ defines the total layer thickness " δ ". Within the range of $R_x = 10^6$ to 10^7 , boundary-layer surveys yield approximately $n = 7$ in the exponent of the equation. The value of "n" increases as a function of the Reynolds number (7). — As seen in figure 2, the distribution in the turbulent layer is "fuller" than that of the laminar layer; i.e. other words, the dynamic pressures close to the surface are much higher, if considering equal total thickness.

Total Thickness. As presented (for example) in (8), the total thickness of the boundary layer is for laminar flow pattern:

$$\delta/x = 5.5/R_x^{1/2} \quad (7)$$

In turbulent flow condition, combination of equations 18 and 19 yields

$$\delta/x = C_f (n+1)(n+2)/2n = 5.14 C_f$$

for $n = 7$. For the same value of n , using equation

28, the total thickness in turbulent condition is found to be

$$\delta/x = 0.154/R_x^{1/7} \quad (9)$$

Considering plane surfaces along which the boundary-layer flow is first laminar, then changing into turbulent state, the thickness at a point x is approximately

$$\delta/x = 0.154 (R_x - R_o)^{6/7}/R_x \quad (10)$$

In this equation, R_o indicates a theoretical number, roughly 30% lower than the critical number R_{x_c} of the surface considered. — The combined functions of boundary-layer thickness as plotted in figure 3 against Reynolds number, resemble those of the friction-drag coefficient in figure 6. As an example, the thickness along a plane wall is plotted in figure 4 for $R_L = 5 \cdot 10^6$. As long as the flow is laminar, the boundary layer grows along the lower curve. Assuming, however, a critical Reynolds number $R_{x_crit} = 10^6$, transition to turbulent flow is reached at $x/l = 10^6/(5 \cdot 10^6) = 0.2$. From there on, the boundary layer thickness increases at a higher rate than before.

Laminar Sub-Layer. Directly at a wall, turbulent oscillations are not possible in the direction normal to the surface. Oscillations in other directions are prevented by viscosity. A certain sub-layer, therefore, remains laminar, even in otherwise turbulent condition. The velocity distribution in the sub-layer is essentially linear (as illustrated in figure 2):

$$\frac{d(w/V)}{d(y/\delta)} = 0.5 (\delta/x) R_x C_\tau \quad (11)$$

- (1) Oberbeck, quoted in Handb. Exp. Physik Wien-Harms Vol. IV, 2; or in Lamb's "Hydrodynamics".
- (2) Drag coefficients in laminar BL flow:
 - a) Janour, Plate at Low Reynolds Numbers, Prague 1947; Trans NACA T. Memo 1316.
 - b) Schoenherr (14,b) results in glycerine reduced by this author to two-dimensional flow.
 - c) Fage, Friction Plates, ARC RM 1580 (1933).
- (3) Prandtl, "Strömungslehre" (1942); English Edition: "Fluid Dynamics", New York 1952.
- (4) Hoerner, Aerodynamics of Screens and Fabrics, Textile Research Journal 1952 p.274.
- (5) Thom and Swart, J. Roy. Aeron. Soc. 1940 p.761.
- (6) Schlichting, "Grenzschichttheorie" (1951); "Boundary Layer Theory" by McGraw-Hill 1955.
- (7) Statistical values in J. Aeron. Sci. 1954 p.705.
- (8) Falkner, Laminar B'Layer, ARC RM 1895 (1941).
- (9) Laufer, Turbulent Channel Flow, NACA T. Rpt 1053.
- (10) Rotta, series of papers on turbulent b'layers: (a) Planck Inst. Göttingen 1950; Trans TMB 242 or NACA TM1344. (b) Ing. Arch. 1950, 277; 1951, 31.

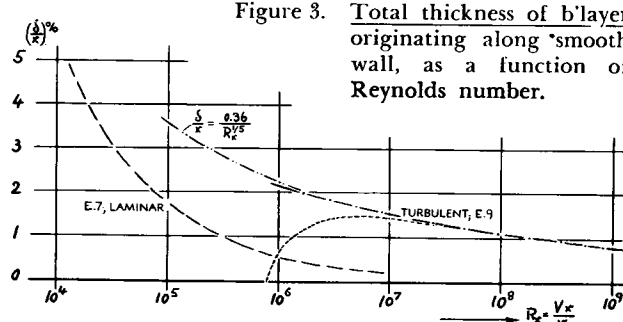


Figure 3. Total thickness of b'layer originating along smooth wall, as a function of Reynolds number.

with C_τ as defined by equation 21. The corresponding sub-layer thickness on smooth (constant-pressure) surfaces, as derived from (6) and from equation 28, is

$$\delta_{sub}/x = K/R_x \sqrt{0.5 C_\tau} = 7.5 K/R_x^{11/12}$$

This thickness ratio decreases roughly in proportion to $1/R_x$. The constant is $K = 5$ (as given in reference 6) for the laminar part of the sub-layer; and $K = 14$ as tested in (9) to the intersection with the exponential distribution (equation 6). These thicknesses are very small. Derived from equations 9 and 12, the sub-layer fraction is approximately

$$\delta_{sub}/\delta_{turb} = 50 K/R_x^{3/4} \quad (13)$$

This function is applicable in the vicinity of $R_x = 10^7$ and 10^8 . The laminar sub-layer usually measures less than a percent of the total turbulent thickness. This means that the sub-layer is only in the order between 1 and 2 times 10^{-4} of the distance x (or body length l). As pointed out in (10), viscosity and surface roughness are essentially effective in the sub-layer, while the remaining and by far larger part of the b'layer is predominantly a dynamic mechanism.

Displacement Thickness. Besides the total thickness, other thicknesses can be defined. The displacement thickness

$$\delta_\Delta = \int [1 - (w/V)] dy \quad (14)$$

is a measure, indicating how far the undisturbed outer flow is removed from the wall because of reduced velocities within the boundary layer. This thickness is

$$\begin{aligned} \text{in laminar boundary layer: } \delta_\Delta &= 0.315 \delta \\ \text{in turbulent boundary layer: } \delta_\Delta &= \delta/(l+n) \end{aligned}$$

where the value of n is ≈ 7 .

Momentum Thickness. The loss of momentum encountered by the boundary layer along its way to a certain point considered, is indicated by the mo-

mentum thickness

$$\delta = \int [(w/V) - (w/V)^2] dy \quad (16)$$

In figure 2, this thickness is represented by the area between the respective velocity- and dynamic-pressure curves. The momentum thickness is

$$\text{in laminar b'layer: } \delta = 0.12 \delta \quad (17)$$

$$\text{in turbulent layer: } \delta = n \delta / [(n+1)(n+2)] \quad (18)$$

Momentum Loss of the Boundary Layer. The mass of air which passes, during the unit of time, through the cross section of the boundary layer, is $\int(b q w dy)$. The momentum per unit time (in pounds) of this flow is $\int(b q w^2 dy)$. The difference between this value and that of the same mass of air at the undisturbed velocity "V" is $\int(b q (wV - w^2) dy)$. After dividing by V^2 , the integral in this expression is identical to the momentum thickness as indicated by equation 16. Hence, (loss of momentum per unit time) = drag = $b q V^2 \delta$. After introducing $q = 0.5 \rho V^2$ and the wetted area S_{wet} of the surface under consideration, the skin-friction drag coefficient is found to be

$$C_f = D_{\text{frict}} / (q S_{\text{wet}}) = 2 \delta / l \quad (19)$$

This equation represents the simplest case (at constant static pressure) of the momentum-loss technique which is widely employed in experimental aerodynamics. The boundary layer thickness is, in other words, a measure of the parasitic resistance originating along the surface. By means of a pressure survey across the wake (boundary layer) of a wing section, for instance, it is thus possible to determine the profile drag of an airplane wing in actual flight (11).

3. FRICTION WITH LAMINAR B'LAYER

Within the range of small and moderately large Reynolds numbers, the flow pattern of the boundary layer is laminar. This means that all particles move along lines which are essentially parallel to each other, with velocities that are locally constant.

Skin-Friction Coefficient. Derived from the viscosity μ (in lb sec/ft²) of the flowing medium, a theoretical solution (12) indicates the local drag coefficient (based on wetted surface area)

$$C_{f\text{lam}} = \frac{d(C_{f\text{lam}})}{d(R_x/R_l)} = \frac{\mu}{q} \left[\frac{dw}{dy} \right]_0 = \frac{0.664}{R_x^{1/2}}$$

where x = distance of the considered surface element from the leading edge and $\tau = C_f q$, in lb/ft², indicating the local shearing stress at the surface. Experimental points are plotted in figure 6; and it is seen that the upper limit for the function's validity is in the vicinity of $R_x = 10^6$. The total or average coefficient "C_f" of a surface is found by integrating the local values along the length (or chord) of the surface considered. As pointed out in (14,a),

$$C_f = C_{f\text{lam}}(k+l)/k \quad (22)$$

where $k = (m - 1)$, and "m" as in equation 28. In case of laminar friction thus:

$$C_{f\text{lam}} = D_{\text{lam}} / (q S_{\text{wet}}) = 1.328 / \sqrt{R_l}$$

The laminar drag (in pounds) is, therefore, proportional to ($C_{f\text{lam}}$ times V^2) a function which is proportional to $V^{0.5}$. The coefficient is plotted in figures 1 and 5, together with results on flat plates, tested in towing tanks or wind tunnels. The lower validity limit of the function is in the order of $R_l = 10^3$, below which the purely "viscous" type of skin friction takes over more and more.

4. TURBULENT BOUNDARY LAYER

At higher Reynolds numbers, after exceeding a stability limit which is treated later, the boundary-layer flow turns turbulent. This means that the flow adjacent to the surface of a body is eddying, with oscillating velocity components parallel and transverse to the main flow direction. Because of these superimposed motions, a certain exchange of momentum takes place between the various "sheets" of the boundary layer. This dynamic mechanism produces shearing stresses which are higher than those in laminar condition. Magnitude and variation of the skin-friction drag coefficient are different from those for laminar flow.

Theoretical Drag Functions. The theoretical analysis of turbulent skin-friction drag is complex; an exact solution has not been established. The available solutions are basically generalizations of experimentally determined velocity distributions across the boundary layer. Among dozens of such statistical functions, the following are the most important ones.

(a) Prandtl and vonKármán, utilizing velocity distributions determined in pipes, found for smooth and plane surfaces (13) :

$$C_\tau = \tau/q = 0.059/R_x^{1/5}; \quad C_f = 0.074/R_\lambda^{1/5}$$

where C_τ and C_f as defined before. The function is applicable for Reynolds numbers below 10^6 . Such derivation from pipe tests was later improved (6) to

$$C_\tau = (2 \log R_x - 0.65)^{2.3}; \quad C_f = 0.455 / (\log R_\lambda)^{2.58}$$

giving adequate answers between $R_\lambda = 10^6$ and 10^9 .

(b) From analysis of velocity distributions across the boundary layer, vonKármán (14,a) derived the similarity rule that $C_f^{-0.5}$ is proportional to $\log(R_\lambda C_f)$. To determine a suitable basic function for the frictional resistance of ships, Schoenherr (14,b) then examined all available experimental results; and he established the equation which is widely used today:

$$\log(R_\lambda C_f) = 0.242/\sqrt{C_f}; \quad C_\tau = C_f / (1 + 3.59 \sqrt{C_f})$$

As shown in figure 5, the "Schoenherr line" appears to be valid up to the highest Reynolds numbers likely to be encountered in human engineering (between 10^9 and 10^{10}). A simpler formula approximating Schoenherr's within $\pm 2\%$ has recently been proposed (14,c) :

$$1/\sqrt{C_f} = 3.46 \log R_\lambda - 5.6 \quad (26)$$

(c) Schultz-Grunow (14,d) tested velocity distributions on a plane wall (rather than in pipes). Expressed by

$$C_\tau = 0.37 / (\log R_x)^{2.58}$$

$$C_f = 0.427 / (\log R_\lambda - 0.407)^{2.64} \quad (27)$$

his function (recently re-examined in reference 14,e) comes close to Schoenherr's "line".

Tabulation of the Schoenherr Function is as follows:

$V^{1/5}$	10^5	10^6	10^7	10^8	10^9	10^{10}
$10^3 C_f$	7.18	4.41	2.93	2.07	1.53	1.17

Practical Equations. Admittedly, all of the known solutions for turbulent skin-friction drag are semi-empirical. Further changes and improvements are therefore possible, as new evidence becomes available. Figure 5 demonstrates, however, that equations 25 and 27 agree well with experimental results obtained on smooth plates or on other surfaces, tested in wind tunnels or towed in water tanks. Schoenherr's function, therefore, seems to be fully adequate for engineering purposes. His equations (and the subsequent equations too) are somewhat inconvenient, however, in their structure. It is useful, therefore, to interpolate certain ranges of the Reynolds number by

$$C_f = K/R_\lambda^{1/m} \quad (28)$$

Between $R_\lambda = 10^6$ and 10^8 , for example, $m = 6$ and $K = 0.44$, thus presenting a simple equation which essentially covers the Reynolds-number range of airplanes. Between $R_\lambda = 10^7$ and 10^9 , the values $m = 7$ and $K = 0.030$ may be used, closely expressing Schoenherr's function. Equation 28 may also be used for the local skin-friction drag coefficient. With $m = 6$ and $K = 0.036$, for example, a formula is obtained which is adequate between $R_x = 10^6$ and 10^8 . — The exponent in equation 28 is always appreciably smaller than that in equation 22 (for laminar boundary-layer flow). The turbulent friction drag (in pounds) is proportional to $V^{11/6}$ or to $V^{13/7}$, thus indicating drag which is "almost" proportional to the square of the velocity. However, because of the wide range of the Reynolds

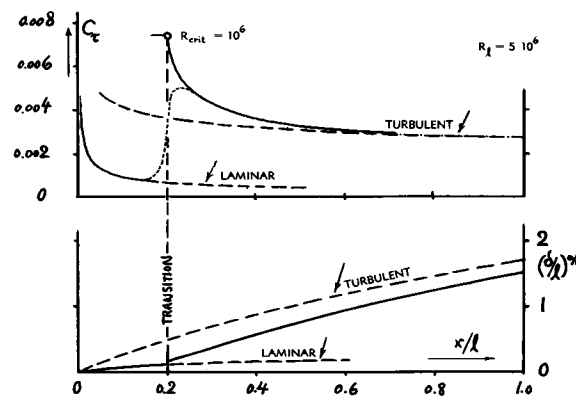


Figure 4. Example of the distribution of boundary-layer thickness " δ " and local drag coefficient " C_τ " along a plane wall having the length " l ". Note: distributions similar to the presented one, have been tested on a foil section (18).

(11) See for instance J.Aero Sci.1940 p.295; or NACA T.Rpt 660. Other sources on wake-survey method: Betz NACA T.Memo 337 (1925); ARC RM 1688 (1936), RM 1808 (1937), RM 2914 (1944); Bollay J.Aeron Sci 1938 p.247.

(12) Blasius, Zeitschr. Mathematik Physik 1908 p.1.

(13) Prandtl, Erg. AVA Göttingen III (1927); vonKármán, Aerod.I.Aachen 1921 or ZAMM 1921 p.233.

(14) Magnitude of turbulent skin-friction drag:

a) vonKármán, J.Aeronautical Sciences 1934 p.1.

b) Schoenherr, Resistance of Plates, Transactions Society Naval Architects Marine Eng. 1932.

c) Hama, Transactions Society NAME 1954 p.333.

d) Schultz-Grunow, New Skin-Friction Drag Law, Lufo 1940 p.239; Transl. NACA T. Memo 986.

e) Landweber, Friction Resistance, Trans Society NAME 1953; also in Yearb.STG 1952 p.137.

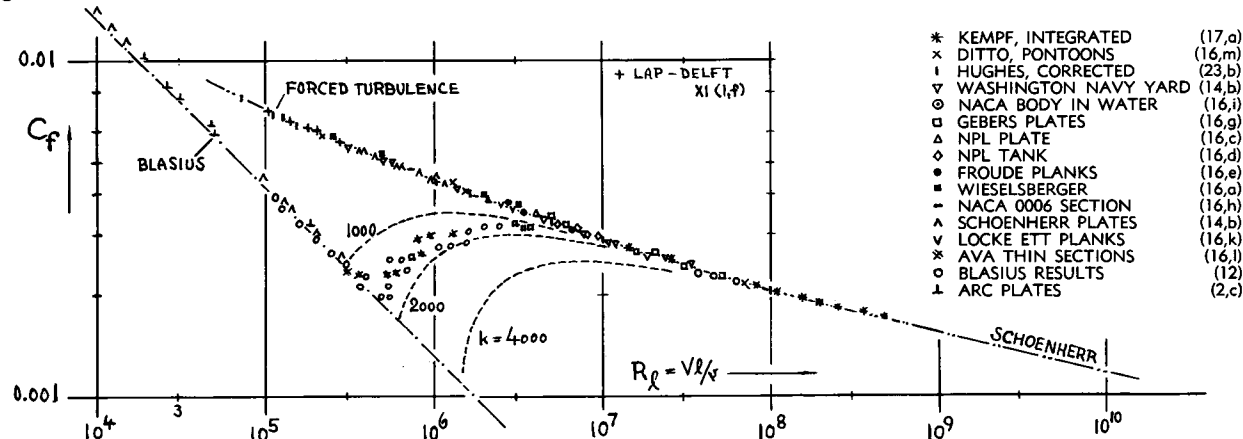


Figure 5. Average or total skin-friction drag coefficient of smooth and plane surfaces (in incompressible flow) in air and in water.

number encountered both in model testing and in full-scale operation of airplanes and ships, much attention is given to a solution as accurate as possible.

The Local Drag Coefficient, denoted in equations 23 to 27 by C_τ , corresponds to the slope of the total or average coefficient against R' number; hence $C_\tau = dC_f/d(R_x/R_\lambda)$, where $R_\lambda = V l/v = R'$ number on "1" which is then replaced by "x" equal to distance from the leading edge of the surface to the location considered. The transition from laminar to turbulent boundary-layer flow takes place within a certain interval " Δx " of the surface considered, as shown for example in figure 4. Theoretically, a sudden transition is assumed, however. As a consequence, at the point of transition or at the critical Reynolds number R_x , the coefficient C_τ suddenly jumps to a peak that is ≈ 10 times the level shortly before the transition, as illustrated in figure 6. Even considering a certain phase of transition, actually measured local coefficients (18) reach values, shortly behind the point of transition, which are several or many times the minimum ahead of the transition.

Transitional Coefficient. With regard to total or average drag coefficient, the transition from laminar

to turbulent boundary-layer flow can be approximated by subtracting from the coefficient corresponding to fully turbulent flow (equations 25 or 28), the decrement

$$\Delta C_f = k/R_\lambda \quad (29)$$

Prandtl (13) originally recommended the constant $k = 1700$ on the basis of certain towing tests in water (included in figure 5). The corresponding critical Reynolds number is $R_x \approx 5 \cdot 10^5$. In various more recent tests, much higher critical numbers have been reached, as illustrated in figure 9. Several transition curves have, therefore, been plotted in figure 5, corresponding to k values up to 4000.

5. FRICTION OF 3-DIMENSIONAL BODIES

Pressure Gradient. On the surface of streamline shapes, the boundary layer develops in a manner that is similar to the way it grows on plane, constant-pressure walls. The velocity distributions within the layer are of the same general type (laminar or turbulent, respectively) as described for plane walls. The pressure distribution along bodies or sections has an influence, however, on boundary layer and

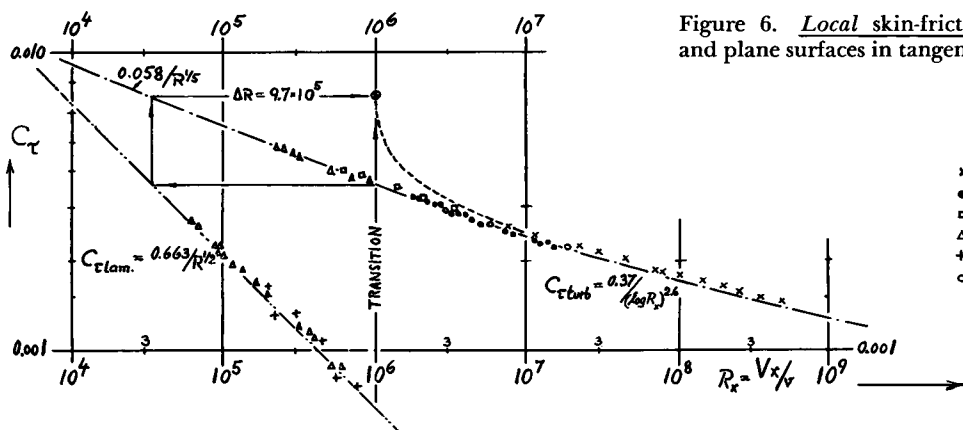


Figure 6. Local skin-friction drag coefficient of smooth and plane surfaces in tangential flow.

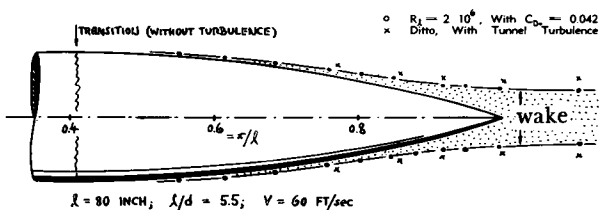


Figure 7. Total thickness of boundary layer developing along body of revolution, as tested in (20,b).

friction drag (19). The layer thickness decreases, and the local drag increases in a negative pressure gradient. Vice versa, thickness increases and drag decreases in a positive pressure gradient; and the local shear force reduces to zero where the flow separates (if at all) from the surface of the body.

Displacement. In three-dimensional streamline bodies, the shape has still another influence by mere geometrical reasons. Along the forebody, where diameter (or width and height) grow in the direction of flow, the volume of the boundary layer is evidently spread out over the growing circumference. Local friction is increased accordingly (20,a). Along the afterbody, the boundary-layer thickness increases, on the other hand, because of the shrinking body diameter. As illustrated in figure 7, upon reaching the pointed end of the body, the ring-shaped cross-sectional area of the boundary layer concentrates into a circle with the approximate diameter

$$d = \sqrt{3 \delta_0 d_{\max}} \quad (30)$$

where δ_0 = basic b'layer thickness, as indicated for instance by equation 9. At the end of an airplane's fuselage, having the usual appendages and surface imperfections, the diameter of the boundary-layer circle approaches that of the body's maximum cross section (S_b). For example the fins at the stern of an airship, accordingly operate within a broad field of reduced velocity. The details of all these variations are usually not considered in practical applications. The average drag of streamline bodies and sections is somewhat higher, however, than that of an equivalent plate (plane surface of equal wetted area and same length and Reynolds number); as explained in the "streamline" chapter.

Axial Cylinder. Upon shrinking the diameter of a cylinder in axial flow, having the length l , the ratio of boundary layer thickness to body diameter d increases. In the extreme case of a thin "line", the cross-sectional area of the boundary layer is transformed into a circle. The contact of the cylinder's surface with the outer flow and its frictional drag are thus increased. For *laminar* boundary-layer flow (21,a), the increase of the coefficient over that of a two-dimensional flat surface having the same length, is approximately

$$\Delta C_f = 2/R_d = 2(l/d)/R_\lambda \quad (31)$$

A drag coefficient including this increment for $l/d = 10$, is included in figure 1. Another theoretical solution (21,c) for the cylinder in axial flow, covering the range of smaller Reynolds numbers, is also shown in the graph ($l/d = 10$). For example, at $R_\lambda = 1$, the skin-friction drag coefficient of that cylinder is ≈ 2.5 times the coefficient of the two-dimensional plate (in tangential flow).

In Turbulent Flow, the described influence of three-dimensionality is estimated (22) to yield a

$$\frac{\Delta C_f}{C_{f0}} = k \frac{1/d}{R_\lambda^{1/5}} ; \quad \Delta C_f \approx 0.0016 \frac{1/d}{R_\lambda^{2/5}} \quad (32)$$

- (16) Results on total skin-friction drag:
 - a) Wieselsberger, Erg. AVA Göttingen I (1921).
 - b) Stack, In VDT, NACA T.Note 364 (1931).
 - c) ARC, In Compressed-Air Tunnel, RM 1804.
 - d) NPL, quoted in J.Aeronautical Sci. 1937 p. 504.
 - e) Froude's Planks, Trans INA 1937 p.120.
 - f) Kempf, Werft-Reederei-Hafen 1925 and 1929.
 - g) Gebers, Schiffbau 1919 or in Erg. AVA III.
 - h) 0006 Section, NACA T.Note 364.
 - i) NACA, Body, T.Note 2854 or T.Rpt 1161 (1954).
 - j) Locke, Stevens ETT Planks in Tank.
 - l) Thin Foil Sections, AVA Göttingen Erg III.
 - m) Kempf Pontoons, Yearb.STG 1951 p.228.
- (17) Experimental results on local skin-friction drag:
 - a) Kempf, Werft-Reederei-Hafen 1929 p.234 & 247.
 - b) Hydrod. Probleme des Schiffsantriebs 1932.
 - c) Dhawan (Caltech), Direct Measurements of Skin Friction, NACA T.Note 2567 or T.Rpt 1121 (1953).
 - d) Peters (MIT), Proc. 5th Intern.Congr.Appl. Mech's 1938.
 - e) Nikuradse, Turbulent B'Layers, Oldenbourg 1942.
- (18) Fage, Airfoil Skin Friction, ARC RM 1852.
- (19) Boundary layer and pressure gradient:
 - a) Ludwig & Tillmann, Shear Forces in turbulent BL's, Ing.Arch. 1949 p.288; also p.207, and ZAMM 1949 p.15.
 - b) Sandborn, Experimental, NACA T.Note 3031.
- (20) Friction on three-dimensional bodies:
 - a) Amtsberg, Yearbook STG 1937 p.177 and 201.
 - b) Simmons, Airship Model, ARC RM 1268 (1929).
 - c) See also NACA T.Rpt 430.
- (21) Laminar BL on cylinder in axial flow:
 - a) Cooper & Tulin (TMB), TMB Rpt 838 (1953).
 - b) Seban and Bond, J'l Aeron'l Sci. 1951 p.671.
 - c) Kelly, J.Aeronautical Sciences 1954 p.634.
 - d) Glauert, Proc.R.Soc. (London) Ser.A 1955 p.188.
- (22) Turbulent BL on cylinder in axial flow:
 - a) Landweber, TMB Rpts 689 (1949) and 761.
 - b) Eckert, J.Aeron Sciences 1952 p.23.
- (23) Frictional drag along edges:
 - a) Okabe, Res.I.Ap.Mech 1953 No.5, Kyushu Univ.
 - b) Hughes, Frictional Resistance in Turbulent Flow, Trans, INA 1952 p.287 and 1954 p.314.
 - c) Townsend, Boundary Layer on Flat Plate of Finite Width, ARC Paper 16,618; FM 2042 (1954).

where k between 0.022 and 0.025. For example, at $R_\ell = 10^6$, and a length ratio $l/d = 10$, the increment is in the order of 1.5%. There is some experimental confirmation (23,b) of this function up to $l/d \approx 600$. For $l/d = 10$, the effect is so small, however, that it cannot be demonstrated in figure 1.

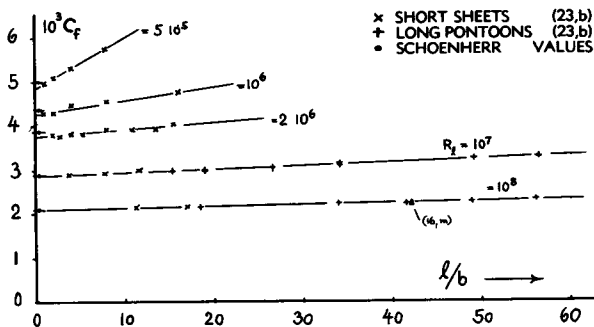


Figure 8. Skin-friction drag coefficient of flat plates (with 2 longitudinal edges) as a function of their length ratio (23,b). Note: Results below $R_\ell = 2 \cdot 10^6$ are debatable because of type and compensation of BL stimulation employed in the tests.

Longitudinal Edges. The edges of a plate in longitudinal flow exhibit an effect similar to that in slender cylinders. On the basis of theoretical boundary-layer functions in laminar flow (23,a), the drag due to a pair of edges in this type of flow is estimated to be

$$\Delta C_f = 2.9(l/b)/R_\ell \quad (33)$$

believed to be valid between $R_\ell = 10^3$ and 10^6 . This drag increment (referred to the wetted area of the plate considered) roughly corresponds to the circumference (2 b) of the "strip" considered as compared to (πd) of the cylinder. — For turbulent flow, figure 8 presents results of sheets and pontoons (each with two longitudinal edges) towed in a water tank. Assuming now that the edge effect follows the pattern of equation 32, evaluation of the tested slopes (above $R_\ell = 10^6$) yields the drag coefficient for a pair of edges

$$C_{\ell 2} = \frac{\Delta D}{q l^2} = \frac{0.0045}{R_\ell^{2/5}} ; \text{ or } \frac{\Delta C_f}{C_{f0}} = 0.03 \frac{l/b}{R_\ell^{1/5}}$$

where ΔC_f is referred to the wetted area (2 b l). This increase of turbulent friction due to lateral edges or that due to curvature (equation 32) is generally insignificant in full-scale aircraft or ship applications. In precise model testing (below $R_\ell = 10^6$), the influence may be noticeable, however. — A different mechanism, involving a secondary flow from the center of the plate toward the edges is proposed in (23,c). It is believed, however, that equation 34 correctly describes terminal conditions at higher l/b ratios, while the solution in (23,c) may apply to ratios below $l/b \approx 5$ — where the effect appears to be negligibly small in the first place.

6. TRANSITION OF B' LAYER FLOW

Origin of Turbulence. In the vicinity of $R_x = 10^6$, the boundary layer originating along an undisturbed, smooth, plane, constant-pressure wall — reaches a critical condition. The dynamic flow forces become predominant over the viscous forces. As a consequence, the layer (still being laminar) exhibits a wave motion. Subsequently this motion breaks up into turbulent oscillations. The so far molecular (viscous) exchange of momentum is largely replaced by a macroscopic exchange of mass; the skin-friction resistance is correspondingly increased. The turbulent transition usually starts at the trailing edge, where the Reynolds number R_x is greatest. Upon increasing R_x above R_{xcrit} , transition point or line move steadily forward. The leading edge is only reached at $R \rightarrow \infty$; hence a certain, more or less small part near that edge always remains laminar.

Stability Limit. If after disturbing somehow the boundary-layer flow, a wave motion is produced, this motion may either be damped (where upon the laminar character continues), or the motion may grow in amplitude thus leading to turbulence. The stability of the boundary layer in this respect has been analyzed (5). In agreement with experiments (25,e), the flow is found to be sensitive only to a certain range of disturbing frequencies. At highest critical Reynolds numbers, these frequencies are in the order of $2(V^2/10^5)$ per second. In standard sea-level air, the resulting frequency is, for example, in the order of 1000/sec for a wind-tunnel velocity of 90 ft/sec; or in the order of 10,000/sec for an airplane flying at 200 mph. In both examples, the frequencies are within the range which can be heard by the human ear. Indeed, transition within the boundary layer can easily be detected through the use of a stethoscope (24). Connected to a small Pitot tube ("needle") placed near the surface to be investigated, this medical instrument makes the turbulent oscillations audible as a noise which is between "hissing" and "thundering". — Theoretical analysis (25,c) also indicates a limit of the Reynolds number below which the b'layer flow is always stable. For constant-pressure surfaces, this lower limit is estimated to be in the order of $R_x = 6 \cdot 10^4$.

Transition. Proper frequencies are a prerequisite for transition. The Reynolds number at which transition really takes place, is then a function of the amplitude of the disturbing influence. Boundary-layer waves can be excited by surface roughness, through mechanical vibrations, by sound waves, or because of the turbulent oscillations in the artificial stream of a wind tunnel. Statistically, to be inde-

pendent of body shape and pressure distribution, a Reynolds number based upon the thickness of the laminar boundary layer (directly ahead of the transition point) is being used to indicate transition. Based upon displacement thickness, $R_D = V \delta_D / \nu = 2650$ has been found in (26,a), for example, in a low-turbulence tunnel. Based upon momentum thickness δ , maximum R_δ values have been reported by other researchers up to 1000, before transition takes place. For constant-pressure surfaces, the critical Reynolds number on length x , is

$$R_{x\text{tr}} = 0.34 R_D^2 = 2.3 R_\delta^2$$

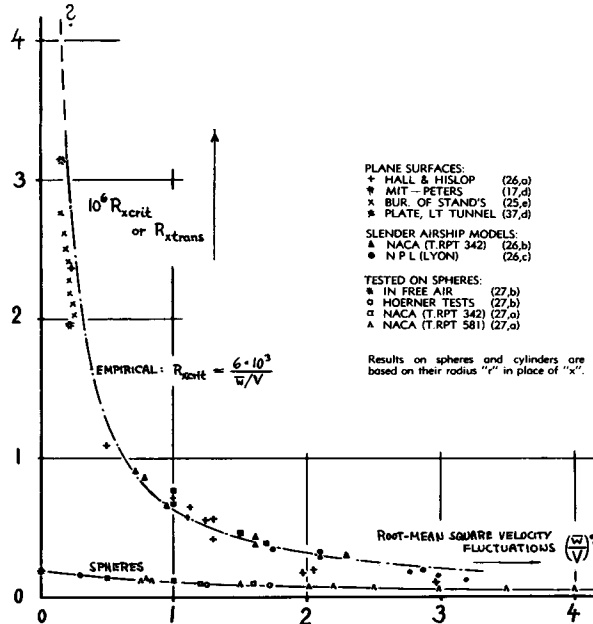


Figure 9. Critical Reynolds number (indicating boundary-layer transition) of plane walls (plates in tangential flow), slender airship bodies, and spheres, as a function of stream turbulence. To make the results on bodies, compatible with those on plane surfaces, the Reynolds numbers of the airship bodies have been based upon 0.5 l and those of the sphere upon the radius rather than diameter.

The values quoted, thus yield critical numbers $R_{x\text{trans}}$ in the order of $2.4 \cdot 10^6$. Still higher values, up to $3.7 \cdot 10^6$ have been found under favorable conditions (see in figure 9).

Stream Turbulence. Figure 9 presents experimental material indicating the critical Reynolds number on plane walls, plotted against the mean-square ratio of the turbulent velocity fluctuations prevailing in the stream of wind tunnels. As a function of this amplitude of the generally isotropic (this means in all directions) and polytropic (this means with various frequencies) oscillations, the critical Reynolds number is seen decreasing at a maximum ratio of more than 20 to one. The frequency of the oscillations is not reported in figure 9. Its influence should be involved, however, in the results. This becomes evident in turbulence tests in the free atmosphere, where the amplitudes are expected to be comparatively large and the frequencies correspondingly low. Sphere tests (27) seem to indicate only very little boundary-layer-affecting turbulence in the atmosphere. — Considerable degrees of turbulence exist behind propellers. Reference (26,d) shows, for example, that the transition point on the suction side of a conventional wing section is moved forward because of the propeller (full-power or idling alike) from 27% to 6% of the chord.

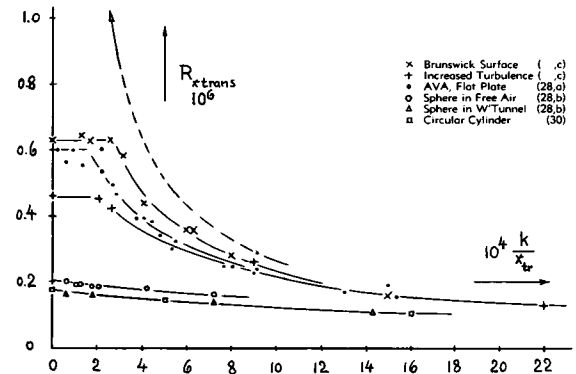


Figure 10. Transition Reynolds number on plane wall and of round bodies, as a function of sand roughness.

Surface Roughness. For roughness, uniformly covering the whole surface, figure 10 shows how the critical Reynolds number steadily decreases as the roughness grain size is increased. Turbulence in the wind tunnel stream has a superimposed effect, roughly cutting off the function due to roughness at certain levels of the critical R' -number. It is suggested that $R_{x\text{tr}}$ grows very high at $(k/x) \rightarrow 0$, provided that turbulence is completely eliminated; and there does not seem to be any permissible grain size then, with respect to transition. However, in turbulent streams, there is evidently some permissible sand roughness the size of which can be read from figure 10. Results on spheres and cylinders, also included in the graph, prove that in such bodies pressure distribution, more than roughness, dictates b'layer transition.

- (24) Pfenninger, Profile Drag, Mitt. 8 Zürich (1943).
- (25) Stability of laminar boundary layers:
 - a) Tollmien, Trans NACA T.Memos 609 and 792.
 - b) Schlichting, Nachr.Ges.Wissensch.Göttingen Math. Phys.Kl. 1933 and 1935; also ZAMM 1933 p.171 or Forschung Ing'wesen 1950 p.65; or (6).
 - c) Lin, Qu.Appl.Math. 1945 II,117;III,218;IV,277.
 - d) J.Aeronaut.Sciences 1951 p.490 and 1953 p.19.
 - e) Schubauer-Skramstad (BOS), B'Layer Oscillations, NACA T.Rpt 909 and J.Aeron Sci. 1947 p.69.
- (26) Transition as a function of stream turbulence:
 - a) Hall-Hislop, Experiments, ARC RM 1843 (1938).
 - b) NACA Airship Models, T.Rpt 342 and T.Note 264.
 - c) Lyon, Airship Models, Aircraft Eng 1934 p.234.
 - d) ARC, Effect of Slip Stream on B'Layer, RM 1957.
- (27) Experiments with spheres in turbulent streams:
 - a) NACA Technical Rpts 342 and 581.
 - b) Hoerner, Lufo 1935 p.42; Transl. NACA T.Memo.

Protuberances. As shown in (29), single but two-dimensional protuberances (for instance a wire with diameter d , placed across the direction of flow at some station x of the length or chord), evidently exhibit a critical size. The Reynolds number $R_{x,\text{tr}}$, at which the transition point begins to move forward from the original station x (located aft of x_d) is a function of the height ratio d/δ_A , where δ_A = displacement thickness of the laminar boundary layer. On the basis of the experimental results in figure 11, the permissible size is estimated to be in the order of

$$k_{\text{crit}} = (0.2 \text{ to } 0.3) \delta_A \quad (36)$$

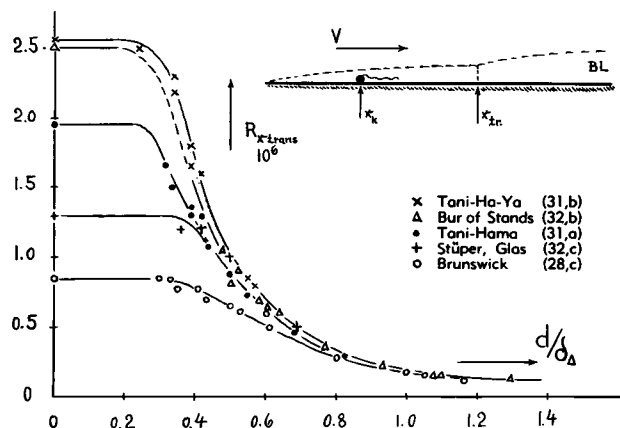


Figure 11. Non-dimensional representation of transition number of plane surfaces for single protuberances (wires across span) placed in the forward part of the surface (with δ_A taken at the place of the protuberance).

Single Elements of Roughness (spaced in lateral direction on a plane wall) essentially show a unique Reynolds number $R_* = w d / v$ at which transition "suddenly" takes place. For spherical elements (with diameter "d"), experiments (32,b) indicate a critical number in the order of $R_{*,\text{tr}} = 600$ defined for "w" = speed within the boundary layer at a distance from the surface equal to the diameter of the spheres tested.

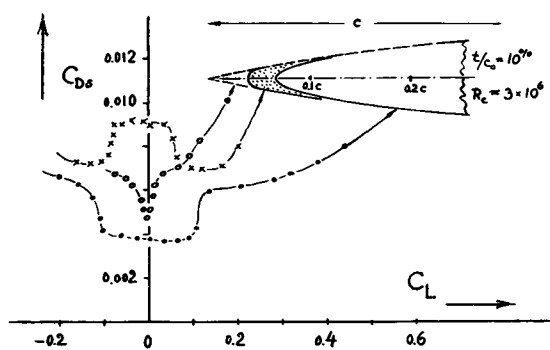


Figure 12. Influence of the leading-edge shape upon boundary layer and profile-drag coefficient of a foil section, as tested in (34).

Forced Transition. Upon increasing the size of a protuberance, transition of the boundary layer flow can be produced directly behind the obstacle. Behind isolated bodies (such as rivet heads, for example) turbulence then spreads out over a wedge-shaped area having a vertex angle (32,a) in the order of 2 times 10° . Turbulent areas with angles of similar magnitude also originate on the surface of wings along the adjoining walls of the fuselage (37,e) or the engine nacelles, and along lateral edges (24). — As found in experimental investigations of two-dimensional protuberances (33), the laminar boundary layer may separate from them. At a short distance behind the obstacle, the flow then turns turbulent; and it reattaches itself in this condition to the surface. — Figure 12 presents the influence of three different leading-edge shapes upon boundary-layer flow and profile drag. A sharp edge forces transition on the suction side immediately upon leaving the symmetrical (zero-lift) angle of attack. The section with a rounding radius at the leading edge exhibits transition on both sides because of a pressure minimum (on each side) in the pressure distribution of this shape. A parabolic shape avoids such distribution; both sides evidently have laminar flow and the profile-drag coefficient shows the "bucket" that is typical of laminar-flow sections.

7. LAMINAR-FLOW FOIL SECTIONS

Theoretical Possibilities. Within the range of small lift coefficients (that is, in case of an airplane at higher flying speeds), the resistance of thin wings consists almost entirely of skin-friction drag. Upon increasing the Reynolds number, the transition point of the boundary layer tends to move forward; the skin-friction drag coefficient increases accordingly, along a transition curve similar to those shown in Figure 5. Postponing, however, the transition to higher Reynolds numbers, by some suitable means; that is, by keeping the boundary layer "artificially" laminar — it is theoretically possible to obtain substantial savings in drag. As shown in figure 13, the skin-friction drag coefficient of plane plates decreases, roughly along straight lines, upon moving the transition point from the trailing to the leading edge. At $R_\ell = 10^7$, for example, the fully laminar resistance is only in the order of 1/7 of the fully turbulent value. Hence, laminarization of wing- and fuselage surfaces of modern high-speed aircraft appears to be an attractive possibility for the aerodynamicist. The graph also shows some experimental results. Beyond $x/c \approx 70\%$ (corresponding to maximum thickness location at between 55 and 60% of the chord), pressure losses along the tail increase to

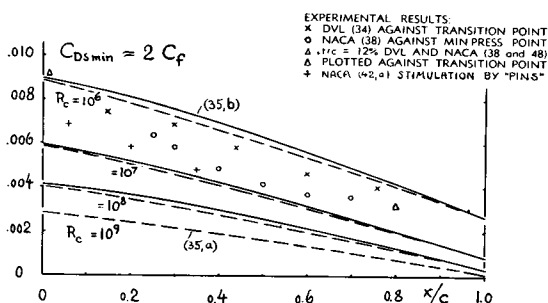


Figure 13. Theoretical (35) and experimental variation of skin-friction drag as a function of transition-point location along the chord of foil sections.

such an extent that the beneficial effect of laminarization is reduced and terminated with respect to total drag.

- (28) Influence of sand roughness:
 - a) Holstein, Friction Plate, ZWB Rpt UM 3110.
 - b) Hoerner, On Spheres, Lufo 1935 p.42.
 - c) Feindt, On Plate, DFL Brunswick Rpt 1956/10.
- (29) Dryden, Review, Journal Aeron Sci. 1953 p.477.
- (30) Fage and Warsap, Effects of Turbulence and Surface Roughness on Drag of Circular Cylinders, ARC RM 1283 (1929). The grain sizes have been determined by author from samples made available by NPL.
- (31) Japanese investigations:
 - a) Ta-Ha-Mit, Aero Res.Inst.Tokyo Univ.Rpt 199.
 - b) Tani and Hama, J.Aeron Sci. 1953 p.289.
 - c) Ta-Ha-Ya, Inst.Sci.Tech.Tokyo Univ. 8 (1954).
- (32) Influence of single roughness elements:
 - a) Scherbarth, Yearbook D.Lufo 1942 p.I,51.
 - b) Schubauer (BOS), BL Transition, J.Aeron.Sci. 1955p.803; also NACA T.Note 3489.
 - c) Stüber, Transition Wire, ZFW 1956 p.30.
- (33) Laminar separation and reattachment investigated:
 - a) ARC RM 1873.
 - b) NACA T.Note 1196 (1947) and 2338 (1951).
 - c) NACA T.Memo 1352.
- (34) Doetsch, Foil Sections in DVL Wind Tunnel, Yearbook D.Luftfahrtforschung 1940 p.I,54.
- (35) Skin-friction as a function of transition:
 - a) Fedjajewsky and Goroschenko, Techn.Wosd.Flota 1940 No.7; Transl NACA T.Memo 822.
 - b) Squire and Young, ARC RM 1838 (1938).
- (36) Influence of pressure distribution:
 - a) Schlichting, Critical R'Number — Pressure Gradient, Yearb.D.Lufo 1940 p.I,97; NACA T.M. 1185.
 - b) Goertler, Influence of Camber on BL Stability, ZAMM 1940 p.138, 1941 p.250; Transl 1588 BMAP.
 - c) Liepmann, Experimental BL Transition on Curved Walls, NACA ACR Rpts, 1943 and 1945.
 - d) Granville, Viscous Drag, TMB Rpt 849 (1953).
- (37) Location of Transition point of sections:
 - a) Calculation, Tech.Wosd.Flota 1940 p.55.
 - b) NACA T.Rpts 636, 637 (1938) and 667 (1939).
 - c) Pfenniger, TH Zürich Heft 13; NACA TM 1181.
 - d) Jones, Flight Experiments, J.Aer. Sci. 1938 p.81.
 - e) Wijker, Netherland NLL Rpt A.1269 (1951).
 - f) Preston and Gregory, Transition and Drag of Laminar-Flow Wing, ARC RM 2499 (1952).
 - g) Lyon, Streamline Bodies, ARC RM 1622.
 - h) NACA, Thin Section, Technical Note 3505.

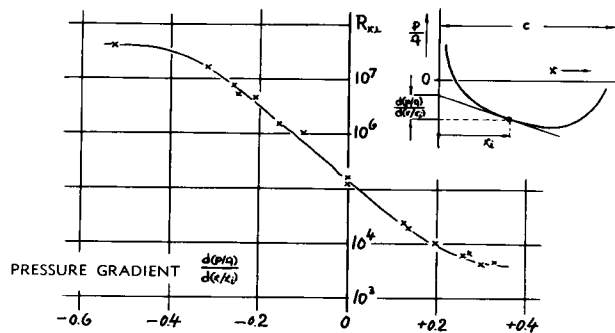


Figure 14. Theoretical prediction of the Reynolds number indicating instability (not yet transition) of the boundary-layer flow, evaluated from (36,a).

Pressure Gradient. The stability limit of the boundary layer is very much a function of the static pressure gradient in which the layer develops. As shown in figure 14, the stability number $R_{x\text{stab}}$ may change in this respect between such limits as less than 10^4 and higher than 10^7 . The analysis indicates that the essential condition for termination of boundary-layer stability, is an inflection in its velocity distribution. Such an inflection in the straight part of the laminar function in figure 2, can "easily" be produced by a positive pressure gradient. A negative gradient, on the other hand, tends to accelerate the part of the boundary layer adjacent to the surface, thus preventing or postponing the formation of inflection and turbulence.

Transition Point. Reaching the point of instability does not yet mean transition from laminar to turbulent flow pattern. An additional distance Δx is required within which turbulence develops. No simple function is available to date for predicting the magnitude of this distance. The point of laminar separation — which is only a function of shape and attitude of the body involved — is accepted as the ultimate location of transition. Another piece of information comes from the investigation of the influence of longitudinal camber or curvature on boundary-layer stability (36,b and c). On convex surfaces, such as at the upper side of foil sections, the stability limit (in terms of local velocity and boundary-layer thickness) is approximately the same as on a plane wall (figure 14). However, on concave surfaces, the stability limit reduces rapidly as the radius of curvature is decreased. For example, for a radius r equal to $10^4 \delta$ (where δ = momentum thickness of the b'layer), roughly representing the cusped tail shape in certain laminar-flow foil sections developed by the NACA (38) — the stability Reynolds number is reduced to the order of 1/2 of the plane-surface value. Concave shape and positive pressure gradient, therefore, combine in these sections to produce transition, shortly aft of the minimum-pressure point. Considering now this

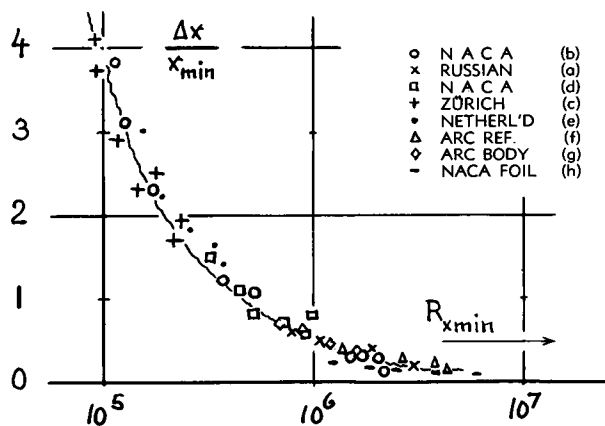


Figure 15. Statistical evaluation of (37) indicating the location of the transition point behind the point of minimum pressure.

point to be a lower limit with respect to transition, figure 15 presents a statistical evaluation of available material. The distance Δx , behind the point of minimum pressure (indicated by "min") decreases steadily as the Reynolds number (on x_{\min}) is increased. Results in (37,h) show, however, that the function suggested in the graph, does not very well apply in peaked pressure distributions, such as found near the LE of thin and/or symmetrical sections at higher lift coefficients. Reference (36,d) shows in this respect, that transition occurs the sooner, the higher the average pressure gradient is, between the point of neutral stability and the transition point.

Location of Maximum Thickness. A way of providing a negative pressure gradient, and to move the minimum-pressure point downstream, is to place the maximum thickness of a body or that of a foil section as far back as practicable. Laminar profiles of this type have been developed in various countries. The NACA (38) has investigated several series of foil sections (for example those beginning with the numbers 64 and 65). One of these sections was employed in the North American "Mustang", a fighter plane which was in active service around 1942. Reference 39 and some experimental points in figure 18 are evidence for the attention which this section has found at that time. — Laminar profiles have a thickness location between 40 and 65% of the chord, in combination with a comparatively pointed nose and possibly with a cusped afterbody. All these characteristics help to produce the desired negative pressure gradient. Since this gradient is also proportional to the thickness ratio t/c , a reasonable minimum value of this ratio is required to make a laminar profile. Figure 16 shows as an example a section with the thickness located at 50% of the chord and the pressure minimum approximately at $x/c = 55\%$.

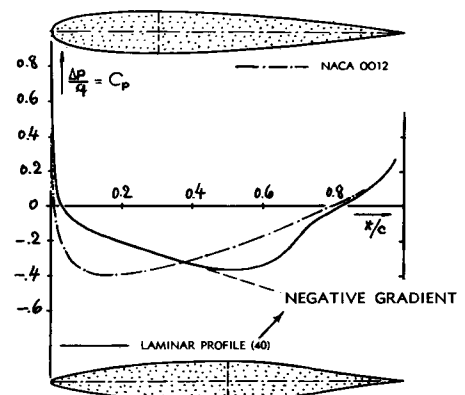


Figure 16. Shape and pressure distribution of two symmetrical foil sections, differing in the location of maximum thickness.

Influence of Lift Coefficient. Figure 17 presents experimental results on a similar section; the minimum drag coefficient is appreciably reduced below that of an "ordinary" section having the same thickness ratio but with the maximum thickness located at 30% of the chord. The reduced coefficient is restricted, however, to a comparatively narrow range around the "optimum" lift coefficient (which happens to be zero in the example). The bucket-shaped part of the $C_D(C_L)$ function usually comprises a $\Delta C_L = +$ and $-$ (0.1 to 0.2). Outside the "bucket", the flow around the foil's leading edge disturbs the boundary layer (on one side) so that it turns turbulent very shortly aft of the edge. Employing a suitable value of section camber, the "bucket" can be placed around the lift coefficient which prevails in the high-speed or cruising condition of the respective airplane, without losing any or much of the laminar effect (38).

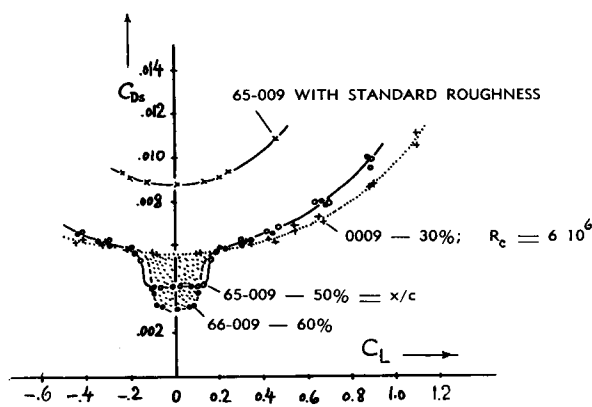


Figure 17. Profile-drag coefficient of various foil sections as reported in (38). Two of the sections show the "bucket"-shaped drag minimum which is typical of laminar-type airfoil sections.

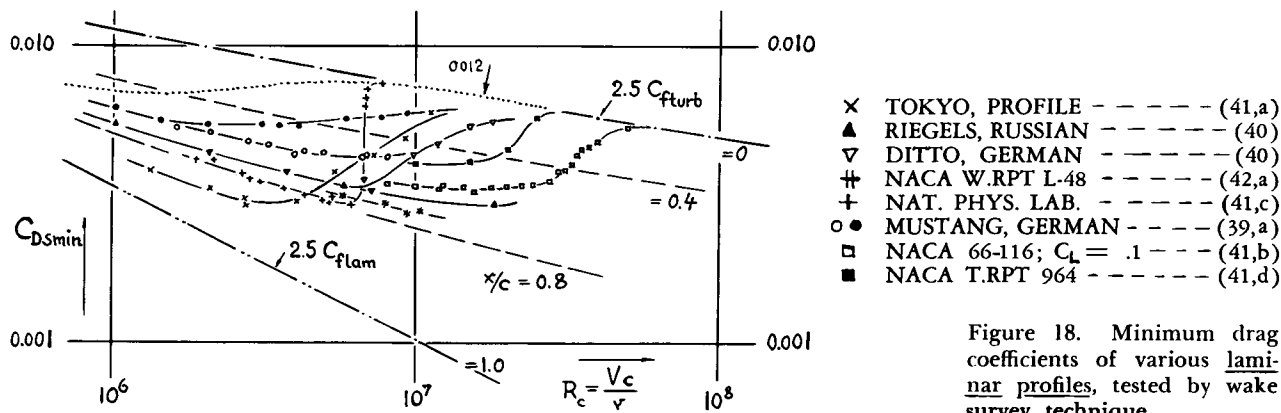


Figure 18. Minimum drag coefficients of various laminar profiles, tested by wake survey technique.

Experimental Results. Figure 18 presents the experimental results of several laminar-type foil sections, as a function of Reynolds number. To show the correlation of these results with the theoretical skin-friction functions, a set of lines has been included representing $(2.125 C_f) = 2.5 C_f$. Doing this, the "2" indicates the two sides of the investigated foils; the "1.25" approximately takes into account the average increased dynamic pressure along the section sides due to their finite thickness. — The graph shows that the drag coefficients of sections with the maximum thickness in the vicinity of 30% of the chord, as they have been common in airplane design for at least 2 decades — approach the fully turbulent skin friction curve above $R_c \approx 10^6$. The coefficients of the laminar type sections, on the other hand, are seen steadily decreasing to and beyond $R_c = 10^7$. Their profile drag is, on the average, only about half as high as that of the "older" sections. Roughly half of the differential between fully turbulent and fully laminar skin-friction drag is saved in this manner. Theoretical lines are also included in figure 18 for transition locations at $x/c = 0.4$ and $= 0.8$.

Stream Turbulence. Upon increasing the Reynolds number above $R_c \approx 5 \cdot 10^6$, several of the investigated sections show a steady forward movement of the transition point. It is suspected that the turbulence of the wind tunnels used in those tests, is at least partly responsible for the movement. It has only been after the development of their Low-Turbulence Tunnel that the NACA obtained the low drag coefficients as shown in the graph. Figure 9 serves as illustration for the influence of stream turbulence on boundary-layer flow. The turbulence in the atmosphere, which might be expected to affect the boundary layer of airplanes, appears to be quite low. It seems to be correct, however, that sound and vibrations produced by aircraft engines, have a noticeable effect on the transition point in the boundary layer. A strong source of turbulence is finally the propeller slip stream, as mentioned in connection with (26,d).

Surface Roughness. As "permissible", we will define such surface imperfections and protuberances that do not show an effect upon the magnitude of drag. Permissible sizes evidently exist in the range of smaller Reynolds numbers, where the transition point of the boundary layer is either to be expected beyond the trailing edge, or where transition is forced by the shape of the foil section (by a cusped tail, for example, or by the laminar separation point). Small Reynolds numbers are not of much concern, however, in aircraft applications. Conditions in the range of higher R' numbers (in the order of 10^7) can be appraised on the basis of generalized functions such as shown in figure 10. For "sand" type roughness (uniformly covering all of the surface) that illustration indicates some permissible lower limit for the size of roughness elements. Reference (38) disagrees with this conclusion in saying that "no roughness detectable to the finger tips should be allowed" on laminar-type airfoils. The imperfections (rivet heads and sheet-metal joints) and possibly paint roughness encountered in practical-construction wings, may have an effect similar to that of distributed sand roughness. It is shown in figure 18 (among others) how the

- (38) Abbott-Doenhof-Stivers, Airfoils, NACA T.Rpt 824.
- (39) Wind-tunnel experiments on "Mustang" section:
 - a) German ZWB Rpts UM 1190 and 1724 (1943).
 - b) British ARC RM 2359 (1946).
- (40) Riegels, Russian Laminar Profiles, ZWB Rpts UM 3040, 3056, 3067 and 3159 (Göttingen 1943, 1944).
- (41) Minimum profile-drag of laminar-flow airfoils:
 - a) "Tokyo LB 24" Airfoil, ZWB Rpt UM 2100.
 - b) Practical-Construction Wings, NACA T.Rpt 910.
 - c) Fage-Walker, NPL Tunnel, ARC RM 2165.
 - d) Several Airfoil Sections, NACA T.Rpt 964.
 - e) NACA W.Rpt L-138 (1944) shows that the 65-418 section, with a minimum coefficient $C_{D_s} = 0.004$ between $R_c = (2 \text{ and } 5) \cdot 10^6$, has values to 0.01 and 0.02 below $R_c = 10^6$ — evidently because of laminar separation from the rear.
- (42) Effect of roughness upon transition:
 - a) Loftin, NACA Wartime Rpt L-48 (1946).
 - b) Fage, EQH 1260 Foil Section, ARC RM 2120.
- (43) Smith and Hilton, Flight Tests on "King Cobra" Having Low-Drag Aerofoil, ARC RM 2375 (1950). See also RM 2485 on maintenance of Laminar-Flow.

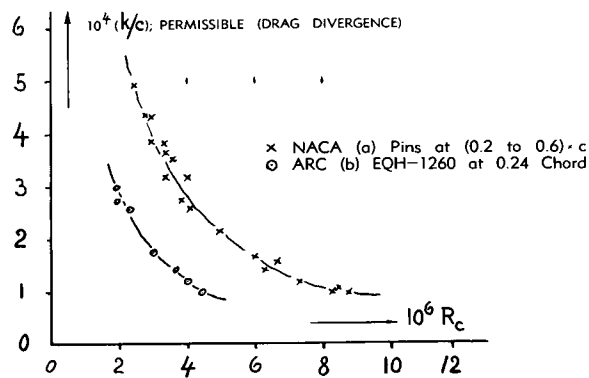


Figure 19. Permissible size of single protuberances on the surface of laminar-type profiles, near zero lift (42).

drag coefficient of such a wing (39,a) starts increasing at a Reynolds number ($3 \cdot 10^6$) which is considerably lower than that of the perfectly smooth model (starting at $7 \cdot 10^6$). Other tests (41,b) confirm the deterioration of laminar characteristics on account of surface imperfections. Figure 17 also demonstrates how laminar flow and low drag are wholly eliminated by placing a narrow sand strip near the leading edge of the foil section. Reference 43 reports on the operational aspects of laminar-type wing sections; and figure 20 shows results of flight tests with a high-speed airplane. After cleaning up the various constructional imperfections of the wing's surface, the drag coefficient is reduced roughly to one third. However, dust (accumulated on the wings at the ground) and insects (picked up during the flight) provide a degree of roughness sufficient to increase the minimum section-drag coefficient from 0.003 to 0.004 and even 0.006 in this example. Nevertheless, there can be a permissible size in *single* roughness elements explained as follows.

Permissible Roughness. It has been concluded from figure 11, and it is stated in the text, that a certain minimum size (height) of *single* roughness elements is permissible without producing turbulence in the boundary layer. The size indicated by equation 36, is in the order of $k/c = 4 \cdot 10^{-5}$, at $R_c = 10^7$ for example. For an assumed length of $c = 10$ ft, the resulting size is $k = 5$ mils, a value which (although small enough) is nevertheless high in comparison to the "sand" sizes considered permissible in turbulent boundary layer (Chapter V). Figure 19 shows the critical size (defined by a divergence of the drag coefficient against that of the smooth foil model) of single protuberances placed at certain stations of the chord of a foil section. The permissible size decreases considerably as the Reynolds number (speed) is increased, roughly in the proportion of $k \sim 1/R_c$. The ARC results on two-dimensional disturbances (across the foil span)

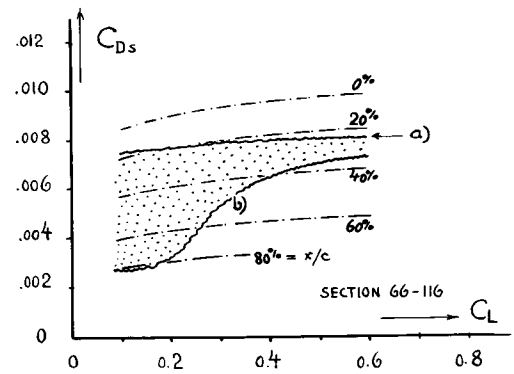


Figure 20. Results of flight tests on the wing of "King Cobra" (43) showing (a) the profile drag "as received" and (b) after reducing the skin imperfections.

roughly agree with those found for plane walls (equation 36). The NACA results on the influence of spanwise rows of "pins" (spaced in lateral direction at 0.033 c) suggest a permissible $k \approx c/10^4$ at $R_c = 10^7$, a value which is about twice as high as that for the two-dimensional protuberances. Some explanation on this type of roughness is given under "single elements".

Boundary-Layer Suction. Another method of keeping the boundary-layer flow laminar, is suction. Through small slots in the surface or through a porous surface material, a suitable part of the laminar boundary layer is sucked into the hollow wing (and ejected downstream somewhere else). For an understanding of the efficiency of this procedure, definition of the resultant drag is necessary. Upon eliminating all of the boundary layer by suction, the momentum loss left behind in the wake would be zero. Reducing, however, the velocity of a stream tube to zero, as is done in suction, means a transfer of the corresponding momentum onto the wing in the form of drag. The power necessary to remove the boundary layer, or "to pump it back to full total pressure", can be expressed in the form of an effective increment of the drag coefficient:

$$\Delta C_D = C_p C_Q \quad (36)$$

where $C_Q = Q/VS = w/V$; and Q = volume of air sucked in the unit of time (ft^3/sec). In the arrangements which are here considered, the volume Q is meant to be that of the two sides of the considered foil sections, referred to the wing area S . " C_p " is a pressure coefficient. In test conditions where the drag is measured by a wind-tunnel balance,

$$C_p = (p_{amb} - p_{ins.})/q \quad (37)$$

is to be used in computing ΔC_D . In a test setup where the profile drag is determined by wake survey (as considered above), rather the total-pressure

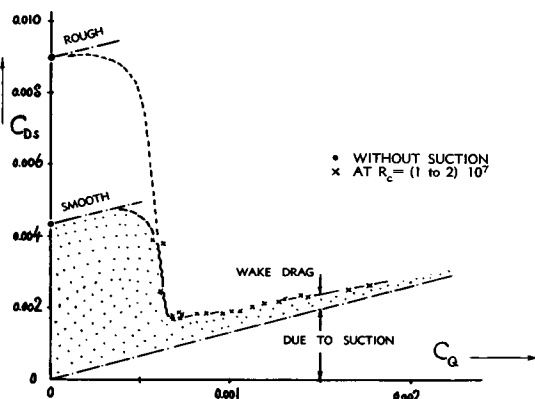


Figure 21. Example for laminarization and drag reduction by means of boundary-layer control. The presented results apply to a 10% thick section (44,a) whose boundary layer is mostly sucked into the hollow wing through the porous skin.

difference between outside and inside

$$C_{p\text{tot}} = (q + p_{amb} - p_{ins.})/q = 1 + C_p$$

must be applied in determining the additional component of drag. Besides some pressure drop across the slotted or porous skin of the wing, the coefficient C_p includes the differential due to section thickness and possibly another differential due to lift. Values for the coefficient are in the order of $C_p = 0.3$ to 0.6 , for slender sections near zero lift.

Reduction of Drag. Figure 21 demonstrates how the profile drag of a section decreases (rather suddenly in the example presented), upon reaching a certain critical volume coefficient of suction. Only very little momentum deficiency is remaining in the wake behind the foil. After adding the drag coefficient equivalent to the energy spent in sucking (equations 36 and 38), the effective or "total" coefficient is obtained. This coefficient shows a minimum value at an optimum suction coefficient. Upon further increasing the volume, the total coefficient increases again. Figure 22 presents optimum total coefficients as a function of the Reynolds number. It is seen that for favorably designed suction foils, drag coefficients can be obtained which are comparatively close to the laminar level.

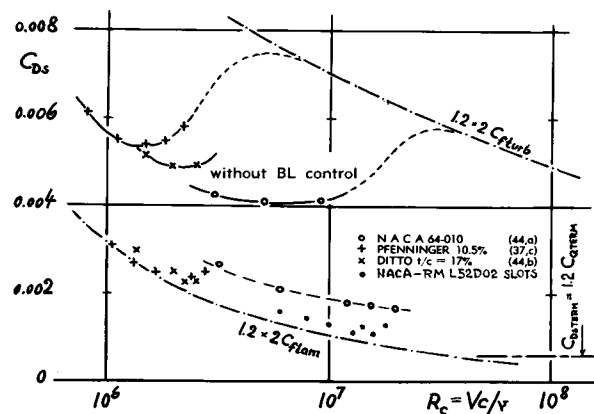


Figure 22. Total profile-drag coefficients of some airfoil sections successfully using boundary-layer control through suction (reference 44).

Required Suction Volume. The quantity of C_Q is important for the size of the suction machinery required. Figure 23 presents optimum experimental values for several sections (at $C_L \approx 0$). The required volume coefficient is essentially proportional to the laminar skin-friction drag coefficient, which is proportional to $1/\sqrt{R_c}$. There is also a theoretical estimate available (6) predicting for a flat surface a coefficient of $C_Q = 0.00012$ and a corresponding drag coefficient $C_f = 0.00024$. It is suggested that these two values (each doubled to account for the two sides of a foil section) are the ultimate levels to which C_Q and $C_{D\text{tot}}$ may possibly reduce at Reynolds numbers between 10^8 and 10^9 . Experiments prove that drag reductions similar to those in figure 22 can also be obtained at higher lift coefficients. For the suction side of the foil, the pressure coefficient roughly increases as tested in (44,c) by $\Delta C_p = C_L$.

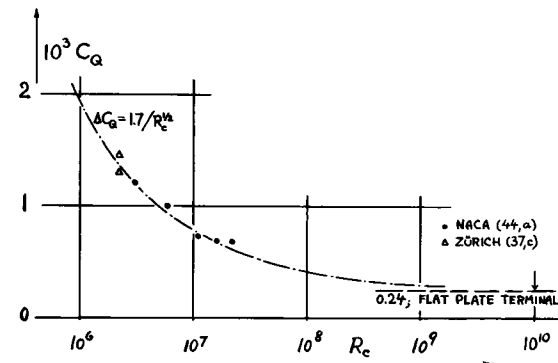


Figure 23. Minimum suction volume required to produce laminar boundary-layer flow in airfoil sections.

(44) Boundary-layer control through suction:

- a) Braslow and Others, Suction on 64-010 Airfoil, NACA T.Rpt 1025 (1951); or T.Notes 1905 and 2112.
 - b) Pfenninger, 17% Airfoil, J.A. Sci. 1949 p.227.
 - c) Raspert, Sailplane, Aeron Engg Review June 1952.
- (45) Lachmann, Laminarization Through Suction; Aer. Engg Review 1954 p.37, or AGARD Rpt AG 14/P5.
- (48) DVL, Airfoils in High-Speed Tunnel, unpublished Rpt Jf-727 (1944).

Surface Roughness in the spaces between openings, holes or slots permitting suction, can have a very detrimental effect upon the drag of these sections. Laminarization through slots is treated in (45); and the influence of surface roughness is explained there

at length. Suction reduces the boundary layer thickness; and the layer grows again between slots. This up and down of thickness has critical limits, an upper one with regard to laminar stability, and a lower one on account of roughness. Turbulent flow is obtained beyond either limit; by under-sucking, respectively, or over-sucking (44,c). Since permissible roughness reduces with speed, maintenance of laminar flow grows more and more difficult, as speed (not Reynolds number), or more precisely (V/\sqrt{v}) is increased. Laminarization through suction is, therefore, a rather sensitive operation. Since the required mechanical equipment (blower and ducts) also adds to the complexity of aircraft, boundary-layer control has so far primarily been considered and tried in airplanes to increase the maximum lift (at low flying speeds, by preventing separation) rather than with a view toward reducing drag at high speeds.

Turbulence Stimulation. Figure 24 shows once more the correlation between transition point and profile drag, in a laminar-type foil section (without suction). As the lift coefficient of the symmetrical shape is changed to positive or negative values, the *suction* side turns turbulent from 20% and even 10% of the chord. The drag coefficient roughly doubles at the same time, although the *pressure* side stays laminar to some 80% (essentially, without being affected by lift). Such laminarization (on the pressure side) evidently takes place in many common foil sections, caused by the natural pressure gradient (at positive angles of attack) between stagnation point and trailing edge. Figure 24 also shows the influence of uniform "sand" type roughness on the characteristics of that foil. Although at α and $C_L = 0$, transition is essentially unchanged by the modest degree of roughness applied, transition at the suction side progresses rapidly upon exceeding an interval of $C_L \approx \pm 0.05$. Note in figure 25 that distributed "sand" type

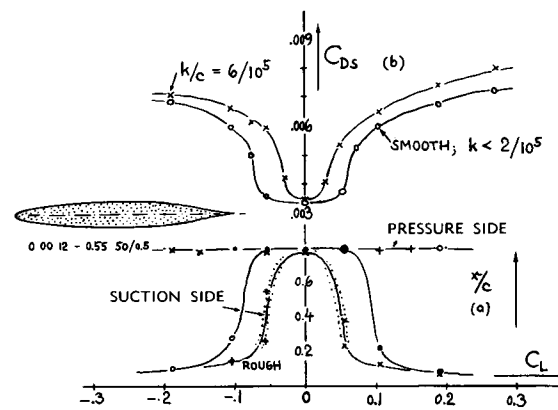


Figure 24. Correlation between minimum section drag coefficient (at bottom of bucket) and location of transition point in the laminar-type airfoil section shown, tested (48) at $R_c = 3 \cdot 10^6$; (a) in smooth condition, (b) with uniform sand type roughness ($k = 6 \cdot 10^{-5}$).

roughness reaches higher drag values corresponding to fully rough condition where the drag coefficient becomes a function of grain size "k" and velocity, rather than of Reynolds number. A corresponding line calculated on the basis of figure 4 in Chapter V, with a factor of 1.3 to account for section thickness, is included in the graph. On the other hand, a roughness strip placed at the airfoil's nose, has primarily a turbulence-stimulating effect, thus increasing the level of the drag coefficient from mostly laminar, to mostly smooth-turbulent condition (without presenting much drag of its own). For both the uniformly distributed sand, and for the turbulence strip, some "permissible" size is evident in figures 24 and 25. Favorable pressure gradients evidently stabilize the boundary layer. The fact that the strip shows a permissible value, appreciably smaller than that of the sand type roughness, must be laid to the considerably higher Reynolds number in testing that foil.

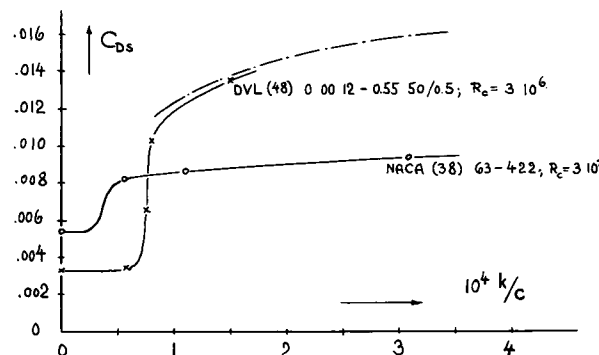


Figure 25. Drag coefficient of two laminar-type airfoils as a function of roughness grain size; (a) DVL (48) with uniform sand-type roughness at $R_c = 3 \cdot 10^6$, (b) NACA (38) with sand strip at nose, at $R_c = 3 \cdot 10^7$.

CHAPTER III — PRESSURE DRAG

In contradistinction to the skin-friction drag (which is a tangential force), pressure drag results from the distribution of forces normal to the body surface. This is also true for the induced drag; and every type of wave resistance (in supersonic flow as well as at the free surface of water) also acts upon the obstacle by way of pressure differentials. Only the viscous pressure drag — that is, pressure drag caused by boundary-layer separation — is treated, however, in this chapter.

1. AT VERY SMALL REYNOLDS NUMBERS

This region of the Reynolds number has been called that of “creeping motion”. Certainly, however, low R'numbers can also be produced by very small dimensions or in a very thin and/or highly viscous fluid. Theoretical functions and experimental results on bodies at small Reynolds numbers are plotted in illustrations later on, together with results at higher R'numbers.

Sphere and Disk. In the same manner as the skin-friction drag (Chapter II), the viscous pressure drag is proportional to the velocity, and not to the dynamic pressure — within the range of smallest Reynolds numbers. Entirely neglecting dynamic components, Stokes (1) has derived the resistance of the *sphere* from the viscous characteristics of the surrounding fluid; thus in non-dimensional form:

$$D/(\mu d V) = 3\pi; \quad \text{or} \quad C_{D_s} = 24/R_d \quad (1)$$

as plotted in figure 10. The drag of a *disk* (in a flow normal to its surface, reference 6), is somewhat smaller, because the wetted area is smaller than that of the *sphere* (considering equal diameter); thus for the *disk*:

$$D/(\mu d V) = 8; \quad \text{or} \quad C_{D_d} = 20.37/R_d \quad (2)$$

as plotted in figure 26. The term $D/\mu dV$ is non-dimensional; the coefficient C_{D_s} is based on frontal area $S_s = (d^2\pi/4)$. It can generally be said that these simple functions apply only at R_d below ≈ 1 .

Pressure Drag Caused by Friction. Within the considered range of extremely low Reynolds numbers, the flow pattern (3) around sphere or disk does not show any separation. To understand the very high drag coefficients, it is helpful to think of heavy oil as flowing medium. The particles closest to the body cling to its surface. Because of the viscous friction within the oil, the outer sheets are dragged by the inner ones, in the direction of the moving body. To maintain this movement of the particles against the body and in relation to each other, a positive pressure originates ahead of, and a negative one behind the body. The corresponding pressure drag is very much different from that due to flow separation as described later. Pressure differentials in viscous flow are the equivalent of skin friction; they are a resultant of the tangential shear forces along the forward and rear surfaces of the body. In the example of the disk (normal to the direction of flow), all of the resistance is necessarily due to pressure. In the case of the sphere, reference 6 indicates that at the very low Reynolds numbers considered, $1/3$ of the drag is due to pressure differentials, while $2/3$ directly correspond to tangential friction. Comparing the disk in normal flow to that in tangential flow (equation 2 in Chapter II), it is found that the “normal” drag is only one and a half times that of the “tangential” value.

Stagnation Pressure. Corresponding to the described flow mechanism, the pressure at the stagnation point is much higher, in the range of low Reynolds numbers, than the dynamic pressure $q = 0.5 \rho V^2$. For blunt-nosed bodies, this so-called Barker effect (4) gives approximately the pressure ratio

$$C_{p_{stag}} = \Delta p_{stag}/(0.5 \rho V^2) = 1 + (6/R_d) \quad (3)$$

where R_d is based on diameter or thickness of the respective body. At $R_d = 0.1$, for instance, Δp_{stag} is in the order of 60 times the dynamic pressure.

Floating Dust. Figure 10 also contains some drag

coefficients determined on tiny air bubbles rising through some sort of oil. It is surprising that (at very low Reynolds numbers) such bubbles have almost the same hydrodynamic properties as solid bodies. Fog droplets floating in air, may also be expected to have similar drag coefficients. Average representative sizes of airborne solids, quoted from (5), are tabulated on this page. Considering as an example, a fog droplet with a diameter of 1 mil, at a sinking speed of 4 ft/min, its Reynolds number is found to be smaller than 0.1; its drag coefficient is higher than 100, as seen in figure 10. Employing Stoke's function (equation 1), the sinking speed of the listed particles is found to be

$$V \approx d^2 (\gamma_{\text{part}} - \gamma_{\text{air}}) / 18 \mu \quad (4)$$

with γ_{part} = weight density of the particle. Neglecting the small quantity γ_{air} , and assuming γ_{part} to be equal to that of water ($\approx 62 \text{ lb/ft}^3$), the sinking speed in standard sea-level atmosphere is approximately given by

$$V \approx 4(d_{\text{mil}})^2 \quad (\text{ft/min}) \quad (5)$$

This speed is also the minimum velocity of the air required in upward direction, to keep the fog droplets "permanently" suspended.

TYPE PARTICLES	DIAMETER	SINKING SPEED
SMOKE PARTICLES	0.1	0.1 inch/hour
ATMOSPHERIC DUST	0.1	0.1 inch/hour
INDUSTRIAL DUST	5	2 inch/min
FOG DROPLETS	20	2 feet/min
PLANT POLLEN	30	5 feet/min
AV. RAIN DROPS	1000	6 feet/sec
DIAMETER IN MICRONS; 1 MICRON = 1/1000 mm = 1/25,000 INCH		

TABLE, listing average sizes and sinking speeds (roughly picked from reference 5) of smoke-, fog- and other particles floating in air.

In Two-Dimensional Flow. As pointed out by Stokes and Lamb (6), analysis of resistance in two-dimensional viscous flow is possible only if certain dynamic terms are taken into account. For symmetrical elliptical cylinders in such flow, the drag coefficient on frontal area is

$$C_{D_*} = \frac{8 \pi / R_h}{[c/(c+h)] + 1.5 - 2.3 \log R_*} \quad (6)$$

where h = height, c = length of cylinder axis in direction of flow and $R_* = V 0.5 (h+c)/\sqrt{\nu}$. For the circular cylinder, $c = h$ and $0.5 (h+c) = d$; therefore:

$$C_{D_*} = \frac{10.9/R_d}{0.87 - \log R_d} \quad (7)$$

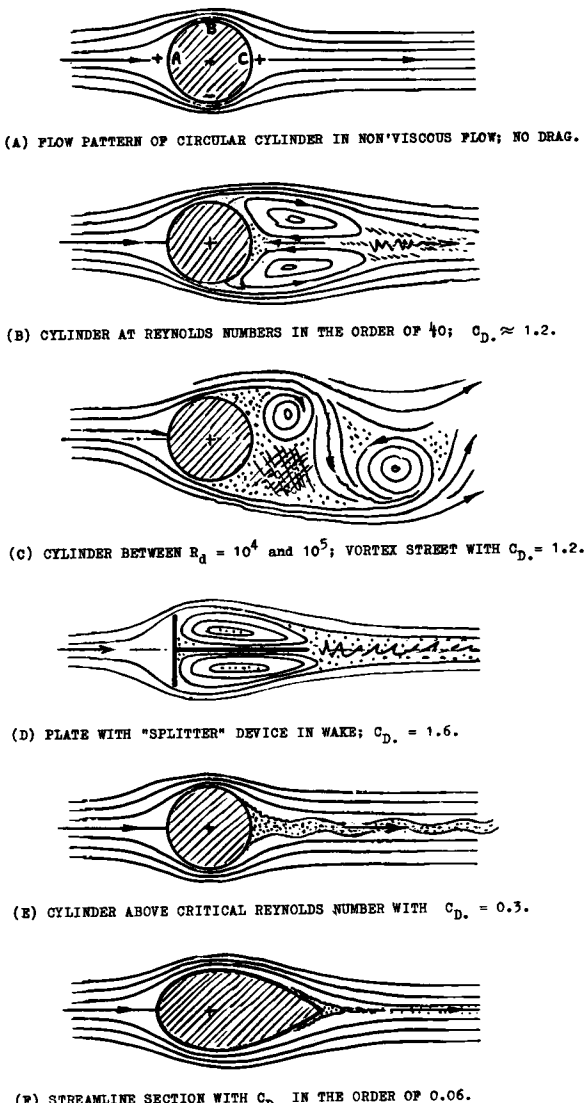


Figure 1. Theoretical and actual flow pattern of two-dimensional bodies.

A corresponding curve is plotted in figure 12 together with experimental results. — For a plate (in normal flow) the "chord" c is zero. Referring the Reynolds number to the height h and with $\log(0.5 R_h) = \log R_d - 0.7$; the coefficient of the plate in two-dimensional flow is

$$C_{D_*} = \frac{10.9/R_h}{0.96 - \log R_h} \quad (8)$$

At extremely small Reynolds numbers, the term $(C_{D_*} \times R_h)$ tends to be proportional to $(1/\log R_h)$. As can be seen in figures 10, 12, 26, these drag coefficients are smaller than those of the corresponding three-dimensional bodies. In three dimensions, a volume of fluid is evidently affected by the viscous forces which, in relation to the frontal area of the body, is larger than in two dimensions.

Intermediate Reynolds Numbers. Above $R \approx 1$, the dynamic forces of the fluid can no longer be neglected. Already below $R = 10$, the flow pattern is, therefore, unsymmetrical in fore- and aft direction; a stationary separation prevails behind the body (3), similar to that as shown in figure 1,b for $R_d = 50$. Above $R = 50$ or = 100, the dynamic forces are predominant over the viscous forces to such an extent as to cause and to maintain the periodic shedding of vortices behind blunt bodies (as in figure 1,c) at a non-dimensional frequency which increases steadily with the Reynolds number. The frequency-indicating "Strouhal number" (see later) then reaches a more or less constant level in the vicinity of $R = 10^3$. Decreasing viscosity and increasing dynamic forces finally produce a constant flow pattern (above $R \approx 10^4$) to be described in the next section.

2. MECHANISM OF FLOW SEPARATION

Within the range of subsonic speeds, non-viscous fluid-dynamic theory expects the flow to close-in behind an obstacle, without any losses. Such flow pattern is illustrated in figure 1,a for the circular cylinder. Positive pressures at the front of the cylinder are counterbalanced by positive pressures of equal magnitude on the rear; the resulting drag is zero. Real flow patterns are different, however.

- ¶(1) Stokes, Trans Cambridge Phil.Soc. 1850 p.8.
- ¶(3) Spheres and cylinders in viscous flow:
a) Vortex System of Sphere, ARC RM 1531 (1932).
b) Flow Past Circular Cylinder, ARC RM 917 (1924).
c) Möller, Hydrodynamic Experiments on the Sphere, Physikalische Ztschr. 1938 p.57.
d) Homann, Viscosity in Flow of Cylinder and Sphere, Forsch'g Ingenieurw'n 1936, 1 and 2; NACA T Memo 1334.
- ¶(4) Barker, Proceedings Roy.Soc.London Vol 101 (1922) p.435; see also Macmillan, Viscous Effects on Pitot Tubes, J'l Roy.Aeron'l Soc. 1954 p.570.
- ¶(5) Data by American Air Filter Co. quoted in Woods "Fan Engineering", by Woods Colchester (England) 1952.
- ¶(6) Lamb, Hydrodynamics. A recent treatment of flow past plates and cylinders in viscous flow is by Tomotika and Aoi in Quart. J'l Appl'd Math's 1950, 1951 and 1953.
- ¶(7) Prandtl, Führer durch Strömungslehre (1941); "Essentials of Fluid Dynamics", New York City 1952. Boundary-layer theory, "Fluid Motion at Low Viscosity", Verhandlungen Internat'l Math.Congress Heidelberg 1904.
- ¶(8) Pressure Distribution of Circular Cylinders:
a) Fage and Falkner, ARC RM 1369 (1931).
b) Konstantinov, Influence of Reynolds Number on Cavitation Flow, Izvest.Akad.SSSR, Otdelenie Tekhn.Nauk 1946 p.1355; Trans'l TMB 233.
c) Hoerner, Fieseler Wasserkanal Bericht No. 2 (1939).
d) Ermisch, Abhandl'g Aerody.Inst. TH Aachen No. 6.
e) Flachsbarth, in Handb'k Exp.Ph.Wien-Harms IV,2.
f) Dryden, BOS Journal of Research Rpt. 221 1930.

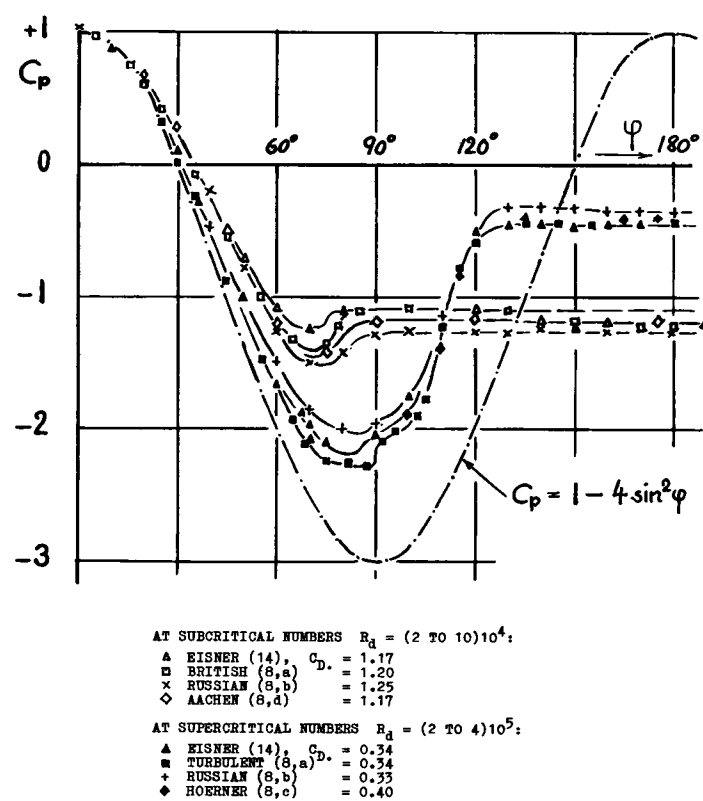


Figure 2. Pressure distribution around the circumference of circular cylinders (tested between walls).

Boundary-Layer Theory. The conception of the boundary-layer theory by Prandtl in 1904 (7) opened the way to theoretical and experimental study of drag and lift. According to this theory, the viscosity of the air is to be considered only within a limited sheet of fluid adjacent to the body surface. Outside this "boundary layer", considering the motion of the air particles against each other, viscosity does not have any noticeable effect. The first effect of the boundary layer is to shift the surrounding potential flow somewhat further outward, corresponding to its displacement thickness (see in Chapter II). Generally, this effect may be unimportant, however, in comparison to the effect which the potential flow, in turn, exerts upon the boundary layer.

Pressure Distribution. Figure 2 presents the pressure distribution around circular cylinders (in flow normal to the axis). The pressure decreases between stagnation "point" (at $\varphi = 0^\circ$) and maximum thickness (at $\varphi = 90^\circ$) from $C_p = +1$ to negative values of appreciable magnitude. If at all, the boundary layer is only favorably affected by the corresponding negative pressure gradient. Between $\varphi = 90^\circ$ and the "rear stagnation point" (at $\varphi = 180^\circ$), potential theory expects full recovery of the static pressure to $C_p = +1$. This does not come

true, however; not only because of the momentum deficiency of the boundary layer, but above all because of a basic change of the flow pattern by way of separation.

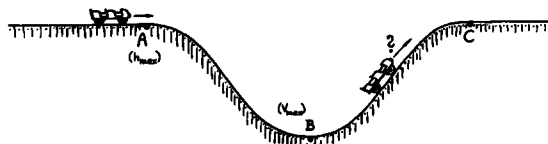


Figure 3. Roller-coaster-car analogy of boundary-layer.

Boundary-Layer Mechanism. Prandtl (7) compares the task of the boundary layer in the described conditions to that of a mechanical ball. In place of the ball, we will consider a roller-coaster car (as found in amusement parks). Such a car may start rolling at point "A" in figure 3, moving down the tracks. During this period, potential energy (corresponding to the elevation of point "A" relative to "B") is transformed into kinetic energy (velocity at "B"). Ascending the "hill" toward "C", kinetic energy is transformed back into potential energy. The roller-coaster car would regain the same elevation as it had at "A", provided that no energy was lost along the way — because of mechanical friction and other resistance. Since such losses cannot be avoided, every hump ("C") in a roller-coaster system has to be lower than the preceding level ("A"). The innermost fluid particles traveling within the boundary layer are in a position similar to that of the car under consideration. Because of viscous losses along the way from the stagnation point ("A" in figure 1,a) along the surface of the cylinder, passing through the point of maximum velocity (at "B"), the particles closest to the body's surface, do not have sufficient kinetic energy left to overcome the adverse (positive) pressure gradient along the rear of the body. The boundary particles, therefore, come momentarily to rest after exhausting their energy, somewhere between "B" and "C". Figure 4 shows what accordingly happens within the bound-

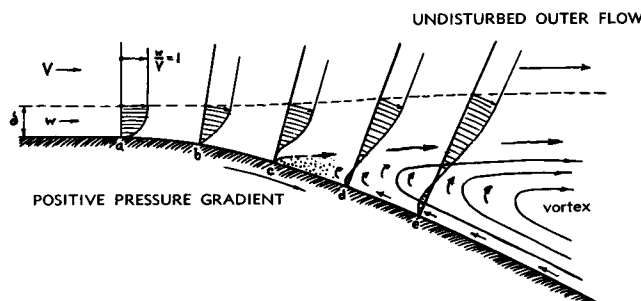


Figure 4. Velocity distribution and flow pattern of the boundary layer in a positive (adverse) pressure gradient, and including separation.

ary layer. At point "a", a layer is shown with a certain thickness and velocity distribution. At "b", the distribution is already somewhat deformed because of the pressure gradient imposed from the outer flow. At "c", the sheet closest to the wall, having the least momentum, is reduced to zero velocity. Subsequently, at "d" in figure 4, the direction of the motion is reversed; particles of the boundary layer are flowing against the direction of the undisturbed flow. These particles are accumulated, the thickness of the boundary layer is accordingly increased and presently the outer flow is separated from the surface of the body. Hence, a vortex is filling the resulting "dead" space, at point "e".

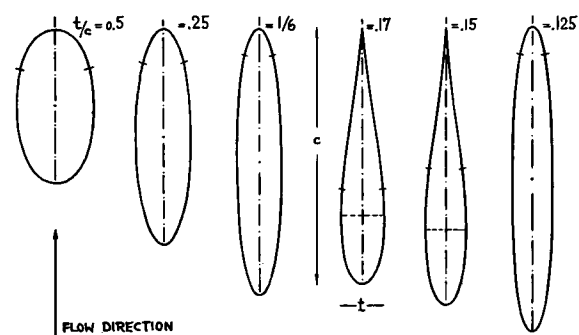


Figure 5. Laminar separation points on several two-dimensional elliptical and Joukowsky shapes, determined by theoretical analysis (9) of the boundary layer flow.

Point of Separation. For laminar boundary-layer flow, the point of separation is a function of body shape only; and it can be found by theoretical analysis (9). As examples, several symmetrical section shapes are shown in figure 5, having theoretical separation points as marked. However, after separation has taken place, the pressure distribution is, of course, different from the non-viscous distribution assumed as basis in the analysis. Actually, separation therefore starts somewhat ahead of the theoretical points. The circular cylinder, for example, has separation from points approximately 10° ahead of the maximum thickness (as shown in figure 1,b and as indicated by the pressure distribution in figure 2, for subcritical Reynolds numbers), while theory predicts separation points 20° aft of the maximum-thickness location. — For turbulent boundary-layer flow, separation cannot be predicted by available theoretical methods.

Drag Due to Separation. Figure 2 shows (among others) that the pressure at the rear side of the cylinders tested, is very much lower than predicted for non-viscous flow conditions. The resultant differential between positive pressures on the forward side and negative pressures at the rear side of the cylinder, represents the pressure drag. In

blunt or bluff and fat shapes, this type of drag is usually many times as high as the skin-friction drag. For example, for the circular cylinder a frictional drag coefficient (corresponding to wetted area and taking into account an average supersonic velocity past the sides) can roughly be assumed in the order of $C_{Df} \approx 0.01$. The tested coefficients $C_{Df} \approx 0.3$ or 0.4 at supercritical R'numbers, and $C_{Df} \approx 1.2$ at subcritical numbers, are thus between 30 and 120 times as high as the component that is *directly* due to tangential shear forces along the surface. Since in this example, viscosity (in the order of 0.01) is the cause of separation and pressure drag (in the order of 0.3, 0.4 or 1.2) — skin friction is realized to be a "trigger" that (in certain combinations of shape and attitude) can set in motion powerful mechanisms of drag.

3. VORTEX SYSTEMS

Upon towing a body through resting air, a more or less regular motion of the fluid particles is left in the "wake" of the obstacle. That is to say, as equivalent of the energy spent in moving the body against the originating drag, momentum is transferred to the fluid.

Vortex Types. In case of laminar friction, a certain volume of fluid particles is accelerated so that it follows the moving body. In a turbulent wake, this type of momentum transfer is combined with a component involved in the manifold motions of the fluid particles against each other. Such motions and other more orderly vortex formations are as follows:

¶(9) Analysis of boundary-layer separation:

a) Bussmann and Ulrich, Yearb'k D.Lufo 1943; see also in reference (10).

b) Howarth, elliptical section with $c/t = 6$, also as a function of lift coefficient, Proc. R'I Soc. A 1935 p. 558.

c) Schubauer and Klebanoff, Separation of Turbulent Boundary Layer, NACA Tech Rpt 1030 (1951).

¶(10) Schlichting, Grenzschichttheorie (1951); or "Boundary Layer Theory", McGraw-Hill 1955.

¶(11) Investigation of double-row vortex streets:

a) Strouhal, Widemann's Annalen der Physik 1878 p. 216.

b) Benard, Comptes Rendus 1908, 1913, 1925, 1926, 1928.

c) VonKármán and Rubach, Mechanism of Drag, Physikalische Zeitschrift 1912 p. 49.

d) The theoretical height ratio of the street (11,c) is $y/x = 0.283$. Vortex arrangements corresponding to this ratio are found at some small distance behind the street-producing bodies. As reported in various places, the height "y" increases, however, considerably further downstream, while the separation "x" essentially remains constant. This dimension is, therefore considered to be a better reference length than the height, in statistical analyses.

(a) Turbulence, equal to vortex formation without much of a regular pattern, originates intensively within every turbulent boundary layer and as a part of more regular systems behind many obstacles.

(b) Stationary vortices are formed in holes and gaps. More or less restricted to their place, they consume but little momentum furnished by the passing outer flow.

(c) A pair of "induced" vortices originates behind wings, as illustrated in Chapter VII. Such vortices can also be observed behind many "non-lifting" bodies as for instance behind fuselages or in the wake of automobiles.

(d) The vortex street to be discussed later on.

Vortex System Behind the Sphere. A vortex system originates behind spheres, first in a stationary form similar to that in figure 1,b — possibly beginning at $R_d \approx 10$. This system develops into an unstable condition as the Reynolds number is increased. Vortex packages are then carried away by the outer flow, in more or less irregular fashion. The line of separation on the surface of the sphere moves back and forth accordingly; and transversal forces appear in the sphere changing direction in time with the separation of the packages. As irregular and unstable as this mechanism may be, a predominant frequency has been found (3, a and c) in the order of $f = 2 V/d$ — approximately constant in the R'number range between 10^4 and 10^5 .

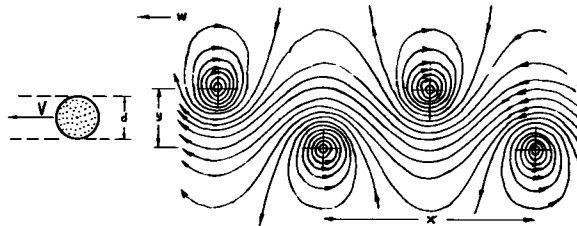


Figure 6. Theoretical pattern of the vortex street (7), seen from a system fixed to the cores. The body producing the street is moving away from it at $(V - w)$.

Vortex Street. A conspicuous type of vortex pattern is found in the wake of two-dimensional bodies, such as cylinders, plates or bluff rods. This comparatively stable system is called "double-row vortex trail" or "vortex street" (11,c). The two sides of the body alternate periodically in releasing a straight vortex. The "street" moves accordingly up and down and the flow pattern as illustrated in figures 1,c and 6, comes into existence. The oscillations are the physical source of the tones in an "Aeolian Harp" produced by wind (Aeolus was the Greek God of the wind). Similar tones can also be heard in telephone poles. — The whole system of the vortex street moves in the same direction as

the body, with the velocity w measured against the resting fluid. Based upon the length "x" of the street (11,d), the drag coefficient is

$$C_{Dx} = D / (q b x) = 1.6 (w/V) - 0.64(w/V)^2 \quad (10)$$

Unfortunately neither the velocity w nor the dimension x can be predicted by theory. Tests on circular cylinders (14), at Reynolds numbers below the critical, indicate $w/V = 1/6$ and $x/d \approx 4.5$. The drag coefficient, calculated as $C_{Dx} = 4.5$ times C_{Dx} (as per equation 10) agrees with the tested value (in the order of 1.15). Theory has thus demonstrated that the equivalent of the drag of bluff bodies such as the cylinder can entirely be contained in the vortex system. It is emphasized that the vortex street is a mechanism which leads to realistic drag coefficients, without introducing any quantitative viscosity values. An assumption must be made, however, concerning existence and dimensional characteristics of the vortex trail.

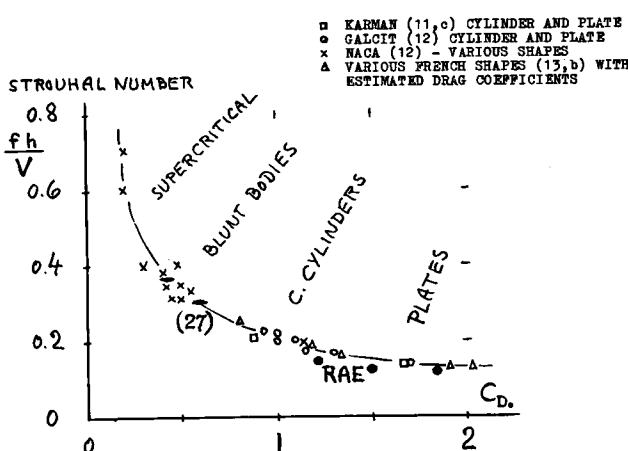


Figure 7. Strouhal number and drag coefficient of various shapes in essentially two-dimensional flow, at Reynolds numbers $> 10^3$.

Vortex Frequency. The number of vortices formed at one side of the "street" in the unit of time, is

$$f = (V - w)/x \quad (11)$$

In non-dimensional form, this frequency is presented by the so-called Strouhal number (11,a) :

$$"S" = f h/V \quad (12)$$

where h = height or thickness of the body producing the street. Available experimental results of essentially two-dimensional bodies (cylinders of various shapes as presented in references 12 and 13) are plotted in figure 7. For the range of Reynolds numbers under consideration (10^3 to 10^6), Strouhal number and drag coefficient seem to be coupled

with each other in a consistent manner. For the circular cylinder (with $C_{Dx} = 1.17$), for example, the dimensionless frequency is in the order of 0.19. The two-dimensional plate (with $C_{Dx} = 1.98$) has " S " = 0.13. Tests with plates and stalled airfoils (at $\alpha = 90^\circ$) of limited span (13,a) show " S " again to be roughly in the order of 0.2. This value correlates quite well with the reduced drag coefficient of such obstacles (in the order of 1.1). The empirical function in figure 7 can be expressed by

$$"S" = 0.21/C_{Dx}^{3/4} \quad (13)$$

Because of high viscosity, the vortex frequencies are lower, however, than indicated by this function, at Reynolds numbers below 10^3 .

General Street Characteristics. As pointed out in (12,a), characteristics of vortex streets are theoretically independent of the bodies producing them. Analysis leads to believe that (above $R = 10^3$) the term " S_x " = $(f x/U)$ is a universal constant, with

$$U = V + \Delta V = V \cdot \sqrt{1 - C_p} \quad (14)$$

indicating the velocity past the wake of the body. As a likely value of the constant, this author suggests

$$"S_x" = f x/U = 0.56 \quad (15)$$

Combining this value with equations 12 and 14, the longitudinal dimension of the vortex street is found to be

$$x/h = ("S_x"/"S") (U/V) = 0.56 \sqrt{1 - C_p} / "S"$$

Solving now equation 11 for w/V , the velocity ratio of the street is found to be

$$w/V = 1 - (x/h) "S" = 1 - 0.56 \sqrt{1 - C_p} / "S" \quad (17)$$

Equation 10 can then be used to determine the drag coefficient $C_{Dx} = (x/h) C_{Dx}$ of vortex-street-producing bodies, provided that " S " and C_p are known (tested). The procedure does not lead to reliable results, however, since w/V is a small differential. It appears that some simpler solution has still to be found. For the time being, the statistical results (particularly in figure 7) are recommended for practical application.

Splitter Plate. By placing a "splitter" plate on the center line of the vortex street, its motions can be considerably affected (12). The Strouhal number is reduced to the order of half the usual value; and the drag coefficient is decreased appreciably. In extreme conditions, a flow pattern may result similar to that in figure 1 (b and d), with a frequency reduced to zero. Some more experimen-

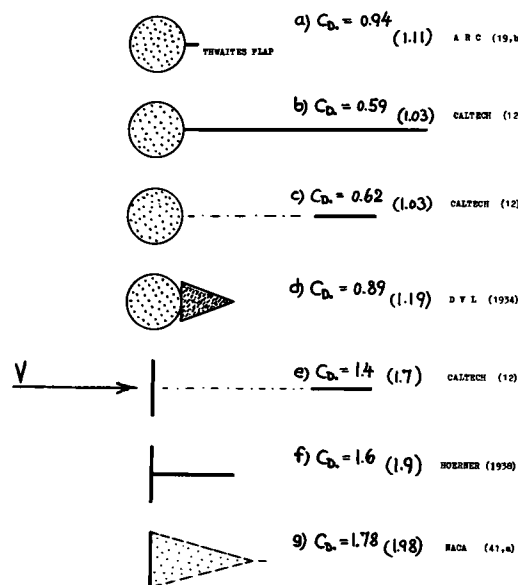
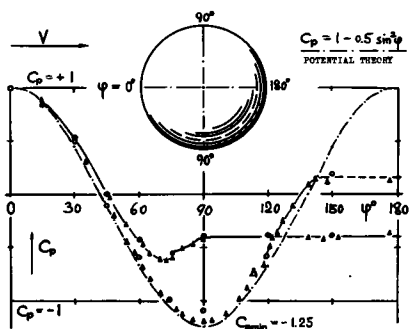


Figure 8. Influence of "splitter" plates (and similar devices) on the drag coefficient of vortex-street-producing shapes (tested between walls). The values in brackets are the drag coefficients without wake interference. The Reynolds numbers (on d or h) are between 10^4 and 10^5 .

tal results regarding the influence of plates and other obstructions interfering with the motion of the vortex street, are presented in figure 8. It should be noted that the drag coefficients obtained in such configurations do no longer follow the function as indicated in figure 7. With respect to the arrangements "d" and "g" in figure 8, we suggest that the reduction of the drag coefficient is not a matter of "streamlining". The wedges attached to the rear of cylinder and plate, respectively, simply reduce the motion of the vortex street.



- AVA (16,h) AT $R_d = 1.7 \cdot 10^5$; $C_{D_0} = 0.45$
- DITTO, BUT AT $R_d = 4.6 \cdot 10^5$; $C_{D_0} = 0.09$
- ▲ ARC (16,g) AT $R_d = 1.6 \cdot 10^5$; $C_{D_0} = 0.47$
- △ DITTO, BUT AT $R_d = 4.2 \cdot 10^5$; $C_{D_0} = 0.14$

Figure 9. Pressure distribution around the sphere.

4. CRITICAL REYNOLDS NUMBER

There are several different types of "critical" R' numbers in fluid dynamics; so for example the one indicating termination of low drag in laminar-type foil sections (Chapter VI), or the one indicating the permissible size of surface roughness (in Chapter V). Termination of laminar separation is the definition of critical Reynolds number as discussed in this section here.

Characteristics of Spheres are extensively reported in (16). As illustrated in figure 10, the sphere has a fairly constant drag coefficient (in the order of $C_{D_0} = 0.47$), within the R' -number range between 10^4 and 10^5 . In the neighborhood of $R_d = 4 \cdot 10^5$ or below this number, the coefficient decreases rapidly, however, to a level in the order of 0.1, which is almost 1/5 of that at Reynolds numbers below the critical. This phenomenon, first recognized by Eiffel and Prandtl, can be explained on the basis of boundary-layer theory, in the following manner.

Laminar Separation. As indicated in the pressure distribution (figure 9) for subcritical Reynolds number, the flow past the sphere separates shortly behind the point of minimum pressure. Figure 1,b shows the corresponding flow pattern of the circular cylinder (at low R' -number).

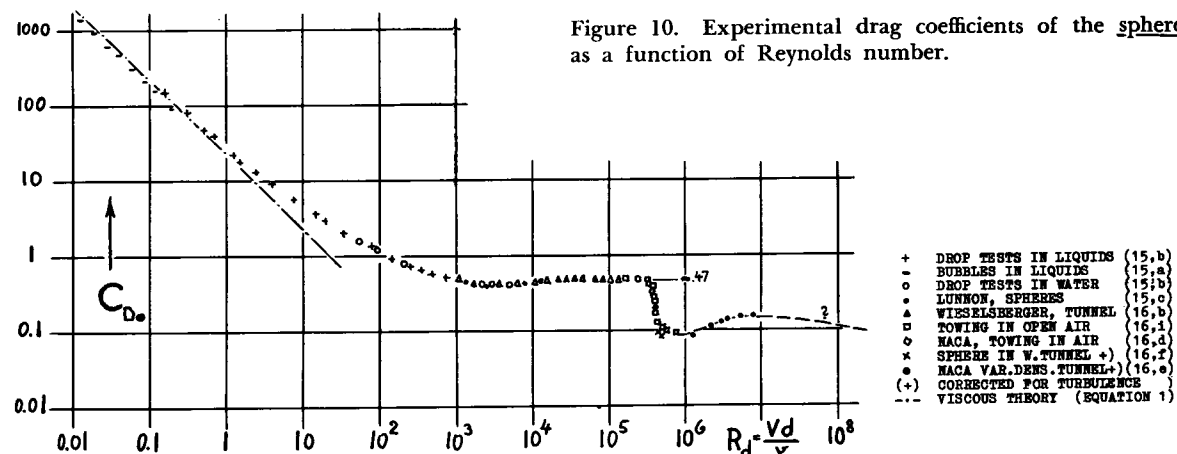
Turbulent B'Layer. Within every turbulent boundary layer, an exchange of mass and momentum takes place between each sheet of the layer and the adjoining ones. This exchange thus represents a continuous momentum transport from the outer flow toward the surface of the body. The resultant losses are higher than in a laminar layer. However, near the surface of the body, the turbulent b'layer carries much more momentum than the laminar layer (as can be seen in Chapter II). Approaching the critical Reynolds number, the b'layer begins to turn turbulent around the equator of the sphere. The sheets nearest to the surface are accordingly boosted in velocity and momentum; and they are therefore better enabled to flow against the positive pressure opposed to their movement along the rear of the body. Subsequently the flow attaches itself

¶ (12) Roshko (Caltech), analytical and experimental studies on drag and flow of two-dimensional bodies:

- NACA T.Notes 2913 and 3169 (1953 and 54).
- Turbulent Wakes, NACA Tech Rpt 1191 (1954).
- Bluff Bodies, Journal Aeron'l Sci. 1955 p.124.

¶ (13) Experimental vortex frequencies:

- Blenk-Fuchs-Liebers, Lufo 1935 p. 38.
- Publ.Sci.Techn.Ministère de l'Air No. 127 (1938).
- Nokkentved, Structural Shapes, Bygningsstatistiky Meddelelser Vol XII No. 3 (Danish, 1941).



to the surface as far as to $\varphi = 150$ or 160° . The drag decreases correspondingly (see in figure 11) to a supercritical coefficient in the order of 0.1 (around $R_d = 10^6$). Figure 9 shows that the supercritical pressure distribution is relatively close to that as predicted by potential theory.

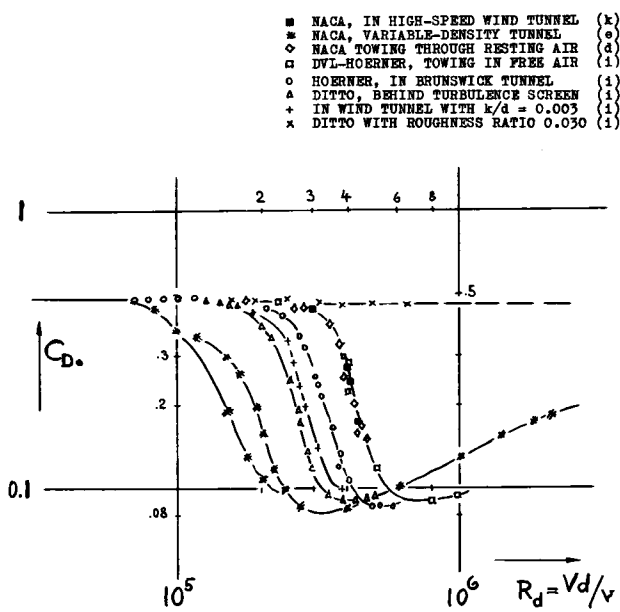


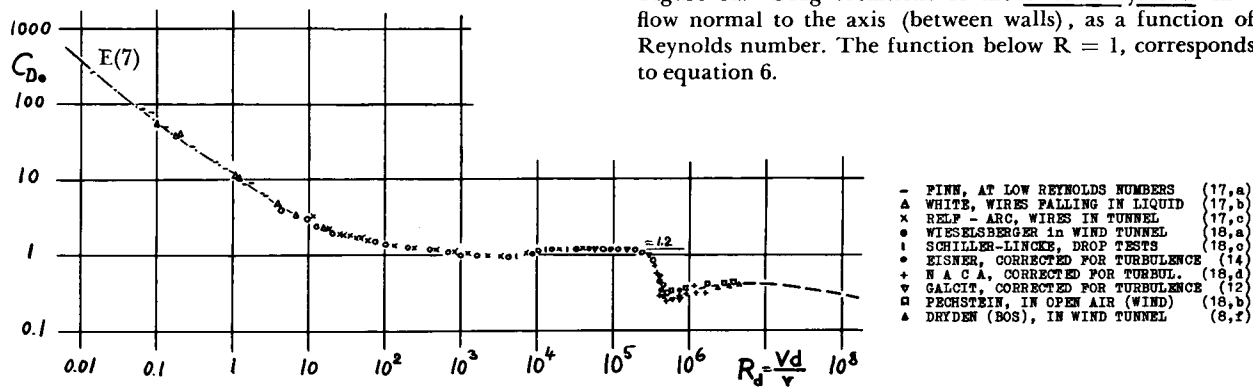
Figure 11. Presentation of typical experimental results on the drag coefficient of the sphere in the critical range of Reynolds number.

Surface-Roughness Effect. There are hundreds of experimental results available on spheres in the critical R' -number range. A small selection taken from (16) is plotted in figure 11. Surface roughness affects the critical Reynolds number appreciably. A plot of R_{dcrit}' of the sphere (arbitrarily defined for $C_{D_0} = 0.3$) against the relative roughness-grain size k/d is presented in Chapter II. To make such sphere results compatible with the results on plane walls (which are also plotted in that graph), the

critical number is based on the radius r (rather than the diameter d). The influence of roughness is also demonstrated in figure 14 presenting the drag coefficient of circular cylinders having various degrees of surface roughness. The supercritical level of the coefficient rises appreciably as a function of the roughness parameter k/d , while the critical R' -number (defined by C_{D_0} half way between subcritical and supercritical level) decreases.

Stream Turbulence. An interesting and famous effect on the critical Reynolds number of round bodies is that of turbulent fluctuations in the wind-tunnel stream. As shown in figure 11 and as plotted in Chapter II, the critical Reynolds number decreases steadily as a function of the turbulent root-mean-square amplitude ratio (\bar{w}/V) contained in the fluid stream. As example of an extremely low number, $R_{dcrit} = 1.5 \cdot 10^5$ is reported from NACA's Variable-Density Tunnel, in its early status (16,e). Carefully designed tunnels show, on the other hand, values around $R_{dcrit} = 3.9 \cdot 10^5$; and values in the order of $4 \cdot 10^5$ were found in undisturbed resting air (16, d and i). The critical sphere numbers are thus suitable to indicate qualitatively the amount of boundary-layer-affecting turbulence present in a fluid stream. — Also the stiffness of the suspension of a sphere in the wind tunnel and mechanical vibrations (16,f), and even sound waves (16,i) have an effect upon critical Reynolds number and resistance of round bodies.

Circular Cylinder. The above-described boundary layer characteristics are identically or similarly found in circular cylinders exposed to a flow normal to their axis. Figure 2 presents the pressure distribution around the cylinder; figure 12 shows the function of the drag coefficient against Reynolds number. In the vicinity of $R_d = 3$ or 4 times 10^5 , the coefficient drops from ≈ 1.18 (in two-dimensional flow) to approximately 0.3. — Figure 13 presents the drag coefficients of other, more or less



rounded, essentially two-dimensional bodies (tested between walls). The critical number is a function of the boundary-layer history as it develops between stagnation point and the location of maximum thickness (or minimum pressure).

¶(14) Eisner, Cylinders in Water, Mitt.Pr.Versuchsanstalt Wasserbau Schiffbau Berlin, Heft 4 (1929).

¶(15) Drag characteristics of spheres in viscous flow:

a) Arnold, Air Bubbles, Philosoph'l Mag. 1911 p.755.
b) Schiller, Drop Tests With Spheres and Disks, Handbuch Exp.Physik Wien-Harms Vol IV,2; also in Ztschr't. Flugtech. Motorluftsch.1928 p.497.

c) Lunnon, Roy.Society A 118 (1928) p.680.

¶(16) Drag Characteristics of Spheres With and Without Turbulence:

a) Eiffel, in "Nouvelles Recherches Résistance de l'Air", Paris 1914 and 1920.
b) Ergebnisse AVA Göttingen Vol II (1923) and Vol IV (1932); also ZFM 1914 p.140.
c) Millikan and Klein Aircraft Engineering 1933 p.169.
d) NACA Tech Reports 185, 253, 342, 558 and 581.
e) Jacobs, In Variable-Density Tunnel, NACA T Note 312.
f) Wiselius, Netherl.Aeron.Inst.Rpt A.950 (1947).
g) British ARC, Spheres, RM 1725 and 1766 (1936).
h) Flachsbarth, Spheres, Physik.Ztschr.1927 p.461.

i) Hoerner, Influence of Reynolds number Turbulence Surface Roughness on Spheres, Lufo 1935 p.42; Trans'l NACA T Memo 777.

k) Robinson, High-Speed, J'l Aeron'l Sci. 1937 p.199.

l) NACA, Journal Aeron'l Sciences 1937 p.199.

¶(17) Drag of Circular Cylinders in Viscous Flow:

a) Finn, Journal Applied Physics 1953, p.771.
b) White, Wires, Proceedings Royal Society London 1946.
c) Relf, Resistance of Wires, ARC RM 102 (1914).
¶(18) Hydrodynamic Characteristics of Circular Cylinders:

a) Wieselsberger, Ergebnisse AVA Göttingen II (1923).
b) Pechstein, In Natural Wind, VDI Zeitschr. 1942 p.22.

c) Schiller and Linke, NACA Tech Memo 715.

d) Welsh, Flight Tests on Cylinders, NACA T Note 2941.

¶(19) Special tests on circular cylinders:

a) Fage and Warsap, Effects of Turbulence and Surface Roughness on Drag of Circular Cylinders, ARC RM 1283 (1929). The grain sizes were measured by the author from samples of the Nat.Phys.Lab.Teddington.

b) Circular Cylinders With "Thwaites Flap", ARC RM's 2611, 2787 and 2829.

5. DRAG OF ROUND BODIES

Origin and characteristics of viscous pressure drag have frequently been investigated, using sphere or circular cylinder as examples. The reason is that with these "simple" bodies, basic characteristics of pressure drag have first been determined — such as the triggering effect of the boundary layer, the phenomenon of flow separation, the critical Reynolds number of round bodies, and the influence of wind-tunnel turbulence.

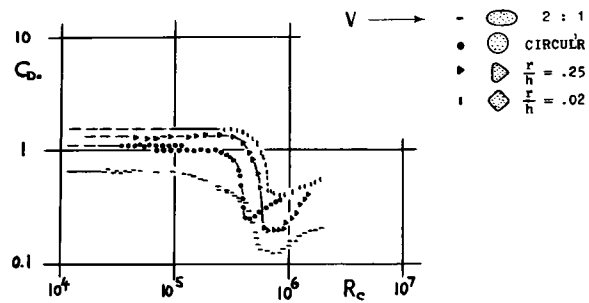


Figure 13. Drag coefficients of several cylinder shapes (tested between walls) in the critical Reynolds-number range; GALCIT (12).

The *Separation Point* in turbulent boundary layer cannot really be predicted by theory. There is some statistical information available, however. It seems that separation takes place when and if the form parameter of the boundary layer " H " = δ_v/δ reaches a certain critical order of magnitude. In the flow along a plane constant-pressure surface, this ratio is $H = 1 + (2/n)$ as can be derived from the b'layer functions in Chapter II. For $n = 7$, for example, $H = 1.29$ on a plane wall. Reference (9,c) reports $H = 2.7$ at the point of separation on some streamline shape. Velocity distribution and shape parameter are functions of pressure distribution along the body under consideration.

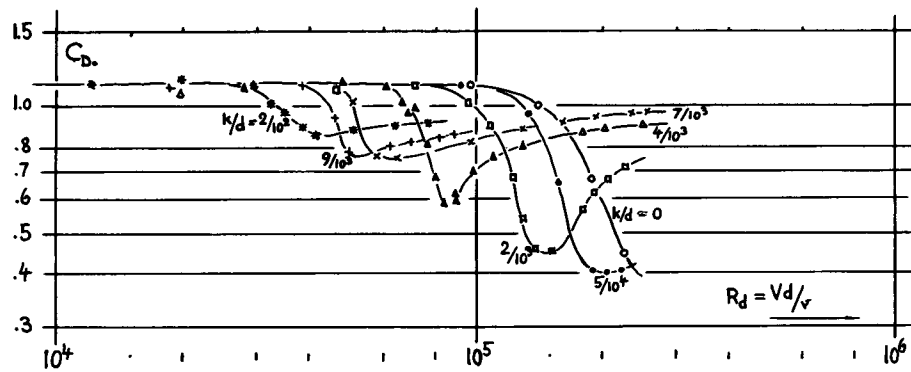


Figure 14. Drag coefficient of cylinders (19,a) having various degrees of surface roughness (sand-grain size "k" as against diameter "d").

Rear-Side Pressure. Flow pattern and pressure in the "dead" space (wake) behind a blunt body cannot really be predicted. Statistical evidence is as follows. At Reynolds numbers above the critical, the pressure distribution around the sphere shows a positive value in the vicinity of $\phi = 180^\circ$. Figure 15 shows correlation between this pressure and the drag coefficient. By a single pressure measurement on the rear side of the sphere, its drag can thus be estimated. This method (16, d and i) is sometimes used, instead of weighing the drag, to determine the critical R'number of a test sphere in the flow of wind tunnels. Figure 16 presents corresponding results for the circular cylinder. Between $C_{D_0} = 0.6$ and 0.3, there is evidently a discontinuity in the experimental function. It is suspected that a change in the pattern of the vortex street may be responsible for this result. In other words, the street may develop only weakly, or may not develop at all under conditions of attached flow (as illustrated in figure 1,e), so that the drag coefficient is smaller than it would be with freely developed vortex trail. For example, drag coefficients are presented in (8, b) which are sometimes on the upper and other times on the lower branch of the function in figure 16 — at overlapping values of the pressure coefficient.

Other Cylindrical Shapes. As seen in figure 13, cylindrical bodies reach a minimum drag coefficient shortly above the critical Reynolds number. As mentioned in connection with figure 16, there is probably reduced vortex activity in this phase. Tests of all these shapes have not been extended very far into the range of higher Reynolds numbers. One general prediction can be made, however. Resistance is evidently a function of the momentum losses which the boundary layer encounters along the way from the stagnation point to the rear of the body. The pressure drag is, in other words, related to the skin-friction drag. The observed increase of cylinder-drag coefficients above $R_d = 10^6$, corresponds to the increase of the frictional coefficient along one of the transition lines shown between $R = 10^5$ and 10^6 in Chapter II. At still higher R'numbers (above $R_d = 10^7$), another decrease of the drag coefficient can be predicted for the round bodies under consideration. This decrease corresponds to the declining course of the skin-friction coefficient in this range of the Reynolds number. It must be understood, however, that compressibility and/or roughness effects may be involved in practical applications where such high Reynolds numbers are obtained.

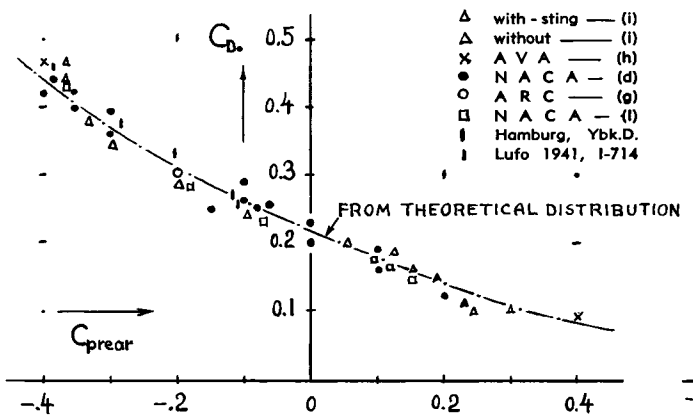


Figure 15. Correlation between drag and rear-side pressure of the sphere; reference (16).

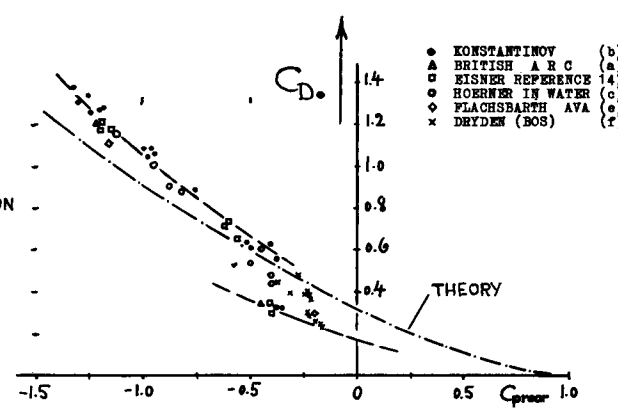


Figure 16. Correlation between drag and rear-side pressure of circular cylinders (8), between walls.

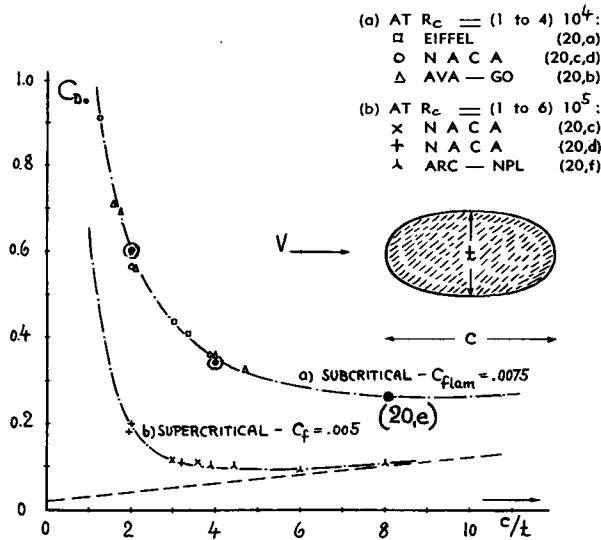


Figure 17. Drag coefficients of elliptical sections, (a) at subcritical R'numbers, (b) above the critical R'number.

Elliptical Sections are represented in figure 17. Equations have been developed similar to those in the "streamline" chapter — giving a suitable interpolation of the tested drag coefficients. At subcritical R'numbers,

$$C_{D_0} = 2 C_{f\text{lam}} (1 + c/t) + 1.1 (t/c) \quad (20)$$

Above the critical R'number range, the coefficient is approximately

$$C_{D_0} = C_{f\text{turb}} (4 + 2 (c/t) + 120 (t/c)^2) \quad (21)$$

Optimum chord/thickness ratios (giving minimum C_{D_0}) are in the order of 9 below, and of 5 above the critical variation of the drag coefficient as against R'number.

¶(20) Experimental results on elliptical cylinders:

- a) Eiffel in *Nouvelles Recherches*, Paris 1919.
- b) AVA Struts, Tech Berichte I (1917) and II (1918).
- c) NACA Tech Note 279 (1928) and Tech Rpt 289.
- d) Jacobs, Streamline Wires, NACA T.Note 480.
- e) Lindsey, Simple-Shape Cylinders, NACA T.Rpt 619.
- f) British ARC, RM 1599 (1934) and RM 1817 (1937).

¶(21) Circular cylinders inclined against flow:

- a) Relf and Powell, Tests of Smooth and Stranded Inclined Wires, ARC RM 307 (1917).
- b) Mustert, Lift and Drag, German Doct ZWB FB 1690.
- c) Kazakevich, Zh.Tekh.Fiz. 1951 p.1111; also Kuznetov, CAHI (Moscow) Rpt 98 (1931).
- d) Thews-Landweber-Plum, Towing Cables, TMB Rpts 418 (1936) and 666 (1948).
- e) Burnsall and Loftin, Pressure Distribution on Yawed Circular Cylinder in the Critical Reynolds Number Range, NACA T.Note 2463 (1951).

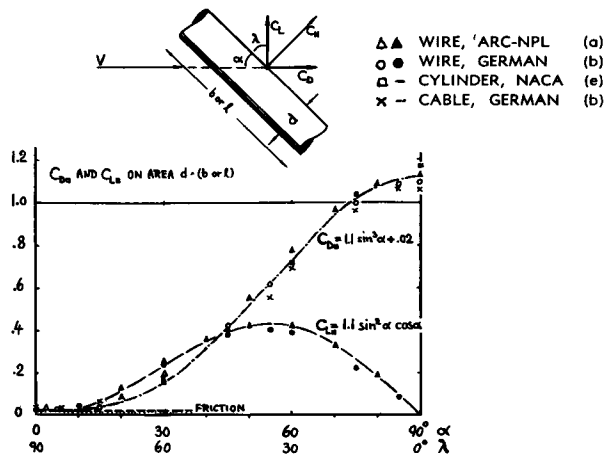


Figure 18. Drag (and lift) coefficients (on area "d" times axial length "l") of circular cylinders, wires and cables; inclined against the direction of flow — at Reynolds numbers below the critical. Reference (21).

Cross-Flow Principle. A principle with quite a number of practical applications (see Index) is very well illustrated by the inclined circular cylinder in figure 18. At an angle of attack " α ", flow pattern and fluid-dynamic pressure forces of such bodies only correspond to the velocity component (and the dynamic pressure) in the direction normal to their axis. Therefore (based on area $S_{\square} = dl$, where l = length along axis) :

$$C_{N_{\square}} = N/qS_{\square} = C_{D\text{basic}} (\sin^2 \alpha \text{ or } \cos^2 \lambda) \quad (22)$$

This force is then split up in the directions of drag and lift; hence:

$$C_{D_{\square}} = C_{D\text{basic}} (\sin^3 \alpha \text{ or } \cos^3 \lambda) \quad (23)$$

$$C_{L_{\square}} = C_{D\text{basic}} (\sin^2 \alpha \cos \alpha \text{ or } (\sin \lambda \cos^2 \lambda))$$

Experimental results in figure 18 on wires, cables and circular cylinders (at subcritical Reynolds numbers) confirm the prediction very well, after adding the frictional component $\Delta C_{D_{\square}} = \pi C_f$.

At Supercritical Reynolds Numbers (that is, with essentially attached flow pattern), cross-flow conditions are different from those at subcritical Reynolds numbers. The pressure drag evidently depends on the skin-frictional losses along the surface, in which the axial velocity component takes part. A rough rule seems to be that between 0 and 50° angle of sweep or yaw " λ ", the drag of a smooth cylinder in supercritical condition, is approximately constant, corresponding to a drag coefficient $C_{D_{\square}}$ on "d" times (b or 1) in the order of 0.2. Reference (21,e) also indicates that the critical speed of a

cylinder (at which the flow attaches to the rear side) decreases as the angle of yaw "λ" is increased; for example from $R_d = 3.6 \cdot 10^5$ for normal flow to $2.0 \cdot 10^5$ (still based on total speed "V") at $λ = 60^\circ$. In conclusion, the cross-flow principle cannot be applied to elements with attached flow pattern (as far as incompressible drag is concerned).

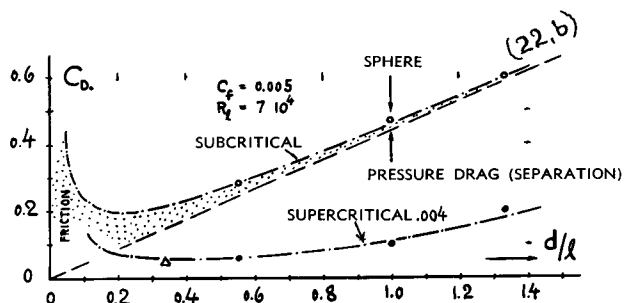


Figure 19. Drag coefficients of ellipsoidal bodies (22); (a) at a subcritical Reynolds number $R'_\lambda = 7 \cdot 10^4$; and (b) above transition, at R' -numbers approaching 10^6 .

Simple Ellipsoidal Bodies are represented in figure 19. The pressure drag caused by laminar separation (at subcritical Reynolds number) can be approximated by a component proportional to the thickness ratio (d/l). Applying the functions as given in the "streamline" chapter, the total drag coefficient in this condition can be approximated by

$$C_{D_0} = 0.44 (d/l) + 4 C_f (l/d) + 4 C_f (d/l)^{1/2} \quad (25)$$

Figure 19 also presents the minimum drag coefficients obtained shortly above the critical transition (see for illustration figures 10 and 11). It appears that equation 31 of the "streamline" chapter can be applied to give an approximate interpolation, using a friction-drag coefficient $C_f = 0.004$.

Half Bodies. A theoretical "half body" extends to infinity in one direction. Theory (23) predicts that such bodies, with a properly streamlined shape facing the fluid flow, do not have any drag. Positive as well as negative pressure differentials press upon the frontal area so that the resultant force is zero. To understand this result, the reader is invited to investigate the pressure distribution of the sphere — which gives a related result. Integrating the theoretical pressure distribution in figure 9 across the frontal area, it is found that the suction forces predominate so that the forebody drag coefficient is negative ($C_{D_0} = -0.125$). The phenomenon of zero or negative forebody drag is also found to some extent in real and viscous fluid flow. Figure 20 gives pressure drag coefficients evaluated from tests (25) on a series of rotationally symmetric body "noses". The first three shapes have a forebody drag

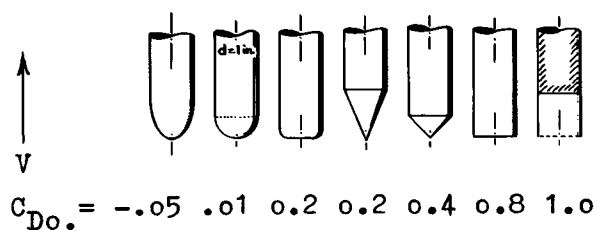


Figure 20. Coefficients indicating the forebody-pressure drag of a series of cylindrical bodies, evaluated from pressure distribution (25,e).

coefficient close to zero. As flow separation starts and grows in the less streamlined and bluffer shapes, the drag coefficient grows rapidly, however.

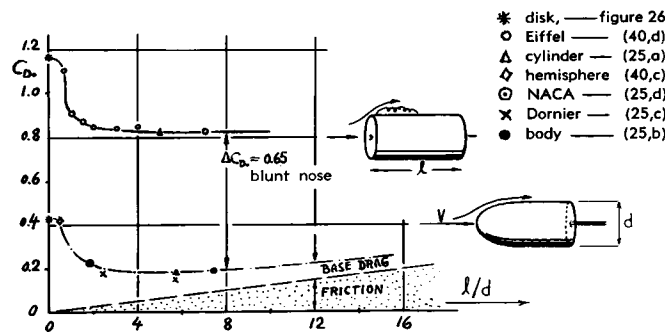


Figure 21. Drag coefficients of cylindrical bodies in axial flow, with blunt shape (in the upper part) and with rounded or streamlined head forms (lower part)—as a function of the fineness ratio l/d .

Parallel-Sided Shapes. Plotted in figure 21 are the drag coefficients of a number of cylindrical bodies in axial flow. Figure 22 shows corresponding results in two-dimensional flow. The drag of these shapes essentially consists of that of the forebody and the base drag originating at the blunt rear end. At zero length ratio, the coefficients of disk and plate are plotted, respectively. Two branches are seen in each graph, one for blunt head form or leading edge, respectively; and the other one representing the experimental results of rounded or streamline shapes.

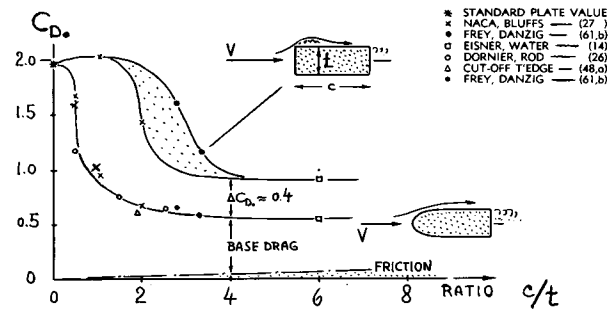


Figure 22. Drag coefficient of "rectangular" sections (tested between walls) with blunt leading edge (upper part) and with rounded shape (lower part), against length ratio.

It is seen that with the blunt forms too, the drag reduces appreciably upon reaching a certain minimum length ratio, which is in the order of $l/d = 1$ and $c/t = 2.5$, respectively. The separated flow reattaches in these cases at some distance aft of the blunt face. With well-rounded noses, the drag reduces quickly to comparatively low values. Some estimated functions are also plotted in the two graphs, indicating the drag contributions due to skin friction and base pressure.

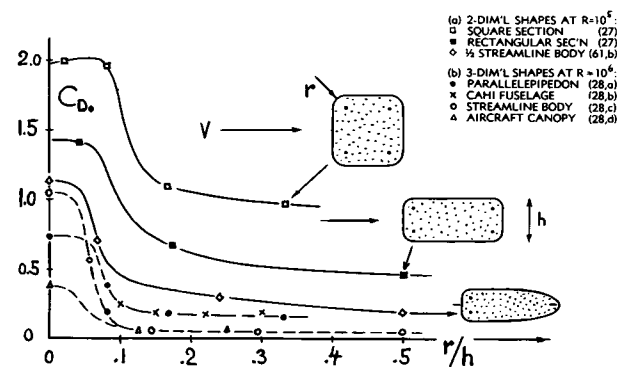


Figure 23. Influence of a rounding radius upon the drag coefficient of various "blunt" bodies (28).

Rounding Radius. "Streamlining" is a continuous variation of shape including (among others) the trend of keeping velocity- and pressure-distribution uniform and smooth. Rounding-off edges in blunt shapes, is a less perfect method of reducing drag. Figure 23 shows nevertheless, what can be accomplished in this manner in two-dimensional as well as in three-dimensional bodies. Above a certain, comparatively small ratio r/h or r/d , respectively, separation from the forward edges reduces progressively. The drag coefficient drops accordingly, between 50 and more than 90%, depending of course upon the shape of the afterbody. The critical

radius ratio (effecting the change in flow pattern) is to some degree a function of Reynolds number; the ratio reduces slowly as the R' -number is increased. As a suitable radius ratio, $r/h = 0.2$ can be recommended for two-dimensional conditions; while $r/d = 0.1$ seems to be adequate for three-dimensional bodies.

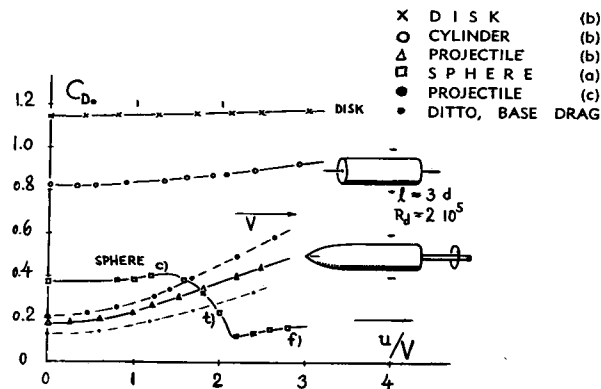


Figure 24. Drag coefficient of rotating bodies (30) as a function of the circumferential velocity ratio.

- ¶(22) Drag Coefficients of Ellipsoidal Bodies:
 - a) Riabouchinsky, Spheres and Ellipsoids, NACA Tech Note 44 (1921); not plotted in figure 19.
 - b) Ergebnisse AVA Göttingen Volume II (1923).
- ¶(23) Theoretical considerations on streamlining:
 - a) Zahm, Simple Quadrics, NACA T. Rpt 253, 1927.
 - b) Smith, Strut Forms, NACA T. Rpt 335, 1929.
- ¶(25) Tests on cylindrical shapes in axial flow:
 - a) Naumann, Cylinders, ZWB Tech Berichte 1943 p.278.
 - b) Schirmer, Airship Shapes, ZWB Report FB 1647.
 - c) Half Bodies on Fuselage, Dornier Report (1937).
 - d) Goodwin, Fuselage Nose Section, NACA RM L9J13.
 - e) Rouse and McNown, Cavitation Pressure Distribution of Head Forms, Iowa University Engg Bull.32 (1948).
- ¶(26) Dornier, Bluff Sections, reported in (41,g).
- ¶(27) Delany and Sorensen, Low-Speed Drag of Cylinders of Various Shapes, NACA T. Note 3038 (1953).
- ¶(28) Influence of rounding radius on drag:
 - a) Pawlowski, Wind Resistance of Automobiles (Basic Body) SAE Journal 1930, July p.5.
 - b) Russian Report on Drag of Fuselage, CAHI Rpt N.519.
 - c) Goethert, Drag Tests on Various Bodies and on Spheres at High Speeds, ZWB Tech Berichte 1944 p.94 and 377.
 - d) Robinson and Delano, Drag of Windshields (Canopies) in Wind Tunnel, NACA Tech Rpt 730 (1942).
- ¶(30) Drag characteristics of rotating bodies:
 - a) Wieselsberger, Physikal.Zeitschr. 1927 p.84.
 - b) Luthander and Rydberg, Rotating Sphere, Physikalische Zeitschrift 1935 p.552.
 - c) Sann, Drag- and Pressure Measurements on Rotating Projectiles ZWB Rpt FB 1048 (1939).

Rotating Bodies. There are a few experimental results available, indicating the drag of simple bodies as a function of their speed of rotation around an axis that is parallel to the direction of the fluid flow through which they move. The influence of rotation seems to be fourfold. First, the boundary layer is thickened because of the added speed component $u = (\text{circumferential velocity}) = d \pi n$, with $n = \text{number of revolutions per time unit}$. In streamline forebodies, this effect causes additional drag (see the projectile in figure 24). Second, the thickened boundary layer is likely to cause separation and additional form drag in the afterbody (see the sphere in supercritical condition at "f"). Third, on account of centrifugal forces in the rotating boundary layer, separation from the base appears to be increased (see the blunt cylinder in the graph). Fourth, the added velocity component affects the stability of the boundary layer, thus reducing the critical Reynolds number of sensitive bodies such

as the sphere. In this respect is tentatively:

$$\frac{R_{crit}}{R_{crit0}} = \sqrt{\frac{V^2}{V^2 + (k \cdot u)^2}} = \frac{1}{\sqrt{1 + (k \cdot u/V)^2}}$$

where $k < 1$ represents a suitable integration constant. This effect is demonstrated in figure 24 at (t); the critical Reynolds number of the sphere as tested is shifted from $R_{dcrit} = 2.9 \cdot 10^5$ (without rotation) to $2 \cdot 10^5$ as shown in the graph at $u/V \approx 1.8$; hence $k \approx 0.6$. The sphere also exhibits the centrifugal effect at "c". Note that the low sphere value $C_{D0} = 0.38$ in subcritical condition (instead of ≈ 0.47) is caused by type and size of the support in these tests by means of a rotating shaft.

The Human Body is similar in aerodynamic shape to a cylinder with a length ratio h/d between 4 and 7. Since human beings vary very much in size and proportions, selection of a reference area is difficult. Figure 25, therefore, presents the drag of an average man in the form of drag area D/q . The drag is predominantly a function of the projected frontal area in the various positions tested. Based on estimated areas, drag coefficients can be determined for the standing positions between $C_{D0} = 1.0$ and 1.3. Without clothing, the drag is between 5 and 10% less than listed.

How Fast a Man Falls. After bailing out of an airplane, and before releasing the parachute, the body of a man accelerates to a terminal velocity the magnitude of which can be derived from $W = D = q(D/q)$. Near sea level (where $q = 0.0024 \text{ lb sec}^2/\text{ft}^4$), the falling speed of a man with $W = 180 \text{ lb}$, is accordingly $V_{ft/sec} \approx 400 \sqrt{(D/q)}$. Employing the drag areas as listed in figure 25 (between 1.2 and 9.0 ft^2), speeds between 130 and 370 ft/sec are thus obtained. Terminal velocities are reported (32,c) between 150 and 180 ft/sec "near sea level"; without specification as to position and attitude during free fall. Another source (32,e) gives a drag area of 5 ft^2 for a "rolling and somersaulting" man. To give a certain scale to all these numbers, it is mentioned that the drag area of a typical fighter airplane is in the order of 6 ft^2 .

The Drag of Ski-Runners has been tested in wind tunnels. In upright position (going down a slope) a drag area $D/q = 5.5 \text{ ft}^2$ is found (32,a) in a smooth wooden model. A similar value ($\approx 6.5 \text{ ft}^2$) can be derived from (32,b) on the basis of an estimated frontal area in the order of 7 ft^2 . Both sources also give results on drag and lift of a ski-jumping man. In the typical "flying" position, with the body leaning forward against and onto the air, the lift area (including the contribution of the skis) is in the order of $L/q = 2.5 \text{ ft}^2$; the maximum lift/drag ratio is in the order of "1".

6. DRAG OF VARIOUS TYPES OF PLATES

All that is said in the preceding section about the critical effect of the boundary layer upon the drag of spheres, applies in principle to all sufficiently rounded bodies, such as the strut sections for instance in Chapter VI. On the other hand, bodies with sharp edges, such as disks and plates in a flow normal to their surfaces, do not show any critical drag decrease. The pressure gradient around the sharp edges would necessarily be extremely high for a flow pattern attached to the rear of a plate — that is, theoretically from $\Delta p/q = -\infty$ at the edge to +1 at the rear stagnation point. No boundary layer, whether laminar or turbulent, can follow the way around the edges of such plates.

Small R'Numbers. Figure 26 shows the drag coefficient of disks and square plates in normal flow, as a function of Reynolds number. Below $R_d = 100$, there is the regime of predominantly viscous flow as discussed in the beginning of this chapter. Approximately at $R_d = 300$, the drag coefficient of the disk shows a peak, as reported from two independent sources. Observation of the flow pattern (35) proves this peak to be due to a change in the pattern of the vortex system behind the body.

Turbulence Effect. Above $R_d = 1000$, the drag coefficient of disks (and other plates) is practically constant up to the highest Reynolds numbers ever tested (approaching 10^7). Because of this stability,

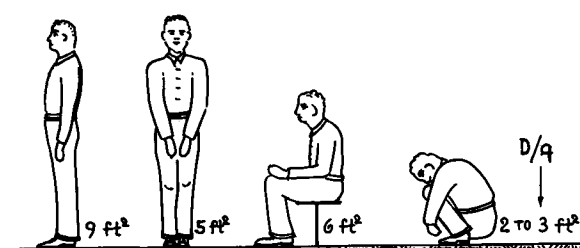
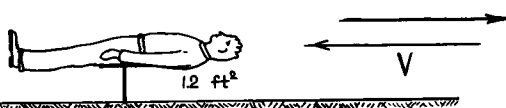
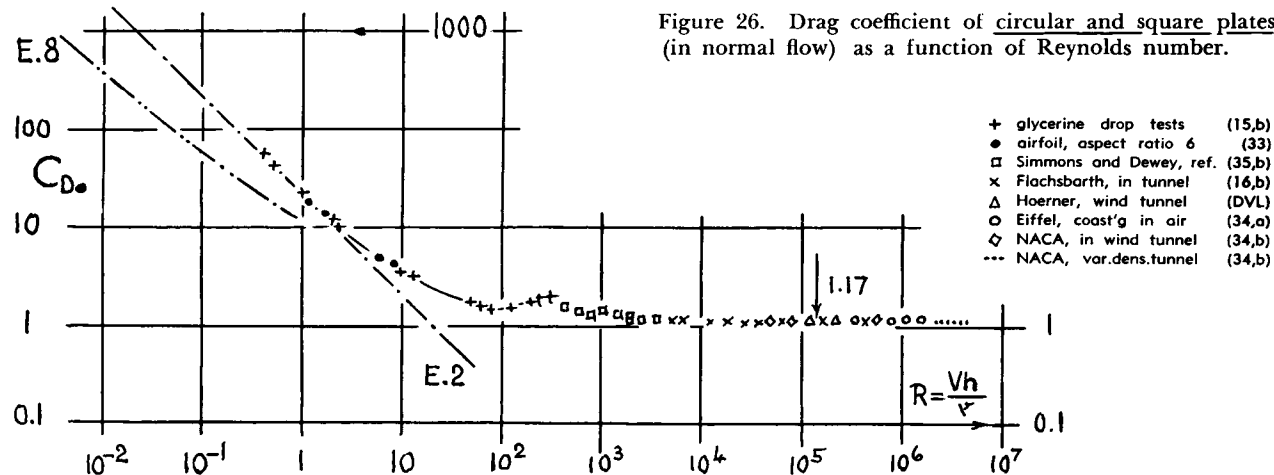


Figure 25. Drag areas (D/q in ft^2) of an average man in various positions, tested in a wind tunnel (31) at speeds between 100 and 200 ft/sec . Specifications: $W = 165 \text{ lb}$; $h = 5.9 \text{ ft}$; $\nabla = 2.6 \text{ ft}^3$; $S_{wet} = 20 \text{ ft}^2$.





the disk is sometimes employed in the calibration of air streams. Drag coefficients reported from numerous wind tunnels do not really show one and the same drag coefficient, however. One explanation for the discrepancies is the blocking effect in closed-type tunnel installations. Figure 27 shows another influence affecting the magnitude of the drag. The coefficient slowly increases with the degree of turbulence in the wind stream (36,b). The total increase as tested is in the order of 5%.

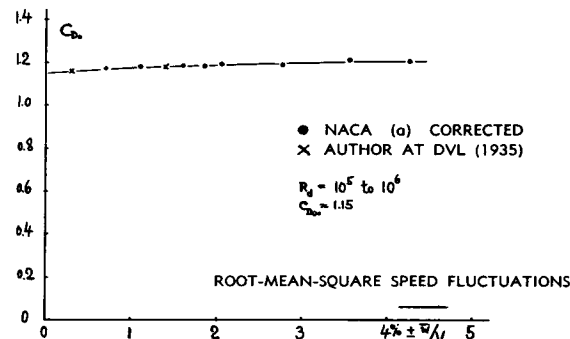


Figure 27. Influence of turbulence on disk drag (36).

"Aspect Ratio". Figure 28 shows how the drag of rectangular plates (and that of cylinders with limited length) varies with their height-to-span ratio h/b . It is surprising how far the effect of the side edges (ends or tips) extends toward the center portion of these bodies. Up to $b/h = 10$, the drag coefficient does not increase appreciably, and at $b/h = 30$, the coefficient is still considerably lower than that of the two-dimensional plate (between end plates). Considering the ends of a rectangular plate as three-dimensional, their dead-space pressure is evidently less negative than that of the "two-dimensional" center. Consequently, a flow of air is induced from the ends along the rear side of the plate and the average pressure is considerably increased. Another way of looking at this phenomenon is to assume that the motion of the vortex street is affected by the "ventilation" from the ends of the plate. The total variation of the drag coefficient is between 1.17 and ≈ 2.0 . Most of the change evidently takes place between $h/b = 0$ and $= 0.1$. Interpolation is suggested by

$$C_{D\bullet} = C_{D0\bullet} [1 - k(h/b)] \quad (29)$$

¶(31) Schmitt, Wind-Tunnel Investigation of Air Loads on Human Beings, TMB Rpt 892 (1954).

¶(32) Other investigations of the human body:

- a) Tani and Mitusi, Aerodynamics of Ski Jumping, Japanese "Kagaku" Vol 21 (1951) p.117.
- b) Straumann, Aerodynamic Tests on Ski Jumpers, Helvetica Physica Acta Vol 14 (1941) p.311.
- c) Terminal velocities of parachutists near sea level, quoted in Journal Aeron'l Sciences 1942 p.293.
- d) "How Fast a Man Falls", Aeroplane 57 (1939) p.445.
- e) Webster, Free Falls and Parachute Descents in the Standard Atmosphere, NACA Tech Note 1315 (1947).

¶(33) Tom and Swart, Airfoil at Extremely Low Speeds, Proceedings Royal Society A, Volume 141 p.761 (1934).

¶(34) Resistance of Plates and Disks:

- a) "Recherches Expérimentales Tour Eiffel", Paris 1907.
- b) Drag of Disks, NACA T.Notes 252 and 253.
- c) AVA Göttingen, Ergebnisse Volume IV (1932).
- d) Ring Plates, AVA Göttingen, Ergebnisse Volume II.
- e) Wick, Inclined Plate, NACA T.Note 3221 (1954).
- f) Smith and Whipple (MIT), Bodies Moving Through Still Air, Journal Aeron'l Sci. 1936 p.21.

¶(35) Flow pattern past plates and disks:

- a) Fage and Johansen, Behind Plates, ARC RM 1104 (1927); and Proc. Royal Society London Vol 116 (1927).
- b) Simmons and Dewey, Disks, ARC RM 1334 (1931).

¶(36) Influence of turbulence on drag of plates:

- a) Schubauer and Dryden, NACA Tech Rpt 546 (1935).
- b) This effect has been discussed by Prandtl (ZFM 1910 p.73) and by Joukowsky (Aérodynamique, Paris 1916).

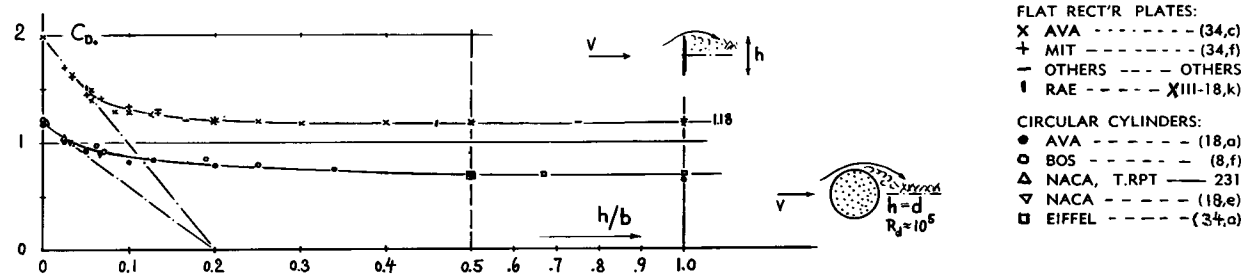


Figure 28. Drag coefficients of rectangular plates and circular cylinders as a function of their height (or diameter) to span ratio.

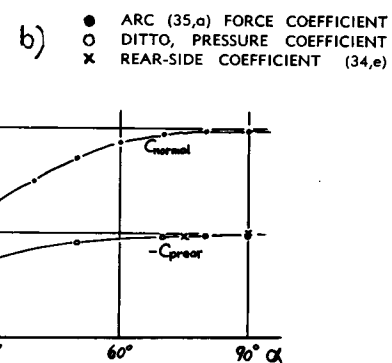
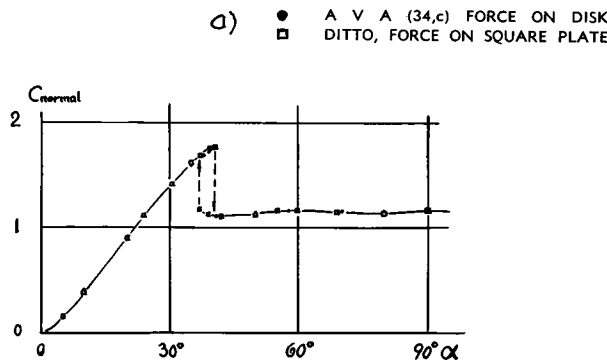
where C_{D_0} = coefficient in two-dimensional flow and "k" a constant in the order of 5.

Rear-Side Pressure. Plates in fluid flow normal to their surface, have highly negative pressures on their rear side. Because of wind-tunnel blocking, some discrepancies are found, however, with respect to the magnitude of the pressure coefficient as reported in various references (37). As likely values are suggested:

$$\begin{aligned} \text{in 2 dimensions } C_{D_0} &= 1.98; \quad C_{\text{prear}} = -1.13; \\ \text{in 3 dimensions } C_{D_0} &= 1.17; \quad C_{\text{prear}} = -0.42; \end{aligned}$$

Plates At An Angle. Upon tilting three-dimensional plates to an angle against the direction of flow, away from $\alpha = 90^\circ$, the normal-force coefficient as plotted in figure 29,a — remains approximately constant between $\Delta\alpha =$ plus and minus $\approx 45^\circ$. This observation seems to be the basis of an old theory of ship sailing. With $C_{\text{normal}} \approx 1.17 \approx \text{constant}$, the lateral component of the sail is $C_L = 1.17 \cos \alpha$, while the drag component is $C_D = 1.17 \sin \alpha$. This analysis can only be correct, of course, in the range of wind-against-sail angles above $\alpha = 45^\circ$ — as they were used in the old-time fully-rigged ships designed for sailing more or less in front of the trade winds.

Figure 29. Normal-force coefficients of plates having square or circular shape (left), and in two-dimensional condition (right), between tunnel walls.



Disk With Hole. As illustrated in figure 30, the drag of a disk (in pounds) is not reduced at first, upon cutting a hole in its center. Beyond $d_i/d_0 = 0.25$, the drag decreases, however, more or less steadily. Based upon the area of the resulting ring, the drag coefficient increases and reaches a limiting value which is identical to that of the rectangular plate with $b/h = \infty$, that is $C_{D_0} = 1.98$. In the wake behind the ring, an annular vortex street must be expected similar to that as observed within the wake of a cylindrical ring (17). Between $d_i/d_0 = 0.6$ and 0.8, evidently some change takes place in the flow pattern. Likely, the organization of the vortex system switches here from the three-dimensional to the two-dimensional type.

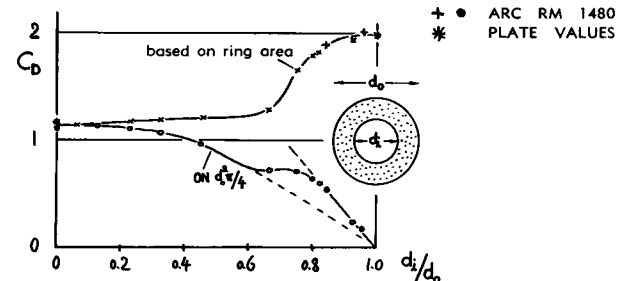


Figure 30. Drag coefficient of annular plates (rings), as reported in (34,d), at $R_{d0} = 10^5$.

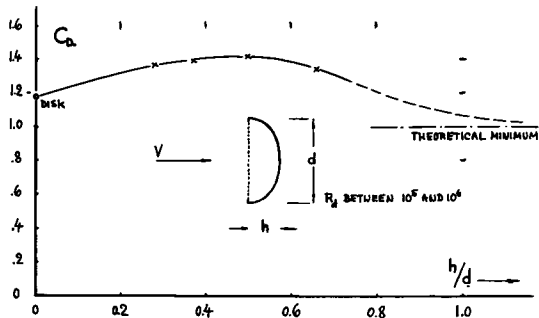


Fig. 31. Drag coefficient of sheet-metal "caps" (40,a) as a function of their height ratio.

Caps and Cups. As large as the drag coefficients of plates may be, there are other shapes exhibiting still higher values. Figure 31 shows the drag coefficient of open cup- or cap-like bodies (similar to parachute canopies). The maximum drag coefficient (on projected area) is obtained for h/d in the order of 0.5, a shape which is \approx hemispherical. Upon further increasing the height ratio, the rear side more and more changes into a wake "fairing". The drag coefficient is, therefore, expected to approach the theoretical minimum which corresponds to full stagnation pressure across the opening.

Figure 32 (near). Drag coefficients of various 3-dimensional bodies (40) at R' -numbers between 10^4 and 10^6 . Note: (•) tested on wind-tunnel floor.

7. DRAG OF WEDGES AND CONES

Figures 32 and 33 present shape and drag coefficient of a number of three- and two-dimensional bodies. All of these shapes have a more or less separated flow pattern; most of them have negative pressure on their rear side; and their drag coefficients are comparatively high.

Angle of Flow. To establish some order in the drag coefficients of various shapes, the geometrical angle is very useful, at which the flow is guided by the body's surface upon separating from its rear side. The flat plate, for example, has such an angle " ϵ " = 90° . A "fold" with a vertex angle of two times 45° , has a separation angle of 90° plus or minus 45° , depending upon the direction of the oncoming flow. Figure 34 demonstrates how the drag coefficient increases as a function of the shape angle. Two branches are found, of course; one for two-dimensional bodies (between walls) and another one for three-dimensional conditions. At " ϵ " = 0, parallel-sided round-nosed shapes have been used in the graph; a hallow, scoop-like body is plotted at 180° .

Figure 33 (right). Drag coefficients (41) of 2-dimensional shapes (between walls) at R between 10^4 and 10^6 . Note: (+) in subcritical flow.

- ¶(37) Information on rear-side pressure of plates:
 a) On disks and small-aspect-ratio plates see: NACA (36,
 a); AVA Ergebnisse IV; reference (40,f).
 b) On plates between walls see: (12), (35,a) and (40,f).
 ¶(40) Experimental results on three-dimensional bodies:
 a) Doetsch, Parachute Models, Lufo 1938 p.577.
 b) NACA, Cup Anemometer, Tech Rpt 513 (1935).
 c) AVA, Hemispherical Bodies, Ergebnisse IV (1932).
 d) Eiffel, Recherches a Tour Eiffel, Paris 1907.
 e) Hemispherical Cup at $R_d = 2 \cdot 10^5$, ARC RM 712 (1919).
 f) Irminger and Nokkentved, Elementary Bodies and Buildings, Copenhagen 1930 and 1936; Transl'n by Jarvis.
 ¶(41) Sections (tested between plates or walls):
 a) Lindsey, Simple Shapes, NACA T. Rpt 619 (1940).
 b) Junkers Wind-Tunnel, Report Ströte V.9609 (1940).
 c) Interference Between Struts, NACA T. Rpt 468 (1933).
 d) Delany-Sorensen, Various Shapes, NACA T. Note 3038.
 e) AVA Göttingen, Ergebnisse II (1923) and III (1926).
 f) Junkers Wind-Tunnel Result on Angle Profile.
 g) Reported by Barth, Zt. Flugwissen 1954 p.309.
 ¶(42) Free-streamline (cavitation) theory:
 a) Kirchhoff, Free Jet Theory, Crelle 1869 (see Lamb).
 b) Bobyleff, Russian Phys.-Chem. Society 1881 (see Lamb).
 c) Riabouchinsky-Plesset-Schafer, Journal Appl. Physics 1948
 p.934, and Review Modern Physics 1948 p.228.
 d) Reichardt, Laws of Cavities, German ZWB UM 6628.
 ¶(43) Neef, Dive Brakes, Fieseler Tunnel Rpt 22 (1941).

SHAPE	REF.	C_d
DISK		0.47
DISK	(c)	0.38
DISK	(c)	0.42
DISK	(e)	0.59
CUBE	(f)	0.80
WEDGE	(d)	0.50
SEPARATION		1.17
WEDGE	(c)	1.17
WEDGE	(b)	1.42
WEDGE	(a)	1.38
CUBE	(f)	1.05

SHAPE	REF.	C_d
DISK		1.17
DISK	(a)	1.20
DISK	(g)	1.16
DISK	(d)	1.60
CUBE	(e)	1.55
WEDGE	(a)	1.55
VORTEX STREET		1.98
WEDGE	(a)	2.00
WEDGE	(b)	2.30
CUBE	(a)	2.20
CUBE	(a)	2.05

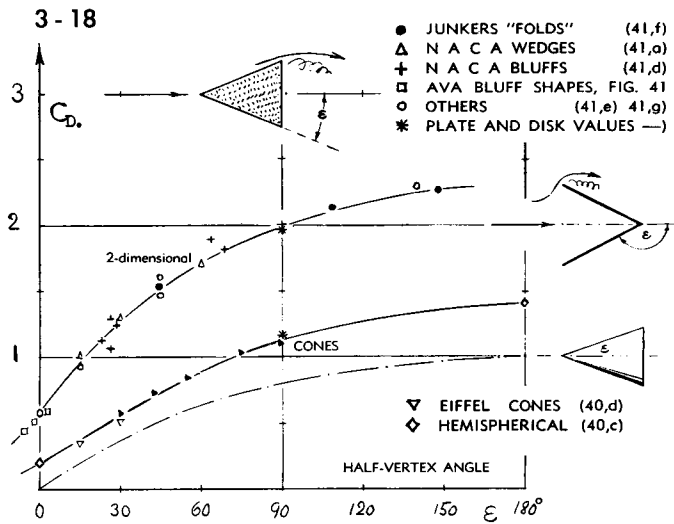


Figure 34. Drag coefficients of wedges, cones and similar shapes as a function of their half-vertex angle. At $\alpha = 90^\circ$ the shape is that of plates in normal flow; between 90 and 180° , "folds" and hollow cones are plotted with their opening against the oncoming stream.

Free-Streamline Theory. Theoretical solutions are existing (42), indicating the drag due to pressure on the front of "folds" and cones. The three-dimensional version is plotted in figure 34; and a certain relation is obvious between this curve (valid for $C_p = 0$) and the experimental function. The theory can be modified by including the negative pressure at the rear side (represented by " C_p ") ; thus:

$$C_{D_0} = C_{D_0 \bullet} (1 - C_p) \quad (31)$$

where C_{D_0} = coefficient for a rear-side pressure equal to ambient pressure ($C_p = 0$). Analyzing, for example the flat plate with $C_p = -1.0$ and with Kirchhoff's theoretical value of $C_{D_0} = 0.88$, equation 31 yields $C_{D_0} = 1.76$. The actually tested value is in the order of 2.0, however. The cavity concept (42) evidently does not represent correctly the vortex-street pattern of this type body. A better approach is by way of vortex-street theory as explained in section 3. Employing equation 13, the drag coefficient of two-dimensional wedges can be calculated on the basis of a tested value for the Strouhal number.

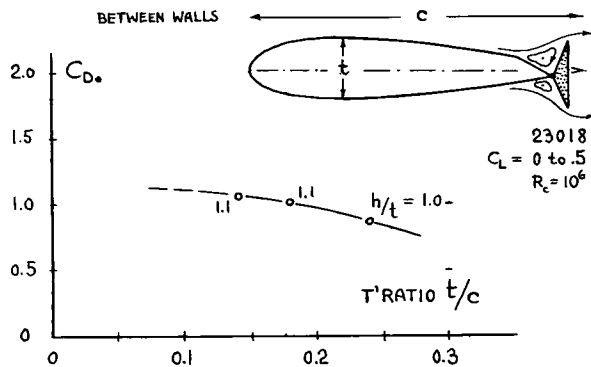


Figure 35. Drag coefficient of a dive-brake flap, deflected from the trailing edge of a wing section (43).

Brake Flap. Figure 35 shows an example where the principle of flow angle is involved. Because of the wing section placed in front of the brake flap, and on account of the stationary vortices in the corners between wing and flap, the angle at which the flow leaves the flap edges, is evidently reduced in comparison to the flow pattern of such plate-like shape in free flow. The drag coefficient decreases, therefore, considerably with the relative thickness of the wing section — from the value $C_{D_0} = 1.8$, taken for free-flow conditions from figure 36, down to approximately half of that value.

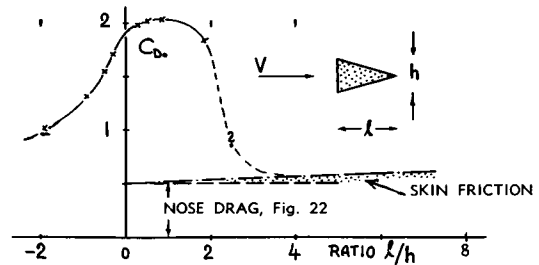
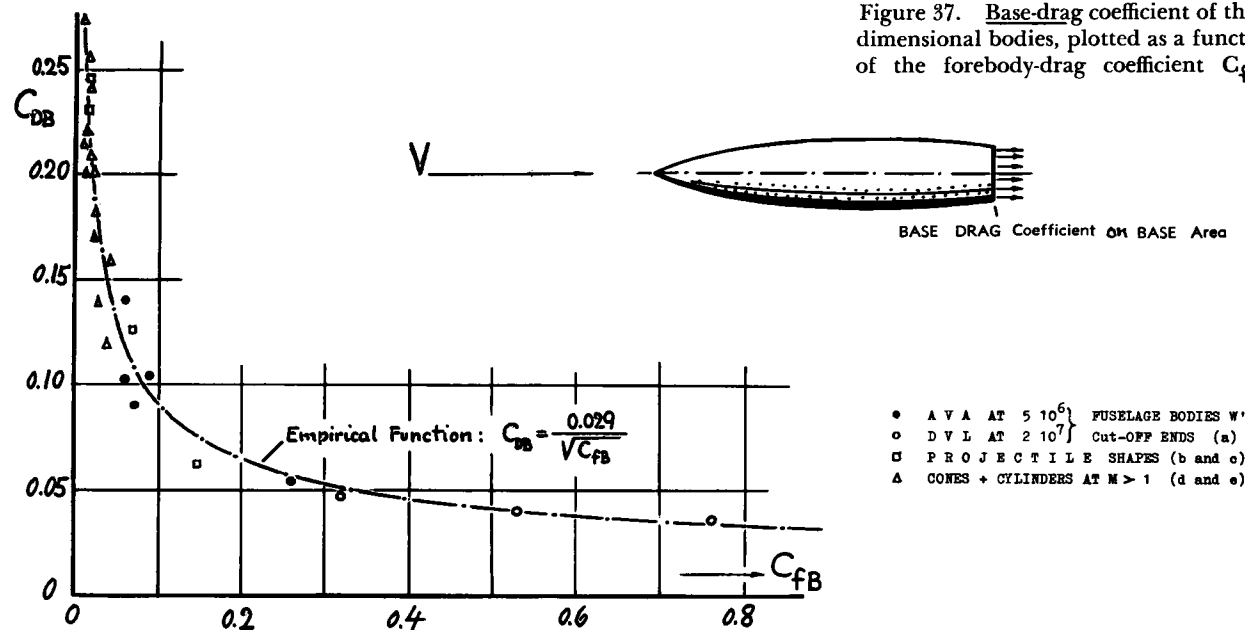


Figure 36. Drag coefficients of wedges, tested between walls, as a function of their length ratio (41,a).

Solid Wedges. Figure 36 presents the drag coefficient of wedge sections as a function of their length ratio l/h . In the range of negative l/h values, the effect of flow angle is seen again. A variation of the length into the wake space (at positive l/h values) slightly increases the drag, at first; unfavorable interference with the vortex street is suggested as explanation. At length ratios above 2, the flow should be expected, however, somehow to reattach itself to the wedge surface, at some distance aft of the forward edges. It is assumed that the drag coefficient then reduces to the comparatively low level indicated in the graph, estimated on the basis of figure 22.

8. BASE DRAG

At the base of projectiles, there originates a pressure drag which is consequently termed "base drag". In principle, the same type of drag is also found behind two-dimensional bodies such as airfoil sections, the trailing edges of which are thickened or cut off. It is possible (45) to correlate the various tested values of base drag with each other, by considering the influence of the boundary layer originating along the forebody.



(a) BASE DRAG OF 3-DIMENSIONAL BODIES

Jet-Pump Mechanism. Examining the flow pattern behind the base of a projectile, it is found to be similar to that of a jet pump. The "jet" (formed by the outer flow), placed like a tube around the space behind the base, mixes with the dead air and tries to pump it away. The static pressure at the base of the body reduces as a consequence.

"*Insulating*" Boundary Layer. Studying available pressure- or drag measurements, the base drag of projectiles is found to depend largely upon the length of the forebody, its surface conditions and the ratio of base- to body diameter. The boundary layer, arriving at the edge of the base, evidently serves more or less as an "insulating" sheet, placed between outer flow and "jet pump" effect, and the dead space behind the base. The effective dynamic pressure of the pump is, in other words, reduced because of boundary layer thickness. This thickness is proportional to the drag originating along the surface of the forebody. As predominant parameter of which the base drag is considered to be a function, we therefore select the drag coefficient

¶(45) Hoerner, Base Drag and Thick Trailing Edges, Journal Aeronautical Sciences 1950 p.622.

¶(46) Base drag on bodies of revolution:

a) Kosin-Lehmann, Fuselages, Yb'k D.Lufo 1942 p.I, 241.
b) Projectile model see reference (30,c).

c) Erdmann (Peenemünde), Drag and Pressure Distribution of Cones and Spheres, German ZWB Lilienthal Rpt 139/1 p.28.

d) Charters-Turetzki, Aberdeen Ball.Res.Lab. Rpt 653.
e) Chapman, Base Drag, NACA Tech Note 2137 (1950).

¶(48) Sections formed by cutting off from trailing edge:

a) AVA Göttingen, Ergebnisse Vol III (1926).
b) Okamoto, Aeron. Institute Tokyo University Rpt 131.
c) Swaty (DVL), 0018 Section, Yearbook D.Lufo 1940.
d) Smith-Schaeffer, Cut-Off 0012, NACA T.Note 2074.
e) Sargent, 0012 With Cut-Off TE, ARC RM 2209 (1942).

¶(49) Sections with thick trailing edges:

a) Engelhardt, Momentum Survey Behind Variable Trailing Edge, Aerodynamic Lab'y TH München Rpt 4/1944.
b) Drescher-Schwenk, In Water, AVA Rpt B 1944/J/17.
c) Barlow, Propeller Shanks, NACA T Rpt 852 (1946).
d) Dornier, "Square" Rods, quoted in (41,g).
e) Strut Sections, Junkers Tunnel Rpt S.1943/85.

¶(50) Wieghardt, Surface Imperfections, Yb'k D.Lufo 1943.

¶(51) Two-dimensional base-drag results at higher Mach numbers NACA RM L8B13, L50E19a and T.Note 3550.

$$C_{fB} = D_{fore} / (q S_B) = C_f S_{wet} / S_B \quad (33)$$

where C_{fB} denotes the "skin drag" of the forebody, meant to include any drag caused by roughness or protuberances. This analysis applies primarily to subsonic flow. A similar treatment of transonic and supersonic base drag is presented in the corresponding chapters.

Base Drag of Three-Dimensional Bodies. The available experiments on projectiles and "fuselages", plotted in figure 37, indicate approximately

$$C_{DB} = D / (q S_B) = 0.029 / \sqrt{C_{fB}} \quad (34)$$

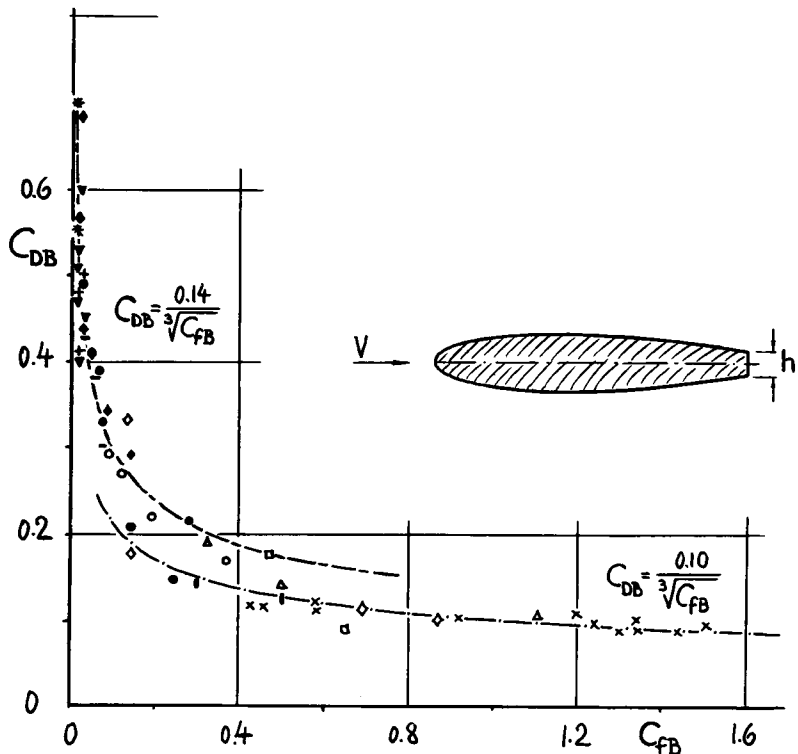


Figure 39. "Base" drag, originating behind the cut-off or thickened trailing edges of foil sections. Coefficients are defined in the text.

with "B" denoting the base. In the case of bodies with a base diameter smaller than that of the forebody, the mechanism of base drag may essentially be the same as with parallel-sided bodies. Referring the base drag to the maximum cross-section area of such bodies, and with forebody-drag coefficient $C_{fB} = C_{Df} \cdot (d/d_B)^2$, equation 34 is transformed into

$$\Delta C_{D_0} = D / (q S_0) = 0.029 \cdot (d_B/d)^3 / \sqrt{C_{Df}}. \quad (35)$$

with C_{Df} representing the forebody drag. Figure 38 shows corresponding results on a smooth fus-

elage body, the trailing end of which was cut off in steps. The fuselage of an average airplane may have a drag coefficient, however, much higher than that of such a smooth body of revolution — possibly in the order of $C_{D_0} = 0.15$, if accounting for surface irregularities and protuberances. For $d_B/d = 1$, equation 35 indicates a corresponding base drag in the order of $\Delta C_{D_0} = 0.09$. To accommodate the tail turret of a bomber, a ratio of $d_B/d = 0.5$ may be sufficient, however. The resulting base-drag coefficient in the order of less than 0.01, is comparatively small; in the order of some 6% of the fuselage drag.

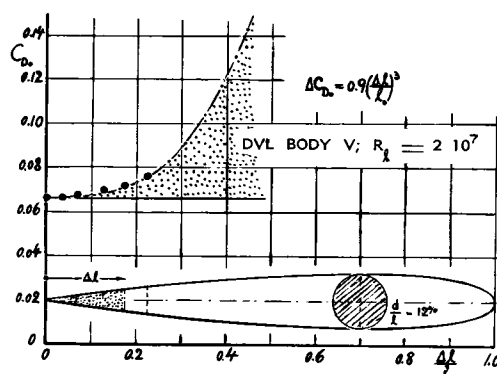


Figure 38. Drag coefficient of a streamline body, whose trailing end is cut off in steps (46,a). In calculating the function, the base diameter is assumed $d_B/d = 2 (\Delta L/L_0)$.

Effect of Boat-Tailing. Rounding or tapering the blunt end of a fuselage body affects the base drag only as far as a round edge is able to "pull" the flow somewhat into the space behind the base. In bodies with C_{fB} in the order of 0.5 and higher, the effect of rounding the cut-off end is expected to be hardly noticeable. In a similar way, the effect of "boat-tailing" the rear end of projectiles, depends upon the boundary-layer thickness and the employed shape of taper. By means of a boat tail, moderate in size ($d_B/d = 0.9$) and in angle of taper (in the order of 5° as against axis) it is possible somewhat to reduce the drag of projectiles. Reference (46,b) shows in such a case a reduction in the order of $\Delta C_{D_0} = -0.07$. For larger taper angles, or in cases where drag and boundary-layer thickness of the forebody are much larger, rather the maximum cross-section area of the body must be considered as "base" and the base drag be determined for the corresponding C_{fB} value (based upon the larger area).

(b) BASE DRAG IN 2-DIMENSIONAL SHAPES

By cutting off or thickening the trailing edge of a wing section, a "base" is formed, flow pattern and "jet-pump" mechanism of which is similar to that as outlined in the foregoing paragraphs for bodies of revolution. Figure 39 shows the available test points, plotted against the same forebody-drag coefficient as defined in equation 33.

Base Drag at Sheet-Metal Joints. Behind certain sharp-edged sheet-metal joints, as illustrated in Chapter V, flow pattern and "base" drag are similar to those at the blunt trailing edge of a wing. The drag of such sheet-metal joints naturally corresponds to the thickness of the boundary layer within which they are placed. Employing the analysis as given in Chapter V, and with the appropriate constant, the base-drag coefficient of sheet-metal joints is found to be

$$C_{D_0} = 0.18 \sqrt[3]{h/\delta} \quad (36)$$

where h denotes the height or thickness of the protruding sheet. The thickness " δ " of the turbulent boundary layer is given in Chapter II. From equations 18 and 19 of that chapter can be derived that

$$C_{fB} = (x/h) C_f = (x/h) 2 (\delta/x) = 0.2 \delta/h$$

Upon introducing $h/\delta = 0.2 C_{fB}$ into equation 36, the base-drag coefficient is found to be

$$C_{DB} = 0.1 \sqrt[3]{C_{fB}} \quad (38)$$

Drag Due to Blunt Trailing Edges. Most of the results in figure 39, indicating the base drag of airfoil sections with blunt trailing edges, show coefficients which are somewhat higher than according to equation 38; thus:

$$C_{DB} = 0.135 \sqrt[3]{C_{fB}} \quad (39)$$

Explanation is found in the flow pattern. Behind two-dimensional bodies with detached flow, we usually have the regulated pattern of the vortex street (figure 6). In the case of the sheet-metal joints, the up- and down movement of such a street is damped, however, or even suppressed by the presence of the wall along which the wake proceeds.

The base drag of the joints is consequently smaller than that of most of the foil sections. — It might be expected in streamline shapes, that the more or less negative base pressure would have an effect upon the pressure distribution of the forebody. Results of such shapes correlate well, however, with experimental points found in parallel-sided shapes (where the pressure distribution is not so much expected to be sensitive).

Profile-Drag Coefficient. The base-drag coefficients (equations 38 and 39) are converted into profile-drag coefficients by multiplying them with h/c :

$$\Delta C_{DS} = k (C_{DS0})^{1/3} \cdot (h/c)^{4/3} \quad (40)$$

where $k = 0.10$ or $= 0.14$, respectively. Figure 40 (as figure 39) shows a transition of the experimental points from one of the calculated curves to the other. Obviously, for small values of h , as long as the trailing edge is thinner than roughly one half the boundary-layer thickness, a regular vortex street does not originate. Results are also available (48, c and d), where vortex activity and base drag are seen to be reduced upon putting a symmetrical foil section at some angle of attack (so that $C_L \approx$ plus or minus 0.1). It is suggested that the vortex street loses stability in unsymmetrical conditions of flow.

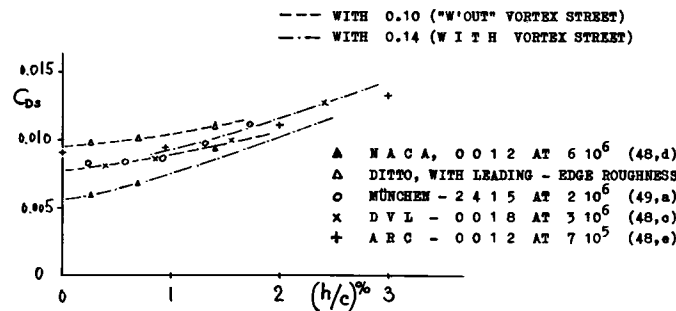


Figure 40. Drag increase of airfoil sections, due to cutting off or thickening the trailing edge.

Laminar Mixing. In supersonic experiments on slender shapes (described in the "transonic" and "supersonic" chapters), there is a marked difference between laminar and turbulent mixing along the wake. Pressure distributions favoring laminar flow are not likely to prevail, however, in ordinary subsonic shapes and at subsonic speeds. It seems that the presented material only represents turbulent mixing. There are also some results included in figure 37 obtained at supersonic (that is, transonic) Mach numbers; they obviously agree with the points corresponding to subsonic (incompressible) experiments. It is found, however, that the results in (51) at Mach numbers between 0.7 and 0.9 (and at mod-

erate R' numbers) correlate with the points in figure 39 only if assuming that their skin-friction drag is, at least to a larger part, laminar.

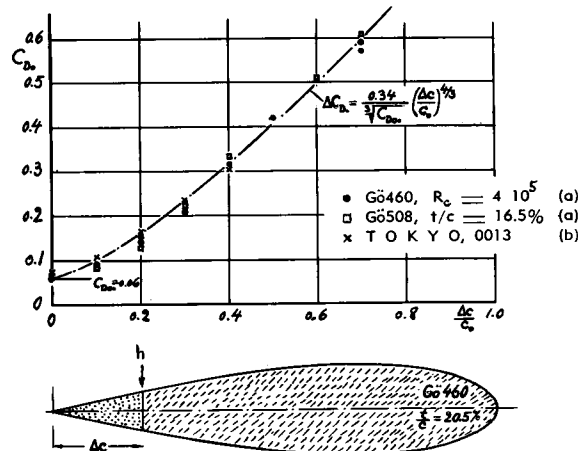


Figure 41. Drag coefficient of foil sections whose trailing edges are cut off in steps. References (48, a and b).

Cut-Off Trailing Edge. In figure 41, minimum drag coefficients are plotted of several airfoil sections the trailing edges of which were cut off in steps. For conventional sections (with the maximum thickness located at $\approx 30\%$ of the chord) the thickness of the trailing edge is approximately

$$h/t = 2(\Delta c/c_o) \quad (41)$$

where c_o denotes the original chord of the section. Replacing in equation 40 the "h/c" by (h/t) (t/c) and substituting $C_{D_{so}} = C_{D_{0o}}(t/c_o)$, an approximate but simple expression is found for the additional drag caused by cutting off the trailing edge of such sections:

$$\begin{aligned} \Delta C_{D_0} &= \frac{D_B}{q S} \\ &= \frac{0.135}{\sqrt[3]{C_{D_{0o}}}} \left[\frac{\Delta c}{c_o} \right]^{4/3} = \frac{0.34}{\sqrt[3]{C_{D_{0o}}}} \left[\frac{\Delta c}{c_o} \right]^{4/3} \end{aligned}$$

This incremental drag coefficient (based on maximum thickness of the section) is plotted in figure 41 together with some experimental results.

Optimum TE Thickness. In the case of wings, the trailing edge does not only affect the drag but also the lift; the maximum lift is somewhat increased. As explained in (45), the airfoil efficiency ratio $C_{L_{max}}/C_{D_{min}}$ reaches a flat maximum between $h/c = 0$ and $\approx 0.4\%$, assuming conventional values for the original lift- and drag coefficients of an airplane. The corresponding permissible thickness of

the trailing edge of a wing is in the order of $1/8$ to 1 inch, depending upon the size of wing and airplane.

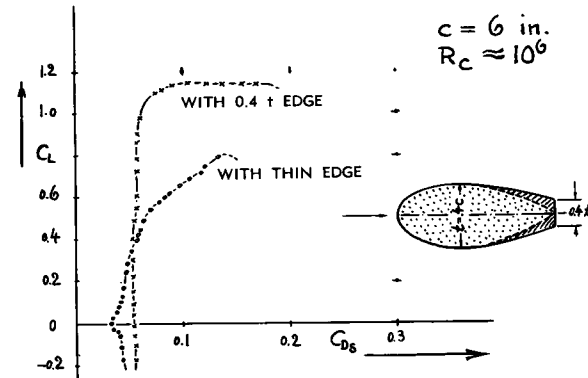


Figure 42. Lift and drag of a 40% thick foil, having square ends and ratio $A = 4$, as tested in a wind tunnel (49,e). The section drag is determined by wake-survey.

Thick Sections. Figure 42 shows another example where a blunt trailing edge is of practical importance. The lift characteristics of a 40% thick section are considerably improved upon employing a thick trailing edge; the maximum lift-drag ratio is increased by some 100% (!). Profiles with high thickness ratios are used at the blade roots of propellers. The flow past such sections is usually somewhat detached from the rear. Thickening the trailing edge, therefore, means "filling out" the dead space. Another series of tests (49,b), carried out on short foil- or strut pieces with geometrical aspect ratios of $b/c = 1.4$ and 2.0, but placed between the walls of a two-dimensional water tunnel, shows drag reductions in the order of 25 and 30% for thickness ratios of $t/c = 57$ and 80% respectively — after thickening their trailing edges up to $h/t = 0.5$ and 0.6. In this case, the flow past the original section (with $h = 0$) is, of course, severely handicapped by interference with the tunnel walls. Similar conditions prevail, however, in the inside of turbo-propeller configurations, where the air flow feeding the jet engine, has to pass between the blade roots of the propeller.

¶ (52) Pressure drop across grids and screens:

- a) Hoerner, AF Tech.Rpt 6289 (Wright Field, 1950).
- b) Eckert-Pflüger, Mesh, Lufo 1941, 142; NACA T.M.1003.
- c) AVA Göttingen, as in reference (53,a).
- d) Scholkmeyer, LFA Braunschweig Rpt 10 Apr 1943.
- e) Adler, Mach-Number Variation, NACA W.Rpt L-23.
- f) Weske, Airfoils in Grids, J'l Aeron'l Sci. 1944 p.369.
- g) Grids, Mitt.Hydrau.Inst. TH München 1 (1926), 2.
- h) Baines-Petersen, Screens, Trans ASME 1951 p.467.
- i) Schubauer-Others, Screens, NACA T.Note 2001 (1950).
- k) Roberston, see in reference (55,c).

9. DRAG OF NON-SOLID BODIES

Grids or screens can be used for wind protection (53,a), as turbulence screens in wind tunnels, as safety grids in the intake ducts of engines (52,a) and in the design of dive brakes or similar devices. The mechanism of flow across pervious sheets of material also helps to explain the drag characteristics of parachutes and wind socks.

Loss Coefficient. The loss of momentum that the flow encounters upon passing through pervious or porous material, is a function of shape and solidity ratio of the elements or ribs composing the sheet. The solidity "σ" is the ratio of the projected solid area S_s to the total area S_a . The pressure drop across screens, perforated sheets or through fabrics — is found by tests in closed channels (ducts). With "1" indicating the conditions ahead of, and "2" behind the obstacle, the loss coefficient is

$$\xi = (p_1 - p_2) / (0.5 \rho w^2) = \Delta p / q_w \quad (47)$$

where w indicates the average velocity in the channel ($w = w_1 = w_2$). In the case of round rods or wires, forming the grid or screen, the flow can be considered to be that through a bunch of nozzles along which the velocity is increased from w to a maximum " w_x ". Subsequently the cross section is 'suddenly' expanded again. The corresponding loss of momentum is indicated (according to Borda; see about diffusers in the chapter on "internal systems"), by the coefficient

$$\xi_{\text{round}} = (\sigma / (1 - \sigma))^2 \quad (48)$$

In the case of grids composed of sharp-edged strips, the flow contracts within the openings to a cross-sectional area which is in the order of $(2/3) S_{\text{open}}$. The loss coefficient is, therefore, equal to that at a higher solidity ratio:

$$\xi_{\text{sharp}} = (0.5 + \sigma)^2 / (1 - \sigma)^2 \quad (49)$$

Experimental data plotted in figure 43 substantiate the two theoretical equations, particularly in the higher ranges of the solidity ratio. The term $1/\xi$ (which can be considered to be the dynamic pressure q_w necessary to produce a certain pressure differential Δp) has, therefore, been plotted in the right-hand part of the graph.

Free-Flow Principle. The loss coefficient of screens and grids having smaller solidity ratios, can be derived from the free-flow drag coefficient $C_{D_{\text{free}}}$ of their elements or ribs, if allowing for the increased velocity $w_x = w / (1 - \sigma)$ within the openings:

$$\xi_{\text{free}} = C_{D_{\text{free}}} \sigma / (1 - \sigma)^2 \quad (50)$$

Using, for example, $C_{D_{\text{free}}} = 1$, the equation approximates the loss coefficient of round-wire screens or grids, up to $\sigma \approx 0.3$. Between this solidity ratio and $\sigma = 0.5$ or 0.6, a transition takes place from this function to that as indicated by equation 48.

Streamline Grids. Using in the last equation $C_{D_{\text{free}}} = C_{D_{\text{streamline}}}$ (c/t), the loss coefficient of grids composed of slender streamline elements can be obtained from their basic profile-drag coefficient $C_{D_{\text{streamline}}}$. Substantiated by tests (52,f) up to $\sigma = 0.5$, the equation shows that such grids have much smaller loss coefficients than round-wire devices. Streamline grids are, therefore, suitable for protection against foreign substances — if placed across the inlet channel of a water turbine or in the intake duct of aircraft engines.

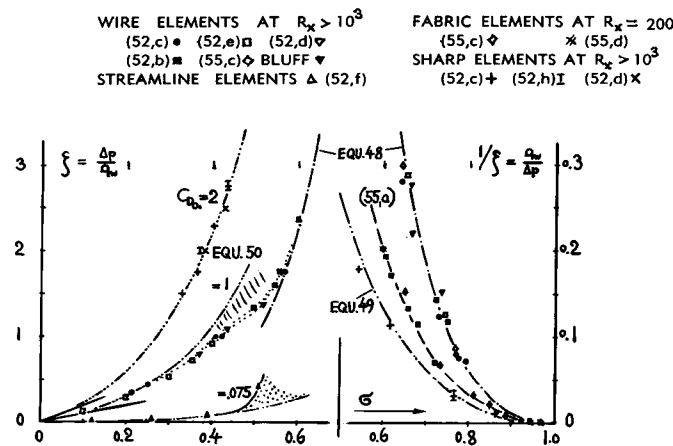


Figure 43. Momentum-loss coefficient across pervious sheets of material (screens and fabrics) as a function of their solidity ratio. Experimental results from (52).

Fine Fabrics, such as parachute cloth, have yarn diameters in the order of $d = 1$ mil. The Reynolds number $R_x = w_x d / v$ is correspondingly small; in the case of a man-carrying parachute during steady descent, in the order of $R_x \approx 200$. In the vicinity of this number, the viscous forces are of appreciable magnitude (as shown in reference 55). Considering a certain solidity, the loss coefficient is therefore 2 or 3 times as high as beyond $R_x = 10^3$, for which range the Borda-type equations (number 48 and 49) are applicable. The loss coefficient of an average parachute cloth is thus in the order of $\xi = 200$ or 300; see experimental points in the right-hand part of figure 43.

Compressibility. The pressure loss across screens and grids increases with the Mach number (52,e). The increment is of the type $\Delta\xi \sim M^n$; and it is unimportant up to Mach numbers $M = w/a$ of about half the critical value. The critical number indicates that the speed of sound is reached within the openings of the porous material considered. At solidities higher than $\sigma = 0.6$, the critical number is approximately

$$M_{\text{crit}} = 0.58 (1 - \sigma) \quad (51)$$

Drag In Free Stream. Upon placing a pervious sheet of material in a free stream—instead of in a closed duct—the velocity w (shortly ahead and behind the surface) is smaller than the undisturbed velocity V . Part of the flow turns sideways in order to get around the obstacle, rather than passing through the sheet. Assuming that $w = 0.5 (V + w_\infty)$; (where w_∞ = wake velocity far downstream), theory (54) gives a function between drag coefficient and loss coefficient:

$$C_{D\alpha} = D/(q S_\alpha) = 1 - ((4 - \xi)/(4 + \xi))^2 \quad (52)$$

This equation agrees with experience, up to $\xi = 1$ and $C_{D\alpha} = 0.6$, as can be seen in figure 44. Beyond this limit, $C_{D\alpha}$ steadily approaches the value of the solid plate or disk ($C_{D\alpha} = 1.17$). Beyond the range of the plot ($\xi = 20$), the drag difference between pervious sheets and solid disks is no longer considerable (less than 5%). As derived from their definitions, the relation between loss- and drag-coefficient is given by

$$C_{D\alpha} = \xi (w/V)^2; \quad w/V = \sqrt{C_{D\alpha}/\xi} \quad (53)$$

By combining available information on the value of ξ with the function in figure 44, it is possible

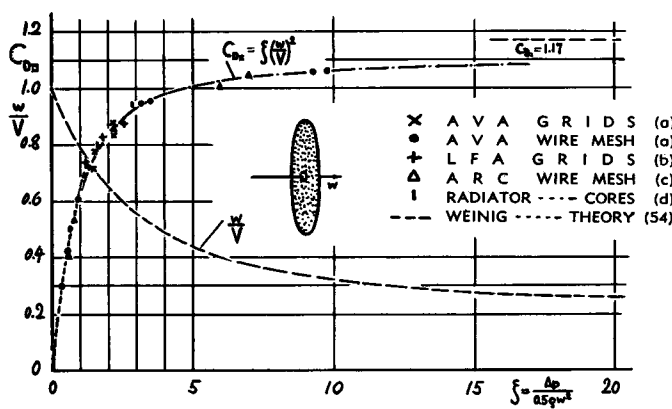


Figure 44. Relation between the drag coefficient of pervious sheets in free normal flow, and the pressure-loss coefficient of the porous material. References (53).

to determine the drag coefficients of pervious obstacles (in normal flow) as a function of their solidity ratio. As an example, the drag of a radiator (core in the open, without duct or fairing) is quoted from (53,d). For a design with $\xi = 3$, the drag coefficient was found by wind-tunnel test to be $C_{D\alpha} = 0.95$; see in figure 44.

Parachutes. Permeability is a function of the loss coefficient (equation 47) across any porous material, with "w" indicating the average velocity shortly ahead or behind the "sheet". Considering the volume flow of air through the opening of a parachute canopy, or through its maximum cross-sectional area S_α , the effective velocity is found to be higher than the "w" obtained from the " ξ " coefficient of the fabric used — approximately in proportion to S_{mat}/S_α . The velocity ratio is increased accordingly, to

$$w_\alpha/V = (S_{\text{mat}}/S_\alpha) \sqrt{C_{D\alpha}/\xi} \quad (54)$$

where S_{mat} = developed area of the material forming the canopy. Using now this ratio as a permeability measure for porous obstacles (rather than that of the material as such), various experimental results of pervious drag "bodies" have been correlated in figure 45. Flat sheets are included in the graph as well as parachutes. It is believed that at higher permeabilities, the shape has little influence on the magnitude of the drag coefficient. Approaching, however, the solid condition (at $w/V = 0$), the external flow pattern is naturally a function of shape. — The outlined procedure is equivalent to calculating the drag coefficient as

$$C_{D\alpha} = \xi (S_\alpha/S_{\text{mat}})^2 (w_\alpha/V)^2 \quad (55)$$

Parachutes and wind socks are further discussed as listed in the Index.

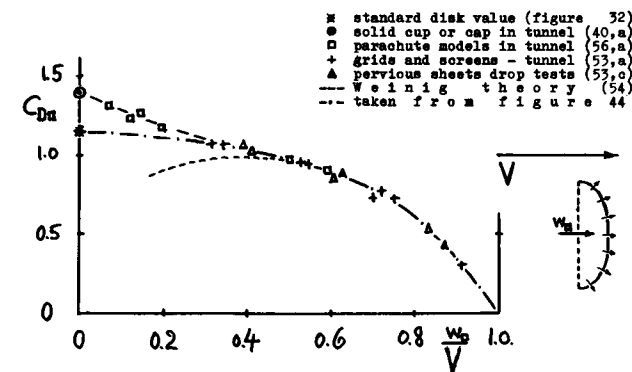


Figure 45. Drag coefficient (on frontal area) of pervious sheets and parachutes, as a function of the velocity ratio w_α/V (defined for maximum cross-sectional area).

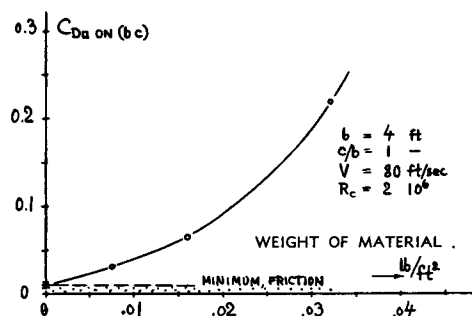
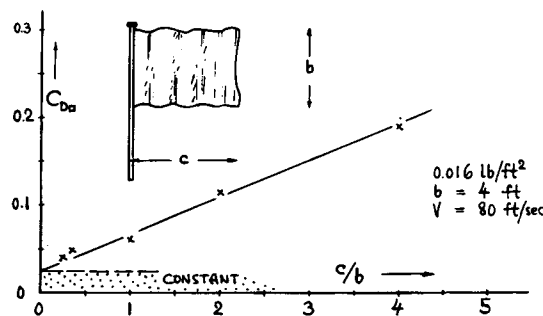


Figure 46. Drag characteristics of fluttering flags (57); as a function of fabric weight (left), and as a function of chord to span ratio (right).

Drag of Flags. Flags are made of porous material (fabric). Their drag is caused, however, by a mechanism different from that as explained in the preceding paragraphs. The minimum drag of a "sheet" in tangential flow corresponds, of course, to the (turbulent) skin friction drag along the two sides; and may thus be in the order of $C_{Df} = 0.01$, assuming C_f to be = 0.005. Tested drag coefficients of flags are considerably larger, however, than the frictional minimum. Additional pressure drag arises by way of flow separation, caused by the flutter of the bunting, which is caused in turn by separation. Two parameters are found in (57) affecting the drag of flags; the chord/span ratio (c/b) and the weight of the fabric (in lb/ft^2). As illustrated in figure 46, there are two components of drag; one representing skin friction plus drag of "batten" or staff ($C_{Df} \approx 0.025$), and a dynamic component representing flutter and separation. For an "aspect ratio" $b/c = 1$, and a material of $0.02 \text{ lb}/\text{ft}^2$, the drag coefficient is in the order of $C_{D\alpha} = 0.1$, a value which is found 10 times as high as the frictional drag estimated above.



10. REDUCTION OF PRESSURE DRAG

Considerable pressure-drag coefficients are always the result of flow separation. Accordingly, to reduce the drag, separation itself must be tackled. Several means have been tried to control the boundary layer; moving portions of the body surface in the direction of flow, guiding the flow around edges through auxiliary foils or vanes, discharging fluid with high velocity into the boundary layer, and finally removal of the retarded boundary-layer material by way of suction.

(a) MECHANICAL DEVICES

Moving Skin. Upon moving, by suitable means, portions of the skin of a body in the direction of flow, the relative velocity between air and body surface, and accordingly the skin friction — can be reduced. The formation of a boundary layer can thus be prevented and flow separation can be avoided. As an example, figure 47 shows the flow pattern around

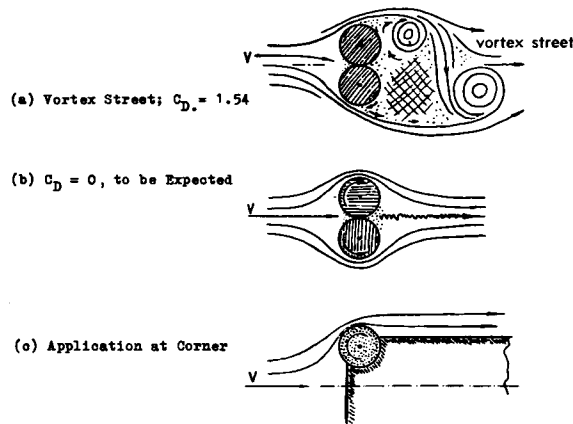


Figure 47. Flow pattern past rotating circular cylinders:
(a) Separated flow pattern with vortex street;
(b) Cylinders as presented by Prandtl (60,a);
(c) An application as suggested in (60,b).

- ¶(53) Drag of previous obstacles in free flow:
 - a) AVA Göttingen, Grids, Ergebnisse Vol IV (1932).
 - b) Scholkemeier, Rpt LFA Brunswick 10 April 1943 (52,d).
 - c) Taylor & Davies, Porous Sheets, ARC RM 2236 and 2237.
 - d) Properties of Radiator Cores, NACA T.Rpt 63 (1919).
- ¶(54) Weinig, Theory of Parachutes, Yearb'k D.Lufo 1940.
- ¶(55) In the viscous range of the Reynolds number:
 - a) Hoerner, Properties of Screens and Fabrics, Textile Research Journal 1952 p.274.
 - b) Dannenberg, Porous Material, NACA T.Note 3094.
 - c) Robertson, Fabrics, Textile Res.J'l 1947 p.167.
 - d) Longnecker, 1950 Thesis Text. Inst. Lowell, Mass.
- ¶(56) Drag characteristics of parachutes:
 - a) Scher and Draper, NACA Tech.Note 2098 (1950).
 - b) More references are under "parachutes"; see Index.
- ¶(60) Experiments with movable-skin devices:
 - a) Prandtl in Ergebnisse AVA Göttingen Vol III (1936).
 - b) Farren, in Goldstein's "Modern Fluid Dynamics" 1938.
- (57) Fairthorne, Drag of Flags, ARC RM 1345 (1931).

a pair of circular cylinders. With the two bodies rotating in the directions as indicated by the arrows, the flow becomes attached all the way along the rear side of the configuration. The drag is consequently reduced, practically to zero. It is doubtful, of course, that any design involving moving surfaces will ever be successful in practical application. Years ago, the "Flettner Rotor", intended to utilize the "Magnus" effect — was an application of this type of boundary layer control. A possible application, suitable to reduce the resistance of blunt shapes, is illustrated in the lower part of the illustration.

Vortex Generators (62). Another "mechanical" means of preventing or postponing separation is "redistribution of momentum in the boundary layer", or "transporting of momentum to the lower regions of the boundary layer" by means of vortex generators or through ramps or wedges placed ahead of the expected separation. Through such "mixing" methods, separation can evidently be somewhat delayed and the lift of wings or wing flaps can be increased. With regard to drag, an equal price has to be paid, however, for avoiding separation in the form of momentum losses in the outer stream.

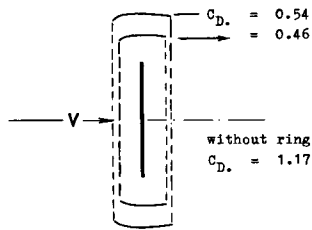


Figure 48. Reduction of separation drag (of a disk) by means of a "ring", tested in various sizes in reference (61,a).

Ring Surface. The flow around sharp edges can considerably be improved by means of auxiliary foils. The most-commonly known application of this method is the leading-edge slot, employed to increase the maximum lift of wings. Considering blunt bodies, the separated flow can be affected by similar devices. As an example, figure 48 shows how the drag of a disk is reduced to approximately 40% of the original value, by means of an annular foil which is placed around it. Such surfaces have been used in the form of the "Townend Ring" (61,a) to improve the flow pattern around radial engines (see in the "internal-flow" chapter).

Guide Vanes. For application in blunt bodies, guide vanes have been investigated (61,b). As an example, figure 49 shows a favorable arrangement of double vanes at the nose and at the base, respectively, of a two-dimensional shape. In either case, the drag is reduced to a fraction of the original

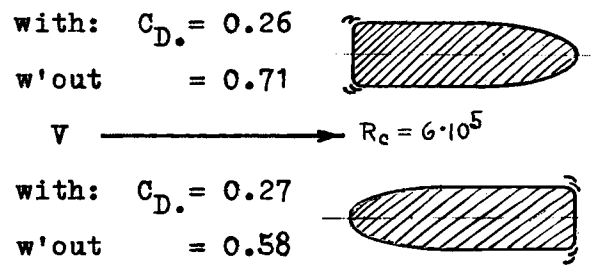


Figure 49. Reduction of pressure drag on a two-dimensional body by means of staggered guide vanes (61,b).

value (without vanes). Auxiliary surfaces similar to these have also successfully been used to reduce the drag of buses. However, employing any such devices, possible interference effects and the drag of the parts necessary to support the vanes, should not be overlooked.

(b) BOUNDARY-LAYER CONTROL

Discharging Fluid. The boundary layer's momentum deficiency can be counteracted by discharging a high-velocity sheet of fluid from within the body considered, tangentially into the layer. Flow separation, if originally existing, may be eliminated in this way. This technique has not yet been utilized in practical applications. So far, successful tests have been conducted with the aim of increasing the maximum lift of a wing section by blowing air over its upper side (63), thus affecting the flow in a way similar to, but more intensively than by wing slats. The maximum lift can be doubled by this method. Discharging of fluid is also of interest in connection with boundary-layer control by suction; the removed volume of fluid has to be discharged at some other place (if it is not consumed in the engine).

Suction Method. The suction variety of boundary-layer control has also been tried for increasing the maximum lift of airfoils. The boundary-layer sheets closest to the surface of the upper side, are removed through openings or slots into the hollow wing by means of a blower (and returned somewhere else into the outer flow). The suction method is also very effective in stabilizing the laminar boundary-layer flow — as described in the "friction" chapter.

Sphere With Suction. As an example of the possible application of boundary-layer suction in bluff bodies, to prevent or to reduce separation, figure 50 presents the drag coefficient of a sphere at Reynolds numbers above the critical — as affected by suction (64). Portions of the rear surface are replaced by

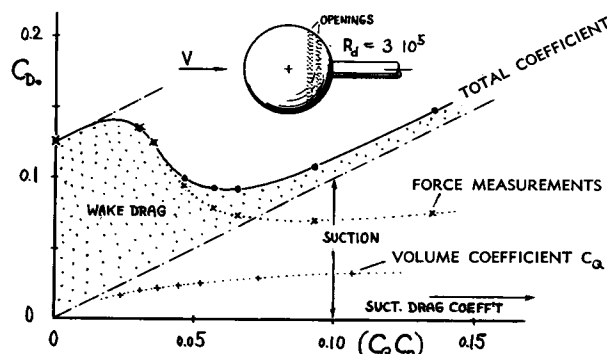


Figure 50. Drag analysis of a sphere, tested with boundary-layer suction at the rear side, to reduce separation.

wire mesh; the air from the boundary layer is sucked through this mesh and discharged sideways into the space outside the wind-tunnel stream. Under these conditions, the drag as measured at the tunnel scales, is reduced from $C_{D_0} = 0.125$ to 0.070. As indicated in the treatment of laminarization through boundary-layer control (in Chapter II), the power expended in the suction machinery can or should be considered in the form of an additional effective drag coefficient. Since in the sphere experiment considered, the original drag coefficients have been determined as forces on the wind-tunnel balance, the procedure is somewhat different, however, from that as described in Chapter II. To obtain the wake-drag coefficient, values of $(2 C_Q)$ have been subtracted from the tested values. Then, to obtain the total effective coefficient, values of $(C_Q C_p)$ have been added to the wake-drag values, with C_p indicating the difference between P_{ambient} and the pressure inside the hollow sphere. As an important result it should be realized that in case of the sphere, the volume coefficient C_Q is at least one order of magnitude larger than in the laminarization technique (Chapter II). As a consequence, the pressure drop across the suction openings is considerable;

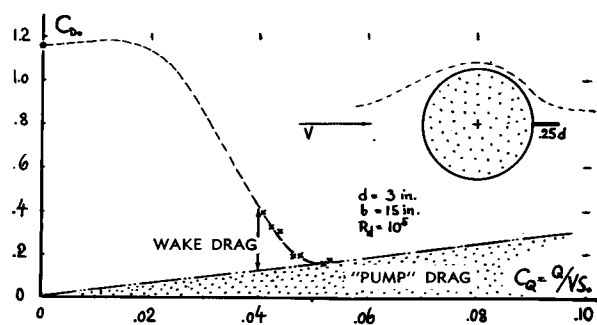


Figure 51. Drag of a circular cylinder (at subcritical R' -number) as a function of suction; from reference (65,a).

the C_p values are high and they increase appreciably with the suction-volume coefficient C_Q . In conclusion, the total drag coefficient of the sphere (as investigated) is reduced only from 0.125 to 0.095 in optimum condition, while the smallness of the minimum wake-drag coefficient obtained (0.013) may only be of academic interest.

Cylinder With Suction. Figure 51 presents results of a wind-tunnel program designed to eliminate separation and to produce circulation (lift) in a circular cylinder. The so-called Thwaite's flap is an important part in this method of boundary-layer control by means of suction through the porous surface of the cylinder — evidently preventing the start of an alternating vortex street. It seems that the minimum value of the suction-volume coefficient C_Q necessary to produce an attached flow pattern, is proportional to $\sqrt{R_d}$ representing the momentum losses of the laminar boundary layer. Reattachment is complete as can be seen in the rear-side pressure coefficient which increases from $C_{p,r} = -1$ (without suction) to +1 (locally at the rear "stagnation point"), above $C_Q = 0.05$ as in Figure 51. The drag as determined in the wake, reduces to zero. Here again, an effective component of drag can be calculated, representing the power expended in pumping the boundary layer material; $\Delta C_{D_0} = (1 + C_p) C_Q$, where $C_p \approx 1.5$ indicating the static pressure differential between inside and ambient space. The minimum total drag coefficient is then found to be in the order of $C_{D_0} = 0.2$. The result is similar to that of the sphere in figure 50.

¶(61) Experiments on Auxiliary foils or guide vanes:
a) Townend, "Townend Ring", J.R.Aero.Soc. Vol 24.

b) Frey, Guide Vanes, Forschung Ing.Wesen 1933 p.67 and 1934 p.105; see also Flügel in Yearb'k ST.G 1930 p.87.

¶(62) Postponing separation by vortex generators:

a) Bursnall, Generators on Lift, NACA Rpt RM L52G24.
b) Stephens-Collins, "Ramps", Austral. ARC Rpt ACA-55.

¶(63) Discharging fluid into boundary layer:

a) Hoerner, Maximum Lift by Blowing, ZWB FB 276.
b) Williams, Blowing Over Flaps, ARC C.Paper 209 (1955).

¶(64) Schrenk, BL Control, Zts.Flugt.M.Luft 1926 p. 366.

¶(65) Preventing separation through suction:

a) Thwaites Flap, ARC RM's 2611, 2787 and 2788; see also NACA T.Note 3498 and Jl Aeron'l Sci. 1948 p.189.
b) Griffith-Type Foil-Sections in Wind Tunnel, ARC RM's 2148, 2149, 2475, 2577, 2647 (1945 to 1953).

Thick Foil Section. Considering suction as a means for preventing flow separation, there is hardly much to be gained in applying it to slender wing sections (at small lift coefficients). A number of experiments have been carried out, however, in England (65) attempting to reduce separation and resistance in comparatively thick foil- or strut sections. Figure 52 presents as an example results of a 30% thick

shape having a cusped rear end with a pair of suction slots. It is possible to reduce the wake in this arrangement to an apparent drag coefficient of 0.001 and 0.006, respectively. Figure 52 shows, however, that the total drag coefficients (obtained after adding $\Delta C_{D_s} = (1 + 0.7) C_Q$) are of appreciable magnitude. With turbulent boundary layer (stimulated at 0.1 chord), there is hardly any advantage found in this type of suction. Only upon combining separation control with laminarization (laminar boundary layer almost to the suction slots), is a considerable reduction of drag (to $\approx \frac{1}{2}$) obtained. The value of $C_{D_{\text{Total}}} = 0.012$ is not lower, however, than that of an ordinary streamline section (with $t/c = 30\%$ at higher R' numbers — as can be seen in the "streamline" chapter. It is, therefore, suggested that suction is not really a favorable means for reducing drag.

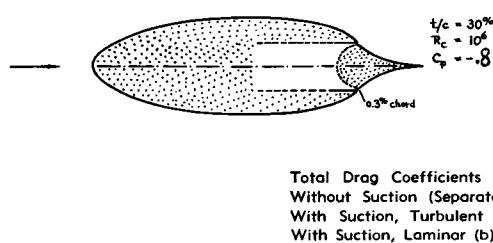


Figure 52. Drag coefficient of a foil section (between end plates) as a function of suction applied to the rear (65,b).
(a) turbulent from 0.1 c: $C_{D_{\text{Wake}}} = 0.005$; $C_Q = 0.015$
(b) laminar flow to slots: $C_{D_{\text{Wake}}} = 0.001$; $C_Q = 0.007$

II. SUPPLEMENTARY NOTES

Since there is more space available on this page, some notes supplementing the topic of pressure drag are added as follows.

Forebody Drag. In the second and third shape shown in figure 53, the value of the negative rear-side pressure coefficient is greater than the total drag coefficient. It is therefore concluded that the forebody drag is somewhat negative, thus confirming what is explained about negative half-body drag in connection with figure 20.

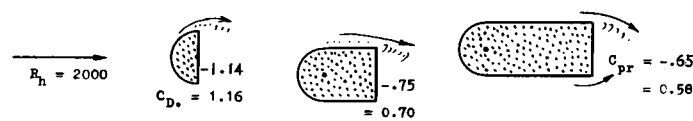


Figure 53. Drag and rear-side pressure of bluff sections (41,g) tested at $b = 30 h$, between end plates.

Leonardo Da Vinci (1452-1519). Figure 55 has been traced from one of Leonardo's drawings (F.55) of flow patterns as he had determined them in water. We might thus call Von Kármán's vortex street "Leonardo's vortex trail" as well, since he is some 450 years ahead, if not in the mathematical treatment, so certainly in discovering this system.



Figure 55. Flow pattern past a bluff obstacle (showing an alternating vortex street), traced from one of Leonardo da Vinci's drawings. — "Del Moto e Misura dell'Acqua", edited by Carusi and Favaro, Bologna 1923.

CHAPTER IV – WIND FORCES ON STRUCTURES

The forces produced by wind in buildings are essentially pressure- and predominantly drag forces (1). Besides buildings, other structures are of engineering interest too with respect to wind — such as bridges, chimneys, and steel masts, for example.

I. WIND CHARACTERISTICS

Speeds. Buildings have to be made strong enough structurally to withstand the maximum wind velocities which, by past experience, can be expected in their particular location. In England, for example, maximum velocities between 70 and 110 mph have occasionally been observed in violent storms (at heights above the ground between 30 and 50 ft) (4,c). In hurricanes moving along the Atlantic coast of the United States, velocities up to 140 mph have been reported. The dynamic pressures $q = 0.5 \rho V^2$ corresponding to the higher speeds quoted, are between 30 and 50 lb/ft². Similar values are assumed in building codes. Appreciably higher speeds (up to 300 or 400 mph) have been mentioned in connection with tornadoes, locally restricted to the narrow path along which they travel. By economical reasons, ordinary buildings are generally not made to stand up against this type of storm.

Boundary Layer. Moving along the surface of land or water, wind develops a boundary layer in a manner similar to that as described in the "friction" chapter. The thickness (height) of this layer is much larger, however, as found on man-made aerodynamic bodies. In steady winds, the thickness has been stated to be higher than 1000 ft. Statistical observation (2,e) indicates that the BL thickness (in ft) is in the order of $\delta = 30$ to 50 times the speed of V_0 (in ft/sec, above the layer). The same source also gives statistical values for the turbulent velocity fluctuations within the Earth's b'layer; their non-dimensional frequency ($f \delta / V_0$) is in the same order of 0.13 to 0.25 as found in wind tunnel investigations of much thinner boundary layers. Man-made structures are usually within the b'layer. Correspondingly the speeds quoted above are not really maximum; rather they are values measured at convenient

places on top of buildings or towers. Figure 1 presents a collection of tested values, plotted in form of the dynamic pressure ratio against an altitude of 10 meters (= 33 ft) and of 100 meters (= 330 ft), respectively. Interpolation is possible in the form of

$$V \sim \sqrt[n]{h} ; \quad \text{or} \quad q \sim \frac{0.5n}{\sqrt[n]{h}} \quad (1)$$

where n is in the order of 6 or 7. Considering as an example, the Eiffel Tower ($h = 300 \text{ m} \approx 1000 \text{ ft}$), the dynamic pressure at the top may be 1.7 times the value at the lower main platform. — Over obstacles and because of various meteorological effects, the distribution may be considerably different from that in the equation. It is said, however, in (2,h) that during 93% of the daytime, the distribution is "logarithmic", a type of function meant to be similar to that in figure 1. Evidently, it is also difficult to define zero altitude of the distribution (where $V \rightarrow 0$) in woods or cities. It is suggested to assume a type of sublayer, roughly corresponding to the average height of trees or buildings, respectively; in which velocity is close to zero.

- QUOTED FROM (a) $h_* = 10 \text{ m}$
- × ON RADIO MAST (d) $= 100 \text{ m}$
- + OVER AIRFIELD (f) $h_* = 10 \text{ m}$
- △ NACA, FIELD (g) $h_* = 10 \text{ m}$
- US WEATHER BR. (h) $= 100 \text{ m}$
- ELEKTROTEKNIKEREN 1949 p.607

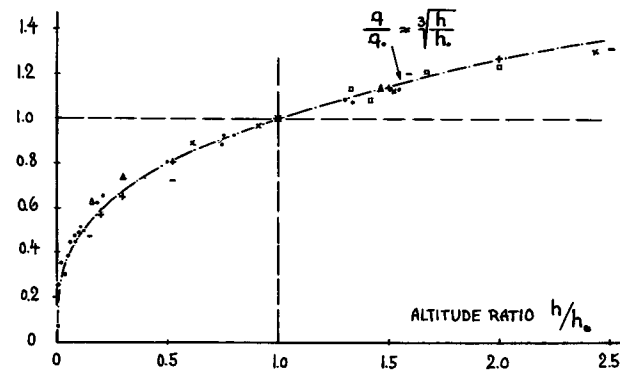


Figure 1. Increase of dynamic pressure with altitude in steady winds, over "smooth" ground surface such as calm water or an airfield; evaluated from (2) with h_* indicating a suitable reference altitude.

Ground Effect. In wind-tunnel investigations and in full-scale calculations there does not seem to be any established rule to account for variation and distribution of speed with altitude, as far as wind loads on buildings and structures are concerned. On the floor of the tunnel or on a ground board, a boundary layer is usually present that is lower than the obstacle investigated. Drag coefficients are then referred to the undisturbed dynamic pressure above the layer. Pressures are given in form of the non-dimensional coefficient

$$C_p = (p_{\text{local}} - p_{\text{ambi}}) / (0.5 \rho V^2) \quad (2)$$

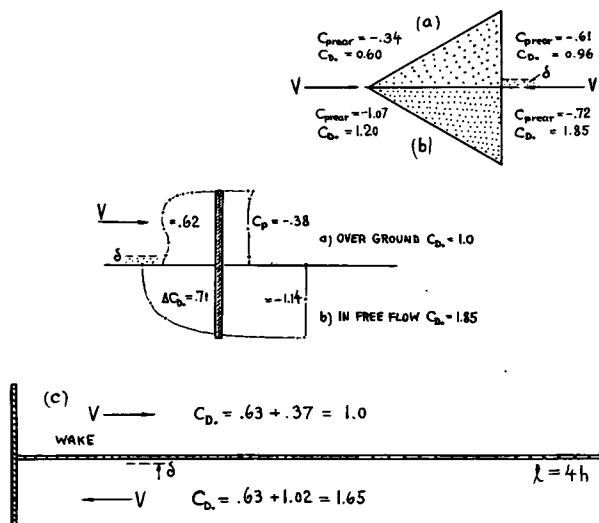


Figure 2. Pressure and drag coefficients of bluff shapes, tested between tunnel walls (3,a) :

- a) half bodies mounted over floor of tunnel,
- b) in free flow (complete double models),
- c) demonstrating influence of "splitter" plate.

Figure 2 shows that the b'layer has a considerable influence upon pressure distribution and drag of simple bluff obstacles. The experiment in part (c) of the illustration demonstrates the influence of the ground on the vortex street developing behind two-dimensional obstacles (see in the "pressure drag" chapter). With the board ("splitter" plate) ahead of the two-dimensional plate, face- and rear-side pressures are somewhat reduced as against conditions in free flow. With the board behind the plate, the vortex street is evidently suppressed; the value of the rear-side pressure is considerably reduced from $C_p = -1.14$ to -0.37 , and the drag coefficient is only \approx half of that in free flow. In a three-dimensional plate (figure 3), the drag coefficient is not affected, however, by the presence of the ground. On the other hand, because of interference with its flow pattern, the drag coefficient of the streamline body in figure 3,b (with b'layer-sensitive flow separation from the rear), is \approx doubled. Since buildings are usually of bluff and three-dimensional shape, the

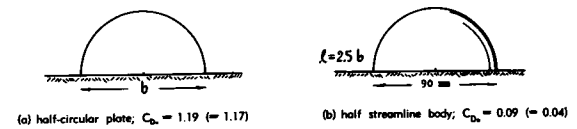


Figure 3. Drag coefficients of two three-dimensional bodies (seen in direction of flow), mounted over a ground surface (3,b), tested at $R_b = 2 \cdot 10^5$ where $b = 90$ mm. The values in brackets indicate drag coefficients in free flow (on double models).

type of their flow pattern does not appear to be affected by the atmospheric boundary layer. The magnitude of their drag coefficients corresponds to the mechanism of protuberances as explained in the chapters on "irregularities" and "interference"; in other words, their drag approximately corresponds to the average dynamic pressure within their height.

2. VARIOUS BUILDINGS

Houses. Figure 4 presents the pressure distribution of a house. There is positive pressure on flat surfaces facing the wind. In the separated space behind the house, the pressure is uniform and negative, between $C_p = -0.2$ and -0.8 (depending on building shape and wind direction). In sharp-cornered buildings, the flow may also be separated from the lateral walls. References (4,b and c) show that the flow can also be separated from the windward side of roofs as illustrated in figure 4 - particularly with slopes smaller than 45° and in taller buildings (with h/l exceeding unity). Figure 5, on the other hand, is an example where the flow reattaches to the windward side of the roof. This illustration also demonstrates that the distribution is little or not at all affected by the particular shape of the rear side. Wind directions different from the one in the two illustrations are investigated in (4). Reference (4,c) also gives information on the mutual interaction between several houses placed one behind the other in a row.

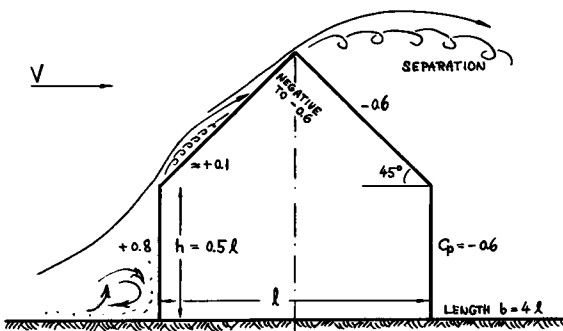
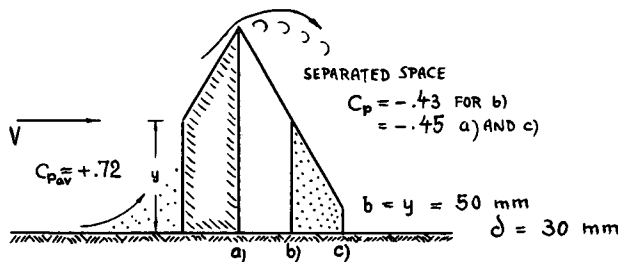


Figure 4. Flow pattern and pressure distribution (on center line) of a simple house shape (4,b).



Internal Pressure. Buildings are usually not really air-tight. The inside pressure is, therefore, affected by the outside distribution. Since negative values are predominant in this distribution, the inside pressure usually assumes some negative value (in the order of $C_p = -0.2$ or -0.3) for a random distribution of leaks. However, by opening windows on the windward (leeward) side, a maximum positive

¶(1) Principles of building aerodynamics are laid down by Pagon in 8 Articles in Engg News Record; Mar, Jul, Oct, Dec 1934 and in Apr, Mar, May, Oct 1935.

¶(2) Wind velocities as a function of altitude:

- Deacon Wind Velocities in the Atmosphere, Porton Technical Paper No. 39, Series No. 10, 1948.
- Paeschke, Physik der Atmosphäre, Vol.24 p.163.
- Wind Near Ground, J.Metr.Soc. Japan, 1952 p.255.
- Wing, Wind Pressure, Electrician 1921 p.6.
- Goddard, BL in Atmosphere, JASci.1935 p.115.
- ARC, Velocity Gradient, RM 1489 (1932).
- NACA, Air Conditions Near Ground, T.Rpt 489.
- Meteorology Atomic Energy, Gov.Printg O. 1955.

¶(3) Resistance of elementary bodies:

- Irminger-Nokkentved; Drag Characteristics, Wind Pressure, Copenhagen 1930 and 1936; Transl by Jarvis.
- Schmid, Wind Resistance of Motor Vehicles, Issue No. 1 of Deutsche Kraftfahrtforschung VDI, 1938.

¶(4) Pressure distribution on houses:

- Ergebnisse AVA Goettingen IV (1932) p.128.
- Chien-Feng-Wang-Siao; Pressure Distribution on Elementary Buildings; Iowa Univ. Rpt for ONR 1951.
- Bailey and Vincent, Wind Pressure on Buildings, Inst'n Civil Engrs. Journ. (London) 1942/43 p.243.

¶(5) Pressure distribution on aircraft hangars:

- Eiffel, Nouvelles Recherches de l'Air (1919).
- Arnstein-Klemperer, Akron Dock, J.A.Sci. 1936, 88.
- Ergebnisse AVA Göttingen Vol IV p.128.

Figure 7. Drag coefficients of simple shapes on ground surface. First 8 bodies from (3,a); then comes a cylinder (8,b) at $R_d = 10^6$, smooth as well as with 8 ribs on outside; finally a square prism (6,b) in two positions.

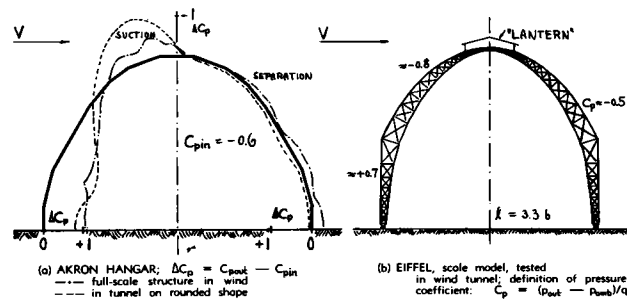
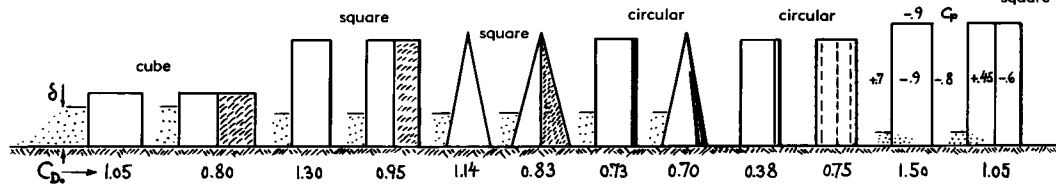


Figure 6. Pressure distribution on airship hangars (5).

(negative) pressure value can be obtained inside the building. This inside pressure then combines with the negative (positive) outside pressure on the leeward (windward) outside of the building, thus producing a maximum pressure differential in the respective wall of the building corresponding to a coefficient $C_p = C_{pout} - C_{pin}$, which can be in the order of 2. For an assumed maximum dynamic wind pressure of 50 lb/ft^2 , the corresponding pressure force in the considered wall is then in the order of 100 lb/ft^2 . The safeguard in such a wall may be the windows. They will probably blow out (or in, respectively), before the wall collapses.

Hangars. Figure 6 shows the pressure distribution on the outside of two hangars. As in circular cylinders ("pressure drag" chapter) a suction peak (in the order of $C_p = -1.2$) appears somewhat ahead of the roof top. Again, the internal pressure is of great importance for the structural safety in a wind storm. Inside pressure coefficients are, for example:

$$C_p = -0.6 \text{ with the hangar doors open}$$

$$C_p = -0.4 \text{ with "lantern" windows open}$$

Positive internal pressures could be produced through openings (windows) in the windward side. Combination of the suction forces near the top of these structures with positive inside pressure may lift the roof off, as it has happened occasionally in strong winds.

Tall Buildings. Figure 7 presents the drag coefficients of various shapes, tested over and in a boundary layer as indicated. The coefficients are similar to those listed in the "pressure drag" chapter. As a function of height h over width b , the coefficients increase in a manner similar to those of plates and subcritical circular cylinders in free flow. Because of

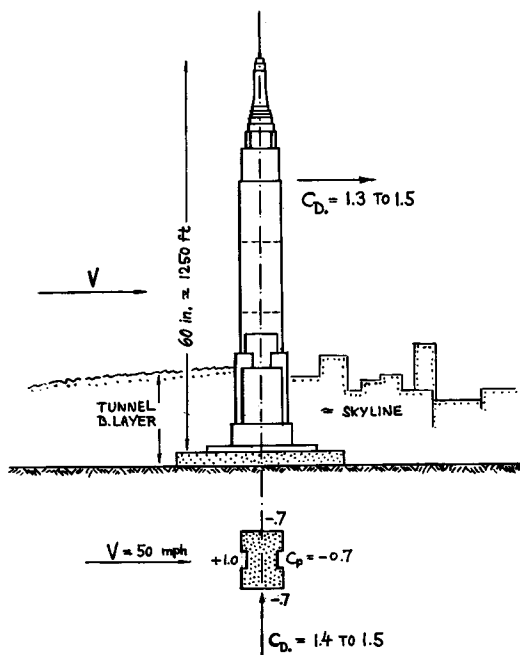


Figure 8. Tests on model of Empire State Building (6,a); note wind-tunnel boundary layer and approximate skyline of surrounding buildings.

this effect and owing to the increase of wind pressure with altitude, the moment due to drag forces might grow sufficiently large to turn-over tall buildings. An experimental investigation was, therefore, undertaken in connection with the design of the Empire State Building (6,a). Figure 8 shows some results, indicating drag coefficients (determined from pressure distribution as well as by force measurements) up to $C_{D\bullet} = 1.5$. For an exposed frontal area (above the sky line) in the order of 100,000 ft^2 , the wind force on the building, in a hurricane blowing at least with 100 mph, at a corresponding dynamic pressure $q \approx 40 \text{ lb}/\text{ft}^2$ — may then be estimated to be roughly 2000 tons. It is not surprising, therefore, that the structure has been reported (6,c) to be bending; so for example by \approx one foot (top against base) in a 40 mph wind.

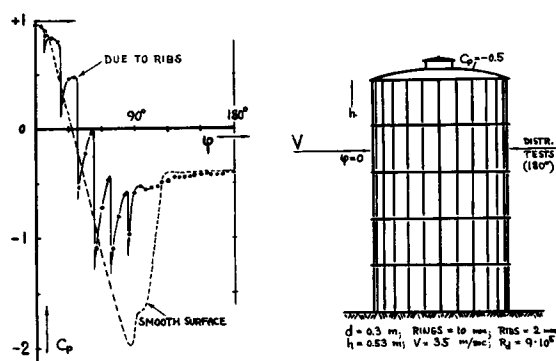


Figure 9. Pressure distribution on the circumference of a gas storage tank (8,a) with smooth surface and with steel ribs on the surface, respectively.

3. CYLINDRICAL STRUCTURES

Storage Tank. The negative pressures at the sides of circular cylinders can have high values, in the order of $C_{p\min} = -2$, as shown in the "pressure drag" chapter. Figure 9 demonstrates, however, that the suction peaks are eliminated by ribs in the outside structure of the storage tank, although the drag is higher in this condition than with smooth surface. With openings in the "lantern" on top of the tank (simulating ventilation openings, if any) an inside pressure is obtained indicated by $C_p = -0.5$.

Chimneys. Drag and pressure distribution of circular cylinders are presented in the "pressure drag" chapter. In full scale, the Reynolds number $R_d = V d/\nu$ is expected to be higher than the critical ($R_d \approx 4 \cdot 10^5$). Reference (7,a) shows, however, that the drag coefficient of a "length of chimney" (tested between end plates) is appreciably increased by surface roughness in the form of mortar gaps between the bricks in old-type chimney construction:

smooth cylinder	$C_{D\bullet} = 0.3$ to 0.4
with smoothed gaps	$= 0.4$ to 0.5
with ordinary gaps	$= 0.5$ to 0.6

These coefficients should not be confused with the higher (subcritical) values at Reynolds numbers below $R_d = 3 \cdot 10^5$ (as shown in the "pressure drag" chapter).

Oscillations. It has been explained in the "pressure drag" chapter that a "vortex street" develops behind bluff obstacles in two-dimensional or similar flow conditions. Fluctuating lateral "lift" forces correspond to the motions of that street; and for the circular cylinder (tested between walls) such forces are reported in (9,a) having a maximum value of $C_L = \pm 0.45$. Cylinders have also been investigated (9,b) suspended in a water stream in such a manner that they were free to oscillate in lateral direction, between springs. For a particular system, lateral force coefficients were evaluated at resonance speed up to $C_L = \pm 1.0$ and ± 1.6 . These values are between 2 and 4 times the fixed-and-rigid-body result quoted above. In oscillating condition, the frequency of the vortex street does no longer correspond to a constant Strouhal number (meaning $f \sim V$) ; rather the vortex shedding seems to be controlled by the motion of the body at its natural frequency. Another investigation (9,c) indicates that in a water tank, "permitting the cylinder to vibrate, raises the resistance up to twice the non-vibrating resistance". In conclusion we may, there-

fore, assume that drag, lateral forces and frequency (or Strouhal number) very roughly correspond to the width "h" over which the cylinder sweeps when oscillating instead of the diameter "d".

In Smoke Stacks, chimneys or other cylindrical shapes, the frequency of vortex street and lateral forces can come into resonance with their natural bending frequency. Oscillations of considerable magnitude can thus be excited by comparatively small aerodynamic forces; possibly leading to the collapse of such structures. For example, wind-excited oscillations of a 150 ft high steel stack with a diameter $d = 4$ ft, are reported in (10,a) beginning at a speed corresponding to a Strouhal number "S" = $fd/V = 0.2$, where f = frequency. These oscillations continued up to twice the speed at which they first started, dangerously shaking the structure. The oscillations could be eliminated in that case by damping devices in the stays holding the stack. Certain modest vibrations are also reported (10,c) to have occurred at one or two particular wind directions in the leeward one of a pair of steel stacks. In these directions, the vortex trail in the wake of the windward stack evidently hit upon the other stack thus exciting its natural frequency.

Pipe Line. Another example of oscillations is reported in (11). A 1000 ft long, 30-inch-diameter gas pipe line, suspended on cables across a river

started swaying up and down (by 5 or 6 ft) at wind speeds in the order of a few mph. It was possible in this case to break-up the vortex street by attaching certain pieces of "splitter" plate (see in Chapter III) to the pipe. Their effect is similar to that of the ground in figure 2,a.

Cables or stranded wires and ropes are used either as electrical conductors (in power lines and in radio antennas) or as supporting devices (in bridges, cable-car lines or as stays as in figure 15). Their basic aerodynamic drag coefficient (figure 10) is similar to the subcritical value of circular cylinders ($C_D = 1.17$). Because of the rough (grooved) shape of their surface, cables are not expected really to show decreased drag coefficients above a critical Reynolds number. However, Reference (12,c) indicates a steady decrease of the drag coefficient of ropes and stranded wires from $C_D = 1.17$ at $R_d = 10^4$ to $C_D = 1.0$ at $R_d = 6 \cdot 10^4$. Wires or cables in electric power lines (or in other applications) also show dynamic (oscillating) characteristics similar to those described in the section on "smoke stacks". The wires in power lines may thus vibrate (and occasionally break) in one of their natural harmonic modes.

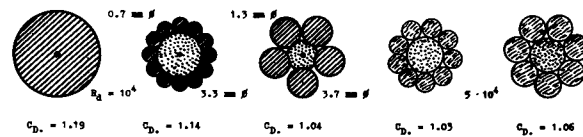


Figure 10. Fluid-dynamic drag coefficients of stranded wires, steel cables and ropes. Three items left by CAHI (12,a); two shapes right by AVA (12,c).

- ¶(6) Dryden and Hill (Bureau of Standards):
 - a) Wind Pressure on Model of Empire State Building, J.Research Nat'l Bur. of Stds Vol.10 (1933) p.493.
 - b) Pressure on Prism, Sci Paper BOS No.523 (1926).
 - c) Rathbun, Tall Building, ASCE Proc.1938 p. 1335.
- ¶(7) Wind pressure on circular cylinders and chimneys:
 - a) Ackeret, Schweizer Bauzeitung 108,2 (1936) p.25.
 - b) Dryden and Hill, BOS J.Research 1930 Rpt 221.
 - c) Pechstein, Large Cylinder, Z.VDI 1942 p.221.
- ¶(8) Pressure distribution on storage tanks:
 - a) Erg.AVA Göttingen III p.144, IV p.134; Naturwissenschaften 1930, 475, Bauwelt 1932 p.550, 692.
 - b) Hankins and Lean, Gas Rese. Board, London 1948.
- ¶(9) Oscillations of circular cylinders:
 - a) Schwabe, Ingenieur Archiv 1935 p.34.
 - b) Petrikat, Oscillations of Weirs; D. Wasserwirtschaft 1941; Forschungshefte der MAN 1952 and 1953.
 - c) Hay, In Towing Tank, Princeton Rpt 1947.
 - d) Thoma, Mitt.Hydraul.Inst. TH Munich No. 8,9.
- ¶(10) Oscillating smoke stacks:
 - a) Scruton, The Engineer (London) 1955 p.806.
 - b) Pagon, Vibrations, Engg News Record July 1934.
 - c) DenHartog, Vortex Wake, Proc.Nat.Acad.Sci.1954
- ¶(11) Baird, Pipe Line, Trans ASME 1955 p.797.
- ¶(12) Characteristics of cables and wires:
 - a) CAHI (Moscow), Investigations, Rpt 33 (1928).
 - b) British ARC, R and M 307 (1917).
 - c) Croseck, Theory of Sailing, Springer 1925.
- ¶(14) Oscillations in electric power lines:
 - a) DenHartog, Tr.A.Inst.El.Engs 1932 Paper 32-91.
 - b) Ruedy, Canadian J. of Research 1935 p.82.
 - c) Galloping, Trns AIEE 1930, 1444 and 1947, 1154.

Galloping Lines. The musical noise in telephone poles has its origin too in vortex streets exciting a suitable natural frequency in the wires strung between them. Generally the street frequencies are too high, however (estimated to be between 10 and 100/sec) to produce amplitudes which might be damaging. — A different type of oscillation has been observed in electric power lines (14). Because of ice and sleet deposited on them and hanging down from them, the wires may obtain a shape exhibiting a certain "lift" curve slope. They are then slightly lifted by wind and they start oscillating up and down at their natural frequency in the order of 1 per second in wires or cables spanning 300 ft between masts. After swinging in this manner for hours or days (!) at amplitudes up to ± 10 ft in winds between 20 and 30 mph, the cables may finally break down. A remedy is to heat the lines where and whenever necessary, for a short time by an over-dosis of current so that the ice melts off.

4. STEEL STRUCTURES

Beams. Radio Towers, some bridges and similar structures are built-up of steel beams and girders. The sections of sharp-edged beams, illustrated in figure 11, show drag coefficients which are close or comparable to those of flat plates. In two-dimensional flow, C_D is in the order of 2 in many cases, with the coefficient based upon projected frontal area.

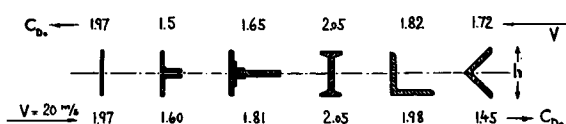


Figure 11. Drag coefficients of various beam sections (15, a) tested on models with $b = (10 \text{ to } 12) \cdot h$ between end plates; $b = 1.5 \text{ m}$.

Girders. Figure 12 shows an example of a bridge girder. Based upon the frontal area of the structure, the drag coefficient of a single girder is $C_D \approx 1.7$; the projected solidity ratio of this girder is $\approx 30\%$. In a pair of girders, the second one is shielded by the first to a certain extent. The drag coefficient of the second girder is, therefore, only $C_D = 0.7$; and the average coefficient of the pair is 1.2. The shielding effect may decrease, however, as the direction of the wind against the structure is selected somewhat different from normal to the girder planes. **Solidity.** It can be seen in (15) that the drag coefficient C_D (on projected solid area) decreases as the solidity (that is, the ratio of the solid to the total area) of a girder is increased, to $C_D = 1.3$ for a solid "beam" of $b/h \approx 9$. Figure 13 gives a statistical analysis on the magnitude of the drag coefficient as a function of solidity. At $S/S_a \rightarrow 0$, beam coefficients are plotted in free flow. At $S/S_a = 1$, three-dimensional solid shapes are used in the graph (such as the disk).

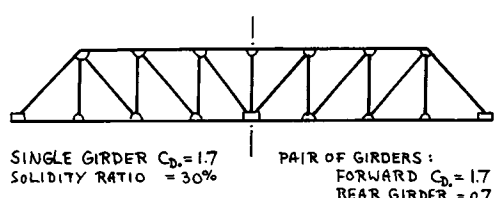


Figure 12. Drag coefficient of bridge girders (16,a).

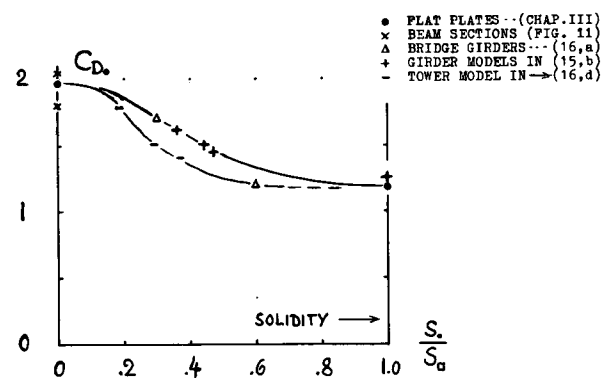


Figure 13. Drag coefficients (on projected solid area S_a) of various steel structures as a function of their solidity ratio.

Bridges, such as the Golden Gate Bridge, for example, at the entrance to the harbor of San Francisco, may be exposed to the full force of strong winds. Figure 14 presents drag coefficients of several shapes of a road-bed structure used in suspension bridges. It is evidently not much of a problem, however, to build bridges (and similar structures) so that they stand up statically against predictable wind forces. Experience with suspension bridges (16,b) has shown, however, that their dynamic behavior (oscillations and flutter), based not only on drag—but also on lift forces, is extremely important.

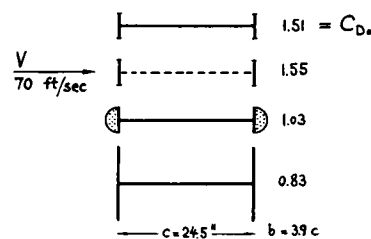


Figure 14. Drag coefficient (on single frontal area) of a bridge structure (road bed plus lateral beams) wind-tunnel tested (16,b) with $A = b/c = 3.9$.

Radio Masts, with triangular or square cross section, supported by stays as shown in figure 15,a, have been built up to 800 ft in height. For undisturbed emission, radio installations are usually located in open terrain or even on mountain tops. They are, therefore, exposed to strong winds. As reported in (18), practical assumptions in their design are a wind pressure (dynamic pressure q) between 30 and 60 lb/ ft^2 , a drag coefficient C_D between 1.5 and 2.0 and a safety factor in the order of 3. While the pull by horizontal antenna cables (if any) at the top of radio masts, is considerable; namely between 1 and 10 tons in larger installations—the wind pressure during a storm (to be determined through the use of figure 13) is still higher, possibly in the order of 50 tons.

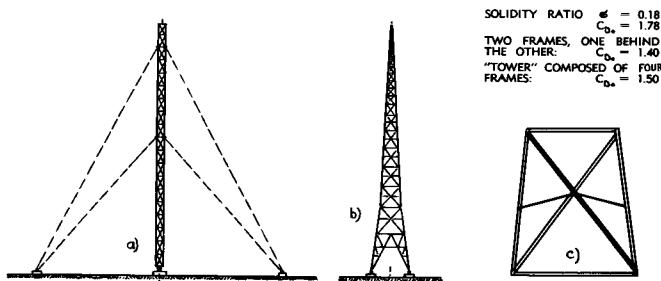


Figure 15. General shapes of radio masts (a) or towers (b), both built in heights up to 800 ft (18); (c) wind forces in a lattice frame (16,d).

Steel Towers are expected to show drag characteristics similar to those of girder bridges. Because of the high drag coefficients involved (C_D , up to 2, on projected area of the structural members), the Eiffel Tower ($h = 300$ m ≈ 1000 ft) has evidently been designed in its characteristic shape; on a rather wide base. Power-line masts and certain radio towers (figure 15,b) are also built in cantilever type (supported from the base, usually on 4 legs). Figure 15,c presents shape and drag coefficients of a typical lattice-design section of such a tower. The mechanism of solidity applies to these structures in the same manner as to girders, so that their drag can be calculated on the basis of the coefficients plotted in figure 13. In a tower built up of 4 frames as in part (c) of figure 15, the contribution of the two lateral frames (parallel to the direction of flow) is only 5% of the drag as indicated for the two sides normal to the wind. That tower has a maximum wind force (in pounds) at a lateral angle between 25 and 35° against the flow, in the order of 10% above the value as in the position normal to the direction of wind.

5. OTHER STRUCTURES

Open Roofs. Pressure distributions on certain shed-type buildings (without walls) are included in (4,b). Taken from another source, figure 16 shows an open roof structure as they are used to protect the platforms in railroad stations. Forces in such roofs can be considerable; a combination of pressure (below) and suction (on top) tends to lift the structure in a manner similar to that of a wing. A particular problem in the roof as illustrated in figure 16, is the effect that the presence of a train can have upon the pressure distribution. While the flow is always separated from the upper side, the positive pressure forces underneath the roof are increased to $C_p = 0.7$ and 0.8, in presence of a train at the leeward side.

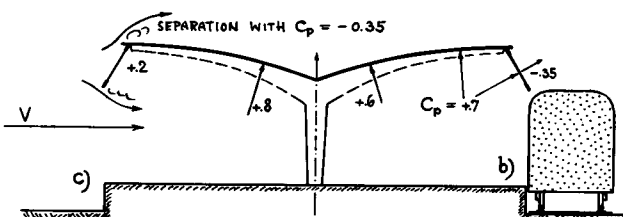
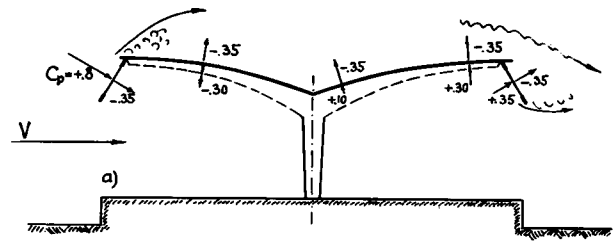


Figure 16. Pressure distribution on the roof over a railroad platform, tested (20) on wind-tunnel model:

- a) without any train;
- b) with train at leeward side;
- c) with train at windward side, the pressure coefficient under the roof is uniformly $C_p = -0.2$.

Sphere. In big exhibitions, "structures of unusual character" are sometimes erected to attract curiosity and attention. One of these has been the "perisphere" as illustrated in figure 17—shown together with the "trylon" described in the subsequent paragraph, at the "New York World's Fair" at Flushing Meadows on Long Island in 1939. Characteristics of spheres are presented in the "pressure drag" chapter. For a diameter of 200 ft, supercritical flow

-
- ¶(15) Aerodynamische Versuchsanstalt Göttingen:
 - a) Various Beam Shapes, Ergebnisse III (1927).
 - b) Experiments on Steel Girder, Erg III (1927).
 - ¶(16) Aerodynamics of steel structures:
 - a) Ower, Resistance of Girder Bridges, by Inst. of Civil Engrs. and Inst. of Struct Engrs (1948).
 - b) Farquharson, Stability of Suspension Bridges, University of Washington Bull. No.116, I (1941).
 - c) Suspension Bridges, Am.Scientist 1954 July.
 - d) NPL, Wind Pressure on Latticed Tower Models, J. Inst'n Electr.Engs 1935 No. 464 p.189.
 - ¶(18) Nokkentved, Radio Masts, Ingenioren 1932 p.347.
 - ¶(20) Aerodyn.Lab. TH München, reported in Kauffmann "Tech Hydro and Aeromechanik", Springer 1954.
 - ¶(22) Klemin and Others (NYU), Aerodynamics For Worlds Fair, Trans AS Civil Engg 1939 p.1449.
 - ¶(24) Eiffel, Travaux Scientifiques à la Tour de 300 Mètres, published in Paris 1900.
 - ¶(26) Additional references on building aerodynamics:
 - a) CAHI (Moscow), Wind Pressure on Roofs and Walls (Railroad Station), Rpt 35 (1928).
 - b) Giovannozi, Building Models, L'Aerotecnica 1935 p.596; see also in Ricerche di Ingegneria 1936 No. 4 p.129 and No. 5 p.105.

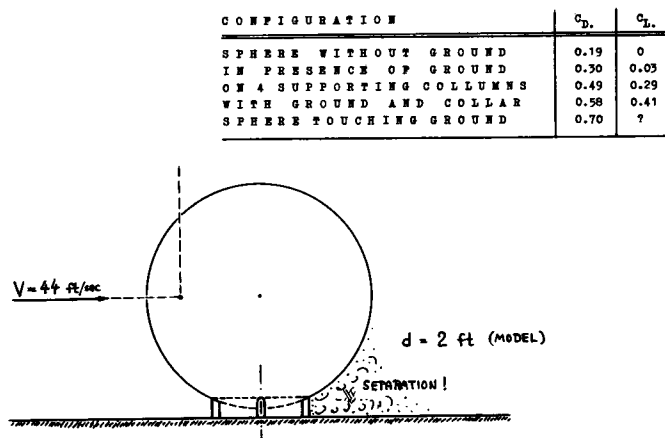


Figure 17. Drag coefficient of a giant sphere ("peri-sphere") as tested in a 1/10 scale model (22).

pattern must be expected at wind speeds above 0.5 ft/sec. The sphere was therefore tested in the NYU wind tunnel (22) on a model having 2 ft diameter at a Reynolds number of $R_d \approx 4 \cdot 10^6$. It is seen that the presence of the ground increases the drag by $\approx 70\%$. The drag is further increased because of "columns" or "collar" needed to support the full-scale structure. An interesting result is that after adding ground and support, a lifting force is produced corresponding to a coefficient " C_L ," between 0.3 and 0.4.

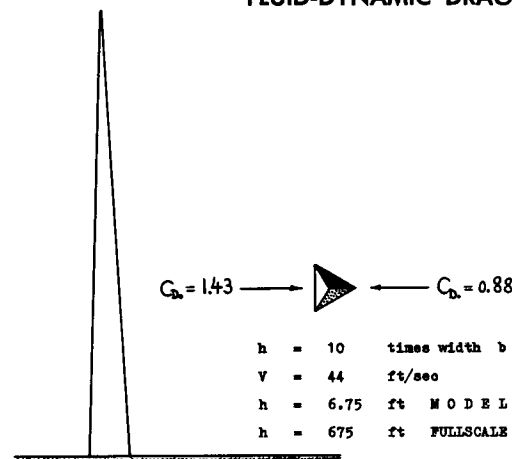


Figure 18. Drag coefficient of the "trylon" as tested in the NYU wind tunnel (22).

"*Trylon*". Figure 18 presents wind-tunnel results on a slender pyramidal shape having $h = 675$ ft, full scale. The drag coefficient varies, of course, with wind direction; between a minimum of 0.88 and a maximum of 1.43. In a hurricane of 125 mph, the corresponding steady-state wind forces would be below and above, respectively, 1,000,000 lb. Here as in smoke stacks (discussed in a preceding paragraph) oscillations caused by vortex shedding, in resonance with the structure's natural lateral bending frequency, might be of importance too.

Statue of Liberty. As a final example of a structure in which wind forces and their exploration by model tests are of importance, the Statue of Liberty is mentioned. Reference (24) says about this 150 feet high monument (erected in New York City harbor in 1886): "Les études que M. Eiffel avait faites sur la résistance au vent des constructions métalliques le désignaient à l'avance pour l'établissement de l'ossature en fer de la Statue de la Liberté de Bartholdi".

CHAPTER V – DRAG OF SURFACE IMPERFECTIONS

The influence of surface imperfections (roughness, protuberances, holes and gaps) upon drag is twofold. First, the boundary layer may be forced to turn turbulent ahead of the transition point as for smooth condition. This type of added resistance is treated in Chapter II. Second, depending upon size and shape, any obstacle on the surface presents a drag of its own. Only this component of resistance; that is, the drag of various surface imperfections in turbulent boundary layer, shall be considered in this chapter.

1. DRAG DUE TO SURFACE ROUGHNESS

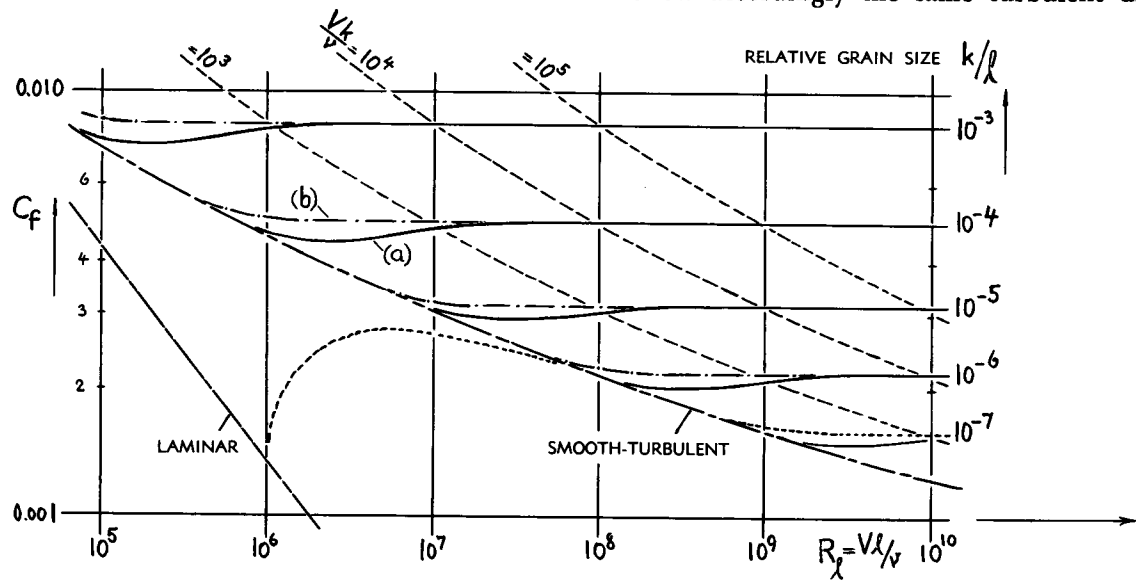
Surface roughness may have an endless variety of grain size, grain shape and concentration. The type which has predominantly been investigated is sand roughness; sand grains of essentially equal diameter are glued to the surface (more or less embedded in lacquer), closely packed against each other. The parameter defining this roughness is simply the grain diameter "k".

Figure 1. Skin-drag coefficient of sand-rough surfaces; (a) as derived from Nikuradse's pipe experiments (1), and (b) as tested and presented in (2).

The drag of a rough surface in tangential flow may not be purely "viscous". Behind every single, sufficiently high protuberance, the flow may locally more or less be separated; and the resultant drag may at least partly be pressure drag. The flow pattern (velocity distribution) across the outer parts of the boundary layer is much the same, however, as that along smooth surfaces (with turbulent boundary-layer flow). The influence of roughness is thus restricted to the sublayer; and roughness may be considered as a substitute for viscosity. If we really want to make a distinction between frictional resistance and drag due to roughness, we may call the latter one "skin drag".

(a) Permissible Grain Size

Critical Reynolds Number. The turbulent boundary layer is characterized by velocity fluctuations in all directions. As explained in Chapter II, there is always a comparatively thin sublayer, however, within which stable laminar flow is prevailing. As long as the protuberances of a rough surface are deeply enough submerged within the sublayer, the surface is, therefore, hydrodynamically equal to a smooth one. As shown in figure 1, the rough surfaces follow accordingly the same turbulent drag



law as the smooth ones — up to certain critical Reynolds numbers. Only above these numbers, the drag coefficient of rough surfaces departs from the smooth and turbulent function which is explained in Chapter II. In other words, as the thickness of the laminar sublayer decreases with increasing R'number, the roughness grains begin to emerge from that layer at certain critical numbers. — The results of two different evaluations are plotted in figure 1. Schlichting's system (1) shows certain "dips" before the constant terminal levels of the drag coefficient are reached. As the critical Reynolds number is approached, the boundary layer (assumed to be turbulent from the beginning) changes into the state of roughness flow, first at (or near) the leading edge, where the ratio k/δ is highest. Within a range of Reynolds number, for example between 10^6 and 10^7 in figure 1, the transition then steadily moves from the leading toward the trailing edge. This travel thus takes place in a direction which is opposite to that of the transition point from laminar to turbulent boundary-layer flow. In Schlichting's experiments, the drag coefficient of the rear portion of the surface is evidently still decreasing with Reynolds number — while the forward portion has already assumed the constant terminal level. The corresponding dip of the drag coefficient is not seen, however, in the results of reference 2. It is suggested that in the latter tests some of the sand grains were protruding from the average level of the rest. Results are known from other investigators (see in reference 3) employing non-uniform grain sizes — which do not exhibit either, the transitional dip of the drag coefficient. It seems that this condition also applies to most physical surfaces, in which a certain number of larger protuberances emerge first from the sublayer, thus covering the dip which can be expected only for uniform roughness structure.

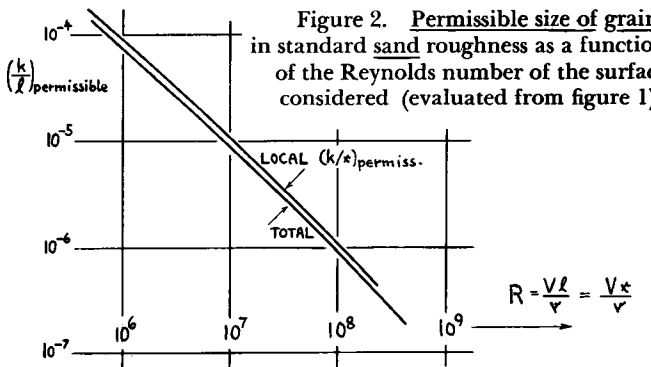


Figure 2. Permissible size of grains in standard sand roughness as a function of the Reynolds number of the surface considered (evaluated from figure 1).

Critical Roughness Size. The critical Reynolds number (or the critical grain-size ratio k/l) shall be defined in figure 1 as the point where the smooth-turbulent function intersects the terminal level indicated by $C_f = \text{constant}$. Figure 2 presents the corresponding critical roughness ratio k/l as a func-

tion of the Reynolds number R . A simple rule can be derived from figure 1; roughly independent of length and R'number of the surface, the permissible sand roughness is defined by the Reynolds number based on average grain diameter "k":

$$R_{\text{critical}} = (Vk/v)_{\text{critical}} = 90 \text{ to } 120$$

The permissible grain diameter is accordingly

$$k_{\text{critical}} \approx 100 v/V \quad (2)$$

Measuring the grain size in mils, it is found for air in standard sea-level condition (with $v = 1.564/10^4$, ft^2/sec):

$$k_{\text{permissible}} \approx 185/V \frac{\text{ft/sec}}{\text{in mil}} \approx 110/V \frac{\text{kts}}{\text{mils}}$$

Hence, as illustrated in figure 3, the permissible size is a function of speed only, at a given altitude (4). This means, for example, that a wing with 10 ft chord, is not permitted to have a larger grain size than a wind-tunnel model having only one ft chord, provided that both bodies are tested at the same speed and in the same atmosphere.

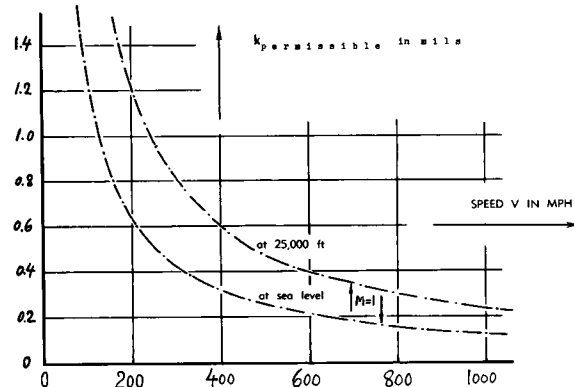


Figure 3. Sand-roughness size in air, permissible on plane walls, as a function of speed.

Influence of Atmosphere. At an altitude of 25,000 ft, the kinematic viscosity (Chapter I) is approximately twice as high as at sea level. As indicated by equation 2, the permissible grain size on the surface of an airplane is consequently twice as high too at this altitude, for equal speeds. Considering, on the other hand, the test conditions in wind tunnels operating with compressed air, as for instance in the Variable-Density Tunnel of the NACA, with a pressure of 20 atmospheres and a kinematic viscosity in the order of only 1/15 of that in free sea-level air, the permissible roughness of wing- or airplane models is found to be very small; namely in the order of only 0.1 mil, at a speed of ≈ 75 ft/sec . — The permissible roughness in water will be discussed in the "hydrodynamic" chapter.

Measuring Roughness. Grain size and structure of physical surfaces can be determined by optical methods (5). The surface is lighted in oblique direction. Using a microscope with a linear enlargement factor of 10 or 20, the grains, contrasted by their shadows, are then optically measured, and a reasonable average size is selected to represent the height or the diameter of the grains. Naturally this method is somewhat arbitrary. Results are furthermore complicated by shape and concentration of the tiny protuberances in physical surfaces.

Type of Surface	Approximate microns	Grain Size d in mils
surfaces like that of a "mirror"	0	0
surface of average glass	0.1	0.004
finished and polished surfaces	0.5	0.02
aircraft-type sheet-metal surfaces	2	0.1
optimum paint-sprayed surfaces	5	0.2
planed wooden boards	15	0.6
paint in aircraft-mass production	20	1
steel plating — bare	50	2
smooth cement surface	50	2
surface with asphalt-type coating	100	4
dip-galvanized metal surface	150	6
incorrectly sprayed aircraft paint	200	8
natural surface of cast iron	250	10
raw wooden boards	500	20
average concrete surface	1000	40

Table A. Approximate values indicating the average grain sizes (diameters) on physical surfaces.

Grain Size in Physical Surfaces. Approximate average grain sizes as found in physical surfaces, are listed in table A. In aviation, camouflage paint may be requested to show a dull surface. Such paint must have accordingly some grain size. At 400 knots, for example, which may be a speed representative of

today's fast long-range airplanes, the permissible grain size is found in figure 3 to be in the order of 0.4 mils (at sea level). It is justified to request, not to exceed this roughness size in manufacturing and painting aircraft. It is not necessary, however, or favorable, as far as *turbulent* boundary layer is concerned, to polish the surface until it shines. The light-alloy sheet metals, commonly used in airplane construction, are generally smooth enough without any further care, up into the transonic range of flying speeds. It is only for portions with laminar boundary-layer flow, especially near the nose of wings or fuselages, that it is favorable to reduce the grain size below the limits indicated by figures 2 or 3. There is an easy chance, on the other hand, of producing grain sizes beyond any permissible limit — just by incorrect handling of the spray gun.

(b) Skin-Drag Coefficients

Terminal Drag Coefficient. The fact that the drag coefficient of rough surfaces assumes constant terminal values, means that these surfaces follow a quadratic drag law. Terminal values have been taken from figure 1 and they have been plotted in *figure 4* against the relative sand-roughness size k/l . Within the most interesting range between $k/l = 10^{-5}$ and 10^{-3} , it is approximately found that

$$C_{f\text{terminal}} = 0.032 \left(\frac{k}{l}\right)^{1/5} \quad (4)$$

Some critical Reynolds numbers are marked on the curve, indicating the limits down to which the terminal values are applicable. Below these numbers, the coefficients of smooth surfaces must be used. The experimental points determined on slender bodies and streamline sections, show drag coefficients that are somewhat higher than those of plane surfaces (thin plates) — because of increased average velocities past their sides.

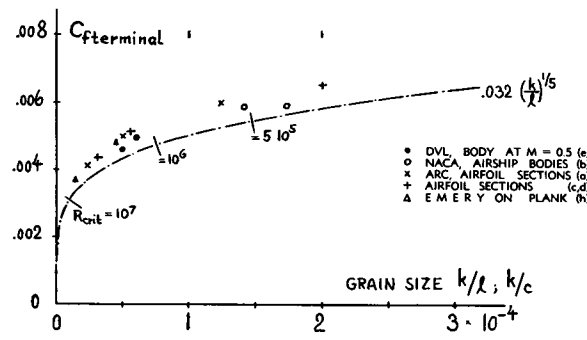


Figure 4. Terminal (constant) skin-drag coefficient of rough surfaces as indicated by theory (1 and 2) and as tested (7). The points are some 10% higher than the theoretical function because of increased average velocity past the slender bodies used in the experiments.

- (1) Prandtl and Schlichting, Drag Law of Rough Surfaces, Werft-Reederei-Hafen 1934 p.1; also Yearb STG 1936 p.416 and Trans ASME 1936; also Trans TMB 258.
- (2) Schultz-Grunow, Rough Plates, Ybk STG 1938 p.177.
- (3) Hama, Smooth and Rough, Trans SNAME 1954.
- (4) Hoerner, Influence of Roughness on Aircraft Characteristics, Ringbuch Luftfahrttechnik Part I A 9 (1937).
- (5) Lichtschnitverfahren by Zeiss and Schmalz.
- (6) Schlichting, Roughness Experiments, Ingenieur Archiv 1936 p.1, also Yearb STG 1937 p.159, and Trans ASME 1936.
- (7) Experimental Results of Terminal Drag Coefficients:
 - a) Airfoil Sections in CAT, ARC RM 1708 and 1789.
 - b) Airship Bodies, NACA T Rpts 342 and 394.
 - c) Hooker, Tests on Airfoil, NACA T Note 457.
 - d) Tests on Airfoil, Document ZWB Rpt FB 642.
 - e) Goethert, On Bodies, ZWB Tech Berichte 1944.
 - f) Young and Others, Flight Tests on Surface Condition (paint, rivets, joints), ARC RM 2258 (1939).
 - g) Young, 0012 Foil, Journal RAS 1950 p.534.
 - h) Allen-Cutland, Emery on Plank, Trans Inst. Engrs and Shipbuilders Scotland 1955/56 see also Shipbdg Shipping Review 1955 p.541.

Equivalent Sand Roughness. To this point, the presented functions of rough surfaces are primarily applicable to "standard" sand roughness. Dealing, however, with physical surfaces, the shape of the roughness grains and their concentration (average distance between grains) — is of hydrodynamic influence too. Various kinds of roughness have been investigated (6) in a special wind channel. The aerodynamic effect of each type is simply indicated by an effective sand-grain size "k". This size or the ratio k/d (where d indicates the average "diameter" of the grains or elements considered) — indicates the size of standard sand roughness which produces the same drag coefficient as the type of roughness investigated. The limitations of the procedure are pointed out later.

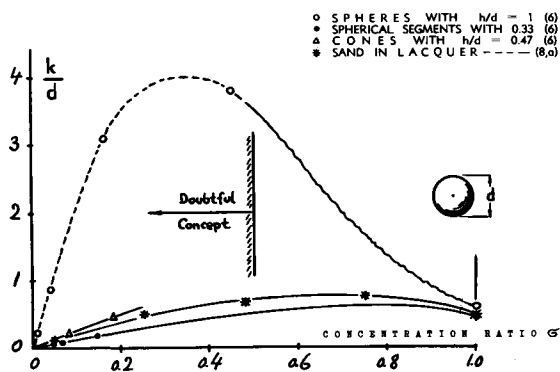


Figure 5. Equivalent sand roughness "k" as a function of roughness concentration.

Grain Concentration. The density or concentration of roughness grains is measured by the parameter

$$\mathfrak{G} = \sum(d^2)/S_{\text{wet}} \quad (5)$$

where d indicates the grain diameter. Some experimental results are plotted against this parameter in figure 5. The equivalent sand-grain ratio k/d , for example of spherical grains, increases considerably upon decreasing the concentration. The grains are

evidently much more effective standing alone than closely packed against each other. A surface with a comparatively thin concentration (around $\mathfrak{G} = 20\%$) may thus present considerable skin drag. Taking, for example, the maximum value for spheres, $k/d = 4$, the corresponding coefficient (equation 4) is expected to be increased to $4^{1/6} = 1.32$ of that of same-diameter standard sand roughness. It should be noted, however, that the spherical shape, if "embedded" in lacquer (8,a) has a very much reduced effect, evidently corresponding to reduced exposure. It can also be noted that at $\mathfrak{G} = 1.0$, all of the investigated shapes (with round plan form) exhibit k values which are lower than that of the somewhat irregular "standard" sand-roughness variety.

Grain Shape. The influence of grain shape is most evident (in figure 5) at intermediate concentration ratios. It is also seen there that the equivalent sand-roughness ratio corresponds to the height ratio h/d of the elements and/or to their shape. Flat elements, for example, have not only smaller k/d but also lower k/h values than the spherical grains. The grains found on painted surfaces may resemble the shape of flat cones or spherical segments. Roughly, figure 5 suggests for these shapes $k/d = 1$ (or a somewhat lower value).

Permissible Grain Size. Using the concept of the equivalent sand roughness, the permissible size of a specific type of elements can also be estimated. For $k/d = 2$, for instance, the permissible size is tentatively only half of that of standard sand grains. Such estimates may be adequate, however, only down to concentration ratios in the order of 0.5. Below this value, there are evidently portions of the surface between the grains, exhibiting lesser drag corresponding to smooth friction. In other words, a few grains distributed over a larger surface cause only small additional drag. However, their permissible grain size must be assumed to be at least as small as for the concentration shown in figure 5 exhibiting maximum drag.

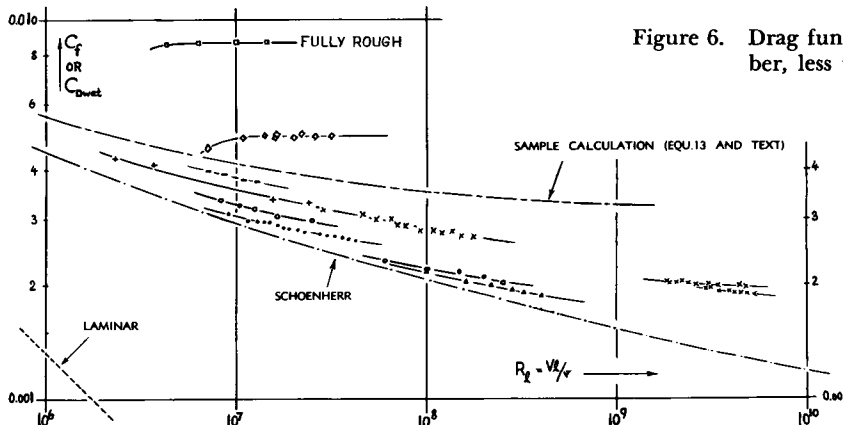


Figure 6. Drag functions having slopes C_f against R' number, less than that of smooth-turbulent friction.

- PAINTED 0012 AIRFOIL (7,g)
- ◊ EMERY ON TANK PLANK (7,h)
- + RIVETS ON SURFACE (8,b)
- TMB NAVY PAINT (8,c)
- GALVANIZED PONTOONS (8,f)
- ▲ PAINT ON PONTOON (8,a)
- × PAINT ON SHIP HULL (8,e)
- SHEET-METAL WING, reported in Ybk.D.Lufu 1939 p.I,95 (8,d)
- x HIRAGA PLANK XI (9,c)

Slope of $C_f(R)$. At Reynolds numbers above the critical, the skin-drag coefficient for standard sand roughness (with $\varsigma = 1$) is constant; the slope of $C_f(R)$ is zero. As explained and demonstrated on revolving cylinders (9), concentration not only affects the critical R'number of roughness, but also the slope of $C_f(R)$. In other words, there may not be a constant "terminal" drag coefficient at all for certain types of roughness. Figure 6 presents some examples; and it is seen that painted and other surfaces exhibit coefficients decreasing against R'number at a rate which is less than that of the smooth-turbulent function. Two examples of coarse-grain coatings are included, however, in the graph—to show the constancy of their drag coefficients. To make the behavior of the painted surfaces understood, a limited number of grains shall be considered again, distributed over a larger area. Tentatively, the surface portions between the grains maintain most of their smooth-surface behavior, including a skin-friction drag coefficient which decreases against Reynolds number. The slope of the total or average drag coefficient of such surfaces will, therefore, be between that of the smooth-turbulent function and a constant terminal coefficient corresponding to grain size. The data in figure 6 and other results have been evaluated in the form of the slope- or exponent ratio m/m_o in the function

$$C_f = K/R_\lambda^m \quad (6)$$

where for smooth surface "m" is in the order of 1/6; see equation 28 in Chapter II. The slope ratios are plotted in figure 7 against the concentration ratio

$$\varsigma = \sum(k^2 \text{ or } d^2)/S_{\text{wet}} \quad (7)$$

The available points are interpolated by

$$m/m_o = (1 - \varsigma)^E \quad (8)$$

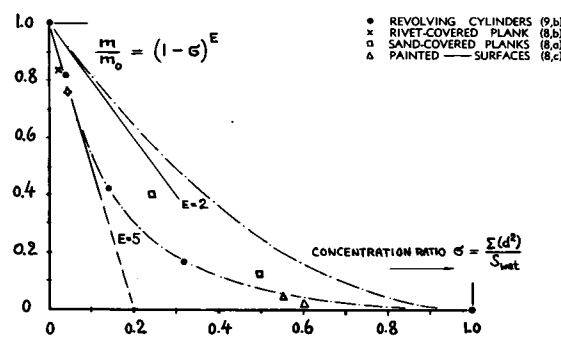


Figure 7. Analysis of the exponent "m" indicating the slope of $C_f(R)$ as a function of concentration.

where $E \approx 5$ for sand-type roughness. It is predicted, however, that this exponent will be smaller for roughness elements which are flatter than spherical grains; possibly in the order of $E = 2$. — The fact that many physical surfaces have drag-coefficient slopes somewhere between that of the smooth surface and a constant level, has been pointed out to exist as early as 1923 (10). Data given in this and other references have been evaluated and listed in table B in the form of the exponent ratio m/m_o . One could reverse the procedure now, and conclude that certain concentration ratios are the equivalent of certain types of roughness, as tested.

Type of Surface	m/m_o	Reference
asphalt-coated	0.8	Hopf (10)
cast-iron	0.8	Hopf (10)
painted plate	0.8	Fig. 7 (8,a)
steel pipe	0.77	Pigot (8,g)
marine paint	0.7	Fig. 7 (8,c)
galvanized pipe ..	0.67	Pigot (8,g)
galvanized metal ..	0.5	Hopf (10)

Table B. Analysis of the slope ratio m/m_o in several types of surface roughness.

Polytropic Grain Size. A surface covered with grains of non-uniform size, may be studied by assuming one basic uniform roughness, combined with some limited number of larger grains. Reference (11) presents experimental results on such surfaces in pipe flow. There are two critical Reynolds numbers, corresponding to the grain sizes involved. At the lower number, the drag coefficient begins to depart from the smooth-turbulent function, assuming a reduced slope from there on. At the second critical R'number, a constant terminal drag coefficient is reached as in uniform sand roughness. Considering next a surface with various grain sizes, the lower critical Reynolds number is expected to correspond to the largest size involved. The terminal level will then be obtained at a number which corresponds to the smallest grain size represented in such a surface.

- (8) Experimental Results on Surface Roughness — Slope:
 - a) Kempf, Yearb. STG 1937 p.159; Trans INA 1937.
 - b) Williams and Brown, Rivets, ARC RM 1855.
 - c) Couch, Ship-Bottom Paints, TMB Rpt 789 (1951).
 - d) Moody, Friction in Pipes, Trans ASME 671, 1944.
 - e) Todd, Skin Roughness, Trans SNAME 1951 p.315.
 - f) Kempf-Karhan, On Ships, Ybk STG 1951 p.228.
 - g) From Pipe Results, Mech'l Engg 1933 p.497.
- (9) Influence of Roughness Concentration:
 - a) Hoerner, Effect of Roughness Concentration Upon Frictional Drag, Jurnal Am.Society Naval Engineers Vol 66 (1954) p.497.
 - b) Revolving Cylinder, NACA Tech Rpt 793 (1944).
- (10) Hopf and Fromm, ZAngMathMech 1923 p.329 and 339.
- (11) Colebrook and White, Experiments With Rough Pipes, Proceedings Royal Society A 1937 p.367.

Practical Procedure. In conclusion, sand-type roughness is realized not to give a complete description of the hydrodynamic characteristics of physical roughnesses. The above considerations of non-uniformity and concentration give the answer (qualitative so far) to many problematic results in correlating the viscous drag of full-scale airplanes and/or ships with model-test results (see also in the chapter on "water-borne craft"). Additional research into this problem is needed. However, for the time being, the procedure as follows is suggested for an appraisal of the drag function in moderately concentrated roughness. (a) The critical Reynolds number is approximately determined on the basis of the predominant or average grain size. (b) The slope of the $C_f(R)$ function (starting at the point on the turbulent skin-friction curve at R_{crit}) is then determined through the use of figure 7. The exponent is found as $m = m_o(m/m_o)$ where m_o as indicated in Chapter II; for smooth-turbulent friction ($m_o \approx 1/6$). (c) Depending on the type of surface (either with a uniform fine grain size, or with underlying smooth portions) there may or may not be a second critical Reynolds number and a constant terminal drag coefficient.

2. DRAG OF SURFACE IMPERFECTIONS

In the following paragraphs, "imperfections" shall be understood to be protuberances (and cavities) the height of which is in the order of or less than the boundary layer thickness. Again, the drag of such imperfections shall only be considered here within turbulent boundary layer. Also the results have almost all been determined on a flat wall.

a) General Mechanism

Effective Dynamic Pressure. A small body, placed within the boundary layer, causes a drag component which corresponds, at least approximately, to the average or effective dynamic pressure of a layer limited by the height h of the body. Basically, therefore, the drag of surface imperfections is smaller than to be expected in free flow or at the wall of a body where no boundary layer is present. From the velocity distribution across the boundary layer (Chapter II), the effective dynamic pressure is derived as

$$q_{eff}/q \approx 0.75 \sqrt[3]{h/\delta} \quad (9)$$

The experimental points in figure 8 show the corresponding trend of $C_D \sim (h/x)^{1/3}$, where the length x of the surface or wall to the location of the protuberance is the measure for b'layer thickness.

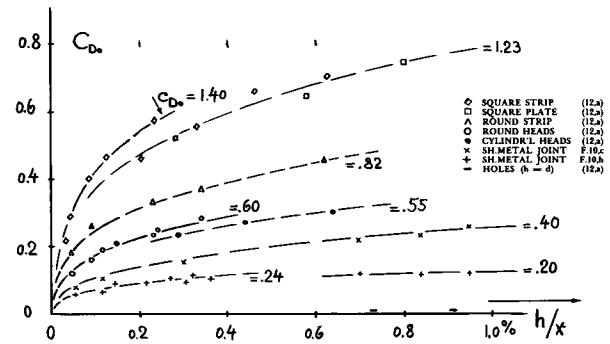


Figure 8. Drag coefficients of elementary surface imperfections as a function of their height ratio.

Independent Drag Coefficient. Accepting the proportion $D \sim h^{1/3}$, it is possible to determine the drag for any height (smaller than δ) — if the same is known for one particular height. Referring now the drag to the effective dynamic pressure (equation 9), an "independent" coefficient is found:

$$c_D = \frac{D}{q_{eff} S} \approx \frac{C_D}{0.75 \sqrt[3]{h/\delta}} \quad (10)$$

The drag of any protuberance with $h < \delta$ in turbulent boundary layer — is sufficiently well defined by means of this coefficient. At Reynolds numbers between $R_x = 10^6$ and 10^7 , the total thickness of the boundary layer on smooth surfaces is roughly

$$\delta/x = 1.6\% \quad (11)$$

with x indicating the distance of the considered point from nose or leading edge of the respective body. Introducing this ratio into equation 10, it is approximately found that

$$c_D = 0.33 C_D / \sqrt[3]{h/x}; \quad C_D = \sqrt[3]{h/x} c_D$$

Of course, this equation applies only to height ratios up to $h/x = 1.5\%$.

Against Reynolds Number. As pointed out in Chapter II, the skin-friction drag coefficient C_f and the boundary layer thickness δ/x — are approximately proportional to $1/R_x^{1/6}$. The drag coefficient of a protuberance on the other hand, is proportional to $(h/\delta)^{1/3}$, as indicated by equation 9. As a function of the R' number of the surface or wall, therefore

$$C_D \sim R'^{1/8} \quad (13)$$

The drag coefficient of the protuberance thus increases with the Reynolds number, while the skin-friction coefficient decreases. The percentage cov-

ered by protuberances (such as rivet heads or sheet-metal joints) of the wetted surface of an average wing may be in the order of 1%. Roughly, 99% of the surface are thus following the laws of smooth skin friction. The corresponding drag coefficient is $C_{f1} = 0.99 \cdot 0.043 / R_x^{1/6}$, as found in Chapter II. The drag component (on the wetted area) due to the protuberances is $C_{f2} = 0.01 C_D$ with $C_D = 0.75 c_D (h/\delta)^{1/3}$, as per equation 10. For an assumed average height ratio $h/x = 0.1\%$, a ratio $h/\delta = 0.0045 R_x^{1/6}$ is derived from b'layer equations in Chapter II; and for an assumed average coefficient $c_D = 0.4$, a coefficient $C_{f2} = 0.0005 R_x^{1/18}$ is finally found. As plotted in figure 6, the total drag coefficient $C_f = C_{f1} + C_{f2}$ decreases with the Reynolds number at a rate which is less than that of the smooth skin-friction coefficient. The example is a confirmation of what is presented in the "roughness" section on the characteristics of moderately concentrated surface roughness. — It should be noted that the interference between protuberances and surface is not taken into account in the simple functions presented.

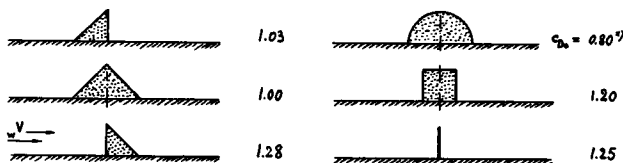


Figure 9. Independent drag coefficient of two-dimensional protuberances, tested (12,a) at $h/\delta = 7.5\%$, and $R_{wh} = 10^4$. (x) decreases at higher R' numbers.

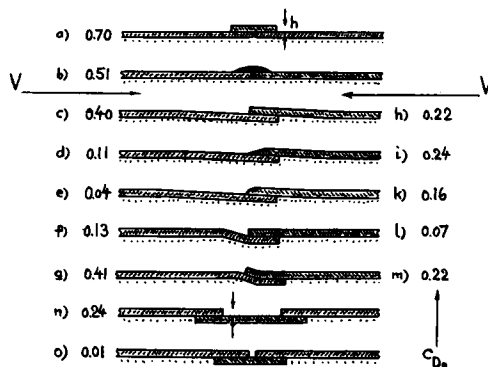


Figure 10. Independent drag coefficient of various sheet-metal joints (12,a), based on thickness "h".

b) Spanwise Protuberances

Spanwise protuberances shall be understood to extend sufficiently far across the general direction of flow. A typical example of this type is a sheet-metal joint running over the span of a wing (or around the circumference of a fuselage).

Drag of Strips. The drag coefficient of sharp-edged spanwise protuberances, shown in figure 9, is rather independent of their specific shape. The flow is always detached from the rear of these strips, just as in free flow. Reference (12,d) also indicates the drag coefficient of wires (used for turbulence stimulation) to be c_D between 0.7 and 0.9 in turbulent b'layer (and between 0.6 and 0.7 in laminar layer).

Sheet-Metal Joints. Among the sheet-metal joints, illustrated in figure 10, the butt joint shows, of course, the lowest drag, $c_D = 0.01$. The highest coefficients on the other hand, are characteristic of the most-protruding and sharp-edged joints, especially (c) and (g) which are directed against the oncoming flow; $c_D = 0.4$. It is worth noticing, however, that by beveling (at 60°) or by rounding the edges of such joints, as in (d) and (e), their drag is reduced, down to 1/4 and 1/10, respectively; a result which is confirmed by another source (12,c). Flat rounding is more effective, however, than same-length beveling. Finally, figure 11 demonstrates that an open joint when facing the fluid flow, has a comparatively high drag coefficient.

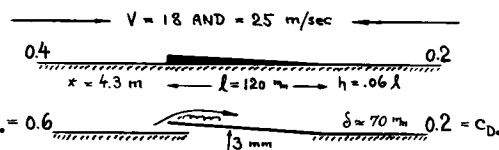


Figure 11. Drag coefficient of a sheet-metal joint (12,b), in "solid" and in open condition.

Waviness. The available experimental data on surface waves are plotted in figure 12. The independent drag coefficient (equation 10) increases approximately as

$$c_{D_s} = 15 (h/l)^2 \quad (14)$$

with l as defined in the illustration. Considering constant wave length (given, for example, between the frames of a fuselage), the drag of a wave in the sheet-metal skin of an aircraft approximately increases as $D \sim h^{7/3} \approx h^2$. Generally, however, the drag of such waves is but small as compared to that of sharp sheet-metal joints.

- (12) Drag Caused by Protuberances in Turbulent Flow:
 - a) Wieghardt, ZWB FB 1563 or Yearb.D.Lufo 1943.
 - b) Tillmann, Rpt KW Inst. Göttingen, Dec 1944.
 - c) Abell, Resistance of Lapped Butt Joints, Liverpool 1931; see also Zeitschrift VDI 1931 p.1431.
 - d) Hughes-Allen, Turbulence Stimulation, Trans Society NAME 1951 p.281.
 - e) Wood, Fittings, NACA T.Note 280 (1928).
- (13) Hood, Waviness on Wing, NACA T.Note 724 (1939).

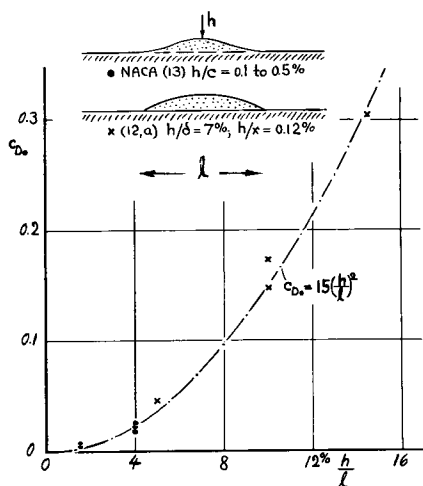


Figure 12. Independent drag coefficient (on projected frontal area) due to surface "waves".

c) Drag of Individual Protuberances

Small bodies, such as bolt- or rivet heads, may be called "spotlike" protuberances. Contrary to spanwise imperfections, they show a three-dimensional flow pattern, of course.

Small Bodies. Among the protuberances illustrated in figure 13, square plates have a coefficient C_D between 1.0 and 1.3. On the average, this coefficient has the same magnitude as in free flow. Further results on plates and disks are presented in the "interference" chapter. In prismatic bodies, the drag

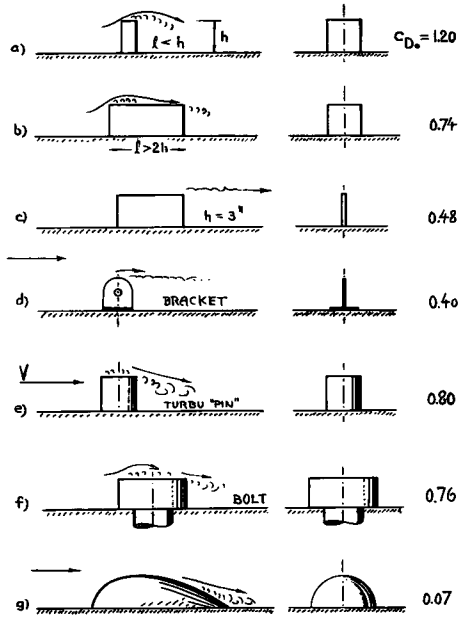


Figure 13. Independent drag coefficient of various three-dimensional protuberances; shapes 'a,b,f,g' from (12,b), "pin" 'e' from (12,d), 'c' and 'd' as in (12,e).

decreases beyond $1 \approx h$, in a manner similar to that in figure 21 of the "pressure drag" chapter, down to a constant level (12,b), with $C_D = 0.74$. Cylindrical "pins" (used in model testing for turbulence stimulation) have comparatively high drag coefficients too. Upon streamlining the little bodies, their drag is considerably reduced.

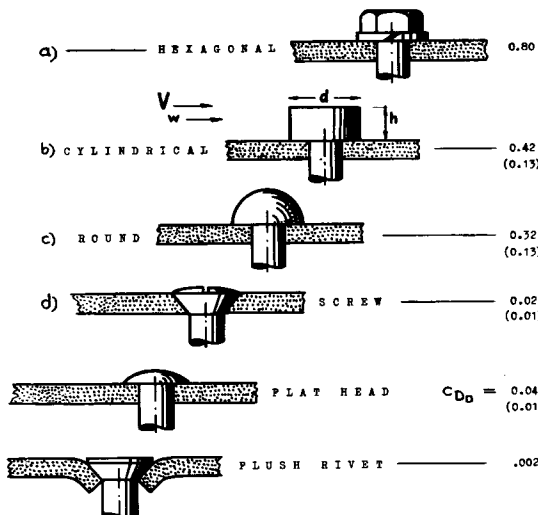


Figure 14. Independent drag coefficient (on $d^2/4$) of bolt- and rivet heads. All shapes tested (12,a) at the same d/δ ratio. Coefficients of the last three heads are based on the effective dynamic pressure as for the first three (corresponding to their height h). The values in brackets apply for supercritical R' numbers.

Bolt- and Rivet Heads. In figure 14, the hexagonal bolt head shows, of course, a high drag coefficient, $C_{D\text{ hex}} = 0.8$, based on plan-form area of the head. In comparison to this shape, flush rivet heads present but a vanishingly small drag coefficient (based upon the same effective dynamic pressure as for the first three heads in the illustration). That such flush heads show a perceptible value of drag after all, is

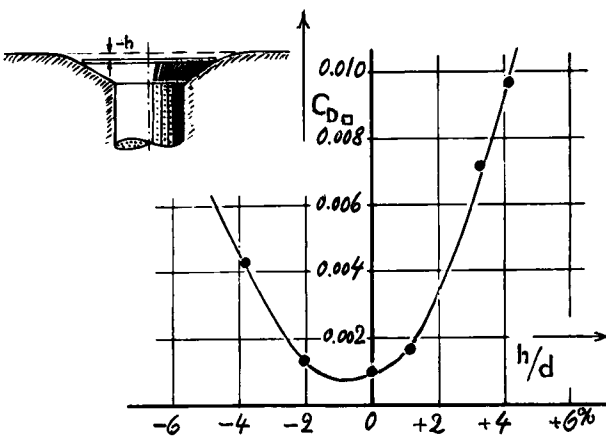


Figure 15. Drag coefficient on $d^2/4$ of a flat rivet head (12,a) tested at $d/\delta = 3$, as a function of its elevation with respect to the surrounding surface.

because of the small groove along their circumference and owing to imperfections in their application. Inevitably the head is often placed, either somewhat too high or too low, in respect to the surrounding sheet-metal surface. A wind-tunnel investigation into this effect is illustrated in figure 15. The minimum drag of the flush-type heads occurs in the vicinity of $h/d = -1\%$. It is thus favorable to set these rivets purposely a little bit lower than flush.

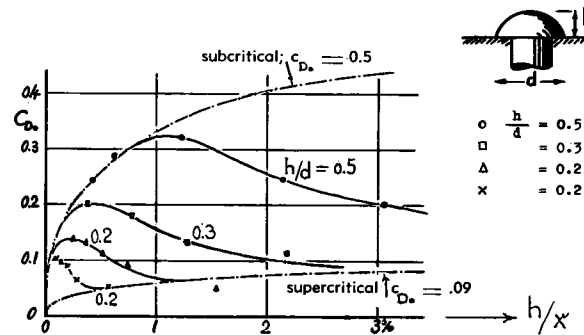


Figure 16. Drag coefficient of round rivet heads in the critical range of their Reynolds number (12,a).

Critical Reynolds Number. Figure 16 demonstrates that the drag coefficient of round rivet heads decreases beyond certain height ratios h/x . The reduction corresponds to that of the drag coefficient of the sphere as a function of Reynolds number as presented in the "pressure drag" chapter. Upon increasing the height h (and the diameter d), the effective R' number of the heads $R_w = d w/v$ increases not only because of the size, but also on account of the effective boundary-layer velocity " w ". Owing to turbulence in that layer, transition to lower drag coefficients starts already around $R_w = 2 \cdot 10^4$. The middle between the limiting conditions ($c_{D_0} \approx 0.3$) is passed at approximately $R_{w\text{crit}} = 8 \cdot 10^4$. This number is only a fifth of that of the sphere in a turbulence-free stream. As in free flow, the independent coefficient of the hemispherical heads drops through the critical range of Reynolds number from around $c_{D_0} = 0.5$ to the order of 0.1

Critical Speed. Assuming a round rivet head with $1/4$ inch diameter, placed within a boundary layer where $w = 0.5 V$, the critical transition of the coefficient takes place between 200 and 1000 mph, if considering an airplane flying near sea level. Conditions above the critical Reynolds number are thus not very likely to be attained; and intermediate drag coefficients within the critical range must be expected for these heads in aircraft applications.

Height Ratio of Round Heads. As illustrated in figure 17, the drag coefficient C_{D_0} (based on dynamic pressure of the outer flow, and plan-form

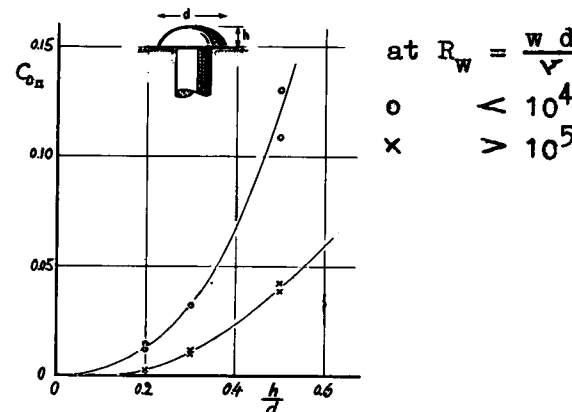


Figure 17. Drag coefficient (on area $d^2\pi/4$) of round heads as a function of their height ratio. Experimental data (12,a) reduced to $d/x = 0.5\%$.

area of the head) increases with the height-diameter ratio at a power between 2 and 3. A round rivet head with $h/d = 0.2$, for example, presents a drag which is in the order of only 10% of that of the hemispherical shape. Such a flat-round head proves, however, to have a drag which is still much higher than that of flush heads (see in figure 15).

Longitudinal Protuberances, extending in the general direction of flow, such as chordwise ridges or sheet-metal joints, for instance, are shown in figure 18. Their drag is approximately twice as high as the skin-friction drag corresponding to their wetted surface. A similar result is found for corrugated sheet metal in figure 23.

In Oblique Flow. In crosswise flow (at $\beta = 90^\circ$) the drag of the strips shown in figure 18, is in the order of 60 times as high as in longitudinal flow (at $\beta = 0^\circ$). The transition between these two directions can roughly be approximated by $D_{\text{pressure}} \sim \sin^2 \beta$.

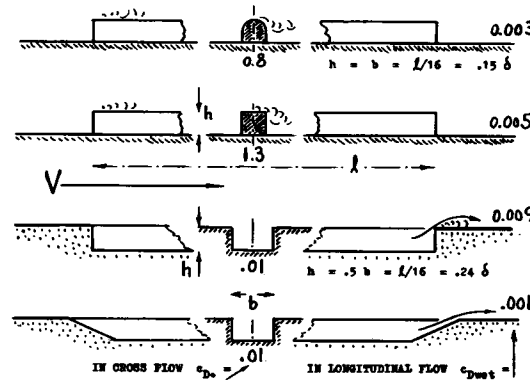


Figure 18. Drag coefficients of strips and grooves (12,a) in longitudinal and in cross flow, as indicated.

d) *Drag of Holes and Gaps.*

The imperfections considered so far, are more or less protruding from the surface on which they are tested. Besides open holes, there are many cracks, gaps and grooves, however, in the skin of airplanes, usually at places where component parts join each other. Such gaps (or holes) do not have a positive height for which an effective dynamic pressure could be defined as per equation 9. As substitute, either the depth "h" or the length (in flow direction) may be used to define coefficients which are comparable to those of positive protuberances.

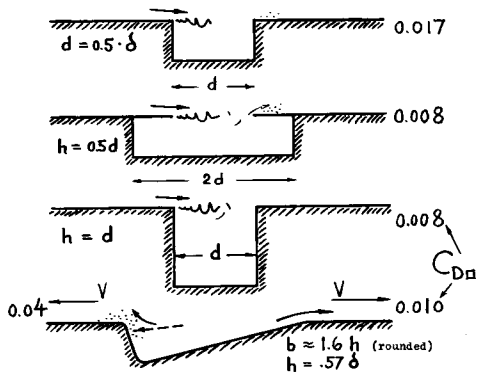
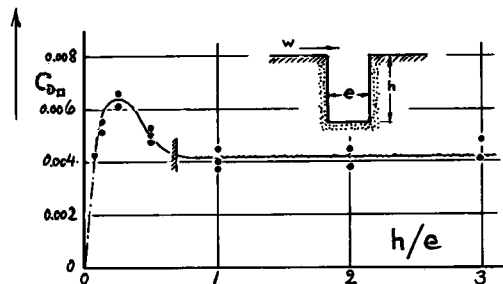


Figure 19. Drag coefficients (on opening area) of several types of holes (12,a,b).

Holes, cut into the skin of aircraft, present a comparatively small drag, corresponding to a coefficient roughly in the order of $C_{D\alpha} = 0.01$ (figure 19). The edge shape of these holes is of some importance. Rounding the downstream edge, reduces the drag. Leading, however, the flow over a rounded (and sloping) edge into the recessed space, increases the drag fourfold in the example as tested.

Figure 20. Drag coefficient (on area e times b) of deep gaps or grooves (12,a,b), tested at $e/x = 0.001$, $e/\delta = .06$, $q_{eff}/q = 0.3$; $C_D = 3.4 C_{D\alpha}$.



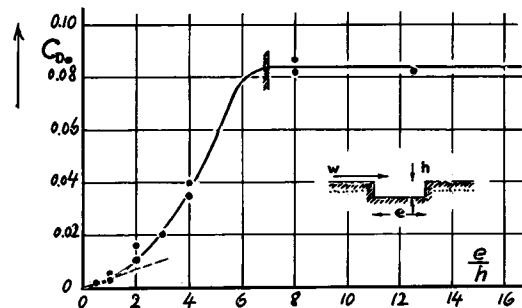
Transverse Gaps. The drag caused by transverse gaps or grooves is a function of their width and depth. A constant coefficient $c_{D\alpha} = 0.014$ (on plan-form area and dynamic pressure corresponding to a height $h = e$) is obtained beyond $h/e = 0.7$; as seen in figure 20. However, the coefficient $c_{D\alpha}$ (on frontal area $b \cdot h$ and dynamic pressure corresponding to the height h), shown in figure 21, reaches the constant value of 0.29 beyond a length ratio $e/h = 7$. This ratio corresponds to $h/e = 0.14$. Between this value and $h/e = 0.70$ (as above), or between $e/h = 1.4$ and 7.0 (as in figure 21), a transition takes place from one regime to the other.

Shape of Edges. Figure 22 shows that the drag of gaps (or grooves) greatly depends upon the shape of the edges and on their position with respect to each other. Rounding the downstream edge, helps to reduce the drag; the flow is smoothly received beyond the gap. Lowering the upstream edge, on the other hand, leads the flow *into* the gap, thus increasing the drag. Employing optimum positions of the two edges, the drag is reduced some 30%, as compared to the original flush configuration.

Sheet-Metal Edges. In modern airplane construction, the edges of gaps are usually formed by sheet metal; and the hollow space inside may be wider than the opening in the skin. As seen in figure 22, the drag is somewhat larger in this case than that of a "solid" gap. By bending the sheet-metal edges up or down, respectively, it is possible, however, to change the drag considerably. In practical production, it appears to be favorable to set the upstream edge as straight as possible and to bend down the downstream edge to a small angle.

Longitudinal Gaps. Grooves, exposed to longitudinal flow are listed in figure 18 together with protruding strips. In contradistinction to the latter ones, the gaps show much smaller drag in transverse flow (at $\beta = 90^\circ$). Obviously the flow jumps easily across such a gap; but it penetrates deeply *into* a longitudinal groove.

Figure 21. Coefficient (on h times b) of shallow gaps or grooves (12,a,b), tested at $h/x = 0.001$ and $h/\delta = 0.06$.



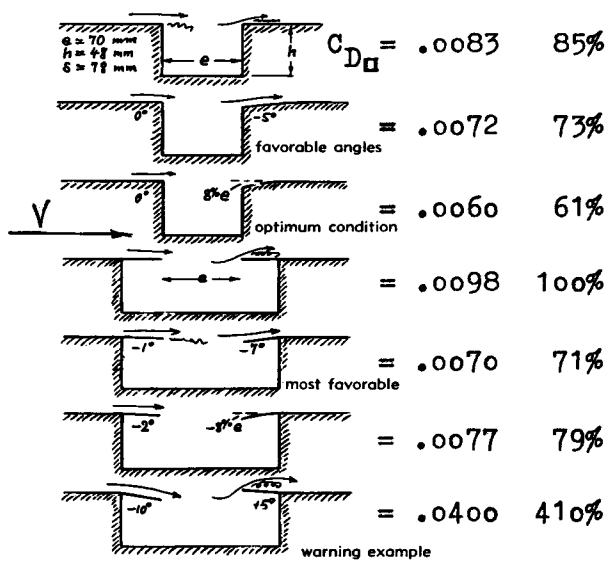


Figure 22. Drag coefficient (on $e \times b$) of a two-dimensional gap, groove or hollow, determined (12,a,b) in a plane wall, as a function of the shape of the edges.

3. IMPERFECTIONS ON STREAMLINE SHAPES

So far, the drag of imperfections has mostly been considered as tested on the plane wall of wind channels (6 and 12). Imperfections, protuberances and other disturbances when placed on the surface of streamline foil sections, are considered as follows.

(a) Imperfections and Protuberances

Surface Roughness. Figure 4 shows that the drag due to roughness uniformly distributed over the surface of streamline shapes is somewhat higher than on a constant-pressure wall. This is evidently so because of the increased velocity along the sides of such bodies. Some more results concerning the drag of airfoil sections having sand-type roughness on

Type of Surface	$10^3 C_f$	$10^5 k/l$	"k" mils
smooth polished finish ..	3.2	(+)	0
well doped linen ..	3.8	(*)	0
bare (oiled) plywood ..	4.5	15	9
Junkers corrugated sheet	5.4	40	24
coarse fabric (taut) ..	6.0	60	36

Table C. Results of wake survey in flight (17) at $R_e = 5 \cdot 10^6$ on wing having $t/c \approx 17\%$. "k" is equivalent sand-roughness size (derived from equation 4; producing the same drag). (+) partly laminar (*) subcritical.

their surfaces, are presented in the "streamline" chapter. Another piece of information is given in table C where results of flight tests on a wing section are listed, indicating type of surface, drag coefficient (obtained by wake survey) and equivalent sand-roughness grain size as explained above. The sectional drag coefficient came out to be essentially constant in these tests, between $C_L = 0.3$ and 0.6.

Corrugated Sheet Metal has been used in the construction of wings and fuselages (particularly by Junkers) in years gone by. For the range of low lift coefficients, figure 23 presents drag coefficients which are not too much above that of the smooth wing at the same Reynolds number. The increment roughly corresponds to the increase in wetted area (in the order of 20%) due to the corrugations. However, in case A, with the corrugations placed on top of the original surface (rather than being cut into the basic model as in "B"), the drag increment amounts to some 40%.

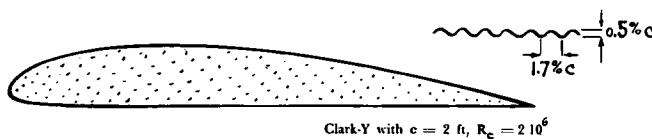


Figure 23. Section drag coefficient of a wing covered with corrugated sheet metal (16).

Sheet-Metal Wing. In case of imperfections placed more or less singly on the surface of streamline shapes, an effect of the type as explained in the "interference" chapter must be expected, due to the positive pressure gradient along the rear of such bodies. As a rough rule, it may be said here that on the after portions of fuselage bodies and of wing sections near zero lift, the drag due to individual protuberances may be in the order of twice as high

- (14) Doetsch, Influence of Surface Imperfections on Drag of Sheet-Metal Wings, ZWB Document (DVL) UM 1233 (1944).
- (15) Day and Schwarzbach (Curtiss Wright), Flight Investigation of Surface Finish (Mud), Jl. Aeron'l Sci. 1946 p.209.
- (16) Wood, Corrugated Surface, NACA T.Rpt 336 (1929).
- (17) Schrenk, Wake Survey in Flight, Lufo 1928 p.1.

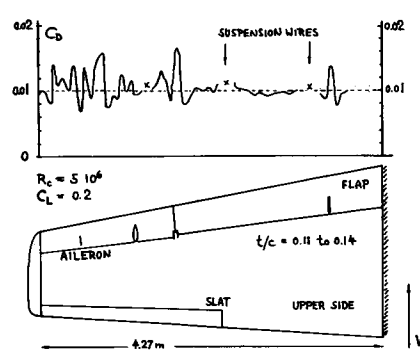


Figure 24. Me-109 sheet-metal wing with slotted flap and aileron, tested by wake survey in wind tunnel (14).

as on a constant-pressure wall. Figure 24 shows the distribution of momentum loss across the span of an Me-109 wing as tested in a large wind tunnel by wake survey behind the wing. The attachments shown on the upper wing side have their traces in the C_{Ds} distribution. Other peaks correspond to the *chordwise* rows of screws used to hold large sheet-metal panels in the lower side. In this reference as well as in other sources, it can be found, however, that a protuberance concentrated in one particular spot, produces a pair of peaks in the wake-loss distribution, while at a short distance behind the obstacle, the flow reattaches, thus leaving no momentum deficiency at its spanwise station. It is also seen in figure 24 that the average drag level is highest within the part of the span where the wing slat (although retracted) is located. The average minimum profile drag coefficient of this wing is slightly above 0.010, while the same type of foil section in smooth and undisturbed condition would have a $C_{Ds} \approx 0.007$ at the Reynolds number as tested.

Surface Condition	C_{Dsmin}
smooth foil section (joints filled with putty, and polished)	0.0063
common service condition (with joints, rivets, camouflage paint)	0.0083
service condition with "thin mud" (from air field)	0.0122
service condition with "heavy mud" (from air field)	0.0175

Table D. Profile drag of 22 (12.8) section, tested in flight by wake survey (15), at $C_L = 0.16$ and $R_e = 1.6 \cdot 10^7$.

Dirt and Mud. In some physical examples of surface disturbance, grain size or any other definition of the imperfections is not readily known. This is usually true for dirt or ice which may collect on the skin of airplane wings. Table D gives an idea on the possible influence of dirt and mud on profile drag. Evidence on the influence of dirt and mud on boundary layer and drag of laminar-type foil sections can be found in the "friction" chapter.

Ice Formation. Ice usually collects at the nose of wing sections. Water has been injected into the stream of wind tunnels (18) and frozen on a wing model. The resulting changes in aerodynamic shape were then simulated in wing models by putting on molded wooden strips. The profile drag coefficient for various conditions is tabulated in figure 25. Airplanes may not only get into trouble because of drag due to, and weight of the ice deposited, but also because of a serious reduction of the maximum lift coefficient in such condition.

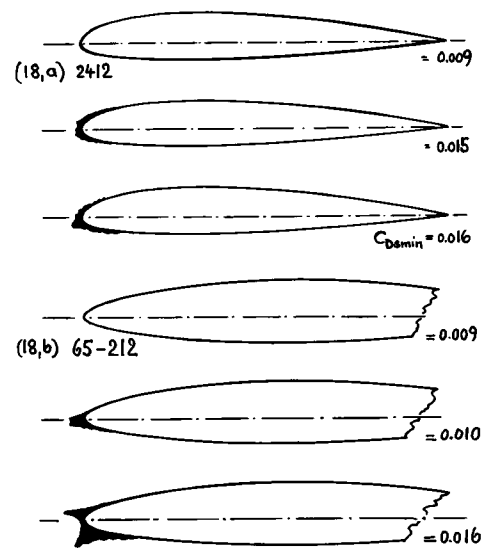


Figure 25. Section drag due to ice formation of two airfoils (18) at low lift coefficients and at $R_e = 10^6$ and 10^7 , respectively.

(b) Drag of Control Gaps

Certain gaps between control surfaces (ailerons, rudders, elevators) and the airplane parts to which they are hinged, are necessary to permit their operation. The airplane designer tries, of course, to keep these gaps as narrow as possible. Nevertheless, they exhibit some additional drag, described as follows:

Longitudinal Gaps. Adjoining the lateral edges of wing slats, landing flaps and control surfaces of airplanes, there are chordwise or longitudinal gaps, with a width in the order of 1/4 of an inch or even wider. Figure 26 indicates comparatively high drag coefficients for such gaps. Information on the variation of this drag as a function of lift coefficient is still lacking. It is suggested, however, that part of the drag is momentum loss due to flow through the gap, while another part may be caused by interference with the flow past the foil section.

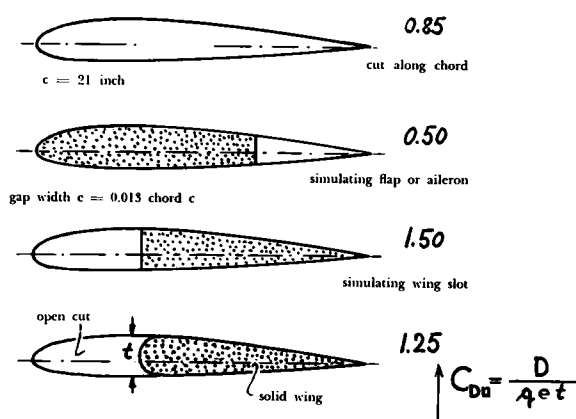


Figure 26. Drag of longitudinal wing gaps, tested (19) on 2412 airfoil at $C_L = 0.1$ and $R_e = 2 \cdot 10^6$.

Gap Width. In spanwise gaps between the noses of ailerons, slotted flaps, elevators or rudders, and the wing or tail surfaces, respectively, definition of gap width is somewhat problematic. After considering, however, what is known about the effect of the edges in the case of spanwise gaps, the definition as illustrated in figure 27 — is adopted for the following analysis of available data on the drag of control gaps. Using the width e , the area $S_g = e b$ is employed as reference for the drag coefficient C_{Dg} . In cases where gaps exist on both sides of the airfoil, the sum of the two widths is to be used.

Experimental Data. Figure 27 indicates how the additional profile drag of conventional wing- or tail surfaces caused by control gaps, increases in proportion

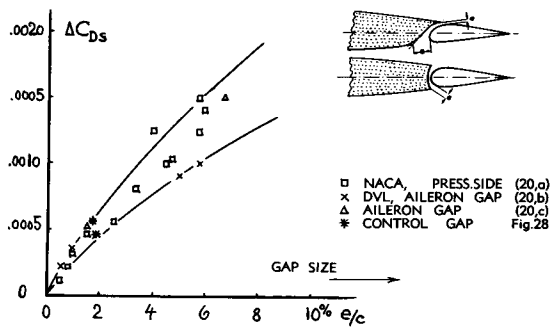


Figure 27. Evaluation of drag due to control gaps.

tion to the gap width. The gap-drag coefficient is accordingly

$$C_{Dg} = \text{between } 0.02 \text{ and } 0.03$$

The lower value applies for the lower- or pressure side of the airfoil section and for thinner sections; the higher value is preferable for the upper- or suction side and for thicker sections. For example, for a ratio $e/c = 5\%$, such as may be characteristic of an average "open"-type control gap, a drag coefficient C_{Dg} is found in figure 22 for a plane wall, below 0.01. The reason why equation 15 gives much higher values is believed to be in the interference effect mentioned above.

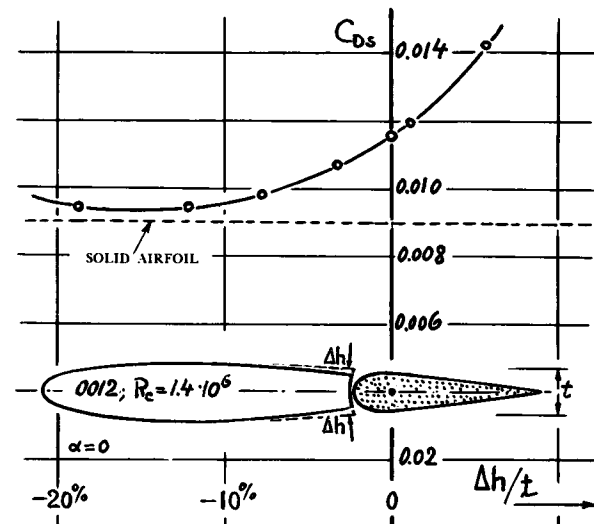


Figure 28. Section-drag coefficient of a horizontal tail surface at zero lift, as a function of the trailing-edge thickness of the stabilizer (19,b).

Positions of the Edges. Figure 28 shows how considerably the drag of a control gap depends upon the position of the two edges in relation to each other. An elevator was attached to the model of a stabilizer, the trailing edge of which was elastically adjustable to various thicknesses (19,b). By decreasing this thickness, the profile drag of the tail surface can be reduced to 76% of the original value (of the configuration having a contour corresponding to the 0012 airfoil section). In comparison to the original gap drag, the reduction amounts to 85%. Similar tests (19,b), employing a thickened elevator, show a corresponding, but somewhat smaller reduction of the drag. For explanation of the impressive effect, it can be stated:

- (a) By changing the position of the front edge as described, the flow is directed against the round nose of the elevator. Any separation of the flow from the flanks of this elevator is subsequently prevented.

- (18) Icing experiments in wind tunnels:
 - a) Gerhardt-Henrich, Yearbk D.Lufo 1940 p.I,575.
 - b) Gray-Glahn, 65-212 Foil, NACA T.Note 2962.
- (19) Engelhardt, Aerodynamic Laboratory TH München:
 - a) Drag of Chord-wise Wing Gaps, Rpt 1/1945.
 - b) Control Surface With Variable Gap, Rpt 3/1944.
- (20) Control-gap statistics:
 - a) NACA Tech Rpts 664 and 677; also T.Rpt 938.
 - b) Doetsch-Kramer, Profile Drag, Lufo 1937 p.173.

- (b) Corresponding to the local curvature of the streamlines, the velocity with which the flow passes over the gap is somewhat decreased.

At any rate, the boundary-layer flow along the elevator is obviously improved, and the pressure drag is considerably reduced, by changing the foil contour as indicated.

Flow Through the Gap. At lift coefficients different from zero, a flow originates through the control gap from the pressure to the suction side of the surface. The profile drag increases accordingly. It is possible, however, to adjust the two stabilizer edges in such a way that a flow through the gap is prevented. Drag reductions similar to those at zero lift can then be obtained as shown in figure 29 for a lift coefficient of $C_L = 0.4$.

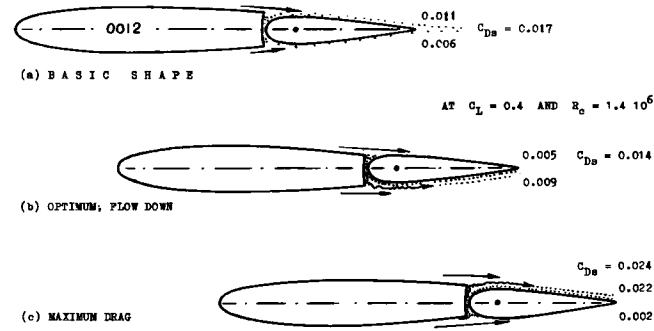


Figure 29. Section drag (by wake survey) of the tail surface as in figure 28, at $C_L = 0.4$. (b) has upper TE of stabilizer lowered, (c) has the lower side displaced upward.

Interference in B'Layer. Coming to the end of this chapter on surface imperfections, figure 30 presents a further example, showing that the drag of protuberances within the boundary layer has characteristics similar to those in free flow. A comparison of this illustration with figure 1 in the "interference" chapter suggests that the second hexagonal head is shielded by the first one. In closest position (at $x/d = 0$), the drag is $\approx 25\%$ of that of two single heads. It should be noted, however, that beyond $x/d = 5$, an interference effect is no longer noticeable. This result too, is in agreement with experience in free flow.

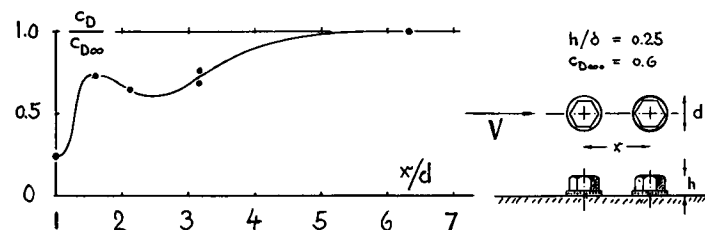


Figure 30. Interference effect between a pair of hexagonal bolt heads tested within the boundary layer of a wall (12,b).

CHAPTER VI—DRAG OF STREAMLINE SHAPES

The discovery of minimum fluid-dynamic drag in slender shapes is evidently very old — as can be seen, for instance, in the ships of the Egyptian Pharaohs. Also Leonardo da Vinci has presented drawings of what we now call "streamline" bodies. Extensive experimental information has been accumulated in our age regarding the aerodynamic characteristics of such shapes, particularly of airfoil sections. Advances in their mathematical treatment have evidently not reduced experimental efforts in modern, large and expensive installations to confirm theoretical predictions and to obtain information in conditions where theory does not apply.

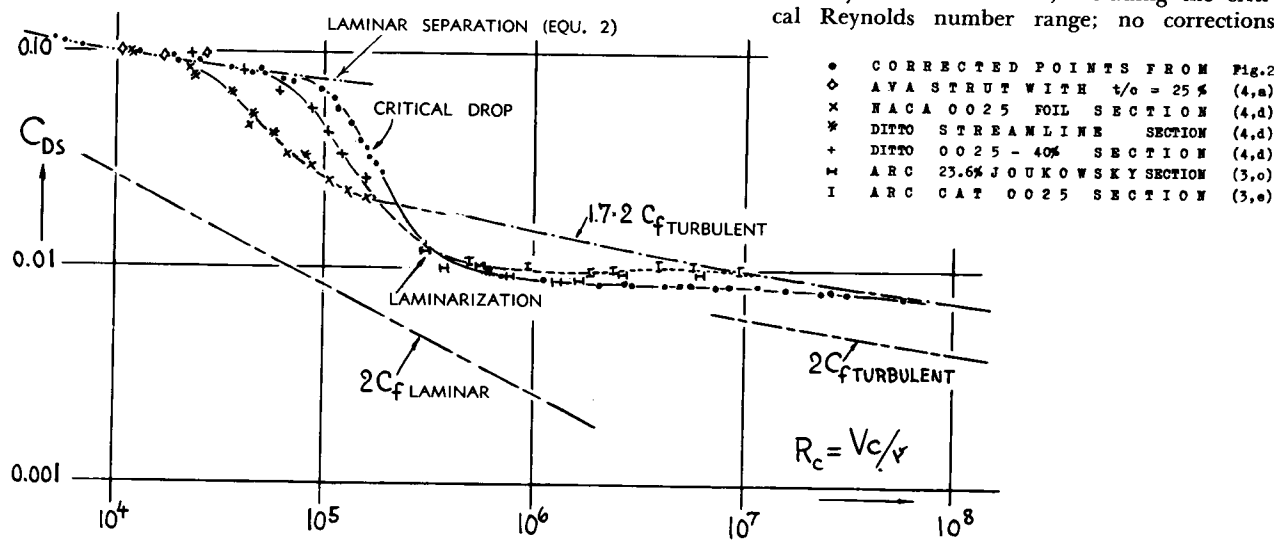
Shape Parameters. Streamline shapes are classified by their thickness ratio t/c (or d/l respectively) the location of maximum thickness x/c (or x/l), the distribution of thickness along chord c or length l (including leading-edge radius and trailing-edge angle), and in wing sections by shape and amplitude of their camber (f/c). In a statistical interpretation of the available experimental material, approximate functions (1) are presented in the fol-

lowing sections, indicating the profile drag of airfoil and strut sections, and the drag of three-dimensional streamline bodies as a function of their thickness or fineness ratio, respectively.

A. DRAG OF WING- AND STRUT SECTIONS

Thousands of wing- and similar sections have been tested within the last ≈ 50 years, primarily in wind tunnels. Two aspects predominate in their development; one is the influence of Reynolds number, the other one is the shape most suitable for particular applications. — The "viscous" or "parasite" drag of wings is usually called "profile" drag. To get away from the subscript "p" which is likely to be confused with the "p" in "pressure", an attempt is made in this book, to substitute "s" from "section". We will, therefore, find " C_{Ds} " = D_s/qS , denoting the section drag coefficient of airfoils and struts (based on "wing" area b times c).

Figure 1. Variation of section-drag coefficient for 25% thick symmetrical sections, including the critical Reynolds number range; no corrections.



1. DRAG AS A FUNCTION OF R'NUMBER

Turbulence. Within the range of small lift coefficients, the drag of airfoil sections is predominantly frictional. Skin-friction drag is very much a function of transition from laminar to turbulent boundary-layer flow, as explained in the "skin-friction" chapter. Results at higher Reynolds numbers are now available from modern low-turbulence wind tunnels (7). Most of the experimental points at lower R'numbers, as plotted in figure 2, have been collected, however, from earlier tests in rather turbulent wind tunnels. Figure 1 presents as an example, results for several $\approx 25\%$ thick sections. The general trend of the drag coefficient is to reduce from the level of laminar separation below $R_c = 10^5$ or 10^4 (in the order of $C_{Ds} = 0.1$ or $C_{D*} = 0.4$)

to the fully turbulent condition beyond $R_c \approx 10^7$ (in the order of $C_{Ds} = 0.01$ or $C_{D*} = 0.04$). This transition over an interval between 10^4 or 10^5 and 10^6 , 10^7 or even 10^8 — can take various ways.

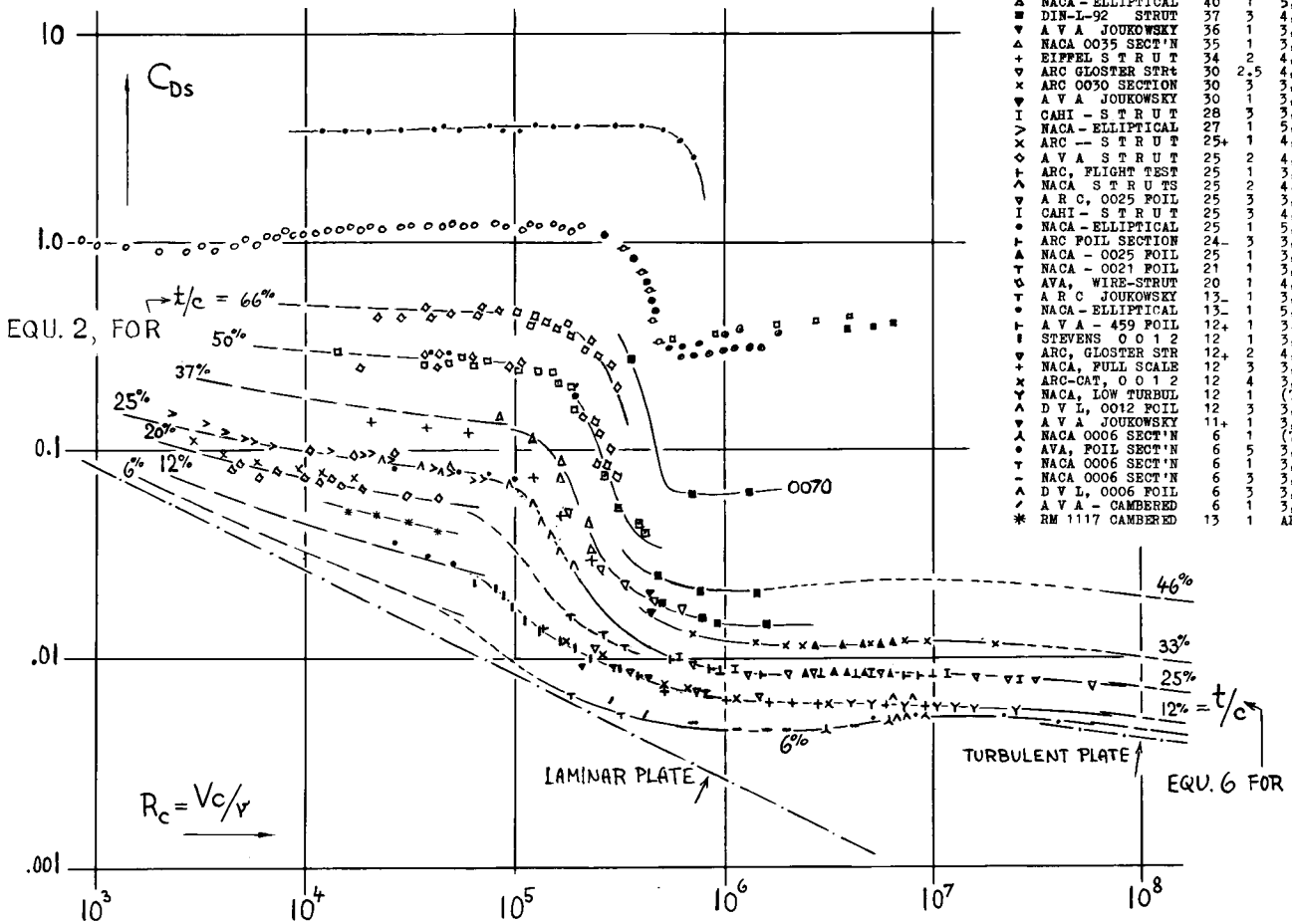
(a) Wind-tunnel stream turbulence produces early and flat transition. At $R_c = 10^5$, variation of the drag coefficient due to turbulence, can be in the ratio of 3 to 1.

(b) The earlier the transition takes place, the sooner the drag coefficient assumes the fully turbulent characteristics.

(c) In low-turbulence streams and in suitable section shapes, the boundary-layer flow along the forebody remains laminar and the drag coefficient is comparatively low, to high Reynolds numbers.

At Reynolds numbers above the critical drop of the drag coefficient, most of the results in figure 2 have been corrected using the method as recommended in (2,a). The so-called turbulence factors "f" = R_{Effect}/R_{Test} applied in figure 2, are consid-

Figure 2. Data on sectional drag (at \approx zero lift) of streamline foil- and strut sections. Many of the experimental results are obtained by wake-survey technique; in others, drag of blunt wing tips has been subtracted from the original values. Drag coefficients at subcritical R'numbers are as indicated by equation 24 (using $C_f = 2.66 \sqrt{R_c}$); at very high R'numbers as given by equation 28 (using C_f as indicated by the Schoenherr equation in Chapter II).



erably higher, however, than quoted in (2,a). They correspond to figure 9 in the "friction" chapter. At R'numbers below the critical drop, a turbulence correction is not needed. The Reynolds number range in which the drop takes place has been shifted, however, in figure 1 in proportion to "f" factors as listed. It would be better, of course, to have experimental data obtained in turbulence-free flow. Applying, however, the corrections mentioned, it is possible to give approximate information on shapes and at Reynolds numbers not available otherwise. It is nevertheless possible, that certain section shapes would have basically different transition if tested in a turbulence-free stream.

Their drag coefficient may, for instance, drop suddenly, possibly involving a hysteresis on increasing or decreasing the speed, respectively.

Reynolds Number Phases. Figure 2 contains more information on small Reynolds numbers and thick (bluff) sections (subject of Chapter III) — than on streamline shapes at higher Reynolds numbers. Characteristics become more evident, however, in a combined presentation. — As a function of Reynolds number, several phases can be recognized in figure 2.

(a) Below $R_c \approx 10^5$, there is the region with completely laminar boundary-layer flow. Sections with intermediate and higher thickness ratios show high drag coefficients, owing to separation of the flow from their rear.

(b) In the range between $R_c \approx 5 \cdot 10^4$ and $\approx 5 \cdot 10^5$, the sections show a critical decrease of their drag coefficient, caused by transition from laminar to turbulent boundary-layer flow (see in Chapter III); in thicker sections, the coefficient drops to $1/3$ or even to $1/10$ of the level below the critical Reynolds number. The critical R'number (based on chord length c) is seen decreasing from near 10^6 for an elliptical section with $t/c = 2$, to around 10^5 for slender streamline shapes.

(c) For some interval of Reynolds number above the critical drop, the transition point of the boundary layer seems to be comparatively fixed (by the pressure minimum). With laminar flow along the forebody, the drag coefficient varies essentially in proportion to the laminar skin-friction drag coefficient.

(d) Another critical phase follows then (in the vicinity of $R_c = 10^6$). Here, the transition point moves steadily ahead, thus causing the drag coefficient to grow again, in a manner similar to that of the skin friction drag coefficient as presented in Chapter II.

(e) Only well beyond $R_c = 10^7$, terminal conditions are obtained at last (in the non-laminar type of sections plotted). Here, practically all of the b'layer flow is turbulent, and the section drag coefficient is proportional to the turbulent skin-friction drag coefficient. This condition is also obtained at considerably smaller R'numbers (10^6) in very turbulent wind-tunnels and/or by surface roughness.

The last two phases are the usual field of practical application in airplane wings. The importance of larger wind-tunnel facilities is thus apparent. Many of the early investigations have been carried out within the critical R'number range. Stream turbulence (reducing the critical Reynolds number) helps, however, in obtaining supercritical, if only qualitative results in small and inexpensive wind tunnels.

- (1) Statistical interpretation of foil-section drag:
 - a) Hoerner, Streamline Shapes, Ybk D.Lu 1942 p. 374.
 - b) Method of using mean-average values for the dynamic pressure, stems from Weinig (Ybk STG 1937).
 - c) Scholz, Slender Shapes, Yearb'k STG 1951 p.244.
- (2) Section-drag corrections (wing-tip drag):
 - a) Regarding wing-tip and turbulence-correction, see NACA T.Rpt 586 and the Appendix of T.Rpt 669.
 - b) Hoerner, Drag of Lateral Edges, Doct ZWB UM 7815 (1943); see Wing Tip Shape, USAF T.Rpt 5752.
 - c) British ARC, RM's 1870, 2110 and 2584.
 - d) 0009 to 0035 Airfoils, NACA T.Rpts 431, 647, 708.
 - e) Doetsch, Foils in DVL Wind Tunnel, Lufo 1937.
- (3) Sections with maximum thickness at $\approx 30\%$ of chord:
 - a) Fage-Falkner-Walker, Experimental Investigation of Symmetrical Joukowski Sections, ARC RM 1241.
 - b) AVA Göttingen Experiments on Joukowski Sections, Ergebnisse Vol III (1926) and Vol IV (1932).
 - c) 0012 and Other Airfoil Sections (Smooth and Rough) in CAT, ARC RM's 1708 and 1789 (1936/37).
 - d) DVL Tests, Doct ZWB FB 642 and Lufo 1937.
 - e) Sections 0015, 0030 and Others in Compressed-Air Tunnel, ARC RM 1804 (1937) and 2584 (1952).
 - f) Symmetrical Sections in Full Scale Tunnel, NACA T.Rpts 647 (0009, 12, 18) and 708 (0025 and 0035).
 - g) 4-Digit Series Modifications, NACA TN 1591.
 - h) NACA at small Reynolds numbers, T.Rpt 58.
 - i) Foils in DVL High Speed Tunnel, ZWB FB 1490.
 - k) AVA, Foil Sections, Erg Göttingen III (1926) p.87.
 - l) 4-Digit Sections in VDT, NACA TN 364 and 457.
 - m) Locke, 0012 and 4415 in Stevens Towing Tank, ETT Memo 42 (1939) and Rpt dated 15 Sept 1939.
 - n) Jacobs-Pinkerton-Greenberg; Airfoils Having Camber Far Forward, NACA T.Rpts 537 and 610.
 - o) Joukowski Sections, ARC RM's 1970 and 2110.
 - p) ARC, Flight Tests on Several Sections, RM 1826.
- (4) Experimental results of strut sections:
 - a) AVA, Tech Ber. Flugzeugmst. I (1917) and II.
 - b) Hartshorn, Seven Strut Shapes, ARC RM 1327.
 - c) CAHI (Moscow) Rpt 33 (1928).
 - d) Jacobs, Drag of Streamline Wires, NACA TN 480.
 - e) ARC, Resistance of Strut Sections, RM 1599.
 - f) Hoerner, Fieseler Water Tunnel Rpts 2 and 5.
 - g) Williams-Brown, Thick Sections, ARC RM 2457.
 - h) Struts at subcritical R'numbers, ARC RM 890.
 - i) Eiffel, 'Nouvelles Recherches' Paris 1914 and 1919.
 - k) Kohler, Drag in Strut Junctures, Lufo 1938 p.143.
 - l) Maxen, Strut Juncutures, Ybk D.Lufo 1940 p.1,599.
 - m) Struts at Low R'numbers; ARC RM 49, RM 256.

2. AS A FUNCTION OF THICKNESS RATIO

The "sectional" drag of a thin plate, exposed on both sides to a tangential flow, is $C_{D_S} = 2 C_f$, with C_f = proper skin-friction drag coefficient as treated in Chapter II. The drag of thin airfoil sections is somewhat higher than this lower limit.

Wing-Tip Drag. Rectangular wing models, used for many years in wind-tunnel investigations of airfoil sections, are often made with square or blunt lateral edges. To obtain the section drag, not only the induced but also the parasitic drag originating at the ends must be subtracted from the readings of the wind-tunnel balance (see for example in reference 2,a). The wing-tip drag is obviously a function of the profile dimensions at the tips. The coefficient of this drag component is, therefore, based on the "tip area" (c_{tip})². Various investigations of wing models concurrently tested with rounded and with blunt lateral edges, have been evaluated. Results have also been obtained by comparing force tests (with blunt ends) to wake-survey results. For lift coefficients equal to or close to zero, figure 3 approximately indicates

$$C_{Dc} = (\Delta D, 2 \text{ edges}) / (q c^2) = 0.15 (t/c)^2 \quad (1)$$

Referring the coefficient to the "frontal" area (t^2) of the tips, the constant value $C_{Dt} = 0.15$ is found for a pair of blunt wing ends. Their drag is similar in nature to that of the bodies in figure 21 of the "pressure-drag" chapter. Equation 1 has been used to correct the experimental results plotted in figure 2; as far as they were obtained from force readings on blunt-ended rectangular wings.

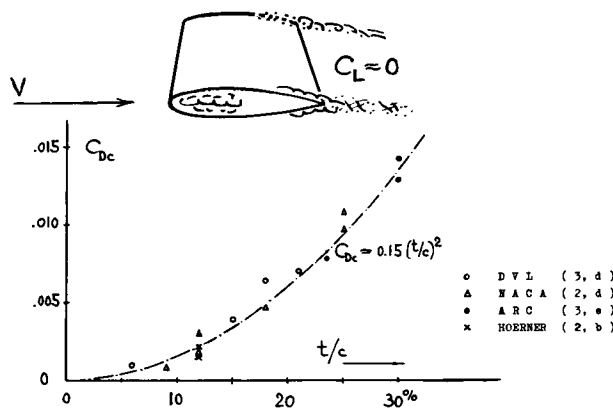


Figure 3. Parasite drag due to square or blunt lateral edges of rectangular wing models, at \approx zero lift. Reynolds numbers R_c above 10^6 .

Faired Edges. A systematic investigation of the characteristics of wing tips (lateral edges) is reported in (2,b). Among the tip forms from this source (illustrated in Chapter VII), the numbers 2 and 5, having favorable shapes, show "negative" tip-drag values in the vicinity of $C_L = 0$. This means, that the parasitic drag of the wing including the two tips, is somewhat lower than the two-dimensional section drag — evidently because of three-dimensional flow conditions around the edges. With C_L close to zero, a pair of these wing tips presents a parasitic drag coefficient in the order of

$$\begin{aligned} C_{Dt_0} &= +0.11 \text{ with blunt edges, number 1} \\ &= -0.04 \text{ with round edges, number 2} \\ &= -0.03 \text{ with sharp edges, number 5} \end{aligned}$$

Results on a 30% thick rectangular model wing are reported in (2,c). For example at $R_c = 5 \cdot 10^6$, the total parasitic drag coefficient on wing area for aspect ratio $A = 6$, is found to be approximately

$$\begin{aligned} C_{D_S} &= 0.0143 \text{ with blunt wing tips} \\ &= 0.0118 \text{ with well-rounded edges} \\ &= 0.0125 \text{ tested by wake survey} \end{aligned}$$

Here again, the rounded ends obviously present a negative drag differential, in the order of $C_{Dt} = (0.0118 - 0.0125) 6/0.3^2 = -0.047$. In conclusion, it appears possible that the drag of a wing with finite span is smaller than in two dimensions.

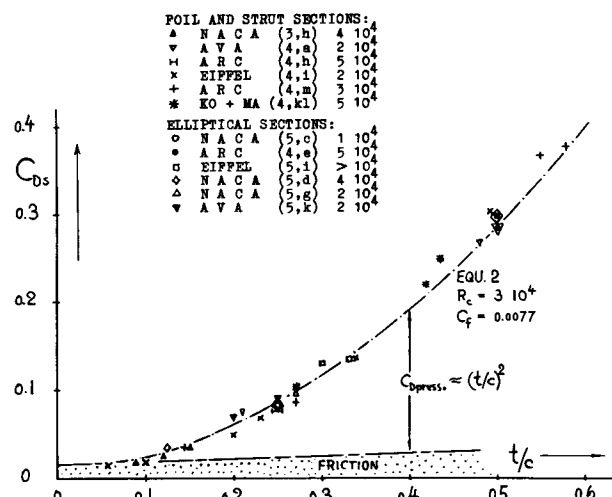


Figure 4. Drag coefficient of streamline and elliptical sections (at \approx zero lift) at subcritical R' numbers.

Low Reynolds Numbers. Streamline wires and compression struts (sections of which are listed in figure 9) are often used in the range of comparatively low Reynolds numbers. As explained in the "pressure-drag" chapter, laminar separation takes place in this phase; and the drag is predominantly due to pressure differentials. The experimental results of streamline (and some elliptical) sections at R_c between $(1 \text{ and } 5) \cdot 10^4$, as plotted in figure 4, can be

interpreted by $C_{Ds} = 2 C_f (1 + \frac{t}{c}) + (t/c)^2$

$$C_{Ds} = 2 C_f (c/t) + 2 C_f + (t/c) \quad (2)$$

The last term represents the pressure drag as described above. For larger thickness ratios, this term becomes predominant; and that is the reason why in figure 1 such sections show apparently constant drag coefficients between $R_c \approx 10^4$ and 10^5 . It is suggested that neither the conventional streamline shapes nor the elliptical sections are optimum in this R-number phase. More efficient shapes might be developed, whenever worth-while applications should arise.

Optimum Wire Shape. Referring the drag coefficient (equation 2) to the area ($b\sqrt{t/c}$), as explained later in the text, a function is obtained that permits to optimize the thickness- or fineness ratio of "streamlined" tension wires:

$$C_{Dcro} = 2 C_f \sqrt{(c/t)} + 2 C_f (t/c)^{1/2} + (t/c)^{3/2} \quad (3)$$

For example, for $R_c = 10^4$, where for laminar b'layer $C_f = 0.0133$, differentiation of this equation leads to an optimum thickness ratio of t/c in the order of 9%.

The Critical Reynolds Number is a function of maximum-thickness location x/c . Several strut sections, for example, with $t/c = 25\%$ have been tested (4,d) in a turbulent wind tunnel. The critical number (defined for 1/2 of the decrement of the drag coefficient) is

$$\begin{aligned} R_{crit} &= 11 \cdot 10^4 \text{ for } x/c = 50\% \\ &= 7 \cdot 10^4 \quad = 40\% \\ &= 3 \cdot 10^4 \quad = 30\% \end{aligned}$$

two of these sections are represented in figure 2. Location and value of the pressure minimum are evidently responsible for the variation of the critical R-number. By the same reason, the 40% thick elliptical section (5,g) in figure 2, should have a critical number appreciably higher than plotted.

It is only to fill the illustration, that the drag coefficient of this section has been plotted using a turbulence factor $f = 1$. — Note, that there are results on strut sections available, obtained in turbulent tunnels, showing supercritical drag coefficients at R_c in the vicinity of $2 \cdot 10^5$. Values are still comparatively high, however, because of the magnitude of the skin friction coefficients involved ($C_{f,turb} \approx 0.006$ and $C_{f,lam} \approx 0.003$). Such sources are, for example, (3,a) (4,d) and (5,i).

Skin-Friction Drag. Because of thickness (displacement), the mean-average velocity around a symmetrical foil section is higher than that of the undisturbed flow, even at zero lift. The supervelocity ΔV and the corresponding increment of the dynamic pressure (Δq) increase roughly in proportion to the thickness ratio t/c . For sections with maximum thickness located at or near 30% of the chord, the differentials are approximately

$$\frac{\Delta V}{V} = \frac{t}{c}; \text{ and } \frac{\Delta C_{Ds}}{2 C_f} = \frac{\Delta q}{q} = 2 - \frac{t}{c} \quad (4)$$

This function basically agrees with theoretical analyses (8); and it is substantiated by experimental results (figure 5). The skin-friction drag also depends, of course, on the location of the boundary layer's transition point on section chord. It appears, however, that in the range between $R_c = 10^6$ and 10^7 , transition on foil sections with maximum thickness at $x/c \approx 30\%$ is governed by the location of the minimum-pressure point rather than by thickness ratio. In other words, in this type of sections,

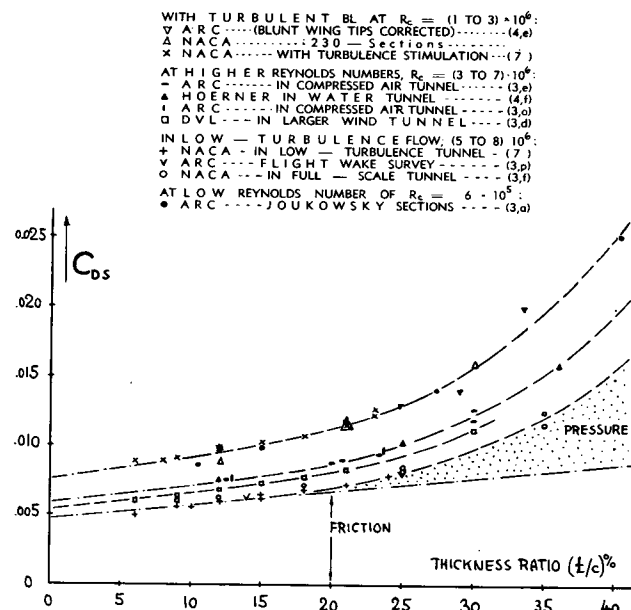


Figure 5. Profile drag coefficient of wing- and strut sections, at higher Reynolds numbers; equation 6.

(5) Experimental Results on elliptical sections:

- a) Dryden, Cylinders in Wind, BOS J.Res.Pap.221.
- b) Delany, Blunt Shapes, NACA T.Note 3038.
- c) Jacobs, Drag of Streamline Wires, NACA TN 480.
- d) Lindsey, Simple-Shape Cylinders, NACA TR 619.
- e) Pechstein, Cylinder in Wind, Zts.VDI 1942 p.22.
- f) Hoerner, Fieseler Wasserkanal Report 5 (1938).
- g) NACA, Elliptical Sections, Note 279 and Rpt 289.
- h) AVA Göttingen, Ergeb II (1923) and III (1926).
- i) Eiffel, Nouvelles Rech Résistance, Paris 1914.
- k) Betz, lenticular "wires", Durand IV p.143.

the location of the transition point is comparatively independent of thickness ratio. The value of C_f to be used in equation 4, should, of course, be that of a thin plate having the same location of the transition point.

Pressure Drag. In addition to the friction drag, there is also a certain pressure- or separation-drag component, originating along the afterbody of foil- and strut sections against the pressure gradient. This component is not included in the theoretical studies (8). Analyzing available experimental results of airfoil sections with $x/c \approx 30\%$, as plotted in figure 5, this drag component can be interpolated by

$$C_{Dpr} / (2C_f) = 60 (t/c)^4 \quad (5)$$

In this equation, $(t/c)^4$ represents the frontal area on which the pressure is acting; and $(t/c)^3$ represents the effect of the adverse pressure gradient along the rear of the section. The pressure or separation drag is assumed to be proportional to the friction drag C_f (along the forebody). The total "viscous" or profile drag of these sections is obtained by adding equations 4 and 5:

$$C_{Ds} / (2 C_f) = 1 + 2 \frac{t}{c} + 60 \left(\frac{t}{c} \right)^4 \quad (6)$$

Thickness Location. Laminar profiles, that is, sections with the maximum thickness located at 40 or 50% of the chord, have a lower supersonic velocity ratio than the "conventional" sections considered so far. The second term of equation 6 is, therefore, reduced in magnitude. The experimental points in figure 6 on "64" and "65" series sections with transition fixed by means of sand strips, are best interpolated by

$$C_{Ds} / (2 C_f) = 1 + 1.2 \frac{t}{c} + 70 \left(\frac{t}{c} \right)^4 \quad (7)$$

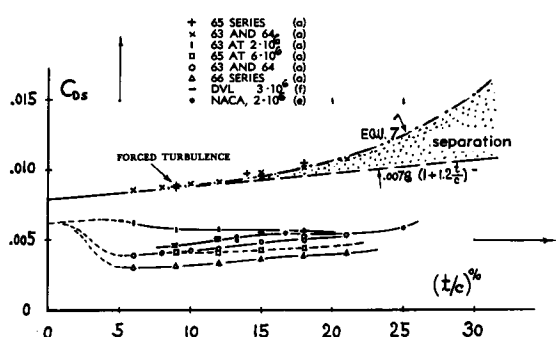


Figure 6. Profile-drag coefficient of laminar-type sections (with maximum thickness at or near 40% of the chord) as a function of thickness ratio (6).

Note that in these sections the value of C_f corresponding to $t/c \rightarrow 0$, is higher than the turbulent skin friction drag coefficient. The sand strips obviously have some pressure drag of their own.

Laminar Profiles. Equation 7 does not agree, however, with smooth-surface laminar-type sections whose drag coefficients are plotted in the lower part of figure 6. In these sections, two effects are fighting each other with respect to drag; that of laminarization and the boundary-layer accumulation or separation near the trailing edge. The third term of the equation represents a penalty in this respect, to be paid to obtain laminarization. In the 64 and 65 series sections, this term is approximately twice as high as that in equation 6 which applies for sections with $x/c \approx 30\%$. Approximately at $x/c = 50\%$, minimum drag is obtained (in conventional thickness ratios and at the R'numbers tested). Beyond this location, pressure and separation drag increase as a function of the wedge angle at the trailing edge. Because of the sensitivity of the boundary layer, the drag coefficient of laminar-type sections shows certain humps and hollows as against thickness ratio. A hollow exists, for example, around $t/c = 15\%$ in the "64" series at $R_c = 6 \cdot 10^6$. The hollow is a function of Reynolds number too. As a consequence of such complex combination of effects, for example, the section 63-0018 exhibits a drag coefficient (at $R_c = 2.5 \cdot 10^7$) that is lower than those of thinner sections. As indicated in figure 6, the drag of all

- ... $t/c = 37\%$ WITHOUT TURBULENCE FROM FIGURE 1
- △ 37 % STRUT SECTION IN WATER TUNNEL (9,e)
- ▲ DITTO WITH $k/c = 3/1000$ AND $= 11/1000$ (9,e)
- ... SMOOTH 0012 WITHOUT STREAM TURBULENCE FIG.1
- Λ SMOOTH 0012 SECTION IN WATER TUNNEL (9,e)
- + 0012 WITH ROUGHNESS $k/c = 1.5/1000$ (9,e)
- × DITTO 0012 WITH GRAIN SIZE $2.8/1000$ (9,e)
- SMOOTH 0012 WITH FORCED TURBULENCE (9,h)
- 0012 WITH $k/c = (2.2; 6.4; 20) \cdot 10^{-5}$ (9,h)
- ◊ 0012 WITH ROUGHNESS $k/c = 1.2 \cdot 10^{-4}$ (9,g)

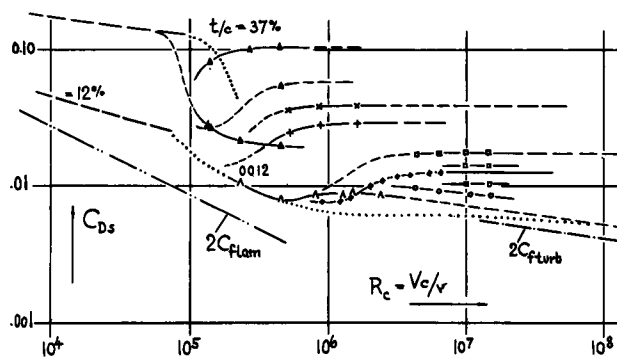


Figure 7. Drag coefficients (at zero lift) of various symmetrical sections having various degrees of surface roughness (9); no corrections applied.

these sections increases, of course, to that of the thin and flat plate (which does not have laminarization due to shape), as t/c approaches zero. At any rate, equation 6 cannot very well be used for predicting the drag of laminar-type foil sections with undisturbed boundary layer flow. Unfortunately, such disturbances are easily produced by dust, mud, insects, imperfections, lateral wing edges (if any), fuselage- or nacelle walls, by the propeller slip stream (if any) and finally by mechanical vibrations (see in the "skin-friction" chapter).

Surface Roughness. Putting into equations 6 or 7 for C_f the proper skin-drag coefficient, as found in the "imperfections" chapter, the profile drag of wing- or strut sections with surface roughness is readily obtained. Available experimental data are plotted in figure 7 against Reynolds number. As explained in Chapter V, the coefficients of rough sections diverge from those of smooth ones at certain critical R' -numbers. Terminal drag coefficients have been taken from figure 7 (extrapolated where necessary) and plotted in figure 8 together with other results. As a function of grain-size ratio (k/l), the drag coefficients evidently have the same trend as the thin plate, whose coefficient was taken from the "imperfections" chapter as $C_{D_s} = 2C_f$. Except for 0012 (9,a), the agreement with equation 6 is good, even at a thickness ratio of 37%.

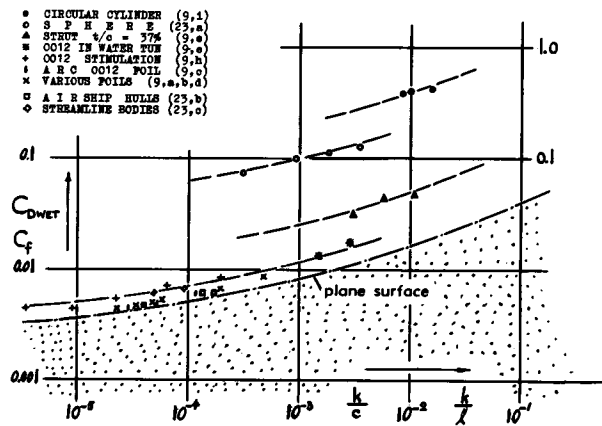


Figure 8. Terminal drag coefficients of streamline and of other shapes as a function of roughness.

3. APPLICATIONS OF STREAMLINE SECTIONS.

To indicate (roughly, by order of magnitude) Reynolds number ranges for various engineering and other applications of streamline sections, *tabulations A* and *B* have been prepared.

APPLICATION	$\frac{c}{inch}$	$V \text{ ft/sec}$	R_e
AVERAGE BUTTERFLY (\$)	1	1	$5 \cdot 10^2$
ZANONIA SEED	2	2	$2 \cdot 10^3$
INDOOR AIRPLANE MODEL	3	6	$1 \cdot 10^4$
SMALL BIRDS	2	20	$2 \cdot 10^4$
SEAGULL (WING CHORD)	6	20	$6 \cdot 10^4$
FREE-FLYING API MODEL	6	30	$1 \cdot 10^5$
HOUSEHOLD FAN (\$)	4	50	$1 \cdot 10^5$
ALBATROS BIRD	8	50	$2 \cdot 10^5$

TABLE A. Reynolds numbers in various small-size applications. (\$) Speed is resultant, wing against air.

Streamline Shapes, suitable at larger Reynolds numbers for application to airplane wings, tail surfaces, and as struts or fairings, have been developed first by empirical means and more recently on the basis of theoretical analysis (of their pressure distribution). Figure 9 displays various typical streamline shapes, arbitrarily blown up to a thickness ratio of $t/c = 40\%$, to show more clearly their characteristics. Among these, (c) gives a simple geometrical method of construction. Ordinates of other section types are found in the references listed (3 to 7). Streamline shapes are generally "fine" and tapered in the afterbody to avoid flow separation. In the forebody, certain marine applications still prefer a sharp (pointed) shape, while in aviation more or less rounded leading edges have been found to be most favorable with regard to the variable angle of attack (and lift) of wings and other applications.

- (6) Experimental results laminar-type foil sections:
 - a) A series of unpublished NACA reports between 1939 and 1945, summarized in T.Rpt 824 (7).
 - b) Loftin, Sections w/out cusp, NACA T.Rpt 903.
 - c) NACA, Circular-Arc Foils, Tech Rpt 1146 (1953).
 - d) Loftin-Smith, 15 Sections, NACA Note 1945.
 - e) Benson-Land-Havens, Testing Strut Sections in Towing Tank, NACA Memo Rpt for Navy Bu'Ships.
 - f) DVL, In Large Wind Tunnel, ZWB FB 1621.
 - g) NACA, Sections to $R_c = 2.5 \cdot 10^7$, Tech Rpt 964.
- (7) Abbott-Doenhoff-Stivers, Summary of Airfoil Data, NACA Tech Rpt 824 (1945); also McGraw-Hill 1949.
- (8) Theoretical calculation of profile drag:
 - a) Squire-Young, Profile Drag, ARC RM 1838 (1937).
 - b) Pretsch, in Yearbk D.Lufo 1938 p.I,60.
 - c) Fedjajewsky and Go, Techn.Wosd.Floata July 1940.
- (9) Experimental results on surface roughness in foils:
 - a) D.Vers.Anst.Luftf., German Doct ZWB FB 642.
 - b) NACA, Technical Notes 364 and 457 (1945).
 - c) Jones and Williams, Roughness on 0012 and Other Airfoils in CAT, ARC RM 1708 (1936) and 1804.
 - d) Schrenk, Momentum Method in Flight, Lufo 1929.
 - e) Hoerner, 0012 and Strut, Fieseler Rpts 2 and 5.
 - g) Relf, 0012 and other Sections, ARC RM 1706 (1936) and 1789 (1937); also Aircraft Eng'g 1936
 - h) Young, 0012 Section, J.R.Aeron'l Soc. 1950 p.534.
 - i) Fage and Warsap, Turbulence and Roughness on Cylinders, ARC RM 1283 (1929). Grain sizes measured by this author from samples of the NPL.

APPLICATION	\circ ft	V knots	R_c
AIRCRAFT STRUT	0.5	100	$5 \cdot 10^5$
SAILBOAT STAY	10	10	$1 \cdot 10^6$
AVERAGE SAILPLANE	4	80	$3 \cdot 10^6$
PERSONAL AIRPLANE	5	100	$5 \cdot 10^6$
AVG FIGHTER AIRPLANE	6	500	$3 \cdot 10^7$
COMMERCIAL AIRPLANE	13	300	$4 \cdot 10^7$
AVERAGE BOMBER WING	12	400	$5 \cdot 10^7$
WATER-TURBINE BLADE (+)	3	15	$6 \cdot 10^6$
SHIP, STRUT in WATER	1	23	$3 \cdot 10^6$
FOIL OF HYDROFOIL BOAT	2	40	$1 \cdot 10^7$
SHIP-PROPELLER BLADE (+)	4	25	$2 \cdot 10^7$

TABLE B. Average Reynolds numbers (on chord length) in various engineering applications. (+) Speed is mean resultant value between blade and fluid.

Section Families. Several more or less systematic series of section shapes have been developed and tested. The more interesting or important ones are as follows:

(a) The wing sections developed by Eiffel (5,i) and at Göttingen (4,a) in the first decade of this century, were thin, sharp-nosed and cambered. They are completely obsolete now as far as airplane wings are concerned. They seem to be suitable, however, at Reynolds numbers below 10^5 (in small birds and in insects).

(b) Round-nosed sections with maximum thickness in the vicinity of 30% of the chord, were next developed in Göttingen (3,k) (for example No. 535, which is a famous sailplane shape), by the NACA (for example "Clark Y") and by the British ARC (for example "RAF-34", reference 3,c).

(c) The first mathematically defined shape was that of the so-called Joukowski sections (figure 9,a) extensively tested in Göttingen (3,b). Their maximum thickness is slightly ahead of 0.3 c; their tail is cusped.

(d) The first realistic family of airfoil sections is the 4-digit series of the NACA (3,f and l) (7) with maximum thickness at 30% of the chord (figure 9,b). An example of this series is

$$\begin{array}{l} 2 \ 4 \ 12 \text{ thickness } t/c = 12\% \\ | \text{ camber location at } 0.4 \text{ chord} \\ \text{camber} = 2\% \text{ of chord} \end{array}$$

Modifications of this series are investigated in (3,g). The 5-digit series (16,g) developed for reduced longitudinal moment (for example "23012") has the same thickness distribution as the 4-digit series.

(e) The NACA 6-series sections (see figure 9,e) with systematic variations of thickness distribution along chord (7), have been developed for favorable pressure gradients. They have partly laminar boundary layer flow (low section drag coefficients); and they are suitable for applications at higher speeds.

An example is

$$\begin{array}{l} 6 \ 4 - 2 \ 12 \text{ thickness ratio } t/c = 12\% \\ | \text{ design lift coefficient} = 0.2 \\ | \text{ location of minimum pressure at } 0.4 \text{ c} \\ \text{NACA series number of this type} \end{array}$$

Reference (6,b) proves, however, that the usually cusped shape of this series is not really important with respect to section drag.

(f) The German classification system also indicates variation of the nose radius. An example is

$$\begin{array}{l} 2 \ 30 \ 12 - 1.1 \ 40 \text{ thickness at } 40\% \text{ c} \\ | \text{ nose radius } r/c = 1.1 \ (t/c)^2 \\ | \text{ thickness ratio } t/c = 12\% \\ | \text{ location of camber at } 30\% \text{ chord} \\ \text{camber ratio } f/c = 2\% \end{array}$$

A similar system is occasionally used in British publications, also indicating the main section-shape parameters.

Foil shapes suitable for transonic and supersonic applications are shown in the respective chapters.

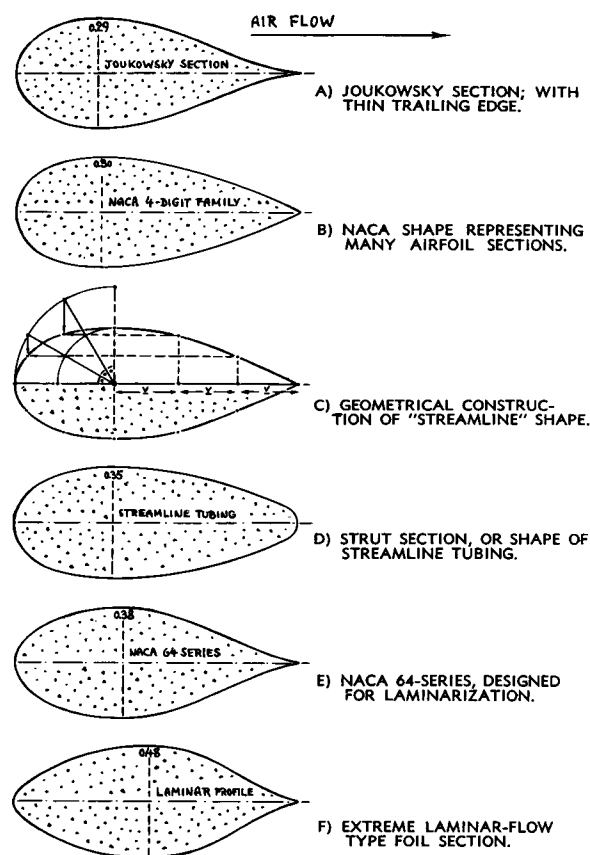


Figure 9. Streamline section shapes, having $t/c = 40\%$.

Wing Sections. Streamline sections have various engineering applications. Depending upon application, various reference areas can be selected for the drag coefficient. For wings and tail surfaces, the plan-form area (leading to C_D or C_{DS}) is most suitable. For other purposes, reference areas and coefficients are preferable as listed in table C.

TYPE OF APPLICATION	REFERENCE AREA	COEFF	$R_e = V c / \nu$
WING OR TAIL SURFACES	"WING" AREA $S = b c$	C_{Dw}	10^6 TO 10^8
FAIRINGS (OR STRUTS)	FRONTAL AREA $S_f = t b$	C_{Df}	10^5 TO 10^7
TENSION WIRES	CROSS-SECTIONAL $b \sqrt{t/c}$	C_{Dw}	10^4 TO 10^5
COMPRESSION STRUTS	"INERTIA" AREA $b^4 \sqrt{c/t}^3$	C_{Dw}	10^5 TO 10^6

TABLE C. Reference areas and R'numbers of wing-, wire- and strut sections, with regard to their application.

Fairings. In the case of fairings put around a given bluff cross section to reduce its drag, section thickness is significant. By multiplying equation 6 with $2 c/t$, the coefficient C_{Dw} , based on maximum cross-section or frontal area is obtained:

$$C_{Dw}/C_f = 4 + 2 \frac{c}{t} + 120 \left(\frac{t}{c} \right)^3 \quad (8)$$

Contrary to the coefficient on plan-form area, this one has a minimum as shown in figure 10. The optimum length ratio of fairings put around two-dimensional obstacles is $c/t \approx 3.7$; the corresponding thickness ratio is $t/c \approx 27\%$. A plot of equation 8 is repeated in figure 11 together with other definitions of the drag coefficient. — To demonstrate the impressive reduction of drag due to streamlining, figure 12 shows a streamline section having the same drag as the much smaller two-dimensional shapes of a plate and a circular cylinder (at supercritical Reynolds number). The drag ratios are in the order of 1 to 50 and 1 to 10, respectively.

Tension Wires. Because of the load they have to carry, the cross-section area is important for streamline wires. To find their optimum shape, the drag coefficient is, therefore, based on the area $S_{cross} = b \sqrt{t/c}$. By multiplying equation 6 with $2\sqrt{c/t}$, the "cross-section coefficient" is found to be

$$C_{Dw}/C_f = 2 \left(\frac{c}{t} \right)^{1/2} + 4 \left(\frac{t}{c} \right)^{1/2} + 120 \left(\frac{t}{c} \right)^{7/2} \quad (9)$$

Minimum drag in this case is obtained at $t/c = 0.19$ or $c/t = 5.3$, as illustrated in figure 11. However, wires may be used in applications below the critical Reynolds number (see in table C). Equation 3 then leads to a much smaller optimum thickness ratio.

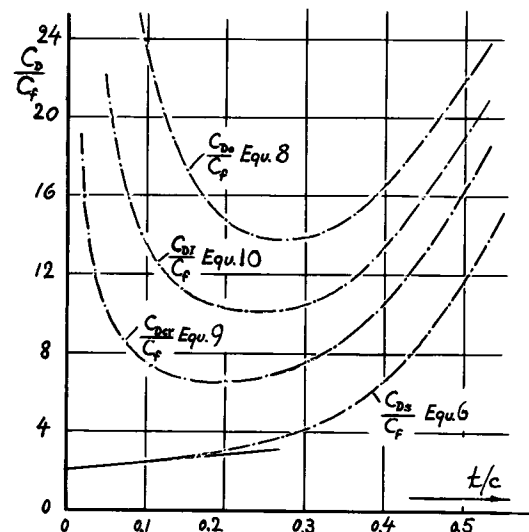
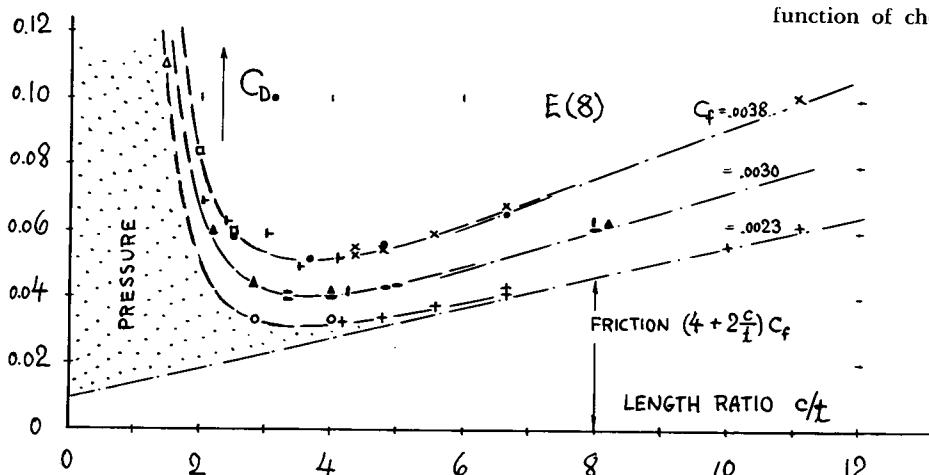


Figure 11. Drag ratios of symmetrical sections, for various practical purposes for which they may be used.

Figure 10. Profile drag coefficients of symmetrical wing- and strut sections, based on frontal area, as a function of chord/thickness ratio.



- In Turbulent Condition:
 - x NACA with sand-strip stim'l'n (7)
 - blunt ends corrected $R_c = 10^6$ (4,e)
 - ARC in CAT at $R_c = 10^6$ (4,g)
- At Lower Reynolds Numbers:
 - J o u k o v s k y (3,a)
 - ▲ Hoerner in water tunnel (4,f)
- At Higher Reynolds Numbers:
 - ARC Flight test $R_c = 6 \cdot 10^6$ (3,p)
 - ARC in CAT at $R_c = 7 \cdot 10^6$ (3,e)
- In Low-Turbulence Flow:
 - NACA Full-Scale Tunnel (3,f)
 - + NACA Low-Turbulence $6 \cdot 10^6$ (6,a)

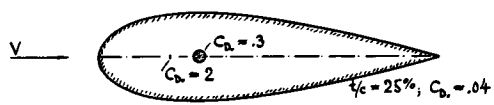


Figure 12. Two-dimensional bodies of equal fluid-dynamic drag; optimum streamline or fairing section, at Reynolds numbers between 10^6 and 10^7 , in comparison to circular cylinder and two-dimensional plate.

Compression Struts. Struts carrying longitudinal pressure loads must be designed so that they do not buckle. The moment of inertia of their cross-section area is to be considered, therefore, in selecting a basis for their drag coefficient. The term $b \sqrt{I}$ can be used as area, with "I" indicating the moment of inertia about the longitudinal section axis. Since for solid sections, this moment is $I \sim (c t^3)$, the area $S_I = b \sqrt{c t^3}$ shall be used. The corresponding drag coefficient, derived from equation 6, is

$$C_{Dl}/C_f = 2 \left(\frac{c}{t} \right)^{3/4} + 2 \left(\frac{t}{c} \right)^{1/4} + 120 \left(\frac{t}{c} \right)^{13/4} \quad (10)$$

The optimum thickness ratio in this definition is in the vicinity of $t/c = 23\%$. However, for consideration of their weight, struts are often made hollow; just tubes are often employed, pressed into a more or less streamline form. Assuming the wall thickness of the tubing to be proportional to the chord c , the same equation (number 9) is obtained as for tension wires. Assuming, however, the wall thickness of the tubing to be proportional to the section thickness t , equation 10 is found again. Actually constructed streamline tubes are probably in between the two cases. Their optimum thickness ratio is accordingly between 18 and 23%.

Function of Reynolds Number. At R'numbers above $R_c = 10^6$, the optimum ratios can be considered to be constant. For subcritical numbers, well below

$R_c = 10^5$, differentiation of equation 2 leads to the optimum thickness ratio with respect to frontal area and C_D of

$$(t/c)_{opt} = 1.63 / (R_c)^{1/4} \quad (11)$$

This ratio is plotted in figure 13 as a function of Reynolds number. Below the critical R'number range, the optimum ratio drops to a minimum of $\approx 11\%$. Optimum values for other applications, as treated above, have the same trends against Reynolds number. A very minimum value is reached by the tension wire with $t/c \approx 5\%$ in the vicinity of $R_c = 8 \cdot 10^4$.

B. SECTION DRAG AS A FUNCTION OF LIFT

Critical Reynolds Number. The range of low, subcritical R'numbers does not have much engineering application, not in airplane wings to be sure. Only in toy-size free-flying airplane models, Reynolds numbers (on wing chord c) can be expected in the order of $R_c = 10^4$. And it is for such application, that a number of foil sections has been tested (10,a). Figure 14 shows the variation of drag- and lift coefficient of a wing model, at fixed angle of attack, as a function of Reynolds number. The wing goes through a critical R'number range in which laminar flow separation from the upper side suddenly disappears. As a consequence, lift increases considerably, and the parasitic or section drag (obtained after subtracting the induced drag $C_{Dl} = C_L^2 / \pi A$) decreases correspondingly. The critical Reynolds number is a function of section shape, lift coefficient, turbulence and so on. The flow mechanism in passing through the critical phase, is basically the same as that of the circular cylinder (and of other "round" shapes) as described in the "pressure-drag" chapter.

Insects and Birds. Figure 14 also demonstrates that a sharp-nosed foil section (such as a thin plate) does not exhibit a critical variation of flow pattern and forces. This is evidently the reason why insects, operating at very low Reynolds numbers, do not have streamline shapes in their wings (10,b). Larger birds, however, operating at R'numbers R_c above 10^5 (such as buzzard and albatross, for example) do have round-nosed (and cambered) wing sections.

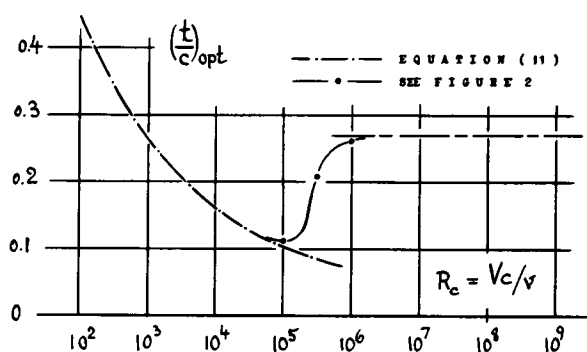
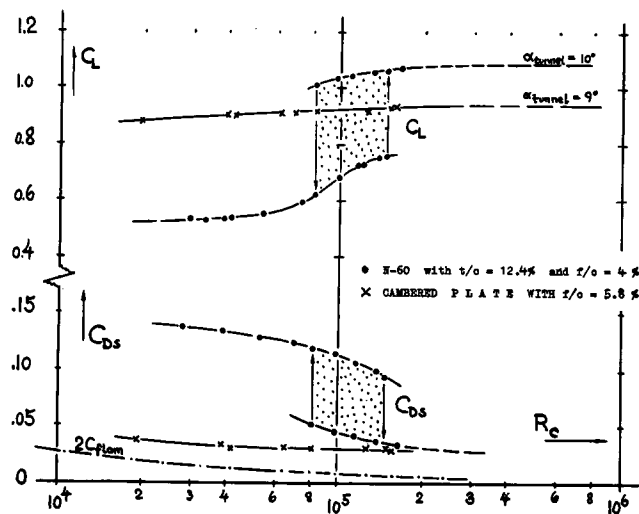


Figure 13. Optimum thickness ratio of fairings (with regard to C_D), as a function of R'number.



Higher R' numbers. At lift coefficients different from zero, the average flow velocity is increased at the upper side of a wing, and it is correspondingly decreased at the lower side. The viscous drag originating on the upper side is consequently higher than that on the lower side. This variation of section drag due to lift can be estimated by applying the same principles as used above in the description of drag due to thickness. The drag is divided into two components. The drag of the upper side is similar to that of half a profile with higher thickness ratio, and that of the lower side corresponds to half a section with lower thickness ratio.

Circulation. From the circulation around a foil section

$$\Gamma = \int w dx = w_{av} 2c = 0.5 C_L V c \quad (\text{ft}^2/\text{sec})$$

follows the average circulation velocity

$$w_{av}/V = C_L/4 \quad (13)$$

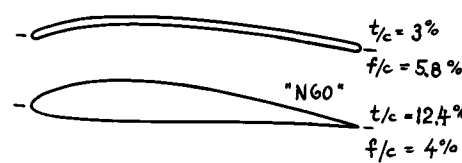


Figure 14. Variation of lift and drag coefficient as a function of Reynolds number, tested (10) at constant angle of attack on wind-tunnel models having $A = 5$. Section drag coefficient obtained after subtracting $C_L^2/\pi A$.

This velocity has one and the same magnitude at upper and lower side of an airfoil section. However, while on the upper side it has the same direction as the general flow (with positive sign), it is directed against the general flow (with negative sign) at the lower side. The difference in the average dynamic pressure, corresponding to circulation, is therefore

$$\Delta q/q = 1 - \left(1 \pm \frac{w_{av}}{V}\right)^2 \approx \pm \frac{C_L}{2} + \frac{C_L^2}{16}$$

The skin-friction drag differentials for the two section sides directly correspond to this equation. In the region of sufficiently low lift coefficients, where $C_L^2 \rightarrow 0$, the upper side makes up completely for the drag reduction of the lower one — as far as friction drag is concerned.

Pressure Drag. A difference in dynamic pressure, Δq , means a subsequent change of the static pressure gradient along the rear of the airfoil section. The pressure component of section drag varies with the third power of this gradient. At the same time, the frontal area of the respective side of the section varies with the angle of attack. The resulting increment of the effective thickness ratio is roughly plus or minus, respectively, $C_L/5$. The pressure-drag component of one side is consequently

$$\left(\frac{\Delta C_{D_s}}{C_f}\right)_{pr} \approx 60 \left(\frac{t}{c} \pm \frac{C_L}{5}\right)^4 \quad (15)$$

Note that on the lower side (negative sign) the pressure drag reduces to zero at a certain lift coefficient; subsequently the function has no more meaning for that side.

Optimum Lift Coefficient. Equation 15 applies only to camber ratios at which the flow smoothly meets the section nose, without any or much flow around it from one side to the other. The optimum or "symmetrical" lift coefficient for which this is true,

- (10) Foil Sections at subcritical Reynolds numbers:
 - a) Schmitz, Aerodynamics of Models, Berlin 1942.
 - b) Kuechemann and Holst, On Aerodynamics of Flying Animals, Luftwissen 1941 p.277.
 - c) See (3,l,m), (4,a,d,h,i,m) and (5,b,d,g,i,k).
- (11) As a function of lift, usually by wake survey:
 - a) German flight test results, Yearb'k D.Lufo 1941 p.I,111 (FB 1456), and Lufo 1929 Issue No. 1.
 - b) NACA, Wake Survey Results, T.Rpts 660 and 667.
 - c) Results, ZWB FM 1576 (Kramer) and 1621.
 - d) Flight Tests on Foil Section Drag, ARC RM 1688.
 - e) Flight Tests by GALCIT, J.Aeron'l Sci. 1940 p.425.
 - f) See results in reference (7).
 - g) AVA Göttingen, Ergebnisse Vol I (1921).
 - h) Foil Sections to $R_c = 2.5 \cdot 10^7$, NACA T. Rpt 964.
 - i) Polhamus, Drag Due to Lift, NACA T.N. 3324.

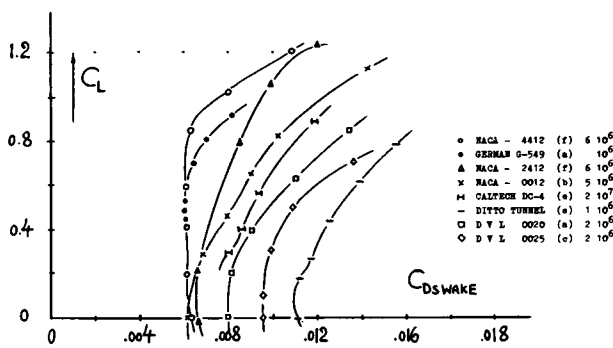


Figure 15. Collection of profile-drag coefficients of various foil sections as a function of lift (11).

is approximately

$$C_{Lopt} = (10 \text{ to } 12) f/c \quad (16)$$

where f/c = camber ratio of the foil section. Figure 15 presents available experimental data on the profile drag of airfoil sections, determined by the only method which eliminates the induced drag — the momentum-loss method (see in Chapter II). C_{Lopt} is roughly indicated by the minimum of the section-drag coefficient C_{Ds} . Combination of equations 14 and 15 yields the drag ratio per section side, with the positive signs to be applied to the upper side and the negative signs to the lower side of the section. Figure 16 illustrates how the viscous drag of a 12% thick airfoil section is shifted from the lower to the upper side, upon increasing the lift coefficient to positive values. The sum of the two drag components increases with C_L . Some experimental points evaluated for optimum lift coefficient, substantiate the calculation, up to $C_L \approx 1$.

Additional Section Drag. Above and below the optimum lift coefficient, the drag increases because of flow around the leading edge and subsequent momentum losses in the boundary layer. The 0012 section for example, in figure 15, shows at $C_L = 1$

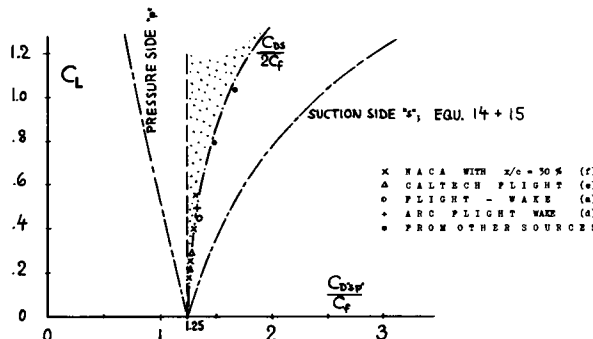


Figure 16. Example with $t/c = 12\%$, of the variation of optimum profile drag as a function of lift, evaluated from (11) for Reynolds numbers between 10^6 and 10^7 .

a section-drag coefficient which is almost twice as high as at zero lift. It has been tried to express the incremental drag by empirical equations (12). A rough but simple function indicating the profile drag of symmetrical (or only slightly cambered) airfoil sections, is

$$\Delta C_{Ds}/C_{Dsmin} = k C_L^n \quad (18)$$

If, or as long as this drag component is proportional to the square of the lift ($n = 2$), it can easily be combined with the induced drag which is also a function of C_L^2 ; see in this respect the "equivalent-aspect-ratio" method as treated in Chapters VII and XIII. In figure 4 of the "drag-due-to-lift" chapter, a component is evident, roughly corresponding to equation 18, with $k = 1$. For example, on the basis of $C_{Dso} = 0.009$ and a wing aspect ratio $A = 7$, the increase of section drag amounts to $\Delta C_{Ds}/C_{Dl} = 0.01 \pi 7 \approx 20\%$.

In Cambered Sections, the drag at $C_L \rightarrow 0$, can be appreciably higher than that at C_{Lopt} . For small camber ratios, between 1 and 2% of the chord, corresponding to C_{Lopt} between 0.1 and 0.2, evaluation of foil-section data (11) with thickness location at $\approx 30\%$ of the chord, suggests a variation of section drag in the form of

$$\Delta C_{Ds} = k C_{Dsmin} (\Delta C_L / \Delta C_{Lmax})^n \quad (19)$$

where $\Delta C_L = (C_L - C_{Lopt})$, positive or negative, $\Delta C_{Lmax} = (C_{Lmax} - C_{Lopt})$, and n between 2 and 3. In all such empirical functions, the boundary-layer changes in laminar-flow type sections are disregarded, of course. These and other sections as well may exhibit irregular variations of viscous drag as a function of lift coefficient (due to pressure-side laminarization, for example) — so that equations 14 through 19, describing continuous variations, can be considered only as idealizations. One more influence comes from the aspect ratio of the wing. It has been shown (11,i) that in small aspect ratios the effective section camber reduces, because of flow curvature. Increments of section drag above those as indicated above are, therefore, found in aspect ratios below those as applied in conventional airplane wings.

Reynolds Number. Figure 17 shows the variation of section drag against R'number, for several airfoils at the lift coefficient $C_L = 0.7$, a value that is well above "optimum". Most of the variation due to partly laminar boundary-layer flow is evidently eliminated; the transition point at the upper side is most likely fixed near the minimum pressure peak.

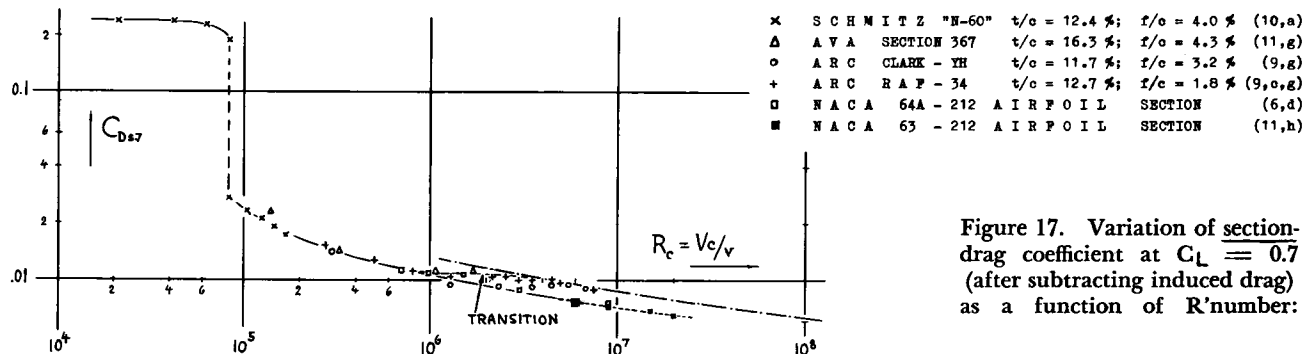


Figure 17. Variation of section-drag coefficient at $C_L = 0.7$ (after subtracting induced drag) as a function of R' number:

Sharp Leading Edges. At optimum lift coefficient, foil sections with sharp leading edges may be expected to have the same drag as similar sections having a favorably rounded leading edge. Figure 18 demonstrates, however, that above and below $C_{L\text{opt}} \approx 0.5$ for $f/c = 5\%$, the viscous drag of this sharp-nosed circular arc section increases considerably above that of comparable round-nosed shapes. The mechanism through which flow around a sharp leading edge is maintained, has found increased attention lately (14). Laminar separation first takes place directly at the edge. Because of turbulent mixing, reattachment is then effected at a location that steadily moves from near the leading to the trailing edge, as the angle of attack is increased. Experience with airfoil sections or plates having sharp edges, proves that in this way appreciable positive pressure gradients can be overcome, without contracting permanent separation. Generation of lift and a fairly high lift-curve slope are thus maintained up to maximum lift coefficients in the order of 1. The section drag increases, however, progressively in this mechanism, as shown in the examples of figure 18. Figure 14 also proves that in sharp-nosed sections, high lift coefficients are maintained down to comparatively low Reynolds numbers — below those that are critical for round-nosed sections. Early experiments in wind (Lilienthal) and in small wind tunnels (Eiffel), at Reynolds numbers below 10^5 , therefore, led to the conclusion that sharp-nosed (and cambered) sections would be optimum for airplane wings. Only after increasing speed (and size) of the test facilities, characteristics were subsequently found in streamline foil shapes, truly superior in

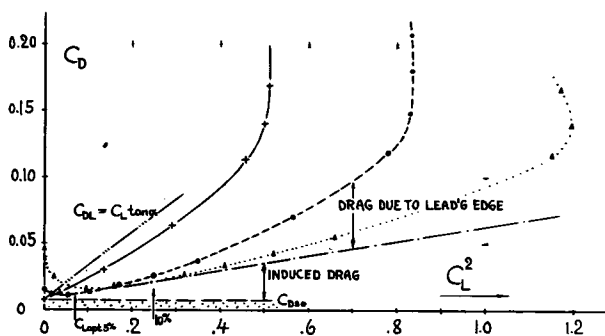


Fig. 18. Drag-lift function of foil sections having sharp LE's, tested with $A = 6$ at $R_c = 6 \cdot 10^6$ (13).

the range of Reynolds numbers as they prevail in full-scale airplanes.

Beyond $C_{L\text{max}}$, the drag of airfoils increases in a manner as shown in figure 19. In the vicinity of $\alpha = 45^\circ$, the lift shows a certain "hump"; and from there on, drag predominates, reaching at $\alpha = 90^\circ$ a maximum roughly equal to that of a flat plate in normal flow (Chapter III). Wings with $A = 5$ or 6, show in this way $C_{D\text{s}} = C_D \approx 1.15$, while in two-dimensional condition (between tunnel walls) $C_{D\text{smax}} \approx 2$. Practical application of high angles of attack is found in helicopter blades and in marine propellers (in reversed operation).

- (12) Formulas for section drag as a function of lift:
 - a) NACA T Rpt 312 (1929); $\Delta C_{D\text{s}} = 0.0093 C_L^{3.3}$.
 - b) Rpt 391 (1931); $\Delta C_{D\text{s}} = 0.0062 (C_L - C_{L\text{opt}})^2$.
 - c) Flight 1932 p.530a and 710a; $\Delta C_{D\text{s}}$ presented as a function of $[(C_L - C_{L\text{opt}}) / (C_{L\text{max}} - C_{L\text{opt}})]$.
- (13) Williams and Others (NPL), Circular-Arc Aerofoils in CAT, ARC RM 2301 (1946) and 2413 (1950).
- (14) NACA, Investigations on BL Reattachment T.Notes 1196 (1947), 1894 (1949), 2338 (1951) and 3505.
- (15) Characteristics at extremely high angles of attack:
 - a) Naumann, Profile to 360° , Ybk Lufo 1940 p.I, 51.
 - b) AVA Göttingen, Ergebnisse Vol III (1926).
 - c) NACA, "Clark Y", Rpt 317 (corrected for block).
 - d) NACA, 0012 Between Walls to 180° , T.Note 3361.

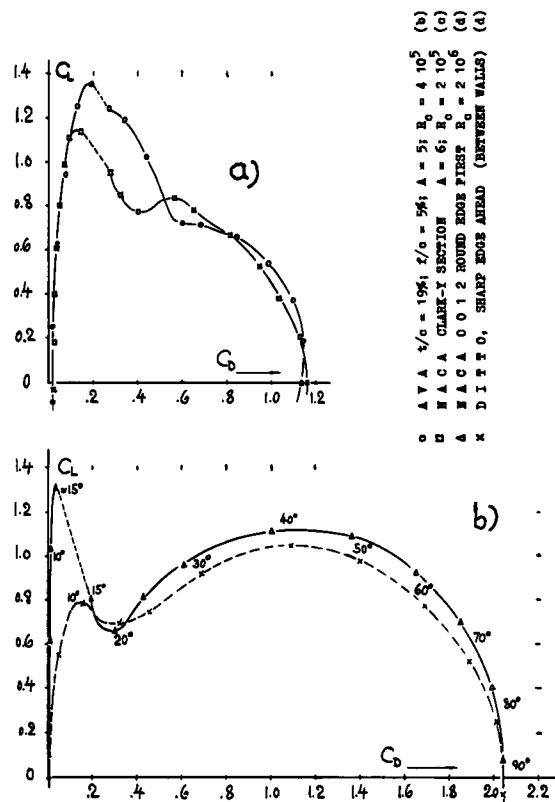


Figure 19. Variation of drag, lift coefficient (15); (a) in finite aspect ratios, (b) between tunnel walls.

Wing Flaps. By deflection of a landing flap, section camber is increased. At higher lift coefficients, flapped sections, therefore, can have less drag than plain airfoils. A certain flap angle is associated with each lift coefficient, providing minimum section drag. Corresponding points are plotted in figure 20, indicating envelopes of the maximum "lift/(section drag)" ratio. Regarding the design of landing flaps, ailerons and control surfaces, figure 20 leads to practical conclusions as follows:

(a) Slotted flaps and similar designs, such as the "double wing" present the least drag in the range of intermediate and higher lift coefficients. Up to certain critical lift coefficients, where evidently a more extended flow separation begins, the profile drag of the slotted sections roughly agrees with the theoretical result as per equations 14 and 15.

(b) Split flaps usually show the highest maximum lift coefficients and the lowest minimum drag values (if retracted into the wing profile). On account of the dead space between the trailing edges of wing and flap (if deflected) the section-drag coefficients of split flaps are about twice as high, however, in the average, as those of the slotted flaps.

(c) In the case of plain flaps, widely used in control surfaces, the flow stays attached to the suction side of the flap within a deflection angle of only plus or minus 10 or 15°. Beyond these angles, the section drag is at least as high as in split flaps.

Wing Slats. Slots (fixed) or movable slats (pioneered in England by Handley-Page) increase maximum lift by preventing flow separation from the upper wing side. Section-drag coefficients associated with their application seem to be excessive at wing-chord Reynolds numbers below $\approx 10^6$ — as shown in (17) for example. It is suggested that the R'number on slat chord (between 15 and 20% of the wing chord), should be well above 10^5 , so that flow separation from slat suction side is avoided. It should be expected that at certain lift coefficients, the section drag coefficient of slotted wings can be as low as with trailing edge flaps. Generally, however, LE slots and slats do not appear to be promising as far as drag is concerned. Their application is rather a necessity in certain wing shapes, to prevent stalling. Figure 20,a presents drag characteristics of an open (fixed) slat. It is seen that in condition (b) with no flow through the slot, drag is comparatively small.

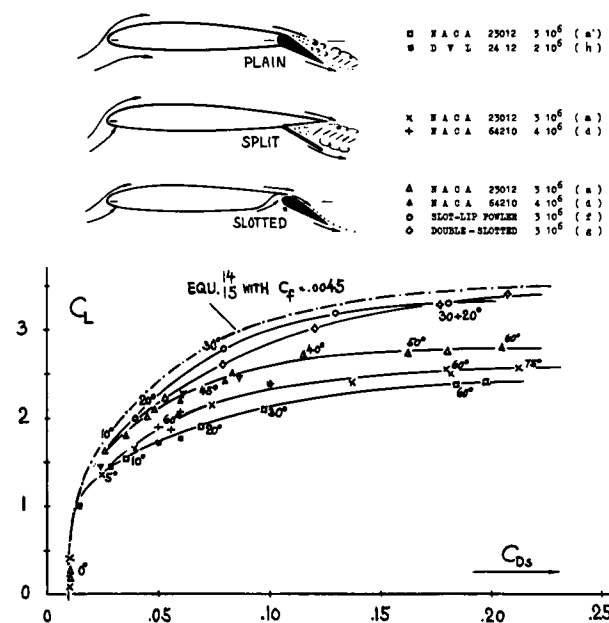


Figure 20. Profile drag of airfoil sections equipped with various types of lift-increasing TE flaps (16).

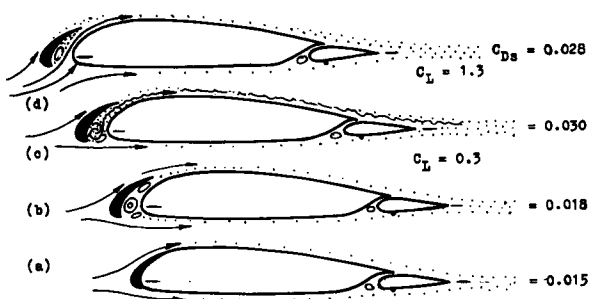


Figure 20.a. Drag (by wake survey) of foil section (Fieseler "Stork") in combination with fixed slat (17.b).

C. DRAG OF STREAMLINE BODIES

Basic Shapes. In distinction from airplane wings (essentially designed for lifting area) engine nacelles and particularly airship hulls are designed with a view to volume. Streamline forms used in these applications, illustrated in figure 21, are generally "fuller", therefore, than the sections in figure 9. Only fighter airplanes (if not having a jet outlet at the tail) and other airplanes (not carrying anything or much in the afterbody) may have more slender basic fuselage contours similar to the NACA 4-digit foil sections. Engine nacelles may have shapes very much dictated by technical functions, such as in- and outlets of cooling air or jet volume and the landing gear which is often retracted into them. In the fuselages of commercial airplanes, a prismatic shape of the middle body is desirable for a convenient arrangement of seats — as in railroad cars. In displacement ships, bow- and stern portions of the hull are made as fine as practicable to reduce (postpone) wave resistance. Generally, the position of maximum thickness has a considerable influence on that of the minimum pressure (dictating boundary-layer transition). Reference (20,a) indicates, for example, on a 17.5% thick body of revolution:

for maximum thickness location $x/c = 0.30, 0.40, 0.50$
a minimum pressure location at $\approx 0.20, 0.35, 0.60$

References (20,b and c) also demonstrate that full forebodies (in distinction from fine or even pointed shapes) have the pressure minimum near the nose.

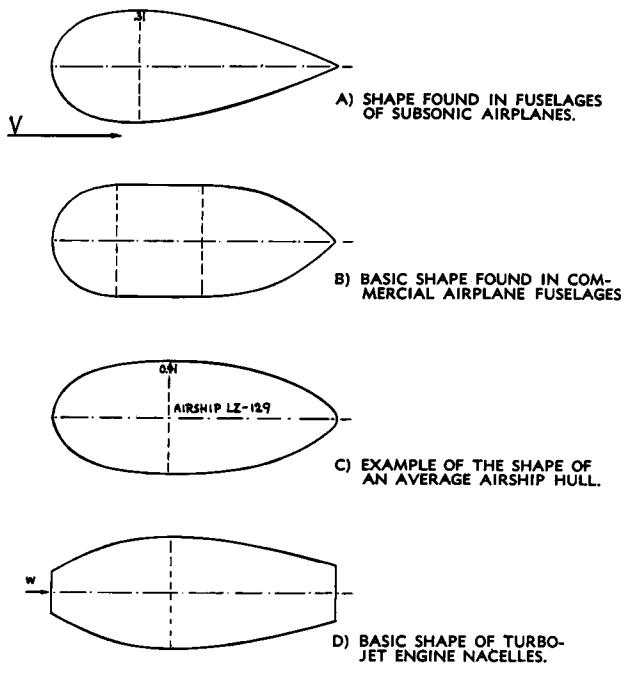
Reynolds Numbers. Approximate average R'numbers (on length l) in streamline bodies are as listed in table D. These numbers are considerably higher than those of the foil sections in tables A and B.

APPLICATION	c ft	V knots	R'
AUTOMOBILE BODY	15	50	$7 \cdot 10^6$
AVERAGE BOMB BODY	5	400	$2 \cdot 10^7$
FIGHTER FUSELAGE	35	550	$2 \cdot 10^8$
COMMERCIAL AIRPLANE	100	300	$3 \cdot 10^8$
BOMB FUSELAGE	100	400	$4 \cdot 10^8$
LARGE AIRSHIP HULL	600	100	$6 \cdot 10^8$
LARGE ROCKET	40	1500	$6 \cdot 10^8$

TABLE D. R'numbers in streamline-body applications.

Experimental Data. Plotted in *figure 22* against Reynolds number, the drag coefficients of three-dimensional bodies generally show trends similar to those of the two-dimensional shapes in *figure 1*. At R'numbers below 10^7 , the experimental points are rather scattered, however. The drag coefficients of two bodies having the same fineness ratio, may be different in the ratio of 1 to 2, for example, at one and the same R'number. The reasons are as follows:

- (a) The support of a body of revolution in the test section of a wind tunnel, is practically impossible without disturbing the flow pattern somehow (by rods or wires attached to the forebody). Also, the wake-survey method of testing drag (which is so successful in testing foil sections) cannot help — since it necessarily includes interference effects too. The method has been applied, however, in (21,h) and (22,a).
- (b) On three-dimensional bodies, pressure minima are basically smaller than in two-dimensional flow. Boundary-layer transition is, therefore, not fixed (as in the 4-digit foil sections for example). Rather, transition is a complex function of shape, Reynolds

Figure 21. Some examples of basic streamline body shapes in engineering applications.

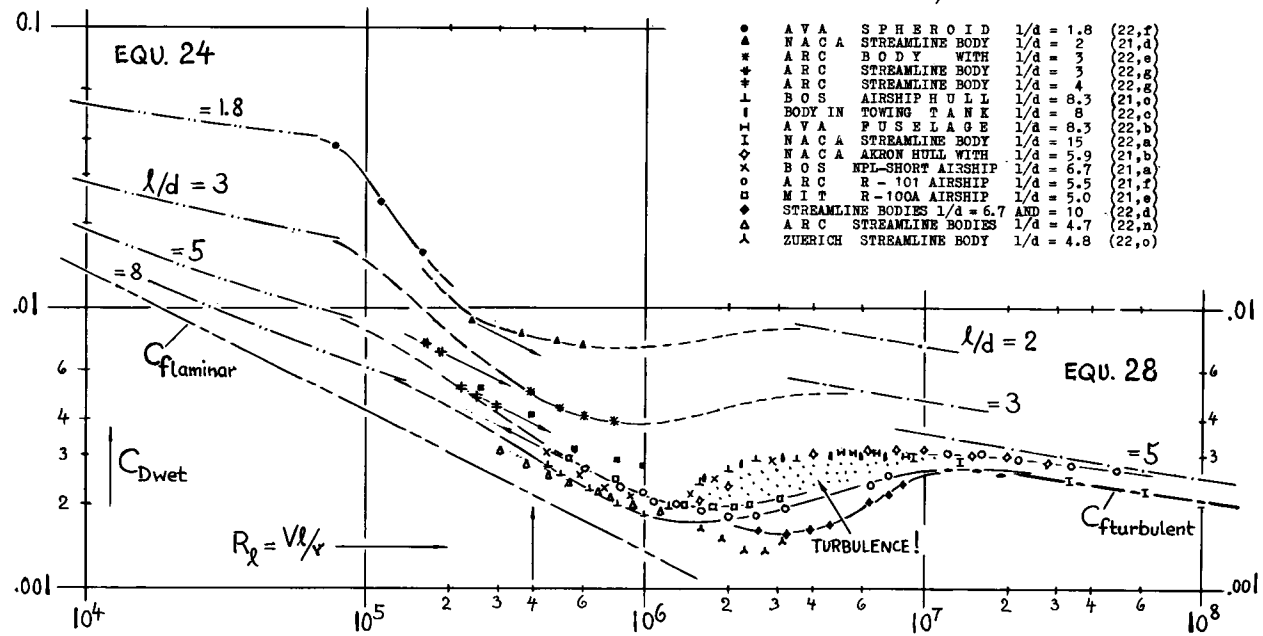
(16) Characteristics of flapped wing sections:

- a) Wenzinger and Others, Airfoils with Various Flap Arrangements, NACA T Rpts 661, 664, 668, 677.
- b) Kramer, Wing Flaps, German Doct ZWB FB 1576.
- c) A bibliography on wing flaps is given in ARC RM 2622, Characteristics of Flaps by Young (1953).
- d) Sivells, Wing with Flaps, NACA T.Rpt 942 (1949).
- e) CAHI (Moscow) Rpt 133; in Fieseler "Stork".
- f) NACA, Fowler Flap, Technical Note 808.
- g) NACA, Double-Slotted Flap, Technical Rpt 723.
- h) DVL, 2412 Foil, Yearb'k D.Lufo 1940 p.I,182.

(17) Characteristics of airfoils with LE slots or slats:

- a) NACA, Tech Note 702 and Tech Rpt 586.
- b) Petrikat, LE Slats, Ybk.D.Lufo 1940 p.I,248.
- c) CAHI Rpt 133, German Transl. Luschau 1936.

Figure 22. Selected results on the drag of rotationally-symmetric bodies (no corrections applied).



number and stream turbulence, similar to conditions in laminar-type foil sections. "Turbulence factors" (not applied in plotting the results in figure 22) would be very large in certain shapes, for example in the order of 10 as in figure 9 of the "skin-friction" chapter.

*1957

At Subcritical Reynolds Numbers. Not a single source was found by the author on streamline bodies in really subcritical condition (below $R_\lambda = 10^5$). Assuming, however, that with separated flow pattern, streamline bodies may have the same drag as spheroids (treated in the "pressure-drag" chapter), it is possible to appraise the subcritical drag (in a manner similar to that of the foil sections in figure 4). Thus the pressure drag is tentatively

$$C_{D_{\text{press.}}} = 0.33 \frac{d}{\lambda} \quad (21)$$

Guided by the later equation 28, the skin-friction drag is estimated to be

$$C_{D_{\text{wet}}} = C_{\text{flam}} [1 + (d/\lambda)^{3/2}] \quad (22)$$

These two coefficients can be converted into one another, using equation 30. The functions then present a pair of asymptotes between which the drag coefficient is

$$C_{D_*} = 0.33 (d/\lambda) + C_{\text{flam}} [3(l/d) + 3(d/\lambda)^{1/2}]$$

Or, based on wetted area:

$$C_{D_{\text{wet}}} = C_{\text{flam}} [1 + (d/\lambda)^{3/2}] + 0.11 (d/\lambda)^2 \quad (24)$$

This function has been used in figure 22 to indicate drag coefficients between $R_\lambda = 10^4$ and $= 10^5$. The optimum fineness ratio, if considering drag based on frontal area, is in the order of $d/\lambda = 20\%$, at $R_\lambda = 10^5$.

Forced Turbulence. Drag predictions in the transitional range around $R_\lambda = 10$ are problematic. Difficulties reduce, however, at higher Reynolds numbers (see in table D) and/or in such applications where boundary-layer transition is forced. In many or most engine nacelles, for example, the b-layer is made turbulent by air intakes, cooling flaps, surface imperfections and the adjoining wing parts. The propeller slipstream (if involved) also produces early transition in nacelles as well as on the fuselage surface (in single-engine configurations). Even in comparatively clean jet engine installations, the boundary-layer may turn turbulent from the rim of the intake opening. In these practical applications, therefore, the irregularities in the drag-coefficient function as seen in figure 22, may not be very important. Airship bodies have accordingly been tested in wind tunnels (21) and ship hulls in towing tanks (see in the chapter on "water-borne craft") with transition forced and fixed by means of sand strips,

wires or turbulence pins placed on the model's surface near nose or stem, or through turbulence screens placed in front of the models. Extrapolation to full-scale Reynolds numbers (above 10^8) is then accomplished in proportion to the turbulent skin-friction drag coefficient. Figure 23 presents a selection of results in which turbulent boundary-layer flow is forced over most of the R'number range investigated. There are many other experimental results available (21) between $R_\lambda = 10^6$ and 10^7 . One group exhibiting the effect of moderate wind-tunnel turbulence is included in figure 22. Between the lowest curve shown there and the "fully" turbulent function in figure 23, the drag coefficient can have any value because of stream turbulence, surface roughness, interference from attached or adjoining parts and as a consequence of shape (position of maximum thickness and fullness — prismatic coefficient). Such results have been excluded from the two graphs, to keep the basic picture clearer.

- (20) Pressure and drag on rotationally symmetric bodies:
 - a) Lange (DVL), Experiments on a Series of Bodies German ZWB FB 1516 (1941), Transl'n NACA TM.
 - b) Neumark, Distribution (Theory), ARC RM 2814.
 - c) Weinig, Foil Sections and Bodies of Revolution, Ybk STG 1937 p.231; see also ZWB FB 1633.
 - d) Young, Drag Calculation, ARC RM 1874 (1939).
 - e) Pritch, 3-Dimensional Bodies, ZWB UM 3185.
- (21) Wind-tunnel results on airship hulls:
 - a) Investigations by BOS, NACA T.Note 264.
 - b) "Akron" Hull in Prop. Tunnel, NACA T.Rpt 432.
 - c) Bur. of Stand., R-33 Hull, Jacobs in Durand III.
 - d) Zahm-Smith, C-Class Hulls in Washington Tunnel, NACA T.Rpt 291 (results do not correlate well).
 - e) MIT Investigation, Aircraft Engg 1934 p.233.
 - f) Two Bodies (R-101) in CAT, ARC RM 1710.
 - g) Fuhrmann, Ybk Motorluftsch. Studieng. 1911/12.
 - h) Lyon, Study of B'Layer, ARC RM 1622 (1934).
 - i) Abbott, Airship Hulls in VDT, NACA T.Rpt 394.
 - k) Two Streamline Bodies, NACA T.Rpt 451 (1933).
 - l) R-101 Hull, ARC RM's 1168 (1926) and 2896.
 - m) C-Class Airship Hulls, NACA T.Rpt 138 (1922).
- (22) Experimental results on bodies of revolution:
 - a) Mottard-Loposer, Parabolic Body Tested in Towing Tank, NACA T.Rpt 1161 (1954); also TN 2854.
 - b) Kosin and Lehmann, Fuselage Aerodynamics, Yearb'k D.Lufo 1942 p.I,241; also Doct AVA 35/1941.
 - c) Weinblum, Streamline Bodies in Towing Tank; Schiffbau 1936 p.411; Yearb'k STG 1937 p.177; Transl'n by TMB.
 - d) DVL, In High Speed Tunnel, Doct J 729/3 (1944).
 - e) Ower, Interference Investigation, ARC RM 1409.
 - f) AVA Göttingen, Spheroids, Ergebnisse II (1932).
 - g) ARC, Series of Streamline Bodies, RM 311 (1917).
 - h) Streamline Bodies in Towing Tank, Hamburg
 - k) NACA Fuselage Bodies in VDT, T.Note 614.
 - l) ARC, Two Streamline Bodies, RM 1271 (1929).
 - m) Goethert, Streamline Bodies in DVL High Speed Tunnel, ZWB Tech Ber. 1944 p.377 (also UM 1222).
 - n) Pannell & Jones, Bodies, ARC RM 607 (1919).
 - o) Mitt.Inst.Aerodynamik TH Zürich No. 13, 1946.

•	F U H R M A N N	SHAPE NO. I WITH $d/l = 16$	\times	(21,g)
◊	A R C - L Y O N	"B" B O D Y WITH $d/l = 20$	\times	(21,h)
×	N A C A - V D T	W I T H $d/l = 12$ TO 16	\times	(21,i)
△	N A C A - V D T	WITH $d/l = 17$ TO $22\frac{1}{2}$ (21,j) AND (22,k)		
+	N A C A - A I R S H I P H U L L	WITH $d/l = 10$	\times	(21,d)
-	B E R L I N	I N T O W I N G T A N K WITH $d/l = 12, 5\frac{1}{2}$ (22,o)		
—	H A M B U R G	I N T O W I N G T A N K WITH $d/l = 13$ \times (22,p)		

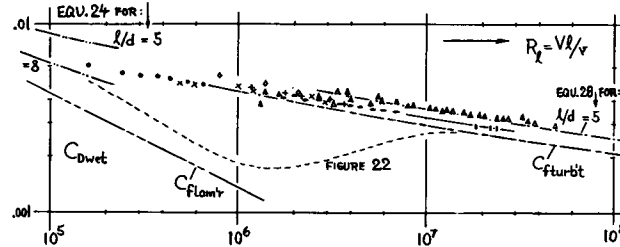


Figure 23. Drag of streamline bodies, tested in turbulent wind tunnels or with turbulence stimulation.

Thickness Ratio. To show their relation to the skin-friction drag coefficient C_f , the experimental results in figures 22 and 23, have been referred to the wetted surface area of the bodies. Employing the same methods as for two-dimensional shapes, the drag in rotationally symmetric conditions can be described in terms of the thickness ratio. In three-dimensional flow, the supervelocity is approximately proportional to $(d/l)^{3/2}$, as can be found in (20). For small (d/l) ratios, the increment of the average dynamic pressure along the sides is accordingly

$$\Delta q_{av}/q = 1.5 (d/l)^{3/2} \quad (26)$$

The frictional drag coefficient corresponds to the average dynamic pressure; therefore:

$$\Delta C_{Df}/C_f = 1.5 (d/l)^{3/2} \quad (26)$$

Interpolating the experimental points in figure 24, the drag component due to flow separation is statistically found to be:

$$C_{Dpr}/C_f = 7 (d/l)^3 \quad (27)$$

The total drag, based on wetted area is consequently

$$C_{Dwet}/C_f = 1 + 1.5 (d/l)^{3/2} + 7 (d/l)^3 \quad (28)$$

The graph shows that the third term of this equation is practically negligible up to $d/l \approx 0.2$.

- (a) AT $R_\lambda = 10^6$ - WITH TURBULENT BOUNDARY LAYER:
 A M A G A - V D T BARE AIRSHIP HULLS (21,a,1)
 A V A - FUHRMANN AIRSHIP BODY (21,g)
 W WITH ROUGHNESS $k/l = 5 \cdot 10^{-3}$ AT $R_\lambda = 4 \cdot 10^6$ (22,d)
- (b) AT $R_\lambda = 3 \cdot 10^6$ - WITH TURBULENT BOUNDARY LAYER:
 D V L - LANGE STREAMLINE BODIES (20,a)
 A R C - LYON AIRSHIP HULL "A" (21,h)
 A H C STREAMLINE BODY (22,g)
- (c) AT $R_\lambda = 10^7$ - WITH TURBULENT BOUNDARY LAYER:
 N A C A - V D T AIRSHIP HULLS (21,i,k)
 D I T T O - NO TURBULENCE STIMULATION (22,k)
 A R C - R-101 AND 102 AIRSHIP HULLS (21,f)
 H S V A AND S T G, STREAMLINE BODIES IN TANK (22,h)
 A V A - FUSELAGE BODY (22,b)
 N A C A - "AERON" AIRSHIP HULL (21,b)
 N A C A - STREAMLINE BODY IN TOWING T. (22,a)
- (d) AT $R_\lambda = 10^6$ - WITH NATURAL TRANSITION:
 D V L - LANGE STREAMLINE BODIES (20,a)
 A R C - OWN BODY EXTRAPOLATED (22,k)
 M I T - AIRSHIP HULL "A" (21,g)
 A R C - C A T R-101 and 102 AIRSHIPS (21,f)
 B O S - AIRSHIP HULLS (21,e)
- (e) TANGENTIAL OPTIMA AT $4 \cdot 10^5$:
 - VARIOUS RESULTS EVALUATED FROM FIG. 22

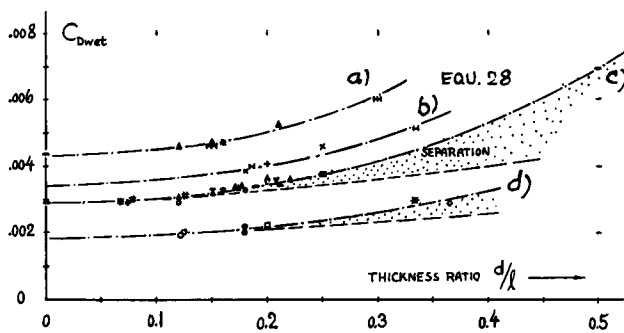


Figure 24. Streamline bodies; variation of drag coefficient (on wetted surface area) as a function of d/λ .

"Laminar" Regime. It appears in figure 22 that between $R = 10^5$ and 10^6 , the drag coefficients of several streamline bodies tested, follow lines which are essentially parallel to the laminar skin-friction function — which means that their drag is proportional to that drag. Equation 28 may, therefore, be applicable. A number of experimental points was taken at, or reduced to $R_\lambda = 4 \cdot 10^5$ (see the lines in figure 22), and included in figure 24. By coincidence they exhibit drag coefficients in the same magnitude as these bodies have in fully turbulent condition at $R_\lambda = 10^7$. Note that with laminar forebody flow, the function cannot continue at thickness ratios below ≈ 0.1 ; transition can no longer be expected then to be fixed near the pressure minimum (whose value reduces together with d/λ). — In not-too-thin bodies, laminarization can be continued to higher Reynolds numbers by placing the maximum thickness further back. An example of this effect is included in figure 22 between (3 and 8) 10^6 in two bodies having the thickness at 0.45 λ . However, since the favorable pressure gradients obtainable in three-dimensional bodies are comparatively small, the laminarization effect cannot be as strong and lasting as in laminar-type foil sections. Also in many applications there may simply not be much of a chance for the b'layer to stay laminar, because of other components of a configuration (such as, for example, wing roots on a fuselage).

Surface Roughness. A few results of streamline bodies having a rough (carborundum- or sand-coated) surface are included in figure 8. Figure 24 demonstrates in two experimental points (22,d) that equation 28 also applies in rough-surface conditions, if using a basic C_f value that corresponds to the relative roughness size k/λ (as explained in the chapter on "imperfections").

Applications. Rotationally symmetric streamline bodies or similar three-dimensional shapes are applied in fuselages, nacelles, airship bodies, ship hulls, floats and in fairings. Suitable reference areas are listed in table E.

APPLICATION	REFERENCE AREA	d/λ_{opt}	$1/d_{opt}$
FAIRINGS AND ENGINE NACELLES	FRONTAL AREA $d^2/4$	0.4	2.5
AIRSHIP- AND BOAT HULLS	VOLUME AREA $\sqrt[3]{V}$	0.3	3
FUSELAGES WITH TAIL SURFACES	SEE REFERENCE (1, a)	0.17	6

TABLE E. Reference areas and optimum ratios of three-dimensional bodies, as a function of application.

Frontal Area. The wetted surface area of streamline bodies is approximately

$$S_{\text{wet}} = (0.7 \text{ to } 0.8) \lambda \text{ (perimeter)}$$

The perimeter is that of the maximum cross-section area, which in rotationally symmetrical bodies is equal to $(d \pi)$. The smaller constant applies to finer shapes, the larger one to fuller shapes (approaching spheroids) as illustrated, for instance, in figure 21. Using an average constant of 0.75, the circumference πd , and the frontal area $S_* = d^2 \pi / 4$, the ratio of wetted to frontal area is found to be approximately

$$\frac{S_{\text{wet}}}{S_*} = \frac{4 \cdot 0.74}{d/\lambda} = 3 \frac{\lambda}{d} \quad (30)$$

Employing this expression, equation 28 is converted into

$$C_{D_*}/C_f = 3(\lambda/d) + 4.5(d/\lambda)^{1/2} + 21(d/\lambda)^2 \quad (31)$$

Optimum Fineness Ratio. With respect to frontal-area coefficient, figure 25 shows a minimum at $\lambda/d \approx 2.7$ or $d/\lambda \approx 37\%$, respectively. Considering aircraft applications, it must be remembered, however, that the flow past streamline bodies is usually disturbed by interference through appendages or other adjoining parts. The optimum fineness ratio of such bodies or that of fairings is consequently higher than 2.7. More information on this subject is available in Chapters VIII and XIII.

▲ TURBULENT CONDITIONS AT $R_x = 10^6$
 ▨ WITH ROUGH SURFACE, EVALUATED FROM FIG'S 8 AND 24
 ○ TURBULENT B' LAYER FLOW AT $R_x = 10^7$
 - OPTIMUM LAMINAR CONDITION AT $R_x = 4 \cdot 10^5$
 ✕ WITH NATURAL TRANSITION AT $R_x = 10^6$

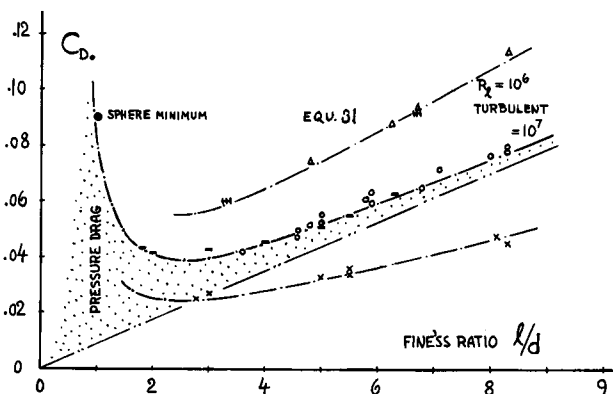


Figure 25. Drag coefficients (on frontal area) of streamline bodies as a function of their fineness ratio. Points evaluated from figures 22 and 23; equation 31.

Volume. For airships, the decisive characteristic is volume. It is, therefore, convenient to refer the drag coefficient to an area derived from volume; that is, to $S_v = (\text{volume})^{2/3}$. This area represents the side of a cube having the same volume "V" as the body considered. The volume of a streamline body is

$$\nabla = C_{\text{pris}} l S_v \quad (32)$$

Where C_{pris} = prismatic coefficient. A value of 0.6 for this coefficient applies to finer fuselage shapes; $C_{\text{pris}} = 0.7$ is approximately correct for airship bodies. Using an average constant, combination of this equation with 30 gives

$$S_{\text{wet}} / \nabla^{2/3} = 4 (l/d)^{1/3} \quad (35)$$

Subsequently, equation 28 is transformed into

$$C_{D\Delta} / C_f = 4 (l/d)^{1/3} + 6 (d/l)^{1.2} + 24 (d/l)^{2.7} \quad (36)$$

As theoretically optimum fineness ratio for airship- and submarine bodies, this equation yields $d/l = 0.25$ or $l/d = 4$. The optimum is, however, rather flat, at $d/l = 0.2$ and $= 0.3$, for instance, the drag is only $\approx 2\%$ larger than the minimum.

Real Bodies. Fuselages and flying-boat hulls differ more or less from the ideal streamline shape, both with respect to contour and cross-section. Usually, therefore, such bodies present drag values, which are somewhat higher than indicated in figures 23 and 25, even if disregarding protuberances, appendages, and interference effects. As equivalent "diameter" of these bodies, " d " = 0.5 ($b + h$) may be used.

Drag Due to Lift. The induced drag of three-dimensional bodies, associated with lift which they usually produce if put at an angle of attack against the flow, is treated to some degree in the "drag-due-to-lift" chapter. In addition to this component of drag, streamline bodies also exhibit some increment of viscous drag — caused by increased average super-velocity around the shape. At positive angles of attack, the boundary-layer has the tendency of accumulating above the stern; and such accumulation is part of the mechanism by which lift originates in the first place in these bodies.

D. SUPPLEMENTARY INFORMATION

To fill the space on this and the next page, some more results are presented, related to the subject of "streamline drag".

Turbulence Stimulation has been mentioned under the heading "forced turbulence" on page 6-16. Figure 26 demonstrates how the drag coefficient of

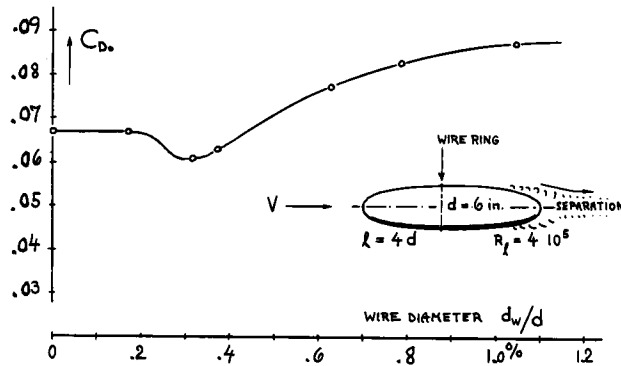


Figure 26. Example of turbulence stimulation by means of a wire ring (26).

- (23) Streamline bodies with surface roughness:
 - a) Hoerner, Reynolds Number Turbulence Roughness on Spheres, Lufo 1935 p.42; Transl'n NACA T. Memo 777.
 - b) NACA, Airship Bodies, T.Rpts 324 and 432.
 - c) DVL, Bodies in High Speed Tunnel, (22,d).
- (26) Jones-Bell, Spheroid, ARC RM 858 (1922).
- (28) Eggers, Reversed 0012 Section and Wedge Function of M; NACA Rpt RM A7C10 (1947).

a spheroid varies as a function of the diameter of a wire ring applied for stimulation. In the first phase, drag is decreased; evidently separation is further reduced in the same manner as in spheres and cylinders (see in the "pressure drag" chapter) within the critical range of their Reynolds number. In the second phase (above $d_w/d = 0.3$) the spheroid's drag increases again. Drag due to, and boundary layer thickness caused by the "trip wire" evidently produce separation to an extent which approaches and then exceeds the original degree of separation. The example presented is extreme insofar as the shape of the spheroid lends itself to separation. The result suggests, however, that some consideration must be given to degree and consequences of turbulence stimulation in model testing.

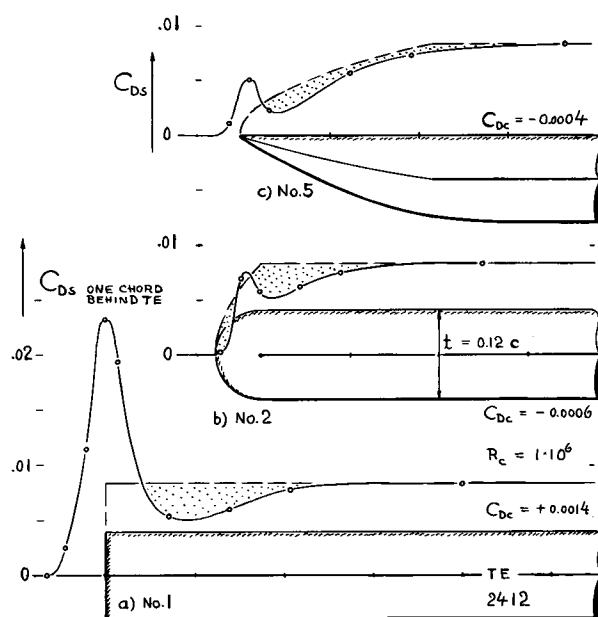


Figure 27. Distribution of sectional drag within the wake of a wing tip. Shape and model tested, is the same as in reference (2,b) of this chapter and in figures 9 and 11 of the "drag due to lift" chapter.

Wing-Tip Drag. It is mentioned on page 6-4, that rounded or sharp lateral edges of a rectangular wing somewhat reduce the sectional drag (at or near zero lift). Figure 27 presents the distribution of parasitic drag as found in the wake of three different tip shapes. Assuming that the sectional drag should correspond to wetted surface or local chord of the wing tip (as indicated in the illustration), certain positive and negative differentials are found. After integrating them, negative values are found in two of the shapes tested, for the drag coefficient $C_{Dc} = D/q c^2$, defined for a pair of wing tips. This result must be explained on the basis of reduced super-velocities past the round and the tapered wing-tip edge, making frictional and pressure drag smaller than in two-dimensional condition.

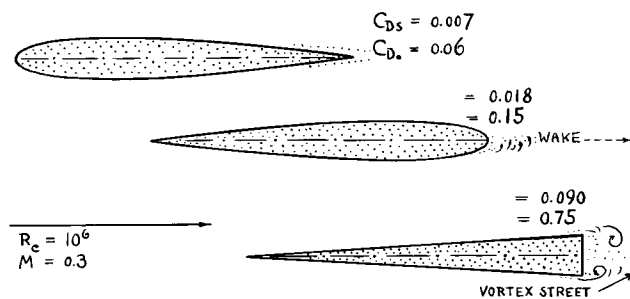


Figure 28. Drag of 0012 airfoil section and of a wedge tested at zero lift between tunnel walls by wake survey (28).

Reversed Flow. Streamline shapes are designed, of course, to be used in their "natural" direction of motion. There may be occasions, however, as mentioned on page 6-13 (in connection with figure 19), where the direction is reversed. Figure 28 presents the drag coefficient (between walls) of a 0012 section at zero lift, tested in both directions. With the round edge trailing, the section drag is more than doubled in comparison to that in the direction of common application. The round trailing end still has an appreciable "streamlining" effect, however. This result is realized when inspecting the wedge shape in figure 28, having a drag coefficient which is ≈ 5 times that of the reversed 0012 section.

CHAPTER VII — DRAG DUE TO LIFT

"Drag due to lift" is meant to indicate components of resistance directly and necessarily associated with the generation of lift — in airplane wings as well as also in bodies such as fuselages, airships, or even automobiles, for example. Predominantly, drag due to lift is *induced drag* and its many variants. The name "induced" refers to the similarity of the fluid-dynamic flow pattern with that of the magnetic field "induced" by electric conductors (1,a). The induced velocities are an essential part of the vortex system left behind the wing; they are the means through which momentum is transferred from the flying wing onto the fluid.

Integral with this vortex system is a permanent downward deflection of the affected stream of air. Upon approaching and meeting the ground, the induced momentum may theoretically again be taken out of this stream and be transferred onto the earth in the form of pressure. In this way an airplane can thus be considered as being supported from the ground. There can also be more than one pair of rolled-up vortices, so for example behind biplanes, cruciform-type wings and in other configurations such as that of a horizontal tail with a fuselage, for instance. Physical pictures of tip vortices are found in (3); see also figures 7 and 8.

1. INDUCED DRAG AND ASPECT RATIO

Basically, lift is produced by deflecting a certain stream of fluid downward from its undisturbed direction. For infinite span, the affected volume of fluid (being proportional to the square of the wing span) is infinite too. For uniform lift distribution, the final or remaining deflection angle and the induced drag are zero accordingly. Considering, however, the limited span of actual wings, induced drag is a price that has to be paid for obtaining the lift needed to support the weight of an airplane.

Lifting Line Theory. Because of the pressure difference between lower and upper side of a lifting wing, a certain flow is started around the wing tips, so to speak. Theory (2) replaces the structure of the wing by a "bound" straight vortex or "lifting line", the circulation of which is of the same magnitude as that of the physical wing. Because of the decrease of circulation toward the wing tips, "trailing" vortices originate along the lifting line. As illustrated in figure 1, a vortex sheet with a more or less constant downwash velocity " w ", leaves the trailing edge of the wing (part "a" of the illustration). Shortly after leaving, however, this vortex sheet transforms itself (it "rolls up") into a pair of tip vortices (b), downwash distribution and flow pattern of which are shown in parts (c) and (d) of figure 1. The circulation in these vortices is the continuation of that in the center of the lifting line.

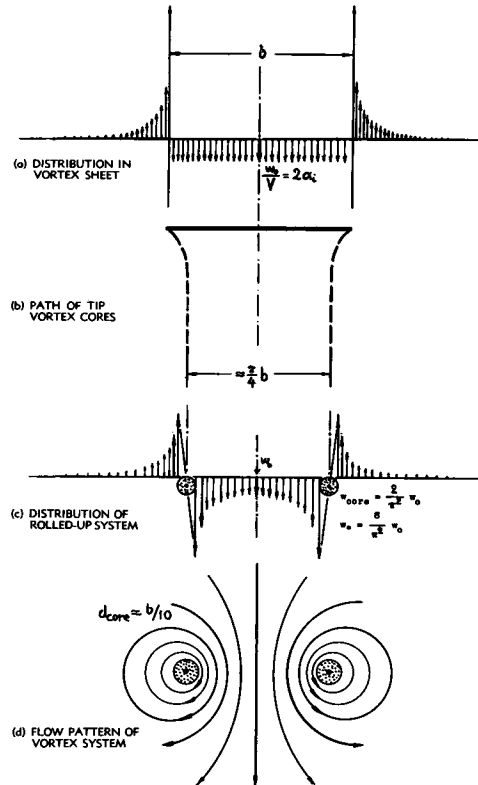


Figure 1. Flow pattern and downwash distribution behind lifting line and/or wings (2 and 3).

Downwash Angle. Theory indicates that the optimum lift distribution over the span of a wing, providing maximum lift for a given angle of attack and minimum induced drag for a given value of lift, is elliptical. The equivalent stream of air deflected by such a wing is that within a cylinder having a diameter equal to the wing span b . Applying now the principle of "force equal to mass times added velocity" to that cylinder of fluid, the fluid-dynamic force is found to be

$$(L \text{ or } F) = q (\pi/4) b^2 V w \quad (1)$$

with w indicating the "vertical" downwash velocity at some distance behind the wing. The average downwash angle is accordingly

$$w/V = 2 C_L / \pi A = 2 \alpha_i \quad (2)$$

where $C_L = L/qS$ = lift coefficient, and $A = b^2/S$ = aspect ratio of the wing considered.

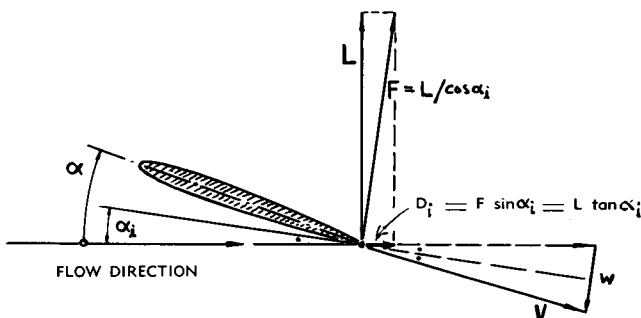


Figure 2. Induced drag, a component of "lift" force.

Induced Angle (2). At the location of lifting line or wing, the flow is deflected by an average angle which is half the final theoretical downwash angle. That angle is the induced angle of attack. As illustrated in figure 2, the force "F" originating in a direction normal to the average direction of the flow in the vicinity of the wing, is therefore tilted backward by the induced angle

$$\alpha_i \approx \tan \alpha_i = C_L / \pi A \quad (3)$$

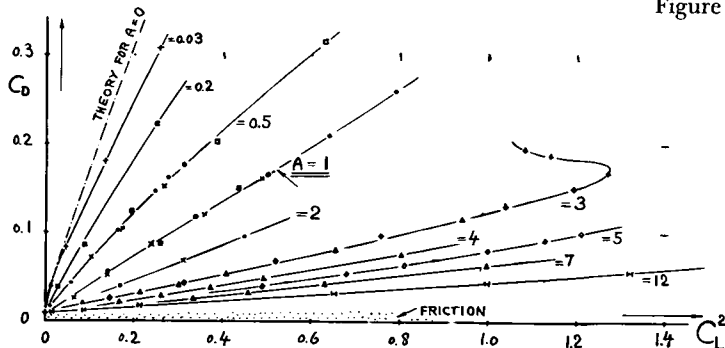


Figure 3. Drag coefficient of various wings (profiled except for 2 small AR plates) as a function of the square of their lift coefficient.

+	WINTER	FLAT PLATE	(36,a)
■	A V A	FLAT PLATE	(4,a)
●	WINTER	$A = .5, = 1, = 2$	(36,b)
□	NACA	CLARK-Y WING	(36,b)
×	A V A	$A = .5, = 1, = 2$	(36,c)
◆	A = 3	B R U N S W I C K	(7,b)
△	A V A	$A = 3 = 4 = 5 = 7$	(4,a)
▣	NACA	TAPERED WING	(4,b)
◊	D V L	RECTANGLE	(4,d)

VII—DRAG DUE TO LIFT

a theoretical function (representing the *induced drag angle*) is obtained, against which experimental results can conveniently be checked. Among the hundreds of such results available from various sources, some more systematic examples are shown in figure 3. By plotting the drag coefficient against the square of the lift coefficient, rather than as a function of this coefficient as such (1,c), the quadratic nature of the induced drag is conveniently demonstrated. At $C_L \rightarrow 0$, a basic profile-drag coefficient is found (in the order of 0.01 or less). In aspect ratios larger than 3, agreement with equation 7 is comparatively close. The straight functions discontinue at higher lift coefficients because of progressive flow separation upon approaching maximum lift coefficient. The limitation is shown in the graph for one aspect ratio ($A = 3$). Plotting now in figure 4, the slopes dC_D/dC_L^2 against $(1/A)$, agreement with theory is found, down to aspect ratios in the order of 1 — if taking the slopes near $C_L^2 \rightarrow 0$. Generally, however, the experimental values are above the theoretical function. An appreciable part of the increment (in the order of 0.01 or even higher) represents the growth of the profile drag against the lift coefficient. The fact that round-ended wings have higher drag due to lift ratios than wings with sharp lateral edges, is discussed later.

In Flat Plates — the theoretically expected suction force near the leading edge of the upper or suction side, cannot develop. Therefore, the pressure force "F" is normal to the plate surface, and the

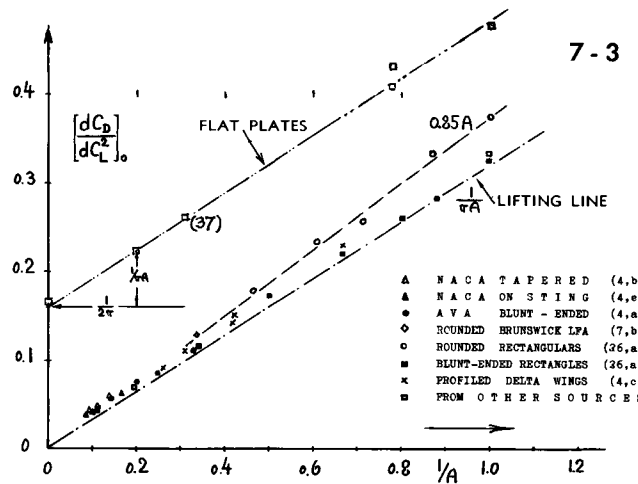


Figure 4. Drag due to lift of various series of wings as a function of $1/(A)$.

drag due to lift is simply a component of the normal force; thus

$$C_{DL} = C_N \cdot \sin\alpha = C_L \tan\alpha$$

The increment of this drag over the induced drag (equation 4) is viscous drag, essentially corresponding to reattaching flow separation behind the sharp leading edge. Assuming now that the lift is still approximately the same as in a profiled wing, the drag due to lift of flat plates is theoretically

$$dC_{DL}/dC_L^2 = d\alpha/dC_L \approx 1/(2\pi) + 1/(\pi A)$$

This drag ratio (included in figure 4) is by $0.5/\pi$ higher than the induced drag.

(I) Historical notes concerning lift and drag:

- a) Glauert says in (2,c): "A line vortex is analogous to a wire carrying an electric current, the strength of the vortex corresponds to the strength of the current, and the induced velocity at any point of the fluid corresponds to the magnetic force due to the electric current".
- b) Account of Lanchester's work by Prandtl in "Generation of Vortices", Paper RAS London 1927.
- c) The polar diagram (C_D against C_L) was introduced by Lilienthal in "Der Vogelflug", 1889.
- (2) On general wing theory:
 - a) Prandtl's Wing Theory, Nachrichten Königl. Gesellschaft der Wi'schaften 1918, 451 and 1919, 107.
 - b) Glauert, "Aerofoil and Airscrew Theory", 1926.
- (3) About rolled-up, trailing tip vortices:
 - a) Bird, Visualization, JAeron'l Sci. 1952 p.481.
 - b) See references (7,b) and (7,d).
 - c) Kraft, Flight Tests, NACA Technical Note 3377.
 - d) Betz, Vortex Systems, ZaMM 1932 p.164.
 - e) Behind swept wings see reference (38,f).
 - f) Kaden, Rolling-Up Analysis, Ing-Archiv 1931, 140.
- (4) Results on drag due to lift and aspect ratio:
 - a) Ergebnisse AVA Göttingen Vol. I (1921).
 - b) Anderson, Experimental and Calculated Characteristics of 22 Tapered Wings, NACA T.Rpt 627.
 - c) Results on Delta Wings, ARC RM 2871.
 - d) DVL, Tunnel Results, ZWB FB 548 and 914.
 - e) NACA, Models at High Speed, Tech Rpt 877.

2. EFFECT OF SHAPE ON INDUCED DRAG

Equations 3 to 7 correspond to elliptical distribution of lift over span of plain monoplane wings placed in an infinite stream of fluid. Any deviation from the elliptical distribution results in a certain increase of the average or effective induced angle of attack. There are also other effects of wing shape (sweep, dihedral) that make the induced drag larger. Various effects of this nature are treated in this section.

Effective Aspect Ratio. The plan forms of airplane wings are rarely elliptical. Also the lift distribution is usually disturbed in airplanes through the addition of fuselage, engine nacelles or other parts. In such conditions, equation 4 can still be applied, however, if using an appropriate correction factor:

$$C_{DL} = (1+k) \frac{C_L^2}{\pi A} = K \frac{C_L^2}{\pi A} = \frac{C_L^2}{\pi e A} \quad (10)$$

As will be described in the subsequent sections, there are certain increments of the induced drag which can be predicted theoretically. Others are known on a statistical basis. Instead of saying now, that the induced drag is so and so much higher than indicated by equation 4, it is in some cases more convenient to say that the effective aspect ratio " $A_t = eA$ ", to be used in that equation, be smaller by a corresponding fraction than the geometrical value. The connection between the two approaches is evidently given by

$$K = 1 + k = A/A_t = 1/e \quad (11)$$

In performance analysis, equation 10 defines the so-called "e" method (see in the "aircraft" chapter) used in correlating the drag due to lift of a complete airplane configuration with the theoretical minimum. In biplanes, the factor "e" is identical to the "span factor" ($e > 1$), indicating their effective span (26,b).

(a) Plan Form and Wing Tip Shape

Lift Distribution. Correction factors have been calculated for rectangular (2,c) and tapered (5) wing plan forms. These factors roughly increase in proportion to the aspect ratio. For tapered (or trapezoidal) shapes, figure 5 has been prepared accordingly, presenting the term " k/A ". The value $k = A(k/A)$ is to be used in the equation

$$C_{D_i} = (1 + k) C_L^2 / \pi A \quad (11)$$

The plan-form-correction represents an induced-drag component which is approximately independent of the aspect ratio. For example, in a rectangular plan form $\Delta(dC_{D_i}/dC_L^2) = k/\pi \approx 0.003$. For taper ratios between 0.3 and 0.4, the additional drag is very small, in the order of 1 or 2% in aspect ratios commonly employed in airplanes. Appreciable increments are indicated only in plan forms that are either extremely tapered or close to the rectangular shape. The theoretical results (figure 5) are appreciably modified, however, by a tip effect to be described later.

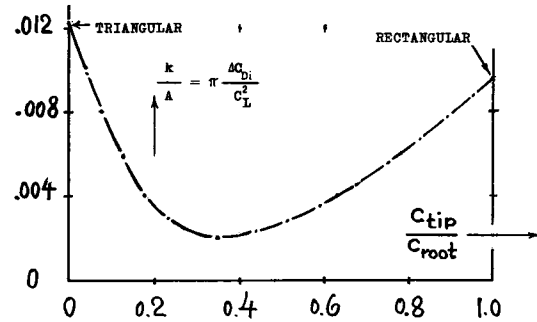


Figure 5. Additional induced drag of tapered wings.

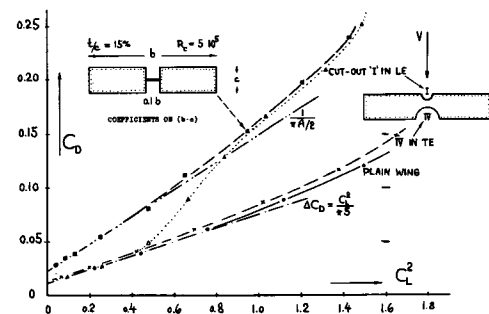


Figure 6. Influence of certain cut-outs in the center of a wing upon drag due to lift (6,a,b).

Cutouts. Figure 6 shows the drag-due-to-lift function of a rectangular wing without and with certain cutouts in its center. Only little drag is added by a cutout in the trailing edge. A (smaller) cutout in the leading edge produces a similar effect up to $C_L \approx 0.65$. At higher lift coefficients, the flow evidently separates behind the gap in the leading edge (6,c). The wing then exhibits essentially the same drag as though the center part was cut out entirely; the drag is roughly doubled in this case. Changes (or sometimes disruptions) of the lift distribution similar to those illustrated in figure 6, can also be produced by fuselages, engine nacelles or other components attached to a wing. Examples of the corresponding additional drag due to lift are presented in the "interference" chapter. Fuselage interference of this type, or cut-outs in the trailing edge of the wing roots, can be favorable, however, with respect to longitudinal stability (by way of downwash).

Tip Vortices. In low aspect-ratio wings, the lateral edges have an important influence upon lift and drag (as described later). A similar but smaller effect of wing tip shape is also found in other aspect ratios. Wing theory assumes that the vortex sheet leaving the "trailing edge" would keep its original distribution of downwash (as in figure 1,a) and would have a span equal to that of the wing. In reality the vortex sheet starts rolling up into the pair of "tip vortices" (figure 1,b,c) as soon as any pressure gradient has developed between lower and upper wing side. Usually, this is near the leading (rather than near the trailing) edge, as illustrated in figure 7. The flow component coming from the lower side combines with the stream along the upper side of the wing tip, thus forming a sharply defined tip vortex. There is sometimes confusion between the pair of rolled-up vortices and those which form the mentioned sheet along the wing span. The latter ones have been called "roller bearings" (2,c), imbedded in the discontinuity between upper-side and lower-side flow. They are not distinct or individual vortices; surveying the space behind the trailing edge of a wing, rather a spanwise sheer flow is found along both sides of the sheet representing the sum of the trailing-vortex circula-

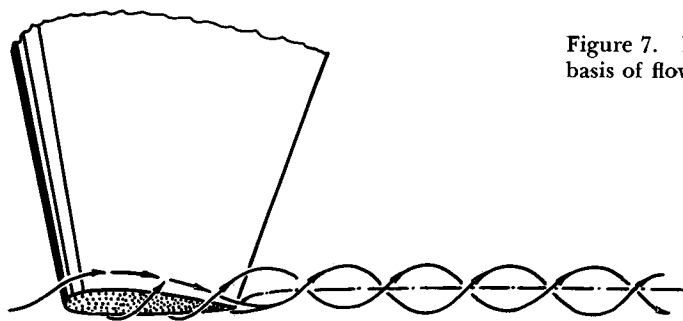


Figure 7. Flow pattern past a wing tip, drawn on the basis of flow observations in a water tunnel (7,a).

tion. In the rolling-up process, this circulation is transferred onto the pair of tip vortices (figure 8). Together with the circulation, the viscous wake (imbedded in the trailing sheet) may also be rolled up into the tip vortices thus filling their cores. The effect that the tip vortices have upon lift and induced drag, is not considered in common lifting-line theory (equation 4) and in applications such as in figure 5. Certain experimental results in larger aspect ratios can be explained, however, by considering the rolling-up process.

Flow Around Tips. As a consequence of "rolling-up", the flow can actually get around the lateral edges of a wing to a certain extent, as shown in figure 8. The effective span is, therefore, shorter than the geometrical span. In other words, a "condition" is theoretically assumed to be fulfilled at the wing tips, similar to the so-called Kutta-Joukowsky condition at the trailing edge of wing sections, to

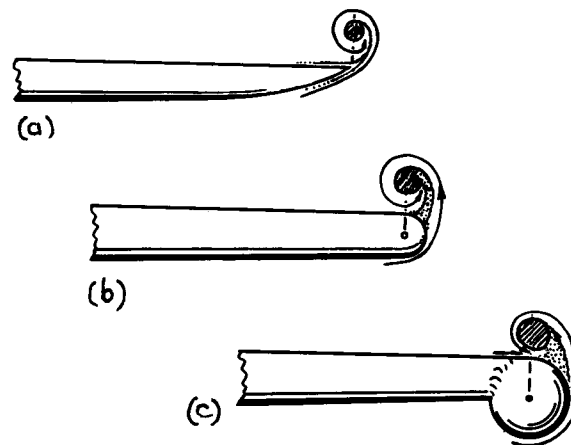


Figure 8. Location of the vortex core in relation to the wing tip; (a) with sharp lateral edge, (b) on wing with round edge, (c) flow around wing-tip tank.

the effect that no flow takes place around the lateral edges. In reality, there is some such flow; and the reduction of effective span as mentioned above, is a function of the wing-tip shape. A series of shapes has, therefore, been investigated on a basically rectangular wing (7,b). Figure 9 presents the plan-form location of the tip-vortex cores. Shapes with sharp lateral edges (numbers 1, 5 and 6) are seen to give the widest effective spans, while rounded edges result in a loss of effective span or aspect ratio.

Figure 9. Wing-tip shape and tip-vortex location of a family of wings (7,b) tested at $A = 3$ and $R_c = 10^6$.

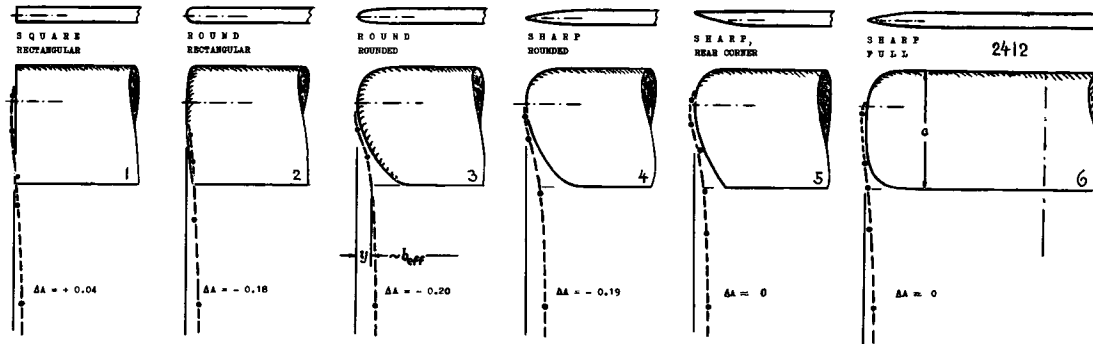


Figure 10 presents lift and drag characteristics for three representatives of the same family of wings. It is seen that the shapes having the widest vortex spans, are generally the ones exhibiting the least drag due to lift.

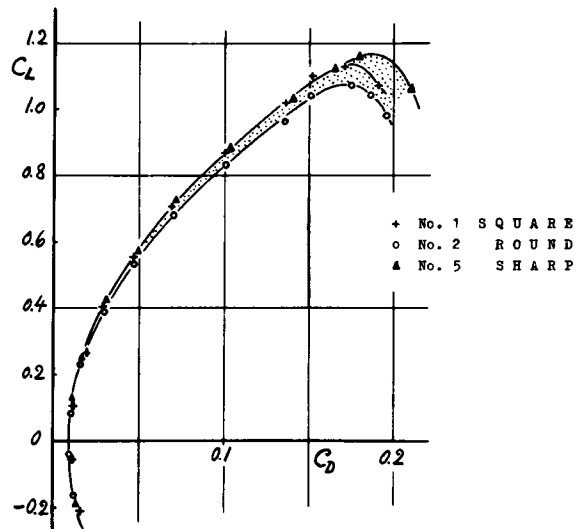


Figure 10. Lift and drag characteristics of 3 of the wings in figure 9; having $A = 3$; tested at $R_c = 10^6$.

Plan Form. Theory predicts minimum induced drag for elliptical lift distribution across the span, which means for un-twisted elliptical plan form. Figure 11 demonstrates, however, directly in one case (number "a" against "c") that a rectangular wing (with sharp lateral edges) does not have a higher drag due to lift than the elliptical wing — while theoretically the rectangular one should have a lift angle higher than that of the elliptical plan form by 0.5° , and a drag function higher by 0.003. The effective aspect ratios of the shapes investigated have been evaluated by comparing their induced angle functions with those as indicated by lifting line theory (equation 4). The differentials " ΔA " thus obtained are believed to apply to all aspect ratios higher than 2. It is seen that the most effective plan forms are the rectangular, the moderately tapered ones and those which have a long trailing edge. The "cut away" shapes, on the other hand, such as "3", "4", "III", and again the elliptical wings (particularly "II") are less effective. In other words, to make the span of the rolled-up vortex system, or the effective span of a wing of given basic shape, as wide as possible, it is favorable to keep the tip vortices apart from each other as far downstream as possible.

Sweep. Another influence found in the tabulation (figure 11) is an angle-of-sweep effect. (a) In distinction from wing "II", the elliptical form "c" has a straight 0.25 chord axis, meaning some negative effective angle of sweep. (b) On the other hand,

WING SHAPE	A	$\frac{d\alpha^o}{dC_L}$	$\frac{dC_D}{dC_L}$	ΔA_i	R_c
1	3.0	18.6	0.123	+ .04	$1 \cdot 10^6$
2	3.0	19.6	.133	- .18	LFA
5	3.0	18.6	.124	≈ 0	2412
4	3.0	19.2	.131	- .19	REF.
3	3.0	19.6	.131	- .20	(7,b)
1	5.0	14.4	0.067	≈ 0	$5 \cdot 10^5$
IV	6.4	13.8	.051	- .03	AVA
II	5.2	14.5	.063	- .04	GÖ
II	5.2	14.2	.060	+ .03	REF.
IV	6.4	13.4	.050	≈ 0	(9,a)
a	5.0	14.5	0.071	≈ 0	$2 \cdot 10^6$
b	5.1	14.5	.073	- .20	REF.
c	5.0	14.5	.071	≈ 0	(9,b)

Figure 11. Aerodynamic performance of 3 families of wings as a function of plan-form and wing-tip shape.

shape "IV" in figure 11 has some positive angle of sweep built into the wing tips. (c) A third piece of evidence is seen in figure 13, where minimum induced drag is found at some 5° positive angle of sweep. (d) Finally, characteristics of profiled "delta" wings are quoted (having straight trailing edges). Theory (figure 5) predicts that their induced drag would be appreciably higher than that for elliptical loading. Some experimental points in figure 4 show, however, that such wings (if tested at higher Reynolds numbers) have induced drag characteristics that are as favorable as those of other common wing plan forms. — In conclusion, a straight trailing edge appears to be desirable with regard to induced drag. The rear plan-form corners again appear to be important for the effective aspect ratio.

Optimum Wing Shape. The results of the "1" to "5" series of wings in figure 11 correlate with the vortex span in figure 9 as well as with the force data in figure 10 — if taking into account both the plan-form influence and the lateral-edge effect. In case of number "5", which is the most favorable one concerning small drag due to lift as well as to minimum sectional drag, it appears that one additional effect is the bent-up shape. Experimental data in (7,c), on a small-aspect-ratio wing, confirm that this feature is important; and it is suggested that some small "end-plate" effect may be involved in this result. Combination of shape "5" with a moderately tapered plan form is believed to be most effective.

(7,d); and there are a few airplanes that have this type of wing shape. In conclusion, the shape of the tips can be more important for the performance of an airplane than the plan form of the wing.

Wing-Tip Tanks. Some wind-tunnel investigations have been published (8) regarding the influence of a pair of external tanks attached to the wing tips as in figure 12. Two effects are evidently involved in this configuration; (a) span and area of the wing are usually increased after adding the tanks; and (b) the tanks may have an effect similar to end plates (characteristics of which are discussed later). Most results correspondingly show an increase in lift-curve slope after adding the tanks; and some of the tests also show a decrease of the drag due to lift. Estimating the influence of round tanks, the fact must be taken into account that the flow passes around their outer sides. As suggested in (8,c), only half of their diameter can thus be considered to be effective as end plates. Using equation 18, the increment of effective aspect ratio due to end-plate effect may, therefore, be $\Delta A/A = +d/b$. It may further be assumed that half of the tank diameter, at each wing tip, is ineffective with respect to the aerodynamic span of the configuration considered. The corresponding reduction in effective aspect ratio is $\Delta A/A = -d/b$. In a configuration where the tanks are attached in a manner so that the wing span is not increased, the two components cancel each other. However, in configurations where the tanks increase the span, the net increment of effective aspect ratio is tentatively

$$\Delta A/A = +0.5 (\Delta b/b) \quad (12)$$

where $(\Delta b)_{\max} = 2 d$ = two tank diameters. The induced drag can be expected to be decreased correspondingly. There may be a parasitic drag component, however, due to interference (with or without flow separation) in the corners between tanks and wing tips — which (increasing with lift) would reduce the favorable effect indicated by the last equation.

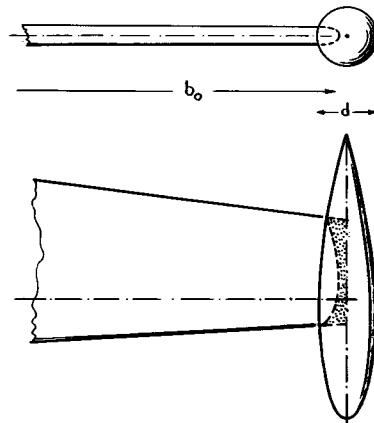


Figure 12. Example of external tank at wing tip.

(b) Twist and Related Effects

Wing Twist. To prevent stalling, the tips of airplane wings are sometimes twisted against the wing roots so that their angle of attack is reduced. Such twisting changes the lift distribution, particularly in the range of low lift coefficients. As indicated in (10), the additional induced drag in wings with nearly elliptical loading is approximately

$$\Delta C_{D_i} = 4 (\Delta \alpha^{\circ})^2 / 10^5 \quad (13)$$

where $\Delta \alpha$ = difference in angle of attack of the wing tips against the center part. A positive component of lift exists in this case in the center of the wing; corresponding negative components are found near the wing tips. The wing thus leaves behind the combined vortex system of one "positive" and two "negative" wings — so to speak. The resulting induced drag is appreciable, even though the total lift of this wing can be zero. For example, an angle of twist $\Delta \alpha = 5^{\circ}$ is expected to reduce the maximum speed of a fighter airplane (which may be 500 knots) by some 10 knots. — Near $C_L = 0$, equation 13 is also applicable to wings with non-elliptic plan form. In rectangular plan forms, at intermediate and higher lift coefficients, the distribution across the span is expected, however, to change in the direction toward elliptical, when twisting the wing tips to more negative angles of attack. At a certain lift coefficient, the induced drag of a twisted rectangular wing will, therefore, have an optimum value.

- (8) Influence of wing-tip tanks on characteristics:
 - a) NACA, Straight and Swept, RM L9J04 + A50K15.
 - b) ARC, On Swept Wing, Current Paper 196 (1954).
 - c) Hartley, Theoretical Load, ARC C.Paper 147.
 - d) RAE, Drop Tanks, ARC RM 2951 (1952).
- (9) Influence of wing plan form:
 - a) AVA Göttingen, Ergebnisse Vol.I (1921).
 - b) Doetsch, Tests of 3 wings, Yearbk D.Lufo 1940.
- (10) Induced drag caused by wing twist:
 - a) Journal Aeronautical Sciences 1936 p.273.
 - b) Hueber, Zeitschr. Flugt. Motorluft. 1933 p.307.
 - c) Lock, About Wing Washout, ARC RM 1769.
- (11) Pearson and Anderson, Characteristics of Wings with Partial Span Flaps, NACA T.Rpt 665 (1939).

Wing Flaps. The variation of the induced drag due to deflection of partial-span landing flaps, is of practical importance in the calculation of take-off, climb and gliding performance of airplanes. The induced drag of such wings is made up of three components:

$$C_{D_i} = C_L^2 / (\pi A) + "v" C_L \Delta C_L + "w" (\Delta C_L^2)$$

with $\Delta C_L = (d\alpha/d\delta) \delta (dC_L/d\alpha)$ indicating the two-dimensional increment of the lift coefficient in those wing parts that are equipped with flaps (δ = flap angle). The first term of the equation represents the basic induced drag, the third term corresponds to the twist equation 13. Numerical values for "v" and "w" are presented in (11), as a function of flap-span ratio and taper ratio of the wing. To give some idea on the magnitude of the additional drag, average and approximate values may be quoted for the various constants involved. Thus assuming for $d\alpha/d\delta$ the value 0.5, and for $dC_L/d\alpha$ the value of 0.1, the induced drag coefficient is found to be in the order of

$$C_{D_i} = C_L^2 / (\pi A) + k_1 C_L (\delta^\circ) + k_2 (\delta^\circ)^2$$

In rectangular or tapered wings, having conventional airplane aspect ratios, the factor k_2 (indicating the twist effect) varies only slightly for flap-span ratios between 0.30 and 0.55; $k_2 \approx 2.3/10^6$. The factor k_1 (indicating a variation of the lift distribution along the span), is a function of the plan form. Representative values of k_1 are included in the tabulation in the next paragraph. This factor is positive for triangular wing shapes (having zero taper ratio); this means that upon deflecting inboard landing flaps the concentration of lift in the center part is furthermore increased in such wings. The factor is negative, on the other hand, for rectangular forms; their lift distribution is brought nearer the elliptical optimum, by deflecting the flaps.

Flaps in Taking Off and Climbing. The induced drag due to flap deflection has a practical bearing upon take-off and climb performance of airplanes. At a lift coefficient of $C_L = 1$, for example, increments of induced drag over the basic drag, are found listed as follows, caused by 10° deflection of a pair of flaps at or near the center of a wing with $A \approx 7$:

for wing shape:	k_1	due to k_1	due to k_2	total
triangular (max. taper) optimum tapered wing	$+5/10^4$	+11%	+ 5%	+16%
zero	0	0 %	+ 5%	+ 5%
rectangular plan form	$-3/10^4$	- 9%	+ 5%	- 4%

The result agrees generally with flight-test experience. Only a comparatively small deflection of partial-span landing flaps can be found favorable during climb in airplanes having tapered wings. Rectangular wings, however, show some increase of their lift/drag ratio at somewhat larger flap angles.

(c) The Form of the Lifting Line

Angle of Sweep. Swept wings (or certain other wing shapes) can have the same induced drag as straight wings of the same aspect ratio — provided that the lift distribution is the same. The distribution across the span of a given wing shape varies, however, with the angle of sweep. In swept-back wings lift is more concentrated near the wing tips. Such concentration can theoretically be eliminated by decreasing the taper ratio. As indicated in (12,f), a ratio $c_{tip}/c_{root} = 0.15$ is needed, for example, to make the lift distribution of a wing having 30° sweepback, near-elliptical. In conventional airplanes, such shape would be extremely hazardous with regard to wing-tip stalling. Realistic swept back wings, therefore, do not have a distribution which would be approximately elliptical, and their induced drag is accordingly somewhat higher than indicated by equation 4. This is not the whole story of the swept wing, however. In a wing, swept back in the plane of the foil sections, the tips drop below the center part, as the angle of attack is increased to positive values. The wing assumes in this way an inverted "V" shape; and the "lift" forces in each panel are more and more tilted backward. As a consequence, the drag due to lift (dC_D/dC_L^2) is appreciably increased. Experimental characteristics from various sources have been evaluated in comparison to similar but straight wings. By plotting the results in the form as in figure 13, a cosine function of the sweep angle is found:

$$dC_L^2/dC_D \sim \cos \Lambda ; \quad dC_D/dC_L^2 \sim 1/\cos \Lambda \quad (16)$$

The origin of this function is shifted, however, at least by 5° , into the range of positive sweep angles.

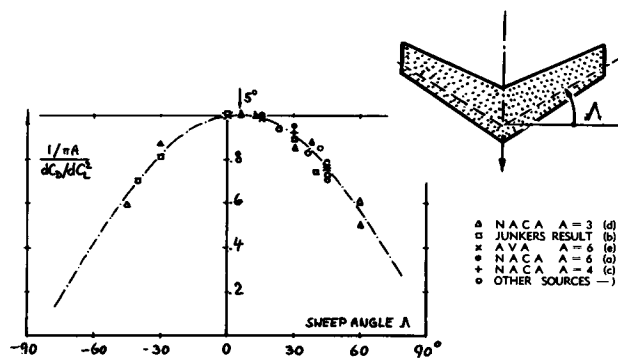


Figure 13. Function indicating the induced drag of swept wings (12), all tested at $R_e \approx 10^6$.

Negative Sweep. Swept-forward wings are rarely considered or applied in the design of airplanes, because of certain unfavorable characteristics in the lateral moments. Theoretically, their lift distribution can nearly be made elliptical by increasing the chord in the outboard portions. As demonstrated in figure 13, their drag due to lift increases with the angle of sweep by the same reasons as outlined in the preceding paragraph. It must be said, however, that swept wings can be designed in which the "V" shape effect is avoided for a certain value of the lift coefficient (by giving them a compensating positive angle of dihedral).

Dihedral. As pointed out in (13,a), when raising the tips of a straight wing to a V-shape position, each wing panel approximately maintains induced characteristics, in the direction normal to the panel, equal to those of a complete straight wing having twice the span of one panel. With reference to the "lift" force normal to each panel (denoted by C_N), the V-shaped wing, therefore, exhibits an induced drag corresponding to equation 4 (if assuming elliptical distribution). The lift of such wing (in vertical direction) is smaller, however, than the sum of the normal forces ($L = N \cos\Gamma$), while the induced (and the parasitic) drag remains unchanged. Expressed in form of coefficients, based upon the panel or developed wing area, therefore

$$C_{D_i} = C_L^2 / (\pi A_s \cos^2 \Gamma) \quad (17)$$

with A_s = developed aspect ratio (from panel dimensions). Upon turning the two panels up, the span between the wing tips is evidently decreased, the effective aspect ratio reduces accordingly and the induced drag function is increased. However, considering a family of dihedraled wings in which the

span between the tips is kept constant, the induced drag function is approximately constant as per equation 4. Results of a more detailed analysis (13,b) are plotted in figure 14. The induced drag is somewhat lower than indicated by the panel approach (13,a); and we may say that "V" shape includes a small effect similar to that of end plates. It appears that equation 17 or 4 should be reduced by $\sqrt{(\cos\Gamma)}$ to approximate the result in figure 14.

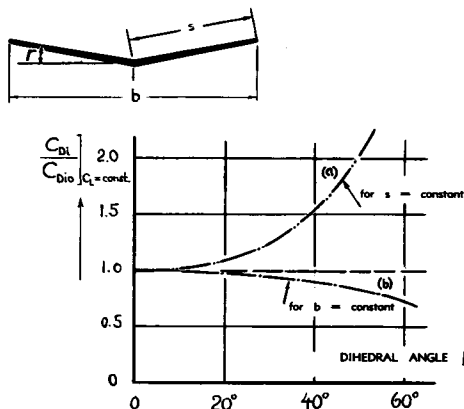


Figure 14. Influence of dihedral on the induced drag; (a) with constant panels, and (b) with $b = \text{constant}$.

"V" Shape Applications. Considering the moderately large dihedral angles applied in airplane wings, the effect upon drag is comparatively small. For an angle of $\Gamma = 6^\circ$ (possibly used in common airplanes), the induced drag increment (in the definition as for equation 17) is in the order of 1%. V-shaped surfaces have also been applied in place of the common tail assembly, combining in their two panels the functions of both the horizontal and vertical tail surfaces. This combination amplifies the complexity of the control characteristics, however. The "V" tail also induces a torsional moment in the fuselage larger than that caused by any ordinary vertical surface.

- (12) Characteristics of swept wings:
 - a) NACA, T.Rpt 627; same as reference (4,b).
 - b) Junkers Results, Rpts S.1943/91 and D.43/46.
 - c) Letko and Goodman, NACA Tech Note 1046.
 - d) Purser-Spearman, Tests, NACA Tech Note 2445.
 - e) Hubert, Yearbk D.Lufo 1937 p.129.
 - f) DeYoung and Harper, Theoretical Span Loading for Arbitrary Plan Form, NACA T.Rpt 921 (1948).
 - g) NACA, Tech Rpt 572 and T. Notes 1093 & 2468.
 - h) Brebner, "Cranked" Wings, ARC RM 2947 (1955).
 - i) ARC, Tests on 45° Swept Wings, RM 2710 (1953).
- (13) On wings having dihedral or V-shape:
 - a) Purser and Campbell, Verification of Vee-Tail Theory and Analysis, NACA Tech Rpt 823 (1945).
 - b) Dätwyler, Mitg Aerodynamik Inst. Zürich, 1934.
- (14) Available theoretical results on end plates:
 - a) Ergebnisse AVA Göttingen Vol.III (1927) p.18.
 - b) Mangler, Analysis, Lufo 1937 p.564 (Transl NACA T.Memo 856), and Lufo 1939 p.219.
 - c) CAHI (Moscow) Technical Report No. 58.
 - d) Rotta, Aerodynamic Characteristics of Wing With End Plate at One Tip, Ingenieur Archiv 1942 p.119.

(d) Influence of End Plates

Adding end plates to a wing (see sketch in figure 15) increases the cross section of the effective cylinder of streaming air deflected by the wing. Less downwash and smaller induced angles of attack are then sufficient in producing a certain lift coefficient.

Height Ratio. Theory (14) considers a lifting line with elliptical loading which is bent up at both ends. The induced drag decreases, and/or the effective aspect ratio increases as a function of the height

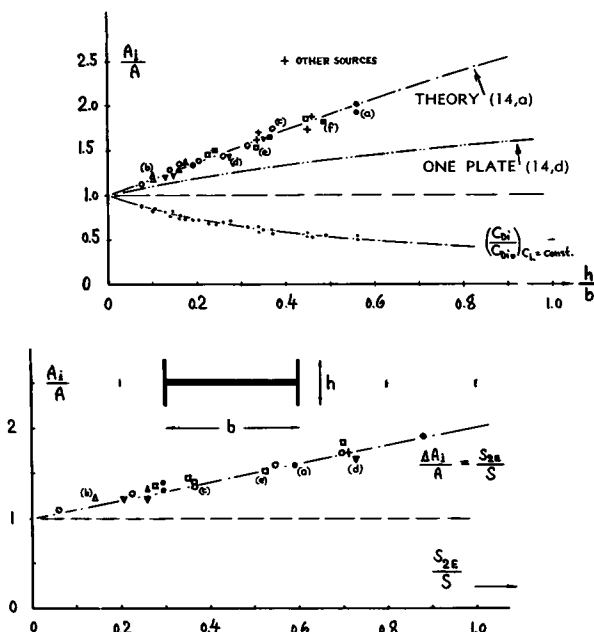


Figure 15. Effective aspect ratio of wings with end plates (15); (a) as a function of height ratio (h/b); and (b) as a function of area ratio (S_{2E}/S).

ratio h/b , as shown in figure 15,a. The effect can be approximated by

$$\Delta A_i/A = k h/b \quad (18)$$

where k is equal to ≈ 1.9 . The effect is rather indifferent as to the particular location and position of the plates, as shown in (15,h). Within reasonable limits, it thus seems to be unimportant, whether the plates are moved up or down in relation to the plane of the wing, or placed nearer to leading or trailing edge of the foil section, or arranged in vertical or laterally somewhat inclined position. Twisting, however, the upper halves of a pair of plates against the lower halves has an effect upon the induced characteristics (15,g).

Area Ratio. Experiments with a family of end-plate shapes (15,c) show that their effect increases somehow as a function of the chordwise dimension. In a way, such plates can be considered as "fences", making it difficult for the flow to get around the wing tips. Accordingly, a longer fence is more effective than a shorter one having the same height. Figure 15,b presents essentially the same experimental data as plotted in part a of the illustration, this time as a function of the area ratio S_{2E}/S , with S_{2E} denoting the sum of the areas of the two end plates. Correlation is found in this manner according to

$$\Delta A_i/A = k S_{2E}/S \quad (19)$$

where k is equal to ≈ 1.1 . Examination of experimental sources reveals, however, that any end-plate area exceeding the wing-chord length, does not contribute much. No such results are in figure 15.

Viscous Drag. The end plates have some profile drag, of course, and some interference drag originating at their junctures with wing or wing tips. On the basis of $C_{DS} = 0.008$, and using the information on the drag of "corners" in the "interference" chapter, the viscous drag, referred to the wing area S , is found to be approximately

$$C_{DS} = 0.008 (S_E/S) + 0.004/A \quad (20)$$

The equation shows that the viscous influence grows as the geometrical aspect ratio of the wing is decreased. Basically, the end plates have at least the drag of a pair of added wing-tip extensions (having the same area). Any such added area naturally produces more lift for the same price of viscous drag. Practical application of end plates in airplanes and/or guided missiles, therefore, seems to be restricted to such designs where the plates can also be utilized for stabilizing or control purposes (16). Even then, improved characteristics predominate in an increase of the lift curve slope in these applications, rather than in the induced drag.

Inboard Plates. Plates have also been investigated in positions inboard the wing tips. Figure 16 presents results of a theoretical analysis (14,b). The effect of the plates decreases upon moving them away from the tips. By reasons of symmetry, their effect reduces theoretically to zero upon approaching the center of the wing. An additional "parasitic" effect in such configurations is shown in the next paragraph.

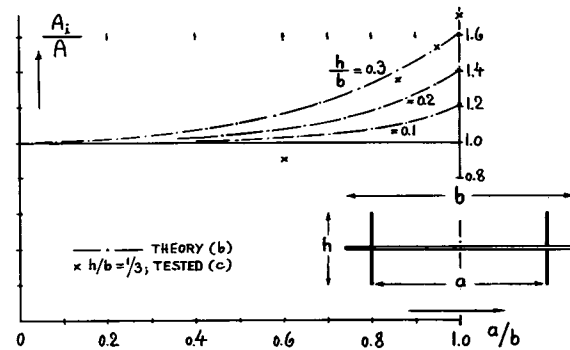


Figure 16. Influence of inboard end plates on the effective aspect ratio of wings (14).

Single End Plates, placed at only one wing tip (14,d), have an effect which is somewhat smaller than half of that of a pair of plates; see in figure 15,a. A practical example of such an arrangement is the vertical tail surface of an airplane with the horizontal surface placed on top (16,b). Figure 17 presents some experimental results on such a configuration. With the plate near the top (or near the bottom), the effective aspect ratio of the fin is increased considerably. With the plate close to $1/2$

of the height of the fin, both the induced lift angle ($d\alpha_i/dC_L$) and the drag due to lift ratio (dC_D/dC_L^2) are increased by some 6% because of *interference* of the plate with the lift distribution of the fin. This effect is further discussed in Chapter VIII under the heading "induced interference".

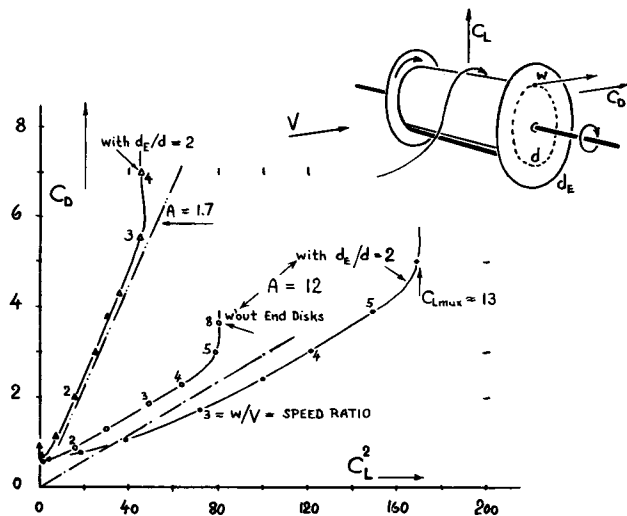


Figure 18. Drag-due-to-lift characteristics of rotating circular cylinders (20,c,e) without and with end disks. Note that in this graph too, plotting $C_D(C_L^2)$ gives fairly straight lines, parallel to induced theory.

- (15) Experimental results on end plates:
 - a) Ergebnisse AVA Göttingen Vol.III (1927) p.95.
 - b) NACA Technical Rpts 201 and 267 (1927).
 - c) NACA Technical Note 2440, A = 4 at R = 10.
 - d) Wadlin-Others, Hydrofoil, NACA RM-L51B13.
 - e) NACA, Tail Surfaces, A = 3 to 6; T.Note 1291.
 - f) On 45° swept wing, NACA Tech Note 2229.
 - g) Clements, Canted Plates, AE Review, July 1955.
 - h) CAHI (Moscow), same as reference (14,c).
- (16) End plate systems in airplanes:
 - a) Root, Empennage Design, J.A.Sci. 1939 p.353.
 - b) Multopp, "T Tails", Aero Digest May 1955.
 - c) Riley, Tail Assembly, NACA T.Note 2907 (1953).
 - d) Results similar to (c) in T.Note 1050 (1946).
- (18) Explanation of the Magnus effect:
 - a) Magnus (1802 to 1870), Abh. Berliner Akad. 1852, Poggendorf Annalen 1853 p.1.
 - b) Prandtl, Die Naturwissenschaften 1925 p.93.
- (20) Experimental results on rotating cylinders:
 - a) Ackeret, Zts. Flugt. M'luftsch. 1925 p.49.
 - b) Reid, Rotating Rods, NACA T.Note 209 (1924).
 - c) AVA Göttingen Ergebnisse Vol.IV (1932).
 - d) Thom, Cylinder with Disks, ARC RM 1623.
 - e) Without end disks, lift of the "A = 1.7" cylinder (c) is so small (in the order of $C_L = 1$) that it cannot well be plotted in the graph.
 - f) Holst, Rotating Wing, ZWB FB 1308 (1940).
 - g) Küchemann, Cylinders and Wings, ZWB FB 1651.
- (22) Applications of rotating cylinders:
 - a) Flettner, Werft-Reederei-Hafen 1924 p.662.
 - b) Ackeret, Rottorschiff, Göttingen 1925.
 - c) "Industrial Applications", Mech.Engg 1927 p.249.
 - d) Klemm investigated the idea of applying rotors in aircraft; see Scientific American, 1925 p.343 and in the August Issue; also 1932 p.362, where a report is given on rotor-lifted airplanes.

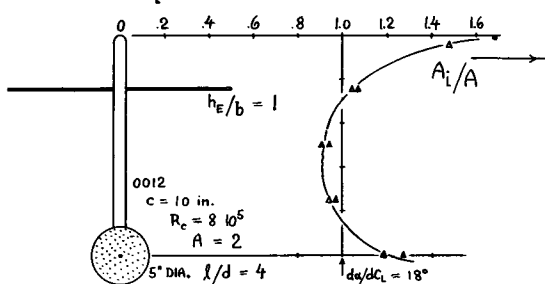


Figure 17. Effective aspect ratio of a vertical tail surface in combination (16,c) with a horizontal plate.

(d) Rotating Cylinders

An interesting application and/or confirmation of lifting-line theory are circular cylinders rotating about their axis (Magnus effect as described in references 18). Lift coefficients (based on span b times diameter d) of considerable magnitude are obtained in this way. Figure 18 presents experimental examples plotted in the form of $C_D(C_L^2)$. Three phases are evident. In the first one, up to velocity ratios w/V in the order of 1 or 2, the drag decreases (separation reduces). In the second phase, the drag increases considerably together with the lift which theoretically reaches a maximum corresponding to $C_L = 4\pi = 12.6$ at $w/V = 4$. Still higher coefficients are obtained, however (on cylinders having larger aspect ratios and fitted with end plates) in the third phase, by applying velocity ratios w/V in the order of 10 or even higher, while the drag increases progressively, because of what we may call "super-circulation".

Drag Due to Lift. Lifting cylinders of finite span exhibit induced drag, of course. Analysis of figure 18 suggests a mechanism as follows. Because of the blunt ends of the cylinders, their effective aspect ratio is reduced, tentatively by $\Delta A = 1$. After adding end plates or "end disks", respectively, this reduction is essentially recovered, however; and on account of the disks as such, the effective aspect ratio is further increased, tentatively by $\Delta A = 2$ ($\Delta d/b$) A, where $\Delta d = d_{EP} - d =$ increment of disk over cylinder diameter. Figure 18 shows that this mechanism can approximately be correct in describing the results. The end disks improve, in other words, the flow pattern past the ends of the cylinders considerably. Their application is effective both with regard to lift (including C_{Lmax}) and induced drag (20,e). Besides a viscous component of drag (in the order of $\Delta C_D = 0.5$), the power necessary to rotate the cylinder (measured in references 20, a and b) can also be taken into account in the form of a drag coefficient. Assuming this power to be due to the

fluid-dynamic friction on the cylinder surface only (that is, disregarding mechanical friction), the equivalent drag coefficient is roughly

$$\Delta C_D = \pi C_f (w/V)^3 \quad (22)$$

Assuming then, C_f to be ≈ 0.003 in the range of Reynolds numbers $R_w = w d / \gamma$ between 10^5 and 10^6 , this drag component is found to be in the order of $\Delta C_D = 0.01 (w/V)^3$. For example at $w/V = 4$, producing a lift coefficient in the order of 8, the increment is $\Delta C_D \approx 0.27$. This much is approximately 10% of the induced drag (at $C_L = 8$) of a cylinder having an effective aspect ratio of $b/d = 10$. All in all, a rotating cylinder of that aspect ratio (with a pair of small end disks) can be expected to have a minimum drag/lift ratio $D/L \approx 1/5$ at $C_L \approx 5$. For comparison, a profiled wing, having the same span as the cylinder, would produce the same maximum lift (in pounds) if made with a chord $\approx (2/3)$ of the span. Its drag/lift ratio at a $C_L = 0.75$ (on wing area), giving the \approx same lift (in pounds) as the cylinder has at $C_L = 5$, is estimated to be $D/L = 1/6$. This value is not very different from that of the cylinder as quoted above. The wing would be much more efficient, however, in the range of smaller lift coefficients.

Flettner Rotor. The lift produced by wind in a rotating cylinder is of some importance in the ballistics of spinning projectiles. The only engineering application of the Magnus effect attempted so far is in Flettner's "rotor ship" (22). Utilizing the wind in a manner similar to that of sailboats, this ship has crossed the Atlantic, propelled (or assisted) by two cylinders rotating about their vertical axes. — Circulation and lift due to rotation are not restricted to the circular cylinder. A rod having the cross sectional shape of a "cross" (20,b) and an ordinary foil section (20,f) have also been tested and found to produce forces similar to those of the cylinder when rotating about their axes.

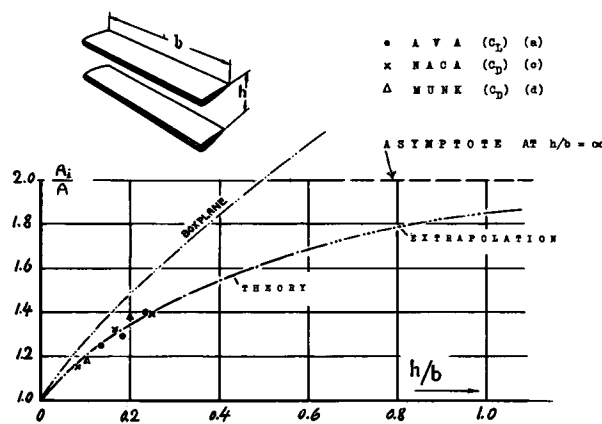


Figure 19. Effective aspect ratios of biplanes (26).

3. DRAG IN VARIOUS WING ARRANGEMENTS

Only monoplane wings, unaffected by any boundaries in the fluid space, have been considered in the preceding sections. Placing now two (or more) wings closely together in biplane-, tandem- or any other arrangement, they have an effect upon each other's aerodynamic characteristics. Several types of such configurations are discussed as follows.

(a) Biplanes and Similar Configurations

Biplane. In the early days of aviation, the biplane was a very popular type of airplane; and its aerodynamic characteristics have theoretically been studied, as a function of gap or height ratio, span ratio, stagger and decalage (26). All these parameters have an influence upon aerodynamic efficiency. However, the most important one is that of the gap ratio "h/b". Aerodynamic characteristics of a biplane composed of two identical panels, each carrying approximately half of the combined load, are indicated in figure 19, in the form of the effective aspect ratio. If defining the geometrical aspect ratio as $A = b^2/S$, where S = combined wing area of the two panels — the effective aspect ratio grows from $A_i = A$ at $h/b \rightarrow 0$, to $A_i = 2A$, at $h/b \rightarrow \infty$. The condition at $h/b = 0$ means a monoplane with the same span, but with twice the chord of a biplane panel. For larger values of h , we have evidently two wings flying independently of each other. This case is treated further under the heading "flying in formation". In the most efficient biplane, the panels are not necessarily equal in dimensions. For example (26,b) for rectangular plan form, with $c_{short}/c_{long} = 0.5$, the optimum span ratio is $b_{short}/b_{long} = 0.75$.

Multiplanes. On the basis of constant span, the induced drag ratio (D_i/L^2) decreases not only as the height "h" of a biplane is increased, but also as the number of panels placed within that height is increased. A number of triplanes has actually been built and flown during the last 50 years. Theoretical analysis (26,a) shows that multiplanes approach as a final limit the condition of the "boxplane". The two (rectangular) panels of such a configuration are connected at each end by means of a piece of foil which can be considered to be an end plate — thus forming a rectangular "box". The effective aspect ratio of this type is included in figure 19. For $h \rightarrow \infty$, the boxplane reaches $A_i \rightarrow \infty$, which means zero induced drag.

Ring Foil. A ring is a shape somehow similar in aerodynamic respect, to that of the boxplane above. On the basis of a sectional lift-curve slope of 2π , analysis (28,a) shows that the effective wing area of a ring-shaped foil is

$$"S" = 0.5 \pi d c \quad (21)$$

where d is wing diameter. The equivalent stream of fluid deflected by such a wing is twice the cylinder defined by the ring diameter d . Therefore, the induced drag is only half of that as indicated by equation 4; and the effective aspect ratio is

$$A_i = 2 d^2 / "S" = 4d/(\pi c) \quad (22)$$

In coefficient form, based upon "S", the induced characteristics of the ring foil are given by

$$dC_{D_i}/dC_L^2 = d\alpha_i/dC_L = 1/\pi A_i = 0.25 c/d$$

These equations mean that lift and induced drag of ring foils are equal to those of two plane wings (flying without affecting each other) having each a span equal to the ring diameter and an area each, equal to 0.25 the developed ring area.

Figure 20 presents experimental results on a ring-shaped airfoil. Based upon $S = 2(dc)$, equation 23 transforms into

$$dC_{D_i}/dC_L^2 = (c/d)/\pi \quad (24)$$

This function is verified in the graph, if assuming an increase of the profile drag as indicated; a result which does not seem to be surprising for the 21%

-
- (26) Theory and results of multiplanes:
 - a) Prandtl, NACA T Rpt 116; Erg. AVA III (1927).
 - b) Munk, Biplane, NACA Technical Rpt 151 (1922).
 - c) Knight and Wenzinger, Wings, NACA T.Rpt 317.
 - d) Munk, Biplane-Triplane Tests, NACA T.Rpt 256.
 - (28) Characteristics of ring-type foils:
 - a) Analysis by Ribner, J.Aero Sci. 1947 p.529.
 - b) Murtry, Experiments, ZWB FB 824/3 (1941).
 - c) Weissinger, Ring Aerodynamics, ZFW 1956 p.141.
 - d) A combination of "ring wing" with turbo-jet engine developed in France; see Yearbk WGL 1954.
 - e) Richter, Ring Aerodynamics, Yearbk WGL 1955.
 - (29) Ground effect on lifting wings:
 - a) Theory, AVA Göttingen, Ergebnisse II (1928).
 - b) NACA, Experimental Data, Technical Note 705.
 - c) Zeitschr.Flugt.M'luftschiffahrt 1932 p.159.
 - d) CAHI Moscow, Experimental Result, Rpt 437.
 - e) ARC, Experimental Results, RM 1847 and 1861.
 - f) Dätwyler, Wings Close to Ground, Mittl Aerodynamik Inst. TH Zürich, 1934; see ZFM 1933 p.442.
 - g) Furlong Sweptback Wing, NACA T.Rpt 1218.

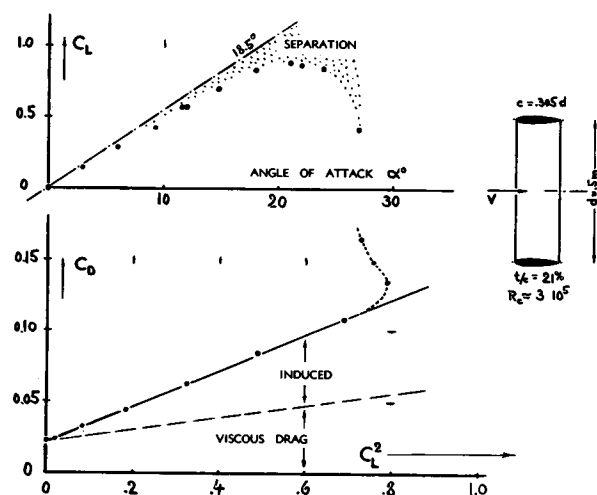


Figure 20. Lift and drag characteristics of a ring shaped airfoil (28,b). Theoretical lift as presented in (28,a).

symmetrical section used in those tests. Ring foils can be used in place of fins for the stabilization of bombs (or for purposes as indicated in reference 28,d). In small aspect ratios, and for small angles of attack (only representing the linear lift term):

$$L = q d^2 \pi \alpha \quad \text{and} \quad D_i = 0.5 L^2 / (q d^2 \pi)$$

Reference (28,d) presents some experimental results approximately confirming this lift function at an aspect ratio $d/c = 0.62$.

Ground Effect. Theory represents the biplane by a pair of lifting lines circulating in one and the same direction. Reversing now the circulation in one of the two vortices, a flow pattern is obtained identified by a plane of symmetry half way between the two. This plane is the fluid-dynamic equivalent of a solid boundary for each of the two "wings". For the lower wing the boundary is a "ceiling" (such as that in a closed-type wind tunnel, for example); for the upper foil, the boundary represents the same influence as that of the ground (the airfield or the runway) upon an airplane wing during take-off or while landing. The downwash behind the wing strikes the ground surface; induced angle and induced drag are accordingly reduced. Figure 21 presents the theoretical prediction (29,a), together with a series of points evaluated from lift- and drag characteristics as tested in wind tunnels in the presence of a ground surface. Below $h/b = 0.3$ or 0.4, the decrement may be approximated in terms of an increment of the effective aspect ratio:

$$\Delta A/A = 0.09 b/h \quad (25)$$

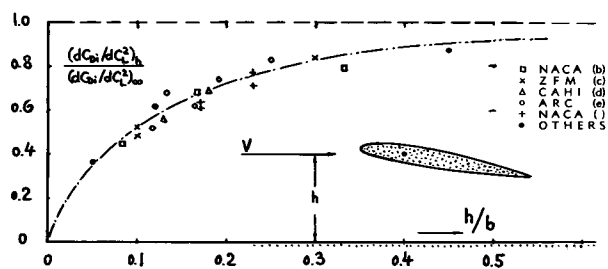


Figure 21. Induced drag of wings flying near ground (29).

Two pairs of points in figure 21 have been evaluated from experimental α_l and C_{Dl} results on a 42° swept wing. They show that the ground effect is also effective in sweepback, with the height h defined to the aerodynamic center of the wing. Considering conventional dimensions of landing gears, the distance between wing and ground is found to be in the order of $h/b = 0.1$. For this ratio, the induced drag function is seen to be approximately half of that in unlimited flow. In other words, the effective aspect ratio is almost twice the geometrical one. The ground effect should, therefore, not be disregarded in take-off and landing calculations.

(b) Wings in Tandem and Similar Arrangements

Tandem Configuration. On the basis of wing theory (26,b) lift and induced drag of two (or more) foils in tandem arrangement, are expected to be equal to those of a single wing having a chord distribution corresponding to the sum of the local chords of the wing panels involved. Using, therefore, an aspect ratio based upon the total area, the combined minimum induced drag of a tandem system is ap-

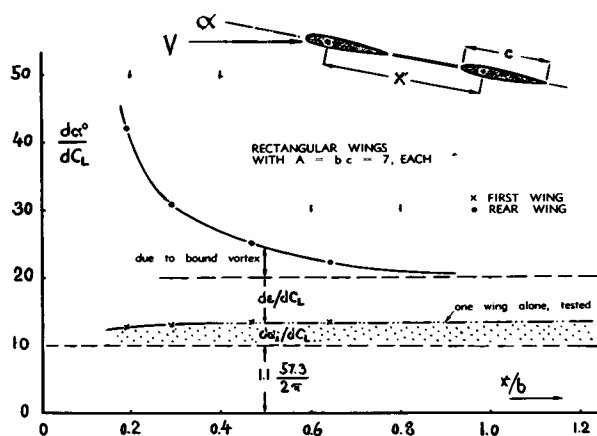


Figure 22. Analysis of the interaction between a pair of tandem wings (30,b).

proximately given by equations 4 to 7. Using induced angles and lift contributions as indicated in figures 22 and 23, the combined induced drag of the systems investigated is found to be approximately in agreement with this prediction. Also in agreement with theory (30,a) the forward foil shows only little effect due to the presence of the rear foil (see in figure 22). The influence of the forward foil upon the rear foil is much more important; the rear foil is "climbing", so to speak, within the downwash field coming from the first foil. The angle of the downwash has a value of $2\alpha_l$, in a not rolled-up vortex sheet (figure 1,a); actually the average value is in the order of only $1.6\alpha_l$. Therefore, the angle at which the lift in the second foil of a tandem system is inclined to the rear — is approximately:

$$\alpha_{l2} = (C_{L2}/\pi A_2) + 1.6 (C_{L1}/\pi A_1)$$

Investigations in (30,c) give some more insight in the mechanism of tandem systems. The larger wing in figure 23, having $A = 6$, has a $dC_D/dC_L^2 = 0.075$, flying alone (without correction as tested in an open-throat wind tunnel). Behind an aspect-ratio-3 foil, the drag function of the larger foil is increased to 0.081, which is not very much above the free-flight value. The wider (second) foil, evidently receives not only downwash, but also upwash (in the outer parts of the span), thus recovering some of the induced drag produced by the forward foil.

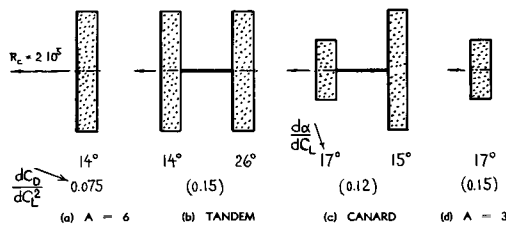


Figure 23. Experimental results (30,c) on the induced characteristics of tandem foils. The values in brackets (not available in the source) have been estimated.

Horizontal Tail. There has been a small French airplane "Pou du Ciel" ("Sky Flea") built in tandem form (combined with some biplane effect). Otherwise, the tandem arrangement has hardly been used in airplane design, obviously because of low efficiency and no structural advantages. The interaction of tandem wings has a practical meaning, however, in the induced drag of horizontal tail surfaces. Depending upon the longitudinal stability of the airplane considered, the tail carries some positive lift load, at least in the range of smaller flying speeds (at higher wing-lift coefficients). Taking into account the aspect ratio of the horizontal surface (usually between 3 and 5), and considering the detrimental effect of the fuselage upon the effective

aspect ratio of the tail (as explained in the "interference" chapter) — the induced drag of the tail surface (subscript "H") is approximately:

$$C_{D_{iH}} = C_{LH} (\alpha_{iH} + \epsilon) \quad (27)$$

with " ϵ " indicating the downwash angle at the location of the tail. The ratio between this drag and the basic induced drag of an airplane is then

$$\frac{D_{iH}}{D_{i0}} = \frac{S_H}{S} \left[\frac{\epsilon}{\alpha_i} \frac{C_{LH}}{C_L} + \frac{A}{A_{iH}} \left(\frac{C_{LH}}{C_L} \right)^2 \right]$$

To illustrate this equation, values shall be assumed, representing common airplane design; $S_H/S = 0.25$, $A_H/A = 0.4$; $\epsilon/\alpha_i = 1$ in gliding condition (with fuselage interference), and = 2 in climbing condition (with propeller slipstream). Using these values together with an assumed ratio of C_{LH}/C_L between 0.1 and 0.3, the induced drag of the horizontal tail is found to be between 4 and 30% of the wing's induced drag. This drag component can thus be of appreciable magnitude and it should not be disregarded in computing the climb performance of airplanes. The additional drag varies greatly, of course, with the longitudinal characteristics (static

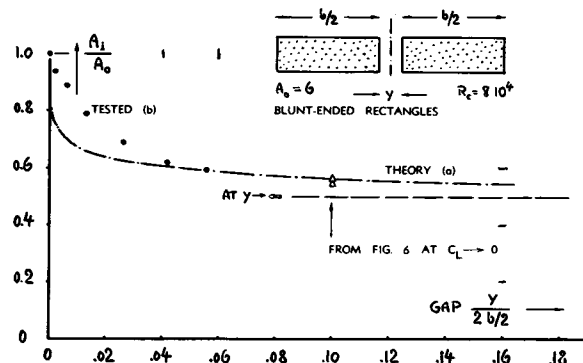


Figure 24. Effective aspect ratio of a pair of wings flying side by side (31).

stability) of the airplane considered. Depending on these characteristics, the induced drag of the horizontal tail surface can have "unexpectedly large values" (30,e) at high speeds (low wing-lift coefficients). — Another example of tandem performance arises when two airplanes combine in a refueling operation (30,f).

(c) Airplanes Flying in Formation

It is known that migratory (and some other) birds like to fly in a staggered or swept formation. Each animal (except for the leader) instinctively takes advantage of the upwash coming from the wing tip of the preceding bird. Theory confirms that this method is suitable to reduce the induced drag.

Longitudinal Gap. Cutting a wing along its center line, roughly means reducing the aspect ratio to half. Figure 24 shows how the effective ratio decreases as a function of the gap between the two halves of such a wing. Theory (31,a) considering two lifting lines (having no physical chord), expects a rapid decrease of A_i/A . Experimental results (31,b) of a rectangular wing (originally having $A = 6$) show, however, that chord and thickness of the square and blunt wing ends are obstructions for the flow through the gap, at least for ratios of y/c below ≈ 0.03 . Beyond $y/b = 0.04$, the configuration in figure 24 approaches the terminal value of $A_i/A = 0.5$ along the theoretical function. The induced characteristics of a pair of such wings, flying side by side, can be derived from the graph.

Flying Side by Side. Considering two or more airplanes flying so closely side by side that their tips touch, their geometric aspect ratio is theoretically increased to twofold or manifold, respectively. In the theoretical analysis (32) each wing is replaced by a "horseshoe" vortex. This is done in such a manner that at a nominal distance equal to zero, certain gaps are considered to be left between the wing tips. Since only the induced drag is affected by the interaction, a practical assumption is made as a basis for the results presented in figures 25, 26 and 27. Considering that the basic wing (in free flight; alone) would have a $C_{D_i}/C_{D_{total}} = 0.5$, the results primarily apply to the optimum lift-drag ratio as may be utilized in long-range flight (at maximum L/D). As shown in figure 26,a the drag decreases as the lateral distance between the planes is reduced, in a manner similar to that in figure 24. For a fixed lateral distance $y = b$, meaning zero gap between the wing tips (permitting however the tip

(30) Characteristics of tandem wings:

- a) Glauert, Tandem Theory, ARC RM 949 (1923).
- b) Luetgebrune, Tandem Tests, ZWB FB 1677.
- c) Eiffel, Résistance de l'Air Aviation, 1919.
- d) Munk's Tests, Vol.II Tech Ber. Flugzeumeist.
- e) Naylor, Wing and Tail, ARC RM 2428 (1954).
- f) See cover picture of A.Eng.Review Nov 1955.

(31) Influence of longitudinal wing gap:

- a) Prandtl-Betz, 4 Abh. Hydro-Aerodynamik (1927), reproduced by Edwards Ann Arbor Mich. 1953; see also Durand's "Aerod. Theory" Vol.IV.
- b) Experiments by Munk and Cario, Technische Berichte der Flugzeugmeisterei Vol.I (1917) p.219.

(32) Schlichting, Analysis of Flying in Formation:

- a) Mitt. D.Akademie Lufo 1942, Transl TMB 239.
- b) Doct ZWB UM 2066 (1944); Transl TMB 240.

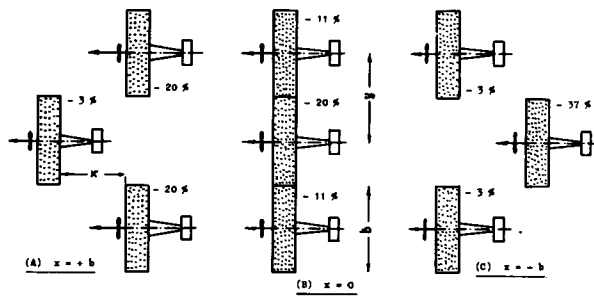


Figure 25. Distribution of drag within the formation of three airplanes (32) flying at $y = b$ and $z = 0$. Average reduction of drag is 14% in all three conditions.

vortices to develop) — the drag decreases steadily as the number of airplanes flying in line is increased (figure 27). Considering as a possibility 5 planes in such a formation, the savings in drag might be in the order of 18%. The effect reduces, however, rapidly (as shown in figure 26,b) upon "staggering" the formation in vertical direction (letting each airplane fly in an altitude which is different from that of the next plane by the value of "z").

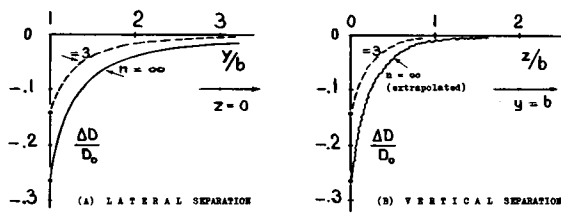


Figure 26. Maximum reduction of drag (32) made possible by flying in formation (as in figure 25), as a function of (a) lateral and (b) vertical separation.

Longitudinal Stagger. As indicated by basic theory (26,b) the arrangement of a formation of airplanes in longitudinal or flight direction, does not have an effect upon the total drag — as long as lateral and vertical distances are kept constant. As listed in figure 25, the total or average drag reduction " $E = \Delta D/D$ " is accordingly one and the same — whether the center wing is flying in the same line with the others, or in front of them or behind. To avoid collisions at the wing tips, therefore, a swept formation (with the wing tips somewhat overlapping laterally) appears to be most favorable in long-range operations; and this is precisely the technique applied by migratory birds. The distribution of the induced drag among the various wings depends upon their individual position. Those in front show almost the same drag as if flying alone. The wings in the rear, on the other hand, show an appreciable decrease of their drag, especially if flying in the center position. To help an ailing airplane home, two others should accordingly fly ahead as indicated in figure 25.

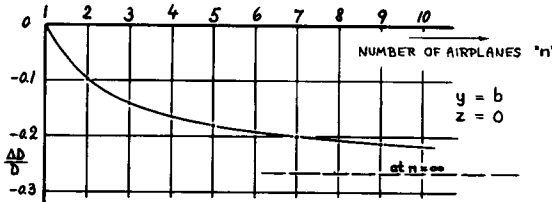


Figure 27. Average or total reduction of drag in formation (as in figure 25) as a function of the number of participating airplanes (32).

4. DRAG IN SMALL ASPECT RATIOS

The principles and results of drag due to lift presented so far in this chapter, are primarily applicable in larger aspect ratios. As the wing chord (not as such existing in lifting line theory) is made longer and longer, it reaches into the space of the "fully" developed vortex system (figure 1,c), thus interfering with its pattern; and the vortex field in turn affects the flow past the foil sections. Essentially there are two locations where such interaction takes place. One is within the span between the wing tips; satisfactory solutions are known for this effect. The other one is at the lateral edges. Only limited information is available regarding the flow pattern past these boundaries and their influence upon lift and drag. Certain answers are suggested, however, in the following paragraphs.

(a) First Component of Drag

Circulation in Small Aspect Ratios (35). The mechanism of circulation in chordwise direction (lifting line), is also present in small aspect ratios. However, every wing (having finite span) produces lift by deflecting a certain stream of fluid. This means that the streamlines passing the foil sections have a certain curvature. In small aspect ratios, the lift is, therefore, lower than predicted by lifting-line theory; the first (linear) term of the lift coefficient is only

$$C_{L_0} = 0.5 \pi A \sin \alpha \quad (30)$$

This function applies to aspect ratios below 1.0 or 0.5. By referring the coefficient to the square of the span, it is seen that the first lift component is no longer a function of the aspect ratio:

$$C_{Lb} = L / (q b^2) = 0.5 \pi \sin \alpha \quad (31)$$

This result indicates that the lift is essentially produced near the leading edge, and that the rear part of the chord is useless, so to speak, in regard to lift. In other words, a condition is reached (below $A = 1$, or $= 0.5$), where maximum possible deflection (downwash angle = angle of attack) is obtained ahead of the trailing edge. One half of the angle of attack (of the first lift term; equation 30) is, therefore, induced; and the corresponding induced drag is

$$C_{D_{\text{Ind}}} = 0.5 C_{L_0} \tan \alpha \approx C_{L_0}^2 / \pi A \quad (32)$$

In other words, the chord effect considered so far, only affects the lift-curve slope; and equation 4 is still applicable for this component of drag.

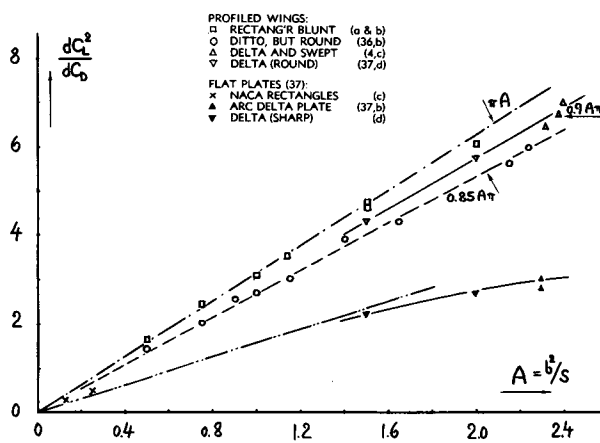


Figure 28. Drag-due-to-lift function of low-aspect-ratio wings, in the range of small lift coefficients; (a) profiled airfoils; (b) flat and sharp-edged plates.

First Drag Term. Figure 28 presents results, evaluated at small angles of attack (near $C_L = 0$), in the form of (dC_L^2/dC_D) which is the inverse of the drag ratio (to make the plot linear). It is seen that profiled rectangular wings with sharp (blunt) lateral edges closely agree with the theory. Wings with round lateral edges have higher drag functions. The effective aspect ratio of such wings is obviously reduced to some .90 or even 80% of the geometrical ratio. A collection of effective aspect ratios is presented in figure 29. Applying these ratios, the induced drag due to the first lift component can be determined through the use of equation 4.

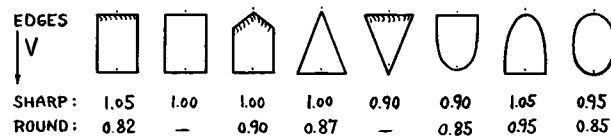


Figure 29. Effective aspect ratios (with respect to linear lift term) of various "wing" shapes with aspect ratios between 0.5 and 1.3 at R_c between $(0.5 \text{ and } 1.0) \cdot 10^6$, evaluated from (36) and (37).

Flat Plates. Not having the same nose-suction effect as profiled wings, plates are expected to have a drag coefficient $C_D = C_L \tan \alpha = C_N \sin \alpha$, as in larger aspect ratios. Considering small angles of attack and not too small aspect ratios, equation 30 (linear lift term) yields in this case

$$(dC_D/dC_L)_0 = (d\alpha/dC_L)_0 = 2/\pi A \quad (33)$$

as plotted in figure 28. Results of plates beveled at the suction side (36,a) do not agree with equation 33. It appears that they develop some favorable suction at their leading edge, so that their drag is reduced. Their function (not included in figure 28) is about half way between profiled wings and plates.

(b) Second Component of Drag

Zero Aspect Ratio. A second, non-linear lift component appears in small aspect ratios. To understand the flow pattern, analysis is useful at $A \rightarrow 0$. In a narrow and straight strip of material, a longitudinal circulation is no longer existing. A different type of lift develops instead, along the lateral edges. A pair of vortices, similar to those in figures 7 and 8 is found somewhat above and parallel to the edges. As derived in (39,a), the normal-force coefficient at $A = 0$, is

$$C_N = k \sin^2 \alpha = C_L / \cos \alpha; \quad k = C_N / \sin^2 \alpha$$

- (35) Linear lift theory of small-aspect-ratio wings:
 - a) Weinig, Lift in Small Span, Lufo 1936 p.405.
 - b) Weissinger, Theory of Swept Wings, ZWB FB 1553, 1942 (Transl NACA T.Memo 1120, see also T.Note 3476); also Expansion of Lifting Line Theory, Mathematische Nachrichten 1949 No. 1 and 2.
 - c) Lawrence, Journal Aeron'l Sciences 1951 p.683.
 - d) Jones, NACA Technical Rpt 835 (1946).
 - e) Falkner, ARC RM 1910 (1943) and RM 2596.
- (36) Investigations of small AR profiled wings:
 - a) Winter, Plates and Wings of Short Span, Forschung 1935 p.40 and 67; Transl NACA TM 798.
 - b) Zimmerman, Clark-Y Foils of Small Aspect Ratio, NACA T.Rpt 431 (1932); also J.Aero Sci.1935 p.156.
 - c) Voepel, AVA Rpt 1946, Transl. RAE No. 276.
 - d) NACA, Sweepback and AR, Tech Note 1093.
 - e) Staufer, Tail Surfaces, Yb.D.Lufo 1940, I,383.
- (37) Experimental results of small AR plates:
 - a) AVA Göttingen, Ergebnisse Vol.IV (1932).
 - b) Jones-Miles, Triangular, ARC RM 2518 (1946).
 - c) Wadlin and Others, Hydrodynamics of Plates, NACA T.Notes 3079 and 3249; or T.Rpt 1246.
 - d) Bartlett, Edge Shape, J.Aero Sci.1955 p.517.

with $k = 2$ as per theory. The square of the angle of attack means physically that the stream of air deflected by the "wing", increases with the angle of attack. In a straight "strip" of this type, the drag due to lift is simply the horizontal component of the normal force; thus

$$C_{DL} = C_N \sin \alpha = C_L \tan \alpha = 2 \sin^3 \alpha = \sqrt{0.5} C_N^{3/2}$$

for $A = 0$ and $k = 2$. The "two-dimensional" flow pattern of the zero-aspect-ratio wing has been interpreted as being that of a flat plate with separated flow pattern. Applying the cross-flow principle (see Index) in combination with the drag coefficient C_D , ≈ 2 of such infinitely long plate in normal flow (at $\alpha = 90^\circ$), equations 34 and 35 are correctly obtained. At small and moderate angles of attack, the strip considered does not have the same flow pattern (vortex street), however, as in the plate exposed to normal flow. Therefore, the empirical result only seems to be coincidental. The flow pattern of the inclined strip, including the two vortices parallel to the lateral edges, may exist without any "true separation" of the flow from the suction side. At any rate, the drag due to lift (equation 35) is very much different from that as indicated by lifting-line theory (equation 4).

Increased Momentum. In aspect ratios higher than zero, the lift of "wings" consists of two components — one corresponding to chordwise circulation (equation 4) and the other one similar to that at zero aspect ratio. For this second component, no explicit solution (except for $A = 0$) has been established to this time. Two schemes (40) have been suggested, however, to explain the non-linear term. The lateral edges of a (rectangular) small-aspect-ratio wing are either assumed to have an effect similar to end plates having a height proportional to the angle of attack, or it is proposed that the size of the fluid stream tube deflected by the wing is increased by a component which is proportional to the angle of attack. Both schemes provide a progressive increase of mo-

mentum, and they thus yield a function which somehow agrees with experimental results of $C_L(\alpha)$. As far as drag due to lift is concerned, these mechanisms do not give correct answers, however, at least not below $A = 1$.

Lateral Vortex Pair. By subtracting the linear lift component as indicated by equation 30, the non-linear component ΔC_L can roughly be isolated from tested values. Such results have been plotted in figure 30 in the form of

$$(\Delta C_L / \sin^2 \alpha) \quad \text{or} \quad (\Delta C_N / \sin^2 \alpha) \quad (36)$$

Admittedly such evaluation is somewhat arbitrary, depending upon the value of $dC_L/d\alpha$ to be assumed for lateral-edge shape and plan form involved in each wing tested. It is seen that the factor k (to be substituted for "2" in equation 34) is larger in sharp-edged wings than in wings having rounded lateral edges. Particularly low components are found in delta wings equipped with round lateral edges (37, d); they are not plotted in the graph. Evaluation of (36,b), not included in figure 30 either, indicates that wing-section camber evidently reduces the second lift term. Values of $(\Delta C_N / \sin^2 \alpha)$ near $A = 0$, are discussed in connection with "streamline bodies".

Second Component. As far as drag is concerned, the component due to the non-linear lift term is expected to correspond to $\tan \alpha$. The total drag due to lift is then

$$C_{DL} = C_{L_0} \tan \alpha_i + \Delta C_L \tan \alpha \quad (37)$$

where $\alpha_i \approx 0.5 \alpha$. In the present state of information, equation 30 may be used for the first and equation 34 (with k as per figure 30) for the second lift component as an approximation. Figure 31 presents the example of a rectangular wing having $A = 0.5$. Equation 37 with $k = 2$ agrees fairly well with the experimental results on profiled wings.

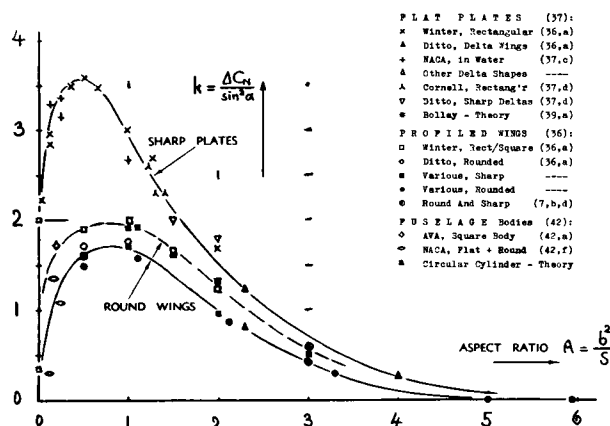


Figure 30. Second (non-linear) lift term of "wings" as a function of aspect ratio.

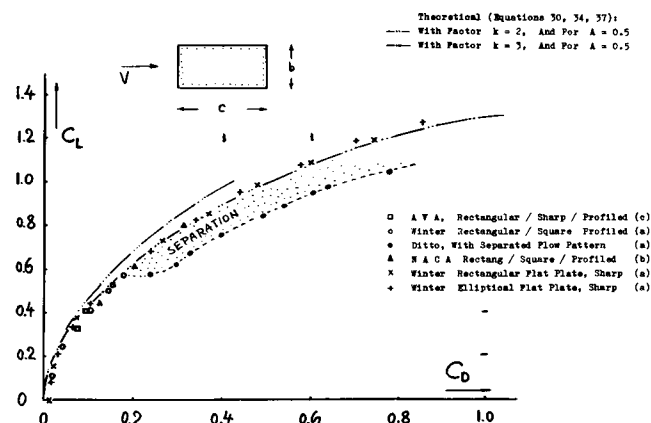


Figure 31. Lift- and drag coefficients (36) of profiled "wings" and flat plates, having an aspect ratio of 0.5.

Similar results are obtained when checking tested characteristics in other small aspect ratios. It is suggested, however, that some (favorable) interaction is present between first and second lift and drag terms.

Plates. Many experimental results have been published on low-aspect-ratio flat plates (37). They show surprisingly high second lift terms; see in figure 30. The fact that these values are far above the theoretical value at $A = 0$, suggests again that the linear lift term is affected by the second term (41). A possible mechanism would be the "end-plate" effect mentioned above, thus increasing the circulation in the small-aspect-ratio wings considered. — Applying equation 35, drag coefficients can be obtained for flat plates of small aspect ratio. The experimental results in figure 31 agree reasonably well with that function. The graph also permits a comparison between plates and profiled "wings". For a given lift coefficient, there is a certain aspect ratio below which the drag-due-to-lift component indicated by equation 35 is less "expensive" than the first component as per equation 33. This aspect ratio is

$$A = 2 k C_L^{3/2} / \pi \quad (38)$$

yielding $A \approx C_L^{3/2}$, for example, for $k = 1.5$. This result is evidently the reason why in small aspect ratios, flat plates (with high k values) can be equal

or even superior to profiled wings of the same planform shape.

Delta Wings. It has also been found (37,d and 38,d) that "delta" wings (small-aspect-ratio triangular shapes with straight trailing edge) have appreciably higher lift coefficients and that they can have equal or smaller drag due to lift when equipped with sharp (rather than with rounded or profiled) lateral edges. It is suggested that the mechanism indicated by equation 38 may give the explanation.

(c) Lift of Streamline Bodies

As the aspect ratio of a profiled "wing" is decreased, the ratio of thickness over span (t/b) increases. Shapes similar to those of streamline bodies are thus obtained, with round or rectangular cross sections, upon approaching $A = 0$.

Lift. Theoretically, streamline bodies such as fuselages, for instance, do not develop lift, or cross-wind forces in any direction. Actually, they exhibit some lift because of the boundary-layer material accumulating at the upper side of their rear end. This lift is of the same nature as that of cone-cylinder bodies (with blunt rear end) as explained in (42,b and g). The upper limit of the linear-lift-curve slope may be defined by equation 31. Figure 32 shows that this value is approached when plotting $dC_{Lb}/d\alpha$ (on "span area" b) against the basic (mostly skin-frictional) drag coefficient $C_{Db} = D/q b^2$. Figure 33 demonstrates that the lift of a streamline body is considerably increased after the body surface was covered with coarse sand. As in wings, the shape of the lateral edges has an effect too upon the magnitude of the lift produced; bodies with square or rectangular cross sections exhibit roughly twice the lift of round shapes.

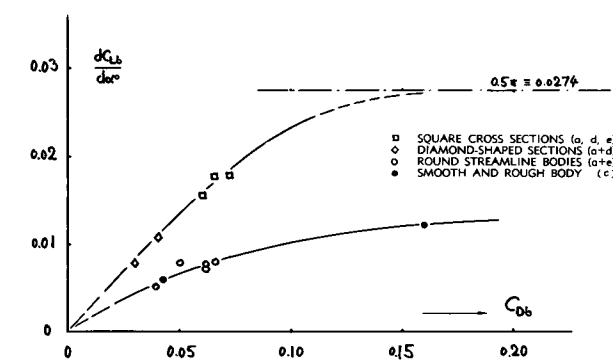


Figure 32. Lift-curve slope (at small lift coefficients) of streamline bodies (42) (with round and square sections) as a function of their drag coefficient.

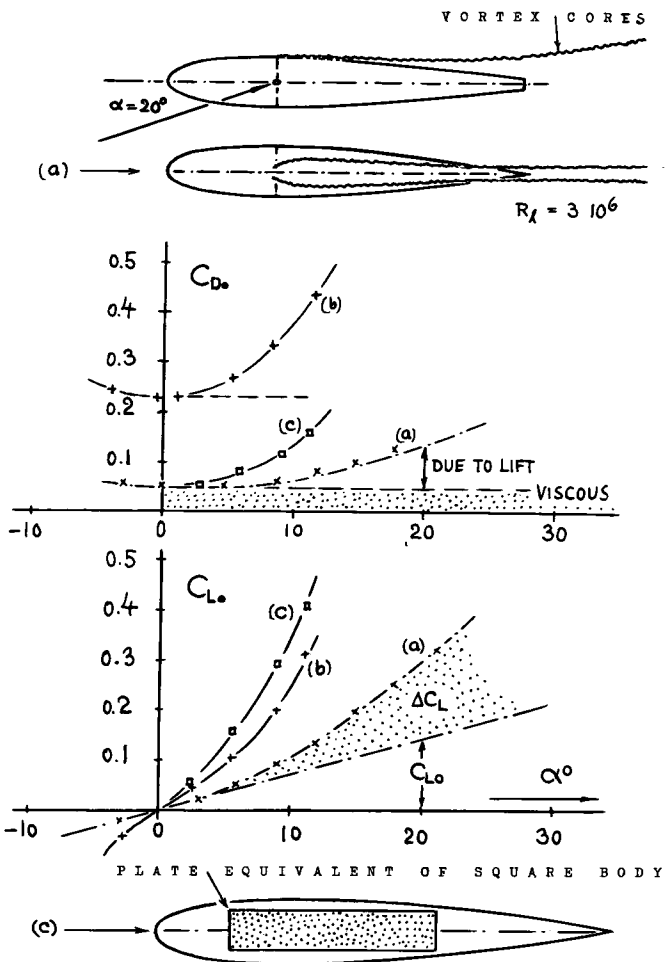


Figure 33. Flow Pattern and lift/drag characteristics of fuselage bodies; (a) in smooth condition (42,c); (b) with rough surface corresponding to $k/l = 1.2/1000$ (42,c); (c) with square cross section (42,a).

Drag Due to Lift. The inset in figure 33 shows the pair of rolled-up trailing vortices originating from the upper side of a streamline body. Note that the lateral vortex separation is considerably smaller than the maximum body diameter. This fact indicates that the effective span is smaller than the geometrical one. In the example of figure 33,a, $dC_{Lb}/d\alpha = (\pi/4) 0.007 = 0.0055$, a value which corresponds to $b_l/b \approx 0.0055/0.0274 = 0.20$. The value of "k" (indicating the magnitude of the second lift term) is found to be ≈ 0.26 . Using the span ratio, and on the basis of $0.26/k = 0.13$, (where $k = 2$ as for the plate at $A \rightarrow 0$) we find an equivalent rectangular plate, giving the same lift and drag (in pounds) as the streamlined body. In the example considered, this plate has a span equal to ≈ 0.20 of the body diameter and a length equal to ≈ 0.13 the body length. — The drag due to lift can be determined on the basis of equation 37. Analyzing the results in figure 33, the lift function was used as tested, however. Here as in other streamlined bodies (for example in reference 42,f), very low "k" values are found at $A \rightarrow 0$; see figure 30. Analysis of figure

33,b reveals that most of the drag increment due to lift is parasitic; and only a minor fraction is induced drag. Corresponding to their higher lift coefficients (see figure 32), bodies with square or rectangular cross sections have drag-due-to-lift coefficients which are considerably higher than those of round bodies (if taken at the same angle of attack); see for example the characteristics of a square fuselage body in (42,a). Effective span and effective chord of bodies with square cross sections are in the order of twice as large as those in round bodies.

Rotating Sphere. It is shown in the "vehicle" chapter that automobile bodies develop lift. Reference (43,a) also demonstrates that a sphere can have lift (in the order of $C_{Lx} = 0.15$, while $C_{Dx} = 0.45$) provided that some orientation is given to the wake by means of a rod placed across the direction of flow. Still higher lift coefficients can be produced in a manner basically identical to that in circular cylinders (as described before in this chapter) — by letting the sphere spin about an axis essentially normal to the direction of flow. Figure 34 shows lift and drag coefficient of a sphere as a function of the equatorial velocity ratio " w/V ". The maximum lift obtained ($C_{Lx} \approx 0.4$) is only a small fraction of the values tested in rotating cylinders. Assuming that all of the drag be induced ($C_{Di} \approx 0.6$ at $C_{Lx} = 0.4$), the effective aspect ratio of the sphere is found (through application of equation 4) to be in the order of $A_i = C_L^2/\pi C_{Di} = 0.4^2/\pi 0.6 \approx 0.09$. This is only a fraction of $(4/\pi)$, the geometrical aspect ratio of the sphere. The reduction properly corresponds to the round shape; and we can conclude that the drag of the rotating sphere is mostly induced drag. — Rotating "spheres" are physically found in tennis-, golf-, baseball- and ping-pong balls. The latter ones can easily be made spinning and they are then seen to travel along a laterally (or otherwise) curved path. Regarding golf- and baseballs, it is suggested that they are comparatively heavy so that any aerodynamic lift that might develop, can have only little effect upon their flight through the air.

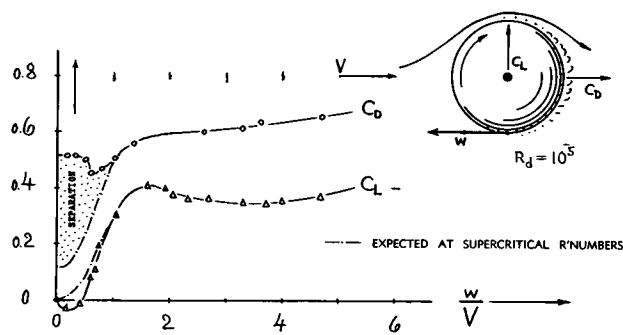


Figure 34. Lift and drag characteristics of a sphere (ping-pong, tennis-, golf- or baseball) spinning about the horizontal cross-wind axis (43,b).

(d) *Parasitic Wing-Tip Drag*

The chord- and lateral-edge effects described in the preceding sections, do not entirely disappear in larger aspect ratios. They are evident there in the form of secondary effects.

Second Lift Term. In figure 30, a quadratic lift term is no longer apparent above $A \approx 4$. This term may still be present, however, although compensated by a reduction of the first lift term (because of boundary-layer losses). Such a lift component is evident in tested pressure distributions of rectangular wings, at the blunt lateral edges. The corresponding drag due to lift as per equation 37 may also be obscured; namely by the end-plate effect of the lateral edges as described in (40,a).

Wing-Tip Shape. The flow around the lateral wing edges causes certain frictional and pressure losses. This type of drag has been investigated (44,a) by means of wake survey across the tip vortices. At

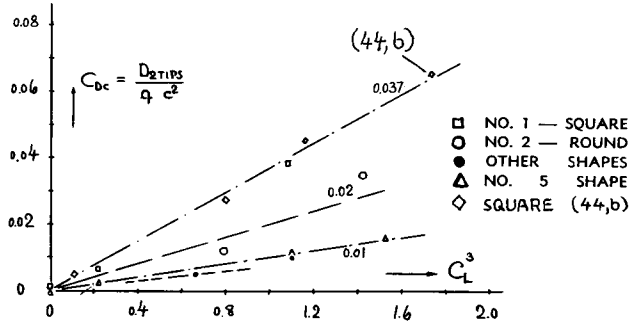


Figure 35. Parasitic wing-tip drag, determined by wake survey, mostly in (44,a), on a 12% thick wing of aspect ratio 3 at $R_c \approx 10^6$. Shapes are as in figure 9.

$C_L = 0$, blunt edges have a drag coefficient C_{Dc} as presented in the "streamline" chapter. Rounded and/or sharp edges show some small negative value at $C_L = 0$; because of the three-dimensional character of flow past the wing tips. As plotted in figure 35 the drag coefficient increases approximately as

$$C_{Dc} = k C_L^3 \quad (39)$$

where $k = 0.01$ for sharp, $k = 0.02$ for rounded, and $k = 0.037$ for blunt edges. The function $C_{Dc} \sim C_L^3$ is of the same type as that of the second-term drag in small aspect ratios (equations 36 and 37). It is not known, however, how much the two types of drag might be identical. At any rate, thin and sharp edges, particularly if bent upward such as number 5 in figure 9, are most favorable. Reference (44,c) gives some instructions on the practical design of this type of wing tip. Roughly, the parasite drag due to lift of this shape is only some 1%, on the average of the induced wing drag.

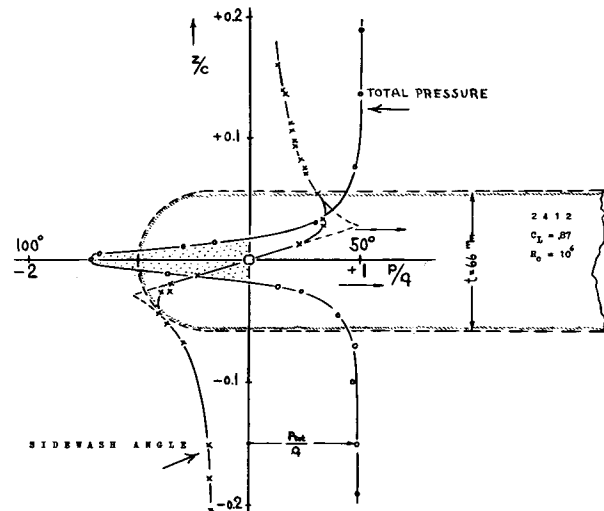


Figure 36. Total pressure (in direction of local flow) and sidewash angle on vertical axis of tip vortex, tested at $x = c$ behind TE of wing shape as shown (No. 2 of 44,a).

Tip Vortex Pattern. As an example, figure 36 presents (a) total pressure and (b) sidewash angle (w/V) where "w" = lateral velocity, measured on the vertical axis of a vortex originating from the rounded wing tip shown (shape number 2 as in figure 9). A core diameter may be defined by extrapolating both the theoretical velocity distribution outside, and the "rotating" distribution inside the core. In the case tested, the diameter is in the order of 5% of the wing chord. The diameter obviously corresponds to the magnitude of the parasitic wing-tip drag. For example, behind the blunt wing tip shape number "1" in figure 9, the diameter was found to be in the order of 7% of the wing chord, so that the cross section of the core is roughly twice that of the core in figure 36. Corresponding tip drag coefficients are plotted in figure 35 at $C_L^3 = 0.65$.

- (43) Lift forces in spheres:
 - a) Krey, Zeitschr. Flugt. M'lufsch. 1931 p. 97.
 - b) MacColl, Rotating Sphere, J.RAS 1928 p.777.
- (44) Investigations into viscous wing-tip drag:
 - a) Hoerner Experiments, ZWB UM 7815 (1943).
 - b) Evaluated from results presented in Prandtl-Tietjens, "Hydro-Aeromechanics" (1934) II p.171.
 - c) Hoerner, Shape of Wing Tips, see (7,d).
- (48) Aerodynamic performance of birds:
 - a) Raspert, Soaring Bird, Aero Engg Rev. 1950 p.14.
 - b) Feldman, TH Zürich, Wind-Tunnel Testing of a Seagull, Aero Review July 1944.
 - c) further references listed in Ybk WGL 1953 p.165.
- (50) Examples for lifting blade rotors:
 - a) Wheatley, Autogiro in Tunnel, NACA T.Rpt 515.
 - b) Payne, Induced Aerodynamics of Helicopters, Aircraft Engg 1956 p.46 and 82.
 - c) NACA, Induced Field, Tech Notes 3690 and 3691.

5. SUPPLEMENTARY NOTES

Some more of the many available results on drag due to lift are presented as follows.

Birds. The formation flying of migratory birds is explained on pages 15 and 16. — A buzzard was ingeniously tested in free flight (48,a) by tracking (following) him in a sailplane. The L/D or D/L ratio of that bird was determined using the calibrated characteristics of the plane as a measure. Two distinct phases are illustrated in figure 37; namely "soaring" and "gliding". Soaring takes place at low sinking speed, with cambered wing section and with wing tip "slot" feathers open. The lowest speed observed is 8.5 m/sec, corresponding to a lift coefficient $C_L = 1.3$ at a Reynolds number $R_c = 1.4 \cdot 10^5$. Gliding takes place between 9 and 23 m/sec. Minimum parasitic drag coefficient on wing area is $C_{D\text{min}} = 0.009$; based on total wetted area, $C_{D\text{wet}} = 0.0034$ at $R_c \approx 2 \cdot 10^5$. Comparison with figure 5 in Chapter II suggests that the flow may be laminar. Figure 37 also presents aerodynamic characteristics obtained on the plaster model of a sea gull (48,b) prepared for testing in a wind tunnel. The drag of this model is considerably higher than that of the buzzard. It seems that in the plaster model, the feathers were not properly reproduced. — The corresponding power loading is 122 kg/HP, while (1/45) HP per kg of animal muscles are considered to be available in "continuous" operation.

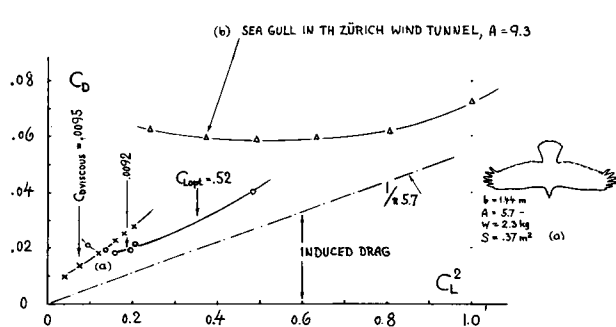


Figure 37. Aerodynamic characteristics of birds (48); of a buzzard (a) and of a seagull (b).

Lifting Blade Rotors. Any type of aircraft using rotating blades, can basically be considered to comply with wing theory (50). Figure 38 shows as an example lift and drag characteristics of an autogiro rotor (which is a rotor not connected to an engine, but driven by the wind). The drag coefficient (based on $d^2\pi/4$) can be split up into a constant component (representing parasitic drag) and into a component $\Delta C_D \sim C_L^2$. The increment is evidently much higher than the induced drag (equation 4). Inasmuch as lift is produced in the blades in a direction roughly parallel to that of the rotor axis, drag due to lift may approximately be $D_L = L \tan \alpha$ where $\alpha = \text{angle of attack measured against the axis}$; and since in small aspect ratios $\alpha \approx 2\alpha_i$, drag due to lift corresponds to equation 35. "Half" of this drag is equivalent to the energy taken out of the wind in driving the blades through the air. In conclusion, autogiro rotors are not efficient in purely aerodynamic respect. They are very efficient, however, in providing lift corresponding to C_L (based on "disk" area) up to "1" with a minimum of structural material and weight. In case of a helicopter, power is supplied to the rotor from the engine. As a consequence, the helicopter produces "induced" velocity and lift = thrust, down to zero speed of advance. Note that the affected mass of air corresponds to a cylinder with a diameter equal to that of the rotor — in the same manner as in wings. Replacing now in equation 1 the forward speed "V" by the induced velocity ($w/2$), the thrust is found to be

$$T = \rho S_{\text{d}} w^2/2 \quad (40)$$

where $S_{\text{d}} = d^2\pi/4$ and $w = \text{slipstream velocity at some distance downstream}$. The power required to produce the slipstream is thrust times speed "w". Combining these two equations, the thrust is found as a function of net power.

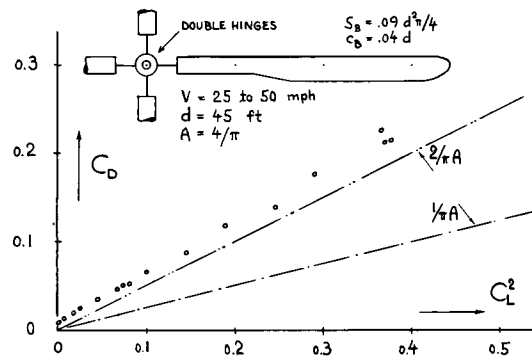


Figure 38. Lift and drag characteristics of an autogiro rotor, as tested in a wind tunnel (50,a).

CHAPTER VIII – INTERFERENCE DRAG

Two bodies "1" and "2", joined so that they touch or penetrate each other, usually present a combined drag D_{1+2} which is somewhat larger than the sum of the individual drag components ($D_1 + D_2$), each measured in free flow. The difference $\Delta D = D_{1+2} - (D_1 + D_2)$ is the interference drag. This type of drag is also present when two or more bodies are placed one behind the other, or when two bodies are near each other (without really touching each other). The mutual interaction between the boundary layer of a surface (wall) and small bodies placed on that wall is interference too. Some consideration is given to the latter subject in the chapters on "surface imperfections" and on "skin friction". Strict calculation of interference drag would be complicated and specific methods to solve such problems according to the principles of theoretical aerodynamics, have not really been developed. The physical phenomena of interference can be stated, however; and approximate but nevertheless reasonable functions can be presented as in the following sections - essentially on a statistical basis.

1. DRAG BETWEEN PAIRS OF BODIES

Shielding Effect. In case of two bodies placed one behind the other, the drag of the second one is usually smaller than in free flow, because of reduced dynamic pressure within the wake of the first body. In the example presented in figure 1, the drag of the second disk is even negative, up to a distance of more than 2 diameters, evidently because of suction behind the first plate. As the distance between the two disks is increased, the drag of the second one gradually approaches the value known under free-flow conditions ($C_D \approx 1.17$). This type of shielding effect can have some consequences in motorcar racing, where a competitor may run for a while within the wake of another car ahead of him. To mention another application, sailing before the wind (using the spinnaker) is one of the few examples where drag is a welcome force (utilized for propulsion). In a sailboat

regatta it is then possible to keep the wind out of a competitor's sails for a while by maneuvering between him and the wind. Figure 1 indicates, however, that there is a limit as to the distance within which a worthwhile effect can be obtained.

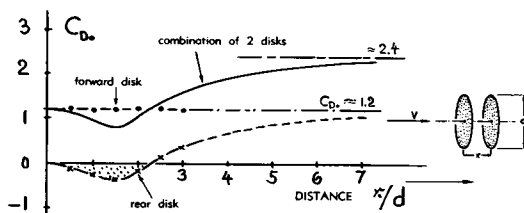


Figure 1. Interaction between two disks placed one behind the other; (reference 1,a).

Circular Cylinders. At the Reynolds number $R_d = 10^5$, the flow pattern of a cylinder is expected to be separated; and the first of the two cylinders in figure 2, correctly shows corresponding drag coefficients. The fact that its drag is decreased within a certain range of distance (particularly at $x/d \approx 2$), can be explained by assuming that the formation of the vortex street (see page 3-6) is reduced by the presence of the second cylinder. — The boundary layer of the rear cylinder is evidently made turbulent by the broad wake coming from the first cylinder, thus producing a supercritical flow pattern with a correspondingly small drag coefficient.

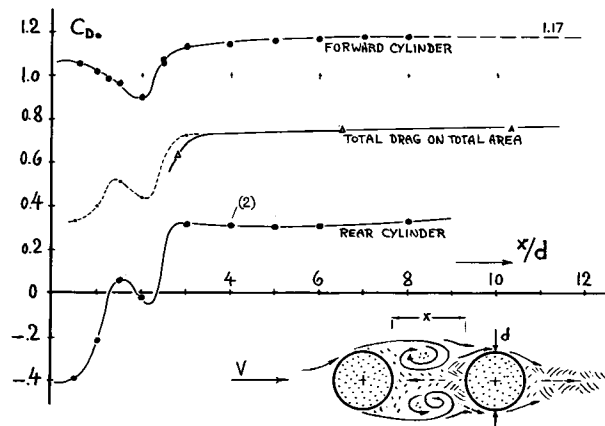


Figure 2. Drag coefficients of two circular cylinders, one placed behind the other.

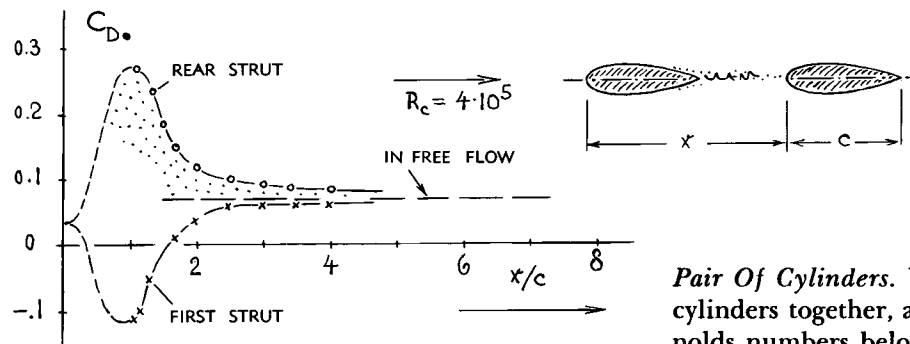


Figure 3. Drag of a pair of strut sections, one behind the other, in tandem (2,a).

Tandem Struts. Interference between the two struts in *figure 3* is basically different from that of the bluff bodies, considered so far. The drag of the rear section is increased (up to fourfold at $x/c \approx 1$). We have to assume that the flow separates from the rear of the second strut because of the momentum deficiency within the wake coming from the first strut. The fact that the drag of the first section is decreased is explained (2) by increased static pressure between the two struts pushing the first one forward, so to speak.

Pair Of Cylinders. Upon bringing a pair of circular cylinders together, as in *figure 5*, their drag (at Reynolds numbers below transition) increases somewhat upon reducing the clearance distance to $y/d = 1$. Below this distance, the pattern of the vortex street switches from that of a pair (originating separately from each cylinder) to a combined system (2,b). Note that the Strouhal number (see page 3-6) reduces from " S " = 0.21 to ≈ 0.10 at $y/d \rightarrow 0$. Upon referring the frequency of the pair of cylinders to their combined "height" of "2 d", the "0.1" transforms into "0.2" as approximately for a single cylinder. The graph also shows that the drag coefficient passes through a minimum, at $y/d \approx 0.9$. We can assume that the amplitude of the vortex street is reduced in this case by way of interference with the jet emanating from the gap between the two solids.

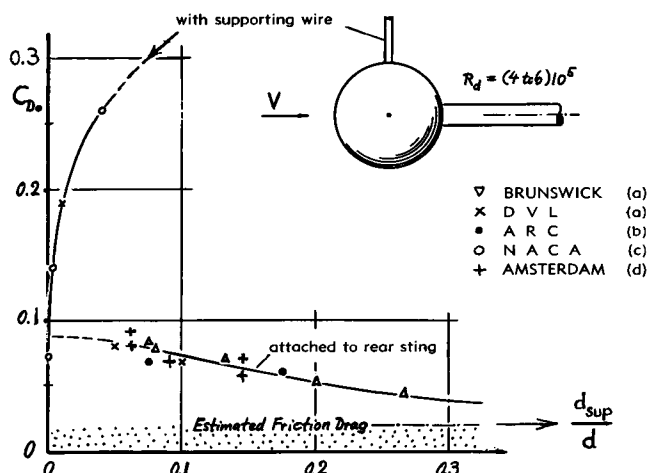


Figure 4. Drag of spheres at supercritical Reynolds numbers, affected by the presence of supporting devices (3).

Sting Support. Examples of favorable interference by placing one solid behind another one, are given in the "pressure drag" chapter (splitter plate and similar devices in *figure 3-8*). Another example is shown in *figure 4*. A "sting", supporting a sphere (tested at Reynolds numbers above transition), fills out the space of the wake, so to speak. As the diameter of this sting is increased, the flow attaches more and more completely to the rear of the body. The final drag coefficient, estimated to be in the order of 0.02, merely represents the skin-friction drag of the sphere.

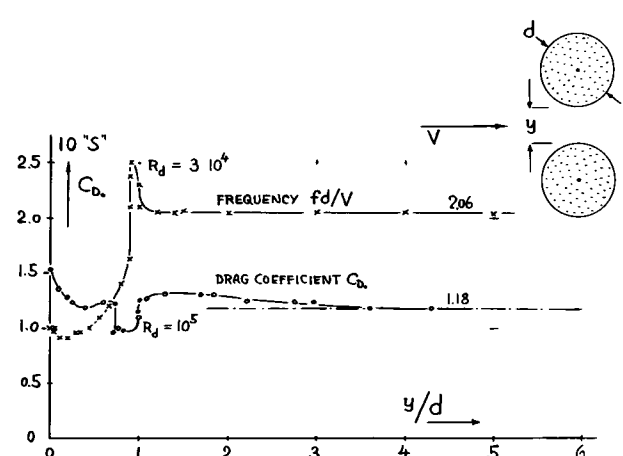


Figure 5. Drag (2,a) (and vortex-street frequency, reference 2,b) of a pair of circular cylinders placed side by side.

Pair Of Struts. Past the sides of round or streamline shapes, the average velocity (just outside the boundary layer) is always increased. In case of the pair of strut sections in *figure 6*, the positive pressure gradient along the rear, automatically associated with that increase of velocity, is evidently responsible for a considerable increase of the drag coefficient, particularly below $y/t = 1$. The two sections form a nozzle between them whose expansion ratio increases as their lateral distance is reduced. The flow through this nozzle separates as the clearance approaches zero.

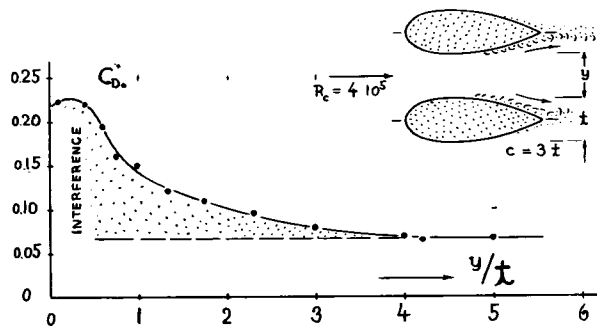
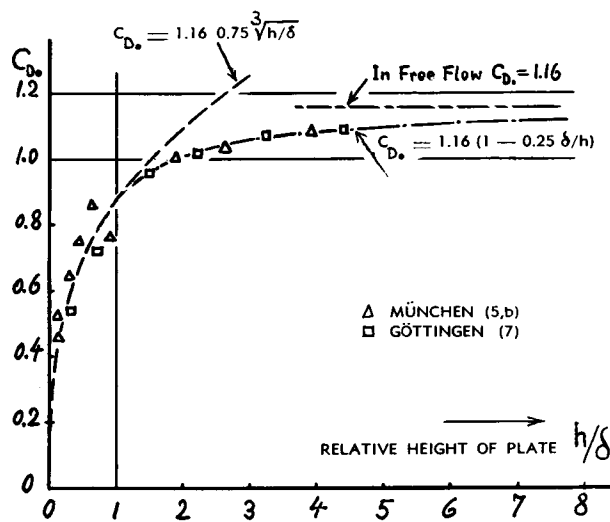
Figure 6. Drag of a pair of struts, one beside the other (2,a).

Figure 7. Drag coefficient of square plates attached to a plane wall, as a function of their height in comparison to boundary-layer thickness.

2. DRAG OF HALF BODIES ON WALLS

The drag of bodies attached to plane (or other) walls, is similar to that of surface protuberances as presented in Chapter V. In comparison to them, the size of the half bodies considered in the following paragraphs is usually much larger, however. This is especially true of aircraft appendages, such as canopies, armament turrets and similar component parts, which may be added to the outer surface of fuselages or wings.

Effective Dynamic Pressure. As a simple case, the drag of a small plate or disk is considered first, attached to a plane wall. Plates in three-dimensional flow have a comparatively constant flow pattern; and their drag adjusts itself to the local average or effective dynamic pressure to which they are exposed. For plate sizes, small in comparison to the thickness of the boundary layer, the effective dynamic pressure is given in equation 9 of the chapter on "surface imperfections". Considering, however, bodies which are higher than the boundary layer, only their bottom is exposed to reduced dynamic pressure. The loss of momentum can, therefore, be considered to be concentrated in a thin sheet. In turbulent flow, the thickness of this sheet is in the order of $y/\delta = 0.25$. Hence the effective dynamic pressure:

$$q_e/q_f = 1 - 0.25 (\delta/h) \quad (1)$$

Figure 7 confirms this calculation. Based upon the effective dynamic pressure, circular and square plates, attached to a plane wall, show "independent" drag coefficients C_D , which (on the average) are of the same magnitude (≈ 1.17) as known under free-flow conditions. An average rough value for the thickness of the boundary layer originating along the surface of aircraft (including some surface imperfections) is

$$\delta \approx 0.02 x; \quad \text{or} \quad \delta/x \approx 2\% \quad (2)$$

with x = distance from the stagnation point of the respective body to the point where the plate (or any other part) is attached. Combining equations 1 and 2,

$$q_e/q_f = 1 - 0.005 (x/h) \quad (3)$$

Two Dimensional Plates. In the case of *two-dimensional* plates (strips) or similar protuberances, the formation of a vortex street is possibly prevented by the wall to which these bodies are attached. As found in (7), their drag coefficient is therefore in the order of $C_D = 1.25$, instead of 1.97 as found in free flow.

- (1) Interference between bodies one behind the other:
 - a) Eiffel, La Résistance de l'Air, Paris 1914.
 - b) Lange (DVL), Antenna Rods. ZWB UM 1238 (1944).
- (2) Drag of pairs of solids:
 - a) Biermann and Herrnstein, Interference Between Struts in Combinations, NACA T.Rpt. 468 (1933).
 - b) Vortex Frequency, J.Aeron.Sci. 1946 p.289.
- (3) Drag of spheres affected by supporting devices:
 - a) Hoerner, Experiments with Spheres (Brunswick and DVL), Luftfahrtforschung 1935 p.42.
 - b) ARC, Wind-Tunnel Turbulence, RM 1662 (1934).
 - c) Bacon-Reid, Spheres, NACA T.Rpt 185 (1928).
 - d) Nat.Luchtvaart Lab. Amsterdam Rpt A.950 1947.
- (5) Engelhardt, Aerody. Laboratory TH München:
 - a) Fuselage-Tail Interference, Rpts 1 and 3/1943.
 - b) Drag of Half Bodies on Walls, Rpt 5/1943.
 - c) Interference on Tail Surfaces, Rpt 4/1943.
 - d) Hoerner, Influence of Fuselage on Tail (5,a), Messerschmitt Rpts TB 54/1942 and 88/1943.

$$\frac{\text{DIAMETER OF DISK}}{\text{FUSELAGE DIAMETER}} = \frac{1}{3}$$

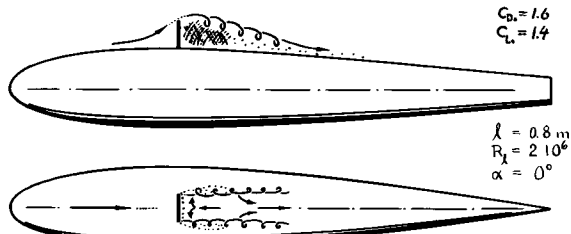


Figure 8. Flow pattern behind a disk attached to a fuselage body as observed in (5,a).

Flow Pattern Behind Added Bodies. The flow pattern behind a disk or any other single three-dimensional body attached to a wall or to the surface of a larger body, has a certain similarity to that of a low-aspect-ratio wing. The added body causes some "lift", directed away from that surface. A corresponding "downwash" and a pair of tip vortices are found behind the obstacle. Dead air might be sucked into the vortex cores. In case of figure 8, a lift was thus measured corresponding to $C_L = 1.4$ (based on frontal area of the added disk). Similar flow patterns and similar lift forces have been observed with other bodies too, as for instance in the case of streamline half bodies and automobiles over a ground surface (see figure 5 in the chapter on "vehicles").

Streamline Half Bodies. Available experimental results are plotted in figure 9, indicating the drag of streamline half bodies (such as canopies or fairings). The location "x" of the added bodies allows an estimate of the boundary-layer thickness. In the range of very low height ratios, up to $h/x = 2\%$ (that is approximately up to $h/\delta = 1$), the drag is proportional to the effective dynamic pressure as indicated by equation 9 of the chapter on "imperfections". Further agreement up to $h/x \approx 6\%$ seems to be coincidental only; rather equation 1 should apply. The suitable independent drag coefficient $C_{D_0} = 0.07$ is about twice as high as may be expected for such bodies in free flow (when restored to complete bodies of revolution). It is concluded, therefore, that the drag increment is due to interference along the base of these bodies. The drag coefficient reduces, however, above $h/x \approx 0.1$. Since the tests considered are made at Reynolds numbers well above transition, the drop of the drag coefficient cannot be explained on the basis of boundary layer turbulence. Rather the flow pattern of streamline half bodies seems to be governed by the thickness of the boundary layer along the wall where they are placed. Above $h/x \approx 10\%$, a flow separation, probably existing at the junction between wall and bodies, gradually disappears; and at height ratios beyond $h/x = 0.3$, or $h/\delta = 15$, the drag coefficient appears to approach the magnitude of 0.03 as known for corresponding bodies in free flow.

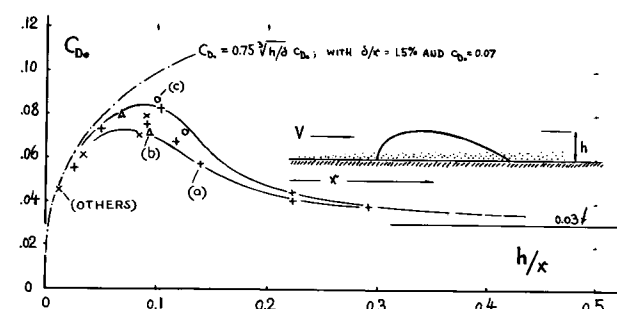


Figure 9. Drag of streamline half bodies placed on a plane wall as a function of their height ratio (6).

Optimum Shape Of Fairings. During the development of an airplane, its outside dimensions usually prove to be too small in some places, because of additional equipment to be built in or to be attached to fuselage or wing. Fairings are placed over these points and parts. The drag of such fairings (bumps or blisters) is a function of their fineness ratio l/h ; as shown in figure 10. Contrary to bodies in free flow, the total wetted surface of the combination of half-body and wall increases but slowly with the fineness ratio (because of that part of the wall which is covered by the body). Approximately only 1/3 of the *First* term of equation 31 in the "streamline" chapter is effective, therefore. Assuming $C_f = 0.004$, the drag coefficient of fairings with higher fineness ratios is thus approximately

$$C_{D_0} = 0.5 C_f (l/h) = 0.002 (l/h) \quad (4)$$

As indicated in figure 10, the optimum length ratio of such fairings is at least $l/h = 10$. This value is between two and three times the corresponding optimum fineness ratio in free flow, which is $l/d = 0.5 \times l/h \approx 2$. Further evaluation of the results in (5,b) indicates that the optimum length ratio (on a plane constant-pressure wall) decreases as the height ratio h/δ is increased beyond the values as plotted in figure 10, possibly approaching $l/h \approx 4$. Figure 11 proves

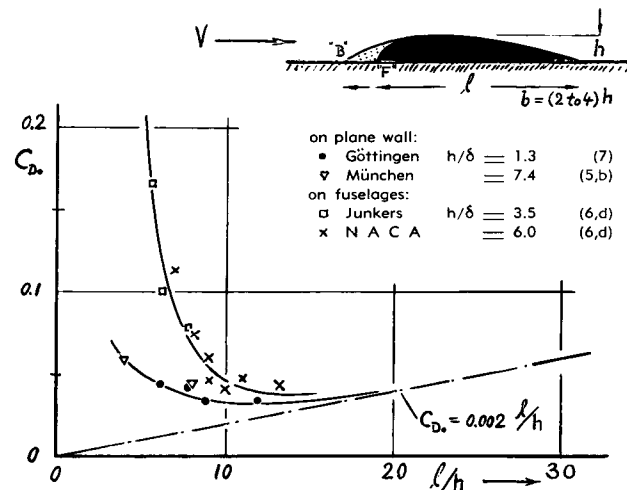


Figure 10. Drag coefficient of fairings (blisters) as a function of their length- or fineness ratio.

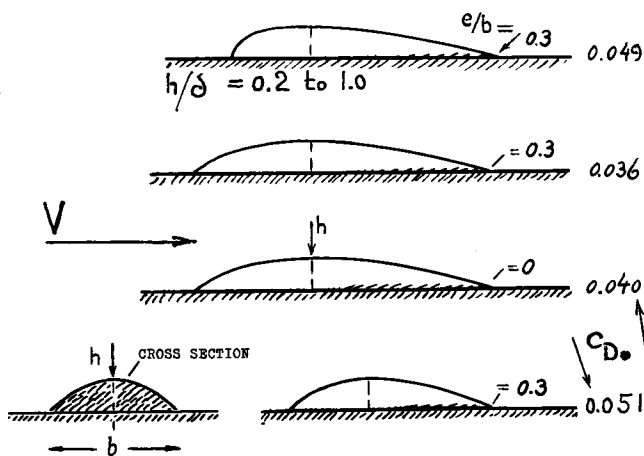


Figure 11. Independent drag coefficients of various forms of fairings (blisters) on plane wall.

that it is also favorable to lengthen (and to flatten) the forebody of the fairings considered, thus avoiding separation ahead of their noses. The minimum coefficient is in the order of $C_{D_0} = 0.03$.

Width Of Trailing Edge. The findings of the preceding paragraph are amplified in figure 12. The drag of body "D" (with pointed rear end) is somewhat reduced after broadening the rear to a trailing edge having a width in the order of $e/b \approx 0.3$. Such a shape has an effect similar to that of a fairing along the lateral edges of the afterbody.

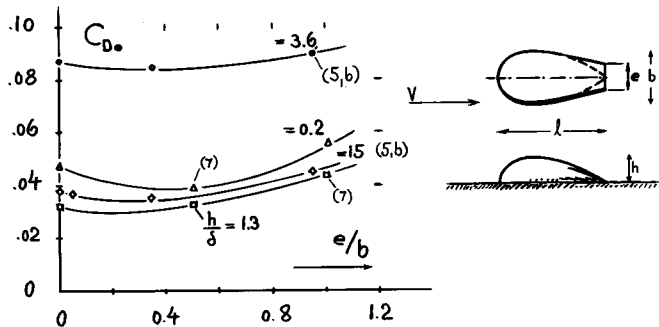


Figure 12. Drag coefficient of streamline shapes on a plane wall as a function of the width of their trailing edge.

(6) Drag of streamline shapes attached to walls:

- See reference (5,b).
 - Küchemann, Goettingen Rpt AVA 1945/A/13.
 - Schmid, Characteristics of Automobiles, Deutsche Kraftfahrtforschung (VDI) Heft 1, 1938.
 - "Others": Reference (7); AVA Rpt 35/41; Messerschmitt Rpt Me-410/11/1943; Junkers Rpt D. 6725; Heinkel Rpt WK 27; NACA T.Rpt 730.
- All these tests are on fuselage bodies. Results as plotted in figure 9 have been reduced to plane-wall conditions.
- Wieghardt, Drag of Surface Protuberances, ZWB Rpt FB 1563 and Yearbk. D.Lufo 1943; supplemented by Tillmann, Rpt K.W.Institut Göttingen 1944.
 - Hoerner, Interference Drag on Three-Dimensional Bodies, German Document ZWB UM 7818.

3. DRAG ON THREE-DIMENSIONAL BODIES

A larger or main body (subscript "m") shall be considered in this section to which smaller parts (primarily disks) are attached or added (subscript "a"). Analysis (9) of experimental results consists of two steps; determination of the drag of the added body, as affected by the main body, and determination of the additional drag arising along the rear of the main body, owing to the presence of the added body.

Drag Of Added Body. Basically, the drag of the added body corresponds to the local dynamic pressure (measured just outside the boundary layer) at the respective place on the surface of the main body. This local pressure is determined either by static-pressure distribution tests or through application of theoretical methods.

$$q_\lambda/q = 1 - (\Delta p_\lambda/q) \quad (5)$$

Taking into account both, the local dynamic pressure and the effective ratio within the boundary layer as per equation 1, the dynamic pressure responsible for the drag of an added body such as plate or disk, is

$$q_e/q = (q_\lambda/q) (q_e/q_\lambda) \quad (6)$$

Boundary-Layer Thickness. The growth of the boundary layer along the forebody surface of a three-dimensional solid is similar to that on a plane wall. Along the afterbody, the growth is stronger, however, by mere geometrical reasons. The volume of the layer in the vicinity of the maximum body thickness is transferred from its annular cross section to that of a circle at the rear end of the body. The radius of this circle is, of course, much greater than the thickness of an annulus containing the same area. Therefore, at the tail of an airplane fuselage (for example), equipped with the "usual" number of appendages and surface imperfections, there is a boundary-layer circle comprising an area almost as large as that of the maximum cross-sectional area of the fuselage itself. The geometrical increase of the boundary layer can be approximated by

$$\delta/(0.02 x) = d/d_x \quad (7)$$

where d = maximum diameter and d_x = local diameter at the station x considered on the afterbody.

Buoyancy Effect. In wind tunnels, the drag of longer models is known to depend upon the static pressure gradient prevailing along the axis of the test section. For instance, a positive gradient (that is, pressure rising in the direction of flow) decreases the pressure

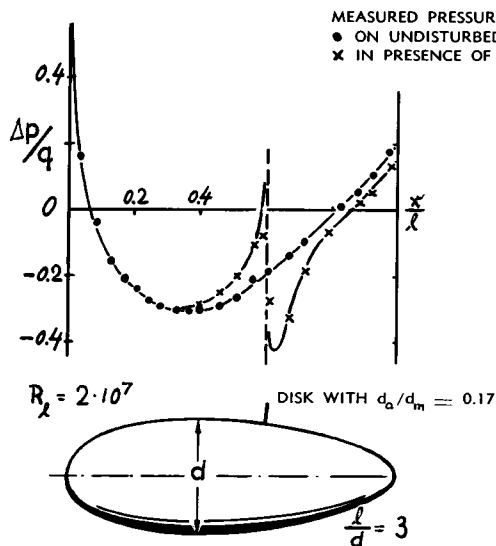


Figure 13. Influence of small disk on pressure distribution along the meridian of streamline body (10).

drag of the tested body; higher pressure affects the rear of the body, thus giving a "horizontal buoyancy" (similar to the vertical buoyancy of a body floating in water). The same effect is present in the case of the disk illustrated in figure 13. Two pressure distributions appear superimposed to each other, the one prevailing on the surface of the main body, and that due to the flow pattern of the disk. The apparent drag of this disk is consequently noticeably lower than that corresponding to the local dynamic pressure (equation 5). The differential due to buoyancy is proportional to the pressure gradient and the volume of the body. In the case of a thin plate, a certain dead space behind the body must be considered as 'volume'. The pressure is transferred through this space to the rear surface of the plate. The experimental results in figures 13 and 14, can satisfactorily be explained assuming such a space having a length four times the height or the diameter of the disk employed. From $\Delta p = 4 d_a (dp/dx)$ indicating the pressure differential on the surface of the undisturbed main body (measured between the disk and the back of the dead space) it follows that the drag due to buoyancy is

$$\Delta C_{D_b} = -\Delta p/q = -4 d_a d (p/q)/(dx) \quad (8)$$

When a certain positive or negative drag force, respectively, due to buoyancy originates on the *added* body, then by reasons of energy or momentum, a corresponding force of the same magnitude, but pointing in the opposite direction, may be expected to be present on the *main* body. This pair of internal forces does not per se affect the total drag of the combination, however. In the end, only drag components resulting from a change of flow pattern (separation) are of interest, either on the main or on the added body.

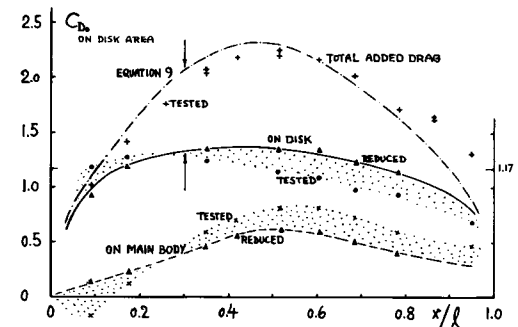


Figure 14. Drag of and due to small disk (as in figure 13). Coefficients on frontal area of disk.

Drag Of Added Body. The drag coefficients of the disk in figure 13, are plotted in figure 14; and they are compared with a calculation as per equations 3 and 6, using a basic coefficient of $C_{D_b} = 1.17$. After allowing for the differential due to buoyancy (equation 8), agreement is found between experiment and calculation. Equation 8 cannot be generalized, however. The flow pattern of a small streamline body, for example, added to the main body, may easily be changed by pressure gradient and boundary layer (figure 9) so that its drag may be increased.

Interference On Main Body. As seen in figure 13, the static pressure on the surface of the main body is noticeably decreased behind the added disk. The main body thus presents an additional pressure-drag component. As mentioned above, part of this drag is an internal force. The rest, however, is the net interference drag caused by the added body on the main body. Figure 14 shows that this component of drag is largest in the vicinity of $x/l = 0.5$. For this location, the positive pressure differential to be overcome by the boundary layer toward the stern of the body, is at its maximum. Ahead of $x/l = 0.5$, the interference drag is considerably smaller. The negative pressure gradients, prevailing along the forebody, evidently eliminate to a great extent the disturbance caused by the added body.

Pressure Gradient. The interference drag is thus related to the pressure gradient. Analyzing some more experimental data (9), an empirical function is tentatively as follows:

$$\Delta D_m/D_a = 1.6 (\Delta p_x/q)^2 / (\Delta x/l) \quad (9)$$

where Δp_x indicates the static pressure difference between the trailing point of the main body and the location x at which the added body is placed; $\Delta x = (l - x)$ denotes the distance between these two points. The interference drag of the main body approximately increases as the square of the pressure

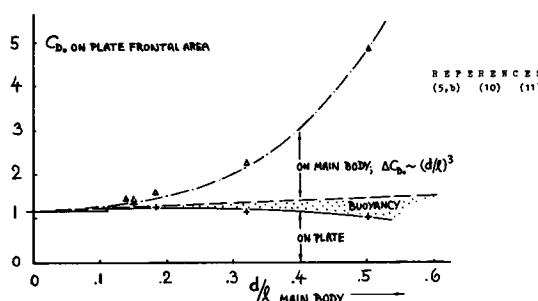


Figure 15. Drag caused by small plates or disks attached at $x/c = 0.5$, as a function of main-body thickness ratio.

difference Δp ; it decreases, however, as the distance Δx is increased. — Equation 9 does not describe very well the interference drag in positions near the stern of the main body (see in figure 14). The added disk obviously affects the boundary layer of the main body by way of increased static pressure (stagnation) ahead of its location. This influence can be taken into account by applying equation 9 for effective positions of the disk ahead of the physical locations by $\Delta x \approx 2 d_a$.

Thickness Ratio. Bodies of revolution show pressure gradients $\Delta p/q$ which, for a certain location x/l , are approximately proportional to their (thickness ratio) $^{3/2}$. The term $(\Delta p_x/q)^2$ in equation 9 is consequently proportional to $(d/l)^3$ and the interference drag may thus be expected to vary accordingly. The few available test points plotted in figure 15, for the location $x = 0.5 l$, confirm the prediction. In case of plain fuselage bodies, with d/l in the order of 0.1 to 0.2, the interference drag is thus comparatively small, in the order of 10% of the drag of the added body. It must be remembered, however, that the drag of the added body may already be increased on account of the aerodynamic influence of the main body, as illustrated, for example, in figure 9. In comparison to the undisturbed drag of a corresponding body in free flow, the total interference drag can therefore be appreciable.

Drag Due to Turbulence. So far, only fully turbulent boundary layer flow has been considered. In positions near the nose of the main body, additional interference drag may arise, however, when the boundary layer (originally still laminar in this region) is rendered turbulent upon adding a small body. For example, such an additional drag increase is found in figure 16, ahead of $x/l = 0.3$; see also (11,g). As mentioned in the "friction" chapter, turbulence spreads behind any spotlike obstacle at an angle of approximately two times 10° . With $2(\tan 10^\circ) \approx 0.3$, the affected triangular area is, therefore, $\Delta S = 0.5 \cdot 0.3 (x_{trans} - x)^2$, where "trans" indicates the original location of the transition line of the boundary layer. Using a differential value between turbulent and laminar skin friction in the order of $\Delta C_f = 0.003$, the additional interference drag due to turbulence is estimated to be

$$\Delta D/q = 0.15 (x_{trans} - x)^2 \cdot 0.003 = 0.00045 (x_{trans} - x)^2$$

The smaller the added body, the higher is the drag coefficient if referred to its frontal area S_a ; thus:

$$\Delta C_D = 0.00045 (x_{trans} - x)^2 / S_a. \quad (11)$$

As shown in figure 17, this type of drag is not of practical importance in added bodies such as plates, at $S_a/S_m = 2\%$. Considering, however, added streamline bodies as illustrated in figures 9 through 12, with drag coefficients in the order of but 0.04, the limit of importance in relation to the basic drag of the added body, may be in the order of $S_a/S_m = 10\%$. In other words, in small sizes, added bodies (such as a rivet head, for illustration) can cause interference drag many times as great as the basic drag of the added body itself.

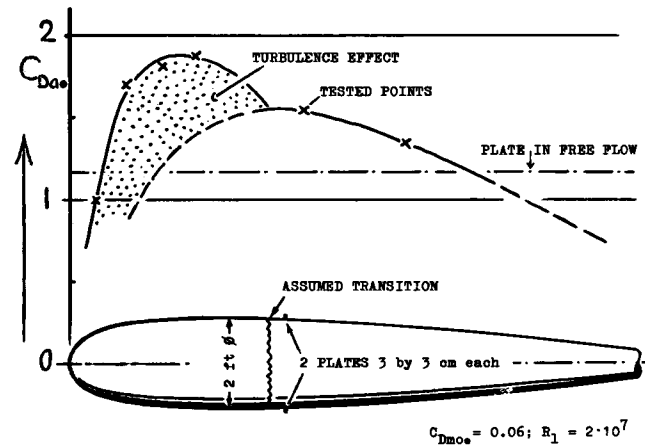


Figure 16. Coefficient (on plate area $S_a = 2 \text{ times } 9 \text{ cm}^2$) of the drag due to a pair of square plates added to a streamline body (11,a) as a function of location.

(10) Ower, Aspects of Mutual Interference Between Parts of Aircraft, ARC RM 1480 (1932).

(11) Interference drag of fuselage bodies:

a) From Messerschmitt Wind Tunnel (1943).

b) Fuselage with Canopy, German Doct AVA 1935/41; this canopy is also evaluated in the "aircraft" chapter.

c) Schoenherr and Reichel, Flight-Test Determination of the Drag of Me/109 Fuel Tank, Messerschmitt Rpts 109/05/L/1944.

d) Armament Turret, Junkers Rpt D.6725.

e) Obenauer-Hoerner, Me-210 Model; ZWB UM 7809.

f) ARC, Windscreens on Fuselage, RM 2235 (1940).

g) Tests on an airship hull similar to those in (a) are reported in NACA T.Rpt 451 (1932).

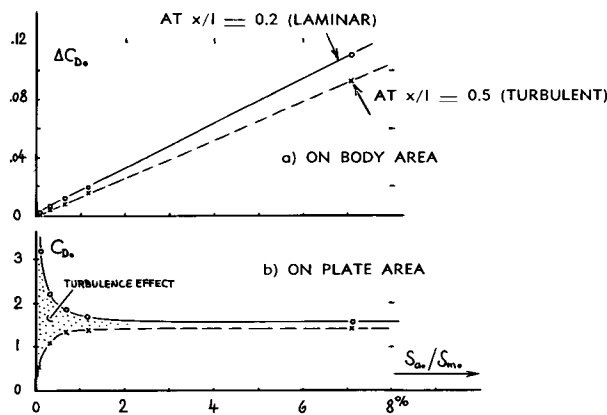


Figure 17. Drag of and caused by two small plates as in figure 16, as a function of their size.

Examples. Knowledge on interference drag of three-dimensional bodies, acquired so far, is employed in the following paragraphs to check several experimental results on fuselage bodies. Doing this, the intention is not to verify the calculation; the available data are too incomplete for this purpose. Rather, method of calculation and order of magnitude of interference drag shall be demonstrated by analyzing tested results.

(a) *Fuselage With Canopy* (11,b). A smooth fuselage body with $d/\ell = 0.12$ and $C_{Dm} = 0.081$ at $R_\ell = 5 \cdot 10^6$, has a smooth canopy with $S_a/S_m = 0.11$ and $h/x = 0.1$, attached to the main body at $x/\ell = 0.33$; $\Delta x/\ell = 0.67$. The drag coefficient of the canopy is estimated through the use of figure 9 to be in the order of 0.07, if attached to a plane wall. The local dynamic pressure ratio at the location of the canopy is estimated to be $q_1/q = 1.07$; the drag coefficient of the canopy is thus $C_{Da} = 1.07 \cdot 0.07 = 0.075$. The pressure difference between canopy location and the rear end of the main body is approximately $\Delta p_x/q = 0.13$. Using equation (9) the increment $\Delta D_m/D_a = 1.6 \cdot (0.13)^2 / 0.67 = 4\%$. The total drag of, and caused by the canopy is thus $C_{Da} = 1.04 \cdot 0.075 = 0.078$. With the canopy in place, a coefficient (based on frontal area of main body) of 0.089 was tested. Based on canopy area, this result indicates a $C_{Da} = (0.089 - 0.081) / 0.11 = 0.073$. In comparison to the drag of the canopy attached to a plane wall (figure 9), the interference drag is but 11%, in this example.

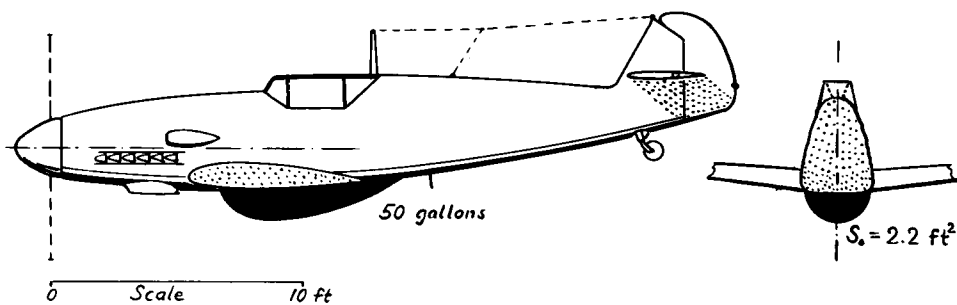
However, in free flow, the drag of the canopy body (completed to an integral body of revolution) may only be $C_{Dc} = 0.04$. Compared to this value, an interference drag is found in the order of approximately 80%, most of which arises on the added body itself. Similar results can be derived from data in (11,f) where the drag of, and due to a canopy (exhibiting a "step" in its contour) is found to correspond to $C_{Da} = 0.11$.

(b) *Fuel Tank of Me-109 Fighter* (11,c). An additional fuel tank attached to the fuselage of the Me-109, is illustrated in figure 18. The additional dynamic pressure and the static pressure gradient subsequently following along the surface of slender fuselage bodies, are usually only small. Tentatively estimating for the location of the belly tank as in the illustration, a $C_p = -0.1$ and a pressure differential $\Delta p_x/q = 0.2$, a drag coefficient is obtained in the order of $C_{Da} = 0.1$. The actual drag of the, and caused by the tank, determined by several flight tests, is larger, however, than corresponding to this coefficient. It is therefore concluded that super-velocity and negative pressure transferred from the wing roots to the location of the tank under the fuselage, must be taken into account. At $C_L = 0.15$, as during the flight tests, the minimum pressure on the lower side of the wing section is in the order of $C_p = -0.4$, due to thickness ratio. Assuming half of this value to be transferred to the location of the tank, the pressure ratios are now $C_p = (-0.1 - 0.2) = -0.3$ and $\Delta p_x/q = 0.2 + 0.2 = 0.4$. Taking as the basic drag coefficient of the tank body for $h/x = 9\%$, from figure 9, a value of 0.08, a $C_{Dc} = 1.3 \cdot 1.4 \cdot 0.08 = 0.15$ is finally obtained. Considering an additional effect due to propeller slipstream, the calculated coefficient satisfactorily corresponds to the tested difference in maximum speed of the Me-109 of $\Delta V = -8$ mph, at an original speed of approximately 300 mph near sea level. The drag coefficient of the tank evaluated from flight tests is $C_{Dc} = 0.16$.

(c) *Gun Turret* (11,d). In case of the Me-109, the added body is at a sensitive place of the main body. Contrary to this condition, figure 19 shows an example where the drag due to an added body is very low. The explanation is as follows: Immediately

Figure 18. Tank under the fuselage of Me-109 (11,c).

ME-109 DATA:		
WING	S	= 172 ft
SPEED SL	V	= 320 mph
DRAG C_D = 0.028		
TANK DATA:		
LENGTH	l	= 7 ft
HEIGHT	h	= 1.2 ft
WIDTH	b	= 2.5 ft
LOSS	ΔV	= -8 mph
DRAG	C_D	= 0.16



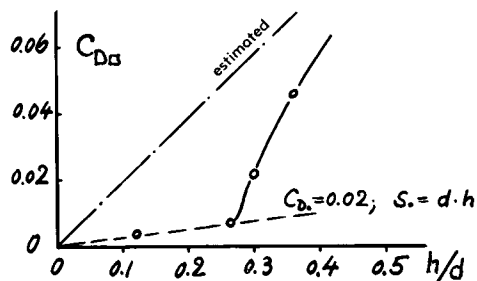
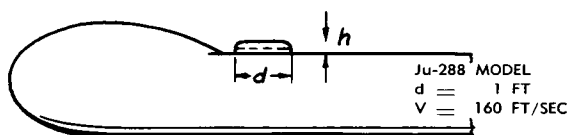


Figure 19. Drag coefficient on area ($d^2\pi/4$) of and due to a "turret" placed behind the crew's compartment of a fuselage (11,d).

behind the cabin of the airplane, there is a region with low dynamic and high static pressure, corresponding to negative curvature of the streamlines. Putting correspondingly favorable values into equations 5 and 9, drag values may be found as low as they were tested (down to $C_{D_a} = 0.02$). With increasing height, the turret emerges, however, from the favorable region; its drag coefficient then increases at a much greater rate.

Interference Method. Calculation of interference drag due to added bodies as described in this section, is somewhat complicated. A simple method of determining this type of drag can be applied, however, in cases where wind-tunnel models (of airplanes, fuselages, nacelles) are tested for drag. Small square plates are attached, in a position normal to the local flow, at proper places on the surface of the model. The drag of and due to these plates is determined and compared to their free-flow value corresponding to $C_{D_a} = 1.17$. If testing in this manner $C_{D_a} = 2.34$, for example, the sensitivity of the place investigated is characterized by the ratio $2.34/1.17 = 2.0$. It is

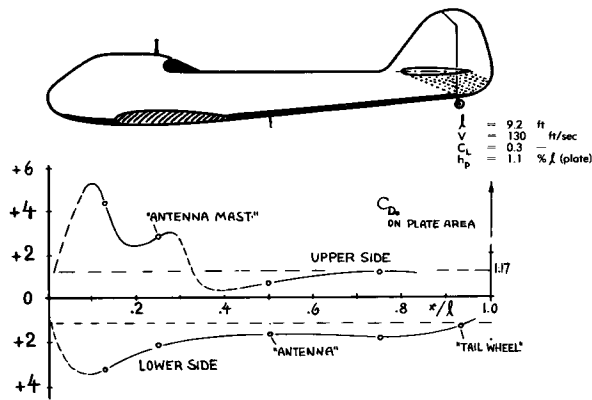


Figure 20. Drag coefficient of and due to a small plate attached to various points of a fuselage (11,e), as shown.

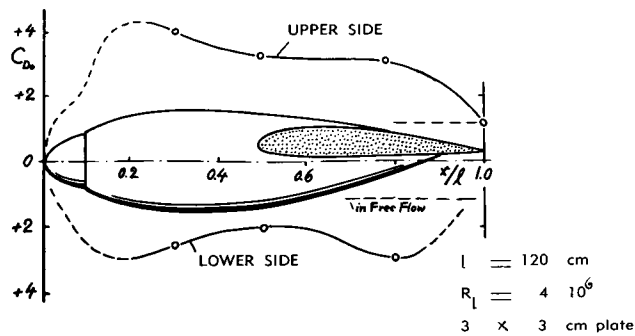


Figure 21. Drag of and due to a plate at various points on the meridian of a nacelle (11,e) at $C_L = 0.3$.

then concluded that other added bodies such as bumps, attachments or armament parts, will also cause a drag that is two times their own basic drag (which may be affected in turn by the conditions on the wall of the main body). Testing in this manner typical bodies such as wings, fuselages or nacelles, data are collected which may generally be used when considering the parasitic drag of airplanes. Figures 20 and 21 present some values indicating the sensitivity of various locations on the surface of fuselage- and nacelle bodies. The most sensitive spot on the fuselage is that on top of the cabin, with $C_{D_a} = (3.9 \cdot 1.17) = 4.5$. The least susceptible point of this body is behind the cabin, where C_{D_a} is estimated to be as low as $(0.3 \cdot 1.17)$. Such a value indicates negative interference drag. The nacelle (in figure 21) is generally more sensitive than the fuselage. Maximum values C_{D_a} between 3 and 4 are reached in some places.

Long Attachments. Long bodies attached to the outside of airplanes, such as antenna rods, landing-gear legs or any type of struts, affect the flow pattern past the main body only by a limited part of their length (close to the main body's surface). The outer ends of such attachments, including for example the wheels of a landing gear, do usually not affect the aircraft body to which they are connected. To study the influence of such attachments, the combination in figure 22 was tested in a wind tunnel (5,b). In

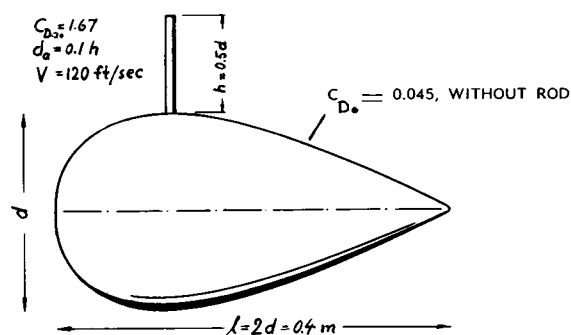


Figure 22. Basic test (5,b) showing the drag of and due to a piece of rod attached to a streamline body.

comparison to a free-flow value in the order of $C_D = 1$ (at a Reynolds number below transition), the rod causes a drag which is almost 1.7 times as high when attached to the comparatively thick main body. A circular-plate tested at the *same* spot had a drag ratio of $6.2/1.17 = 5.3$. Comparing the two ratios with each other, it is concluded that only about $1.7/5.3 = 0.32$ of the total length of the rod is responsible for interference drag. The value 0.32 means a length equal to about 16% of the maximum main-body diameter in figure 22. This value may thus be used as a rough rule, indicating the effective height of such added bodies when calculating their interference drag. Analyzing the drag of a sphere according to figure 4, suspended by a vertical wire, approximately the same result is obtained as from figure 22.

4. WINGS (STRUTS) AND WALLS

Interference drag also originates at points where wings, struts or tail surfaces join or penetrate the fuselage, or where different parts of the tail assembly join each other. As simplest case, the drag of a wing or strut joining a plane wall, is considered first.

Interference Drag in Corners. When a wing or strut adjoins a wall (or an end plate), the boundary layers of both, the wing and the wall join each other. Subjected to the pressure gradient along the rear of the foil section, the boundary layer is further retarded; and additional pressure drag (i.e., interference drag) arises. This type of drag is independent of the span of the respective wing or strut. The drag coefficient is, therefore, most suitably based upon the dimensions of the wing section, that is either on the "chord area" c^2 or the "thickness area" t^2 .

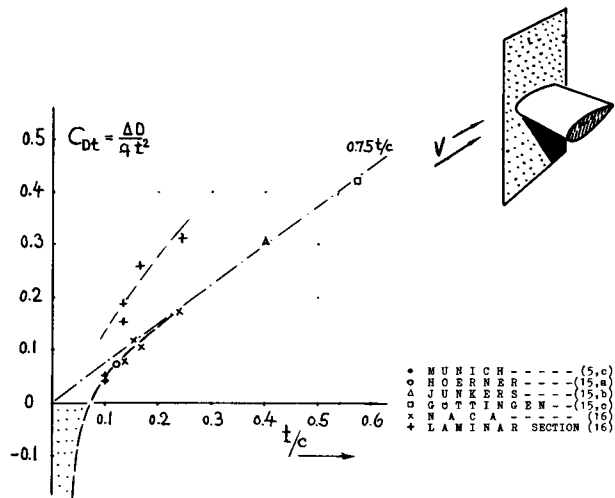


Figure 23. Interference drag originating at the junction of wings or struts with a plane wall.

Boundary-Layer Thickness. The interference drag originating from foil-wall junctions is expected to be a function of the thickness of the boundary layer at the wall. Experimental evidence on this question is not conclusive. Results in (5,c) suggest that the interference drag in thin sections (with $t/c \approx 10\%$) decreases as the b'layer is thickened (to a maximum of $\delta/c = 8\%$); most likely on account of the decreasing dynamic pressure prevailing within that layer. The experimental data plotted in figure 23 even suggest that the interference drag will be negative, at thickness ratios below $t/c \approx 8\%$. In a similar manner, figure 34 shows negative interference drag for the combination of a fuselage with a horizontal tail surface — when drag and boundary-layer thickness of the fuselage are increased by surface roughness. Investigation of a strut section (2,a) with $c/t = 3$ indicates, however, that the interference drag increases as the boundary layer at the location of the strut grows in thickness, at least up to $\delta/c = 3\%$. The points in figure 23 are valid for ratios in the order of $\delta/c = 10\%$, such as found, on the average, in wing-fuselage junctions. The results can be interpolated in the form of

$$C_{Dc} = \Delta D/qc^2 = 0.8(t/c)^3 - 0.0003 \quad (11)$$

indicating a value of $C_{Dc} = -0.0003$ for the flat plate (having $t/c = 0$). Referring the coefficient to the thickness area:

$$C_{Dt} = \Delta D/qt^2 = 0.75(t/c) - 0.0003/(t/c)^2 \quad (12)$$

as plotted in the graph. Reference (16) indicates that laminar-type sections (with maximum thickness at 50% of the chord) have higher interference drag coefficients than sections with $x/c = 30$ or 35%; see corresponding points in figure 23.

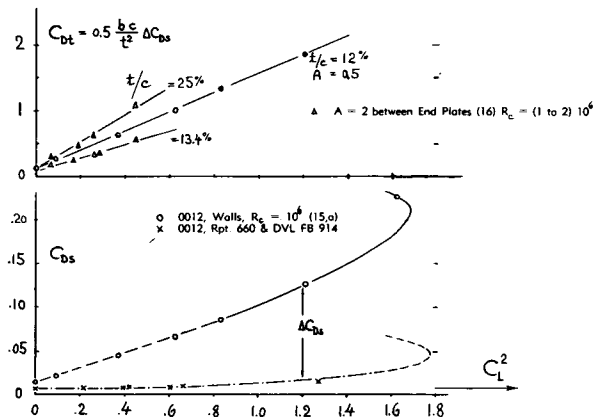


Figure 24. Drag of wings placed between two walls of a water tunnel (15,a) and between end plates (16), respectively; as a function of the lift coefficient.

Influence of Lift. Because of the lift which a wing adjoining a wall, may produce, the pressure gradient on the upper side of the junction is increased (and that on the lower side is somewhat decreased). Therefore, as shown in figure 24, total drag and interference drag appreciably increase with lift coefficient. In case of the 0012 foil, the span of the wing model is very small ($b = 0.5 c$). The coefficient C_{Dt} evaluated from the lower part of the graph, for one junction, is therefore somewhat larger than that of the 13.4% thick section which was tested at $A = b/c = 2$. At any rate, the interference drag approximately increases as the square of the lift coefficient.

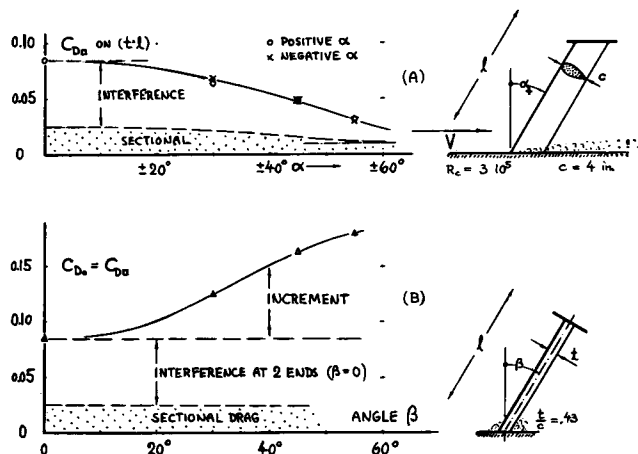


Figure 25. Total drag of the piece of strut as shown (17) as a function (a) of the angle of pitch and (b) of the lateral angle of inclination.

Inclined Struts. Figure 25 presents experimental results on a piece of strut, inclined against the wall (or end plate) to which it is joined. (a) Upon tilting the strut in longitudinal direction, the pressure-drag component decreases corresponding to the "cross-flow" principle (as explained on page 3-11). (b) When inclining the strut in lateral direction, its interference drag grows, most likely because of increased separation in the narrower one of the two corners.

- (15) Drag of foil sections between tunnel walls:
 - a) Hoerner, Fieseler Water Tunnel Rpt 5 (1939).
 - b) 40% Strut Section, Junkers V.1064(1941).
 - c) Drescher and Schwenk, Thick Sections in Water Tunnel, AVA Goettingen Rpt 1944/J/17.
- (16) Benson, Land and Havens, Struts Between End Plates in Towing Tank NACA Memo Rpt 1942.
- (17) Maxen, Wind Tunnel Tests on Struts joining a Wall (Plate), Yearb. D. Lufo 1940 p.I,599.
- (18) Interference drag in strut and foil junctions:
 - a) Kohler, Strut Junctions, Lufo 1938 p. 143.
 - b) ARC Tailplane (at $M = 0.5$), RM 2138 (1941).
 - c) NYU, Tests for Gibbs and Cox, Inc. 1952.
 - d) Hoerner, Tail Surfaces, ZWB UM 7812 (1942).

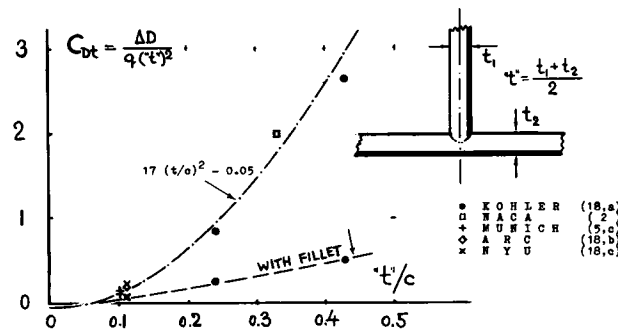


Figure 26. Interference drag coefficient (on area t^2) of wing- and strut sections; with and without fillets.

Strut Junctions. Upon attaching a wing (or a strut) to the fuselage at a place of positive pressure gradient, the interference drag must be expected to be increased over the values as indicated by equation 11. The same problem arises when putting together two foils in form of a "T", or crosswise, as is often done in tail surfaces with "end plates" attached to the tips of the horizontal part. The pressure gradients of the two foils evidently combine with each other in retarding the boundary layer. Another example of this type of interference is the junction between two struts. Such junctions, in the form of a "T", exhibit interference drag as plotted in figure 26. That drag can be approximated by

$$C_{Dt} = \Delta D / (qt^2) = 17 (t/c)^2 - 0.05 \quad (13)$$

or based on "chord area", by

$$C_{Dc} = \Delta D / (qc^2) = C_{Dt} (t/c)^2 \quad (13)$$

The negative term accounts for the reduced dynamic pressure within the boundary layers of the two struts. The interference drag (without fairing) is comparatively high. Assuming, for instance, a thickness ratio of $t/c = 0.3$, which is close to the optimum of strut sections in free flow, an interference drag is found as illustrated in figure 27. The drag originating from the junction of two such struts, is as great as that of a piece of strut having a length "b" equal to 10 times the strut chord.

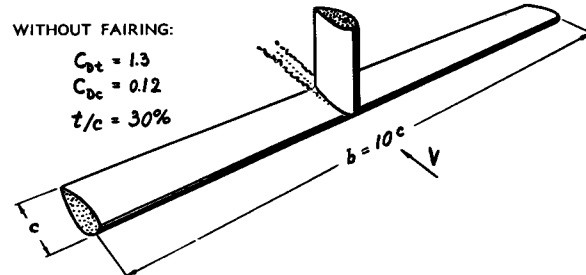


Figure 27. Demonstration of the magnitude of interference drag originating at the junction of two struts. The interference drag is as great as the original drag of the larger piece of strut.

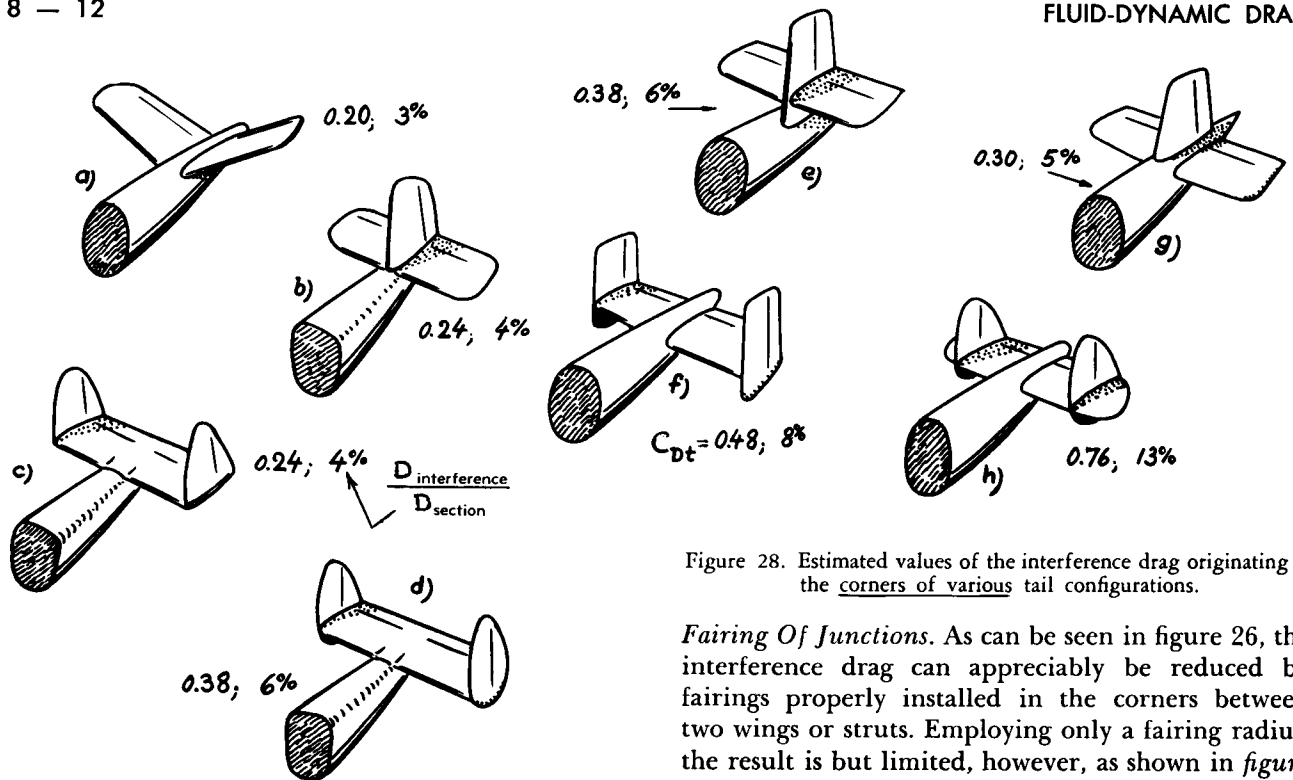


Figure 28. Estimated values of the interference drag originating in the corners of various tail configurations.

Tail Configurations produce interference drag at their junctions with the fuselage as well, as in the corners formed between their horizontal and vertical parts. The interference drag of the various types of tail configurations shown in figure 28 was estimated on the basis of the following data: Thickness ratio of the employed sections $t/c = 10\%$, aspect ratio of the horizontal surface $A_H = 4$, of the vertical surface $A_V = 2$, sectional drag coefficient $C_{Ds} = 0.01$. The drag originating on the fuselage walls was taken from figure 23 as $C_{Dc} = 0.05$ (t/c)² = 0.0005. For a two-corner foil junction, a value of $C_{Dt} = 0.14$ was taken from figure 26, thus giving for one corner a coefficient $C_{Dc} = 0.07$ (t/c)² = 0.0007. Using the two underlined values, the interference drag of the configurations illustrated in figure 28 was calculated corresponding to the number of corners in each case. This number varies between 4 and 12. The interference drag varies accordingly between 3 and 13% of the basic profile drag. Theoretically, the "V" type (number "a") is the optimum; there are only four corners on such a tail assembly, and these corners are at the fuselage. More common types having low interference drag are numbers "b" and "g". Configurations with "end plates", such as numbers "f" or "h", present the largest interference drag, because of the high number of corners. Moreover, the type "h", with the horizontal foil laterally extending beyond the vertical surfaces, is inefficient with respect to lift-curve slope too; the flow around the horizontal parts outside the end plates is disturbed on account of the two adjoining corners.

Fairing Of Junctions. As can be seen in figure 26, the interference drag can appreciably be reduced by fairings properly installed in the corners between two wings or struts. Employing only a fairing radius, the result is but limited, however, as shown in figure 29. The optimum radius is small, in the order of 4 to 8% of the wing chord. As shown in figure 30, the interference drag of a strut junction can thus be reduced to 10% of the unfaired configuration or less by means of a fairing extending one strut chord beyond the trailing edges. Fillets of this type have especially been developed for wing-fuselage junctions (24, a, b).

Junction Angle. In a manner similar to that in figure 25, the interference drag between two wings or struts increases as the corner angle is decreased from 90° . Using the optimum fairing radius as found in figure 29, the interference drag between a wing (or tail surface) and a profiled "end plate" is reduced by 20%;

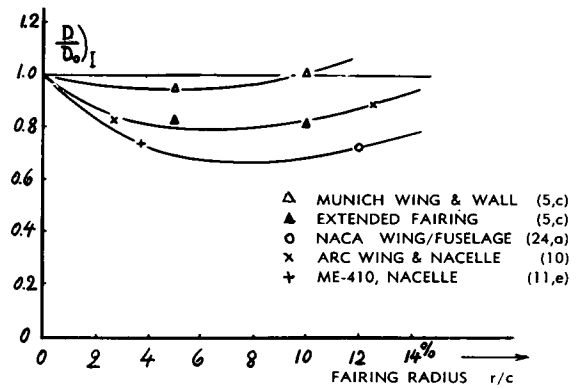


Figure 29. Interference drag in corners between wings or tail surfaces and walls, fuselages or nacelles, as a function of the fairing radius.

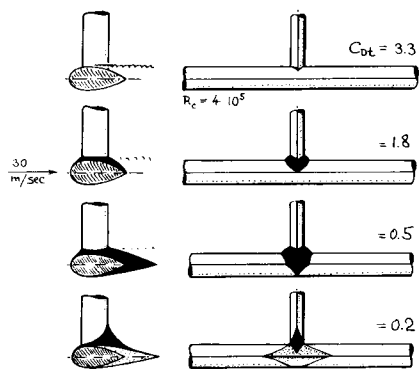


Figure 30. Influence of various fairings on the interference drag originating from the junction of two struts (18,a) having $t/c = 43.5\%$ each.

as shown by the experimental result in figure 31. Employing the round shape "c", the interference-drag coefficient appears to be negative, if using in the evaluation the original foil areas for reference (as in "a" or "b" of the illustration). Considering, however,

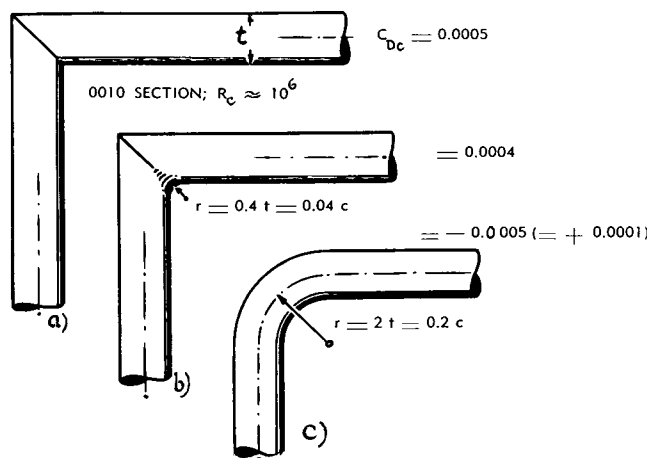


Figure 31. Interference drag originating in the corner where two wing or tail surfaces join each other (5,c).

- (20) Information on interference drag of wings:
 a) Jacobs, Airfoil Characteristics Affected by Protuberances, NACA T.Rpts 446 and 449 (1933).
 b) Hoerner, Interference Drag of Bodies Attached to Wings, ZWB Rpt UM 7844 (1945).
 (21) Induced interference drag in wings:
 a) Fuselage and Horizontal Tail, ref. (5,a,c).
 b) Junkers, Basic Tests on Body-Wing Interference, Rpt Stroete V. 7561 and V.7649 (1939).
 c) Muttray, Aerodynamic Combination of Wing and Fuselage (Longitudinal Plate) Lufo 1934 p.131 and Ringbuch Luftfahrttechnik Section I A 4 (1937).
 d) Abbott, Airship with Fins, NACA T.Rpt 394 (1931).
 e) Riley, Horizontal Tail, NACA T.Note 2907.
 f) NACA, Plate in Center of Airfoil, W.Rpt L-660.
 g) Huebner-Pleines, Glide Control, ZFM 1932 p.455.
 h) NACA, Pressure Distribution on Horizontal Tail, T.Note 1539; and in Wartime Rpt L-227.
 i) W.Rpt L-227 shows load distributions on the horizontal tail of the P-40 fighter. The "hole" in the center is ≈ 3 ft wide against 12.8 ft span ($\approx 25\%$) while fuselage width $\approx 10\%$ only.

that upon rounding the corner, the wetted surface of the configuration reduces, the positive but small interference-drag coefficient $C_{Dc} = 0.0001$ or $C_{Dt} = 0.01$ is obtained for shape "c" in figure 31.

5. INTERFERENCE DRAG ON WINGS

There are two types of interference drag originating on wings, first a parasitic component, corresponding to boundary layer and pressure losses, and second a component of additional drag, caused by derangement or interruption of the lift distribution due to an added body.

Parasitic Interference. The drag of, and due to protuberances placed spanwise on a wing has been evaluated from experiments (20,a) in a manner similar to that on three-dimensional bodies (section 3). The drag coefficient of such two-dimensional protuberances is approximately

$$C_{Dp} = D_p / (qS_a) = c_D \cdot (q_f/q) (q_e/q_f) \quad (14)$$

with c_D indicating the independent drag coefficient (based on effective dynamic pressure as explained on page 5-6). The interference drag arising at the rear of the wing section, corresponds (20,b) to location and pressure gradient in a manner similar to that as indicated in equation 9; hence

$$\Delta D_m/D_a = 0.4 (\Delta p/q)^2 / (\Delta x/c) \quad (15)$$

Calculations on the basis of the last two equations agree fairly well with the mentioned tests, for the upper wing side as well as for the lower one, and also at smaller as well as larger lift coefficients. Figure 32 gives an example of this statistical analysis at $C_L = 0.2$.

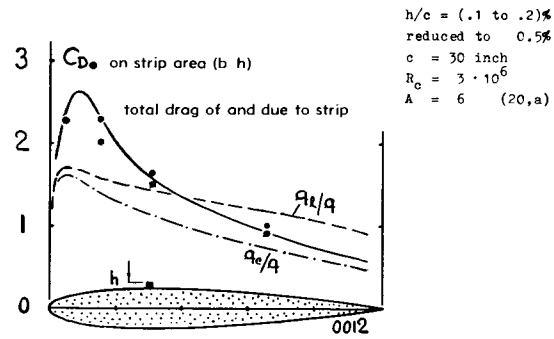


Figure 32. Coefficient (on projected strip area) indicating drag of and due to a square strip (20,a) placed along the span on the suction side of a wing.

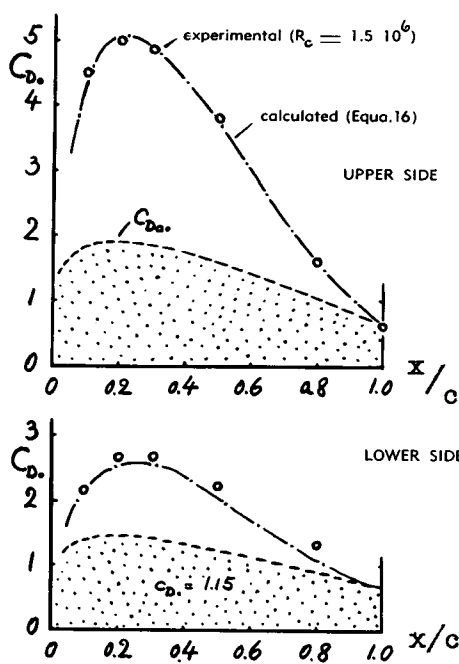


Figure 33. Experimental (11,e) and calculated drag of and due to a square plate having $h/c = 4.1\%$ on the Me-210 wing ($t/c = 15\%$; $A = 7.2$) at $C_L = 0.3$.

Isolated Protuberances. Figure 33 shows the drag of, and due to a small square plate placed on the upper and lower side, respectively, of a 15% thick wing. By statistical analysis of several tests (20,a), the following equation was found for the interference drag caused by such isolated protuberances on the rear of the wing:

$$\Delta D_m / D_a = 1.1 \cdot (\Delta p/q)^2 / (\Delta x/c) \quad (16)$$

The constant in this equation is smaller than that of equation 9 (for three-dimensional bodies), but greater than that in equation 15 (for spanwise protuberances). Figure 33 shows that the resulting drag coefficient,

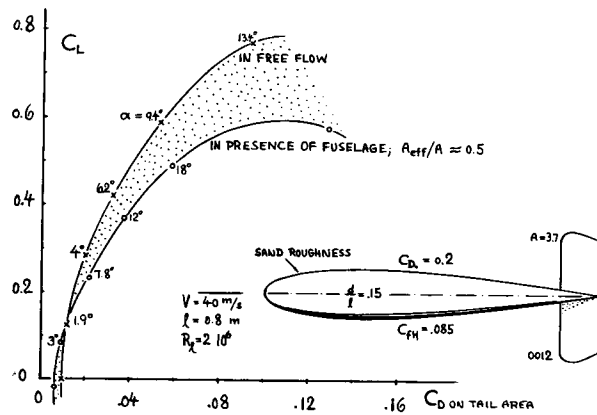


Figure 34. Drag of a horizontal tail surface as affected by the presence of the fuselage (5,a,d). Drag and lift coefficients are based on horizontal area.

based on the plate's frontal area, exhibits values up to 5, when placed on the suction side of this wing. This value is more than four times as high as the coefficient of the plate in free flow, and approximately five times as high as that on a plane wall (with a boundary-layer thickness equal to that on the wing surface).

Induced Interference Drag. Any bluff obstacle placed at a certain point of a wing, somehow changes the spanwise lift distribution. Provided that the change takes place in a direction away from the elliptical optimum of that distribution, the induced drag of the wing is consequently increased. This is without doubt the case if the disturbing bluff body is of such size that the lift distribution is more or less interrupted. The wing may then be compared to one having a longitudinal gap; and such a wing, "cut in two", has the characteristics of a pair of wings flying closely side by side as shown in figure 24 of the "drag due to lift" chapter. Their effective aspect ratio is reduced, and in the limiting case (with a sufficiently wide gap) lift- and drag forces correspond to the individual aspect ratios of the two wing parts.

Dynamic-Pressure Hole. An obvious example of "interruption" is found in the horizontal tail surface at the end of the fuselage. The "hole" in the distribution of the dynamic pressure within the wake of the fuselage is equivalent to a longitudinal gap as above. Lift distributions are presented in (21,h) showing a local reduction to approximately half the theoretical values at the junctions of a horizontal tail with the fuselage. Figure 34 demonstrates how the lift of a particular horizontal surface is reduced, accordingly, and how the drag due to lift is increased at the same time. Analysis of the lift curve slope (by way of $d\alpha_i/dC_L$) indicates that in this case most of the drag increment is of induced origin, rather than

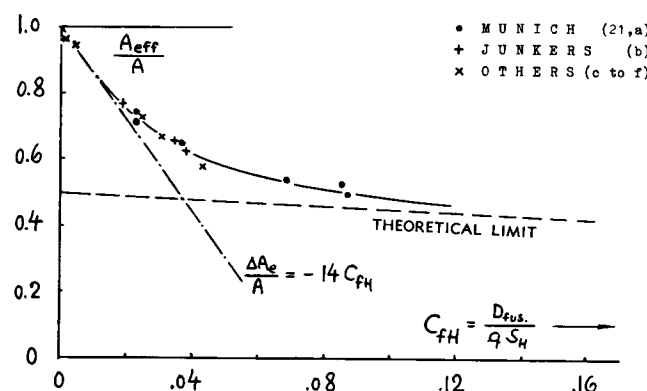


Figure 35. Influence of the fuselage (or other obstructions) upon the effective aspect ratio of the horizontal tail (or of a wing, respectively).

due to parasitic loss of momentum. — A measure for the size of hole or gap in relation to the dimensions of the tail surface, is the coefficient

$$C_{fH} = D_{fus} / (q \cdot S_H) \quad (17)$$

Figure 35 presents a number of points evaluated on the basis of tested "lift angles" ($d\alpha/dC_L$), indicating the ratio of the effective aspect ratio " A_i " as a function of C_{fH} . This type of interference is also evident in (21,f), where a thin friction plate is tested, placed at the suction side on the centerline of a wing. Up to about $C_{fH} = 0.015$, the effect can be approximated by

$$\Delta A/A = -15 C_{fH} \quad (18)$$

The induced drag is then

$$C_{Di} = (C_L^2/\pi A) (1 - \Delta A/A) \quad (19)$$

and (combining with equation 18) the increment of the induced drag, for small C_{fH} values, is found to be

$$\Delta C_{Di} \approx (C_L^2/\pi A) 15 C_{fH} \quad (20)$$

Some induced drag is also included in equation 16; analysis shows, however, that this component can only be in the order of 5% of the parasitic drag of the small plates investigated. It is concluded, therefore, that two cases must be distinguished in wing interference: One case due to small and isolated added bodies, behind which the flow closes-in again without really affecting the lift (equation 16); and the other one due to larger and/or chordwise extending protuberances, causing lasting separation at the suction side of the wing and a noticeable dent in the lift distribution (equation 20). It is also obvious that two-dimensional protuberances (as per equation 15) do generally not add to induced drag.

Horizontal Tail. The induced drag of horizontal tail surfaces is basically high, in so far as the tail has to "climb" within the downwash of the wing (as explained in the "due-to-lift" chapter in connection with tandem wings). The drag of the tail is furthermore increased because of the reduction in effective aspect ratio as indicated in figure 35, possibly in the order of 50%. The tail's total drag due to lift can thus reach a magnitude of 20% of the induced drag of the wing, assuming conventional airplane dimensions. This additional drag seems to be one important explanation for the poor lift/drag ratios of airplanes when approaching the landing field at higher lift coefficients (in power-off flight).

Glide-Path Control. By deflecting a plate or flap from the upper side of a wing, the lift-over-drag ratio can very effectively be reduced — if so desired when approaching a landing field. Assuming an airplane with $A = 6$ or 7, the induced drag is in the order of $C_{Di} = 0.05$, at $C_L = 1$. Assuming now a plate deflected in the center of the wing, near the point of minimum pressure, its drag coefficient is in the order of $C_{Da} = 10$ (as per equation 14). For a plate having a size $h = b = 10\%$ of the average wing chord; that is for $S_{a.} \approx 0.0015 S_{wing}$, the coefficient defined by equation 17, is $C_{fH} = (10 \cdot 0.0015) = 0.015$. Figure 35 gives the resulting effective aspect ratio A_i in the order of 0.8 of the geometrical ratio. The induced drag with deflected drag flap thus corresponds to $C_{Di} = 1/\pi \cdot 0.8 A = 0.06$, at $C_L = 1$. Referring the differential produced by the plate $\Delta C_{Di} = 0.06 - 0.05 = 0.01$, to its frontal area, the additional drag of the wing, caused by interference, amounts to $\Delta C_D = 0.01/0.0015 = 7$; and the total drag coefficient of and due to the plate is $C_D = 10 + 7 = 17$. Coefficients of this magnitude can be recalculated from flight tests with a device as described, reported in (21,g). The drag values obtained for constant lift are in the order of 15 times the drag coefficient of the plate in free flow.

6. WING-BODY CONFIGURATIONS

The interference drag originating in wing-fuselage and engine-nacelle configurations is also twofold; namely parasitic as well as induced.

Parasitic Interference. The interference drag of a number of wing-fuselage and fuselage-tail configurations has been evaluated and plotted in figure 36. The function obtained brings to mind the corre-

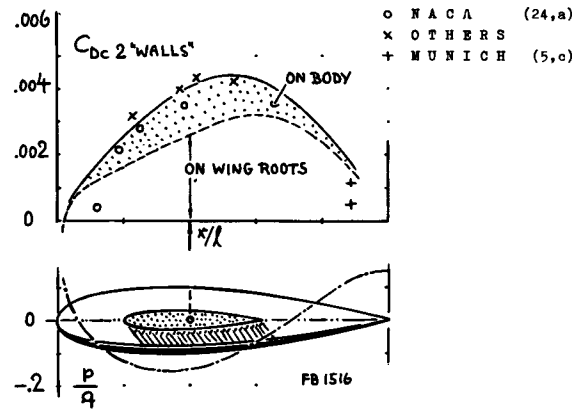


Figure 36. Interference drag (at $C_L \approx 0$) originating in the corners of various wing (or horizontal-tail) and fuselage (or engine-nacelle) configurations.

sponding curve in figure 14. Interference drag is comparatively small with the wing near the body's nose; and the drag reaches a maximum for locations somewhat aft of the maximum thickness. Interference drag is small again for arrangements near the rear end of the body. Figure 36 presents only the interference component of drag. Actually, when adding the body to the wing, the combined wetted area reduces, particularly on the wing. Such combinations may, therefore, have a total drag which is lower than the sum of the free-flow drag values of the two component parts measured independently — even though the interference drag as plotted, has a positive value. Practical conclusions for zero or low lift coefficients are as follows:

(a) *Wing-Fuselage Junctions.* Conventional wing-fuselage combinations have locations x/l (as defined in figure 36) between 0.2 and 0.4. Their interference drag considerably varies, therefore, with the particular position of the wing. At any rate, their interference drag decreases if moving the wing forward.

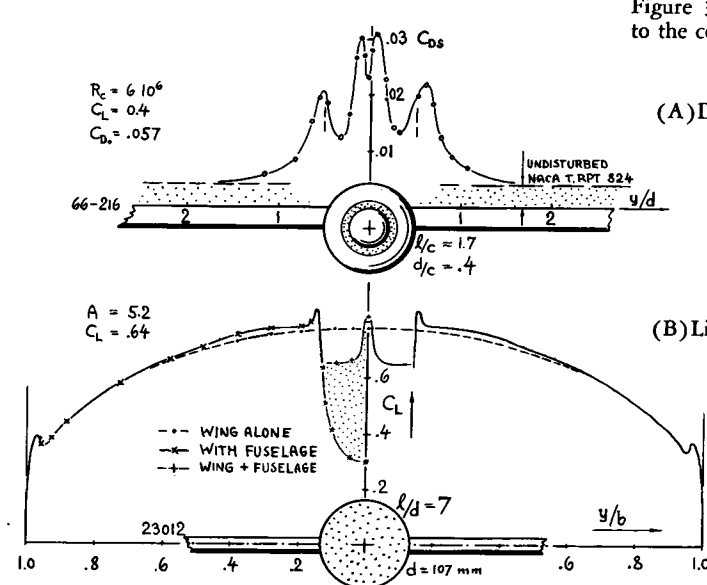
(b) *Slender Engine Nacelles.* Nacelles usually cover the range of intermediate " x/l " values in figure 36. In this range, the interference drag is comparatively constant; in the order of $C_{Dc} = 0.004$. This amount may be compared with the profile drag coefficient of the employed wing section. Assuming a $C_{Ds} = 0.008$, the interference drag is then found to be approximately as large as the sectional drag of a wing portion with the span $b = c \times (0.004/0.008) = 50\%$ of the wing chord. The wing area covered by an average nacelle (with a fineness ratio $l/d = 5$ and a length ratio $l/c = 1.5$) corresponds to a span portion $\Delta b = 25\%$ of the wing chord. A rough but simple rule is therefore, that the parasitic interference drag of engine nacelles

(at \approx zero lift) is approximately equal to the section drag of a wing area twice as large as the wing portion covered by the nacelle. The profile drag as such of that piece of wing does not appear, of course, in the total drag of the combination, since the piece is covered by the nacelle. Therefore, the net total of added drag is \approx equal to one times the profile drag of the part of the wing area defined above.

(c) *Tail Surfaces.* The points in figure 36 evaluated for horizontal tail surfaces, are comparatively low. Increased thickness of the boundary layer near the stern of the main body is evidently responsible for the result. Figure 34 even proves that the interference drag of tail surfaces at the end of fuselages (at zero lift) can very well be negative.

(d) *Propeller Blades* may be considered to be foils. The interference drag originating at their roots can then be appraised on the basis of figure 36. Usually the roots have sections which are much thicker (in relation to their chord) than wing sections. Assuming, for example, $t/c = 50\%$, a value of $C_{Dt} = 0.4$ is found in figure 23. Considering a propeller with three blades and a disk loading coefficient $C_T = \text{thrust}/(\text{dynamic pressure}) \text{ per (disk area of the propeller)} = 0.10$ (corresponding to high-speed conditions of average airplanes), the decrease of propeller efficiency due to interference drag of the blade roots is found to be in the order of 1% of the thrust. This effect may be considered to be small. It can be concluded, however, from figure 36, that the most favorable location of roots (and hub) of a propeller will be at the very nose of engine nacelle or fuselage, respectively. In other words, covering the hub of the propeller by an extra large spinner, is not found to produce higher propulsive efficiencies (22).

Figure 37. Lift and drag distribution as affected by bodies added to the center of wings. Coefficients are based on wing dimensions.



(A) Drag in the wake of a wing-nacelle combination (25,f).

(B) Lift from pressure distribution on wing + fuselage (24,d).

" α " Flow. At lift coefficients different from zero, the displacement of a fuselage (or nacelle) produces increased angle of attack or angle of flow at the wing roots, corresponding to what we may call " α flow" (23,c). A pair of peaks appears accordingly in the span-wise lift distribution, as shown in *figure 37*. The circulation of wing or wing roots is transferred to fuselage or nacelle, to some degree (as predicted by theory). Including some lift originating at the rear end of the body (owing to separation; indicated by dotted line in the illustration), the configuration may even exhibit a lift curve slope slightly higher than that of the wing alone. For example, wind-tunnel tests in (24,a) indicate an increment in the order of 4% for a body having a diameter equal to 1/10 of the wing span. Referred to the piece of wing covered by the fuselage, the increment is in the order of 30 or 40% of the lift ordinarily produced by that part of the wing. The effect can, therefore, be considered to be similar to that of a local increase of wing chord. Because of the parasitic losses along the wing roots, as shown in the upper part of *figure 37*, the drag increment due to lift (dC_D/dC_L^2) of the configuration can be expected to be larger than in the wing alone. Such result is evident in most of the configurations presented in *figure 38*. Here as in similar arrangements, it may also be that the lift distribution (particularly of a rectangular wing) is made "more elliptical" because of fuselage interference, so that the induced drag of the configuration might be slightly reduced.

Body Displacement. Because of the displacement of the fuselage (or engine nacelle), the average flow velocity at the wing roots is increased along the upper side in low-wing configurations; and it is increased at the lower side in high-wing arrangements. The lift is shifted accordingly by more or less constant differentials ΔC_L , which are positive in low-wing and negative in high-wing configurations. The variation can be considered to be the equivalent of that due to a wing flap deflected in the center of the wing. The differentials are suitably referred to the wing area corresponding to the width of the fuselage or nacelle (subscript "b"). For a fuselage with $d = 0.1 b$, the C_{Lb} is in the order of +or- 0.1. The longitudinal position of wing versus fuselage has an effect too, upon ΔC_L . Reference (25,a) indicates that with the wing far forward, the ΔC_L of a high-wing configuration switches from negative to positive, while for positions of the wing far aft (as usual in engine nacelles) ΔC_L is appreciably more negative in the high-wing arrangement tested. Engine nacelles (one nacelle tested in the center of a wing model) exhibit considerably higher differentials, in the order of $\Delta C_L = \pm (0.2 \text{ or } 0.3)$, for low-wing and high-wing installations, respectively. *Figure 40* presents an example in this respect. Nacelles have an effect upon the circulation of the wing section, around which they are placed, similar to flaps. In fact, the ΔC_L value can easily be changed by deflecting the trailing edge (or some sheet-metal tab) behind a nacelle (25,c). An example of this effect is illustrated in figure 16 of Chapter XIII.

Wing-Fuselage Angle. In a symmetrical mid-wing configuration (with symmetrical foil section) lift and induced drag are zero at zero angle of attack. However, when the fuselage is set at some angle of incidence in relation to the wing, certain lift differentials are obtained. For explanation, the fuselage has been considered a "wing". This might be correct for fuselages having sharp lateral edges. It cannot

-
- (22) Tests on the aerodynamic effect of spinners:
 - a) Biermann and Hartmann, NACA T.Rpt 642 (1938).
 - b) Stickle Kreiger Naiman, NACA T.Rpt 725 (1940).
 - (23) Theoretical treatment of wing-body configurations:
 - a) NACA, Loading of Wing + Fuselage, RM L52J27a.
 - b) Vandrey, Yearbk D.Lufo 1938 p.I,158.
 - c) " α " flow is described by Multhopp Lufo 1941p.52, is shown in Ybk D.Lufo 1941 p.I,11, and further evaluated in Ybk D.Lufo 1942 p.I,11 and 366.
 - d) Pepper, Wing + Fuselage, NACA T.Note 812.
 - (24) Experimental data, wing-fuselage configurations:
 - a) Jacobs and Ward, Interference Wing and Fuselage, 509 Combinations, NACA T Rpt 540 (1935).
 - b) Sherman, Interference of Wing and Fuselage, NACA T. Rpt 575 (1936); and T.Notes 640,641,642 (1938).
 - c) Möller, ZWB Rpt FB 1318 and Ybk D.Lufo 1942.
 - d) Gimmerl, Pressure Distribution on Wing-Fuselage Combination, German Doct ZWB FB 1710 (1942).
 - (25) Experimental data on wing-nacelle configurations:
 - a) NACA, Nacelle Position, T.Note 1593 (1948).
 - b) ARC, Summary on Nacelles, RM 2406 (1939).
 - c) Wind-Tunnel Tests on Ju-288 in DVL Tunnel, 1940.
 - d) Others: Junkers Rpt S.392; Me-328, DFS Rpt 1942/6.
 - e) Junkers, Engine Nacelles, Rpt S.392 (1941).
 - f) Ellis, Drag of Nacelle, NACA W.Rpt L-696 (1942).
 - (26) Novotny, Wind-Tunnel Investigation of Me-264 Model, German Doct ZWB (AVA) 1942/W/341.

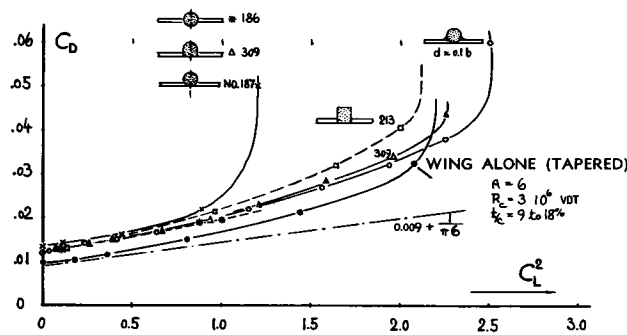


Figure 38. Drag coefficient as a function of the square of the lift coefficient as tested (24,a,b) on various wing-fuselage configurations.

be claimed, however, that a fuselage with well-rounded cross-section shape would perform as a wing. Rather an accelerated flow around the sides of the fuselage (the "α" flow) is started (or changed) as the fuselage is turned to a certain (usually negative) angle of attack against the wing. The resulting lift differential evaluated from results in (24) is in the order of

$$\Delta C_{Lb} = -0.07 \Delta\alpha^o \quad (21)$$

where $(\Delta\alpha)$ indicates the angle of the fuselage axis against the wing's zero lift line.

Induced Drag Due To Body. In the preceding two paragraphs, certain displacement effects of fuselage- and nacelle bodies have been reduced to equivalent local changes in the wing's angle of attack. It is, therefore, possible to estimate the increment of the induced drag on the basis of ΔC_L values, by applying the theory of partial-span wing flaps as presented in the "drag-due-to-lift" chapter. In the range of $b_b/b = 0$ to 0.2, where " b_b " indicates the body, the constant in equation 10 of that chapter is on the average 0.035. Applying that function, additional induced drag is obtained for small lift coefficients as follows:

$$\Delta C_{Db} = 0.035 (\Delta C_{Lb})^2 \quad (22)$$

with the subscript "b" indicating that the coefficient is based on the area (c times b_b). Figure 39 gives some proof for the correctness of this equation, with ΔL referred to S_e (rather than to the " Δb " area.) Equation 22 reads accordingly

$$\Delta C_D \approx 0.015 (\Delta C_{Lb})^2 \quad (23)$$

Example. In conventional airplanes, the fuselage may be set to an angle in the order of minus 4 or 5° against the zero-lift line of the wing section. Equation 21 indicates a corresponding $C_{Lb} = -0.32$. An addition-

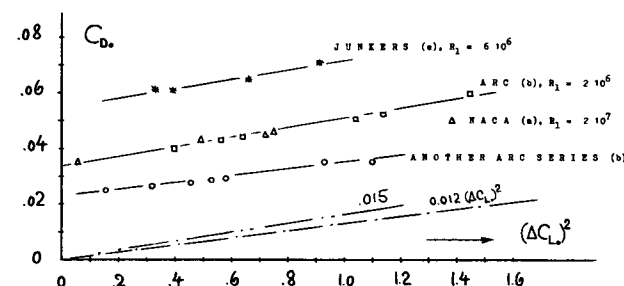
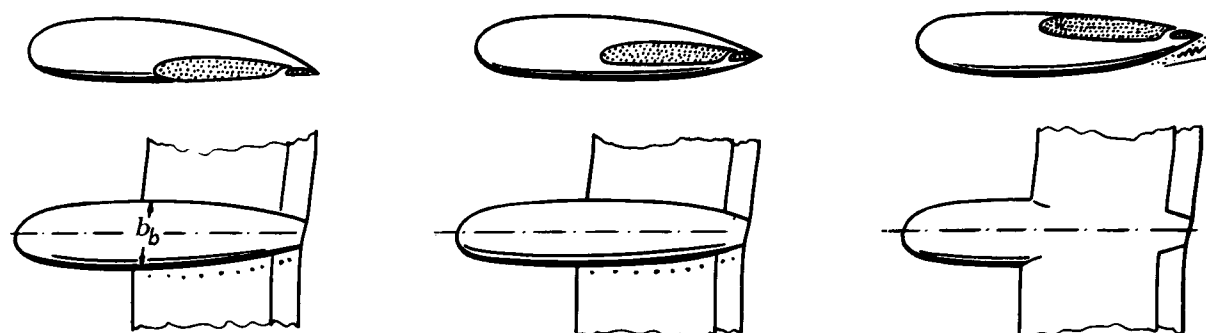


Figure 39. Drag of engine nacelles (tested in the center of wing models; reference 25) as a function of the lift differential caused by installing them.

al value of $C_{Lb} = -0.10$ applies for an assumed high-wing configuration. For a total of -0.42 , equation 22 yields an additional induced drag corresponding to $\Delta C_{Di} = 0.0007$ for an assumed $b_b/b = 0.1$. This component represents about 3.5% of the high-speed drag coefficient of an average fighter airplane (with a total drag coefficient of ≈ 0.02). The equivalent loss in maximum speed is in the order of 1.5 %. Based upon the maximum cross-section area of the fuselage, the induced drag increment is in the order of $\Delta C_{Dc} = 0.1$, representing at least 50% of the drag which a smooth fuselage may have in free flow. Based upon the "chord area" (c^2), a $C_{Dc} = 0.0035$ is obtained. Comparing this value to those in figure 36, the calculated induced drag appears to be in the same order of magnitude as the parasitic interference drag originating in the wing-fuselage corners. However, in case of a low-wing configuration, the influences of angular and vertical position of the fuselage in relation to the wing, more or less cancel each other.

Figure 40. Lift differentials caused by, and drag forces of and due to engine nacelles when added to a wing in various positions (25,e). Drag coefficients are based on the nacelle's frontal area; the lift differentials are referred to the area (c times b_b).



(a) LOW WING; $C_D = 0.061$
 $C_{Lb} = +.19$, $C_{Di} = 0.004$

(b) MID WING; $C_D = 0.053$
 $C_{Lb} \approx 0$, $C_{Di} = 0$

(c) HIGH WING; $C_D = 0.076$
 $C_{Lb} = -.27$, $C_{Di} = 0.008$

Nacelles. Equation 22 is also believed to be roughly applicable for those places on the wing span where the engine nacelles are usually installed. Figure 40 shows the results of a systematic investigation of the comparative merits of low- and high-wing configurations. It is seen that the mid-wing arrangement has the lowest drag coefficient. High-wing and low-wing combinations exhibit higher coefficients corresponding to their positive and negative lift differentials, respectively. Drag differentials calculated through the use of equation 22, explain at least half of the increments as tested. The other half is most likely a parasitic component.

Still larger values can, of course, be expected at higher lift coefficients. Protuberances on wing fillets, such as bolt heads or sheet-metal joints are thus very undesirable. Figure 42 also illustrates the effect of interference plates in various places of an airplane model, for two lift coefficients. Two of the locations tested are seen to have low sensitivity; and their sensitivity does not increase as the lift coefficient is increased. One of these is above or below the forward end of the fuselage (a); the other one at the upper or lower side of the engine nacelles (d). Locations on the wing roots (b and c) are again found to be very sensitive, particularly at higher lift coefficients.

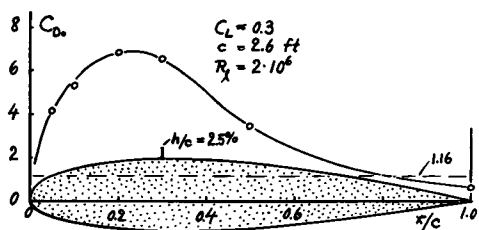


Figure 41. Drag of and due to a square test plate on the upper wing-root fillet of an airplane model (11,e).

Interference Method. The same testing technique as described for three-dimensional bodies can also be used in the investigation of interference effects on wings. One very sensitive location is on the wing roots (in the corner between wing and fuselage). Figure 41 indicates in this case a maximum value of $C_{D_s} = 7$ and a drag ratio $7/1.17 = 6$, at $C_L = 0.3$.

6. CONCLUDING REMARKS

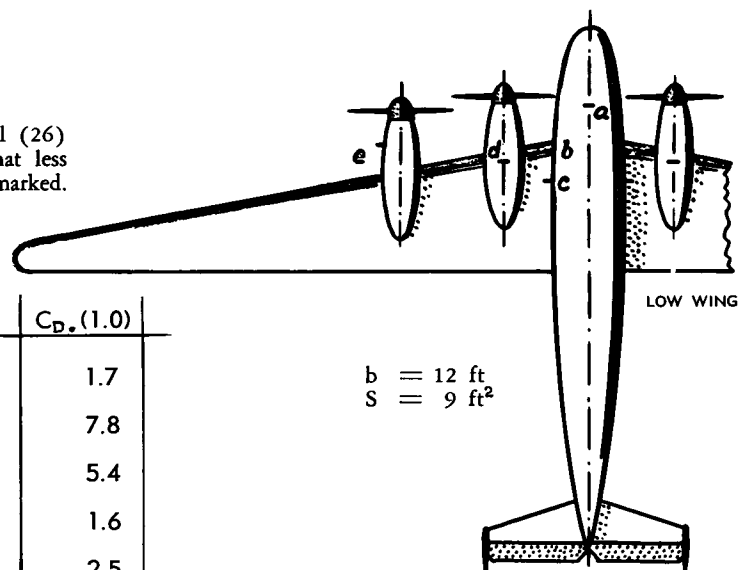
Besides the examples presented in this chapter, there are other configurations shown in other parts of this book whose characteristics are, or may be considered as being the result of mutual interference between components. Typical examples are:

- | | | |
|----------------------------------|------|-------|
| (a) "splitter" plates (v'street) | page | 3-7 |
| (b) body with guide vanes | page | 3-26 |
| (c) wing-tip fuel tanks | page | 7-7 |
| (d) automobiles and ground | page | 12-1 |
| (e) windshields and canopies | page | 13-2 |
| (f) radial engine cowlings | page | 13-4 |
| (g) wing and engine nacelles | page | 13-6 |
| (h) external stores (tanks) | page | 13-16 |
| (i) slipstream effect | page | 14-15 |

(28) Jones (NPL), Experiments on Rigid Parachute Models, ARC RM 2520 (1953). See also (51) in Chapter XIII.

Figure 42. Interference investigation of an airplane model (26) by means of small test plates. The plates were somewhat less than one square inch in size, attached to the points as marked.

Location of Plates	Representing	$C_{D_s}(0.2)$	$C_{D_s}(1.0)$
a) Above or below the fuselage	windshield or gun turret	1.7	1.7
b) On wing fillet near wing nose	surface, skin imperfections	3.6	7.8
c) Wing-root fillet near 1/2 chord	imperfections or attachments	3.6	5.4
d) Above or below the nacelles	oil cooler or carburetor inlet	1.6	1.6
e) On the sides of the nacelles	engine parts, exhaust stacks	3.5	2.5



Biplane and tandem wings too (pages 7-12 and 7-14) represent an interference mechanism. Roughness elements may also be considered as interfering with the surface on which they are placed; see turbulence stimulation on pages 2-10 and 6-19, and roughness on laminar-type foil sections (page 2-13). Vice versa, the boundary layer interferes with roughness elements

(such as imperfections, page 5-6). Interference effects of appreciable magnitude are also found in Chapters X and XI, caused by the free surface of water (wave drag, spray and ventilation). More and different examples of interference are furthermore presented in Chapters XV, XVI and XVII, dealing with compressible and/or supersonic flow conditions.

Parachute. As a final example of interference drag, the combination of a parachute cap with a comparatively large and bluff "load" (simulated by a disk) is presented in figure 43. It is seen that the canopy's drag coefficient reduces appreciably when placing the "load" as shown. Note that not only the drag of the canopy, but also the total drag of the combination is decreased below that of the canopy alone (connected to the wind-tunnel balance).

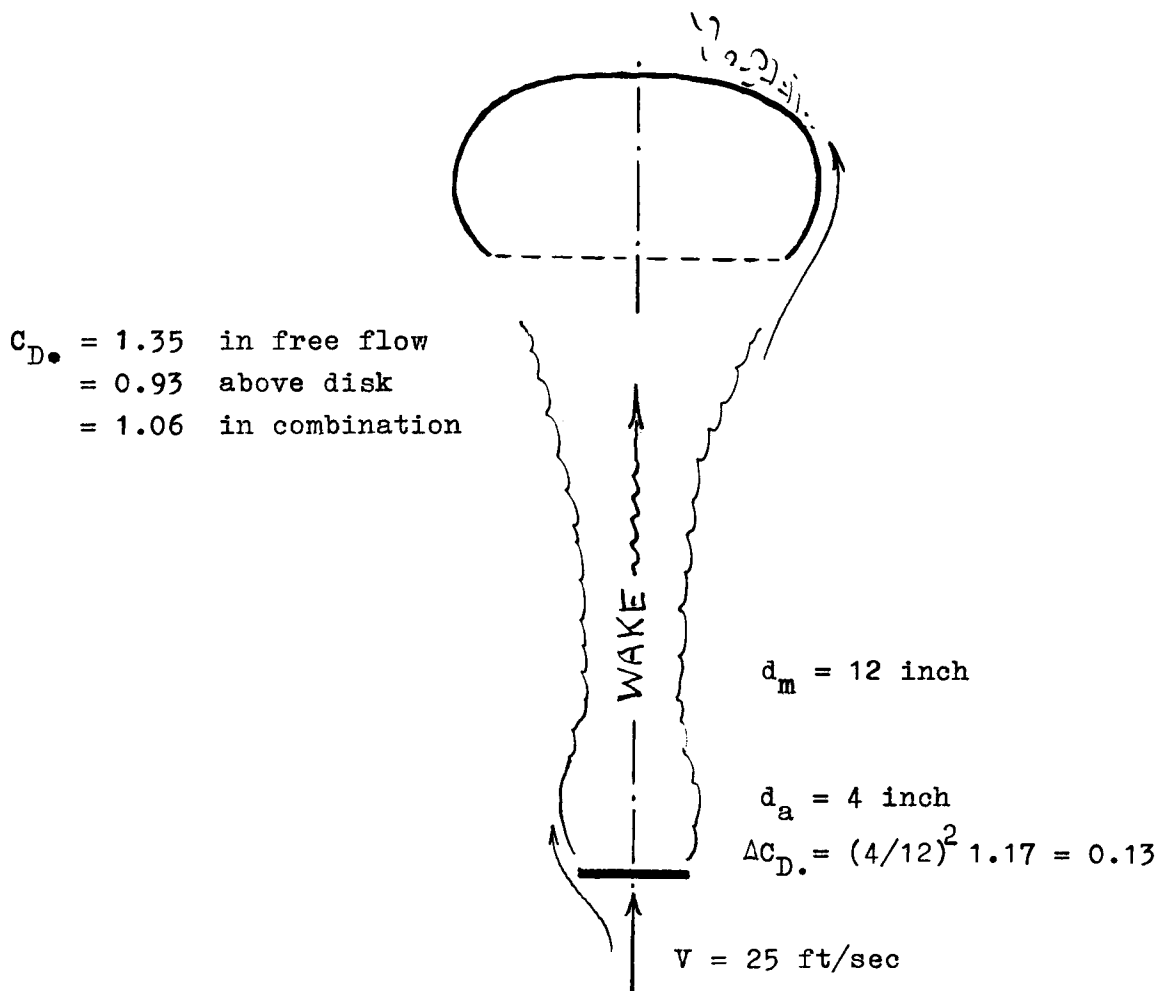


Figure 43. Drag of a parachute canopy (sheet-metal model) without, and in presence of a large and bluff "load" simulated by a disk (28).

CHAPTER IX — DRAG DUE TO INTERNAL-FLOW SYSTEMS

This chapter deals with the aerodynamic characteristics of radiators and cowlings (used for aircraft engines) and with ventilation systems in any type vehicles. The aerodynamic drag connected with these installations consists of an internal component corresponding to the loss of momentum encountered by the flow when passing through the internal system, and an external component — which is parasite drag originating from inlet, housing (if any) and outlet of the system.

A. MECHANISM OF DUCTED SYSTEMS

All internal flow systems can be reduced to the mechanism of a duct with inlet, an expanding part (diffuser), an obstruction, a contracting part (nozzle) and an outlet. As an example of such system, one type of radiator installation is shown in figure 1. A certain stream tube is isolated from the outside flow, led into the aircraft or vehicle, and discharged somewhere, back into the outside flow (1).

Loss Coefficient. As illustrated in figure 1, the flow of air varies considerably in velocity, dynamic pressure and static pressure on its way through the duct. Under loss-free conditions, the sum of static and dynamic pressure would remain constant all the way, as indicated by Bernoulli's theorem (see Chapter I):

$$p_{\text{total}} = p + q = \text{constant} \quad (1)$$

Actually, the air flow encounters momentum losses, primarily due to obstacles (such as the radiator core) and expansions of the cross-section area of the duct. The corresponding decrements in total pressure are best given in the form of the loss coefficient

$$\xi = \Delta p_{\text{total}} / (0.5 \rho w^2) \quad (2)$$

where w indicates the average velocity in the cross section of the duct in which a particular loss occurs. The term

$$\xi (w/V)^2 = \Delta p_{\text{total}} / (0.5 \rho V^2) \quad (3)$$

refers each loss component to the dynamic pressure of the undisturbed external flow. All losses can thus be added up. Because of $(w/V)^2$, the smallest cross sections tend to contribute the largest losses, and vice versa.

Intake Diffuser. To reduce the velocity through the duct system, a diffuser is usually placed directly behind the intake opening. A considerable part of the desired deceleration occurs ahead of the opening, however, as indicated in figure 1. In case of air scoops, used as intake for the combustion air of engines or for ventilation purposes, frequently no diffuser is provided at all; and the deceleration entirely takes place in front of the opening. In either case the efficiency of the intake is indicated by

$$\eta_{\text{in}} = (\Delta p_w + q_w) / (0.5 \rho V^2) = \Delta p_{w\text{total}} / q$$

where "w" indicates conditions at the end of the diffuser or in a suitable cross section inside the duct. Combining equations 3 and 4, the loss coefficient of the diffuser is found to be

$$\xi_{\text{in}} = (1 - \eta_{\text{in}}) / (w/V)^2 \quad (5)$$

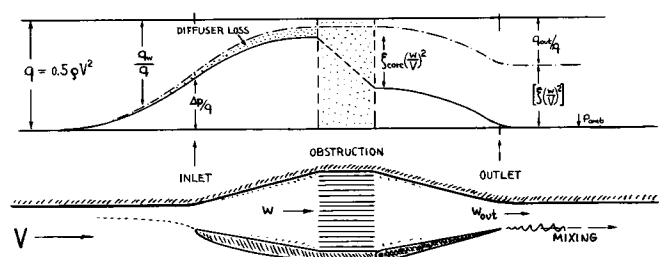


Figure 1. Pressure variations in a ducted radiator system. Conditions as shown, roughly correspond to $\eta_{\text{in}} = 90\%$, $\xi_{\text{core}} = 7$, and $w/V = 0.25$.

where ξ_{in} tends to be constant in many installations. As a consequence, η_{in} usually decreases with w/V , as illustrated for example in figure 5. In the form of equation 5, the diffuser losses (which can be considerable because of boundary-layer separation) can be added to other loss components (as per equation 3).

The Rate Of Flow through the duct is a function of the difference in total pressure between intake and outlet, and therefore a function of the internal losses of momentum. The sum of these losses shall be written as

$$\sum [\xi_n (w_n/V)^2] = [\xi(w/V)^2] \quad (6)$$

where n indicates the cross section in which the individual loss is incurred. The average dynamic pressure in the outlet opening is then indicated by

$$\begin{aligned} q_{out}/q &= (p_{totout} - p_{out})/q \\ &= 1 - [\xi(w/V)^2] - C_{pout} \end{aligned} \quad (7)$$

where $C_{pout} = \Delta p_{out}/q =$ static pressure coefficient in the plane of the outlet. Equation 7 can be solved for the velocity ratio through the outlet:

$$w_{out}/V = \sqrt{1 - [\xi(w/V)^2] - C_{pout}} \quad (8)$$

The rate of flow through any other cross section (S_w) of the duct corresponds to the respective area ratio; hence

$$w/V = (S_{out}/S_w) \sqrt{1 - [\xi(w/V)^2] - C_{pout}} \quad (9)$$

By varying the outlet area (by means of an adjustable flap), the rate of flow through an internal system can conveniently be controlled. In the limiting case of large outlet openings, that is for $q_{out}/q \rightarrow 0$, equation 7 yields the velocity ratio

$$(w/V)_{max} = \sqrt{(1 - C_{pout})/\xi_w} \quad (10)$$

where " ξ_w " denotes the sum of the internal losses, referred to the dynamic pressure of the considered cross section (subscript "w").

Intake Area. Within certain limits, the rate of flow through the duct system is independent of the cross-sectional area of the intake. However, for a very small inlet area, increased momentum losses are likely to occur along the diffuser which necessarily follows the narrow entrance. If on the other hand, the inlet area is too large, with the air "overflowing" the edges, certain losses will originate on the outside because of flow separation.

Internal Losses. The internal losses of momentum result in external drag. This means that some fraction of the engine power of a considered airplane or vehicle is consumed to maintain the flow through every ducted system. The drag corresponding to the internal losses of momentum ("M") equals (mass flow) times (velocity decrement); thus $C_{pout} = 0$:

$$D_M = \rho S_a w (V - w_{out}) = 2 S_a q_w (V - w_{out})/w$$

where "w" indicates conditions in the cross section (S_a) of the duct chosen for reference. In the case of radiator installations, for example, this reference section is that of the core.

Outlet Pressure. The static pressure around the outlet opening is not always \approx equal to the ambient pressure. Because of a scavenging effect of the external flow upon the outlet, Δp_{out} is often somewhat negative. Through application of flaps, deflected to a position extending into the external flow, it is also possible to obtain pressures to the order of $C_{pout} = -0.5$. The outlet presents the corresponding drag component

$$\Delta D = -\Delta p_{out} S_{out} \quad (12)$$

to be added to equation 11. The two functions then give the drag coefficient

(13)

$$C_{Dw} = 2(w/V)(1 - w_{out}/V) + (\bar{C}_{pout} S_{out}/S_a) \quad (13)$$

By introducing equation 8 into this function, the coefficient of drag due to internal losses of ducted systems from inlet to outlet is found to be

$$C_{Dw} = 2 w/V \left[1 - \sqrt{1 - [\xi(w/V)^2] - C_{pout}} \right] + \bar{C}_{pout} S_{out}/S_a \quad (14)$$

For $C_{pout} \rightarrow 0$, the equation is plotted in figure 2.

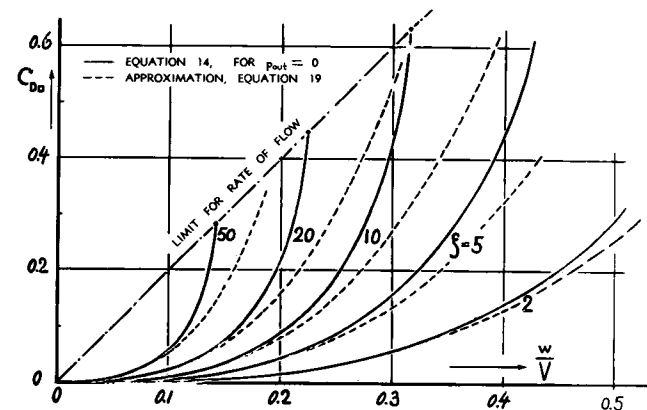


Figure 2. Drag due to internal losses of ducted radiator systems (equations 14 and 19) for $C_{pout} = 0$.

B. DRAG OF RADIATOR INSTALLATIONS

The "internal" drag of ducted engine radiators corresponds to theory as presented in the preceding section. The external drag is found through evaluation of experimental results. In a realistic analysis, it is also necessary to consider the influence of heating as well as some effect of compressibility upon the flow through the system.

1. Considerations For The System.

Surface Cooling. Every transfer of heat between two fluids is proportional to the area of the partition adjacent to both mediums. Radiators or heat exchangers are consequently designed with as large a surface as practicable. A surface of considerable size is available in the wings of airplanes; and attempts have been made, at least experimentally, to use the wings as radiators. The turbulent skin-friction drag is theoretically expected to decrease somewhat with an increase of temperature within the boundary layer (2,a). Considering, however, the heated wing as a ram-jet mechanism (2,b), the location must be taken into account at which heat is transferred. A propulsive force (negative drag component) can only be expected when and if transfer takes place in a region where the static pressure is higher than the ambient pressure. Since the average differential Δp is negative over most of the wetted wing surface, the resultant thermodynamic thrust may thus be negative or identical to drag. For this and other practical reasons (such as vulnerability), surface cooling has never really been utilized in airplane design.

Aircraft Radiators. Roughly 15% of the heat produced by burning gasoline in reciprocating engines has to be removed from the cylinder walls. In liquid-cooled engines this is accomplished by means of radiators. Concentrating a system of tubes and fins within a small volume, an internal surface is obtained which is in the order of 100 times the frontal area of the radiator core. This size cooling area is thus of the same order as that of the airplane wings.

Ducting Of Radiators. The transfer of heat through the cooling elements of a radiator core is approximately proportional to $w^{0.8}$ of the internal flow. The skin-friction within the openings of the core is, on the other hand, proportional to $w^{1.8}$, considering turbulent boundary-layer flow. From these two relations results the ratio

$$\frac{\text{pressure loss}}{\text{heat transfer}} \sim \frac{w^{1.8}}{w^{0.8}} = w \quad (15)$$

The internal drag of a radiator, therefore, reduces as the velocity of the cooling air flow is reduced. Low velocities are obtained by placing the radiator within a duct; that is, behind a diffuser as illustrated in figure 1. After passing through the radiator core, the air is accelerated again by means of a convergent duct (nozzle) and discharged through an outlet. Figure 7,d presents one example where the *total* drag of and due to a belly-type radiator installation is very high, because of insufficient ducting.

Radiator Size. The frontal area of the radiator core, required to give the desired heat transfer, is $S_{\square} \sim 1/w^{0.8}$. Large cores are consequently needed for low velocity ratios " w/V ". Besides being heavy, such radiators may also present a higher external drag. Development of aircraft radiators has arrived at core sizes which, under climb conditions of an airplane, require a maximum rate of flow in the order of $w/V = 0.3$. The rate at maximum aircraft speed is then only in the order of $w/V = 0.1$ (depending of course, upon the speed range of the respective airplane). The corresponding ratios of the dynamic pressure within the duct are $q_w/q = (w/V)^2 = 0.3^2 = 0.09$ and $= 0.1^2 = 0.01$, respectively. Such conditions are very effective in reducing radiator drag.

2. Internal Radiator Drag.

Since the frontal area of the core S_{\square} is the most significant parameter of a radiator installation, the aerodynamic characteristics, that is the drag coefficient $C_{D\square}$, the internal velocity w , and the loss coefficient ξ_w , are consistently measured in, or referred to this area.

Radiator Cores are tested for pressure drop in closed channels. Between front- and rear side, there is a difference in pressure Δp_{core} which, based upon the constant dynamic pressure of the channel flow shortly

(1) Mechanism and analysis of ducted systems:

- a) Schlupp, Ringb.Luft'technik III A 24 (1940).
- b) Capon, Cowled Systems, ARC RM 1702 (1936).
- c) RAE, Cooling Aerodynamics, ARC RM 2498 (1947).

(2) Analysis of wing-surface cooling:

- a) Fedjajewski, Skin Friction of Heated Bodies, CAHI Moscow) Rpt 516 (1940).
- b) Surface Cooling, Ringb.Luft'technik III A 23.
- c) Gloster and Supermarine Wing, ARC RM 1311 (1929).

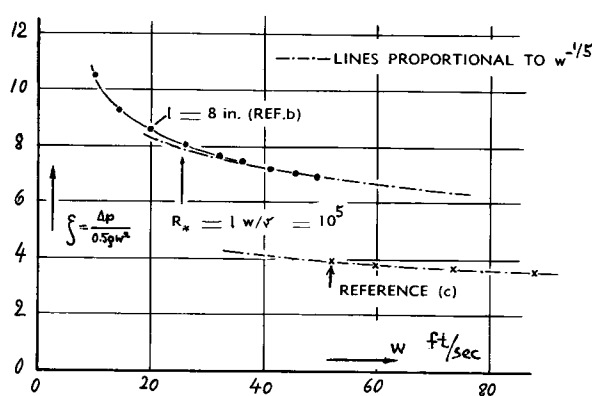


Figure 3. Pressure-loss coefficient of typical radiator cores, tested in closed channels (3).

ahead or behind the core, gives the loss coefficient

$$\xi_{core} = \Delta p_{core} / q_w = (p_1 - p_2) / (0.5 \rho w^2) \quad (16)$$

Conventional radiator cores have ξ_{core} between 5 and 10. The pressure differential is mostly due to skin-friction drag within the openings of the core; the loss coefficient decreases, therefore, with the velocity w (that is, with the Reynolds number), as shown in the examples of figure 3. Above $w \approx 20$ ft/sec, the drag of the tested cores appears to be roughly proportional to the turbulent skin-friction coefficient (as treated in Chapter II):

$$\xi_{core} \sim 1/w^{1/5} \quad (17)$$

Diffuser Efficiency (4). Radiator intakes, installed at the surface of fuselages, wings or nacelles, can severely be affected by the boundary layer originating ahead of them. For example, in the arrangement illustrated in figure 4, the flow is completely detached from the upper side of the diffuser; there is even a return flow through the upper part of the core. Such conditions lead to losses comparable to those in a sudden expansion of the cross section of the duct. Based upon the dynamic pressure in the duct following such expansion, theory (4,e) predicts:

$$\xi_{in,max} = (S_d/S_{in})^2 \quad (18)$$

where "in" denotes the inlet section of duct or diffuser, respectively. The example in figure 4 (without BL control) essentially corresponds to this maximum loss coefficient. The diffuser efficiency is $\eta_{in} \approx 65\%$ at $w/V = 0.13$; the equivalent loss coefficient (equation 5) is $\xi_{in} = 21$, based on $0.5 \rho w^2$ (where w = average nominal velocity across the section in which the core is located). This ξ value is in the order of twice the loss coefficient of the core. The total drag of the radiator system is correspondingly high, and the maximum rate of flow available for "fully" opened inlet and outlet flaps is comparatively small.

Boundary-Layer Control. Through addition of a small slot at the entrance, in figure 4, providing "bleed-off", it is possible to remove the boundary layer before it enters the diffuser and to obtain an efficiency $\eta_{in} = 97\%$ (at the velocity ratio of $w/V = 0.13$). The corresponding loss coefficient is only $\xi_{in} = 1.5$. Drag-and rate-of-flow characteristics are improved accordingly. It must be considered, however, that the flow through the slot too, presents some loss of momentum. Its magnitude is estimated to correspond to $\Delta C_{Dn} \approx 0.02$, as far as the configuration in figure 4 is concerned. Another method of preventing the boundary layer from getting into the diffuser, is illustrated in figure 5. The intake opening is somewhat removed from the surface of the aircraft; the boundary layer is guided sideways by means of a "neck" or a "groove". The resultant loss coefficient of the diffuser $\xi_{in} = 3.2$ is considered to be low for an expansion ratio of $S_d/S_{in} = 6$. Ratios of this magnitude, with diffuser efficiencies above 90% are superior to values quoted for diffusers placed in longer ducts (4), where the boundary layer is fully developed.

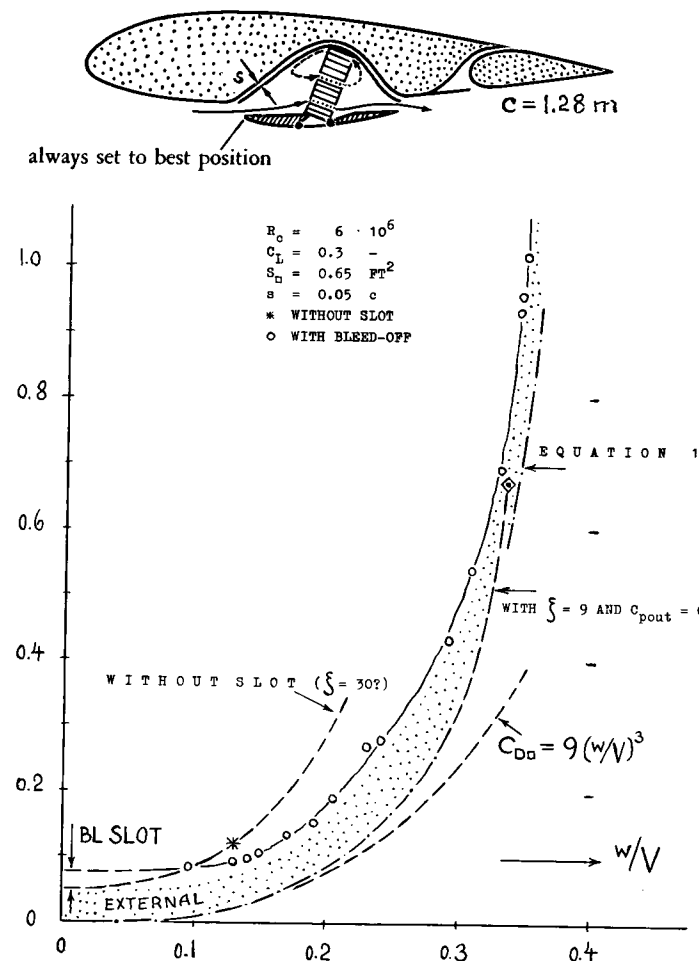


Figure 4. Drag characteristics of a wing radiator (6,d) with (and without) boundary layer control. Similar results are reported in 1,c).

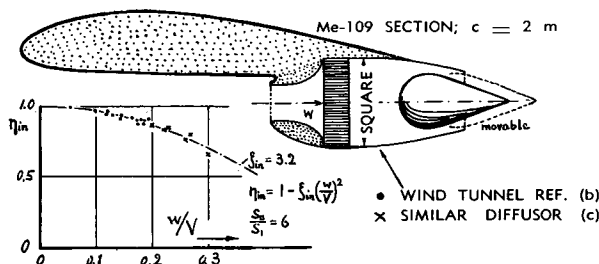


Figure 5. Aerodynamic efficiency of a well designed inlet diffuser (6,b).

Momentum Drag. For certain configurations and in the range of lower flow rates it may be permissible to assume $p_{out} = p_{ambi}$, meaning $C_{pout} = 0$. Using furthermore the approximation $\sqrt{1-x} \approx (1-0.5x)$, equation 14 is simplified to

$$C_{D\Delta} = (w/V)^3 \xi_w \quad (19)$$

where "w" indicates that " ξ " is defined for the duct section where the velocity is "w". This function for the internal drag indicates the trend which is usually found when testing the drag of radiator installations. As illustrated in *figure 2*, the equation is sufficiently accurate, only if used for values of $\xi(w/V)^2 < 0.4$, however.

Outlet Pressure. *Figure 4* shows that equation 14, applied with $C_{pout} = 0$, sufficiently well describes the internal drag up to flow ratios in the order of $w/V \approx 0.3$. To obtain ratios higher than this, the outlet flap must be opened into the outer flow, so that a negative outlet pressure is obtained. Those points in the graph, highest in both drag coefficient and flow ratio, can be checked by equation 14, if pressure values in the order of $C_{pout} = -0.2$ are used.

Drag Due To Leaks. With the outlet flap near the closed position, such as under high-speed flight conditions, there is a positive pressure within the duct in the order of magnitude of the dynamic pressure $0.5 \rho V^2$. Since this pressure can be appreciably high, a noticeable volume of air may be forced out of the radiator housing through the cracks and gaps which usually exist on mass-production installations. From flight reports (6,e) it is learned, for example, that in the case of the Me-109, the air flow through such leaks attained a rate of flow (measured in the cross section of the core) corresponding to w/V between 0.05 and 0.10. Passing through leaks, the air is usually not discharged in down-stream direction. The momentum of the outflow is, therefore, mostly lost; and equations 14 and 19 must be changed, to indicate the maximum possible internal drag coefficient.

$$C_{D\Delta max} = 2 (w/V) \quad (20)$$

In case of the Me-109 (similar to the installation in *figure 4*) the drag due to leaks is estimated to be in the order of $\Delta C_{D\Delta} = 0.1$, with "closed" outlet flap. This drag component is larger than the external parasitic drag of the installation.

3. External Radiator Drag.

The external drag of a radiator installation depends upon location, shape, and size of the enclosure in which it is housed. Results of a basic wind-tunnel study are presented in *figure 6*. Shapes, suitable to house radiators, near or at the trailing edge of the wing, show drag coefficients in the order of $C_D = 0.06$, based upon the protruding frontal area.

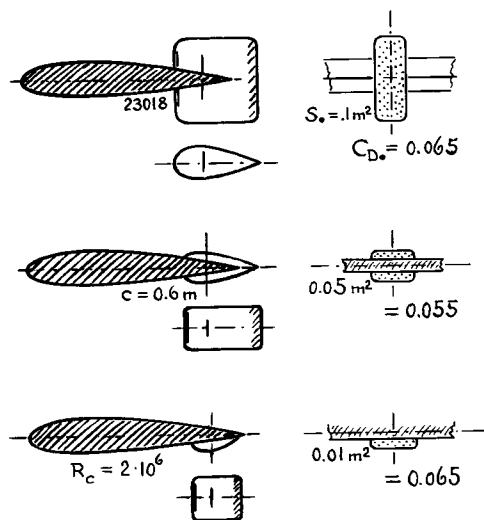


Figure 6. Drag coefficients of three shapes (6,a) suitable to house wing radiators.

- (3) Pressure loss across radiator cores:
 - a) Dickinson-Kleinschmidt, NACA T.Rpt 63 (1919).
 - b) Ducted Radiators, Ybk D.Lufo 1938 p.II,281.
 - c) see in reference (9,b).
 - d) Becker-Baals, NACA Wartime Rpt L-6 (1944).
- (4) Efficiency of diffusers:
 - a) NACA Tech Notes 1610, 2888, 3066, 3124.
 - b) Aircraft Engg 1939 p.267; ARC RM 2751 (1953).
 - c) Ing. Archiv 1940 p.361; VDI Forsch.Heft 76 (1909); Naumann, ZWB FB 1705(1942); Vüllers Z.VDI 1933 p.947; Nikuradse, Forsch.Arbeit VDI No. 289 (1929); Kroener, Forschungs Arbeit VDI No. 222 (1920).
 - d) Little-Wilbur, NACA T.Rpt 1201 (1954).
 - e) Borda, Expériences sur la résistance des fluides, Mem. de l'Académie Royale des Science Paris 1763 and 1767. With regard to minimum efficiency of diffusors see engineering handbooks.
 - f) ARC, Conical Diffusers, RM 2751 (1953).
 - g) NACA, Two-Dimensional Diffusers, Tech Note 2888.
 - h) NACA, Roughness in Diffuser, Tech Note 3066 (1954).

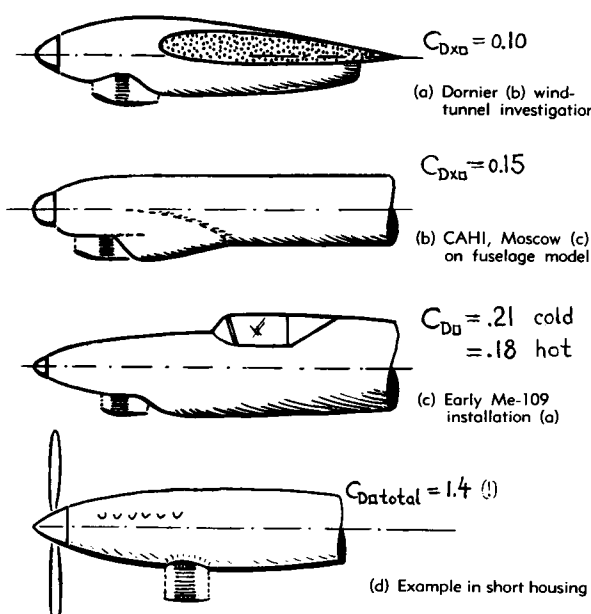


Figure 7. Shape and drag of several belly-type radiator installations (8).

Evaluation Of Tests. In wind-tunnel tests, the "external" and "internal" drag components are usually measured together. Considering, however, that the momentum drag is comparatively small up to $w/V \approx 0.1$, and assuming reasonable values for the internal loss coefficient ξ_w , it is possible to analyze experimental results and to find approximate values for the external drag. From the data presented in figures 7 and 8, conclusions are derived as follows:

(a) *Drag Near $w/V = 0$.* Within a certain range of flow ratios, the total-drag function of a radiator installation runs roughly parallel to the curve of the momentum drag. The difference indicates minimum external drag. At or near $w/V = 0$, this type drag is sometimes considerably higher than at intermediate rates of flow. The additional drag is caused by boundary-layer losses and flow separation at the *outside* of the radiator housing. At $(w/V) \rightarrow 0$, the air in front of the radiator duct is forced to turn sideways and to flow around the rim of the intake opening. The duct is thus *overflowing*, similar to a vessel into which too much water is being poured.

(b) *Belly-Type Radiator.* Among the various installations, the belly type shows the highest external drag coefficients, evidently because of added frontal area. It is possible to decrease this area by placing the core inside the fuselage (or the nacelle), and thus to reduce the external drag of the installation. The external coefficient is between $C_{D0} = 0.1$ and 0.2 , as shown in figure 7. To keep the internal drag low, it is of primary importance for this type radiator to remove the boundary-layer in front of the intake.

(c) *Ring Radiators.* The most favorable type of installation appears to be the "ring" radiator (figure 8), placed within the nose of fuselage or nacelle. The low drag coefficients observed for this type ($C_{D0} \approx 0.04$) seem to be attributable to the elimination of any added frontal area. Variations of the ring radiator are the "double spinner" and the "drum radiator" (figure 8), both designed to obtain maximum utilization of the limited space between propeller and engine.

Wing Radiators. Figures 4, 5 and 9 illustrate several wing installations. Locations on the lower wing side can produce small external drag coefficients, particularly in designs where the core is recessed into the wing. Note that the high total drag coefficient of the Me-109 configuration in figure 9 is caused by blunt shape, external roughness and internal leakage. Two examples in figure 9 (a and b) show that installations within the wing proper, with intake through the section nose and outlet at the suction side can also have low drag coefficients. Local flow angles at the nose vary considerably, however, with the angle of attack of the wing. Internal efficiency is, therefore, restricted to a certain range of the lift coefficient. Figure 10 presents an example of the wing-nose inlets investigated in (9,d). For the staggered position of the inlet lips as shown, internal recovery is $\eta_{in} \approx 100\%$ between $C_L = 0.2$ and 0.6

Lift Due To Intake. At lift coefficients above 0.5 , the drag coefficients of the wing with the inlet opening as shown in figure 10, are somewhat lower than those of the bare wing at equal lift coefficients. It is suggested that the intake and the flow into the wing (and from there sideways out of the wind tunnel) have an

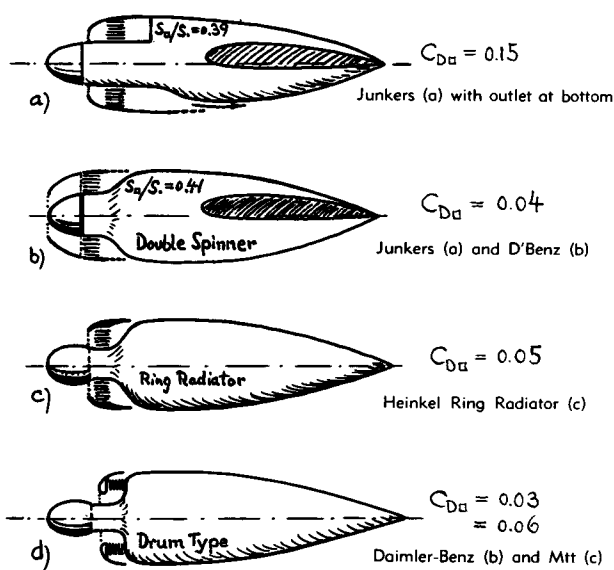


Figure 8. Shape and drag of ring-type radiators (5).

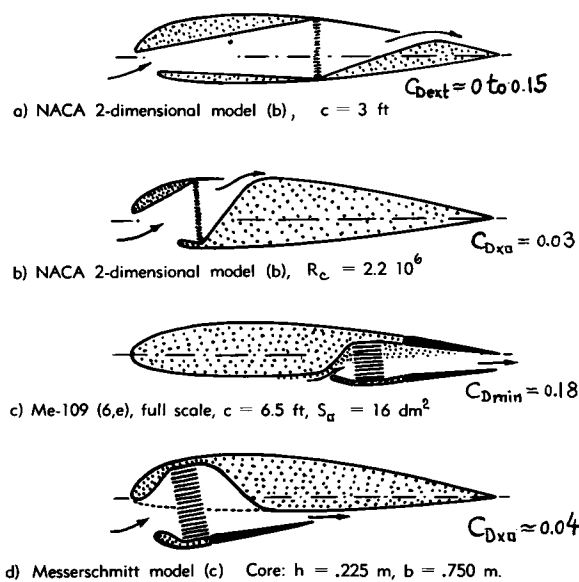


Figure 9. Shape and drag of several wing-type radiator installations (6)(9).

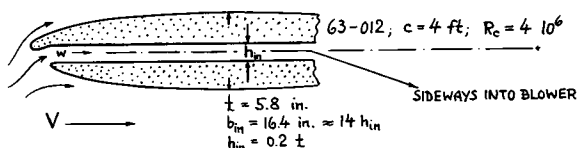


Figure 10. Shape of a favorable wing-nose inlet (9,d).

- (5) Investigations of ring-type radiators:
 - a) Junkers, Ring Radiators and "Double Spinners", Rpts D.5673 (1936), S.278 and S.367 (1941).
 - b) Daimler-Benz, Wind-Tunnel Investigations of Ring Radiators, Rpt 21 (1941) and Rpts by Luftschiffbau Zeppelin 600/185 (1941) and 600/237 (1943).
 - c) Heinkel, Wind-Tunnel Investigation of Ring and Drum-Type Radiators, Rpt ENB 82 (1942).
- (6) Wind tunnel investigations of wing radiators:
 - a) Braune, Cowlings, Blohm and Voss Rpt S322 (1944).
 - b) Ehrhardt, Nacelle-Type, ZWB UM 7858 (1944).
 - c) Kanold, Radiator, Messerschmitt Rpt TB 111.
 - d) Junkers, Wing-Installed Radiator with Boundary-Layer Control, Wind-Tunnel Rpt S. 1942/103.
 - e) Messerschmitt, Me-109; Rpts Feb 1932, Aug 1939, Nov 1939; also 109/10/L/1941 and 109/15/L1/1942.
- (8) Belly-type radiator installations:
 - a) Barth, Yearbook D. Lufo 1943.
 - b) CAHI, Various Installations, Rpt 517 (1940).
 - c) see reference (6,e).
 - d) Worth, Engine Cooling, J.SAE 1937 p.315.
- (9) Characteristics of wing-nose inlets:
 - a) Winter, Radiator, Messerschmitt Rpt Sept. 1944.
 - b) Harris-Recant, Ducts, NACA T Rpt 743 (1942).
 - c) Nelson-Czarnecki, NACA W.Rpt L-407 (1943).
 - d) Dannenberg, LE Inlets, NACA T.Note 3126 (1954).
- (10) Characteristics of radial-engine cowlings:
 - a) Theodorsen, NACA T.Rpts 592 through 594 (1937).
 - b) Theodorsen, Principles, J.A. Sci. 1938 p.169.
 - c) Theodorsen, Nose-Slot, NACA T.Rpt 595 (1937).
 - d) Schlupp, Ringb.Luft'technik, III,A,25 (1940).
 - e) Robinson-Becker, NACA T.Rpt 745 (1942).

effect similar to that of boundary layer control by suction, thus improving the flow past the upper side of the wing (at higher angles of attack). The fact that the maximum lift coefficient (in the order of $C_{L_{max}} = 1.35$) is slightly increased after adding the intake opening, seems to confirm this explanation. At any rate, as far as drag is concerned, carefully designed wing-nose intakes can be favorable. Duct and radiator arrangement inside the foil section, may be problematic, however, with respect to the spar or other structural members of the wing.

C. DRAG OF ENGINE INSTALLATIONS

There are particularly two types of engines for which internal and external aerodynamics have been investigated; namely air-cooled (radial-type) reciprocating engines and the modern turbo-jet powerplants.

1. Engine Cowlings.

Air-cooled engines are usually housed within cowlings of the type developed by the NACA (10,a,b,c). This is not only done to reduce the considerable drag of an open installation (see in Chapter XIII), but also to improve the cooling of the engine cylinders.

Internal Characteristics. Although the appearance of a cowled radial engine is very similar to that of a ring-radiator installation (figure 8), the internal flow conditions are somewhat different:

- a) The opening ratio or "conductivity", that is the ratio of the open area across the cylinder- and baffle system to the total frontal area of the engine, is smaller than that of conventional radiator cores; $f = S_{open} / S_{\square} \approx K < 0.1$.
 - b) The pressure drop between the intake and the space behind the baffled cylinders is higher than that through an average radiator core.
 - c) The flow velocity between the cylinder fins is approximately twice as high as that through radiator openings. The flow ratio w/V , on the other hand, (with $w = Q/S_{\square}$, where Q as defined below) is in the order of only 1/4 of that of an average radiator installation.
- Internal characteristics of air-cooled engines could very well be handled through the methods presented for radiator installations. Because of the differences outlined above, analysis is preferred, however, in the form as follows

Conductivity (10). For a given cowling design, the pressure differential between front and rear of the engine is a measure for the rate of flow. Between the cylinder fins, the velocity is on the average

$$w_{f_l}/V = k \sqrt{\Delta p/q} \quad (22)$$

where k is a factor smaller than, but near unity. From measurements taken on a test stand, the "conductivity" of an engine is found to be

$$K = Q/(S_a V \sqrt{\Delta p/q}) \quad (23)$$

where Q denotes the volume of air passing through the system per unit time, and S_a the frontal area of engine cowling or nacelle. The corresponding velocity ratio is approximately

$$w/V = Q/(S_a V) = K \sqrt{\Delta p/q} \quad (24)$$

In average air-cooled aircraft engines, this ratio is in the order of 0.10 during climbs and in the order of 0.03 at high flying speeds. Combining equations 22 and 24

$$f = S_{open}/S_a = K/k \quad (25)$$

Assuming $k = 1$, the value $K \approx f = S_{open}/S_a$ represents the effective opening ratio or conductivity of the engine. The magnitude of K is between 5 and 10% for baffled installations. Without baffles the conductivity would be in the order of $K = 0.3$ to 0.6.

Internal Losses. Substituting in equation 24 the term $\xi(w/V)^2$ for $\Delta p/q$, the loss coefficient is found to be

$$\xi = 1/K^2; \quad \text{and } K = 1/\sqrt{\xi} \quad (26)$$

For $K = 0.05$ to 0.10, high loss coefficients are found in this manner for baffled engines, in the order of ≈ 100 to 400. By comparison, therefore, the losses occurring in the intake diffuser are of little practical significance. — Combining and substituting equations 24 and 26 into equation 14, the internal drag coefficient of radial engines is found to be

$$C_{D_{in}} = 2 K \sqrt{\Delta p/q} \left[1 - \sqrt{1 - (\Delta p/q)} - C_{pout} \right] - C_{pout} (S_{out}/S_a) \quad (27)$$

For small flow ratios, the approximation

$$\sqrt{1 - (\Delta p/q)} \approx (1 - 0.5 \Delta p/q) \quad (27)$$

can be used; and the outlet pressure C_{pout} may be assumed to be zero. The resulting simple formula for the internal drag is:

$$C_{D_{in}} = K (\Delta p/q)^{3/2} \quad (28)$$

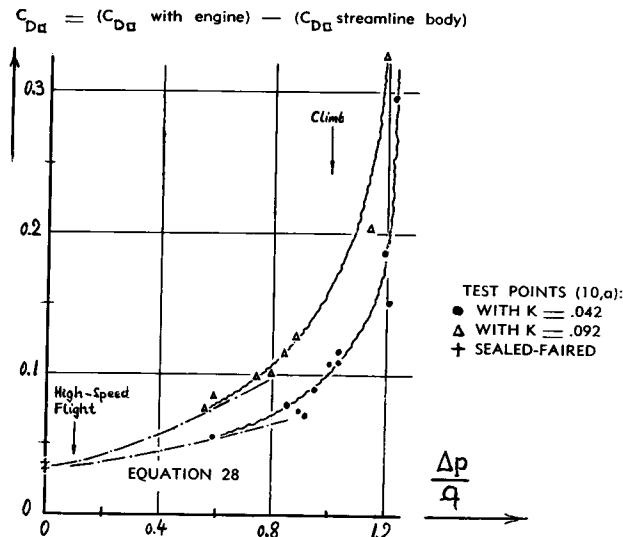
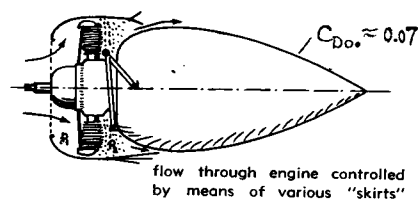


Figure 11. Drag due to cooling of a radial engine, tested (10,a) and analyzed for two values of conductivity.

The experimental points plotted in figure 11 are obtained from tests with an unheated engine installation, for two different values of conductivity. Equation 28 expresses the internal drag with sufficient accuracy up to about $\Delta p/q = 0.4$. Beyond this flow ratio, the more complete equation 27 must be used to describe the drag. Here, as in the case of radiators, assumptions must also be made for the magnitude of the outlet pressure at high flow ratios. For example, the highest test points in figure 11 are around $\Delta p/q = 1.2$. The corresponding outlet pressure coefficient must be $C_{pout} = 1.0 - 1.2 = -0.2$. Putting this value into equation 27, theoretical points are found which agree sufficiently well with the experimental results in that particular condition.

External Drag. As in the case of ring radiators (figure 8), the increment of *external drag*, caused by the cowled installation of a radial engine can be comparatively small. In figure 11 for example, $C_{D_{ext}} \approx 0.035$. Some more experimental data on cowled radial engines are presented in Chapter XIII.

Streamline Cowling. The engine nacelles and cowlings investigated in (10), represent modest aircraft installations as around 1937. Cowlings and nacelles have been developed since, so that they are suitable for higher speeds, having higher critical Mach numbers (10,e) and (12,c). The arrangement in figure 12 can be considered as an extreme example, with the

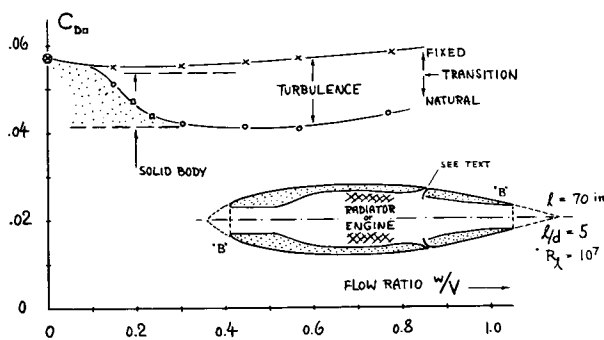


Figure 12. Total drag coefficient (on maximum frontal area S_{D}) of radiator or engine installation housed in a streamline nacelle, without and with turbulence stimulation (11).

powerplant (whatever type it may be) assumed to be located near the maximum diameter of the streamline nacelle- or fuselage shape. After subtracting the internal drag (which is not at issue in the investigation quoted), the external drag is obtained. Both the streamline body without openings, and the ducted body at flow ratios (based on frontal area of the body) between 0.3 and 0.6, have some laminar flow along the forebody. The drag is equally increased in both conditions, after fixing transition near the nose by means of a carborundum strip. At any rate, the external or parasite drag caused by inlet and outlet of the cooling flow, is practically reduced to zero in these conditions. However, at small rates of flow and without stimulation of turbulence, the ducted configuration shows higher drag coefficients than the solid body. The inlet opening is evidently "overflowing" in this case; and the flow around the rim of the opening produces boundary layer turbulence in a manner similar to that as caused by the carborundum strip. — As an alternative for the discharge through the rear end of the body, an annular outlet slot (at 63% of the body length) has also been investigated (see in figure 12). The external drag of this configuration is somewhat higher than with the tail outlet (ΔC_{D} is between 0.005 and 0.010). With either outlet, the external drag coefficient (0.04 to 0.06) is considerably smaller than those of the old-type nacelle installations quoted later, in Chapter XIII, (having total drag coefficients between 0.15 and 0.21).

2. JET-ENGINE INSTALLATIONS

"The change in aircraft propulsion from the piston engine to the turbojet engine moved the slipstream from outside the airplane into its interior" (13,a). Engine thermodynamics are not a subject of this book. The external drag caused by the air inlet of these engines, shall be considered, however.

Body-Nose Inlet. Figure 13 presents a basic body-nose inlet suitable for higher and possibly supersonic speeds. At velocity ratios (with w defined for the inlet area) above $w/V = 0.6$, the external drag of the configuration is \approx equal to that of the solid streamline body (tested on the sting support as shown). The internal recovery is close to 100% up to $w/V = 1$.

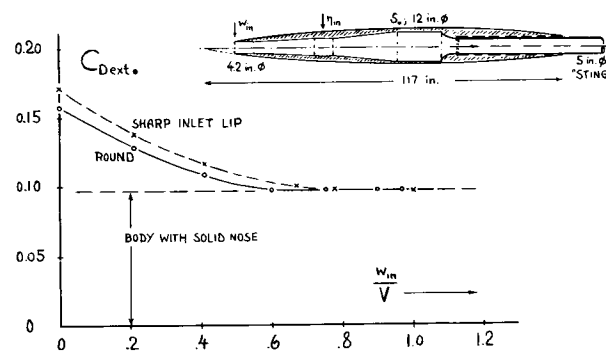


Figure 13. External drag of a ducted body of revolution (12,a).

Internal Characteristics. Inlet openings (scoops) at both sides of the fuselage are employed in several modern fighter airplanes (13,a). To obtain adequate internal efficiency (recovery η_{in}), boundary layer control is frequently applied by means of a "bleed-off" slot between wall and scoop opening. It seems, however, that certain installations for turbo-jet engines are markedly different from radiator installations with respect to the average or predominant value of the inlet velocity ratio; which may be in the order of $w_{\text{in}}/V = 1$. To obtain such ratios, engine installations do not necessarily rely on aerodynamic pressures at in- and outlet opening. The flow is maintained down to zero speed of advance — by means of the engine compressor. As a consequence, stagnation of the boundary layer ahead of the intake opening may not be such a problem as in radiator intakes. The installation in figure 14 (with a small "hump" inside the opening) has an internal loss coefficient $\xi = 0.1$ at flow ratios w/V between ≈ 0.6 and ≈ 1.7 . The configuration in figure 15 does not have either, a specific control of the boundary-layer at the side of the fuselage. Yet the recovery ratio is $\eta_{\text{in}} = 0.9$ at $w/V = 0.3$ to 1.5 and at C_L between 0.4 and 1.0.

- (11) Becker, Streamline Body, NACA T.Rpt 1038 (1951).
- (12) Development of body-nose intlets:
 - a) Blackaby-Watson, NACA T.Note 3170 (1954).
 - b) Baals-Smith-Wright, NACA T.Rpt 920 (1948).
 - c) Nichols, With Spinner, NACA T.Rpt 950 (1949).
- (13) Fuselage intlets for turbo jet engines:
 - a) Lockheed F-80 side intlets and McDonnell wing-root intlets, Aero Digest April 1951 p.75.
 - b) Holzhauser, Air-Induction, NACA RM A51J19a.
 - c) Keith, Wing-Root Inlet, NACA T.Note 3363 (1955).
 - d) Nichols, Submerged Scoop, NACA T.Note 3437 (1950).

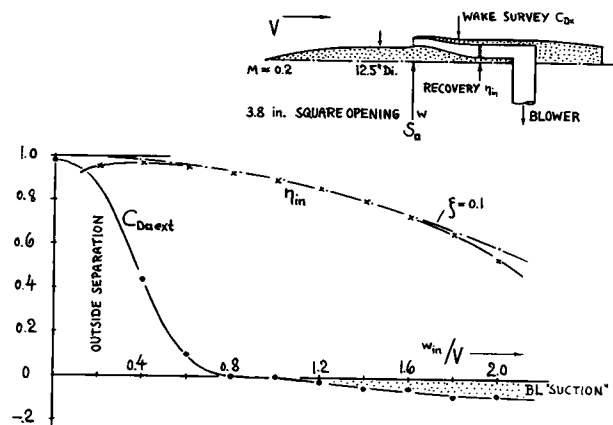


Figure 14 Characteristics of a scoop-type air-induction system designed to be used for a jet engine (13,b).

Scoop Intake. Figure 14 presents characteristics of an "air-induction" system to be installed as a pair at the sides of a fuselage. In the vicinity of $w_{in}/V = 1$, the external drag caused by the intake is zero. At ratios below $w/V = 0.8$, the inlet opening is "spilling"; considerable parasite drag is caused by separation from the outside, up to $C_{D_{in}} = 1$ (based on opening area). At flow ratios higher than unity, a negative drag component is evident. It is suggested that the inlet favorably affects the external flow past the afterbody by way of what we may call boundary-layer control.

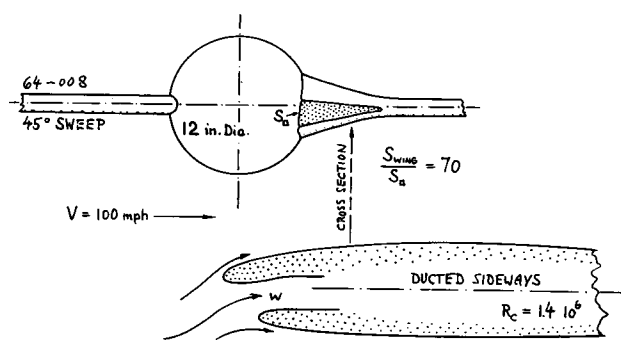


Figure 15. Triangular inlet for a turbo-jet engine in the wing root (13,c). For comparison(left): wing without inlet.

Wing-Root Inlet. Another location for a pair of intakes is at the wing roots as in figure 15. The inlet lips are properly staggered (as in figure 10), to provide internal efficiency at intermediate and higher lift coefficients. To compensate for the increase in wing thickness (necessary to house one engine at each side, half in the wing and half in the fuselage), the root chord is increased roughly 100%. In a manner similar to that of the wing-nose inlet in figure 10, the external drag of the configuration with inlet reduces steadily with the lift coefficient — in comparison to the bare wing configuration (left side of drawing) at equal lift. Here again, the flow past the outside (along the

wing-root corners) is evidently improved on account of boundary-layer "suction". The lengthened wing root may also be considered as a fairing. At any rate, lift at equal angle of attack is increased through addition of the engine installation. With the engines built-in, the same lift coefficient is, therefore, obtained at an angle of attack which is smaller than that of the bare-wing configuration. Comparing, however, drag coefficients at equal angles of attack, slightly positive increments of the external drag coefficient are found for the configuration including the engine installation.

Lift Due To Inflow. Another way of analysis also helps to explain the increment of lift as found in the wind-tunnel test. The mass of air taken-in through each opening is deflected into the direction of the wing chord. The corresponding component of lift is

$$C_{Ld} = 2(w/V)\sin\alpha \quad (29)$$

Applying this equation to the configuration in figure 15 as a correction, external drag coefficients due to the engine installation are obtained in the order of $C_{D_{in}} = 0$ at $C_L = 0$ and $C_{D_{in}} = 0.05$ (based on inlet area) at $C_L = 1$.

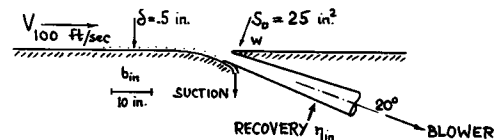


Figure 16. Example for a submerged-type air-induction system, utilizing boundary layer suction, investigated for a high-speed turbo-jet engine installation (13,d).

Flush-Type Intake. On account of forced flow in turbo-jet engine installations, a flush-type intake opening can be applied such as in figure 16. Note that the boundary-layer control slot at the entrance does not effect the external (parasite) drag. The suction slot is helpful, however, in raising the internal efficiency from $\eta_{in} = 70\%$ (without slot) to the order of 90% (at $w/V = 0.5$ to 1.5), when applying suction quantities corresponding to

$$C_{Qd} = Q/(V \delta_\Delta b_{in}) \approx 2 \quad (30)$$

where δ_Δ indicates the displacement thickness of the boundary layer ahead of the opening and b_{in} the spanwise dimension of the opening. The external drag coefficient due to the engine installation (on inlet area), including a component corresponding to the suction quantity "Q", is between $C_{D_{in}} = 0$ and 0.03, at $w/V = 0.8$ to 1.6.

D. HEAT AND COMPRESSIBILITY EFFECTS.

So far, radiator and engine installations have been treated without consideration of heat. Heat is transferred, of course, in engine-cooling systems. Heat is also introduced through compressibility at higher speeds as applied in modern airplanes. Heat as treated in this section, changes the internal conditions of cooling systems; and it thus changes their momentum drag.

1. Influence Of Cooling Heat (14)

Radiator Core. Because of heat transferred from the cooling liquid, the air flow is accelerated along the core openings. The friction drag within the openings increases accordingly. Also, the acceleration requires an additional pressure differential. The loss coefficient under "hot" conditions is therefore:

$$\xi_* = \xi_0 (T_{amb} + 0.5 \Delta T) / T_{amb} + (2 \Delta T) / (f^2 T_{amb})$$

where f = area ratio of the openings to the total cross section of the core, T_{amb} = temperature of the ambient air, ΔT = temperature increase of the air while passing through the core, and $(T_{amb} + 0.5 \cdot \Delta T)$ = average temperature of the heated air within the core openings. Full-scale experience shows that the temperature increment is in the order of

$$\Delta T = 0.7 (T_{liquid} - T_{amb}) \quad (32)$$

Practical core designs have opening ratios in the order of 0.7. The average temperature difference ($T_{liquid} - T_{amb}$) is in the order of 120°F for water and some 190°F if glycol is used as cooling medium in place of water. In practical cases, equation 31 yields an increase of the loss coefficient between 10 and 20%.

Propulsion. The heated radiator duct is, in principle, a ram jet. The diffuser provides the compression needed for the operation of such a system, and the core adds the heat to the air. Finally, the portion of the duct between core and outlet serves as nozzle through which the jet is discharged. The resultant

force (drag or thrust) of the heated radiator system can be calculated by the same methods as previously outlined for unheated systems. Taking into account the reduced density of the air passing through the outlet:

$$\rho/\rho_{out} = T_{out}/T_{amb} = 1 + (\Delta T/T_{amb})$$

equation 8 (applied for $C_{pout} = 0$) then becomes

$$w_{out}/V = \sqrt{[1 - [\xi_*(w/V)^2]]} \rho/\rho_{out} \quad (34)$$

and equation 14 transforms into

$$C_{D\alpha} = 2(w/V) \left[1 - \sqrt{[1 - [\xi_*(w/V)^2]]} (1 + (\Delta T/T_{amb})) \right] \quad (35)$$

The "hot" loss coefficient as indicated by equation 31 must be used in this equation. Depending, therefore, upon the magnitude of ' ξ ' and the flow ratio w/V , the resultant differential of internal drag can be either positive or negative.

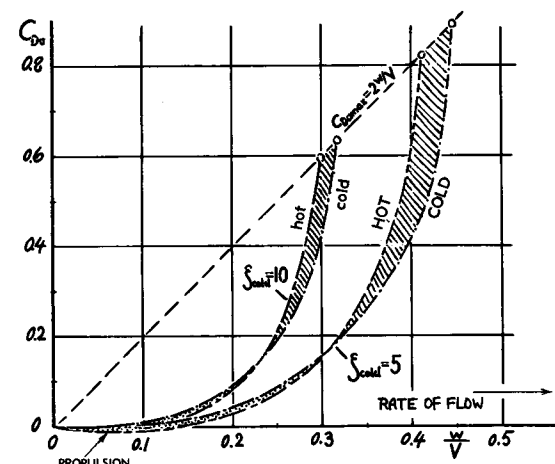


Figure 17. Theoretical internal drag coefficients of two radiator installations, without and with heating (14).

Practical Conclusions. Figure 17 shows as an example the calculated drag coefficients of a ducted radiator system for both the cold and the heated condition, for two representative loss coefficients. In the range of low flow ratios, up to $w/V = 0.10$ or even $= 0.15$, a propulsive force can be expected. Its magnitude is small, however, in comparison to the external drag (listed for instance in figures 4, and 6 to 8). Up to about $w/V \approx 0.10$, the difference between the cold and the heated radiator is roughly

$$\Delta C_{DM\alpha} = -(0.1 \text{ to } 0.2) w/V \quad (36)$$

At higher flow ratios, beyond $w/V = 0.2$, or $= 0.3$, the increased pressure loss across the core is predominant; and heated radiators then have drag values larger than in cold condition. Wind-tunnel results are presented in (14,a) qualitatively confirming the results derived above.

(14) Influence of heating on radiators:

- a) Goethert, Aerodynamic Drag of Radiators Including Heating, Lufo 1938 p.432; Trans NACA T.Memo 896.
- b) Meredith, Cooling in Ducts; ARC RM 1683.
- c) Schlupp, see in reference (1,a).
- d) Rauscher-Phillips, J.Aeron.Sci. 1941 p.167.
- e) More correctly, heat transfer is $\sim (w)^{0.8}$.

In Air-Cooled Engines, the average temperature differential between the cylinders and the ambient air is higher than in radiators; $(T_{\text{liqu}} - T_{\text{amb}})$ is in the order of 250 to 350°F, and $(T_{\text{liqu}} - T_{\text{amb}})/T_{\text{amb}}$ = 0.5 to 0.7. The parameter $(\Delta T/T_{\text{amb}})$ needed in equations 31 and 35, therefore, attains values up to 0.5. Under high-speed flying conditions, with $(\Delta p/q)_{\text{cold}} \approx 0.15$ and $(w/V)_{\text{cold}} \approx 0.03$, for example, an engine with $K_{\text{cold}} \approx 0.07$ is expected to show a conductivity that is decreased as per equations 26 and 31 to $K_{\text{hot}} \approx 0.063$. The decrement is some 10%, which means that the loss coefficient is increased from ≈ 200 to about 240 (that is, by some 20%). Because of the temperature parameter in equation 35, the resultant coefficient of internal drag is nevertheless decreased from $C_{D_{\square}} = 0.006$ to -0.003 . Considering the internal system alone, the engine installation thus shows a propulsive thrust component (negative drag). In the range of higher flow ratios (corresponding to climb conditions of average airplanes), the heated stream of cooling air is still expected to provide a drag reduction in the order of $\Delta C_{D_{\square}} = -0.005$, in comparison to the cold engine at the same mass rate of flow.

2. Influence Of Compressibility.

The external drag of radiator installations increases at subsonic Mach numbers according to the principles outlined in Chapter XV. In this section here, consideration is limited to the influence of compressibility upon internal characteristics.

Increase Of Temperature. Ahead and within every cooling system, the air is decelerated from the flight velocity V to the velocity within the openings of the radiator core or between the fins of the engine cylinders. This velocity is w/f where "w" = nominal velocity within the cross section of core or engine cowling, and "f" = opening or porosity ratio $S_{\text{open}}/S_{\square}$ of core or engine area, respectively. Because of the increase of pressure associated with deceleration, a corresponding part of the dynamic energy of the air flow is transformed into heat. The increase of temperature (16) within the cooling openings is given by

$$\Delta T/T_{\text{amb}} = 0.2 M^2 [1 - (w/V)^2/f] \quad (37)$$

This increment has a certain influence upon the internal flow characteristics of radiators and air-cooled engines. Since there is no additional energy being fed into these systems, a propulsive component similar to that as found in connection with radiator heating, cannot be expected from compressibility, however.

Radiators. Assuming, for example, in an average radiator installation $w/V = 0.15$, $f = 0.7$ and $M = 0.8$, the air temperature within the core openings is increased by some 40°F. For water, the average temperature difference between the hot fluid and the cooling air is thus reduced from some 120 to 80°F. To maintain the same cooling effect, the flow ratio w/V must therefore be increased, at least in proportion to $120/80 = 1.5$, in this case (14,e). The internal drag is consequently increased, as found through application of equation 35, by some 150%. However, at flow rates in the order of $w/V = 0.1$ (as can be assumed to be prevailing when flying at $M = 0.8$), an increase of the *internal* drag by 150% only means an increment in the order of $\Delta C_{D_{\square}} = 0.01$, a value which may be small in comparison to the external drag of such an installation.

Air-Cooled Engines. Since the velocity through the openings between fins and baffles around air-cooled engine cylinders is generally higher than that through the openings of radiator cores, the increase in temperature as indicated by equation 37 can be comparatively small. For an engine with $K = 0.07$, for example, with $\Delta p/q = 0.2$ and $w/V = 0.03$ (as in high-speed operation of an airplane), the expected temperature increment at $M = 0.8$ amounts to some 20°F which is in the order of not more than 7% of the average temperature differential $(T_{\text{liqu}} - T_{\text{amb}})$ of air-cooled engines. The corresponding increase of internal drag may be negligible in many cases.

-
- (15) Becker-Baals, Heat and Compressibility Effects in Internal Flow Systems, NACA T.Rpt 773 (1943).
 - (16) Derived from treatment in Chapter XV.
 - (18) Drag characteristics of air scoops:
 - a) Boeck, Air Scoops, Messerschmitt TB 38 (1941).
 - b) Barth, Tests, Tech Berichte, ZWB 1939 p.95.
 - c) Schirmer, Ventilation, Tech Rpt Luftsch. Bau Zeppelin No. 500/237 (1931) and 500/264 (1932).
 - (19) Drag of ventilation openings:
 - a) Rogallo, Internal-Flow Systems, NACA T.Rpt 713. This source presents experimental results on many different types of openings, and some theoretical information.
 - b) Winter, Tests at TH Graz, reported by Hoerner, German Doct, ZWB UM 7843 (1945).
 - c) Rokus and Troller, J.Aeron.Sci. 1936 p.203.
 - (20) Winter and Jacklitsch, Suction Effect Behind Radiator Flaps, ZWB Tech Berichte 1944 p.309.
 - (21) Hewins and Reilly (Newport News), Condenser Scoop Design, Trans Society NAME 1940.
 - (22) Characteristics of vents and drains:
 - a) Baeuerle, Pipe Ends, ZWB UM 3220 (AVA 1945).
 - b) Vick and Silhan, Drains Discharging into Subsonic Transonic Streams, NACA T.Note 3359 (1955).
 - c) Dewey and Vick, Outlets, NACA T.Note 3466 (1955).

E. INLET AND OUTLET OPENINGS

Air scoops are primarily used to feed air into the cylinders of reciprocating aircraft engines. Similar intakes are sometimes employed in ventilation systems. After passing through the airplane cabin or the vehicle compartment that is to be ventilated, the flow of air may then be discharged from some type of outlet. The internal drag of such systems can be calculated on the basis of the equations presented in section "A" of this chapter. The drag of inlet and outlet devices can also be studied separately.

1. Drag Of Air Scoops

Momentum Drag. The minimum drag of the intake device of a ducted system is equivalent to the momentum of the stream tube which is diverted from the external flow into the opening. Disregarding the boundary layer on the body surface at which the intake is mounted, the momentum drag of a scoop corresponds to equation 20. In fact, three of the shapes illustrated in figure 18 and the two in figure 19 are designed in such a manner that the boundary-layer does not get into the opening. In the scoop in figure 20, some volume of boundary layer is obviously taken in. Therefore, here as in figure 21, the definition of $C_D = 2 (w/V)$ is no longer perfect; the momentum drag must be expected to be somewhat smaller. For example, results in figure 22 suggest a constant of 1.8 in place of the "2" in equation 20.

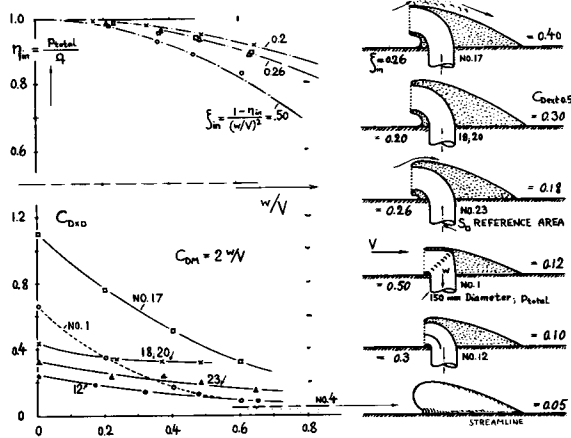


Figure 18. Shape, internal recovery and drag of several air scoops (18,a).

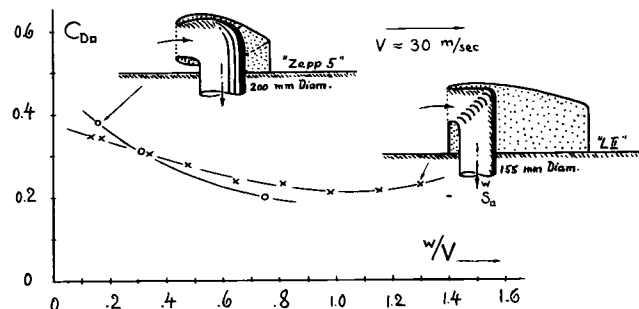


Figure 19. External drag coefficients of two airship-type engine scoops (18,c).

The External Drag of an air scoop or inlet opening is found after subtracting the internal or momentum drag from the measured total drag. In figures 18 to 21, the external component is seen decreasing with the flow ratio. A minimum is found in the vicinity of a certain " w/V " value which depends upon external and internal shape, particularly of the "mouth". Below this ratio the openings are "overflowing"; for sharp opening edges, the external drag coefficient then reaches values of C_{Dext} up to 1.0, at $w/V \rightarrow 0$. By reducing the entrance diameter in relation to that of the duct, it is possible to obtain optimum shapes for certain desired flow ratios. The range of these ratios is increased by rounding the rim of the inlet opening. The most favorable scoops present external coefficients below 0.1.

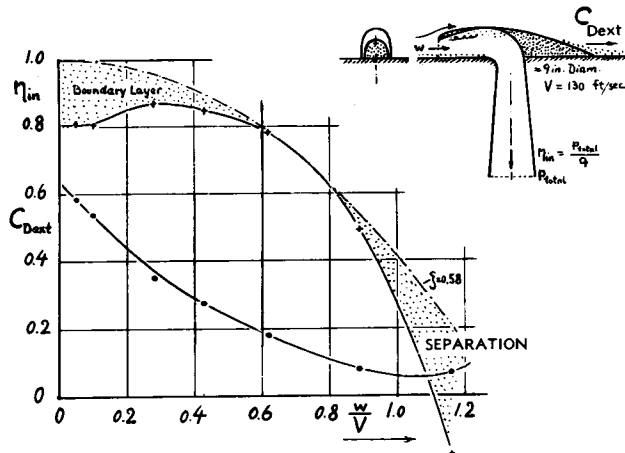


Figure 20. External and internal coefficients of a scoop (18,b) evaluated on the basis of $C_{DMa} = 2 w/V$

Internal Losses. As far as drag is concerned, it does not matter how the momentum is "lost" inside a ducted system. For the operation of an engine it is important, however, how much of the dynamic pressure is recovered. Figures 18 and 20 give several examples in this respect; and equation 5 indicates the connection between the recovery ratio η_{in} and the intake loss coefficient ξ_{in} . It is seen that those shapes in figure 18 whose inlet opening is somewhat removed from the wall, have much lower loss coefficients than the other scoops including that in figure 20, which have the opening adjacent to the wall.

2. Drag Of Ventilation Systems

Ventilation is needed to supply fresh air to the interior compartments of aircraft and other vehicles, for venting of fuel tanks, and to cool engine parts or other equipment.

(a) Drag of Inlet Openings.

Drag coefficients of some typical inlet openings are presented in figures 21 to 23. The smallest drag coefficients ($C_{D\Delta} = 0.1$) are found for "streamline" openings similar in shape to the air scoops of figure 18.

Blunt Scoops. Obliquely cut-off pipe ends have the highest external coefficients, up to $C_{D\Delta} = 1.5$, depending upon the ratio of height to diameter. Figure 23 shows three scoops with "blunt" entrance shape. The total drag coefficient of two of these shapes is approximately constant (independent of flow ratio) as shown in the graph for one of them. Upon increasing w/V , momentum drag evidently replaces more and more the external (parasite) drag. Drag is large, particularly in the flared shape.

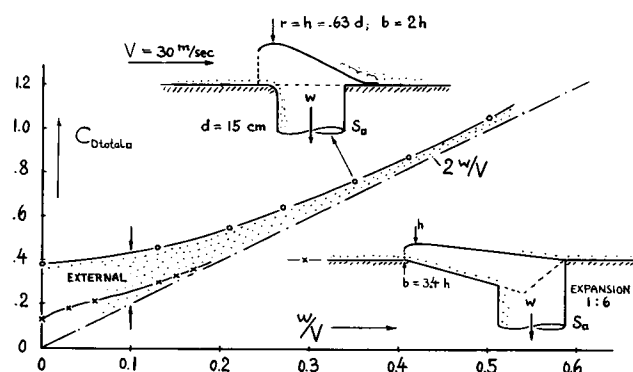


Figure 21. Drag of two sheet-metal ventilation intakes (19,b); (a) scoop type, (b) conical inlet.

Flush Inlets. External drag is, of course, a function of the protruding frontal area of the inlet scoop. The recessed type in figure 24 has an average pressure coefficient in the order of $C_p = +0.32$. With respect to drag, the graph indicates some value at $w/V \approx 0$. In the range of higher flow ratios, the total drag is considerably below the value as per equation 35. It is suggested that in this case (where only boundary-layer material is taken into the duct), the momentum drag coefficient (referred to the cross-section area of the duct) roughly equals the pressure coefficient C_p .

SHAPE OF OPENING	C_{Dmin}	AT w/V	ξ_{in}
a)	1.0	> 1	2.7
b)	.15	0.9	2.0
c)	.10	0.8	1.7
d)	.35	> 1	2.7

Figure 22. Aerodynamic characteristics of several inlet openings (air scoops), tested in (19,a). Height (diameter) of the scoops $h = 2$ to 6 inches; thickness of boundary layer (without openings, at same location, $\delta = 1$ inch). Drag coefficient based on $d^2\pi/4$.

Internal Characteristics. With regard to internal losses, figure 20 presents the inlet efficiency of a streamline opening. As mentioned before, the total pressure inside the intake is a function of the boundary layer originating ahead of the opening. Although in the case as illustrated, the thickness of this layer is but 1% of the height of the opening, the pressure recovery at $w/V = 0$ is only 81%. The boundary layer evidently accumulates in front of the inlet. The loss coefficient (equation 2) reaches a minimum of $\xi = 0.58$ in that example, in the vicinity of $w/V = 0.7$. — Holes, simply cut into the surface of a wall, have a recovery close to zero. Such openings can only take-in air by means of positive static pressure superimposed to the location of the opening, or if there is a negative pressure gradient provided somewhere inside the duct, such as by a blower. However, the recessed type of opening in figure 24, has a recovery in the order of 30% without artificial help. Still better characteristics are obtained with the opening in figure 28, designed to be used in the condenser cooling system of steam-powered ships.

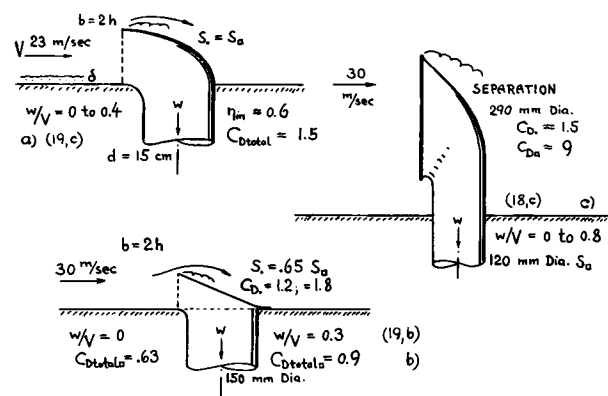
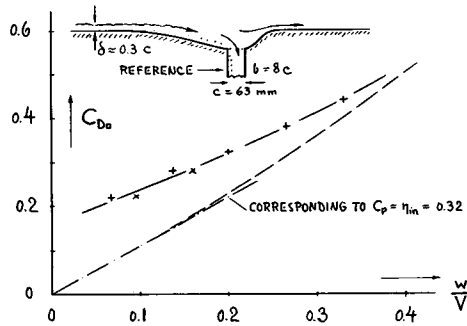
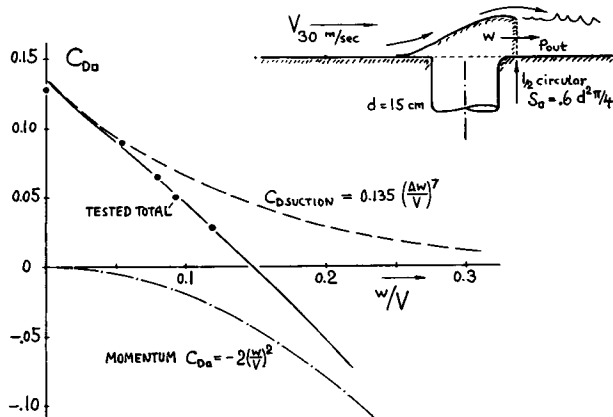


Figure 23. Characteristics of three "blunt" scoops.

Figure 24. Drag of a recessed type of air intake (19,c).(b) *Drag of Outlet Openings*

In some ventilation systems, outlet openings are not provided at all. The flow of air fed into the passenger compartment of an airplane or under the hood of an engine, may escape at random through gaps or openings in the skin of the craft. Under such conditions, the momentum of the outflow is usually wasted, so that equation 20 represents the final value of the internal drag of such systems. It is more economical, however, to install suitable outlet openings such as the more favorable ones in figures 25 to 28. Provided that the outlet discharges in downstream direction, the internal drag in these systems reduces, and the rate of flow is increased.

Figure 25. Total drag coefficient of an outlet opening, tested (19,b) and analyzed.

(24) Ramshorn, Wind-Tunnel Investigation of Double-Spinner Models, Rpt by BMW (Munich) presented at Propeller Meeting at DVL April 1940.

(25) NACA, Rotating Cowling, Rpt RM A54G14.

(26) Efficiency of three-dimensional diffusers:

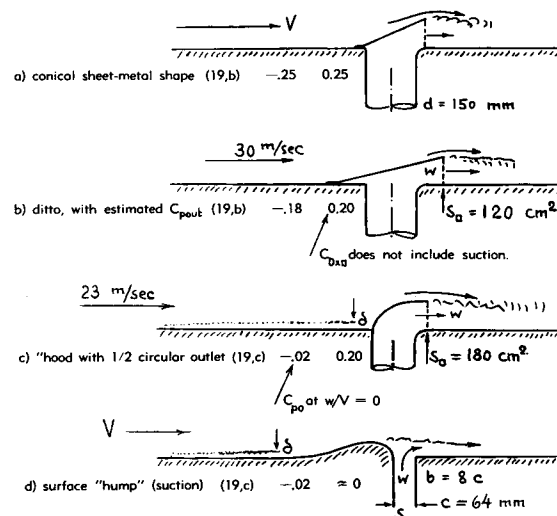
a) Gibson, Diffusers, Proc.Roy.Soc. London A No.563 1910 p.366 and Trans Roy.Soc. Edinburgh 1913 Part 1 p.97.

b) Peters, Ing.Archiv 1931 p.92; NACA T.Memo 737.

Momentum. Equation 9 (indicating rate of flow) and equation 14 (indicating momentum drag) are also applicable to ventilation systems. It is convenient, however, to measure w in the cross section of the inlet- or outlet section, respectively; to refer the drag coefficient to the corresponding cross-section area, and to reduce the internal loss coefficient of the system to the same area. Considering an outlet opening separated from the rest of the system, a thrust component is obtained (originating within the elbow or some other place ahead of the discharge opening). Applying equation 13, this thrust, equal to negative drag, is found to be

$$C_{Doutlet} = -2(w_{out}/V)^2 \quad (40)$$

By subtracting this component from the drag measured, for instance, on a wind-tunnel balance, the external drag coefficients are obtained as plotted or listed, respectively, in figures 25, 26 and 27.

Figure 26. Suction pressure and external drag coefficient at zero flow, of several outlet openings.

Drag Analysis. In figure 25, an analysis is presented of the drag of a typical outlet opening. After subtracting the "negative" internal component, indicated by equation 40, there remains an external drag coefficient. This component is subdivided into two parts, some parasite drag originating on the exterior of the outlet, and the "base" drag which corresponds to the negative pressure (if any) behind the opening. As far as outlet nozzles (directed downstream) are concerned, analysis of experiments (20) indicates that this pressure varies with the flow ratio roughly as

$$C_{pout} = C_{pout0} [(V - w_{out})/V]^6 \quad (41)$$

where C_{pout0} indicates the negative "base" pressure at $w/V = 0$, corresponding to the shape of the outlet.

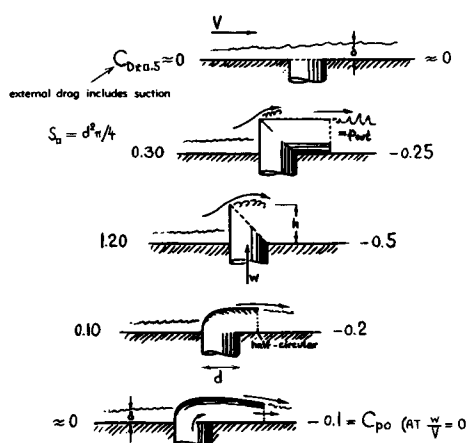


Figure 27. External drag coefficient (at $w/V = 0.5$; on $d^2 \pi / 4$) and suction pressure coefficient (at $w/V = 0$) of several outlet shapes (19,a). Boundary-layer thickness $\delta = (0.3$ to 0.5) d .

A plot of this function helps to understand the variation of the drag coefficient in figure 25. Referring velocity ratio and drag to the downstream-directed outlet opening (S_a) the total drag coefficient of a ducted system is

$$C_{Dq} = D/qS_a = 2 k (w/V) - 2 (w/V)^2 + C_{Dxout} - C_{pout}$$

The first term is as in equation 20. The second term represents the jet thrust of the stream leaving the system. " C_{Dxout} " indicates the external (parasite) drag, excluding the suction pressure at the outlet (if any), which in turn is added as the last term of the equation. The factor in the first term is $k = 1$ or somewhat smaller than that (in cases where boundary layer material is taken into the system).

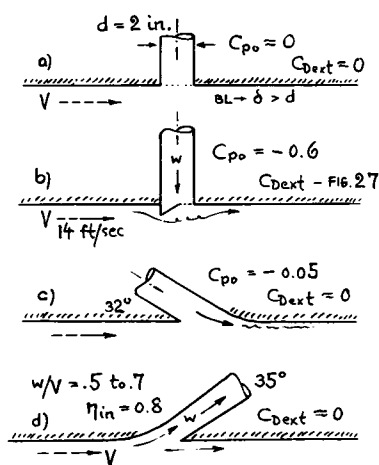


Figure 28. Pressure coefficients (and estimated drag coefficients) of several marine-type condenser-water outlets (21) and of one inlet opening.

Streamline Openings. The most favorable inlet openings may be the scoop types (in figures 18 through 22). Among the outlet openings (shown in figures 25 to 28), the hood-like shapes have the lowest drag coefficients. Judging, however, the merits of inlets and outlets, the pressures provided by them, must be considered too. It is favorable in this respect, to place a diffuser directly behind the intake. In regard to the outlet it is usually favorable to place a diffuser ahead of that opening and to increase its geometrical size, rather than to employ an outlet shape which, on account of its more negative pressure coefficient, may help to obtain the desired rate of flow.

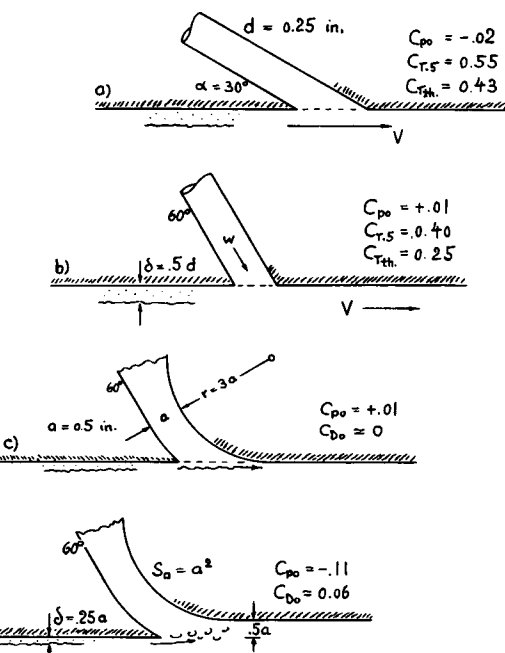


Figure 29. Characteristics of several flush-type discharge openings (22,c). Subscript "o" indicates $w/V = 0$; subscript ".5" denotes conditions at $w/V = 0.5$.

Outlet Thrust. Wind-tunnel tests (22,c) on various flush-type outlet openings give information on drag as a function of discharge ratio (w/V). Figure 29,c indicates zero drag for $w/V = 0$. Shape "d" has a small external drag coefficient (in the order of 0.06). Assuming that in the straight outlets, the discharging jet does not turn around the downstream corner where the pipe meets the outer surface — the thrust "T" of the outlet is theoretically

$$C_T = T/(q S_a) = 2 (w/V)^2 \cos \alpha \quad (44)$$

Tested coefficients are larger, however, as listed in figure 29,a and b for $w/V = 0.5$. Some suction evidently originates at the downstream edge of the openings, thus pulling the discharged stream somewhat around.

Vent Openings. Figures 30 and 31 present outlet pressures and drag coefficients of various pipe ends used as vents (without in- or outflow) for aircraft fuel tanks and as drains in places where oil drippings or water may accumulate. The highest suction pressures are produced by pipes cut off in a direction parallel to the general flow. The lowest drag coefficients (on frontal area) are found in the inclined shapes.

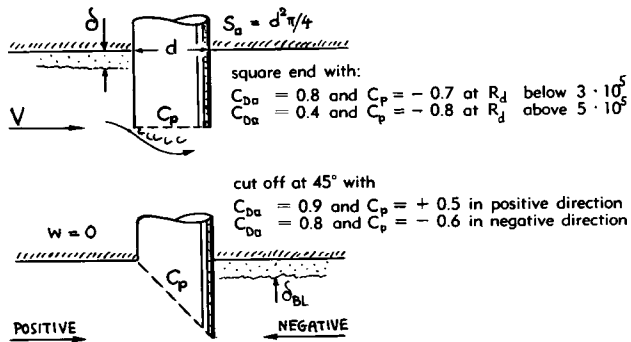


Figure 30. Drag and suction pressure of simple vent openings.

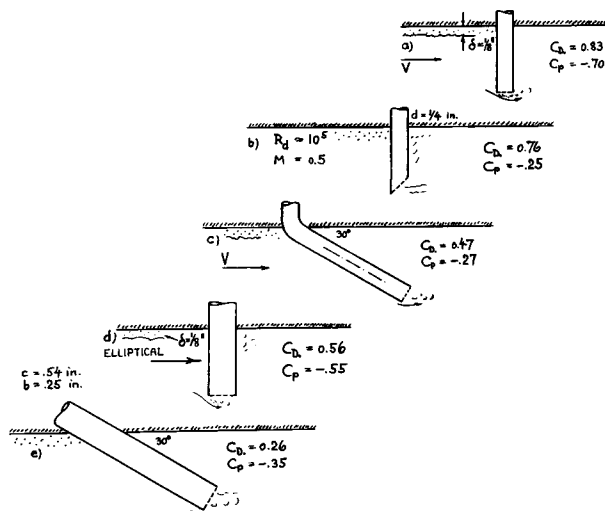


Figure 31. Drag of various simple types of protruding vents (22,b) at $w/V = 0$. Shapes (a) to (c) are pipe ends; shapes (d) and (e) are of elliptical cross section. Drag coefficients on projected frontal area.

SUPPLEMENTARY NOTES

Efficiency Of Diffusers. There are several definitions of efficiency possible. We will apply the pressure ratio as follows:

$$\eta_p = (p_2 - p_1) / (q_1 - q_2) \quad (50)$$

where "2" indicates average conditions at the larger, and "1" those at the smaller end of the diffuser. Efficiency is a function of the area ratio (S_2/S_1) as well as of the opening angle " 2ϵ ". Figures 32 and 33 present experimental results on diffusers placed within ducts, where the velocity distribution ahead of the expansion may have reached a final shape similar to parabolic. This is not the condition found in air-intake openings of engine or ventilation systems. It is felt, however, that the material presented may help to understand the mechanism of "diffusion". — As a function of area ratio, equation 18 indicates a lower limit for the efficiency. Figure 32 shows that diffusers with opening angles (2ϵ) above 90° follow that equation closely. Figure 33 demonstrates maximum

efficiencies in the order of 90% for diffuser angles (2ϵ) between 5 and 10° . Above this range, efficiency decreases rapidly to (and below) the level as indicated by equation 18. Between (2ϵ) = 50 and 100° , it is suggested that fluctuations, with the flow swinging from one side of the diffuser to the other, produce additional losses of momentum. Flow separation can be reduced or postponed by certain obstacles such as screens or by vanes. One obvious remedy is the application of partitions, dividing a diffuser into a number of smaller units, each having a reduced angle. — Analysis of the experimental material leads to certain optimum dimensions of a diffuser. The optimum length ratio is very roughly

$$(l/d_1)_{opt} = 3 (S_2/S_1) - 1 \quad (51)$$

This empirical function applies to three-dimensional diffusers, under the conditions as stated above, at area ratios (S_2/S_1) between 1 and 5.

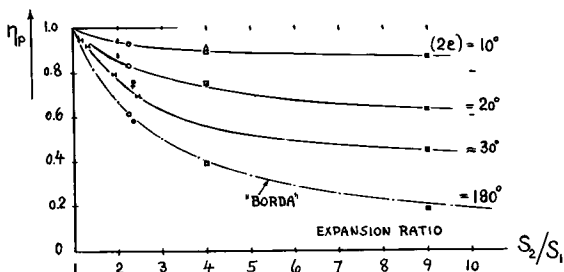


Figure 32. Efficiency of conical and similar diffusers as a function of the expansion ratio (S_2/S_1).

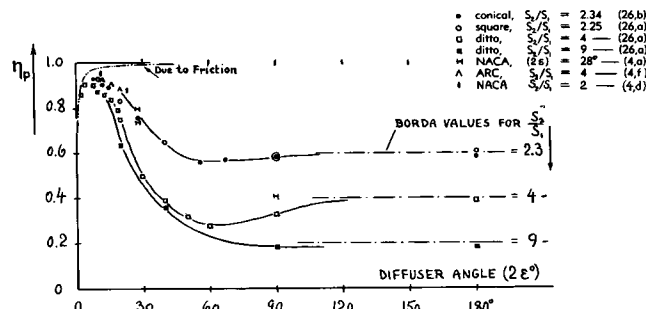


Figure 33. Efficiency of conical and similar diffusers as a function of the expansion angle (2ϵ).

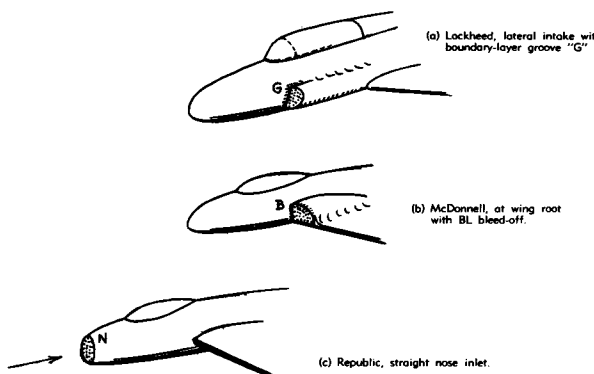


Figure 34. Three examples of intake openings for jet engines housed within the fuselage.

Fuselage Inlets have been discussed on pages 9-9 and -10. Figure 34 gives an illustration of three different methods of getting the required volume flow of air into jet engines housed within the fuselage. The nose inlet "N" takes-in air with high efficiency; it is subsequently difficult, however, to get the air flow ducted past the pilot's compartment into the engine. The other two types of intake need some boundary layer control as noted, in order to obtain adequate internal efficiency.

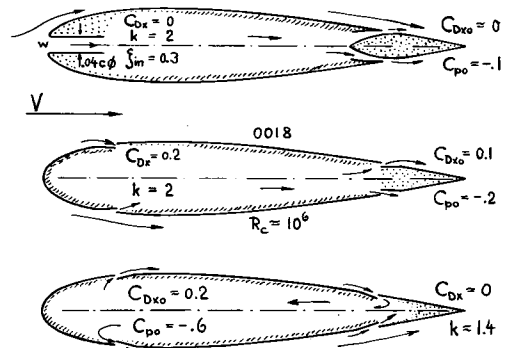
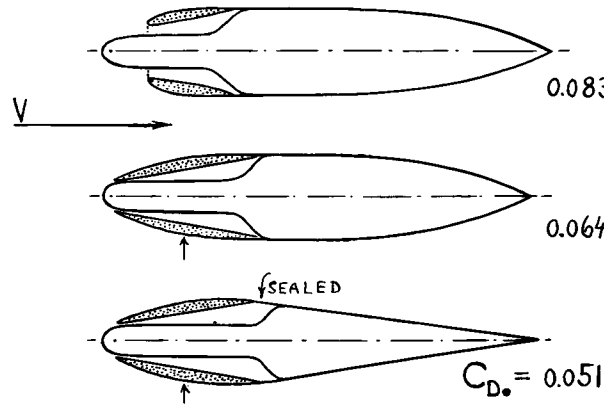


Figure 35. Two examples each (19,a), of inlet and outlet openings in a streamline foil section.

Ventilation Openings. Figure 35 presents examples of inlet and outlet openings demonstrating the influence of location on a simple type of wing section. Intake is favorable either at the stagnation point or within the boundary layer near the trailing edge. In regard to outlet, a forward location provides more-negative pressure coefficients, while aft locations give a lesser drag coefficient (down to zero). Attention is invited to other valuable statements made at the end of reference (19,a).

Figure 36. Drag coefficient of three smooth nacelle models (having ≈ 1 ft diameter and $1/d = 5$), designed to house a radial engine, tested at 37 m/sec and $R_L = 4 \cdot 10^6$. The outlet openings are closed and faired (zero internal flow). The slender forebody shape of the last two forms provides smooth external flow and a high critical Mach number ($M = 0.8$ in comparison to 0.6 in the first shape). The reduction of drag between second and third shape is essentially due to decreased wetted area. The source (24) also gives some proof for the correctness of equation 29 (indicating lift produced by internal flow). To accommodate a propeller, the cowling has to be cut at the location marked by arrow. The resultant "Double spinner" (rotating with the propeller) is a device considered for application in modern turbo-prop installations; see for example (25).



CHAPTER X — HYDRODYNAMIC DRAG

Within the larger field of fluid dynamics, the term "hydrodynamic" can refer to incompressible flow characteristics in any fluid, including air at low Mach numbers. Water tunnels have accordingly been used for aerodynamic testing. In the following, however, "hydrodynamic" is meant to indicate flow characteristics which are typical of liquids. Among the liquids involved in engineering applications, the water is predominant by far. Therefore, "hydrodynamic drag" essentially means that of bodies moving through water. Boats and ships are not treated, however, in this place. The chapter is subdivided, describing characteristics in fully submerged condition, in cavitating flow, and those of bodies piercing the surface.

Fish. Observation of fish has led to the conclusion that the hydrodynamic efficiency in moving through water is high. Fully laminar flow must be assumed, for example, to explain speeds up to 40 ft/sec as produced by a barracuda (1,a) having $W = 30$ lb, $l = 4$ ft and $R_d \approx 10^7$. Rather than claiming that the slimy skin (1,e) of such animals would reduce the frictional drag — it is suggested that the absence of any noisy, rattling or vibrating mechanisms (such as in all man-made craft or in wind tunnels and towing tanks) favors maintenance of laminar boundary-layer flow, up to and beyond a Reynolds number $R_d = 10^7$. This appears to be quite likely upon inspecting figure 9 in the "skin friction" chapter (1,d).

Critical Reynolds Number. Partly laminar skin-friction is a continued difficulty in the tank testing of ship hulls; it makes their viscous drag indeterminate. Forced stimulation of turbulence is, therefore, nowadays applied at least in smaller models and in fuller shapes. Disregarding such stimulation, there appears to be some systematic difference, however, in the transition Reynolds numbers as found in water and in air, respectively. As explained in the chapter on "pressure drag", drag coefficient or rear-side pressure coefficient of smooth spheres or circular cylinders can be used as an indication for the turbulence level in a stream of fluid. Results of such tests are plotted in figure 1, against the critical speed $V_{crit} = R_{crit} v/d$. It is seen that the critical Reynolds number generally increases with speed. This means that in one

A. FULLY SUBMERGED BODIES

All that has been said in previous chapters about boundary layer, Reynolds number, skin friction, flow separation, pressure drag, lift (if any) and so on — basically also applies to bodies placed in a stream of water. Disregarding the phenomenon of cavitation, therefore, the following first section primarily needs to amplify the aerodynamic findings by presenting characteristics which are peculiar to water and possibly different from those of the same shapes in air.

Skin Friction. It should be noted that in the "skin friction" chapter, experimental results are included on skin friction, obtained by towing plates or pontoons in water tanks. Schoenherr's function of the turbulent drag coefficient (equation 26 in that chapter; based on experiments performed both in air and in water), is becoming more and more the preferred formulation, used in the prediction of skin-friction drag of ship hulls. So, basically there is no difference between water and air with respect to frictional drag, if using the non-dimensional formulation of drag coefficient C_f as a function of Reynolds number R_d .

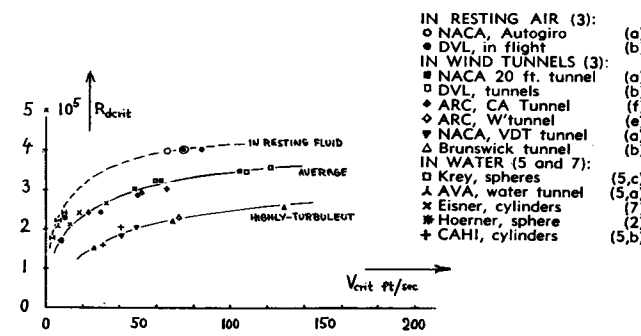


FIGURE 1. Transition R'number of spheres and cylinders, in air and in water, as a function of critical speed.

and the same tunnel, for instance, a smaller sphere passes the critical phase at a somewhat higher, and a larger sphere at a somewhat lower Reynolds number. Experiments in water are generally at lower speeds than those in air (with sphere diameters in the same order of magnitude). Plotting against the critical speed, shows that the available experimental points correlate fairly well with each other, on several levels of turbulence. Whether or not the result is accidental or is justified by some physical law is not known, however, to the author. It appears, at any rate, that under similar stream conditions (resting or moving fluid, respectively), the critical number in water may roughly be in the order of half of that in air.

Foil Sections. The turbulence effect in water is also demonstrated in figure 2, where the profile-drag coefficient of a laminar-type foil section, tested by wake survey in a towing tank (4,a) is seen to be on the turbulent level — while in a wind tunnel, the same section shows predominantly laminar flow up to $R_c = 7 \cdot 10^6$. Results on the 0012 foil section in air and water, are also plotted in the graph. Variation of the drag coefficient against R-number, appears to be shifted, approximately in a ratio of 1 : 2, because of the turbulence effect mentioned above.

Surface Roughness. It is explained in the chapter on "surface imperfections", that the influence of surface roughness on turbulent skin-friction drag only starts at certain "critical" Reynolds numbers. For sand-type roughness, the coefficient C_f is then only a function of the roughness grain size "k". Figure 3 has been prepared for average water, with a viscosity $\nu \approx 1.3/10^5$, (ft^2/sec). The critical or "permissible" sand-grain size is approximately

$$k_{\text{mil}} = 14/V_{\text{ft/sec}} = 8/V_{\text{knots}} \quad (1)$$

Comparing conditions in water at comparatively small speeds, with those of airplanes at their much higher speeds, the permissible sand-type roughness

FIGURE 2. Minimum drag coefficient of 0012 and of laminar-flow-type foil sections, tested by wake survey in towing tanks and in wind tunnels (4).

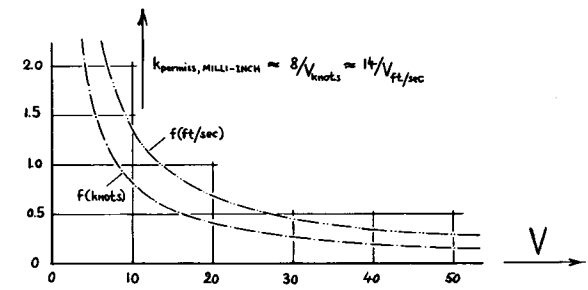
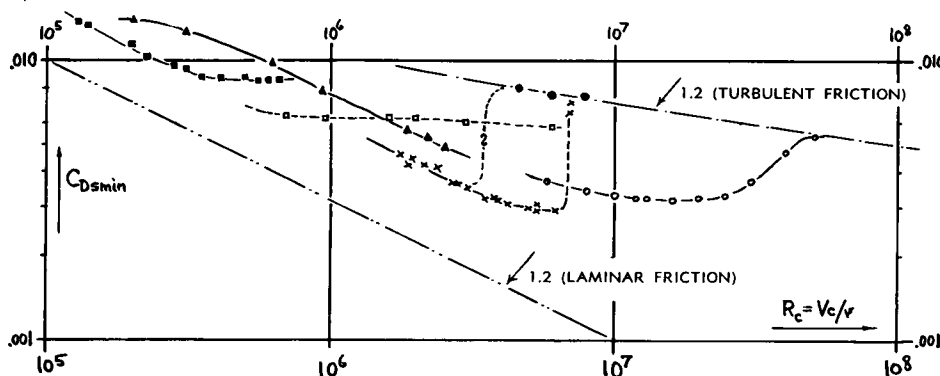


FIGURE 3. Permissible size ("diameter") of particles or grains on surfaces in tangential water flow.

size in these two cases, appears to be in the same small order of magnitude; for example, of 0.5 mil at 16 knots in water. The rough and average values in *table A* show that in ships, the grain size is usually well above the permissible. For example, surfaces treated with common marine paint, grow too rough at speeds in the vicinity of 4 knots. Information on drag above the critical roughness Reynolds number is given in Chapters VI and XI.

Type of Surface	k (mil)
polished — shining — smooth	0
aeronautical production paint	1
"smooth" marine paint (6,a)	2
bare steel plating (6,c)	2
average galvanized metal (6,c)	6
Navy hot plastic coating (6,a)	9
ordinary wood in water (6,c)	20
average concrete surface (6,c)	50
average barnacle growth (6,b)	200

Table A. Rough indication of average grain sizes (diameters) in physical surfaces.

Pressure Drag. Some of the experimental results on spheres and cylinders presented in the chapter on "pressure drag" have been obtained in water tunnels or towing tanks. Results in water, on other deeply submerged, two-dimensional bluff shapes in non-cavitating and non-ventilating flow are presented in figure 4. Most of the coefficients can be checked against those of corresponding shapes listed in the illustrations of the Chapter III. The coefficients of such

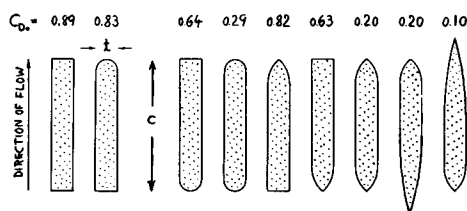


FIGURE 4. Drag of various shapes (7,a) in two-dimensional flow, towed in water (between end plates); $c \approx 1$ ft, $V = 12$ ft/sec, $R_C \approx 10^6$, $c/t = 6$.

- (1) Information on drag of fish:
 - a) Gero, Power and Efficiency of Large Salt-Water Fish, Aeron'l Engg Review January 1952 p.10.
 - b) Taylor, Analysis of Swimming Animals, Proc. Roy. Society (London) Ser.A 1952, No. 1117 p.158.
 - c) Gawn, Fish Propulsion, Trans INA 1950 p.323.
 - d) The alternative explanation is that the biological efficiency of fish is higher than expected. The thrust/weight ratio is up to 2.5 and 5.0; see "Novitates", Am. Mus. Nat. History No. 1601, 1952.
 - e) Tank Experiments on Pikes, Zts. der Vergleichenden Physik 1932 No. 2. A pike was towed alive (anesthetized), with and without slime, and also a wax model.
- (2) Hoerner, experiments on spheres:
 - a) Towing in Air by Airplane, Reference 3,b.
 - b) Gibbs & Cox Corp. In Water by Boat, 1952.
 - c) In Water-Tunnel, Fieseler Rpt 2 (1939).
- (3) Characteristics of spheres tested in air:
 - a) Mostly in Wind Tunnels, NACA Tech Rpt 558.
 - b) Hoerner, Experiments with Spheres Turbulence Roughness Lufo 1935 p.42; Translation NACA T.Memo 777.
 - c) DVL in Large High-Speed Tunnel, see in (b).
 - d) AVA (Winter), Large Tunnel (No. VI), 1939.
 - e) In Wind Tunnel, British ARC RM 1662.
 - f) In Compressed-Air Tunnel, ARC RM 1832.
- (4) Characteristics of foils tested in water:
 - a) Fage and Walker, Laminar-Flow Aerofoil in Froude Tank, British ARC RM 2165 (1948).
 - b) Townsin, Low-Drag Hydrofoil, Paper INA, 1954/5.
 - c) For Comparison in Wind Tunnel, NACA TR 910.
 - d) Locke, 0012, Stevens ETT, T. Memo 42 (1939).
- (5) Critical Reynolds numbers in water:
 - a) Drescher, Spheres, Yearbk D.Lufo 1941, p.I,714.
 - b) Konstantinov, Cylinders, see reference 18,e.
 - c) Krey, Sand Grains and Spheres in Water, Mitteilungen Pr.Versuchsanstalt W'bau Schiffb. Berlin Rpt No. 1 (1921).
- (6) Influence of roughness in physical surfaces:
 - a) Couch, Friction Tests of Ship-Bottom Paints, Taylor Model Basin Rpt 789 (1951).
 - b) Amtsberg, on Ship Hulls, Schiffbau 1937 p.135.
 - c) Hopf-Fromm, Z.A.Math.Mech. 1923 p.239, 339.
 - d) Kempf, Ybk.STG, 1937,159; TransINA 1937, 159.
 - e) Todd (TMB), Trans Society NAME 1951 p.315.
 - f) Moody, Pipe Friction, Trans ASME 671 (1944).
- (7) Drag of bluff shapes in water:
 - a) Eisner, Drag Characteristics of Cylinders in Towing Tank, Mitt.Pr.VAWS Berlin 1929, No. 4.
 - b) ARC, Drag of Sea Anchors, ARC RM 425.
 - c) Guide Vanes on Cylinder, TMB Rpt 504.

shapes can be considered to be comparatively constant with regard to Reynolds number. *Figure 5* gives drag characteristics of several "sea anchors" and "disks". The "bucket" shape has characteristics similar to those of parachutes (Chapter XIII). The high drag coefficient of the "collared" disk is caused by wiggling and swaying motions; these too are similar to those of parachutes.

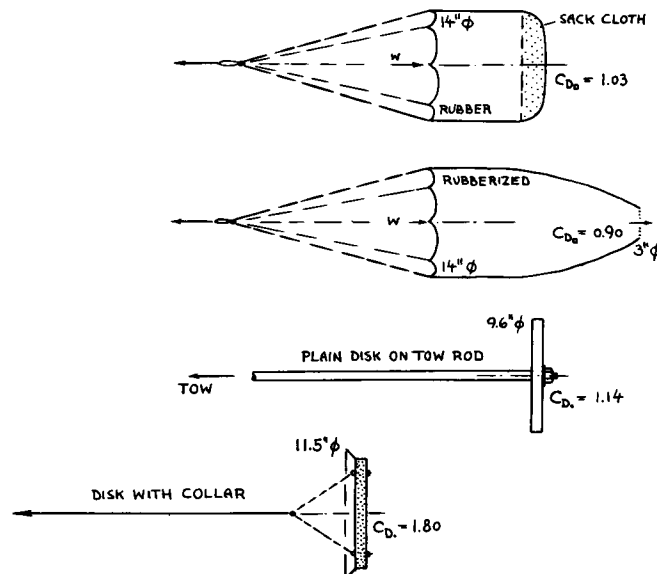


FIGURE 5. Drag coefficients (on S.) of sea anchors and disks (7,b) tested in towing tank.

Guide Vanes. Results on reducing drag due to separation, by means of guide vanes, are presented near the end of the "pressure-drag" chapter. *Figure 6* demonstrates that the drag of cylinders (at subcritical R' -numbers) can be reduced by adding a pair of guiding plates or vanes, respectively. Vibrations caused by the "vortex street" originating from the cylinder are successfully eliminated in this manner, or changed to permissible frequency and amplitude, for example in submarine periscopes.

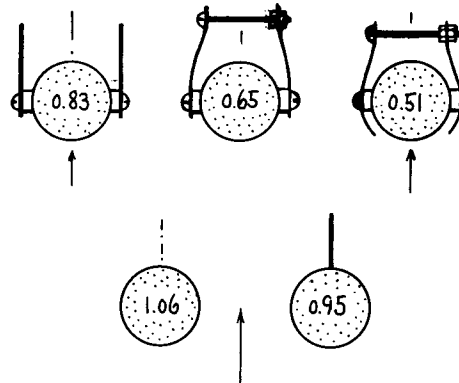


FIGURE 6. Drag coefficient C_D of a cylinder ($d = 15/16$ inch, length = 2 ft below end plate) tested in water (7,c) at 7 knots (at $R_d = 7 \cdot 10^4$). Drag and oscillations are reduced by means of guide vanes as shown. Screws placed 2.5 cylinder diameters apart.

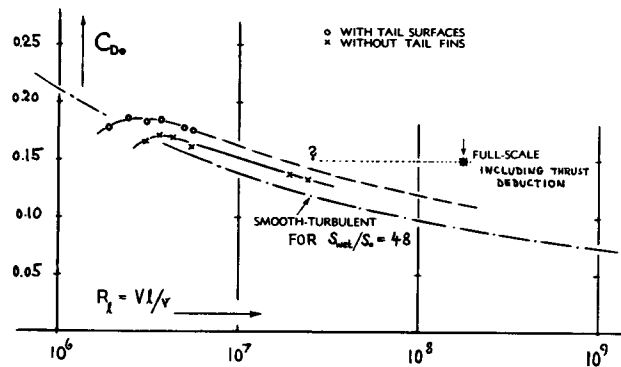


FIGURE 7. Drag coefficient of a torpedo having $1/d \approx 15$, model and full scale; (8) and (17,e).

Streamline Bodies. The drag of streamline bodies basically corresponds to the drag coefficients presented in the chapter on "streamline bodies". Figure 7 presents as an example the drag coefficient of a torpedo, tested in a wind tunnel, towed in a tank and as evaluated from full-scale runs (where fins and surface roughness are present, not simulated in the models). In proximity of the water surface, additional drag originates in these and in any other type of bodies — because of the deformation and a wave pattern produced in that surface by the displacement of the moving solid. This drag component is treated in the chapter on "ships and boats".

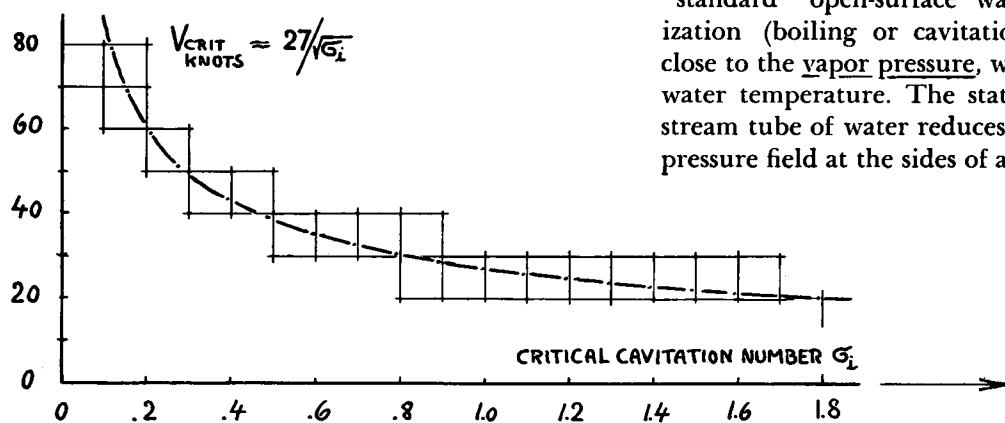
B. DRAG CHARACTERISTICS IN CAVITATING FLOW

To be complete, it is mentioned here that the compressibility of water is "very" small. The corresponding speed of sound (or of pressure propagation) is very high in water (in the order of 4700 ft/sec). Hence there does not seem to be any practical application in sight, where compressibility would have to be considered in streaming water. However, the phenomenon of cavitation restricts very much the speed up to which a flow pattern in water can be expected to be identical to that around the same shape in an air stream. Above a critical speed, a mechanism takes over which is different from that in non-cavitating condition. Two aspects of cavitation can be presented with engineering accuracy as of this time; the critical speed and/or pressure at which cavitation *starts*, and the drag of selected bodies in the final phase of full cavitation.

1. Fundamentals Of Cavitation

Mechanism Of Cavitation. Some fundamentals and analyses of cavitation are presented in (10). Vaporization is the growth of a bubble. Gas-filled bubbles (usually microscopic in size, called nuclei) must be present first, either within the stream of water or hidden in "crevices" at the surface of solid obstacles or walls. Without them, water does not vaporize (boil or cavitate) at all. In most engineering applications, the volume of air contained in water is near or even above saturation, a status which, for example, corresponds to some 2% of air measured by volume, in "standard" open-surface water. Therefore, vaporization (boiling or cavitation) usually starts at or close to the vapor pressure, which is a function of the water temperature. The static pressure of a certain stream tube of water reduces when entering the low-pressure field at the sides of an obstacle. Approaching

FIGURE 8. Standardized critical cavitation speed (defined in text) as a function of G_i .



the level of the vapor pressure, very small air-filled bubbles appear first. Subsequently, the water vaporizes into these bubbles, thus forming continuous and larger voids (steady-vapor or "sheet" phase). At the rear end of or behind the obstacle, the vapor condenses again, while air bubbles (in some form) remain in the wake.

Cavitation Number. The tendency or preparedness of a water flow to cavitate, is indicated by the cavitation number (10,d)

$$\sigma = (p_{\text{ambi}} - p_{\text{vap}})/q \quad (2)$$

where $q = 0.5 \rho V^2$. At standard temperature (59°F) the vapor pressure is comparatively low; $p_{\text{vap}} = 33 \text{ lb}/\text{ft}^2$, corresponding to a head of 0.53 ft fresh water. This is less than 2% of the sea-level atmospheric pressure. Therefore, disregarding the value of p_{vapor} (at p_{ambient} equal to or higher than the atmospheric pressure), the cavitation number appears approximately as the ratio of the undisturbed static to the dynamic pressure of a flow of water.

Critical Speed. Disregarding the value of p_{vapor} , the critical dynamic pressure at any free water surface is

$$q_{\text{crit}} = 0.5 \rho V_{\text{crit}}^2 = p_{\text{at}}/\sigma_i \quad (3)$$

where σ_i = "incipient" cavitation number. On the basis of an atmospheric pressure (at sea level) of $p_{\text{at}} = 2120 \text{ lb}/\text{ft}^2$ (corresponding to a water head of 34 ft), and for an average sea-water mass density of $\rho = 2 \text{ lb sec}^2/\text{ft}^4$, the corresponding "standard" critical cavitation speed at the free surface of water is

$$V_{\text{crit}} = 46/\sqrt{\sigma_i} \quad (\text{ft/sec}) = 27/\sqrt{\sigma_i} \quad (\text{knots})$$

as plotted in figure 8. For bodies submerged at some depth "h" below the surface, the critical speed is higher in proportion to $\sqrt{(34 + h)/34}$, with h in ft.

Erosion. There are two consequences of cavitation, a change in hydrodynamic forces, and erosion. With regard to erosion, it seems that the predominant effect is the mechanical hammering (impact) at spots where vapor-filled cavities suddenly collapse upon the surface of the body involved. As an example, figure 17 presents the cavitation phases of a hydrofoil- or turbine-blade section (in two-dimensional flow). There is a final "super-cavitating" flow pattern in which the cavity collapses *behind* the body. Erosion does not occur in this phase; that is, not on the body that produces cavitation and cavity.

2. Onset Of Cavitation

In engineering applications, it is usually desirable to avoid cavitation. Knowledge of the critical conditions at which cavitation first starts, is therefore important.

Critical Cavitation Number. The static pressure exhibits a minimum value somewhere at the surface of an obstacle. The corresponding reduction of the static pressure is indicated by

$$(p_{\text{min}} - p_{\text{amb}})/q = C_{p\text{min}} \quad (5)$$

For the critical condition of $p_{\text{min}} = p_{\text{vapor}}$, combination of equations 2 and 5 tentatively leads to the critical cavitation number

$$\sigma_i = -C_{p\text{min}} = |C_{p\text{min}}| \quad (6)$$

where the subscript "i" (from incipient) indicates the onset of cavitation. In experiments, the onset is determined by visual observation, by watching the sound level associated with the collapse of vapor bubbles, or by the divergence of lift-, drag- or other hydrodynamic coefficients from their undisturbed levels.

Three-Dimensional Shapes. Figure 9 presents the critical pressure coefficients of a series of three-dimensional head shapes (at zero flow angle), as a function of their length ratio x/d . In slender shapes (as long as the flow is attached to the sides), the critical number is approximately equal to the absolute value of the minimum pressure coefficient. It is seen that the cone-cylinder combinations have considerably higher critical coefficients than the more streamlined forms; this means, of course, that the streamline shapes can stand a considerably higher speed before cavitation starts.

-
- (8) Drag of Torpedo, German Doct ZWB UM 6421.
 - (10) Information on the mechanism of cavitation:
 - a) Ackeret, Investigations in Cavitation, Tech Mech & Thermodynamik Vol. 1 of Forschung Ing'wesen 1930 p.1; Transl TMB No. 20 and NACA T.Memo 1078.
 - b) Eisenberg, Mechanism of Cavitation, TMB Rpts 712 (1950) and 842 (1952); see also in Forschungs-hefte für Schiffstechnik No. 3/4 (1953).
 - c) Knapp, Cavitation, Mech Engg 1954 p.73.
 - d) Thoma, Trans World Power Conf. 1924, 2p.536.
 - e) Daily, Layer, ASME Paper No. 1955-A-142.

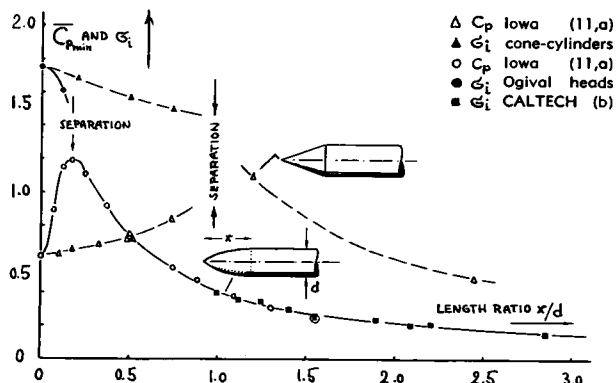


FIGURE 9. Pressure coefficient and incipient-cavitation number of 2 series of three-dimensional head shapes (11).

Vortex Cavitation. The minimum pressure around a given obstacle does not always occur at its surface. The minimum may be found within the vortex cores originating from the tips of propeller blades, for example. Vortices are also present in the separated flow pattern past blunt or bluff bodies, such as plotted near $x/d = 0$ in figure 9. In these shapes, cavitation starts within the fluid (at some distance away from the body's surface) at cavitation numbers G_i which can be appreciably higher than the absolute value of the minimum-pressure coefficient as measured on the surface of the solid. In the conical shapes of figure 9, flow separation is, of course, more predominant than in the rounded forms. The transition from separated to attached flow conditions is possibly discontinuous.

Disk. Figure 10 presents the flow pattern past a fully-cavitating disk. The pressure within the cavity is comparatively constant and \approx equal to the vapor pressure. A steep positive pressure gradient accompanies the transition (or collapse) of the cavity into the wake. The critical cavitation number of the disk is $G_i = 0.73$, indicating onset of cavitation in a ring-shaped vortex (18,b). Steady-state cavitation from the rim of the disk starts at $G = 0.55$; this value is practically equal to the non-cavitating pressure coefficient at the rear of the disk ($C_{p\text{rear}} = -0.54$) as reported in that source.

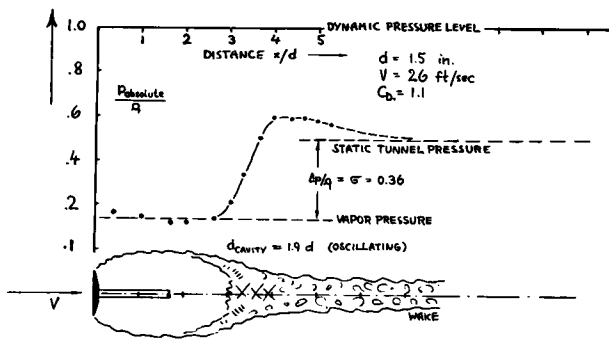


FIGURE 10. Flow pattern of a cavitating disk, and static pressure along the axis (18,b).

Round Bodies. Critical cavitation numbers of circular cylinders (tested between walls) are marked in figure 15. Cavitation starts in the separated space behind the cylinder ($G_i > |C_{p\text{min}}|$). The coefficients also depend upon the basic flow pattern corresponding to subcritical or supercritical Reynolds number, respectively (see in the "pressure-drag" chapter). At subcritical numbers, deviation of the drag coefficient only starts at cavitation numbers which are appreciably lower than G_i as defined by the first appearance of cavities. Roughly, drag divergence starts when $G \approx |C_{p\text{min}}|$ on the cylinder surface. — The incipient cavitation number of the sphere at supercritical Reynolds numbers is in the order of 1.8, while $C_{p\text{min}} \approx -1.1$ in this case (16).

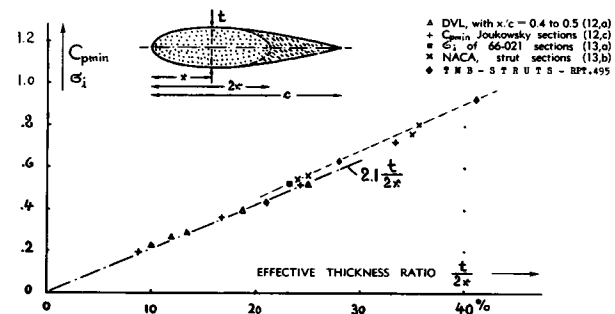


FIGURE 11. Pressure coefficient at the sides of symmetrical foil sections (at zero lift) and cavitation number.

Streamline Sections. Figure 11 presents pressure characteristics of symmetrical foil sections at zero angle of attack. Assuming that the influence of the afterbody upon the flow pattern past the forebody may be of secondary importance, the coefficients are seen to increase in proportion to the thickness ratio of an equivalent, approximately elliptical section as illustrated. The result

$$G_i \approx |C_{p\text{min}}| \approx 2.1(t/2x) \quad (7)$$

exhibits a constant which is close to the theoretical value of 2.0 for elliptical sections.

Delay Of Cavitation. Even on the basis of a sufficient number of "nuclei" in the water, cavitation may not exactly start at reaching vapor pressure. As demonstrated in the lower right-hand part of figure 9 and in figure 11, good agreement between G_i and $|C_{p\text{min}}|$ is evidently obtained in non-separated flow patterns, up to values in the order of 1.0. Experiments at such values (16) on small-size bodies have shown, however, that the onset of cavitation is delayed (it occurs at $G_i < |C_{p\text{min}}|$). Substituting the low-pressure field of a body for its size, the same effect is found at the leading edge of a foil section such as in figure 12, at lift coefficients sufficiently different from $C_{L\text{opt}}$, where high $|C_{p\text{min}}|$ values appear in a narrow peak. Possibly the height of this peak is cut down somewhat,

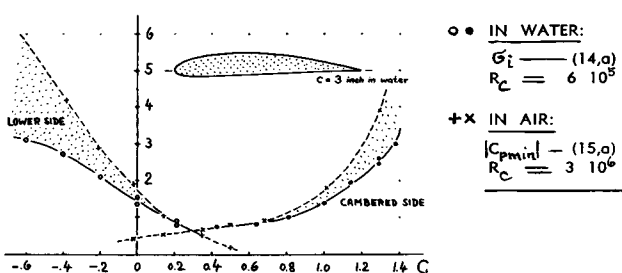


FIGURE 12. Comparison of G_i and $C_{p\min}$ for 4412 section, tested in water- and wind tunnel, respectively.

because of air-bubble content, before the onset of cavitation becomes visible. Whatever the explanation may be, there is a delay in the onset of cavitation (as plotted in figure 13) in the order of

$$\Delta G_i = 0.08 C_{p\min}^2 \quad (8)$$

Similar (and even larger) differentials are found when comparing the cavitation tests in (14,c) with the pressure distribution for the 64-006 section used, as reported in (15,b). It can be argued, however, that in the latter investigation the Reynolds number is almost 10 times that in the towing tank. In conclusion, critical cavitation numbers are not always \approx equal to the $C_{p\min}$ values; they may be higher (in separated flow patterns) or somewhat lower (in small body sizes or narrow minimum-pressure peaks).

- (11) Characteristics of three-dimensional head shapes:
a) Rouse & McNown, Cavitation and Pressure Distribution, Iowa State Univ. Engg Bull. 32 (1948).
b) Knapp, Ogives and Spherogives, CALTECH Hydrodynamics Laboratory Rpt 1945.
- (12) Pressure distribution of symmetrical sections:
a) Forces and Pressures on Airfoil Sections, German Doct ZWB (DVL) FB 1621 (1943).
b) 15% Foil Section, Ybk. D. Lufo 1941 p.I,101.
c) Series of Joukovsky Sections, ARC RM 1241.
d) Schubauer, Elliptic Cylinder, NACA TR 652 (1939).
- (13) Cavitating strut sections, see in Chapter X X.

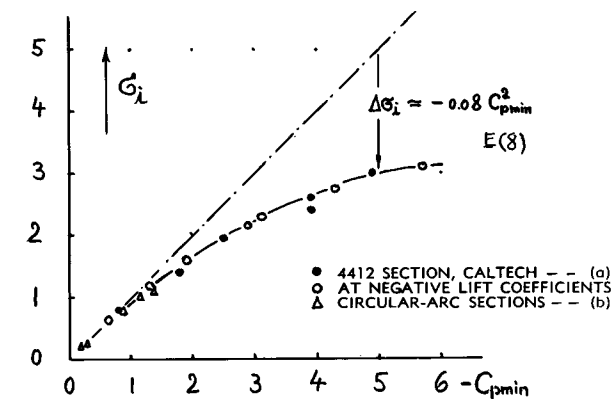


FIGURE 13. Statistical analysis of the "delay" of cavitation in peaked pressure distributions (14).

3. Drag Coefficients In Cavitating Flow

Sharp-Edged Bodies. In fully cavitating condition, the drag of an obstacle evidently corresponds to an average positive pressure component on its face and to the uniform negative pressure within the cavity (at the rear side). For $G = 0$ (that is, for cavity pressure equal to ambient pressure, distribution and value of the face pressure have been calculated for wedges (17,a) and they have experimentally been determined for cones (17,b), as a function of the half apex angle " ε ". These functions are plotted in figure 14. Since the flow pattern is essentially determined by the shape of the face in these bodies, the drag is (within reason) independent of the form of the afterbody. Upon increasing ε from zero to finite values, the flow pattern past the forebody changes as explained in (17,b). The drag coefficient of the type

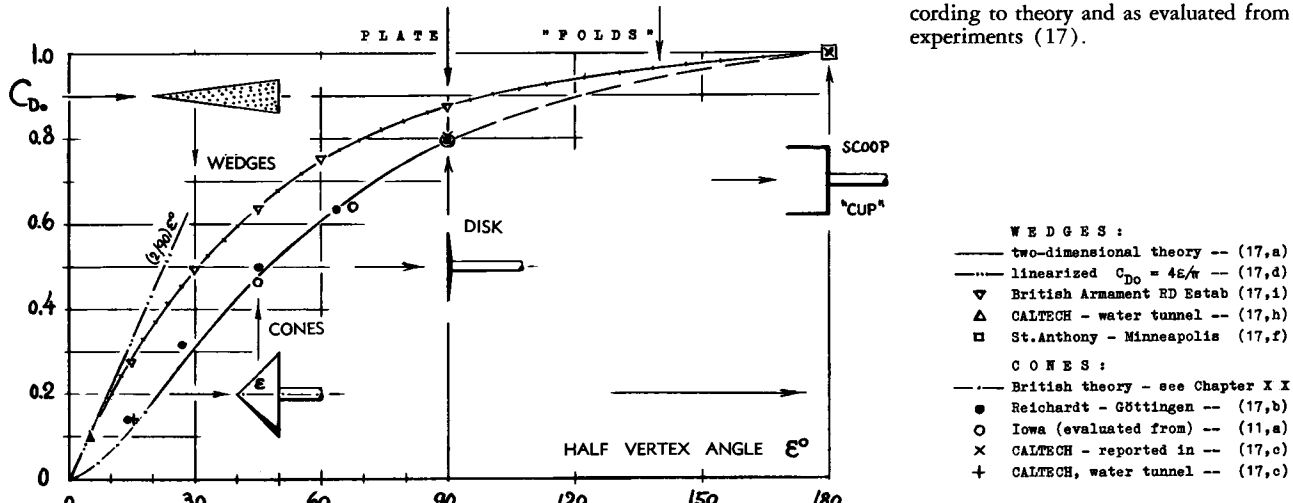
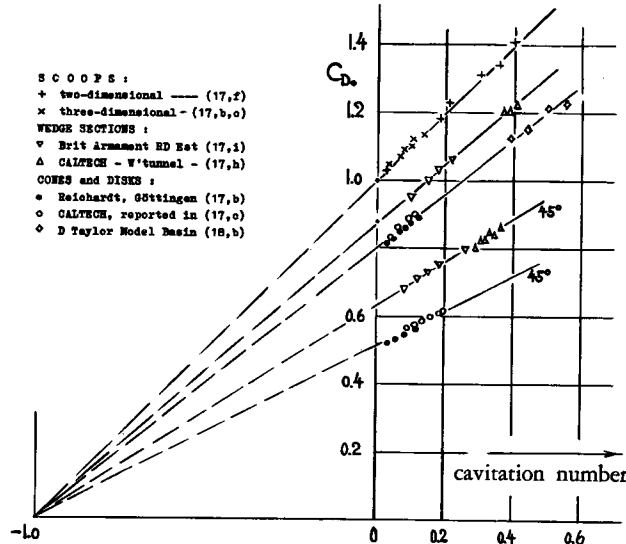


Figure 14. Drag coefficients of wedges and cones at zero cavitation number, according to theory and as evaluated from experiments (17).



of bodies considered is accordingly expected to increase as

$$C_D = C_{D_0} (1 + \sigma) \quad (9)$$

where C_{D_0} = coefficient for $\sigma = 0$. The experimental results for disks and of cones in figure 15 confirm this mechanism very well. As demonstrated in Chapter XX, the drag functions of slender wedges (struts) and of slender cones are different, however.

Spheres and hemispherical heads (noses) have a drag coefficient at zero cavitation number $C_{D_0} = 0.29$, as indicated by analysis (18,f) and confirmed by tests (18). The coefficient as plotted in figure 15a, then begins to increase as indicated by equation (9). It seems, however, that spherical shapes do not have a fixed minimum pressure point (from where cavitation would start at all speeds). As a consequence, upon approaching the line $C_{D_0} = \sigma$, there seems to be a tendency for the coefficient to grow along that line. This means that drag in cavitating condition would be equal to that due to the negative pressure in the cavity at the rear side or base of sphere or hemisphere.

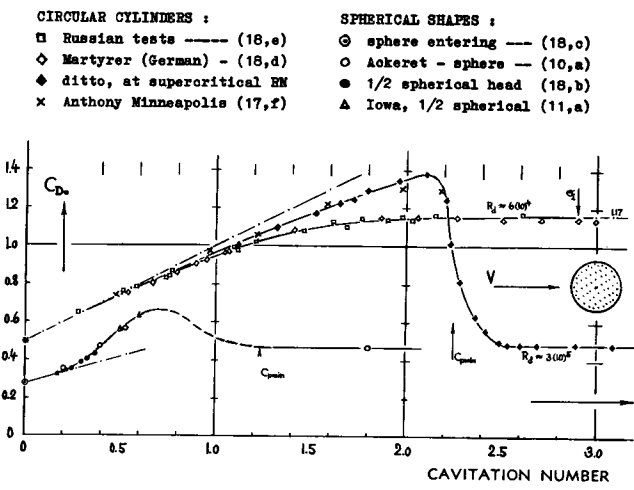


FIGURE 15. Drag coefficients of various bodies in cavitating flow as a function of cavitation number.

Circular Cylinder. On circular cylinders (in cross flow) cavitation must be expected to start from the minimum pressure point, somewhat ahead of the maximum thickness. Figure 15 demonstrates that the transition to non-cavitating flow, is a function of the Reynolds number. Below the critical number, which is somewhere above $R_d = 10^5$, the flow pattern changes from cavitating to separated, without any spectacular consequence. On the other hand, when testing at Reynolds numbers above $(3 \text{ or } 4)10^5$, flow pattern and drag coefficient change from the attached condition at higher cavitation numbers, to the cavitating type, at cavitation numbers around 2. In other words, at Reynolds numbers above the critical (see Chapter III) the drag coefficient of circular cylinders in cross flow, doubles or triples after cavitation has started. As the cavitation number is further decreased toward zero, the coefficients both above and below the critical R_d -number reduce together, approximately following equation (9); and they evidently meet the theoretical (18,a) value $C_{D_0} = 0.5$, at $\sigma = 0$.

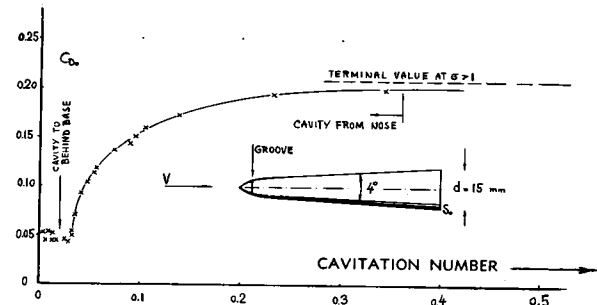


FIGURE 16. Drag of a water-entry missile (17,e). The groove near the nose is expected to produce a cavity into which the missile then enters with small drag.

Figure 16 presents drag characteristics of a particular part-conical missile shape (designed for under-water application). As the cavitation number is decreased, the drag coefficient reduces steadily, while the cavity grows longer and longer. As the cavity reaches the body's base, the coefficient is $C_{D_0} \approx 0.05$ (or slightly less); and it stays approximately constant from there to $\sigma = 0$. For a true cone of the same thickness ratio, $(d/\ell) \approx 0.19$, equation 12 indicates a coefficient $C_{D_{0e}} = 0.063$. Both values are but a fraction of the "terminal" value in non-cavitating flow (which is slightly above $C_{D_0} = 0.20$).

Figure 15a. Drag coefficients of circular cylinders, spheres and hemispheres, as a function of cavitation number.

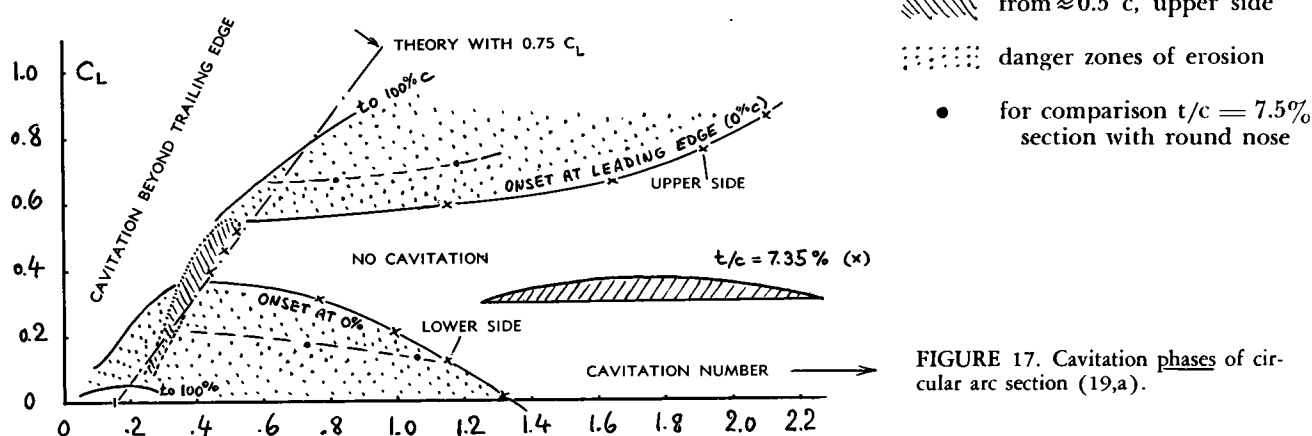


FIGURE 17. Cavitation phases of circular arc section (19,a).

- (14) Cavitating foil sections (cambered):
 - a) Daily (Caltech), Cavitation on Hydrofoil Section, Trans ASME 1949 p.269.
 - b) Balhan, Propeller-Blade Sections in Cavitating Flow, Wageningen Publication 97 (1951).
 - c) King and Land, Sweepback and Cavitation of Hydrofoils, NACA Rpt RM L52J10.
- (15) Pressure distributions tested:
 - a) On 4412 Section, NACA Tech Rpt 563 (1936).
 - b) On 64-006 Section, NACA T.Note 1923 (1940).
- (16) Kermene, McGraw, Parkin (Caltec); Cavitation Inception and Scale Effects, Trans ASME 1955.
- (17) Drag of Cavitating Wedges and Cones:
 - a) Wedge Theory, in Lamb's Hydrodynamics (paragraph 78); or in Birkhoff's "Hydrodynamics".
 - b) Reichardt, Cavitation Bubbles German Docts ZWB UM 6606, 6616, 6620 and 6628 (1944 & 1945); Transl 766 Brit.Ministry of Aircraft Production.
 - c) Plesset-Schaffer, Cavity Drag, Rev. Modern Physics 1948 p.228 and J.Appl'd Physics 1948 p.934.
 - d) Tulin, 2-Dimensional Theory, TMB Rpt 834.
 - e) Albring, Fluid-Dynamic Characteristics of Weapons, German Doct ZWB UM 6421 (1944).
 - f) Silberman, St.A.Falls Hydr Lab Minn Rpt 59 (1958).
 - h) Waid, Wedges, CALTECH Rpt E-73.6 (1957).
 - i) Cox & Clayden, Wedges, J.Fluid Mech 1958 p 615.
- (18) Characteristics of round bodies in cavitating flow:
 - a) Brodetsky, Theory, Proc. R. Soc. London A No.
 - b) Eisenberg, Cavities, TMB Rpt 668 (1948).
 - c) Sphere Entering Water, J.Appl.Phys. 1948, 1109.
 - d) Martyrer, Cylinder and Foils, in "Hydrodynamische Probleme", Hamburg 1932.
 - e) Konstantinov, Circular Cylinders, Russian 1946; Transl TMB No. 233. Note: Drag coefficients have been reduced by 10% for tunnel influence.
 - f) Sphere, Annalen der Physik 1927 p.697
- (19) Experimental results on cavitating foil sections:
 - a) Walchner, Circular-Arc Sections in "Hydrodyn. Probleme", Hamburg 1932, Transl NACA T. Memo 1060; Continuation on round-nosed sections in Rpts and Transl No.330 (1947) Brit.Min. Aircraft Production.
 - b) Martyrer, Cylinder and Foils, see (18,d).
 - c) Numachi, Sections ≈ 12% thick in Forschung 1940 p.303; 6% thick in Trans ASME 1953 p.1257.
 - d) Kermene, Water Tunnel Tests of NACA 4412 and Walchner Profile "7" Noncavitating and Cavitating, Rpt 47-5 by Hydrodyn.Lab. Caltech (1956).
 - e) Parkin, Circular Arc and Flat Plate, Rpt 47-6 by Hydrodynamic Laboratory Caltech (1956).

Size Of Cavity. Referred to the maximum cross-section area of the cavity S_{cav} , the drag coefficient is generally $C_{D_{\text{cav}}} = D/qS_{\text{cav}} \approx \sigma$. The size of the cavity in two-dimensional or three-dimensional flow can, therefore, be estimated on the basis of drag coefficient and cavitation number.

4. Cavitating Hydrofoils

Certain rudders (under the stern of ships), the various fin-like rudders of submarines and the "fins" presently used in the electro-hydraulic control of rolling ship motions — are basically hydrofoils. We may also consider the blades of propellers to be "foils". Not to speak of hydrofoil boats (in Chapter XI), cavitation is bound to occur in all these applications, as a certain critical speed is reached or exceeded.

The Inception Of Cavitation in symmetrical foil sections (at zero lift) has already been indicated in figure 11. Considering now a lifting foil, its pressure distribution is composed of a component due to thickness (equation 7) and a component corresponding to lift. In cambered sections, there is an "optimum" lift coefficient, at which the streamlines meet the section nose smoothly. As a function of camber ratio (f/c), this smooth or "symmetrical" entrance occurs (in non-cavitating condition) at

$$C_{L_{\text{opt}}} = (10 \text{ to } 12) f/c \quad (13)$$

Figure 17 gives an illustration of cavitation zones as determined for a circular-arc section with $f/c = 0.5$ or $0.075 = 3.75\%$, having a $C_{L_{\text{opt}}} = 0.45$. With respect to minimum pressure and incipient cavitation, operation in the vicinity of $C_{L_{\text{opt}}}$ provides the highest possible speeds without cavitation, for a given foil section. Assuming now that the pressure differentials due to lift and due to thickness (equation 7) are super-

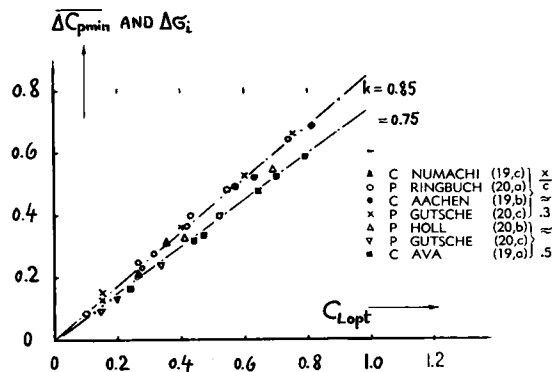


FIGURE 18. Due-to-lift component of pressure coefficients for foil sections in the vicinity of their optimum lift coefficient; "C" = cavitating, "P" = pressure distribution test.

imposed to each other, the component due to thickness can be subtracted. Figure 18 presents the remaining component " ΔC_L ", thus attributable to lift. It seems that the experimental points are grouped according to the location of maximum thickness along the section chord. In each group, cavitation results are seen to be in good agreement with the minimum-pressure coefficients. The component due to lift is approximately

$$\Delta C_L = |\Delta C_{p\min}| = k C_L \quad (14)$$

where k is between 0.75 and 0.85. It is emphasized that this function applies only in the vicinity of $C_{L\text{opt}}$. Figure 17 shows that upon operating a foil section beyond some differential ΔC_L above or below $C_{L\text{opt}}$, ς_L values are obtained which are considerably higher than those determined by application of equations 7 plus 14. The graph also shows that the differential $\pm \Delta C_L$ of a slightly round-nosed section is appreciably higher than that with a sharp leading edge (having same thickness and same thickness location).

Cavitating Plate. The normal-force coefficient of a cavitating flat plate (or thin foil section with flat

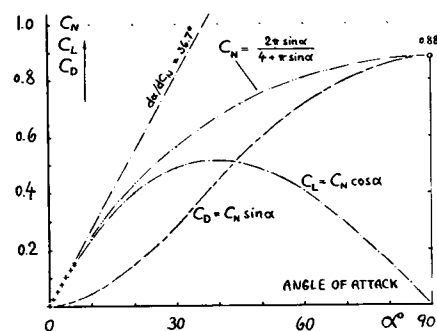


FIGURE 19. Characteristics of flat plates (or of plane pressure sides) in two-dimensional fully-cavitating flow (21,a) at $\Sigma = 0$. Experimental points (+) are for circular-arc sections (19,a) with $t/c = 2.5$ to 7.5%.

pressure side) in two-dimensional flow, is theoretically (21,a) for $\varsigma = 0$:

$$C_N = \frac{2\pi \sin \alpha}{4 + \pi \sin \alpha} \quad (15)$$

Figure 19 presents this function and some experimental results (obtained between tunnel walls) confirming the theoretical prediction. For $\varsigma \rightarrow 0$, reference (21,d) presents the solution

$$C_L = 0.5 \pi \alpha (1 + \epsilon) \quad (16)$$

thus including the suction side pressure (ς). Note that the first term of this equation represents a quarter of the lift in non-cavitating (two-dimensional) flow. The same result in the first term is also obtained from equation 15 for small angles of attack where " $\pi \sin \alpha$ " in the denominator is negligibly small in comparison to "4". Unfortunately, equation 16 is no longer correct enough at cavitation numbers exceeding certain small values. For $\alpha = 10^\circ$, the limit is below $\varsigma = 0.1$, for example.

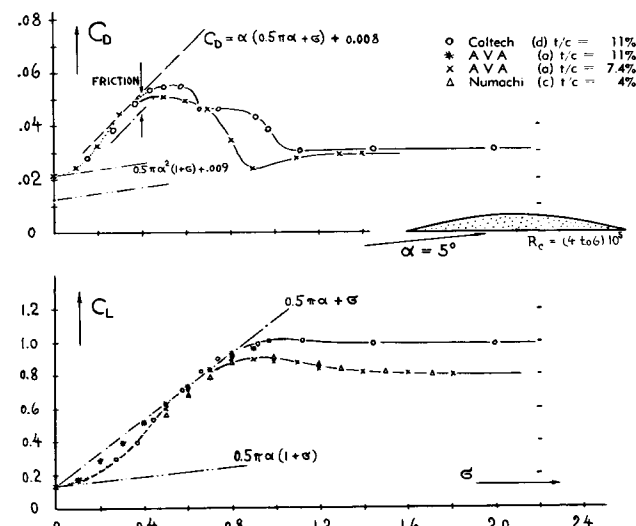


FIGURE 20. Lift and drag coefficients of circular arc sections tested between walls at $\alpha = 5^\circ$, as a function of cavitation number (19).

Circular Arcs. The pressure drag of a cavitating flat plate in two-dimensional flow, is simply a component of the normal force:

$$C_{DP} = C_N \sin \alpha = C_L \tan \alpha \quad (17)$$

Figure 20 presents the variation of lift and drag coefficients of thin circular arc sections (tested at $\alpha = 5^\circ$ between walls) as a function of cavitation number. In fully cavitating condition (with cavity extending from leading edge to beyond trailing edge) these sections are expected to have the same characteristics as

flat plates. Figure 20 shows several phases with respect to cavitation number. (a) In non-cavitating condition, indicated in the right-hand part of the graph, the lift coefficient corresponds to angle of attack and camber of the sections involved. (b) As the cavitation number is reduced below a certain critical range (where cavitation develops), the lift coefficient decreases, while the drag coefficient increases somewhat. (c) Approaching $\sigma = 0$, lift- and drag coefficient decrease together. — Equation 16 only applies below $\sigma \approx 0.1$, in the example plotted. Between there and $\sigma \approx 0.6$, the experimental results somehow agree with the numerical results of reference (21,d). There are other points (19,a), however, which would not fit very well into the presentation of figure 20. It is suggested that the Reynolds number (which is below 10^6 in all experimental results available so far) may have an appreciable influence particularly in sections with a more or less rounded leading edge. Another theoretical function proposed in (21,b) seems to set an upper limit for the lift in cavitating flow:

$$C_L = 0.5 \pi \alpha + \sigma \quad (18)$$

This equation (also plotted in figure 20) appears adequately to describe the lift of flat pressure sides in two-dimensional fully cavitating flow, roughly at angles of attack $\alpha < (10\sigma)$ and/or at cavitation numbers $\sigma > 0.1 \cdot (\alpha)$. At the other ends of the ranges thus indicated, "full" cavitation will also be limited; (a) above certain " σ " values, the cavity will no longer reach beyond the trailing edge; and (b) below certain angles of attack, the cambered side of circular-arc sections such as evaluated in figure 20, is bound to interfere with the formation of the cavity. Figure 21 gives another example where equation 18 seems to be confirmed by experimental points. Note that in this illustration the lift coefficient diverges from the straight line representing the equation, at both ends of the angle-of-attack range tested. Above $\alpha = 5^\circ$, transition takes place to theoretical function

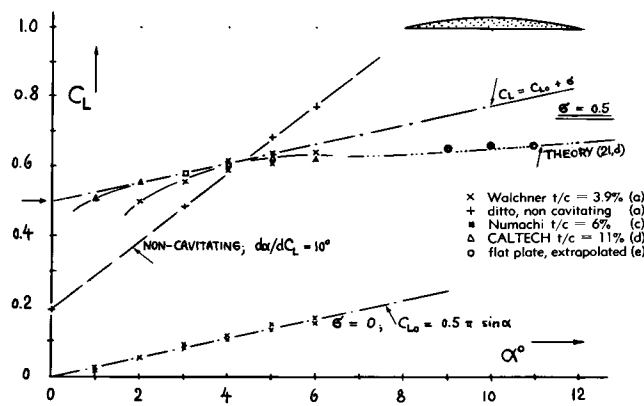


FIGURE 21. Lift coefficient of circular arc sections and of flat plate at constant cavitation numbers (19).

and experimental results quoted from (19,d). Whenever equation 18 applies, the drag of cavitating flat plates or that of flat pressure sides (in two-dimensional fully cavitating flow) will be

$$C_D = (2/\pi) C_L \cdot (C_L - \sigma) + C_f \quad (19)$$

where C_f = friction drag coefficient of the pressure side.

Cambered Plate. Although lift and drag of even the simplest type of cavitating hydrofoil is not susceptible to plain and explicit treatment, some qualitative statements can be made on the influence of camber upon the characteristics. In non-cavitating two-dimensional flow, the lift of a cambered plate is

$$C_L = 2 \pi \sin(\alpha + 0.5\gamma) \quad (20)$$

where γ = angle of the trailing edge against the chord line of the arc. In fully cavitating flow, theory (21,d,f) indicates that the component due to camber is

$$dC_L/d\gamma = \pi(7/16) \quad (21)$$

thus presenting a slope which is $(7/16)$ of that in equation 20. The lift component produced by camber is also independent of " σ ". — Both suction side and pressure side have forwardly inclined resultant forces, so that the drag due to lift is smaller than that of the flat plate. A cambered plate has been tested in (19,e); for lift coefficient of $C_L = 0.3$, for example, at $\sigma = 0$, the flat plate requires an angle of attack of $\alpha = 14^\circ$ while a plate corresponding to $\gamma = 8^\circ$ (camber ratio $f/c = 3.5\%$) needs an angle (measured against chord line) of only $\alpha = 6.5^\circ$. The pressure drag ratio decreases accordingly from $D_p/L \approx 0.2$ to ≈ 0.1 . It is proposed that the pressure-side drag can be zero (except for friction) while (in fully cavitating condition) the suction side drag corresponds to $(L \sin \alpha)$. The drag due to lift can thus be reduced appreciably by proper pressure-side camber.

- (20) Pressure distribution on cambered sections:
 - a) Ringbuch Luftfahrt-Technik, Section IA, 11, by German Ministry of Aviation, 1938.
 - b) Holl, Propeller Sections, Forschung 1932 p.109; see "Hydrodynamische Probleme", Hamburg 1932.
 - c) Gutsche, Mitt. Pr.VAWS Berlin, Vol.10 (1933); Ybk.STG 1936 p.277, 1938 p.125 and Vol.41 (1940).
- (21) Theory of cavitating foil sections:
 - a) Green, Gliding Plate, Proc. Cambridge Phil. Soc. 1936; also 1935 and 1938.
 - b) Betz, Proc. 3rd Internat. Congr. Tech Mechanics Stockholm 1930, Vol.I p.411.
 - c) Bollay, Planing, Proc. 54th Internat'l Congr. Appl. Mechanics 1939 p.474.
 - d) Wu, 2-Dimensional Fully Cavitating Hydrofoils, Caltech Hydrodynamics Lab. Rpt 21-17 (1955).
 - e) Tulin, Supercavitation, TMB Paper (NPL;1955).
 - f) Wu-Perry, Hydrop. Lab. Caltech Rpt 47-4.

Airfoil Sections with round leading edges, such as "Clark Y" (19,c) and "NACA 4412" (19,d and e), have also been tested in cavitation tunnels. Since in sections of this type, value and location of the minimum pressure are not fixed as in thin plates or circular arcs, cavitation may not at all be a steady-state phenomenon (see the results on 4412 in reference 19,d).

Finite-Span Foils. Utilizing equation 18, the angle of attack of fully cavitating finite-span (but higher-aspect-ratio) hydrofoils may tentatively be

$$\alpha = (2/\pi) (C_L - \varsigma) + (C_L/\pi A) \quad (27)$$

Note that (within the limitations of equation 18) the " ς " component of lift does not require a sectional angle of attack. The last term of equation 27 is the induced angle of attack (see in Chapter VII). The pressure drag (including induced drag) of *flat* plates or that of sections having plane pressure sides, corresponds again to equation 17. It can be concluded from (21,d) that this analysis holds only for comparatively small angles of attack. For each angle of attack, the validity limit is approximately indicated by the lift coefficient that the section would have in non-cavitating flow (indicated by $C_L = 2\pi \sin \alpha$). Two foil sections have been investigated in a towing tank (22), simulating cavitation by ventilation. Employing the same technique as described in connection with the half-body in figure 26, ventilation was obtained at angles of attack above 10° . Figure 22 shows that in ventilating-cavitating flow, the cambered section is much more favorable than the flat plate.

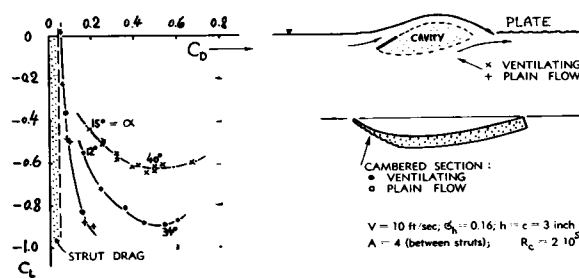


FIGURE 22. Characteristics of two "foil" sections, towed between end struts in tank near surface (22); with and without ventilation.

In Small Aspect Ratios (below $A = 1$), only the linear term of the lift coefficient (see in the "drag-due-to-lift" chapter) can tentatively be predicted. Keeping the induced angle as in non-cavitating flow ($\alpha_i = C_L^2/\pi A$) and increasing the sectional angle fourfold,

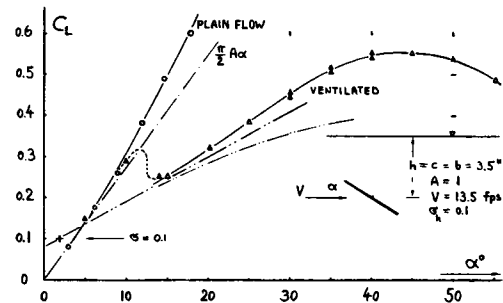


FIGURE 23. Lift of a ventilated square flat plate (22). Note that the hump at $\alpha \approx 12^\circ$ would probably not occur in cavitating flow. The "cavitation" number is explained in the section on surface-piercing bodies.

the total angle of attack of fully cavitating small-aspect-ratio flat plates is tentatively

$$\alpha = (5/\pi) (C_N/A) - (4/\pi) (\varsigma/A) \quad (28)$$

A square plate ($A = 1$), has been tested in a towing tank (22), simulating cavitation by ventilation (through a hollow strut). The lift coefficient $C_L = C_N \cos \alpha$, plotted in figure 23, shows basic agreement with the theoretical equation. The lift increments at angles of attack higher than $\approx 14^\circ$, represent the second, non-linear lift term in the small aspect ratio tested. This component (explained in the "drag-due-to-lift" chapter) is not included in equation 28. The total pressure drag of the flat plate is indicated by equation 17.

For Zero Aspect Ratio, consideration of the velocity component normal to a plate-like strip of material (cross-flow principle; see reference 21,c) in combination with the flat-plate value in figure 14, leads to

$$C_N = (1 + \varsigma) 0.88 \sin^2 \alpha \quad (29)$$

Pressure drag simply corresponds to $C_D = C_N \sin \alpha$.

-
- (22) Hoerner, Square Plate and Cambered Sections in Gibbs & Cox, Inc. Towing Tank (1953).
 - (23) Wave-drag of surface-piercing struts:
 - a) Havelock, Proc.R.Soc. London A 1923 p.571.
 - b) Tank Tests by Shiells, Trans INA 1953.
 - (24) Experiments on surface-piercing struts:
 - a) Kaplan, Stevens ETT Rpt 488 (1953).
 - b) Ramsen and Vaughan, NACA T.Note 3420.
 - c) Coffee and McKann, NACA T.Note 3092 (1953). This reference also describes the method of separating the wave drag from the total drag of such surface-piercing struts.
 - d) Benson and Land, Hydrofoils in NACA Tank, NACA Wartime Rpt L-578 (1942).
 - e) Hoerner, Gibbs & Cox Corporation (1953).
 - f) Dingee, Stevens ETT Rpt 472 (1953).

C. DRAG OF SURFACE PIERCING SOLIDS

Besides cavitation, the most important effect which makes flow patterns in water different from those in air, is that of the free surface. Bodies such as struts or submarine periscopes, in a more or less vertical position, penetrating through the water surface, are treated in this section. At higher Froude numbers, the predominant characteristics of such solids are spray and ventilation.

1. WAVE AND SPRAY DRAG

At Small Froude Numbers. Reference 26 reports on flow pattern and resistance of surface-piercing circular cylinders and of flat plates (normal to the flow). At $F \rightarrow 0$, their drag coefficient is identical to that of shapes having vertical length equal to twice the submerged dimension h . In other words, the water surface has the same effect as a solid "ceiling"; it does not change its plane shape. The drag coefficient at $F \rightarrow 0$ is accordingly in the order of $C_D = 1.2$ for the flat plate in figure 28; and it is roughly between 0.7 and 1.0 for the circular cylinders in figure 27, depending upon their height or length ratio $2h/d$ (see in Chapter III).

Wave Drag. Considering now a surface-piercing strut having a streamline shape, its friction or profile drag is comparatively small. As the Froude number is increased from zero, a deformation of the water surface takes place. Water is piling up at the front, and a certain hollow forms behind the solid. The resulting additional drag is wave drag. Figure 24 shows the theoretical coefficient of this component of drag for double-arc sections. After two or three initial steps (humps and hollows), the wave-drag coefficient reaches a maximum at the Froude number $F_c \approx 0.5$;

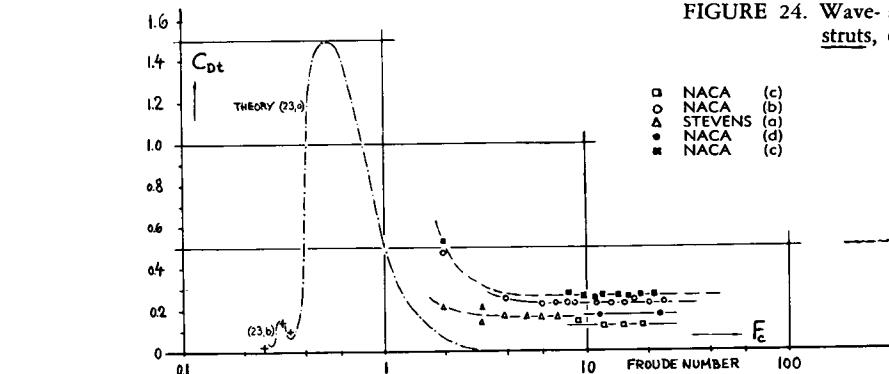


FIGURE 24. Wave- and spray drag coefficients of surface-piercing struts, evaluated from tank tests (24).

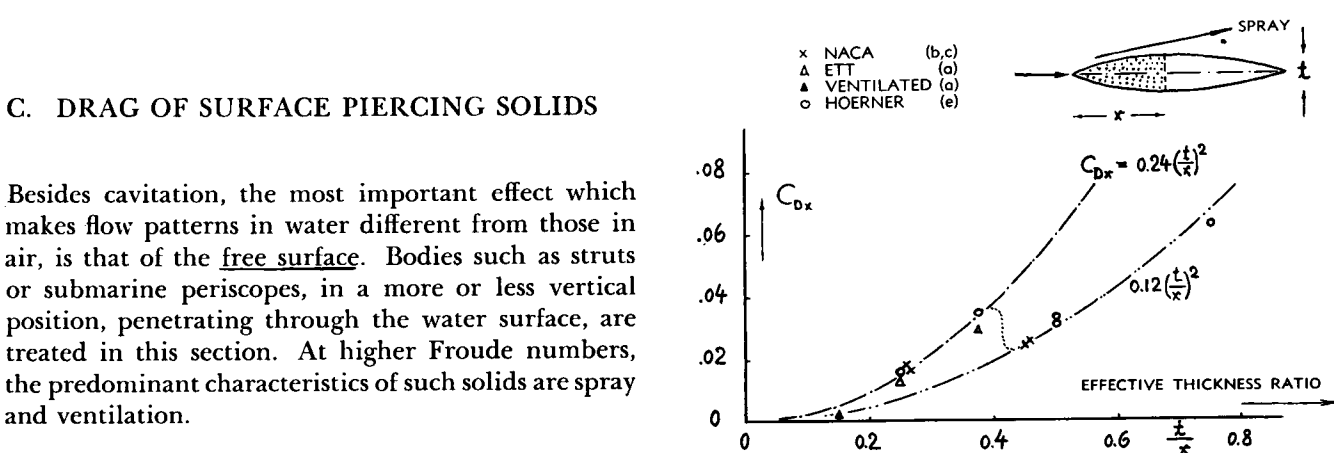


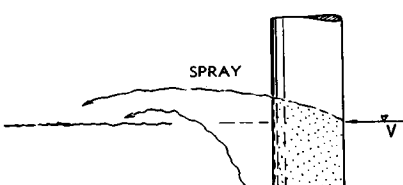
FIGURE 25. Spray-drag coefficient (on x^2) as a function of forebody thickness ratio.

above which it steadily reduces to zero — as far as theory goes.

Spray Drag. As usual, theory only considers infinitely small deformations of the water surface, a condition which is truly correct for a strut section with $t/c \rightarrow 0$. Actually, the wave produced by the penetrating strut, breaks up, so to speak, at Froude numbers above $F_c = 0.5$. Water piling up along the forebody of the strut section continues upward and sideways into the air, thus forming "spray". Jets of water, "shot" into the air, evidently mean another component of drag. Evaluation of towing-tank tests (figure 24), yields the spray-drag coefficient (based upon forebody length x ; $C_{Dt} = D/qx^2$) as plotted in figure 25. Further evaluation leads to the general spray-drag coefficient

$$C_{Dt} = D_{Spray}/(q t^2) = 0.24 \quad (31)$$

an empirical function which applies to Froude numbers, roughly above $F_c = 3$. Figure 25 shows that in the neighborhood of $t/x = 0.4$, something happens to the flow pattern (possibly ventilation at the trailing edge?). At thickness ratios above $t/x \approx 0.4$, the spray-drag coefficient is only in the order of $C_{Dt} = 0.12$.



pressed by a Froude number (see in the chapter on "water-borne craft") on depth h :

$$F_h = V/\sqrt{g \cdot h} \quad (33)$$

2. DRAG DUE TO VENTILATION

Mechanism Of Ventilation. One obvious condition for the formation of air-filled spaces is the presence of a negative pressure field into which air can be attracted by way of suction. The second prerequisite for the maintenance of larger and permanent air-filled cavities (ventilation, see reference 27,b) is evidently a "duct" through which air is channeled from the water surface down to the negative-pressure area.

Ventilation And Cavitation. Under certain conditions, cavitation can be simulated by feeding air into the separated space behind a blunt or bluff body. In true cavitation, the pressure within that space is equal to the vapor pressure. The equivalent cavitation number of a ventilated pattern is then found by replacing the vapor pressure (in equation 2) by the absolute static pressure in the air-filled void. Such simulation is satisfactory for a certain class of sharp-edged bodies (as for example very nicely demonstrated on cones in reference 17,b). — Ventilation of the half-body presented in figure 26, was made possible by means of hollow (air-ducting) end plates, between which the strut model was towed in horizontal position. The static pressure in the air-filled pocket is, therefore, equal to the atmospheric pressure; and the pressure differential is

$$\Delta p = (p_{ambi} - p_{pocket}) = q C_p = \gamma h \quad (32)$$

where γ = weight density of water and where the pressure coefficient $C_p = \Delta p/q$, is a function of the particular body shape. The depth can also be ex-

pressed by a Froude number, it is found that in ventilating flow patterns, the negative pressure at the rear side of an obstacle corresponds to

$$|C_p| = |\Delta p/q| = \gamma|h| / (0.5 \rho V^2) = 2/F_h^2 = \sigma_h \quad (34)$$

This means that in these conditions, $(2/F_h^2)$ replaces the " σ " number of a tentatively equivalent cavitating flow pattern.

Half-Body. In case of the shape in the lower part of figure 26, the minimum surface pressure occurs somewhere between leading and trailing edge. The flow passes the trailing edges essentially in a direction which is parallel to the axis of the body. From the experimental fact that the drag coefficient of this body is approximately

$$C_D = \sigma_h = 2/F_h^2 \quad (35)$$

it must be concluded that the drag of the forebody is close to zero (28). Result and flow pattern are basically different from those in cavitating flow. Cavitational separation would start from the minimum-pressure points, rather than from the trailing edges. Similar reasoning seems to apply to the case of the blunt shape in the upper part of figure 26. In conclusion, drag coefficients in ventilating condition are not generally the same as in cavitating flow,

Depth Of Pocket. In case of bluff surface-piercing bodies (rods or cylinders), a natural ventilation channel is evidently provided by the separated space at the rear side of such shapes. "Dead" liquid is sucked down through the channel and replaced by air. The negative pressure required for the formation of a ventilation pocket, is a function of shape as well as velocity. Applying equation 34 for the bottom of the

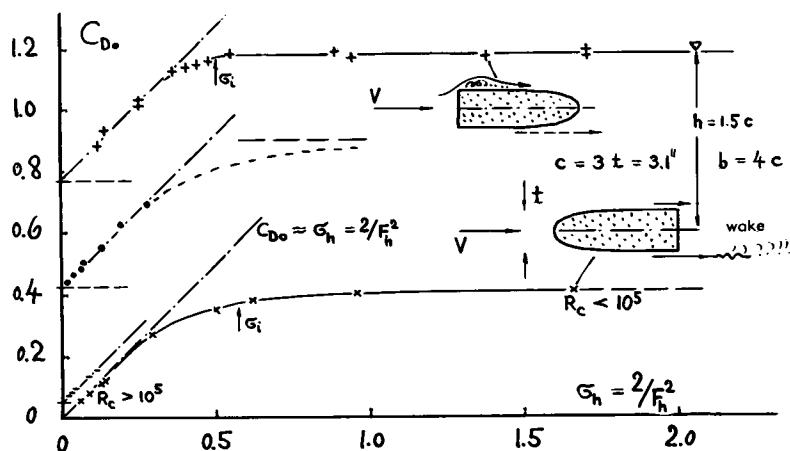


FIGURE 26. Drag coefficients of two "strut" sections (tested between end struts) and of two surface-piercing "struts" in ventilating flow. "h" indicates average static depth of submergence of the bodies tested.

- $\times +$ Between hollow end struts ————— (25)
- \bullet circular cylinder ————— (figure 27)
- $-$ streamline strut ————— (figure 29)

pocket (having the depth h), evaluation of underwater photographs (24,a) and/or the tested functions of C_D . (F_h) yield values as follows:

shape of body	figure	C_{pb}	F_{hcrit}
wedge section	29	-0.19	3.2
circular cylinder	27	-0.62	1.8
normal flat plate	28	-1.00	1.4

The listed Froude numbers also represent the "critical" speed at which the poCKET reaches the bottom of a strut having the submerged length " h ".

Circular Cylinder. In fully-ventilated condition, the average pressure differential between pocket and ambient liquid evidently corresponds to $1/2$ the submerged length h . Equation 35, therefore, changes for the surface-piercing condition to

$$\Delta C_D = 1/F_h^2 = \sigma_{h/2} \quad (36)$$

The equation represents a rear-side drag component which is constant (in pounds or in any other unit at Froude numbers above F_{hvent}) for a given body at $h = \text{constant}$. Figure 27 shows that this function serves very well in the interpolation of the experimental points of various circular cylinders (at sub-critical Reynolds numbers), on the basis of a constant "residuary" coefficient in the order of $C_D = 0.49 \approx 0.5$. The total drag coefficient of such surface-piercing cylinders, at higher Froude numbers, is therefore

$$C_D \approx 0.5 + (1/F_h^2) = 0.5 + \sigma_{h/2} \quad (37)$$

Note that in this equation the σ function is different from that in cavitating flow (equation 9).

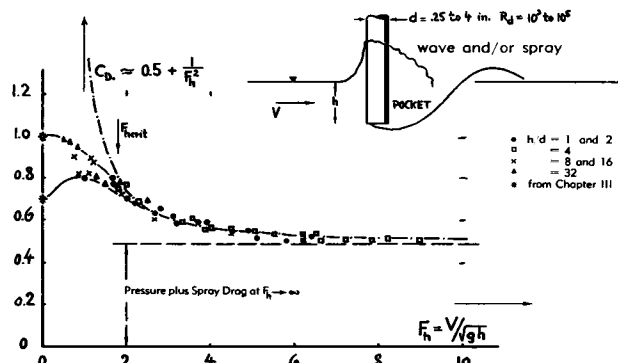


FIGURE 27. Drag coefficient of surface-piercing circular cylinders (on area d times h), as a function of Froude number (26,a).

A Surface-Piercing Plate (normal to a ventilating flow) has separation points which coincide with the minimum pressure points. Cavitation theory can, therefore, be applied. Using for rectangular small-aspect-ratio plates the value $C_D = 0.8$ (see in figure 14), equation 9 together with $\sigma_{h/2} = 1/F_h^2$, yields the drag coefficient in fully ventilated condition:

$$C_D = 0.8(1 + \sigma_{h/2}) = 0.8 + (0.8/F_h^2) \quad (38)$$

Some additional drag must be expected as a consequence of the deformation and disturbance of the water surface. At the higher Froude numbers considered, this drag component is of the type corresponding to a constant coefficient based upon width (thickness) such as that of the spray-drag in figure 24. Analysis of the experimental points in figure 28 suggests a $C_{D\perp} = 0.3$. Referred to the frontal area ($b h$), the spray drag component is

$$\Delta C_D = 0.3 b/h \quad (39)$$

Corresponding lines are shown in the graph.

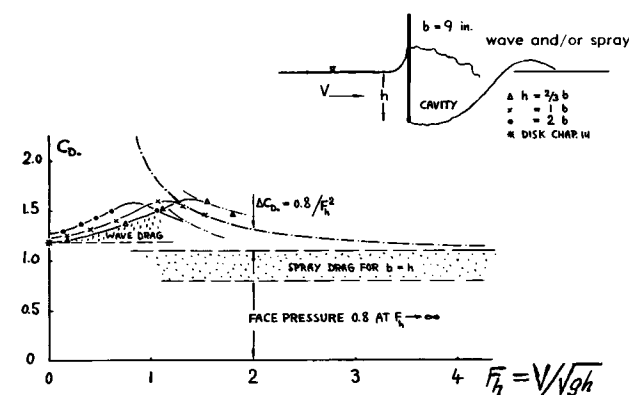


FIGURE 28. Drag coefficient of surface-piercing flat plates (on area b times h) as tested in (26,b).

- (25) Hoerner, Towing-Tank Tests on Ventilated Bodies, Gibbs & Cox for ONR, Tech Rpt 15 (1953).
- (26) Hay, Princeton School of Engineering Rpts:
 - a) Investigation of Cylinders, October 1947.
 - b) Experiments on Parallelepipedons, May 1947.
- (27) Saunders, "Hydrodynamics in Ship Design":
 - a) Text to be published by Soc.NNAME, 1959?
 - b) Saunders differentiates between "ventilation" as in flying-boat steps, for instance, and "air leakage" as it may occur in hydrofoils, for example. A third term is "air entrainment".
- (28) It is pointed out in Chapter III that physical "half bodies" can have negative drag.
- (30) Von Kármán, in Trans. Soc.NNAME 1936 p.327.
- (31) At Fnumbers above 2, the results in figures 27 through 30 can be represented by straight lines, if plotting against $(1/F^2)$.
- (32) The hydrodynamic characteristics and examples presented in this chapter are by no means complete. The criterion that the author has applied in selecting and evaluating them, is availability of results rather than the need for specific information.

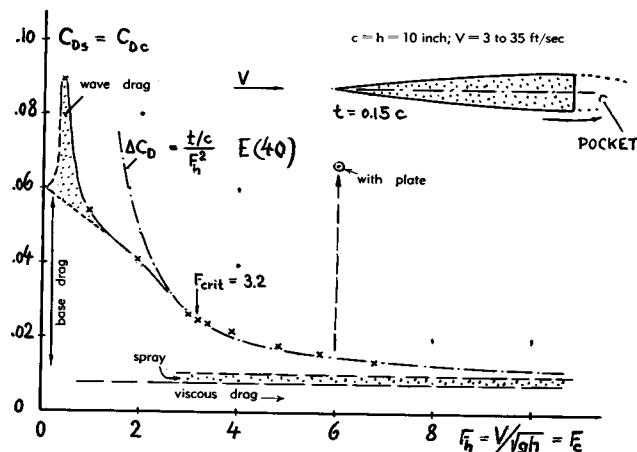


FIGURE 29. Drag coefficient of a surface-piercing strut having a blunt trailing edge (24,a.)

Ventilated Strut. Figure 29 presents the drag coefficient of a slender surface-piercing strut. The blunt trailing end of the 1/2 ogival section facilitates ventilation. Analysis yields a skin-frictional, a spray-drag and a ventilation component of drag. Assuming a suitable section-drag value (see in the "streamline" chapter) and a $C_{Dt} = 0.24$ (from figure 25), a constant part $\Delta C_{Ds} = 0.008 + 0.003 = 0.011$ is obtained. The remaining component corresponds to equation 36:

$$\Delta C_{Ds} = g_h(t/c) = (t/c)/F_h^2 \quad (40)$$

where "s" indicates "section" as in Chapter VI.

Ventilation Plate. In the ventilating examples considered (figures 27, 28 and 29), the total drag coefficient decreases as ventilation takes place. To prevent air entrainment or "leakage" (27,b) along a surface-

piercing strut, a fence-like "subsurface plate" (27) can be used (as for example in outboard motor shafts). Adding such a plate (closely below the water surface) to the strut in figure 29, ventilation is completely eliminated. As tested at a Froude number $F_c = F_h = 6$, the drag coefficient is considerably increased, namely from 0.015 to 0.067. Including the drag of the plate proper, the new value represents a base-drag coefficient (on area S_b) of $C_{Db} = 0.057/0.15 = 0.38$, a value which appears to be in line with similar values presented in the "pressure-drag" chapter under the heading of "base drag".

Inclined Shaft. Upon inclining a surface-piercing circular cylinder (such as the inclined propeller shaft of a hydrofoil boat, for example) to an angle of attack " α ", the "cross-flow principle" (see Index) can be applied. Equation 37 then changes to

$$C_{Ds} = 0.5 \sin^3 \alpha + (\sin \alpha / F_h^2) \quad (41)$$

based on diameter times wetted length of the shaft. This equation agrees well with the experimental points in figure 30, after adding a value of 0.01 for skin friction.

Angle Of Yaw. Figure 31 presents the hydrodynamic coefficients of a slender surface-piercing strut (having a rounded lower end; a shape which might possibly be used as a rudder), plotted against angle of yaw " β ". At $\beta \approx 15^\circ$, ventilation suddenly takes place; the lateral lift reduces considerably. Drag in this condition is somewhat higher than $C_D = C_L \tan \alpha$. An explanation is found in the convex shape of the pressure side, which can also produce negative lateral lift forces at smaller angles of yaw.

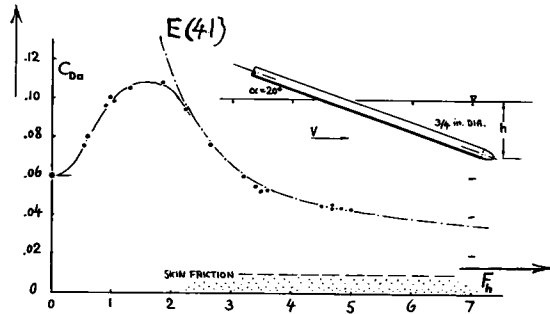


FIGURE 30. Drag coefficient of an inclined surface-piercing (and ventilating) shaft (25).

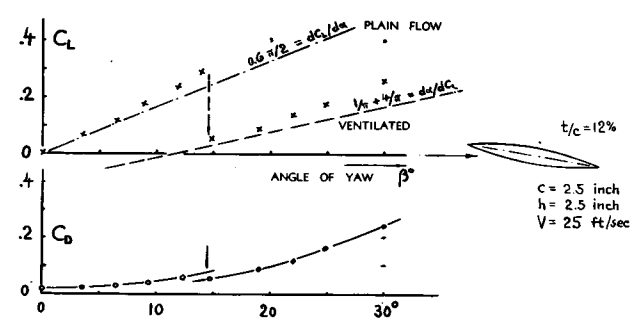


FIGURE 31. Coefficients (on area \$c\$ times \$h\$) of a surface-piercing strut as a function of yaw angle (24,f).

CHAPTER XI—RESISTANCE OF WATER-BORNE CRAFT

Principles of drag in water are presented in Chapter X, including such influences of a free surface as spray and ventilation. Depending upon speed, most of the drag components explained in that chapter can be involved to certain degrees in the various types of water-borne craft. In addition, a disturbance of the free water surface is usually left behind every moving ship or boat, the equivalent of which is "wave resistance". This type of drag is particularly discussed in the first section of this chapter, dealing with "displacement vessels". Resistance components related to wave drag are found in "planing" boats, treated in the second section. Principles, characteristics and performance of "hydrofoil boats" are then presented at the end of this chapter.

A. RESISTANCE OF DISPLACEMENT VESSELS

All larger ships carry their weight by means of buoyancy, a fact that is evident in the term "displacement vessel". Detailed drag characteristics of hulls are extensively presented in various textbooks (1). In contrast to these books, the following section shall primarily explain the basic aspects of the subject; it shall then give results in a more general fashion; and it shall present only examples of specific hydrodynamic characteristics, rather than a complete treatment of hull resistance. Inasmuch as the text corresponds with the general fluid-dynamic approach of this book, this section is likely to appear as unorthodox to naval architects who are used to somewhat different terms and concepts. The author's aerodynamic background is also responsible for the fact that "viscous" form drag is treated more extensively than wavemaking drag.

Naval architects speak of "resistance" rather than "drag". Both terms are alternatively applied, however, in this text.

1. GENERAL PRINCIPLES

Notation. Certain terms and many symbols as applied in the aerodynamic chapters of this book (listed in Chapter I), are also used in this section, as far as applicable. Beyond these, to describe the shape of hulls, a system of coefficients is widely used, which in non-dimensional form can be written as follows:

length-beam (on waterline) ratio	l/b
beam against draft ratio	b/h
prismatic coefficient $C_{pris} =$	∇/lS_\bullet
volumetric coefficient $C_V =$	∇/l^3
wetted surface ratio, either as	S/l^2
or on displacement volume:	$S/\nabla^{2/3}$

where l = waterline length, $\nabla = W/\gamma$ = displaced volume of water (with W = weight of the craft in lb, and γ = weight density of water in lb/ft³) S_\bullet = maximum submerged cross-sectional area ("maximum section") and "S" or S_{wet} = wetted surface area. Some of the coefficients and ratios listed, are still widely used in dimensional form. — The displacement weight is usually given in tons, and then denoted by " Δ " in this text. Among the many definitions of tonnage, three are important here, the "short ton" = 2000 lb (in aviation), the "long ton" = 2240 lb (in naval architecture), and the metric ton = 2205 lb (in Continental Europe).

Resistance Coefficients. In presenting resistance or drag, two methods are basically used:

(a) Presentation of the ratio drag "D" over weight "W" (where W corresponds to the displaced volume of water); this ratio is very convenient in engineering applications.

(b) A coefficient based on dynamic pressure ($q = 0.5 \rho V^2$) and upon the wetted area of the hull, is more significant in presenting the frictional or "vis-

cous" components of resistance:

$$C_{Dwet} = D/(q S) = 2 (D/W) (\nabla/l^3)/((F_l^2 (S/l^2))$$

The drag/weight ratio is obtained as follows:

$$(D/W) = 0.5 C_{Dwet} F_l^2 (S/l^2)/(\nabla/l^3) \quad (2)$$

The wetted surface area of a hull is not only a function of its size, but also of its shape. Surface ratios should be presented together with the results in every towing tank investigation. In case of the Taylor series of hull forms (1,b and 13,a), the wetted surface approximately corresponds to

$$S = 2.6 \sqrt{\nabla l} ; \quad S/l^2 = 2.6 \sqrt{\nabla/l^3} \quad (3)$$

Model Testing. The drag of displacement hulls consists of two predominant components; skin friction and wave resistance. Since the two are governed by different laws (the one corresponding to Reynolds number, the other to Froude number), it is basically impossible to simulate correctly full-scale conditions in towing tanks (unless full-scale dimensions can be used). The common procedure is to satisfy the dynamic law (producing the proper wave pattern), and to correct (reduce) the skin-frictional component on the basis of Reynolds number. It should be noted in this respect, that the gap in R'number between tank models and full-scale vessels is very great, in the order of 1 to 100, as can be seen in figure 9, for example — or even 1 to 1000, when comparatively small models are used investigating larger and/or faster vessels.

Turbulence Stimulation. In 10 to 20 ft long hull models, towed at a Froude number of $F_l = 0.1$ (where wave-making is usually negligibly small), the Reynolds number is between (3 and 4) 10^6 . On the basis of what is presented in Chapter II, mostly turbulent flow might thus be expected to exist within the boundary layer. However, the negative (that is, decreasing) pressure gradient produced by hull shape (displacement), can stabilize the boundary layer flow along the bow up to larger R'numbers. As shown in two examples in the left-hand part of figure 1, the "viscous" drag coefficient may then vary as a function of R'number in a manner similar to that of streamline bodies or sections as presented in several figures of Chapter VI. Stimulation of turbulence by means of certain generators placed near the stem (7) is therefore advisable and it is nowadays applied in routine tank testing. However, depending upon the size of such stimulators (sand strips, wires or pins placed on the model's bow), the resistance of hull plus stimulation elements can vary appreciably at one and the same speed or Reynolds number (as demonstrated for example in figure VI-26).

The Froude Number, named after William Froude (1810 to 1879), is an indication of the ratio of "dynamic" forces (such as lift or frictional drag) to the "static" forces (representing gravity and weight) involved in the flow and wave pattern in proximity of and at the surface of water. Considering a body, such as a ship's hull, moving along the surface — there are two types of pressures acting upon the obstacle, static or buoyant pressures, and dynamic pressures. The latter ones are proportional to $(l^2 q V^2)$, with l indicating a suitable dimension of the body; and the former ones are proportional to the submerged volume of the body, or to l^3 . The ratio of the dynamic to the static pressures or forces is thus

$$\frac{\text{dynamic forces}}{\text{static forces}} = \frac{l^2 q V^2}{\gamma l^3} = \frac{V^2}{gl}$$

The root of this ratio is the so-called "Froude number" $F_l = V/\sqrt{gl}$. This number is one of the most useful tools in the analysis of tests in, or in proximity of the water surface. Also, problems in the field of aviation involving size (weight) and aerodynamic forces could or should be studied on the basis of a Froude number. The number represents, in this respect, the "square-cube" law, meaning that the weight of any structure grows at a higher rate than any of its areas exposed to fluid-dynamic forces (in wind or water). As far as ships are concerned, the square of the Froude number (based on a suitable dimension of the hull) can also be interpreted as a wave length ratio. The length of the transverse waves (in deep water, from crest to crest) formed by the ship's motion is

$$\lambda = 2\pi V^2/g \quad (6)$$

The square of the F'number (on hull length l) is then a measure for the ratio

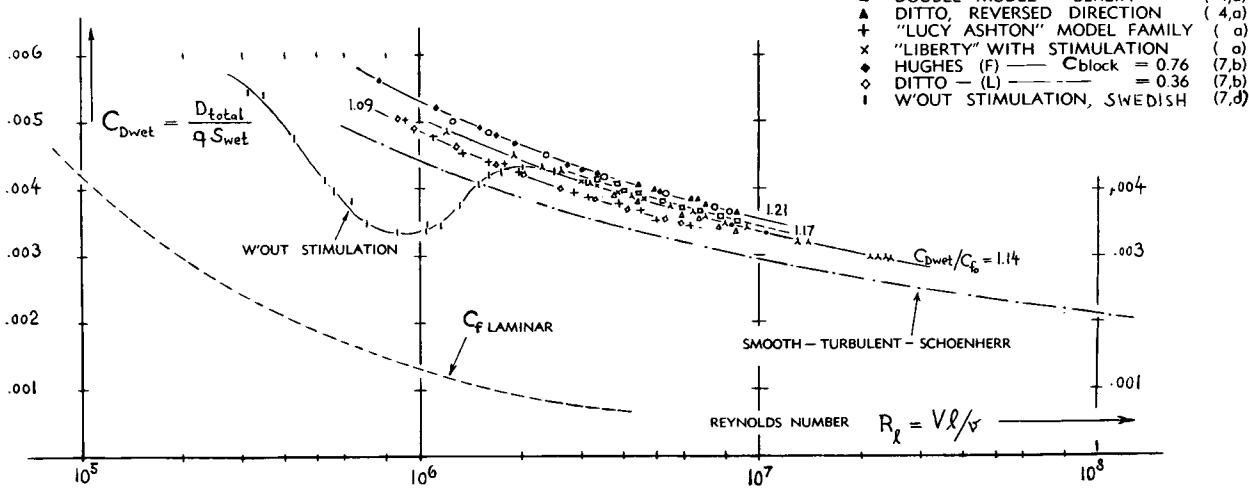
$$\lambda/l = 2\pi(V^2/gl) = 2\pi F_l^2 \quad (7)$$

This equation means that at one and the same Froude number, the wave pattern produced by model or full-scale ship has the same shape and the same dimensions in relation to those of the hull.

(1) Texts dealing with ship hydrodynamics:

- a) The Papers of William Froude (1810-1879) by Inst. Naval Architects, London 1955.
- b) Taylor, Speed and Power of Ships, Washington Govt. Printing Office 1933 and 1943, see reference 13,a.
- c) Rossel-Chapman, Principles of Naval Architecture Soc.NAME and MIT, 1939, 1949 (to be revised 1957).
- d) Van Lammert, Troost, Koning, Resistance Propulsion Steering of Ships, Stam (Holland) 1948.
- e) Saunders, Hydrodynamics in Ship Design, to be published by Soc.NAME in 1957/58.
- f) Lap, Fundamentals of Ship Resistance, a series of lectures published in Internat.Shipt.Progress 1956 and 1957.
- g) Todd, Fundamentals of Testing, Tr. SNAME 1951 p.850.

Figure 1. Non-wave-making or "viscous" resistance coefficient (at Froude numbers below ≈ 0.15) of various hull models and of some model families (geosims), compared with Schoenherr.



2. DRAG CAUSED BY FRICTION

Skin-friction along the hull usually plays the predominant part in larger displacement vessels. For example, in trans-Atlantic liners, frictional drag (in the definition of this book, including form and roughness effects) accounts for more than 75% of the total resistance. In freighters and tankers the percentage is even appreciably higher, approaching some 95% at Froude numbers below 0.15.

Extrapolation Method. The prediction of full-scale ship resistance is traditionally based on towing-tank tests. The procedure (first introduced by William Froude) is generally as follows:

(a) After subtracting a standardized minimum value for the skin-frictional drag (in England corresponding to Froude's plank experiments, in the United States according to Schoenherr), the so called "residual" drag ratio is obtained.

(b) For each full-scale speed, this component is then combined with frictional resistance determined for full scale Reynolds number through the use of the same friction function (Froude or Schoenherr, respectively).

(c) Since all this is done with and for smooth hull surface, full scale resistance is never correctly obtained. In the United States, the discrepancy is then eliminated by a "roughness allowance" corresponding to the incremental coefficient $\Delta C_f = 0.0004$.

(d) Another method advocated in some European quarters, is to assume a certain equivalent sand-type

roughness (as explained in Chapter V) thus providing a constant friction drag coefficient. The corresponding grain sizes are between 0.1 mm for smaller "boats" and 0.2 mm for larger vessels under realistic service conditions (8,f).

Inasmuch as the details of these methods are somewhat obsolete in comparison to the present state of at least qualitative hydrodynamic knowledge, they are not treated further (not in their original and still accepted standard form) in this text. This is particularly true for the "residual" component of resistance which is a mixture of wavemaking with "viscous" or parasite drag.

Turbulent Friction. The most suitable formulation of skin friction drag as a function of Reynolds number, is the "Schoenherr line", presented in Chapter II. At small Froude numbers (where we do not expect any wave drag worthwhile to be considered), towing-tank tests on scale families of hull models (called "geosims") with smooth surfaces (and with suitable turbulence stimulation, at least in the smaller sizes) have repeatedly shown that their drag varies in proportion to (or parallel to) this function of the plane-wall skin friction drag coefficient C_f ; see figure 1. This illustration is very similar to the graph in figure 23 of Chapter VI, in which the smooth, but turbulent drag coefficient of airplane hulls is presented. Other skin-friction "extrapolators" have been promoted in recent years (2,e) — more on statistical grounds than on the basis of strict physical reasoning. They are part of a discussion now going on for 50 years on this subject. Approach and analysis as in the following paragraphs are not generally accepted; they rather reflect the author's opinion on the mechanism of "viscous" resistance.

Three-Dimensionality. The latest word regarding skin friction is "three-dimensional extrapolator", suggesting that bodies such as hulls may have a slope of the frictional drag coefficient C_f against R'number R_λ that would be significantly different from the plane-wall function. Nature and magnitude of the three-dimensional "edge effect" in rectangular plates are explained on page 2-8. On the same page, it is also pointed out that the skin-friction drag of a circular cylinder (having a length $l = 10 d$) in axial flow (tentatively representing the hull of an average ship) does not have a skin-friction drag coefficient significantly different from that of a plane surface; that is, not above a Reynolds number of $R_\lambda \approx 10^6$. Lateral curvature should, therefore, be disregarded in the discussion of full-scale resistance of ships. Slopes of C_{Dwet} against R_λ , larger than that of Schoenherr's function are suggested, sometimes to be the result of difficulties in the stimulation of turbulence (particularly in "geosim" families and in fuller bow shapes).

Thickness Effect. Flow separation from the afterbody is or can be avoided in slender streamline shapes. As pointed out in the "streamline" chapter, the drag of such bodies increases, nevertheless, with the thickness ratio (diameter/length), because of increased momentum losses in the boundary layer. The increment is twofold.

(a) Equation 26 of the "streamline" chapter indicates an increment of frictional drag due to increased mean-average velocity along the sides of streamline bodies, in proportion to $(d/l)^{3/2}$. Using in displacement vessels, the volumetric coefficient V/l^3 in place of the thickness ratio "d/l", the drag increment due to *supervelocity* (mean-average increment of tangential speed along the hull) can thus be expected to be

$$C_{Dwet} \sim \sqrt{V/l^3} \quad (9)$$

This function is confirmed in figure 2 within the range of smaller volumetric coefficients. Increased velocity means reduced static pressure at the bottom of the hull. "Squatting" (an increase of draft "h" while under way) is therefore a measure for this component

of additional drag (4,d):

$$\Delta C_f / C_{f_0} \approx 0.5 g \Delta h / V^2 \quad (10)$$

The squatting effect is expected to grow with the b/h ratio of the hull. It may therefore be more than coincidence in figure 2, that hulls with a beam ratio $b/h = 3$ show appreciably higher increments than those with $b/h = 2$.

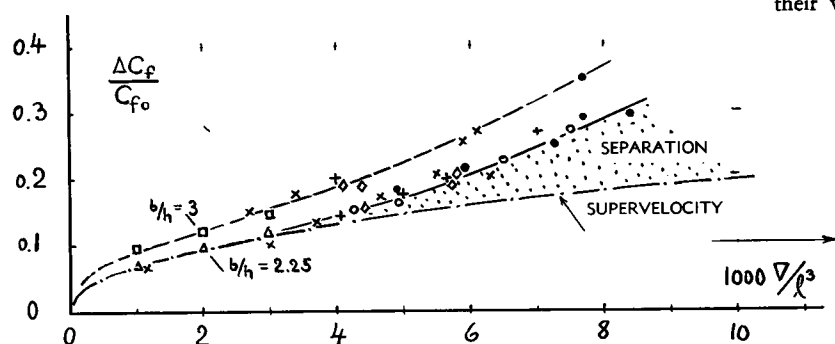
(b) A second increment of "parasitic" drag caused by skin friction in streamline solids, is a component of pressure and possibly separation drag (see in Chapter VI). This term is approximately of the form

$$\Delta C_f \sim (V/l^3)^o \quad (11)$$

where $o > 1$. As demonstrated in (4,d) and (10,b), the pressure drag component is also increased by shortening the length of the so-called run in a hull (that is, by making the afterbody shorter and/or fuller).

Surface Roughness. Principles of fluid-dynamic roughness are explained in the first section of Chapter V. As far as ships are concerned, this author believes that an explanation of the discrepancies in frictional resistance mentioned above, can easily be found in the complex roughness structure of the wetted surface of the full-scale ships. It has been mentioned in this respect (on page 10-2) that clean hulls with common marine paint on their plating, will grow hydrodynamically rough at a speed of ≈ 4 knots. In distinction from the laboratory type of sand roughness (see in the chapter on "imperfections"), the grain size is not uniform, however, in commercial paints or coatings (9,a). Because of this and/or because of reduced roughness concentration, the influence of which is explained on page 5-4, there can be a very extended transitional range of the Reynolds number, in which the slope of the skin-friction coefficient C_f against R'number gradually reduces. Surface imperfections such as butts, laps, welds and rivet heads in the plating

Figure 2. Non-wave-making, "viscous" resistance of bare hulls (with maximum beam at \approx midship), as a function of their volumetric coefficient.



- | | | |
|---|---|--------|
| △ | TAYLOR SERIES, FOR $b/h = 3.25$ | (13,a) |
| □ | DITTO, $b/h = 3.00$, $C_{f, \text{prism}} = 0.6$ | (13,a) |
| ○ | SERIES "60" FOR $b/h = 2.50$ | (13,b) |
| ◊ | VARIOUS JAPANESE MODELS | (4,b) |
| × | VARIOUS SWEDISH MODELS | (4,c) |
| ● | HUGHES (NPL), REFERENCE | (4,e) |
| + | FROM CERTAIN OTHER SOURCES | ----- |

of a ship (flow mechanism and drag of which are extensively treated in Chapter V) can also be considered to be roughness with low concentration. An example of their drag coefficient as a function of R'number is presented in figure 6 of the chapter mentioned. The transitional phase can very well be so extended that a terminal *constant* skin-friction drag coefficient is not yet reached at the highest speed of a ship. This mechanism, further treated in (8,b) and supported by the experimental evidence in figure 8, provides an explanation why in many experiments on full-scale vessels (as for example in 8,c), a constant drag coefficient (as expected on the basis of sand-type roughness) usually does not come true.

Fouling. Grain sizes likely to be found in physical surfaces, are listed in tables on pages 5-3 and 10-2, including those in marine-type paints and coatings. For most practical purposes, the wetted surface of ships must be expected to be in the "rough" regime of hydrodynamic boundary-layer flow. Consideration of roughness still has to go further in ships, however. Even if the skin plating would be made sufficiently smooth in building a ship — fouling (marine growth) will make a hull hydrodynamically "rough" within a comparatively short time. To give an indication of the magnitude of the effect, some statistical information on total drag at specified speeds, taken from (1,b) has been plotted in figure 3 against the time after docking (cleaning and painting). It is seen that after a year in service, the total drag (mostly frictional, at cruising speed) of naval vessels may possibly be doubled. As a biological phenomenon, fouling (such as start and growth of barnacles) depends very much upon environmental conditions, such as in ports and

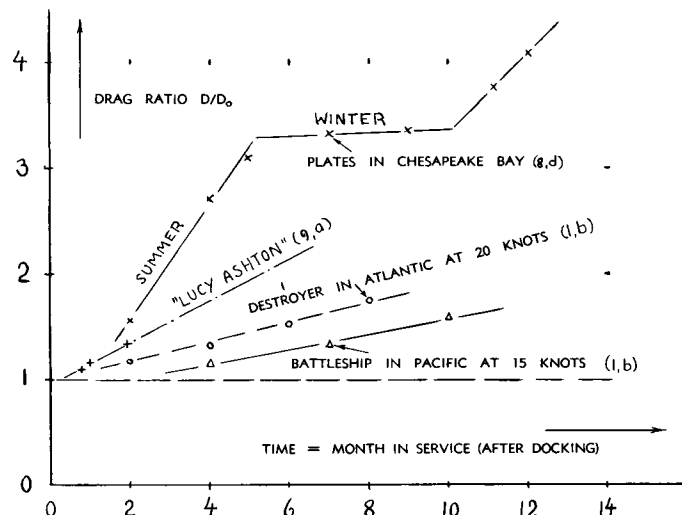


Figure 3. Increase of total resistance (which is essentially frictional plus appendage drag) of ships due to fouling.

anchorage areas. Figure 3 proves in this respect that when lying still, fouling progresses considerably faster than when moving. Investigation of certain test plates lying in Chesapeake Bay (8,d) also shows that fouling stops during Winter time, while it increases at an alarming rate (in that case) in the Summer. In conclusion, the frictional drag coefficient of ships is "never" constant; it usually increases appreciably with time because of fouling. Docking can therefore be of greater importance with respect to the performance of a ship than hull shape and other design characteristics. The period between dockings for a well-kept liner, is in the order of half a year.

3. MODEL-FULL-SCALE CORRELATION

In finer shapes, wave resistance is negligibly small at Froude numbers below ≈ 0.1 . Even after excluding this component, correct prediction of "viscous" or "parasitic" full-scale resistance remains problematic, however.

Drag of Barges. To show in form of an extreme example, that non-wavemaking drag is not always explicitly related to skin friction, drag of barge-like "boxes" is presented first. — Besides the pressure drag cumulatively caused in round shapes and also in streamline bodies by boundary-layer losses (as explained on pages 3-4 and 6-6), there is also the more "violent" type of pressure or "eddy-making" drag originating from bluff obstacles by way of *flow separation*. Particularly in case of sharp edges from which separation takes place, this type of drag does

- (2) Correlation of resistance along friction line:
 - a) Weitbrecht, Tank Tests, Yearb.STG 1933 p.329.
 - b) VanLammeren-VanManen-Lap. Scale Effect on "Victory Ships," Trans INA 1955 p.167.
 - c) O. Schlichting, Yearbook STG 1951, p.55.
 - e) "Extrapolators" different from the Schoenherr line are proposed by Telfer (Trans INA 1927 and 1950) by Troost and Lap (Intern.Shipbldg Progress 1954 p.5 and 1956 p.573) and by Hughes (Trans INA 1950 and 1954; see also Discussion in Schiff und Hafen Feb and July 1955 by Wieghardt, and comments in the following reference).
 - f) Granville, Viscous Resistance, Trans SNAME 1956.
- (3) Experimental results on barge shapes:
 - a) Hay, Tank Tests, Princeton Univ.Engg. Rpt 1946.
 - b) Hay and Runyon, Parallelepipedons, 1947.
 - c) Hay, Blunt Forms, Mar. Engr. Nav. Arch. 1950 p.339.
 - d) Allan, Barges, Trans INA 1948 p.154.
 - e) Taggart, Barge Hulls, Am.Soc.Naval Eng. 1956 p.781. Additional drag due to skegs, needed for stabilization, is between 30 and 100% of the basic hull resistance.
- (4) Information on "viscous" form drag:
 - a) Graff and Horn, STG Forschungsheft 10 (1939).
 - b) Tamiya, Intern'l Shipbldg. Progress 1954 p.55.
 - c) Nordström, Swedish Stat Exp't Tank Rpt 1954.
 - d) Graff, Form Resistance, Yearb.STG. 1934 p.193.
 - e) Hughes (NPL), Form Resistance, Trans INA 1954.
 - f) Eggert, Trans. Soc.NNAME 1935 p.139; 1939 p.303.

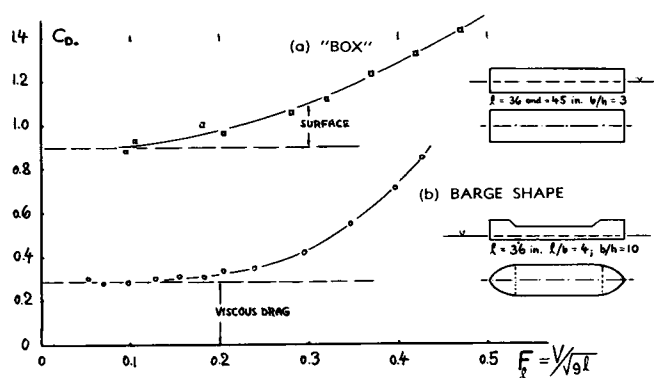


Figure 4. Drag coefficient of simple barge forms (3,a,b,c) on statically submerged frontal area.

usually not, or at least not appreciably vary as a function of skin friction along the forebody. The drag coefficient of such bodies is, therefore, comparatively constant when plotted against Reynolds number, as shown in numerous examples in Chapter III. Figure 4 presents drag coefficients (on projected submerged frontal area "S") of some barge-type hulls. In the form of a blunt "box", pressure drag caused by flow separation is very high. In fact, in the example as shown, the drag is roughly 10 times as high as the frictional drag estimated on the basis of the wetted surface area of the box. By rounding the forefoot edge, the drag coefficient can be reduced to 0.4, as shown in figure 5. Similar reductions are obtained (3,b) by bending up the ends of the bottom. Rounding the ends in plan form, is suitable too for reducing the "eddy making" drag of such barge shapes (figure 4). Rounding is generally more effective at the bow than at the stern. It is desirable, however, in practical applications, to keep the plan form \approx rectangular and to have symmetrical ends, so that the barges can be towed in either direction. — Barges are used at small speeds. For example at $V = 3$ knots, the Froude number of a 200 ft long barge is below $F_x = 0.1$. Wave-making is, therefore, considered to be negligibly small. Reference (3,a,b,c) gives information, however, regarding the resistance of various "boxes" at higher Froude numbers.

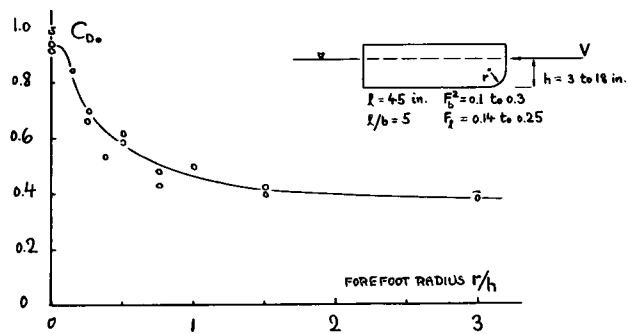


Figure 5. Drag of a "box" or barge shape as a function of its forefoot radius (3,a,b,c).

Hull Appendages are either additions indispensable (such as rudders, propeller shafting, struts or bossings); or they are desirable in the operation of vessels (such as bilge keels, stabilizing fins and possibly certain naval equipment). Appendages may sometimes have a bluff shape (such as possibly in struts supporting the propeller shaft); and they may then have a basic drag coefficient (due to flow separation) which is high and which, in a manner similar to that of the barges noted above, does not decrease with R' number. "Streamline" shaping of appendages has widely been accepted, however, in modern ship design. In models equipped with appendages, laminar separation may also take place from certain of these appendages (such as struts in particular) thus leading to total drag coefficients appreciably higher than corresponding to the Schoenherr line. Such appendages are, therefore, usually not reproduced in tank models when testing resistance; and their drag is added on the basis of experience.

Frictional Appendage Drag. The drag of bilge keels may be estimated on the basis of their wetted area; experiments (9,b) seem to confirm such analysis, if not taking into account the fact that a strip of the hull surface is covered by the keels. An increment of 2 or 3% of the "viscous" hull resistance is thus found for this item. In rudders, sharp edges (if any) and gaps (if any) between them and "deadwood" or rudder-post should be taken into account. Including such imperfections and certain parts needed to support and to move the rudder, a section-drag coefficient of at least 0.02 (on projected lateral area as in Chapter VI) may be assumed. Depending upon configuration (single behind deadwood; or twin in less disturbed flow), the mean-average dynamic pressure of the wake flow passing the rudder is less than the full pressure corresponding to the ship's speed. Assuming a ratio of 0.5, the drag coefficient on the rudder's wetted area is then $.5(0.02)0.5 = 0.005$. For a wetted rudder area possibly in the order of 4% of the hull's surface, the drag contribution of the rudder is then estimated to be some 6% of the total "viscous" drag of a ship. Stabilizing fins (such as developed by Denny Brown or Sperry) may have a projected "wing" area of 200 ft² for a 400 ft long ship. On the basis of $C_{D_S} = 0.01$, their drag may then be in the order of 3% of the "viscous" ship resistance (5,c).

Propeller Shafting. In twin- (and in quadruple-) screw ships, the propeller shafts are either supported by struts (or "brackets"); or they are housed in and supported by fin-like bossings. Investigations on an experimental twin-screw craft (9,a) show that the two methods, illustrated in figure 6, roughly yield the same net drag increment in the order of 6 or 7% of the hull's total "viscous" resistance. Referred to the bossing's added wetted area, a coefficient of C_f =

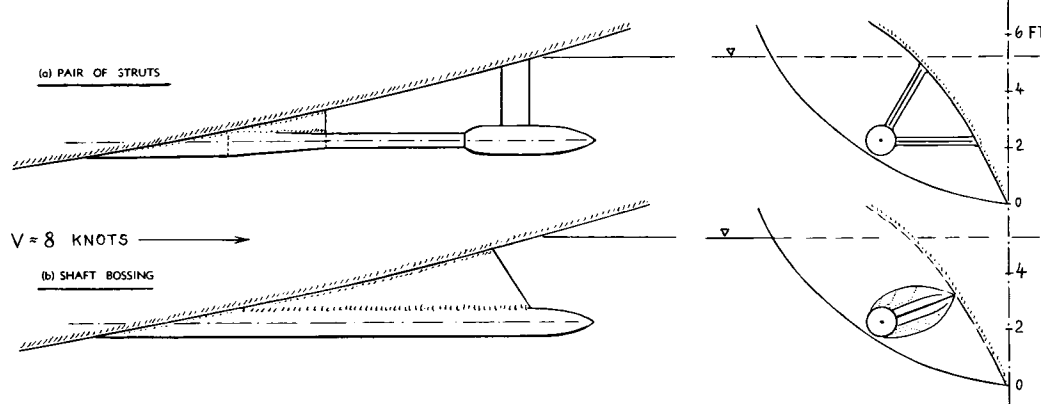


Figure 6. Example of propeller shafting tested full scale (9,a)
(a) with struts (brackets) and (b) with "streamline" bossings.

0.008 is obtained. This value is more than 3 times the hull's coefficient which is $C_{Dwet} = 0.0024$ (as plotted in figure 8). We therefore have to assume that the bossings have some form drag, and/or that they also cause an appreciable amount of interference drag along the hull, of the type as described in Chapter VIII. As a rough rule, we may thus assume that bossings have a drag corresponding to wetted area, increased 100% (or more) because of interference. Analysis of the shaft plus strut system as in figure 6,a, shows that approximately 45% of the drag increment are due to shafting and bearings (corresponding to a value of $C_f \approx 0.005$ on their wetted area), and that the other 55% evidently originate from the struts,

having $t/c = 1/3$, and their junctions with hull and bearings, respectively. Applying the interference coefficient $C_{Dt} = 0.25$ (taken from figure 23 in Chapter VIII) for a total of 8 junctures, a total drag of the shaft and strut system is obtained which is roughly double the tested value. It can be concluded that the average or effective dynamic pressure along the stern and at the location of the struts (and their junctures) is roughly half of the undisturbed pressure (corresponding to $0.5 \rho V^2$). Tank-model tests, also reported in (9,a) on the same configuration of shaft and struts, show an increment of the ship's drag coefficient which is on the average double the increment as tested full scale. For the Reynolds numbers in the model tests, on strut chord (between 10^4 and 10^5) figure 2 in Chapter VI proves that flow pattern and drag coefficient can be expected to correspond to laminar separation (with $C_{Ds} \approx 0.10$). This result thus bears out what is said above about tank testing of such appendages. — Reference (1,f) explains in particular how in twin-screw vessels, size (wetted area) and drag percentage of shafting vary as a function of the hull's prismatic coefficient. Added resistance in a ship having $C_{Pris} = 0.8$ may only be as high as 3 or 4%.

(5) Resistance of ship appendages:

- a) About Bilge Keels, Ybk. STG 1933 p.360.
- b) Propeller Shafting see in reference (9,a) 1955.
- c) The estimate does not include increments to be expected from the motions of a vessel at sea, and in faster ships those possibly caused by cavitation.
- d) The fact that drag of certain appendages is of frictional nature, thus expected to decrease as a function of Reynolds number, is taken into account by referring the added resistance to that of the hull.
- e) Mandel, On Appendages, Trans SNAME 1953 p.464.

(6) Aerodynamic resistance of ships:

- a) Föttinger, Yearbook STG 1924.
- b) Hughes, Model Experiments, Trans INA 1930 p.310.
- c) Hemke-Carson, Streamlining Superstructure of Ships, Marine Engeneering. Shipping Review 1936 p.603, 685.
- d) Wind resistance of "Lucy Ashton" (9,a) corresponds to $C_{Dw} = 1.25$ to 1.36 at zero wind angle.
- e) Aerodynamic drag coefficient of "Victory Ship" model (tested by Endert, Trans INA 1955 p.167) is $C_{Dw} = 0.95$ at zero angle, and $C_{Dw} = 1.25$ between $\beta = (20$ and $23)$.
- f) Frontal area above waterline may be $\approx 0.5 b^2$.
- g) Report on Wind Resistance Experiments by Shipbuilding Research Association of Japan No. 1 (1954); quoted in (1,f), indicates $C_{Dw} \approx 0.8$ in head wind, ≈ 1.0 in wind from astern, $C_{Dw} = 1.25$ in beam wind (based on lateral area). Removal of all equipment (mast, derricks, bulwarks, rails, winches) reduces the aerodynamic drag by 7%; rounding of bridge-house front by 12%.

Condenser Water. Some inlet (scoops) and outlet openings used to drive cooling water through the condensers of a ship are shown on page 9-16. Since the water is usually discharged in a direction normal to the skin of the hull, its momentum (whatever there is left) can be considered to be completely lost. As derived from the principles set forth in Chapter IX, the "internal" drag therefore corresponds to

$$D/q = Q/V \quad (15)$$

where Q = volume of water per unit time. Statistically, a certain percentage of thrust \equiv resistance of the ship is to be expected for the condenser-water component of drag. This component is roughly in the order of 1% of the total resistance.

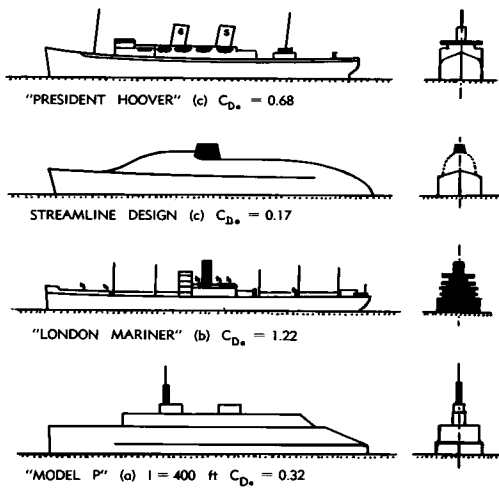


Figure 7. Aerodynamic or wind resistance of several ship models (6). The coefficient C_{D_a} is based on projected frontal area of hull (above waterline) plus superstructure.

Wind Resistance. Considering the mass-density ratio of water against air in the order of 840, the air drag of hull and superstructure may not appear to be important. However, heading into the wind, the dynamic pressure corresponds to the square of ship-plus-wind speed. As a consequence, the *aerodynamic drag* can be an appreciable fraction of the total resistance that a ship encounters on her way through the elements. Figure 7 presents a few samples of the aerodynamic drag coefficient (based on frontal area of the ship above the waterline), as tested in wind tunnels (6). With respect to the apparent wind (wind in relation to the moving ship), the component of aerodynamic drag in the direction of motion increases above the values given in the illustration, by 20 or 30% to a maximum at wind angles between 20 and 35° off the bow. Figure 7 also shows certain attempts of streamlining. To demonstrate the relative importance of such efforts, we may consider a freighter with an assumed ratio of $S_{\text{wet}}/S_* = 15$ (where "wet" indicates the area wetted by water, while S_* is the frontal area of the ship above the waterline). Using a $C_{D_{\text{wet}}} = 0.003$ (at speeds without much wavemaking resistance) and a $C_{D_a} = 1.1$ (assumed on the basis of figure 7 and reference 6,d), the function

$$D_{\text{air}}/D_{\text{water}} = (C_{D_a}/C_{D_{\text{wet}}}) (S_*/S_{\text{wet}})/840 \quad (16)$$

then leads to a ratio of some 3%. Thus, wind resistance is not entirely negligible. This component of resistance (as well as that due to condenser water flow) does not appear, however, in accepted formulations of ship resistance. Considering next a head wind with a speed (against water) equal to that of the ship, the aerodynamic drag will be quadrupled, thus possibly amounting to 12%. Applying a streamline type of superstructure, at least half of this component could be avoided.

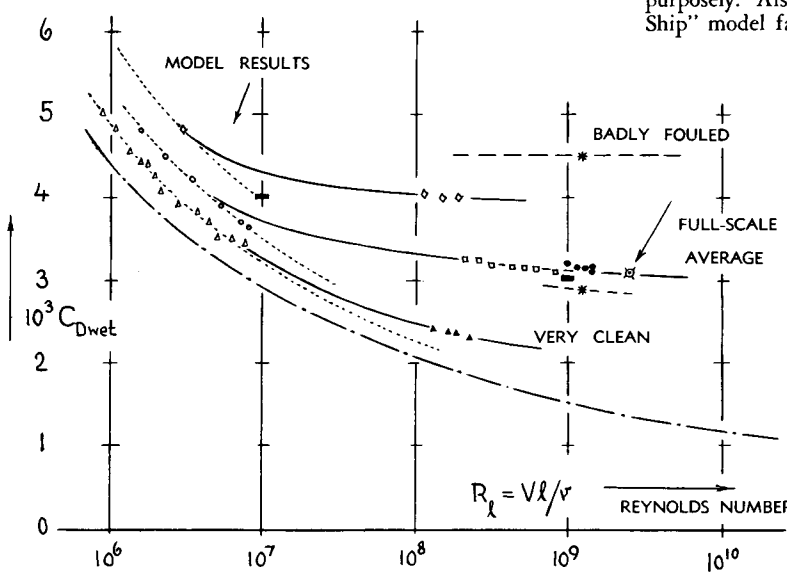
Sum of Increments. The drag components considered in the preceding paragraphs, add up as follows:

shaft bossings	7%	(9%)
rudder	6%	(7%)
bilge keels	2%	(2%)
condenser water	1%	(1%)
wind resistance	3%	(3%)
total increment	19%	(22%)

Reliable experimental information confirming the various components is limited. The total of their resistance (not referring to items such as wind drag) is usually quoted (1) to be between 15% of the hull resistance for single screw vessels and some 30% for multiple-screw ships (equipped with shaft bossings or struts). Although the estimate made above may not be correct quantitatively, the mechanism proposed in the following paragraph may nevertheless be true.

Friction Belt. The drag caused by appendages is a function of size and location. In regard to location, practically all of the appendages are usually placed well inside the "friction belt" (expression for boundary layer and/or wake). Increasing now the Reynolds number from that of a model investigation (say at 10^6) a 1000 fold (to $R_\lambda = 10^9$), the thickness of belt and wake is appreciably reduced. In two-dimensional flow, boundary-layer thickness is proportional to the skin-friction coefficient C_f . Comparing conditions at $R_\lambda = 10^9$ with those at 10^6 , the BL thickness is therefore reduced in proportion to $C_{f9}/C_{f6} = 0.35$. As explained in the chapter on "imperfections", the drag of bodies located within that boundary layer is consequently increased to $(0.35)^{-1/3} \approx 1.4$. The appendages "emerge", so to speak, more and more from the deeper layers of the friction belt. For an assumed drag of the appendages concerned, in the order of 15% of the total, another $\approx 6\%$ may thus be added (5,d) at an R'number of 10^9 . Repeating, however, the analysis for three-dimensional conditions (as they certainly exist around the stern of a hull) a factor of ≈ 1.2 is obtained, and a corresponding increment of only 3%, as listed in parentheses in the tabulation above. Note that as a consequence, the appendage drag is expected neither to be a constant percentage of the Schoenherr Line resistance, nor to correspond to a constant $\Delta C_{D_{\text{wet}}}$.

FIGURE 8. Correlation of model and full-scale total drag coefficients of various vessels. Note that the "Greyhound" and "Youdachi" results are not the same as presented in (8,c) and that certain points have been omitted purposely. Also the "Hamburg" results are joint with those of the "Victory Ship" model family, which is meant to be a possibility rather than a fact.



▲ "LUCY ASHTON" MODEL FAMILY (9,a)
○ "VICTORY-SHIP" MODEL FAMILY (2,b)

- + measured predominant grain size in mm
- *) measured barnacle size = 3.5 mm
- x equivalent sand roughness grain size corresponding to terminal C_f level

Vessel and Source	l_m	C_{Dwet}	k_{mm}
▲ "Lucy Ashton" very smooth ship with fresh paint (9,a)	52	.0020	0.02 _x
* same ship, but marine paint (9,d)	120	.0028	0.18
* same ship, but badly fouled *) (9,d)	120	.0045	2.6 _x
□ "Yudachi" evidently clean (9,c)	71	.0030	0.14
◎ "Bremen" from skin plate (8,c)	275	.0031	0.55
● "Hamburg" from skin plate (8,c)	201	.0030	0.48
◇ "Greyhound" by W. Froude (9,b)	52	.0039	0.37
- naval vessel as in figure 9 (10)	116	.0029	0.08 ₊

Propulsive Efficiency. Inasmuch as full-scale performance is also a function of propulsive efficiency, it is mentioned here (a) that the recovery of momentum obtained by the propeller operating within the wake of the hull ("wake fraction" minus "thrust deduction") is known to be full-scale a few percent lower than determined in model tests (see reference 1); and (b) that propeller efficiency as determined in a uniform tunnel flow, may in actual operation be a few percent lower because of the deep velocity and dynamic-pressure "holes" found behind deadwood, bossings or shaft-strut systems.

Roughness. Figure 8 presents a re-evaluation of several sets of experimental results obtained on full-scale vessels. While these data are "old", interpretation by the author is new. The most important result is that all of the results show a more and more reducing slope of $C_f(R)$, in a manner explained on pages 5-4 and 11-4. Assuming, for example, for the "Hamburg" a basic ratio (due to thickness) of $C_f/C_{f_0} = 1.2$, the frictional resistance of this vessel at cruising speed (without wave-making and appendage drag, but including roughness) corresponds to $C_f \approx 2 C_{f_0}$ where C_{f_0} = smooth-turbulent coefficient as defined by the Schoenherr function. Average C_f/C_{f_0} ratios of the ships tested, also tend to correlate with each other when plotted against their average cruising speed. The fastest vessels tested tend to have the highest ratios, in this respect and vice versa; a result which corresponds to the fact that the critical speed in regard to roughness depends upon the grain size rather than the dimensions of the craft (see on pages 5-2 and 10-2).

- (7) Stimulation of turbulence in hull models:
 - a) Couch and Hinterthan, Methods for Stimulation, TMB RPT 726 (1950). Results ----- are for 20 ft model of "Liberty Ship."
 - b) Hughes and Allan (NPL), Trans. Soc. NAME 1951 p.281.
 - c) Ridgely-Nevitt (Webb), Appendix in ref. (13,e).
 - d) Nordström, Publ. No. 18 Swed. Shipb. Exp. Tank (1951).
- (8) Surface roughness in hulls:
 - a) See in reference (9,a) 1953 and 1955.
 - b) Hoerner, Mechanics of Roughness → Concentration, Journal Am. Soc. of Naval Engineers 1954 p.497.
 - c) Kempf, Werft-Reederei-Hafen 1924 p.521, 1929 p.234; Yearb. STG 1937 p.159; Trans INA 1937 p.109.
 - d) McEntee, Drag due to Fouling, Trans SNAME 1915.
 - e) Results of a "plank ship" (9,c) are plotted in figure 6 of Chapter V, showing reduced slope of $C_f(R_L)$.
 - f) Weitbrecht, Standardized Roughness, Internat. Towing Tank Conf. Berlin 1937, Mitt. Pr. VAWS No. 32 p.20.
- (9) Full-scale investigations of ship resistance:
 - a) Denny, Conn, Lackenby, Walter, Livingston-Smith; Resistance of "Lucy Ashton", Trans INA 1951 p.40, 1953 p.350, 1955 p.109 and 1955 p.525.
 - b) "Greyhound" by W. Froude; see reference (1,a).
 - c) Hiraga, Planks and Ships, Trans INA 1951 p.284.
 - d) Amtsberg, Roughness, Schiffbau 1937 p.135.
- (10) Analysis of one particular vessel:
 - a) These data on a Naval vessel have been made available by the Taylor Model Basin. Appendages were reproduced in the model. Trials conducted in 1950.
 - b) Hoerner, Analysis of Viscous Ship Resistance, Internat. Shipb. Progress 1954 p.156.

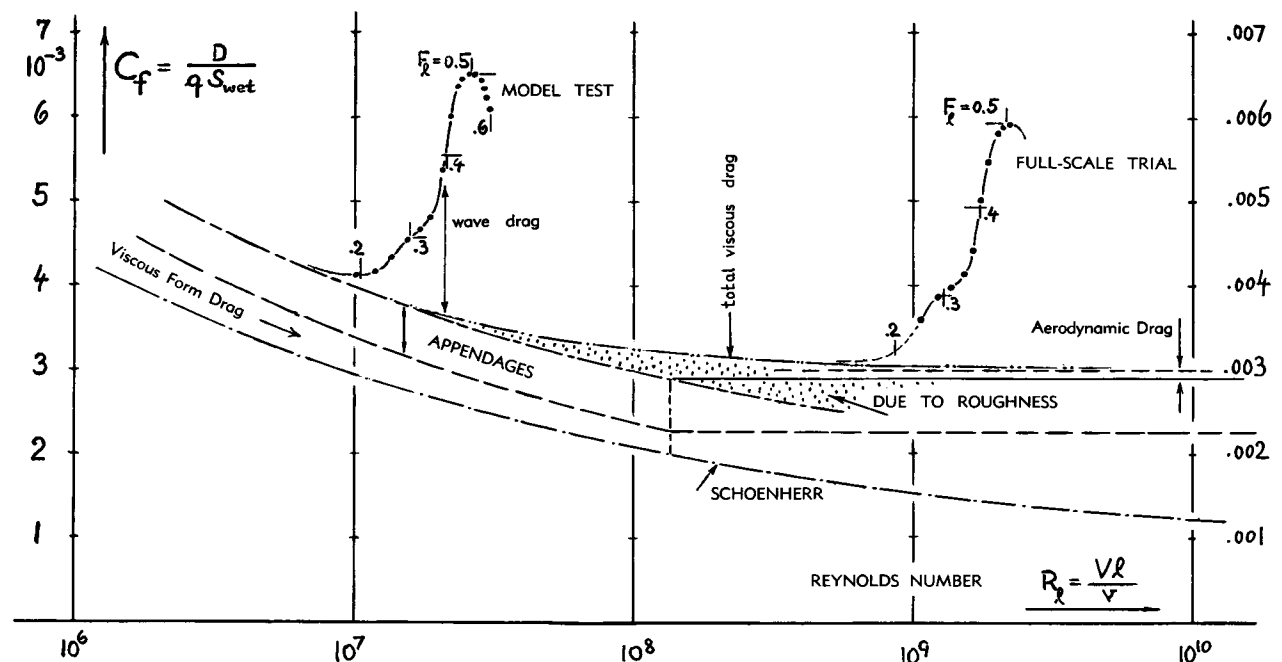


Figure 9. Tank-model and full-scale trial tests (45 days after dry-docking and painting) of a naval vessel (10); having $I = 283$ ft, $\Delta = 3200$ tons and $\nabla/I^3 = 2/1000$.

Correlation. Figure 9 presents the example of a naval vessel, analyzed through application of the methods and principles mentioned. The drag increment corresponding to hull thickness ratio (figure 2) is estimated to be 15% of the Schoenherr function. The drag area (D/q) of the appendages (rudder, shafting and others), reproduced in the model is assumed to be constant, corresponding to a $\Delta C_f = 0.0006$ (which is $\approx 20\%$ of the "viscous" resistance at full-scale Reynolds number). Trials of the vessel were undertaken after 45 days out of dry-dock and painting, in Atlantic waters at 80° F. With respect to surface roughness under these conditions, it is suggested in the illustration, that a constant drag coefficient would be reached at speeds slightly above the maximum of the ship. From the smooth-turbulent drag function of the model to that constant level, a transition line is shown whose slope reduces gradually from that of the Schoenherr line (at $R_L \approx 10^7$) to zero (when reaching the constant level, if at all). Beginning, shape and termination of the transition are governed by concentration (see page 5-4) and size distribution of the roughness "grains" or "elements", as found in the wetted surface of the vessel tested, under the fouling conditions at the time of trial. Some of the assumptions made in producing figure 9, are heuristic, of course. None of them is believed to be unreasonable, however, and the agreement thus obtained suggests that the analysis is physically correct. As far as the vessel as such is concerned, "viscous" or "parasite" resistance at $R_L = 10^9$ corresponds ten-

tatively to the drag coefficients (on wetted area) as follows:

Schoenherr Line value	$C_f = 0.0015$
added drag due to roughness	$= 0.0005$
added drag due to thickness	$= 0.0003$
drag of model appendages	$= 0.0007$
aerodynamic resistance	$= 0.0001$
total non-wavemaking	$C_f = 0.0031$

On the basis of this breakdown, roughness accounts for $1/3$ of the increment over the Schoenherr value. It is suggested, however, that some fraction of what is labelled "appendages" (as tested on the model) should rather be blamed on roughness too. A final conclusion derived while making this analysis, is simply that in the end, summation of a sufficient number of comparatively small components helps very much in arriving at resistance values compatible with full-scale experience.

Extrapolation Method. Considering the mechanics of viscous form drag, appendage resistance, interference and "polytropic" roughness as described above, it can be concluded that none of the simple "extrapolators" proposed (2,e) can directly lead to a correct prediction of full-scale resistance. A physically correct breakdown of drag (as attempted in these paragraphs) should open the door, however, to more realistic formulations. Indeed, figure 9 represents an attempt of doing that by taking steps as follows:

- use the smooth-turbulent Schoenherr function as basis;
- estimate the increment due to thickness on the basis of figure 2;

- (c) determine the drag of the appendages by experiments or through application of the methods set forth in certain chapters of this book;
- (d) find the *terminal* level of the "viscous" drag coefficient on the basis of an empirical or standardized skin roughness grain size;
- (e) determine the coefficient due to aerodynamic drag (and that corresponding to condenser-water flow);
- (f) find or assume a transition from the line corresponding to smooth-turbulent skin friction to the constant terminal level.
- (g) add wave resistance, which is to be evaluated from towing-tank tests in a manner similar to the method used in splitting off the "residual" drag.

A procedure possibly to be utilized for the step in "f", is indicated on page 5-4. The "limiting" grain size (as proposed in step "d") representing the roughness of the "smooth" spaces in between the larger "grains", brush marks, imperfections and fouling particles of the hull's surface — may of course vary very much with time and between different ships. This grain size is $k \approx 0.05$ mm in the illustration. A magnitude of $k = 0.1$ mm could possibly be adopted as a realistic standard, thus taking into account some fouling. A larger vessel will then correctly be on a lower drag level than a shorter ship. Figure 8 gives some confirmation of this mechanism in combination with the principle of the more and more reducing slope of $C_f(R)$. It is felt that among the existing methods, that of the American Towing-Tank Conference, of adding to the Schoenherr function the residual resistance as well as a standardized roughness allowance of $\Delta C_f = 0.0004$, comes closest to the result outlined above.

4. WAVE RESISTANCE

Nature of Wave Drag. Leonardo da Vinci (1452 to 1519) is quoted to have stated that a hull "pushes aside and in front of itself a great quantity of water". This is not correct in finer shapes; in fact in a non-viscous and non-spraying liquid, the particles will eventually return to their original location, after a ship has passed. Corresponding to the increased static pressure at the bow of a hull, the water level rises in the vicinity of the stem. On the other hand, at the sides of the hull, particularly in the vicinity of the shoulders, the static pressure is decreased. Since gravity tends to reduce any deviation from level condition, a wave system originates from the bow (beginning with a crest), and a similar (but weaker) system from the stern (beginning with a trough) of every displacement vessel. Each of these systems has lateral and transverse components, as explained in textbooks on the subject (1). In each wave, water particles perform a so-called orbital motion, up and down, back and forth, approximately in circles (in the manner of a Ferris wheel). Thus the particles essentially remain at their original location; and it is only the wave *shape* that appears to travel along the water surface. The momentum transferred from the moving vessel onto the water particles travels with the waves, however. Wavemaking is thus a dissipation of energy which means resistance against the motion of the ship. As far as the hull is concerned, wave drag appears in the form of a net longitudinal component of the pressure distribution along the hull.

Humps and Hollows. Theory of drag due to wave-making has been developed (12). After integration of the static pressures around a given hull, it is possible to predict wave resistance. It is demonstrated in (12,e), that on the average, the transverse and the divergent part of a wave system, each roughly contributes half of the wave drag. The transverse waves determine, however, the interference between bow and stern system. Depending upon whether the two systems are in phase or not, they can add to each other or they may partly cancel each other (12,b). As a consequence, the drag coefficient of displacement hulls shows "humps" and "hollows" as a function of speed, as shown in figure 10. Based upon the length " λ " (from crest to crest) of the transverse waves, humps of the wave-drag coefficient appear at Froude numbers

$$F_\lambda = V/\sqrt{g\lambda} = 1/\sqrt{2\pi n} = 0.4/\sqrt{n};$$

where $n = 2, 4, 6 \dots$

(12) Wave-drag theory, presented by:
 a) Havelock, numerous studies between 1908 and 1952; a bibliography is given in (e).
 b) Wigley, Calculated and Measured Wave Resistance, Trans INA 1944 p.41, 1948 p.92 and 1949 p.41.
 c) Weinblum, Papers between 1930 and 1952 partly in Yearb.STG, also in other places, such as in J.Am.Soc.Nav. Engs. 1952 p.251. A systematic treatment of the subject is also given in Yearb.STG 1953 p.186.
 d) Havelock, Water Effect, Trans SNAME 1951 p.13.
 e) Lunde, Linearized Theory, Trans SNAME 1951 p.25.

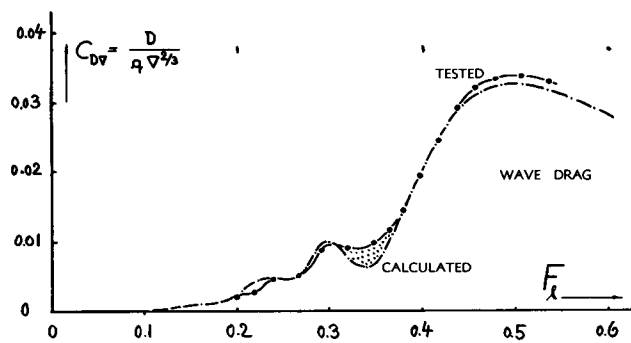


Figure 10. Comparison of calculated with tested wave drag by Wigley (12) for hull No. 829; having $b/h = 1.5$; $C_{\text{pris}} = 0.64$ and mid-section coefficient = 2/3.

The corresponding critical numbers are 0.28 and 0.20, while at 0.16 and 0.14 and so forth, wave drag is comparatively small. Actual critical numbers based on the hull's water-line length (rather than on its effective wavemaking length) are higher than the theoretical ones; among them, $F_L \approx 0.3$ indicates the most important hump. Another "last" hump appears in the vicinity of $F_L = 0.45$. The corresponding hump speeds are approximately

$$V_{\text{critknots}} = (0.75, 1.0, 1.5) \sqrt{\frac{1}{f_L}} \quad (19)$$

The drag coefficient hollows are between these speeds. — Because of the viscous wake at and aft of the stern, the second wave system is always weaker than the bow system. As a consequence, interference is smaller than predicted by theory. As pointed out in (12,d), the greatest discrepancy between theoretical analysis and experience is in the hollow between $F_L = 0.3$ and 0.4, a fact which is also illustrated in figure 10.

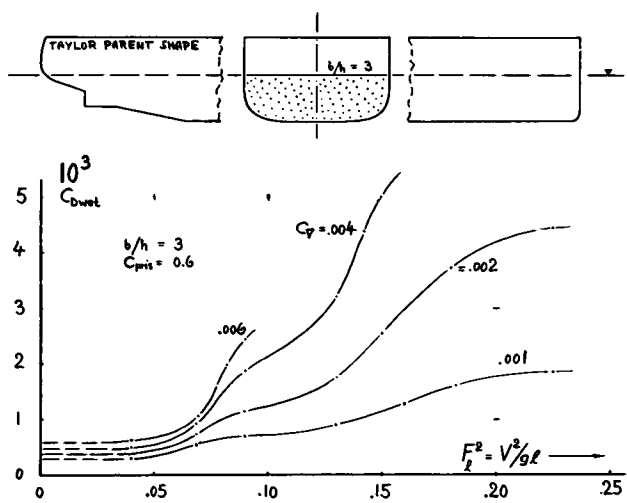


Figure 11. Residual drag coefficient (form + wave drag) of Taylor Series (13,a) for constant prismatic coefficient, plotted against the square of Froude number.

Froude Number. Since theory is complex (no explicit, let alone simple formula is available), the magnitude of wave resistance is customarily derived from model tests in towing tanks. Some trends of this drag component can be stated, however, as indicated by theory (12,c). As a function of Froude number, for example, the average wave drag (disregarding the humps and hollows) is expected to grow as

$$D_W/W \sim F_L^m \quad (20)$$

where $m \approx 4$. Because of the humps and hollows superimposed, this trend is not clearly evident in experimental results. Optimum designs, such as in figure 15, show however, that equation 20 is confirmed in a limited range of Froude number. Figure 9 also demonstrates that wave resistance (including humps and hollows) is essentially the same in full scale as in model testing. Minor changes can be expected, however, on account of the fact that the thickness of the friction belt in full scale (affecting the formation of the stern system) is smaller than in any tank model. It may be stated in this connection that even without a second system (from the stern) humps and hollows must be expected, depending on whether or not one of the transverse waves coming from the bow "lifts" the stern up, thus pushing the hull forward.

Volumetric Coefficient. Under limited conditions, theory also predicts that wave drag tends to grow as

$$D_W \sim b^n \quad (22)$$

with $n = 2$ or smaller. Some evidence of this trend is seen in figure 11 at higher Froude numbers, where b is represented by $(V/l)^3$. Small values of the volumetric coefficient in the order of $C_V = (1 or 2)/1000$ are therefore preferable at such numbers, as for example in destroyers. To say it in other words, vessels designed for operation at higher Froude numbers are made as long and slender as practicable in order to reduce wavemaking. However, if increasing the draft in proportion to the beam, volume and displacement weight also grow as b^2 . As a consequence, the residual resistance ratio (D/W) is not very much affected by an increase of C_V . Even in the vicinity of the last hump (at $F_L \approx 0.5$ for example in figure 9), Taylor's Series of hull forms (13,a) indicates (for $C_{\text{pris}} = \text{constant}$) that (D/W) is comparatively constant (between 0.04 and 0.05), at least up to $C_V \approx 2/1000$ which is as far as tested at higher speeds. In the range of small Froude numbers, variation of C_V between 3 and 7/1000 does not affect the "residual" resistance coefficient (on wetted area) very much. Cargo ships and tankers are, therefore, made comparatively fat and bulky in order to carry as much volume as possible in a given length of hull.

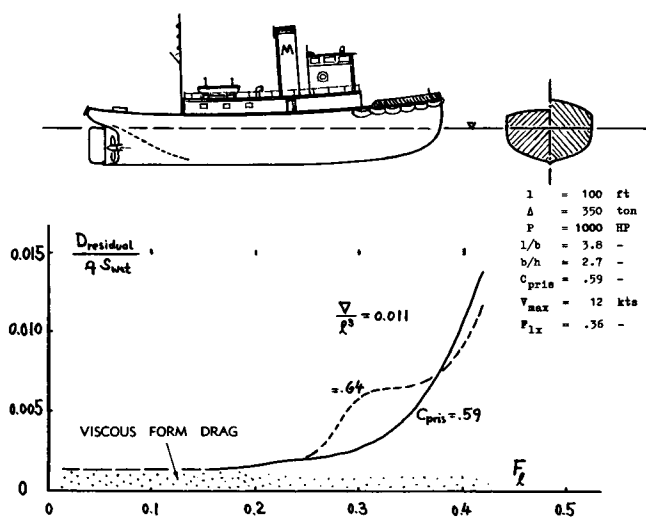


Figure 12. Residual drag coefficient of a typical (bare) tugboat hull (13,c).

Prismatic Coefficient. In contrast to the volumetric coefficient (indicating "thickness" as such), the prismatic coefficient indicates distribution of thickness. Figure 12 shows that by increasing this coefficient (making bow and stern fuller), wave resistance coefficient (and bow-stern interference) at $F_L \approx 0.3$ are considerably increased. Figure 13 presents as an example, the drag ratio D/W for $F_L = 0.3$. In the vicinity of the hump, found at this Froude number, "it pays to reduce the prismatic coefficient as far as possible" (12,c). The graph shows accordingly an optimum $C_{\text{pris}} \approx 0.5$. Such a coefficient means narrow entrance angle and hollow shape at bow and stern; see figure 13. Reducing the coefficient further (while $\nabla/1^3$ is constant), results in shapes that are extremely wide in beam and extremely fine at the ends. Taking into account frictional resistance (which is not included in figure 13), prismatic coefficients are considered optimum in modern vessels, approximately as follows:

for motorboats, destroyers, cruisers,	
liners, battleships	$C_{\text{pris}} \approx 0.60$
for average passenger ships	≈ 0.65
for average freighters	≈ 0.70
for very slow cargo ships	≈ 0.80

(13) Tank-model results on displacement hulls:

- a) Gertler, Reanalysis of Test Data for Taylor Series, TMB Rpt 806 Govt. Printing Office, Washington, D.C.
- b) Todd-Forrest, Experiments on Merchant Ship Forms Series 57 and 60, Trans SNAME 1951 and 1953.
- c) Roach-Taggart, Tugboats, Trans SNAME 1954 p.593.
- d) Almy, Hughes, Meek, Ferguson; Experiments on a Series of 0.65 Block Coefficient Forms, Trans INA 1954.
- e) Ridgeley Nevitt, Trawler Hulls, Trans SNAME 1956.
- f) St.Denis, Transom Stern, Mar.Eng. July 1953 p.53.
- g) Hunnewell, Coast Cutters, Trans SNAME 1937 p.81.
- h) Bragg, Bulbous Bows, Trans SNAME 1930.
- i) Resistance can also be influenced by a hydrofoil placed at the forefoot; Abkowitz Trans SNAME 1953 p.65.

Maximum Section. It has been mentioned that the wave system originating from the stern is comparatively weak. With regard to wave resistance, it is, therefore, favorable to make the forebody of a ship finer than the afterbody. Doing this, the maximum cross section of the hull (or the parallel middle body, respectively) is naturally moved aft. Shortening of the afterbody may lead to "viscous" flow separation from the stern, however; at least in hulls with larger volumetric coefficients. The finer forebody shape may, therefore, be confined to the waterline, while the section area curve is more or less kept symmetrical fore and aft. Experimental results on this subject (12,b) show that a shorter bow increases wave resistance, particularly in the vicinity of $F_L \approx 0.24$ and ≈ 0.33 (in the type of hull investigated). The center of buoyancy should accordingly be somewhat aft of midships at Froude numbers F_L between 0.15 and 0.30. However, at Froude numbers below 0.15, a position of the center of buoyancy ahead of midships is preferable with regard to "viscous" form drag originating along the stern, as mentioned above.

Wavemaking Length. Alterations of hull shape may be considered in terms of wavemaking length. The effective length of a hull (with respect to humps and hollows) is reduced (and the effective Froude number is increased) by raking or cutting away the stem (as for example, in the "Maier Form") or by applying a "counter stern". The wavemaking length is increased (and the effective Froude number is decreased) by adding a "bulbous bow" and by "cruiser" or transom type sterns. By proper design, it is thus possible to make the cruising speed of a ship coincide with a hollow in the wave-making resistance, rather than with a hump. Such design efforts are particularly rewarding in regard to the hump at $F_L \approx 0.3$. Figure 12 demonstrates, as an example, how this hump is not only decreased but also shifted (whatever there is left) to higher speeds, by reducing the prismatic coefficient.

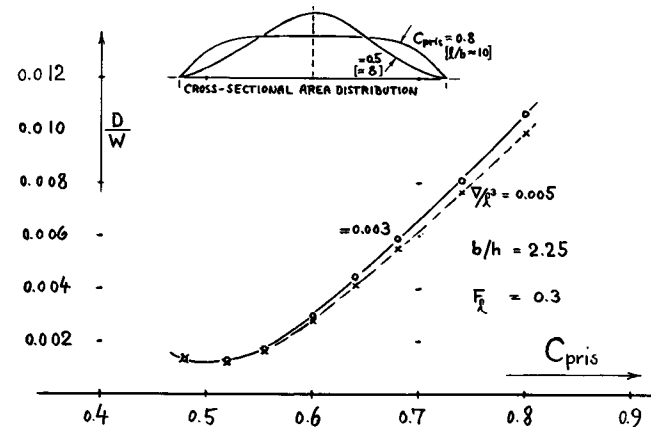


Figure 13. Residual drag (form + wave drag) of Taylor series (13,a) at hump Froude number $F_L = 0.3$. Note that at this Froude number, results for different b/h ratios and for different volumetric coefficients are roughly the same.

In Shallow Water, the propagation speed of a wave has the limiting maximum value

$$V_x = \sqrt{g H} \quad (22)$$

where H = depth of water. For example, in 40 ft of water, the critical speed is 36 ft/sec = 21 knots. A displacement craft going at this speed, then produces a solitary wave, similar to that at the last hump, at $F_L \approx 0.45$, in deep water; and its wave drag (in lb or in the form of the D/W ratio) in this condition is approximately as high (14,a) as in deep water at that F-number. At lesser speeds, wave resistance is roughly as high as in deep water at such a higher Froude number at which the transverse system has the same wave length, and the same position of humps and hollows along the length of the hull as in the shallow-water condition. Resistance in shallow water can thus be presented in terms of

$$V/V_x = V/\sqrt{g H} = F_L \sqrt{1/H} \quad (23)$$

Up to some 0.7 of the critical speed, the influence of shallow water on ship resistance is considered to be very small. Shallowness is, therefore, not so much a problem in itself. Rather, it grows important in combination with a lateral restriction as we may find it in inland waterways, such as particularly in canals. The flow pattern is much more complicated then. Theoretical solutions are available, however, for such conditions (14,c,d,e), both for wave resistance and for "viscous" drag (affected by blockage).

In Seaway. The drag of displacement vessels has been discussed so far on the basis of a perfectly smooth water surface. Actually, the water is rarely calm; and ocean waves have been reported with heights up to 70 feet between crest and trough. Not too much is known in a systematic way, about the influence of a seaway upon the hydrodynamic drag of ships. Figure 14 shows one example, however, in which a model was towed against regular waves (considered to be "long") in a tank. The increment of the mean-average total drag is in general moderately high; and the increment is suggested to be proportional to beam times wave height. However, in a comparatively narrow speed range, time-average resistance is roughly doubled; and it may even be increased more in other combinations of vessel and seaway. In this range, the frequency of wave encounter is in synchronism with the natural pitch and heaving motions of the vessel investigated. As a function of the predominant wave length, therefore, ocean-going ships have a critical speed at which not only the resistance is very much increased, but where also their structural strength and the comfort of the passengers is considerably af-

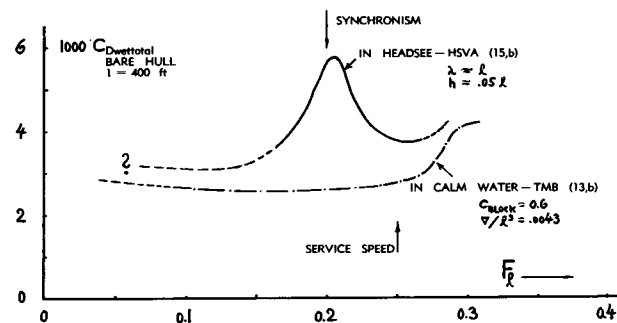


Figure 14. Resistance of a dynamically similar merchant-ship model, tested in regular tank waves (15,b). At synchronism, heaving and pitching show amplitudes larger than those of the wave train.

fected. At this speed, the drag increment is predominantly of the wave-making type due to plunging in and out of the water (15,a). Ocean waves are not regular and records of their predominant height and length in a developed storm are not always consistent. To give some indication of the parameters involved, it may be mentioned, however, that the critical speed of a larger liner is between 20 and 30 knots and those of a 400 ft "Victory" ship between 15 and 20 knots, when going against a seaway produced by one of the more severe storms on the Atlantic. Not only because of drag, but also with regard to discomfort and possible damage (slamming), a ship must then either stay above the critical speed, or after "falling out of step", continue at a speed somewhat below the critical range (15,d).

(14) Resistance in shallow water:

- a) O. Schlichting, Yearbook STG 1934 p.127.
- b) Schmidt, Torpedo Boats, Schiffbau 1938 p.100.
- c) Kreitner, Theory, Werft-Reederei-Hafen 1934.
- d) Schuster, Flow Pattern, Yearbk STG 1952 p.224.
- e) VanManen and VanLammeren, Model and Ship Trials in Shallow Water, Trans Soc.NNAME 1956.

(15) Resistance in sea waves:

- a) Kreitner, Resistance, Trans INA 1939 p.203.
- b) 7th Intern. Conf. Ship Hydrodynamics, Sweden 1954.
- c) Kempf, "San Francisco" in Waves, Trans SNAME 1936 p.195 (also in Werft-Reederei-Hafen 1936 p.363).
- d) Motions in Waves, Trans SNAME 1955 p.140, 190.

(16) Performance of various types of displacement ships:

- a) Woolland, British Vessels, Shipb. and Marine Eng. Builder July 1956; J.Am.Soc.Naval Engrs 1956 p.727.
- b) Parkes, German and Japanese, Trans INA 1949 p.427.
- c) Stewart, Ore Carriers, Trans NE Coast Institution Engineers Shipbuilders 1953/4 p.409.
- e) Ship dimensions are restricted by passages such as through the Panama Canal, to $b \approx 110$ ft; and by the low-tide depth of water in ports, to a draft of some 35 ft.
- f) Super-tankers are being built in sizes up to 85000 tons, and considered to be built up to 100000 tons. To stop them from 15 knots, may take 15 minutes and/or 2 miles, at full backing power.

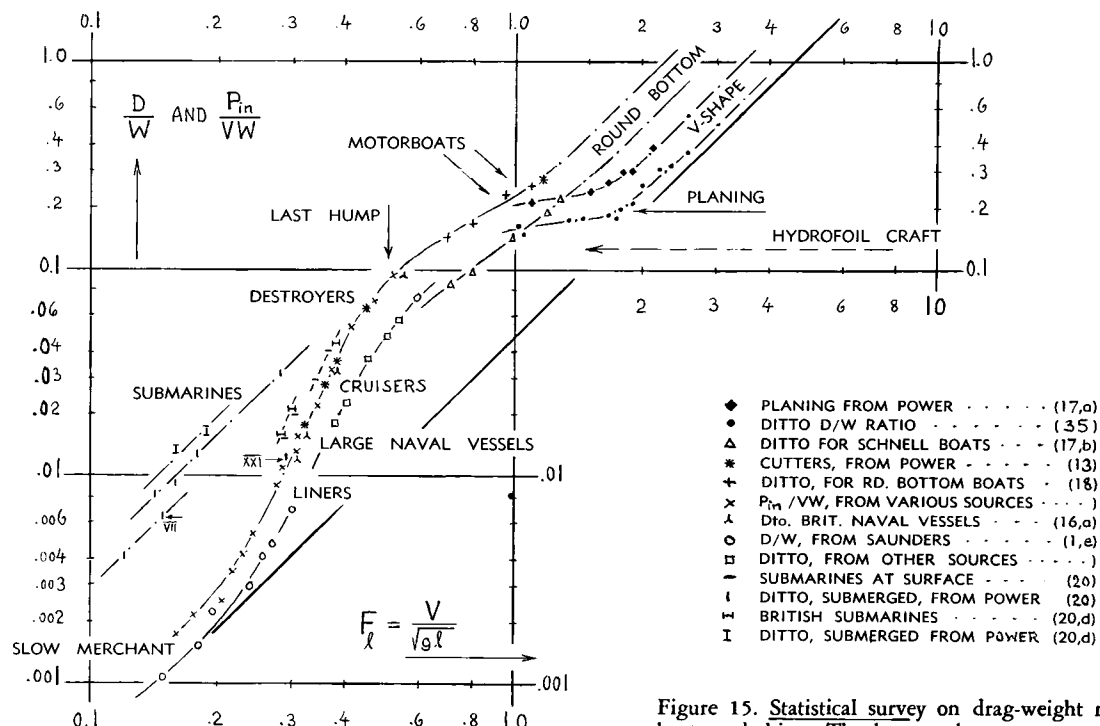
5. TYPES OF DISPLACEMENT VESSELS

Statistics. For the reader not so familiar with naval architecture, *table A* gives a rough idea on dimensions, speeds and similarity parameters with which we are dealing in ships. "Optimum" total resistance ratios of vessels and boats have also been collected from various sources, and presented in *figure 15*. Below $F_L \approx 0.2$, drag is essentially proportional to the square of the speed (skin friction, no wave making). Humps and hollows (due to wave resistance) are not found in the statistical plot; they are evidently avoided by proper hull shape in each particular design. Between $F_L = 0.3$ and 0.4 we find drag increasing as the 4th power of speed. This trend reflects the theo-

retical expectation of wave resistance growing at this rate (12). Beyond $F_L \approx 0.5$ (representing the speed of the so-called "last" hump) the slope of $D(V)$ reduces again. The ratio $P_{in} / (V W)$, in pounds of "engine thrust" per pound of displacement weight, with P_{in} indicating installed or brake horsepower, is higher than the resistance ratio D/W as derived from model tests, because of mechanical losses, propeller efficiency and factors such as method of rating and reserve power provided. Thus, what we may call total efficiency " η ", is between 0.6 and 0.7, indicating the difference between the two functions plotted in the graph. The discontinuity at $F_L \approx 0.6$ is due to various differences between the adjoining two classes of craft ("destroyers" and "motorboats"). The overall increase of the drag ratio as a function of Froude number is very large. The ratio ranges from well below 1% in slow merchant vessels to nearly 10% in destroyers; and it grows beyond that in all types of motorboats.

TYPE OF SHIP	Ref.	tons	l,ft	l/b	V/l^3	C_{pris}	BHP	V,kts	F_1	R_1
average tank model	(--)	1	20	-	--	--	--	4	0.27	$1 \cdot 10^7$
6 m sail boat	(F.19)	4	23	4	1.20%	--	--	6	0.36	$1 \cdot 10^7$
small motorboat	(--)	5	30	4	0.65%	.60	150	15	0.80	$6 \cdot 10^7$
a "launch"	(13,g)	30	55	4	0.60%	.60	300	14	0.59	$1 \cdot 10^8$
average blue whale	(--)	85	80	-	0.16%	--	--	10 ?	0.33	$1 \cdot 10^8$
small C.G. cutter	(13,g)	200	85	4	0.60%	.60	500	14	0.38	$2 \cdot 10^8$
average tug boat	(13,c)	300	100	4	1.05%	.59	1000	10	0.30	$2 \cdot 10^8$
av'ge fishing boat	(13,e)	300	100	5	1.05%	.65	600	10	0.30	$1 \cdot 10^8$
coaster motorship	(1,e)	750	155	6	0.70%	.75	400	11	0.25	$3 \cdot 10^8$
submarine surfaced	(20)	800	200	12	0.35%	.50	2500	17	0.35	$5 \cdot 10^8$
Coast Guard cutter	(13,g)	2000	300	-	0.26%	--	5000	18	0.32	$7 \cdot 10^8$
average destroyer	(1,e)	3000	400	10	0.17%	.60	70000	36	0.50	$2 \cdot 10^9$
average cargo ship	(1,d)	9000	400	7	0.50%	.75	4000	14	0.18	$6 \cdot 10^8$
old-type cruiser	(16,a)	9000	650	9	0.20%	--	80000	32	0.38	$3 \cdot 10^9$
average tanker	(1,d)	20000	500	7	0.58%	.75	5000	14	0.18	$8 \cdot 10^8$
cargo-passenger	(1,e)	20000	600	8	0.33%	.70	15000	20	0.23	$1 \cdot 10^9$
modern tanker	(--)	40000	600	7	0.55%	.70	20000	17	0.20	$1 \cdot 10^9$
Atlantic liner	(--)	60000	900	9	0.30%	.60	100000	29	0.31	$3 \cdot 10^9$
average battleship	(16,a)	45000	800	8	0.31%	.65	160000)	30	0.32	$3 \cdot 10^9$
aircraft carrier	(--)	60000	900	8	0.30%	.65	280000)	32	0.32	$4 \cdot 10^9$
new super-tanker	(16,f)	100000	950	7	0.42%	--	45000	18	0.17	$2 \cdot 10^9$

TABLE A. Dimensions and performance characteristics of various displacement-type vessels. Data in each type actually may vary very considerably as a function of time and conditions of operation and so on. Therefore, this list is only intended to show the possible order of magnitude of dimensions and similarity parameters involved. Power in Naval vessels is usually "secret"; it is possible, however, to make estimates on the basis of figure 15. Values shown in parentheses, are estimated in such a manner or by other methods. The various numbers listed do not necessarily represent vessels that have existed at one time or another, or which may be existing at this time.



Motorboats. Small boats, going at higher speeds, have Froude numbers exceeding those investigated in the Taylor Series. Figure 16 presents the characteristics of a bare round-bilge hull, up to $F \approx 1.1$. The maximum of the coefficient (at $F = 0.5$) is ≈ 3 times that of the skin friction drag. Beyond the hump, the coefficient reduces to the level of 0.004. Referring this coefficient to the square of the beam, b , the value $C_{Db} = D/qb^2 = 0.02$ is obtained. A considerable part represented by this coefficient is spray drag. All components, viscous, spray, appendage, air drag, of such boats seem to end up as $D \sim V^2$, in the range of very high Froude numbers.

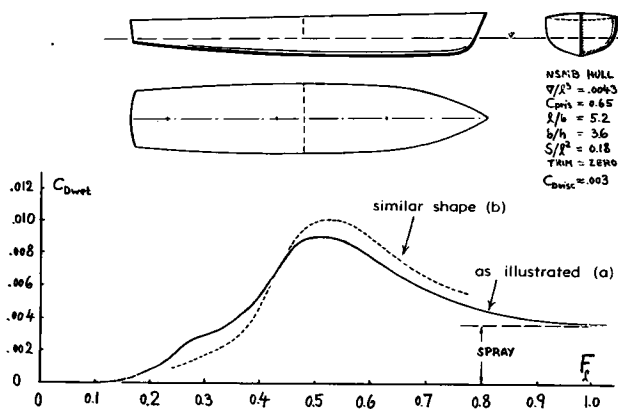


Figure 16. Wave- and spray-drag coefficient of round-bilge motor-boat hulls (18).

Figure 15. Statistical survey on drag-weight ratio of all types of boats and ships. The lower values represent total D/W ratios as derived from tests on tank models; the higher values indicate an "effective" drag ratio (including losses in the propulsion system) as derived from installed horsepower in full-scale trials. For explanation of planing and hydrofoil craft, see later in the text.

Planing? The round-bilge hulls in figure 16 should not be confused with planing hulls (see in section B of this chapter). Converting the drag coefficient into the resistance ratio (equation 2), it is seen that their (D/W) does not reach an approximately constant level as in planing boats (see in figure 15). Also, the drag ratio increases to much higher values as the Froude number is increased. Round bottoms or hulls with round bilges are poor in regard to planing; they do not produce much lift, if put at an angle of trim. In fact, reference (34) demonstrates that there is basically no lift at all in a streamlined body (having a tapered afterbody). Because of their cambered shape, such bodies even develop negative lift (suction) at their bottoms (see equation 10), the amount of which becomes objectionable at Froude numbers above $F_l \approx 1$. Operation of such hulls simply becomes impossible at these speeds; and it is only after adding "chine strips" (making the flow break away from the sides of the body) that some positive planing lift is finally obtained. To avoid squatting in destroyers, certain measures are taken in the design of their hulls. Part of such efforts is the transom shape of the stern (13,f), which helps to keep the bottom straight, thus reducing suction. As far as motorboats are concerned, many of them are not of the planing type either (as long as they have round bilges). Just a transom stern is not enough to make them planing.

SURFACED:			SUBMERGED:		
$\Delta = 770$			$\Delta = 870$	TONS	
$V = 17.7$	MAXIMUM		$V = 7.6$	KNOTS	
$P = 2800$	(DIESEL)		$P = 375$	BHP (ELECTRO)	
$C_D = 2.5/1000$			$l = 222$	FT	

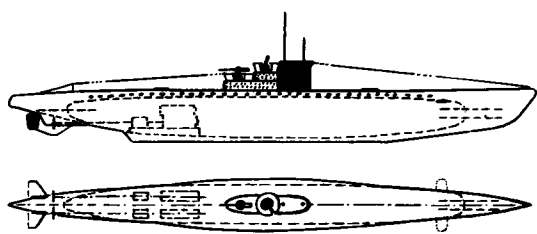


Figure 17. Shape and principal dimensions of the German submarine, Type VIIc, predominant during World War II. Horizontal surfaces added by author.

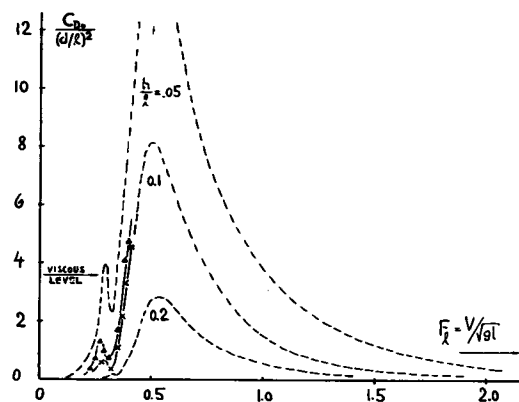
SUBMARINES. Although specific towing-tank data on submarines are not available, information on the German "U" boat development during World War II has been published (20). Figure 17 shows the essential dimensions of their predominant design (type "VII") during World War II. Drag ratios, evaluated for this and other boats, are included in figure 15. In surface operation, submarines show resistance ratios slightly higher than those of other displacement ships. The difference can be explained on the basis of skin-friction drag (due to smaller Reynolds number and because of their long and slender shape).

- (17) Information on "Schnell" Boats:
 - a) Tietjens, Schnellboote, Yearb.D.Lufo 1937 p.I,361 and Werft-Reederei-Hafen 1937 p.87 and 106.
 - b) Graff HSV, Werft-Reederei-Hafen 1935 p.334.
- (18) Round-Bilge Motorboat Hulls:
 - a) De Groot (Wageningen), Resistance of Motorboats, Intern.Shiptb. Progress 1955 p.61. Series includes volumetric coefficients between 2 and 7/1000.
 - b) Nordström, Small Boats, Teknisk Tidskrift 1936.
- (20) Characteristic of submarines:
 - a) Schade, German Development, Trans SNAME 1946.
 - b) Starks, "U" Boats, Trans INA 1947 p.291.
 - c) Hilmar, Undersea Craft, Paper SNAME 1952.
 - d) Sims, British Submarines, Trans INA 1947.
- (21) Wave drag of submerged streamline bodies:
 - a) Weinblum, Amtsberg and Bock; Tests on Wave Resistance of Immersed Bodies of Revolution, Mitteilungen Preussische Versuchsanstalt Wasserbau Schiffbau, Berlin 1936; also Schiffbau 1936; Transl.234 by Taylor Model Basin.
 - b) Weinblum, Bodies of Revolution with Minimum Wave Resistance, Ingenieur Archiv 1936 p.104.
 - c) Wigley, Trans INA 1953 p.268; also in Shipbuilding and Marine Engine Bldr. 1953 p.273.

In Submerged Operation — the wetted area of a submarine is appreciably increased over that in surface operation. Analysis of the boat as per figure 17, gives a total drag coefficient (based on maximum frontal area including conning tower, and for an assumed propulsive efficiency of 70%) — in the order of $C_D = 0.15$. For a fineness ratio $l/b = l/h = 12$, this value is considerably higher than that of smooth bodies as found in the "streamline" chapter. Referring the coefficient to the estimated wetted surface area, $C_{Dwet} = 0.0048$ is obtained. At the Reynolds number corresponding to the boat's trial conditions, at $R_\lambda = 3 \cdot 10^8$, the skin-friction coefficient is $C_f = 0.0018$. Thus, the resistance as tested is 2.7 times the Schoenherr value. Most of the increment is evidently caused by the open-type conning tower, having a frontal area of almost 30% of that of the hull body. Other contributions come from the periscopes, guns, rails, all types of attachments and the many openings in the outer hull needed for filling or emptying the buoyancy tanks. As a consequence, the resistance of submarines in submerged condition, is usually higher than in surface operation (at the same speed). Figure 15 also shows (in the left hand side) that in the absence of any noticeable water-surface reaction, the drag ratio approximately varies as the square of speed or square of Froude number. This means an approximately constant drag coefficient, in the order as derived above. It can then be concluded from the graph, that at Froude numbers around $F_\lambda = 0.5$, deeply submerged submarines (without wave drag) can have a smaller drag coefficient than in surface operation. Another advantage in deeply submerged boats, both in regard to resistance and passenger comfort, is the elimination of bad-weather effects (waves).

Streamlining. On the basis of wind-tunnel and towing-tank investigations, the Germans also developed the more advanced submarine type "XXI". The hull had a continuous shape; the conning tower was more streamlined; and the guns were integrated into the tower. Based on a realistic engine-power value (20,a), the improvement over type "VII" is appreciable (see point marked in figure 15).

SUBMERGED BODY. Deeply submerged, a streamline body may have the same low drag coefficient as the hull of an airship. In proximity of the water surface, such a body experiences wave drag, however, in basically the same manner as surface vessels do. Figure 18 presents the theoretical prediction (21,c) on the magnitude of the wave-drag of slender spheroidal bodies, plotted against Froude number for several values of the submergence ratio h/l . After subtracting values for the basic, mostly skin-frictional drag of certain bodies tested (21,a) their wave-drag component has been separated. The results agree sufficiently well with the theoretical prediction. The



wave drag has a maximum "at" the surface (at $h \approx 0$). To give the graph a scale, the viscous drag of the tested bodies is indicated at $C_{D_v} \approx .05$. The wave drag decreases sharply with submergence. It may roughly be said that this drag becomes unimportant at ratios larger than $h/d = 5$. Submarines may travel below $h = 5 d$. However, with the periscope out of the water or in "snorkeling" operation, their submergence is between 1 and 2 hull diameters. Considering now as a theoretical example, a length in the order of 200 ft and a speed of 20 knots, the Froude number is right at the maximum of the wave drag in figure 18. Thus, when operating in proximity of the water surface, the wave drag of a fast submarine can roughly be of the same order as its basic streamline-body drag; and her total resistance ratio will then be very high (figure 15).

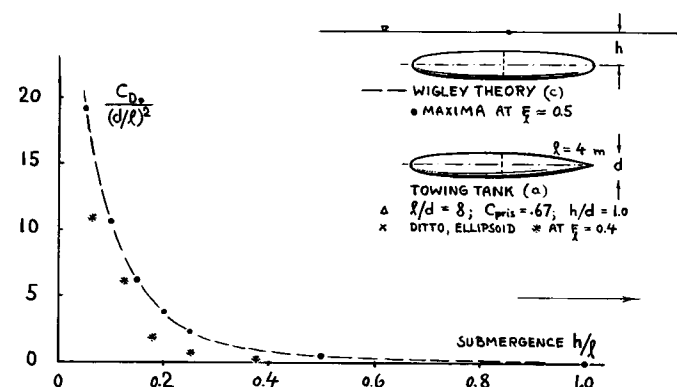


Figure 18. Wave-drag coefficient of submerged streamline bodies, as predicted by theory and as tested (21), as a function of Froude number and submergence ratio.

Sailboats. Performance of sailing craft rests in the combined application of aerodynamic forces (in the sail system) and hydrodynamic effects in the hull. Within the scope of this book, only the hydrodynamic aspects shall be considered, however. As an example, figure 19 presents drag coefficients of a 6-meter yacht.

Wave Drag. The volumetric coefficient of sailing yachts is comparatively high. The 6-meter boat in figure 19 has such a coefficient in the order of $C_V = W/\rho l^3 = 12/1000$; while displacement ships usually have between 1 and 4/1000. An appreciable fraction of the displacement is concentrated in the keel and deeply submerged, accordingly. For example, the 6-meter boat quoted has a static draft h approaching the size of the beam b , while displacement ships may have beam ratios b/h between 2.2 and 3.5. The total drag ratio of the yacht in figure 19 (without heeling) as a function of Froude number is approximately equal to that of other "optimum" displacement vessels (as in figure 15).

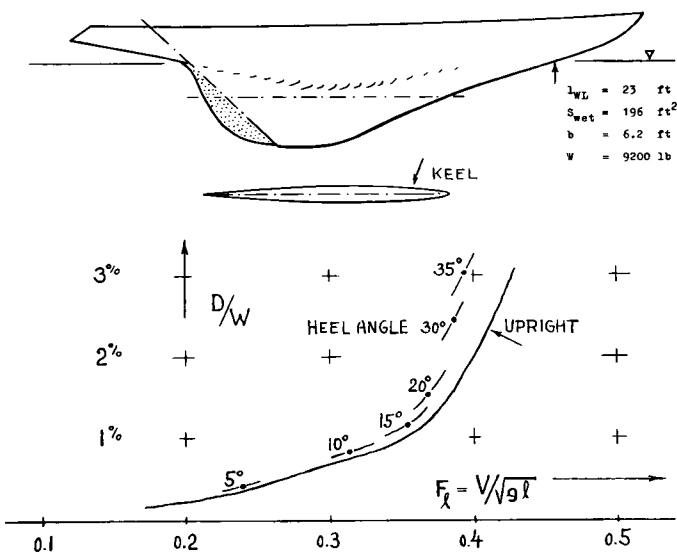


Figure 19. Full-scale resistance characteristics of 6-meter sail boat "Jill", predicted from model tests (25,a) upright as well as heeling, as indicated, with corresponding leeway.

$$C_{latK} = F_{lat}/q S_K = (S_S/S_K) (C_{latS}/840)$$

where "840" indicates the density ratio of water against air, "S" = sail and "K" = "keel". For example, in the 6-meter yacht as per figure 25, the lateral area of the keel (plus hull to the static waterline) is in the order of 70 ft^2 , while the sail area is between 400 and 500 ft^2 . The lateral lift coefficient in the sails, based on a dynamic pressure corresponding to an apparent or relative wind speed V_S assumed to be 15 knots, may be in the order of $C_{\text{lat},S} = 1.0$. The lateral coefficient of the hull (based on craft speed against water, V_K , in the order of 5 knots) is then at the level of less than 0.1. Figure 19 shows, nevertheless, an increase of hull-drag caused by sideslipping (leeway) and heeling (in close-to-wind condition) up to more than 50% of the total drag in straight and upright motion. Assuming that frictional and wave-making drag of the hull is not appreciably changed by the angular position, the increment must essentially be "due to lateral lift". Calculation of such drag in small aspect ratios ($A \approx 0.3$ in the submerged part of the hull in figure 25) is unfortunately complex (see Chapter VII). It is possible, however, through numerical application of equations 32 through 37 of the chapter quoted, to obtain by order of magnitude the increments (and their progressive trend) as reported in the illustration.

Beam Wind. The mechanism of induced drag found in sailing craft, can also exist in displacement vessels proceeding in a beam wind. Based upon their lateral projected area above the waterline, reference (6,e) indicates an aerodynamic drag coefficient in the order of $C_D = 1.2$. To counteract the corresponding lateral force in hull and superstructure, an angle of yaw in the order of 10° may be required in a wind having a velocity equal to the ship's speed of advance. The resultant hydrodynamic drag due to lateral lift is then estimated (on the basis of equation 35 on page 7-18) to be in the order of 10% of the vessel's non-wave-making resistance.

(25) Fluid-dynamic characteristics of sailboats:

- a) Davidson, Studies of Sailing Yacht, Trans SNAME 1936 p.288; also Trans ASME (Jl.Ap. Mech's) June 1936.
- b) Croseck, Segel Theorie, Springer Berlin 1925.
- c) Wells, Scientific Sailboat Racing, 1950.
- d) Morwood, Sailing Aerodynamics, New York 1954.
- e) Sail Aerodynamics are also treated in Trans SNAME 1915 p.1, and in 1925; J.RAS 1930 p.880; Yearbk.STG 1933 p.228; ZAMM 1941 p.308.

(30) "Circulation" does not mean that fluid particles really go around a foil section in something similar to a "circle". The term only means an added component flow velocity. In case of a planing plate, the water surface approximately represents the streamline meeting the stagnation point. This line has something of a discontinuity, insofar as the spray is a component of the flow which should go over the top of the surface in order to make the pattern perfect.

(31) Basic theory of planing:

- a) Wagner, Gliding, Z.Ang.Math.Mech 1932, p.193 or Yearbk.STG 1932 p.205. Transl. NACA T.Memo 1139.
- b) Weinig, Lufo 1937 p.314; NACA T.Memo 845.
- c) Bollay, Proc. 54th Int.Congr. Appl'd Mechs 1938 p.474.

B. CHARACTERISTICS OF PLANING CRAFT

Planing means "gliding" or "skimming" over the surface of water, rather than "plowing" through it as displacement vessels do. Beginning with the earliest experimental versions, particularly all water-based airplanes seem to have been equipped with planing-type floats. Also, all modern power-driven racing boats are of the planing variety, reaching top speeds between 70 and more than 200 mph in various classes.

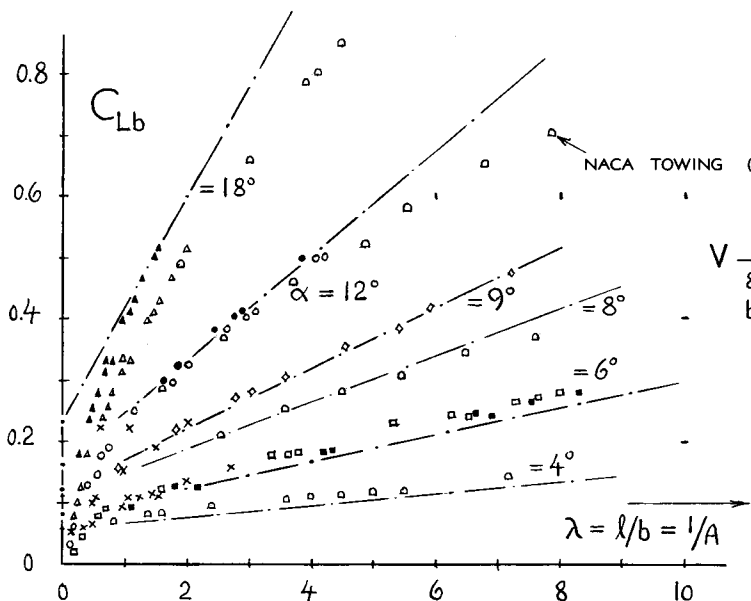
1. THEORY OF PLANING

No theoretical solution for lift and drag of planing surfaces has been established so far. Hundreds of tank tests are available, however; and a large bibliography reporting and discussing them.

Two-Dimensional planing can be understood as a limiting case of hydrofoiling (with submergence $h \rightarrow 0$). At high Froude numbers (no buoyancy and no "wave" drag), a properly cambered surface with $b = \infty$ (in two-dimensional flow), riding on top of a solitary wave, can be considered as the lower face of a foil (30) in infinite flow (31). Its lift curve slope is simply half of that of the complete foil; the lift angle is accordingly

$$d\alpha/dC_L = 1/\pi = 57.3/\pi = 18.3^\circ \quad (21)$$

The drag due to lift of this theoretical surface is zero. Real planing surfaces are essentially straight (no camber). Assuming that their lift (in two-dimensional flow) may still correspond to equation 21, their drag due to lift is no longer zero, however; rather it is a component of the force normal to the surface considered. Momentum or energy is dissipated in the form of spray. This is about all the information available by way of exact theory. All other formulations (33) are statistical; a number of them are adaptations of aerodynamic wing theory, "corrected" for aspect ratio and other effects on the basis of experimental results.



OPEN SYMBOLS ON RUNNING-WATER,
FILLED SYMBOLS ON STATIC LENGTH
X FROM REFERENCES (32,a and b)

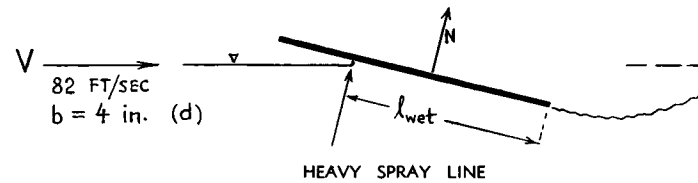


Figure 20. Lift coefficient of flat rectangular planing surfaces (32,d) as a function of wetted length ratio.

BUOYANT LIFT. In a flat plate inclined against the water surface at the angle α , the trailing edge is submerged at $h = 1\alpha$, where 1 is the not very well defined average *wetted length*. The component of buoyant lift corresponds to the displaced volume of water; hence approximately

$$L_B = 0.5 \rho h 1 b = 0.5 \rho \alpha l^2 b \quad (22)$$

The lift thus obtained is basically the same as that due to " ζ " in cavitating or ventilating flow ($\zeta \equiv 1/F_h^2$), as explained in Chapter X. The coefficient based on the square of the span is then

$$C_{Lb} = L_B / (0.5 \rho V^2 b^2) = g 1 \alpha / (V^2 A) = \alpha / (A F_\lambda^2)$$

where A = wetted aspect ratio = b/l . However, since the wetted length is usually somewhat longer than corresponding to submergence, the component of buoyancy lift can be somewhat smaller (33,a) than indicated by the equation. In high-speed and low-angle operation, the component comes to be negligibly small — because of the magnitude of F_λ^2 .

Beginning Of Planing. At small Froude numbers, the buoyant component of lift can be an appreciable if not predominant fraction of the total lift. There is no well-defined Froude number, however, at which it could be said that planing "begins". The only designation possible is to define arbitrarily a certain percentage of buoyancy in comparison to the total weight (which includes the dynamic lift) of a planing craft — as the condition where planing can be considered to be established. Because of the complex nature of planing, such a definition cannot easily be derived. Considering, however, small angles of attack and excluding very high wetted-length ratios, only the

linear small-aspect ratio lift term (of equation 26) may be taken into account. Using equation 23, the ratio is then

$$\frac{\text{Buoyant lift}}{\text{Dynamic lift}} = \frac{\alpha / (A F_\lambda^2)}{\alpha \pi / 4} = \frac{4 \lambda}{\pi F_\lambda^2}$$

Arbitrarily assuming now that planing is considered to "take over" where this ratio is equal to 20%, the corresponding Froude number is

$$F_{\lambda*} = 1.6; \text{ or } F_{b*} = 1.6 \sqrt{\lambda} \quad (25)$$

This value is indicated in figures 23 and 26; and it is seen that a point of increased deviation in the functions plotted, is roughly met by the equation.

SMALL ASPECT RATIOS. Many practical applications of planing exhibit small wetted aspect ratios. As explained in the chapter on "drag due to lift", there are two components of lift in such 'wings'; a linear term corresponding to circulation (30), and an approximately quadratic term originating along the lateral edges. The two types of lift are found in planing surfaces too. Below $A \approx 1$ (or above $\lambda = 1$), interpretation of experimental results on flat and rectangular planing "bottoms" (at higher Froude numbers) is tentatively possible on the basis of

$$C_{Lb} = L / (\rho b^2) = (\pi/4) \sin \alpha \cos \alpha + k (\sin^2 \alpha / A) \cos \alpha$$

where $\lambda = 1/A$ = wetted length ratio. The factor k is a function of the aspect ratio possibly similar to that as shown in the "drag-due-to-lift" chapter. Note that the experimental points plotted in figure 20, follow curved lines, which means that k is not con-

stant. In fact, k may be expected (31,c) to reduce to 0.88 as $\lambda \rightarrow \infty$, resulting in a lift- or normal-force coefficient as given in equation 29 of the "hydrodynamic" chapter. One difficulty in the analysis is evidently proper definition of an effective length "l". Spray increases the "wetted" length; and it is not clear that the length indicated by the "heavy spray line" has sufficient significance in regard to lift. Correlation of the experimental points in figure 20 with the equation (applied for $k = 2$) is quite good when using the static wetted length (at rest, rather than the running length). Another definition of length would be to the stagnation line as tested in (32,f). For small angles, the function reduces to

$$C_{Lb} = (\pi/4)\alpha + k\lambda\alpha^2 \quad (26)$$

In Higher Aspect Ratios, a planing surface may also be considered to be a foil in "cavitating" flow, with the air space being a large cavity having the cavitation number $\zeta \approx$ zero. Using the two-dimensional theory as plotted in figure 19 of the "hydrodynamic" chapter, the force on the pressure side of a flat plate in this condition, at small angles of attack, approximately corresponds to

$$C_L \approx C_N \approx 0.5\pi(\alpha - \alpha_i) \quad (27)$$

Introducing for the induced angle at the surface $\alpha_i = 2 C_L / \pi A$, where "2" = biplane factor, the

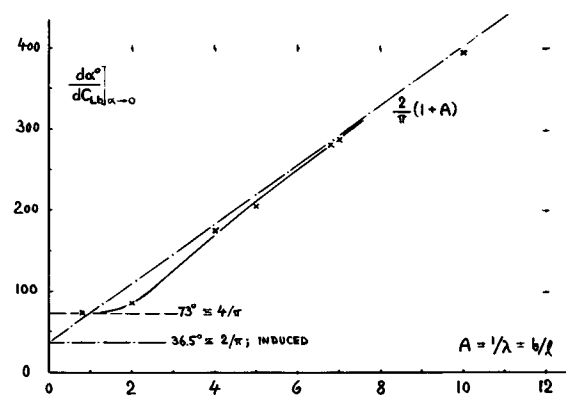


Figure 21. Lift angle of flat planing surfaces (32,d), mostly at higher wetted aspect ratios.

lift angle of planing plates having larger wetted aspect ratios is found to be approximately

$$\begin{aligned} d\alpha/dC_L &= (2/\pi) + (2/\pi A) \\ d\alpha/dC_{Lb} &= (2A/\pi) + (2/\pi) \\ &= 36.5^\circ (1 + A) \end{aligned} \quad (28)$$

The first term is the "sectional" angle of attack, while the second term represents the "induced" angle. Figure 21 shows that agreement with experimental points is very good at aspect ratios above 4. Below this value, a transition takes place to the constant value of 73° (first term in equation 26) for small aspect ratios.

Drag of Planing Plates. The pressure drag of flat planing plates is a component of the normal- or lift force, respectively:

$$D_p = D_i + D_{spray} = N \sin\alpha = L \tan\alpha \quad (29)$$

The increment of this drag over the "induced" drag represents the spray produced by straight bottoms. Including now a skin-frictional component, the drag (at higher Froude numbers) is indicated by the coefficient

$$C_{Db} \approx k_1 C_{Lb} \tan\alpha + k_2 \lambda C_f \quad (30)$$

and the drag-lift ratio is

$$\begin{aligned} D/L &= k_1 \tan\alpha + k_2 C_f / C_L \\ &= k_1 \tan\alpha + k_2 \lambda C_f / C_{Lb} \end{aligned}$$

To solve this equation, the function $C_{Lb}(\alpha)$ has to be known; and that is the reason for presenting above, all the functions on planing lift.

-
- (32) Experiments on prismatic bottoms:
 a) Sottorf, Planing Experiments, Werft Reederei Hafen 1929, 1932, 1933; Trans NACA T.Memos 661 and 739; also Yearbk D.Lufo 1937 p.I,309 and 320, also Lufo 1937 p.157; see NACA T.Memos 860 and 1061; also Yearbk D.Lufo 1937 p.I,320.
 b) Sambraus, Lufo 1936 p.269; NACA T.Memo 848 (b).
 c) NACA Tech Notes 509 (1934), 648 (1938), 2804, 2842, 2876, 3052 (1952 & 1953).
 d) Weinstein and Kapryan, Planing Characteristics of Flat Plates, NACA T.Note 2981 (1953).
 e) Korvin-Kroukovsky and Others, Stevens ETT Investigations, Inst.Aeron'l Sci. SMF Papers No.166 through 170, 229, 244, FF-2, FF-6 and FF-11 (1948 to 1955).
 f) Kapryan and Boyd, Pressure Distribution of Prismatic Surfaces, NACA T.Note 3477 (1955).
 g) Springston-Sayre, 50° Deadrise, TMB Rpt 920 (1955).
 h) Christopher, Shallow Water, NACA T.Note 3642.
 i) McBride, Spray by Planing, NACA T.Note 3615 (1956).
 k) Further towing tank results up to $1/b = 7$ and $\alpha = 30^\circ$ together with a comprehensive evaluation of practically all available results from other sources, are presented by Shuford, "Theoretical and Experimental Study of Planing Including Effects of Cross Section and Plan Form", NACA T.Note 3939 (1957).

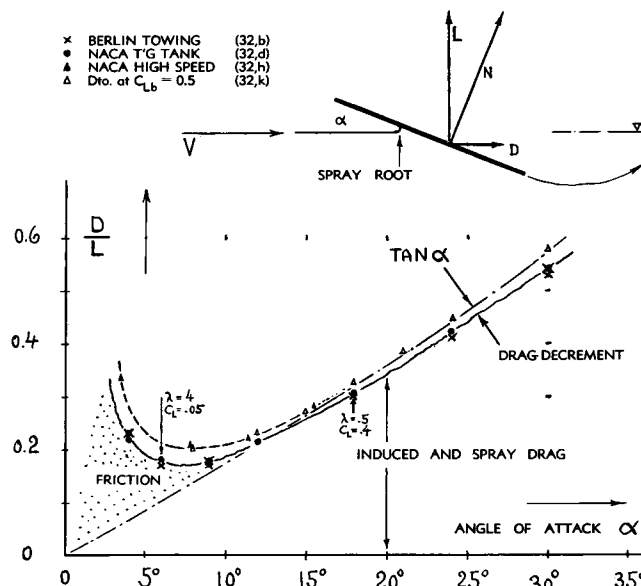


Figure 22. Drag/lift ratio of flat planing surface (32,d) for $C_{Lb} = 0.2 = \text{constant}$.

The Skin Friction component in the last equation is a function of wetted length. Figure 22 shows the drag/lift ratio of a flat plate at constant lift coefficient (C_{Lb} , based on the square of the beam). When increasing the angle of attack, wetted length and wetted area and the λ ratio, therefore, decrease. Under these conditions, drag reaches a minimum at an angle at which pressure drag is approximately equal to skin friction drag (at $\alpha \approx 7^\circ$ in the graph). The skin friction drag can be laminar, in smaller models; and it can be expected to be turbulent in full-scale applications. As to its magnitude, it has been stated (32,a,d) that at higher angles of trim, spray rubbing against the foremost part of the surface (essentially in the direction of motion) reduces the frictional component noticeably. In fact, the data in figure 22 (from two different sources), with D/L dropping below the theoretical minimum corresponding to $\tan \alpha$, force us to postulate a *negative* skin-friction drag component. The only means of explaining this result seems to be the presence of a stream of spray, *strongly* increasing as a function of the angle of attack. There is another reason, however, because of which frictional drag can also be somewhat *higher* than corresponding to one of the well-known skin friction functions. The streamlines passing along the bottom diverge to the sides. A number of them thus leaves the surface not at the trailing, but at the *lateral* edges. Average "rubbing" length and effective Reynolds number are thus smaller than corresponding to wetted length; and the drag coefficient C_f can then be higher than indicated, for example, by the Schoenherr function. Evidence of this influence (in the order of 5%) is found, for example, in (32,d) and i) at angles of and below 6° ; read also (33,e).

Camber. Straight (prismatic) surfaces have been considered in the preceding paragraphs. The drag due to lift could be reduced, however, by proper camber. Experiments (32,a and 38) confirm this prediction, showing optimum drag ratios in the order of 12% for λ in the order of 1.0 — thus indicating drag reductions (in comparison to straight plates) between 15% and 40% respectively. However, in planing boats, camber is usually zero along the afterbody; and it is more or less *negative* along the forebody.

Planing On Shallow Water has been investigated in (32,h). Down to clearance distances of " z " = b , hardly any influence is noticeable of shallow water upon lift and drag. At lesser distances, lift obtained for a certain angle of attack, increases; for example 40% for $z = b/4$ (where z is measured from the trailing edge). Drag corresponds, of course, to the angle of attack (equation 31), and thus reduces when getting into shallow water.

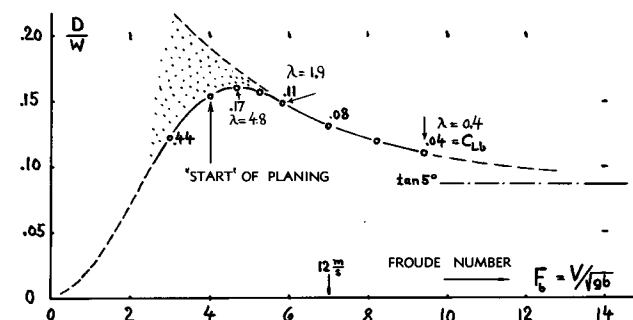


Figure 23. Drag-load ratio of a flat planing surface (32,a) as a function of Froude number; for $\alpha = 5^\circ \approx$ optimum, $b = 300$ mm, $W = 50$ kg, $W/\sqrt{gb}^3 = 1.85 = \text{constant}$.

(33) Statistical analysis of planing:

- Locke, Flat-Bottom Planing, Navy BuAer Rpts (1948 to 1950); J.Aeron Sci 1949 p.184.
- Shuford, Review of Planing Theory and Experiments, a comprehensive study, NACA T.Note 3233 (1954).
- Sottorf, Ybk.D.Lufo 1937 p.I,320; NACA TM 1061.
- Proposed empirical formulations for flat rectangular bottoms, when planing at higher Froude numbers, are: $C_L \sim \sqrt{A}$, for $\alpha = \text{constant}$ (33,a and c); $\Delta C_L \sim \alpha^2$ for second lift term (33,a); and $C_L \sim \alpha^4$, to account for ΔC_L (32,e).
- The wetted length increases at higher angles of attack over the static value (so for example at $\alpha = 18^\circ$ in figure 20). Reference (32,d) reports, however, that the wetted length is reduced because of aerodynamic stagnation within the narrow space under the forebody, at angles of attack of and below 6° .
- Murray, On Planing Hulls, Trans SNAME 1950 p.658.
- A thorough theoretical analysis of planing facts is presented in (32,k). Results of that study (published while this chapter was being printed) are similar to those given in this section.

type planing bottoms:

$$C_{L\Gamma}/C_{Lo} = \cos\Gamma \cos(0.6\Gamma + 0.4 \cdot 90^\circ)/\cos(0.4 \cdot 90^\circ)$$

The constants have been selected to suit the experimental results in figure 24. The decrease of lift with the angle of deadrise is considerable. With respect to inverted "V" bottoms (at negative angles in figure 24), the function developed suggests a somewhat increased lift efficiency; although impact may be objectionable in this type of bottom. The drag of V-shaped planing bottoms is approximately

$$D/L = (\tan\alpha + \lambda C_f/C_{Lb})/\cos\Gamma \quad (33)$$

Considering as an example, a deadrise angle $\Gamma = +15^\circ$, the pressure drag of an average straight planing bottom is found to be some 20% higher than that of a plane plate having the same wetted dimensions. As found in (32,c), the decrease of lift due to V-shape and the D/L ratio can appreciably be reduced, however, by horizontal flare (at the lateral edges) or by vertical chine strips as sketched in figure 24. These modifications evidently increase the effective span, without increasing impact in waves.

Motorboats. In figure 15 is shown that displacement-type motorboats experience a continued increase of their drag-weight ratio as a function of Froude number. By planing, it is possible to keep the drag ratio in the order of 18%, up to appreciably higher speeds. Figure 25 presents some towing-tank results on a family of planing-type hulls (35). At intermediate Froude numbers, the drag ratio reduces as the beam is increased. This variation corresponds to that in figure 26 where for a certain speed and load, span or beam is varied in a family of flat plates. The increase of span has practical limits, however, in V-bottom shapes.

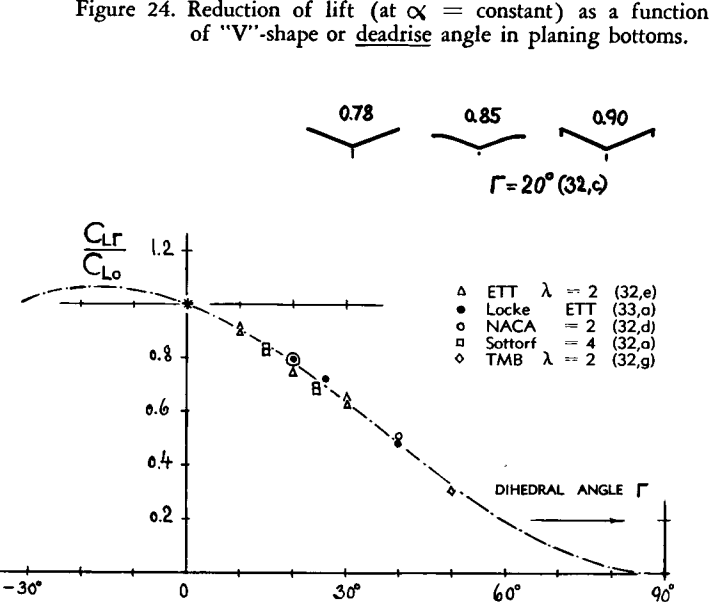


Figure 24. Reduction of lift (at $\alpha = \text{constant}$) as a function of "V"-shape or deadrise angle in planing bottoms.

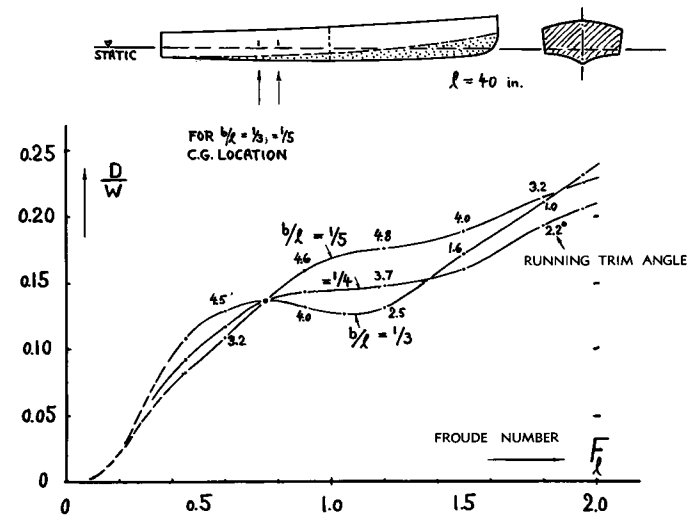


Figure 25. Drag-weight ratio of 3 V-bottom motor boat hulls (35), having a volumetric coefficient $V/1^3 = 3/1000$.

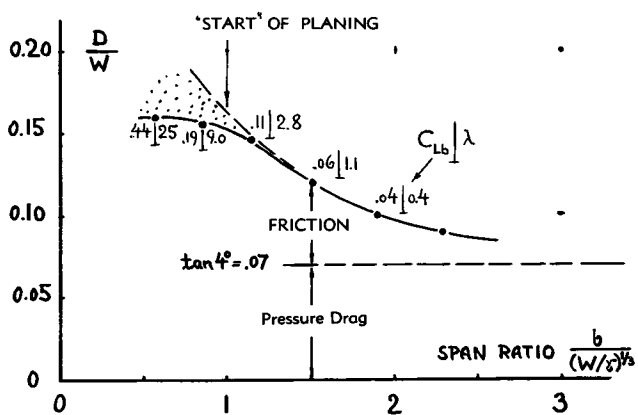


Figure 26. Drag-weight ratio of flat planing surfaces (32,a) with $W = 18 \text{ kg}$, $V = 6 \text{ m/sec}$, $\alpha = 4^\circ \approx$ optimum, as a function of beam or span ("b" between 0.15 and 0.60 m).

TRIM — has an important influence upon planing characteristics (see in figure 22). In hulls such as in figure 25, trim depends on shape, center-of-gravity location, and speed. The variation is best demonstrated in the hull having $b/\lambda = 1/3$. At "F" numbers between 0.5 and 1.0, the trim angle (against the static waterline as shown) is comparatively high; $\approx 4^\circ$. Between $F_F = 1$ and $= 2$, the angle decreases, however, down to 1° . The drag doubles in the same interval, because of skin friction along a wetted area which is too large for that speed range. At high speeds, optimum planing would be on the rear end of the bottom at a reasonable trim angle, a condition which is not compatible with any fixed center-of-gravity location in this type of craft. At Froude numbers above 1.0 or 1.5, the drag ratios of the hulls in figure 25 are nevertheless lower than those of displacement-type motorboats such as in figure 16, for example.

POWER AND SPEED. Drag ratios and full-scale results of motorboats are plotted in figure 15. Comparing them to bare-hull results (figure 25), it can be found that the contribution of appendages to drag in these craft is considerable (in the order of 30% of the bare-hull resistance). Between $F_F = 1$ and 2, planing motorboats show an approximately constant drag-ratio level. In this range, the installed power for boats including appendages corresponds to the ratio $P/(V W) \approx 0.24$. Consequently:

$$V_K \approx 550 / (0.24 \cdot 1.7 \cdot 2240) \quad (\text{BHP}/\Delta) \approx 0.6 \text{ BHP}/\Delta$$

where $P_{in} = 550 \cdot (\text{BHP})$ = installed power, V_K = speed in knots and Δ = displacement in long tons. At higher speeds, planing craft are less efficient; there may be losses due to cavitation in the propeller, and some aerodynamic drag is to be expected (as pointed out in the "hydrofoil" section). As a consequence, power required is somewhat higher than indicated by the last equation.

Seaplane Hulls (and floats) usually have a "step" in their bottom (36,d) to facilitate their balance and to control their aerodynamic angle of attack. As the speed is increased, these craft rise onto the step (located below the center of gravity). Figure 27 shows as an example the drag characteristics of such hulls for certain loading coefficients

$$C_\Delta = W/\gamma b^3 \quad (34)$$

(not to be confused with C_V). The drag ratio reaches a maximum at a Froude number in the order of $F_b = 3$, which corresponds to F_F between 1.0 and 1.5 in the examples shown. The reduction of drag theoretically to be expected in the planing phase (above $F_b = 3$) is not clearly evident in most of the towing-tank results available (36). The formation of spray and its interaction with the hull is responsible for added resistance, as explained in the next paragraph. Details of afterbody shapes suitable to minimize the spray effect are described in (36,f). The hydrodynamic drag in planing condition (at the level of $D/W \approx 18\%$ as in figure 27) is of appreciable magnitude. Resistance above hump speed decreases, however, by one reason not shown in figure 27; $D = (D/W) W$ reduces naturally, as " W " = weight carried by water is "unloaded", when the aircraft becomes more and more air-borne. Also, resistance is not at all the only consideration in the design of a suitable hull. Modern development of flying boats prefers comparatively large length-beam ratios (in the order of $l/b = 15$.) A narrow beam provides for smooth landing (small impact accelerations) in rough water, while increased water resistance (during take-off) is made up in these designs by powerful engines. Note that a hull shape with a height in the order of $h = 3 b$ (corresponding to narrow beam) also helps keeping the propellers out of waves and spray.

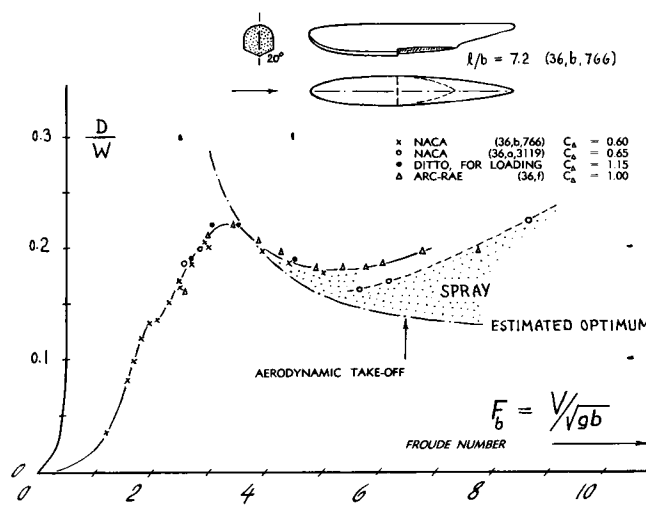


Figure 27. Examples for the drag/weight ratio of typical flying-boat hulls.

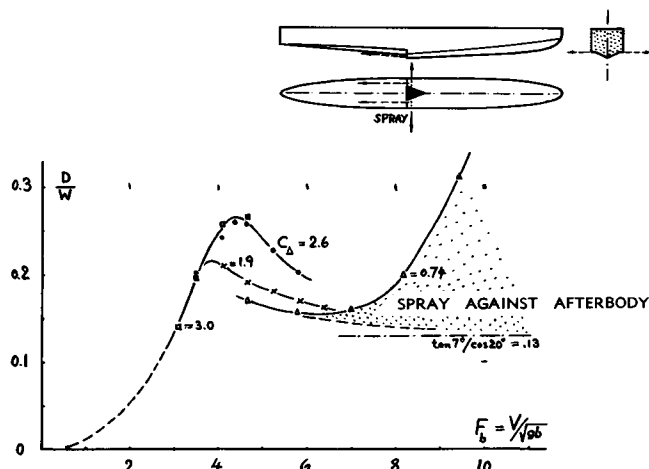


Figure 28. Drag-weight ratio of an airplane float (32,a) as a function of Froude number. Float data: DVL No.7, at $\alpha = 7^\circ$ = constant, $1/b = 9.2$, $b = 0.3$ m. Coefficient $C_D = W/\gamma b^3$.

Floats. Figure 28 presents the hydrodynamic drag characteristics of an airplane float. Here again, favorable trim angles are made possible by application of a step. For the angle of 7° as investigated, the drag ratios plotted for various loading coefficients C_D , should theoretically all end up at the level of $(\tan 7^\circ)/0.94 = 0.133$, where "0.94" is as per equation 33 for 20° angle of deadrise. At higher speeds, only a very small wetted area is sufficient, however, to support the given load. Because of the bottom's V-shape, the wet-

ted span reduces, therefore, to that of a small triangle as indicated in the drawing. As a consequence, spray washes sideways and along the bottom of the afterbody, thus increasing the drag considerably. To avoid this effect, the afterbody of seaplane hulls (in which the same effect takes place as shown in figure 28) is very often cut away at the bottom and at the sides.

Skis. Rather than using floats, attempts have also been made of starting and landing airplanes on skis (see, for example, reference 39). Figure 29 shows the drag ratio of one such arrangement as tested in a towing-tank. At low velocities, with fully submerged skis, resistance is comparatively high. After emerging (getting the airplane onto the skis), the drag reduces, however. The pressure drag then corresponds to the trim angle τ as marked plus the angle at which the skis are set against the fuselage axis (4.5°).

RACING BOATS. All modern power boats used in the various racing classes, are of the planing variety (so-called "hydroplanes"). As an example, the repeated Gold-Cup winner "Slo-Mo-Shun" (37) may be mentioned, having:

$$\begin{array}{ll} l = 28 \text{ ft} & W = 4300 \text{ lb} \\ P = 1600 \text{ HP} & V_x = 178 \text{ mph} \end{array}$$

This boat is planing on two side "sponsons", and "riding" on the half submerged propeller aft. The overall ratio of the craft at the very high Froude number (on hull length) of $F_x = 8.7$, is approximately

$$P_{in}/(V W) = (1600 \cdot 550)/(260 \cdot 4300) = 0.8$$

Besides the low efficiency of the fully-ventilated propeller, an appreciable component of aerodynamic drag is included in the "total" resistance ratio.

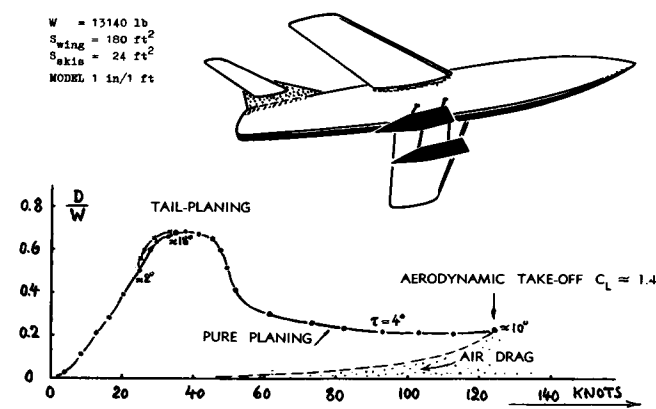


Figure 29. Total (aerodynamic and hydrodynamic) drag ratio of an airplane model on skis (38,a). Dimensions are indicated full scale. The pressure drag corresponds to the trim angle " τ " as marked, plus the angle at which the skis are set against the fuselage axis.

- (34) Hydrodynamics of streamline bodies:
 - a) Weinflash, Streamline Fuselage NACA RM L9L21a (1949).
 - b) Weinflash-Fontana, Streamline Bodies, NACA RM L54K22. See also L52B11 and L55F20 on pressures.
- (35) Davidson and Juarez, Tests of 20 Related Models of V-Bottom Motorboats Series 50, Stevens ETT Rpt No. 170 for TMB (No. R-47) (1941, revised 1949).
- (36) Hydrodynamic characteristics of flying-boat hulls:
 - a) NACA T.Notes 464, 470, 488, 491, 504, 509, 535, 539, 541, 545, 551, 563, 566, 574, 590, 635, 638, 656, 668, 681, 716, 725, 836, 858, 1782, 2297, 2481, 2503, 3119.
 - b) Parkinson, NACA T.Rpts (543) (1937) and 766.
 - c) ETT, NACA W-105 (1944) and T.Note 1182 (1947).
 - d) Attempts of eliminating the step introducing air by means of ducts and discharging same through exit vents onto the afterbody planing bottom, are reported by Hamilton, Full Scale Flying Boat Hull, ARC RM 2899 (1956).
 - e) Parkinson, In Waves, NACA T.Note 3419 (1954).

In regard to take-off resistance, this reference reports a "large effect" of rough water (against waves). Methods of analysis have not yet been established for such conditions.
- f) Owen, In RAE Seaplane Tank, ARC RM 2976 (1955).
- g) Sottor, Characteristics of Floats, Yearbk D.Lufo 1937 p.I,309; Translation in NACA T.Memos 704 and 860.
- (37) "Slo-Mo-Shun", quoted from various magazines.
- (38) Characteristics of water-borne skis:
 - a) Wadlin, NACA RM L7I04 (1947) and L9C03 (1949).
 - b) Dingee, "Skids", Stevens ETT Rpt 742 (1953).
 - c) Wadlin-McGehee, 6 Hydro-Ski Forms, NACA RM L9L20.
 - d) See also results in reference (32,k).
- (39) "Bases Unlimited", Aeron'l Engg Review June 1955.

wave drag is approximately

$$C_{Dw,h} = D_w / (q b h) = 0.5 C_{Lh}^2 / F_h^2 \quad (40)$$

C. HYDROFOIL BOATS

A hydrofoil is the equivalent of an airfoil; it serves to produce lift by "flying" in water. Basic characteristics of submerged foils are presented in Chapter X. Their most specific application is in hydrofoil boats which have been slowly developing during the last 50 years. Characteristics of hydrofoils moving in horizontal direction, in proximity of the water surface, are therefore treated as follows.

WAVE DRAG IN TWO DIMENSIONS. Deeply submerged, a hydrofoil is basically expected to have the same fluid-dynamic characteristics (in terms of lift-and drag coefficients, aspect ratio, induced angle of attack and so on) as an airplane wing flying in air. In proximity of the water surface, these characteristics are usually considerably different, however. If disregarding the range of the smallest Froude numbers (below $V/\sqrt{g h} \approx 0.4$, where h = submergence of a horizontally arranged foil) the water surface is deformed by the pressure field around the moving hydrofoil. In two dimensional flow (with infinite span), a wave train originates above the foil as sketched in figure 30. The orbital motions in this train represent a transfer of momentum from foil to water. The hydrofoil, therefore, has a drag due to lift, even in two-dimensional condition, stemming from its "bound vortex" or "lifting line". Figure 30 presents a theoretical prediction of this type of wave drag, as a function of Froude number based on depth of submergence "h" (to the quarter point of the foil chord). The wave drag coefficient reaches a maximum at $F_h = \sqrt{2}$; and it reduces to zero as $F_h \rightarrow \infty$. For higher Froude numbers (say above $F_h = 5$),

where $F_h = V/\sqrt{g h}$, and the coefficients are based on the area span b times submergence h . In conventional notation (on foil area equal to span b times chord c), the drag coefficient is

$$C_D = C_{Dh} h/c$$

$$dC_D/dC_L^2 = (dC_{Dh}/dC_L^2) c/h \quad (41)$$

If presenting equation 40 in this form, it is seen that at $F_c = \text{constant}$, wave drag attenuates rapidly as the depth of submergence "h" is increased.

Induced Drag. Typical hydrofoil boats are designed to operate at higher Froude numbers, where the wave drag as per figure 30 is of lesser importance. Because of the limited span of their foils, they have a "trailing-vortex" drag, however. In deep submergence, this type of drag is identical to the induced drag of airplane wings (as described in Chapter VII). Upon approaching the free water surface, the induced drag is considerably increased. Approximately beyond F_h or $F_c = 10$, a horizontal hydrofoil of finite span has approximately the same fluid-dynamic characteristics as the lower panel of a biplane. Applying, therefore, mechanism and results of biplanes as presented in the chapter on "drag due to lift", the function in figure 31 is obtained, thus indicating the minimum "induced" drag of a hydrofoil moving under the free surface:

$$C_{Dl} \approx K C_L^2 / (\pi A) ; \quad dC_{Dl}/dC_L^2 \approx K / (\pi A)$$

with K between 1 and 2. Strictly, lift, induced angle and induced drag are not equal in the otherwise equal two panels of a biplane. The average effective dynamic pressure of the lower panel is somewhat reduced. Its induced drag is consequently somewhat higher than indicated in the equation. As pointed out in (51,c), the lift in the lower panel of a symmetrical biplane is accordingly reduced some 5%; and the induced drag in the definition as in equation 42 may be increased some 10%.

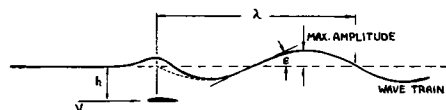
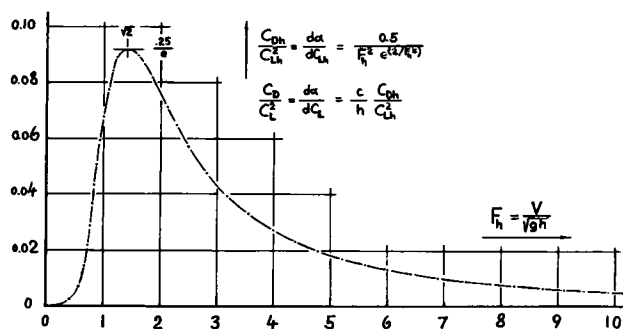


Figure 30. Universal function of hydrofoil wave drag (50) in two-dimensional deep-water flow.

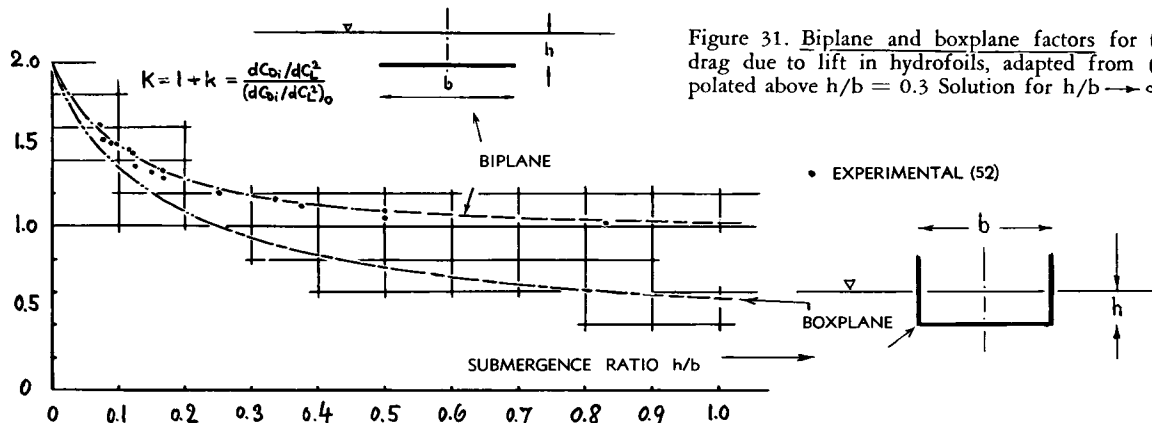


Figure 31. Biplane and boxplane factors for the calculation of drag due to lift in hydrofoils, adapted from (51,a) and extrapolated above $h/b = 0.3$. Solution for $h/b \rightarrow \infty$ in (53,a).

End Struts. In hydrofoil boats, a structural connection is needed between foil and hull, by means of struts or bent-up foil ends. One possibility is the "boxplane" arrangement as included in figure 31. Both from there and in figure 32 it is seen that the drag due to lift of such configuration is appreciably lower than without the end struts. With respect to structural foil strength and in regard to lateral stability, this type of arrangement may not be feasible, however. The struts (or additional supports) are usually placed about 1/3 halfspan inboard.

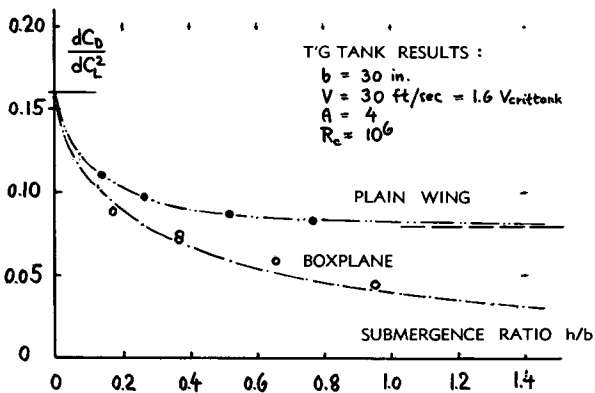


Figure 32. Drag-due-to-lift ratio of a hydrofoil with and without end struts (52,a) as a function of submergence.

STRUT INTERFERENCE. As described in the "interference" chapter, some additional parasite drag originates in the corners between struts and foil. The lift distribution across the span of a hydrofoil is affected to some degree by the presence of struts; and the induced drag may be increased as explained in the "interference" chapter. For example, a single strut in the center of the foil may increase the drag due to lift by some 10%. In a pair of struts (each at 2/3 of the half span) their interference effect may combine with a partial end-strut effect, similar to the one described above, in such a way (51,b) that the drag due to lift of the configuration is (by coincidence) approximately equal to that of a plain foil (without struts). This seems to be the explanation for the fact that many of the experimental results on strut-supported foils (52) agree well with biplane theory, which does not take into account neither parasite nor induced strut interference.

WAVE DRAG IN FINITE SPAN (53). At higher Froude numbers (say above $F_h = 10$), the "bound-vortex" wave drag can be approximated by

$$C_{Dw} = 0.5 k C_L^2 / F_h^2 \quad (43)$$

where k as plotted in figure 33. This component is important only in large-size hydrofoil boats at low speeds (higher lift coefficients).

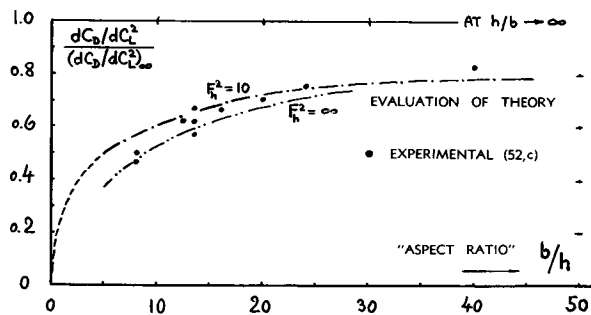


Figure 33. Evaluation of finite-span "wave" drag ratio.

- (50) Keldysch, Lawrentjew, Kotschin, Vladimirov; Wing Below Surface of Water (Two-Dimensional Theory and Biplane Concept), Summarized in CAHI(Moscow) Rpt 311(1937); Translations ATI157689, ZWB No. 311 (German), R.Bull.1-8 SNAME and NACA T.M.1341 (see also 1335).
- (51) Biplane and boxplane factors:
 - a) Adapted from Ergebnisse AVA Göttingen Vol.II (1923) and Vol.III (1927).
 - b) Hoerner, Influence of End Plates Struts and Nacelles, Gibbs & Cox for ONR Tech Rpt 14 (1953).
 - c) Diehl, Biplanes, NACA Tech Rpt 458 (1933).

Shallow Water can reduce wave drag appreciably. At the critical speed

$$V_* = \sqrt{g H} \quad (44)$$

in any consistent system of units, where H = depth of the water — the bound-vortex wave drag reduces to zero. Towing-tank experiments on hydrofoils are very often performed above the critical speed. This is the reason why in the material presented on the following pages, "wave drag" is no longer mentioned. Every finite-span hydrofoil retains, however, the "induced" drag as outlined above (60).

Wave Angles. Characteristics of airplane wings in tandem arrangement are discussed in the chapter on "drag due to lift". In hydrofoils (in horizontal position near the water surface), the problem is more complex, because of the wave pattern generated in that surface. In two-dimensional condition, a wave train follows the hydrofoil, with a propagation speed equal to foil speed. As presented in (50) for deep water, the flow angle within that train (against the horizontal, positive for upwash) at a submergence h equal to that of the foil, is

$$\varepsilon/C_{Lh} = (\cos(1/F_x^2)) / (F_h^2 e^{(2/F_h^2)}) \quad (45)$$

with x = distance behind the quarter point of the foil chord. The humps and hollows in the train are thus a function of the separation Froude number

$$F_x = V/\sqrt{g x} \quad (46)$$

The wave angle has its first positive (upwash) maximum at

$$\cos(1/F_x^2) = +1; \quad F_x^2 = 0.5/2\pi; \quad x = 2\pi V^2/g$$

If now placing at this location, a second two-dimensional foil at the same submergence as the first foil, producing the same lift, it is possible to recover the wave drag of the first foil. The second foil cancels in this case the wave motion behind the first foil, leaving behind a completely undisturbed water surface. Real foils are, of course, not two-dimensional. Their "bound-vortex" wave train has reduced amplitudes; and the drag corresponding to their lateral wave system ("induced" or "biplane" type) cannot be recovered. Therefore, at higher Froude numbers, wave-drag recovery does not seem to be promising.

TANDEM FOILS. As pointed out in the chapter on "drag due to lift", the rear wing in a tandem configuration operates in the downwash field produced by the first wing. Here again, the water surface has an appreciable influence upon the flow pattern. A swept or "V" shaped lateral wave system originates above each foil tip. The outer branches of these two systems

carry sideways momentum, corresponding to part of what is called in this text "induced" drag. The inner branches meet at a distance behind the foil which is theoretically $\approx 1.4 b$; and there they form a "roach". Evaluation of the flow field behind a hydrofoil (52,d) shows that below and behind that peak, the flow angle is comparatively constant and slightly negative, thus indicating downwash. The downwash angle is evidently that of a wing in presence of a solid "ceiling". Such ceiling effect is equal to the ground effect as explained in the "lift" chapter. Therefore, the average downwash angle below and behind the roach is approximately

$$\varepsilon/C_L = 2''k''/(\pi A) \quad (48)$$

where " k " = $(2 - K)$, with K as plotted in figure 31 as a function of the submergence ratio h/b .

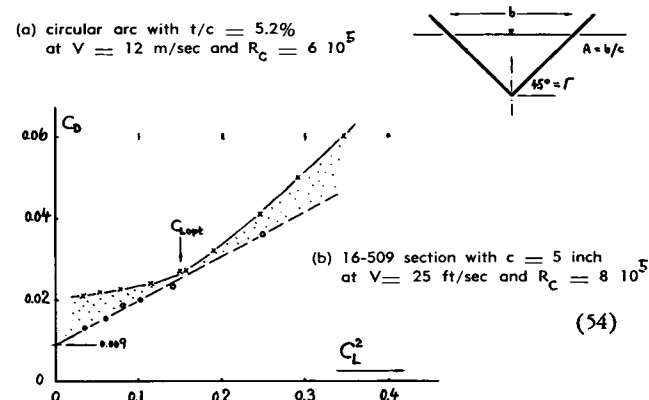


Figure 34. Drag-lift characteristics of surface piercing "V" shaped hydrofoils.

Surface-Piercing Foil. Figure 34 shows the drag characteristics of two hydrofoils, having "dihedraled" surface-piercing ends. Hydrodynamic coefficients and aspect ratio of such foils are based upon the projection of the submerged area, with b measured between the piercing points. At $C_L^2 \approx 0.16$, one of the two foils shows a minimum dC_D/dC_L^2 . The corresponding lift coefficient $C_L = \sqrt{0.16} = 0.4$ is the "optimum" or "symmetrical" value corresponding to camber ratio f/c of the foil section used:

$$C_{Lopt} \approx (10 \text{ to } 12) f/c \quad (49)$$

Above and below this coefficient, parasitic losses are caused by flow around the sharp leading edge of that particular foil. The effect can considerably be reduced by applying aviation-type rounded leading edges, as shown in the other foil in figure 34. It should generally be noted that aspect ratio and drag due to lift of the surface-piercing type of hydrofoils considered, change appreciably with submergence, because of the geometrical variation of span as a function of submergence.

V-SHAPED FOIL. The induced drag of V-shaped wings is explained in the chapter on "drag due to lift". Dihedral as such does not affect the induced drag function C_{Dl} (C_L^2), with coefficients and aspect ratio as defined above. Replacing now foils as those in figure 34, by a "box" having equal submerged span and equal enclosed area between panels and water surface, approximate induced characteristics can be determined (through the use of equation 42 and figure 31). The boxplane factor for such foils, tentatively corresponds to the average submergence ratio

$$h_{av}/b = 0.25 \tan \Gamma \quad (50)$$

where " Γ " = angle of dihedral. *Figure 35* demonstrates, however, that the drag due to lift is higher than calculated, even at the optimum lift coefficient. It must, therefore, be concluded that effective span and aspect ratio are smaller than the projected geometrical values, and that probably some parasitic drag (spray) originates at the piercing ends.

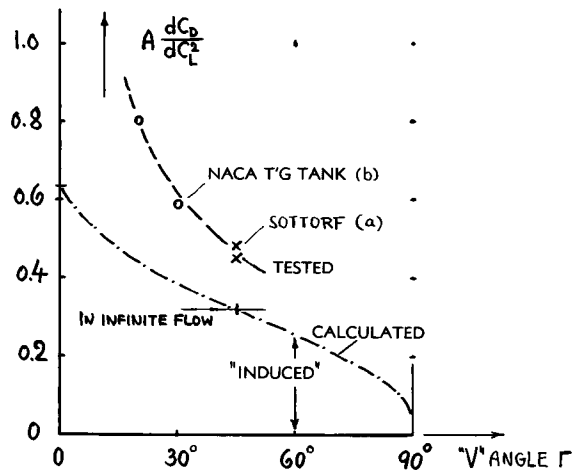


Figure 35. Variation of drag-lift function (at C_{Lopt}) of surface-piercing hydrofoils (54) against their "V" shape angle. Coefficients and aspect ratio are based on submerged projected span (between piercing points).

VENTILATION. At higher lift coefficients, "ventilation" breaks in, along the piercing foil ends, thus causing a considerable reduction of lift coefficient and lift-curve slope. *Figure 36* shows the critical lift coefficients for a particular family of hydrofoils having sharp-nosed sections. The critical values C_{Lx} (where full ventilation occurs) are obviously related to the optimum lift coefficient corresponding to section camber (equation 49). Here again, a moderately rounded leading edge improves characteristics. Another means of preventing (or postponing) ventilation are "fences" (54,a) placed at the upper foil side near the piercing points.

- (52) Towing tank tests on fully-submerged hydrofoils:
 - a) Wadlin, Fontana, McGehee, Shuford; End Plates, End Struts, Submergence; NACA Tech. Rpt 1232 (1955).
 - b) Wadlin, Ramsen, McGehee; Aspect-Ratio-10 Hydrofoil, Report by NACA RM L9K14a (1949).
 - c) Sutherland and Kaplan; Various Hydrofoils, Stevens ETT Rpts 406, 410, 417, 418, 429 (1951).
 - d) Wadlin-Ramsen-Vaughan, Flat Plates in Water, NACA Technical Rpt 1246 (1955); also T. Note 3908.
 - e) Hydrofoils, NACA W.Rpts L-757, L-766 (1942).
- (53) Theory of finite-span hydrofoils:
 - a) Wu (Caltech), J.Math and Physics (1954).
 - b) Breslin, G&C Tech Rpt for ONR No.16 (1954).
- (54) Tests on surface-piercing hydrofoils:
 - a) Sottorf, German Doct ZWB FB 1319 (1940).
 - b) Benson and Land, NACA W.Rpt L-758 (1942).

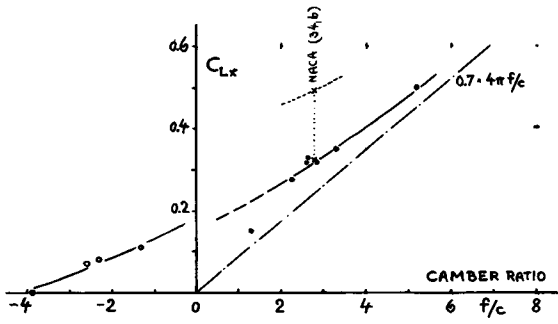
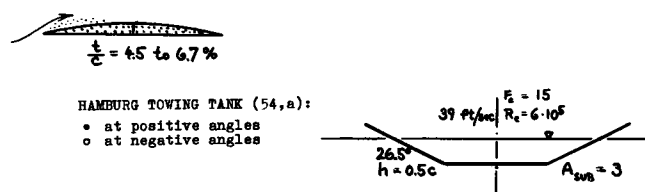
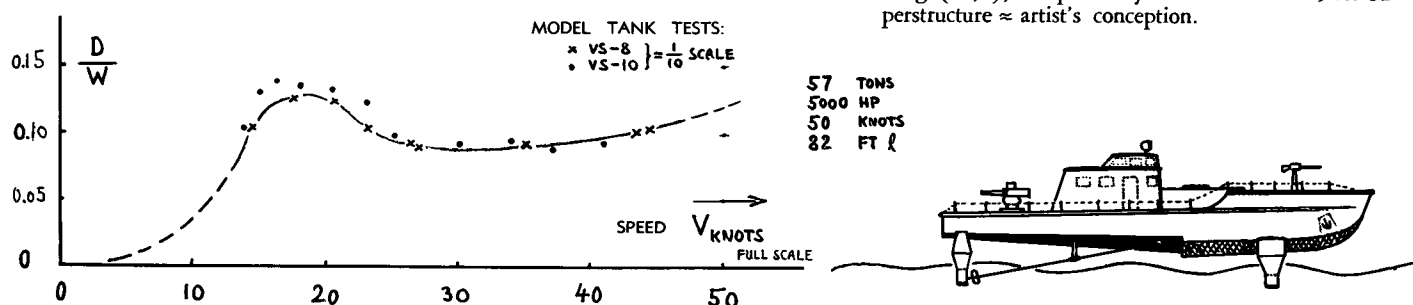


Figure 36. Lift coefficient at which ventilation takes place (all over span), as tested for a particular family of surface-piercing hydrofoils (54,a).



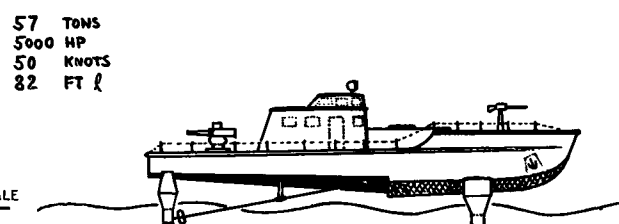


HYDROFOIL BOATS have necessarily more than one foil (required for balance and stability), somehow involving a tandem effect. The struts (or bent-up ends) needed to connect the foils to the hull, also add to the drag by way of spray – as presented in Chapter X. As a consequence, and also including the drag of a rudder and of propulsion parts, the basic “parasite” drag of such boats (in flying condition) is roughly twice the profile drag of the foil proper. On account of the biplane effect, some downwash, some wave drag; owing to additional section drag due to lift; and because of the induced strut-interference phenomenon described above, the drag due to lift may roughly be twice the minimum induced drag as indicated by lifting-line theory ($C_{D,i} = C_L^2 / \pi A$). Therefore, to indicate the order of magnitude of their drag, the following equation can be applied to average hydrofoil craft:

$$C_D = C_{D_0} + C_{D,L} \approx 0.016 + 2 C_L^2 / \pi A \quad (51)$$

For exa. for $A = 6$, this equation gives a minimum drag ratio for $C_L \approx 0.4$ in the order of $D/L = 8\%$ – which is about the average optimum (at cruising speed) for this type craft. Figure 37 shows, as an example, the tested ratio D/W of such a boat with a surface-piercing foil system in tandem. The craft has a take-off hump, a minimum-drag-maximum-range speed, and a top speed – all similar to the phases in the operation of an airplane.

Figure 37. Example of Hydrofoil Boat. Design Schertel-Sachsenberg (55,b), completed by Russians in ≈ 1946 . Superstructure \approx artist's conception.



POWER AND SPEED. Some survey on hydrofoil boats is presented in (55,a). Such craft have been built between 1 and 80 tons, with 20 to 5000 HP, going at up to 60 knots. In designing hydrofoil boats, the drag ratio at design speed can be considered to be constant. In other words, this ratio is approximately independent of craft size, speed, or Froude number, if keeping the lift coefficient C_L constant. This coefficient can be considered to be the equivalent of a Froude number, however. The power required to propel this type craft is then

$$P_{in} \sim D V \sim W V ; \quad P_{in}/\Delta \sim V \quad (52)$$

Figure 38 presents tested maximum speeds of hydrofoil- and planing boats, plotted against their power loading P/Δ . In addition to the hydrodynamic resistance, there is evidently some aerodynamic drag too. Considering a narrow size range in the category of motorboats, the aerodynamic component is roughly

$$P_2/\Delta \sim V^3 \quad (53)$$

The graph gives evidence of such a component. Some cavitation losses in the screw propulsion are probably involved too. – Also included in the graph are results of some planing and displacement-type motorboats. Dynamically-lifted craft are superior in performance above some 30 knots; or more precisely, at Froude numbers above $F_L = 0.8$ or 1.0, as shown also in figure 15. At equal power loading, hydrofoil craft have a $\approx 30\%$ higher speed than planing craft.

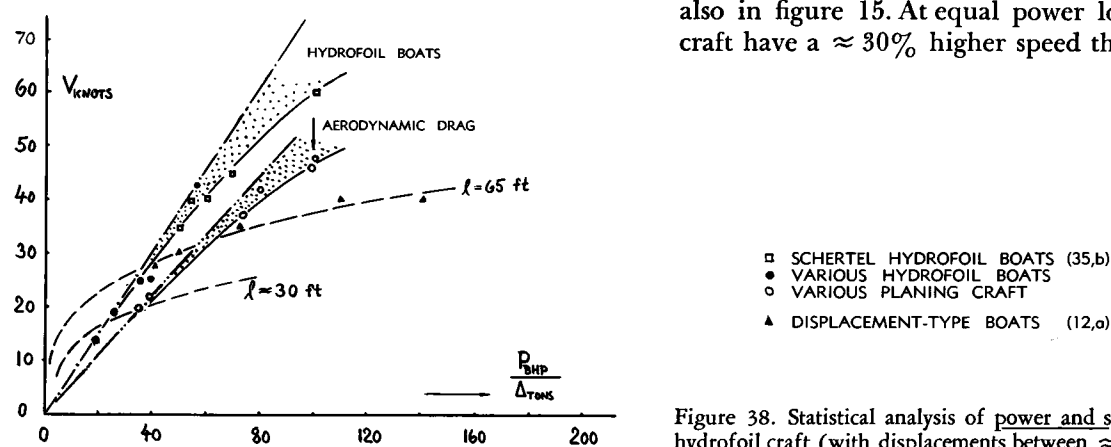


Figure 38. Statistical analysis of power and speed of planing and hydrofoil craft (with displacements between ≈ 1 and ≈ 100 tons).

SMALL ASPECT RATIOS. Hydrofoils considered so far, usually have "higher" aspect ratios, comparable to those as applied in airplane wings. However, for the purpose of lifting water-based airplanes out of the water (take-off) and to withstand the impact upon landing (at comparatively high speeds, and into waves), much smaller ratios (and smaller relative sizes) are considered suitable. As explained in the "lift" chapter, theory of such "wings" has not been completely established. Analysis of small-aspect-ratio hydrofoils is accordingly limited. As an example, the normal-force coefficient of one such foil or plate, respectively, is presented in figure 39 for two submergence ratios. Deeply submerged, with $h > (0.2 c) = 1.6 b$ at the leading edge (LE), the function is evidently of the same type as presented for similar "wings" in the "drag-due-to-lift" chapter (with a "k" value above 3). At the shallow submergence of $h_{LE} = 0.025 c = 0.2 b$, lift is reduced. It is suggested that part of the reduction corresponds to the biplane effect as outlined before. — The drag of the flat plate considered is simply $C_D = C_L \tan \alpha$; plus some small frictional component.

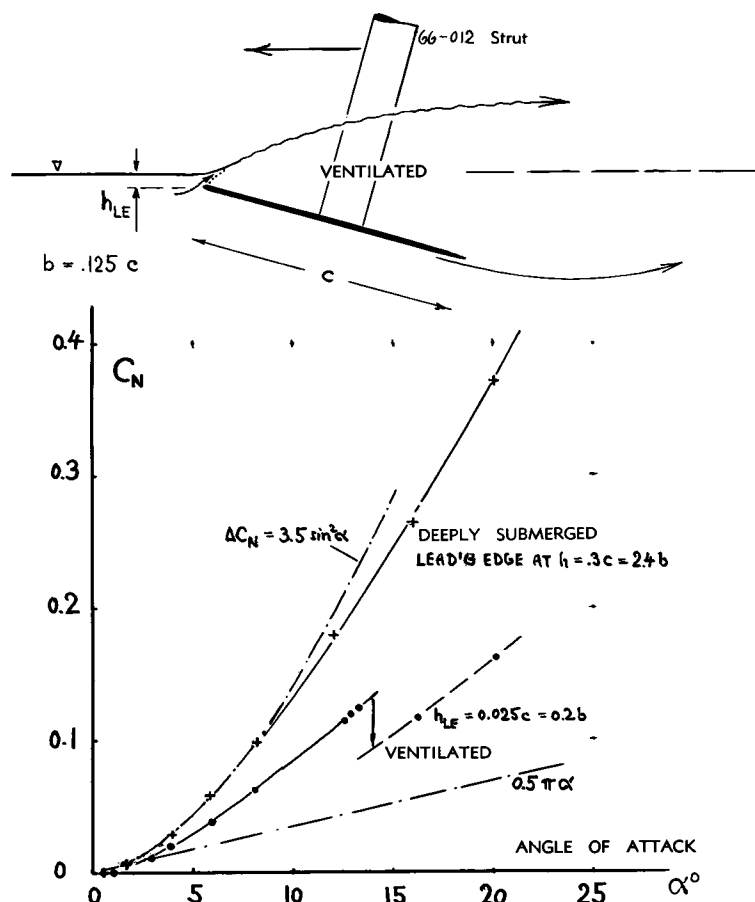


Figure 39. Normal-force coefficient of a small-aspect-ratio flat plate (56) at two different submergence ratios. Chord $c = 20$ inch, $A = 0.125$, $V = 25$ ft/sec.

VENTILATION along the strut employed to support the plate in figure 39, occurs as indicated. Applying low-aspect-ratio wing theory with a sectional lift angle $(d\alpha/dC_L) \approx$ equal to 4 times $(0.5/\pi)$, the linear term of the lift- or normal-force angle of a ventilated plate is found to be

$$\alpha = 4 C_N / (\pi A) + K C_N / (\pi A) - 4 S_h / (\pi A)$$

where $K =$ biplane factor and $S_h = 1/E_h^2$ as explained in the "hydrodynamic" chapter. Figure 23 of that chapter presents, as an example, the lift coefficient ($C_L = C_N \cos \alpha$) of a square flat plate (having $A = 1$) as tested in a towing tank, ventilated by means of a hollow supporting strut. For a submergence ratio of $h/b = 1.0$, the biplane factor is $K = 1.01 \approx 1$. The last function, therefore, reduces to equation 28 of the "hydrodynamic" chapter, under the conditions as tested. An application of small-aspect-ratio hydrofoils, ventilated or in plain flow, is found in aircraft-type "hydro-skis", in submerged operation during take-off or "landing"; as described in the section on "planing craft".

(55) On Hydrofoil Boats:

- a) Survey by Buermann, Leehey, Stilwell; Trans Soc. NAME 1953 p.242. See also "Life" 27 Sept 1954 p.56.
- b) Schertel-Sachsenberg Boats, Chapter on "Hydrofoil Boats" in Handbook der Werften, Hansa Hamburg 1952. See also "Schiff und Hafen" 1953 p.103; "Hansa" 1952 p.1090, and Sachsenberg Docs. No. 24 and 30 (Towing Tank Hamburg, 1943).
- c) Büller, Hydrofoil Boats, Yearb.STG 1952 p.119.
- d) Grunberg, Sustentation Hydrodynamique par Ailettes; L'Aérotechnique No. 174, Supplement of l'Aéronautique No. 217 June 1939 p.61; also Tank Tests by NACA in RM L52D15.

- (56) Wadlin, Ramsen, Vaughan; Rectangular Plates (Hydrofoils) Having Aspect Ratios of 1.0, 0.25 and 0.125; NACA T. Notes 3079 & 3249 (1954), or T.Rpt 1246.

- (57) Hoerner, Gibbs & Cox Corporation Towing Tank (1953).
- (60) It is a matter of choice whether to call the drag due to lift of a hydrofoil "induced" or "wave drag". However, in order to distinguish between the two components, the terms are used as explained in the text. Consideration of the combined vortex and wave system of a hydrofoil also leads to the statement that a water wave represents a vortex. The wave resistance of ships is thus realized to be the equivalent of a vortex system; and it becomes in this way also related to certain examples of vortex-bound pressure or separation drag as described in Chapter III.

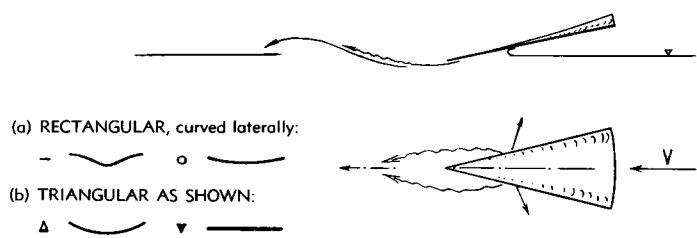
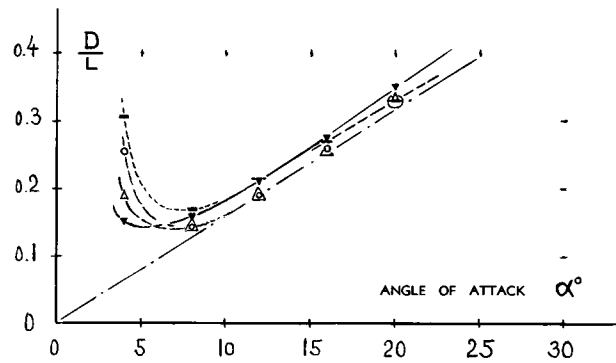


Figure 40. Lift-drag ratio of four differently shaped hydro-skis (38,c). Evaluation for $W = L = 4$ to 6 lb, at $V = 25$ to 30 ft/sec planing speed. Wetted area in the order of 0.1 to 0.3 ft^2 at $\alpha = 4^\circ$ and of 0.02 ft^2 at 20° .

Hydro-Skis. When using plate-like skids or skis similar to the plates just described, in airplanes, their planing characteristics are at least as important as their performance in submerged condition. Reference (38,c) gives some information on shape details in hydro-skis. Some D/L ratios evaluated from the experimental data, are plotted in figure 40. The influence of shape is as follows:

(a) Lateral curvature in otherwise straight skis, can be expected to reduce lift and efficiency below that of a flat bottom. No clear indication is found in this regard, in figure 40.

(b) A comparison between the rectangular and triangular shapes shows a small difference in favor of rectangular plan form.

At higher angles of attack, the drag/lift ratios of all ski shapes in figure 40, are for practical purposes equal to $\tan\alpha$.

CHAPTER XII – DRAG OF LAND-BORNE VEHICLES

Drag or resistance of land-borne vehicles such as automobiles and railroad conveyances, is twofold; namely mechanical (in the wheels or at the points in contact with the ground) and aerodynamic. Essentially the latter is treated in this chapter, being presented in the form of the non-dimensional drag coefficient C_D . (based on the frontal area S_0). Chapter I must be consulted to determine the drag (in pounds) as a function of speed for a given-size vehicle.

A. DRAG OF MOTOR VEHICLES

Among land-borne vehicles, the automobile is particularly interesting as far as aerodynamic drag (1) is concerned — because “everybody” drives or uses this facility so often.

1. EXPERIMENTAL METHODS

Road Tests. A number of investigations on the road are known, such as described in (2), measuring the drag of automobiles according to the principle of “drag equals mass times deceleration”. Since drag values resulting from this method include the drag components originating in the tires and within part of the mechanical system of the vehicle, additional tests are required on special stands (9) to determine the “rolling resistance”. This resistance is to be subtracted from the total drag as determined by road tests in order to arrive at the net aerodynamic drag.

Wind Tunnel Tests. Modern wind tunnels, developed for aeronautical research, are also very suitable

for measuring the aerodynamic drag of automobiles, either on models or by placing the vehicles themselves into larger test installations. Contrary to road conditions, the artificial air stream is blown against the resting vehicle, in such investigations. Proper representation of the road surface, which in actual operation is not fixed in relation to the vehicle, must therefore be given consideration.

Ground Plate. The simplest reproduction of the ground is a plane plate placed under the vehicle. Since such a plate is exposed to the same air flow as the automobile model itself, a boundary layer originates which, by way of interference, can considerably change the flow pattern around the model. Results obtained with this type of ground representation are listed and compared with other methods in figure 1. It is seen that a fixed plate leads to drag coefficients that are usually slightly higher than with proper simulation of the road surface. To reduce or to avoid ground-plate interference, attempts have been made (3,d) and (4,e) to remove the boundary layer by suction. It appears, however, that drag coefficients obtained in this way are somewhat too high.

Image Method. In the so-called image method (3,c,e) and (4,c), the ground plate is entirely omitted. A second, identical or symmetrical, model of the vehicle is placed upside down with the wheels against those of the first model. Theoretically, because of the symmetry of the system, no air particles will penetrate the imaginary road surface — in an ideal stream of air.

Figure 1. Drag coefficients of several automobile models, determined by various techniques of simulating road or ground surface; (a) ground plate with suction, (b) values in brackets were obtained on similar shapes.

WIND - TUNNEL TECHNIQUE →	W/O GROUND	FIXED - PLATE	W/ PLATE & SUCTION	FULL - SCALE
STREAMLINE CAR (JARAY) (3,e)	0.19 (89%)	0.23 (107%)	-- --	0.21 (100%)
1/2 STREAMLINE CAR (3,e)	0.36 (97%)	0.38 (102%)	-- --	0.37 (100%)
1936 PASSENGER CAR (3,e)	0.50 (97%)	0.53 (103%)	0.53 (104%)	0.52 (100%)
STANDARD CAR (3,e)	0.52 (96%)	0.56 (103%)	0.55 (102%)	0.54 (100%)
LEY AUTOMOBILE MODEL (4,e)	0.29 (97%)	0.27 _a (88%)	0.31 (104%)	-- -- -- b --

Actually, the flow between the two models is more or less turbulent and separated, however. Velocity components are, therefore, crossing the plane of symmetry back and forth. Also, the formation of the vortex system aft of the vehicle may be affected by the non-existence of the road surface. It is suggested that the method could be improved by placing a plate *behind* the double model, thus preventing the motion of larger vortices across the plane of symmetry — without interfering directly with the flow pattern past the underside of the vehicle.

Moving Ground. The most perfect reproduction of the road surface in a wind tunnel is through the use of a belt, moving at proper distance (close to the wheels) under the model, in the same direction and with the same speed as the artificial flow. The test results listed in *figure 1* show differences between the various test methods. As far as available, data obtained by the moving-belt technique are considered as most representative of full-scale conditions. The differences in drag coefficient found for other methods are comparatively consistent. Except for extreme streamline shapes, the fixed plate also appears to give reasonable results.

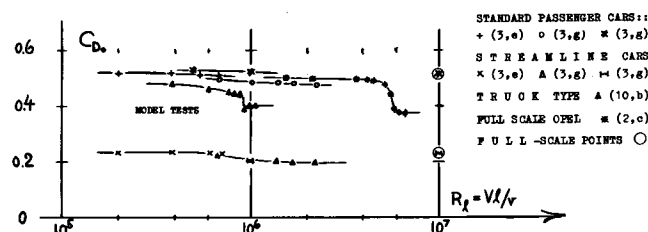


Figure 2. Drag of several automobile shapes (mostly tested in wind tunnels) as a function of Reynolds number.

Reynolds Number. In agreement with facts as presented in other chapters on the influence of R' number on skin friction, separation and drag, some effect should be found in automobiles too. *Figure 2* shows a small decrease of the drag coefficient with R' number (speed) as found in wind tunnel tests. A sudden drop is found in one example, reminding of the behavior of rounded bodies as explained at length in the "pressure-drag" and "streamline" chapters. Two full-scale points are included in the graph at $R_f = 10^7$. Whether they are on the same level as, or higher or lower than the model results, is also a function of geometrical similarity.

Model Similarity. Proper representation in models, of all protuberances and other details of the actual vehicle (including, for example, the shape of the underside) is of importance. A number of automobile types have been tested (3, g), both full-scale on the road and through tunnel models, in which internal air flow, window frames, door hinges, ornate-

ments and the rough and open underside were reproduced as accurately as possible. On the average, the full-scale drag values seem to be slightly higher than the model results. Usually we can be satisfied with wind tunnel results under two conditions; namely that the model similarity is adequate (including underside and internal air flow) and that the ground representation is adequate. Results on a number of passenger cars are presented in *figure 3*, obtained either by such wind-tunnel testing or from full-scale investigations on the road (5).

2. DRAG OF BASIC SHAPES.

There are numerous wind-tunnel results available concerning the aerodynamic drag of automobiles; a few of them are presented in the illustrations. Readers who are more deeply interested in the findings of such tests, may study references 3 and 4. Certain mechanisms of drag are discussed as follows.

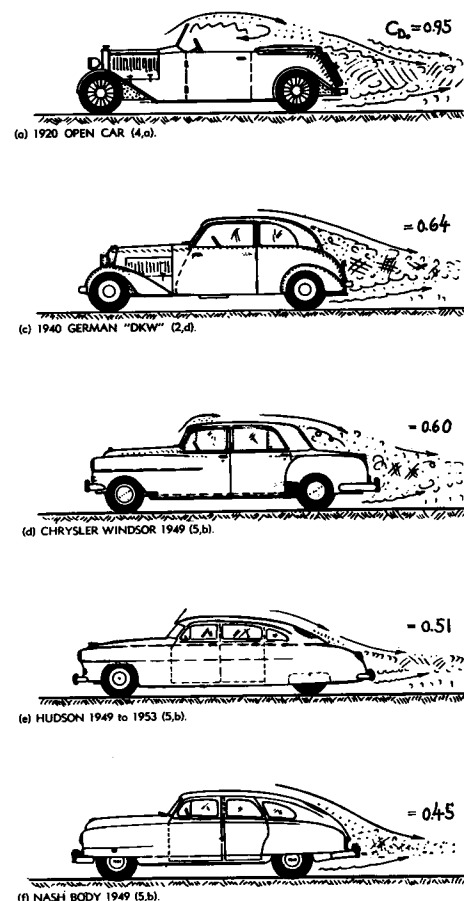


Figure 3. Drag coefficients of "standard" passenger cars, tested either in wind tunnels on geometrically similar models or by deceleration of the full-scale vehicles.

Skin-Friction Drag. Considering average passenger cars traveling at ≈ 50 mph, the Reynolds number is in the order of $R_\ell = VL/\nu \approx 10^7$, where l = total length of the vehicles. The corresponding skin-friction drag coefficient (for mostly turbulent boundary-layer flow) is roughly $C_f = 0.003$, as found in Chapter II. The wetted-surface area of a passenger car is in the order of 9 times the projected frontal area. Taking into account the increased dynamic pressure around the car body (by a factor of 1.5) the drag component due to friction is found to be in the order of $C_{Df} = 1.5 \cdot 9 \cdot 0.003 = 0.04$. The aerodynamic drag of conventional passenger cars is on the average ≈ 10 times as high as the skin-friction.

Separation Drag. The largest drag coefficients are obtained with open convertibles (such as in figure 3, a) and in blunt box-like shapes (as in figures 4, a and 13, a). A systematic series of smooth basic automobile bodies is investigated in (4, e). Figure 4 presents some of these and some other results:

- (a) By rounding the front end, the drag coefficient is reduced to the order of $C_D = 0.3$.
- (b) Rounding the rear end does not really reduce drag. Adding, however, a tapering tail, lowers the drag coefficient almost to $C_D = 0.1$.
- (c) Rounding the lateral edges (which are sharp in the shapes quoted from reference 4,e), produces streamline shapes (without long tails; figure 4-e,f) exhibiting drag coefficients as low as 0.13.

-
- (1) An extensive treatment of practical aerodynamics is found in "Aerodynamik des Kraftfahrzeugs" by Koenig-Fachsenfeld, Umschau Verlag Frankfurt.
 - (2) Deceleration tests, automobiles on the road:
 - a) Essers, Autom.tech Rundsch 1927, 359, 384.
 - b) Agg, Proc. 6th Highway-Res. Board Wash. 1928.
 - c) Hoerner, Testing Drag of Automobiles by Deceleration, Zeitschrift VDI 1935 p.1028.
 - d) Weiss-Sawatzki, D. Kraftf.forschg VDI No. 66.
 - e) Hoerner, Drag of a "Plymouth" Under Actual Road Conditions, Automotive Industries 1951, 15 Sept., p.43.
 - (3) Wind-tunnel techniques for automobile models:
 - a) Klemmin, J.A.S. 1934, 198; AutomInd. 1934, 140.
 - b) Schirmer, Automobiltech Zts. 1935 p.176.
 - c) Ono, Ground Representation, J.A.Sci.1935, 40.
 - d) Stalker, Suction, J.Aero'l Sci.1934 p.151.
 - e) Schmid, Automob't Zts. 1936, No.17, D.Kraftf. forschg VDI No.1, 1938;and Zts.VDI 1938 p.188.
 - f) Mueller, Forschg Ingenieurwesen 1939 p.220.
 - g) Sawatzki-Weiss, Autom.tech Zts. 1941; (2,d).
 - h) Gruson, Comptes Rend.Ac.Sci. Paris 1937,473.
 - (4) Automobile models tested in wind tunnels:
 - a) Klemperer, Zts. Flugt. M'luftsch. 1922 p.201.
 - b) Tietjens, Tr.ASME 1932, 235; Tr.SAE 1932.
 - c) Heald, BOS J.Res. 1933 p.284, 871; 1934 p.863.
 - d) Mauboussin, Models, L'Aéronautique 1933.
 - e) Lay, Model & Road, J.SAE 1933 p.144, 177, 261.
 - f) Hoerner, Survey, Zeitschrift VDI 1934 p.1261.
 - g) Andreau, Sci. Aérienne 1934, 285; J.Soc.Ing. Auto 1934, 2577; 1935, 34; Autom.Engr 1935, 75, and pages 113, 147.
 - h) Flugt.Inst. Stuttgart, Autom.Zts. 1935 p.331.
 - i) Reid, J.SAE 1935,180; Autom.Engr 1936, 252.
 - k) Kamm, Automobiltech Zeitschrift 1939 p.447.
 - l) Giquaux, Automobile Engineer 1935 p.33.
 - m) Möller, Volkswagen, Automobt.Zts. 1951 p.74.
 - (5) Full-scale vehicles tested other than in (2):
 - a) Conrad, Public Roads 1925 p.203.
 - b) Nagler and Razak, "Automobile Moving People Through Air", SAE Quarterly Trans 1950 p.530.
 - c) Lockwood, American Highways 1929 No.2.

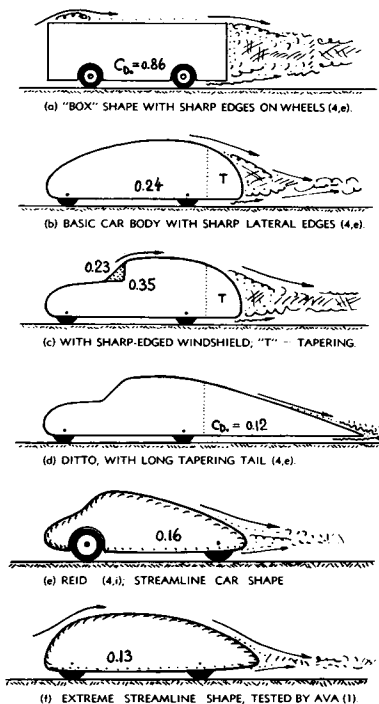


Figure 4. Drag coefficients of several smooth wind tunnel models (tested over fixed ground plate).

Aerodynamic Lift. The shape of automobiles is, of course, adjusted to the condition of moving in proximity of the road surface; the lower side of the body contour is nearly a straight line, and the upper side is curved somehow. The resulting pressure distribution yields an aerodynamic lift similar to that of an airplane wing (of extremely small aspect ratio). The two tip vortices, necessary components of the corresponding flow pattern, can be observed when traveling behind an automobile over a dusty road or through smoke or snow flakes. Based on frontal area, passenger cars have aerodynamic lift coefficients

as listed in figure 5. For example, for a coefficient of $C_{L_0} = 0.4$ (estimated to apply to today's conventional body shapes) the lift is in the order of 60 lb when driving at 50 mph (and = 240 lb at 100 mph). The lift coefficient is evidently highest in bodies with well rounded tops (figure 5,b), down-sloping tails (figure 5,a) and with sharp lateral edges (figure 4, b to d). It appears that the lateral edges of the windshield (figure 4,c) have a decisive part in producing a lifting flow pattern (favoring flow over the top of the car). "True" streamline shapes (figure 4,g or 5,e) do not have much of a lift coefficient.

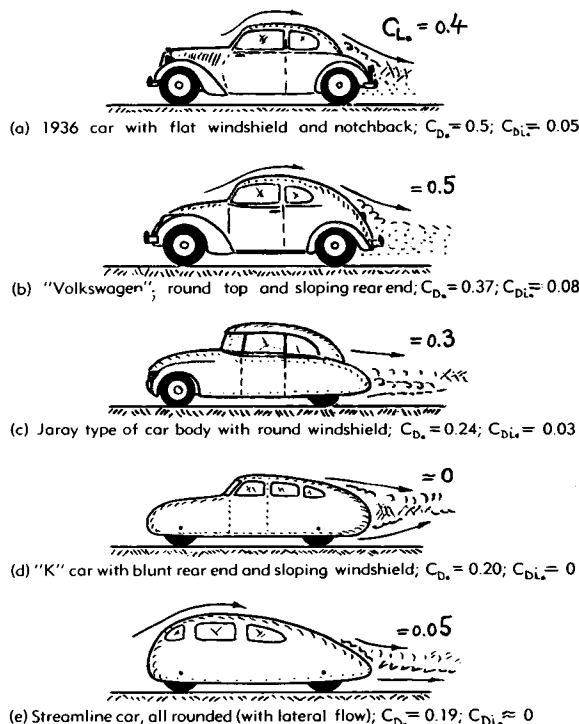


Figure 5. Lift coefficients (on frontal area) of several types of passenger cars, as tested in a wind tunnel (6,b).

Induced Drag. Lift presents induced drag (which can be appraised on the basis of wing theory as outlined in Chapter VII. In a simple analysis we may assume that $S_0 = b h = b^2$, which means that the height h equals the "span" b of the car. Using equation 4 of the mentioned chapter, the coefficient of drag due to lift is then found to be

$$C_{D_{L_0}} = C_{D_{lb}} = D_L / (qS_0) = C_{L_0}^2 / \pi \quad (1)$$

For a coefficient $C_{L_0} = 0.4$ (as quoted above), the corresponding drag coefficient is $C_{D_{L_0}} = 0.05$.

Wrap-Around Windshield. Lift and drag due to lift can basically be reduced by giving the car body a shape which facilitates flow along the lateral sides, rather than over the top. Figure 6,a shows an early attempt in this regard, exhibiting a shape which is tapered in the horizontal plane, thus ending in a vertical trailing edge. A more realistic automobile

shape is that of the European Jaray (between 1930 and 1940) particularly explained in (1). Figures 5.c; 6,b and 10,c give examples of his designs in which the flat windshield is replaced by a well-rounded front. It seems that the "wrap-around" windshield (popular since 1955) can produce similar results. In this shape, not only the loss of momentum is reduced in getting around the corner posts, but lift and drag due to lift can also be reduced and \approx avoided. It seems to be important, however, in this respect that the windshield be properly faired into the lateral body sides (without obstruction by rain gutters and the like).

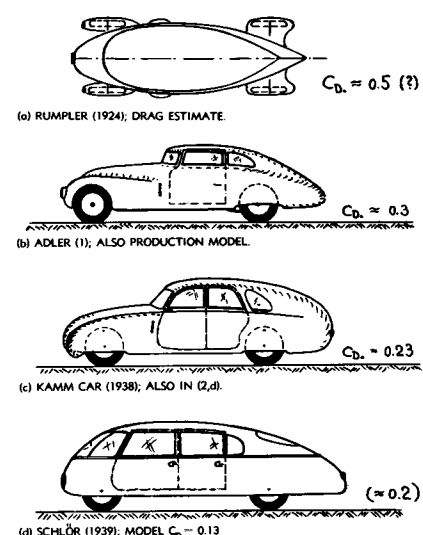


Figure 6. Examples for shape and drag coefficient of several experimental streamline cars.

Blunt Rear End. Considering that most vehicles are operated and parked in city traffic, and are housed in garages; extended "tails" are impractical. Another obstacle to streamline shapes is the fact that in ordinary "family cars" height and width of their after-bodies must leave enough space to accommodate passengers in the rear seat. It is subsequently not very favorable to give the upper side of the body a steep downward slope (as for example in figure 5, a and b). The air flow is not likely to follow such a contour, and the resulting flow separation means pressure drag. It is preferable, therefore, in bodies with restricted length, to design them with a more or less blunt, suddenly cut-off end, the projected area of which is smaller, however, than that of the maximum cross-section area of the car body. Figure 6,c shows an experimental car having a comparatively blunt end. The drag coefficient of $C_{D_0} = 0.23$, tested for this automobile (with faired and smooth underside) on the road, is low indeed. The blunt end (also shown in figure 12) presents some "base" drag, of course, as treated in the "pressure-drag" chapter — estimated to be in the order of $\Delta C_{D_0} = 0.05$ (based on S_0) for the car in figure 6,c. A factor which helps

explain why this shape and other similar designs (7, a) nevertheless have small drag coefficients, is the reduction of lift (see figure 5,d) and drag due to lift ($\Delta C_D \approx -0.08$ as per equation 1) in comparison to conventional shapes exhibiting attached flow over a rounded and down-sloping top.

3. DRAG DUE TO OPERATIONAL PARTS

Automobiles as we buy and use them, generally show higher drag coefficients (listed in figure 3) than quoted for similar model shapes in the preceding paragraphs. The explanation is found in the many necessary (and unnecessary) accessory parts used in the operation of motor vehicles.

Protuberances. Figure 7 presents an analysis of the drag of a "sedan" typical of the years between 1930 and 1940, with drag components compiled from various wind-tunnel and road investigations. The final, comparatively high drag coefficient is not surprising after listing and adding the drag of all parts and protuberances which were or still are attached

to the outside of this type of car. Among these are: license plates, bumpers, headlights, rear view mirror, spot light, fender flaps, door handles, hinges, locks, antennas, window frames, windshield wipers, ornaments and on older models: spare tires, running boards, and horns. The drag of protruding parts and the interference drag caused by them on the main car body, can be appraised through application of the methods outlined in Chapter VIII. As an example, the drag of an outside rear-view mirror, placed at the side of the windshield, may be "calculated". In free flow, the drag coefficient of such a disk-like part is $C_{D_0} = 1.2$. In the vicinity of the front corner post of the car compartment, the average local dynamic pressure (of the air flowing around this corner) is estimated to be 1.6 times as high as in the undisturbed flow; the drag coefficient of the "added" body is, therefore, concluded to be $C_{D_{a0}} = 1.6 \cdot 1.2 = 1.9$. Considering the interference caused by the obstacle at the rear of the car body, the additional drag is estimated to be in the order of 60%. The total drag of and due to the mirror is thus given by the coefficient (based on frontal area of the mirror) of $C_{D_0} = 3$. Based on frontal area of the car, the additional drag coefficient is in the order of $\Delta C_D = 0.015$, which represents between 2 and 3% of the total aerodynamic drag of a modern passenger car. This much may not be critical in any respect. However, several similar protuberances may, when added up, give a total effect well worth considering. By eliminating (building-in) a number of component parts (such as the headlights) and by other improvements in form (particularly after adopting a sloping windshield), the aerodynamic drag of passenger cars has been reduced between 1930 and 1950. As shown in figure 3, the most advanced U.S. passenger cars now have drag coefficients between 0.4 and 0.5. These values are still \approx twice as high, however, as those obtained in certain experimental cars (listed in figure 6).

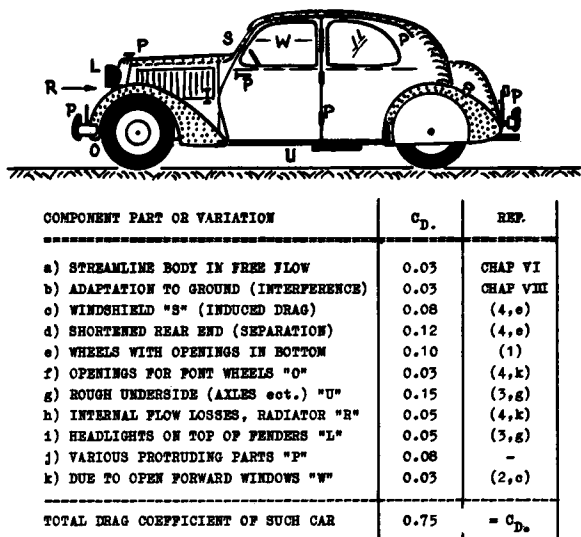


Figure 7. Analysis of the aerodynamic drag of an average European 1930-to-1940 passenger car (sedan) derived from model- and full-scale tests as quoted.

- (6) Concerning aerodynamic lift of automobiles:
 - a) Heald, J.Research Nat'l.Bur. Stand. 1934 p.871.
 - b) Sawatzki, VDI D.Kraftf.forsch Heft 45, 1941.
- (7) Automobile bodies with blunt rear end:
 - a) Everling, Verk' Woche 1939; Mo'kritik 1939.
 - b) Kraft.Inst. Stuttgt, Autom't.Zts. 1940 p.550.

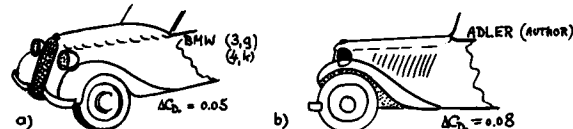


Figure 8. Drag of and due to fender-mounted headlights.

Headlights. Figure 8 presents two examples of drag due to fender-mounted headlights. In arrangement (b) the headlights are obviously in the narrow entrance of an expanding passage between hood and fenders. Referred to the frontal area of the headlights, the drag coefficient is between 2 and 4 — values which can be explained on the basis of interference, as treated in the chapter on this subject.

Underside. The biggest single avoidable aerodynamic drag component in today's passenger cars is in the rough underside. Withdrawn from the view of the motorist, there are axles, gear boxes, brake cables, springs, brackets, tanks, mufflers, holes and sharp edges in the frame — all of them exposed to the air stream. *Figure 9* presents some experimental evidence showing differential coefficients ΔC_D between 0.1 and 0.3 caused by such roughness of the underside. It is inevitable, of course, that some cut-outs be provided around the wheels, particularly in the front end where the wheels must also have space for turning (*figure 9,b*). Another model result is quoted in (1); by covering the underside of a bus, the drag coefficient is reduced from $C_D = 0.40$ to 0.27. The stock-produced "Tatra" car (Czechoslovakia) is built with a fairly smooth (flat) underside. The road-tested drag coefficient of this car, $C_D = 0.31$, is correspondingly low (1). Also the Volkswagen has a comparatively smooth underside.

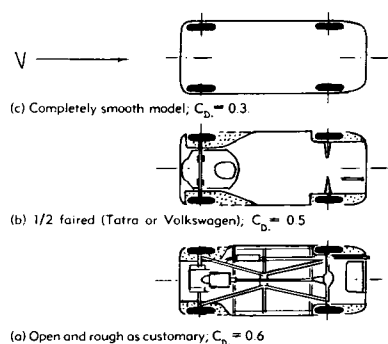


Figure 9. Shape of the underside and drag coefficient of a passenger car model (3,g).

Sun Visors at the upper edge of the windshield, used as protection against sun, heat, rain and snow, resemble very much the slots or slats sometimes applied at the leading edge of airplane wings. They would be useful in reducing drag if the bend between windshield and car top still was as sharp as in most old-time automobiles (*see figure 3,d*). Applied to modern cars, sun visors were found (5,b) to give an additional drag coefficient in the order of 0.04 (on the car's S.). It is suggested, however, that shape and setting (angle of attack) of these vane-like devices are critical, and that smaller drag increments could be obtained through proper development in a wind tunnel.

Wheel Openings. A certain controversy in modern automobiles is the question of having the wheels enclosed in the main body or laterally covered somehow. In a number of cars this has been done as far as the rear wheels are concerned. Since the front wheels

require additional space for turning, it seems that in only one stock-produced car (*figure 3,f*) fenders have been extended so as to cover most of the front wheels. Wind tunnel investigations (4,k) indicate an increment of the drag coefficient in the order of $\Delta C_D = 0.02$ due to a pair of wheel openings (front or rear approximately alike).

Open Windows. By opening the front windows of the car in *figure 10,b*; the drag coefficient was found to be increased by an increment between 0.03 and 0.04. It should generally be noted, however, that the influence of a disturbance (such as open windows or wheel housings) is small in automobile bodies which have high drag coefficients to begin with. Closing the top of a car similar to that in *figure 3,a* — the author found the drag coefficient reduced from 0.95 to 0.75. A sliding top over the front seat (available in a few European cars) produces an increment of $\Delta C_D = 0.1$ as reported in (1).

Cooling Air. The flow of air through the engine radiator as conventional in today's automobiles, is poor in aerodynamic respect. The drag differential listed in *figure 7* gives a coefficient based on frontal area of the radiator core, in the order of $C_{Dq} = 0.4$. As explained in the chapter on "internal flow", the momentum loss of the air flowing through the system, considerably depends upon shape and direction of the outlet. In automobiles, the air usually escapes at random, through the open bottom. The corresponding drag is then in order as quoted above. If, however, the cooling air would be discharged downstream by means of a suitable exit nozzle, some negative drag component (jet thrust) might be obtained on account of the energy transferred to the cooling air by the engine fan (and some heating.)

Streamlining. By summing-up drag components as analyzed in the last paragraphs, it is possible to predict the minimum drag of an automobile. A suitable streamline body, may have a basic drag coefficient of $C_D = 0.07$ (including ground interference) and an increment due to 4 wheels plus cut-outs in the car bottom in the order of $\Delta C_D = 0.10$, thus giving a first minimum in the order of 0.17. Next, assuming token values for induced drag, internal flow and external protuberances (including the windshield installation) of 0.01 each, a more realistic minimum in the order of $C_D = 0.2$ is obtained. Many enthusiastic attempts have been made during the last 50 years to give the passenger car a "streamline" shape. *Figure 6* shows several examples. Full-scale drag coefficients have been obtained in experimental vehicles as low as the 0.2 estimated above — a value which is less than half of that as found in modern stock cars (*figure 3*). The various needs of traffic, the convenience of the people riding in these vehicles, and last

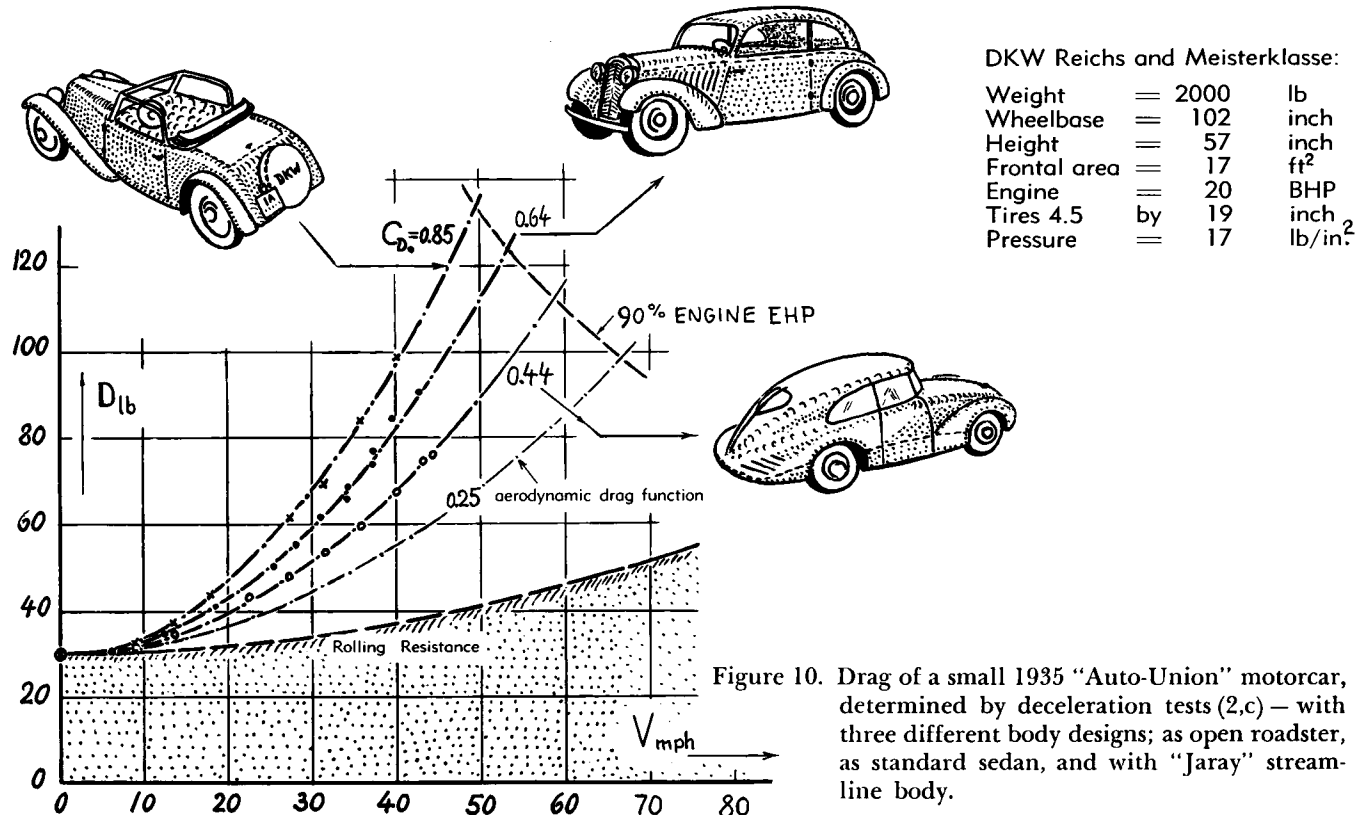


Figure 10. Drag of a small 1935 "Auto-Union" motorcar, determined by deceleration tests (2,c) — with three different body designs; as open roadster, as standard sedan, and with "Jaray" streamline body.

but not least a shiny appearance are evidently given preference over fuel saving aerodynamic efficiency. As an example, the 1949 to 1954 "Hudson" may be mentioned. This automobile having a low-slung and efficient streamline body shape did have all chances of obtaining a drag coefficient as low as those in figure 6 — by making the underside smooth and by adding a properly wrapped-around windshield. Actually, the tested coefficient of this automobile was $= 0.5$, however (see figure 3,e).

value of mechanical friction within the wheel bearings, a considerable amount of drag is caused by the external friction and the internal deformation of the rubber tires. This rolling resistance is approximately proportional to the load under which the wheels are moving. For a given type of tire, the rolling coefficient K_R = resistance/load, in pounds per pound, primarily depends upon the inflation pressure "p", and to a minor extent upon the speed of the vehicle. Considering treaded passenger-car tires in the range of their design loads, tests (9) on German low-pressure tires as of 1935 to 1940 indicate an average coefficient

$$K_R = 0.005 + \frac{0.15}{P' (\text{lb/in}^2)} + \frac{0.000035 (V_{\text{mph}})^2}{P' (\text{lb/in}^2)}$$

Assuming an average inflation pressure "p" = 26 lb/in^2 , the rolling resistance of these tires at 90 mph is twice as high as at $V \rightarrow 0$. A smaller fraction of the speed-dependent component of the equation is aerodynamic drag caused by "viscous" friction and by a centrifugal pumping effect at the surfaces of wheels and tires. The rolling resistance of the tires is $D_R = K_R W$. The power corresponding to rolling resistance is

$$P_{R,\text{HP}} = K_R W_{lb} V_{\text{mph}} / 375 \quad (4)$$

4. EFFICIENCY OF PASSENGER CARS.

Rolling Resistance. Figure 10 presents the total drag of one and the same passenger car chassis, with 3 different body shapes; namely as an open "roadster" as a standard two-door "sedan" and with an experimental Jaray-type of body — all tested by deceleration technique on the road (2,c). Disregarding a small

- (8) Schmitt, Power for Cooling of Automobile Engines, Deutsche Kraftf.forschg VDI, No.45 1940.
- (9) Rolling resistance of automobile tires:
 - a) Schmid, Autom.techZeitschr. 1936 No. 17.
 - b) Kluge & Haas, D.Kraftf.forschg VDI No. 26.
 - c) Stonex (Gen. Motors), SAE J. 1949 Dec p.18.

Power Required. To show the importance that the aerodynamic drag can have, the power shall be calculated required to drive an average passenger car over a level and smoothly-paved highway in calm atmosphere. The aerodynamic drag is

$$D_{\text{air}} = C_D \cdot 0.5 \rho V^2 S. \quad (5)$$

The corresponding power (in a consistent system of units) is

$$P_{\text{air}} = D_{\text{air}} V = C_D \cdot 0.5 \rho V^3 S. \quad (6)$$

Introducing the standard sea-level density ($\rho_0 = 0.0024 \text{ slug/ft}^3$), measuring the speed in mph and the frontal area in ft^2 , the power is

$$P_{\text{air, HP}} = C_D \cdot S \cdot \frac{\rho}{ft^2} (V_{\text{mph}})^3 \cdot 6.8 / 10^6 \quad (7)$$

Assuming a frontal area $S = 25 \text{ ft}^2$, the corresponding power is plotted in figure 11 for three different values of the aerodynamic drag coefficient. Considering the mechanical efficiency of the transmission system of such an automobile to be $\eta = 90\%$, the assumed power of the engine (100 BHP) is sufficient to bring the car up to maximum speeds between 83 and 112 mph — provided that suitable gear ratios are installed.

Fuel Economy. Assuming that $C_D = 0.5$ represents the aerodynamic quality of today's passenger cars; the maximum possible speed of the automobile assumed (on smooth and level road) is somewhat over 90 mph. The average driver may not consider speeds of this magnitude. However, by changing the body

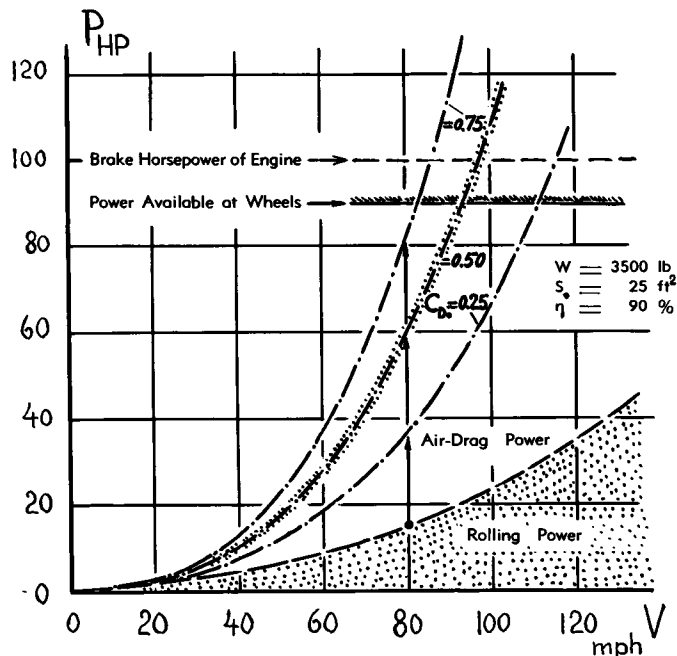


Figure 11. Calculated engine power required to overcome rolling resistance and aerodynamic drag of an average U.S. passenger automobile.

shape so that the drag coefficient is reduced from 0.5 to 0.25, for example — between 25 and 50% of the usual fuel consumption can be saved, at speeds between 40 and 80 mph. On the other hand, an open convertible with an assumed $C_D = 0.75$, results in a fuel consumption which is at least by the same percentages higher than that of the conventional "sedan"-type car. Another advantage of a low-drag car is increased acceleration. Integration of the curves in figure 11 between $V = 0$ and $= 50 \text{ mph}$, shows an increase in acceleration by some 7% — due to reducing the aerodynamic coefficient from 0.5 to 0.25.

Optimum Speed. Considering once more the total drag plotted in figure 10, the most economical speed of an automobile, yielding the highest mileage, is theoretically at $V \rightarrow 0$. Of course, this consideration does not include the characteristics of the engine and the transmission ratio between engine and rear axle, both of which have an important influence upon total efficiency. In fact, in one small car tested by the author for fuel consumption, a speed in the order of 20 mph was found to give the highest mileage; other modern cars are reported to be most economical in regard to fuel consumption at around 30 mph. Again, these optimum speeds may only be academic — since everybody wants to travel faster than at 20 or 30 mph, and most people are ready to pay for speed.

5. DRAG OF OTHER MOTOR VEHICLES

Trucks. The "boxes" in figures 4 and 13 resemble the shape of van-type trucks (or trailer trucks). The resistance of a platform-type "semi-trailer" combination as tested by deceleration technique (10, a) is plotted in figure 12. Assuming that equation 2 might apply to wheels and tires of this heavy vehicle (there is no better information known to the author), the aerodynamic drag has been separated. The drag coefficient thus obtained, in the order of 1.4, appears to be reasonable for the bluff and rough shape considered.

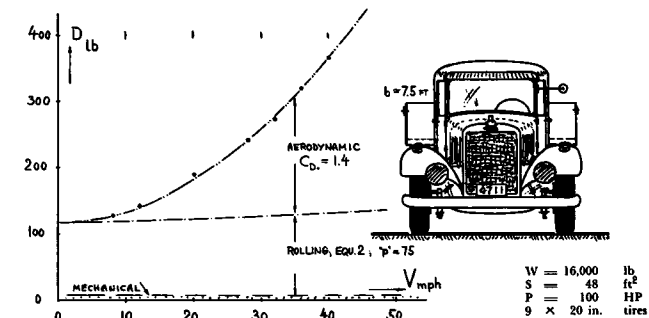


Figure 12. Drag of a 1938/39 semi-trailer truck ("cab" plus hitched-up trailer; total of 3 axles), determined by deceleration technique on the road (10,a).

Omnibuses. Because of their size, buses have absolute aerodynamic drag values higher than those of ordinary passenger cars. Based upon their frontal area, they present drag coefficients, however, in the same order as comparable shapes in figure 3. From wind-tunnel tests, illustrated in figure 13, it is learned again that sloping down the rear end does not decrease the drag. Roughness of the underside causes an increment in the order of $\Delta C_D = 0.15$. — Many modern omnibuses are similar in their basic shape to that of figure 13,a. Note, that by rounding the edges (around the front side) the drag coefficient is reduced to $C_D = 0.46$ for this "box" shape, from 0.86 as in figure 4,a. Figure 13 also contains results on the German "Volkswagen" truck (also produced as a "limousine"). By rounding the front end, the drag coefficient is reduced from 0.73 to 0.44. These values apply to smooth wind-tunnel models, however. The information as quoted for shape "c" suggests that full-scale buses will probably have coefficients higher than listed by a ΔC_D , in the order of 0.2.

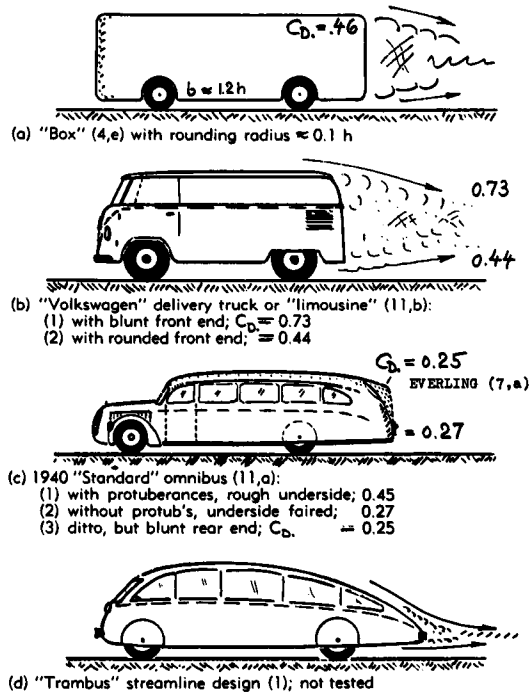


Figure 13. Drag coefficients of several types of omnibuses as tested on wind-tunnel models.

- (10) Concerning resistance of trucks:
 - a) Trucks, Public Roads Vol.23 (May 1942).
 - b) Möller, Volkswagen Truck, Aut.Zts. 1951 p.l.
- (11) Regarding drag of omnibuses:
 - a) FKFS, Automobt.Zts. 1936, 143 and 1940, 550.
 - b) Volkswagen see reference (10,b).
- (12) Racing car, unpublished German information.
- (13) Aerodynamic drag of motorcycles:
 - a) Sawatzki, D. Kraftf.forschg VDI No.18, 1938.
 - b) Scholz, NSU, Umschau 1951, 691; Z.VDI 1953.

Racing Cars. Besides air drag, other characteristics have a decisive influence on the outcome of a race — such as acceleration (selection of optimum gear ratio) performance of the brakes (in suddenly slowing down upon entering one of the two 180° curves of closed race tracks) and last but not least quality and endurance of engine and tires. Some attention has nevertheless been given to the aerodynamic drag in racing cars. Figure 14 presents the drag coefficient of one particular car as tested on the full-scale vehicle in a larger wind tunnel. The open wheels of this car, desirable for continued inspection by the driver during the race, for brake cooling and for quick wheel changes, naturally add to the aerodynamic drag. Racing cars designed for speed records on straight courses (such as Daytona Beach or Bonneville Salt Flats) are usually fully streamlined, however, with the wheels enclosed in the car's main body. In either type, momentum loss and drag due to internal cooling air flow appears to be more important than in ordinary passenger cars, because of the powerful engines.



Figure 14. 1934 "Auto Union" racing car, tested (12) in the large DVL wind tunnel (Berlin). The projected frontal area is $S_0 = 1.13 \text{ m}^2$.
 (a) "original" condition (with axles exposed and with radiator flow); $C_D = 0.65$
 (b) wheel and axle fairings; $C_D = 0.50$.

Motorcycles. In case of motorcycles, an area is not really obvious to which a drag coefficient could be referred. The drag must, therefore, be presented in the form of the "drag area" $D/q = D/(0.5 \rho V^2)$ usually given (in the English-speaking countries) in ft^2 . For standard sea-level condition, the drag is then

$$D_{lb} = 0.0026 (D/q)_{ft^2} (V_{mph})^2 \quad (9)$$

where the constant is equal to 0.5 ρ times a factor to account for the conversion from ft/sec to mph . Figure 15 shows the results of some wind-tunnel tests. Deceleration tests of the author (2,c) indicate a drag area of 6.0 ft^2 for a 1935 NSU motorcycle with the driver and with a rider on the back seat, both sitting nearly upright. In comparison to a modern fighter airplane which has a drag area in the same order (see in the "aircraft" chapter) the drag of a motorcycle (including driver) must be considered to be large. The reason is evidently found in the aerodynamically

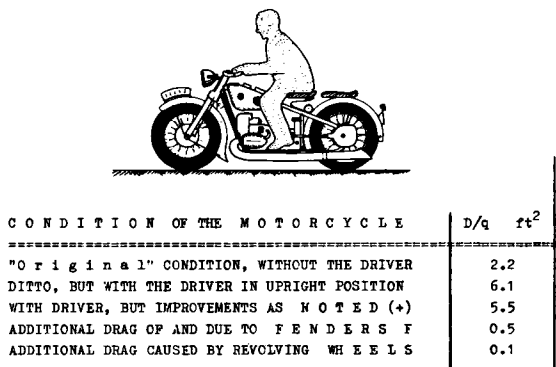


Figure 15. Aerodynamic drag values of motorcycles, derived from wind-tunnel tests (13,a) of three such vehicles (BMW, NSU, and Viktoria), all within the same power group (500 cm^3 cylinder volume); (+) improvement = disk-like fairings at the sides of the wheels plus fairing around the upper part of the wheel fork.

rough and bluff design of these vehicles, including steel tubing and usually neglecting any fairing. A considerable part of the drag is also due to the driver (see "human beings" in the "pressure drag" chapter). The driver can reduce the drag appreciably by bending down, "lying" down onto the tank as in figure 16,a. Number "b" of that illustration finally shows that the drag area can be reduced to 1.5 ft^2 by putting a streamline shell around vehicle and driver. With the shape as illustrated, a world speed record of 290 km/h has been obtained in 1951 over a distance of 1 km, using an engine of 500 cm^3 cylinder volume, boosted to put out $\approx 100 \text{ BHP}$ (!)

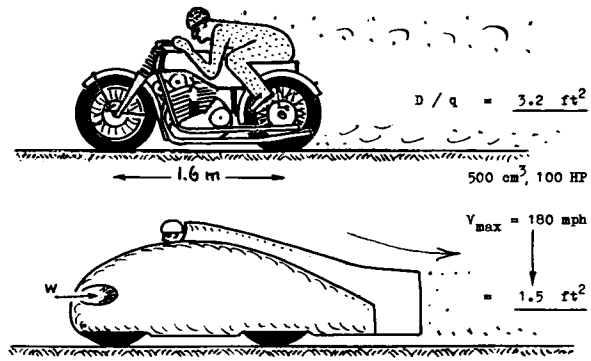


Figure 16. Drag area of an NSU motorcycle (13,b), determined by wind-tunnel investigation in original and in fully streamlined condition.

B. DRAG OF RAILROAD VEHICLES

1. Locomotives And Power Cars.

Rail Cars. Motor cars, that is self-powered railroad (or street) cars, running singly, have drag coefficients similar in character to those of automobiles. The available results of wind tunnel tests are listed in figure 17. The flow pattern past these more or less box-like vehicles is similar to that of prismatic bodies in the pressure-drag chapter. Accordingly, drag coefficients between 0.2 with well-rounded nose, and 0.8 with blunt front end can be expected. Tested values are in the order of 0.5. An attempt on radical streamlining (16,c) demonstrates that the drag coefficient could be reduced to as low as 0.08; or at least to 0.19 if permitting window frames and similar surface imperfections.

The Steam Locomotive is a complex piece of machinery. In the old-time "standard" models, the outside shape is or was usually very rough, exhibiting all types of levers, rails, instruments, pumps, pipes and other devices. As illustrated in figures 18, 19 and 20, the

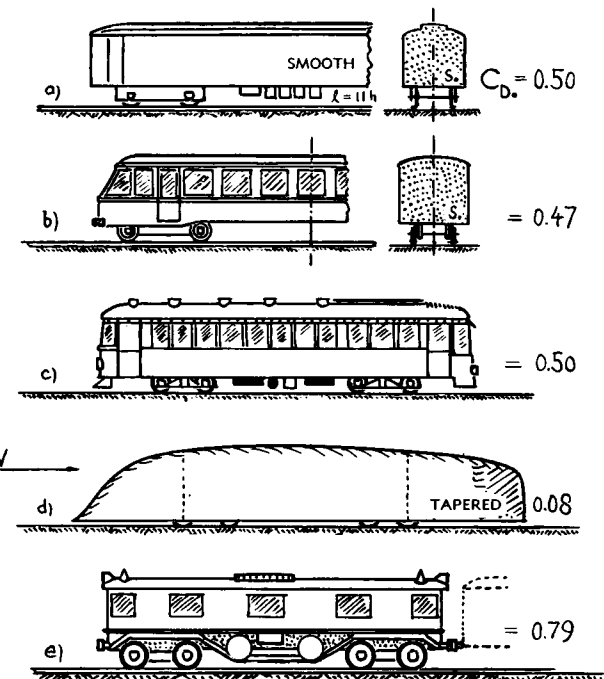


Figure 17. Aerodynamic drag coefficients of various powered rail-car models (16)

- Smooth model (a).
- Model with more details (b).
- Streetcar with details (c).
- Extreme streamline shape (c); with window frames and rough underside $C_D = 0.19$.
- Electric Engine (c) in front of train.

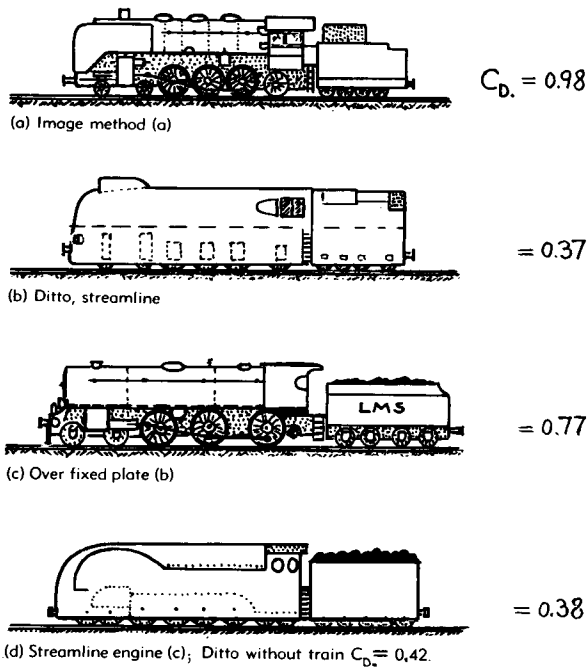


Figure 18. Drag coefficients of "standard" and streamline locomotives tested on wind-tunnel models in front of trains or so-called tail cars (17).

drag coefficient is correspondingly high, between 0.7 and 0.9 (tested in front of a train or some type of a "tail car"). By fairing the smoke-box front with a hemispherical cover (17,b), the drag coefficient can be reduced by 0.17. By fairing, in addition to the front end, the wheels and the upper side of the tender, and after covering all pipes, hand rails, levers, gaps, and protuberances, the drag coefficient is reduced to less than 0.4. An ideal shape (entirely smooth and faired) even shows $C_D = 0.16$ (again tested in the presence of a train or a tail car placed behind the locomotive model).

- (16) Aerodynamic drag of rail cars:
 a) Ergebnisse AVA Gottingen Vol.III, 1926 p.161.
 b) See L'Aerotecnica 1934 p.482.
 c) Tietjens Ripley, Trains, Trans ASME 1932.
- (17) Air resistance of railroad vehicles:
 a) Nordmann, Aerod. Drag of Railroad Vehicles, Organ Fortschr.Eisenbahnw. 1935, 395; Zts. VDI 1938, 515.
 b) Johansen, Air Resistance of Trains, Proc. Institute Mech'l Engineers Vol 134 (1936) p.91.
 c) Griffin, Streamlining Effect on Air Drag of Steam Locomotives, Journal ASME 1948 p.515.
 d) Lipetz, Tr.ASME 1937, 617; RW Mech.Eng. 1935, 496.
 e) Klemm, Aerodynamics of Railway Trains, R'way Mech.Eng. 1934 p. 315, 312, 282, 357; same as in (d).
 f) Nocon, in Glasers Annalen 1931 p.99.

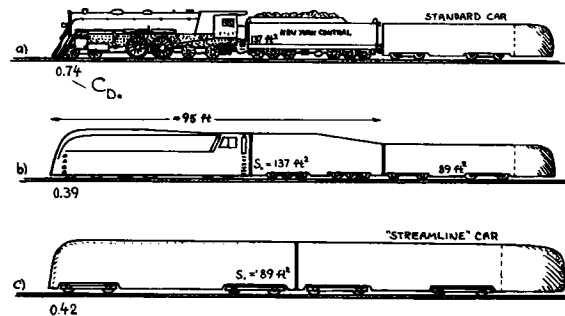


Figure 19. Aerodynamic drag coefficients of three types of railroad engines, model-tested in (17,d and e).

- (a) "Standard" locomotive. Based on $S_0 = 137 \text{ ft}^2$:
 $C_D = 0.74$ with "tail car" (fairing)
 = 0.97 with 1 car + tail car
 = 1.17 with 2 cars + tail car
 = 1.27 with 3 cars + tail car
- (b) Streamline locomotive. Based on 137 ft^2 , the coefficient is $C_D = 0.39$ with tail car.
- (c) Electric power car. Based on $S_0 = 89 \text{ ft}^2$:
 $C_D = 0.42$ with tail car
 = 0.52 with 1 car + tail car
 = 0.64 with 2 cars + tail car

Power Cars — that is, cars driven by electric motors, have drag coefficients similar to those of rail cars. An example of a rather rough car of this type is included in figure 17. By rounding the front end (as done in more modern Diesel engines) a coefficient in the order of $C_D = 0.4$ may be expected (in front of a train). Figure 19 indicates a $C_D = 0.42$ for a power car plus "tail car". After subtracting an estimated value for the tail car, a drag coefficient in the order of 0.3 is obtained for that smooth power car model running in front of a train.

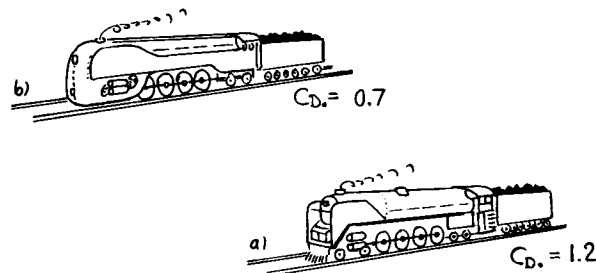


Figure 20. Drag coefficient (17,c) of a steam locomotive (without train); a) "standard" design, b) streamlined shape. The base drag coefficient of this locomotive (no train behind) may be in the order of $\Delta C_D = 0.2$.

2. Drag Of Railroad Trains

Railroad Cars. Assuming for an average passenger car a ratio of "wetted" surface area to frontal area in the order of 15, and a skin-friction drag coefficient of 0.003, the minimum drag coefficient of one such car, being pulled with others in a train, is estimated to be $C_{Df} \approx 0.05$. The "standard" cars, with rough undersides, and other protuberances, and with open gaps around the diaphragms, show approximately four times this minimum value as listed in table A.

Car Condition	REF.	C_{Df}
"Standard" Car (+)	(17, f)	0.18
"Standard" Car model	(17, d)	0.15
"Standard" Car model	(17, b)	0.17
With Fairied Gaps	(17, b)	0.16
With Fairied Underside	(17, b)	0.13
Streamlined Design	(17, d)	0.11
"Ideal" Streamline Car	(17, b)	0.05

Table A. Aerodynamic drag coefficients of railroad-passenger cars, tested on wind-tunnel models, except for (+) which is from draw-bar tests on actual vehicles on the tracks.

Protuberances. It is mentioned above that old-type steam locomotives are rough in aerodynamic respect because of the many parts protruding from their surface. Some protuberances are also found on railroad passenger cars, such as generators and battery boxes, for example, at their underside. As a supplement to the various inlet devices as treated in the "internal flow" chapter, figure 21 presents drag coefficients of several ventilation intakes and outlets designed for application in railroad vehicles. The air scoops have

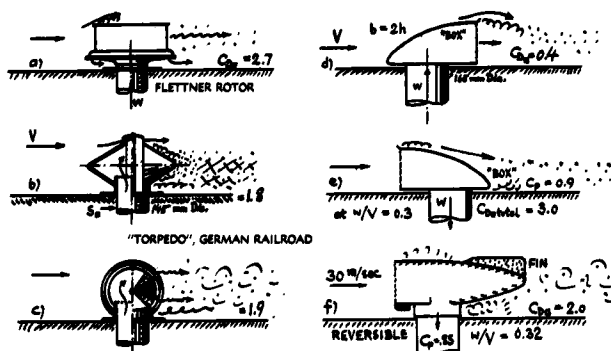


Figure 21. Total drag coefficients (on duct area) of railroad ventilation devices (18):
 (a) is a rotating "exhaust fan".
 (b) and (c) give suction (discharging).
 (d) and (e) can serve as outlet or inlet.
 (f) is a weather-vane type of scoop.

high drag coefficients because of their unnecessarily blunt shapes. The outlets are primarily designed to provide the "desired rate of flow", without consideration for the aerodynamic drag. Usually these devices are shaped symmetrically to give the same effect in both directions of travel as required in railroad operation. In most of these shapes, the total drag coefficient is in the order of 2, based upon the duct area $d^2 \pi / 4$; and roughly in the order of 1, based upon external frontal area. It is mentioned in the sources of these results (18) that such devices necessary in the operation of passenger trains, may represent 20% of their total aerodynamic drag. Table A confirms this estimate, showing $C_{Df} = 0.18$ for a full-scale car while for a smooth model $C_{Df} = 0.15$ only.

Model Scale. As in the case of automobiles (treated in the preceding section), the aerodynamic drag of railroad vehicles can be and has been determined either by testing wind-tunnel models or by tests with the actual equipment on the tracks. The length of a passenger train (composed of an engine and 6 passenger cars) is in the order of 500 ft. A medium-size wind tunnel can, on the other hand, only accommodate a model length of some 10 ft. The model scale is thus in the order of 1 to 50, and the corresponding difference in Reynolds number must be considered when predicting the aerodynamic characteristics of trains.

Aerodynamic Drag Law. While in the power cars above (as in automobiles) the influence of Reynolds number can be small, aerodynamic conditions of long railroad trains are basically different. A considerable fraction of the drag is directly caused by friction along the wetted surface of such trains. The minimum of this drag is

$$C_{Df} = C_{fturb}(S_{wet}/S_*) \quad (11)$$

The ratio of the wetted area of a train to the frontal area is approximately

$$S_{wet}/S_* = 2 [(1/b) + (1/h)] \quad (12)$$

where l = length of the train, b = breadth and h = height of the cars. For an average railroad car, this ratio is in the order of 15. The area ratio of a train with engine and 6 cars, as illustrated in figure 22, is thus in the order of $S_{wet}/S_* = 100$. Applying now equation 11 with the turbulent coefficient as presented in the "skin-friction" chapter, a minimum coefficient $C_{Df} = 0.4$ is obtained for the usual Reynolds number range of model tests on such a train, between $R_f = 10^6$ and 10^7 . Proceeding from wind-tunnel to full-scale conditions (which are at R' numbers between 10^8 and 10^9), the skin-friction component of the drag coefficient of this train reduces some 50%. The coefficient of the pressure drag, on

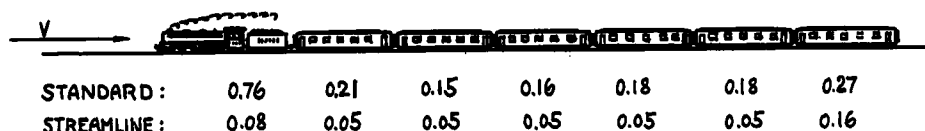


Figure 22. Distribution of aerodynamic drag among the components of a railroad train, as found in wind-tunnel tests (17,b). The standard train has a total drag coefficient $C_{D_0} = 1.9$, the streamline model has $C_{D_0} = 0.5$.

the other hand, assumed to be equal to the difference between the tested drag and the calculated minimum drag of the train, may approximately be considered to be independent of the Reynolds number. Two extreme types of trains are analyzed in this manner, in figure 23, a "standard" one (illustrated in figure 22), and a streamline train. The pressure-drag coefficient is reduced by streamlining (that is by fairing the undersides, and the gaps between the cars) from 1.4 to 0.1. The percentage decrease of the total aerodynamic drag coefficient due to Reynolds number, is of course highest in the streamline shape. Between wind-tunnel and full-scale conditions (at $R_\lambda = 5 \cdot 10^8$, corresponding to $V = 100$ mph) the reduction is more than 40%. Such a difference must certainly be taken into account.

Base Drag. Behind the last car, the flow separates from its "base". Considering a train with 6 or more cars and a total aerodynamic drag coefficient of the model train in the order of $C_{D_0} = 2$, the boundary layer at the end of the train could be expected to occupy a space the cross-sectional area of which is in the order of 10 times the base area. Derived from

figure 37 of the "pressure-drag" chapter, the corresponding base-drag coefficient would be approximately 0.02, while for a streamline train with $C_{D_0} = 0.5$, the base-drag coefficient would be 0.04. Train tests consistently show much higher values, however, as listed in table B. An explanation for this result is suggested in the next paragraph.

Type of TRAIN	REF.	C_{DB}
"Standard"	(17, f)	0.09
"Standard"-Type Train	(17, b)	0.10
With Tail Fairing	(17, b)	0.09
Streamline-Type Train	(17, d)	0.11
"Ideal" Streamline Train	(17, b)	0.15
Ditto With Tail Fairing	(17, b)	0.11

Table B. Base-drag coefficients of trains.

Flow Pattern. As a function of local Reynolds number (position among the other cars of a train) the drag coefficient of an individual car might be expected to decrease with distance from the front end. This does not come true, however, as shown in figure 22. Note: If the first car behind the engine has a higher drag coefficient than the following ones; this is evidently because of the gap behind the tender. By increasing the height of this tender (fairing the upper side), the drag coefficient of the train was reduced by 0.14. — Generally, a fairly constant drag coefficient seems to exist for the cars in line of a train.

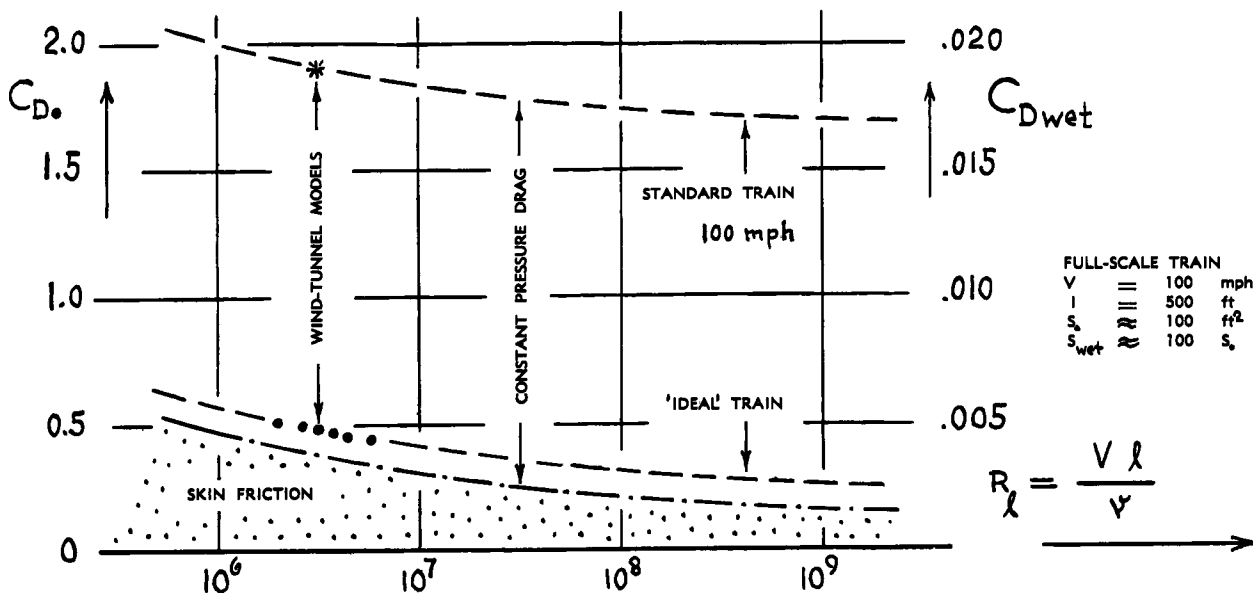


Figure 23. Drag variation of a railroad train (locomotive + six passenger cars), as a function of Reynolds number, evaluated from (17,b).

(18) Schirmer, Ventilation Openings, Tech Rpts Luftsch.bau Zeppelin No. 600/83 (1934), 600/119.

This fact suggests a flow pattern past trains different from that of three-dimensional bodies of moderate length, in free flow. In a manner similar to that illustrated in figure 8 of the "interference" chapter, it may be true that the boundary-layer material is shifted to both sides, away from the train, in form of a vortex pair. Not all of the dead air thus arrives at the edge of the base of the last car. The average dynamic pressure, responsible for the friction drag along the train and for the base drag discussed in the preceding paragraph, is correspondingly higher than expected in a flow pattern similar to that of plate friction. Whether this analysis is correct or not, can only be decided by detailed observation of the flow along such a train. Should it be so, it would mean that the effective aerodynamic length of trains may be in the order of one or two cars. Corresponding to this length, the effective Reynolds number to be considered in figure 23 — would also be reduced; the skin-friction component of drag would be somewhat increased, accordingly.

3. Efficiency Of Railroad Trains.

Traction Resistance. Disregarding the thrust required to climb ascending sections, considerable mechanical resistance originates within the wheel bearings of railroad vehicles and due to deformation of, and friction between wheels and rails. The resistance caused by the friction in oil-lubricated, plain journal bearings increases theoretically with speed. However, in real operation, the oil temperature also increases with speed; the corresponding resistance may, therefore, be considered as being approximately constant as against speed. The rolling resistance originating on account of elastic deformations of wheels and rails, is also independent of speed. These two components give the first two terms of the following formula, developed from (19,a), for the ratio of resistance to weight (in pounds per pound):

$$K_R = 0.0007 + (2.8 n/W_{lb}) + 0.00001 V_{mph} \quad (14)$$

With an axle loading, that is with (train weight "W") / (number of axles "n") in the order of 22,000 lb, the resulting constant part of the coefficient of mechanical resistance is $K_{R_0} = 0.2\%$. — The third term of the equation indicates the "dynamic" resistance caused by jolts over the rail junctions, and due to other (swaying) motions of the vehicles. This component seems to increase in proportion to the speed. At 100 mph, the mechanical resistance is thus approximately 1.5 times as high as at $V \rightarrow 0$.

Wheel Ventilation. Due to skin friction and because of a pumping effect roughly similar to that of a centrifugal blower, the revolving wheels absorb a certain power. The corresponding additional aerodynamic drag is not included in the usual model tests (the wheels are simply not made to turn). From experiments with automobile and motorcycle wheels (3,e) and (13,a) this type drag is estimated to be

$$D/q = D / (0.5 \rho V^2) = (0.05 \text{ to } 0.14) \text{ ft}^2 \quad (15)$$

per one wheel. Assuming a value of 0.1 ft², the four wheels of an average automobile present an additional aerodynamic drag in the order of but $\Delta C_D = 0.005$, which is in the order of 1% of the aerodynamic drag of such a vehicle. In railroad trains, the number of wheels is much higher; the drag due to the wheels is, therefore, noticeable as illustrated in figure 25.

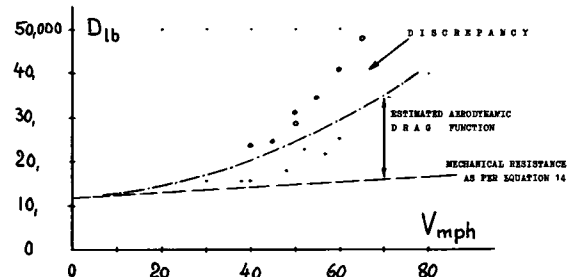


Figure 24. Resistance of a 70 car mixed freight train, draw-bar tested behind locomotive (22). Average weight = 43 short tons per car; total weight \approx 3000 tons. Length of train \approx 3000 ft; frontal area $S_f \approx 100 \text{ ft}^2$.

Freight Train. Figure 24 presents the resistance of a freight train as specified, selected from the results in (22). After applying equation 14 for the mechanical resistance, a component is left over which is expected to be aerodynamic drag. The experimental points in the upper part of the graph do not correlate, however, with a quadratic function of air drag. While some other points in the lower part of figure 24 could be understood on the basis of tail wind (reducing the aerodynamic drag appreciably), wind does not help analytically to explain the trend of the upper points. It is, therefore, suggested that the mechanical resistance in these trains may be different from that as indicated by equation 14; and that the equation should contain a cubic term. The author does not have any better explanation as of this time. At any rate, assuming the quadratic air-drag function as shown in the graph, a drag coefficient of $C_D = 18$ is obtained from the train of 70 cars behind the engine. Divided by the number of cars, the resulting coefficient is $C_D = 0.26$ per car. In comparison to those listed in table A, this value appears to be reasonable if considering that the freight cars do not have equal height. The steps and gaps in the contour of a "mixed" train cause appreciable aerodynamic drag.

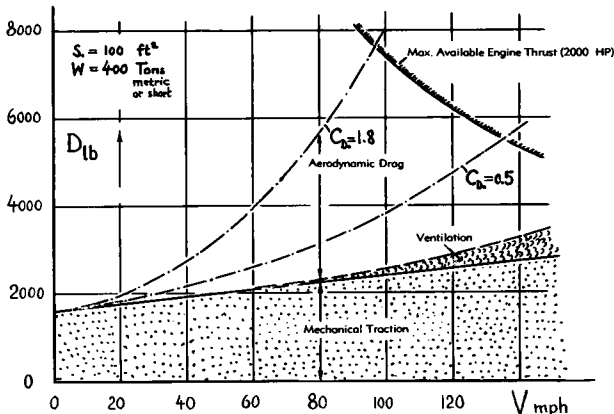


Figure 25. Analysis of mechanical and aerodynamic drag of a train, consisting of an engine and 6 passenger cars as illustrated in figure 22.

Total Train Drag (19,e). For illustration, calculated mechanical resistance as well as the aerodynamic drag of a representative railroad passenger train, consisting of an engine and 6 cars, are plotted in figure 25. The aerodynamic drag of the "standard" train equals the mechanical resistance, at a speed somewhat above 60 mph. By streamlining the train, so that C_{D_s} is reduced from 1.8 to 0.5 (as in the model tests; figure 23) the required engine power can be reduced by 34% at 60 mph, by 46% at 80 mph, and by more than 50% at 100 mph. A number of more or less streamlined trains are in operation in the United States; other (light weight) trains (the so-called "Talgo" type train, the General Motors train and Train "X" built by Pullman-Standard) are being introduced as of this time (21). The savings in fuel made possible by reasonable streamlining appear to be appreciable. The cars of these trains are also made lower, thus presenting smaller frontal and surface areas (reduced aerodynamic drag); and they are lighter in weight, thus having less mechanical resistance.

- (19) Mechanical traction resistance of RR vehicles:
 - a) Davis, General Electric Review 1926 p. 685.
 - b) Vogelpohl, Zeitschrift VDI 1935 p. 851.
 - c) Trans ASME 1937, Paper RR3, p.329.
 - d) Andrews, T.Inst.Locomot.Engg 1954, 91.
 - e) For lack of more-conclusive information, equation 14 is assumed to apply in the analysis.
- (21) Lightweight Trains, "Fortune" July 1955 p.110.
- (22) Tuthill, Freight Train Resistance, Univ. Illinois Engg Exp.Sta Bull. No.376 (1948).
- (24) Ower, Streamline Body Interference, ARC RM 1480. Table 8 of the source applies to two disks.
- (25) Rolling resistance of airplane tires:
 - (a) Wetmore, Wheels, NACA T.Rpt 583 (1937).
 - (b) Frank & Kranz, German ZWB FB 1037 (1939).
- (28) Christy, in Rod and Custom, February 1956.
- (30) Engine ratings: "Where does power go?"; SAE 1956.

Vehicle Size. An interesting aspect in land-borne vehicles is a comparison of aerodynamic drag referred to the vehicle volume. Using for a streamline train a frontal drag coefficient of $C_{D_s} = 1$ and for a passenger car $C_{D_s} = 0.5$, the coefficient based on $V^{2/3}$ (see in the "streamline" chapter) is roughly $C_{D_s} = 0.1$ for the train and $= 0.3$ for the automobile. This result can be considered to be a consequence of the "square-cube" law or the Froude number, as explained in the chapter on "water-borne craft". The volume (number of passengers) grows faster than the (frontal or wetted) area, as the size of a certain-type vehicle is increased.

B. SUPPLEMENTARY NOTES

Since there is space left at the end of this chapter, some supplementary information concerning the drag of land-borne vehicles is added as follows.

Interference. For terminology and principles see in Chapter VIII. Figure 26 demonstrates the extent to which the drag of a streamline body is increased through addition or presence of a comparatively small obstacle. Even without touching the "main" body, the "added" disk still has an appreciable effect upon flow pattern (separation from the rear) and drag coefficient of that shape. — It must be said, however, that the effect would be less for a main body having, to begin with, some separation and a correspondingly higher drag coefficient. For example, in an average automobile with $C_{D_s} = 0.42$ (which is 10 times the drag coefficient of the streamline body in figure 26), the increment due to the added disk might only be half of the value indicated in figure 26.

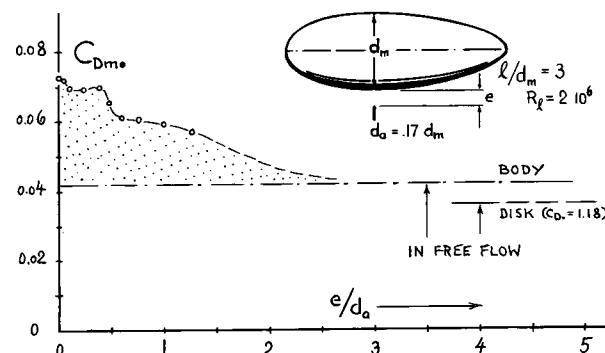


Figure 26. Drag caused by the presence of a small disk (with $S_{d_a}/S_{b_m} \approx 3\%$) placed near a streamline body (24). The drag of the disk in free flow represents 86% of the streamline shape's undisturbed drag.

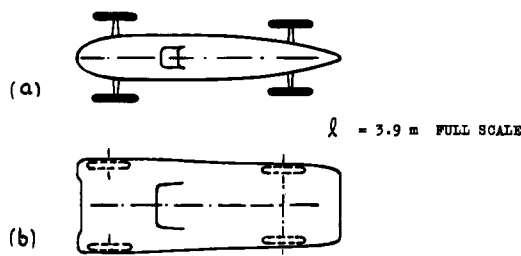


Figure 27. Drag area of a sports or racing car (4,h), determined by wind-tunnel tests on a 1/6 scale smooth model. Drag coefficients C_D are as follows:

- (a) with exposed wheels ($S_e = 0.82 \text{ m}^2$):

 - 0.27 without any fairings
 - 0.17 with rear wheel fairings
 - 0.15 without wheels, but with axles

- (b) with wheels enclosed ($S_e = 1.26 \text{ m}^2$):

 - 0.23 wheel housings open at the sides
 - 0.19 with covered wheel housings
 - 0.22 ditto, and with 2 head lights
 - 0.23 and with spare wheel on rear
 - 0.25 "0.19" with 0.5 m^2 bottom opening

Sports Car. Figure 27 shows shape and drag characteristics of one and the same chassis of a small sports or racing car, (a) with wheels and axles in the open, and (b) with the wheels housed within a wider car body. The aerodynamic drag area $D/q = (C_D \cdot S_e)$ of the wide type (having $S_e = 13.5 \text{ ft}^2$) is seen to be larger (between 2.5 and 2.9 ft^2) than that of the model with exposed wheels ($S_e = 8.8 \text{ ft}^2$ and $D/q = 2.2 \text{ ft}^2$). Tunnel tests on the racing car in figure 14 have shown, however, that by putting suitable fairings around the axles, the drag coefficient of that car can be reduced by $\Delta C_D = 0.04$. If doing this to the car in figure 27,a the two body shapes will approximately have equal drag.

Rolling Resistance. Some information on rolling resistance " D_{Ro} " of airplane type tires is given in (25). Resistance ratios D_{Ro}/W , tested at speeds between 10 and 40 mph, are approximately between:

0.6 and 1.0%	on concrete surface
1.5 and 2.5%	on dry and "firm" turf
6.4 and 7.7%	on average "soft turf"

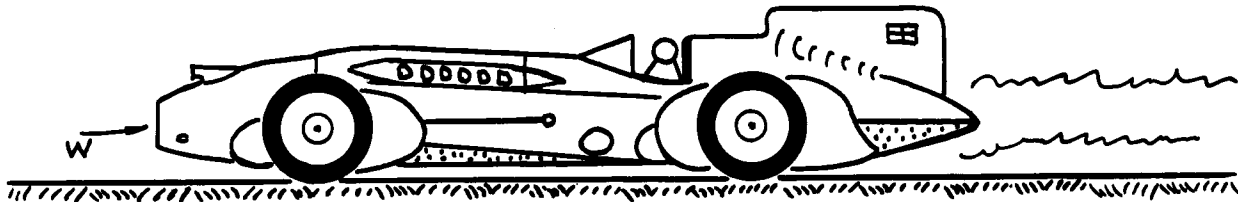


Figure 28. "Streamline" shape of Malcolm Campbell's "Blue Bird" ($W \approx 10000 \text{ lb}$), with which he drove home several world speed records. Quoted from (28), the car made 174 mph with 450 BHP, 206 mph with 900 BHP, 254 mph with 1500 BHP (1933, as shown in the illustration), and finally 300 mph with 2500 BHP. Assuming 20% mechanical losses, and allowing an average rolling drag of $(0.05 \times 10,000) = 500 \text{ lb}$ on the Daytona Beach sand, an aerodynamic drag coefficient C_D is obtained between 0.40 and 0.45 (on estimated 20 ft^2 frontal area). This coefficient is between those listed in figure 14 and the unrealistic model results quoted in figure 27.

CHAPTER XIII

DRAG OF AIRCRAFT COMPONENTS AND ACCESSORIES

Many experimental data are compiled in this chapter, indicating the drag of various components and accessory parts of aircraft. The experimental material presented, serves as illustration for various mechanisms of aerodynamic drag, treated in other chapters in more basic form. Referring to these chapters, the results, selected from an ever-growing fund of published reports, are explained and analyzed as far as necessary or suitable. The examples presented may also simply be used for direct information on certain drag-producing component parts and accessories of aircraft.

1. DRAG OF FUSELAGES

Smooth fuselages might have a drag which is close to that of streamline bodies having the same fineness ratio. There are some reasons, however, because of which the drag may also be considerably larger than that as presented in the "streamline" chapter.

Fineness Ratio. In case of oval or rectangular cross section, the equivalent fineness ratio of three-dimensional bodies may be taken as

$$1/\text{"d"} = 2 \frac{1}{(b+h)} \quad (1)$$



CONFIGURATION	(I,a)	(I,b)	(I,c)	(I,d)
bare fuselage body	0.15	0.10	0.16	0.08
with opening & pilot	0.19	—	0.18	0.15
with a windshield	0.23	0.15	0.20	0.20
with cockpit & engine	0.59	0.46	0.32	0.37
Reynolds number R_L	$7 \cdot 10^5$	$1 \cdot 10^7$	$1 \cdot 10^7$	$2 \cdot 10^6$

Figure 1. Drag coefficients (on frontal area) of several fuselages of small open-cockpit airplanes.

where b = width and h = height of the shape. Introducing this fineness ratio into equations 28 or 31 of Chapter VI, a minimum drag coefficient of fuselages can be obtained. For example, on the basis of $C_f = 0.003$ as found in Chapter II for a Reynolds number ($R_L \approx 10^7$) the drag coefficient of a fuselage having $1/d = 6$, is found to be $C_{D_{\text{min}}} = 0.0034$ or $C_D = 0.061$. Note at this point that $1/d = 6$ is not an optimum fineness ratio in regard to drag; fuselages have to have some length to give the tail a sufficiently long moment arm (and to place the horizontal tail away from the bound-vortex downwash behind the wing's trailing edge). The coefficients for bare shapes listed in figures 1, 5 and 7, are higher than the C_D calculated above; either on account of fineness ratios higher than assumed, or because of turbulence (and support interference) in the wind-tunnel.

Open Cockpits. Figure 1 gives a general idea as to the extent to which the drag of a fuselage is increased on account of the accommodations required to house the pilot (and the engine). The drag coefficient of an open-cockpit fuselage with windshield is thus increased over the basic value, on the average by an increment $\Delta C_D \approx 0.05$. Referred to the frontal area of the windshield, coefficients in the order of $C_{D_{\text{min}}} = 0.5$ are obtained. Figure 2 shows attempts of reducing the drag of an open cockpit (a) by means of a fairing *behind* the pilot's head and (b) by placing the pilot into the (properly shaped) opening of a *hood*. Of course, open cockpits are rarely found any longer in today's airplanes.

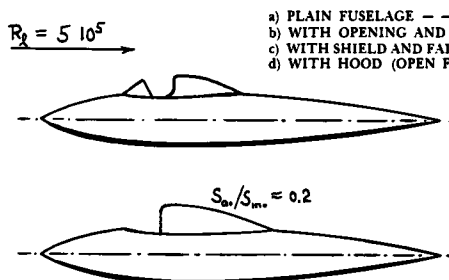


Figure 2. Drag coefficient (on original frontal area) of an open-cockpit fuselage (1,b).

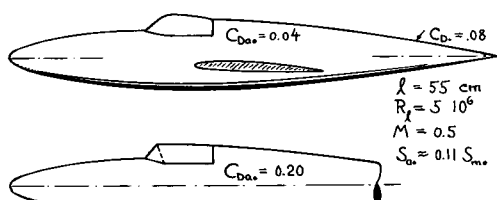


Figure 3. Drag coefficient of a canopy (a) with rounded, and (b) with sharp-edged shape (2,f).

Canopies. Figure 5 shows two basic methods of providing the pilot of an airplane with the necessary vision out of an enclosed cabin. The drag of and due to a canopy has been extensively discussed in the "interference" chapter. The drag of canopies is also shown in figures 3 through 5. Based upon the frontal area of the added shape, drag coefficients are found below $C_{D_a} = 0.1$ for reasonably smooth shapes (including interference effects). Figure 6 presents results of a more systematic investigation at a Reynolds number (on canopy length) in the order of $3 \cdot 10^6$. It is seen that the optimum length ratio is not really included in these tests. Minimum drag (on frontal area) is found at fineness ratios (l/h and l/d , respectively) which are appreciably higher than in streamline bodies (see Chapter VI). The data in (2,e) also permit to make a guess at the optimum length ratios each of the forebody (to the maximum thickness or height of the canopy) and of the afterbody. For either portion of the canopy, $(l/h)_{opt} \approx 6$, so that the total ratio $(l/h)_{opt} \approx 12$ as shown in figure 6. This result is similar to that as found for blisters (bumps) on plane walls in the chapter on "surface imperfections". The fact that in the optimum shape, the maximum thickness is roughly located at half the canopy length, is also different from conditions in free flow. Figure 6 indicates a theoretically possible minimum coefficient (on frontal canopy area) of less than $C_{D_a} = 0.04$. Of course, such slender shapes do not appear to be very practical, neither as to their structural length nor in regard to the pilot's field of vision.

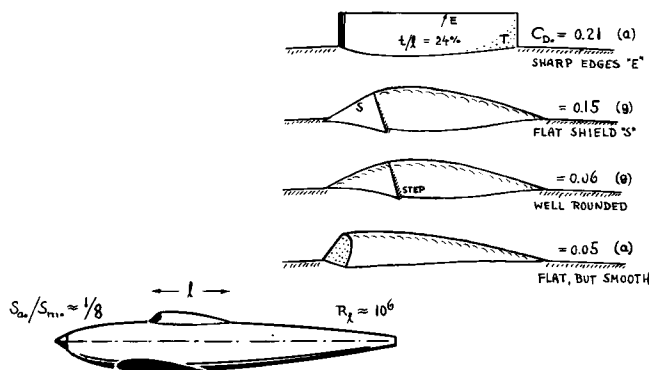


Figure 4. Drag coefficients (based on frontal area of canopy) of several shapes selected from (2,a and g).

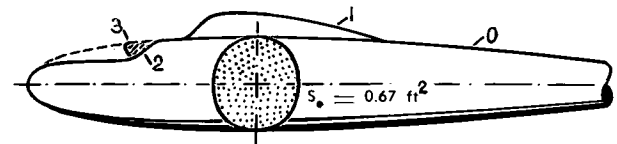


Figure 5. Drag of a fuselage (on basic area S_b) with several means of providing vision for the pilot (2,b).

Drag Of Windshields cut "into" the fuselage body is of a magnitude similar to that of canopies put on top of the fuselage. This is shown in figures 5 and 7. One reason for the magnitude of their drag may be the fact that after adding the windshield, the boundary layer of the main body is made turbulent at least over some portion of its circumference. Figure 7 shows the influence of the particular shape of the windshield. It appears that rounding the lateral edges is equally important as rounding the upper edge of the shield. Coefficients on frontal "window" area are between 0.06 and 0.31.

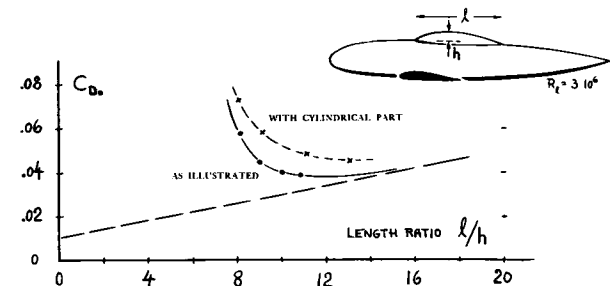


Figure 6. Drag coefficient (on frontal area) of a canopy (2,e) as a function of its length ratio l/h .

Surface Roughness. Sharp edges around the front of canopies add, of course, to their drag (see figure 3). Reference (2,e) also indicates that the increment of the canopy drag coefficient due to a step (at the location marked by the "h" in figure 6) amounts to $\Delta C_{D_a} \approx 0.02$. Roughly $\Delta C_{D_a} = 0.01$ is caused by a "strip" in place of the step. Taking these and other surface imperfections of actually constructed canopies (or windshields) in account, their drag is likely to be appreciably higher than the more favorable values presented in the illustrations of this section.

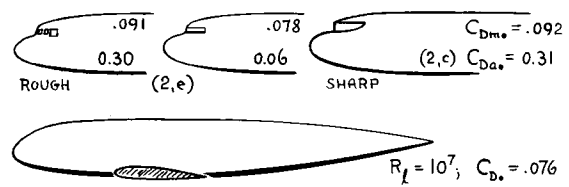


Figure 7. Drag caused by undercut windshields. Shapes (a) and (b) are taken from (2,e); form (c) from (2,c).

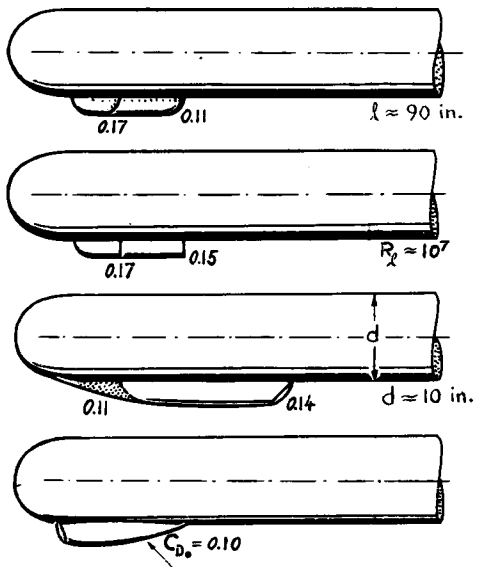


Figure 8. Drag (on added frontal area) of several appendages (3,a,b), designed to be used for armament or other devices.

Armament. Figure 8 shows several methods of incorporating a gun stand (or the smooth housing of any similar device) in the nose section of a fuselage. Depending upon the individual shape of these appendages, their drag coefficient (on projected frontal area) is between $C_{D_a} = 0.10$ and 0.17 . Of course, the complete "remote-controlled" gun installation in figure 9 has an appreciably higher drag, in the order of 40% of that of the fuselage.

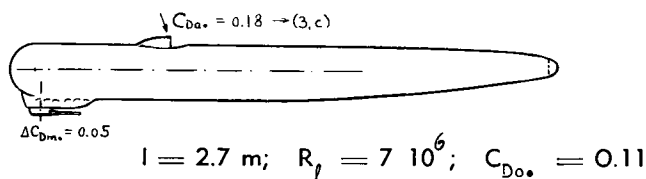


Figure 9. Drag caused by installation of gun turret (3,b).

- (1) Drag of fuselages and open windshields:
 - a) ARC RM 465 (1919); quoted in NACA T.Rpt 236.
 - b) ARC RM 112; quoted in NACA T.Rpt 236.
 - c) Weick, Full Scale Airplane, NACA T.Note 271.
 - d) Washington Navy Yard, Aero Rpt 459 (1931).
- (2) Drag characteristics of canopies and windshields:
 - a) Hartley-Cameron-Curtis, Wind-Tunnel Tests on the Design of Cabins, ARC RM 1811 (1937).
 - b) Brennecke, Wind-Tunnel Investigation of Various Fuselages, AVA Rpt 1935/41.
 - c) MIT, Fuselage Drag, J.Aeron.Sci. 1936 p.276.
 - e) NACA, Drag of Canopies, T.Rpt 730 (1942).
 - f) Heinkel, Two Canopies, Rpt SK.140 (1941).
 - g) RAE, Fighter Models, ARC RM 2535 (1951).
- (3) Drag of various armament appendages:
 - a) Dornier Tunnel Rpts 12 (1937) and 102 (1941).
 - b) Fuchs, He-177 Fuselage Models, Heinkel Wind-Tunnel Rpts WK 61, 101, 114 & 133 (1939 to 1941).
 - c) Heinkel, He-111 Fuselage, Document WK 27.
 - d) Messerschmitt, Gun Openings, Rpt WKB 3/1943.
 - e) Cut-Off Fuselage, Yearbk D.Lufo 1942 p.1,241.

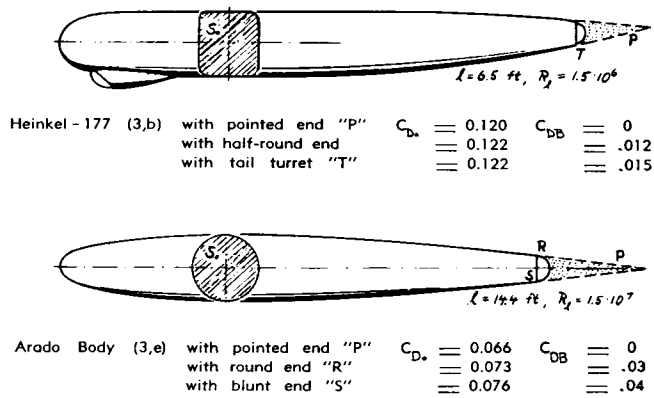


Figure 10. Drag due to tail turret (or a cut-off tail).

Tail Turrets. Figure 10 presents data of two tail turrets. Their drag is essentially that caused by cutting off the rear end of the respective fuselages. As explained in Chapter III, the base drag originating behind these turrets, is a function of the "skin drag" of the fuselage bodies, including appendages and protuberances. Case (b) in figure 10, having a completely smooth body, is therefore not realistic. Assuming that the drag coefficient of the fuselage in part (a) of the illustration might grow to $C_{D_a} = 0.15$ after adding a windshield and all types of surface roughness (and the wing roots) as in a real airplane, a base drag coefficient in the order of $C_{D_B} = 0.01$ is obtained. Under due consideration of the area ratio $S_B/S_a \approx 0.2$ or less, the drag coefficient due to such tail turrets is found to be in the order of only $\Delta C_{D_m} = 0.002$ (based on frontal fuselage area). This drag increment is but between 1 and 2% of the assumed fuselage drag.

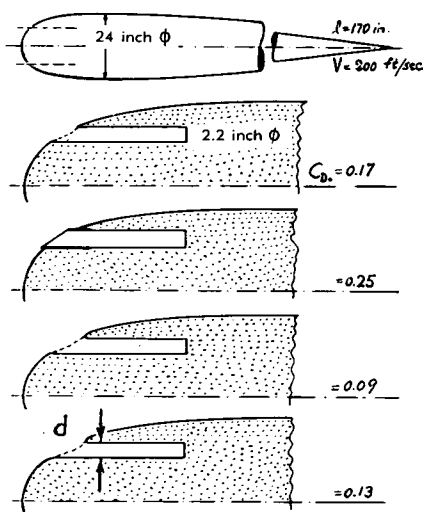


Figure 11. Drag coefficients (on opening area $d^2 \pi / 4$) caused by gun holes (3,d) in the nose of a fuselage.

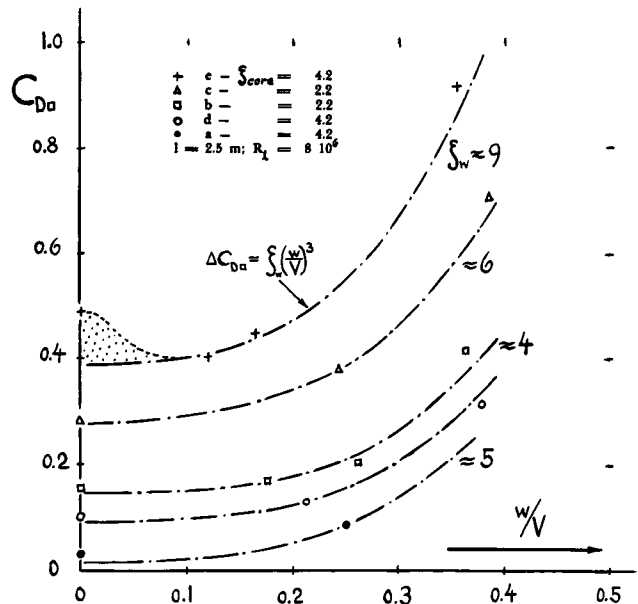
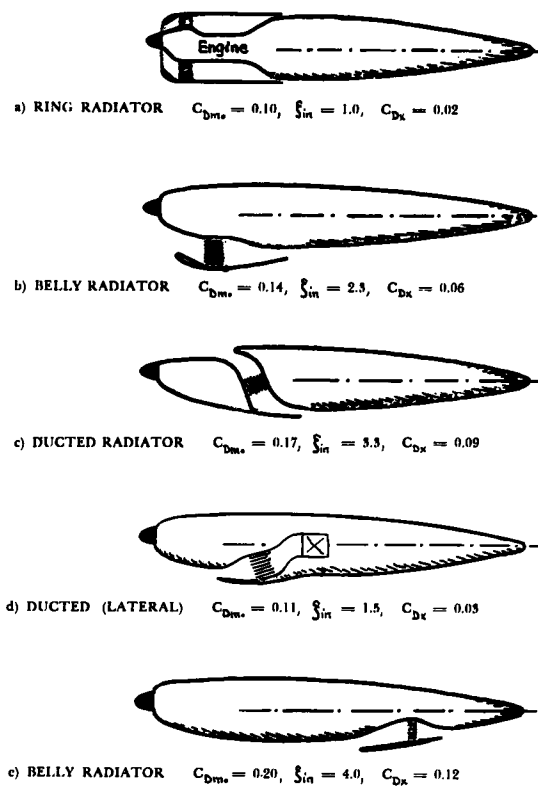


Figure 12. Drag of a fuselage (4,a) ducted in various ways to accommodate a radiator.

Drag Due To Guns. Figure 11 presents the drag caused by the installation of a gun in the nose of a fuselage. Regarding the hole through which the gun barrel protrudes, it is favorable to make the downstream edge as round as practicable. The drag coefficient is then reduced to half of that with sharp edge. This result agrees with the characteristics of surface gaps as presented in the chapter on "imperfections". The additional drag of the gun barrels (not shown in Figure 11) is indicated by a coefficient C_{D_g} = 0.2 to 0.4, based upon the frontal area of these barrels; depending, of course, upon the length at which they protrude from the opening.

Radiator Installations. Figure 12 presents drag characteristics of a fuselage in combination with several ducted radiator installations. The drag coefficients as indicated are a function of the internal momentum drag of the radiators (see Chapter IX in this respect). It is seen that all configurations in which the radiator housing as such, or inlet and outlet protrude from the fuselage body, have the highest drag coefficients. To account for the relative size of radiator against fuselage, the values (included in figure 12) $C_{D_{\text{fr}}} = D/(q S_{\text{fr}})$ based on cross-section area S_{fr} of the radiator core, should be used. The increment of the fuselage drag then corresponds to

$$\Delta C_{D_u} = C_{D_u} (S_{\text{fr}}/S_{\text{fr}}) \quad (3)$$

Engine Installations. Figure 1 gives some information on the drag caused by old-type installation of radial engines in the nose of fuselages. Figure 13 shows two attempts of fairing-in or cowling such an engine. A "spinner" is not a very effective means of reducing drag. A sizeable reduction of drag is accomplished through the NACA-type cowling (discussed later under "nacelles"). The drag coefficient of the fuselage configuration is nevertheless increased because of the engine installation, from 0.15 to 0.25, which means a $C_{D_u} = 0.10$ for the engine (including some "internal" drag).

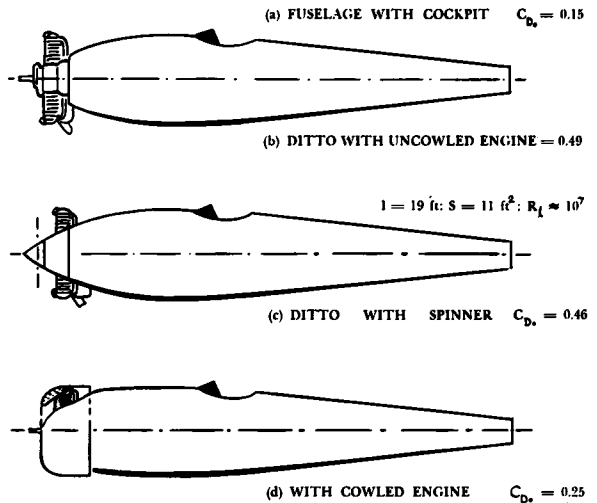


Figure 13. Drag coefficient (on basic frontal area) of a fuselage with radial-engine installation (4,b).

Leakage. Even after including the drag of all the appendages discussed in this section, the drag of a real fuselage (or that of an engine nacelle) may not be complete. As shown in wind-tunnel investigations (5), a considerable increment of drag can be caused by all types of "leaks" (inlets and outlets through cracks and gaps and holes) in the skin of fuselage, engine cowling and canopy (or in the nacelles). This type of internal flow can be estimated through application of the methods presented in Chapter IX. In a simplified analysis, essentially flush openings shall be assumed; and the outlet momentum shall be considered to be lost (discharge does not take place in downstream direction). Because of the "sudden" intake through small openings into larger internal spaces, the inlet momentum is also lost, which means that $\eta_{in} \rightarrow 0$ and $\xi_{in} \rightarrow \infty$. As a consequence, the rate of flow is only a function of the local static pressures at the openings; hence:

$$C_Q = Q/VS_{\square} = \sqrt{(p_{in} - p_{out})/q} \quad (4)$$

where $Q = \text{ft}^3/\text{sec}$, $S_{\square} = \text{area of the openings}$ (inlet or outlet, whichever is smaller). The maximum possible drag due to this internal flow is then

$$C_{DQ} = 2 w_{\square}/V = 2 C_Q = 2\sqrt{(p_{in} - p_{out})/q} \quad (5)$$

based on the same S_{\square} and with w_{\square} = velocity through S_{\square} . However, in cases where boundary-layer material is taken in through the inlet openings, the factor "2" is too large. A constant smaller than "1" seems to be more appropriate for random intake through openings in the skin of an aircraft. The difficulty in applying this equation lies, of course, both in measuring the inlet and outlet openings existing in a given structure, and in the proper estimation of the average pressure differential between the openings. Assuming (quite arbitrarily) a pressure coefficient (in the right side of equation 5) of 0.5 and an average inlet or outlet area equal to 1% of the frontal area of a fuselage, the equation (used with a constant = 1) yields an increment of the drag coefficient $\Delta C_D \approx 0.01 \cdot 0.5 = 0.005$. This much is in the order of 5% of the basic drag of a fuselage. The leak drag can be appreciably higher, however, in engine and radiator installations where full total pressure may prevail inside (purposely "taken in"). As a consequence, the pressure coefficient is at least "1" and the factor in equation 5 is "2". The corresponding increment for

a 1% leak-area ratio (as above) is $\Delta C_D = 0.02$, a value which is in the order of 20% (or more) of the basic fuselage (or nacelle) drag. Wind-tunnel tests on a full-scale fighter airplane (5,b) have revealed that $\approx 10\%$ of the total parasite drag of the craft was caused by leaks.

2. DRAG OF ENGINE NACELLES

The drag of and due to engine nacelles has two additional components, the interference effects as described in Chapter VIII, and the drag caused by the air flow through the engine, principles of which are outlined in the "internal chapter". Some more information and practical applications connected with both of these aspects are presented as follows:

(a) Drag Of Smooth Nacelle Bodies

Slim Shapes. A number of less common nacelle shapes are shown in figure 14. The fact that the thin "shaft" ("a") has a drag coefficient (on frontal area) roughly twice as large as that of common nacelle bodies, may be attributable to the magnitude of its wetted area in comparison to S_f (fineness ratio). The result that the "flat" type presents a drag which is considerably higher in the vertical (number "e") than in the horizontal arrangement (number "d"), can be explained on the basis of separation in the four corners between wing and nacelle, formed in the upright position.

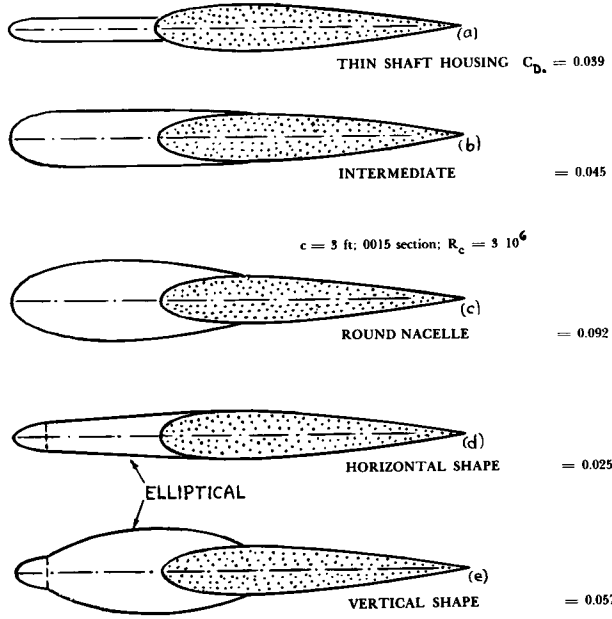


Figure 14. Drag coefficients of several "slim" engine nacelles (7,c) at zero lift.

(4) Radiators and engines in fuselages:

a) CAHI (Moscow), Fuselage Ducts, Rpt 517 (1940).
b) Weick, Cowlings, NACA T.Rpt 314 (1929).

(5) Drag caused by structural leaks:

a) Patterson, Leak Drag, ARC RM 1883 (1938).
b) ARC, Tests on "Hurricane", RM 2562 (1953).

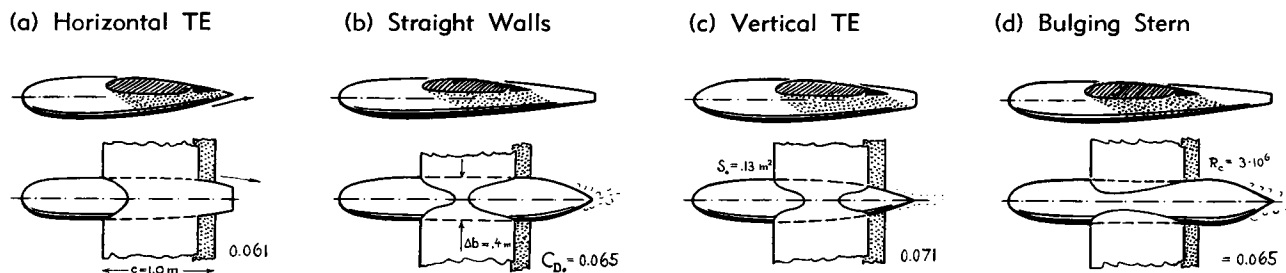


Figure 15. Drag of a high-wing nacelle (7,a) showing various modifications of length and shape in the afterbody.

Induced Drag. Figure 15 shows results of an investigation (in a high-wing configuration) undertaken with the intention of reducing the *parasitic* drag of a nacelle by modifying the shape of the rear end. It is seen, however, that extending the length of the nacelle beyond the trailing edge of the wing and other modifications do not help at all. More important is evidently the *induced* drag caused by the local variation of lift due to the nacelle. This type of drag (explained in the "interference" chapter) can effectively be controlled by adjusting the wing's trailing edge (within the part of the span "covered" by the nacelle), in such a way (9) that the lift differential is reduced to zero. Figure 16 presents some results in this respect, selected from the vast material in (8,b). It is seen there, that the mid-wing configuration has the smallest drag; that in a high-wing arrangement, a wide and horizontal trailing edge of the nacelle increases the drag further; that a vertical trailing edge does not help to reduce the drag (because of additional wetted area); and finally that a piece of "flap" at the trailing edge (with an area roughly equal to the frontal area of the nacelle) reduces lift differential and drag appreciably.

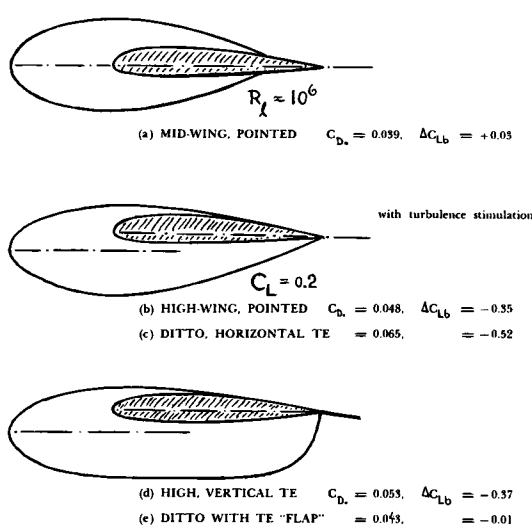
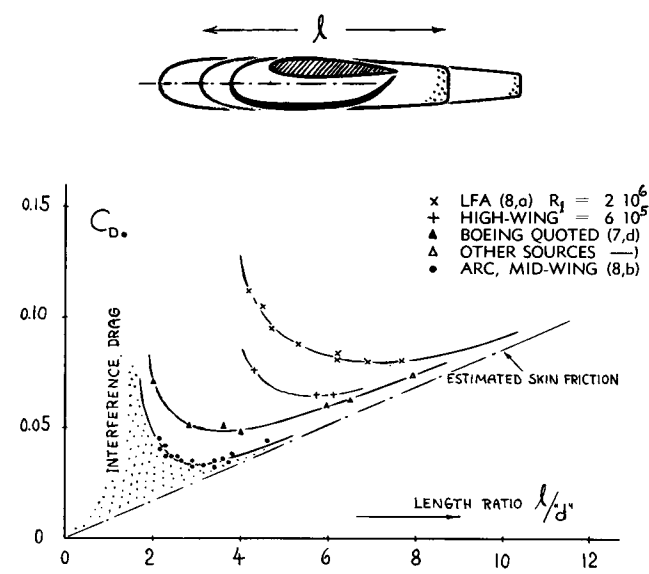


Figure 16. Drag coefficients of smooth engine nacelles, selected from the material in (8,b).

Length Ratio. Figure 17 presents the total drag of and due to smooth nacelles, tested in several more or less systematic series in which the length ratio ℓ/d or ℓ/c is varied while "d"/c is more or less kept constant. Analyzing their drag, the frictional component is found to be responsible for the increase in the right-hand part of the illustration. Interference drag (separation) produces, on the other hand, the sharp increase of the total drag in the left-hand part. Between the two extremes, there is an optimum ratio, which in the mid-wing family (8,b), is in the order of $\ell/d = 3$, thus coming close to that as found in streamline bodies (see in Chapter VI). The minimum drag coefficient (in the order of $C_D = 0.033$) is also close to that in free flow.

The High Wing configurations (8,a) in figure 17 have a minimum drag coefficient and an optimum fineness ratio, both of which are roughly twice as high as those of the mid-wing family (8,b). The reason for this result is most likely found in parasitic interference effects along the junctions between wing and nacelle. It is suggested that any high-wing configuration, with all volume of the nacelle body

Figure 17. Drag of several series of smooth engine nacelles (8) as a function of their length ratio ℓ/d .

on one side of the wing section, may have interference effects (adverse pressure gradient and subsequent boundary-layer losses) corresponding to the total displacement of the nacelle—while mid-wing arrangements (with one half of their volume above, and the other half below the wing) may have characteristics corresponding to only half their thickness ratio ("d"/1). We therefore have now two reasons in favor of mid-wing configurations; namely reduced parasite drag as well as less induced interference. It is also shown in Chapter IX that such nacelles can be built with an external drag that corresponds only to their skin friction.

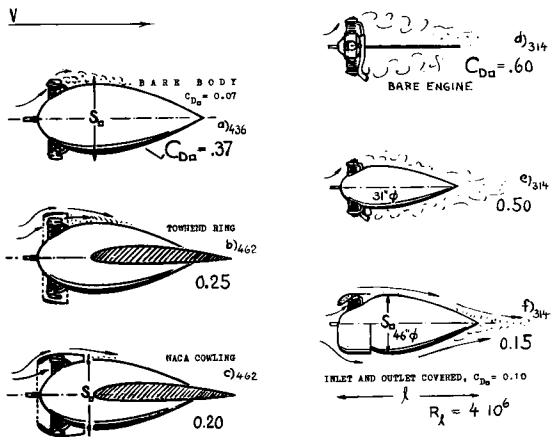


Figure 18. Drag coefficients (on maximum frontal area S_0 as indicated) of radial-engine nacelles in various phases of cowling. References (4,b) and (10,a).

(7) Drag of smooth nacelle bodies:

- Junkers, Tunnel Investigation in Praha (1941).
- Vertical and longitudinal position and angle of setting is found in NACA T.Note 1593 (1948).
- MIT Results, quoted in J.A.Sci. 1941 p.219.
- Boeing Results in "Perkins and Hage" p.97.
- NACA, Thickened Wing Roots, W.Rpt L-390 (1943).

(8) Drag of nacelles as a function of length ratio:

- Arado Wind-Tunnel Tests in Braunschweig 1943, Supplement to Yearbk D.Lufo 1942 p.1,241.
- Smelt-Davidson, Nacelles, ARC RM 2406 (1950).
- Note: Many other "optimum" values are reported in (b), between 0.023 and 0.037, evidently depending on other parameters such as relative size and turbulence stimulation on the surface of wing and nacelle.

(9) Hoerner, Longitudinal Stability Investigation of Ju-288, Rpt Junkers Kobü-Ew 947 (1941).

(10) Drag of radial-type engine nacelles:

- NACA, Radial-Engine Nacelles, T.Rpts 313 (1929, fuselage); 314, 505 (tandem), 506 (on biplane), 507 (pusher type) and 745 (1942, high speed).
- Wood, Tests of Nacelle Combinations in Various Positions, NACA T.Rpts 415, 436, 462 (1932/33).
- NACA, Streamline Engine Nacelles, W.Rpt L-299.
- For vertical position of nacelles see "interference" chapter and NACA T.Rpt 750 (smooth body).
- The Townend Ring, J.Royal Aeron.Soc. 1930; also "Historical Survey" in Aircr.Engg. 1934 p.100.
- Theodorsen, NACA Tech Rpts 592, 595 (nose-slot cowling) and 596, including internal theory.
- Jacobs, Nacelles in VDT, NACA T.Note 320 (1929).
- ARC, Wing-Nacelle Interference, RM 1414 (1930).

(b) DRAG OF DUCTED NACELLES

Cowlings. Figure 18 shows design and drag of radial-engine installations. It is seen that the coefficient of the bare engine (supported in the wind tunnel on a sting) is not very much reduced by adding the nacelle body "e"; although configuration "a" shows a more favorable result. Around 1930, efforts were, therefore, made to reduce the drag by means of fairings or cowlings placed around the protruding cylinders. The so-called Townend Ring ("b" in figure 18; see also in references 10,e,f), similar in shape and effect to the ring surfaces presented near the end of Chapter III, reduces the total drag of a nacelle between 30 and 50%. A still greater reduction of drag (and an improvement of cooling characteristics) is obtained by the NACA cowling ("c" and "f"). Almost entirely hiding the engine, this type cowling eliminates between 80 and 90% of the external drag caused by the protruding cylinders as in "a" and "e" of the illustration. Note that in all the results presented on radial engines, their internal drag is included. The magnitude of that drag component is shown in Chapter IX, as a function of "K" and $(\Delta p/q)$. Very roughly, a component of $\Delta C_{D_a} = 0.1$ may be assumed to represent the average internal drag of cowled radial engines.

Wing Interference. Two of the nacelles shown in figure 18 are mounted on a wing, thus including a certain increment due to interference. Figure 19 presents the drag characteristics of other types of mountings, above and below the wing. Because of the plump nacelle shape and strong interference effects, the drag is very much increased in all positions at the suction side of the wing, particularly for the

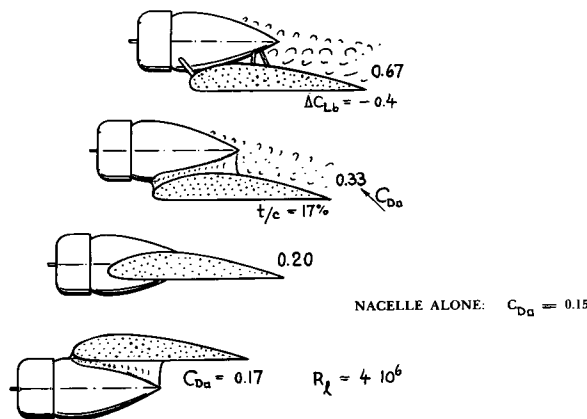


Figure 19. Drag of several radial-engine installations, demonstrating interference with wing (10,b).

rough type of strut mounting. It should also be noted that the ΔC_L values are negative in all examples quoted, including positions on the suction side of the wing, where theory (Chapter VIII) rather expects a positive increment of lift. This type of nacelle produces evidently so much separation that the lift is reduced regardless. The induced drag corresponding to ΔC_L is not of any importance, however, in comparison to the high external (and internal) drag components of this type engine installation. The optimum arrangement in figure 19 is below the wing (where the average dynamic pressure is somewhat reduced, at $C_L = 0.4$ as tested).

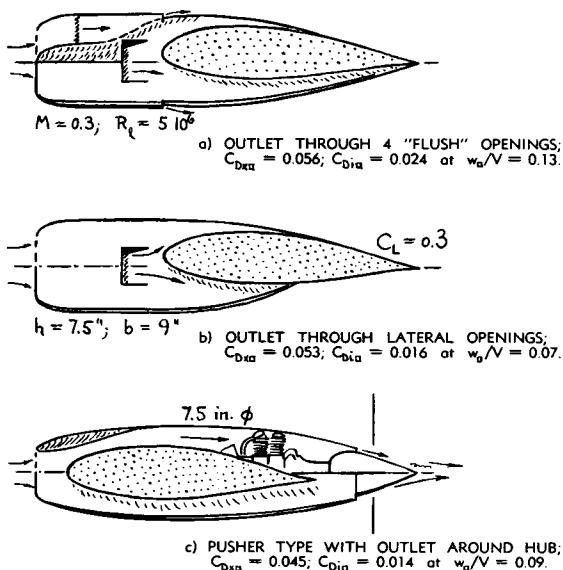


Figure 20. Drag coefficients of several nacelles, varying in type and location of the outlet (10,c).

Inlet — Outlet. Because of the short distance between engine and propeller, the original NACA cowling has a comparatively bluff shape (which is no longer suitable for today's faster flying speeds). Another reason for external drag coefficients appreciably higher than those of solid nacelle bodies, is evidently the presence of the outlet at a location likely to be sensitive with regard to interference drag (causing pressure drag at the rear of the nacelle). Figure 20 shows results on slender nacelles with several outlet modifications. Form "a" has the discharge concentrated in two pairs of outlets; form "b" has only lateral outlets. Configuration "c" has outlets around the hub of the pusher propeller. This last nacelle has an external drag coefficient comparable to those of smooth and solid streamline nacelle shapes (as presented for example, in figure 17).

Jet Engines require a flow more or less straight through the nacelle. For them, mid-wing installations are therefore more problematic than for reciprocating engines, with respect to the wing's spar which cannot very well be cut out to permit the engine duct or the whole jet engine to be installed. Two solutions of this problem have been developed. One is the installation of a pair of engines, one in each wing root (with the structural members "wrapped" around). Reference (7,e) proves that arrangement of engines, partly within the fuselage and mostly in a thickened and lengthened wing root can be accomplished with some appreciable reduction of the drag due to the engines, as compared to the installation in a pair of nacelles. The other method, of adding 2 or 4 jet engines, is to support each of them by a "neck" or "pylon" below and more or less ahead of the wing. The information given in the later section on "external stores" suspended from the lower side of the wing may be applied to engines installed in this manner.

Lift. All drag coefficients of fuselages and nacelles, presented so far in this chapter, are approximately minimum values for each configuration, as far as the lift of the wing is concerned on which they are mounted. The drag coefficients listed are usually applicable for lift coefficients C_L between 0.2 and 0.3. Figure 21 shows how the drag of and due to nacelles varies as a function of lift. Mid-wing configurations have an optimum lift coefficient (where $C_{D_{nac}}$ is minimum) in the order of $C_L = 0.2$. Low-wing nacelles show drag coefficients increasing with lift coefficient, while the coefficient of underslung types may somewhat reduce as C_L is increased. — The variation due to lift has evidently two components, a parasite part (caused by boundary-layer growth and separation) and an induced component (which may or may not be constant, depending upon configuration and the variation of the flow pattern due to separation, if any).

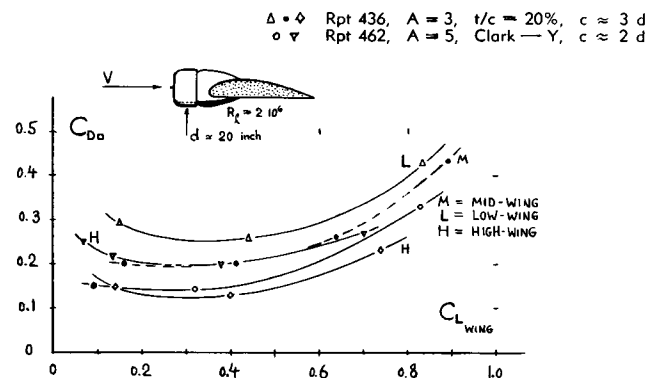


Figure 21. Drag coefficient $C_{D_{nac}}$ of engine nacelles as a function of the lift coefficient of the wing on which they are installed (10,b).

3. DRAG OF FLOATS AND BOAT HULLS

In regard to their aerodynamic drag, flying-boat hulls, and floats are similar to fuselages. However, since their lower side is specifically designed for the purpose of taking off from, and landing on water — the drag of these bodies is somewhat higher than that of comparable streamline or fuselage bodies.

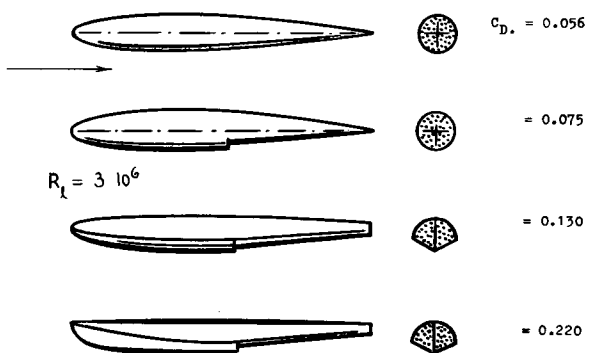


Figure 22. Drag of a float (12,a) developed from a basic streamline body by adding step and chines.

Chines. Figure 22 shows how the aerodynamic drag of a float growth upon developing its final shape from that of a basic streamline body of revolution. It is seen that the addition of the sharp chines (needed to make the bottom effectively planing on the water) increases the drag appreciably. Because of the sharp deck line in their forebody, the drag coefficient of floats can be several times as high as that of the basic body. A well-rounded deck (in the third shape of figure 22) may keep the drag within acceptable limits, however. Figure 23 proves that the drag increment due to chines is comparatively less in flying-boat hulls.

- (12) Aerodynamic drag of seaplane floats:
 - a) Diehl, Navy Yard, "Engineering Aerodynamics".
 - b) Cowley, Model Tests for "Schneider Trophy" Contest, ARC RM 1296 through 1299 (1928).
 - c) Floats and Boats, Luftwissen 1939 p.101.
 - d) NACA, Full Scale, W.Rpt L-238, presents Coefficients between $C_{D_0} = 0.15$ and 0.21; $C_{D_A} = 0.04$ and 0.06.
- (13) Aerodynamic drag of flying boat hulls:
 - a) Smith and Allen, Review on Flying Boats, including data from NACA T.Notes 1305 to 1307 and 1686, T.Rpts 766 and 1144; ARC RM 2896 (1954).
 - b) Aerodynamics and Hydrodynamics, NACA T.Rpt 766.
 - c) Riebe and Naeseth, Refined Flying Boat Hull, NACA Tech Note 2489 or Tech Rpt 1144.
- (14) Drag of steps on seaplane hulls:
 - a) Hartman, NACA Technical Note 525 (1935).
 - b) Diehl, NACA T.Rpt 236; also quoted in his "Engineering Aerodynamics" p.290.
 - c) See results on floats in reference (12,b).
 - d) Hamilton Flying Boats, ARC RM 2899 (1956).
 - e) ARC Rpts: RM 2708 (1945) 2834, 2896 (1955).
 - f) NACA, Tech. Notes 1307 (1947) and 2762 (1952).

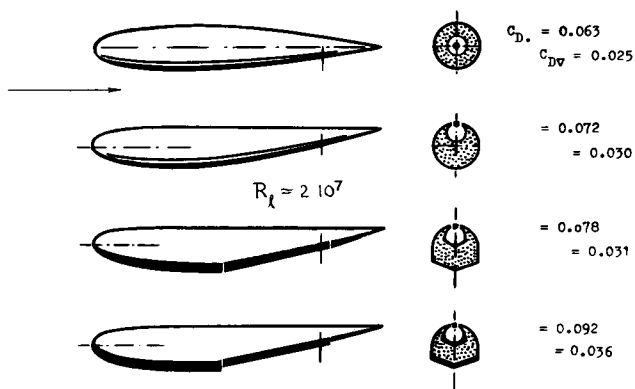


Figure 23. Drag of flying-boat hull (14,a), developed from streamline body having same length and same displacement.

Fineness Ratio. Figure 24 presents the drag coefficient (on frontal area) of a series of smooth seaplane hull models as a function of their fineness ratio (defined in equation 1). The optimum ratio with respect to drag on frontal area, seems to be in the vicinity of 5. Based on $(volume)^{2/3}$, a minimum drag coefficient is obtained at $l/d \approx 9$, corresponding to $l/b \approx 13$ in the hull family tested. Modern development of flying boats tends toward comparatively high length/beam ratios, up to 20 or even higher (not to be confused with the l/d ratio). A considerable increase of the height ratio (h/b) to the order of 3 and higher goes hand in hand with that development; and this increase makes wetted area and frictional drag larger than those in a comparable streamline body of revolution.

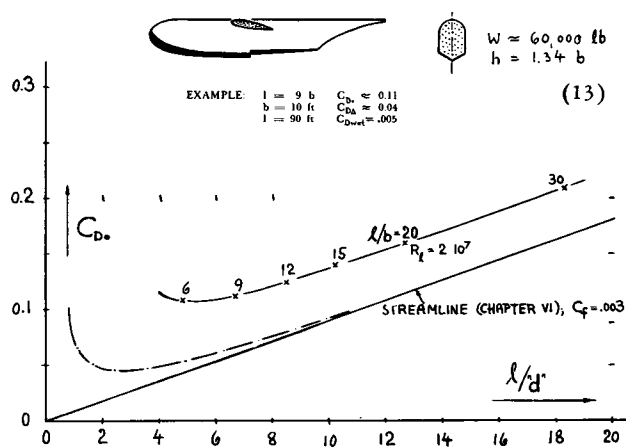


Figure 24. Drag coefficient of a series of flying-boat hulls as a function of their fineness ratio l/d .

Steps. Steps cut into the lower side of floats and flying boats are necessary to break the suction of the water, and to keep the airplane balanced at angles of attack desirable for short take-off. The drag of these steps, plotted in figure 25, can be calculated in

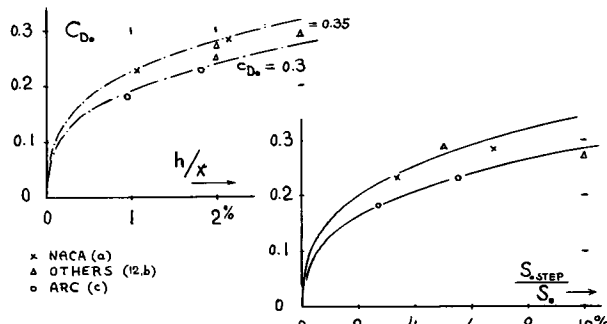


Figure 25. Drag coefficient of and due to steps (14) in the bottom of floats and flying boats; (a) as a function of height ratio (x = distance from nose) and (b) against frontal area ratio.

a way similar to that of sheet-metal joints. Selecting from the material presented in Chapter V, an "independent" coefficient $c_{D_0} = 0.2$, the drag coefficient of steps (based on frontal step area) is suggested to be

$$C_{D_0} = 3 \sqrt[3]{(h/x)} \cdot 0.2 = 0.6 \sqrt[3]{(h/x)} \quad (8)$$

where h = height of step and x = distance between body nose and step. Drag coefficients in figure 25, recalculated from experimental results on floats and hulls, are some 50% higher than the theoretical value. The increment is evidently caused by interference originating behind the step along the rear of the boat body. Part "b" of figure 25 presents the same drag coefficients as a function of the frontal area ratio.

Step Fairing. During flight, the step is not needed. By deflecting a flap or by any other mechanism, the step may therefore be faired, after taking off. *Figure 26* (shape "c") shows that most of the step drag can be eliminated in this way. The attempt shown as number "b", "streamlining" the step in the plan form, is not very successful. Another method of eliminating the step drag is proposed in (13,c). Both body and bottom of the hull terminate together in a vertical edge, while the afterbody is replaced by a "boom", high in the air. The low drag coefficient of this type hull (in the order of $C_{D_0} = 0.045$) is also brought about by elimination of wetted area.

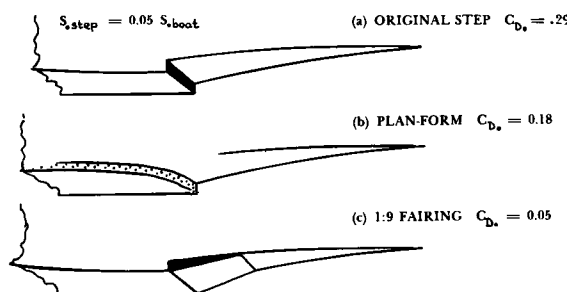


Figure 26. Variation of step drag coefficient due to shape and fairing (14,d).

4. DRAG OF LIFTING SURFACES

Principles of drag due to lift are presented in the "lift" chapter; and the parasitic drag of airfoil sections is treated in the "streamline" chapter. All that is left to be considered here is, therefore, a number of supplementary items (such as the drag of tail surfaces) and the drag caused by devices such as brake flaps.

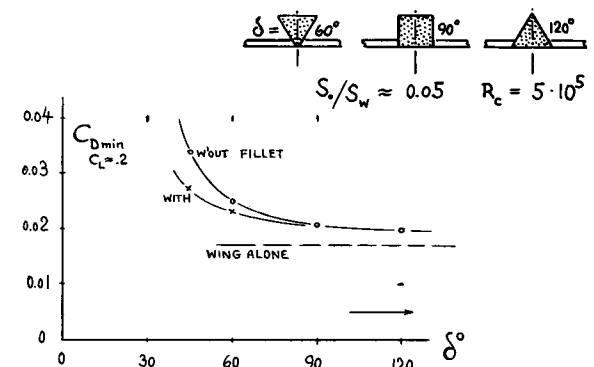


Figure 27. Drag of a wing-fuselage configuration as a function of the angle along the wing roots (15).

Interference Drag. The parasitic interference along the wing roots is among others a function of the angle in the corner between wing and fuselage wall. *Figure 27* shows that the drag increases considerably as the angle δ is decreased below some 90° . — The extensive and systematic investigations in (16) have often been quoted and evaluated, showing the influence of shape, relative position and that of fairings (fillets) upon the drag of wing-fuselage combinations. Interference is, of course, particularly strong at higher lift coefficients. *Figure 28* shows the variation of the parasitic drag (obtained after subtracting $C_{D_0} = C_L^2 / \pi A$) at a lift coefficient $C_L = 1$, as a function of the vertical location of wing against fuselage. The lowest drag is obtained in mid-wing arrangement (or slightly above) where 15% of the wing area is covered by the fuselage body. The parasitic interference drag is largest in low-wing condition, where an expanding passage is formed between fuselage and the rear of the wing's suction side. A lesser peak of interference drag is found in the high-wing configuration. Both the high-wing and particularly the low-wing drag can appreciably be reduced by means of suitable fillets, design instructions for, and aerodynamic characteristics of which are given in (16).

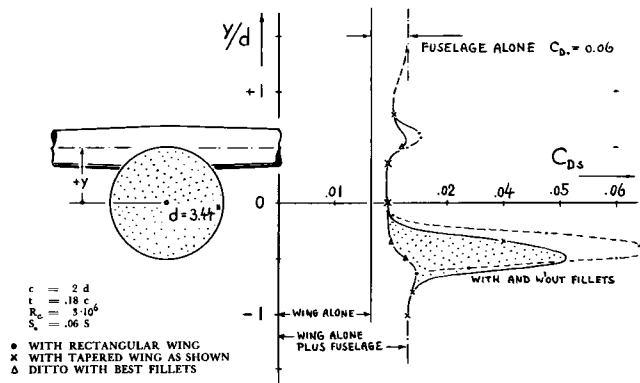


Figure 28. Parasite drag coefficient of a wing-fuselage configuration at $C_L = 1.0$, evaluated from (16).

Dive Brakes are desirable in the tactical operation of military airplanes (as glide-path control or when approaching a target in "stuka" fashion), reducing their speed to values which can be considered to be safe with regard to their operation and/or structural strength. An effective means of providing high drag coefficients is the flat plate, with C_{D_0} roughly between 1.2 and 2.0. Attaching such a plate or flap to the wing of an airplane, presents certain problems, however. One of these is the balance of the airplane (avoiding a change in longitudinal trim). Most wing-brake configurations have, therefore, a pair of "flaps", one above and one below the wing section (see figure 30).

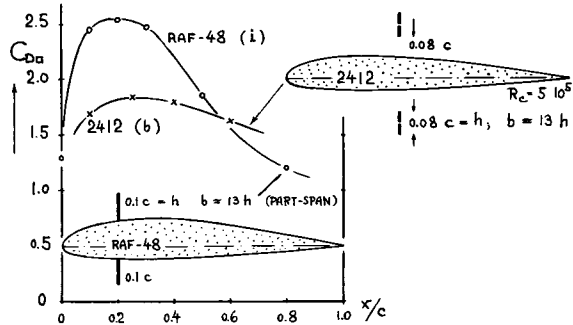


Figure 29. Drag coefficient of 2 pairs of dive brakes (18) as a function of their location on wing chord.

Results reported in (18,i) suggest, however, that "brake" flaps on the lower wing side (at a location comparatively far forward) can also perform to satisfaction, when used for glide-path control and when an increase of the lift coefficient is desirable.

Brake Location. Figure 29 shows that maximum effect is obtained near maximum thickness of the wing section, where local dynamic pressure and interference effects are largest. The thickness of the wing section also contributes directly to the effect. If one refers the drag to the "total" projected area corresponding to a height equal to $(2h + t)$ where t = section thickness, one obtains a roughly constant maximum coefficient in the order of $C_{D_0} = 1.3$ for solid brake flaps, a value which is slightly higher than that of three-dimensional plates in free flow. The whole space between the outer edges of the plates is evidently "wake" in this case; the drag of a pair of brake flaps increases accordingly with the wing's thickness ratio. Perforated flaps or flaps having a gap between them and the wing surface, do not follow this rule, however. Among the configurations shown in figure 30, "a" and "c" (with the brake flaps located near the wing's trailing edge) have comparatively small drag coefficients. The low drag of a TE flap (tested in two-dimensional flow) is explained in figure 35 of the "pressure-drag" chapter. It shall be mentioned here that two-dimensional investigations (be-

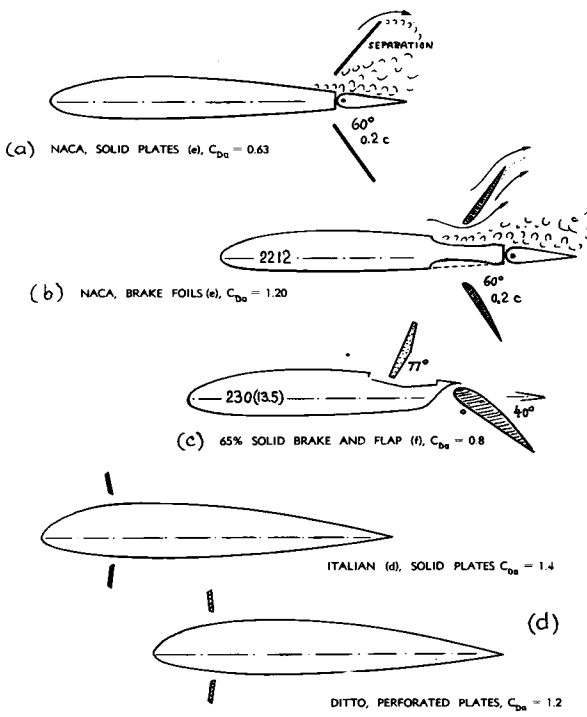


Figure 30. Drag coefficient (on sum of "flap" areas) of various types of wing brakes (18), all part span.

- (15) Muttray, Low-Wing Configurations, Erg AVA IV p.89; Lufo 1928 p.33; Ringbuch Luftf.technik IA4.
- (16) NACA, Investigation of Wing-Fuselage Combinations:
 - a) Tech/Rpts 540 and 575, from 1935.
 - b) Tech/Notes 641 and 642, to 1938.
- (18) Characteristics of brake flaps:
 - a) ZWB, Wing with Brake Flaps, Rpt. FB 1689.
 - b) Voepel, Yearbk D.Lufo 1941 p. 82.
 - c) Me-109 Investigation at the AVA, 1939.
 - d) Lattanzi, Transl NACA T.Memo 1161 (1949).
 - e) Toll and Ivey, NACA W.Rpt L-56 (1945)
 - f) Purser and Liddell, NACA W.Rpt L-549 (1942).
 - g) ARC, RM 1864 (1939), 2211 and 2689 (1948).
 - h) NACA, Spoiler Ailerons, T.Rpt 1034 (1950).
 - i) Davies-Kirk, Air Brakes, ARC RM 2614 (1951).
 - k) ARC, Plates and Brakes, C.Paper 251 (1956).

tween tunnel walls) are of lesser practical importance, since flow conditions in full-scale brake designs are always more or less three-dimensional. A comparatively effective arrangement is the number "b"; its drag coefficient is almost twice as high as that of the number "a". The difference is suggested to be in the flow pattern as indicated in the illustration.

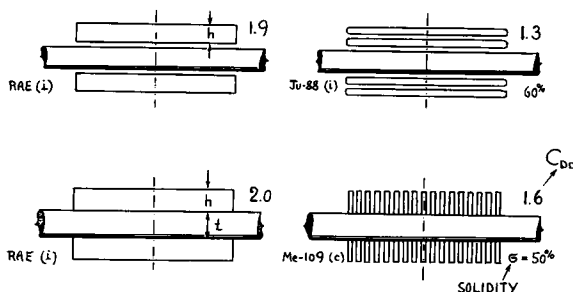


Figure 30a. Drag of and due to dive brakes (18); solid flaps (left side); latticed and rake-type flaps (right side); all part-span; t/c between 12 and 14%; x/c between 30 and 40%.

Pervious Flaps. A vortex street originates behind plates in two-dimensional (or similar) flow (as pointed out in Chapter III). Extending solid flaps from the upper and lower surface of a wing can, therefore, cause heavy vibrations, on the flaps themselves and on the affected wing parts (ailerons and landing flaps). In addition, the wake originating behind the flaps possibly interacts with the horizontal tail surface of the aircraft (buffeting). All these troubles disappear, however, after employing flaps that are perforated or which are otherwise divided into a number of strips or smaller parts. The size of the vortices behind such pervious flaps corresponds to that of the elements. The general pattern of the wake is, therefore, more that of an irregular turbulent flow. — The drag of pervious sheets is basically treated in Chapter III. Figure 30,a gives some information on the drag of lattice- and rake-type dive-brakes in comparison to that of solid flaps. The drag coefficient (on flap area S_{fl}) of and due to a pervious flap is somewhat smaller than that of the solid type (in three-dimensional flow). The shape of the elements forming latticed or rake-type "flaps" has an influence upon

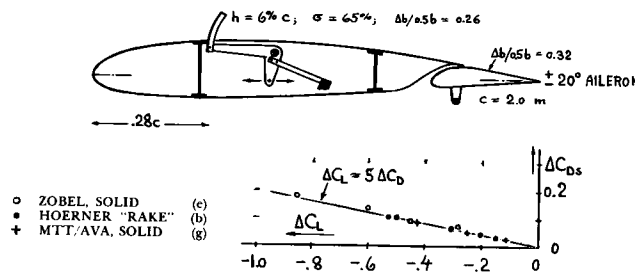


Figure 31. Variation of lift produced by spoiler "flaps" (19). Drawing shows experimental installation of a rake-type spoiler system (19,b) in the Ju-88 bomber.

their drag. The most efficient cross section of a "strip" (giving maximum coefficient C_{D_s} ; on blocked area) is that of a "fold", with the open side against the stream (19,b).

Spoiler Control. The rake-type brake devices in figure 30 can also be used in the spoiler-type roll control of airplane wings, replacing the standard type ailerons (19). Figure 31 shows the arrangement of one such design using a "rake" form of spoiler. For small values of the drag coefficient C_{D_s} , caused by skin-friction and boundary-layer growth (in two-dimensional flow) theory (19,a) expects a variation of the lift coefficient in the order of

$$\Delta C_L = -7.5 C_{D_s} \quad (9)$$

Spoiler tests have been evaluated (by taking into account the induced drag which reduces appreciably after the lift coefficient has dropped). The graph in figure 31 shows a variation of lift coefficient associated with the variation of section-drag coefficient produced by extending a spoiler from the wing's suction side, similar to that as indicated by equation 9. The constant is "5", however, instead of "7". Increased parasite drag in connection with decreased lift in one side of a wing means yawing moments in the direction of a turn which an airplane may perform by utilizing spoiler control. Tunnel experiments and a full-scale experimental application, described in (19,b), indicate that a control system superior to that of ordinary ailerons (avoiding any time delay as found in other spoiler applications), is found in the combination of a rake-type spoiler with a pair of comparatively short ailerons of the conventional type.

Tail Surfaces. Chapter V gives information on the drag caused in tail surfaces by the gap necessary to permit deflection (and balance) of the elevator and rudder, respectively. Also, the detrimental influence of the fuselage upon the induced effectiveness of the horizontal tail is described in the "interference" chapter. Examination of various experimental results indicates an average basic drag coefficient of tail surfaces in the order of $C_{D_s} = 0.01$ within the range of $C_L = \pm 0.2$, and for deflection angles within $\pm 5^\circ$. — Horizontal as well as lateral tail surfaces are not really "producing" lift. It may rather be said that elevator or rudder is deflected in most operations, in order to reduce the lift of the respective surface. Only then can the airplane assume the extreme positions of "tail-first" landing and sideslipping, respectively — while stabilizer or fin, respectively, is at an angle of attack opposing the direction of motion. To say it in other words, the horizontal tail has usually a *positive* (upward) lift force during a three-point landing operation; stabilizer and elevator are thus "fighting" each other, so to speak.

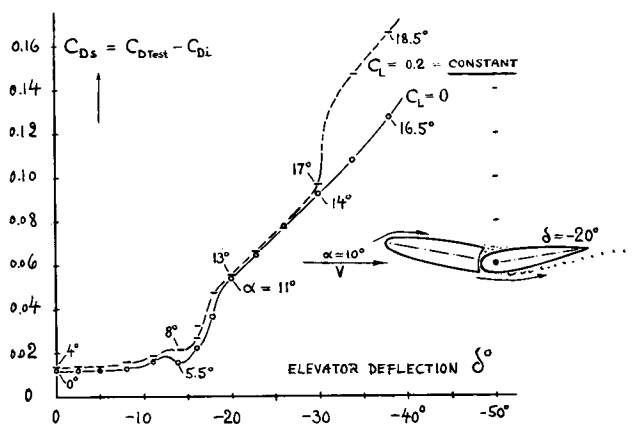


Figure 32. Variation of section drag coefficient of a horizontal tail surface (21) at constant C_L .

Elevator Deflection. Figure 32 presents the parasitic or sectional drag coefficient of a horizontal surface (obtained after subtracting from the tested total drag the calculated induced drag), plotted against the elevator angle for two constant lift coefficients ($C_L = 0$ and $= + 0.2$). Note that while deflecting the elevator, the angle of attack of the stabilizer is changed so that $C_L = \text{constant}$. Four phases can be observed in the illustration. Between plus and minus 12 or possibly 15° elevator (or rudder) deflection, the flow is fully attached. Between minus 12 and 18°, flow separates from the suction (lower) side of elevator (or rudder). Beyond some -19° , drag continues to increase when further deflecting the elevator (or rudder). Then, at some -30° elevator (or rudder) angle, for a lift coefficient $C_L = + 0.2$, flow separation also takes place from the suction (upper) side of the surface; drag increases correspondingly. As an example, a

horizontal tail may be considered, with the elevator 30° up, while the stabilizer is at a positive angle of attack between 10 and 15°. For an assumed resultant lift coefficient equal to zero, figure 32 then indicates a coefficient in the order of $C_{Ds} = 0.09$, a value which is some 9 times the basic section-drag coefficient as mentioned above.

Asymmetric Engine Power. When flying a twin-engine airplane with one propeller stopped (because of engine failure), the moment due to the remaining one-sided thrust must be compensated by a suitable deflection of the rudder. The lateral tail force required is obviously

$$|F_{lat}| = |\text{thrust}| (y/x) = |\text{drag}| (y/x) \quad (10)$$

where "x/y" is the ratio of the tail's moment arm ("x") to that of the propeller ("y"). Applying the induced-drag equation (Chapter VII) to both the vertical tail and the wing of the airplane, the induced drag ratio is found to be

$$\frac{D_{ilat}}{D_{iwing}} = \left[\frac{F_{lat}}{T} \right]^2 \left[\frac{D}{L} \frac{b}{h} \right]^2 = \left[\frac{y D b}{x L h} \right]^2 \quad (11)$$

where h = effective height of the vertical tail surface. To give an example, $x/y = 3$; $D/L = 0.1$; and $b/h = 3$ may be assumed. The induced drag ratio is then in the order of 10%. As explained in (22), the airplane is necessarily sideslipping in the maneuver considered. Therefore, some additional drag originating in fuselage, engine nacelles and in the tail surfaces must also be expected.

-
- (19) Characteristics of wing-flow spoilers:
 - a) Theory of lift as a function of b'layer: ZFM 1932 p.277, 1933, p.439; Lufo 1934 p.26; Schlichting in "Boundary-Layer Theory" 1954.
 - b) Hoerner, Development of Spoiler-Control System, Dr.-Ing. Thesis Tech Hochschule Berlin 1941.
 - c) British ARC, RM's 1251, 2319, 2491, 2586.
 - d) NACA Tech Rpts 439, 443, 494, 517, 602, 605, 664, 706; Tech Notes 1015, 1079, 1123, 1245, 1294, 1404 and 1409; J.Aeron.Sci. 1950.
 - e) Kramer-Zobel (DVI) German Docs ZWB FB 583 (1936), FB 964 (NACA T.Memo 1307) and FB 1304.
 - f) V.Doepp, Junkers Rpt S.387 (1941).
 - g) Messerschmitt, Spoiler, ZWB Rpt UM 7860 (1944).
 - (21) Goethert, Experimental Results of Horizontal Tail Surfaces, Ringbuch Lufo Section IA 13 (1940), on the basis of ZWB Rpts FB 552, 553 and 953.
 - (22) Flight on asymmetric engine power:
 - a) Wright, Aircraft Engineering 1950 p.350 & 374.
 - b) Jones, Sideslip Performance, ARC RM 1455 (1932).

5. DRAG OF LANDING GEARS

Landing gears are made retractable in all modern high-speed airplanes. The drag of fixed "under-carriages" used in old-type, and still used in small and slow airplanes, is avoided in this manner. However, in taking off and in landing, airplanes have to have their landing gear out, so that aerodynamic consideration of the devices needed for moving along the ground is still important.

Reference Area. The drag coefficient of airplane wheels and landing gears may conveniently be based upon the area S_{d} , equal to tire width times outer diameter. Referring the drag of fairings, wheel forks and struts, and that of whole landing gears to that area (or to the sum of the wheel areas, respectively), the size of these parts and their drag is properly considered to be proportional to wheel- and tire size.

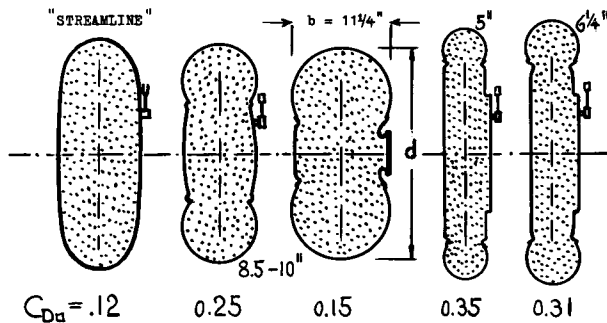


Figure 33. Drag coefficients (based on area $b \cdot d$) of several airplane wheels (25), tested at $R_d \approx 2 \cdot 10^6$.

Wheels. Figure 33 presents drag coefficients of several types of bare wheels. Their drag can appreciably be reduced by covering the sides or by giving the "hub" such a shape that the sides are no longer hollow. Attempts are made in (25,a) of reducing the drag of wheels by placing a streamline housing around them. Although the shape is improved in this way, the frontal area is increased, of course; $C_{D_a} = 0.14$ was tested for a typical shape. Figure 35 presents an example where a wheel housing is comparatively beneficial (reducing the interference drag between wheel and struts). Figure 34 demonstrates how the drag of wheels (defined as total drag minus drag of the struts "alone") is increased because of interference through the adjoining landing-gear struts.

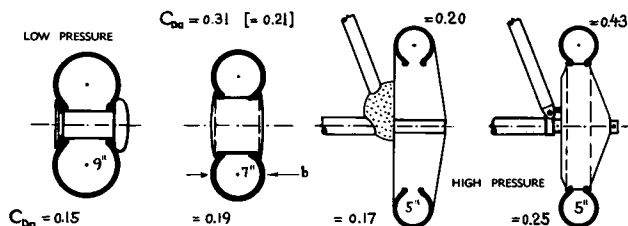


Figure 34. Drag of and due to wheels (25,e). The bracketed value is for faired junction; coefficients in the lower line are for wheels alone.

Fixed Gears. Among the non-retractable landing gears shown in figures 35 and 36, the single-strut gears have the least drag. Combining the wheel housing with that of the strut, the "trouser" type designs give adequate space for the shock-absorbing mechanism of the strut, with aerodynamic drag coefficients still smaller than those of the multiple-strut designs. The latter's drag is high because of interference between wheels and struts (see figure 34) and also between struts, fuselage and/or wing. Landing gears extending from the lower side of engine nacelles have shorter struts or "trousers" respectively. Figure 36 indicates, however, that their drag is approximately the same as without nacelle; interference is obviously stronger in the nacelle configurations.

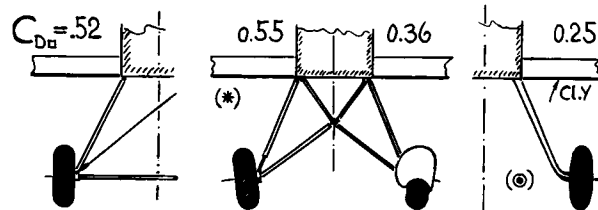


Figure 35. Drag coefficients of several landing gears designed for a 3000 lb airplane (25,a). Wing chord $c = 7.2$ ft; $R_c = 5 \cdot 10^6$. All struts streamline with $t/c = 1/3$; (*) with round tubing has $C_{D_a} = 1.30$. "Standard" 8.5×10 inch tires with 25.3 inch outer diameter, except for (◎) which is "streamline".

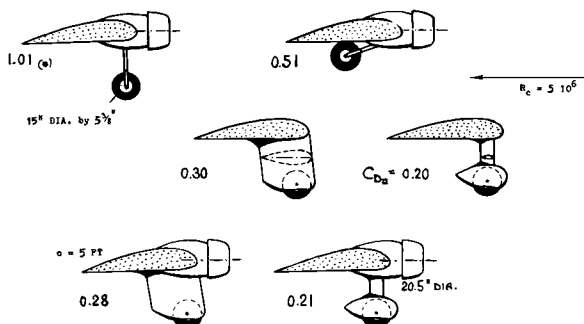


Figure 36. Drag coefficients (on wheel area S_{d}) of a landing gear designed for a 16,000 lb. airplane (25,a); (*) this coefficient is believed to be subcritical with respect to the R' number of the circular strut.

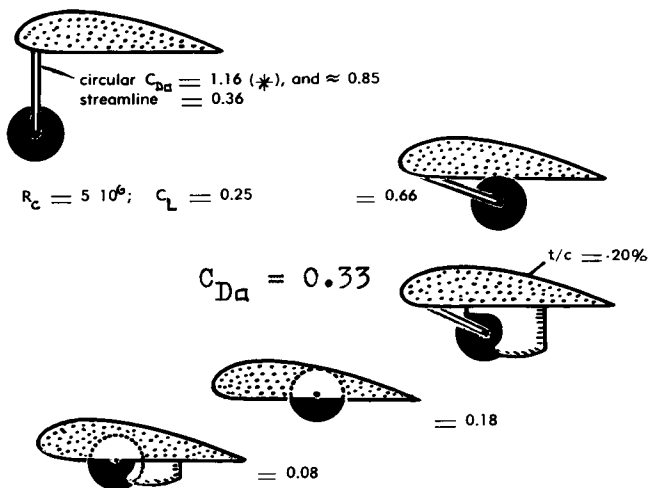


Figure 37. Drag of partly retracted landing gear (25,a), represented by coefficients on wheel area "S_D"; (*) this coefficient most likely applies to subcritical flow conditions; the value 0.85 is estimated for supercritical R'numbers.

Retractable Landing Gears (it seems) are often designed without much care for the aerodynamic shape in the extended position. The drag coefficient (based on wheel area) is in the order of $C_{Dg} = 0.6$ or 0.8, as indicated in figures 37 and 38, for configurations built with cylindrical struts. These values do not even include the openings in the wing, the fuselage, or the nacelle, respectively, necessary to receive the gear in the retracted position. Considering an example with an assumed coefficient $C_{Dg} = 0.8$ and a ratio of the area of a pair of wheels to that of the wing of the airplane in the order of 1%, the additional drag of such landing gear in extended position, is found to be between 25 and 50% of an average airplane's parasite drag. Such a component of drag should not be overlooked in the calculation of take-off, gliding-, and landing performance of airplanes. The drag of this type landing gear in lowered position can be (and sometimes is) reduced by giving the struts some streamline shape and/or by closing again the cover flaps of the openings in the skin of the craft, after letting the gear down. It is clear, however, that such a device cannot help shortly after

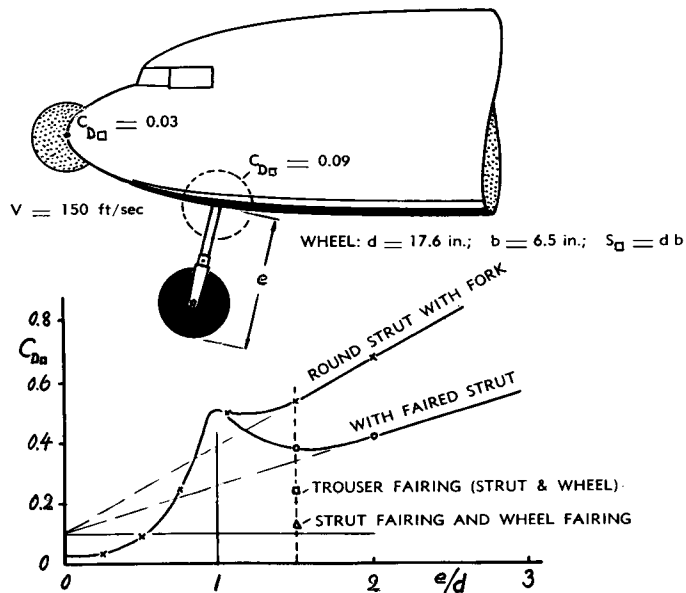


Figure 38. Drag coefficient (on wheel area S_D) of a retractable wheel in the nose of a fuselage (25,a).

taking off, when the gear is being retracted. — *Figure 37* indicates that partly retracting the landing gear, reduces the drag considerably, down to the order of but 10% of that in fully extended position. *Figure 38* shows a critical wheel position (at $e/d = 1$) where the drag reaches a maximum. Generally, part-retraction is not really applied. It is evidently felt, that while employing a mechanism for pulling up the wheels, they should as well be retracted entirely into wing, fuselage or engine nacelle (provided that there is sufficient space available to do so).

Tail Wheels. Simple skids (25,a) used in smaller airplanes, have approximately the same drag as faired tail wheels—if designed to support the same weight. Because of the fork necessary to support tail wheels, their drag is comparatively high ($C_{Dg} \approx 0.6$). *Figure 39* shows that a streamline housing enclosing the wheel as far as practicable, cuts down the drag to half the original value. Sometimes, the tail wheel has also been made retractable. In most of the modern high-speed airplanes, the tail wheel has been replaced, however, by a nose wheel (as in figure 38).

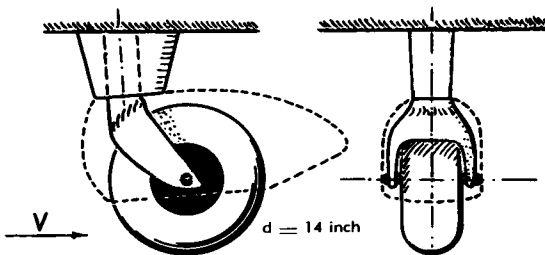
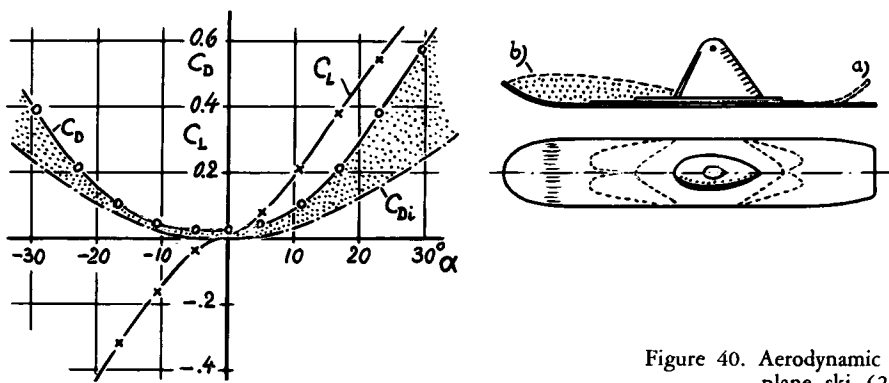


Figure 39. Drag of tail wheel (25,b). Coefficient $C_{Dg} = 0.58$ (without fairing), $= 0.49$ (with rear fairing), $= 0.41$ (with forward fairing), $= 0.27$ (with complete fairing).

- (25) Drag of various landing gears:
 a) Herrnstein-Biermann, Airplane Wheels Fairings Landing Gears; NACA T.Rpts 485, 518, 522 (1934/1935).
 b) Fuchs, Tail Wheel, Heinkel Rpt WK 20 (1937).
 c) ARC, Wheels Undercarriages, RM 579, 1479, 1691.
 d) Evaluations of (a) in Luftwissen 1936 p.188 and in Ringbuch Luftfahrttechnik IA8 (1937).
 e) Bradfield, Wheels and Mudguards, ARC RM 1479.
 (26) Kohler, Airplane Skis, Luftwissen 1937 p.6.



DRAG COEFFICIENTS ON
PLAN-FORM ----- AREA:
MINIMUM: $C_D = 0.03$
DUE TO (a) $\Delta C_D = +.07$
DUE TO (b) $\Delta C_D = -.02$

Figure 40. Aerodynamic lift and drag characteristics of an airplane ski (26).

Skis. Airplane skis present aerodynamic characteristics similar to those of "wings" of extremely small aspect ratio (see in Chapter VII). The aspect ratio of the ski in figure 40 is, for example, $A = b^2/S = 0.19$ only. The drag due to lift corresponding to this ratio, determined through the use of the equations presented in the chapter mentioned, is considerable in comparison to the minimum parasitic drag of such a ski.

6. DRAG OF EXTERNAL LOADS

Loads which cannot readily be stowed within fuselage or wing of airplanes, or which are to be dropped during the flight (bombs) are attached to the outside of aircraft. Their drag is twofold; they have a drag of their own and they cause some interference drag.

Streamline Tanks, employed to carry additional fuel, have usually the shape of streamline bodies. Originally, such tanks were sometimes attached to existing bomb racks, primarily under the wings. Number "j"

in figure 41 shows that their drag is comparatively high in this condition ($C_{D_0} = 0.26$), evidently because of interference effects within the narrow spaces between wing, supporting parts and tank. The purpose of such tanks, to increase the range of the airplane, is thus curtailed to a considerable extent by the added drag. Fairing the bomb rack by means of a sheet-metal collar, somewhat reduces the drag coefficient (see number "i" with $C_{D_0} = 0.13$). The "neck" is obviously too thick in this case, however. The most favorable method of carrying a tank underneath the wing, is that on a streamline pylon (number "n" in figure 41). Figure 42 shows the drag added by the presence of the pylon (increasing with its length); and it indicates one component of interference drag between tank and wing which decreases to zero as the clearance distance is increased to and beyond $y/d = 0.5$. Including the pylon drag, the minimum is found in the vicinity of $y/d = 0.2$ or 0.3 for two of the configurations investigated and in the order of 0.5 for the others. Experimental results in (30,n) indicate that in this type of suspension, tank locations under or ahead of the wing's leading edge (such as they are applied in modern jet engine nacelles) are very favorable (giving drag coefficients in the order of $C_{D_0} = 0.05$, including pylon and interference).

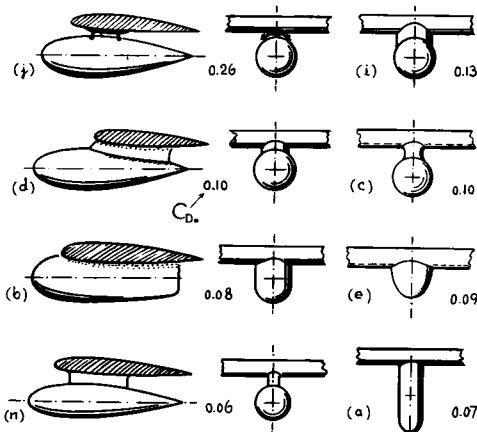


Figure 41. Shape and drag coefficient of various external stores (tanks) mounted under the wing (30).

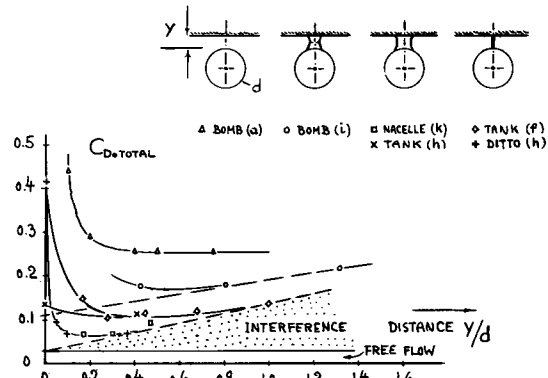


Figure 42. Drag coefficients of several tanks (and bombs) suspended by means of a neck or pylon underneath a wing (30), as a function of the clearance ratio y/d .

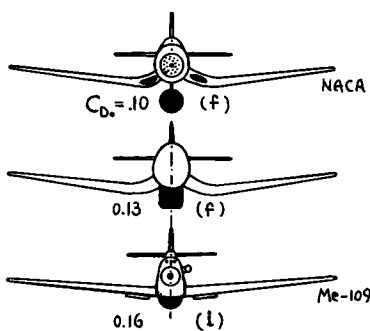


Figure 43. Examples of external tanks under the fuselage of low-wing airplanes (30).

"Belly" Tanks. A "belly" type tank, mounted under the fuselage of the Me-109 is analyzed in Chapter VIII, having a coefficient $C_{D_0} = 0.16$. In addition to this tank, figure 43 presents three arrangements under the fuselage of fighter airplanes, two of them in "belly" form. It is seen that suspension by means of a "pylon" yields a smaller drag coefficient. Generally, the place under the fuselage of low-wing airplanes, does not appear to be very favorable, however, to attach an external tank. Figure 41 "e" shows a "belly" shape mounted under a wing with a drag coefficient of 0.09. Increasing the height to breadth ratio of such tanks, a "nacelle" type is obtained as in "b" of the illustration. Further modifications of this type are reported in (30,a). Minimum drag is found in a shape having a height ratio in the vicinity of $h/b = 5$, approximately as in "a" in figure 41. However, because of its foil-like form, developing lateral forces, such a tank may not be very desirable.

Streamline Arrangements at the upper side of the wing are presented in figure 44. The second form, a low-wing nacelle-type tank, has of course an induced drag component similar to that of "b" or "e" in figure 41. Shifting, however, such a tank to the rear, and giving it a flat and wide "beaver tail" pointing upward (thus eliminating the induced drag component), the lowest drag coefficient ($C_{D_0} = 0.03$) is obtained among all arrangements quoted.

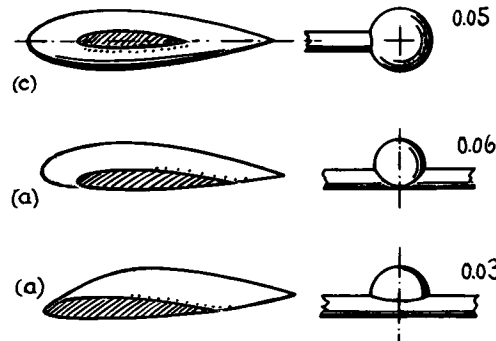


Figure 44. Drag coefficients of tanks (31) attached to the upper side or at the tips, respectively, of wings.

Wing-Tip Tanks. Many modern fighter planes and some other airplanes are equipped with wing-tip tanks. Their influence on effective aspect ratio and induced drag is discussed in the "lift" chapter. Regarding their parasitic drag (at small to moderately large lift coefficients), shape "c" in figure 44 indicates a drag coefficient in the order of $C_{D_0} = 0.05$.

Range. For illustration, a small fighter airplane may be considered with a "drag area" at cruising speed, $f = D/q = (C_{D_0} S) = 8 \text{ ft}^2$ and a regular fuel load " F " = 200 gallons. Through addition of a pair of external tanks with a total of $\Delta F = 200$ gallons of fuel, the range of this airplane may theoretically be increased by 100%. Actually, the tanks increase the drag area by $\Delta f = C_{D_0} S$. Consequently, with " R " denoting the range of the airplane under specified conditions,

$$\frac{R + \Delta R}{R} \approx \frac{1 + (\Delta F/F)}{1 + (\Delta f/f)} \quad (15)$$

Assuming in the considered example a frontal area of each tank $S = 2 \text{ ft}^2$, the range is increased to only ≈ 1.77 times the original value, for an unfavorable tank drag coefficient of $C_{D_0} = 0.26$ (as in figure 41,j). With the most favorable coefficient listed in figure 44 ($C_{D_0} = 0.03$), the range ratio is 1.97, which is essentially equal to the value simply corresponding to the number of gallons aboard.

- (30) Drag of external stores (tanks) under aircraft:
 - a) Russian Catalog, Bombs and Stores, Moscow 1940.
 - b) Dornier, Do-217 External Tanks, Rpt 74, 1940.
 - c) Dornier, Do-217 Flight Test with Tank, 1940.
 - d) Me-264 Wind Tunnel Tests Rpt AVA 42/W/34.
 - e) Owen-Becker-Nogg, Tanks, RAE Rpt 8146.
 - f) Pepper, Auxiliary Tanks, NACA W.Rpt L-371.
 - g) RAE, Drop Tanks on Swept Wing, ARC RM 2951.
 - h) Junkers, Wind-Tunnel Tests on External Tanks Ju-288, Rpts D.6372 and 6633 (1939/40).
 - i) Messerschmitt, 109 Flight Tests, Rpt 16/L/1943.
 - k) Wiesener, Force- and Pressure-Distribution on Combination of Wing with Tank, ZWB Rpt UM 1090 (1943).
 - l) Hoerner, The Drag of Bombs Hung from the Outside of Airplanes, ZWB Rpt UM 7814 (1943).
 - m) Arado, Pair of Jet-Engine Nacelles, LFA 1943.
 - n) Silvers and Spreemann, NACA RM L7K20 (1947).
 - o) Pylon tanks also in NACA RM L50L12 and L51D26.
- (31) External stores at upper side and at tips of wing:
 - a) Hütter, External Store "Doppelreiter" on Upper Side of Wing, Document ZWB UM 4592, 1944.
 - b) NACA, Wing-Tip Tanks, RM A5F02 and L9J04.
 - c) Messerschmitt, Tip Tank, Darmstadt 1943.

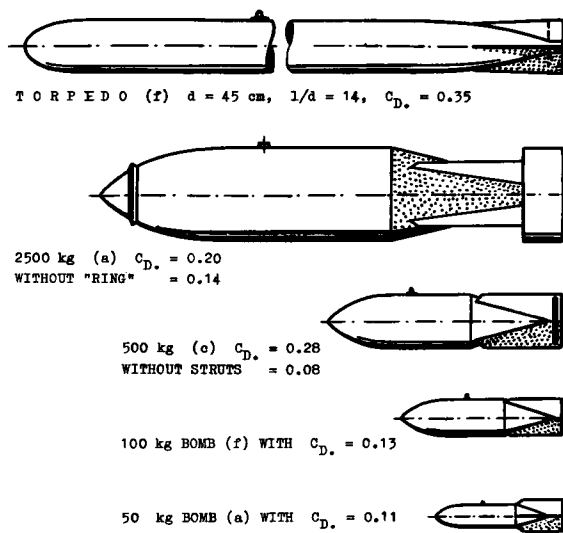


Figure 45. Drag coefficients of bombs and of one torpedo (32) in free flow (at subcritical speeds).

Bombs as such are treated in the "transonic" chapter. In this section here, bombs are primarily considered being carried on the outside of airplanes. Inasmuch as this application is restricted to subsonic speeds, the drag of bombs is presented without accounting for any effects of compressibility. The drag coefficients of bombs in free flow, listed in figure 45, are several times as high as those of comparable streamline bodies. The additional drag is caused by the comparatively bluff shape as well as by fins and other protuberances, such as attachments needed to support bombs under the wing or the fuselage of an airplane. The drag coefficient is at least $C_{D_0} = 0.09$. Bombs with the fins stiffened by means of round struts show values up to $C_{D_0} \approx 0.3$. The additional drag due to a nose ring (favorable to get such a bomb *into* water at the side of ships) is $\Delta C_{D_0} = 0.05$. The drag coefficient of aircraft torpedos corresponds to their length. Figure 45 shows a tested value of $C_{D_0} = 0.35$.

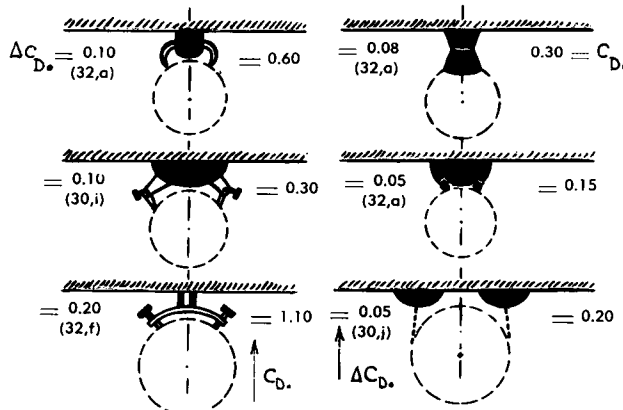


Figure 46. Drag of several bomb racks (and similar devices). The coefficients, of the racks as well (ΔC_{D_0}), and those of the complete configuration (with bombs attached, indicated by C_{D_0}), are based in each case upon the respective bomb's frontal area.

Bomb Racks. In order to support a bomb and to keep it safely in place, a rack is needed. After dropping the bomb, the rack usually remains exposed to the air stream. The drag of such racks is comparatively high. Based on frontal area of the bomb which the rack is designed to carry, figure 46 shows drag values which are in the same order as those of the bombs themselves. The drag of the protruding parts can be estimated on the basis of their frontal area and the following drag coefficients:

for streamline fairings around rack $C_{D_0} = 0.1$
for arms (rods and other blunt parts) $C_{D_0} = 1.0$

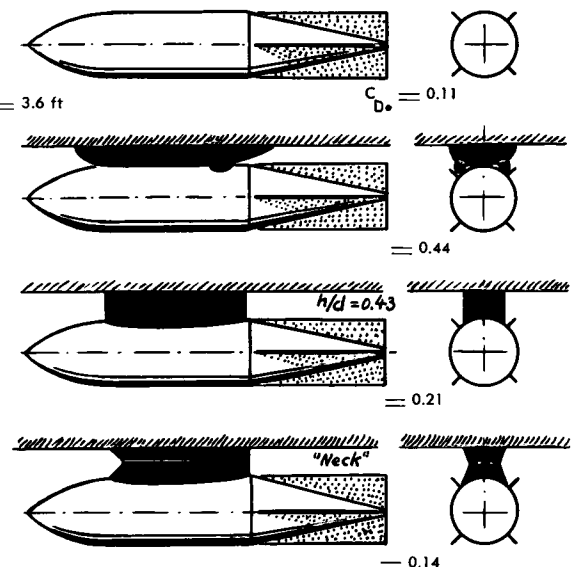


Figure 47. The drag coefficient of a 50 kg bomb (32,a) in combination with various racks or necks, respectively.

Neck Suspension. Figure 47 shows several methods of suspending a bomb under a wing or fuselage. The additional drag of a bomb rack and due to the interference between this rack, the bomb and the wing, is in the order of $\Delta C_{D_0} = 0.3$. The most favorable type of suspension is by means of a neck or pylon; the minimum drag increment caused by such an arrangement corresponds to only $\Delta C_{D_0} = 0.03$.

Interference Drag. Basically, bombs (with higher drag coefficients) cause an interference drag which is larger than that due to tanks (having lower drag coefficients). In regard to the angular position of bombs (or tanks) against the lower side of the wing (or the fuselage respectively), the smallest total drag is found in the vicinity of $\Delta\alpha = -3^\circ$ (measured against wing chord); that is, with the tail of the bomb somewhat closer to the adjoining wing side than with the nose. If placing two or more bombs (or nacelles or external stores) closely beside each other, their drag may be increased because of mutual interference.

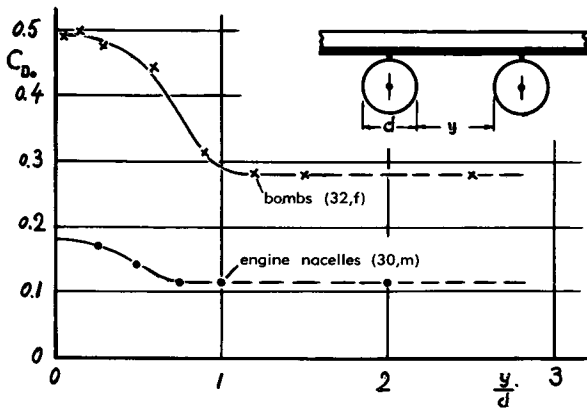


Figure 48. Drag coefficients of pairs of bombs and tanks (or nacelles), respectively, as a function of their lateral distance.

However, beyond a lateral distance of approximately $e = d$, figure 48 does not show interference any longer. Placing, on the other hand, two bombs behind each other, their total or average drag coefficient is reduced; as can be seen in figure 49. Within the wake of the forward bombs, the drag of the rear bombs is evidently smaller than in unobstructed flow.

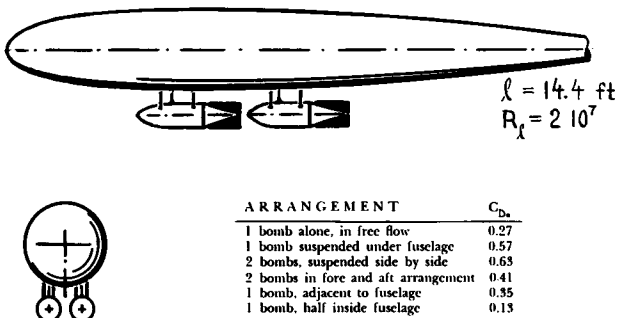


Figure 49. Drag of bombs in several arrangements, suspended under the fuselage of an airplane (32,e).

7. DRAG OF MISCELLANEOUS PARTS

(a) Drag Of Cylindrical Parts

Drag characteristics of circular (and other) cylinders are treated in Chapter III, as a function of Reynolds number, surface roughness and angle of inclination. Certain applications in aircraft are discussed as follows.

Fairings. Gun barrels sticking out of bombers, in directions crosswise to the air flow, present considerable drag due to their cylindrical shape, particularly in the range of Reynolds numbers below transition. These drag forces may also curtail handling and aiming of the guns, because of the moment about the center of their rotation. Figure 50 shows some attempts of reducing the drag of cylindrical bodies by adding fairings to their rear side. The results are small, however; the gap in the surface between cylinder and fairing, and the bluff shape of the half-cylindrical nose, evidently prevent the flow from getting sufficiently far attached to the rear of the fairings. Similar results are obtained using sleeve-type fairings, presented in figure 51. Sleeves can be attached in such a manner that they adjust themselves automatically to the direction of the air flow when applied to gun barrels or other aircraft equipment. By increasing the chord of the fairing and/or by thickening the trailing edge (as described in Chapter III) it is furthermore possible to increase the critical Mach number (see Chapter XV) from ≈ 0.55 to ≈ 0.70 in the shapes presented in figure 51.

FAIRING	$C_{D, SUB}$	$10^5 R_{crit}$	$C_{D, SUPER}$
→ (+) NONE	1.20	1.5 TO 4.0	0.40
→ (+) CONE	0.88	2.5 TO 4.0	0.32
→ (+) TAPERED CONE	0.80	2.0 TO 3.5	0.29
→ (+) TAPERED CONE	0.82	2.0 TO 3.5	0.24
→ (+) TAPERED CONE	0.73	1.50 TO 3.0	0.16
→ (+) TAPERED CONE /gap	0.95	1.0 TO 2.0	0.24
→ (+) TAPERED CONE /gap	?	?	0.13
STREAMLINE	0.35	0.5 TO 1.0	0.05

Figure 50. Influence of various fairings on drag of circular cylinder (35,a), at R' numbers above transition.

- (32) Drag of bombs, attached to aircraft:
 - a) Heinrich, Wind-Tunnel Investigation of Wing with Bombs, ZWB UM 4574 (FGZ 1944); Transl by Cornell Aeron.Lab 1949.
 - b) Arado, Wind-Tunnel Investigation of a Pair of Jet Engines at the LFA Brunswick 1943.
 - c) Göther, Investigation of Bombs SC-50, -250, -5000, Document ZWB FB 1663.
 - e) Kosin, Fuselages, Yearbk D.Lufo 1942 p.I,241.
 - f) Russian Bomb and Tank Catalog (30,a).
 - g) Hoerner, Bombs, Messerschmitt Rpt TB 85/1943.
 - h) Stoney-Royall, Smooth Shapes, NACA RM L56D16.
 - i) NACA, Full-Scale Bombs, W.Rpt L-131 (1944).
- (35) Means of reducing drag of circular cylinders:
 - a) Kramer, Unpublished DVL Tests, 1934.
 - b) Junkers, Sleeve-type Fairings in Junkers High-Speed Tunnel, Rpts S.1943/85 and S.1944/13.
 - c) Guide Vanes for Periscopes, TMB Rpt 504 (1945).

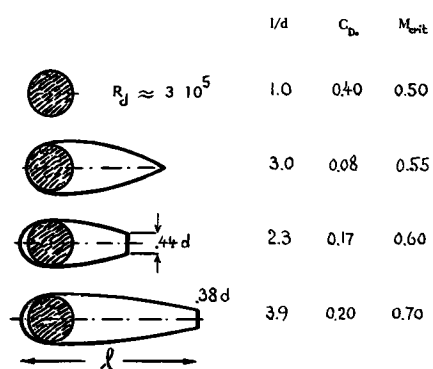


Figure 51. Drag of sleeve-type fairings (35,b), to be used around gun barrels, at R' numbers above transition.

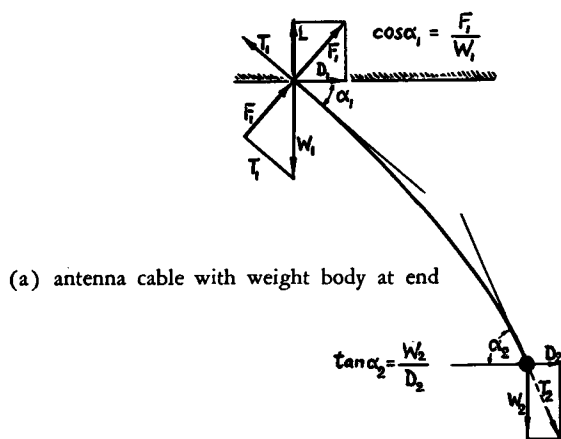
Cables may be used to tow one airplane behind another one, or as antennas. Aerodynamic characteristics of cylinders inclined against the direction of flow, correspond to the "cross-flow" component of velocity (normal to the cylinder axis; as explained on page 3-11). The shape of an antenna cable towed without a weight at its end is that of a straight line (if disregarding oscillations). The angle of inclination is

$$\tan \alpha = (W - L)/D \quad (18)$$

where W = weight, L = lift and D = drag. The pressure drag then corresponds to

$$C_{Dq} = C_{D0} \sin^3 \alpha \quad (19)$$

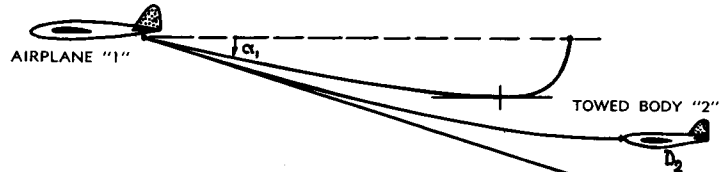
where C_{D0} = basic drag coefficient of the cylinder (at $\alpha = 90^\circ$); for example, $C_{D0} \approx 1.1$ for circular shape at subcritical Reynolds numbers. With a weight at the end of the cable, conditions are as illustrated in figure 52,a. The angle α_2 corresponds to drag and weight (if no lift) of the body attached to the end of the cable. The angle α_1 is found by putting into equation (18) the values for W , L and D of cable plus weight body.



Towing another airplane, as illustrated in figure 52,b, the lift of that airplane must also be taken into account. At point "1", the total values of weight, lift and drag of cable plus towed body must be put into equation (18) to obtain α_1 . An angle must first be assumed, in this case. The proper lift and drag forces of the cable are then found through the use of the cross-flow equations on page 3-11. Iterating the calculation, the correct solution for α_1 is finally found. At point "2" the angle is also found through application of equation (18), using for W , L and D the values of the towed airplane. For $L = W$, for example, $\alpha_2 = 0$. In many practical cases, the shape of the tow cable may already be sufficiently well defined by the angles α_1 and α_2 . The drag of the cable can then be calculated by integration along the length of the cable.

Refuelling Hose. During certain in-flight refuelling operations, the "second" airplane (as in figure 52,b) may move in below the tail of the "first" plane, so that it carries part of the hose's drag. For a known or assumed shape, the drag can then be integrated along the length of the hose. However, owing to the diameter "d" being appreciably larger than that of cables, the Reynolds number $R_d = V d/v$ is likely to be supercritical. Reference (37) indicates that for this condition, the cross-flow principle does not apply any longer. Rather, the drag coefficient (on diameter times length) of smooth cylinders is roughly independent of the angle between flow and axis; in the order of $C_{Dq} = 0.2$. It may be doubtful, however, that the surface of an armored type of refuelling hose would actually be smooth.

Figure 52. Shape and forces in towing cables



(b) one airplane towing another airplane

(b) Drag Of Stopped Propellers

The drag of stopped propellers is important for range and endurance of a multi-engine airplane, one or more engines of which may be out of order.

Blade Angle. With an *average* blade angle (measured at 0.7 radius) close to zero (measured between blade and plane of rotation), the flow past a stopped propeller is detached from the rear of the blades. Their drag is consequently similar to that of plates in a flow normal to their surface. Figure 53 shows drag coefficients between 1.0 and 1.2 for this condition (based on developed blade area). Variation of the drag coefficient with blade angle " β " might be expected either to be similar to that of flat plates at angles of attack near 90° (meaning $C_{D\Delta} \sim \cos\beta$, as suggested in the "pressure drag" chapter), or to correspond to the cross-flow principle (page 3-11, meaning that $C_{D\Delta} \sim \cos^2\beta$). The experimental points in figure 53 are well interpolated by

$$C_{D\Delta} = 0.1 + \cos^2\beta \quad (20)$$

where "0.1" = "residual" coefficient at $\beta = 90^\circ$.

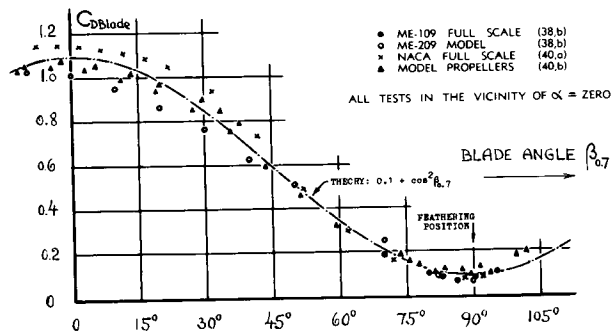


Figure 53. Drag of stopped (blocked) propellers as a function of the blade angle (at 0.7 radius).

Induced Drag. Because of the twisted shape of the propeller blades and/or owing to blade angle, some portion of the drag presented in figure 53 is induced by nature. This component is particularly evident in the vicinity of $\beta = 90^\circ$ where the drag coefficient of the blades is in the order of $C_{D\Delta} = 0.07$ to 0.12 . Not more than 0.01 or 0.02 may be attributable to the profile drag of the blades (including that of the roots). The rest can be explained by applying equation 13 of Chapter VII (indicating the induced drag of a wing caused by twist), if assuming for the blades an effective twist angle between 40 and 50 .

Tilted Propellers. With the airplane at a certain angle of attack and at a corresponding lift coefficient, the average angle of attack of a feathered blade (at $\beta = 90^\circ$) or a stopped propeller in *horizontal* position, is different from zero. This angle of attack is responsible for an additional component of induced drag. As explained in (39,a), the blades of a tilted propeller approximately present the same lift as a wing with an area corresponding to the projection of the blade areas in vertical direction. This means that the lift is zero at $\alpha = 0$ and $\beta = 0$, and that it increases in proportion to $\sin\alpha$ as well as to $\sin\beta$. Assuming for an average propeller blade an effective aspect ratio (equal to "propeller radius" over "average blade width") in the order of 7, the resulting lift curve slope of a feathered three-bladed propeller is estimated to be in the order of $dC_L/d\alpha^\circ = 0.04$ (based on developed blade area). The coefficient of induced drag corresponding to propeller lift is then found to be in the order of

$$(22)$$

$$C_{Di} = D_i / q S_{Bl} = (dC_L/d\alpha^\circ)^2 \alpha^2 / \pi A = 0.0002 \cdot (\alpha^\circ)^2$$

Ahead of the wing of an airplane, the angle of attack at the location of the propeller and its blades is larger, however, than the geometrical angle —

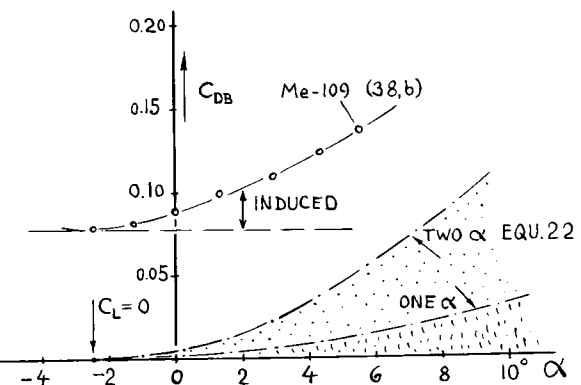


Figure 54. Drag of a feathered (stopped) tractor propeller as a function of the airplane's angle of attack (38,b).

- (36) Pabst, Towed Cables, Ybk D.Lufo 1941 p.I,574.
- (37) Bursnall, Yawed Cylinders, NACA T.Note 2463 (1951).
- (38) Drag of locked propellers:
 - a) Braked Locked Freewheeling, J.A.Sc. 1936 p.237.
 - b) Ehrhardt, Stopped, Yearb.D.Lufo 1942 p.I.
- (39) Propeller characteristics at angle of attack:
 - a) Ribner, Formulas, NACA Tech Rpt 819; and "Propellers in Yaw", T.Rpt 820, 1945.
 - b) For upwash ahead of wing, see NACA Technical Notes 2957 (1953), 3675 and 3738 (1956).
- (40) Negative thrust in propellers:
 - a) Hartman, Negative Thrust of Adjustable Pitch Propeller, NACA Tech Rpt 464 (1933).
 - b) Naumann, Tested, Yearb.D.Lufo 1940 p.I,745.
- (42) Characteristics of ejection seats:
 - a) Frost, Review, Aero Engg Rev. Sept 1955.
 - b) For pictures of ejection seats, see "Popular Mechanics" 1953 and "Popular Science" 1954.
 - c) Viggiano, Full-Scale Ejection Seat in Wind Tunnel, Air Force Tech Rpt 5578 (Wright Field, 1949).

because of the "upwash" corresponding to the circulation of that wing. This angle is approximately

$$\frac{d\alpha^\circ}{dC_L} = 57.3 / (4\pi x/c) = 4.5^\circ / (x/c) \quad (23)$$

where x = distance measured from the quarter point of the wing section. Figure 54 demonstrates that the increase of the drag coefficient of feathered propellers with the angle of attack as tested, is at least partly explained by this analysis.

Windmilling Propeller. A propeller, if not adjusted to feathering position, may keep rotating in case of engine failure. Similar conditions also prevail in power-off dives. The rotational speed of the propeller then depends upon the negative torque (due to mechanical friction) of the engine; and the drag must be determined through the use of proper propeller coefficients (40). This problem seems to exceed the scope of this book. For a rough estimate, the following procedure may be employed, however. In the case considered, the propeller operates as a windmill driving the engine. The power required to do this, is in the order of 10% of the rated power of the engine, at the respective speed of rotation. The efficiency of the "windmill" in transforming the "drag power" into rotational power, is estimated to be less than 50%. The drag of a propeller in this condition is consequently at least

$$D = (0.1/0.5) (n_{wind}/n_{rated}) (P_{rated}/V)$$

where D , P and V are used in a consistent set of dimensions as, for example, in the lb-ft-sec system.

(c) Ejection Seats

Ejection seats, designed to catapult the pilot safely out of a high-speed airplane, have been developed in recent years (42).

Drag. The problem as illustrated in figure 55, is to shoot the seat up at a velocity large enough to carry it over the airplane's fin—while the aerodynamic drag accelerates the ejected mass downstream. The drag area (D/q) of a seat suitable for the escape of a pilot (including rests for feet, arms and head, and including an auxiliary parachute pack, see illustrations in reference 42) varies between 4 and 9 ft^2 , depending on its angular position (42,c).

Trajectory. In a rough analysis it may be assumed that the seat be ejected in a direction normal to the airplane's axis, that its ejection speed "w" be constant and that the dynamic pressure to which the seat is exposed after leaving the cockpit, would be constant and equal to $q = 0.5 \rho V^2$. Under these simplified conditions, the path of the seat in relation to the aircraft is defined by $y = w t$, where t = time, and by

$$x = g 0.5 \rho V^2 t^2 (D/q)/W \quad (26)$$

For the speeds and the weight of seat plus pilot ("W") as indicated in figure 55, the parabolic trajectory is then given by $x \approx 0.16 y^2$. In a more complete analysis, several other effects have to be considered too, such as the angular position of the seat, and the positive or negative lift forces which develop as a function of that angle. Reference (42,c) indicates lift areas (L/q) varying between $+ 2.5 \text{ ft}^2$ (for the seat tilted forward to some 60° , and $- 2.0 \text{ ft}^2$ (near the upright position as shown in the illustration).

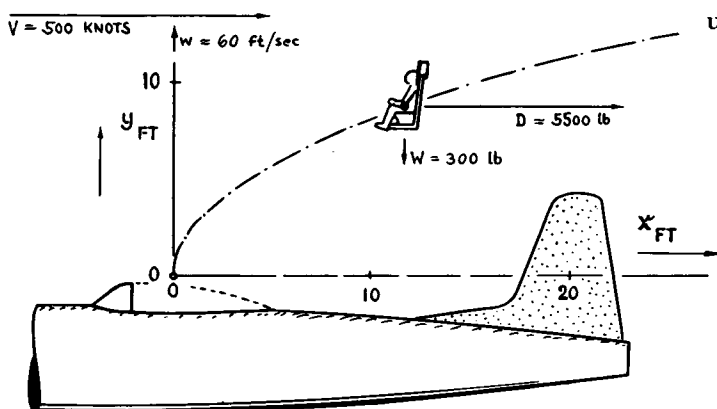


Figure 55. Example of mechanism and trajectory of an ejection seat (42).

8. CHARACTERISTICS OF PARACHUTES

Aerodynamic and other properties of parachutes are a fascinating subject. After years of trial-and-error development, they are now in a phase of more systematic study (50). Basic characteristics of porous and pervious shapes are indicated in figures 44 and 45 of Chapter III. Specific information on parachutes is presented as follows.

Basic Shape. Figure 31 in the "pressure drag" chapter suggests that a canopy shape near to hemispherical may give a maximum drag coefficient (in the order of $C_{D\Delta} = 1.4$). Indeed, most types of parachutes have a similar shape. If designed and sewed together as flat circles, such parachute canopies have approximately an inflated diameter of $2/3$ of the laid-out cloth diameter. The ratio of their inflated frontal area (S_Δ) to that of the developed area of the fabric (S_\square) is consequently in the order of 0.45. The drag coefficient referred to canopy area is then $C_{D\Delta} = 0.45 C_{D\Delta}$. Using a suitable drag coefficient and the weight of load plus parachute "W", sinking speed or "rate of descent" can tentatively be calculated as

$$U = \sqrt{2 W / (\rho C_D S)}; U_{ft/sec} = 29 \sqrt{W / (C_D S)}$$

where $\rho_2 \approx 0.0012$ (lb sec/ ft^4) in sea-level conditions. The problem is much more complicated, however, as explained in the following paragraphs.

Permeability. The material (textile fabric) of which parachutes are usually made, is more or less porous by nature. Its permeability is the average speed of the flow of air passing through the material, at a short distance ahead or aft of the textile sheet. In the United States, this speed is determined for a pressure differential Δp_{test} corresponding to 0.5 inch of water (ASTM standard) and quoted in ft/min. An aver-

age parachute cloth may have a permeability of "150 ft/min", for example. However, the real permeability speed corresponds to the pressure differential

$$\Delta p = q C_{D\Delta} \quad (31)$$

where $q = 0.5 \rho V^2$. Within the range of Reynolds numbers of average cloth (across the pores, as defined in reference 50,a), the variation of permeability with pressure can be approximated by

$$w/w_{test} = (\Delta p / \Delta p_{test})^{0.6} \quad (32)$$

where "test" indicates standard testing differential (equal to $2.6 \text{ lb}/\text{ft}^2$ in the U.S. and equal to $52 \text{ lb}/\text{ft}^2$ in Great Britain). — The effective permeability of a canopy is that through its opening circle. This velocity is larger than that through the material in proportion to the area ratio S_Δ/S_\square . Combining this function with equations 31 and 32, the *effective permeability of parachute canopies* is found to be

$$w_{eff} = w_{test} (S_\Delta/S_\square) (0.5 \rho V^2 C_{D\Delta} / \Delta p_{test})^{0.6}$$

The speed ratio as used in figure 57 can be determined from this equation as

$$w/V = w_{test} (S_\Delta/S_\square) V^{0.2} (0.5 \rho C_{D\Delta} / \Delta p_{test})^{0.6}$$

Fortunately, "V" appears only under the fifth root in this equation, so that in gliding parachutes, this speed may be replaced by "U" as defined later in the text.

Flow Pattern. Fundamentals of porous sheets are explained on pages 3-23 and 24. The drag coefficient decreases as a function of permeability, expressed in figure 45 of Chapter III by the velocity ratio (w/V). The equations on page 3-24 permit to calculate the drag coefficient of very porous parachutes (with $w/V > 0.5$; see figure 57) on the basis of the properties of the canopy material, applying equations 33 and/or 34 for the effective permeability. Characteristics below $w/V \approx 0.5$ (comprising the majority of designs and applications) are different, however. Figure 56 shows how a stream of air attaches itself to one side of the canopy thus causing a lateral "lift" force owing to the suction on that side. Wind-tunnel tests on sheet-metal "caps" (51,c) and on certain models made of cloth (52), show the lateral force and the corresponding moment about the center of the load (between 1 and 2 diameters below the canopy opening). The lateral "lift" pulls the canopy sideways. Under favorable conditions, the parachute therefore glides at a certain angle $\gamma^\circ = (90 - \alpha^\circ)$. In other cases, the system of canopy and load assumes a more or less regular state of oscillating or "coning" motion, with flow separation and suction force of the canopy changing in two or more directions.

(50) Fundamentals of parachutes:

- a) Hoerner, Drag Characteristics of Parachutes, Air Force Tech Rpt 6201 (Wright Field 1950).
 - b) Heinrich, Survey, Aero Engg Rev. 1956 p.73.
 - c) Brown, "Parachutes", Pitman (London) 1951.
- (51) Experimental results on sheet-metal shells:
- a) Ergebnisse AVA Göttingen Vol IV (1932).
 - b) Breevort-Joiner, Anemometer, NACA T.N. 489.
 - c) Doetsch, Parachute Models, Lufo 1938 p.577.
 - d) Jones, Compilation of Data, ARC RM 862 (1923).
 - e) ARC, Perforated Plates and Caps, RM's 2520 and 2523; also Porous Sheets in RM's 2236 and 2237.

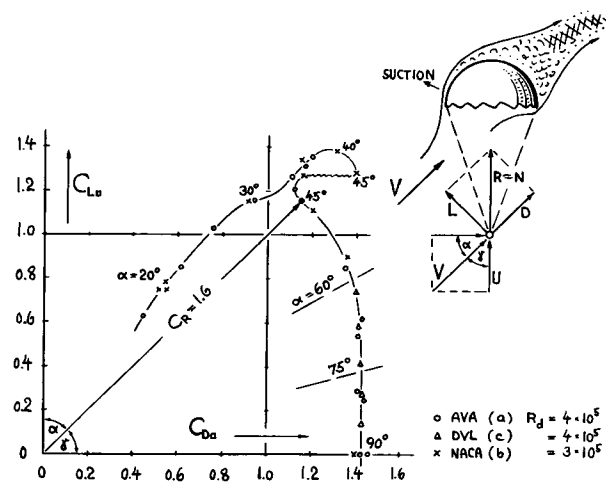


Figure 56. Aerodynamic characteristics of hemispherical shells, rigidly suspended in wind tunnels (51).

Gliding Parachutes. Figure 56 shows the aerodynamic characteristics of parachute- or canopy models made of sheet metal. The stable equilibrium of these models (around a point approximately 1.3 times the diameter beneath the canopy) is between $\alpha = 40$ and 50° . Such parachutes may, therefore, assume this stable position and keep steadily gliding at an angle $\gamma = (90 - \alpha)$ in the vicinity of 45° against the vertical (in relation to the air space, as found in 51,c). The weight of parachute and load is supported in this case by the resultant aerodynamic force $R = \sqrt{D^2 + L^2}$. This resultant is essentially identical to the force normal to the opening circle of the canopy (within the region of $\alpha = 90^\circ \pm (45 \text{ or } 50)^\circ$). For ex-

ample, in the vicinity of $\alpha = 45^\circ = \gamma$, the resultant force coefficient is $C_R \approx 1.65$, in figure 56, based on resultant velocity "V" (in the direction indicated by α or γ , respectively). For the descent of the parachute, the vertical component of V , that is the sinking speed "U", is of more practical importance; and during full-scale tests in open air, only this component $U = V \sin\alpha = V \cos\gamma$, is usually timed. Referring the resultant- or normal-force coefficient to this speed, an effective, "vertical", or "weight coefficient" may be defined:

$$C_{Wd} = W / (0.5 \rho U^2 S_d) = C_R / \sin^2 \alpha \approx C_N / \sin^2 \alpha$$

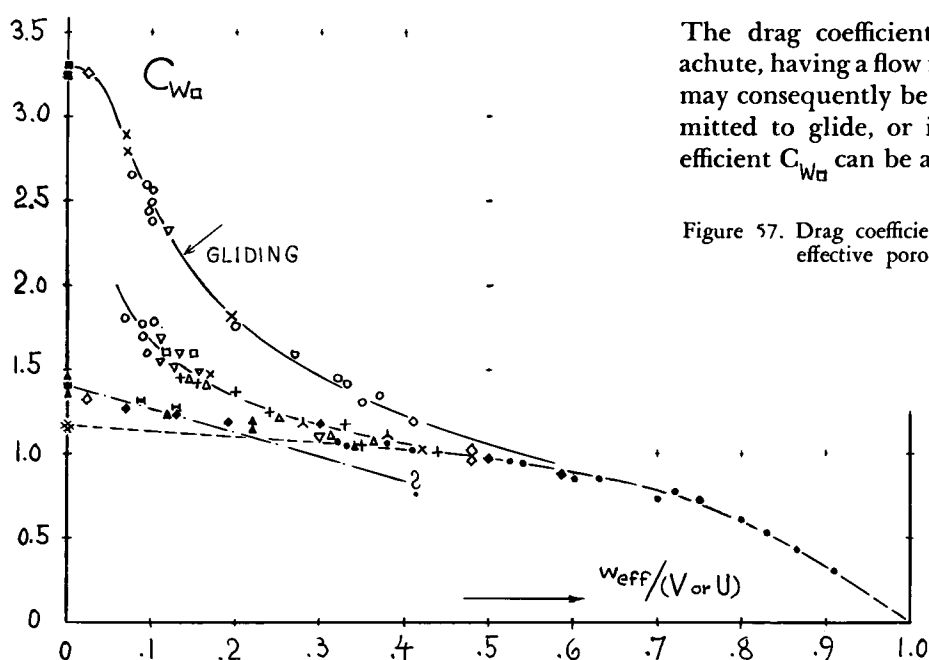
Characteristics in figure 56, with $C_R = 1.65$ at $\alpha = 45^\circ = \gamma$, thus yield a coefficient $C_{Wd} = 3.3$, as plotted in figure 57 at $w/V = 0$. This value is twice the "resultant" coefficient. It should be noted, however, that the angle of stable gliding is also a function of the rigging-line length. That length could be such (longer than considered above) that stability is obtained in the point of the function in figure 56 farthest away from the origin. This point corresponds to $C_{Rd} \approx 1.8$ and $C_{Wd} \approx 3.6$. The rate of descent of a *gliding parachute* can then be determined through the use of equation 30, introducing " C_W " in place of " C_D ".

Drag (Permeability). Drag and/or weight coefficients of parachutes are plotted in figure 57 against their effective permeability ratio determined through the use of equation 34. Assuming $C_{Dd} = 1.4$ as "basic" drag coefficient, the coefficient of parachute canopies restrained from gliding (reference 52,b and c), is reduced by permeability, tentatively as

$$C_{Dd} = 1.4 (1 - w/V) \quad (36)$$

The drag coefficient of an average personnel parachute, having a flow ratio in the order of $w/V = 10\%$, may consequently be reduced to $C_{Dd} = 1.26$. If permitted to glide, or if made gliding, the weight coefficient C_{Wd} can be as high as 3.3 (as derived above).

Figure 57. Drag coefficient of parachutes as a function of their effective porosity (indicated by the flow ratio w/V).



GLIDING AND OSCILLATING:	
×	GOODYEAR (54,c)
○	WRIGHT FIELD (54,a)
□	FULL SCALE, FREE FALL: NACA, N.1315 (56,b)
▽	WRIGHT FIELD (56,c,d)
OSCILLATING IN W'TUNNELS:	
+	R.A.E (ARC) (52,g)
△	BROWN (HIS FIG.53; 50,c)
×	NACA, N.1869 (52,b)
■	NACA, HIGH SPEED (52,h)
◆	NACA, N.2098 (52,b)
RESTRAINED (METAL) MODELS:	
■	CUPS AND CAPS (51,b,c)
*	STANDARD DISK VALUE (—)
◇	CANOPY CAP (52,a)
▲	PERFORATED CAPS (51,e)
●	POINTS AS IN FIG. III-45

However, this coefficient quickly drops from that level as a function of the speed ratio (w/V). For example, the parachute mentioned above (with $w/V = 0.1$) is expected to have a coefficient in the order of $C_{W\alpha} = 2.4$ (if really gliding). At $w/V = 0.2$, the coefficient is almost reduced to half the maximum value. Pressure distributions around the canopy reported in (51,e) clearly show that the lateral suction force (illustrated in figure 56) is eliminated by a sufficient rate of flow through the material, particularly through the "skirt" or through a strip of material adjacent to the rim of the canopy. Assuming that the drag coefficient is approximately constant within the range of $\alpha = (90 \pm 20)^\circ$, as seen for instance in figure 56, the "resultant" coefficient is

$$C_{Ra} \approx C_{Da} \approx 1.4/\sin \alpha \quad (38)$$

Combining this one with equation 31, the "weight" coefficient is found to be

$$C_{Wa} = 1.4/\sin^3 \alpha \quad (39)$$

Reversing this equation, it is thus possible approximately to recalculate glide angles from the weight coefficients plotted in the upper part of figure 57. At $w/V = 10\%$, for instance, $C_{Wa} = 2.4$; $\sin^3 \alpha = 1.4/2.4$; $\alpha = 56^\circ$; and the glide angle (against the vertical) $\delta = 90 - \alpha^\circ = 34^\circ$.

Oscillating Parachutes. Full-scale drop tests (56) yield drag or weight coefficients usually smaller than the value of 2.4 calculated in the last section, in the order of less than $C_{Wa} = 1.8$ (or $C_{Do} = 0.8$ based on developed area of the canopy material). Steady gliding only occurs under certain favorable conditions. Parachutes

may as well assume a more or less obvious oscillating state, produced and maintained through dynamic interaction between canopy forces and the suspended load. Model tests (54,a) show that gliding prevails at smaller speeds while oscillations (with amplitudes to $\pm 20^\circ$) are predominant at intermediate rates of descent. Some 200 full-scale drop tests have been evaluated at Wright Field (quoted in reference 50,a). Parachutes with cloth diameter between 22 and 24 ft, made of textile material with a permeability corresponding to ≈ 130 ft/min ASTM, carrying between 150 and 200 lb load, show two preferred conditions; oscillating (with $C_{Wa} \approx 1.6$) and gliding (with $C_{Wa} \approx 2.4$). The chances of gliding against oscillating are roughly one to three. It thus seems that most parachute descents in practical operation are of an irregular oscillating type, likely combined with some gliding. Coefficients C_{Do} , evaluated from full-scale drop tests, are usually between 1.4 and 1.8, thus falling into the space between the two limiting conditions plotted in figure 57. Considering a man-carrying parachute with a total weight of 200 lb, a diameter of the laid-out cloth in the order of 26 ft, and a corresponding frontal area of the inflated canopy of approximately 250 ft^2 — the rate of descent at sea level density will approximately be

$U = 23 \text{ ft/sec}$	for $C_{Do} = 1.26$, restrained
$U = 20 \text{ ft/sec}$	for $C_{Do} = 1.60$, oscillating
$U = 16 \text{ ft/sec}$	for $C_{Do} = 2.40$, if gliding

Model Testing. In wind tunnel investigations, parachutes or models of them may be connected to the balance system at the junction point of their suspension lines. This arrangement does not reproduce *dynamic* conditions of a parachute descending through the air. However, such tunnel tests usually show severe oscillations; and they may thus accidentally give drag coefficients of the same magnitude as found from drop tests. To overcome the limitations of tunnel testing, parachute models made of various types of textiles, have been investigated by dropping them — among others, from the 175 ft high ceiling of the airship dock at Akron, Ohio (54,c). Figure 58 presents some such results together with available full-scale data. Gliding is reported for the larger coefficients in the left-hand part of the graph, oscillations for the results at intermediate and higher speeds. As a function of speed (varied by changing the load), the "weight" coefficient reduces appreciably. Certain groupings can be found in the graph as to canopy size as well as on the basis of permeability (indicated in the U.S. standard manner in ft/min as explained above). One explanation (50,b) for the change of flow pattern and weight coefficient is simply a consideration of dynamics; which then should give correlation on the basis of Froude number (see in Chapter XI). Two or three other reasons are suggested as follows:

- (52) Experimental results on parachute models:
 - a) Heinrich, Stability, ZWB Rpt FB 1780 (1943).
 - b) Investigation of Parachutes in Wind Tunnels and in Free Air, NACA T.Notes 1315, 1869, and 2098.
 - c) Taylor and Davies, Characteristics of Porous Sheets, ARC RM 2236 and RM 2237 (1934).
 - d) Scher, Cluster of Parachutes, NACA RM L53G07.
 - e) Jones, Restrained Models, ARC RM 2520 (1953).
 - f) Stimmmer, Tunnel Tests and Analyses, Guggenheim Airship Institute Rpts 1948 and 1949.
 - g) Johns-Auterson, Parachutes, ARC RM 2335 (1944).
 - h) Schueler-Evens-Johnson, NACA Memo Rpt 1944.
- (53) Knacke, Design and Use of Ribbon-Type Parachutes, AMC Memo Rpt MCREXE-672-19LL (1948).
- (54) Drop tests of parachute models:
 - a) Knacke, Model Parachutes Comparison Tests, AMC Memo Rpt MCREXE-672-12B (1949, Wright Field).
 - b) Floating in Spinning Tunnel, NACA RM L51J18.
 - c) Stimmmer and Ross (Goodyear) USAF Tech Rpt 5867 (8 volumes, Wright Field, 1952/1954).
- (56) Full-Scale drop tests on parachutes:
 - a) Penrod-Maison-McDonald, J.Aeron Sci 1947 p.303.
 - b) Webster, Falls and Descents, NACA T.Note 1315.
 - c) Some Wright Field results are quoted in (50,a).
 - d) Knacke, Size, Memo WCEEH 1951 (Wright Field.)

- GOODYEAR, 11.9 FT ϕ , DROP, 100 ASTM (54,c)
- + WRIGHT FIELD, 3.8 FT ϕ MODEL FLAT (54,a)
- ▽ A R C , 1 m ϕ CLOTH MODELS RM 862 (51,d)
- × 24 TO 30 FT ϕ FLAT FULL SCALE (140) (56,c)
- I 48 FT ϕ SKIRTED FLAT, 100/150 ASTM (56,d)
- 24 FT ϕ "SPHERICAL", 200 FT/MIN ASTM (56,d)
- ◇ 15 FT ϕ "RING-SLOT", 17% POROSITY (56,d)
- BROWN, 4 FT ϕ FLAT ($w/V = 0.38$) (50,c)
- △ GOODYEAR, 11.9 FT ϕ , 20/26% POROSITY (54,c)
- ▼ GOODYEAR, "GUIDE-SURFACE" TYPE (54,c)

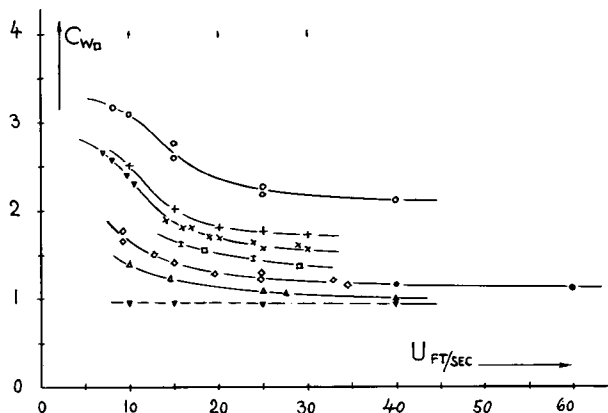


Figure 58. Variation of the drag coefficient of parachute models (made of fabric) as a function of vertical speed.

(a) *Reynolds Number* is not involved with regard to canopy shape. Within reasonable limits as to viscous friction and compressibility, respectively, the drag coefficient of bluff bodies is not susceptible to variations of size and speed. However, the flow through the canopy material is a function of R' number (based on conditions within the pores, as presented in (59,a).

(b) *Aeroelasticity*. Permeability of textile fabrics is, among others, a function of tension and elastic deformation in the material. For example, maximum elongations in parachute cloths are reported in (59,b) between 15 and 30%. We may therefore conclude that the geometrical porosity " $1 - \zeta$ " (see page 3-23) can be increased by $\Delta\zeta$ between 0.3 and 0.6, in the extreme case just before breaking. Assuming that the tension may only be 10% of that at breaking, $\Delta\zeta$ can still be in the order of 0.03 or 0.06, a differential that might mean an increase of geometrical porosity by 30 or 60%. Figure 43 in Chapter III shows how permeability increases as a function of porosity. Inasmuch as tension in a given canopy is proportional to the dynamic pressure, the drag coefficient decreases as the speed is increased (see figure 58).

(c) *Parachute Size*. The drag coefficient also decreases somewhat as the size of a certain type of parachute is increased (keeping the design speed \approx constant). In this respect, see the coefficients in figure 58 of full-scale chutes for 24, 48 and 100 ft developed diameter. This effect too can be explained on the basis of tension. Assuming that forces in the canopy be proportional to the load, tension (in lb/ft) is obtained increasing in

proportion to the diameter of the canopy (at $V =$ constant). The drag coefficient decreases, therefore, as size and permeability are increased. Inasmuch as figure 57 indicates a strong decrease of C_W as a function of permeability-ratio, small variations of the parameters indicated in (a), (b) and (c) are likely to produce the effects as shown in figure 58.

Rigging Lines. Inflated diameter and shape of the canopy are affected by the length of the rigging lines. Figure 59 shows how the drag coefficient (believed to be on projected frontal area, in restrained condition) increases, as the length of the lines is increased. One set of tested points indicating the projected area ratio, suggests that the shape is as much involved in the result as the magnitude of the inflated area.

- BROWN, 4 FT ϕ FLAT AT 60 FT/SEC (50,c)
- DITTO, "SHAPED" ("45° Brit.PERM.) (52,g)
- △ GOODYEAR, 11.9 FT ϕ , EXTEND.SKIRT (54,c)
- + - GOODYEAR, FLAT, 100 FT/MIN ASTM (54,c)
- × - WRIGHT FIELD TUNNEL MODEL --- (54,a)

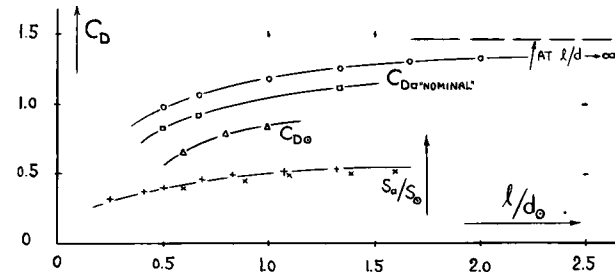


Figure 59. Variation of parachute drag coefficient as a function of rigging-line length.

Ribbon-Type. Figure 57 indicates that above $w/V = 0.3$, the drag coefficient of porous parachutes equals that of flat sheets having the same flow ratio w/V . Parachutes with such flow ratios have been developed, to eliminate oscillations which are highly undesirable in certain applications. Ribbon-type parachutes (50,b and 53) have porosity ratios ($1 - \zeta$) between 20 and 40%. The loss coefficient (defined in the "pressure drag" chapter) corresponding to the latter value, is $\xi = 7.7$. The resultant flow ratio is $w/V = 0.65$, and the drag coefficient $C_{D_{RIB}} = 0.82$. Figure 57 shows that the drag coefficient of this parachute fully corresponds to the theoretical value.

"Shaped" Canopies. Besides the "flat" type parachute (also called a "parasheet" in reference 50,c, "gathered" by suitable rigging lines), other designs have been developed (50,b). So-called "shaped" canopies (sewn together, for example in the form of a hemispherical shell) have essentially the same aerodynamic characteristics as the flat type. It is possible, however, to save some material, so that the drag coefficient based on developed canopy area (indicating an aerodynamic "efficiency") attains somewhat higher values.

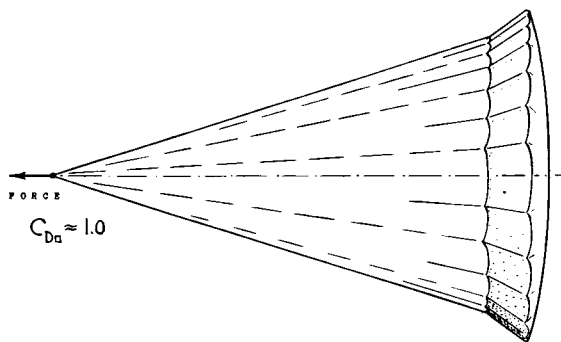


Figure 60. Shape and drag of guide surface parachute (57).

Guide Surface. An entirely different type is the so-called "guide-surface" parachute, a "conical" shape particularly designed and used for stabilization of bombs, mines and torpedos, for missile recovery and for rescue from high-speed aircraft. *Figure 60* shows form and drag coefficient of this type of parachute. Coefficients are based, in this case, on the area corresponding to *constructed* diameter. The inflated diameter is estimated to be some 5% smaller. The value of the drag coefficient corresponds to the canopy shape which is not too favorable for producing drag. Inasmuch as guide-surface parachutes never glide, since they hardly oscillate (only by $\pm 1^\circ$) and because they are made of very tight (and heavy) material—their drag coefficient is practically constant (see in figure 58). Guide-surface chutes have been developed for and tested (57) at speeds approaching that of sound. For a diameter of 6.5 ft, steady-state drag forces are thus obtained in the order of 30 or 40,000 lb.

Conclusions. The parachute problems listed in this section have not yet been solved analytically. Concept and consequences of aeroelastic tension as outlined above do not seem to be generally accepted. It should be agreed, however, that model testing is problematic in the field of parachutes. To get away from the confusion thus existing, some drag coefficients are tabulated as follows, believed to apply to average *full-scale* conditions:

flat-type ("parasheet") oscillating	$C_{D_a} = 1.7$
average ribbon type (20% porosity)	$C_{D_a} = 1.0$
guide-surface type (see figure 60)	$C_{D_a} = 1.0$

One more influence on permeability and drag of parachute canopies to be mentioned, is rain. Reference (59,c) reports that permeability of fabrics can be reduced to zero by wetting.

9. DRAG OF TOW TARGETS

Towed "windsocks" and similar devices are used as practicing targets for anti-aircraft artillery.

"Windsocks". *Figure 61* presents several shapes designed to be towed behind aircraft. Most of them are built in the form of windsocks, inflated and kept in shape through an opening in front. Provided that this opening is wide in comparison to the diameter of the socks, drag coefficients of cylindrical shapes are comparable to those of previous sheets as indicated by the equations on page 3-24. — By making the material wet (that is, by reducing its porosity), the drag is noticeably reduced in one case (shape "c"). The flow is evidently reattached to the outer side of that cone. Upon reducing porosity, the pressure losses across walls and bottom of the cone are reduced too; and the total drag comes out smaller than in dry condition.

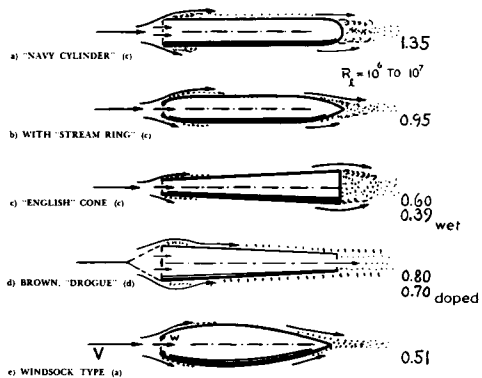


Figure 61. Drag coefficient (on frontal area) of various tow targets, built in the form of windsocks (60).

- (57) Stable guide-surface parachutes:
 - a) Heinrich, ZWB FB 1780 (1943); Transl ATI-42978; See also (50,b) and USAF Tech Rpt 5853.
 - b) Reported by Cook Laboratories in (59,b).
- (59) Properties of parachute fabrics:
 - a) Hoerner, Aerodynamic Properties of Screens and Fabrics, Textile Research J. 1952 p.274.
 - b) Wright Air Development Center, Symposium on Parachute Textiles, Tech Rpt 1954-49.
 - c) Swallow, RAE Tech Note Chem 1248 (1955).
 - d) Brown, Tension and Porosity, ARC RM 2325 (1944). Most fabrics open up; but some do not.
 - e) Shape of and tension in canopies are analyzed in ARC RM 2118 (1942); theory.
- (60) Characteristics of tow targets:
 - a) Windsocks and Flags, Focke-Wulf Rpt 27 (1933).
 - b) Fleischhacker, Flight Tests on Tow Targets, Rpt Erprobungsstelle Tarnewitz, 19 July 1940.
 - c) Migotsky, Anti-Aircraft Target, NACA W.Rpt L-760.
 - d) Brown, "Drogues", in reference (50,c).
- (65) Drag of dive brakes attached to fuselages:
 - a) Wright, Speed Brake, NACA RM L8B06; see A7K28.
 - b) Fail-Owen-Eyre, Plates and Brakes, ARC C. Paper 251.

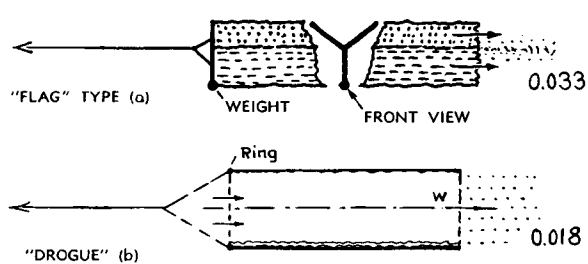


Figure 62. Drag coefficient of "flag" type towing targets (60), referred to total wetted area.

Flag Type. One of the "socks" in figure 61 ("d" with the larger diameter ahead) has an open bottom. Drag is somewhat reduced in this shape. The cylindrical shape in figure 62 (stiffened at the leading edge by a metal ring) has the comparatively low coefficient $C_{D\alpha} = 0.42$ (for "tight" fabric). Based on wetted area, the coefficient is $C_{Dwet} = 0.018$. The flag type

("a") built up of three sheets of textile fabric has a drag similar in magnitude (in pounds) to that of "c" or "e" in figure 61. Based on wetted area, its coefficient is in the order of 0.03 which is almost 7 times the turbulent skin friction drag of $C_f \approx 0.0045$ at $R_\ell = 10^6$. The additional drag is caused by supporting rods (at the leading edge) and by flutter, the consequences of which are shown in figure 46 of Chapter III. As a target, such a device is not inferior to windsocks. Referring the drag to the visible lateral area (equal to length times height), a coefficient is found which is in the order of those of the streamline windsocks described in the next paragraph.

Streamlining the shape, including a reduction of the inlet opening, the drag coefficients of windsock targets are cut down to $C_{D\alpha} = 0.56, 0.51$ and 0.35 , respectively. However, with regard to stability (steadiness in the air), the flag type targets may be more desirable.

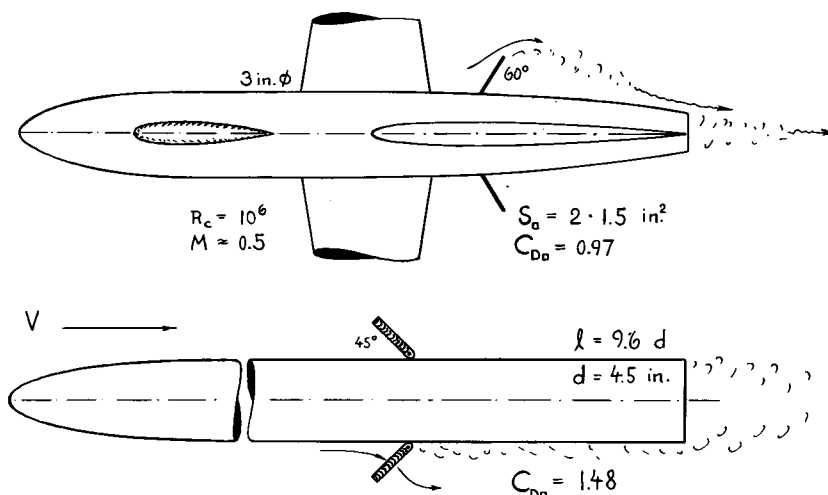


Figure 63. Drag of and due to dive-brake flaps deflected from the sides of fuselages:

- (a) Pair of solid square plates on the fuselage model of an experimental airplane (65,a).
- (b) Pair of "flaps" composed each of a set of guide vanes, deflecting the air stream (65,b).

The plates have a drag coefficient similar to that in free flow (without fuselage). The cascades of guide vanes are more effective, producing ≈ 1.5 times the drag of the plates. Similar to that in figure 30(b), their flow is locally deflected outward, thus "losing" more momentum than in any plate device. This fact is also evident in the lift (or lateral force) of a configuration using only one of the two guide-vane flaps, corresponding to $C_{L\alpha} = 1.26$. In other words, flow pattern and characteristics of the cascade type of brake are those of a low aspect ratio wing rather than those of a bluff obstruction.

CHAPTER XIV — DRAG OF COMPLETE AIRCRAFT

The drag of many aircraft components, large and small, has been presented and expounded in other chapters, including aspects such as Reynolds number, surface roughness and interference. An analysis is now undertaken in this chapter of total drag corresponding to the performance of aircraft in full-scale operation. Such analysis also demonstrates a synthetic method of predicting full-scale performance by realistically computing the drag of the component parts, by taking into account surface roughness and interference effects and by including internal losses — through application of the many theoretical functions and/or statistical rules developed and/or quoted in this book.

on the basis of thickness ratio (d/l) and turbulent skin-friction drag coefficient C_f (as a function of R' number; Chapter II). — The type of drag coefficient preferred in airship aerodynamics is C_{Dv} , based on $(\text{volume})^{2/3}$ as explained in Chapter VI. Inasmuch as the coefficient C_{Dwet} (based on wetted area) directly displays the predominant source of airship drag, this definition is used, however, in figure 1. — Fine-ness ratios (l/d) applied in most airships are far above the values found to be optimum in Chapter VI (1). Hull-fin interference, stability and control characteristics and possibly the dimensions of hangars seem to be responsible for higher ratios (up to $l/d = 10$, in older designs).

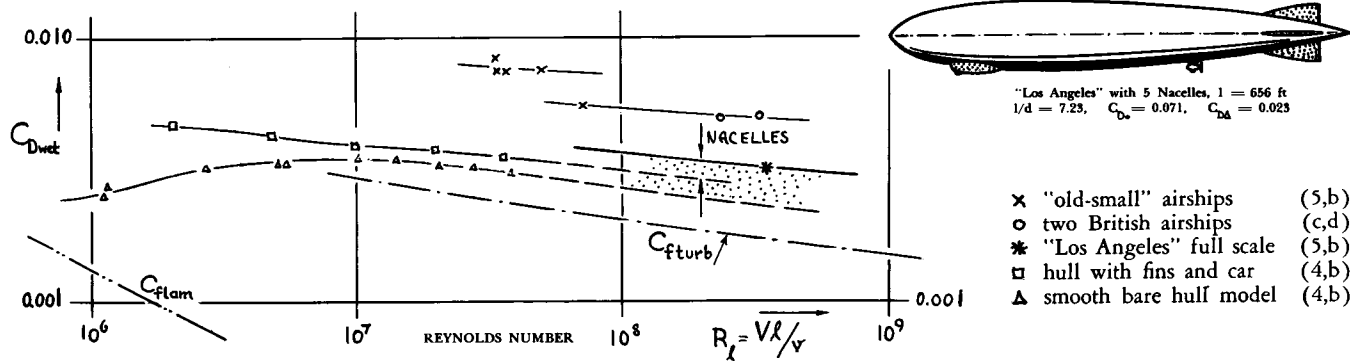
Fins. Reference (4,b) gives experimental information on the drag of a "Goodyear-Zeppelin" airship model having $l/d = 7.2$. At a Reynolds number $R_l = 2 \cdot 10^7$, drag coefficients of the bare hull are $C_{Dv} = 0.023$, or $C_{Dwet} = 0.072$, or $C_{Dwet} = 0.0032$, (1). Addition of a set of 4 smooth fins having a "foil" area $S_{fin} \approx S_*$, increases the drag by $\approx 12\%$, while the added wetted area is $\approx 8\%$ of that of the hull body. Similarly, reference (4,c) indicates an increment of 9% for a set of 6 fins with $S_{fin} \approx 0.6 S_*$ and a wetted area ratio of approximately 9%. Other model tests, on a "Zeppelin" airship (with $l/d = 6$) at $R_l = 5 \cdot 10^6$ are reported in (4,e). Addition of 4 fins having a total "foil" area equal to S_* or a wetted area equal to 11% of that of the bare hull, causes an increase of

1. DRAG OF AIRSHIPS

Big airships are no longer with us. They were developed in one phase of aviation at considerable cost; and they have been replaced by the "heavier-than-air" type of aircraft. All that is left today in the field of airships are "blimps" (colloquial for small airships).

Hull. The drag of bare and smooth airship hulls is extensively presented in the "streamline" chapter. Applying equation 28 of that chapter, the theoretical drag of a bare and smooth hull can easily be predicted

Figure 1. Drag coefficient of airships (on wetted area of their hulls); comparison of model- and full scale results.



the drag coefficient on wetted area by 24%. In conclusion, the drag of and due to fins is larger than corresponding to their wetted area. The increment is evidently caused by interference along the hull's tapering stern.

Car. The second major appendage of each airship is the "car". Many more or less bluff shapes of cars and engine nacelles have individually been tested (6); drag coefficients are $C_D \approx 0.1$ for smooth cars, and up to ≈ 0.6 including openings and radiators. Their drag in presence of the airship hull and the interference drag caused by them on the hull, could be predicted by applying the principles outlined in Chapter VIII. Practically all of the appendages investigated in that reference are obsolete, however. The most advanced airships ever built, had cars integrated into the bottom of the hull, similar in shape (if not in size) to canopies or windshields as presented in Chapter XIII. Evaluated from (4,b and c), a drag coefficient on frontal area of such cars is found in the order of 0.1. Inasmuch as the frontal area is only $\approx 1\%$ of that of the hull, the car drag is not of great importance.

Engine Nacelles, installed in several pairs at the sides of airship hulls, have never been developed to a degree of streamline efficiency comparable to that of the shapes used in modern airplanes as presented in Chapters IX and XIII. The drag of nacelles can readily be predicted by applying the principles set forth in the "interference" chapter. As an example, a number of nacelles may be assumed with a total frontal area in the order of $S_{a\bullet}/S_{m\bullet} = 0.01$, each having a drag coefficient of $C_{Dn} = 0.5$ (a value indicating a comparatively rough shape, and including the drag of the structure by which each nacelle is supported from the hull). Based on hull frontal area, the drag of and due to the nacelles will then be in the order of $\Delta C_{Dm} = 0.01 \cdot 0.5 \cdot 1.2 = 0.006$, where "1.2" indicates a factor accounting for interference. The drag of and due to the nacelles is then in the order of 10% of the hull drag. Such a component of drag is indicated in figure 1.

Full-Scale deceleration tests (similar in method to those on automobiles, discussed in Chapter XII) have been made on a number of airships. Reference (5,a) yields drag coefficients C_D between 0.08 and 0.10 at $R_\ell \approx 10^8$ for a series of "Zeppelin" airships having displacement volumes between 2 and 3 million ft³, a diameter of 78 ft and fineness ratios between 8 and 9. These drag values as well as those of other "smaller" and "older" airships (plotted in figure 1) are considerably larger than the total drag that can be obtained by adding to the basic hull drag the components due to car, fins and nacelles as estimated above. It is suspected that at the time when these ships were in operation (at and before 1918), the appendages

were very bluff in shape, suspended and kept in place by means of struts and cables; and that the engine radiators were of the open type, thus increasing the drag of the nacelles very much. — Reference (5,d) yields $C_{Dv} = 0.038$ or $C_{Dwet} \approx 0.0045$ (on hull plus fin area), for a full-scale configuration with 5 engine nacelles (275 HP each) at $R_\ell \approx 2 \cdot 10^8$, (where the basic $C_f = 0.0018$). We will assume that general surface roughness, all sorts of small protuberances (vents, handling attachments, rudder gaps) and the suspension of the engine nacelles (interference) may be responsible for the still existing gap between these values and those which can be determined on the basis of skin friction.

Reynolds Number. The drag coefficients of roughness elements and of bluff parts can be assumed to be essentially constant if plotted against Reynolds number. The total drag coefficient of airships may, therefore, be assumed to be composed of a constant component and of another component which varies in proportion to the turbulent skin-friction drag coefficient. If, for instance, half of the total drag (as tested at one particular R'number) is considered to be constant, then the coefficient is found to vary against the Reynolds number in proportion to $1/R^{1/2}$, and not in proportion to $1/R^{1/6}$ as in plain friction flow. Corresponding lines are shown in figure 1, roughly indicating the variation of the drag coefficient of fully equipped full-scale airships as a function of Reynolds number. Correlation is found in this manner between model- and full-scale results, at least for the more streamlined "Los Angeles". A more detailed method of correlation and/or extrapolation against R'number is presented for ships, in Chapter XI.

-
- (1) Drag coefficients and optimum shapes on pages 6-18 and 19.
 - (4) Drag characteristics of airships:
 - a) Many results on bare hulls are presented and quoted in the "streamline" chapter.
 - b) Abbott, Airships in VDT, NACA T.Rpt 394 (1931).
 - c) Abbott, Hulls and Appendages, NACA T.Rpt 394(1932).
 - d) CAHI (Moscow) Report 151 (1932).
 - e) Quoted in "Ringbuch Luftf. Technik" Section IA15.
 - (5) Drag of airships determined by deceleration:
 - a) Zeppelin results, quoted in NACA T.Rpt 117 (1921).
 - b) Thompson and Kirschbaum, NACA T.Rpt 397 (1931).
 - c) Pannell-Frazer, Rigid Airships, ARC RM 668 (1919).
 - d) ARC, Airship R.32 Tests, RMs 811, 812, 813 (1921).
 - (6) Diehl, Fuselages Cars Nacelles, NACA T.Rpt 236.
 - (10) Drag characteristics of the Me-109:
 - a) 109 Parts, Aero Lab. TH Munich Rpt ZWB UM 7821.
 - b) Messerschmitt, Glide Tests Me-109, 1940.
 - c) Sahliger, Drag- and Lift Measurements of the ME-109 in the Full-Scale Tunnel at Chalais-Meudon, ZWB Rpt UM 7801 (Messerschmitt 1943).
 - d) Flight Tests 109 Radiator, Messerschmitt Rpts "18 Aug 1939", 109/10/L1941, 109/15/L1942.
 - e) Messerschmitt, Tunnel Model, ZWB UM 7857 (1944).
 - (12) Hoerner, Me-109 Analysis, unpubl. Rpt 1946.

2. DRAG ANALYSIS OF A FIGHTER AIRPLANE

Because of the author's personal experience with that particular airplane, and on the basis of wind-tunnel investigations and flight tests carried out on and for this airplane, the maximum-speed drag of the Messerschmitt "Me-109" is presented and analyzed as follows — thus showing the application of some of the methods outlined in this book.

(a) Full-Scale Performance

The prevailing type of the Me-109 produced in 1944 was the series "G", illustrated in figure 2. The principal dimensions and data are

total wing area	$S = 172 \text{ ft}^2$
wing span	$b = 32 \text{ ft}$
aspect ratio	$A = 6.1 -$
overall length	$\ell = 29 \text{ ft}$
gross weight	$W = 6700 \text{ lb}$
wing loading	$= 39 \text{ lb}/\text{ft}^2$
maximum speed	$V = 610 \text{ km/h}$
reciprocating engine	$= DB 601A$
maximum power	$P = 1200 \text{ hp}$
in altitude of	$z = 22000 \text{ ft}$

Besides exhaust stacks and a pair of wing radiators, the airplane had the following parts exposed to the air flow: Tail wheel (14 inch diameter), antenna wire with mast on upper side of fuselage, two machine guns with portholes on top of engine cowling, partly open housings for the retractable landing gear

and a comparatively blunt canopy. Figure 2 shows size and location of these parts. The maximum speed as listed in "km/h" is 380 mph, or 330 knots.

Thrust. The efficiency of the variable-pitch propeller is estimated to be $\eta = 0.85$ at a high-speed disk loading of $C_T = T/qS_o \approx 0.07$. The effective thrust is then:

$$T = \eta P/V = 0.85 \cdot 1200 \cdot 550/560 = 1000 \text{ lb}$$

with "V" in ft/sec, "P" as above and "550" indicating the conversion factor for HP. To this value, the thrust produced by the exhaust of the engine is to be added. In the case of reciprocating engines, this component is in the order of

$$\Delta T_{lb} = (0.11 \text{ to } 0.13) P_{HP} \quad (2)$$

provided that the exhaust pipes are adjusted in downstream direction. In case of the Me-109, the jet thrust is in the order of 140 lb. The total thrust at maximum speed is then $(1000 + 140) = 1140 \text{ lb}$. Considering steady horizontal flight, the value of the total drag of the airplane is equal to that of the thrust. At a dynamic pressure $q = 184 \text{ lb}/\text{ft}^2$, the "drag area" is consequently

$$D/q = C_D S = 1140/184 = 6.2 \text{ ft}^2 \quad (3)$$

The resultant drag coefficient (on total wing area of 172 ft^2)

$$C_D = 0.036; \text{ or } C_{Dwet} \approx 0.0105$$

on total wetted area of 590 ft^2 , indicates an airplane with comparatively poor aerodynamic efficiency (the Me-109 was first designed in 1935; size and output of the engine were \approx doubled between then and 1944).

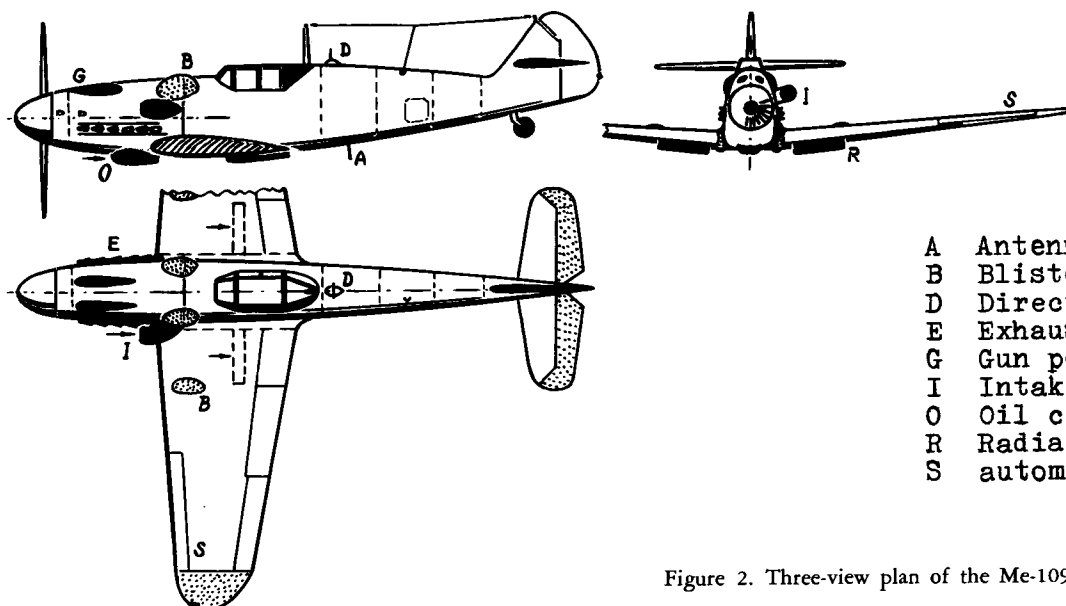


Figure 2. Three-view plan of the Me-109-G (1944.)

Induced Drag. For the given flight condition, the lift coefficient is $C_L = (W/S)/q = 0.21$. Because of flow around the wing tips (see in the "drag-due-to-lift" chapter), the effective aspect ratio is estimated to be reduced from 6.1 to 5.8. Considering planform, the induced drag is increased by some 2%. Consequently:

$$C_{D_i} = 1.02 \cdot 0.21^2 / (\pi \cdot 5.8) = 0.0025$$

$$D_i/q = 172 \cdot 0.0025 = 0.42 \text{ ft}^2 \quad (5)$$

There is no twist built into the wing of the Me-109. Subtracting the induced drag area from the total area, the tested parasite drag area is found to be $D_{par}/q = 5.8 \text{ ft}^2$.

(b) Drag Of The Wing

Skin Friction. The average wing chord of the airplane is $S/b = 5 \text{ ft}$. The Reynolds number corresponding to maximum speed is thus $R_c = V c/\nu = 1.1 \cdot 10^7$. The skin-friction drag coefficient of a smooth and plane surface at this R'number is approximately $C_f = 0.0028$. Because of the sheet-metal gaps behind the slats and owing to the propeller slipstream, the flow of the boundary layer past the wing surfaces of the Me-109 is "fully" turbulent, however. Furthermore, the skin of the Me-109 is coated with camouflage paint, the average grain size of which is in the order of $h \approx k = 1 \text{ mil}$. This value exceeds the permissible size. The drag coefficient corresponding to a grain size of $k/l \approx h/c = 1.7 \cdot 10^{-5}$ is in the order of $C_f = 0.0035$, as found in the chapter on "imperfections". The drag area of the wing panels (outside the fuselage) is accordingly $D/q = 1.28 \cdot 2 \cdot 0.0035 \cdot 150 = 1.35 \text{ ft}^2$, where "1.28" indicates the influence of section thickness (Chapter VI). The thickness ratio is $t/c = 14.2\%$ at the roots and 11.3% near the wing tips.

Surface Imperfections. The wing surfaces of the Me-109 are covered with numerous small protuberances such as sheet-metal joints and rivet heads, and with other irregularities such as gaps and holes. Number and size of these imperfections were determined on the airplane and added up in groups, separately for the two wing sides. The *lower* side has the following:

Type of Imperfection	Area ft^2	C_D or C_{Df}	$D/q, \text{ft}^2$
29 ft lateral sheet-metal edges	$S_+ = .16$	0.10	0.013
36 ft lateral surface gops	$S_+ = .75$	0.05	0.038
50 ft longitudinal edges	$S_+ = .17$.004	0.001
500 bolt heads	$S_+ = .40$	0.01	0.004
3500 flush rivet heads	$S_+ = 1.5$.0014	0.002
several sheet-metal blisters	$S_+ = .07$	0.10	0.007

The gaps are chiefly those around the covers of the retracted landing gear. Included in the sheet-metal edges are those of the many other covers of the Me-109 wing, bolted to the lower side by means of the 500 bolts as listed. The drag coefficients used in the table are selected from the various graphs in Chapter V. The total drag area of this wing side is $D/q = 0.065 \text{ ft}^2$. At the upper or suction side of the wing, the drag area due to imperfections is much smaller; $D/q = 0.011 \text{ ft}^2$. Imperfections on that side are carefully covered with filler, or they are avoided by suitable design in the first place. Referring the drag of the imperfections to the *exposed* wing area ($172 - 22 = 150 \text{ ft}^2$), additional skin-drag coefficients are obtained in the order of $\Delta C_f = 0.065/150 = 0.0005$ for the lower, and $\Delta C_f = 0.011/150 = 0.0001$ for the upper wing side. After adding these increments to the basic coefficient of 0.0035, the skin-drag coefficients are found to be 0.0040 for the lower, and 0.0036 for the upper side. Taking into account the influence of thickness as well as that of lift (as explained in the "streamline" chapter), the average dynamic pressure ratio is 1.16 at the pressure side and 1.42 at the suction side, respectively. The section drag coefficient of this "actual-construction" wing is then

$$C_{Ds} = 1.16 \cdot 0.0040 + 1.42 \cdot 0.0036 \approx 0.010 \quad (8)$$

The corresponding drag area is $D/q = C_D S = 1.47 \text{ ft}^2$.

Additional Components. The following sources of drag, common to both sides, are found on the Me-109 wing:

Drag Source	Area ft^2	C_D or C_{Df}	$D/q, \text{ft}^2$
Aileron gaps on both wing sides	$S_+ = .70$	0.025	0.018
Aileron hinges on lower side	$S_+ = .06$	0.5	0.030
Balance weights on the ailerons	$S_+ = .09$	0.3	0.027
Gaps at the sides of the slots	$S_+ = .07$	1.3	0.090
Gaps beside ailerons and flaps	$S_+ = .06$	0.5	0.030
Air-speed Pitot-static tube		—	0.010
2 Position lights on wing tips	$S_+ = .02$	0.1	0.002
2 Blisters on upper wing side	$S_+ = .20$	0.1	0.020
2 Holes around landing gear	$S_+ = 3.5$	0.04	0.140

Most of the drag coefficients are again taken from the graphs in Chapter V. Others are known from specific wind-tunnel tests (10,a) on the respective parts. Including some interference drag near the trailing edge caused by the parts, the total of the additional items is in the order of $D/q = 0.40 \text{ ft}^2$.

(c) Drag Of The Fuselage

Skin Friction. Because of the propeller slipstream, the flow of the boundary layer along the fuselage may be assumed to be turbulent from the beginning. For an average grain size of the camouflage paint coat of $k = 1$ mil, that is for $k/l = 2.8/10^6$, the skin-drag coefficient is taken from Chapter V to be in the order of $C_f = 0.0025$. The drag of all sheet-metal joints, gaps and rivet heads is again computed according to their number and size, and through the use of the drag coefficients listed in Chapter V. The resultant drag area is $D/q = 0.069 \text{ ft}^2$. Referring this drag to the wetted surface of the fuselage, which is $S_{\text{wet}} = 250 \text{ ft}^2$, the additional drag corresponds to $\Delta C_f = 0.0003$, and the total coefficient is $(0.0025 + 0.0003) = 0.0028$. Accounting for the increased dynamic pressure along the sides of the fuselage by a factor of 1.07 (see in the "streamline" chapter), the drag coefficient (on wetted area) is increased to $C_{D\text{wet}} = 1.07 \cdot 0.0028 = 0.0030$. For a wetted area of 250 ft^2 , the corresponding drag area is $D/q = 0.75 \text{ ft}^2$.

The Appendages listed in the following table present drag components, computed on the basis of frontal area and by means of drag coefficients selected from figure 3,b (for the canopy) and figure 39 (for the tail wheel) in Chapter XIII, and from reference 10,a (for the antenna mast). The *interference* drag caused by these "added" bodies is estimated on the basis of the principles and equations derived in Chapter VIII. The canopy has so many edges around the window panes, and some gaps to permit the cockpit to be opened, that its final drag value is almost twice that of the smooth shape. The total of the fuselage's appendages yields $D/q = 0.63 \text{ ft}^2$

Appendage	Area, ft^2	C_D	Interference	$D/q, \text{ft}^2$
Pilots Canopy	$S_a = 1.00$	0.10	19%	0.12
Irregularities	50%	0.08
Tail Wheel	$S_a = 0.50$	0.58	0	0.29
Antenna Mast	$S_a = 0.14$	0.17	19%	0.03
Antenna Parts	0.03
Antenna Stick	$S_a = 0.03$	1.50	10%	0.05
Gun Installation	0.03

Wing Interference. Interference drag caused by adding the fuselage to the wing is twofold; induced and parasitic. The lift variation due to low-wing configuration may correspond to a $\Delta C_{Lb} = L/q b_{fus} c$ less than +0.1 (see Chapter VIII). The corresponding constant component of induced drag is negligibly small. For the parasitic interference drag, an amount is estimated equal to that of the fraction of the wing covered by the fuselage. For a ratio $b_{fus}/b = 0.1$, and for a chord of 7 ft at the wing roots, the interference drag is found to be $D/q = C_D S = (0.01 \cdot 7$

$0.1 \cdot 32) = 0.22 \text{ ft}^2$. Including this value and that of the appendages above, the drag area of the fuselage is found to be $D/q = 1.60 \text{ ft}^2$. Referred to the frontal area $S = 9 \text{ ft}^2$, the drag coefficient is $C_{Df} = 1.60/9 \approx 0.18$ which is more than twice the value of the bare fuselage body.

Slip Stream. The fuselage, all of its appendages and the wing roots are located within the propeller's slip stream. This means that they are subjected to an average dynamic pressure which (at maximum airplane speed) is estimated to be 10% higher than that corresponding to flight speed. Including the slip-stream effect, the fuselage's total drag area is finally found to be $D/q = 1.1 \cdot 1.60 = 1.75 \text{ ft}^2$.

(d) Drag Of Appendages

Engine Installation. The exposed parts of the engine installation consist of a number of necessary items near the nose of the fuselage, such as the air scoop and the oil cooler for instance, and of the two radiators underneath the wings (see figure 2). The following tabulation gives their drag characteristics.

Component Part	Area ft^2	C_D	Interference	$D/q, \text{ft}^2$
Air Scoop	$S_a = 0.2$	0.3	12%	0.067
Intake Momentum	$S_a = 0.2$	0.4	0	0.080
Exhaust Stacks	$S_a = 0.1$	0.5	12%	0.056
Oil Cooler	$S_a = 0.75$	0.2	12%	0.168
Ventilation Openings	$S_a = 0.1$	0.9	12%	0.100
Wing Radiators	$S_a = 3.7$	0.18	---	0.660
Total of the Engine Installation	---	---	---	1.131

The coefficient of the air scoop is estimated on the basis of figure 18 in Chapter IX. The momentum of the air volume taken in through the air scoop presents a drag force as indicated by equation 20 in the "internal" chapter, corresponding to an estimated flow ratio of $w/V = 0.2$. The drag of the ventilation openings is determined through the use of a drag coefficient found in figure 23,b of the same chapter. The interference drag originating along the fuselage (because of engine parts), is found to be 12% of their basic drag (as per equation 9 in Chapter VIII). The drag of a radiator similar to one of the Me-109's twin wing radiators is presented in figure 4 of Chapter IX; $C_{Dq} \approx 0.1$, at an assumed $w/V = 0.15$. Only 0.04 of this is expected to be momentum drag. However, flight tests carried out with and without the radiators installed (10,d) indicate drag coefficients C_{Dq} between 0.15 and 0.21. These comparatively high coefficients correspond to poor aerodynamic design and considerable internal leakage.—The total drag area of and due to the engine components is multiplied by the slip-stream factor "1.1" as above; thus $D/q = 1.1 \cdot 1.13 = 1.24 \text{ ft}^2$.

Tail Surfaces. Not counting the portion covered by the fuselage, the horizontal tail surface presents an area of 25 ft^2 . The vertical-surface area is 11 ft^2 . For a grain size of the surface in the order of $k = 1 \text{ mil}$, the skin-drag coefficient is $C_f = 0.004$, as found in Chapter V. Due to a thickness ratio of $t/c = 10\%$, the section-drag coefficient is $C_{Ds} = 2.12 \cdot 0.004 = 0.0096$. Surface imperfections are accounted for in a manner similar to that as outlined above for the wing. The corresponding drag area is $D/q = 0.007 \text{ ft}^2$ for the horizontal, and 0.009 ft^2 for the vertical tail surface. The profile-drag coefficient is increased accordingly to 0.010, including the drag of the control gaps. Considering the boundary layer originating along the fuselage, the interference drag of the junctions between tail surfaces and fuselage walls is assumed to be zero. The parasite-drag area of the tail assembly is then $D/q = 0.010(25 + 11) = 0.36 \text{ ft}^2$. — On account of the (negative) lift of the horizontal tail surface, a small induced drag component may exist in the high-speed condition considered, in the order of $D/q = 0.01 \text{ ft}^2$.

Compressibility. The sum of all parasitic drag components considered, is $D/q = 5.14 \text{ ft}^2$. At maximum horizontal speed in 22,000 ft altitude, the Mach number of the Me-109 is $M = 0.55$. As explained in Chapter XV, only a certain fraction of the total parasite drag established in the last paragraphs, increases as a function of Mach number. Assuming in this respect a fraction of 10%, that is 0.52 ft^2 , the additional drag on account of compressibility, indicated by equation 55 of the chapter quoted, is

$$\Delta D/q = ((P)^3 - 1) 0.52 = 0.38 \text{ ft}^2 \quad (11)$$

where the Prandtl factor " P " = 1.2. Including this component, the "synthetic" parasite drag area is $D/q = 5.6 \text{ ft}^2$, a value that can be accepted as being sufficiently close to the 5.8 ft^2 recalculated above from the high-speed performance (thrust) of the airplane. It is possible, of course, to find values which are plus/minus 5 or more % off the correct drag area, just by assuming drag coefficients for the various component parts, somewhat higher or lower than they should be, within the range of accuracy of the information available.

(e) Results Of Me-109 Analysis

Parasite Drag Coefficient. The various drag components calculated in the foregoing paragraphs are plotted in figure 3. Not including induced drag, or momentum drag of the engine's air intake, and not counting the drag of the tail wheel, the resultant drag coefficient (on wing area of 172 ft^2) is $C_{Ds} = 0.028$. A coefficient of $C_{Ds} = 0.030$ was tested (10,c) in this condition in "la soufflerie la plus grande" at Chalais-Meudon near Paris in 1941 by placing a full-scale Me-109 in that tunnel. The difference in the coefficient is easily explained on the basis of Reynolds number. On wing chord, the number is $R_c = 4 \cdot 10^6$ in the tunnel, while in flying condition $R_c \approx 2 \cdot 10^7$.

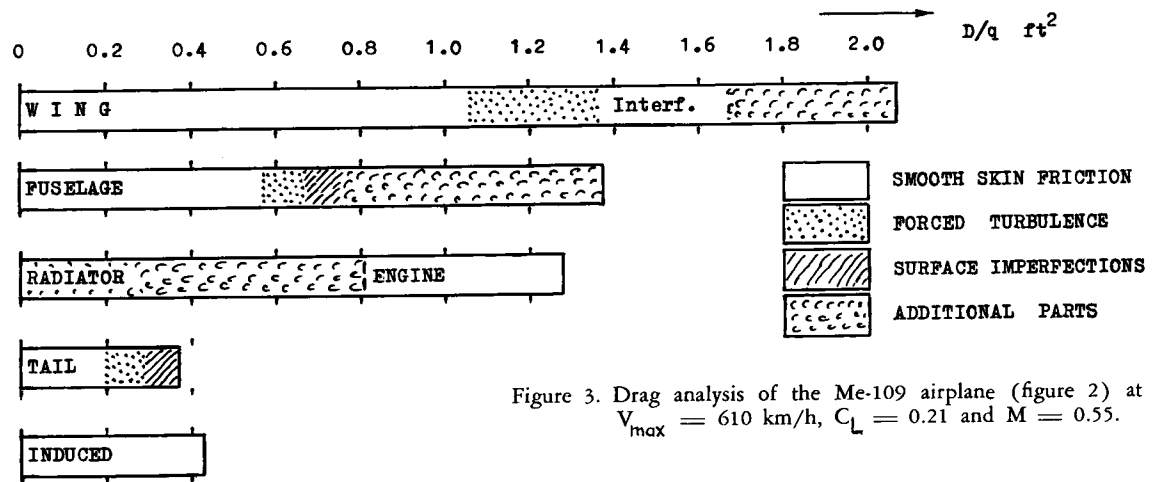


Figure 3. Drag analysis of the Me-109 airplane (figure 2) at $V_{max} = 610 \text{ km/h}$, $C_L = 0.21$ and $M = 0.55$.

Main Components. The drag analysis of the Me-109 shows that the drag of an actual-construction airplane can realistically be predicted "from scratch", by applying the methods developed in this book, particularly in reference to surface imperfections and interference effects. Considering distribution of the total drag, percentages are found as follows:

wing, including surface roughness	37.5%
fuselage, with roughness and canopy	13.7%
tail surfaces, including roughness	6.9%
engine and radiator installation	23.3%
appendages (as armament and tail wheel)	11.4%
induced drag (at maximum speed)	7.2%

- (13) Drag characteristics of Heinkel He-70 airplane:
 a) Full scale (Zts.Flugt.Motorluft Dec. 1933):
 $W = 3330 \text{ kg}$; $S = 36.5 \text{ m}^2$; $V_{\max} = 235 \text{ mph}$, with
 maximum power of 660 HP at sea level.
 b) Jones and Smyth, Models, ARC RM 1709 (1936).
 c) Results quoted in J.Aeron.Sci. 1940 p.425.
- (14) Full-scale performance of airplanes:
 a) Richards, "Cleanness", J.Roy.Aeron Soc. 1950 p.137.
 b) Hoerner, Skin Friction Analysis, Lufo 1935 p.188.
 c) Collection of Airplane Data in Aviation Week, 14 March 1955.
 d) Jane's "All the World's Aircraft", Volumes since 1909.
 e) RAE, "Spitfire" and "Mustang", ARC RM 2535 (1951).
 f) Sinclair, Vickers Viscount J.SLAЕ May 1956 p.3.
 g) Military Aircraft, Flight 1956 p.699.
 h) Clarkson, Efficiency, The Aeroplane 1938 p.474.
 i) NACA, Qualities of Douglas DC-3, Tech Note 3088.
 k) DeHav."Comet", The Aeroplane, 6 Jan, 6 July 1956.
 l) Fahey, U.S. Army Aircraft 1908 to 1946 and USAF Aircraft 1947 to 1956, by "Ships and Aircraft", Falls Church (Va.).
 m) Hall, Ryan "Spirit of St. Louis", NACA T.Note 257
 n) Fischer-Poturzyn, Junkers and World Aviation, Munich 1935.
 o) Littlewood, Trends in Transport, J.A.Sci.1953 p.225.
 p) From publications in aeronautical magazines.

The engine installation presents more drag (in this case) than the fuselage without appendages. The share of the radiator on total parasite drag, which is almost 16%, must be considered to be very high.

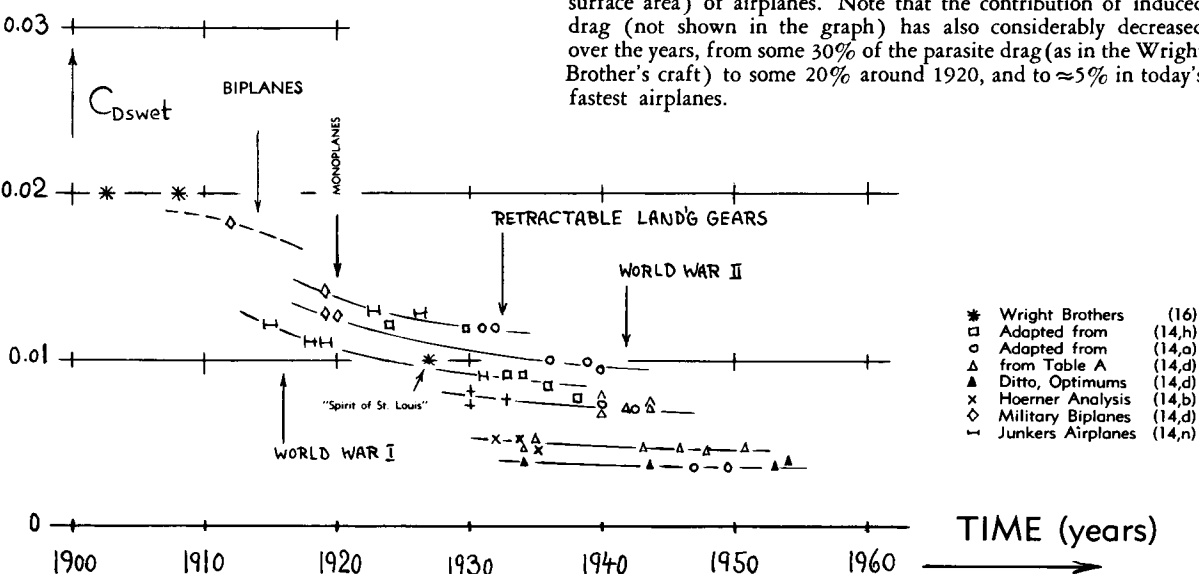
Aerodynamic Efficiency. Considering drag on the basis of origin, the following breakdown is found for the Me-109:

skin-friction drag (smooth surface, turbulent)	33%
surface roughness and surface imperfections	15%
exposed parts, especially those of the engine	33%
interference drag (including that due to parts)	6%
influence of compressibility (on 10% of drag)	6%
induced drag under maximum-speed conditions	7%

Several definitions are possible for an aerodynamic "efficiency" ratio

$$\eta_{aero} = D_{useful}/D_{total} \quad (12)$$

depending upon what is understood as "useful" or "necessary" or "unavoidable". Considering, for instance, in the last tabulation, the skin-friction drag and the induced drag as minimum limit of the useful drag, the efficiency of the Me-109 is but 40%. This figure indicates that more than half of the total drag of this airplane could theoretically be avoided by extremely clean design and faultless construction of skin and details. If rebuilding the Me-109 in a manner that η_a would reach 100%, the maximum speed would be increased from 610 to some 800 km/h, if using the same power plant.



3. PERFORMANCE OF OTHER AIRPLANES

Performance of airplanes is a function not only of aerodynamic drag, but also of lift and weight. Essentially two aerodynamic aspects are considered as follows; drag at maximum speed (where the lift coefficient is comparatively small) and drag as a function of lift.

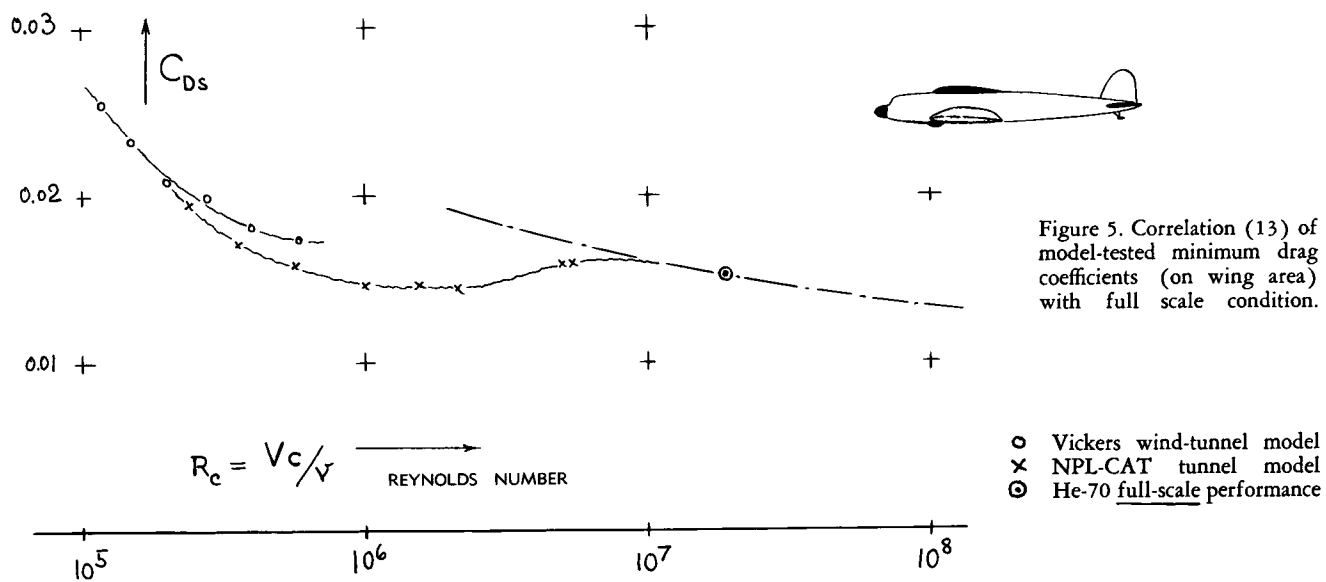
(a) Maximum Speed Performance

A large proportion of model testing in the field of shipbuilding (XI) and of land-borne vehicles (XII) is simply done to find the magnitude of "resistance" which is then used to predict full-scale power requirements. This is not really done in the development of airplanes; that is, not by testing truly similar models in wind tunnels. Rather, full-scale drag is estimated on statistical basis, or it is calculated by means of methods similar to those presented in this book.

Aerodynamic Cleanliness. Maximum speed is of course a function of drag; and drag (per unit of wetted area) is a matter of design, constructional expenditure and application of the airplane. For example, the wire-braced airplanes of the era between 1903 and 1920 (beginning with the Wright Brothers' famous craft) had a very low aerodynamic efficiency. Figure 4 indicates for them a drag coefficient (on wetted area) in the order of some 6 times the theoretically possible

minimum corresponding to turbulent skin friction. The graph then shows the influence of the so-called World Wars I and II upon development. Between 1930 and 1940 the drag coefficients were still comparatively high in the airplane types in general service at that time — while a few experimental and/or progressive designs had values comparable to the more advanced airplanes of today. Since the Wright Brothers' days, airplanes have very much been "cleaned up", so that the drag of those particularly designed for high speed, is now approximately equal to their skin friction drag (assumed to be turbulent). One more experience can be mentioned, namely that military airplanes usually start out comparatively clean, and that the various requirements of armament and operation may finally make them into "Christmas Trees" (see Chapter XIII in regard to appendages).

As a Function of R'number — figure 5 presents a correlation of model-tested drag coefficients of a certain airplane design, with a value recalculated from full-scale performance. The wind-tunnel results have been obtained on *smooth* models and at R'numbers below completed transition. The fact that some of the model data are on the same level as the full-scale point, is only accidental. Using truly similar models (including roughness and internal flow) and forcing transition (by turbulence stimulation of the boundary layer), we would obtain considerably higher coefficients, as indicated by the line meeting the full-scale point. This mechanism is fully realized in ship-model testing (Chapter XI) where skin friction is purposely made turbulent, and is then reduced analytically in proportion to the basic functions presented in Chapter II (equation 25). With respect to airplanes, it is the very purpose of this book to establish and to present a method of predicting full-scale drag



"from scrap", including items which cannot very well be imitated in a model, such as leakage for example, and surface imperfections (which would be likely not to be similar in a boundary layer thickened by turbulence stimulation).

Drag Breakdown. Drag of two or more (comparatively modern) airplanes has been analyzed in the manner outlined in section 2 of this chapter. Principal results are as follows:

Junkers Ju-88 Bomber. This airplane, put into service in 1940, has the following data:

gross weight	$W = 22000 \text{ lb}$
wing area	$S = 560 \text{ ft}^2$
maximum speed	$V = 280 \text{ mph}$
aspect ratio	$A = 6.3 -$
maximum power	$P = 1900 \text{ HP}$
at altitude	$z = 18000 \text{ ft}$

Assuming a propeller efficiency of 78%, and taking into account 250 lb of exhaust thrust, the drag area is found to be $D/q = 20 \text{ ft}^2$; $C_D = 0.036$. Analysis

gives the following distribution:

induced drag of the wing	4.1 ft^2	21%
parasite drag of wing	7.0 ft^2	35%
drag of the fuselage	3.1 ft^2	16%
drag of tail surfaces	2.0 ft^2	10%
drag of the nacelles	3.6 ft^2	18%

The induced drag has a much higher percentage in this case (at $C_L = 0.35$) than in the case of the Me-109 or other fighter airplanes. The profile-drag coefficient of the wing, including imperfections and aileron gaps is $C_{D_s} = 0.0125$, which is approximately twice the drag of an ideal (smooth and undisturbed) wing with $t/c = 13.5\%$. The drag coefficient of the fuselage, based on frontal area of 21 ft^2 , is $C_D = 0.15$. The profile-drag coefficient of the tail surfaces is in the order of 0.11 for 13% thickness ratio. The drag coefficient on total wetted area, in the order of $C_{D_wet} = 0.010$, is comparatively high. It can therefore be concluded that this airplane (with a pair of rather "bluff" engine nacelles and with all sorts of military equipment) was not very efficient in aerodynamic respect.

YEAR	AIRPLANE	TYPE	b(ft)	S(ft^2)	W(lb)	"POWER"	z(ft)	V,kts.	C_D	C_{D_s}	C_{D_wet}	NOTES
1903	Wright-Brothers	RP biplane	40	510	750	12 HP	0	26	0.074	0.046	0.020	17 December 1903
1927	"Spirit of St.Louis"	RP personal	46	319	(3000)	223 HP	0	112	0.033	0.029	0.010	Lindberg - Atlantic
1938	Fieseler "Stork"	RP S T O L	47	280	2700	240 HP	0	95	0.066	0.061	0.014	fixed wing slots
1935	Messerschmitt-108	RP personal	34	173	2800	230 HP	0	160	0.018)	0.016)	0.009)	modern - personal
1945	Piper "Cub"	RP personal	35	179	1500	135 HP	0	110	0.032)	0.029)	0.009)	struts + landg.gear
1948	Beech "Bonanza"	RP personal	33	178	2700	220 HP	0	169	0.018)	0.016)	0.005)	retracted landg'gear
1950	Cessna "170"	RP personal	36	175	2200	140 HP	0	122	0.032	0.029	0.009	struts + landg'gear
1942	Messerschmitt-109	RP fighter	32	172	6700	1200 HP	22000	330	0.036	0.033	0.0095	with bluff radiators
1943	N.A. P-51 "Mustang"	RP fighter	37	235	10000	1380 HP	20000)	380	0.020	0.017	0.0040	w'laminar profile
1943	Messerschmitt-262	TJ fighter	34	233	10800	2500 lb	10000	450	0.022	0.021	0.0059	"first" jet plane
1944	Messerschmitt-163	RO interceptor	31	186	8000	1500 lb	13000	500	0.013	0.012	0.0035	rocket-powered
1946	Lockheed P-80	TJ fighter	39	238	11000	4000 lb	J-33	480	0.021	0.020	0.0050	holds speed record
1932	Junkers "Ju-52"	RP passenger	98	1190	22000	2000 HP	5000	170	0.032	0.028	0.0080	corrugated skin
1934	Douglas "DC-2"	RP passenger	85	940	18000	1400 HP	7000	185	0.021	0.018	0.0045	"first" modern
1934	Heinkel "He-70"	RP passenger	49	390	7300	660 HP	0	203	0.013	0.012	0.0038	very clean design
1946	Lock "Constellation"	RP passenger	123	1650	80000	8000 HP	14000	300	0.019)	0.017)	0.005)	modern airliner
1951	Douglas "DC-6B"	RP airliner	117	1463	100000	7600 HP	16000	325	0.019)	0.017)	0.005)	large airliner
1953	De Havilland "Comet"	T airliner	115	2120	150000	42000 lb	37000	440	0.016)	0.014)	0.0037)	large turbo-prop
1954	Vickers "Viscount"	TP airliner	94	960	65000	7600 HP	35000	300	0.017)	0.015)	0.004)	British turbo-prop
1940	Heinkel "He-111,H"	RP bomber	74	942	25000	2600 HP	13000	200	0.026	0.023	0.0070	now an "old" bomber
1940	Junkers "Ju-88,A"	RP bomber	66	590	25000	2000 HP	18000	245	0.036	0.028	0.0079	in World War II
1942	Boeing "B-17,G"	RP bomber	104	960	52000	4000 HP	14000	270	0.028	0.024	0.0070	in World War II
1943	Messerschmitt-210	RP bomber	54	390	21000	2300 HP	19000	310	0.028	0.024	0.0070	in World War II
1943	Boeing "B-29,B"	RP bomber	142	1730	153000	8000 HP	14000	305	0.033	0.030	0.0077	atomic bomb carrier

TABLE A, showing dimensions and performance of a very few among the hundreds or thousands of airplane types developed since 1903. Note that power (or thrust, respectively) and maximum speed are both a function of altitude, and that information on both of them is usually less accurate than on the dimensions of an airplane. The drag coefficients are evaluated from maximum speed performance; values in parentheses are only estimated. The years quoted are usually not those of the first appearance of the particular airplane types; rather they are the years in which those airplanes became predominant or in which they had power and performance as listed. Successful airplane designs usually undergo considerable and repeated changes in this respect. Also, one and the same type may have different performance values, as a function of load and/or equipment carried. Ratios such as W/S , P/S , P/W or $A = b^2/S$ and $S_{wet}/S = C_D/C_{Dwet}$ can be derived from the data as listed. The letters under the heading "type" indicate the type of propulsion; RP = reciprocating engine plus propeller, TJ = Turbo-jet propulsion, TP = turbo-propeller combination, RO = rocket power. The "power" of jet-type engines is usually given in pounds of static thrust.

Messerschmitt Me-262. The production version of this first type of jet airplane ever used in actual service, has the following data:

gross weight	$W = 10600 \text{ lb}$
wing area	$S = 233 \text{ ft}^2$
maximum speed	$V = 520 \text{ mph}$
aspect ratio	$A = 7.2 -$
thrust power	$P = 2900 \text{ HP}$
at altitude	$z = 7000 \text{ ft}$

The drag area corresponding to these conditions is $D/q = 5.0 \text{ ft}^2$; $C_{D\text{wet}} = 0.006$. Analysis shows the following distribution:

induced drag of the wing	0.1 ft^2	2%
parasite drag of the wing	1.6 ft^2	32%
drag of the fuselage	1.6 ft^2	32%
drag of the tail surfaces	0.7 ft^2	14%
drag of the two nacelles	1.0 ft^2	20%

An increment of 15% due to compressibility (see Chapter XV) at a Mach number of 0.67 is included in the total value. The surface imperfections are small in case of the Me-262. The profile-drag coefficient of the wing is only 0.0073; the coefficient of the fuselage is only 0.08, based upon a frontal area of some 19 ft^2 . The drag of the jet engine nacelles is appreciable; particularly caused by interference with the wing.

Wetted-Area Drag Coefficient. Assuming that most of the drag of an airplane is skin friction, and that the rest is somehow an added percentage, drag areas "f" = (D/q) can statistically be considered as a function of total wetted area (of wing plus nacelles plus fuselage plus tail). Table A presents some such results, evaluated from performance data of various airplanes published in (14). Certain groups can be identified as per period of time and application. Commercial airplanes (and military cargo airplanes) have usually somewhat lower drag coefficients than comparable military combat planes. As an example for low aerodynamic efficiency, the Fieseler "Stork" is listed in the table. This airplane was not designed for fast or continued flying; rather its purpose was to fly as slowly as practicable, replacing the helicopter type of aircraft which was not yet available at that time (1937). The "Stork" was consequently constructed as light as possible, equipped with a non-retractable landing gear, and fitted with a fixed wing slot all over the span ($C_{L\text{max}} = 3.4$, including the additional lift due to propeller). — It is also seen in the table as well as in figure 4, that at one and the same time, the drag coefficient $C_{D\text{wet}}$ may vary as much as between 0.014 (for the "Stork") and 0.004 (for "P-51, Mustang", a very progressive fighter airplane for its time). It is also seen that the drag coefficient of a certain type of airplane decreases with time; so for example from 0.008 (for Junkers-52 in 1933) to 0.005 (for "Constellation" in 1947) and to 0.004 or less (for "Viscount" in 1955).

Sweep. Figures 6 and 7 show examples of modern highly efficient airplanes. The two airplanes do not really reach any critical (near-sonic) speeds. It is therefore suggested that the swept shape of their wings is primarily a matter of arrangement.

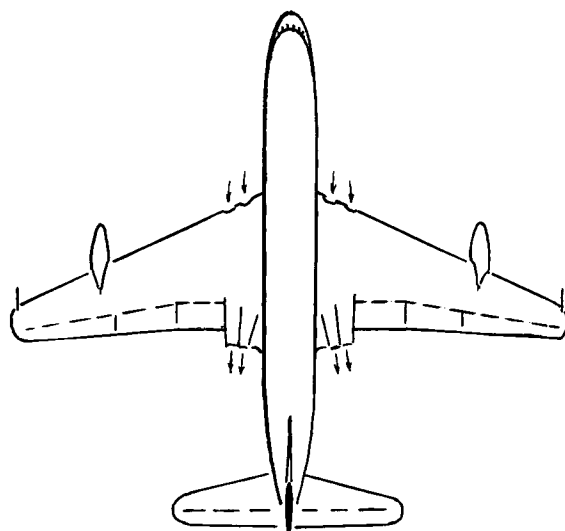


Figure 6. Plan-form view of a modern turbo airliner, De Havilland "Comet 4" (1956), developed from "Comet 1" (1949).

$$\begin{aligned} W &\approx 150000 \text{ lb} & T &\approx 42000 \text{ lb} \\ b &= 115 \text{ ft} & V_x &\approx 450 \text{ kts} \\ S &= 2120 \text{ ft}^2 & Z &\approx 37000 \text{ ft} \end{aligned}$$

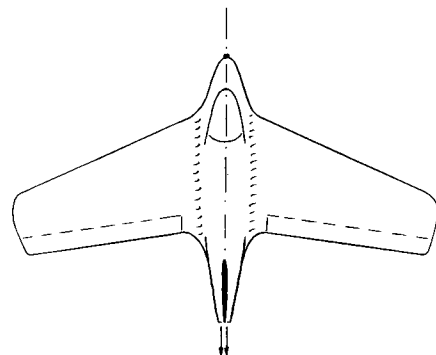


Figure 7. Plan-form view of Me-163 interceptor fighter, first successful rocket-powered airplane (1944). $W = 9000 \text{ lb}$, $b = 31 \text{ ft}$, $S = 186 \text{ ft}^2$, $V_{\text{max}} \approx 1000 \text{ km/h}$ (1941, in smooth and clean condition). Climb speed $11600 \text{ ft/min}/\sqrt{\text{ft}}$.

Aerodynamic Efficiency can have various definitions. Assuming as an average skin-friction drag coefficient (including the influence of wing- and fuselage thickness) the value of 0.003, aerodynamic efficiency is approximately indicated by

$$\eta_a \approx 0.003/C_{Dwet} \quad (15)$$

where C_{Dwet} represents the parasitic drag at high or cruising speed. Efficiency increases from some 15% (Wright Brothers in 1903) to some 100% in more or less experimental or not completely outfitted, clean airplanes as of today.

Maximum Speed is not only a function of drag, but also of power installed. Power is evidently

$$P = 0.5 \rho V^3 C_D S \quad (16)$$

It follows from this function (in a fixed altitude; with $\rho = \text{constant}$) that $V_{\max} \sim \sqrt[3]{P_{\max}/S}$. Figure 8 presents some statistical information in this form. The available data correspond to drag coefficients (on wing area) between 0.015 and 0.035. It must be mentioned at this point, however, that compressibility (Mach number) sets a limit to the maximum speed obtainable with subsonic types of aircraft; see Chapter XV.

Seaplanes and flying boats, data of which are not included in our statistical survey, are basically handicapped by the type of configuration, ruggedness and structural accommodations necessary for operation in, out and onto water. Some information on their drag is presented in Chapter XIII.

Figure 8. Statistical survey on maximum speed of airplanes (14) as a function of their power ratio P/S . Note that performance depends not only on power, but also upon altitude, type of airplane (loading and equipment) and aerodynamic refinement, such as a retractable landing gear, in particular.

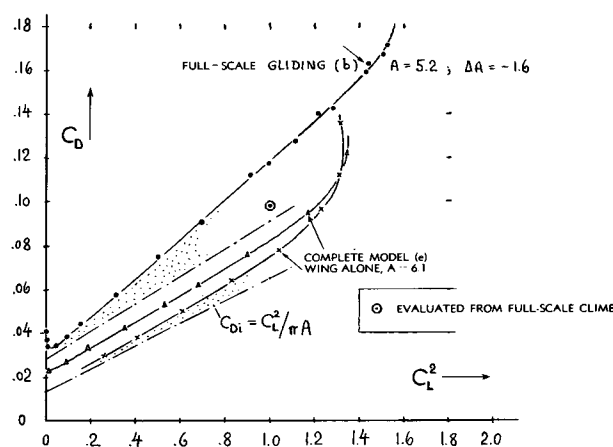
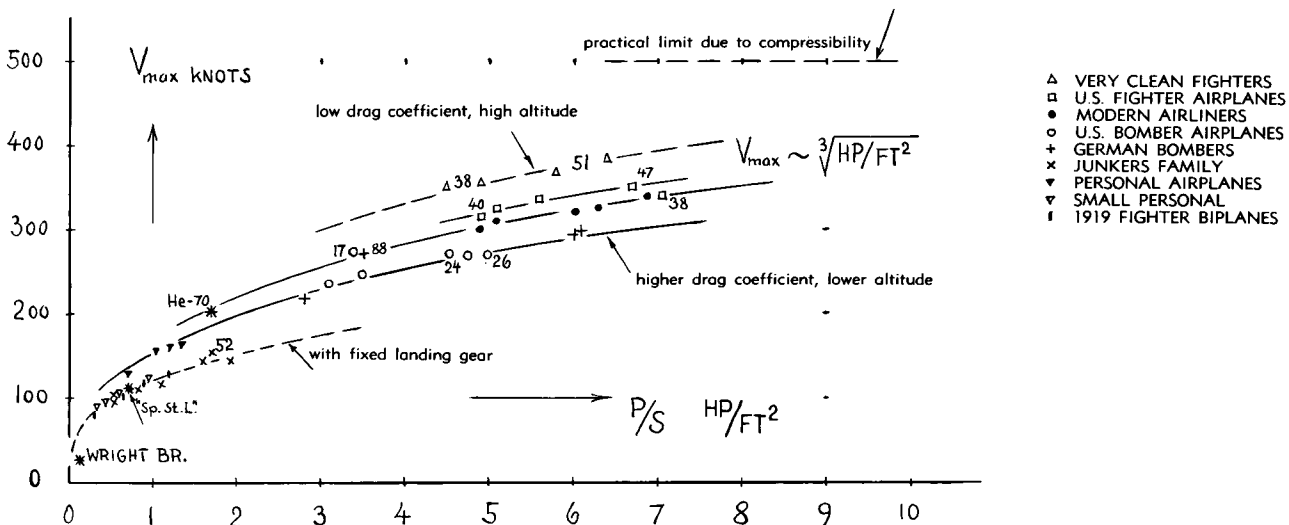


Figure 9. Drag coefficients of the Me-109 (10), plotted versus the square of the lift coefficient.

- (15) Airplane models in wind tunnels:
a) NPL, He-70 Airplane, ARC RM 1709 (1936);
see "Boundary Layer and Wake", J.Aeron.Sci. 1940 p.425.
b) RAE, Tunnel Tests on Fighters, ARC RM 2535(14,e).
- (16) Dimensions and performance characteristics of the Wright Brothers airplane, as given in the Smithsonian Institution in Washington (DC).
- (18) Principles and application of $C_D(C_L^2)$ method:
a) Oswald, General Formulas and Charts for the Calculation of Airplane Performance, NACA Tech.Rpt 408 (1932); also Tech.Rpt 654 (1939).
b) Driggs, Aircraft Analysis, Paper RAS London 1949.
- (19) Characteristics of sailplanes:
a) Lippisch, Sailplane Performance, Lufo 1934 p.127.
b) Murray, Wing and Fuselage, Lufo 1934 p.131.
- (20) Airplane drag as a function of lift:
a) ARC, Junkers Full Scale and Model, RM 945 (1924).
b) ARC, Glides of Bristol Fighter, RM 1133 and 1146; also with propeller in RM 937, 1083, 1085.
c) Raspet, Cessna-120, Aeron.Soc.India J. 1952 p.115.



(b) Drag Due To Lift

Drag due to lift is primarily induced drag (Chapter VII). However, other components of drag also increase as a function of lift coefficient, as shown for the foil section drag (Chapter VI), the interference drag (Chapter VIII), and the drag of other aircraft parts (Chapter XIII).

$C_D(C_L^2)$ Method. The type of plot presented in figures 9 and 10 is based upon the assumption or approximation that all increments of the drag coefficient might, at least on the average, be proportional to the square of the lift coefficient. Such an approximation is encouraged by similar plots, in figures 24 and 38 of the "interference" chapter and by a number of graphs in the "due to lift" chapter. The concept of $C_{DL} \sim C_L^2$ has, therefore, led to a method of performance calculation sometimes called the "e" method (18). In form of an equation thus:

$$C_D = C_{D_0} + (dC_D/dC_L^2)C_L^2 \quad (18)$$

where C_{D_0} = parasite drag coefficient, obtained by extrapolation to $C_L^2 = 0$. The drag due to lift is then indicated in terms of the induced drag:

$$C_{DL} = C_L^2 / (\pi e \cdot A) \quad (19)$$

where "e" (usually smaller than unity) indicates an equivalent or effective aspect ratio $A_e = eA$. In other words, the aspect ratio of the wing or airplane, the performance of which is to be calculated, is considered to be decreased by the factor $e = A_e/A$. The effective aspect ratio, similar in definition to that employed in Chapter VII, thus leads to a polar diagram which approximately describes the characteristics of the actual airplane. Interpolating the tested points in a plot such as in figure 9 by a straight line, the "e" factor is determined by the slope (dC_D/dC_L^2) in relation to that of the minimum possible induced drag ($C_L^2/A\pi$).

Analysis Of Me-109. Figure 9 presents drag characteristics of the Me-109, as a function of lift, tested on a wind tunnel model (10,e) as well as in full scale (gliding). The 1939 version of the Me-109 (designated "E") differs from the model G (as considered in the first section of this chapter) chiefly by shorter wing tips; the wing area is but 162 ft² and the aspect ratio is only 5.2. The full-scale drag due to lift slope (dC_D/dC_L^2) is consequently greater than that of the model. — A drag analysis of the Me-109, similar to that presented for maximum-speed condition (in Section 2), has also been made (12) for $C_L = 1$, a condition

that approximately corresponds to minimum sinking speed of that airplane. Induced drag is, of course, based on aspect ratio. Section drag as a function of lift is estimated, using equation 18 in Chapter VI. At $C_L = 1$, the drag of the radiator corresponds to a flow ratio of $w/V = 0.27$. Finally, the horizontal tail presents increments of appreciable magnitude, both of induced drag as explained in Chapter VII and of parasite drag (as shown in figure 32 of Chapter XIII). The total drag in power-off flight as plotted in figure 9 is approximately composed of a basic parasite component of (" C_{Dmin} " = 0.029) and a component due to lift, which is approximately proportional to C_L^2 (as explained above). The latter component may roughly be broken down as follows:

type of drag	dC_D/dC_L^2	%
Parasite wing drag (including parts)	0.010	11
induced drag of the wing ($A = 5.2$)	0.061	69
drag of and due to fuselage	0.009	10
parasite drag of the tail surfaces	0.004	4
induced drag of the horizontal tail	0.005	6
total drag due to lift	0.088	100

Full-scale characteristics in figure 9 also differ from the model results in the value of minimum drag coefficient (the model is too smooth).

Effective Aspect Ratio. Inasmuch as parasitic drag is not related to induced drag and aspect ratio, the concept of "e" does not have a theoretical basis. The differential $(1 - e)$ should be expected to increase in proportion to the aspect ratio "A". Representation of the effective aspect ratio by

$$\Delta A = (e - 1)A \quad (20)$$

is therefore preferred in this book. The differential ΔA is obtained by comparing a tested $C_D(C_L^2)$ function against the theoretical minimum; thus

$$\Delta A/A = ((dC_D^2/dC_L^2)/\pi A) - 1 \quad (21)$$

The drag-due-to-lift coefficient of the Me-109-E at $C_L = 1$, corresponding to $dC_D/dC_L^2 = 0.089$, is by 0.027 larger than that of the induced drag (as indicated by lifting line theory), in the power-off condition represented in figure 9. The increment (about equally caused by tail, sectional wing drag and fuselage interference) is appreciable. In terms of an effective decrease of the aspect ratio, the value "0.027" corresponds to $\Delta A = -1.6$. The "gliding ratio" is $L/D = 1/0.117 = 8.6$, at $C_L = 1$. The maximum of this ratio is ≈ 9.6 at C_L between 0.6 and 0.7. — The Me-109-G model (in figure 9) has a lesser drag-due-to-lift slope $(dC_D/dC_L^2 = 0.061)$, not only because of its larger aspect ratio, but also on account of its greater smoothness. In terms of the effective aspect ratio, the result is $\Delta A = -0.9$ for the model of the 109-G.

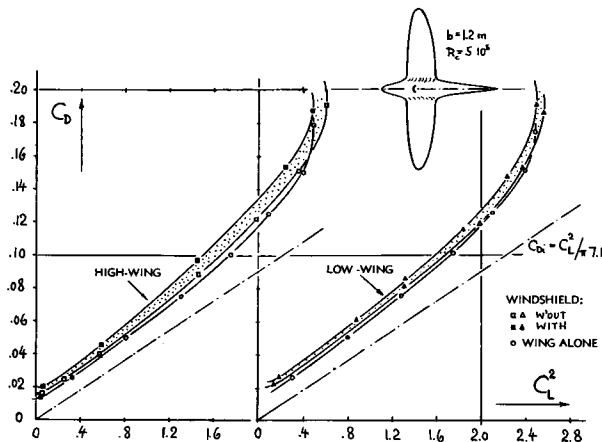


Figure. 10. Drag-due-to-lift characteristics of a sail-plane model (19,b), tested at $R_c = 5 \cdot 10^5$.

Sailplane. Figure 10 presents the drag and lift characteristics of a sailplane tested on a model in the configurations as indicated. The low-wing type is more favorable than the high-wing arrangement, particularly after adding a minimum size windshield. Based on its frontal area (equal to 1/300 of the wing area), the drag of the canopy corresponds to $C_{D_0} \approx 0.8$ at $C_L \approx 0.5$, roughly alike for the two configurations tested. However, at $C_L = 1.4$, the coefficient is $C_{D_0} = 1.9$ for low-wing and = 3.1 for high-wing arrangement. These values remind of the results found for plates (disks) presented at the end of the "interference" chapter. Figure 10 also demonstrates the limitations of the $C_D(C_L^2)$ concept. The lines obtained are not really straight. They can only be approximated by straight lines within a certain range of the lift coefficient, which in the highly cambered section applied in the sailplane considered, may be between $C_L = 0.4$ and 1.0.

Optimum Lift. An important point in the drag and lift characteristics of an airplane is the lift coefficient where C_D/C_L is at a minimum. This point is found by the tangent line through the origin as drawn, for illustration, in the lower part of figure 11. In wings or in airplane configurations in which the drag component due to lift (C_{DL}) is sufficiently well proportional to the square of the lift (C_L^2), the total drag

coefficient at the point of $(D/L)_{min}$ or $(L/D)_{max}$ is two times the parasitic or minimum coefficient:

$$C_D = 2 C_{Dmin}; \text{ or } C_{DL} = C_{Dmin} \quad (22)$$

Assuming that $C_{DL} = C_{D1}$, the statement (21) can also be made that at the optimum point considered:

$$C_{DS} = C_{D1}; \text{ or } C_D = 2 C_L^2 / (\pi A) \quad (23)$$

Sinking Speed. The significance of the point where (D/L) is minimum, is demonstrated in the upper part of figure 11. Every wing or airplane has basically its maximum range or most favorable gliding performance at the speed corresponding to the lift coefficient ($C_L = 0.9$, in the example) at which the (C_D/C_L) ratio is minimum. The connection between upper and lower part of the illustration is approximately given by

$$V = \sqrt{(2W/\rho S)} / \sqrt{C_L} \quad (24)$$

$$w = \sqrt{(2W/\rho S)} (C_D/C_L)^{1.5} \quad (25)$$

The latter equation also shows that minimum sinking speeds (maximum ceiling and smallest turning circle) are obtained at a speed "V" corresponding to the C_L value at which $(C_D/C_L)^{1.5}$ or (C_D^2/C_L^3) is minimum. That lift coefficient is always above the value at which $(C_D/C_L) = \text{minimum}$. The minimum "drag ratio" of the sailplane in figure 11 is 3.2%; the corresponding "gliding ratio" (L/D) is 31, obtained in an aspect ratio $A = 19$. Other high-performance sailplanes have been built with still higher aspect ratios, up to the order of 30.

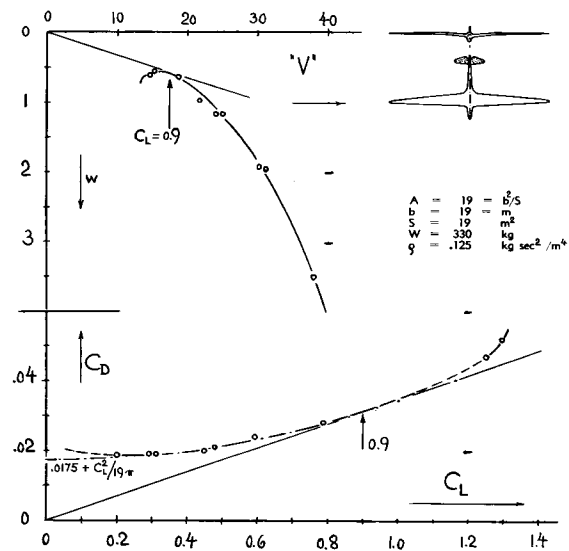


Figure 11. So-called speed polar diagram (upper part) and drag-lift function (lower part) of the high performance sailplane "Sao Paulo" (19,a).

(21) Lanchester: "An aerodrome (airplane) will travel the greatest distance on a given supply of energy when its aerodynamic (due to lift) and direct (parasitic) resistances are equal to one another."

(c) Influence Of Thrust

Analysis of flight performance is not directly a subject of this book. Inasmuch as drag is a principal basis of performance calculation, it is believed, however, that the influence of thrust (propeller or jet) on drag due to lift must be explained.

Lift Due to Thrust. In a combination of wing plus propeller (and slipstream), the lift is usually increased over that of the plain wing. Theoretical analysis (22,a) indicates for airplane configurations of conventional design (with propeller diameter "d"

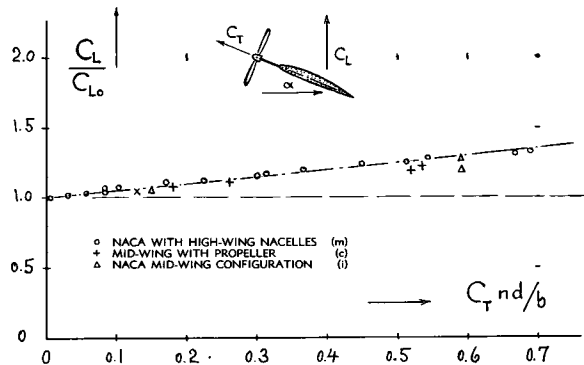


Figure 12. Increment of lift due to tractor-propeller thrust in various airplane configurations (22). Theory as per equation 30.

- (22) Influence of slipstream on lift and drag:
 - a) Smelt-Davies, Increase of Lift, ARC RM 1788 (1937).
 - b) Pleines, "Bussard", Lufo 1935 p.142.
 - c) Stüber, Wing-Propeller Interaction, Ringbuch Luftftech. Part IA12 (1939); also Lufo 1935 p.267, 1938 p.181.
 - d) Muttray, Running Propeller, Lufo 1938 p.181.
 - e) NACA, Systematic Nacelle-Propeller Combinations, T.Rpts. 415, 436, 462, 505, 506, 569 (1932 to 1936).
 - f) ARC Reports RM 1512, 1624, 1797 (1932 to 1937).
 - g) Hoerner, Fieseler "Stork", Yearbk D.Lufo 1939 p.I,238.
 - h) Aiken, Air Load Distribution, NACA T.Note 1729.
 - i) Kuhn-Draper, wing-propeller combinations for vertical take-off, NACA T.Notes 3304, 3360, 3364.
 - k) NACA, Distribution of Air Load, T.Note 1729 also RM L9B10 (wing, fuselage, tail).
 - l) Rethorst, In VTOL Aircraft, Aero Engg. Review Oct 1956 p.42; see also his Dr. Thesis to be published
 - m) NACA, 4-Engine Airplane, Tech Note 3789 (1956).
 - n) Thompson, Pusher Tractor Propellers, ARC RM 2516.
- (24) Squire-Young, Calculation of Induced Drag Due to Propeller Slipstream, ARC RM 2368 (1950).
- (26) Schrenk, Interaction Between Airframe and Engine Installation, ZFM 1927 p.399 and 1931 p.695 & 721.
- (28) The wetted area of airplanes is on the average roughly: $S_{wet} = (2S) + (0.3S, \text{ for tail surfaces}) + (1.3S, \text{ for fuselage}) + (0.3S, \text{ for twin nacelles, if any})$; where $S = \text{projected wing area}$.

in the order of the wing chord) an approximate increment

$$\Delta C_L \approx 0.5 C_T C_{L0} n (d/b) \quad (30)$$

where $C_T = T/qS_0$; $S_0 = d^2 \pi/4$; $n = \text{number of propellers installed}$; and $(d/b) = \text{propeller diameter in relation to wing span}$. Figure 12 proves that the equation correctly describes certain mid-wing arrangements. Flapped wings (22,i) and configurations with some basic flow separation above the fuselage (22,g) show higher increments, however, in the order of twice that as predicted by the equation. Low-wing airplanes too (22,h) have increments in somewhat increased order of magnitude. Reference (22,e) gives similar results for low-wing combinations. Other experimental results in this source show that in high-wing nacelle configurations, the increment is less, possibly only half of that as indicated by equation 30. It evidently matters whether the slipstream is blowing in the direction of, or against the wing's circulation.

Climbing. The thrust of an airplane does not only vary with speed; in full-power climb, thrust is also different from that in steady and straight horizontal flight at one and the same speed. Inasmuch as drag due to lift is of primary importance in prediction and/or analysis of climb performance, we will consider an airplane at constant effective power (tentatively made possible by means of a variable-pitch propeller). The thrust available is, then

$$T \sim 1/V; \text{ and } C_T \sim C_L^{3/2} \quad (31)$$

Figure 13 presents an example confirming this trend; and there are other sources (22) showing similar results.

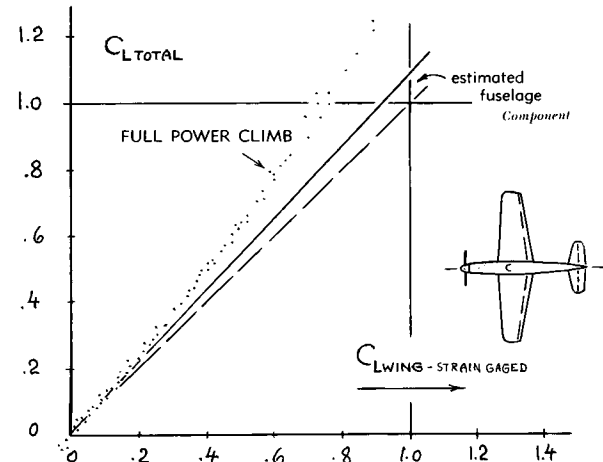


Figure 13. Coefficient of total lift (corresponding to weight) of North American "Mustang" (22,k) in full-power flight, plotted against that of the lift produced in wing panels and the horizontal tail (measured by strain gages). The differential is essentially due to propeller slipstream.

Drag Due to Slipstream is twofold. First, the parasitic drag of the airplane's components located within the slipstream is increased, approximately in proportion to the increased dynamic pressure within the stream. This type of drag is mentioned in the M-109 example in Section 2. Second, the lift increment as per equation 30 results in additional (or in a different component of) induced drag. It is clear then that in an airplane with operating propeller, the simple concept of one certain effective aspect ratio can no longer be adequate. In other words, the effective aspect ratio is a function of power or thrust applied. This mechanism becomes very much evident in the extreme case of "STOL" (short take-off and landing) or "VTOL" (vertical take-off and landing) aircraft (22,l). They develop lift \approx thrust at $V \rightarrow 0$; and their effective aspect ratio consequently approaches infinity in that condition. — The component of drag corresponding to the increment of lift due to thrust as explained above, is tentatively

$$\Delta C_{D_i} = \Delta C_L \alpha'_i = \Delta C_L C_{L_0} / \pi A \quad (33)$$

where α'_i is the induced angle of the wing *without* propeller, at the lift coefficient " C_{L_0} ".

Climb Performance. As a simplified case, a midwing airplane may be considered, with a lift increment as per equation 30 and a drag increment as indicated by equation 33. Inasmuch as C_{D_i} corresponds to an " α'_i " determined on the basis of C_{L_0} (rather than $C_L = C_{L_0} + \Delta C_L$), the total drag due to lift (dC_D/dC_L^2) of the airplane with running propeller should then be expected to be somewhat smaller than in gliding condition. To confirm this effect, full-scale climb performance of the Me-109-E has been analyzed. Corresponding to a value of $C_L^3/C_D^2 = 110$ obtained at $C_L = 1$, the drag coefficient in full and maximum power condition is found to be $C_D = 0.095$. Figure 9 shows that this value is smaller than that derived from glides (without power). The differential corresponds to a ΔC_L value produced by propeller and slipstream, roughly in the magnitude as indicated by equation 30.

In Jet Airplanes the mechanism of lift caused by thrust may partly be identical to that as outlined above for tractor propellers. Note that the volume of air taken in by a jet engine is deflected within the duct through the airplane's angle of attack (as mentioned in Chapter IX in connection with wing- and fuselage-side inlets). Here as in pusher-type propellers (22,e) a different type of lift differential is also produced by the thrust as such; namely

$$\Delta L = T \sin \gamma \quad (35)$$

$$\Delta D \equiv \Delta T = (1 - \cos \gamma) T_0 \quad (36)$$

where γ = flight-path angle against the horizontal. — It is difficult, of course to draw a line between net thrust and effective drag of an airplane. In a correct analysis of performance, this has to be done, however. — In jet engines we may roughly assume constant thrust (rather than constant power) over the airplanes most favorable climb-speed range. In this case,

$$C_T \sim 1/V^2 \sim C_L \quad (38)$$

which means a straight increase of the apparent lift-curve slope. For that part of the lift increment directly being a component of thrust, equations 35 and 36 lead to

$$\Delta C_D = \Delta C_L (1 - \cos \gamma) / \sin \gamma \approx 0.5 (\Delta C_L) \sin \gamma \quad (39)$$

Since γ is larger than α'_i , this type of drag due to lift is higher than that as indicated by equation 33. The analysis leads to the conclusion that pusher-type propellers as well as jet engines, are basically somewhat less effective in regard to climb performance than tractor-type propellers.

Pusher Propeller. Reference (22,n) shows that in a model configuration at $R_c = 6 \cdot 10^5$, efficiency of a tractor propeller is $\approx 4\%$ lower than that in pusher arrangement, because of forced boundary layer transition on the nacelle body. If eliminating laminar boundary layer, the pusher type may have an efficiency slightly superior over that of the tractor propeller. In regard to lift increment, the pusher type is less efficient, however, as predicted above.

Performance Calculation. Only two or three single points in the polar diagram of an airplane (and their vicinity) are predominantly utilized in routine performance calculations; namely that for V_{max} , that for optimum climb and the value of $C_{L_{max}}$ (for take-off and landing). The suggestion (26) to determine performance without the aid of a complete $C_D(C_L)$ function, therefore, appears to be reasonable; and it is proposed to establish statistical material for the climb condition, on the basis of " ΔA " as defined in equation 21, taking into account power or thrust (possibly in the form of T/W or T/S).

(32) Otto Lilienthal, "Der Vogelflug als Grundlage der Fliegekunst", published in Berlin 1889.

(33) Orville Wright (1871-1948) and Wilbur Wright (1867-1912) made 4 flights on the 17th of December 1903 at Kitty Hawk (N.C.). The longest of these flights was 852 ft, 59 seconds against a 20 mph wind, a few feet above the ground. The Wright Brothers' airplane and its data are on exhibition in the Smithsonian Institution in Washington (D.C.). See also McFarland, "Papers of W. and O. Wright," McGraw-Hill.

(d) The First Powered Airplane

First Aircraft. The first balloons (by Montgolfier as well as by Charles) ascended in 1783. Experimental airships ("dirigibles") were developed between 1852 and 1900, leading to Santos Dumont's flights in 1898 and 1901 and to the first of the Zeppelin air-

ships in 1900. Otto Lilienthal (1848-1896), see reference (32), may be claimed to be the most successful man, repeatedly to have made gliding flights, covering distances to 250 m = 800 ft between 1892 and 1896. Roughly ten years later, the Wright Brothers perfected and demonstrated what is recognized to be the first successful, powered and man-carrying airplane (33). Figure 15 presents a view and some evaluation of their craft. Flight was achieved in the vicinity of the optimum lift coefficient ($C_L \approx 0.6$). The parasite drag coefficient is high, of course, because of many struts and wires, and on account of engine installation and pilot, both placed in open air.

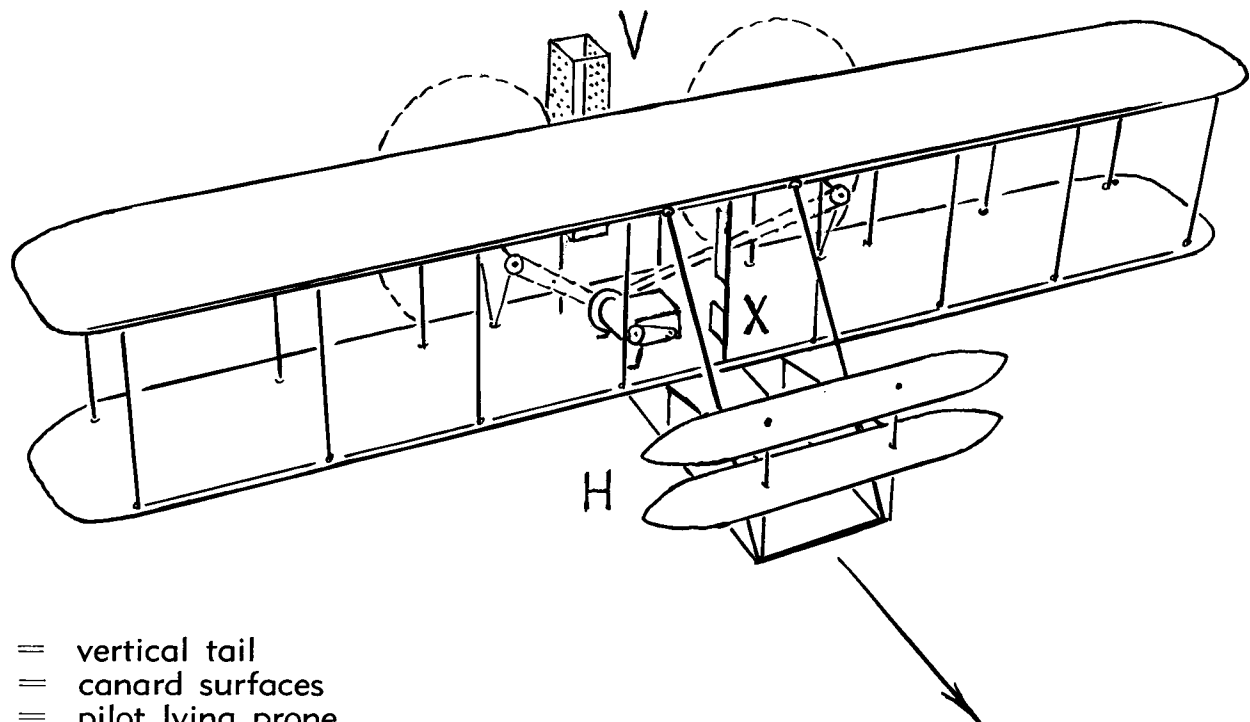


Figure 15. View of the 1903 Wright Brothers' canard-type pusher-propeller airplane (33), having $b = 40.3$ ft, $c = 6.5$ ft, $S = 510$ ft 2 , $W = 605$ lb plus pilot ≈ 755 lb. For a reported speed ("indicated", against wind) of 31 mph, the lift coefficient is $C_L = (755/2.5 \cdot 510) = 0.59$. Applying biplane theory (Chapter VII) the induced drag coefficient is estimated to be $C_{D,i} = 0.028$. The Wright Brothers' gasoline engine is reported to have developed 12 HP. Assuming a mechanical efficiency of 0.92 and a propeller efficiency of 0.71, the total drag is found to be $D = \eta P/V = 0.65 \cdot 12 \cdot 550/45.5 = 94$ lb. The corresponding drag coefficient is $C_D = 94/(2.5 \cdot 510) = 0.074$. This value is roughly two times the coefficient "due to lift" (which is the induced drag coefficient as above, plus an appreciable component of parasitic drag due to lift). It can therefore be concluded that the world's first powered airplane flight was performed at or near the lift coefficient for optimum gliding. The gliding ratio is $L/D = C_L/C_D = 0.59/0.074 = 8$. Other flights of the Wright Brothers in the years following their historic deed, in airplanes of much the same dimensions, were made with the aid of "stronger" engines (such as 27 HP, for example, in 1908).

CHAPTER XV — SUBSONIC INFLUENCE OF COMPRESSIBILITY ON DRAG

At moderately high speeds (as they are applied in most of our "utility" airplanes, both in the commercial and in the military field) aerodynamic theory and experimental investigations consider the air as essentially being incompressible. In fact, the pressure differences occurring on the surface of bodies exposed to the velocities used in most of the older wind tunnels, or those around airplanes at lower speeds, are small in comparison to the ambient pressure of the atmosphere. At a Mach number of $M = 0.3$, for example, corresponding to a velocity of $V \approx 100$ m/sec ≈ 330 ft/sec ≈ 230 mph or ≈ 200 knots (at sea level), the "impact" at the stagnation point is only 2% higher than the dynamic pressure $0.5 \rho V^2$. During the first 30-year period of their development, the practical aerodynamic problems of powered airplanes (except those at the tips of propellers) have, therefore, been treated almost exclusively without taking compressibility into account. However, during the last decade, many airplanes have been flown to level-flight speeds in the order of 400 knots (to Mach numbers in the order of $M = 0.9$) - let alone a number of experimental airplanes which already have exceeded the speed of sound considerably. The compressibility of the air thus cannot be neglected any longer. In this first chapter dealing with the subject, essentially subsonic characteristics shall be presented, up to and including the so-called critical Mach number.

1. ELEMENTS OF COMPRESSIBILITY

The Velocity of Sound is the natural speed at which vanishingly small local variations of static pressure are propagated through the air space, away from their source. This speed is basically

$$"a" = \sqrt{k g R T} \quad (1)$$

where k = ratio of the specific heats (c_p/c_v) of the fluid considered, g = acceleration due to gravity, R = gas constant and T = absolute temperature, with all these values in a consistent system of units. In atmospheric air (up to an altitude of some 300,000 ft) $k = 1.405 \approx 1.4 = 7/5$; and the speed of sound accordingly:

$$"a" = 66 \sqrt{T} \quad (\text{ft/sec}) \quad (2)$$

where T is measured in centigrades or °Kelvin. Under "normal" sea-level conditions, with $T = 273 + 15 = 288$ °K (or = 518 °Fabs), the sonic velocity of the air is " a " ≈ 1116 ft/sec ≈ 761 mph ≈ 661 kts ≈ 340 m/sec or ≈ 1210 km/h (3). Between sea level and some 35,000 ft of altitude, the speed of sound reduces to ≈ 0.87 of that at sea level; and it remains essentially constant within the stratosphere, where the average temperature is considered to be in the order of 218 °K (or 392 °Fabs) up to some 100,000 ft of altitude. In water, on the other hand, the speed of sound is so extremely high (≈ 4800 ft/sec at room temperature), that under none of the ordinary practical conditions, compressibility effects have to be taken into account.

Mach Number. Regarding the pressure distribution around a body exposed to compressive fluid flow, the velocity of this flow in comparison to that of the propagation of sound (which is a pressure variation) — is a measure (4,a) for the degree to which com-

(1) Modern Textbooks on the subject of compressibility are, for example: (a) Liepmann-Puckett's "Aerodynamics of Compressible Fluids" (Wiley 1947) and Liepmann-Roshko's "Elements of Gasdynamics" (Wiley 1957); (b) excellent physical interpretations of compressive phenomena are presented by Prandtl in "Essentials of Fluid Dynamics", London 1952; (c) by von Kármán in J.Aeron.Sci. 1941 p.337 and in Proc. First US Congr.Appld.Mechs. 1951 (Edwards, Ann Arbor) or in Vol.V of "Jet Propulsion — High Speed Aerodynamics"; and (d) by Goethert in USAF Wright Field Inst.Technology Lecture Notes as of 1948. (e) The first version of this chapter was the author's report ZWB Doct UM 7810(1944); CADO Tech Rpt F-TR-1188-IA (Wright Field, 1948).

pressibility is involved. This ratio is the

$$\text{Mach number} = M = V/a \quad (3)$$

As pointed out in J.Aeron.Sci. 1948 p.352, the square of the M'number has a direct physical significance. The "numerator represents a measure of the directed kinetic energy of the flow", while "the denominator represents the random kinetic energy of the molecules". — Considering now, for example, a number $M = 1$, the speed at which a body moves against the air particles, is equal to the velocity at which a "warning" can be given of the approach. No warning is given, accordingly, at speeds above that of sound. This sudden type of approach has basic consequences listed as follows.

Stagnation Pressure. Because of thermodynamic compression, the pressure at the stagnation point is increased over the ambient static pressure by an amount which is higher than the dynamic pressure $q = 0.5 \rho V^2$ (as in any incompressible fluid). The increased pressure, called "stagnation" pressure, is presented in figure 1 of Chapter XVI. As far as subsonic speeds, up to $M = 1$, are concerned, the function can be developed into

$$"q"/(0.5 \rho V^2) = 1 + (M^2/4) + (M^4/40) + \dots$$

For example, at $M = 1$, the pressure increment amounts to almost 28%. The aerodynamic pressure and friction forces, originating on all other parts of bodies in uncompressed fluid flow (outside the vicinity of the stagnation point), are not related to the stagnation pressure, however. The aerodynamic coefficients are, therefore, based now as in incompressible fluid flow, upon the dynamic pressure ($0.5 \rho V^2$) which is then somewhat more a mathematical than a physical value (that is, it cannot any longer directly be measured by means of a Pitot-static instrument).

Prandtl-Glauert Rule. Along the sides of slender (streamline) bodies, velocity increments as well as local static pressure differentials are both increased by approximately the same percentages as against the ambient values. As far as two-dimensional bodies (foil sections) are concerned, the lower limit of the increment is given by the "Prandtl-Glauert rule" (2). This rule indicates that a section, exposed to a flow of compressible fluid, shows the same velocity increments and the same pressure differentials as a certain reference section having a thickness and an angle of attack (that is, all dimensions perpendicular to the direction of flow) increased in proportion to the Prandtl factor

$$"P" = 1/\sqrt{1 - M^2} = 1/\beta \quad (5)$$

as plotted in figure 1. A number of attempts have been made (2,c) of improving the rule by introducing second-order terms. One effect thus taken into account simply concerns the difference between ($C_{p\text{com}}/C_{p\text{inc}}$) and $(\Delta V/V)_{\text{com}}/(\Delta V/V)_{\text{inc}}$. It is believed, however, that the second-order term in the pressure coefficient as a function of the thickness ratio (t/c) is usually cancelled by progressive boundary layer losses. Another correctly suggested modification, is to replace in equation 5 the ambient Mach number by the somewhat increased local Mach number at the surface of the solid considered. All modifications proposed tend to make the compressibility factor larger when approaching the critical Mach number, particularly in higher thickness ratios. Inasmuch as the increment is but small (for typical airfoil sections) and since certain increases in pressure and lift coefficients can also be explained on different levels (4), the author proposes that it usually does not pay, in engineering applications, to complicate the original rule by introducing higher order terms.

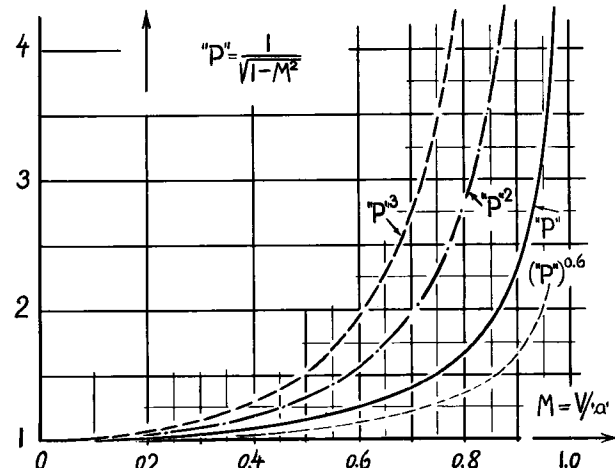


Figure 1. The Prandtl factor (equation 5) and certain of its powers, plotted as a function of Mach number.

Stagnation Temperature. In non-compressive flow — the Bernoulli principle states that the sum of static and dynamic pressure is constant, as long as there is no momentum added or taken away in a given mechanism of flow. Approaching a stagnation point (indicated by $V = 0$) the momentum of the air particles is transformed into static pressure. In a compressive flow, part of the fluid energy is changed into heat, however. The increase of temperature at some place in the vicinity of the stagnation point is generally indicated by

$$\Delta T/T_{\text{am}} = 0.5 (k - 1)(V^2 - w^2)/a^2 \quad (6)$$

where T = absolute temperature and where w indicates the local velocity at the point considered, within

the flow or on the surface of a body. With the aid of this equation it is possible, for instance, to determine the increase of temperature due to compressibility within the core of a radiator (Chapter IX). In air (with $k = 1.4$) the ratio is

$$\Delta T/T_{amb} = 0.2 M^2 (1 - (w/V)^2) \quad (7)$$

and under normal sea-level conditions (with $T_{amb} = 288 \text{ }^{\circ}\text{K}$) the temperature at the stagnation point (where $w = 0$) corresponds to

$$\Delta T = V^2/21600 \quad (8)$$

measured in degrees K and with V in ft/sec. For example, at $M = 1$, the increase of temperature is approximately 0.2 of the ambient absolute temperature, or very roughly $100 \text{ }^{\circ}\text{F}$ under normal sea-level conditions, thus approaching (on a very hot summer day) a total temperature equal to that of boiling water.

2. DRAG CHARACTERISTICS OF BLUFF BODIES

There are many bluff shapes, the drag coefficients of which do not distinctly vary as a function of skin friction (see Chapter III). Their drag as affected by compressibility, corresponds to principles described as follows.

Plates. In a rough analysis, the drag of blunt body shapes, showing a flow pattern entirely separated from their rear side, may be considered as consisting of two components. The first of these is the resultant of the mostly positive pressure distribution on their forward side. The corresponding positive "nose pressures" may be assumed to vary in proportion to the stagnation pressure as indicated by equation 4. Regarding the negative pressure within the separated space at the rear side or "base" of such bodies, we will tentatively assume that this second component of pressure drag may (within reason) not be affected by subsonic compressibility. Considering, for instance, the *two-dimensional flat plate* whose drag coefficient is plotted in figure 2, the coefficient at low Mach numbers $C_{D0} \approx 1.98$, is known (see page 3-16) to be composed of ≈ 0.85 due to "nose" pressure and of 1.13 due to "base" pressure. Assuming the nose pressure to vary in proportion to equation 4, the drag coefficient of this plate is suggested to be

$$C_{D0} = 1.13 + 0.85 (1 + 0.25 M^2) \quad (9)$$

The coefficient of a square section, also plotted in figure 2, follows the same function — up to a certain

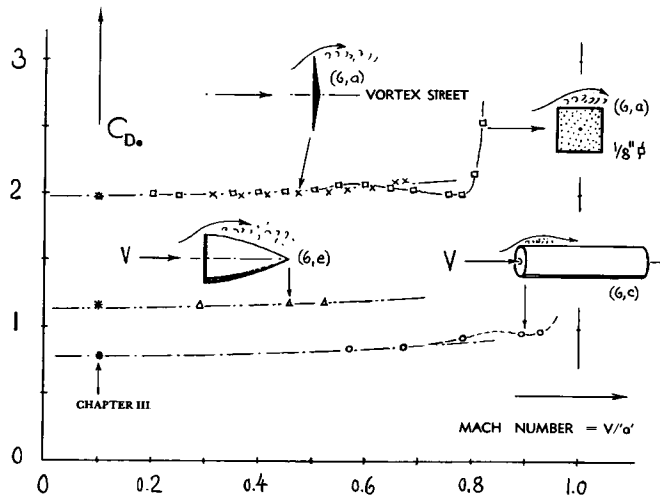


Figure 2. Drag coefficients of sharp-edged or *blunt bodies* with separated flow patterns, as a function of Mach number.

(2) Prandtl-Glauert compressibility rule:

- a) Prandtl (1922), in *Führer durch die Strömungslehre* (1942) or in "Essentials of Fluid Dynamics" (London 1952).
- b) Glauert, ARC RM 1135 (1927) or Proceedings Royal Society London A Volume 118 (1927/28) p.113.
- c) Improvements of the rule are presented by von Kármán-Tsien (J.Aeron.Sci. 1941 p.337), by Hantzsche-Wendt (see NACA T.Memo 1030), by Kaplan (NACA T.Rpts 794 and 834), by Laitone (J.Aeron.Sci. 1949 p.639), by Van Dyke (NACA T.Notes 3390, and in J.Aeron.Sci. 1954 p. 647), and by Weinig (J.Aeron.Sci. 1956 p.279).
- d) Further Discussion in J.Aeron.Sci. 1955 p.270 and 284.
- e) As explained by Kaplan in NACA Tech Rpt 894, the critical Mach number is part of a transonic *similarity system*. The lowest-order approximation yields $M_{crit} = 1 - 0.9(t/2x)^{2/3}$. However, this function fits the results as plotted in figure 19, only to $t/(2x) \approx 0.1$.

- (3) Could we not agree, educated as we are, on only two measures for speed, one per second and one per hour, and abandon Mr. Fahrenheit (1686 to 1736) at the same time?
- (4) Footnotes on compressibility:

- a) The Reynolds number corresponding to a given Mach number is $R_x = M l/\lambda$, where l = body dimension (in ft) and $\lambda = y'/a' = 1.4/10^7$ ft at standard sea level, and $= 3.5/10^7$ ft in 30,000 ft of altitude, for example.
- b) Certain humps in pressure and lift coefficients found at and somewhat above the critical Mach number, may be caused by the recompression and re-attachment phenomenon discussed later. Compressive wind tunnel *blockage* may also contribute to make pressure and lift coefficients appear higher (and/or the Mach number lower) than predicted by the Prandtl-Glauert rule. Evidence for an opposite tunnel influence is found in NACA Technical Note 3607 where in an *open-throat tunnel*, critical Mach numbers have been recorded that are by ≈ 0.04 higher than those in figure 19.

(5) Drag of double-wedge foil sections at subsonic speeds:

- a) Humphreys, Pressure 10% D'Wedge NACA TN 3306.
- b) Lindsey-Daley-Humphreys, Flow and Force Characteristics of several Supersonic-Type Airfoil Sections Tested at Subsonic Speeds, NACA T.Notes 1211 (1947).
- c) Solomon, 4 and 6% D'Wedges, NACA Doct. RM A6G24.
- d) Daley-Lord, 6% Sections, NACA T.Notes 3424 (1949).
- e) Hilton, D'Wedges, ARC RM 2057 and 2196 (1943/44).

Mach number to be discussed later (6,g). The blunt body of revolution also plotted in that illustration, essentially representing a disk, can be interpolated by

$$C_{D\bullet} = 0.45 + 0.7 (1 + 0.25 M^2) \quad (9)$$

Blunt Cylinder. The drag coefficient of circular cylinders in longitudinal flow is in the order of $C_{D\bullet} = 0.8$, as shown in figure 21 of Chapter III. Most of the drag of such cylinders corresponds to the stagnation type of pressure on their forward face. The components of surface friction at the sides ($\Delta C_{D\bullet} \approx 0.05$) and of base pressure (in the order of $\Delta C_{D\bullet} = 0.03$ as found in figure 37 of Chapter III) are comparatively small. Considering them as unaffected by compressibility, the drag coefficient of the blunt cylinder as in figure 2 may then be expected to be

$$C_{D\bullet} = 0.08 + 0.74 (1 + 0.25 M^2) \quad (10)$$

The graph shows that the drag of the bluff bodies considered, is reasonably well interpolated by the functions derived. Similar equations can also be written for other sharp-edged bodies for which the components of nose- and base drag are known.

Wedges. Figure 3 presents (among others) the drag coefficient of a 12% thick wedge section, tested in two-dimensional flow (between tunnel walls). If assuming that in such a slender wedge, pressure drag

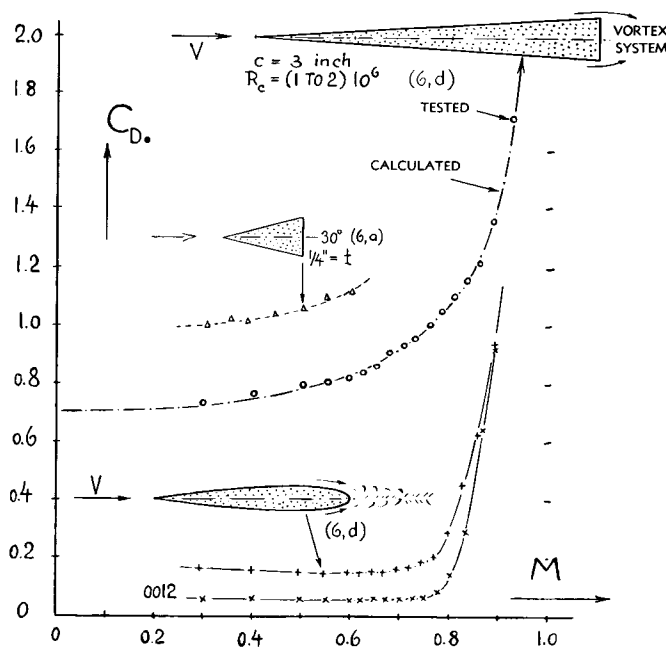


Figure 3. Drag coefficients (on frontal area) of three 12% thick sections, including a wedge and a reversed 0012 section (6,d) as a function of Mach number.

essentially originates behind the blunt base, we may speculate that the negative *base pressure* is somehow related to the negative pressure developing along the forebody, reaching a minimum at the trailing edges of the wedge section considered. We may furthermore assume that the value of the corresponding pressure coefficient $C_{p\min}$ increases as a function of Mach number in proportion to the Prandtl factor "P". Tentatively, therefore:

$$C_{D\bullet} = 2 C_f (c/t) + C_{Df\text{fore}} + "P" C_{DB_0} \quad (11)$$

The experimental results of the 12% thick wedge in figure 3 can be interpolated very well with the help of this equation when assuming for the forebody drag a value of $C_{Df\text{fore}} = 0.1$. The base drag coefficient at $M \rightarrow 0$ may then be $C_{DB_0} = 0.6$; and the total coefficient grows as a function of Mach number, as plotted in the graph. If assuming that the pressure coefficient $C_{p\min}$ at the trailing edges of the wedge is equal to that of the base pressure, the critical Mach number of this flow pattern (as determined through the use of figure 19) must be expected roughly to be $M_{crit} = 0.65$. The experimental points in figure 3 do not show any discontinuity, however, at or above this number. — The much thicker wedge included in the same illustration, does not conform with the simple analysis as per equation 11. The drag of *this wedge* is suggested to be some combination of stagnation with rear-side-pressure function, the values of both of which are expected to grow as the Mach number is increased.

The Reversed 0012 section, also shown in figure 3, has a much lower drag coefficient than the 12% wedge; and the coefficient does not increase before reaching $M \approx 0.7$. The flow pattern past the base of this section is obviously quite different from that of the wedge, and more similar to that of airfoils.

Strut Sections. The flow pattern past rounded shapes is more complicated than that around sharp-edged bodies, the reason being that the B'layer still has some influence upon separation and drag coefficient. Figure 4 presents experimental results on two fat strut shapes. Within the range of smaller Mach numbers, the 25 and 40% thick sections show drag coefficients that are up to 3 times the values to be expected for comparable streamline sections as presented later (in part 4). Comparison of the coefficients with those in figures 2 and 10 of Chapter VI, indicates that these sections are in the transitional range of Reynolds number (the coefficients are "half way" between the subcritical and supercritical levels, respectively). Separation is evidently assisted by laminarization (corresponding to thickness location at 50% of the chord); and it is aggravated by the comparatively short and bluff shape of the afterbody.

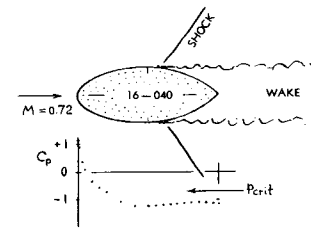
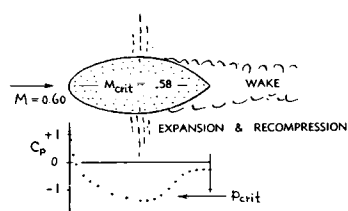
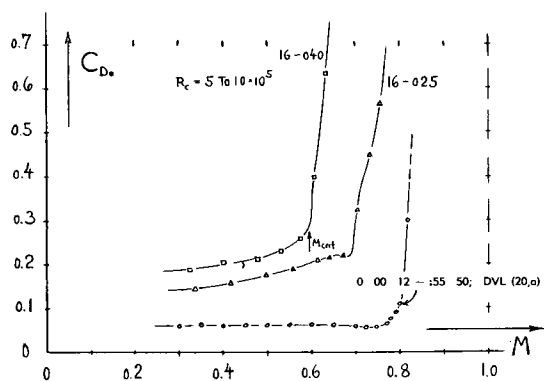


Figure 4. Drag and flow characteristics of fat strut sections (involving separation in compressive flow (12,a).

The Drag Divergence Mach numbers of the sections in figure 4, agree with those in figure 19 (possibly just by accident). Their flow pattern is very well described in (12,a) on the basis of "schlieren" pictures in combination with pressure distribution results. The illustration shows two typical conditions:

(a) at lower Mach numbers, up to $M \approx 0.60$, the flow pattern includes some separation from the afterbody of the sections (as explained above).

(b) at higher M'numbers (as at $M = 0.71$) separation is more extended, starting out from under the root of the oblique shock front as shown in the sketch.

Further discussion of the supercritical flow pattern of foil sections in general is presented in Chapter XVI. One conclusion to be drawn from the strut experiments at this point, is that laminarization produced by shape (12,b) and then increased by means of compressibility, can lead to serious separation and to correspondingly high drag coefficients. High-speed application of laminar-type shapes to struts and fairings may thus be problematic, even at higher R'numbers. An alternative solution may be found in the "half-streamline" struts as presented in figure 7.

- (6) Compressive drag of sharp and *bluff* solids:
 a) Lindsey, Drag of Simple Shapes, NACA T.Rpt 619.
 b) Robinson-Delano, Windshields, NACA T.Rpt 730.
 c) Naumann, Drag of Blunt Cylinder in Axial Flow, German ZWB Tech.Berichte 1943 p.278.
 d) Eggers, 12%Wedge and Reversed 0012 Section, NACA Doct. RM A7C10. See also figure 28 in Chapter VI.
 e) The blunt solid of revolution shown in figure 2, is the afterbody of the shapes as in figure 34 (39,a).
 f) Flow Pattern Past 40° Wedge, see ARC RM 2321.
 g) Note that in small-tunnel results such as in (a) the Reynolds number is comparatively low. Experimental points below $M = 0.3$ (where R on "h" = 1/4 inch, is in the order of $4 \cdot 10^4$) have therefore been omitted in plotting the graph (figure 2.).
- (7) Drag of *spheres* in compressive fluid flow:
 a) Charters-Thomas, Spheres, J.Aeron.Sci. 1945 p.468.
 b) Goethert, in ZWB Lilienthal Rpt 127 p.83.
 c) Ferri, R'and M'Number, Atti Guidonia 67/69 1942 p.49; also reported by Eula in Aerotecnica 1940 No. 1.
 d) Tada, Japanese Navy Tests, J.Japan Soc.Aeron.Engg. 1956 p.(135). These high-speed results on spheres and cylinders are severely affected by tunnel blockage. The points included in figures 6 and 10 have, therefore, arbitrarily been plotted against 16% increased M'numbers.
 e) Results in (17,a) indicate that at Mach numbers of 0.8 and 0.9, respectively, the drag coefficient of the sphere does not vary as the Reynolds number is changed between (2 and 8) 10^5 . One aspect of such tests that should not be overlooked, is *surface roughness*, however. It is believed to be difficult to produce aerodynamically smooth models or full-scale craft for, or to keep them clean at speeds in the order of 1000 ft/sec, where the permissible grain size of roughness or dust may be in the order of 0.1 mil (see Chapter V).
 f) Millikan, Tunnel Calibration, J.Aeron.Sci. 1948 p.69.
- (8) Drag of *cylinders* in compressive fluid flow:
 a) Lindsey, Drag of Cylinders, NACA T.Rpt 619.
 b) Matt, Drag of Circular Cylinders, ZWB Doct FB 1825 and ZWB Tech.Berichte 1944 p.47.
 c) Frenzl, Cylinders, ZWB Tech. Berichte 1942 p.61.
 d) Heaslet, Theory, NACA T.Rpt 780 (1944).
 e) Delany-Sorensen, NACA Tech Note 3038 (1953).
 f) Gowen-Perkins, Cylinders f(RM), NACA T.Note 2960.
 g) Knowler, Cylinders at High Speed, ARC RM 1933.
 h) Ferri as in reference (7,c).
 i) The dip in the drag coefficient of the circular cylinder is investigated in particular in (8,g). As indicated in figure 20 of Chapter XVI, the dip obviously correlates with a variation of the base-pressure coefficient.

Circular Cylinder. As stated in Chapter III, the net resultant of the pressure forces originating on the forward side of round bodies, can very well be somewhat negative. For the purpose of this analysis, we will simply assume that the forebody drag of such shapes may approximately be zero. In other words, most of the drag of round bodies is "base" drag. In a manner similar to that assumed above (for wedges), the base pressure is likely to be related to the minimum pressure shortly ahead of the separation boundary; and the absolute value of the coefficient of this pressure may increase as a function of Mach number as indicated for two-dimensional conditions by the Prandtl-Glauert rule (equation 5). This analysis (rough as it may be) seems to be reasonably well confirmed by the experimental evidence plotted in figure 5 for the cylinder at Reynolds numbers below the range of BL transition, up to the critical Mach number, where the speed of sound is locally first reached (at the minimum pressure points on the circumference of the cylinder).

The Sphere, represented in figure 6, shows the same type of variation of the drag coefficient against Mach number as the cylinder. It can be speculated, however, that below the critical M'number (and at R'numbers below that of BL transition) the growth of the drag coefficient corresponds to a three-dimensional compressibility rule (possibly in the form as in equation 44) rather than to equation 5.

At Supercritical R'Numbers. Drag coefficients of round bodies at Reynolds numbers *above transition* (where flow separation is considerably reduced) are also plotted in figures 5 and 6. It is suggested that the experimental functions may somehow be related to those of airfoil or strut sections and streamline bodies, respectively, as explained in parts 4 and 7 of this chapter. The relative increase of their coefficients is appreciable, evidently corresponding to the "extreme" thickness ratio involved. In the vicinity of $M = 0.75$ and 0.55 , respectively, the difference between the conditions of subcritical and supercritical Reynolds numbers — disappears. Evidently, the flow pattern then separates to the same degree, at larger as at smaller Reynolds numbers (7,e).

Above the Critical Mach Number, drag is a transonic phenomenon (as treated in Chapter XVI). Characteristics shortly above that number are of importance, however, in the determination of the speed at which in a number of body shapes, drag and other force coefficients first diverge appreciably from their subcritical level. For example, the drag coefficient of the circular cylinder as in figure 5, steadily continues growing after passing the critical Mach number (determined from pressure distribution) for an interval of appreciable magnitude (in the order of $\Delta M = 0.2$). An explanation for this phase is readily found in the supersonic expansion phenomenon as explained later in connection with the flow around "sharp" leading edges of foil sections.

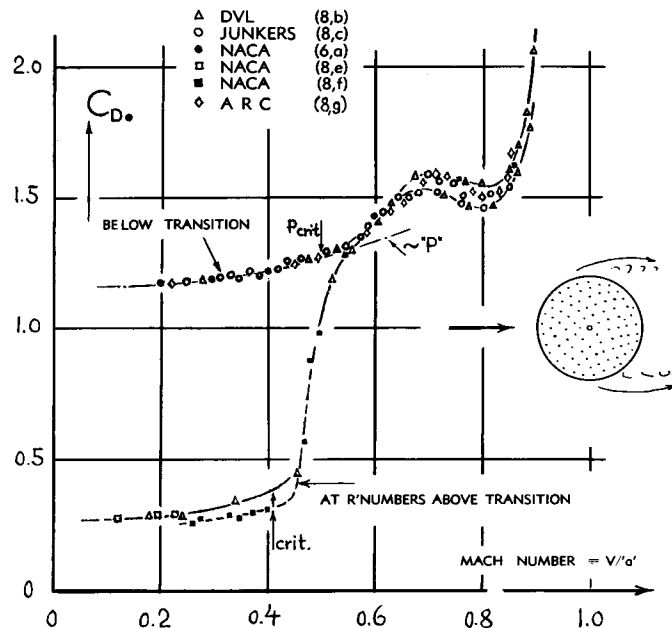


Figure 5. Drag coefficients of circular cylinders, tested (8) between walls in various wind tunnels (a) at subcritical R'numbers, and (b) at R'numbers above transition.

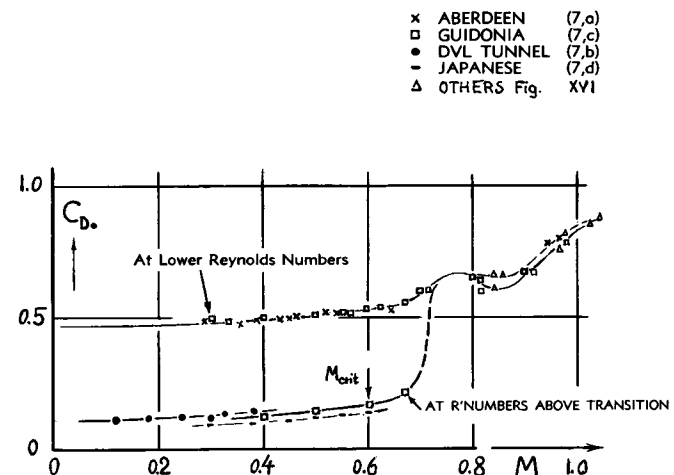


Figure 6. Drag coefficients of the sphere (7) as a function of Mach number; (a) at subcritical R'numbers, (b) above the critical R'number.

Up-Down-Up. A pronounced "dip" in the coefficient of the cylinder takes place in the vicinity of $M = 0.8$. The explanation of this dip must be found in a favorable interaction between the local supersonic field of flow existing at and behind the location of the cylinder's maximum thickness, and the flow pattern within its wake. Tentatively, this interaction is as follows. After passing the points on the circumference of the cylinder where the streamlines are closest to each other, at sonic speed, the velocity continuous increasing, and the static pressure decreasing accordingly, as in a Laval nozzle. The stream tubes involved, necessarily expand when doing this, in a manner that seems basically to be the same as in the Prandtl-Meyer type of expansion (described in Chapter XVII). It is then suggested that by means of increasing volumetric *displacement*, the stream tubes involved tend to reduce separation. On the basis of the *negative pressure gradient* associated with expansion, it can also be claimed that boundary layer separation, originally caused by a strong positive pressure gradient, may effectively be reduced by the gradient's reversal. Inasmuch as in a circular cylinder the rear-side pressure is of appreciable magnitude ($C_{pB} \approx -1.1$ at small Mach numbers, and possibly $= -1.4$ at $M \approx 0.7$) a modest reduction of separation by means of the mechanism suggested, may very well lead to the dip of the drag coefficient as indicated in figure 5.

Half-Streamline Shapes. The circular cylinder is not at all the only shape in which the described "re-attachment" takes place. Besides the sphere (in figure 6) the square section in figure 2 also shows the "up-down-up" tendency (between $M = 0.6$ and 0.8). A very pronounced "dip" is found in (9,d) on a 53% thick section having a blunt trailing edge. The drag

coefficient (of a comparatively short piece of "strut" or propeller shank) is reduced from $C_{D0} = 0.47$ at $M = 0.3$, to 0.23 at the dip Mach number of 0.66. Another example is shown in figure 7. The four "half-streamline" shapes presented in the graph, permit some more speculation as follows:

(a) The dip in the drag coefficient is only found in sections having comparatively full leading edges (and/or in shapes with a sufficiently tapered after-body). Disregarding the "base", section III, with a "streamline" (that is, more elliptical) forebody, does evidently not have separated spaces where such separation could be reduced by some favorable supersonic interaction.

(b) The dip does evidently not take place in longer shapes such as number "V-a" in figure 7, where the supersonic flow field is located far ahead of the base and/or the boat-tailed rear end of the section.

A further piece of information is found in figure 2, where the "plate" does not exhibit any dip. It is suggested that separation from the rear side of this shape cannot be reduced by the influence of the supersonic field of flow as described above.

Canopies. Further insight into the mechanics of bluff-body drag in compressive fluid flow, can also be obtained from the results on canopies (or windshields) as reported in (6,b). Corresponding to their characteristics, the canopies as tested, fall into three categories, examples of which are shown in figure 8:

(a) There is first of all the streamline type, characteristics of which correspond to the principles as pointed out later in the section on "streamline bodies". Drag is low in this group; the drag-divergence Mach number is comparatively high.

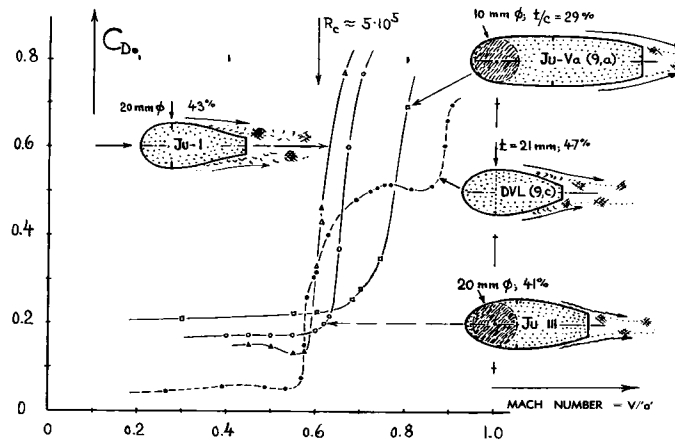


Figure 7. Drag coefficients of several half-streamline "strut" or fairing sections; mostly from (9,a).

(9) Half-streamline sections at high Mach numbers:

- a) Half-streamline Fairings, Investigated in Junkers High-Speed Tunnel, Junkers Doct S.1944/13-8. Inasmuch as this tunnel is a two-dimensional but open-jet type (struts tested between walls), results are considered to be reliable.
- b) Hoerner, Series of Antenna Rods, investigated in large open-throat high-speed tunnel at Brunswick LFA in 1944. Inasmuch as the facility used in testing the rods was a large-size and open-jet type tunnel, the "creeping" character of the results in figure 9 cannot be caused by any tunnel deficiency.
- c) Matt, Streamline Rods, DVL Doct J.900/27 (1942).
- d) Barlow, Short Pieces of "Shanks", NACA T.Rpt 852.

(12) Experimental results on strut-type sections:

- a) Daley, Fat Foil Sections, NACA T.Note 1657 (1948).
- b) NACA T.Note 480 confirms that rearward position of thickness increases the critical Reynolds number.

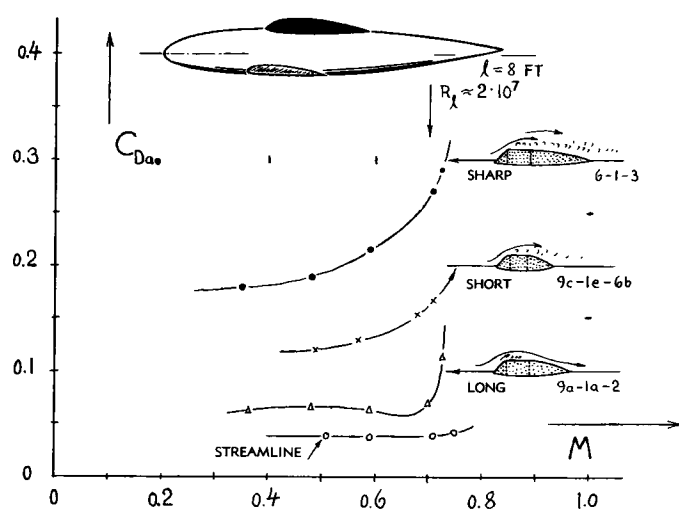


Figure 8. Drag coefficients (on their frontal area) of a family of canopies. Note: inasmuch as the results as reported in the source (6,b) are significantly affected by wind-tunnel blockage, a rough correction has been applied by multiplying the Mach number with 1.4.

(b) The sharp-edged form of canopy "6-1-3" has basically a high drag coefficient ($C_{D_0} = 0.2$) thus suggesting a separated flow pattern. The drag coefficient then increases as a function of Mach number, roughly in proportion to the stagnation pressure (as explained in connection with the blunt bodies presented in figure 2.) Canopy "9-1-6" although having a somewhat rounded head shape, is evidently so short that a re-attachment of the flow separating from the edge of the windshield cannot take place, neither at low Mach numbers, nor with the help of supersonic expansion as explained above. As a consequence, the drag coefficient of this canopy shows the same variation against "M" as the really blunt type "6-1-3".

(c) The afterbody of shape "9-1-2" (having the same forebody shape as canopy "9-1-6") is comparatively long. Re-attachment evidently takes place in this form, facilitated by what we may call a longer mixing length (distance between the origin of separation and the rear end of the canopy). As a consequence, the drag coefficient of this type shape reduces above $M \approx 0.6$ (in the example shown in the illustration) thus showing a "dip" similar to that in the "round" bodies discussed above.

From these canopy tests, it can generally be concluded again, that dips result from the interaction of a localized supersonic flow field, with boundary layer and separation. The compression shock eventually following the supersonic field, at still higher M-numbers, has an unfavorable effect, however, upon separation. The drag coefficients of all canopy shapes investigated (and those of all streamline bodies and foil sections as well) finally grow into values of very appreciable magnitude.

Antenna Rods. Figure 9 presents results of a series of more or less streamline "rods" (9,b), made from sheet metal and designed to be used as radar antennas. The drag of these rods, tested by clamping them to a dynamometer at the heavier of their ends, is higher than and different from that of comparable foil or strut sections obtained from typical wind-tunnel investigations. Reasons are as follows:

(a) Being hand-made experimental specimens, the surface of the rods was comparatively rough and somewhat irregular, in places. Welding seams also result in the thick trailing edges, at least in two of the shapes as shown.

(b) The 1 m long rods (having a geometrical aspect ratio of 17 or 18) are tapered from 100 mm at the clamped end, down to a chord length of 20 mm at the tips. Corresponding to a sheet-metal thickness of 1.5 mm, the tips have therefore no longer much of a shape similar to those shown in the illustration.

(c) The Reynolds number (on chord length) is comparatively low. It reduces from $R_c = 5 \cdot 10^5$ at $M = 0.7$ for the larger end, to $1 \cdot 10^5$ at the tips.

As a consequence of the properties listed, all of the rods tested show a "creeping" increase of the drag coefficient, beginning at Mach numbers well below the critical (9,b). These results are proposed to be an example of possible differences between realistic full-scale performance and the usual wind-tunnel testing under more or less idealistic conditions.

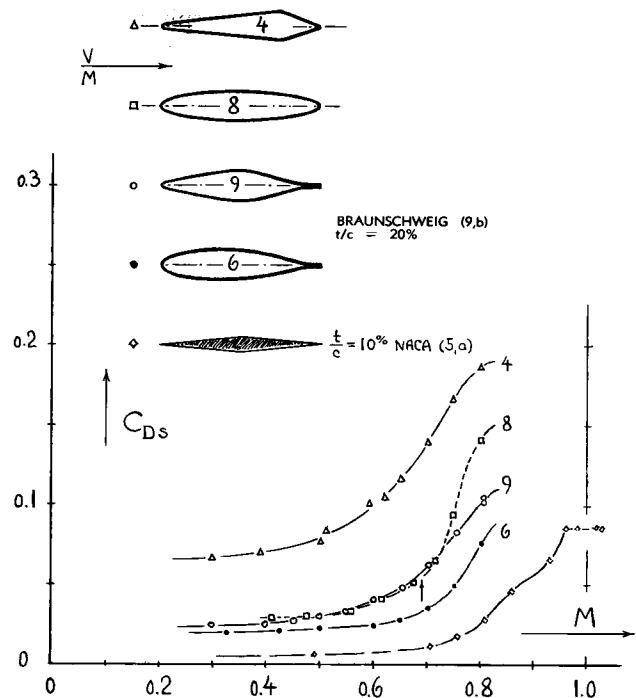


Figure 9. Results of a series of half-streamline sheet-metal antenna rods, investigated in a high-speed wind tunnel (9,b), and of one double-wedge foil section (5,a).

3. SKIN FRICTION IN COMPRESSIVE FLOW.

On Plane Wall. Within the boundary layer originating along the plane wall, as for instance on a thin plate in longitudinal flow, the air particles are retarded; directly at the wall, the speed is \approx zero. Decreasing velocity, means increasing temperature, as indicated by equations 6 or 7. At higher Mach numbers, an appreciable proportion of the dynamic energy taken away from the fluid flow by surface friction, is thus transformed into heat. Because of increased temperature, the density of the air within the boundary layer is reduced; at the rate of $\rho \sim 1/T$. Skin-friction coefficients in compressible fluid flow are, therefore, smaller than those as presented in Chapter II. In case of laminar boundary-layer flow, the effect of reduced density is to a large degree cancelled, however, by a simultaneous increase of viscosity, the magnitude of which is roughly $\mu \sim T$. The reduction of the laminar skin-friction drag coefficient as a function of Mach number is therefore so little (see in figure 2 of Chapter XVII) that within the range of subsonic speeds, this coefficient may as well be considered as being constant.

Turbulent Boundary Layer. As far as subsonic speeds are concerned, the turbulent skin-friction drag coefficient as plotted in figure 3 of Chapter XVII, may be interpolated by

$$C_{f,com} = C_{fo} (1 - 0.09 M^2) \quad (14)$$

At $M = 1$, for example, this type of skin-friction drag is thus reduced on account of compressibility by 7%. We may, therefore, say that an "insulating" sheet of warm air is placed between body surface and outside flow, or that the surface is "lubricated", so to speak, by means of thinner air.

BL Stability. Theoretical studies (16) have been undertaken to determine the stability of the laminar boundary-layer flow (along a straight constant-pressure surface) in a compressible (and heat conducting) fluid, as distinct from that under incompressible conditions (as discussed on page 2-8). It appears that heat transfer is a most important parameter. Predictions are as follows:

(a) Stability is *reduced* in case of an insulated surface (no heat transfer). At $M = 1$, for example, the minimum possible critical Reynolds number of an insulated surface is thus reduced to roughly $1/2$ the value as known for incompressible fluid flow. Stability is further reduced when heating the surface from the inside.

(b) Stability can be *increased* by withdrawing heat through the surface. At $M = 1$, for example, cooling of the skin of an aircraft down to $T_{wall} \approx 0.8 T_{amb}$ or by the differential $\Delta T \approx -(0.4 T_{amb})$ or $\Delta T \approx -(0.3 T_{stag})$ is theoretically expected to stabilize the BL flow almost indefinitely. Thermodynamic BL characteristics are discussed further in Chapter XVII.

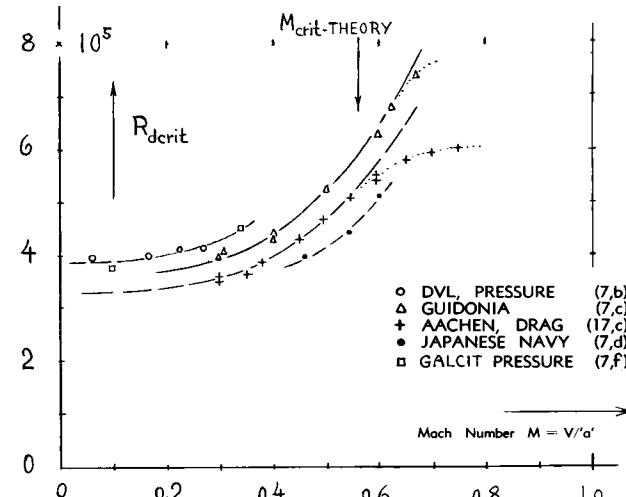


Figure 10. Critical R' number of the sphere (17) defined by passing through $C_{D_0} = 0.3$, as a function of Mach number.

- (14) Skin-friction in compressible fluids:
 - a) Reference is made to (10) in Chapter XVII.
 - b) Fedjajewsky, Turbulent Friction, CAHI Rpt 516 (Moscow 1940).
 - c) Hoerner, Influence of Compressibility Upon Drag, ZWB Doc UM 7810 (1944); USAF Tech Rpt F-TR-1188-IA, (Wright Field, 1948).
 - d) Solution for laminar flow in fig. 2 of Chap.XVII.
- (16) Boundary layer transition in compressible flow:
 - a) Lees, Analysis of BL Stability, NACA Tech Notes 1115 (1946) and 1360 (1947), and T.Rpt 876 (1947).
 - b) Gazley, Review of Data, J.Aeron.Sci. 1953 p.19.
 - c) See also reference (16) in Chapter XVII.
- (17) Influence of Mach number on critical Reynolds number:
 - a) Ferri, Sphere, Atti Guidonia 67-69 (1942) p.49; also reported by Eula in Aerotecnica 1940 No. 1.
 - b) Hoerner, Compressibility and Transition Point of BL, USAF Tech Rpt F-TR-2184-ND (Wright Field, 1948).
 - c) Naumann, Drag of Spheres, ZWB Rpt FB 1778 (1943).

BL Transition. Stability of the laminar boundary-layer flow is also closely connected with the *pressure gradient*, as explained in Chapter II. Since pressure coefficients vary as a function of Mach number, stability and laminar character of the boundary layer are in this manner affected by compressibility. The negative gradient between the stagnation point of a sphere, for instance, and its equator is increased corresponding to the Prandtl-Glauert rule, or rather as indicated by the equivalent rule for three-dimensional flow conditions (to be explained later). As shown in figure 10, the critical Reynolds number of the sphere (where the drag coefficient passes through $C_{D_0} = 0.3$) is, therefore, found growing appreciably as a function of M'number; ΔR_{crit} is roughly proportional to M^3 .

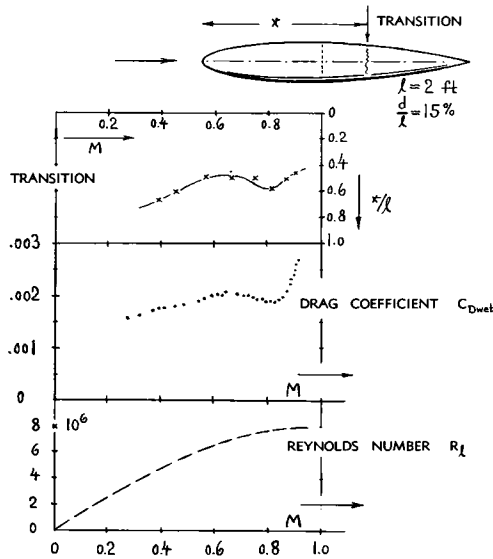


Figure 11. Correlation between drag coefficient, transition point, Mach- and R'number of a "fuselage" body (39,b).

Laminarization. The transition point of the boundary layer of the body illustrated in figure 11 is seen moving downstream as the Mach number is increased from $M = 0.65$ to 0.82 . In the same interval, the drag coefficient decreases accordingly. Applying this experience to *laminar-type foil sections* (as treated in Chapter II) it can be predicted that the stability of their boundary layer and the corresponding low profile-drag coefficients can be favorably affected by compressibility (provided that their surface is smooth enough for the high speeds involved; see footnote 7,e). Evidence of the stabilizing influence of compressibility (by way of negative pressure gradient) is also found in figure 35 (at subsonic speeds) and in certain results presented in Chapter XVI (at transonic speeds), such as on smooth missile shapes where continuous negative pressure gradients may develop between stagnation point and body tail.

Surface Roughness. Equation 14 (valid for smooth-turbulent friction) may be academic, insofar as at higher speeds, skin friction of aircraft is likely to correspond to surface roughness (as explained in Chapter V). In fully developed roughness flow, the drag coefficient is no longer a function of Reynolds number. It may therefore be expected (as explained in reference 14,c) that the coefficient of rough surfaces (when tested at speeds where roughness-type flow has developed in the BL) fully corresponds to reduced BL density; and that the reduction due to compressibility would thus be larger than for smooth surfaces as indicated by equation 14. Hence tentatively:

$$C_{f_{com}} = C_{f_{inc}}(1 - 0.12 M^2) \quad (15)$$

Drag characteristics of two slender streamline bodies having surfaces made "completely" rough by coating

them with carborundum grains, are presented later (in figure 36). Provided that laminarization does *not* take place under such conditions, the conclusion can be drawn that the skin-drag coefficients of these shapes decrease as a function of Mach number, approximately as indicated by equation 15.

4. DRAG OF FOIL AND STRUT SECTIONS

Skin Friction drag of foil sections in compressive fluid flow can be calculated similarly as shown in Chapter VI. The friction coefficient " C_f " to which the section drag coefficient " C_{D_s} " is related (as in equation 6 of the "streamline" chapter), must be replaced, however, by a value reduced as per equation 14 (for smooth and turbulent condition) or equation 15 (for rough-surface flow). An increase of supersonic velocity must then be taken into account as indicated by the Prandtl-Glauert rule (equation 5). Simultaneously, however, the density of the air within the boundary layer is decreased because of the mean-average negative pressure prevailing at the section sides. Semi-theoretical analysis in (14,c) suggests that the two effects roughly cancel each other. Therefore, the frictional component of section drag may approximately correspond to

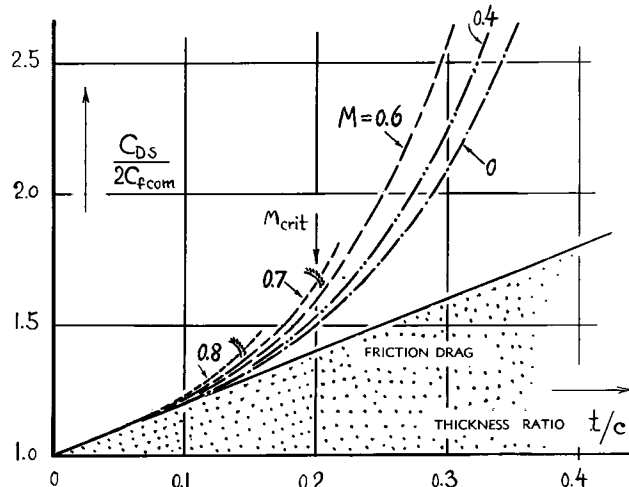
$$C_{D_{fric}} = 2 C_{f_{com}}(1 + k t/c) \quad (16)$$

where $k = 2$ for thickness location at 0.3 chord and $k = 1.5$ for high-speed type sections with locations between 0.35 and 0.45 of the chord. Because of $C_{f_{com}}$ (as in equations 14 or 15, respectively), the frictional component of the section drag coefficient can thus be expected slowly to decrease as the Mach number is increased.

Pressure Drag. In incompressible flow, pressure drag of streamline airfoil and strut sections grows in proportion to $(t/c)^4$ as indicated in Chapter VI (equation 6). The component $(t/c)^1$ of this term, indicating the frontal area of the section, remains constant upon changing from incompressible to compressive flow. However, applying the Prandtl-Glauert rule, the component $(t/c)^3$, representing the influence of the positive pressure gradient along the rear of the section sides, is to be increased by the Prandtl factor (equation 5). Tentatively (14,c), therefore, the pressure drag component of slender streamline sections varies as

$$C_{DP}/(2 C_{f_{com}}) = 60 (P)^3 (t/c)^4 \quad (17)$$

Combining this function with equation 16, the profile-drag coefficient of sections having the maximum



- (19) General remarks on experimental results:
 a) Some of the results quoted in (20) and in other footnotes, and many others (not referenced) are severely affected by compressive *blockage* in smaller closed-type wind tunnels. See in this respect Mair-Gamble, Blockage Corrections, ARC RM 2033 and 2527; or Herriot, NACA T.Rpt 995 (1950).
 b) In all such functions, plotted against Mach number, an influence of Reynolds number (usually increasing as a function of tunnel Mach number) is naturally included.
 c) While results as a function of R'number, are usually presented in larger and logarithmic-scale graphs, those as a function of M'number always seem to be reported in comparatively small scales, thus obscuring the finer variations of the drag coefficient. Figure 18 proves, however, that results from high-speed wind tunnels can very well be consistent and that they can show the same variations as a function of R'number as those from larger low-speed facilities.
 d) Almost all modern results on airfoil section drag are obtained by wake-survey technique.
 e) "Creeping" transition into the critical M'number phase as shown, for example in (20,a and m) can be explained on the basis of increasing B'layer separation.

Figure 12. Drag coefficient ratio (at $C_L = 0$) of symmetrical airfoil and/or strut sections having the maximum thickness located at 30% of the chord, as a function of thickness ratio and Mach number — calculated through application of equation 18.

thickness at 30% of the chord, is found to be

$$C_{DS}/(2 C_{fcom}) = 1 + 2(t/c) + 60(P^3)(t/c)^4$$

with C_{fcom} corresponding to Reynolds number, surface condition and boundary layer flow. Figure 12 demonstrates that section drag as obtained through application of this equation increases as a function of thickness ratio at a rate which is somewhat higher than for incompressible flow (at $M \rightarrow 0$). Considering, however, the fact that " C_{fcom} " decreases as the Mach number is increased, the increase of pressure drag may very roughly be cancelled in sections having thickness ratios between 9 and 15%. Figure 13 presents theoretical and experimental profile-drag coefficients, as a function of Mach number. To simplify conditions, a constant basic friction-drag coefficient $C_{fcom} = 0.00285$ was assumed when calculating the theoretical lines in the graph. Agreement thus obtained is encouraging. It must be said, however, that a number of experimental results from other sources (19,a) show increases of the drag coefficient which are appreciably higher than those in figure 13. In fact, a decrease of the coefficient as it can be expected to occur in smaller thickness ratios (on the basis of equation 14) is rarely confirmed in experimental investi-

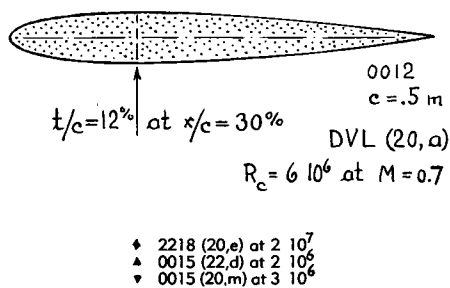
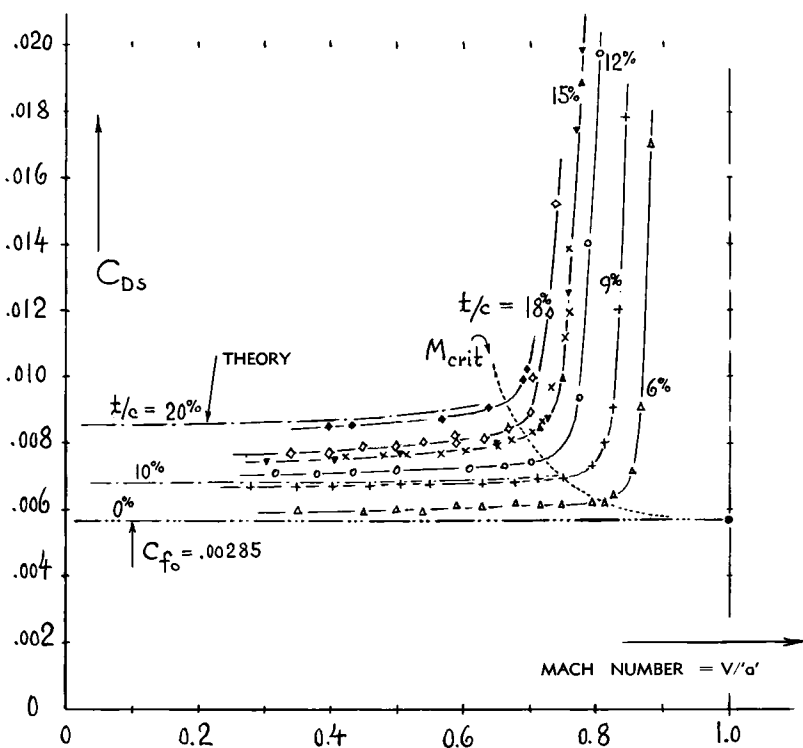


Figure 13. Drag coefficients (at $C_L = 0$) of a family of symmetrical foil sections (with maximum thickness at 30% of the chord); (a) tested in a large-size wind-tunnel (20,a); and (b) calculated as per equation 18 for $C_f = 0.00285 = \text{constant}$.

0015 at transonic speeds,
see (36,e) in Chapter XVII.

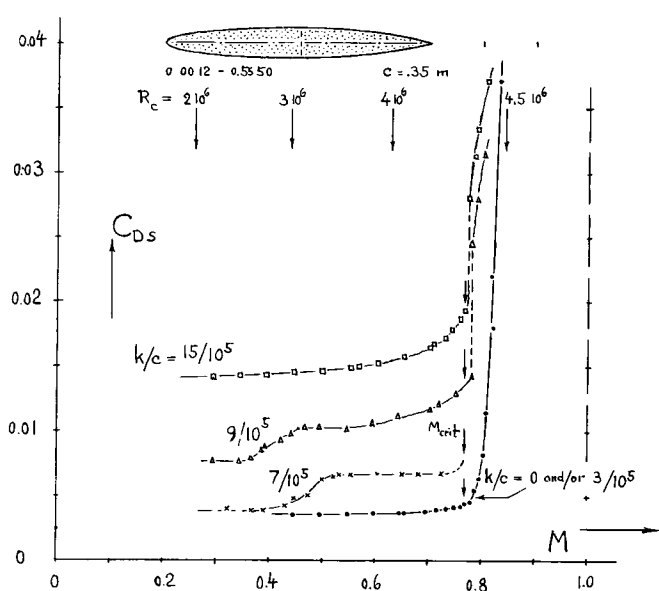


Figure 14. Drag coefficient of a foil section, in smooth condition as well as completely coated with carborundum having grain sizes "k" as indicated (20,a).

gations (19,b). At smaller R' numbers (such as at $R'_c \approx 5 \cdot 10^5$, for example) transition from subcritical Mach numbers into the critical phase appears to be "creeping" (19,e) possibly to such a degree that drag divergence cannot very well be defined.

Surface Roughness. Figure 14 presents experimental information on the drag of a rough-surface foil section in compressive fluid flow. By comparison of the coefficients (at $M \approx 0.5$) with those of rough surfaces in figure 4 of Chapter V and with those of laminar-type sections in figure 18 of Chapter II, conclusions can be drawn as follows:

(a) The grain-size ratio of $3/10^5$ does not affect the drag at all. This ratio is below the no-longer-permissible as defined in figure 2 of Chapter V.

(b) The ratio of $7/10^5$ does not produce fully developed roughness flow. The drag coefficient may represent turbulent friction, however. Note that the level above $M = 0.5$, roughly corresponds to that with $k/c = 9/10^5$, at $M = 0.3$.

(c) Grain sizes corresponding to $k/c = 7/10^5$ and $= 9/10^5$ cause a transition of the drag coefficients from a lower to a higher level (between $M = 0.35$ and 0.50). It is suggested that in $7/10^5$, this transition is from laminar to turbulent, while in $9/10^5$, transition from smooth-turbulent to roughness-type boundary-layer flow seems to take place.

(d) The level of the drag coefficient corresponding to $k/c = 15/10^5$, indicates "fully" developed roughness-type B'layer flow (See Chapter V).

(e) The decreasing trend of fully-rough skin-friction drag coefficients predicted by equation 15, is not confirmed by these experimental results. In fact, two among the three functions presented in the graph, show that the coefficient increases as the Mach number is increased. Here, as in all results on smooth airfoil sections (such as in figures 13 and 17, for example) the influence of Mach and Reynolds numbers upon laminarization and boundary layer transition, is evidently superimposed to the simple functions as presented in the text above (19,b). In other words, the value of C_{f_0} or $C_{f_{com}}$ being the basis of "viscous" or section drag, is not constant; and the value is evidently not even constant in the "fully" rough shapes as in figure 14 where some chord fraction near the leading edge can be assumed to be laminarized by means of a negative pressure gradient (in spite of roughness).

(f) At Reynolds numbers corresponding to full-scale application in aircraft (above 10^7), the influence of roughness upon laminar-type foil sections can be expected to be more severe than in the model experiments considered.

Strut Sections. By multiplying equation 18 with c/t , the drag coefficient (based on frontal area) is obtained of strut sections and fairings (with maximum thickness at 0.3 chord):

$$C_{D_s}/C_{f_{com}} = 4 + 2(c/t) + 120(P')^3(t/c)^3 \quad (19)$$

The experimental results on the "fat" sections in figure 4 are not suitable for comparison with this equation (because of laminar-type flow separation). Other reliable results on sections having thickness ratios larger than those of "airfoils", thus representing "struts", do not seem to be available. Disregarding the "half-streamline" shapes as in figures 7 and 9, the fattest foil section presented in this chapter is the 18% thick shape in figure 13.

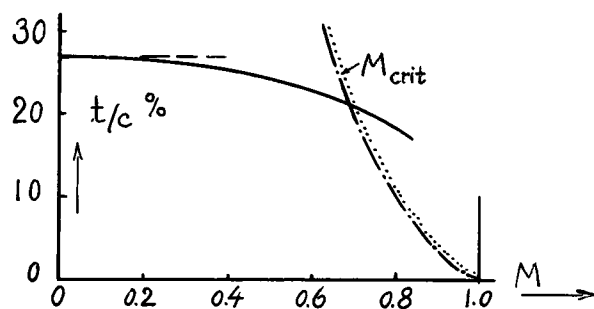


Figure 15. Optimum thickness ratio of *fairing or strut* sections (giving minimum drag in relation to their frontal area) as a function of Mach number.

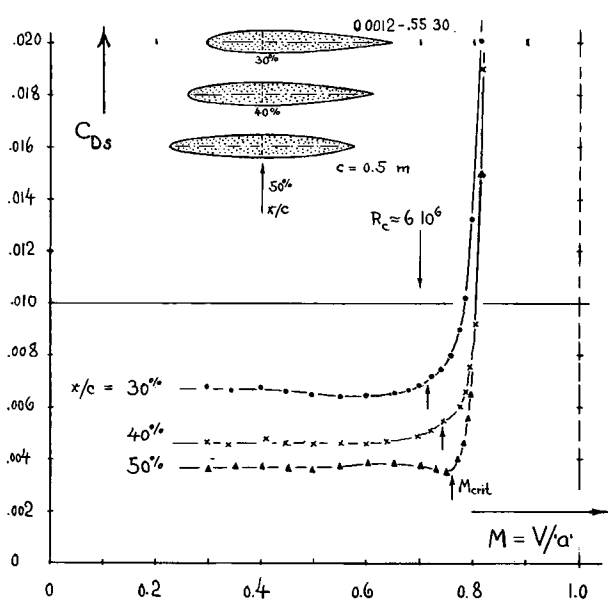


Figure 16. Drag coefficients at zero lift of symmetrical sections, varying in the location of maximum thickness (20,a).

Optimum Thickness Ratio. As demonstrated in Chapter VI, strut sections have an optimum thickness ratio (giving minimum drag in relation to frontal area). This ratio, found by differentiating equation 19, and plotted in figure 15, decreases slowly with the Mach number. Upon reaching the critical M'number, the function plotted in figure 19 has to be considered, however, in order to avoid the strong increase of drag likely to take place when exceeding that number. The optimum ratio then decreases very rapidly as against Mach number.

◊ $t/c = 10\%$ at $x/c = 42\%$ (20,l)
 ♦ ditto with forced turbulence
 ○ $t/c = 10\%$ at $x/c = 40\%$ (20,h)

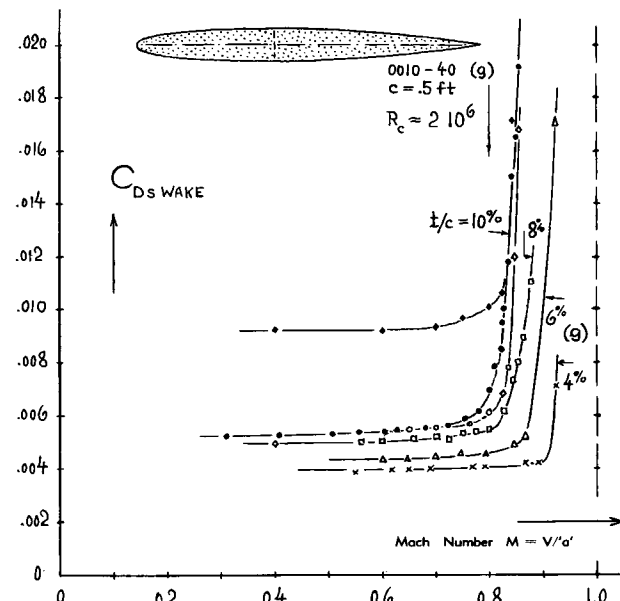


Figure 17. Drag coefficients at zero lift of several *laminar type* NACA airfoil sections (20,g) having $x/c \approx 38\%$; and of other similar airfoil sections.

- (20) Experimental results on *airfoil sections* as a function of Mach number are now so numerous that only the more systematic or more illuminating publications can be quoted:
 a) Goethert, DVL Airfoil Characteristics at High Speeds, reported in ZWB Docs FB-1910, 1490 and 1506 (1942), in Tech Berichte ZWB 1944 p.235; in NACA T.Memos 1203 and 1240; and in reference (1,d).
 b) NACA, Tech Notes 1129, 1813, 2670 and 3871.
 c) Stack-VonDoenhoff, NACA Tech Rpt 492 (1934).
 d) NACA, Documents RM A9G18 and L7E08 (free fall).
 e) ARC Reports RM2058 (Blocking), and 2555 (Flight).
 f) Feldmann, Symmetrical Foils, ETH Zürich Heft 14.
 g) Berggren-Graham, Symmetrical Foils, NACA TN 3172.
 h) NACA 0010-40 Free Fall (RM A9G18), combined with foil section 64A010 tested in wind tunnel (T.Note 3871).
 i) Stack, Airfoils at High Speeds, NACA T.Rpt 763 (1943).
 k) Stivers, "64A" Foil Series, NACA T.Note 3162.
 l) Rogers, Tests on 10% Airfoil, ARC RM 2863 (1956).
 m) Mair, 0015 Model Size, ARC RM 2527 (1951).
 n) Hemenover, Cambered Foil, NACA T.Note 2998.

Laminar Flow Sections. The equations developed so far, are primarily valid for sections with the maximum thickness located at or near 30% of the chord, such as they were "conventional" in airplane design for many years. Applying now the same methods to laminar-type sections as represented by equation 7 in Chapter VI, the variation of their sectional drag with Mach number, could also be estimated. The mechanism of laminarization due to shifting maximum thickness aft, is confirmed in figure 16. As mentioned while discussing characteristics of this type of sections in incompressible flow (page 6-6) their drag coefficient may be erratic, however, as a function of Reynolds number; and therefore as a function of Mach number as well. In a way, such behavior is evident in the up and down variations as in figure 16, while figure 17 shows slowly increasing trends in all

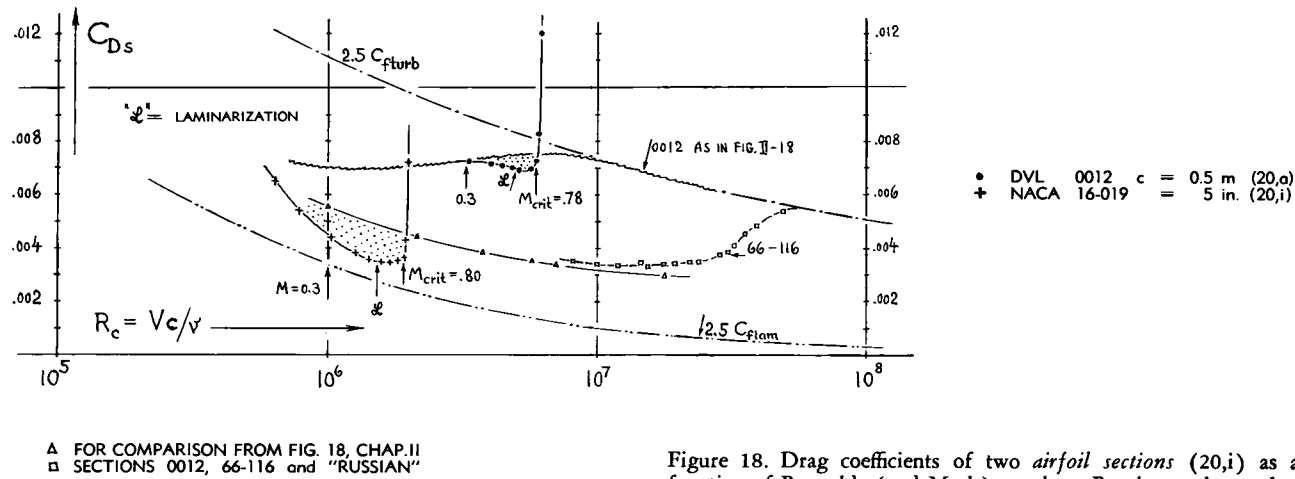


Figure 18. Drag coefficients of two airfoil sections (20,i) as a function of Reynolds (and Mach) number. Results on three other sections shown for comparison from figure 18 in Chapter II.

sections tested (19,b). *Figure 18* (drawn to a larger C_D scale; see footnote 19,c) demonstrates systematic variations, as a function both of Reynolds and Mach number. By comparison with results on other foil sections (taken from figure 18 in Chapter II) it is seen that the critical M' number terminates the low-drag phase of the laminar-type foil section at a Reynolds number far below the range in which "creeping" transition takes place in non-compressive fluid flow (or at Mach numbers considerably below the critical). Although accurate prediction of full-scale drag of "laminar" sections remains problematic (see text on pages 2-13 and 6-6), three statements may nevertheless be made:

(a) Compressibility is expected to help *preserve the laminar character* of boundary layer flow by means of increased favorable pressure gradients (see page 15-10). By comparison with the theoretical skin friction functions (included in figure 18) it is found that in the laminar-type section, the expected laminarization really takes place, at least up to $R_c \approx 1.5 \cdot 10^6$. A similar result seems also to be evident in the 0012 section in the vicinity of $R_c = (4 \text{ and } 5) \cdot 10^6$. — Note that the difference between the two sections with regard to Reynolds number corresponding to M_{crit} , reflects different model sizes applied in the tunnel tests. Termination of the subcritical drag functions is not completely sudden, however. There is obviously some interval ahead of M_{crit} where compressibility and/or conditions near the critical speed (such as tunnel vibrations?) have some influence upon transition so that the drag coefficient starts rising steadily.

(b) Reynolds numbers in full-scale applications of laminar foil sections are above 10^7 , while those in the available high-speed wind-tunnel results are only

somewhat above 10^6 . After consulting figure 18, it appears doubtful, therefore, whether or not the low drag coefficients as in figures 16 and 17 are applicable to full-scale conditions of airplanes (even if proper consideration is given to the item as follows).

(c) The permissible surface roughness grain size is already very small at the higher speeds of ordinary airplanes (see page 5-2). Considering now speeds increased to the subsonic limit as given by the critical Mach number of the wing section, surface roughness under realistic conditions of hardware construction and aircraft operation, may really be expected to be problematic. There can, on the other hand, a relieving influence of compressibility be suspected, insofar as the permissible grain size (or the permissible R' number for a certain grain size) may be increased on the basis of a heated and lower-density boundary layer.

(22) Pressure distribution on airfoil sections:

- a) See NACA Tech Rpt 832 and Tech Note 3162.
- b) Goethert, 0015 Section, Yearbk D.Lufo 1941 p.1,101, and 148; 12% sections in ZWB Tech Ber. 1944 p.235.
- c) Incompressible Distribution, ZWB Doct FB 1621.
- d) Graham-Nitzberg-Olson, Distributions, NACA T.R.832.
- e) Busemann, High Speeds, including local supersonic field with shock-free recompression, J.A.Sci.1949 p.327.

5. CRITICAL MACH NUMBER OF WINGS

Definition. Most of the compressibility effects, considered in the preceding section, have only a moderate effect upon flow pattern and drag. Shapes of streamlines and boundary layer characteristics are of the same type as in incompressible flow. Whatever changes there are as a consequence of subsonic and subcritical compressibility, they are usually small; and aerodynamic characteristics can be obtained by adding certain corrections to those in incompressible flow. Such conditions begin to change, however, when and if at certain points on the surface of solid bodies, the velocity of sound is locally first attained and/or slightly exceeded. The corresponding Mach number in the undisturbed flow (at some distance away from the solid investigated) is called the *critical* Mach number. The number at which the critical condition first becomes evident in a more or less distinct change of the aerodynamic forces, is the "*divergence*" Mach number. In many cases, the value of this number is acceptably close to that of the critical number (which can accurately be determined from pressure distribution tests) and it may then be so designated in text and/or illustrations. Under certain conditions, the drag-divergence Mach number may be considerably higher than the critical number, however.

Prandtl Factor. The critical Mach number (but not the divergence number) is open to calculation. We will assume that the maximum local supersonic ratio ($\Delta V/V$) on the sides of a two-dimensional streamline shape (airfoil section) is known under incompressible conditions. In a compressive flow of gas, this ratio is then expected to increase corresponding to the Prandtl-Glauert rule (equation 5). The critical Mach number is obtained when

$$M(1 + (P_* \Delta V/V)) = 1 \quad (20)$$

where ' P_* ' = Prandtl factor (as in equation 5) determined for the imaginary local Mach number $M_* = (1 + \Delta V/V) M_{crit}$. The critical Mach number can then be evaluated from:

$$(1/M_{crit}) = 1 + (P_* \Delta V/V) \quad (21)$$

Example. For a supersonic ratio $\Delta V/V = 0.1$, we obtain the "imaginary" Mach number $M_* = (1 + \Delta V/V) M_{crit} = 1.1 M_{crit}$. We thus have to estimate the value of M_{crit} first; and we can do that for the purpose of this example by looking into figure 19 where we may tentatively pick a value of 0.80. We then obtain $M_* = 0.88$ and ' P_* ' = $1/\sqrt{1 - M_*^2} = 2.1$. Using these values, equation 20 yields $0.80(1 + 0.21) = 0.94 \neq 1$. This procedure has to be repeated (iterated) until that equation is satisfied. The correct critical number in the example selected is M_{crit} between 0.81 and 0.82.

Airfoil Sections. There are many experimental results of airfoil and strut sections, and of some elliptical cylinders, indicating that the drag-divergence Mach number of these bodies is near the predicted critical Mach number. Figure 19 presents evidence in this respect, with the critical number plotted against the supersonic ratio ($\Delta V/V$). In case of elliptical section shape, the theoretical ratio is exactly $\Delta V/V = t/c$, where t/c = thickness ratio. Considering now average streamline sections with maximum thickness located at known location "x" on the chord, and with roughly elliptical forebody shapes (to the position x), we may tentatively assign to them the effective thickness ratio

$$(t/c)_e = t/(2x) \quad (22)$$

This thickness ratio is suggested to be an acceptable measure for the supersonic ratio (23,a). The graph presents critical Mach numbers, applicable to practically all symmetrical streamline sections and to those of slender elliptical sections, at and near zero lift; and it is seen that the approximation is suitable for engineering purposes.

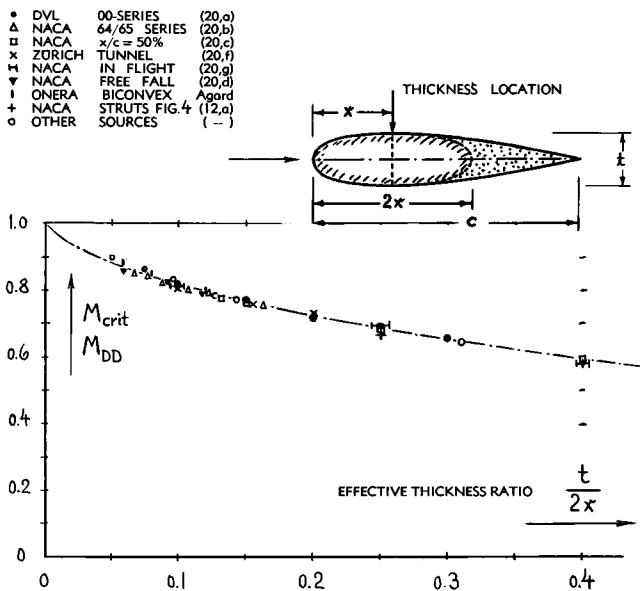


Figure 19. Critical Mach number of symmetrical airfoil and strut sections (at zero lift) as indicated by theory (see text) and as evaluated from drag divergence in various experimental reports (20), as a function of their forebody thickness ratio ($t/2x$) which is approximately equal to the supersonic ratio ($\Delta V/V$).

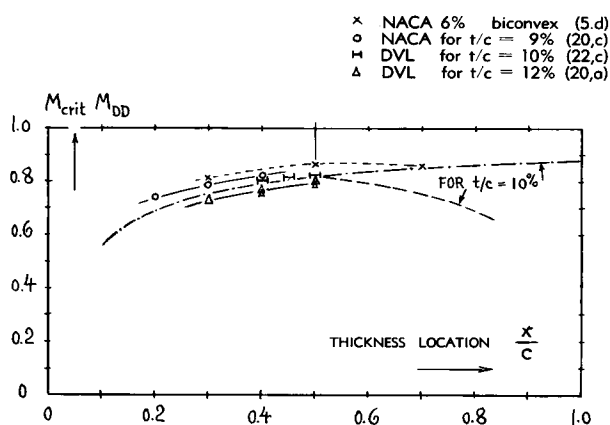


Figure 20. Influence of thickness location along foil chord upon critical or drag-divergence Mach number.

Thickness Location. Figure 20 displays the influence of thickness location in respect to section chord. Minimum supersonicities and highest critical Mach numbers are obtained for a location at $x/c \approx 0.5$ or possibly aft of this station. Besides laminarization through negative pressure gradient, reduced supersonicities are thus the reason for the development of modern airfoil sections, having their maximum thickness between ≈ 0.35 and ≈ 0.50 of the chord. The continuation of the line in figure 20 beyond $x/c = 0.5$ is computed on the basis of the equivalent forebody thickness ratio (as defined in figure 19). Considering instead the thickness ratio corresponding to the afterbody shape, smaller critical numbers are obtained, of course, corresponding to the lower branch line in the graph, originating from $x/c = 0.5$. Inasmuch as a growing boundary layer can be expected somewhat to "fill up" the tapering after end of a foil section, actual results may be inbetween the two branches.

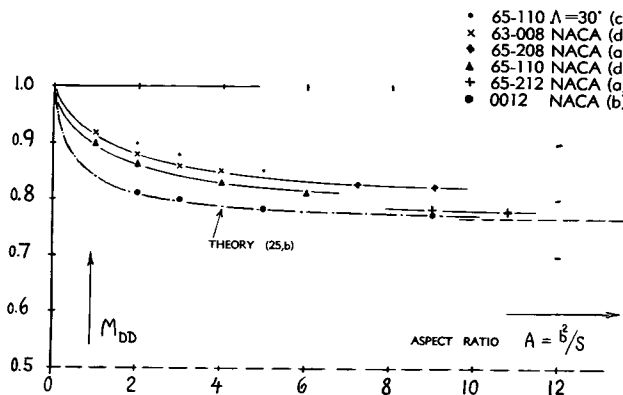


Figure 21. Critical Mach number of various wings as a function of their aspect ratio (26). Theory as in (25,b).

Blunt Trailing Edge. By moving the maximum thickness to the trailing edge, the forebody thickness ratio is effectively reduced; and the critical Mach number is possibly increased as indicated in figure 20 by the upper line. Sections with a corresponding blunt and/or boat-tailed trailing edge have been proposed and tested, primarily at transonic and supersonic speeds (see Chapters XVI and XVII). Analysis of such sections on the basis of figure 39 in Chapter III, shows conditional advantages in the vicinity of their critical Mach number. Drag of such sections at speeds below the critical number is bound to be so high, however, that their usefulness can justly be questioned.

Finite Wings having aspect ratios as applied in airplanes are usually considered to have locally a two-dimensional type of flow pattern along the chordwise sections. In compressive fluid flow (at higher speeds, approaching the critical Mach number) the presence of the three-dimensional wing tips provides considerable relief, however, for supersonicities and pressure differentials as they have been explained above to arise corresponding to the Prandtl rule. Theory (25,c) indicates that the three-dimensional relaxation can be accounted for by applying to free-stream conditions an effective reduction of ambient speed or M' number.

Figure 21 presents the corresponding increase of the critical Mach number. It is seen that in the range of aspect ratios above 8 or 10, the flow pattern is so much two-dimensional, that the critical M' number can very well be predicted through application of the Prandtl rule (or as shown in figure 19). Below that range, the critical number increases above that of the employed (two-dimensional) airfoil section as indicated. A substantial increase is found below $A = 2$, approaching from there the ultimate limit at $M = 1$. One set of experimental points in figure 21 proves that the aspect-ratio effect also applies to swept wings.

M_{crit} (Lift). Of course, supersonicities at the surface of a wing are also a function of its lift coefficient, or more precisely of the maximum local lift coefficient (28). It has been pointed out in connection with cavitation in hydrofoils (on page 10-10) that the velocity fields due to displacement (section thickness) and corresponding to lift, can approximately be superimposed to each other. Picking up the two components from the "hydrodynamic" chapter, the combined maximum supersonicity ratio for sections having a thickness location between 0.35 and 0.40, is predicted to be

$$(\Delta V/V) \approx (4/3) (t/c) + 0.7 C_L \quad (24)$$

The due-to-lift term is valid only for the, and in the vicinity of the "optimum" lift coefficient (23,b) how-

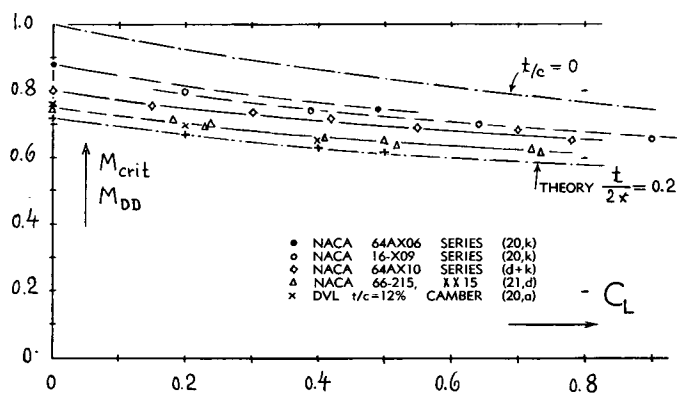


Figure 22. Critical M'number of cambered airfoil sections as a function of their "optimum" lift coefficient (23,b).

ever. Figure 22 presents the function, evaluated for $t/c = 0$, and $= 15\%$, respectively. Experimental data from various sources agree reasonably well with the theoretical prediction, if disregarding some "exceptions from the rule" to be described later under the subheading of "drag dip". It may be said that the "optimum" critical Mach number for any thickness ratio reduces as a function of lift coefficient, very roughly in proportion to that at $t/c = 0$; and that at $C_L = 0$, it is of course, equal to that as plotted in figure 19. — Regarding the critical Mach number of symmetrical sections and/or of cambered sections at lift coefficients sufficiently *different* from their respective "optimum" values, a presentation of facts and some explanation of these facts is given in the following paragraphs.

Recompression. In one-dimensional gas dynamics, "recompression" of a supersonic stream of fluid is expected to take place by means of a shock (equal to a sudden pressure jump); and a shock always means a loss of momentum which in turn appears in the form of an increment of pressure drag in the obstacle which is the cause of all these phenomena. It has been pointed out, however (22,e) that *within a localized field of flow* (extending laterally only a short distance away from the body producing that field) the static pressure can very well return to the ambient level without the help of a shock. In other words, within a certain limited range of the Mach number, *recompression* can take place without a corresponding increment of drag. Confirmation of such flow pattern is obviously found in figure 23 where, at a lift coefficient of $C_L = 0.4$, the drag coefficient of the straight foil section, at Mach numbers above 0.65, is lower than that of the "properly" cambered section (24). Indeed, the coefficient of the symmetrical section does not increase at all after passing the critical Mach number (determined from pressure distribution, at $M = 0.575$ as marked). Such a "delay" of drag divergence does not occur in ordinary streamline sections at their correct design angle of attack (such as $\alpha = \text{zero}$ in symmetrical sections). Rather, "DD" Mach numbers appreciably exceeding the respective critical Mach numbers, are only found, at angles of attack or lift coefficients at which a sharp flow around the leading edge (23,c) takes place thus producing a sharply peaked pressure distribution. It is stated in (1,d) that in such cases, conditions for shock-free recompression are particularly favorable; and we can conclude that a certain delay in the growth of the drag coefficient is thus effected. Even if assuming that after exceed-

(23) Supercavities in hydrofoil sections:

a) This ratio has also been used on page 10-6 as a measure for the susceptibility of hydrofoil sections to cavitation. It is to be understood, however, that replacing streamline foil shapes by equivalent elliptical sections can only be done within reasonable limits as to thickness location (x/c) and particular section shape.

b) The "optimum" is that lift coefficient at which in a given cambered foil section, the entrance of the leading edge into the streamlines is smooth or "symmetrical". The magnitude of $C_{L\text{opt}}$ is indicated by equation 13 in Chapter X.

c) Curiously enough, similar conclusions are obtained in Chapter X, with respect to critical cavitation numbers in peaked pressure distributions.

(24) By some reason, the 2% camber section shown in figure 23 has a drag coefficient (at subcritical M'numbers) considerably lower than that of both the 4% and the 0% camber section.

(25) Compressibility in finite aspect ratios:

a) Goethert, Modified "Rule", D.Lufo 1941 p.I,156.
b) Hess-Gardner, "Ellipsoids", NACA T.Note 1792(1949).

c) Anderson, Aspect Ratio, J.Aeron.Sci.1956 p.874.

(26) Wings of finite aspect ratio in wind tunnels:

a) Hamilton-Nelson, 6 Wings, NACA T.Rpt 877(1947).
b) Stack-Lindsey, Low A' Ratios, NACA Tech Rpt 922.
c) Adler, Straight and Swept Wings, NACA RM L7C24.
d) NACA Documents RM A51A12 and A53C19.

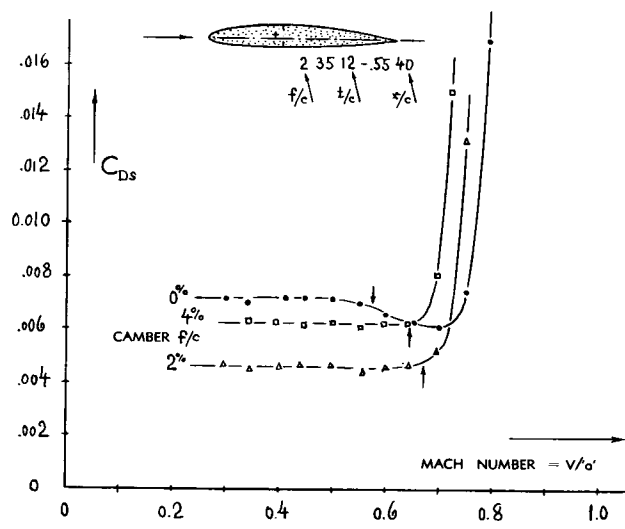


Figure 23. Section drag coefficients of three shapes differing in camber (20,a) at $C_L = 0.4 = \text{constant}$; (a) cambered corresponding to lift; (b) with intermediate camber (24); (c) straight airfoil section.

ing the critical Mach number by some interval, a compression shock does occur, it can then be argued that the loss of momentum involved may at first be comparatively small. The shock may take place in oblique direction and it may not extend very far into the outer flow.

Drag Dip. In the vicinity of $M = 0.7$, the symmetrical airfoil in figure 23 (tested at $C_L = 0.4 = \text{constant}$) exhibits a pronounced dip of its drag coefficient. This dip appears to be similar in shape to those as observed on bluff bodies (in the earlier section on this subject); and it is suggested that the mechanics of the dip are the same as explained in connection with those bluff bodies. In other words - the boundary layer re-attachment taking place at the suction side, aft of the leading edge of comparatively sharp-nosed airfoil sections, at lift coefficients different from $C_{L\text{opt}}$ - this re-attachment is evidently improved by an expanding supersonic flow taking place around the airfoil's nose (see in Chapter XVII under the sub-heading of "Prandtl-Meyer"). As a consequence of this mechanism, in combination with the recompression phenomenon as explained above, the drag coefficient may perform an "up-down-up" variation as, for example, in figure 25, in the more-sharp-nosed section. This variation evidently corresponds to that of sphere and cylinder in figures 5 and 6, where the flow pattern partly re-attaches at Mach numbers in the vicinity of 0.8. Supersonic expansion, elimination of separation through such expansion and shock-free recompression, all these phenomena and their influence upon lift and drag forces are confirmed by "schlieren" pictures and pressure distributions presented in (22). It is shown in particular that shock-free recompression can occur from velocities as high as 1.4 times that of sound, and that full separation (at M_{crit}) from a sharp leading edge (at an angle of

attack corresponding to an original $C_L \approx 0.5$) is fully eliminated by means of supersonic expansion so that the lift coefficient increases to ≈ 0.7 (thus forming a hump as mentioned in footnote 4,b). The report quoted also presents dips in the drag coefficients of two of the sections tested, as a consequence of "supersonic" re-attachment; it also proves that dips can only occur when and if the flow pattern is somehow separated, to begin with. Reference (22) shows, finally, that whenever recompression takes place by means of a "real" shock, the drag coefficient is comparatively high because of the negative expansion pressure preceding the shock and on account of flow separation starting anew in combination with the shock.

As a Function of Lift Coefficient, the parasitic or section drag coefficient increases in a manner as explained in Chapter VI. Keeping now $C_{\text{Lift}} = \text{constant}$ (as for example in figure 23, rather than the angle of attack) there is no strong reason why the increment of the drag coefficient due to lift should increase as a function of Mach number over the value as indicated in equation 15 of the chapter mentioned. This statement is, of course, restricted to speeds and lift coefficients below the critical Mach number. Both figures 23 and 25 confirm the conclusion.

Peaked Distributions. Details of the interaction between expansion zones, shock fronts and the boundary layer (or vice versa) are reported in (27). The interaction is found to depend upon the status of the B'layer. For a turbulent (and *thick*) layer, recompression is likely to take place in form of a shock. Conditions in combination with a laminar (and accordingly *thinner*) boundary layer are more conducive to the Prandtl-Meyer type of expansion, and to shock-free recompression as described above. These prerequisites are evidently fulfilled in the case of flow around comparatively sharp leading edges. We can therefore make the statement that "peaked" pressure distributions over the surface of an airfoil section do not lead to Mach numbers that would be indicative of drag (and other forces') divergence. Peaked distributions may rather be expected to have drag-divergence Mach numbers that are considerably higher (23,c) than the critical number (corresponding to locally reaching sonic velocity). Drag divergence numbers of symmetrical airfoils (having not too round noses) therefore reduce only little as the lift coefficient is increased from zero. Within reason (not exceeding coefficients in the order of $C_L = 0.3$ or 0.4) their M_{DD} values are then higher, of course, than those as plotted in figure 22. Figure 24 presents as an example the drag-divergence Mach number of a foil section as a function of the lift coefficient. The differential ($M_{DD} - M_{\text{crit}}$) reaches values between 0.3 and 0.4, at certain lift coefficients.

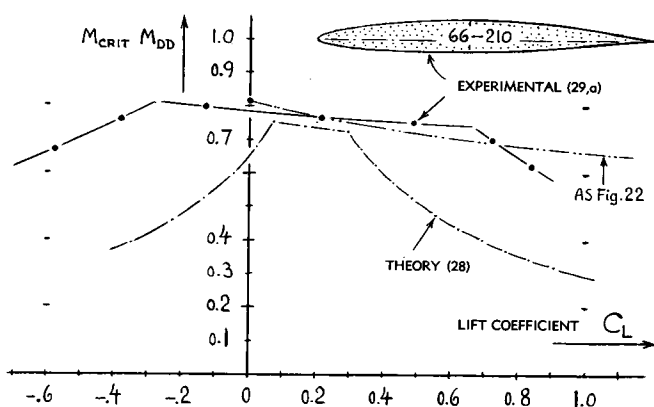


Figure 24. Drag-divergence Mach number of a foil section (29,a) cambered corresponding to $C_{L\text{opt}} \approx 0.2$, as a function of lift coefficient.

Nose Shape. Figure 25 shows the section drag coefficient at $C_L = 0.4$ of two symmetrical foil sections varying in thickness location and in the shape (radius) of the nose. Drag divergence in the 0012 section approximately coincides with the critical Mach number of this section (determined from pressure distribution). The sharp-nosed section shows a pronounced up-down-up variation however; and the total "delay" in drag divergence amounts to $\Delta M \approx 0.3$ as against M_{crit} and to $\Delta M \approx 0.17$ in comparison to that of the 0012 section. The reason for this result is to be found in the boundary layer development. The BL flowing into the space of supersonic expansion is evidently thin (and possibly laminar) in the sharp-nosed section; and it is thicker (and possibly turbulent) in the more round-nosed section. If finally relating the sharp-nosed section to a section properly cambered for $C_L = 0.4$, the increment of M_{DP} reduces to less than 0.1. Such value (corresponding to $\Delta V \approx 50$ knots) is still worthwhile, however, to be considered in the design of subsonic airplanes.

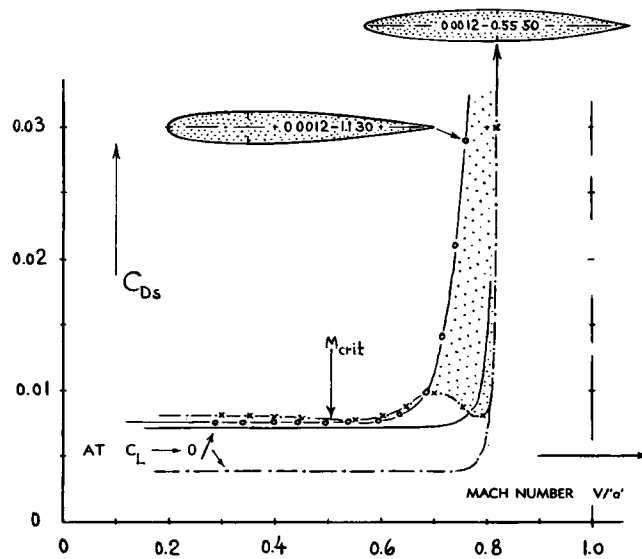


Figure 25. Parasitic drag coefficient of two airfoil sections (20,a), differing in the shape of the nose, at $C_L = 0.4$.

- (27) Boundary layer shock interaction:
 - a) Liepmann, BL and Shocks, J.A.Sci. 1946 p.623.
 - b) Ackeret, Mitt. ETH Zürich No. 10; NACA T.Memo 1113.
 - c) Interferometric Flow Pattern, NACA T.Note 2801.
- (28) Theoretical guidance in respect to the critical Mach number of airfoil sections as a function of camber and lift coefficient is given in NACA T.Rpt 824 (1945), "Summary of Airfoil Data" by Abbott-Doenhoff-Stivers (also available as a book). As explained in the text, pressure distributions do not have much significance, however, in regard to drag divergence, when they are "peaked".
- (29) Foil sections cambered for supercritical M' numbers:
 - a) Graham, Experiments, NACA T.Notes 1396 and 1771.
 - b) Woersching, Negative Camber, J.A.Sci. 1951 p.361.
 - c) ARC, Negative Camber, RM 2460 (1947).
 - d) Summers, Camber in 64AX10, NACA T.Note 2096.
 - e) Goethert, ZWB Doct FB 1910 (1940); see Ref.(20,a).
 - f) BL Re-attachment also in NACA T.Notes 1211 & 3804.
- (30) Theoretical principles of swept wings:
 - a) Ringleb, Oblique Flow, NACA T.Memo 1158.
 - b) Ludwieg, Critical Mach Number, ARC RM 2713 (1947).
 - c) Jones, Principles of Cross Flow and Swept Wings, NACA T.Rpts 835, 851, 863, 884 and 902 (1946 to 1948).
 - d) Neumark, Critical Mach Number, ARC RM 2821 (1949). This publication claims that all previous efforts including (b) and (c) of predicting the critical Mach number of swept wings have been erroneous.
 - e) Neumark (d) calls such wings "yawed" or "swept", while wings with "c" kept constant in the direction of the undisturbed fluid flow are "sheared". Most of the NACA testing (32) is done on wing families with chord defined in the direction of flow (such as in figure 30).
 - f) Küchermann, Flow Mechanism, ARC RM 2908 (1956).
- (31) Characteristics of wings in oblique flow:
 - a) Pressure Distribution by Lippisch, ZWB Doct FB 1669 (1942), and by Koch, ZWB Doct UM 3006; NACA T.Memo 1115.
 - b) Jacobs, Sheared Flow, Ing.Arch. 1952 p.418.
 - c) Beavan, Yawed Airfoils, ARC RM 2458.

Flap Camber. The flow mechanism explained above and/or the underlying experimental facts have also led to proposal, design and investigation (29) of foil sections whose camber line is *reflexed* in such a way that they may produce the desirable delay of drag (lift and moment) divergence. Camber is negative in such sections near the leading edge; and it is positive for most of the rest of the chord. Figure 23 proves, however, that at Mach numbers below drag divergence, the losses of momentum in the flow around the leading edge and the readiness for separation in the symmetrical section, are evidently higher than in the properly cambered section. In other words, the straight shape is not the most favorable one at lower speeds. It is suggested, therefore, that in a high-speed airplane, camber and drag divergence Mach number of the wing could possibly be controlled to advantage, by means of trailing and/or leading edge flaps.

6. CHARACTERISTICS OF SWEPT WINGS

The principle of "cross flow" is explained in Chapter III in connection with inclined circular cylinders. The same principle if applied to the plan-form shape of wings, makes it possible to increase the maximum speed of subsonic type airplanes appreciably.

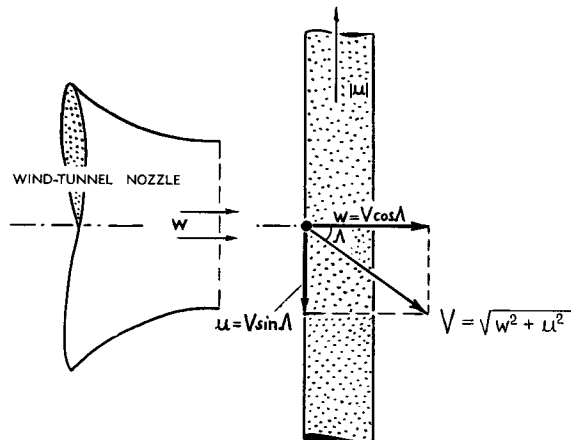


Figure 26. Experiment explaining the principle of "cross flow", or "sideslipping" in the panels of swept wings.

Cosine Component. Considering a straight (cylindrical) piece of wing moving against the air at an angle of yaw ("side-slipping"), we can split the resultant velocity "V" into two components, one blowing in the direction of the wing's axis or spar, and the other in the direction of the wing panel's chord, normal to its axis. If neglecting skin-friction, the former component ($V \sin \Lambda$) can then be disregarded. The wing's displacement effects (pressure and lift forces) must, on the other hand, be expected to correspond to the dynamic pressure of the other flow component ($V \cos \Lambda$). To make the flow pattern thoroughly understood, the imaginary experiment illustrated in figure 26 may be studied. An infinitely-long airfoil (in the form of a large ring, for instance) is assumed to be moving in lateral direction, across the open jet of a wind tunnel, at the velocity "u". *Disregarding skin friction*, it is then obvious that the "potential" flow pattern of, and the pressure forces (31) originating in the piece of foil bounded by the edges of the tunnel's jet, are a function only of the component "w". However, the resultant velocity at a certain point

of the airfoil, in relation to the air particles, discharged from the tunnel's nozzle,

$$V = \sqrt{w^2 + u^2} \quad (26)$$

is evidently larger than "w". Assuming now that the resultant velocity "V" be sonic (at $M = 1$), the speed "w" can very well be subsonic, below the critical Mach number, and even very small, all depending upon the value of "u" with which the foil is driven across the tunnel's jet. A practical application of this principle is the *swept wing* (swept either way, back or forward) in which each panel is in the steady-state condition of sideslipping at the reduced "effective" speed

$$w = V \cos \Lambda \quad (27)$$

while the airplane as a whole moves straight ahead, at the resultant "full" speed "V". The wing's angle of sweep " Λ " evidently corresponds to the velocity component "u" as in the wind-tunnel experiment described; thus:

$$\sin \Lambda = u/V \quad (28)$$

Swept-Wing Definition. In dealing with swept wings, a definition of their geometry is necessary. In subsonic aerodynamics we will consider as the angle of sweep that of the 1/4 chord line. As "chord" of the foil sections to be used in the theoretical analysis of this chapter, we shall define the dimensions measured in each panel, in the direction normal to the quarter-chord axis (30,e). Section shape and thickness ratio are determined accordingly. This definition may then lead to the assumption that upon sweeping the panels of a wing, the "effective" thickness ratio, measured in the direction of the wing's motion, would be reduced in proportion to $\cos \Lambda$. This is not the correct approach to the problem, however; and the mechanism as in figure 26 should always be remembered. As to the aspect ratio of swept wings, the basic definition of $A = b^2/S$ still applies, where b = span measured as the straight distance between the wing tips. As a consequence, the aspect ratio reduces upon sweeping the panels of a wing, in proportion to $\cos \Lambda$. Aspect ratios of swept wings are easily overestimated when looking at them. One evidently considers the dimensions of the panels, rather than the ratio b^2/S . For example, the wing as depicted in figure 29, has an aspect ratio of only 4, while that of the panels, so to speak, i.e. when sweeping them into straight-wing position, is almost ≈ 8 .

Pressure Drag. The cross-flow principle described (which may also be called "cosine principle", because of equation 27) is independent of compressibility (33). It obtains higher significance, however, under compressive conditions of fluid flow. Using equation 6 on page 6-6, the frictional coefficient to be applied then corresponds to equation 14 or 15,

respectively. The second term of the function quoted, reduces in proportion to $\cos \Lambda$. With respect to the third term, representing pressure drag, experiments on two 20% thick airfoils in oblique flow (tested in yawed or sheared position between tunnel walls, reference 31,c; by pressure distribution) confirm the prediction that the pressure coefficients reduce in proportion to $\cos \Lambda$. The *pressure-drag* component reduces accordingly. To obtain this term properly, the drag which it represents, is first calculated in the form of a coefficient based on the dynamic pressure $0.5 \rho w^2$; and then referred to $0.5 \rho V^2$. When introducing the Prandtl factor (as in equation 5) this factor must be determined as a function of the Mach number corresponding to "w" rather than to "V". As a result we obtain tentatively

$$C_{Ds} = 2 C_{f_{com}} [1 + k(t/c) \cos \Lambda + 60 (\bar{P}_\Lambda^3) (t/c)^4 \cos^2 \Lambda]$$

where k between 1.5 and 2.0, depending upon the thickness location of the foil section applied, and where

$$\bar{P}_\Lambda = 1/\sqrt{1 - M^2 \cos^2 \Lambda} \quad (31)$$

represents the Prandtl factor defined in the direction of "w", i.e. normal to the foil axis. As far as wings are concerned, with thickness ratios in the order of 10%, the pressure drag component is comparatively small. A direct reduction of section drag (at subcritical speeds) is, therefore, not expected to be spectacular if applying angles of sweep, say in the order of 30°. Experimental results in figures 30 and 31 (and other evidence found in reference 32) do not show conclusively much of this type of reduction of section drag effected by sweeping the wing panels.

Inclined Struts. By multiplying equation 30 with (c/t) , the drag coefficient (based on frontal area) of struts and two-dimensional fairings is obtained. Figure 27 shows experimental results obtained by sweeping two of the antenna rods previously quoted. A considerable decrease of the drag coefficient is evident (33). Because of the particular test conditions

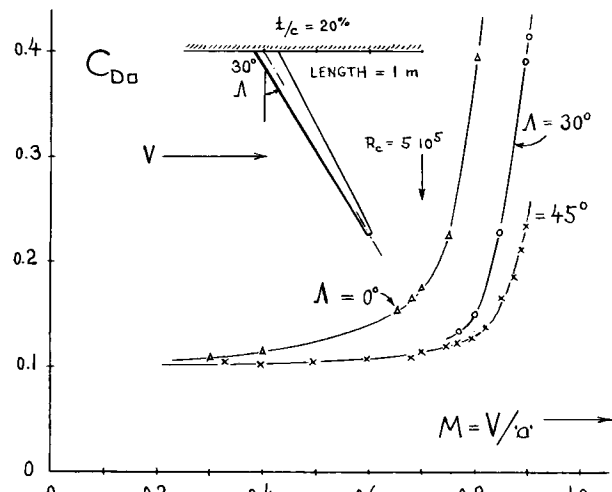


Figure 27. Drag coefficient (on original frontal area S_D) of a 20% thick strut (antenna rod No. 6 as in figure 9 and reference 9,b) in oblique flow, i.e. in a position inclined against the oncoming flow by the angle Λ .

listed in connection with figure 9, a quantitative evaluation is not very well possible, however. Other results specifically confirming the analysis, have not come to the attention of the author. To be conservative in making predictions, the square of the cosine in the last term of equation 30, was then *arbitrarily* reduced to a plain " $\cos \Lambda$ "; so that the drag of inclined struts may now correspond to

$$C_{D_s} = C_{f_{com}} (2 (c/t) + 4 \cos \Lambda + 120 (\bar{P}_\Lambda^3) (t/c)^3 \cos \Lambda)$$

The function is plotted in this form in figure 28, for some selected values of Mach number and chord/thickness ratio. To arrange struts (wherever they may be used) in an inclined position, thus appears to be promising. An example for the application of such "struts", is as protection devices placed across the intake openings of jet (or of other air-fed) engines, without reducing the ram pressure, and/or choking the inflow too much. It must be noted, however, that the coefficient as in the equation and as in figure 28, is based upon the "frontal" area normal to the strut axis. When inclining the strut, it will then be of importance whether or not the length (or span) is kept constant.

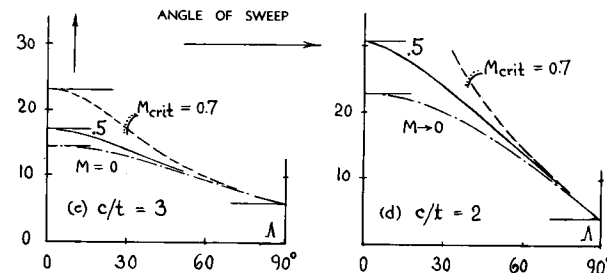
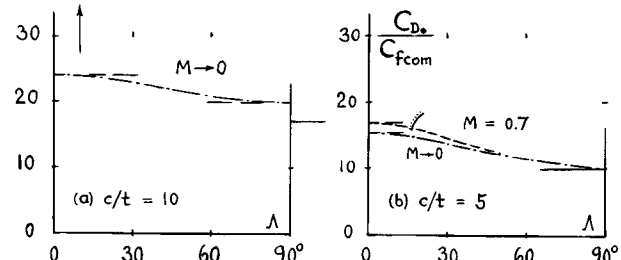


Figure 28. Evaluation of a function derived in the text, demonstrating possible drag reductions of struts and/or fairings obtainable by inclining them against the direction of flow.

Critical Mach Numbers. Considering a swept wing as being composed of two sideslipping panels, it may at first sight seem to be possible to fly with such a wing beyond the speed of sound, without having at any point of its surface a shock or any other disturbance of the potential flow caused by exceeding a critical speed. To explain this apparently paradoxical statement, the experiment as in figure 26 can help again; and the gas-dynamic equations of fluid flow can be satisfied by considering as the "reservoir" or "stagnation" pressure the total pressure corresponding to "w" rather than to "V". On the basis of equation 27, the "critical" Mach number would then be

$$M_{\text{crit}} = M_{\text{crit0}} / \cos \Lambda \quad (36)$$

where M_{crit0} = critical number of the straight wing. This M' -number is indeed an *upper* limit, and it is plotted as such in figure 29 for $M_{\text{crit0}} = 0.8$. For reasons of symmetry, the centerline of every swept wing is exposed to straight flow, however, essentially having the velocity "V". The theoretical limit of the critical Mach number of larger aspect ratio wings is unity, therefore, (at the limiting sweep angle of 90°). Between that limit and the critical Mach number of the unswept (straight) wing, the "lower" critical number varies as indicated by analysis (30,d).

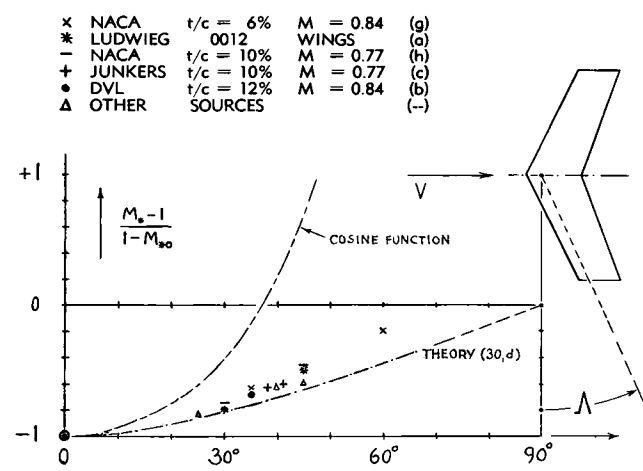


Figure 29. Critical Mach number of larger-aspect ratio wings (32) as a function of their angle of sweep. Theories are evaluated for $M_{\text{crit0}} = 0.8$ corresponding to a thickness ratio of $t/(2x) = 11\%$, at zero lift.

Figure 30 presents as an example the drag coefficient (at $C_L = 0$) of a 12% thick wing both in straight form and for an angle of sweepback of 45°. The critical or drag-divergence Mach number is increased from 0.70 to almost 0.90, thus confirming our presentation.

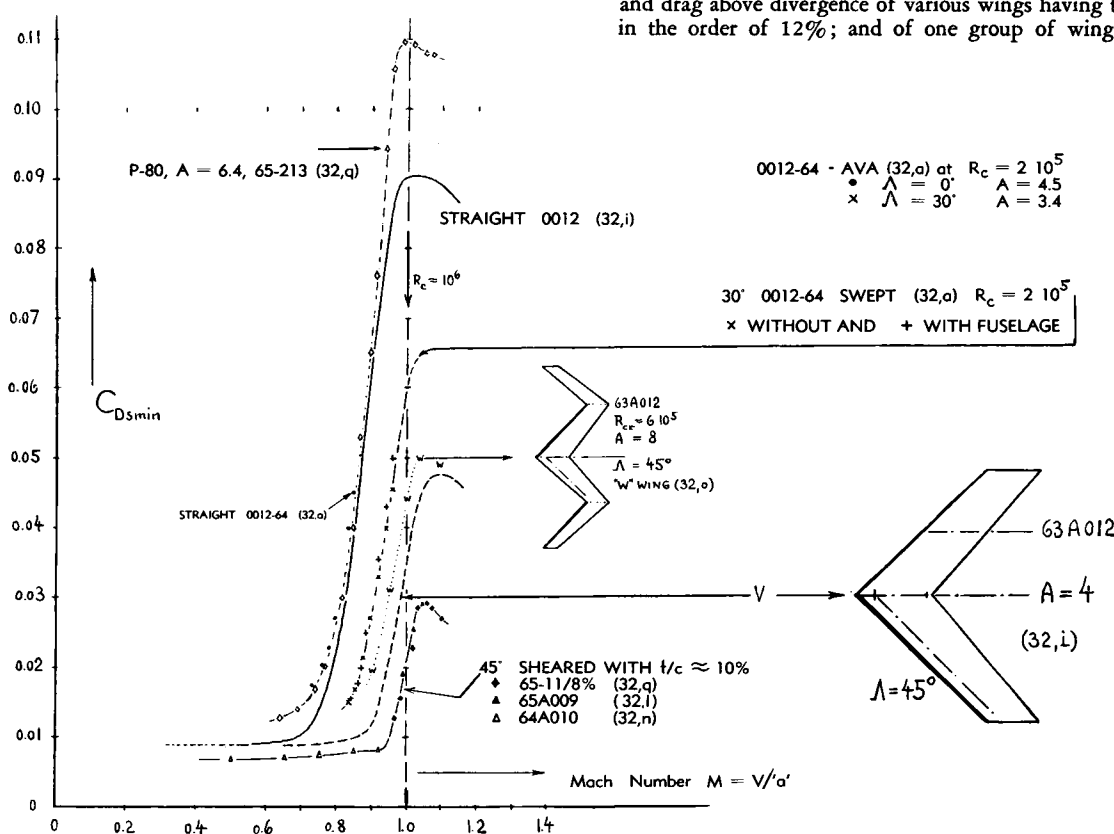


Figure 30. Influence of sweep (32) upon critical Mach number and drag above divergence of various wings having thickness ratios in the order of 12%; and of one group of wings with $\approx 10\%$.

Example. By plotting the critical Mach number of swept wings in the manner as in figure 29, the experimental results obtained by testing pairs or groups of wings, each having a common thickness ratio, collapse approximately upon a common function. To explain the graph, we will consider an example. For $t/c = 12\%$ and $t/(2x) = 20\%$, the critical M'number of a straight wing may be $M_{*0} = 0.72$ (as in figure 19). After sweeping the wing panels to $\Lambda = 45^\circ$, we find the value of ≈ -0.5 in the graph (figure 29). The critical M'number is then $M_{*0} = 1 - 0.5(1 - 0.72) = 0.86$. The increment is 0.14 in this case; and the corresponding increase of the maximum speed of an airplane using this wing is possibly between 80 and 90 knots.

Center Part. The fact that the experimental points as plotted in figure 29 do not very well agree with the theoretical function as indicated, is not alarming at all. Only small portions of the center part (and possibly spots at the wing tips) exhibit sonic speeds at the lower boundary, while the rest of the wing panels can go on without any disturbance (as explained above) to speeds and Mach numbers corresponding to the cosine function. With respect to drag, only some "creeping" divergence is expected, accordingly, to start at the lower Mach-number boundary, originating from the wing's center part. This divergence may not be important, and it may not well be noticeable when picking M_{DD} values from plots of C_D as a function of M (such as in figure

31, for example). Reference (30,d) also explains the influence of section shape. In a swept-back wing, the most favorable thickness location on the wing's center line, is ahead of 0.5 chord, where the three-dimensional relaxation in the "arrow head" of a swept wing is strongest. However, in swept-forward wings (as in figure 53, for example, a type considered by simple theory to be "equal" to a swept-back wing) the optimum location of thickness on the center line is somewhat aft of 0.5 chord (34). At lift coefficients different from zero, swept-forward wings also become more loaded in the center; and this direction of sweep will then really be not as favorable as the swept-back type (in which the tips rather than the center are more loaded at lift coefficients different from zero).

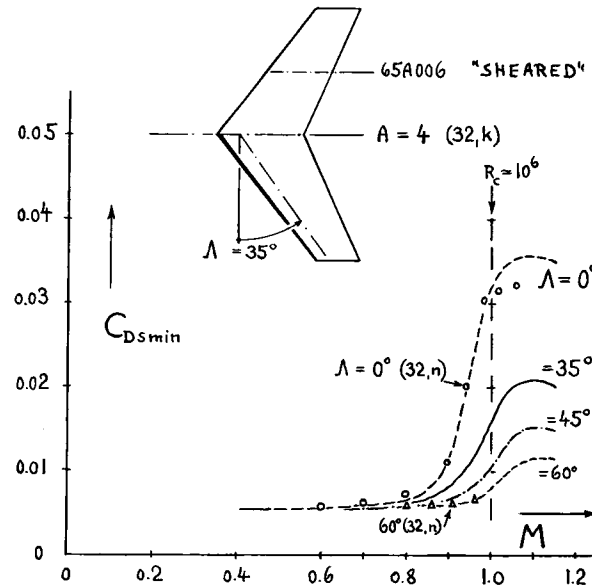


Figure 31. A family of 6% thick swept wings tested by transonic bump technique (32,k).

- (32) Experimental investigation of swept wings:
 - a) Ludwig, Swept Wings at High Speeds, ZWB Lilienthal Rpt 127 p.44; AVA Rpt 1940/8/14; Transl. ATI 6963.
 - b) Goethert, High-Speed Tests of Swept Wings, ZWB Rpt FB 1813; Lilienthal Rpts 127 and 156 (1942).
 - c) Frenzl, Swept Wings Tested in the Junkers High-Speed Wind Tunnel, Junkers Rpt S.1943/58.
 - d) Kolb, Free-Fall Tests by DVL, Wright Field RPT 1949.
 - e) Mathews-Thompson, Falling Body, NACA T.Note 1969.
 - g) NACA, T.Note 3867 and Documents RM L9B25, L9G27, L51D13 and L52K04.
 - h) NACA Documents RM L6J01a and L50K27.
 - i) NACA Bump Tests 12% Wings, L51C26, L51H30.
 - k) NACA Bump Technique on 6% Thick Wings, Documents RM L9A21, L9H22, L9I08, L9K10a, A51A12.
 - l) Polhamus, Summary of NACA Bump Tests, RM L51H30.
 - m) Whitcomb, Pressure and Pattern on 35° and 45° Swept Back and Forward Wings, NACA Docs RM L50K27/28.
 - n) NACA, High-Speed Tunnel Results, Documents L51D13 (to 60° Sweep) and A52D01 (to $R_c = 10^7$).
 - o) "W" and "M" wings have been tested by Morrison, NACA Documents RM L50H25a and L52E14a.
 - p) Holmes, 6 Wings with 40° Sweep, ARC RM 2930.
 - q) Weaver, P-80 Wings on Bump, J.A.Sci.1948 p.28.
- (33) Figure 25 in Chapter VIII proves that inclination reduces the drag of a strut (at low Mach numbers) appreciably. Interference with the wall (also reducing with the angle of sweep) overshadows other effects in that example, however.
- (34) This result corresponds correctly to the reversal theorem as explained in Chapter XVI.

Swept-Wing Characteristics. As far as subsonic speeds are concerned, the primary incentive for the development of swept wings comes from the beneficial influence of sweep upon their critical Mach number. By postponing transonic effects such as shocks, it is expected that undesirable consequences in regard to trim, stability, vibrations and drag can be avoided altogether. This effect is particularly evident in thicker foil sections (such as in figure 30). Figure 31 demonstrates, however, that a combination of sweep with thin foil sections increases the drag-divergence Mach number to between 0.9 and 1.0. Sweep has also considerable influence upon the rise of the drag coefficient *above* the critical Mach number. This effect is also evident in figure 31. Another parameter affecting the transonic drag rise as well as the critical Mach number, is the wing's *aspect ratio*. Its influence upon M_{crit} is as shown in figure 21.

Sheared Wings. The critical Mach numbers of "sheared" wings (30,e) with foil sections defined and kept constant in the general direction of motion, are somewhat lower than those of the class of swept wings as defined in the beginning of this section. A few experimental points obtained on wing models of the sheared type, are included in figure 30. For example at $\Lambda = 30^\circ$, the difference in the critical or drag-divergence Mach number between the two definitions of sweep may be in the order of $\Delta M = 0.02$ or 0.03 .

"W" Wings. A variation of the swept wing, designed to avoid wing-tip stalling (a property representing the primary disadvantage of sweep-back) is the "W" shape an example of which is included in figure 30. The addition of 2 more "kinks" where the "cross" flow cannot develop, somewhat reduces the drag-divergence M' number, and it increases the transonic drag to a certain extent—as in comparison to plain swept wings. The reversed shape, in form of an "M" has also been investigated (63) essentially showing the same drag function as the "W" wing (32,a and o).

Delta Wings. There is a particular type of "swept" wings, triangular in shape, flying point-first, and having a straight trailing edge. This class of wings could be treated by applying the functions derived in the previous paragraphs, on the basis of the sweep angle corresponding to their maximum-thickness line. The aspect ratio of typical "delta" wings is comparatively small, however; for example $A = 2$, for a vertex angle of $30/60^\circ$. In such small A' ratios, the flow pattern is much more three-dimensional than two-dimensional. An alleviating effect of a nature similar to that as shown in figure 21 is, therefore, found in delta wings. More information on this type of wing is given in the "transonic" chapter, where swept wings are also discussed further.

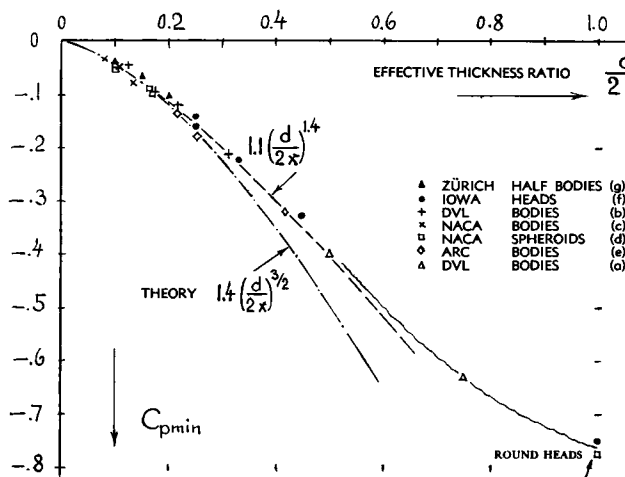


Figure 32. Low-speed experimental minimum pressure coefficients (36) on the surface of spheroids and streamline bodies, plotted against their effective diameter/length ratio $d/(2x)$.

7. CHARACTERISTICS OF STREAMLINED BODIES

The flow past three-dimensional bodies cannot be described by linear equations. Treatment of supersonicities, pressure gradients, form-bound drag and their variation as a function of Mach number, and the prediction of the critical Mach number are therefore not as straight-forward and comparatively simple as in two-dimensional conditions. Some approximate analysis is as follows.

Skin Friction. The drag coefficient of "conventional" bodies of revolution (with maximum diameter located between 0.3 and 0.4 of the length) is approximately indicated by equation 28 of Chapter VI. As in two-dimensional sections (explained before) the skin friction component is expected to correspond to the basic coefficient as in equations 14 or 15, respectively. Without further modification, thus:

$$C_{Df\text{wet}} = (1 + 1.5(d/1)^{3/2}) C_{f\text{com}} \quad (40)$$

Supervelocities in three-dimensional flow conditions are appreciably smaller (for one and the same thickness or diameter/length ratio, respectively) than in two-dimensional flow. Figure 32 presents a collection of experimental points indicating the minimum pressure coefficients found at the sides of rotationally-symmetric streamline bodies. As in figure 19, an equivalent or effective thickness or diameter/length ratio $d/(2x)$ has been used in plotting the graph; and this ratio is that of the forebody (to the maximum thickness at x) completed to a full double-symmetric shape having the length $(2x)$. For such spheroidal shapes, theory (35,c) predicts that the ratio of supervelocity grows as $(d/1)^{1/4}$. The graph indicates approximately

$$C_{p\text{min}} = -1.1 (d/2x)^{1/4} \quad (41)$$

Actual supervelocity ratios may then correspond to

$$\Delta V/V = 0.5 (d/1)^{4/3} \quad (42)$$

These functions apply particularly well to diameter/length ratios between 5 and 30%, thus covering practically all streamline shapes. Tests on half-body heads (combined with a cylindrical afterbody) show only slightly lesser ratios.

Compressibility Rule. The original Prandtl-Glauert rule refers only to slender two-dimensional bodies, that is to airfoil sections. For three-dimensional bodies, the rule has a more complicated form. As formulated in (37,a), the supersonicities and negative pressure differentials developing in compressible flow along the sides of rotationally symmetric bodies are $(P)^2$ times as high as on a similar body of reference the dimensions of which, measured in flow- or flight direction, are 'P' times as long as those of the actual body. Utilizing equation 41, the pressure differentials (in the form of C_p) on the assumed more slender reference body have a relative magnitude of only $(1/P)^{1/4}$. According to the rule, the differentials on the actual body are then predicted to be $(P)^2$ times as high as on the reference body. The ratio $(P)^2 / (P)^{1/4}$ finally indicates the pressure ratio. Thus in explicit form:

$$C_{p\text{com}}/C_{p\text{ref}} = (P)^{0.6} \quad (44)$$

This ratio is plotted in figure 1. Pressure distribution tests reported in (36,c) essentially confirm this function.

- (35) Incompressible theoretical velocities on spheroids:
 - a) Maruhn, Theory, Yearbk D.Lufo 1941 p.I,135.
 - b) Hoerner, in "Aerodynamic Drag", 1951 p.203.
 - c) Evaluation of (a) J.Aeron.Sci. 1951 p.770.
- (36) Supersonicities tested on bodies of revolution:
 - a) DVL, Streamline Bodies, Reference (39,a).
 - b) Lange (DVL), Distribution, ZWB Doct FB 1516.
 - c) NACA, Streamline Bodies, RM L53L28a and A5G17.
 - d) NACA, On Spheroids, RM L52D30 and T. Rpt 1155.
 - e) ARC, In Wind Tunnel, RM 1061, 1622 and 1480.
 - f) Iowa University, reference (11,a) in Chapter X.
 - g) VanDriest, Spheroidal Heads, Zürich ETH No. 16.
- (37) Compressibility function for 3-dimensional bodies:
 - a) Goethert, Extension of Prandtl Rule, ZWB FB 1275 and Yearbk D.Lufo 1941 p.I,156(NACA T.Memo 1105).
 - b) Advances in aerodynamic theory have confirmed the formulation as under (a). References, functions and experimental verification are presented by Matthews, "Pressure Distributions About Bodies of Revolution", in NACA Tech Rpt 1155 (1953).
 - c) Pressure distributions at higher and at transonic speeds are reported in NACA Documents RM A50E09, L53H04 and L53L28a; and in Tech Rpt 1155.
- (39) Drag of streamline bodies $f(M)$:
 - a) Goethert, Family of Fat Bodies, DVL Doct Jf.707/2 (1944), or ZWB Lilienthal Rpt 127 or ZWB Tech Berichte 1944 p.94 and 377 (corrected results).
 - b) Drag Characteristics of 8 Slender Bodies, DVL Doct Jf.729/3 (1944); reported by Melkus in AVA Rpt 1946/Z/11; quoted by Riegels in Yearbk WGL 1952.
 - c) Zobel, Low-Drag Bodies, ZWB FB 1801 and UM 2036.
 - d) NACA, Large-Size Body, see reference (50,b).
 - e) Thommen, Martin Fund Student Paper IAS 1956 p.115.
 - f) NACA Documents RM L5E03, L7K12 and L9C11.
 - g) Lopatoff, Spheroid, NACA RM L51E09.
 - h) Mason, External Stores, NACA Doct. RM L53J22.
 - k) Fin-Stabilized Gun-Fired Bodies, NACA RM L56D16.
- (40) Critical Mach number of streamline bodies:
 - a) NACA, Various Free-Flight Results, reported in Documents RM L7K12, L8A05, L9F02 and L50I08a.
 - b) NACA, Parabolic Body in Flight, RM L9I30.
 - c) NACA, in Tunnels, RM L9C11, L52F06, L53L28a.
 - d) DVL Bodies as in reference (39,a).

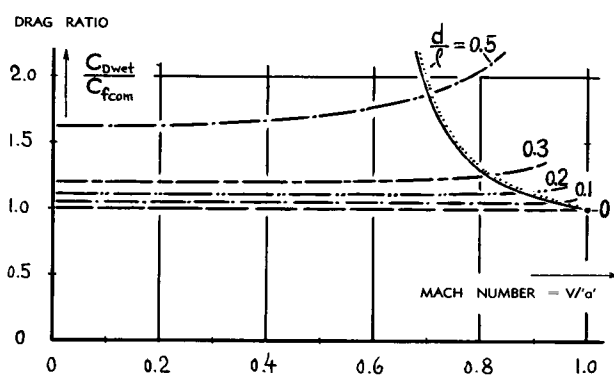


Figure 33. Drag ratios of a family of streamline bodies of revolution calculated through the use of equations 40 plus 45, plotted as a function of Mach number.

The Pressure Drag of a body of revolution as given in equation 28 of Chapter VI, corresponds to the frontal area represented in that equation by $(d/l)^1$, while the influence of the pressure gradient along the after-body (producing growth and possibly separation of the boundary layer) corresponds to $(d/l)^2$. Applying now the three-dimensional compressibility rule together with the trend as given in equation 44, the pressure drag in three-dimensional fluid flow can be approximated by

$$C_{DPwet} = C_{fcom} 6 (P)^{1/2} (d/l)^3 \quad (45)$$

This component of drag can thus be smaller than in incompressible fluid flow (because of C_{fcom} reducing against M as in equations 14 or 15, respectively); or it can be larger (because of the modified Prandtl factor). The function is plotted in figure 33, together with the skin-friction component (as per equation 40) in the form of a drag ratio. It can readily be seen that this ratio is approximately constant (is independent of Mach number) as far as slender streamline shapes are concerned (up to $d/l \approx 0.2$ or 0.3), over most of the subsonic range below the critical M' -number. On the basis of equation 14 (for smooth-turbulent boundary layer flow) the drag coefficient (rather than the ratio as plotted) is then expected to decrease slightly as the Mach number is increased. Confirmation is not easily found, because of experimental difficulties in supporting low-drag bodies at high speeds without interfering with pressure distribution, boundary layer flow and separation (if any). Figure 34 presents available results on a family of comparatively fat streamline bodies, some of which seem to verify the theoretical prediction. Other bodies (such as that in figure 11, for example) exhibit considerable variations of the drag coefficient, caused by shifting of the boundary layer's transition point under the combined influence of the wind tunnel as such (stream turbulence?) and that of Reynolds and Mach number, respectively.

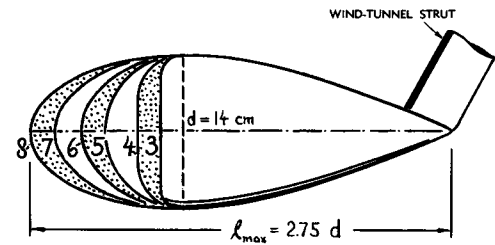
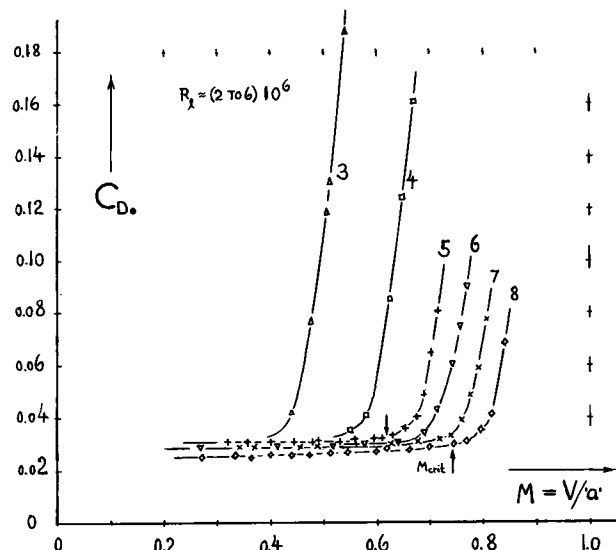


Figure 34. Drag coefficients of a family of fat streamline bodies of revolution (39,a) as a function of M' -number.

Streamline Bodies. There are only a few "reliable" experimental results available (39) on high-speed drag of streamline bodies. The results plotted in figure 35 confirm that the critical or drag divergence Mach number of slender bodies is comparatively high (up to and above $M = 0.9$). They also show that (in the absence of interference effects from other aircraft parts and/or disturbing support devices in wind tunnels) drag of such bodies below M_{crit} simply corresponds to skin friction. At Mach numbers above the critical, their coefficient increases steeply, however.

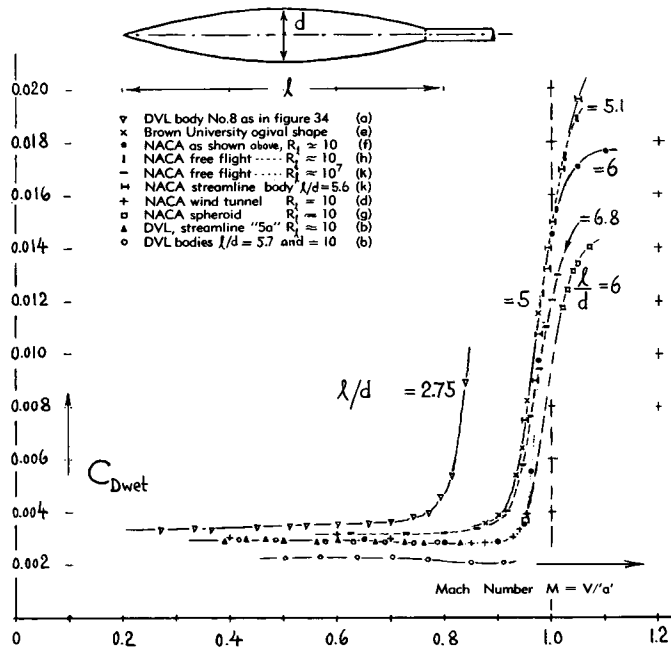


Figure 35. Drag coefficients (39) of several streamline and of two ogival bodies of revolution as a function of M' -number. Note that in the results of (f) and (g) a value of 0.003 has been added for skin friction (which was not included in the coefficients derived from pressure distribution).

Rounding Radius. Figure 34 also permits to obtain an idea on the influence and the importance of a rounding radius (in this type of body shape) upon the drag-divergence Mach number. While at sub-critical M' -numbers, a certain critical radius can be determined, below which separation suddenly takes place (see on page 3-13), such a critical radius is not evident with regard to drag divergence. Rather, the value of M_{crit} increases more and more, as the forebody (nose) of the shape investigated, is made longer and finer.

- (42) Drag of straight-wing-fuselage configurations:
 - a) Whitcomb, Experiments, NACA RM L50L07.
 - b) Knappe, Fuselage + Canopies, Heinkel Doct. SK.140.
 - c) See references (59,a and b.).
- (44) Interference drag in compressive fluid flow:
 - a) See Engine Nacelles in reference (47).
 - b) Knappe, Interference Drag of Crossed Pair of Airfoils, Heinkel Wind-Tunnel Doct WK 210 (1944).
 - c) Hoerner, Compressibility Interference Drag, Evaluation of (b); USAF Wright Field Rpt F-TS-1518-RE (1947).
 - d) Wilson-Horten, 64-Series Airfoils Balance-Tested Between Walls of Tunnel, NACA Document RM L53C20.
 - e) NACA, Airfoils Between Tunnel Walls, see (20,i).
- (45) This method needs to be developed further. Application in this form, as suggested, and statistical evaluation of experimental results is found at the end of this chapter.
- (46) The fact that the interference component increases as M is reduced below 0.6 or 0.5 (contrary to the ('P')³ method) must be explained by Reynolds-number, boundary-layer and turbulence effects.
- (47) Interference drag of smooth engine nacelles:
 - a) See "Meteor" Nacelles in reference (59,b).
 - b) Boltz-Beam, Body of Revolution and Wing Nacelle Combination, NACA Doct. RM A50E09; see also RM A9K01 and A50A13 on other configurations of the same models.
 - c) Jordan, Propeller Slipstream, NACA T.Note 2776.
- (48) Drag of aircraft canopies and windshields:
 - a) Knappe, Windshields, Heinkel Doct SK.140 (1941).
 - b) Beaven (NPL), Windscreens, ARC RM 2235 (1940).
 - c) See "Spiteful" Cabins in reference (59,a).
 - d) See the family of windshields in (6,b).
 - e) DVL, Me-262 Fuselage, Doct J.900/60 (1944).

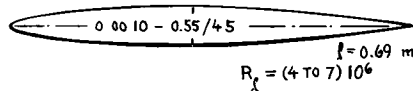
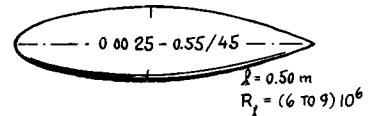
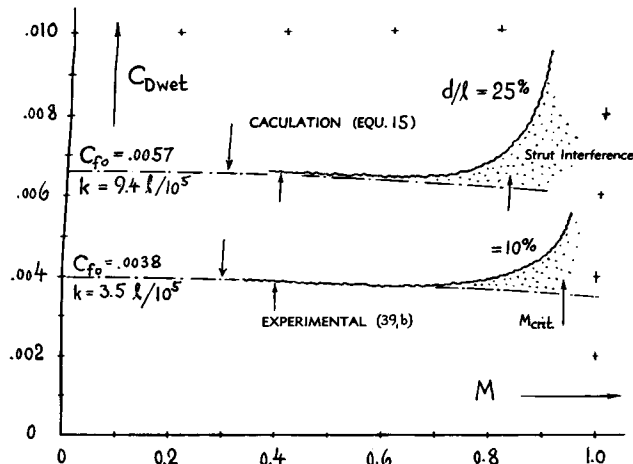
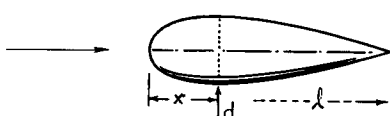
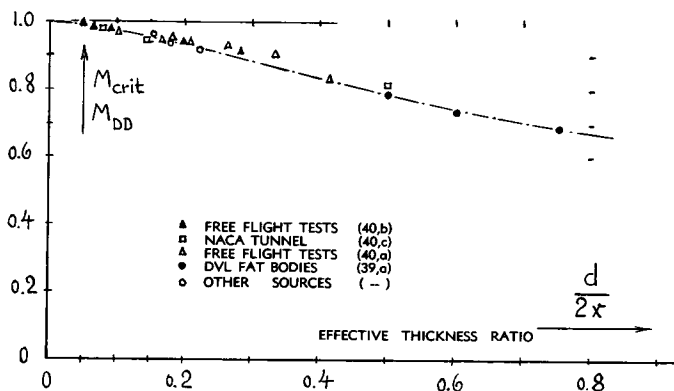


Figure 36. Drag coefficients of two "fully" rough bodies of revolution (39,b) as a function of Mach number.

Rough Bodies. In bodies "fully" covered with carbondum grains, the influence of R_f number may be expected to be eliminated. The reduction of the drag coefficient of the two streamline bodies presented in figure 36, can therefore be claimed to be a confirmation of the theoretical predictions (equation 15 in combination with the constancy of the ratio as in figure 33). The "creeping" increase of the coefficient, starting at $M \approx 0.65$ is most certainly caused by *interference* with the essentially two-dimensional strut (similar to that in figure 34) used to support the models firmly in the wind tunnel. Without such interference, the drag coefficients must be expected to continue along the theoretical lines up to the critical Mach numbers as marked in the graph.

Critical Mach Number. Inasmuch as (on the basis of equal thickness or diameter/length ratio, respectively) the supersonicities on the surface of three-dimensional bodies are appreciably smaller than those of airfoil sections, their critical Mach number is higher, of course. Considering, however, the critical number on the basis of equal incompressible supersonicity ratio, the statement can be made that bodies of revolution experience critical Mach numbers only slightly higher than those of airfoil sections. Figure 19 (in which a scale of $\Delta V/V$ is included) may thus be consulted to obtain first and conservative information on the critical Mach number of three-dimensional bodies. Figure 32 can be utilized in this connection to estimate the supersonicity ratio. The critical Mach number of streamline bodies can be determined more correctly, however, by applying the modified compressibility rule as described above, in combination with the statistical information on spheroids in equation 42. The critical number is then found by replacing in equation 21 the ' P_* ' by ' $(P_*)^{0.6}$ '. The resultant function plotted in figure 37 is reasonably well confirmed by experimental drag-divergence results from various sources, evaluated on the basis of the equivalent diameter/length ratio $d/(2x)$. To give an example, a fuselage with an effective fineness ratio of 5, that is with $d/(2x) = 20\%$, has a critical Mach number in the order of 0.9, while a wing with $t/c = 10\%$ may have an $M_{crit} \approx 0.84$, and at a lift coefficient of 0.2, even a value of $M_{crit} = 0.79$, only.

Figure 37. Critical and/or drag divergence Mach number of 3-dimensional streamline bodies (40) as a function of their effective diameter/length ratio.



8. DRAG OF AIRCRAFT COMPONENTS

Upon combining wing, fuselage and nacelles (if any) into an aircraft configuration, and when adding necessary or desirable parts such as canopies or external stores, the resultant total resistance is usually larger than the sum of the drag components tested singly (see Chapter VIII). The resultant *interference drag* is usually increased on account of compressibility. A number of configurations exhibiting interference effects is considered as follows.

Wing Plus Fuselage. It has been shown in the paragraphs dealing with slender "airfoil sections" that their parasitic drag coefficient is roughly independent of the Mach number (up to its critical value). The drag coefficients of slender three-dimensional bodies (such as the fuselage and possibly the nacelles of an airplane) may even be expected to decrease with Mach number, on account of skin friction (equation 14). Yet, wind-tunnel investigations of more or less complete airplane models at Mach numbers exceeding 0.4 or 0.5, usually indicate an appreciable increase of the drag coefficient of such configurations. Figure 38 shows the drag coefficient of a fuselage when added to a wing. It appears that the drag of and due to the fuselage increases steadily as a function of Mach number. Considering one of the underslung designs of external stores in figure 45 as being similar to a fuselage, that graph also confirms the increasing trend of the drag coefficient of such combinations as a func-

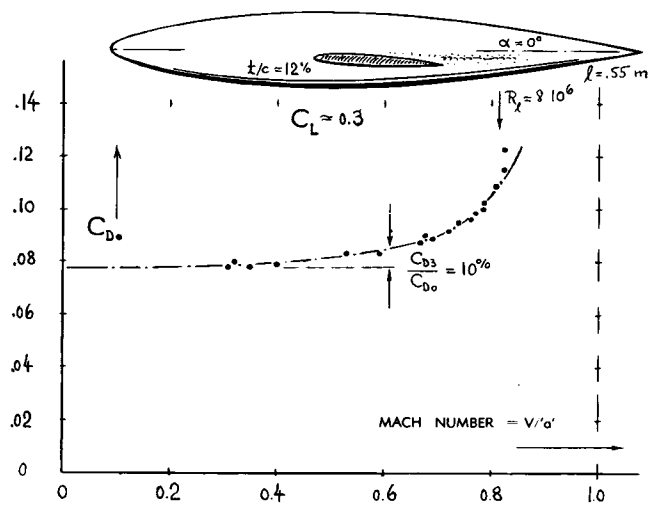


Figure 38. Drag coefficient of a *fuselage* (42,b), including interference effects with the wing to which it is added.

tion of Mach number. This growth is caused by interference in the various corners of aircraft configurations. Evidence of and examples for the interference component are presented as follows, while a statistical evaluation is undertaken in the next section of this chapter.

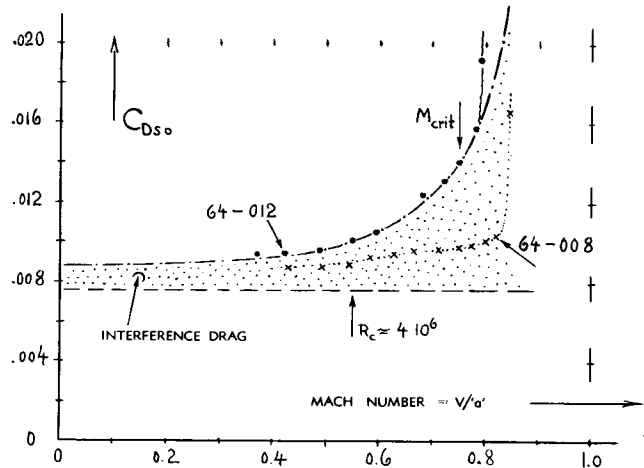
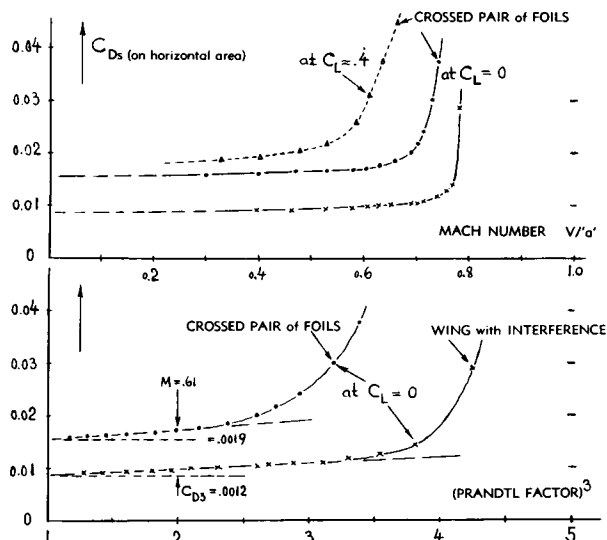


Figure 39. *Balance-tested* drag coefficient of two airfoils spanning the test section of a high-speed wind tunnel, *wall to wall* (44,d).

Wing-Wall Interference. Figure 39 presents examples of interference drag apparently originating from the wall junctures of airfoil models spanning the test section of a high-speed closed-type wind tunnel. The "viscous" drag coefficient of the foil sections as such corresponds to the principles of streamline shapes as presented in Chapter VI; and the coefficient of a particular section, can be expected essentially to remain constant as a function of Mach number (as in figure 13, for example). So then, the increment as found for the 12% airfoil in figure 39, is claimed to be chiefly interference drag originating from the wall junctures. Upon consulting figure 23 in Chapter VIII, coefficients " C_{Df} " can be estimated for this type of drag. For 2 wall junctures, and for a "wetted" aspect ratio "A" (between the walls, which is = 3, in the test considered) the increment of the drag coefficient caused by wall interference (at $M \rightarrow 0$) is then

$$\Delta C_{Ds} = 2 C_{Df} (t/c)^2 / A \quad (48)$$

Since interference drag is a consequence of adverse pressure gradients, the component ΔC_{Ds} may now be expected to increase as a function of Mach number in proportion to some higher power of the Prandtl factor (figure 1). There is unfortunately some tunnel blockage involved in the results plotted (also growing as a function of Mach number). Further evaluation is, therefore omitted. — Another airfoil (with $t/c = 8\%$ only) also represented in figure 39, shows, by comparison, hardly any interference effect. Figure 23 of Chapter VIII gives the explanation; the interference coefficient is evidently close to zero at $t/c = 8\%$.



Crossed Wings. Figure 40 presents the parasitic drag coefficient of a crossed pair of wings, tested between tunnel walls as indicated. There are then 8 corners in this configuration in which interference drag can develop; and this fact is the reason for presenting this particular configuration at this point. As in the case of figure 39, it is speculated that the component of the drag coefficient attributable to interference, may grow in proportion to a higher power of the Prandtl factor. After trying various powers, it was found that the coefficient of the configuration as tested approximately lines up straight when plotting against $(P)^3$, as shown in the lower part of the illustration. The interference drag of this configuration thus follows a function similar to that of the pressure component in equation 17. Another example in figure 40 (at $C_L = 0.4$) also demonstrates that the interference drag and its growth as a function of Mach number, increase as the lift coefficient (of the horizontal foil) is increased.

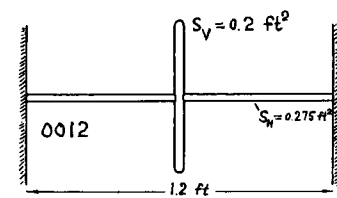


Figure 40. Drag characteristics of a *crossed pair* of airfoils, tested (44,b) between tunnel walls, plotted against Mach number (upper part) and against the cube of the Prandtl factor (in the lower part).

Plotting Against $(P)^3$. We know that the pressure drag of airfoil sections as well as the parasitic interference drag approximately grows in proportion to a higher power of "P". We may also believe that the induced increments, due to wing twist and caused by fuselage and nacelle interference (see Chapter VIII) may grow as some power of "P". Assuming then that the drag of an airplane *directly* stemming from skin friction may not materially be affected by subsonic compressibility, we can conclude that the rest of the parasitic drag may correspond to a component coefficient increasing as a function of Mach number in proportion to an average power of the Prandtl factor between 2 and 3. Tentatively, we will select " 3 ". Plotting then the total drag coefficient against $(P)^3$, the fraction affected by compressibility can approximately be isolated, as demonstrated in the example in figure 40. At $(P)^3 = 2$, corresponding to $M = 0.61$, the increasing part of the coefficient is expected to be twice as large as at $M = 0$. The difference of the coefficient between $M = 0.61$ and $M \rightarrow 0$, thus indicates the part of the total coefficient which increases with the Mach number according to the assumed function.

Nacelles. The lower part of figure 41 presents the drag coefficient (on wing area) of a swept wing for the bare wing as well as in combination with the nacelle as shown. The drag-divergence Mach number is appreciably reduced. The nacelle body was also tes-

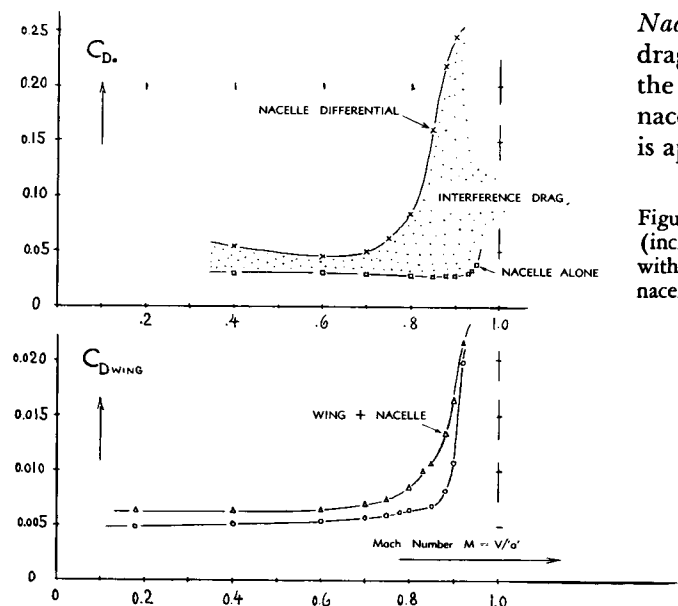
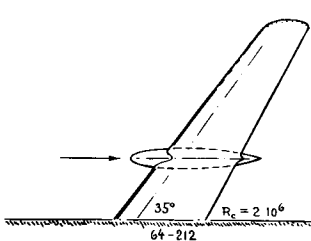
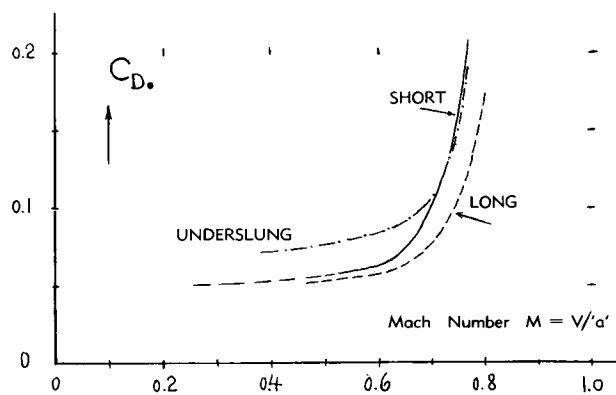


Figure 41. Drag characteristics (47,b) of a smooth *engine nacelle* (including wing interference), (a) drag coefficient of the wing without and with the nacelle, (b) coefficient of and due to the nacelle, based on its frontal area.





ted "alone". The upper part of the illustration shows its comparatively low coefficient; and it demonstrates that the critical Mach number of this body (in the order of 0.94) is appreciably higher than that of the wing ($M_{DD} \approx 0.86$). The nacelle drag coefficient has also been evaluated from the results of wing plus nacelle as against "wing alone"; and the corresponding drag coefficient (on frontal area of the nacelle) is plotted too, in the upper part of figure 41. This coefficient is significantly higher than that of the body alone, the difference representing interference drag. At higher Mach numbers, the interference component grows into very considerable values, approaching some 8 times (!) the drag of the nacelle alone (46). The plot also demonstrates the "creeping" character of interference drag. Other experimental results (on behalf of the "Meteor") are plotted in figure 42. It is seen that the long nacelle has the lowest drag coefficient and the highest drag-divergence Mach number. An underslung nacelle has increased drag; most of the increment being induced drag as treated later in this chapter.

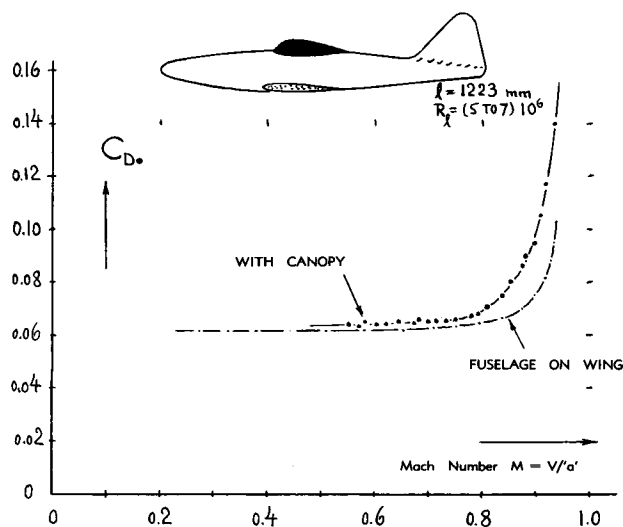


Figure 42. Drag coefficient of and due to different shapes of engine nacelles, tested on behalf of the "Meteor" (59,b).

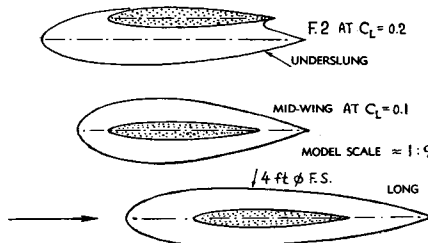


Figure 42. Drag coefficient of and due to different shapes of engine nacelles, tested on behalf of the "Meteor" (59,b).

Canopies. The drag of several more or less bluff canopy shapes is discussed as a more general phenomenon in section 2 of this chapter. Reference (6,b) also gives, at least qualitative information as to the radii required at the junctures of fore and afterbody, respectively, with a cylindrical middle body, in order to minimize flow separation and compressibility effects upon separation, in cases where a true streamline shape cannot be applied. Characteristics of three more shapes are presented in figures 43 and 44. Among these, the latter illustration shows an appreciable reduction in the value of the drag-divergence Mach number. It is suggested that a type of *transonic area rule* (described in Chapter XVI) may be responsible for this result, as opposed to that in figure 43 where canopy and wing are not at the same longitudinal station of the fuselage as they approximately are in figure 44. The bluff shape, in figure 43, shows the familiar dip (upon approaching $M = 0.8$) the mechanics of which are described in section 2 of this chapter.

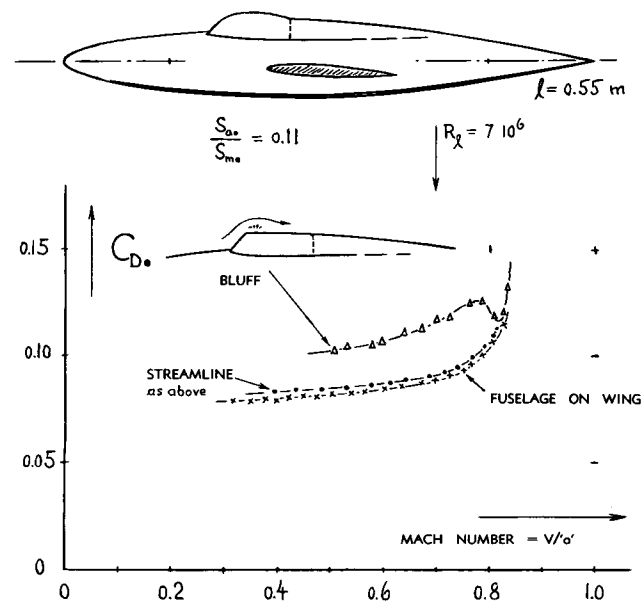


Figure 43. Drag characteristics of a fuselage (including wing interference) with and without canopies added (48,a).

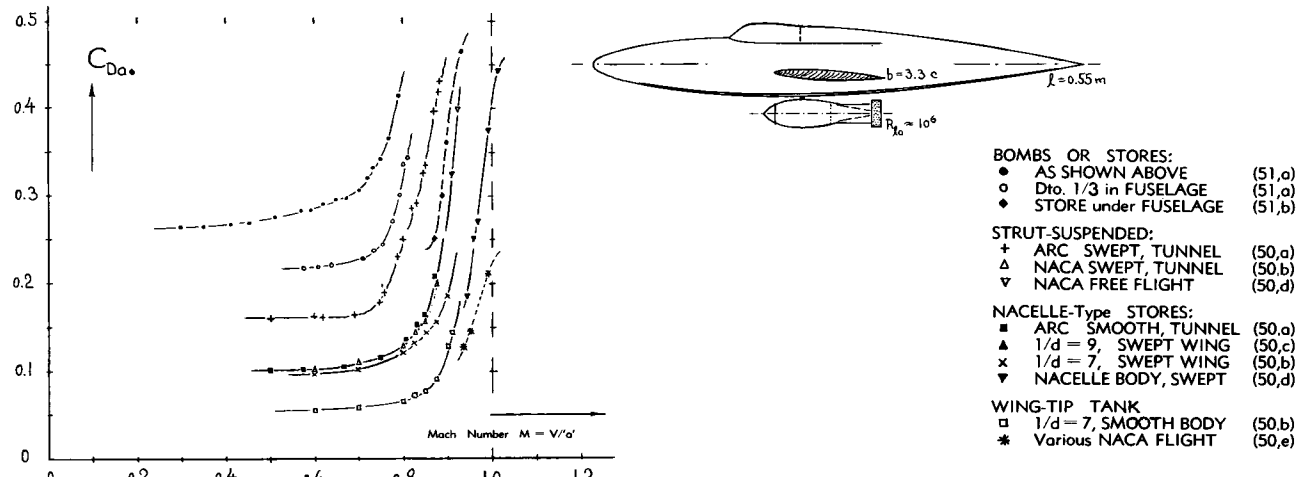


Figure 45. Drag characteristics of several *external stores* (50) and of a *bomb* (51) attached to airplane models.

Propeller Slipstream. The influence of a jet of air, simulating the slipstream of a propeller upon a nacelle-body and wing configuration, is described in (47,c). For a speed within the jet equal to 1.1 times the general speed, total drag is increased between 5 and 10%. On account of the slipstream, the drag divergence number of the wing drops from 0.78 to 0.76 (at $C_L = 0$); and with the nacelle in place (in symmetrical mid-wing arrangement) M_{DB} is reduced from 0.77 to 0.76 (as on the wing alone). We may, therefore, conclude that the three-dimensional character of configuration and flow pattern relieves the supvelocities which are to be expected along the wing roots. This statement even seems to apply to lift coefficients between 0.4 and 0.5 as included in the investigation quoted.

External Stores (and/or smooth nacelle bodies) are represented in figure 45, where their drag coefficients are plotted (based upon frontal area, and including interference effects in regard to wing or fuselage, respectively). Since wind-tunnel tests at transonic speeds are not always reliable, some available free-flight results have been added to the graph. These data show usually somewhat smaller coefficients (and/or higher Mach numbers for a certain level of the coefficient) than closed tunnel results on configurations of comparable type. The wing-tip type of tank presents the least added drag. Reference (50) also shows that the drag divergence Mach number of a wing is not reduced by adding a pair of tip tanks. Nacelle-type tanks (somehow integrated with the wing) have drag coefficients appreciably higher than those of the wing-tip tanks, while pylon-, neck-, or strut-suspended under-wing stores exhibit the highest drag coefficients (likely because of the two-dimensional character of the "pylon"). Most of these external stores produce a "creeping" increase of the drag coefficient as against Mach number, a result which is evidently indicative of the fact that the disturbance of the wing by the added bodies, is a *local* effect of interference involving progressively increasing flow separation, as a critical speed is exceeded. Reference (50,a) shows in this respect that critical (sonic) pressures are obtained at the juncture of a wing-tip tank at $M = 0.65$, for example, while drag divergence only becomes really obvious at $M = 0.82$.

Bombs, carried on the outside, are not desirable, of course, in high-performance airplanes. Their drag coefficients at lower speeds correspond to those as presented in Chapter XIII. Figure 45 shows that the drag-divergence number (as far as its value can be estimated) is comparatively low (in the vicinity of $M = 0.7$). The increase of the drag coefficient is "creeping". Comparison with free-flight results on a similar but smooth "store" shape (without fins, results of which are also included in the illustration) suggests that some tunnel blockage is involved.

(50) Drag of *external aircraft stores*:

- RAE, Drop Tank Models, ARC RM 2951 (1956).
- Spreemann, External Stores, NACA RM L9J06.
- NACA, Wing Tip Tanks, RM L52J22.
- NACA, Free-Flight Tests, RM L50G17a and L51D26.
- NACA, wing-tip tanks at transonic speeds, NACA Documents RM L54F29a, L51K02, A52J21 and L51L27.

(51) Bombs and stores *under fuselage*:

- Grütter-Knappe, Bomb, Heinkel Doct. SK 183 (1946).
- Mason, External Store, NACA RM L53J22.

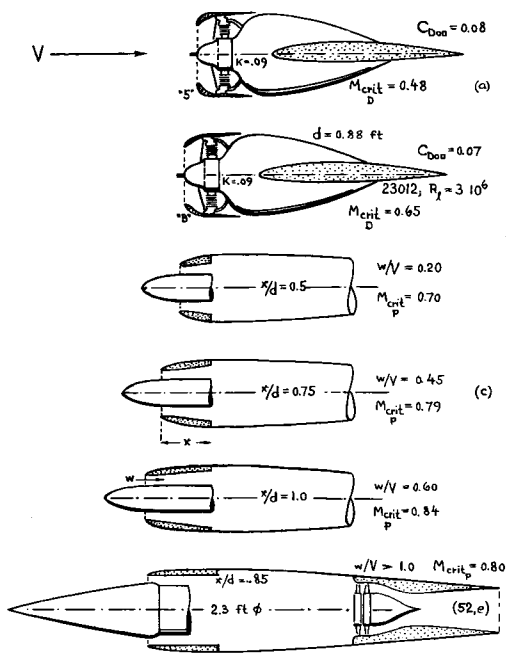


Figure 46. Critical Mach number of several *engine cowling shapes* (52), determined on the basis of pressure distribution ("P") and/or drag divergence ("D") respectively.

Engine Cowlings are treated at length in Chapters IX and XIII. With respect to compressibility, the shape of their inlet opening is sensitive, of course. Figure 46 demonstrates how the critical or drag-divergence Mach number grows from 0.25 as found for the worst of the now "old-time", comparatively short and bluff cowling shapes, to numbers above 0.80, in the more modern, more slender and more streamline types. Here as in all aircraft components, avoiding or postponing the critical or drag-divergence Mach number, is of primary importance in regard to drag. Pressure distributions on cowlings are therefore investigated in (52,c) for various inlet shapes and as a function of the inlet velocity ratio. Three shapes reproduced in figure 46, are typical "optimum" designs, selected from that source. One word of caution may be added, however, to the effect, that pressure peaks in the distribution around cowlings, do not necessarily lead to drag divergence upon reaching the "critical" Mach number (53). This effect is well demonstrated in figure 47, where we find a "delay" in the order of $\Delta M = 0.1$. Here as in figure 46, the length of the inlet cowling is the most important parameter in regard to the value of M_{crit} or M_{DD} , respectively. Below drag divergence, coefficients of cowled nacelles, tested alone, are roughly equal to those as presented in Chapters IX and XIII.

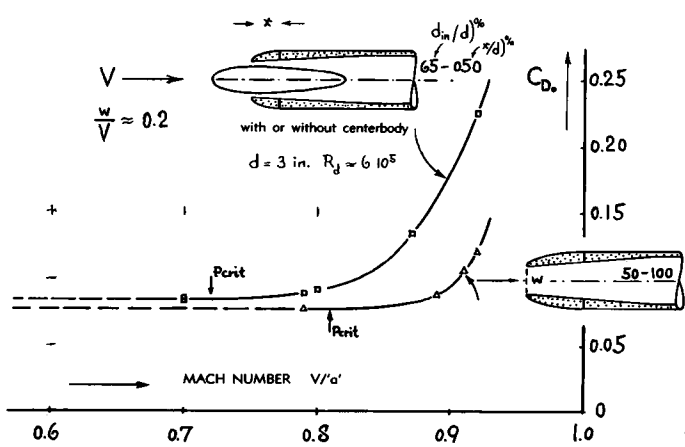


Figure 47. Two examples of engine *inlet openings* (52,d) suitable either for air-cooled reciprocating, for turbo-jet or for turbo-prop engine installations.

Radiators or inlet openings, respectively, investigated in (59,a) for example, show drag characteristics similar to those of engine cowlings. For constant setting of their control flaps, their coefficient is essentially constant (independent of Mach number) up to a critical speed where shock induced separation obviously starts from the outside shape.

Dive Brakes. Bluff bodies such as those in figure 2, exhibit drag coefficients that increase only slowly as a function of Mach number. In a similar manner, dive brakes (sharp-edged plates or flaps) consistently show comparatively constant or slightly increasing coefficients. For example, a pair of flaps deflected from the fuselage sides (54,a) has a drag coefficient C_D varying between 0.9 and 1.0. A wing flap (similar in shape to one of those in figure 30 of Chapter XIII) investigated on the "Vampire" model (59,b) has a coefficient $C_D \approx 1.0$ essentially constant to $M = 0.8$.

9. DRAG OF AIRPLANE CONFIGURATIONS

The drag of wings, fuselage bodies, engine nacelles and other component parts is presented in previous sections of this chapter. The drag of airplane configurations as a whole, is considered as follows.

(a) INDUCED DRAG OF WINGS

Lifting Line. Induced drag as defined by lifting-line theory (in Chapter VII) is basically related to lift, and not directly to geometrical parameters such as the angle of attack. In simple wings at subsonic speeds, this type of drag is, therefore, independent of compressibility, if considered in the form of $C_{Di} = C_L^2 / (\pi A)$. There are certain exceptions, however, where drag is a function of the geometrical angle of attack rather than of lift and induced angle, such as particularly in flat and sharp-edged plates (see in Chapter VII). Provided that the lift-curve slope of such "wings" increases as a function of Mach number (as indicated by the Prandtl rule) their drag due to lift can, therefore, be expected to reduce as the Mach number is increased.

Induced Interference Drag. The lift differential caused by adding a fuselage or a pair of nacelles to a wing, as explained on page 8-18, may also be assumed to be increased in proportion to the Prandtl factor (56). The increment of induced drag due to a fuselage or a nacelle, indicated by equation 22 (in chapter VIII) may consequently be increased to

$$\Delta C_{Di} = 0.035 (\Delta b/b) ('P')^2 \Delta C_{Lbo}^2 \quad (51)$$

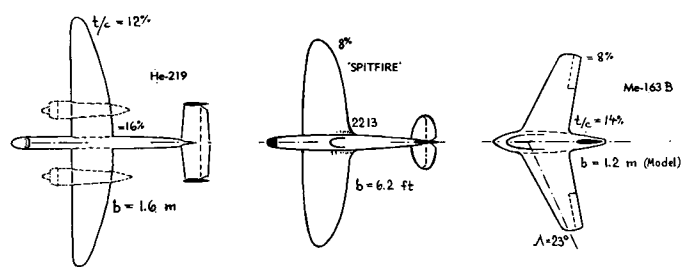
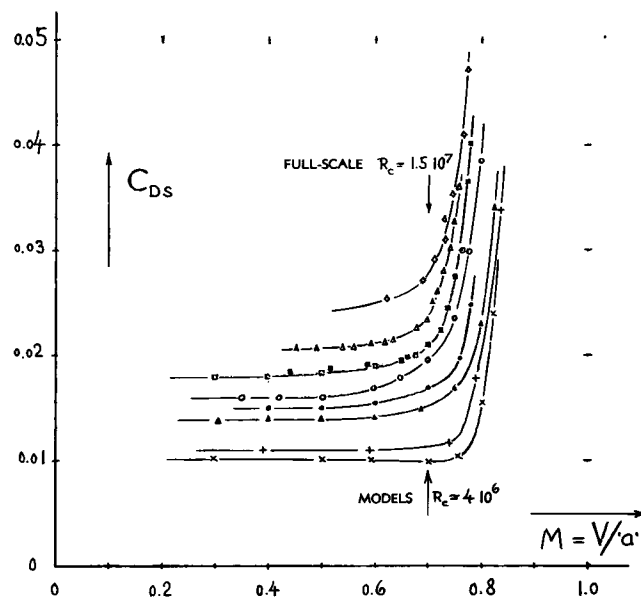
The corresponding loss of maximum speed (quoted on page 8-18 as being in the order of 1.5%) is then expected to be \approx doubled, on account of compressibility (for an original speed corresponding to $M = 0.76$). Figure 45 includes an example where induced interference is evident in the high-wing arrangement of a nacelle. The induced increment is always combined with a parasitic increment, however; and these two components are evaluated together in section (c).

Twisted Wings. It is explained in Chapter VII how the induced drag is increased by twisting the wing tips in relation to the center part. Although the Prandtl rule as quoted in section 1, is only valid for two-dimensional flow conditions, it may tentatively be applied (56) as an approximation to the three-dimensional case of a twisted wing. As indicated by equation 13 in Chapter VII, the additional drag of such a wing is proportional to the square of the angle of twist. We conclude, therefore, that

$$\Delta C_{Di} = ('P')^2 (\Delta \alpha)^2 / 10^5 \quad (50)$$

Considering as an example, a fast subsonic fighter airplane, with an original maximum speed of 500 knots ($M = 0.76$), the loss of speed due to twist is tentatively found to be increased from 10 knots (as found for 5° twist in incompressible flow on page 7-7) to some 20 knots. Figure 48 includes an example (the "Me-163") where an appreciable increment due to wing twist is evident.

-
- (52) Drag of *engine cowlings* at high speeds:
 - a) Robinson-Becker, Radial Engines, NACA T. Rpt 745.
 - b) Baals-Smith-Wright, Nose Inlets, NACA T.Rpt 920.
 - c) Nichols and Keither, Systematic Group of Cowlings with and without Spinners, NACA T.Rpt 950 (1949).
 - d) Continuation of (c) in NACA T.Notes 2685 and 3436.
 - e) Nichols, Transonic Inlet, NACA T.Note 2685.
 - (53) Critical and drag divergence Mach numbers are defined on page 15-15; the flow pattern past "peaked" pressure distributions is expounded on page 15-18.
 - (54) Drag of *dive-brake flaps*, attached to airplanes:
 - a) Fuselage Brake, NACA Doct RM L8B06.
 - b) See "Meteor" and "Vampire" in reference (59,b).
 - (56) We may also think of using a lesser power of "P".
 - (57) Hamilton, 4-Engine Model, NACA W.Rpt A-69.
 - (58) DVL high-speed wind-tunnel tests (mostly Lindemann):
 - a) Me-262 Model, DVL Doct J 900/4 (1942).
 - b) Knappe, He-177 Model, Heinkel Doct SK 148 (1942).
 - c) Me-163B Model, ZWB Doct UM 1085 (1943).
 - d) Ju-287 Model, ZWB Doct UM 1345 (1944).
 - e) Comparison of Various Types, ZWB UM 1306 (1944).
 - f) Lienarz, Comparison, ZWB Doct UM 7823 (1944).
 - (59) British RAE results on drag at high speeds:
 - a) RAE Staff, Tunnel Tests on "Spitfire", "Spiteful", "Attacker" and "Mustang" Fighters, ARC RM 2535(1951).
 - b) RAE, "Meteor" and "Vampire" Models, ARC RM 2504.
 - (60) Full-scale results on drag at high speeds:
 - a) Kaiser, Me-109 Dives, Messerschmitt 109/12/L/1943.
 - b) Me-262 Flight Test Rpts 262/01 and 02/L/1943.
 - c) NACA, P-51 Dive Tests, W.Rpts A-62 and L-78 (1945).
 - d) Highton-Plascott-Clarke, Flight Tests and Dives of "Meteor IV" Fighter, ARC RM 2748 (1949).



- | | | |
|--------------|-----------------------|--------|
| ◊ Me-109-G | FLIGHT TEST | (60,a) |
| ▲ NA P-51 | FLIGHT TEST | (60,c) |
| ■ 'SPITEFUL' | IN WIND TUNNEL | (59,a) |
| □ 'SPITFIRE' | IN WIND TUNNEL | (59,a) |
| ○ He-219 | WITHOUT NACELLES | (58,e) |
| • 'METEOR' | WITHOUT NACELLES | (59,b) |
| ▲ Me-262 | STRAIGHT WING | (58,g) |
| × | AT $C_L = 0$ | (58,c) |
| + | DITTO WITH 6° W'TWIST | (58,c) |

Figure 48. Drag coefficients as a function of Mach number of several complete *single-engine* (no-nacelle) type airplane models (58) and of two full-scale airplanes (60).

(b) PARASITIC DRAG OF AIRPLANES

Drag coefficients (essentially at $C_L = 0$) of a number of airplane configurations (complete models) and of a few full-scale airplanes (determined by glide or dive tests) are presented in figures 48 to 51.

Fighter-Type Airplanes (single-engined, no nacelles) have a comparatively constant drag coefficient, as against Mach number. Figure 49 also demonstrates agreement between full-scale results and model experiments. The steep increase of the drag coefficient at Mach numbers above the critical, as found in so many wind-tunnel model tests, is confirmed in particular, by such full scale experiments. It is suggested, however, that the airplane as tested has been a "clean" experimental specimen, not yet "cluttered" with all the attachments and equipments possibly to be added when putting the aircraft into realistic service. This conclusion is emphasized by full-scale results of the Me-109 included in figure 48. Looking at that illustration from a statistical point of view, it is also seen that the critical or drag-divergence Mach number decreases systematically as the basic drag coefficient is increased.

The "Meteor", represented in figure 50 is a British twin-jet-engine fighter airplane (developed around 1945, it seems). Agreement between full-scale and model-tested drag coefficients (whatever agreement is found in the graph) can be said to be accidental rather than genuine. It seems that the influence of Reynolds number ($2 \cdot 10^7$ full scale as against $5 \cdot 10^5$ in the model) combines with that of increased surface roughness in the full-scale tests, in such a manner that the total drag coefficient comes out roughly equal. There is also some "creeping" increase of the coefficient in the model results (beginning at $M \approx 0.65$) probably caused by low-R'number fuselage and nacelle interference with the wing. This effect is evidently reduced at the much higher numbers of the full-scale investigation; the drag coefficient of the real airplane increases at a lesser rate, accordingly.

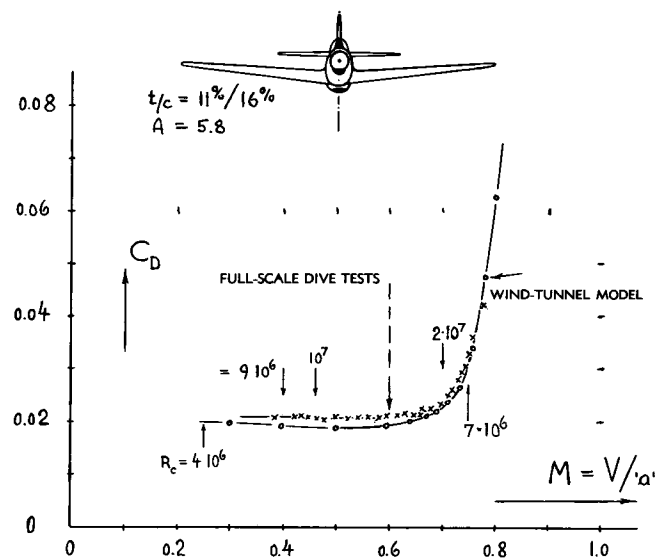
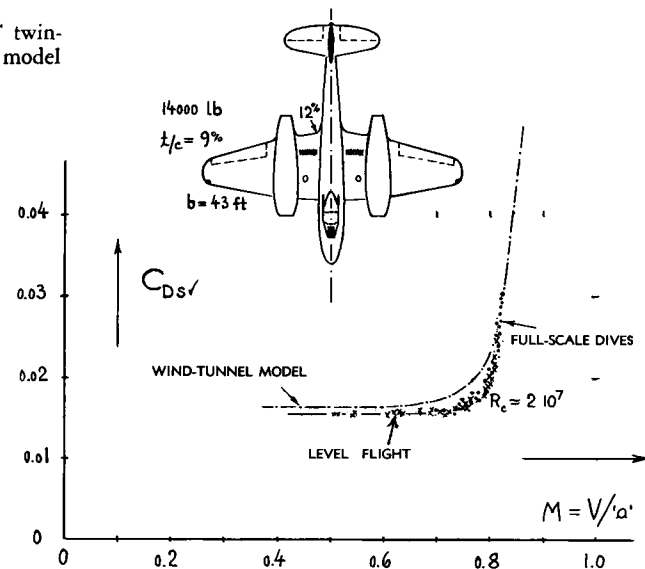


Figure 49. Drag characteristics (60,c) of North American P-51 fighter airplane (World War II period), (a) as tested on a wind tunnel model, and (b) as determined by full-scale dives.

Figure 50. Drag characteristics of British Gloster "Meteor" twin-engine fighter airplane, (a) as found on a wind-tunnel model (59,b), and (b) as tested full-scale (60,d).

Twin-Engine Configurations. The "Meteor" is already an airplane carrying two engine nacelles. Figure 51 presents results on two more twin-nacelle configurations. The He-177 (not designed to be flown at higher Mach numbers, but investigated nevertheless) shows a high-level drag coefficient and a low drag-divergence Mach number (corresponding to a root thickness ratio of $t/c = 17\%$ or $t/(2 \cdot x) = 28\%$). Because of strong interference effects in the nacelles (as explained in section "b") such configurations have basically higher drag coefficients, a higher growth of the drag coefficient as against Mach number and a lower critical M'number, than single-engine (no-nacelle) airplanes. British designers have apparently realized this fact and their more recent high-speed twin-engine airplane types have the machinery more or less built into wing and/or fuselage, accordingly—while in the United States pylon-suspended (easily maintainable and exchangeable) arrangements seem to be preferred in multi-engine airplanes.

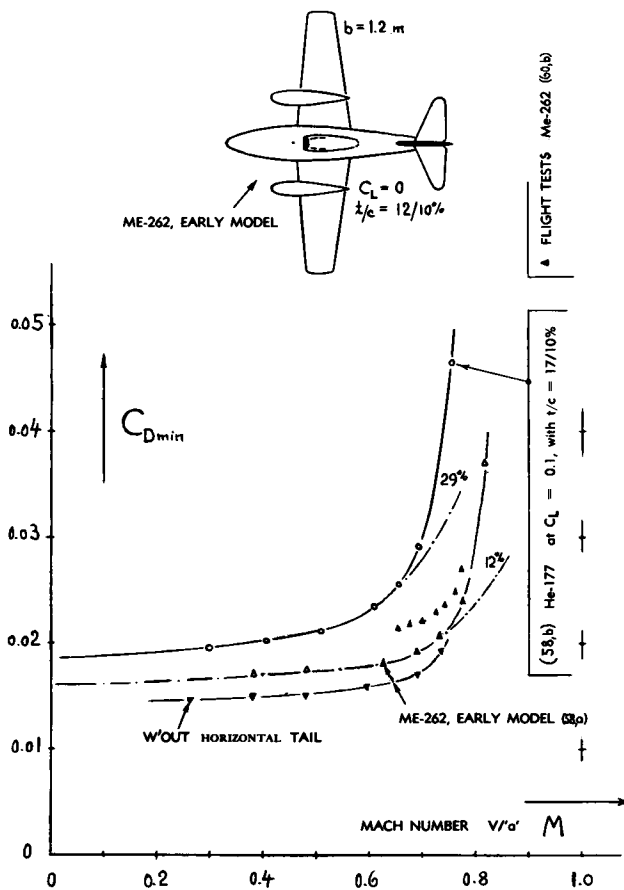


(c) STATISTICAL COMPRESSIBILITY METHOD

Characteristics of component parts of airplanes and those of complete configurations are presented in the preceding sections of this chapter. In order to arrive at a simple engineering type of drag prediction for higher subsonic Mach numbers, a statistical evaluation is presented as follows.

Interference. It is proposed (as in connection with figure 40) to divide the drag of average more or less "clean" airplanes and other configurations (such as missiles) into two basic components. One of these corresponds to an essentially constant subsonic type of coefficient. The other one is expected to increase as a function of Mach number, possibly in proportion to $(P)^3$. We will now designate the latter component as " C_{D3} ", with the subscript "3" reminding of the exponent of the Prandtl factor. When applying this method, experimental points are suitably plotted against a scale of $(P)^3$ (as done in the lower part of figure 40). Such plotting presents two more advantages. First, extrapolating the test points to $"P" = 1$, the incompressible value (C_{D0}) of the coefficient is easily obtained. Second, the critical or drag-divergence Mach number is found more accurately than when plotting against M . The Prandtl factor thus serves as a convenient function for interpolation and statistical evaluation (45) of available experimental data. It is clear, however, that the method does not work in cases where considerable variations take place as a function of M 'number because of boundary layer transition shifting back or forward (such as in figures 11 and 49, for example).

Figure 51. Drag coefficients of two tunnel-tested twin-engine-nacelle airplane configurations (58).



TYPE OF BODY OR CONFIGURATION

	C_{Dwet}	C_{D3}/C_{D0}	REFER.
smooth 12% airfoil section (with \approx turbulent BL)	0.0034	1%	fig 14
fuselage, coefficient including wing interference	0.0045	4.3	fig 43
fuselage (with canopy) including wing interference	0.0045	11%	fig 43
external store (on wing) including interference	0.0045	7%	fig 45
nacelle (added to wing) including interference	0.0050	23%	fig 42
airfoil mounted wall to wall in wind tunnel	0.0043	14%	fig 40
crossed pair of foils, mounted between tunnel walls	0.0045	11%	fig 40
fuselage coefficient including wing interference	0.0029	2%	(58,f) Me-328 tested at DVL
wing plus fuselage combination, wind-tunnel model	0.0038	6%	
complete twin-nacelle airplane model in tunnel	0.0052	22%	
horizontal tail (on fuselage) with interference	0.0053	22%	
Me-163, very smooth wind-tunnel model at $C_L = 0$	0.0032	0%	fig 48
same Me-163 wind tunnel model, but at $C_L = 0.1$	0.0038	3%	fig 48
"Meteor" (with twin nacelles) full-scale results	0.0040	3%	fig 50
"Meteor" (with 2 nacelles) smooth tunnel model	0.0042	6%	fig 50
Ju-287 smooth wind-tunnel model without nacelles	0.0035	5%	fig 53
Ju-287 complete wind-tunnel model, with nacelles	0.0048	11%	fig 53
"Spitfire" fighter complete wind-tunnel model	0.0043	6.9	fig 48
P-51 fighter, complete but smooth tunnel model	0.0048	11%	fig 49
Me-262 wind-tunnel model, without nacelles	0.0035	5%	R 58,a
Me-262 complete wind-tunnel model, with nacelles	0.0040	12%	fig 51
4-engine airplane, complete (smooth) tunnel model	0.0053	19%	fig 53
He-177 complete (but smooth) wind-tunnel model	0.0051	29%	fig 51

TABLE — presenting some statistical values indicating the percentage of the drag coefficient of airplanes and other body configurations — approximately increasing in proportion to the cube of the Prandtl factor.

Airplane Configurations. After splitting up the drag of an airplane (or any other configuration) into the two components described above, its coefficient as a function of Mach number corresponds to

$$C_{Dcom} = C_{D0} + ((P)^3 - 1) C_{D3} \quad (55)$$

Applications of this function are shown in figures 51 and 53. Model-tested values of the drag coefficient are very well interpolated when assuming that certain percentages (as noted in the graphs) of the basic coefficient (C_{D0}) may vary in proportion to $(P)^3$. The drag characteristics of the various configurations plotted on the preceding pages, and some other configurations such as wings plus nacelles, for example, have been evaluated in the manner as described above. The resultant drag coefficients (C_{D0} in the form of C_{Dwet} , and C_{D3} represented by the ratio C_{D3}/C_{D0}) are listed in the TABLE reproduced on this page. As far as complete airplanes are concerned, it is seen that the ratio (C_{D3}/C_{D0}) varies between 5% for very clean single-engine designs, some 8 to 13% for other airplanes (without nacelles) and up to 22 or 23% for multiple-engine configurations (having nacelles on their wings). If assuming percentages of $C_{D3}/C_{D0} = 10\%$ (and 20%, respectively) it can be calculated that commercial airplanes, for example, operating at comparatively low speeds (around 300 mph), have less than 5% (or 10%, respectively) drag

increase on account of compressibility. Military airplanes, on the other hand, flying at higher (but not yet critical Mach numbers) can be expected to show drag increases between 10% (or 20%, respectively) and 20% (or 40%, respectively). For example, the four-nacelle configuration in figure 51, represents such an increment of 37% (when flying at the critical Mach number).

Importance of Interference. Among the configurations listed in the TABLE, nacelles installed on wings show the highest percentages, up to 47% if referred to the incompressible drag of and due to such nacelles. As outlined in Chapter VIII at length, combination of a nacelle with a wing presents considerable interference drag. It is evidently this type of drag in particular, which causes the drag coefficient of airplanes to increase appreciably at speeds still below the critical Mach number. Interference drag thus takes on an increasingly important role when flying at higher speeds. To reduce interference in high speed airplanes, it therefore appears advisable to apply extended wing-root fillets, to avoid lift differentials and induced interference drag (see Chapter VIII) in wing-body configurations; and it may pay to increase the fineness ratio of nacelles and possibly to enlarge the wing area, thus reducing lift coefficient and subsequent pressure gradients along the suction side. Any increase of wetted area incurred in doing all this, may not be too objectionable insofar as skin friction does not lead into any *critical* conditions such as all types of the displacement-bound pressure drag do.

Based on Wetted Area, the drag coefficient of a body with pure skin-friction drag, may roughly be in the order of 0.003. Any amount exceeding this value, very roughly indicates the pressure-drag component. The "wetted" area drag coefficient of airplanes or other configurations may thus be a suitable parameter against which the percentages listed in the TABLE (on the preceding page) can be plotted.

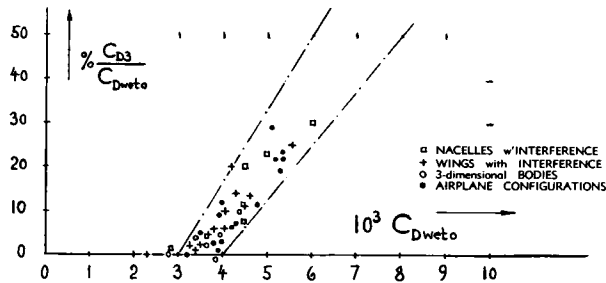


Figure 52. Statistical drag percentages of airplane and other configurations approximately growing in proportion to the cube of the Prandtl factor, plotted against their wetted-area drag coefficient.

Figure 52 proves that in this way, some systematic order is obtained among the various experimental results that originally seemed to have comparatively arbitrary rates of drag increase on account of subsonic compressibility. Approach and method presented are, of course, of a statistical nature. Utilization of the Prandtl factor is partly heuristic, rather than correct (45). It is felt, however, that simplicity is also an important quality in methods to be used in engineering applications. The fact that some of the results in figure 52 are close to the percentage line starting from $C_{Dweto} = 0.004$ can be explained by assuming that certain parts of the configurations tested have individual drag coefficients, *not* sensitive in regard to Mach number. The beginning of the C_{D3} component is shifted, accordingly, to somewhat higher C_{Dweto} values. It must concurrently be expected that the method does not directly apply to configurations involving bluff shapes such as dive brakes or as those in the second section of this chapter.

(d) SWEPT-WING CONFIGURATIONS

Fuselage Interference. Drag characteristics of one (very clean) swept-wing airplane configuration are included in figure 48. Considering the results (62,a) included in figure 30, it is found that a smooth fuselage body does not make any or much of a difference when added to a swept wing. Similar results are available in (62,e) where tests on swept wings are reported without and with a fuselage added. Inasmuch as the supersonicities are usually highest in the center of a swept wing, the fuselage may thus be considered serving as a fairing (or as a local increase of sweep angle) covering the most sensitive part of the wing. Speaking in terms of the transonic area rule (see Chapter XVI) it may also be speculated that wing-fuselage interference is reduced when sweeping the wing, because of a more favorable distribution of displacement along the axis of the aircraft configuration. In conclusion, swept-wings may not exhibit any or much of a reduction of their critical Mach number when adding a slender fuselage.

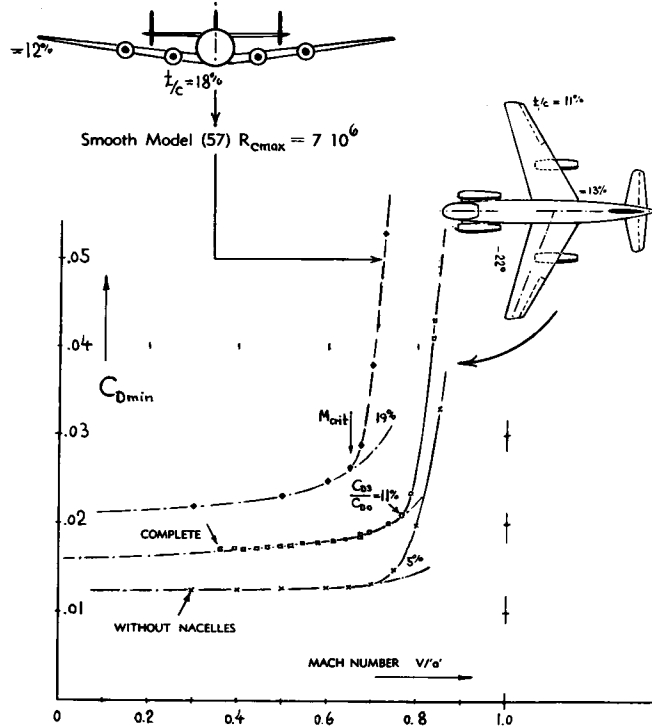


Figure 53. Drag coefficient of the model of the *swept-forward* Ju-287 airplane type (58,d), with and without engine nacelles, and of a smooth 4-engine airplane model (57).

- (62) Drag of *swept-wing* configurations:
 a) Ludwieg and Others, *Swept-Wing Configurations*, AVA Göttingen Rpts 1940/8/7, 1940/8/13, 1940/8/14.
 b) Junkers-287, as in reference (58,d).
 c) Whitcomb, Combinations, NACA T.Rpt 1273.
 d) Boddy-Morrill, Interference, NACA RM A7J02.
 e) A favorable fuselage effect is indicated by experiments in NACA RM L50L07, K28 and K27; and L52K04.
 f) King-Pasteur, Tapered Wings, NACA T. Note 3867 (1956); see also RM L52K04 on other combinations.
 g) Küchemann, *Contouring Theory*, ARC RM 2908(1956).

Fuselage Contouring. Certain attempts have been made (62,g) of improving the characteristics of swept wings by "contouring" the fuselage walls in such a way as to accommodate the cosine type of transonic flow over the wing panels, and to permit this type of flow also to develop along the wing roots. Practical results confirm expectations insofar as the increase of the drag coefficient above the critical Mach number is somewhat reduced.

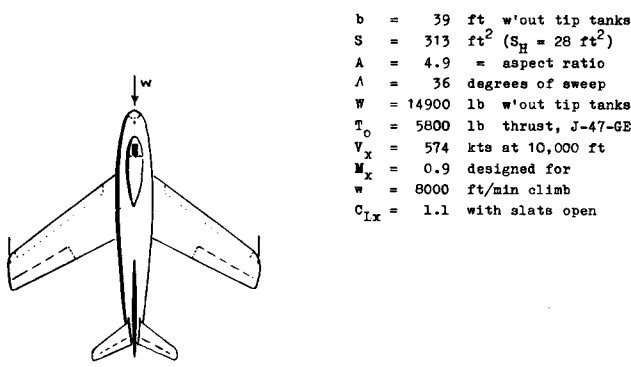


Figure 54. North-American "P-86 *Sabre Jet*" fighter airplane (65,b) as an example of swept-wing application.

"P-86" Fighter. The gain in maximum subcritical speed to be obtained by applying a reasonable angle of sweep, is not really spectacular, if taking into account increased structural expenditures as well as certain complications in the handling qualities of such airplanes. However, to show that the mechanics of swept wings are not just laboratory results, the example of a successful airplane incorporating a sweep angle of 35°, is presented in figure 54. For a wing section thickness ratio of 12%, and a location at 40% of the chord, the effective ratio is found to be 0.12/0.8 = 15%. The corresponding critical Mach number of a straight wing (as found on the basis of figure 19) is $M_{\text{crit}} = 0.77$. Indeed, we have a full-scale maximum level-speed result of the straight-wing "P-80" (65,a) slightly exceeding this Mach Number. For an angle of sweep of 35° (as in the "F-86") the critical M'number is raised to ≈ 0.84 (as per figure 29), thus representing a gain of 9%. The record speed flown by the "P-86" in 1952 in level flight close to seal level corresponding to a Mach number in the order of 0.87 was obtained with a special wing, however (65,b). Of course, the critical M'number is not a "wall" or "barrier" rigidly limiting the maximum speed of an airplane. The steep increase of the drag coefficient above the critical speed, for example in the order of 100% for an increment of $\Delta M = 0.05$, naturally places the level speed limit closely above the drag-divergence M'number. Statistically, therefore, knowledge of wing thickness ratio and angle of sweep, permits to make an estimate on the maximum speed potential of a subsonic type of airplane.

10. DRAG ABOVE DRAG DIVERGENCE

Above the "critical" Mach number, we are in the *transonic* regime, specifically treated in the next chapter. Inasmuch as subsonic-type airplanes are occasionally also driven beyond that M'number, their drag characteristics under such conditions are considered in this chapter, however. "Critical" conditions in any aircraft configuration are first reached in the wing. Drag divergence and drag increase, primarily of *airfoil* sections and of three-dimensional wings are evaluated accordingly.

The Critical Mach Number can be considered to be part of the transonic similarity system as explained in Chapters XVI and XVII. Some correlation of critical and/or drag-divergence Mach numbers of foil sections has been obtained accordingly (71,d). Prerequisites of such similarity are not really fulfilled, however, in foil sections above drag divergence; i.e. stagnation, viscosity, flow separation and compression shocks (not included in the theoretical analysis) are most certainly involved. Critical and/or drag-divergence M'numbers are treated (on a different basis) in sections 5, 6 and 7 of this chapter.

Nature of Drag at Supercritical Mach Numbers. Several graphs presented in this chapter demonstrate that after exceeding the drag divergence Mach number, the drag coefficient of airfoil sections increases rapidly, eventually reaching values (at $M \approx 1$) which may be 10 times as high as those below the critical M'number. Based upon *frontal area*, a 10% thick foil section (see figure 11 in Chapter XVII) may thus exhibit a maximum transonic coefficient in the order of $C_D = 1$. Drag at this level is pressure-bound, of course. Corresponding distributions along the surface of a symmetrical foil section (at $C_L = 0$) are shown in figure 55, together with wake-survey results. Phases are as follows:

- At and below the critical M'number, the pressure distribution is essentially of the same type as in non-compressive fluid flow. The drag coefficient of the section in figure 55,a is 0.009; and the wake simply represents the momentum loss of the boundary layer.
- At $M = 0.80$ (in that particular foil section) we see that a supersonic expansion takes place along the section's forebody, attaining a maximum speed at $x = 0.64 c$, corresponding to a local M'number of ≈ 1.2 . The supersonic flow then breaks down aft of this station by way of a shock (because the downstream pressure gradient is no longer sufficient to maintain

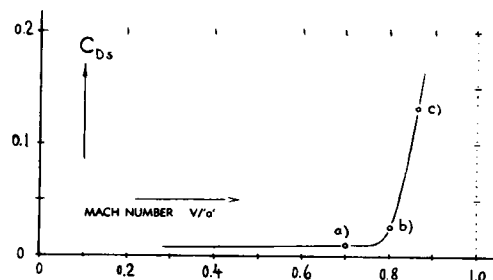
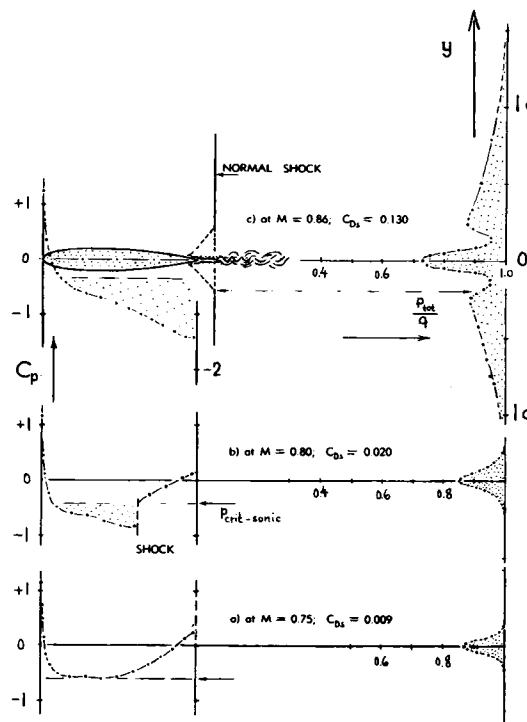


Figure 55. Pressure distribution, flow pattern and wake characteristics of a 15% thick foil section (70,a) at three higher subsonic Mach numbers.



(63) See also in Chapter XVI on "cranked" wings.

(65) Full scale speed-records of fighter airplanes:

- a) Lockheed "P-80 Shooting Star" obtained a world speed record of 623 mph \approx 540 kts, flown on a hot summer day near sea level in 1947. The Mach number corresponding to 38 °C is 0.79. A special wing was built for the record attempt with a maximum thickness ratio of 11% at \approx 45% of the chord, while the standard version of this type has 65-213 sections (see J.Aeron.Sci. 1948 p.28 and 31). Wind-tunnel results on these wings are included in figure 29, 30.
- b) Dimensions of the North American "F-86A" are given in NACA T.Rpt 1250 (1955). The wing has 2° twist. Foil section is 0012-64 at the root and 0011-64 at the tips (both modified). Leading edge slats are needed to prevent wing-tip stalling. The "F-86E Sabre Jet" set a world speed record in 1952 "in California", of 698.5 mph \approx 610 kts.
- c) Other results: Gloster "Meteor" as in figure 50 with $t/c = 12\%$, attained $M = 0.82$; "Me-163" as in figure 48 with $t/c = 13\%$ and $\Lambda = 23^\circ$ reached $M = 0.83$.

(70) Flow pattern and characteristics of foil sections:

- a) Goethert, Pressure and Forces of 0015 (40) Section at High Speeds, Yearb.D.Lufo 1941 p.I, 101 and 148; see also in ZWB Tech. Berichte 1944 p.235.
- b) Daley, Characteristics to $M = 1$, NACA T.Note 3607.
- c) Rogers, Foil Section at High Speeds, ARC RM 2863.
- d) Daley, 6-Series in Open Tunnel, NACA TN 3607.

(71) Analysis of drag rise above critical Mach number:

- a) Nitzberg, Drag Past Critical, NACA T.Note 1813.
- b) ARC, Analysis of Shock Drag, RM 2401 and 2512.
- c) Oswatitsch, Analysis of Drag Increase, ARC RM 2716.
- d) Similarity in regard to M_{DD} has been considered in ARC RM 2715, in NACA RM A51A12 and in (a).
- e) Anderson (25,c), Aspect Ratio, J.Sci.1956 p.874.

(73) Interaction between boundary layer and shocks:

- a) Liepmann, Interaction Between BL and Shock Waves, J.Aeron.Sci.1946 p.623, and in NACA Tech Rpt 1100.
- c) Turner, 6% Foil at $M \approx 1$, Australia ARL Rpt. A.99.
- d) Love, Shock-Induced Separation, NACA T.Note 3601.
- e) Lindsey, BL and Pressure Rise, NACA T.Note 3820.
- f) Pressure Required for Separation, J.A.Sci.1953 p.858.
- g) Lange, Shock-Induced Separation, NACA TN 3065.
- h) Wood, LE Flow Separation, NACA T.Note 3804.

the expansion). This shock does not cause separation (in this particular case), and the flow continues to the trailing edge. The wake pattern shows a somewhat enlarged drag area, however, the larger part of which is believed to be due to increased BL thickness, while a smaller part may directly correspond to the momentum losses across the shock.

(c) At $M = 0.86$ (the highest number tested in that investigation) the shock has reached the trailing edge. The strong negative pressure gradient corresponding to an expansion to a maximum local M'number of ≈ 1.6 , is likely to prevent flow separation. Behind the shock (at a distance aft of the trailing edge equal to 3 times the chord, where the survey was made) we now recognize two different components of drag. The viscous boundary-layer type is concentrated near the wake's center line; while the momentum deficiency in the two "wings" of the wake represents the losses in the upper and lower branch, respectively, of the compression shock, reaching up and down some 2 foil chords each. Wake traverses similar to that at $M = 0.86$ in figure 55, are also reported in (73,c).

BL Separation. As the Mach number is increased within phase (b) as described above, the shock moves toward the trailing edge where it ultimately forms the tail wave as in supersonic flow. While moving, the shock also increases its intensity. Interaction between the shock and the boundary layer is a function of Reynolds number (with laminar or turbulent BL status, respectively) and foil-section shape (thickness

ratio) as well as angle of attack (lift coefficient). The resultant flow pattern has been studied in elementary form (73). Velocities within the boundary layer are (at least partly) subsonic, of course. The compression (pressure jump) taking place across the shock, is easily transmitted, therefore, through the "lower" sheets of the boundary layer, not only downstream but also *upstream*. Boundary layer material may then be backed up into the space ahead of the shock, thus giving rise to an extended oblique forward "leg" of the shock wave. Schlieren pictures presented in (73,c) and in (70,b) prove that the double-dip wake distribution as shown in figure 55,c, corresponds to the combination of an oblique shock wave (originating along boundary layer and/or viscous wake) with a final *normal shock* (located in the vicinity of the trailing edge). Such a shock pattern has been sketched in the illustration, accordingly. The two lateral peaks in the wake distribution thus indicate locations somewhat outside the junctures of the weak oblique with the strong normal shock waves. An extreme example for BL separation is also shown in figure 4, where at $M \approx 0.7$, and at a number $R_c = 8 \cdot 10^5$ (at which in that case, the BL is still laminar) the flow is "completely" separated from the afterbody. However, in slender shapes (and as long as the boundary layer is thin) separation may *not* take place (as for example, in figure 55,b where compression continues aft of the shock to even positive values of the coefficient). The pressure differential required to produce separation has also recently been investigated (73). Inasmuch as separation is a function of the pressure gradient (supersonic expansion ahead of the shock) and the shock intensity a function of BL and wake thickness, the mechanism as a whole cannot properly be predicted, however, by theoretical analysis.

Growth of Drag Coefficient. The pressure loss in a stream tube going through a shock, is a known quantity. Analysis (71) of the corresponding drag of a foil section is involved, however, let alone any consideration of boundary-layer interaction and flow separation as mentioned above. For practical purposes, we therefore revert to a statistical approach. Evaluating the drag functions in figures 13 and 17, it is thus assumed that the rise of the drag coefficient of the foil sections tested may correspond to

$$\Delta C_D \sim (\Delta M / (1 - M_{DD}))^3 \quad (36)$$

where $\Delta M = M - M_{DD}$ and $M_{DD} = M'$ number where drag divergence takes place. Figure 56 presents results from various sources and on different families of airfoil sections, plotted against the M' number parameter as in the equation. Best correlation among the various foil sections in figure 13 is then obtained when referring the drag coefficient to the area ($b \sqrt{t c}$) which thus represents some mean between "wing" and frontal area. However, coefficients in this form would

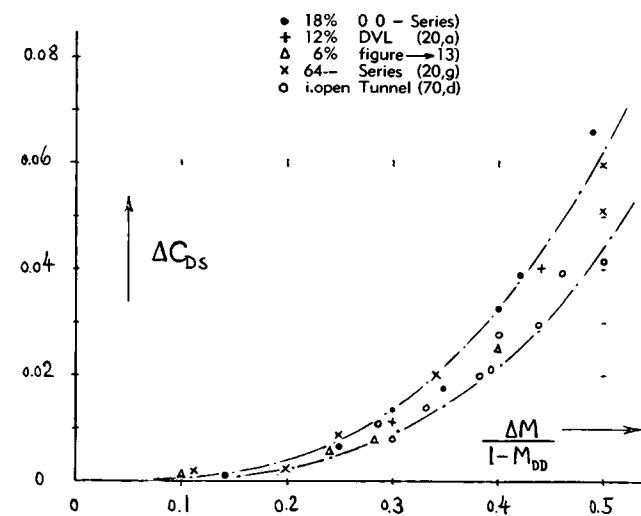


Figure 56. Increment of section-drag coefficient above M_{DD} , evaluated from results such as in figures 13 and 17.

not be very convenient to be used in practical applications. Rather, we have therefore plotted coefficients in the usual definition. The incremental drag of foil sections is then indicated by

$$\Delta C_{Ds} = K (\Delta M / \Delta M_D)^3 \quad (58)$$

where $\Delta M_D = (1 - M_{DD})$ and where K is a function of thickness ratio, section shape and lift coefficient (considered within the limits of ± 0.1). We can tentatively say that

$$\begin{aligned} K &= 0.35 \text{ for 6-series foils in open tunnel} \\ &= 0.40 \text{ for foil sections with } t/c \approx 6\% \\ &= 0.50 \text{ for thicker and for 6-series foils} \end{aligned}$$

Testing conditions (4,b) are thus equally important as the secondary parameters. The seemingly simple result is very much a function also of the value of M_{DD} assumed in the evaluation of the experimental results (in figure 56) or selected in any application of the method.

Aspect Ratio. Figure 56 represents the drag rise of airfoil sections (tested under two-dimensional flow conditions). Three-dimensional fluid flow as in finite-aspect-ratio wings, offers significant *relaxation*, however, for pressures and forces in the transonic regime of fluid flow. The drag rise above M_{DD} reduces accordingly. This effect is analytically treated in (71,e). For practical purposes, and for aspect ratios not lower than those usually applied in subsonic-type airplanes and for M' numbers not too far above divergence, results of that analysis can be simplified very much. The drag coefficient of a finite wing is then equal to that of the foil section (as in equation 58) shifted to a higher Mach number by the differential

$$\bar{\Delta M}/M = (\bar{\Delta w}/V)(1 + 0.2 M^2) \quad (59)$$

where $M \approx M'$ number at which the finite-span wing is flying. The average (integrated) velocity relaxation corresponds to

$$\bar{\Delta w}/V \approx 0.2 (t/2x) \lambda / (1 - M^2) \quad (60)$$

where x as defined in figure 19, and $\lambda = 1/A = "c"/b$. Figure 57 shows this function, evaluated for $t/2x = 10\%$, for an assumed average value of $M = 0.85$ and for a drag differential (equal to drag rise above divergence Mach number) of $\Delta C_{DS} = 0.01$. Experimental points confirm the theoretical function for aspect ratios above 5. At ' λ ' values above 0.2, higher-order terms (available in reference 71,e) have to be added. The analysis also predicts that ΔM should increase in proportion to $t/2x$. However, experimental results obtained in 0012 airfoils, are not higher in the graph than wings with 8 and 9% thick sections (possibly because of tunnel effects).

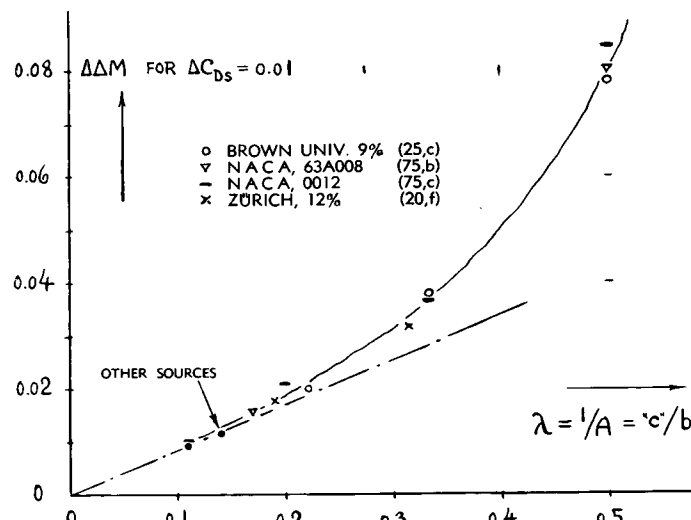


Figure 57. Increment of M' number at which $\Delta C_{DS} = 0.01$ is obtained in finite wings, as a function of their ' λ ' ratio.

Practical Result. Experimental results (such as in figures 30 & 31 and in footnote 75) and analysis (71,e) yield equally, not only a reduction of the drag rise as such, but also a reduction of its rate as indicated by the exponent in equation 58. Analysis of experimental data tentatively leads to the function

$$\Delta C_{DS} = (K/10^3) (10 \Delta M / \Delta M_D)^n \quad (62)$$

where K as in equation 58, $\Delta M_D = (1 - M_{DD})$ and the exponent possibly

$$n = 3/(1 + \lambda) \quad (63)$$

It is only after repeated application of these statistical functions that more definite constants could be obtained.

Complete Airplanes. The most sensitive component part of an airplane (in regard to compressibility) is its wing. We have so far covered in our analysis only wings, accordingly. Comparison of the results on complete airplanes (in figures 48 through 50) with those on wings (such as presented in figures 30 and 31, and in Chapter XVII) reveals, however, that their drag increase is noticeably higher. Also, the growth of the drag coefficient is found to be still higher in multi-engine (nacelle-type) configurations (see figure 53). Tentatively the *maximum* slope of the coefficient above drag divergence, for average aspect ratios, is:

$$\begin{aligned} dC_D/dM &= 0.40 \text{ for airplane wings alone} \\ &= 0.70 \text{ for smooth configurations} \\ &= 0.90 \text{ for multi-engine airplanes} \end{aligned}$$

(75) Transonic experimental results on wings:

- a) For subsonic results see footnotes (20) and (26).
- b) Nelson, Straight Wings, NACA T.Note 3501 & 3502.
- c) NACA, Straight Wings, Tech Rpts 877 and 922.
- d) "Bump" tests such as in (b) show generally a creeping increase of the drag coefficient below and at divergence (because of wall interference). Closed-tunnel results such as (a) and (c) show, on the other hand, some tunnel blockage, particularly in larger aspect ratios. Correct values may be between the results obtained by those two methods.
- e) For results on swept wings see footnote (32), figures 30 and 31, and footnote 60 in Chapter XVI.

Angle of Sweep. Sweeping the panels of a wing means postponing the "upper" critical Mach number from $M = 1$ to $M = 1/\cos \Lambda$. In the terminology as in figure 56, the parameter $\Delta M_D = 1 - M_{DD}$ can then be replaced by $\Delta M_{D,\Lambda} = (1/\cos \Lambda) - M_{DD}$ so as to make that graph possibly applicable to swept wings.

Another, not so complicated method of obtaining the drag rise of swept wings, is presented in figure 58. It is suggested that the variation of the drag rise (at Mach numbers not too much above divergence) approximately corresponds to

$$\Delta C_D = (\sin^3 \Lambda) \Delta C_{D_0} \quad (65)$$

Where ΔC_{D_0} = drag increment of a *straight* wing having the *same aspect ratio* as the swept wing. A physical explanation of the reduction is obtained when considering a swept wing to be the sum of a straight piece (representing the center part and increasing in drag as indicated by equation 62) and of the two panels (whose drag coefficient is taken not to be affected by the increase of M beyond M_{DD}). The size of that center part then determines the function as in figure 58. That graph also reflects the variation of the maximum transonic drag coefficient as shown in figure 43 of Chapter XVI.

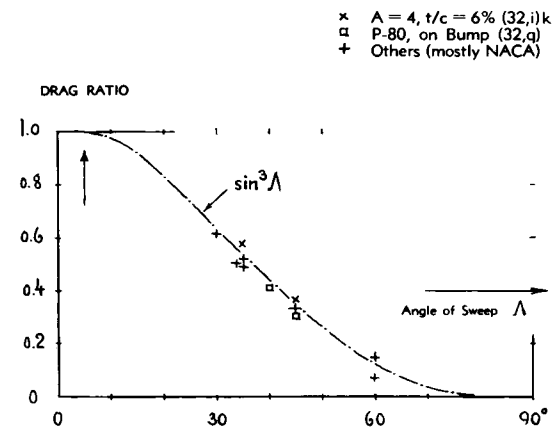


Figure 58. Reduction of the drag rise of finite-span wings above drag-divergence Mach number, as a function of their angle of sweep.

CHAPTER XVI — DRAG AT TRANSONIC SPEEDS

An extended range of speeds in the vicinity of $M = 1$, is generally called "transonic". Fluid-dynamic characteristics are found in this phase different from those in the subsonic as well as in the truly supersonic regimes of flow. Inasmuch as any increase of maximum aircraft speeds leads first into this range, consideration of drag at Mach numbers in the vicinity of unity, is of great practical importance, of course (1). Specifically, flow patterns shall be understood to be transonic in character, whenever supersonic speeds are combined with localized phases of subsonic flow. The transonic regime can thus be considered to begin at the critical Mach number, which is treated as such in Chapter XV. At supersonic speeds, on the other hand, subsonic-type flow characteristics are found, for example, on delta wings (at least at their leading edges) up to Mach numbers in the order of 2. Indeed, a subsonic component of flow never disappears in blunt and in many bluff body shapes where the compression wave, originating from the forward face, is always detached. Separating subjects into such that are to be treated in this chapter and others which properly belong into the next chapter, dealing with supersonic characteristics, is often impossible, accordingly. Among the characteristics presented in this chapter, are bluff bodies, cones and swept wings, in particular. Treatment of straight wings is concentrated, however, in Chapter XVII.

1. ELEMENTS OF TRANSONIC FLUID FLOW

Cross-Section Area. Considering a stream tube in non-compressive flow, its cross-sectional area varies as a function of speed in such a manner that the volume flow (in ft^3/sec) is always constant; law of continuity. Considering next an obstacle affecting the velocity within the stream tube, the cross-section area increases accordingly when approaching a stagnation point; and it reduces when passing the sides of a solid body. We can also say that the average velocity of the fluid flow around the solid, must increase because of its displacement (thickness). Thermodynamic consideration of a stream tube in compressive fluid flow leads eventually to entirely different results, however. Upon increasing speed, and decreasing static pressure accordingly, the density (in lb/ft^3) of the gas considered reduces, and the specific volume (in ft^3/lb) increases significantly. Figure 1 shows the corresponding development of the stream tube's cross-sectional area S_a . This area reaches a minimum at sonic speed where the static pressure (in air) is $p_1 = 0.528 \cdot p_o$, with subscript "o" indicating the "reservoir" pressure (5). At the speed corresponding to local $M = 1$, the variation of density is such that $dS_a/dV = 0$. This result means that upon increasing the speed, say from $M = 0.99$ to 1.00 , or from $M = 1.00$ to 1.01 , the cross section area S_a of a stream tube remains, for all practical purposes, *constant*. The area ratio of the tube (as plotted in figure 1) is $S_a/S_{\min} = (\rho \cdot "a")/(\rho V)$; and the continuity law is now $S_a \rho V = \text{constant}$. At speeds above $M = 1$, the relation between velocity and required cross-section area of the stream tube considered is thus qualitatively reversed; and (to say it in different words) the area increases as the speed is further increased. For $k = 1.4$ (as in air under almost all practical conditions) the area ratio is

$$S_a/S_{\min} = ((1 + 0.2 M^2)/1.2)^{3/2}/M \quad (1)$$

-
- (1) Theoretical advances in the transonic field, experimental information and their dissemination in form of articles, papers and reports have been so numerous within the last years, that a special chapter has been provided for the treatment of this subject. As the flux of new information continues, further expansion and revision of this chapter is bound to be desirable after some time.
- (2) Gas-dynamic and/or thermodynamic functions and principles can be found in (a) many text books and/or in the sources listed in footnote (1) of Chapter XV; (b) see Bailey in J.Aeron.Sci. 1944 p.227; (c) most suitable for engineers is Liepmann-Roshko's "Elements of Gasdynamics" (Wiley 1957).

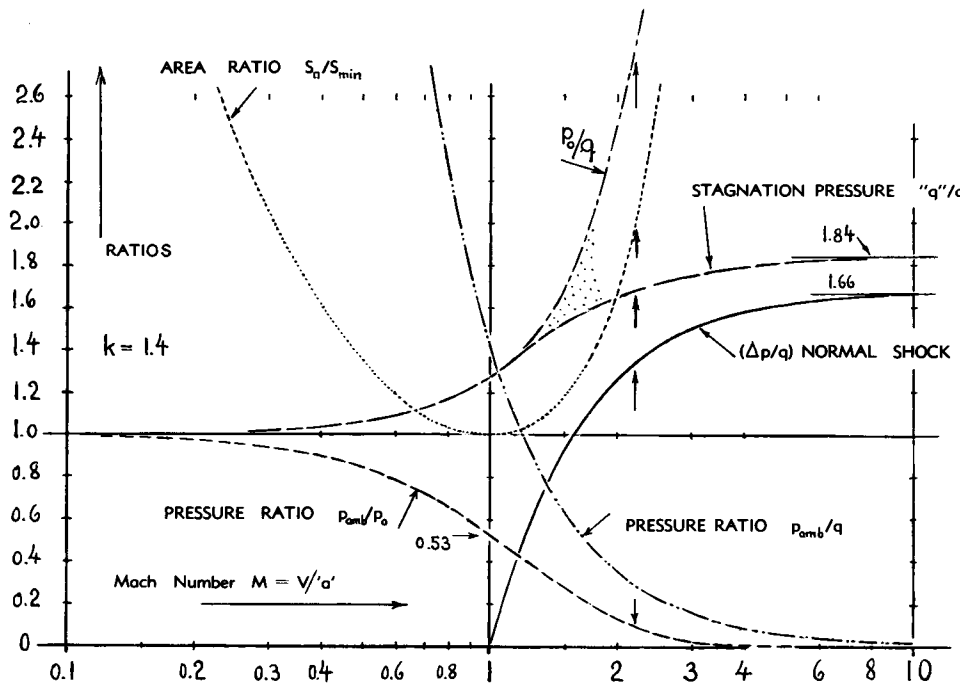


Figure 1. Basic one-dimensional thermodynamic pressure functions and the area ratio of a stream tube, as a function of Mach number (based on ambient velocity of sound).

Laval Nozzle. A famous engineering application of the thermodynamic functions plotted in figure 1, is deLaval's expanding nozzle originally used in steam turbines operating at supersonic speeds. Fluid flow (of steam, gas or air) in such a nozzle reaches sonic speed within the narrowest section. The velocity then continues increasing into the expanding part of the nozzle, while pressure and density continue decreasing and the *specific volume* keeps on increasing so as to fill the expanding cross-sectional area of the nozzle by progressive expansion. One important feature of such nozzle flow is the fact that the so-called critical speed in the "bottleneck" corresponds to $M = 1$ (based on thermodynamic conditions within that section). As far as wind tunnels are concerned, those designed for supersonic speeds, all have the Laval-nozzle-type of expansion. For the very high Mach number of 10 (for example) the geometrical expansion ratio is in the order of 536, as indicated by equation 1.

Free Air Testing. The drag of projectiles has been and still is measured by recording their path-time history during free flight in ballistic ranges (7,e,f); and this technique has recently been developed to very high velocities (4,e). Because of the difficulties explained in the next paragraph, related methods have also been developed for testing bombs, missiles and similar configurations in the atmosphere after dropping them (4,g) from airplanes or after propelling them somehow into higher altitudes (4,c). Special test "vehicles" have been developed for this purpose, particularly by the NACA, involving multiple-channel telemetering devices. All of these methods make use of the free air space, where available cross-section areas are extremely large and where reflections of pressure waves are \approx zero accordingly.

Transonic Wind Tunnel. In a subsonic tunnel the average velocity across the test section "simply" increases so as to permit the total volume flow of air to pass the model placed in that section. Considering, however, conditions of a compressive fluid flow in a closed-type tunnel, any increase of velocity at $M \approx 1$ does not help, insofar as the stream tubes cannot any longer contract (because of $S_0/q = \text{constant}$ or $V_0 = \text{constant}$) when increasing their speed. Ordinary closed-type tunnels, therefore, start "choking" at speeds corresponding to $M = 0.9$ (let us say, or at even lower speeds depending upon the geometrical and aerodynamic blockage ratio). Efforts in the development of wind tunnels (particularly in the United States after World War II) have solved this problem now (4,b) by giving the test section slotted walls through which a certain expansion is permitted, without reflection of the pressure field produced by the model placed in that section.

"Critical" Pressure. The static pressure in the throat of a Laval nozzle (producing supersonic speeds) is always equal to $0.53 P_0$ (as marked in figure 1) and it is called the critical pressure. In the free stream of a compressive fluid, this pressure corresponds to sonic velocity obtained at the point where that pressure is found. In form of a coefficient, the critical or "sonic" pressure differential (in air with $k = 1.4$) is indicated by

$$C_{pcrit} = (0.75 (1 + 0.2 M^2)^{3.5} - 1.43)/M^2$$

This coefficient is zero at $M = 1$; it is negative at subsonic, and positive at supersonic speeds.

Normal Shock. Considering again the one-dimensional stream-tube flow as in figure 1, we will assume that the velocity is supersonic, say at $M_1 = 2.2$. If now leading that tube into a field of increasing static pressure, deceleration and recompression take place, usually in a sudden and discontinuous manner, i.e. in form of a shock. For constant cross-sectional area (as in a duct) the velocity then returns to a subsonic value. The pressure differential corresponds to

$$\Delta p/q = (4/M^2) (M^2 - 1)/(k + 1) \quad (2)$$

where q = dynamic pressure of the undisturbed supersonic stream. In the example considered, the increment is $\Delta p/q = 1.32$ (as indicated in the graph by an arrow). Referred to the undisturbed ambient pressure, the increment is $\Delta p/p_{amb} = (\Delta p/q)/(p_{amb}/q) = 1.32/0.295 = 4.5$, and the total static pressure behind the shock is $p_2/p_{amb} = 1 + 4.5 = 5.5$. The pressure jump is also accompanied by a temperature increase. "Total pressure" or *enthalpy* (= thermodynamic potential) does not reach the same value as was prevailing at the same speed (V_2) when first accelerating the stream tube, as in the nozzle of a wind tunnel. As explained in Chapter XVII, the entropy increases accordingly in the "irreversible" process of a shock. To say it in different words, as a consequence of viscosity within, and heat-transfer across a shock wave, a momentum deficiency is left behind, thus representing the equivalent of the "wave drag" experienced by the obstacle.

Stagnation Pressure. At transonic and supersonic speeds, stagnation \equiv deceleration of air particles in front of every blunt obstacle, occurs in two steps;

first in form of a sudden increase of pressure across a detached shock wave (in the form as explained above) and second, in form of a steady adiabatic increase (at velocities which are then subsonic) when approaching the stagnation point of the obstacle. The total increase, that is, the stagnation pressure increment denoted by "q" (with quotation marks to make it distinct) is higher than the dynamic pressure $q = 0.5 \rho V^2$; thus for $k = 1.4$ as in air:

$$\begin{aligned} "q"/q &= 1.84 - (0.76/M^2) + (0.166/M^4) \\ &\quad + (0.035/M^6) + \dots \end{aligned} \quad (4)$$

Figure 1 shows that this pressure ratio increases steadily, up to the limiting value of 1.84 at $M \rightarrow \infty$. In the example considered above, the pressure finally reaches " q " $/q = 1.69$. Again referred to p_{amb} , the total increment is $1.69/0.295 = 5.7$, and the total pressure corresponds to $p_* / p_{amb} = 5.7 + 1.0 = 6.7$. The isentropic stagnation pressure (5) corresponds, on the other hand, to $p_*/p_{amb} = 1/0.094 = 10.7$ (as marked in the graph.) The difference between the two ratios represents the pressure loss across the shock, resulting in $\Delta p/q = (10.7 - 6.7)(p_{amb}/q) = 4.0/0.29 = 1.16$.

Static and Dynamic Pressures. Substituting in the equation of the dynamic pressure, $q = 0.5 \rho V^2$, the velocity V by M ('a'), and the velocity of sound

$$'a' = \sqrt{p/\rho} \quad (6)$$

the relation between dynamic pressure and ambient static pressure " p_{amb} " is found to be

$$q = 0.5 k p_{amb} M^2 = 0.7 p_{amb} M^2 \quad (7)$$

where $k = 1.4$ for air in tropospheric and stratospheric applications. This equation (also plotted in figure 1 in the form of p_{amb}/q) is found to be useful in converting aerodynamic coefficients that are sometimes given in the form of

$$(force or pressure)/(p_{amb} S) \quad (8)$$

into the more conventional and "standard" coefficients, based upon dynamic pressure, rather than upon the absolute static pressure.

The Minimum Pressure which can possibly be reached in a gaseous fluid is that of vacuum, and is thus equal to zero. The corresponding pressure difference $\Delta p_{min} = |p_{amb}|$ based upon the dynamic pressure is

$$p_{amb}/q = 2/(k M^2) = 1.43/M^2 \quad (10)$$

As illustrated in figure 1, this pressure ratio decreases considerably as the Mach number is increased, ultimately approaching zero, as $M \rightarrow \infty$.

-
- (3) Thermodynamic effects including their influence upon skin friction are treated in Chapter XVII.
 - (4) Transonic testing techniques:
 - a) Weaver, Bump Technique, J.A.Sci.1948 p.28.
 - b) Wright-Ward, Transonic Tunnel, NACA T.Rpt 1231.
 - c) Thompson, Flight Research at Transonic and Supersonic Speeds, Proc. Internat. Aeronautical Conf. 1949, p.582.
 - d) Delsasso, Free Flight Ballistics, J.A.Sci.1948 p.605; see also references (42,c and m).
 - e) Charters, Gas Gun for Firing Models up to $M = 20$, see in Shell Aviation News December 1956 p.12.
 - f) Free-flight Testing, see references (51) to (53).
 - g) Kell-RAE, Falling Test Vehicle, ARC RM 2902.

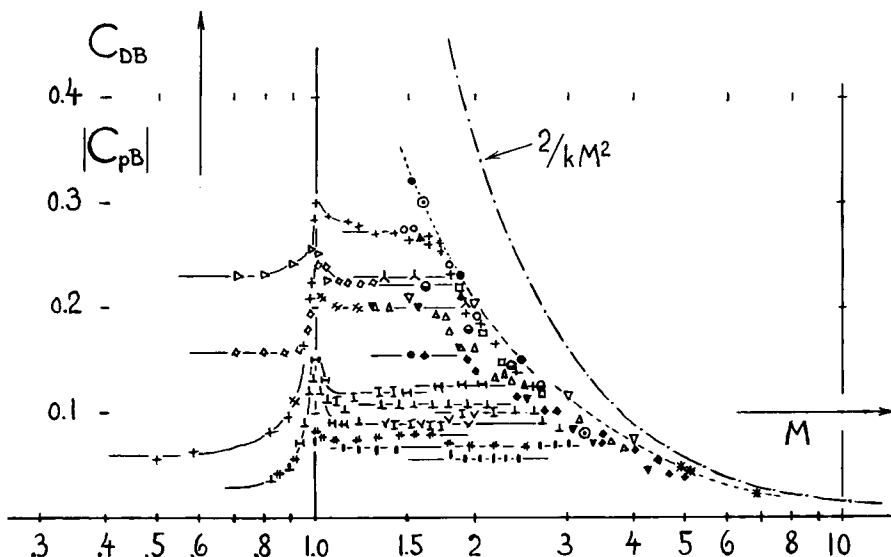
2. BASE DRAG AT TRANSONIC SPEEDS

Base drag at transonic speeds has received extensive consideration within the last 10 years, evidently on behalf of guided missiles where (after "brennschluss") the outlet opening of the rocket motor produces an appreciable value of suction drag. No basic or complete solution of the problem has been established, however; and none of the semi-theoretical correlations found (13) (16) seems to be better than statistical evaluation of the available experimental material. Some such evaluation, presented as follows, is also guided by the principles laid down in Chapter III on the same subject under non-compressive conditions.

Function of M. Figure 2 presents a compilation of the available data on drag originating past the base of three-dimensional bodies, such as projectiles and missile shapes. Three phases are evident; (a) a rise of the coefficient upon approaching $M = 1$ (with a peak at $M \approx 1.0$), (b) a "transonic" range in which the coefficient is comparatively constant (9,a) and (c) a "supersonic" regime in which the coefficient decreases steadily as the Mach number is further increased.

"Subsonic" Phase. Some comparatively modest increase of the base drag coefficient in the subsonic phase, is apparent in several of the experimental results of figures 2 and 11. The increment can be explained on the basis of a local increase of speed along the sides of the body and past the base, which in turn can be expected to develop corresponding to subsonic compressibility rules (see Chapter XV under the subheading of "wedges"). Such an increase may first take place in proportion to a certain power of the Prandtl factor. Approaching $M = 1$, the maximum local velocity may then be appreciably above the sonic speed; and the interaction (mixing) with the dead space must be intensified to such a degree that the drag coefficient is raised to the peak values as shown in figure 2 (and even more so in figure 11). — Two of the bodies represented in figure 2, show very low base-drag coefficients at subsonic speeds. Analysis on the basis of figure 37 in Chapter III, indicates that values in the low order of $C_{DB} = 0.05$ correspond to the high forebody drag coefficient $C_{fB} \approx 0.3$. It is thus suggested that in the two cases considered, some flow separation from the rim of the conical head may have existed, thus producing $C_{fB} \approx 0.3$ as postulated above. It must then be assumed that between $M = .8$ and 1.0 the flow around the shoulder of the cone improves progressively by means of a Prandtl-Meyer type of supersonic expansion (see Chapters XV and XVII on this subject), so that the base drag coefficient increases accordingly.

Figure 2. Base drag coefficients (on base area S_B) of various simple projectile and missile body shapes as a function of Mach number.



- (a) PLAIN "CYLINDRICAL" PROJECTILE BODIES:
 - + J. H. UNIVERSITY FLIGHT WITH FINS (7,g) (7,o)
 - λ I/d = 12 IN WIND TUNNEL AT 5 10^7 (7,m)
 - △ ABERDEEN BALLISTIC RANGE ($\approx 2 \cdot 10^6$) (7,e)
 - AACHEN WIND TUNNEL, PRESSURE DISTR. (7,d)
 - ▲ KOCHEL CONE-CYLINDER BODIES ($\approx 10^6$) (7,c)
 - ◆ NACA VARIOUS REPORTS (13,a,b,g) (7,k)
 - ▼ NOL 60° CONE-CYLINDER (FIGURE 8) (7,h)
 - OAL WIND TUNNEL ($\approx 2 \cdot 10^7$) REPORTED IN (7,g)
 - ▷ VIRGINIA, SMOOTH PROJECTILE SHAPE (7,g)
 - * "CYLINDRICAL" MISSILE WITH FINS (8,g)
 - ◊ "STRAIGHT" MISSILE BODY $R_f = 3 \cdot 10^7$ (7,n)
 - * AT HIGH MACH NUMBERS REPORTED IN (7,g)
- (b) VARIOUS SIMPLE BODY SHAPES:
 - KOCHEL, BEHIND SPHERE AT $R_d \approx 10^6$ (7,c)
 - NOL, BEHIND DISK REPORTED IN (7,p)
 - ▽ NPL STRAIGHT 2×10^6 CONE ($> 10^6$) (7,l)
- (c) BOAT-TAILED MISSILES WITH FINS:
 - FLIGHT TEST ON SLENDER SHAPE (8,h)
 - H RM-10 MISSILE IN FLIGHT AT $R_f \approx 10^8$ (8,e)
 - + DITTO 1/2 SCALE FLIGHT ($3 \cdot 10^7$) (8,e)
 - ⊕ RM-10 MISSILE AT $R_f = 8 \cdot 10^7$ (8,f)
 - | DITTO 1/2 SCALE AT $R_f = 3 \cdot 10^7$ (8,f)
 - □ I/d = 28 WIND-TUNNEL TEST (8,o)

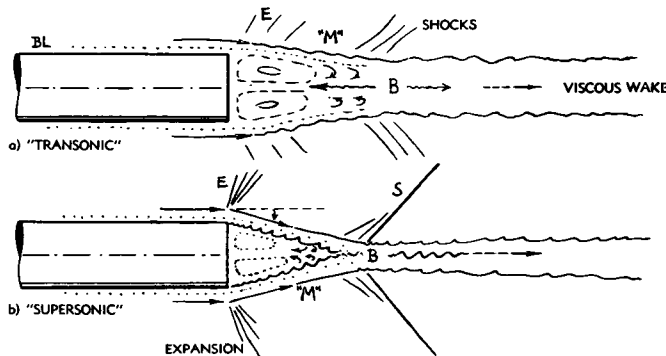


Figure 3. Basic Flow pattern past the base of a three-dimensional projectile or missile body.

- (5) The subscript "amb" generally describes conditions in the undisturbed ambient fluid space (at or near the location of the flying object). In the system usually considered by engineers (aircraft moving through given air space at \approx constant altitude) the speed of sound is constant. The Mach number as used in this book is generally based on ambient air temperature, accordingly; and not on any local, "sonic" or other speed of sound. The subscript "o" indicates the isentropic stagnation or absolute "reservoir" pressure, while " $q = p_* - p_{amb}$ " refers to the actual stagnation pressure p_* (obtained by way of a normal shock plus subsequent adiabatic compression).
- (6) General information on transonic and supersonic flow:
 - a) NACA, Shape of Shock Waves (Cones) T.Note 2000.
 - b) NACA, Tables of Various Mach Number Functions, Tech.Rpt 1135 and Tech.Note 3981 (1957).
- (7) Base pressure and/or drag on 3-dimensional bodies:
 - b) Stamm, Pressure Distribution Behind Flying Bodies, ZWB Rpt UM 8103; see NACA Tech.Memo 1101.
 - c) Erdmann, Drag of Cones and Spheres, Pressure Distribution at Supersonic Speeds; ZWB Lilienthal Rpt 139/1 p.28; also in RAE T.Note Aero 1742.
 - d) Bach (Aachen), Pressure, ZWB Doct UM 6057 (1945).
 - e) Charters, Ballistic Contributions, J.A. Sc.1947, p.155.
 - f) Charters and Turetsky, Base Pressure Free Flight, Aberdeen Proving Ground, BRL Rpt 653 (1948).
 - g) Hill (John Hopkins), Base Pressure at Supersonic Speeds, J.Aeron.Sc.1949 p.153 and 1950 p.185.
 - h) Kurzweg, BL and Base Pressure, J.Aeron.Sc.1951 p.743. Additional information on the cone-cylinder bodies in this source, stems from unpublished NAVORD reports.
 - k) Reller-Hamaker, $M = 2.73$ to 4.98 , NACA T.N. 3393.
 - l) Gadd, See (25,g), ARC Current Paper No. 271 (1956).
 - m) Petersen, "Cylindrical" Body, BRL Aberdeen BB Rpt 44.
 - n) Hart, Transonic Flight Finless Body, NACA RM L52E06.
 - o) Faro, "Cylindrical" Missiles, J.H.Univ. BB Rpt 106.
 - p) Behind Disks, NAVORD 1950; see in J.A.Sc.1951 p.141.
 - q) Walberg IAS Martin Fund Student Paper 1956 p.128.
- (8) Drag and pressure on parabolic bodies:
 - a) NACA Documents RM E50D10 and 28.
 - c) Hasel and Others, NACA Document RM L52A14.
 - d) Welsh-Moraes, Flight Tests, NACA RM L51E18.
 - e) Evans, RM-10 Missile Flight and Tunnel, NACA T.Rpt 1160 (1954); see also other reports in (51).
 - g) "Straight" Missile, NACA Document RM L50I28a.
 - h) Flight Tests Boat-Tailed Missile, NACA RM L51J29.

Flow Pattern. Figure 3 shows the flow pattern past the base of a cylindrical body as it has been sketched and presented in many publications. In comparison to the conditions explained in Chapter III, the pattern is, of course, modified by the supersonic expansion and compression phenomena as indicated in the illustration. Studies have been made (16) to determine the influence of "mixing" taking place along the boundary (or sheer layer at "M") between external flow and dead space. Other investigators (13) try to give an analytical interpretation of the expansion observed at "E". In all these efforts, location of and flow conditions at the "bottleneck" (at "B") is found to be the critical item. Some qualitative explanations are presented in the following paragraphs.

"Transonic" Phase. Between $M = 1$ and an upper limit of M between 1.5 and 2.5 (or even higher, depending upon wake diameter), figure 2 displays several roughly constant levels of the base drag coefficient (9,a). Considering the corresponding flow pattern (in figure 3,a) we realize that the "bottleneck" is "open" in this phase (9,e) in such a manner that we have a re-entry (backflow) of fluid material (9,c) from the wake aft of the conical compression shock into the dead space (adjoining the base surface). The compression shock ("S") terminating the supersonic flow arriving at and proceeding beyond the base, may not have much of an influence upon the flow pattern in the wake, under these conditions. As a consequence, this pattern may then primarily be a function of subsonic-type "viscous" mixing rather than the specific consequence of supersonic effects. As explained in Chapter III, the boundary layer developing along the length of the forebody may thus be the most important and tentatively a universal parameter against which the various levels of the drag coefficient in the transonic regime can be correlated. Since that thickness is not directly known, the wetted surface ratio S_{wet}/S_B , or in case of cylindrical afterbodies simply the total length ratio " l/d ", may then be utilized in a statistical evaluation such as presented in figure 4.

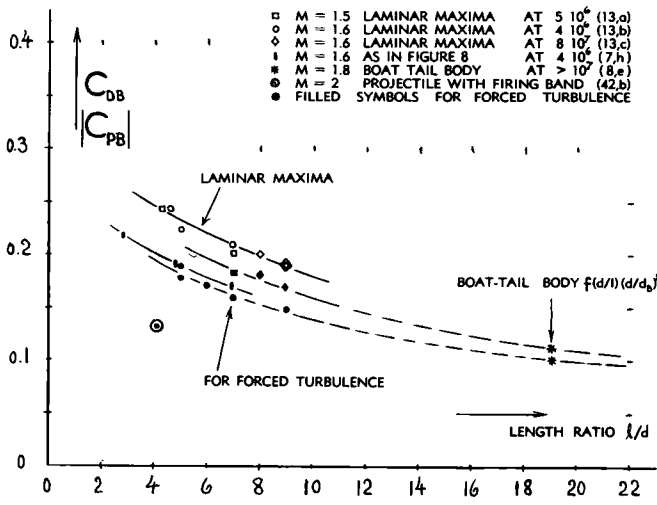


Figure 4. "Transonic" base drag coefficient of smooth projectile (and missile) bodies plotted versus their length ratio.

The value of base-drag or base-pressure coefficient reduces systematically as the length ratio is increased. There is some difference, however, between base drag developing from laminar and turbulent boundary layer flow, respectively. The turbulent boundary layer exhibits a considerably higher loss of momentum than a laminar layer. Suction and base drag for turbulent condition are less, accordingly, than for laminar flow (on the basis of equal wetted-area ratio).

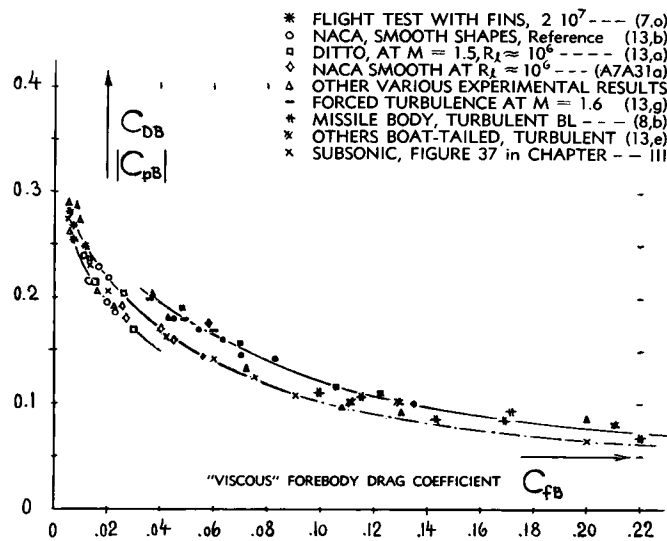


Figure 5. Correlation between "transonic" base-pressure drag coefficient and the "viscous" forebody drag coefficient.

"Viscous" Forebody Drag. Another way of presenting base-drag coefficients, is by plotting them against the same forebody drag parameter (9,b) as in Chapter III. The resulting graph (figure 5) shows an empirical function very similar to that in figure 37 of that chapter. Indeed, a set of points taken from that illustration is included in figure 5; and it comes close to the two or three branches as found for "transonic" speeds. Mixing and suction (now considered on the basis of the same forebody drag coefficient C_{fb}) are somewhat stronger in fully turbulent flow than in a mixing flow which begins in laminar fashion (and then turns turbulent). Other discrepancies found in the graph, can be explained by the uncertainty in selecting proper values for the skin-friction drag coefficient (9,d). The result seems to prove, nevertheless, that within a certain transonic regime, base drag is an essentially "viscous" phenomenon.

Terminating M'number. The "transonic" type of flow pattern (described in the preceding paragraph) is obviously facilitated by a heavy "viscous" wake (laminar or turbulent, but heavy) produced by a long forebody, a rough forebody surface and/or by a forebody whose diameter (determining wetted surface) is larger than that of the base surface (in parabolic or

boat-tailed shapes). Under all conditions, there is a limiting Mach number, however, above which that flow pattern discontinues. As the M'number is increased, a Prandtl-Meyer type of expansion (explained in the introductory section of Chapter XVII) takes evidently place around the rim of the base (9,f). It is suggested that such expansion can only develop to any significant degree when and if the "bottleneck" is "sealed," so that backflow is prevented and an effective ejector-type scavenging or pumping effect is obtained along the mixing surface (as in figure 3,b). The experimental results in figure 2 show that the terminating M'number corresponds to the transonic level of the base drag coefficient. That number can thus be comparatively high, under conditions where the base-drag coefficient is low.

"Supersonic" Phase. The presence of the dead space as shown in figure 3,b converts the afterbody into a somehow conical shape. The base drag then corresponds to the conical shock wave ("S") originating from the vicinity of the "bottleneck"; and it is apparent that the base drag is then essentially wave drag. As shown in figure 2, the coefficient decreases accordingly, as a function of Mach number, in a manner similar to that of wedge-like afterbodies as presented in Chapter XVII. As pointed out in (13,g) turning angle (corresponding to the boundary of the conical dead space in figure 3,b), expansion pressure and base pressure, are all a function of location of and flow pattern through the bottleneck ("B" in figure 3,b). None of these parameters can be predicted, however, without first knowing one or two of the others. An upper limit is imposed to the base drag, however, by the minimum possible static pressure, corresponding to vacuum. For $p = 0$, equation 10 then yields the maximum possible base-drag coefficient. The experimental points in figure 2 suggest a certain percentage

- LAMINAR MAXIMA ···· $l/d = 2$
- TURBULENT MINIMA FIGURE 8
- + VARIOUS POINTS FROM FIGURE 2
- ✗ MINIMUM VALUES FROM FIGURE 2

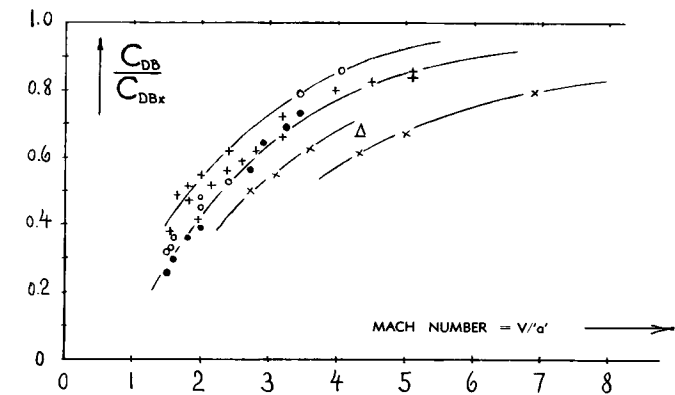
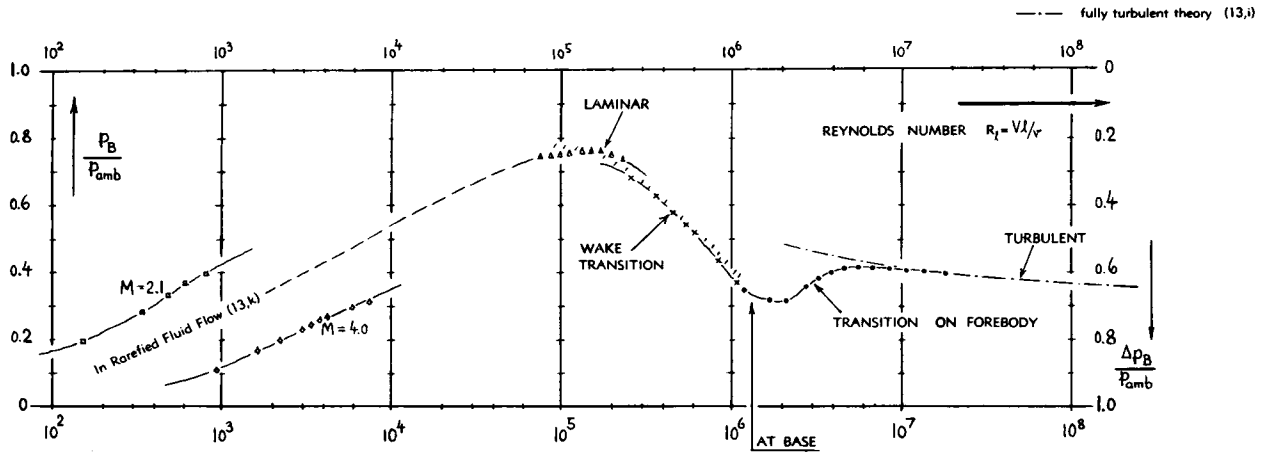


Figure 6. "Supersonic" base-pressure ratio of 3-dimensional "cylindrical" bodies as a function of M'number.

Figure 7. Various phases of wake mixing and base pressure behind a cone-cylinder combination, as a function of R' number.

✓ NPL on projectile models at $M = 2.5$, quoted in Howarth's "Mod. Dev. Fluid Dynamics", 1953 p.701.

△ KAVANAU (13,4) $M = 2.84$ | 60°Cone plus cylinder
x N.P.L. (13,1) $M = 3.0$ | Cylinder
● PRINCETON (13,d) $M = 2.95$ | $l/d \approx 3.4$



of the theoretical maximum; so that the coefficient in this phase is tentatively:

$$C_{DB} = K (1.43/M^2) \quad (14)$$

(9) Notes on transonic flow past the base of bodies:

- a) This "transonic" constancy of the base-drag coefficients of cylindrical bodies is not a generally accepted fact. Analyses as in (13) and (16) rather tend to produce a continuation of the "supersonic" function into the transonic phase (as found indeed in two-dimensional conditions as in figure 11). Constant base-drag coefficients are clearly presented, however, for parabolic bodies such as in (51) for example.
- b) The forebody of a streamline or pointed body at transonic Mach numbers, also produces an appreciable amount of *wave drag*. This type of drag generally appears in form of momentum losses extending sideways into the space of supersonic fluid flow. Wave drag, therefore, does not appear in the boundary layer and/or in the viscous wake developing along the obstacle; and it usually does not noticeably affect velocities, flow pattern and pressures at and past the base of "cylindrical" base-ended bodies. It is, therefore, proper to use in the definition of " C_{DB} " only the "viscous" skin drag components (frictional as well as due to surface roughness and/or flow separation, if any). Such consideration of momentum losses in the BL (rather than body geometry and Reynolds Number) permits to include the effects of surface roughness and attachments placed on the surface of the forebody.
- c) This type of *back flow* is specifically mentioned by Wick in "Effect of Boundary Layer on Flow Through Abrupt Area Change" (J.Aeron.Sci. 1953 p.675).
- d) For fully laminar flow pattern, the skin-friction coefficient was assumed to be equal to that as presented in Chapter II. For "turbulent" boundary-layer flow, a mixed composition was estimated on the basis of M' number, R' number and body shape.
- e) It appears that the diameter of such open throats and that of the downstream wake (in the transonic phase) roughly corresponds to the constant ratio $d_B/d_B = 2 C_{DB}$.
- f) A limited expansion around the rim, followed by a weak shock, has experimentally been determined (13,g) thus producing absolute rim pressures noticeably below the pressure in the center part of the base.

The ratio (17,a) $K = C_{DB}/C_{DBx}$ is not constant, however, within the series of test points plotted in figure 6. Rather, the ratio increases as a function of Mach number; and it seems that K approaches unity as $M \rightarrow \infty$.

Reynolds Number. Since "viscous" mixing is an important part of the flow pattern (see figure 3), boundary layer and Reynolds number of the forebody can have considerable influence upon base drag. Mixing as a function of R' number has, therefore, been studied (16,c); and five or more distinct phases have been found to exist:

(a) At *very low* R' numbers (in the order of 10^3) flow conditions are completely laminar, of course. Large *viscous forces* obviously produce base-drag coefficients of appreciable magnitude (13,k). This phase (in the left-hand part of figure 7) is only of practical importance, however, under rarefied conditions of fluid flow.

(b) At *low* R' numbers (in the order of 10^5 on body length) the boundary-layer flow and the shear flow past dead space and wake are still laminar. Suction as a consequence of laminar mixing is weak, the value of the *absolute* pressure is high accordingly; the pressure differential $\Delta p_B = (p_{amb} - p_B)$ representing base drag, is low.

(c) As the Reynolds number is increased (very roughly from 10^5 or 10^6 to 10^6 or 10^7) transition from laminar to turbulent type of mixing takes place *along the wake*. As the transition point moves toward the base, the intensity of mixing thus increases considerably. As a consequence, the *absolute* base pressure reduces appreciably; and the base-drag coefficient increases accordingly. Correlation is obtained (13,b) in the higher R'number part of this phase when plotting base-drag or base-pressure coefficients (at constant Mach numbers) against the parameter $(l/d/\sqrt{R_f})$. This parameter represents the thickness of the BL arriving at the rim of the base, corresponding to length "l" and to the laminar skin-friction drag coefficient of $C_f \sim 1/\sqrt{R_f}$ (as presented in Chapter II).

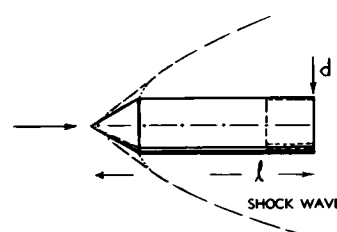
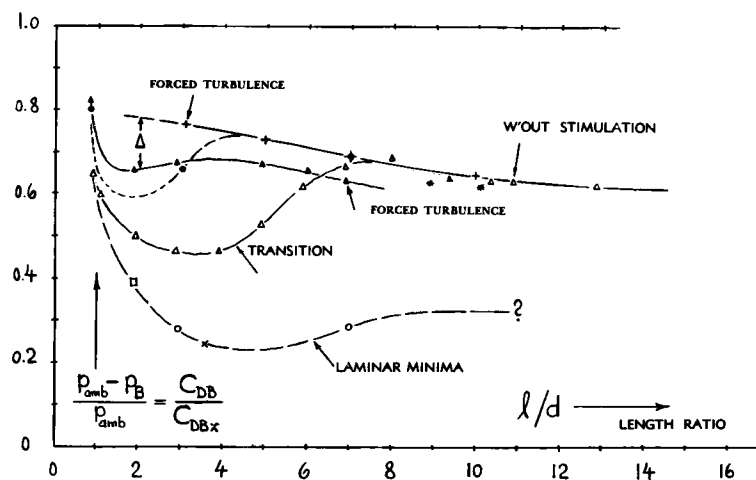
(d) The base pressure p_B then reaches a minimum (and the base drag a maximum) at the, and for a certain interval above the R'number at which the transition point reaches the body's base (as marked in the graph). Mixing is most efficient in this condition; while the essentially laminar "viscous" forebody drag is near minimum.

(e) As the Reynolds number is further increased, the skin-friction drag coefficient C_f evidently grows along one of the transition lines as shown in figure 5 of Chapter II. Boundary layer thickness and momentum losses of the fluid flow arriving at the rim of the base, are increased accordingly. The scavenging or pumping effect of the shear flow past the dead space behind the base is then reduced; the base pressure increases again and the base drag reduces to some degree.

(f) Transition from laminar to turbulent type of flow along the surface of the forebody may finally be "complete"; or turbulent flow may be forced by *stimulation* elements placed near the nose of the forebody. Correlation is then obtained (13,b) by plotting base-drag coefficients against the parameter $(l/d/\sqrt{R_f})$ where the fifth root represents the simplest approximation to turbulent skin friction (see Chapter II).— In full-scale applications, phases "a" and "b" may not be of much importance (14), if disregarding rarefied conditions (see Chapter XVIII). It appears, however, that laminar BL flow and/or laminarization by means of supersonic expansion along the smooth surface of missiles (no firing bands as in artillery shell) is very well possible to numbers in the order of $R_f = 10^7$.

Forebody Shape. An important difference between supersonic and subsonic flow is found around "corners". While at subsonic speeds, separation is likely to occur and boundary-layer transition is \approx *certain* to take place, neither one of these two events must necessarily be expected under supersonic conditions. So for example, flow pattern and skin friction past the comparatively bluff cone-cylinder configuration as in figures 7 and 8, are entirely laminar to Reynolds numbers between $(1$ and $2) \times 10^6$ (based on body length) at Mach numbers between 2 and 4. The forebody shape does have an influence, however, upon flow pattern and parasitic drag developing along the surface. Figure 8 demonstrates, for example, that a more slender, and ogival shape (+) has a higher base-drag coefficient (because of lesser viscous forebody drag) than the bluffer cone shape (Δ) tested under the same (forced-turbulence) conditions. Transition (in the wake as well as subsequently along the surface of the forebody) is also a function of shape. The sharp corner in the contour of the 60° cone-cylinder combination (in figures 7 and 8) induces transition at lower Reynolds numbers, while smooth ogival shapes such as in (7,h) and (13,h) preserve laminar flow to considerably higher R'numbers.

Figure 8. Base pressure and base drag of a cylinder-cone combination, at $M = 3.24$ as a function of length ratio.



2 x 30° CONE PLUS CYLINDER AT $M = 3.24$:

Δ	NOL (7,h) NATURAL TRANSITION AT	$R_d = 3 \cdot 10^5$
Δ	NOL (7,h) FORCED TURBULENCE AT	$R_d = 3 \cdot 10^5$
*	NOL (7,h) FREE FLIGHT TESTS AT	$R_d = 3 \cdot 10^6$
•	NPL (7,l) MAXIMUM VALUES AT	$R_l = 2 \cdot 10^6$
○	NPL (7,l) MINIMUM VALUES AT	$R_l = 2 \cdot 10^5$
□	KAVANAU (13,f) AT $M = 2.84$ and	$R_l = 2 \cdot 10^5$
×	KOCHEL (7,c) AT $M = 3.10$ and	$R_l = 2 \cdot 10^5$
+	NACA (13,h) OGIVAL SHAPE AT 3.24 and	$\approx 5 \cdot 10^6$

□ NATURAL	TRANSITION	$R_f = 6 \cdot 10^6$	(7,k)
◊ NATURAL	TRANSITION	$R_f = 3 \cdot 10^6$	(7,h)
▀ LAMINAR	MAXIMA	$R_f = 3 \cdot 10^6$	(13,e)
×	WITH FINS	$R_f = 1 \cdot 10^7$	(7,o)
○ LAMINAR	VALUES	$R_f = 2 \cdot 10^6$	(13,b)
△ LAMINAR	MAXIMA	$R_f = 6 \cdot 10^6$	(13,c)
▽ TURBULENT	NATURAL	$R_f = 1 \cdot 10^6$	(13,g)
+ LAMINAR	MAXIMA	$R_f = 4 \cdot 10^6$	(13,b)
* FORCED	TURBULENCE	$R_f = 4 \cdot 10^6$	(13,b)
■ FILLED SYMBOLS FOR FORCED TURBULENCE			

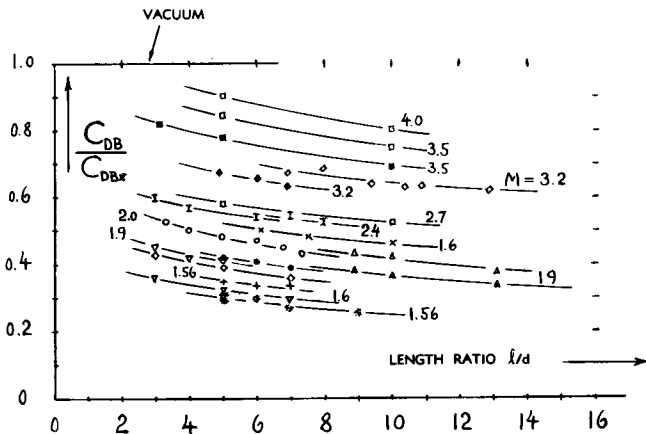


Figure 9. "Supersonic" base drag ratio (at certain constant Mach numbers) as a function of length ratio l/d , representing the ratio of wetted forebody area over base area.

- (13) Influence of viscosity on base pressure:
 - a) Chapman-Perkins, At $M = 1.5$, NACA Tech Rpt 1036.
 - b) Chapman, Correlation, NACA T.Rpt 1051 (T.N. 2137).
 - c) Bromm-Goodwin, R'Number, NACA T.N. 3708(1956).
 - d) Bogdonoff (Princeton), J.Aeron.Sci. 1952 p.201.
 - e) Grigsby-Ogburn, Cone-Cylinder, NACA RM L53H21.
 - f) Kavanau, at $M = 2.84$, J.Aeron.Sci. 1954 p.257.
 - g) Love, Analysis for Turbulent BL, NACA T.N. 3819.
 - h) VanHise, R'Number Wake Transition, NACA T.N. 3942.
 - i) Cope (NPL), ARC Current Paper No. 118 (1946/53).
 - k) Kavanau, At Very Low R'Numbers, J.A.Sci. 1956 p.193.
- (14) A bullet (1 inch in length and thus considered to be the smallest practical application) flying at $M = 2$ or at ≈ 2200 ft/sec, has an R'number, on length, above 10^6 . A shell (say 1 foot in length) moving at the same speed at 30,000 feet altitude has a number $R_f \approx 5 \cdot 10^6$.
- (16) Analysis of free-boundary mixing process:
 - a) Chapman, Laminar Mixing, NACA T.Rpt 958.
 - b) Gooderman and Others, Turbulent, NACA T.Rpt 963.
 - c) Crocco-Lees, Mixing Theory, J. Aer.Sci. 1952 p.649.
- (17) Notes on "supersonic" type of base drag:
 - a) When plotting experimental results, the base drag coefficients as in figure 2 (and in other graphs) are suitably replaced by the ratio $C_{DB}/C_{DB,L} = \Delta p_B/p_{amb}$, where "x" refers to the limiting coefficient as indicated by equation 10, and where $\Delta p_B = p_{amb} - p_B$.
 - b) It seems, the possibility of 'separation' from the rim of the cone has not really been considered in other sources. Reynolds number, turbulent versus laminar boundary layer flow and mixing theories are discussed instead. Proof for the correctness of the separation hypothesis is found in low minimum base drag coefficients, the values of which do not correlate with results on configurations with finer conical nose shapes; see "Δ" in figures 6 and 8. Schlieren pictures in (13,f) show also directly a heavy boundary layer, the "viscous" wake, a fully open "bottleneck" and the absence (weakness and /or diffusion) of a shock wave otherwise expected to originate from the wake.

Length Ratio. The $30^\circ/60^\circ$ cone-cylinder body as in figure 7, has extensively been investigated in various places as well (7,l) (13,d,f,k) as with length ratios varying between 0.9 and 12.9 (7,h). At $l/d \approx 0.9$, representing the cone without a cylinder added, suction pressure is strongest. Suction and/or base drag then reduce appreciably as cylinder length is added; and it is believed that this effect is due to an interference of the afterbody with the mixing process. We may assume, for instance, that the flow loses momentum when getting around the cone's shoulder. The lowest branch (○) in figure 8, corresponds to fully laminar flow conditions (at $R_f \approx 2 \cdot 10^5$) as described above under "b". The intermediate branch (△) represents conditions where the Reynolds number increases in proportion to the body length. Two effects are thus superimposed. Taking results from other sources (●) into account, it can be concluded, however, that between $l/d = 0.9$ and ≈ 5 , a change takes place in the flow pattern; and it is believed that this change is a re-attachment of the flow (17,b) aft of the cone's rim and the establishment of "full" supersonic expansion around that corner. Suction and base pressure are increased as a consequence; and they reach maximum values at certain ratios which in turn are a function of R'number. This mechanism is further illustrated by a series of test points obtained with Blasius stimulation (▲). It appears that re-attachment is facilitated by forced turbulence as early as at $l/d = 3$ (at the particular R'number as in those tests) while without this effect, a similar flow pattern is only obtained at $l/d \approx 7$. However, stimulation is seen to produce base-drag coefficients smaller (because of increased BL thickness) than those obtained by natural transition. This difference is consistent and genuine. Finally (above $l/d = 8$, in figure 8) the base drag reduces slowly as further length is added, on account of increasing viscous forebody drag. It should be noted that this variation is different from that in figure 7, where the base drag increases above $R_f = 10^7$ because of the reducing trend of the skin-friction drag coefficient along the forebody.

Wetted Surface Ratio. The thickness of the boundary layer arriving at the rim of the base grows with the forebody's area, or with the area ratio S_{wet}/S_B . Inasmuch as in shapes with cylindrical rear end, this ratio is proportional to the length ratio (l/d), this parameter is thus employed in figure 9 in correlating base-pressure or drag coefficients (17,a) from various sources. The values of the ratios plotted (each set of points at $M = \text{constant}$) reduce systematically as a function of that parameter, in a manner similar to, but not as strongly as the function plotted in figure 4. The mechanics of "supersonic" base drag are more complex, however, insofar as C_{DB} generally reduces as a function of M (as in figure 2). Presenting the results in the form of the base-pressure or base-drag ratio (as in figure 6) does not help much either, in-

sofar as this ratio increases as a function of Mach number. As long as we do not have a basic and simple "solution" for this type of base drag, further correlation appears to be futile. Qualitatively, it can be said, however, that the base drag must be expected to decrease as a function of the forebody-drag coefficient in a manner similar to that as shown in figure 5. It then follows that base drag is not only a function of geometry and Reynolds number, but also of forebody-surface conditions (*roughness*, attachments, firing bands and so on). A single point (◎) has been added in figure 4 demonstrating this effect.

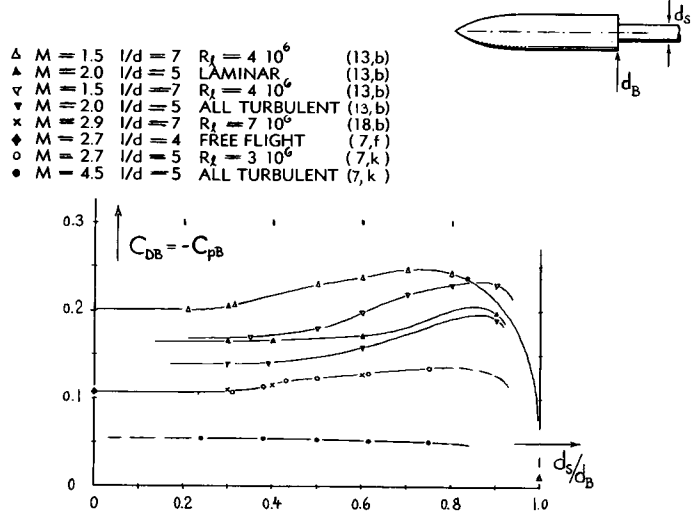


Figure 10. Base pressure (drag) coefficient as a function of sting diameter ratio.

Sting Effect. When testing three-dimensional bodies such as streamline or projectile- and missile-type shapes in wind tunnels, they need to be supported in such a manner that the flow pattern is not disturbed to any significant degree. The preferred method of supporting blunt-based solids, is by means of a sting contacting the model from downstream. Figure 10 shows the influence of sting diameter upon base drag for smooth and slender forebody shapes at Mach numbers between 1.5 and 4.5. It appears that the sting has the largest influence at "transonic" M'numbers, where the "open" bottleneck seems to be filled and "closed" by the sting. At M'numbers above "2", diameter ratios below 0.4 appear to be permissible. At ratios in the vicinity of .8, most of the experimental results show an appreciable increase of the pressure (drag) value. The three-dimensional flow pattern past the base is evidently converted into a more two-dimensional (annular) pattern, in this case. At $M = 4.5$, ratios up to .6 or 0.7 do not seriously affect the value of the base pressure tested.

Rocket Nozzle. Base drag has an interesting consequence in the arrangement of the rocket-jet nozzle within the base of a missile. There is usually an annular clearance space left open around the nozzle.

Full-scale investigations on experimental rockets (24) indicate, for example at $M = 2$, a base drag coefficient C_{DB} in the order of .1 in "power-off" condition. For a jet pressure equal to ambient pressure, the base pressure in the annulus is reduced to a C_p in the order of -0.05 . In "power-on" condition, the "annulus" is subjected to the pumping effect both of the outside flow and of the jet discharging through the rocket nozzle. The value of the base-pressure coefficient is increased, accordingly, to the order of ≈ -0.2 , while the total pressure in the rocket jet reaches a value between (2 and 3) times the ambient pressure, corresponding to a $C_{p\text{total}}$ (on dynamic pressure of the outside flow) between 0.7 and 1.0. For a diameter ratio of 0.9, and an annulus-against base-area ratio of $\approx 20\%$, the base pressure thus takes away some 4% of the rocket thrust, so to speak. It might be simple, however, to extend the nozzle to somewhat beyond base and base diameter of the rocket vehicle, so that the drag in the annulus is avoided.

Boat Tail. "Streamline" type projectile or missile shapes, having a base diameter smaller than the maximum of the forebody, are called "boat-tailed". Their drag is discussed later, together with the wave drag originating from the boat-tail sides. In regard to base drag, figure 2 demonstrates that the character of drag and flow pattern in boat-tailed missile bodies is usually "transonic". Contrary to figure 3,a, the compression shock is bound to be located closer to or even at the base, however, thus permitting the "bottleneck" to stay open to higher limiting Mach numbers (to $M \approx 3$ or 4, as in figure 2). As far as the magnitude of suction pressure is concerned, the mechanism as a function of forebody-drag coefficient C_{fB} (as in figure 5) can very well be applied in *slender and slowly tapering* body shapes to explain and/or to predict the value of the pressure coefficient. The wetted area ratio S_{wet}/S_B of such bodies is evidently proportional to (l/d) as in figure 4, times $(S_w/S_B) = (d/d_B)^2$. Results of one experimental investigation have been plotted in that graph as an example. The points (*) obviously continue the functions obtained at lesser length or area ratios (on bodies having cylindrical ends with $d_B = d$). Other such points can be evaluated from (8,a) for ratios of $(l/d)(d/d_B)^2$ in the order of 30. The same and other results are included in figure 5 plotted against estimated forebody-drag coefficients " C_{fB} ". It must be said, however, that flow conditions past the base of boat-tailed missiles (such as the NACA's RM-10, see footnote 51) are not very consistent. The "transonic" results of such shapes in figure 2 show certain ups and downs; and it is sometimes not clear whether the boundary layer or the telemetering devices play tricks on us in this phase. Reference (8,e) demonstrates, however, that a stable condition at the RM-10 base is reached at R' numbers (on body length) above 10^7 . Below this number, the flow along the forebody is essentially

laminar. Because of smaller R' numbers (between 10^6 and 10^7) the pressure coefficients of boat-tailed bodies in reference (13,c) (having $l/d = 8$) do therefore not correlate very well on the basis of C_{PB} . A reason for this result is most likely laminar-type and shock-induced separation from the end of the "boat tail". Separation also takes place in projectiles in cases where the boat-tail angle exceeds a certain permissible value (see the later section on this subject).

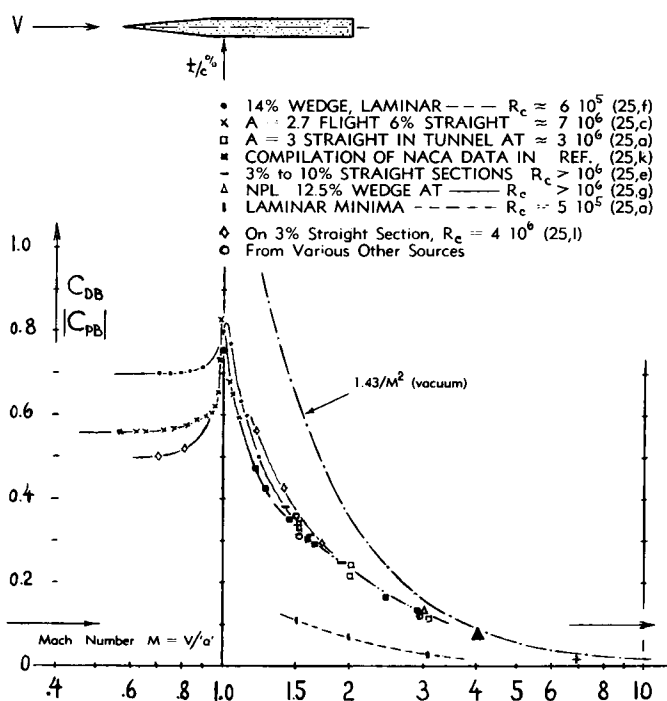


Figure 11. "Base" drag originating from the blunt trailing edge of airfoil sections, as a function of M number.

- (18) Influence of sting support on base pressure:
 - a) Perkins, At $M = 1.5$, NACA T.Note 2292 (1948).
 - b) See the information in reference (13,b).
 - c) Cahn, At Transonic Speeds, NACA Doct. RM L56F18a.
 - d) Donaldson, At $M \approx 2$, Aeron.Quart. 1955 p.221.
 - e) Love, Summary on Base Drag, NACA Doct. RM L53K12.
- (22) Interference of tail surface on base pressure:
 - a) Spahr-Dickey, Fin, NACA T.Note 2360 (1951).
 - b) Tail-Wing Interference, NACA T.Note 2360.
 - c) Hart, Fins and Sting in Flight, NACA RM L52E06.
 - d) Love, Fins and Sting, NACA Doct. RM L52J21a.
- (24) Base drag around rocket outlet nozzles:
 - a) NACA, Rocket Jet Effect, RM L50I18 and L51J29.
 - b) Cortright, Aeron'l Engg.Review, p.59.
- (25) Experimental results on two-dimensional base drag:
 - a) Chapman, Blunt TE's, NACA T.Rpt 1109 (TN 2611).
 - b) Chapman, included in NACA T.Rpt 1051 (13,b).
 - c) Morrow, Flight Tests, NACA T.Note 3548(L50E19a).
 - d) Chapman, TE Thickness, NACA T.Note 3350(1955).
 - e) Goin, Blunt T'Edge Wings, NACA Doct. RM L52D21.
 - f) Sawyer, Cylinder and Wedge, NACA Doct. RM L8B13.
 - g) Gadd, as in (7,l); also NPL Symposium Rept. 1955.
 - h) Stanton, Cylinders in Tunnel, ARC RM 1210 (1928).
 - i) Chapman, Supersonic Airfoils, NACA Doct. RM A9H11.
 - k) Chapman, Compilation, NACA Conference Rpt 1950.
 - l) Dugan, On 3% Airfoil, NACA Doct. RM A52E01.

Fin Interference. While projectiles are usually stabilized in their flight by "spinning" them, missiles are generally kept in direction by means of fins (similar to those of airships, bombs and/or torpedoes). These fins can affect base pressure in several ways. They may change status and thickness of boundary layer and/or wake; and they can thus either increase or decrease the base-pressure coefficient, in the order of $\pm 10\%$ in "straight" projectile shapes such as in (7,g,n,o) for example. This type of interference can be much stronger, however, in boat-tailed missile bodies, whose flow pattern is more sensitive. Reference (8,c) shows, for example, an increase of the base-drag coefficient from practically zero (for laminar flow at $R_\lambda = 3 \cdot 10^6$) to $-C_{PB} = 0.11$, which is a value close to that in forced-turbulence condition (0.12). It is suggested that some laminar separation (from the boat tail) ahead of the base, is eliminated in this case through addition of the fins. Another interference effect of fins is directly a consequence of their pressure field. For common locations (adjoining or somewhat ahead of the base) this effect seems to be comparatively small. For positions with the fins' afterbodies extending beyond the base, the influence can be expected to depend upon the pressure differential between fins and base space. This differential may be negative (in particular for fins with higher thickness ratios) or it may be positive. For a typical missile configuration (RM-10 in reference 8,c) with four 10% thick and 60° swept fins, the value of the negative base-pressure coefficient (tested with fixed boundary-layer transition) is, for example, increased on account of the fins, from $-C_{PB} = 0.09$ to 0.13. When moving the fins further back in this swept configuration (by some 50% of their chord so that they protrude that much beyond the base), it might be possible to reduce the base drag by letting the positive part of the fins' pressure field corresponding to a measured differential of $\Delta C_p \approx 0.05$ "impinge" upon the dead-air space behind the base.

Blunt Trailing Edges. The two-dimensional equivalent of the "base" of a projectile, is a thick and blunt trailing edge as we find it in wedges, for example, or in airfoil sections whose rear end has been cut off or thickened. Figure 11 presents available experimental results, mostly on shapes with flat and parallel sides. Contrary to the characteristics of three-dimensional bodies (in figure 2) there is no \approx constant "transonic" level found in any of the sections investigated. Two-dimensional mixing is obviously more effective, so that "sealing" of the "bottleneck" (as in figure 3,b) is easier obtained. The sketch in figure 13 displays a very narrow wake "throat", accordingly. It should also be noted that the downstream wake shows the familiar fluctuating vortex "street" pattern (see Chapter III). In conclusion, the "base" drag of two-dimensional and of finite-span airfoils as well, has usually a "supersonic" character.

Maximum Base Drag. Two-dimensional base-drag characteristics follow the principles outlined in connection with three-dimensional projectile- and missile bodies (under the subheadings of "viscous forebody drag", "supersonic phase" and "Reynolds number"). To show how far the influence of R'number (corresponding to that in figure 7) can go in two-dimensional base flow, some laminar minima (1) are included in figure 11 (obtained at $R_c = 2 \cdot 10^5$). As in three-dimensional bodies (see figure 9) the turbulent maximum drag values are somewhat lower than the maximum suction pressure (drag) coefficients obtained (in the vicinity of $R_c = 10^6$) for laminar BL along the foil sections (26,a).

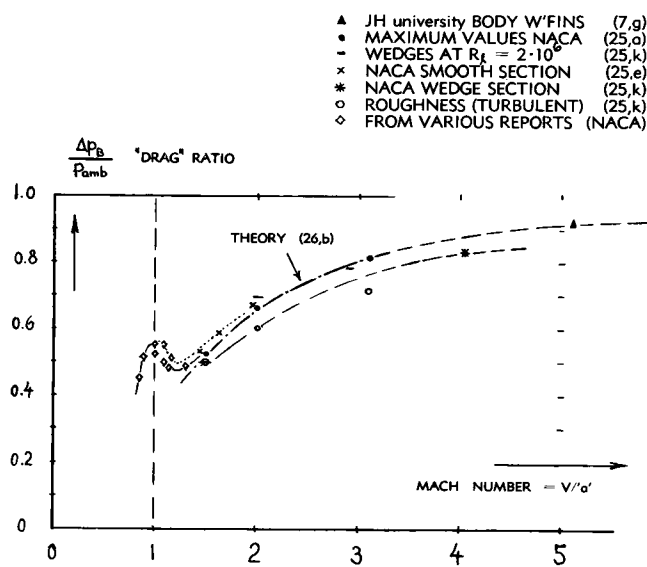


Figure 12. Variation of suction-pressure or base-drag ratio of several blunt-ended airfoil sections as a function of Mach number.

Figure 12 shows the variation of pressure or drag ratio (17,a) as a function of Mach number. The highest experimental points essentially agree with a theoretical solution (26,b) for two-dimensional flow involving no or comparatively thin boundary layers. This (numerically solved) solution, obtained "without the aid of any experimental data", is thus supposed to indicate a lower limit of the base pressure or an upper limit of the corresponding base drag. Results from tests at Reynolds numbers (between 10^6 and 10^7) where the boundary layer is still laminar over most of the foil section chord, are seen to agree with the theoretical function very well.

-
- (26) Theoretical analysis of 2-dimensional base drag:
 a) Chapman, NACA T.Rpts 1051 and 1063 (T.N.2264).
 b) Korst, Base-Pressure Theory, J.Appl.Mech.1956 p.593; see also J.Aeron.Sci. 1954 p.568.
 c) Klunker, Supersonic Drag, NACA T.Note 2828(1952).

"Transonic" Phase. Figure 12 demonstrates that the agreement between experimental results and the limiting theory (26,b) discontinues as the Mach number reduces below ≈ 1.3 . Indeed, tested drag coefficients are higher than indicated by the theory. We must thus conclude that in a comparatively narrow transonic range of the Mach number, the flow pattern past base (and forebody) is different from the one assumed in the theoretical formulation. As a possible reason for increased base drag, presence and mechanism of a vortex street (see Chapter III) in combination with supersonic effects is mentioned at this point.

Forebody Drag. Figure 13 presents an attempt of correlating the base pressure (drag) ratio (17,a) with the viscous forebody coefficient (9,b)

$$C_{fB} = C_{Ds} (c/h) \quad (18)$$

where C_{Ds} = "viscous" section drag coefficient. Inasmuch as this coefficient is not usually measured separately, most of the C_{fB} values used in plotting the points in figure 13 have necessarily been calculated (or estimated, respectively; see footnote 9,d). To demonstrate the application, we will consider a blunt-ended foil section with $t/c = 5\%$, flying at $R_c = 10^7$, where laminar boundary layer flow is still possible with the help of some negative pressure gradient. The skin-drag coefficient $C_{Dso} \approx 2 C_f$ is then expected to be in the order of 0.002 for laminar and of 0.006 for turbulent flow. For thickness of the trailing edge $h = t$, the corresponding coefficients on base area are $C_{fB} = 0.04$ and $= 0.12$ respectively. For a Mach number $M = 1.5$, the base

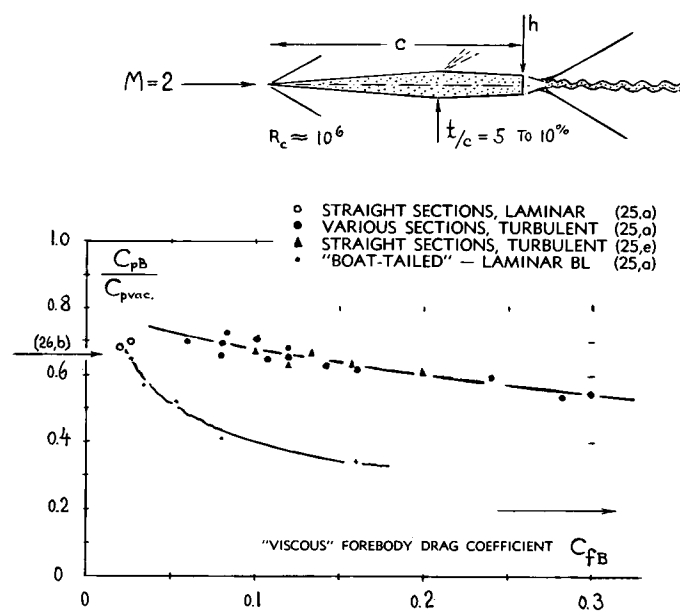


Figure 13. Correlation between base drag and "viscous" forebody-drag coefficient, for a blunt-ended foil section.

drag coefficient corresponding to vacuum (as shown in figure 11) is $C_{DB} \approx 0.6$. Using the two C_{FB} values as found above, figure 13 then yields the two base drag coefficients $C_{DB} = 0.6 \cdot 0.6 = 0.36$ and $= 0.6 \cdot 0.65 = 0.12$, respectively. The sum total of the coefficients, for section and Mach number considered (not including the forebody *wave* drag which is assumed to be independent of boundary layer and base flow) is:

$$\begin{aligned} C_{DFB} + C_{DB} &= 0.04 + 0.36 = 0.40 \quad (\text{laminar}) \\ &= 0.12 + 0.39 = 0.51 \quad (\text{turbulent}) \end{aligned}$$

The laminar boundary layer flow is thus more desirable in this particular case (where $h = t$). Other combinations of TE thickness ratio and Mach number leading to similar results, or to opposite results respectively, can be found by going through the same procedure. Further analysis, including wave drag on forebody and tapering afterbody, is presented in Chapter XVII.

Boat-Tailing. Boundary-layer flow is usually laminar in transonic wind-tunnel tests (unless stimulation is applied). As explained in Chapter XVII, laminar flow is also not unrealistic in full-scale supersonic applications. There are a number of points included in figure 13, at C_{FB} below 0.1, showing considerably reduced base pressure (drag) ratios. It appears that all of these were tested in the presence of laminar B'layer. However, all the low values were also obtained on heavily boat-tailed shapes. Rather than blaming the result on laminar "mixing", it is therefore suggested that an interaction between shock wave and B'layer is taking place under these conditions, thus resulting in some influence of the higher pressure behind the tail shock wave upon the pressure level at the base.

3. BLUFF BODIES AT TRANSONIC SPEEDS

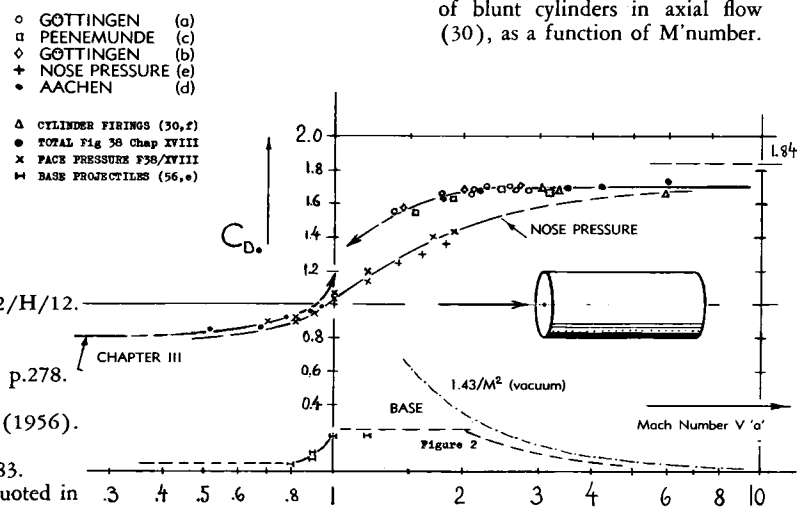
(a) Drag Of Blunt Bodies

The *Blunt Cylinder* as in figure 14, exhibits a fully detached and rounded shock wave (of the form as illustrated in figure 20). The average positive pressure coefficient on the cylinder face is, therefore, closely related to the stagnation pressure as indicated by equation 4 or in figure 1. Disregarding a negligibly small component of skin friction, the forebody drag coefficient of the blunt cylinder may accordingly be:

$$C_{D_{fore}} = K_{fore} ("q"/q) \quad (20)$$

where the factor is tentatively $K_{fore} = 0.90$, as found from pressure distribution tests in (30,e); see the (+) points in figure 14. The total drag coefficient increases accordingly, while the transonic base-drag coefficient remains at a constant value of ≈ 0.2 . Approximately at $M = 2$, the base pressure coefficient can be expected to begin decreasing in the manner as pointed out in general in Section 2 of this chapter and as shown in particular in figure 2. Tentatively, the base drag component may be assumed to be 0.6 of the maximum possible function (corresponding to vacuum). A computed drag function is obtained in this manner, matching and extrapolating the experimental points in figure 14 very well. It so happens that the total drag coefficient assumes a roughly constant level, tentatively terminating at $C_{D_0} \approx 1.65 = 0.9 \cdot 1.84$, where 1.84 = terminal stagnation pressure coefficient as in figure 1. Somewhat different factors and values for the two components of drag can, of course, be assumed or they may eventually be tested.

Figure 14. Drag characteristics of blunt cylinders in axial flow (30), as a function of M'number.



- (30) Drag of and pressure on *cylinders* in axial flow:
 a) In Wind Tunnel, AVA Docts. 1940/8/1, 1942/H/12.
 b) AVA Göttingen, see reference (42,e).
 c) Peenemünde, see references (7,c)(42,a).
 d) Naumann, Subsonic, ZWB Tech.Berichte 1943 p.278.
 e) Nose pressure distribution, reference (36,b).
 f) Long, Firings to $M = 8$, NAVORD Rpt 4382(1956).
- (32) Drag of *bluff bodies* at high speeds:
 a) Hansche-Rinehart, Cubes Fired, J.A.Sci.1952 p.83.
 b) British Tunnel Tests on Various Bluff Bodies, quoted in Aberdeen BRL PG Report 425 (1943).
 c) Strassl, Beveled Cylinders, AVA Doct. B 1942/H/12.
 d) Schardin, Schlieren Pictures, ZWB Litl.Rpt 139/1.

Bluff Heads. Reference (30,a) proves that the length of cylinders in supersonic axial flow does not noticeably affect their drag coefficient, i.e. not between $l/d = 2$ and 5 as tested. The same source also shows that beveling the forward end of such cylinders, reduces the pressure drag coefficient on that end as indicated in figure 15. All of the *bluff* shapes in that illustration exhibit total drag coefficients which are comparatively constant between $M = 2.0$ and 3.4. Assuming the base-drag component to be $C_{DB} = 0.2$ (see figure 2), approximate wave-drag or nose-pressure coefficients can be obtained; see figure 15. They show then that beveling, tapering, rounding and/or pointing reduces that type of drag significantly. Figure 16 presents the total drag coefficients of such solids at $M = 2$, as a function of the length or fineness ratio (x/d) of their forebody shape.

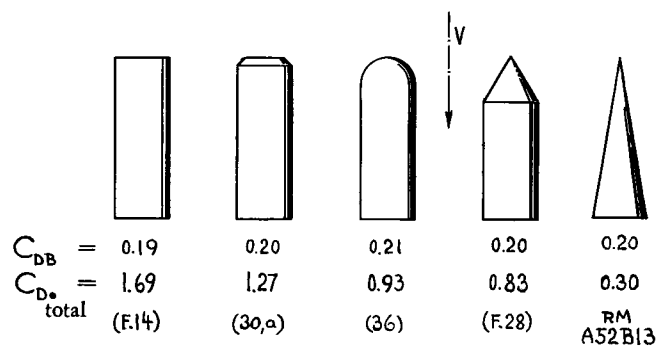


Figure 15. Drag coefficients of several more or less blunt or bluff-ended circular cylinders in axial flow at $M = 2$.

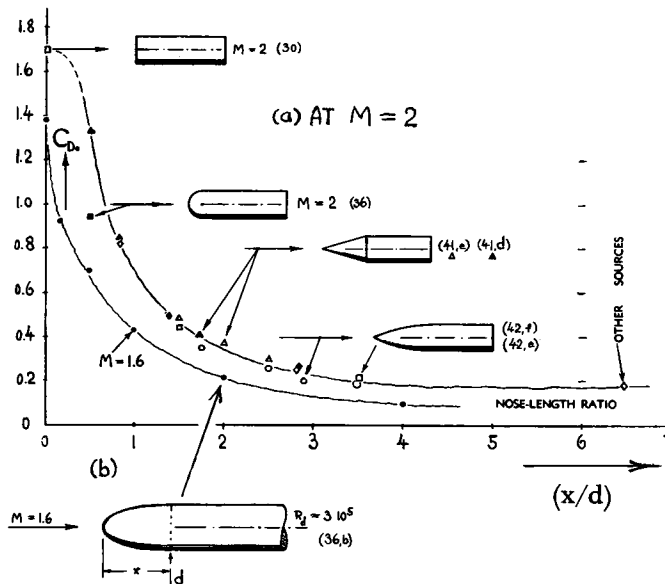


Figure 16. Drag coefficients of various more or less bluff, rotationally-symmetric shapes, as a function of their forebody length ratio; (a) total drag of bodies as indicated, at $M = 2$; (b) forebody drag (head pressure) of a group of spheroidal heads (36,b) at $M = 1.6$.

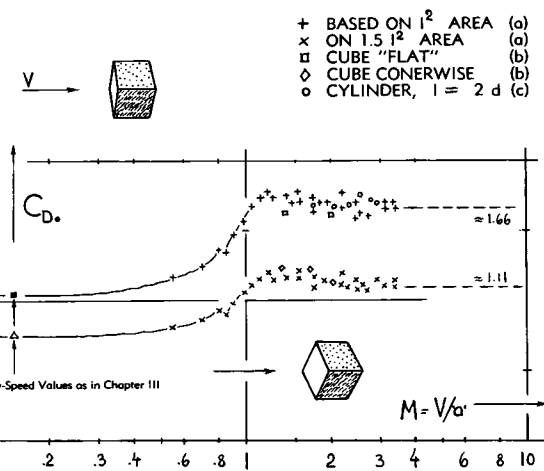


Figure 17. Drag coefficients of *rotating cubes* fired through a ballistic range (32,a).

Rotating Cubes. The drag of steel cubes somehow rotating in an uncontrolled manner, was tested by firing them through a ballistic range at speeds up to 4000 ft/sec. Figure 17 presents the average drag coefficients obtained, originally based on a frontal area equal to $1.5 l^2$ where l = edge length of the cubes tested. This area roughly represents an average projected frontal area of the cubes when rotating. By coincidence, the drag coefficients are then somehow compatible with those of cubes from a different source (32,b) tested in "cornerwise" position. Actual frontal areas are $S_* = l^2$ for the "flat" cube, $= \sqrt{2} l^2$ for edgewise motion, and $\approx 1.7 l^2$ for all positions with one of the corner points first. After referring the drag coefficient to the area l^2 (as in a "flat" cube) the points are also more or less compatible with results (32,b) on cubes in a position where two of the faces are normal to the direction of the fluid flow. The rotating cubes thus represent average conditions between all positions statistically possible.

Two-Dimensional Plate. Blunt bodies such as the cylinder in figure 14, or as plates and/or disks in supersonic fluid flow in a direction normal to their forward face, always exhibit a fully detached and rounded shock wave pattern. It has been found on bluff wedges (33,a) that under these conditions the pressure distribution along the sides begins with $p = 1.893 p_*$ at the LE; and it ends at $p \approx p_*$ at the shoulder (where p_* = critical pressure corresponding to sonic speed). Experimental results for a certain wedge obtained at various transonic M' numbers, therefore, collapse into one distribution function when plotting p/p_* against wedge length or thickness. Shape of, and pressure drag coefficient corresponding to this distribution are thus a function of wedge angle (and not of M' number). This type of similarity is utilized as follows to predict the average

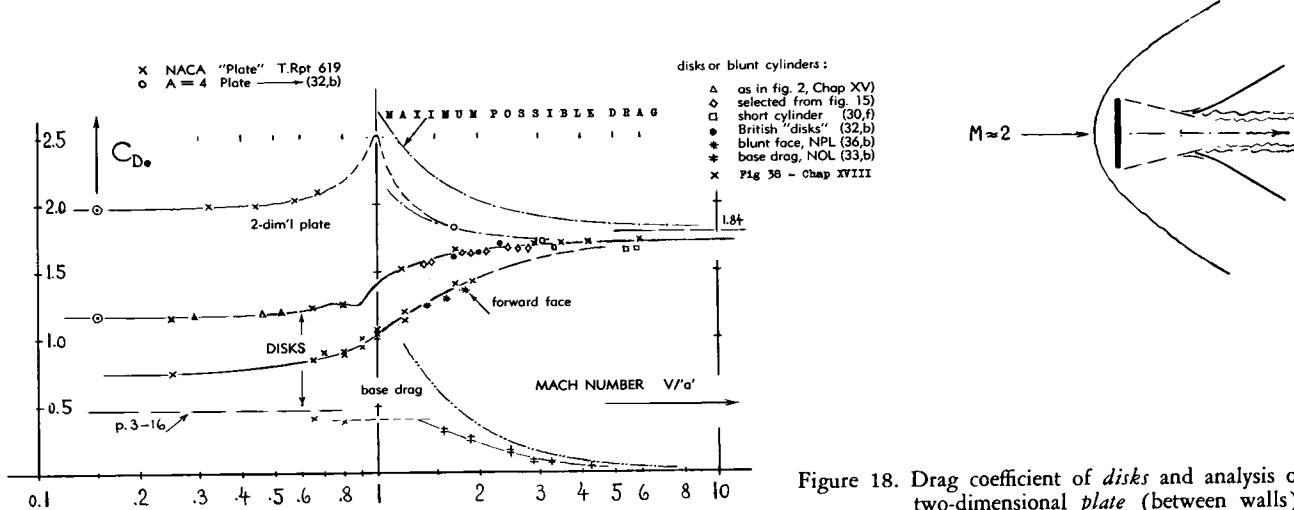


Figure 18. Drag coefficient of disks and analysis of two-dimensional plate (between walls).

pressure coefficient on the *forward face* of a flat plate in two-dimensional normal flow, at "transonic" speeds:

$$C_{D_0} = K \left(\frac{q}{q} \right) - 2 \left(1 - K \right) / (k M^2) \quad (21)$$

where " q/q " = stagnation pressure coefficient as in equat. 4, and K = factor indicating the fullness of the pressure distribution. For a wedge angle of $2 \cdot 90^\circ$, as in a plate or in a blunt and square leading edge, it was found that $K = 0.92$ (33,a) and $K = 0.94$ (36,b) respectively. Applying an average factor of 0.93 (and for $k = 1.4$ as in air) a face-pressure drag coefficient of $0.93 \cdot 1.84 = 1.71$ is thus obtained for $M \rightarrow \infty$.

Bluff Wedges. "K" values to be used in equation 21 have been evaluated for a few "wedges", including the flat plate (having $\varepsilon = 90^\circ$). They are plotted in figure 19 as a function of the half-apex angle " ε ". At $\varepsilon = 180^\circ$, the theoretical value of $K = 1$ is

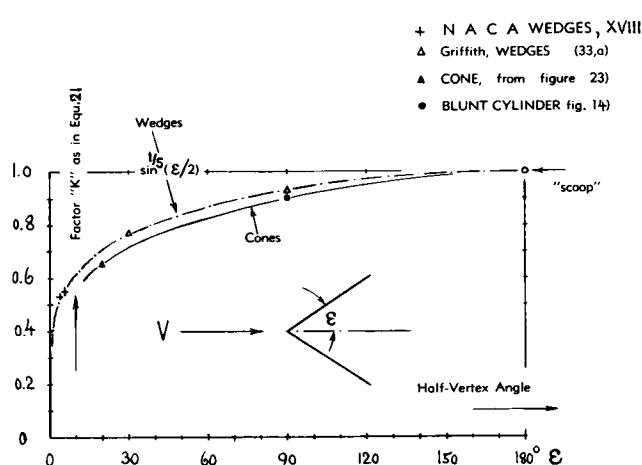
applied indicating "scoop" type shapes (such as "cups" or other open and sharp-edged forms). The available points for two-dimensional shapes can then be interpolated by.

$$K = \sin(\varepsilon/2) \quad (22)$$

For conical shells" (moving point-first or moving with the opening against the air-stream, respectively) there is a second line indicating coefficients somewhat lower than for the two-dimensional wedges and "folds", respectively. Selecting the proper coefficient, the drag corresponding to positive face pressure can then be calculated through the use of equation 21 (for "any" Mach number). The method ceases to be applicable, however, as soon as the bow shock wave attaches itself to the body surface (as in slender cones and/or wedges). A very similar method of drag analysis is also applied in Chapter XVIII, where characteristics of bluff bodies are further considered, under "hypersonic" conditions (33,c).

Further analysis and improved "K" values, see Chap. XVIII.

- (33) Results on blunt heads and disks:
 - a) Griffith, Wedge Theory, J.Aeron.Sci.1952 p.249.
 - b) NOL Experimental Results on Disks, as in (7,p).
 - c) Blunt bodies appear to be a case where the distinction between "subsonic", "transonic", "supersonic" and "hypersonic" gets lost to a large degree.
 - d) Face pressure, included in reference (36,b).
- (34) Drag of spheres at transonic/supersonic speeds:
 - a) Hélie, Traité de Ballistique, Paris 1884.
 - b) Charters & Thomas in J.Aeron.Sci. 1945 p.468.
 - c) Clark & Harris, Pendulum, J.Aeron.Sci. 1952 p.385.
 - e) Hodges, Tech Rpt T-656 (1949) N.M.School of Mines.
 - f) Ferri, R' and M'Number, Atti Guidonia 67, 68, 69 (1942) p.49; also by Eula in Aerotecnica 1940 No. 1.
 - g) See Erdmann, reference (7,c), Peenemünde.
 - h) NOL, Firings at $M = 8.7$, unpublished 1956.
 - i) Lehnert, Base Pressure, NAVORD Rpt 2774 (1953).

Figure 19. Factor "K" to be used in equation 21, in order to determine the transonic and/or supersonic forebody wave-drag coefficient of blunt bodies and bluff cones or wedges.

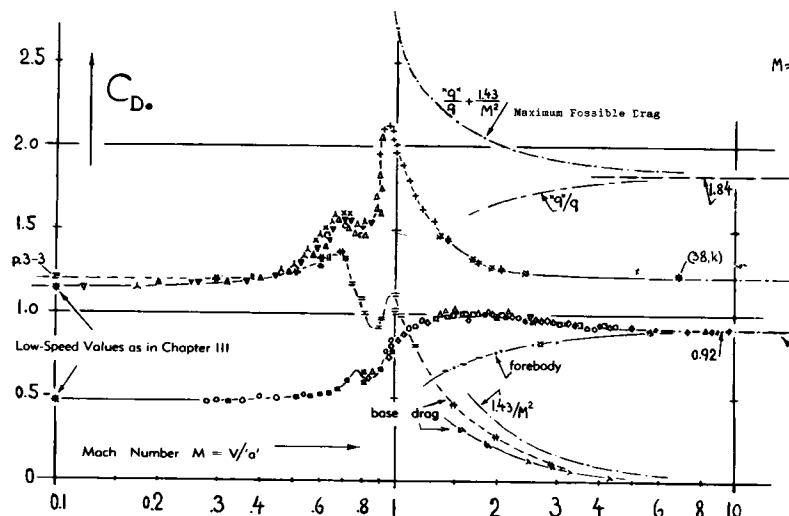
Base Pressure. The detached-shock mechanism as described in the preceding paragraph, is now tentatively applied to the three-dimensional case of a *disk*. For the face of a blunt-ended circular cylinder, the factor K was found (36,b) to be 0.88. Figure 19 suggests, however, that a value of 0.90 might be more consistent with other results. Applying now this factor to the disk, its face pressure is then determined through application of equation 21. In regard to rear-side or base pressure, figure 18 shows a tested function (33,b) very roughly corresponding to $\approx 65\%$ of the maximum possible differential corresponding to vacuum (equation 14). The drag coefficient of the disk at higher supersonic speeds is thus tentatively

$$C_{D_0} = 1.62 + (0.1/M^2) \quad (24)$$

Assuming that the drag of a disk may be equal or similar in magnitude to that of a short cylinder in axial flow, values have been selected among those in figure 14 in such a manner that the total drag coefficient (as found for those cylinders) is equal to the sum of face pressure coefficient as tested (36,b) plus base drag coefficient as determined behind disks (33,b). The resultant function is a likely indication for the drag coefficient of disks at transonic and supersonic speeds. — Supersonic results on two-dimensional plates (tested between walls) do not seem to be available. We may make a guess, however, concerning the negative pressure at their rear surface; and we will assume this pressure possibly to correspond to 75% of the coefficient indicated by vacuum (see figure 12). Adding to equation 24, the drag coefficient of a plate between walls is then tentatively:

$$C_{D_0} = 1.72 + (0.3/M^2) \quad (25)$$

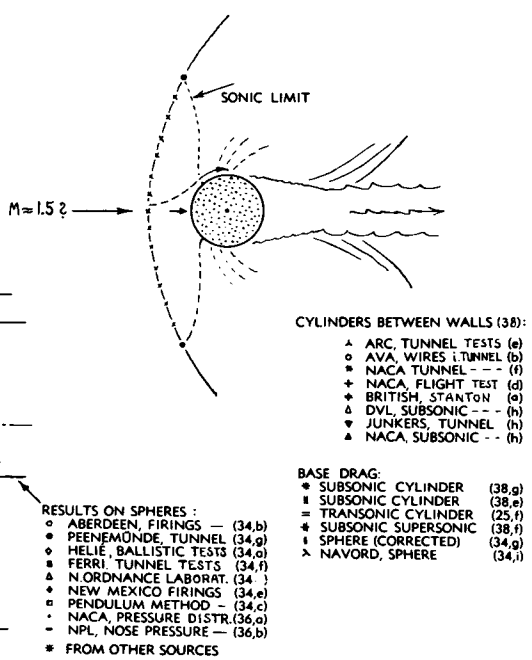
This drag coefficient is plotted in figure 18 together with that of the disk. The "synthetic" functions (for the disk as well as for the plate) are qualitatively confirmed.



(b) Drag Of Rounded Shapes

Spheres. Figure 20 presents a transonic and supersonic continuation of the drag function of spheres as in figure 6 of Chapter XV. Schlieren pictures (34,b) show that the separation point on the surface of the sphere moves from $\approx 15^\circ$ ahead, to $\approx 20^\circ$ aft of the "equator". It could then be speculated that there may be some variation of the drag coefficient, at transonic and supersonic speeds, as a function of Reynolds number and boundary layer development. Tests in ballistic ranges (34,b,e,h) between $R_d = 10^4$ and 10^6 , seem to indicate only comparatively small variations. Experimental results only at such higher R' -numbers are plotted in figure 20. Characteristics at "very small" R' -numbers are discussed in Chapter XI X as a subject of rarefied fluid flow. — Results of pressure distribution tests on hemispherical head shapes, included in figure 20, may be considered also to represent the forebody-drag coefficient of spheres. Between $M = 1.5$ and 2.0, this component corresponds to approximately 44% of the stagnation pressure (as in figure 1). The percentage grows, however, as the M' -number is increased. At M' -numbers between 5 and 7, the pressure at the surface of the sphere is found (36,c) and (38,k) to correspond to a hypersonic type of distribution, as described in Chapter XVIII. The result is a terminal pressure drag coefficient of $C_{D_0} = 0.92$ (for hemispherical heads as well as for spheres) as indicated in the graph.

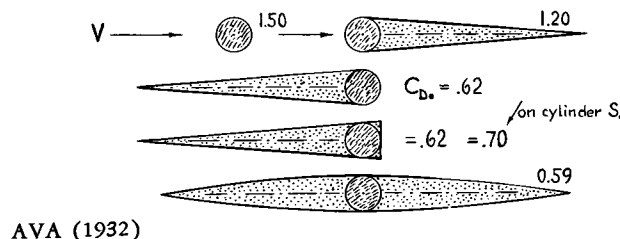
Figure 20. Drag coefficients as a function of M' -number (a) of spheres; (b) of circular cylinders (between walls).



Base Drag. The rear-side or base-drag coefficient of the sphere (as tested, see figure 20) increases from $\approx 50\%$ of the maximum possible value (corresponding to vacuum) at $M = 1.5$, to some 70% of that function at $M = 3.0$, thus presenting a growth of the ratio similar to the lines in figure 6.

Spheroidal Head Shapes of varying length ratio have been investigated by pressure distribution method in (36,b), between $M = 1.4$ and 1.8. Figure 16 demonstrates how the nose drag coefficient of a cylinder in axial flow decreases from the value as found for the blunt form (see figure 14) by giving the forward end a spheroidal shape more and more increasing in fineness ratio x/d .

Cylinder in Cross Flow. Drag coefficients of circular cylinders in two-dimensional flow (tested between tunnel walls) are presented in figure 20 over the "full" range of the Mach number. The up-down-up irregularity at higher subsonic M'numbers (treated at length in Chapter XV) is seen to correlate very well with base-drag results. The drag coefficient then reaches a transonic peak slightly above 2.1. At supersonic M'numbers, the base-drag coefficient is on the average in the order of $\approx 70\%$ of the value corresponding to vacuum, as tested between $M = 1.5$ and 2.9 and as included in the illustration. On account of the base pressure, the total coefficient reduces considerably (between $M = 1$ and 2). The component due to positive pressure on the forward side of the cylinder is in the order of 0.66 of the stagnation pressure. Extrapolating the total coefficient to higher M'numbers, this value tentatively indicates the terminal level, while the base-drag component reduces to zero; see again under "hypersonic characteristics" in Chapter XVIII.



AVA (1932)

Figure 21. Drag coefficient of a circular cylinder (tested between tunnel walls, reference XVII) at $M = 1.5$, without and with various fairings.

Cylinder Fairings. Since the mechanism of supersonic drag is different from that at subsonic speeds (or in incompressible fluid flow) the influence of form upon drag is also different. A series of simple section shapes, possibly to be used as fairings around circular cylinders, are presented in figure 21. The single wedge with the cylinder ahead, has a much higher drag coefficient than in the sharp-edge-first direction. This result demonstrates again that in transonic and supersonic flow, stagnation pressure on any type of bluff shape leads to high drag coefficients, while at supersonic (but not at transonic) speeds, drag due to negative base pressure can be comparatively low. In fact, at $M = 1.5$ as tested, the drag of the wedge (moving sharp-edge-first) is only slightly larger than that of the biconvex section included in the illustration for comparison. Characteristics of blunt-ended foil sections are further treated in Chapter XVII.

Elliptical Cylinders. We do not have results on elliptical cylinders as such. A series of half-body type elliptical "edges" has been investigated, however, by pressure-distribution method (36,b). Figure 22 shows how the drag coefficient (on frontal area) reduces as the leading edge is made elliptical with a more and more increasing length or fineness ratio x/t .

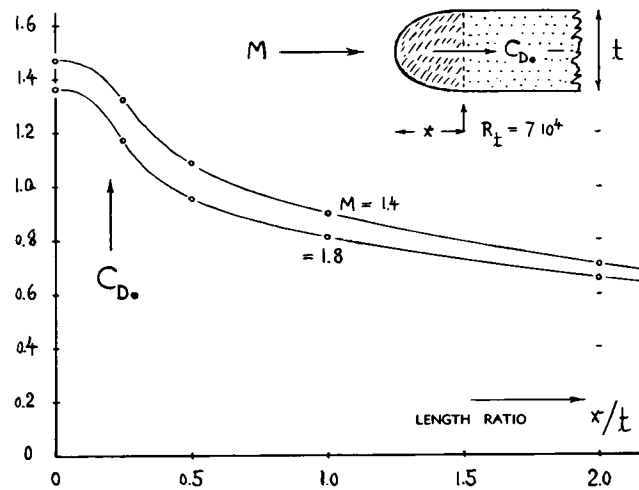


Figure 22. Drag coefficient of a 'leading edge' from pressure distribution (36,b) as a function of the length ratio x/t .

- (35) Influence of Reynolds number on spheres:
 - a) Charters (Aberdeen) as in reference (34,b).
 - b) May and Witt, Free Flight, J.Aeron.Sci.1953 p.635.
 - c) May, Firings at Small R'Numbers, NAVORD Rpt 4392.
- (36) Characteristics of spheroidal heads:
 - a) NACA, Hemispherical Noses, RM A52B13 & L52K06.
 - b) Holder-Chinneck (NPL), Supersonic Flow Past Series of Half-Body Shapes, Aeron.Quarterly 1954 p.317.
 - c) GALCIT, Bluff Bodies, J.Aer.Sci.1956 p.177 & 1054.
 - d) References (c) and (38,k) prove that the Newtonian type distribution does not very well apply to cones.
- (38) Circular cylinders in high-speed cross flow:
 - a) Stanton, Pressure Distribution, ARC RM 1210 (1928).
 - b) Ludwieg, Drag of Wires, AVA Doct 8/16/1939.
 - c) Welsh, Transonic Flight Tests, NACA T.Note 2941.
 - e) Knowler-Pruden (NPL), ARC RM 1933 (≈ 1942).
 - f) Gowen-Perkins, R' and M'Numbers, NACA T.Note 2960.
 - g) Orlin, Hydraulic Analogy, NACA T.Rpt 875 (1947).
 - h) Various test points at subsonic speeds correspond to those plotted in figure 5 of Chapter XV; in figure '20'.
 - k) Penland, Cylinder and Sphere, NACA RM L54A14.

4. TRANSONIC DRAG OF SLENDER BODIES

The shape of projectiles and missile bodies designed for transonic and supersonic speeds, shows usually a pointed nose and a more or less blunt and flat base. Drag due to separation from that base is treated in the second section of this Chapter. Disregarding some skin-friction, the rest of the drag of such bodies corresponds to compression waves (shocks) originating from the forebody and its more or less conical nose, and possibly from the afterbody (if boat-tailed).

Conical Flow is theoretically treated as a half-infinite pattern of flow, a substitution which accounts for pressure (which is then constant along the cone length) and drag on cones of finite length and/or of conical nose shapes in truly *supersonic* axial flow. However, at subsonic and transonic speeds, the pressure on the surface of a physical cone starts from an (infinitely small) stagnation point; and it reduces from there to values below ambient pressure at the cone's rim or shoulder. At high subsonic speeds, the flow pattern undergoes changes similar to those described elsewhere (in Chapter XV and in this chapter here). Theoretical methods have been established describing and correlating these changes, and the subsequent variation of the pressure drag coefficient across the transonic range, by means of similarity functions (40).

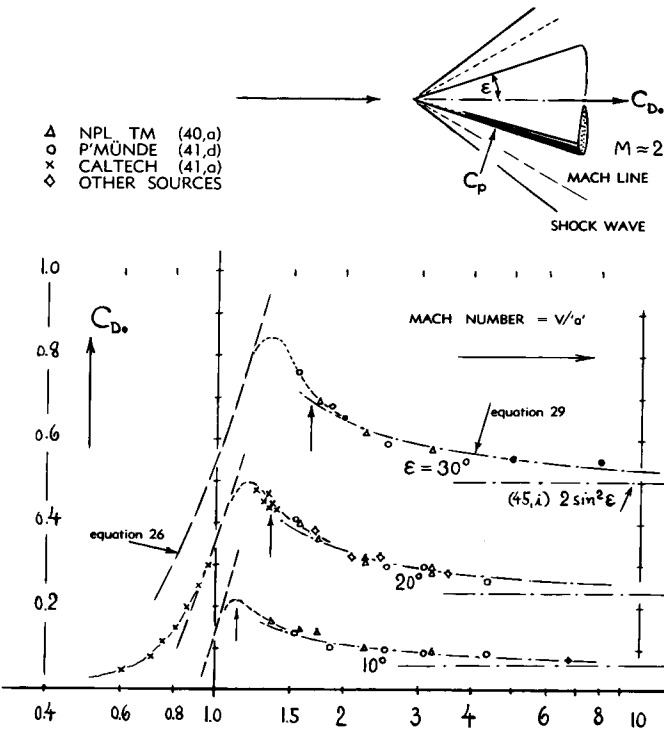


Figure 23. Theoretical (40) and experimental (41) drag coefficients of various conical heads at transonic and supersonic Mach numbers.

Most of these methods employ certain linearized terms, however, so that transonic applications are only realistic for very small cone angles (45). Really suitable parameters to be plotted (45,f) are also complex; "a source term has to be subtracted out" (2,c). Rather we are using, therefore, a statistical approach. One component of the similarity system (41,a) (40,e) is utilized, however, in figure 23, indicating the slope of the drag coefficient across $M = 1$; thus:

$$dC_{D*}/dM = (4/(k+1)) \cdot (1 - 0.5 C_{D*}) \quad (26)$$

where $C_{D*} =$ drag coefficient at $M = 1$, and $k = 1.4$ for air.

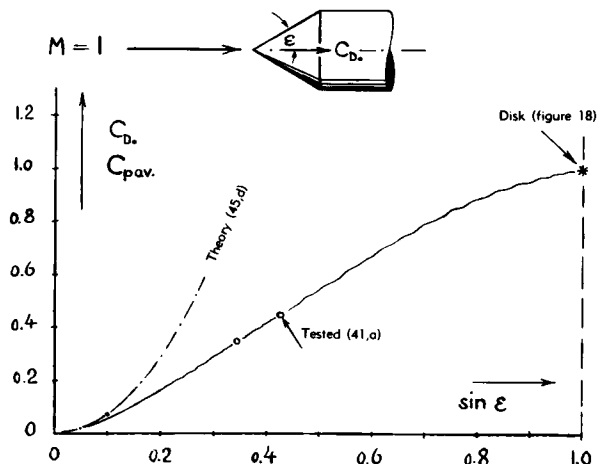


Figure 24. Drag coefficient of conical heads at $M = 1$.

At $M = 1$. Besides the transonic result in figure 23, we have only another point from the same source (41,a) indicating drag at $M = 1$. These two points are plotted in figure 24 in combination with a theoretical solution (45,g) and with a value estimated for the disk (which is a cone with $\epsilon = 90^\circ$) on the basis of figure 18. The correlation thus obtained looks encouraging. Tentatively, therefore, the empirical function as indicated in the graph, can be used for the cone part of cone-cylinder configurations at $M = 1$. A value of $C_{D*} = 0.56$ has accordingly been taken for $\epsilon = 30^\circ$ and plotted in figure 28 together with the slope function (equation 26) thus indicating a likely continuation across $M = 1$, of the experimental results obtained in supersonic wind tunnels. — The drag coefficient of the conical noses in figure 23, reaches a peak closely above $M = 1$; and it then connects to the supersonic function described as follows.

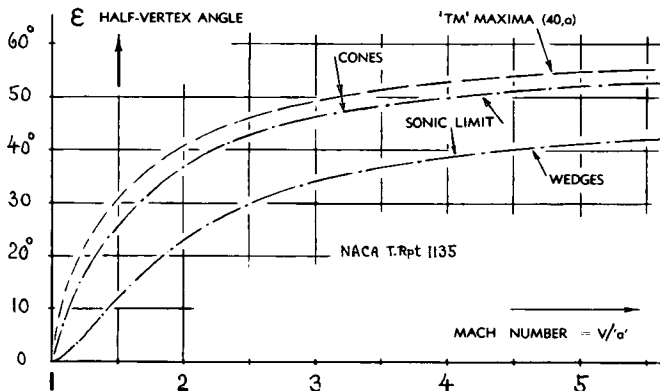


Figure 25. Maximum permissible half-vertex angles of cones (40,a) and wedges (6,b) at which the shock wave detaches from point or leading edge, respectively.

Supersonic Cone Flow. Within the transonic range, the shock wave is detached from the point of the cones considered; and the front is round rather than conical. Figure 25 shows the Mach numbers at which the shock then attaches itself to the point. This event does not immediately terminate the mixed transonic regime, however. The flow pattern only becomes truly supersonic at certain slightly higher Mach numbers also indicated in the graph. Above the latter numbers, the pattern is "conical" which means according to the results of theoretical (40) and experimental studies, characteristics as follows:

(a) The shock wave is truly conical, at least to the point where the expansion waves originating from the cone's shoulder interfere with the compression wave.

(b) The angle of the conical wave is larger than that of the cone, a property which is (at least qualitatively) equal to that in theoretical two-dimensional wedge flow.

(c) The pressure distribution along the cone surface is uniform (a property which is different from that in the transonic range).

(d) Velocities and/or local Mach numbers are constant along "rays" originating from the cone point. In spite of these apparently well defined conditions, there is no *explicit* solution available, predicting pressure and drag of cones at supersonic speeds. It has been possible, however, to determine the wave drag by numerical evaluation (40,a). The theoretical results, plotted in figure 23 for 3 selected cone angles, are sufficiently well confirmed by experimental results. As a function of the cone angle " ε " (at $M = \text{constant}$) the drag coefficient increases, roughly in proportion to $(\varepsilon)^{1.6}$. Figure 26 presents the coefficient in this form, for $M = 2$. The thickness ratio of the cone is obviously

$$d/x = 2 \tan \varepsilon \quad (27)$$

Substituting this ratio for the angle ε , the pressure coefficient is found increasing approximately as $(d/x)^{1.5}$.

Regarding cones under hypersonic conditions of flow, see J.Aeron. Sci. 1951 p.529, 631, 641 and (74) in Chapter XVII.

- (39) The graph in figure 25, indicating another type of "critical" Mach number, is a very useful aid in the analysis of tested, or in the prediction of transonic and/or supersonic drag coefficients.
- (40) Pressure and drag on *conical heads*; theory:
 - a) Taylor-Maccoll, Theory, Proc.Royal Soc.A 1933 p.278.
 - b) Tabulated evaluation of (a) see reference (6,b).
 - c) Ehret, Hypersonic Similarity, NACA T.Note 2250.
 - d) See also "streamline bodies" in footnote (45).
 - e) Similarity at $M \approx 1$, also in NACA T.Rpt 1094.
 - f) Parker, Optimum Shape, NACA T.Note 3189.
 - g) MIT, Theoretical Cone Tables, published in 1947, discussed by Roberts in J.Aeron.Sci.1954 p.336.
 - h) Characteristics of non-symmetrical cones are reported in J.A.Sci. 1953 p.513, 563; also NACA T.Notes 2236, 2515.
- (41) Pressure and drag of cones, experimental:
 - a) Solomon, Transonic Pressure Distribution, NACA T.Note 3213; J.Aeron.Sci. 1953 p.627.
 - b) Johnston, Cones and Wedges, J.A.Sci.1953 p.378.
 - c) Bergdolt, Transonic, J.Aeron.Sci.1953 p.751.
 - d) Cones in Peenemünde Tunnel, see reference (7,c).
 - e) Ferri, Guidonia Tests, NACA W.Rpt L-152 (1945).
 - f) Drougge, 2° 45° Cone in Transonic Flow, Medd.No. 25 (1948) of Swedish Flygtek. Försöksanstalt (FFA).
 - g) Eggers, Minimum-Drag Bodies, NACA T.Note 3666.
 - h) Sommer, Blunted Cones, NACA Doct. RM A52B13.

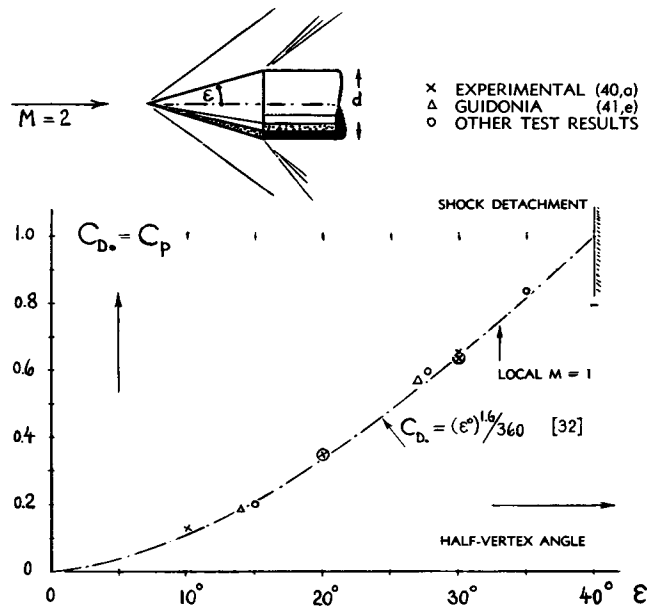


Figure 26. Pressure-drag coefficient of *conical heads* at $M = 2$, as indicated by theory (40,a) and as tested.

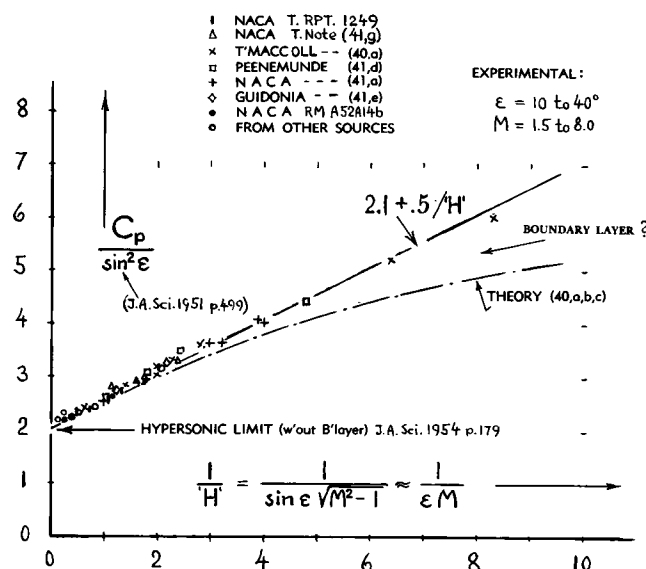


Figure 27. Supersonic pressure-drag coefficient of conical heads, presented in the form of "hypersonic" similarity parameters.

Supersonic Similarity. At higher *supersonic* Mach numbers, pressure and/or nose drag of cones or conical points can conveniently be correlated on the basis of a hypersonic similarity law (40,c,d) by plotting the quantities as in figure 27. It is seen that available experimental data collapse very well when applying this system. The function has practical limitations, however, at both ends of the M' -number parameter. The influence of boundary-layer displacement (at small cone angles and/or at high M' -numbers) is explained in the "hypersonic" Chapter.

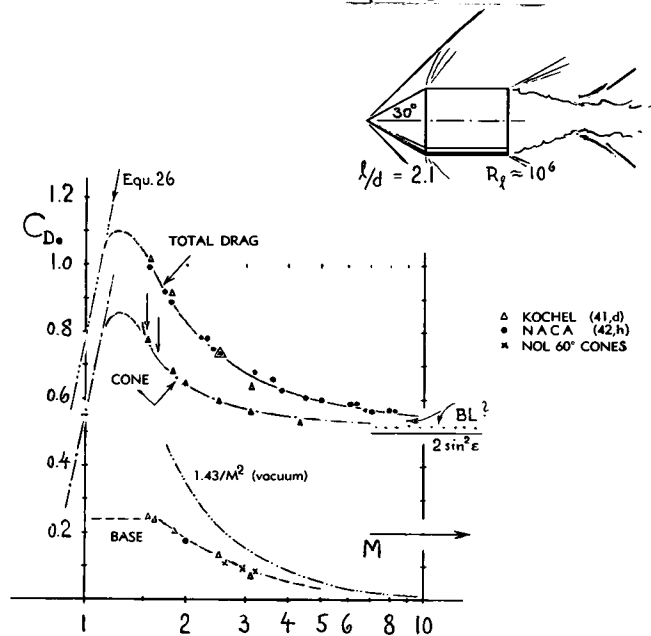


Figure 28. Drag components of a simple and smooth cone-cylinder configuration (42,h).

On the other hand, at smaller Mach numbers (slightly above the "transonic" regime) experimental results consistently seem to indicate drag coefficients higher than indicated by infinite cone theory. On the basis of figure 27,

$$C_{D_0} = 2.1 \sin^2 \epsilon + 0.5 (\sin \epsilon / \sqrt{M^2 - 1}) \quad (29)$$

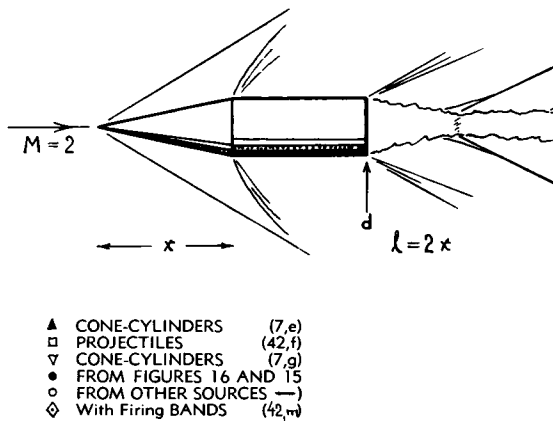
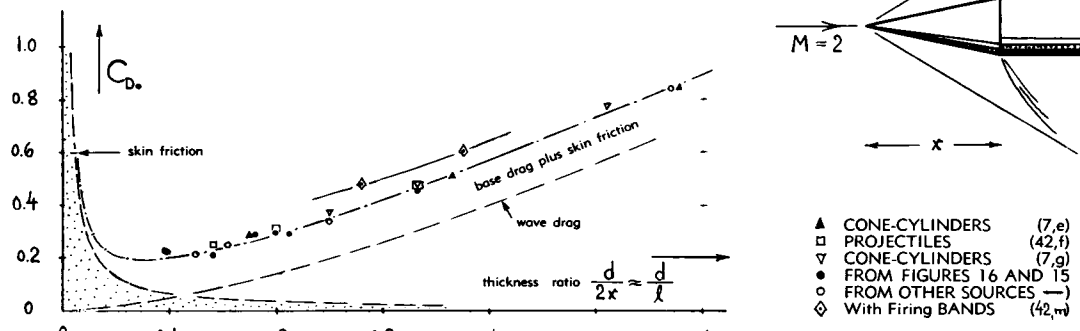
is therefore suggested as a simple approximation. The similarity terms as plotted, do not have a direct meaning for the engineer. Values of C_p as a function of M can easily be computed, however, by means of the last equation; and then be plotted as, for example, in figure 23.

Non-Symmetrical Cones have also been investigated (40,h). In comparison to a circular cone (having the same length and the same-size cross-section area) wave drag is expected slightly to be *reduced* in such shapes; for example, by 3% in a 2 : 1 elliptical cone, and by some 6% in an essentially triangular shape (at M' -numbers between 2 and 9).

Cone-Cylinders. By combining the information available on conical heads, with that on base drag (in section 2 of this Chapter) the drag of simple cone-cylinder configurations can be predicted. Figure 28 presents experimental results on one particular combination, together with an analysis of the drag components involved. The skin-frictional part is comparatively small. The base-drag and cone-pressure components add up properly, except for the highest M' -numbers tested. The total-drag coefficients between $M = 6$ and 8 seem to indicate the presence of some boundary layer (effectively increasing the cone angle). — Downwards, the experimental function is extrapolated across $M = 1$, in the manner as pointed out before (under the subheading "at $M = 1$ ").

Optimum Fineness Ratio. Figure 29 presents an analysis of the drag coefficient of smooth cone-cylinder configurations (at $M = 2$) as a function of their thickness ratio " d/l ". The total length of the bodies is assumed to be $l = 2x$. The total drag, including friction, then reaches a minimum (in relation to frontal area) at or below $d/l = 0.1$. The optimum body thus has a ratio (l/d) above 10 (at $M = 2$ as in the graph). Based on volume (as explained in Chapter VI) the optimum length ratio (carrying the most volume at the expense of a certain drag value) is even higher, somewhere above 15. It must therefore be concluded that the shape of projectiles (with a length ratio l/d in the order of only 5) is dictated by considerations other than aerodynamic drag — such as diameter and working area of the cartridge for example. It seems, however, that modern guided (or not-guided) missiles have, on the average, greater fineness ratios than typical projectiles, shells or bullets.

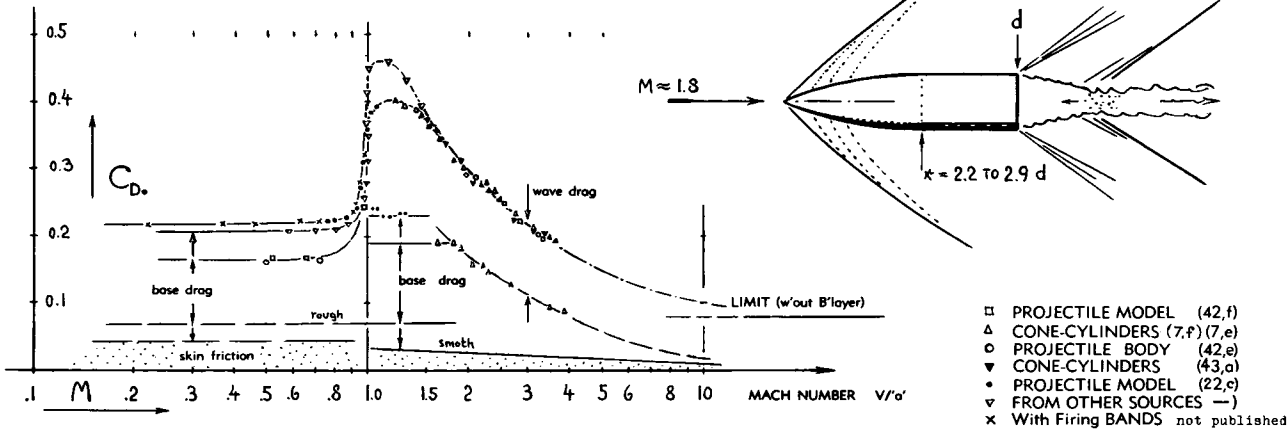
Figure 29. Total drag coefficient of, and analysis of that coefficient, at $M = 2$, for a simple cone-cylinder configuration, as a function of diameter/length ratio.



Ogival Noses, such as used particularly in projectiles, can roughly be approximated by pieces of cones fitted to their shape. Assuming then that (at least in truly supersonic flow) the drag of each element may correspond to the local angle of inclination “ ε ”, the wave drag of such shapes can be appraised on the basis of equation 29. Doing so, an optimum shape (giving a minimum of wave drag in relation to constant frontal area) can be determined by trial-and-error. More elaborate methods have also been applied (40,f). The optimum shape is somewhere between conical and parabolic or ogival (as in many projectile bodies). Preferably, the surface angle “ ε ” should be larger at and near the point (41,g) and smaller, respectively, when approaching the “shoulder” where the nose joins the more or less cylindrical afterbody. The drag differential between equal-length noses may be in the order of — 10% for the optimum shape in comparison to the cone, while the truly ogival shape has a wave drag possibly 10% higher than that of the cone. Experimental results in figure 31 confirm this analysis, if considering that only \approx half of the drag of the shapes presented is wave drag (while the other half is base drag at the M' number as tested). As a function of Mach number, ogival noses have drag characteristics similar to those of cones (see figure 23).

- (42) Projectile bodies at supersonic speeds:
 - a) Erdmann, ZWB Lilienthal Rpt 139/1 p.28.
 - b) Ferri, German-Italian Tests, NACA W.Rpt L-152.
 - c) Kent, Firings, Mech.Engg.1932 p.644.
 - e) Walchner, ZWB Lilith.Rpt 139/1; NACA T.M.1122.
 - f) AVA Göttingen, Tunnel Tests, Doct. 8/14/1939.
 - g) Naumann, A.Inst.Aachen May 1942 for “Rheinmetall”.
 - h) Allen, Configuration (as in figure 28) Tested in NACA Hypersonic Wind Tunnel, Agard Rpt AG17/P7 (1954) p.333; J.Appl.Phys. 1950 No. 11; NACA RM A52A14b.
 - k) Aachen, Projectile Models, ZWB Document FB 1048.
 - m) Eberhard, Shell, Artil. Monatshefte 1912 p.833.
- (43) Boat-tailed projectile-type bodies:
 - a) Lehnert, 9 Models, ZWB Doct. Lilienth. Rpt 139/2.
 - b) Walchner, Projectile Bodies, ZWB Lilienthal Rpt 139/1 (NACA Translation T.Memo 1122).
 - c) Jack, Theory on Boat-Tail Pressure and Wave Drag, NACA T.Note 2972 (1953); with other references quoted.
- (44) An example of an experimental shell (J.A.Sci.1948 p.39) has $d = 4.5$ inch (diameter), muzzle velocity $V_x = 2000$ ft/sec, $M \approx 1.7$, $R_g \approx 5 \cdot 10^6$, $C_f = 0.002$ (turbulent). The rate of spin is roughly such that the circumferential velocity is $\approx 10\%$ of V . Skin friction has been measured by telemetering the deceleration of spin (same source).

Figure 30. Transonic and supersonic drag characteristics of smooth projectile bodies (42).



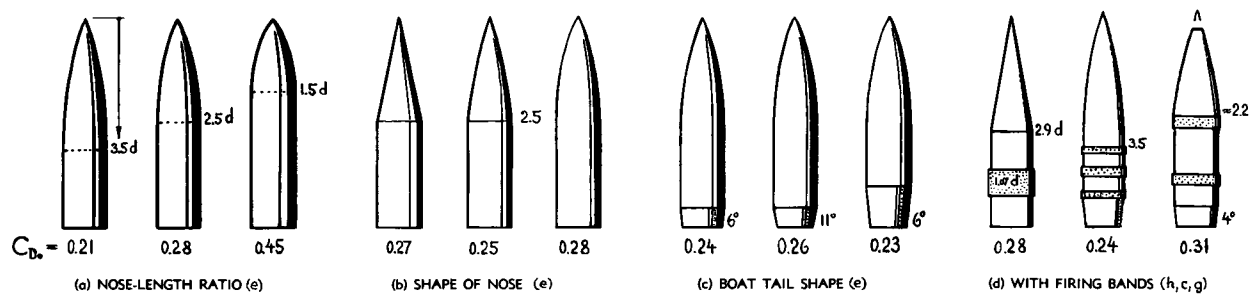


Figure 31. Drag coefficients of various smooth projectile bodies, tunnel-tested at $M = 2$; (42).

Projectiles (44) are most likely the first bodies ever tested (by firing them) at transonic and supersonic speeds. The cone-cylinder configurations in figure 29 can already be considered to represent smooth projectile or shell shapes. Figure 30 shows drag characteristics of this, and of the more familiar type with ogival head form. Skin friction is comparatively small in these bodies, particularly at supersonic speeds (see Chapter XVII). "Transonic" base drag corresponds to the functions in figures 2 and 5. The wave drag originating from the forebody is similar to that in figure 23; for the shapes as tested, this component approximately corresponds to a conical head of 2 times 11° (see then equation 29). Including tested base drag coefficients (7,f) the drag of those smooth projectile bodies is thus explained. The fact that (in figure 30) five different shapes give one and the same experimental function should not be construed, however, as indicating that "all" projectiles would have the same drag characteristics. Results on similar shapes have simply been selected from the material available, so that a common function is obtained in the illustration.

Roughness. Real mass-produced projectiles (shell) are not at all as smooth as the models represented by figure 30. To make them spin, they also have one or two firing bands protruding from their surface. "Viscous" drag (including separation aft of the bands) is *increased*, accordingly. The base drag must then be expected to be somewhat *reduced* (as can be concluded from figure 5). As an example, figure 4 includes one single point (O) showing a reduction from $C_{D_B} = 0.20$ to 0.13 caused by the addition of a firing band to a projectile shape. In regard to total drag, figure 31,d demonstrates an increment, however, over that of smooth shapes. Base drag is thus more than replaced by additional forebody drag.

Boat-Tailing. Figure 31 presents several groups of projectile models, all tested at $M = 2$, showing certain shape effects. The strongest influence is that of the nose length or fineness ratio x/d . The illustration shows also the influence of boat-tailing upon the drag coefficient. Upon reducing the base area, the base drag is effectively reduced in two ways. First, the area is reduced upon which negative base pressure can act; and second, the magnitude of the suction pressure coefficient is reduced in the manner as explained in the "base pressure" section, in connection with figure 5. The experimental results plotted in figure 32 show, accordingly, an appreciable decrease of the base-drag component. However, when departing from the cylindrical shape of the projectile's afterbody, additional wave drag is produced along the boat tail. Utilizing the information presented further down, in the paragraph on "streamline bodies", that drag can very well be estimated. For the purpose of this particular application, we may say that the absolute value of the wave-pressure coefficient on the conical boat tail portions in figures 31 and 32, is equal to that on a corresponding piece of cone having the same slope (indicated by " ε ") as in the forward end of the projectiles considered. We can thus apply the function as in figure 27, or any suitable interpolation formula, such as equation 29, for example. For $M = 2$ (as in figure 26) the wave drag corresponds to

$$C_{Dw} \approx (\varepsilon^\circ)^{1.6} / 360 \quad (32)$$

For an average boat-tail angle of 7° , we then obtain the second drag component plotted in figure 32. For that particular angle (and at $M = 2$) minimum total drag is obtained at $S_B/S_* \approx 0.2$, corresponding to $d_B/d \approx 0.4$.

Boat-Tail Angle. Equation 32 indicates, of course, that the wave drag originating from a boat tail, reduces appreciably as the tail angle is reduced. As far as projectiles are concerned, a straight cylindrical shape is desirable, however, in regard to the mechanics of firing and rifling. The boat-tail length is kept short, therefore, as shown in figure 31. Optimum angles (giving minimum total drag) are then between

5 and 10° . When applying larger angles, the flow simply separates from the boat tail, particularly when firing bands are placed on the forebody, thus increasing BL thickness ahead of the boat-tail portion. For full separation, the body then assumes approximately the same base- and total-drag coefficients as for a "cylindrical" shape (with the boat tail cut off). Figure 32 shows how this happens upon reducing the area ratio below 0.5 or 0.4 (under the particular conditions as tested). In each type of body, we have a \approx constant fore-body coefficient corresponding to wave drag plus skin friction. The base drag decreases as the base area ratio is reduced, while the boat tail's wave drag increases until separation takes place, eventually.

Parabolic Bodies, with cut-off or thickened (blunt-based) rear end, are applied in certain missiles, thus providing a natural outlet opening for the nozzle of the rocket-motor. When finally coasting (after "brennschluss") without jet, base drag must, of course, be taken into account. Figure 32,b presents the drag characteristics of a family of such bodies, at $M = 1.93$. The variation of the components of the drag coeffi-

(45,g) Yoshihara, Cone-Cylinder at $M = 1$; Wright Field Rpt, see Proc.Midwest.Conf. Fl.Dy.Univ.Mnnesota 1953.

- (45) Theoretical characteristics of "streamline" bodies:
 - a) vonKármán-Moore, Bodies, Trans ASME 1932 p.303.
 - b) Lighthill, Bodies of Revolution, ARC RM 2003(1945); and Quart.J.Mech. and Appl.Math. 1948 p.90.
 - c) Fraenkel, Evaluation of (b) Theory, ARC RM 2842.
 - d) Heaslet-Spreiter, Three-Dimensional Transonic Flow, NACA T.Note 3717 (1956).
 - e) Statements in certain of the available references (not listed here) saying that a particular "solution" is "complete" and that it applies to *all* speeds from subsonic to hypersonic Mach numbers, are misleading. In the fine print it is usually found that such solutions only apply to "very slender" shapes.
 - f) A discussion of transonic similarity principles as developed by Oswatitsch and Berndt, is included in (d).
 - g) Yoshihara, Solution for Cone at $M = 1$, evaluated in (d).
 - h) Hayes, Transonic Similitude, J.A.Sci.1954 p.721; this paper gives a clear exposition of conditions at $M = 1$.
 - i) VanDyke, Supersonic Theory, J.Aeron.Sci.1951 p.161; see also NACA T. Rpt 1081 (1952).
- (46) Experimental investigation of streamline bodies:
 - a) Danforth, Wing-Flow Method, NACA RM L7K12.
 - b) Figure 35 in Chapter XV shows a few results on streamline bodies extending to and slightly beyond $M = 1$.
 - c) Lopatoff, Spheroid, NACA Doct. RM L51E09.
 - e) Pressure distributions in NACA Documents RM L51L07a, L52D21a, L53H04 and L53L28a.
 - f) Skin friction in NACA Docts. RM L51B12 and L52A14.
- (48) Boat-tailed missile-type or parabolic bodies:
 - a) Chapman-Perkins, NACA T.Rpt 1036 (1951).
 - b) Bromm-Goodwin, 7 Bodies, NACA T.Note 3708.
 - c) See Footnotes (8,a) and (8,d).
 - d) Adams, Theoretical Analysis, NACA T.Note 2550.
- (49) Separation from the boat-tail is clearly demonstrated by schlieren pictures in NACA T.Rpt 1036.
- (50) Analysis of "optimum" body shapes:
 - a) Sears, Projectile, Qu. Appl. Math. Vol. 4 p.361 (1947).
 - b) Ward, Bodies, Quart. J. Mech. Appl. Math. 1949 p.75.
 - c) Graham, Aero.Quart. 1955 Pt. 2 p.99 and NACA T. M. 1421.
 - d) Heaslet, Ducted Shapes, NACA Tech. Rpt 1256(1956).

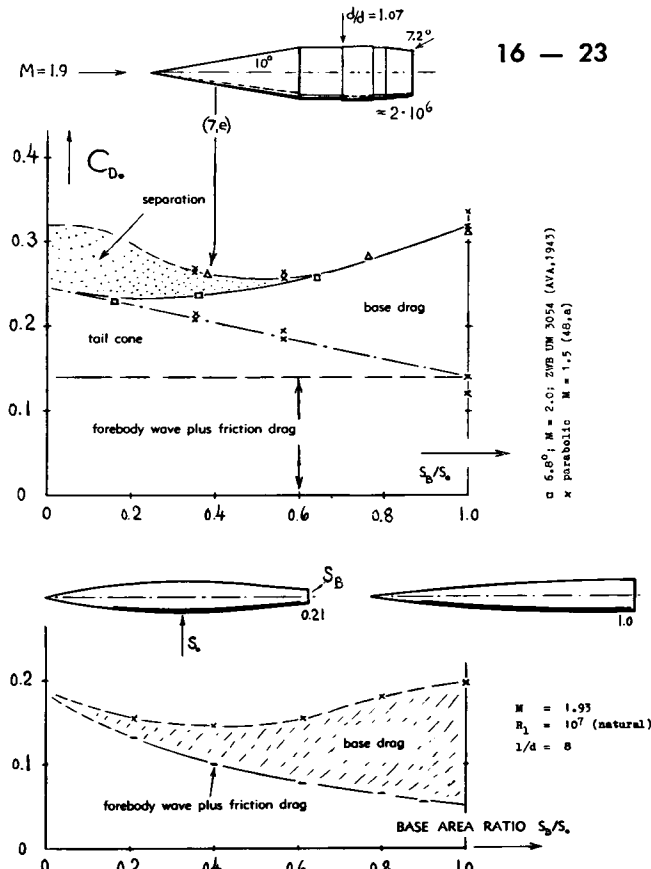


Figure 32. Drag analysis of *boat-tailed* bodies at $M \approx 2$;
(a) various "cylindrical" projectile models and
(b) a group of parabolic missile shapes (48,b).

cient as a function of base-area ratio is different from that of the projectiles insofar as the shape of the forebody in the group investigated, changes together with the area ratio. Minimum drag is obtained at a similar ratio, however ($S_B/S_0 \approx 0.4$). Flow pattern and drag coefficients of parabolic bodies are also a function of Reynolds number. At R' numbers below the range of BL transition, shock-induced separation from the rear end (ahead of the base) is easily found (49). Such separation can be eliminated or postponed by introducing (forcing or stimulating) turbulence. Consequences are:

- a) The suction pressure at the base is increased because of increased BL momentum and stronger turbulent mixing. Based upon the forebody's frontal area, the increment may be in the order of $\Delta C_{D_0} = 0.02$.
- b) The forebody drag is increased because of friction. For example, at $R_1 = 3 \cdot 10^6$, $C_{f,turb} \approx 0.003$ and $C_{f,lan} = 0.001$ (or even smaller); the corresponding increment of the body's coefficient is in the order of $\Delta C_{D_0} \approx 0.03$.
- c) Wave drag is increased because of expansion along the boat tail. This component roughly replaces the pressure drag due to separation.

Depending upon the magnitude of the various components involved, the total drag is then changed; and it is certainly increased as far as the skin-friction component is concerned.

Double Cones. For rotationally-symmetric bodies in transonic and supersonic flow, having somehow tapering or pointed afterbodies, it seems there is no simple solution available among the theoretical treatments listed. Reference (45,c) presenting an evaluation of the essentially linearized and slender-body theory in (45,b) permits an, at least qualitative, appraisal of the pressure forces originating along tapering afterbodies, however. For example, the drag of *double cones* as in figure 33, is equal to that of the forebody (as per figure 27 or as indicated in figure 23) plus a basic amount for the afterbody (assumed to have the same but negative surface slope as the forebody) equal to that of the forebody, plus a component of "interference" wave drag. For the double cone, this component (reflecting increased expansion around the body's "shoulder" corresponding to an angle of deflection twice the cone angle " ϵ ") is roughly equal to 100% of the basic cone-drag coefficient. In other words, the wave drag of the *afterbody* is really twice that of the forebody, in the case of the double cone considered. Including skin friction (assumed to correspond to $C_f = 0.002$) we thus find an optimum thickness ratio for the double cone configuration in the order of $d/l = 5$ or 6% only. The graph also demonstrates that a single cone (having a base-drag coefficient in the order of $C_{DB} = 0.2$ as in figure 2) presents drag values appreciably smaller than those of the double cone, at diameter/length ratios above $\approx 15\%$. Comparison with the cone-cylinder configuration in figure 29, shows on the other hand, that base drag is less expensive than "conical" drag at diameter-length ratios below 10%. All this analysis is made for $M = 2$. Corresponding results can also be worked out for other M'numbers. We could also evaluate certain optimum boat-tailed shapes (somewhere between the three types considered).

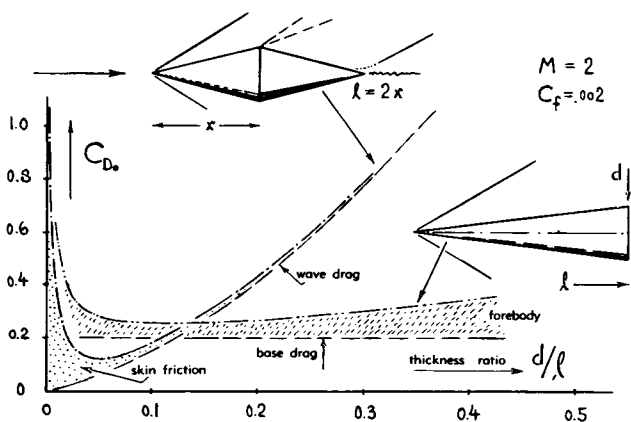


Figure 33. Theoretical drag coefficients of single and double cones at $M = 2$, as a function of diameter ratio.

Critical M'numbers:
at $M = 1.4$ Max. Fin Drag
at $M = 3.0$ Base Drag
at $M = 1.2$ 14° Cone Drag
at $M = 3.0$ 46° Cone Point

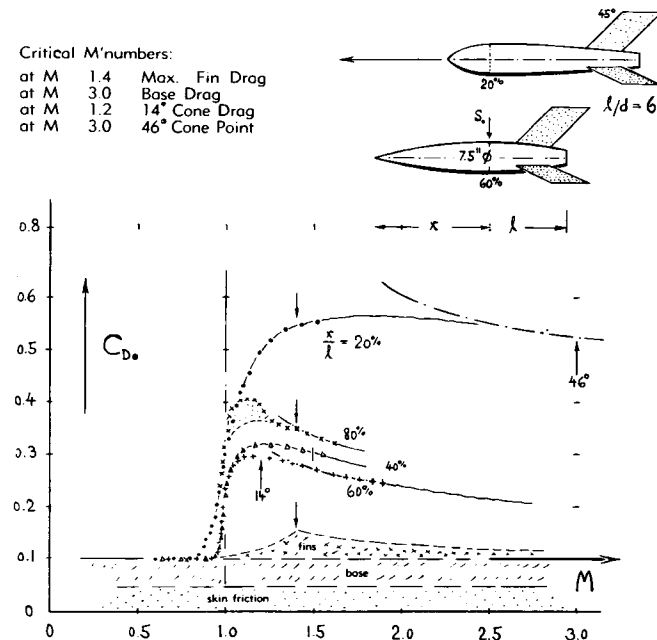


Figure 34. Transonic drag characteristics (52,b,c) of a series of fin-stabilized bodies of revolution, varying in the location of maximum thickness.

Streamline Bodies, to be applied in transonic and supersonic flow, are meant to be more or less slender shapes, having a *pointed nose* and a somehow tapering afterbody form, possibly ending in a point as in the subsonic type of "streamline" bodies. Finding optimum body shapes has recently become a mathematical venture (50). Inasmuch as viscosity is not included in such theoretical studies, their practical consequences are not too great, however. As far as simple "streamline" bodies are concerned, anything between conical and ogival is close to "optimum". An approximation to such a shape is, for example, the combination of a more or less conical head with a cylindrical middle body and a conical afterbody. Reference (45,c) predicts for such a combination an afterbody wave-drag coefficient equal to that of a head cone having the same vertex angle, with no "interference" effect, as long as the middle portion is long enough (say, with a length in the order of that of fore and/or after cone). We can then conclude that slender parabolic shapes (such as that of the missile in figure 37, for example) follow approximately the same principles, and that the supersonic wave drag of a symmetrical body of this type (with maximum thickness at 50% of its length) is approximately, and/or at least, equal to twice the forebody drag. Experimental results to prove these predictions are practically non-existent (46,b). The tested total drag coefficients of bodies such as those of the missiles, for example, shown on these pages, are to some degree the consequence of viscous skin friction variations. A systematic series of tests on fin-stabilized "parabolic" bodies (52) permits some evaluation, however, in respect to the drag of the body as such.

"Critical" M'Numbers. Flight-tested drag coefficients of a group of bodies having a fineness ratio $l/d = 6$, are presented in figure 34. After subtracting a value for skin-friction plus base-pressure drag (assumed to be equal to the subsonic drag coefficient in the order of 0.1), the rest is wave drag originating from the body as well as from the fins. Corresponding to an angle of sweep of 45° , the critical M'number of the latter ones is $1/\cos 45^\circ = \sqrt{2}$. Above this number, the fin drag coefficient (calculated through application of the principles presented in the "supersonic" chapter) is as indicated in the graph. The "critical" M'number of the body proper corresponds to the vertex angle of the conical point. The Mach numbers at which "supersonic" cone flow becomes fully established (see figure 25) are indicated in the graph. It is only above these latter numbers, that we can expect a truly supersonic flow pattern and a "supersonic" drag function for each of the shapes investigated. Cone angles equivalent to each of the streamline bodies, have empirically been determined in such a manner that the "supersonic" drag function calculated on the basis of equation 29, matches in each case the tested drag coefficients. It is then realized that the 'bluffest' nose shape (corresponding to $x = 0.2 l$) has a very wide "transonic" phase (extending to $M \approx 3.0$ and that this fact is the reason for the rising trend of the drag coefficient for this shape (as far as tested). The coefficient grows within this phase to a level appreciably above those of the other three bodies represented in the graph.

Thickness Location. The cone angle discussed above is of course a function of the thickness location of the bodies considered. Figure 35 shows the total drag coefficient of the fin-stabilized configurations plotted as a function of x/l . Minimum drag (at $M = 1.5$, as at other M'numbers between 1.0 and 1.6) is obtained for a location at $x \approx 0.55 l$. The wave-drag components originating from fore and afterbody, respectively, are obviously "balanced" at this location.

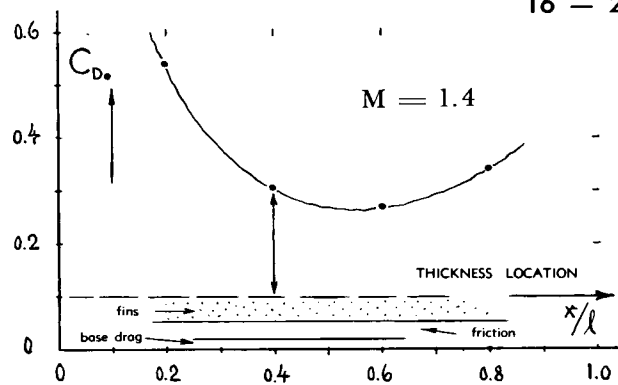


Figure 35. Total drag coefficients of several fin-stabilized bodies (of the type as in figure 34) as a function of their thickness location.

Transonic Drag. Information on the wave drag of conical and/or streamline shapes at transonic speeds (where the bow shock wave is *detached*) is mostly empirical to this time. Figure 23 shows characteristics of a particular conical head; transonic characteristics of other cones are as suggested in the graph.

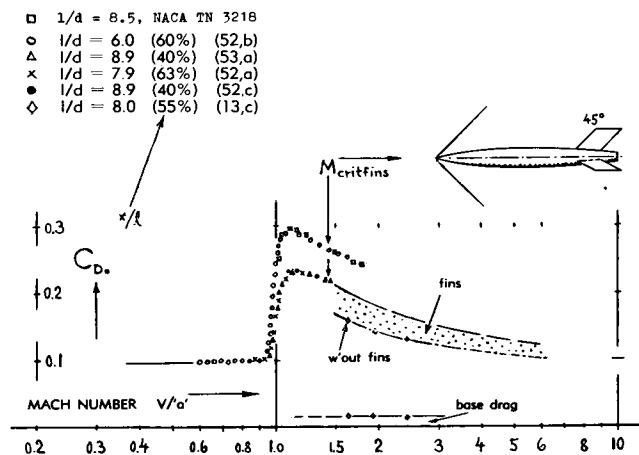


Figure 36. Transonic drag coefficient (on frontal area) of flight-tested fin-stabilized missile models (52).

Fin-Stabilized Missile. The drag coefficient of a "streamline" missile at transonic speeds is presented in figure 36. Drag divergence (at $M \approx 0.95$) corresponds to the body shape (see figure 37 in Chapter XV) while the lower critical number of the thin fins having a 45° angle of sweep (see figure 19 in Chapter XV) seems to be slightly higher than that of the body. The steep increase of the coefficient at $M \approx 1$ is similar to that of the streamline shapes in figure 34. The M'number for shock attachment (and for "supersonic" type of flow) at the body's conical nose is roughly $M = 1.1$. The shape of the drag function above this M'number is partly dictated by the fins, whose drag coefficient is expected to reach a maximum at their upper critical M'number (which is in the order of 1.4). From there on, pure supersonic functions should be expected of the type as indicated in the graph.

- (51) Aerodynamic investigation of RM-10 missile:
 - a) Evans, Tunnel and Flight Tests, NACA T.Rpt. 1160.
 - b) Jackson, Drag and Base Flight Tests, NACA TN3320.
 - c) Hasel, in Supersonic Tunnel, NACA Doct. RM L52A14.
 - d) Czarnecki, NACA T.Rpt 1240 (T.Notes 3165&3166)
 - e) Carros, Correlation of Results, NACA T.Note 3171
 - f) Piland, Finless Flight Model, NACA Doct. RM 54H09.
- (52) Transonic drag of fin-stabilized streamline bodies:
 - a) Alexander-Chauvin-Rumsey, NACA RM L8A05.
 - b) Katz, Thickness Position, NACA RM L9F02.
 - c) Hart-Katz, Several Shapes, NACA RM L9I30.
 - d) Thomson, Thickness Location, NACA RM L8A28b.
 - e) Welsh-Moraes, Slender in Flight, NACA RM L51E18.
 - f) Katz, Nose Fineness, NACA Doct. RM L7B19.

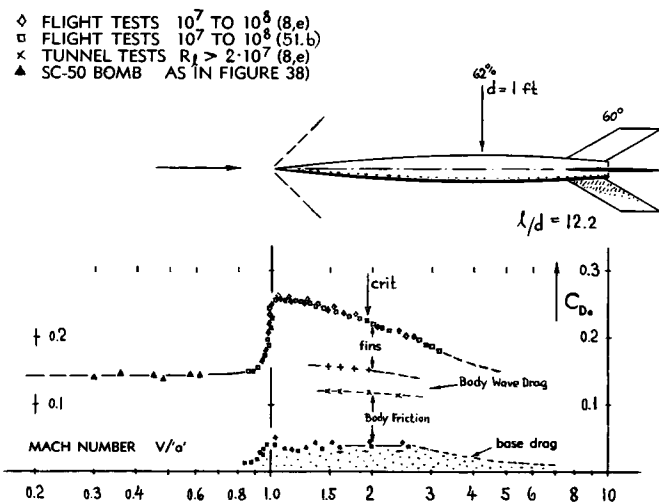


Figure 37. Subsonic to supersonic drag characteristics of the NACA's RM-10 experimental missile (51).

The RM-10 Missile is an experimental "vehicle" developed and extensively tested by the NACA (51) full-scale as well as on tunnel models, as a standard configuration suitable for transonic and supersonic speeds. The upper critical M'number of the 60° swept fins is in the vicinity of 2. A small hump or discontinuity can be expected, accordingly, at that number. Tunnel-tested values for base, skin-friction and forebody-wave drag are indicated in figure 37. Using these components and what is known about their variation as a function of M'number, the missile's drag coefficient is then extrapolated into the range above $M = 3$, where tests have not yet been carried out. In spite of the fins, the total coefficient is lower than that of the projectile shapes as in figure 30, particularly at Mach numbers between 1 and 2.

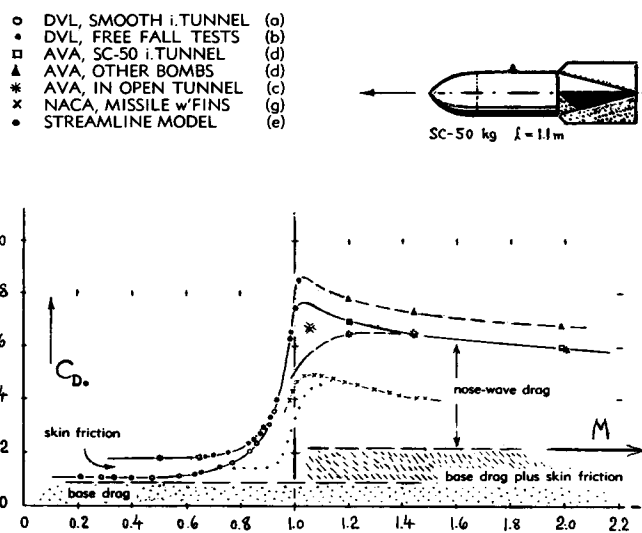


Figure 38. Transonic drag characteristics of "SC-50" and of similar bombs, as determined on wind-tunnel models and by full-scale free-fall tests (55).

Drag of Bombs. Figure 38 presents the drag characteristics of one particular bomb (and those of similar configurations) from subsonic, through transonic and into supersonic speeds. Approaching $M = 1$, the drag coefficient increases from a level of $C_{D_0} = 0.1$ or 0.2, to a maximum value of ≈ 0.8 ; a fact that can only be explained on the basis of flow separation combined with a compression shock originating from afterbody tail-cone shoulder or wake, respectively. For a boat-tail angle of the SC-50 bomb between 18 and 19° , a separated flow pattern can be expected at supersonic speeds. The drag is then essentially that of a comparatively bluff "projectile" shape without boat tail. On the basis of figure 5 we can estimate a corresponding "transonic" base-drag coefficient in the order of 0.11. At higher supersonic Mach numbers, the total drag coefficient is correctly at a level roughly equal to that of the bluntest shape in figure 34. However, within the extended transonic phase, drag characteristics of the bombs are entirely different from those of the parabolic bodies (in figure 34), exhibiting above all the high peak values between $M = 1.0$ and 1.2 (as described above). The reason for this difference must be in the afterbody shape. — For comparison, figure 38 also includes results on a smooth and *streamline* bomb model (55,e). Subsonic magnitude and slope of the drag coefficient at $M \approx 1$, are appreciably lower than those of the "SC-50" bomb. Flow pattern and drag components of that "streamline" shape are thus close to those of the missile configurations (as in figures 34 and 36).

Rounded Noses. The drag coefficient of the sphere is shown in figure 20. A hemispherical head is also represented in that illustration. All such "round" shapes display a certain drag component rising across the transonic regime in proportion to the stagnation pressure as in figure 1. Rounding now the conical tip of a streamline body in the manner as shown in figure 39, some such influence of stagnation-pressure can very well be expected. The graph demonstrates that a really rounded nose shape, having a frontal area corresponding to the ratio of $(d_{no}/d)^2 = 0.78^2 = 0.6$, produces significantly increased drag coefficients. Analysis suggests that the coefficient should further grow, as indicated in the graph. The drag function is then similar in character to those of the bluff-nosed bodies in figures 34 and 38. Round noses are also systematically investigated (53,c) on a conical body having a length $l = 3 d$. At Mach numbers between 3 and 7, the optimum diameter ratio (giving minimum drag on frontal area) is approximately 15%. At $M = 2$, that ratio is $\approx 25\%$, growing further as the M'number is reduced further.

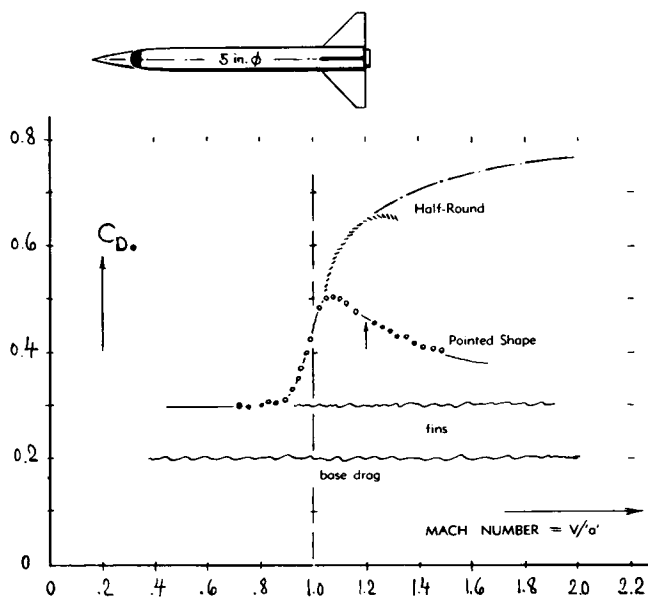


Figure 39. Drag characteristics of fin-stabilized body, flight-tested for three different nose shapes (53a).

- (53) Influence of nose bluntness on drag:
 - a) Hart, Nose Shape, NACA Doct. RM L50I08a.
 - b) Influence of Conical Shields Ahead of Body Nose, NACA RM L6J16a, L6K08a and L8L07a.
 - c) NACA, Blunt Cone Nose, Doct. RM A52B13.
 - d) NACA, Documents RM L6D10, L6G27, L7B19, L9C11.
 - e) Hart, Transonic Flight, NACA RM L51E25.
 - f) Stalder, Hemispherical Head with Spike, NACA T.Note 3287. Drag is defined in this report for $p_B = 0$.
- (54) In several graphs (figures 34, 36, 37, 38, 40) a constant coefficient has been assumed for skin friction. Actually, that coefficient must be expected to reduce as the Mach number is increased.
- (55) Transonic drag of fin-stabilized bombs:
 - a) Goethert, Tunnel Tests, ZWB Doct FB 1663 (1942).
 - b) Goethert-Kolb, SC-50 kg Drop Tests, ZWB Document UM 1173 and Tech.Berichte 1944 p. 252; NACA TM 1186.
 - c) Roth-Hahn, "Fritz" Bomb, AVA Doct 1941/8/13.
 - d) Weber, Various Bombs, ZWB Doct UM 3127 (1944).
 - e) Stoney-Royall, Series of Bombs, NACA RM L56D16.
 - f) Aberdeen Ballistic Res.Laboratory Rpt No. 647.
 - g) NACA, "Cylindrical" Missile, Doct. RM L50I08a.

Conical Shield. Tests have been carried out on a round-nosed body with a rod sticking out ahead (53,b). By means of a "windshield" (conical point on that rod) protruding 1.6 body diameters ahead of a round nose similar to the one in figure 39, drag is reduced from $C_{D_0} = 0.82$, by $\Delta C_{D_0} = 0.19$, at $M = 1.4$; while a pointed body shape extending to the same distance, has an only slightly lower drag coefficient ($C_{D_0} = 0.62$). Similar results are reported in (53,f) for a "spike" protruding from a hemispherical head shape by \approx one head diameter.

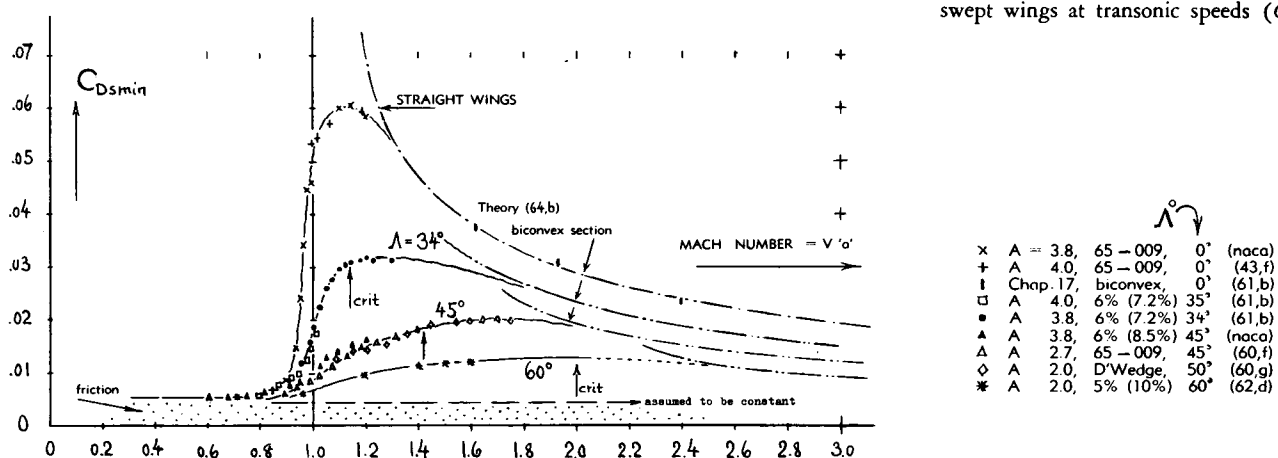
5. DRAG OF SWEPT AND POINTED WINGS

Swept wings and the related type of "pointed", "conical" and/or triangular wings are specifically suitable (at least in respect to drag) to be used at transonic speeds.

(A) CHARACTERISTICS OF SWEPT WINGS

Experimental Results. Some experimental results on swept wings at high subsonic speeds and at $M \approx 1$, are presented in figures 30 and 31 of Chapter XV. Partly the same and other drag coefficients are plotted in figures 40 (and in 42) continuing those functions across the transonic range. Most of the results in figure 40 have been obtained by free-flight technique (60) on "yawed" type wings. Note that results of two "sheared" wings are included in the graph. One of these, with 45° angle of sweep and with a 65A006 foil section (defined in the direction parallel to the axis of symmetry) corresponds to an 8.5% "yawed" type wing as indicated. The other one, having $\Lambda = 60^\circ$ and a 64A005 section, represents a $\approx 10\%$ thick yawed-type wing. The thickness ratio of a "yawed" wing is simply that of a "sheared" wing multiplied with cosine Λ .

Figure 40. Drag coefficient of "yawed" type swept wings at transonic speeds (65).



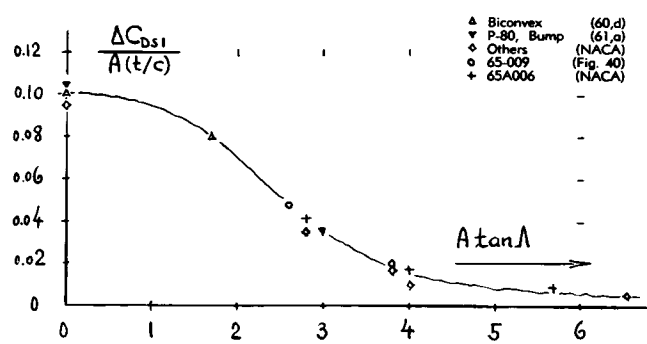


Figure 41. Drag of small-aspect-ratio swept wings at $M = 1$, correlated on the basis of transonic area rule.

Drag Rise. Swept wings at subsonic speeds are treated in Chapter XV, including their critical Mach number (page 15-22). The drag rise above M_{DD} is described on page 15-38 and illustrated in figure 56 of the same chapter. At and in the vicinity of $M = 1$, available experimental results on small-aspect-ratio wings can be correlated on the basis of the transonic area rule (see in a later section of this chapter). Application of this rule suggests that the type of plot as in figure 49 can also be made for a group of swept wings having the parameter $(A \tan \Lambda) = \text{constant}$. We have plotted in figure 41, for $M = 1$, the corresponding slope parameter

$$\Delta C_D / (A t/c) \quad \text{as a function of} \quad (A \tan \Lambda) \quad (37)$$

The result (only to be expected to be correct for small aspect ratios and/or for larger angles of sweep) is similar in character to the $(\cos)^3$ function in figure 43.

$M(\max)$. The drag coefficient of larger-aspect-ratio straight wings reaches a peaked maximum value at or in the close vicinity of $M = 1$. We may, therefore, also call this number " $M(\max)$ ". Corresponding to the cross-flow or cosine principle as explained in Chapter XV (see figure 26 in that chapter), the upper critical Mach number of swept wings and the corresponding value of $M(\max)$ for the wing panels (rather than for the whole wing) is increased to

$$M(\max) = 1/\cos \Lambda \quad (38)$$

To say it in different words, at this Mach number, the leading edges of cylindrical wing panels come in contact with the Mach cone originating from the vertex point; and the Mach angle in this condition is simply

$$\mu(\max)^\circ = 90^\circ - \Lambda^\circ = \epsilon^\circ \quad (39)$$

In conclusion, the drag coefficients of swept wings are expected to show maximum values at or near $M(\max)$ rather than at $M = 1$.

"Supersonic" Drag. At Mach numbers above $M(\max)$, linearized theory (64, b) gives explicit answers in regard to the wave drag of swept wings. If defining the foil-section thickness ratio (t/c) in the plane normal to the panels' edges (as in Chapter XV), the wave drag due to thickness can be written as

$$C_{D\Lambda}/C_{D0} = \cos^2 \Lambda / \sqrt{1 - (\tan^2 \Lambda / (M^2 - 1))} \quad (42)$$

where C_{D0} represents the wave drag at zero angle of sweep (see Chapter XVII). The wave drag of wings with symmetrical double-wedge sections, then corresponds to

$$C_{D\Lambda}/(t/c)^2 = 4 \cos^2 \Lambda / \sqrt{M^2 - 1 - \tan^2 \Lambda} \quad (43)$$

Figures 40 and 42 show that this function decreases as the Mach number is increased, in a manner similar to that of straight wings. The graph also shows that the level of the wave-drag coefficient reduces significantly as the angle of sweep is increased. This is true for "yawed" type swept wings, i.e. when defining the section thickness ratio (t/c) as above. However, when considering "sheared" wings (where the panel's foil-section chord is defined in the direction of flow or flight) the drag coefficient comes out to be *higher* in swept wings than in straight wings. The theoretical wave drag coefficients for this type of swept-wings are obtained from those shown in the illustrations, by multiplying them with $1/\cos^2 \Lambda$. Coefficients for wings in this definition of sweep, eventually reduce to those of straight wings, i.e. at higher supersonic Mach numbers (63).

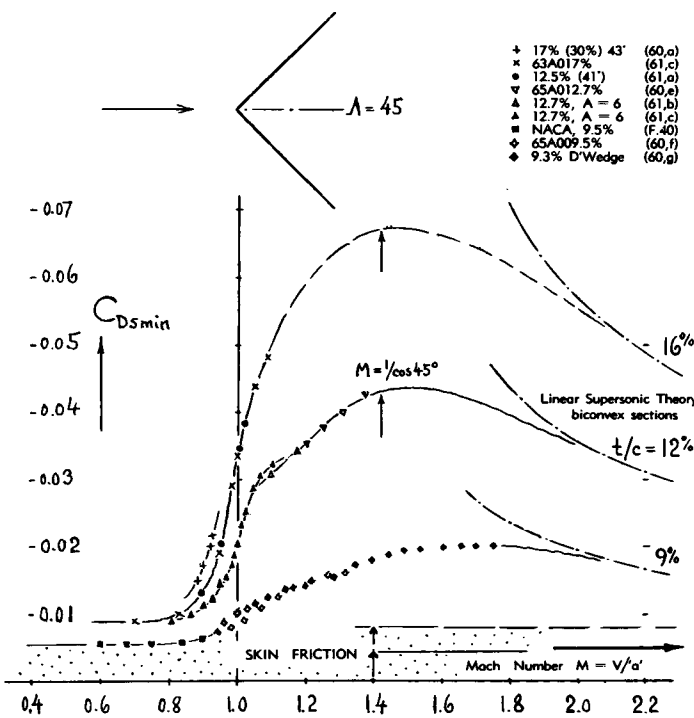


Figure 42. Drag coefficient of wings having 45° angle of sweep, but varying in thickness (and aspect) ratio (65).

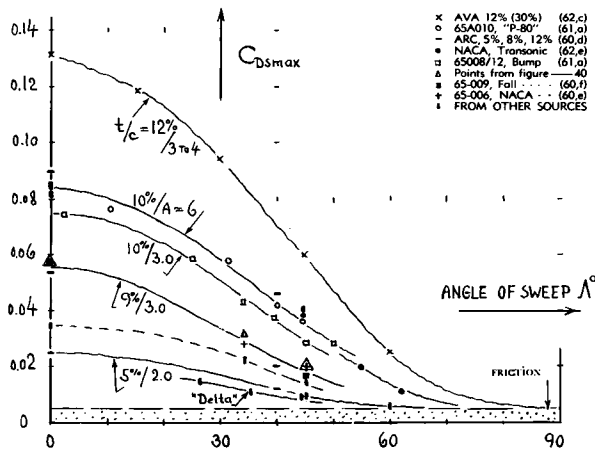


Figure 43. Maximum (see text) transonic drag coefficients of non-lifting wings as a function of the angle of sweep.

Transonic Hump. The experimental results in figures 40 and 42 are expected (65) somehow to connect across the transonic range to the lines representing supersonic theory. Such theory also predicts a certain peak to occur at M_{∞} (max) as defined by equation 39. It seems, however, that the theoretically possible peaks of the drag coefficient do not come true. Rather, extended "humps", such as suggested in figures 40 and 42, may be expected instead. Such hump values are plotted in figure 43. Inasmuch as transonic results on swept wings, extending to and beyond M_{∞} (max) are rare, "maximum" values have also been included in the graph, "as measured" (63). They do not correctly represent the maximum coefficients; they may give an indication, however, of the variation to be expected as a function of the angle of sweep. It is seen that the transonic coefficients of swept wings having constant foil sections, reduce ap-

preciably as the angle of sweep is increased. The test points suggest that roughly:

$$C_{Dw\lambda} / C_{Dw0} = \cos^n \lambda \quad (40)$$

where n is between 2.0 and 2.5 for "sheared" wings and probably between 3.5 and 4.0 for "yawed" wings.

Thickness. Besides the angle of sweep, other parameters have of course an effect upon the transonic drag of wings, such as aspect ratio and thickness ratio in particular. If assuming that pressure or wave drag at or near $M = 1$ increases as $(t/c)^{5/3}$ (as in two-dimensional foil sections, see Chapter XVII) the results in figure 43 may collapse onto a common line when plotting

$$C_{Ds\lambda} / (t/c)^{5/3} \text{ or } C_{Ds\lambda} / (t/c)^{2/3} \quad (41)$$

instead of the plain coefficient. Figure 42 demonstrates the influence of the thickness ratio on the drag of a group of wings having a 45° angle of sweep. Combination of low thickness ratio with a suitable angle of sweep (and possibly with a low aspect ratio) thus tends to produce transonic drag coefficients which are only a fraction of those found in the ordinary subsonic type of airplane wings. In fact, employing an angle of sweep of 60° in combination with $t/c = 6\%$ ("yawed") or 3% ("sheared"), a transonic drag function is obtained hardly to be distinguished from the skin friction component ($C_{Ds} \approx 0.005$).

Drag Due to Lift. As in the case of straight wings (see in Chapter XVII) the drag-due-to-lift ratio of swept wings applied at Mach numbers where the LE flow pattern is "supersonic", is expected to be equal to their "lift angle"; thus for conditions where $\mu > \epsilon$,

$$dC_d / dC_L^2 = d\alpha / dC_L = 0.25 \sqrt{M^2 - 1 - \tan^2 \lambda} \quad (44)$$

Inasmuch as the angle of attack required to produce a certain lift coefficient in swept wings under "supersonic" conditions, is smaller than in straight wings, this type of drag is expected to be lower than in those wings.

Transonic Theory. Within the transonic M' number range (where the wing panels are *swept behind* the Mach cone originating from the vertex point) conditions are more complicated. Because of the subsonic-type of flow, a certain suction force can be expected to originate "around" the leading edge. For "slender" wings (where $\sqrt{M^2 - 1} / \tan \lambda$ is small) there is a solution available for this type of flow pattern (discussed in the section on "conical wings"). Some theoretical analysis is also presented in (64, d). It appears, however, that suction does often not develop to any significant extent. We will therefore revert to a statistical approach.

-
- (60) Free flight tests on swept wings at transonic speeds:
 a) Kolb, Swept Wings, unpublished DVL results (1944).
 b) Mathew-Thompson, Rectangular and Swept, NACA T. Note 1969; see Proc. Int. Aeron. Conf. 1949 p.582.
 c) See the references under (36).
 d) Kell, Falling Test Vehicle, ARC RM 2902 (1955).
 e) NACA, Docts. RM L6L24, L7C05, L52F30.
 f) Mathews-Thompson, 65-009 Wings, NACA T. Rpt 988.
 g) Pittel, Tapered Wings, NACA T. Note 3697 (1950).
 (61) Transonic results by tunnel "bump" technique:
 a) Weaver, P-80 Tests, J. Aeron. Sci. 1941 p.31.
 b) Polhamus, Summary, NACA T. Note 3469 (L51H30).
 c) NACA Docts. RM L9B25, L9G26, L50A12, L50B03a.
 d) Turner, Family of Wings, NACA T. Note 3468 (1955).

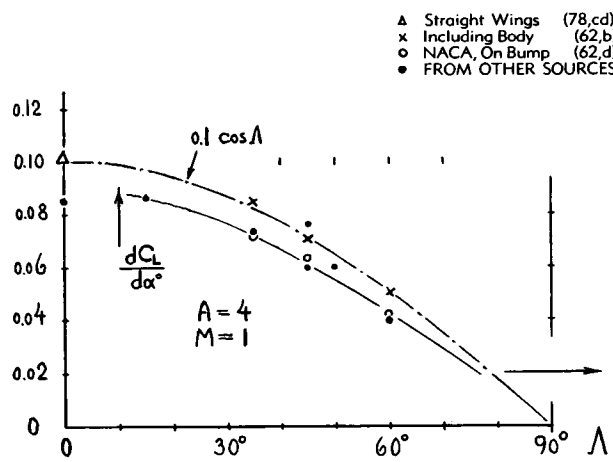


Figure 44. Lift-curve slope at $M = 1$, of various wings, having $A = 4$, as a function of their angle of sweep.

Lift Angle. As long as LE suction does not develop, the combined (induced plus wave) pressure drag simply corresponds to the angle of attack. As for "supersonic" LE, we will thus assume that

$$C_{Dw} = C_L \tan \alpha; \quad dC_D/dC_L^2 = d\alpha/dC_L \quad (45)$$

To obtain drag due to lift, we then have to know the "lift angle". In aspect ratios larger than "small", experimental results may be used. *Figure 44* shows as an example, the L-curve slope at $M \approx 1$ of various swept wings, all having an aspect ratio of 4 (and airfoil sections of or similar to 65-006, tested at $R_c \approx 10^6$). Without any claim as to complete theoretical justification, we make the statement that the lift-curve slope reduces in proportion to the cosine of the angle of sweep (68).

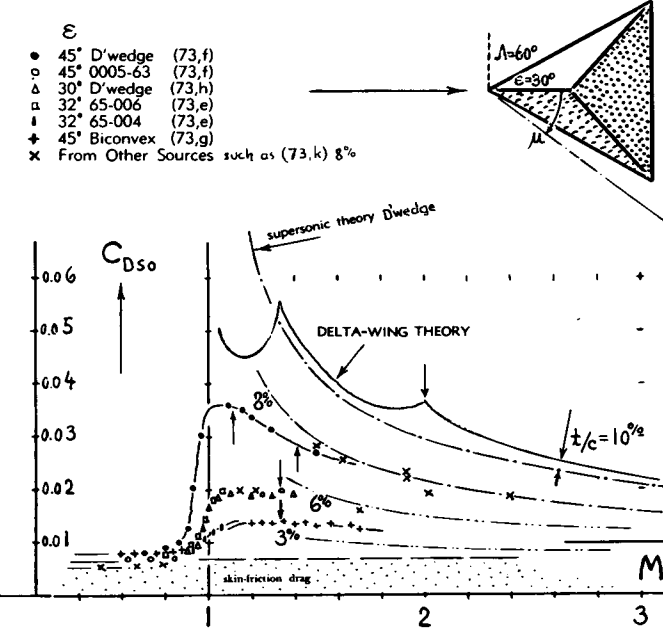


Figure 45. Wave-drag coefficients of various "delta" wings at transonic and supersonic speeds.

(B) POINTED AND/OR TRIANGULAR WINGS

Triangular and/or delta wings could be considered to be variants of swept wings. In practical applications they always have small aspect ratios, however. Under such conditions, their flow pattern is "conical", in a manner similar to that of circular cones as described in a previous section of this chapter; and their treatment is different from that of swept wings, accordingly.

"Critical" M'Numbers. Triangular wings such as those in figure 45 for example, are theoretically expected to have three different "critical" Mach numbers; corresponding to the angles of sweep at the trailing edge, at the line on which the maximum thickness is located and at the leading edge. A "delta" wing (having a straight trailing edge) encounters a first critical at $M = 1$, and a last critical when the leading edges come in contact with the Mach cone originating from the vertex point. The Mach number corresponding to the leading edge angle, is as indicated by equation 38, when considering Λ to be the sweep angle of the leading edges. Below this number, the edges are thus called "subsonic" while above that M'number, they and the rest of "delta" wings are subjected to an entirely supersonic type of fluid flow. The characteristics of such wings can accordingly be presented as a function of the parameter $\tan \varepsilon / \tan \mu$, where $\varepsilon^\circ = 90^\circ - \Lambda^\circ$. Inasmuch as $\tan \varepsilon = A/4$ and $\tan \mu = 1/\sqrt{M^2 - 1}$, characteristics can also be presented against the "reduced" aspect ratio

$$A \sqrt{M^2 - 1} = 4 (\tan \varepsilon / \tan \mu) \quad (46)$$

Thickness Line. The coefficient of drag due to thickness is expected to show a peak at $\tan \varepsilon / \tan \mu = 1$, i.e. at the Mach number where $\mu = \varepsilon$. The "critical" Mach number corresponding to the angle of sweep indicating the location of maximum thickness, in terms of $\tan \varepsilon / \tan \mu$, is defined by $\tan \varepsilon / \tan \varepsilon_t$ where "t" denotes the vertex angle of the thickness or ridge line. For "delta" wings (with straight trailing edges), the critical condition due to thickness corresponds to

$$(\tan \varepsilon / \tan \mu) = 1 - (x/c) \quad (47)$$

where x = location of maximum thickness on chord "c". Thus, in case of the wing as in figure 46, that critical condition is found at $\tan \varepsilon / \tan \mu = 0.5$, corresponding to $M = 2$ where the drag coefficient shows theoretically another peak value. To obtain a really substantial reduction of drag, it thus appears to be useful to keep the thickness line swept behind the Mach cone. One method of doing this, is to

move the *location* of maximum thickness forward. As an optimum for wings such as those in figures 45 and 46, theory (70,e) predicts a location in the vicinity of $x/c = 12\%$. Experimental results are included in that graph for a delta wing (73, i) having a thickness location at 18% of the chord. These results and other data (73,c) show that the variation of drag as a function of thickness location does not conform very well with the theoretical prediction.

No Peaks! A linearized, but three-dimensional theoretical solution (70, e) has been applied to the particular case of a 10% thick double-wedge 60° "delta" wing, plotted in figure 45. It becomes then evident that the highest peak (as indicated by *theory*) occurs at the critical Mach number corresponding to the thickness line (rather than to that of the leading edge), a result which agrees with that of swept wings (where the thickness line is usually \approx parallel to the quarter-chord line). Experimental results demonstrate again the differences between theory and reality. The theoretically expected peaks do not come true. In fact, one can hardly find any correlation at all in figure 45, at transonic Mach numbers, between theory and experiment (76).

-
- (62) Transonic tunnel tests on *swept wings*:
 - a) Goethert, Arrow-Type Wings, ZWB Doct. FB 1813.
 - b) Luoma, Family of Wings, NACA RM L51D13.
 - c) Ludwig, ZWB Lilienth. Rpt 127 (AVA 1940/8/14).
 - d) NACA RM A9D25, A9J24, L52E14, L52K04, L53B02.
 - e) Ellis-Hasel, see reference (73,d).
 - f) Vincenti, 60° *Swept Forward*, NACA RM A8E05.
 - g) Kemp, $A = 4$ at $M = 1.4$, NACA Doct. RM L50G14.
 - (63) Swept wings are generally suitable to be used at high subsonic and at sonic speeds. This is evidently the reason for the lack of experimental points at higher transonic and at super-sonic speeds. Combination of sweep with low aspect ratios leads to "delta" wings to be discussed in the next section.
 - (64) Analysis of swept wings at supersonic speeds:
 - a) Busemann, "Arrow"-Type Wings, Lufo 1935 p.210; see also ZWB Lilienthal Rpt 164.
 - b) VonKármán, Supersonic Principles, J. A. Sci. 1947, 373.
 - c) Nonweiler, "Supersonic" Swept Wings, ARC RM 2795.
 - d) Cohen, Supersonic Characteristics, NACA T. Rpt 1050.
 - (65) With respect to the functions presented in *figures 40 and 42*, it should be noted that certain experimental results on swept wings exhibiting peak values between $M = 1.0$ and 1.3 (not shown), cannot be considered to be realistic for such wings if tested without body interference. The drag coefficients must necessarily continue to rise so that they eventually meet the functions as indicated by linearized theory. The "supersonic" lines in the right side of the two graphs are calculated for biconvex section shapes, for which the constant is 5.3 instead of 4.0, in the equation indicating their wave drag (see Chapter XVII).
 - (68) It is also suggested that the mechanism as explained on page 7-8, is involved in these results.
 - (69) We will define "delta" wings to be triangular shapes flying point first and having a straight trailing edge, such as in the Greek letter ' Δ '. Note that the thickness ratio t/c of such wings is defined in the direction of motion (as on the center line). An "arrow-head" wing is similar to the "delta" shape; it has a swept trailing edge, however.
 - (70) Theoretical analysis of *pointed wings*:
 - a) Jones, Low-Aspect-Ratio Pointed Wings, NACA T. Rpts 835, 851, 863, 1032, 1033, 1107; also T. Note 3530.
 - b) Grant, Arrow Wings, NACA T. Note 3185 (1954).
 - c) Cooper, Optimum Foil Sections, NACA T. Note 3183.
 - d) Brown, Triangular Wings, NACA T. Rpt 839 (1946).
 - e) Puckett, Supersonic Wave-Drag Theory of Small AR Wings, J. Aeron. Sci. 1946 p.475 and 1947 p.567.
 - f) Robinson, Delta Wings, ARC RM 2548 (1946).
 - g) Fowell, Delta-Wing Solutionis, J. A. Sci. 1956 p.709.
 - h) Beane, Biconvex Delta Wings, J. Aeron. Sci. 1951 p.7.
 - i) Spreiter, Transonic Similarity, NACA T. Rpt 1153.

Other "Conical" Shapes. Theory applies not only to triangular or "delta" wings, considered in the preceding paragraphs, but also to a large family of other plan forms fitting basically into the same type of conical flow. Such shapes are in particular those which can be obtained from the "delta" wing (as in figure 45) by sweeping the trailing edge either back (by moving the center point forward - see footnote 69) thus approximating swept and highly tapered wing shapes, or by sweeping that edge forward (thus producing a *diamond* shape). Optimum locations for the three characteristic lines (of LE, thickness and TE) can theoretically be found for operation at particular Mach numbers. The critical numbers in all such shapes can easily be determined by introducing into equation 38 each of the three sweep angles (of LE, thickness location and TE).

Reversal Theorem. By turning a conical type wing around through 180°, i.e. by reversing the direction of flow or motion, the three critical Mach numbers obviously remain the same as in the original direction. Reversed-flow equalities go further, however. As derived and pointed out by several authors (71) the *theoretical* aerodynamic forces of *all* three-dimensional low-aspect-ratio wings are identical in supersonic flow upon reversing the direction of flow or flight (72). Considering as an example a "delta" wing, the wave-drag components of fore- and afterbody somehow correspond to the sweep or vertex angles of leading and trailing edges, respectively. Flying point first, the forebody drag may be small accordingly, and the afterbody drag larger. In the reversed direction, the forebody component is then large, and the afterbody drag is smaller. The sum of the two components of wave drag is constant. A triangular wing was drag-tested, both in the point-first and in the reversed direction (73, a). The results essentially confirm the theoretical prediction. Different development of the boundary layer is likely to have some influence, however, when reversing the direction (72).

Trailing Edge. The Mach number, "critical" in regard to the trailing edge, is $M = 1$, for a straight form of the edge. The corresponding value of $\tan \epsilon / \tan \mu$ is zero. Theory does not include a solution for this condition. It is possible, however, to correlate experimental results of "delta" wings (having straight trailing edges) at $M = 1$, on the basis of the transonic area rule. Such results are included in figure 49.

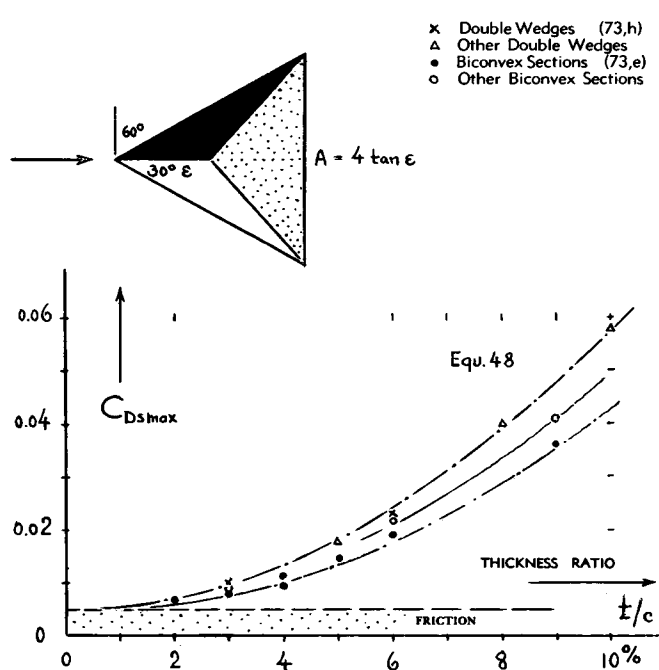


Figure 46. Maximum transonic drag coefficients of "delta" wings as a function of foil section thickness ratio.

Maximum Transonic Coefficients of "delta" wings are plotted in figure 46. Thinking again in terms of the transonic area rule (see a later section of this chapter) slender wings can be expected to show a pressure-drag coefficient (based on frontal area) increasing in the same manner as that of a streamline or conical body (such as shown in the left corner of the graph in figure 24). Referring then the coefficient to the wing area,

$$C_{D_{s\infty}} \sim (t/c)^2 \quad (48)$$

is tentatively obtained for "delta" and similar wings at $M \approx 1$. Figure 46 seems to confirm this analysis.

"Lift-Curve Slope". In "supersonic" condition (that is, when $\epsilon > \mu$) the drag due to lift of triangular (and that of similar shapes) is simply a function of the angle of attack, in the manner as indicated in Chapter VII for flat plates; and the lift coefficient is simply equal to that in two-dimensional supersonic flow (see Chapter XVII). This range of the function is

plotted in the right-hand part of figure 47 as a horizontal line. For the "subsonic" type of leading edge, there is some flow around that edge to be expected. This flow is maximum near $\tan \epsilon / \tan \mu \approx 0$, i.e. when ϵ is small in comparison to the Mach angle μ . Lift and lift-curve slope are then equal to those in uncompressed fluid flow (74, b); see Chapter VII. In terms of "slender" wing similarity, thus:

$$\sqrt{M^2 - 1} (dC_L/d\alpha) = (\pi/2) A \sqrt{M^2 - 1} \quad (55)$$

Figure 47 shows (among others) that this function applies up to "effective" aspect ratios $A \sqrt{M^2 - 1} \approx 1$. In addition to this linear component of lift, a second non-linear component can be expected in small-aspect ratio wings. This second term, treated at length in Chapter VII, does not seem to be very large, however, in "delta" wings.

Slender Wings. A consequence of the LE flow mentioned above, is a *suction* force at the edge. As in subsonic fluid flow, drag can then be expected to be reduced by a certain component of "thrust" corresponding to that suction. For slender wings, i.e. for "pointed" wings in conditions where the parameter $\sqrt{M^2 - 1} / \tan \Lambda$ is small, theory (74, b) predicts a minimum drag due to lift corresponding to

$$dC_D/dC_L^2 = (\lambda/\pi) + (A(M^2 - 1))^{1/2}/8\pi \quad (56)$$

where $\lambda = 1/A$. In terms of "delta"-wing similarity as used in figure 47, this component corresponds to

$$(dC_L^2/dC_D) \sqrt{M^2 - 1} = 4\pi (\tan \epsilon / \tan \mu) \quad (57)$$

as plotted (in reversed manner) in the left part of that graph. Experimental points prove, however, that LE suction does not always materialize. Without such suction, the drag due to lift of small-aspect-ratio wings (up to $A \sqrt{M^2 - 1} \approx 1$) is then twice as high as with developed LE suction.

Drag Due to Lift. The simplest method of presenting the function as indicated by equation 56, is by plotting the parameter as in figure 47. However, without LE suction, drag-rise simply corresponds to

$$dC_D/dC_L^2 = d\alpha/dC_L \quad (60)$$

as shown in the graph by plotting lift-curve slope values (\bullet) in the same manner as the (C_L^2/C_{DL}) function. Experimental results also show that drag due to lift can generally be some 10% higher than indicated by theory (including or excluding suction, respectively). The reason for this result is obviously found in a certain lift deficiency caused by development of and/or shock-wave interaction with the boundary layer.

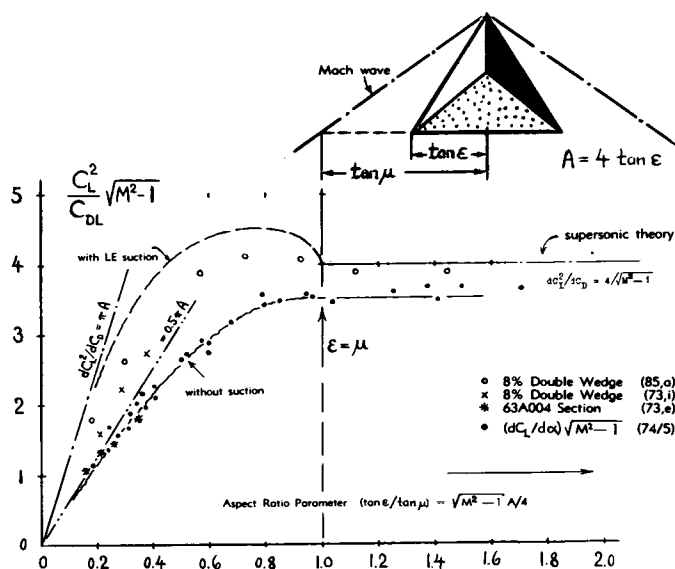


Figure 47. Drag due to lift function of triangular or "delta" wings, as a function of their "aspect ratio". It is shown by Lampert (J.Aeron.Sci.1957 p.667) that, at $\tan \epsilon / \tan \mu = 1$, the shock wave does not attach to the leading edge. As a consequence, lift has not developed yet to the "supersonic" level at that point. Experimental values recover, however, as $\tan \epsilon / \tan \mu$ is further increased.

- (71) Presentation of transonic reversal theorem:
 - a) The theorem has been discussed and/or treated by various authors; see J. Aeron. Sci. 1947 p. 373, or 1949 p.496, or J. Appl. Phys. 1950 p.159.
 - b) Further treatment in NACA Tech. Rpts 986 and 1119.
- (72) The reversal theorem is interesting. It does not mean, however that a reversed wing would also have the same "viscous" properties and/or the same behavior in respect to lateral motions, for example. As a consequence, the reversal theorem does not have a direct engineering application.
- (73) Experimental investigations of pointed wings:
 - a) Kehl, "Zitterrochen" Tunnel Tests, ZWB Documents UM 3122 & 3161; see NACA T. Memo 1159.
 - b) Lange-Wacke, Series of Small AR Wings, ZWB Documents, translated as NACA T. Memos 1146 and 1176.
 - c) Vincenti, Comparison, NACA T. Note 2100 (1950).
 - d) Ellis and Hazel, Supersonic Investigation of Triangular and Sweptback Wings, NACA T. Note 1955 (1949).
 - e) Emerson, Clipped Delta Wings, NACA T. Note 3671.
 - f) NACA Documents RM A9L01 and A50K24.
 - g) NACA, 90° Delta Biconvex, RM A51D30 and A51F21.
 - h) Welsh, 60° Delta, NACA T. Note 3650 (1950).
 - i) Love, 22 Triangular Wings, NACA T. Rpt 1238 (1955).
 - j) Page, Wing and Body, NACA Tech. Note 3872 (1957).
 - k) Continuation of (i) at $M = 4$ and 7, RM L52K19.
- (74) Analysis of small-aspect-ratio lifting wings:
 - a) VonKármán, Supersonics, J. Aeron. Sci. 1947 p.373.
 - b) Jones, Theory of Low AR Wings, NACA (70,a); also J. Aeron. Sci. 1950 p.307; 1951 p.75; 1952 p.813.
 - c) Adam-Sears, J. Aer. Sci. 1953 p.85; also 1952 p.424.
 - d) Henderson, Optimum Delta Wings, NACA TN2858.
 - e) Brown, Triangular Wings, NACA T. Rpt 839.
 - f) Lomax, Slender Wing Theory, NACA T. Rpt 1105.
- (75) Experimental results on lifting "delta" wings:
 - a) See most of the references under (73).
 - b) Petersen, With End Plates, NACA RM A53J14.
 - c) Hatch, LE Suction in Delta Wing, NACA RM L53I08.
- (76) It is said in (70,i) that "the range of applicability of linear theory increases as the aspect ratio decreases". Thinking, however, in terms of transonic area rule, there should not be any sharp drag peaks in three-dimensional wings such as in figure 45 — a conclusion which is indeed confirmed by the experimental results.

Optimum Wing Shapes. Equation 56 is part of a general theoretical analysis (70 and 74) encompassing large "families" of wings. For example, for elliptical loading, minimum drag is obtained as indicated by

$$dC_D/dC_L^2 = \sqrt{M^2 - 1} \sqrt{(1/16) + (M^2 - 1)/(\pi A)^2}$$

For $A \rightarrow \infty$, this equation yields the function as for two-dimensional supersonic flow (Chapter XVII). For $A \rightarrow 0$, we obtain the induced-drag formula as for uncompressed fluid flow. In regard to frontal area, the optimum foil section is either the double wedge, or when disregarding base drag, the single wedge. With respect to wing volume, double-arc or biconvex shapes are optimum.

Wing Tips. In a manner similar to that as mentioned in Chapter VII in regard to the performance of highly tapered wings, the pointed tips of delta wings are not very effective in transonic and in supersonic flow. Clipping them (73, e) so that the taper ratio is increased from zero to the order of 0.1, increases the slope of the lift coefficient, and it reduces the drag rise due to lift accordingly. Reference (75, b) also shows that adding end plates, improves the lift-curve slope, and it reduces drag due to lift further.

6. DRAG OF AIRCRAFT CONFIGURATIONS

So far, we have considered in this chapter the transonic drag characteristics of more or less simple and elementary shapes such as pointed bodies, for example, and "delta" wings. Upon integrating these with each other and with other component parts into an "aircraft" configuration, certain interference effects (different from those expounded in Chapter VIII) have to be taken into account. Through discovery of the "area rule" a few years ago, a new approach has evidently been established in the analysis of all types of solid shapes and their configurations, not only in the transonic but in the supersonic regime of fluid flow, as well. We will try to explain principles and to present practical results.

(A) THE TRANSONIC AREA RULE

Drag Rise. Cones (as in figure 23), streamline bodies such as those in figure 34, and small-aspect-ratio wings as presented in figure 45, all these three-dimensional shapes exhibit a more or less steep rise of the drag coefficient when approaching $M = 1$. Through systematic experiments (77, a) it was then found that the drag of small-aspect-ratio wing plus slender-body

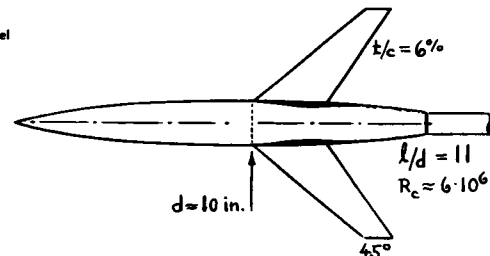
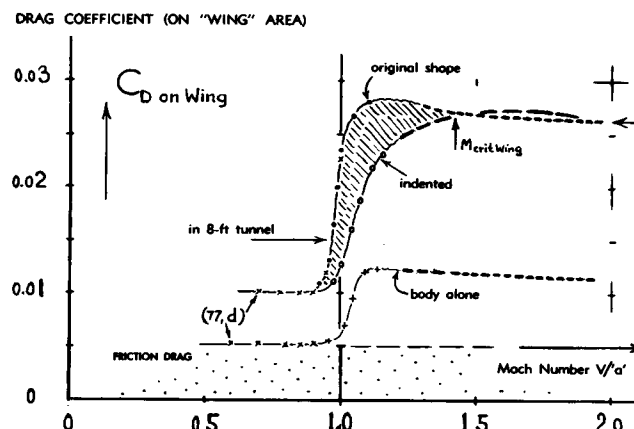


Figure 48. Drag of a wing-body configuration (77,a) in the transonic Mach-number range, demonstrating the area rule.

configurations "is primarily dependent on the axial distribution of cross-sectional area normal to the air stream". It thus appears that at transonic speeds, the "extensive" flow field is approximately the same for the wing-body combination as for the body with the displacement (volume) of the wing "wrapped around" at the proper location. The shape including the "bulge" is thus the body *equivalent* in regard to wave drag to the wing-body configuration; and the two have approximately the same pressure drag coefficient (suitably based on total frontal area).

Indentation. A "smooth-streamline" shape has obviously less drag than the "bulging" equivalent body, not only on the basis of frontal area, but also because of a more favorable shape. Minimum drag is then obtained in a wing-body configuration by *re-distributing* the combined cross-sectional area in the same manner as that of a streamline body having the highest possible fineness ratio. This is done in the "airplane" shown in figure 48, by taking away from the sides (and from top and bottom) of the fuselage the *volume* of the wing. The graph proves that such body indentation *postpones* the transonic drag rise effectively, thus reducing the drag at $M \approx 1$ significantly (79). Drag reduction is less spectacular at Mach numbers above unity; and it fades out upon approaching $M \approx 1.5$ (in the particular example as in figure 48). Some drag reduction can also be obtained by *adding* to a given configuration volume in such places where the original distribution has indentations, so that a smoother effective shape is thus produced.

Wing Similarity. The simple *area distribution* concept explained above, is a limiting case, correctly applying only to rotationally-symmetric bodies in combination with very-low-aspect-ratio wings. Within limits, results on wings varying in aspect ratio and thickness ratio, can thus be correlated with each other on the basis of the area rule, which then simply appears as a "sonic" similarity rule. A wing with $A = 1$ and $t/c = 0.10$, for example, can be expected to have the same drag coefficient (at $M = 1$ and

based upon frontal area) as a wing with $A = 2$ and $t/c = 0.05$; simply because $A(t/c) = 0.10 = \text{constant}$. In terms of the area rule, the two wings have one and the same (rectangular) axial distribution of cross-section area ($b \cdot t$). Figure 49 presents experimental results; and these results are seen to line up properly against $A(t/c)$. A more complete transonic similarity rule is shown to apply to these same wings, and to still other combinations of A 'ratio and thickness ratio, in figure 12 of Chapter XVII. Up to $A(t/c)^{1/3} = 1.1$, we can derive from that graph that

$$\Delta C_{D_0} = 2.3 A(t/c) \quad (55)$$

This function agrees sufficiently well with the experimental results in figure 49. It also appears that the *maximum* transonic pressure-drag coefficient can be correlated against $A(t/c) \rightarrow$ see the uppermost experimental function in figure 49. Finally, results on triangular or "delta" wings can also be correlated very well with each other, as shown by the lowest branch in the graph.

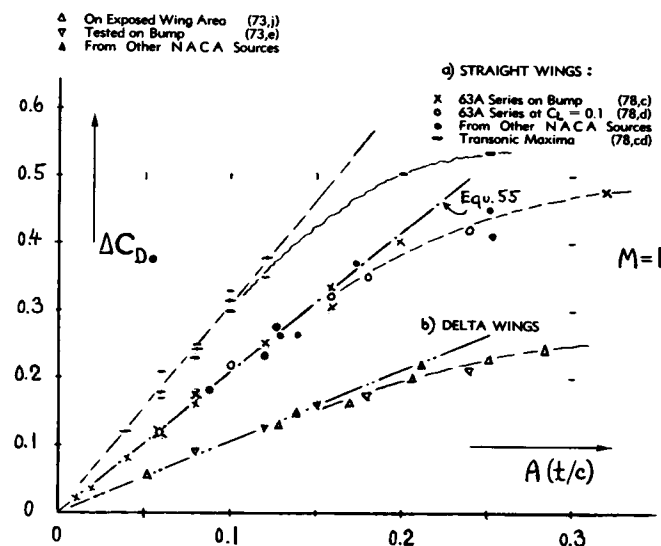


Figure 49. Drag of straight and of triangular wings at $M = 1$, presented in terms of transonic area rule.

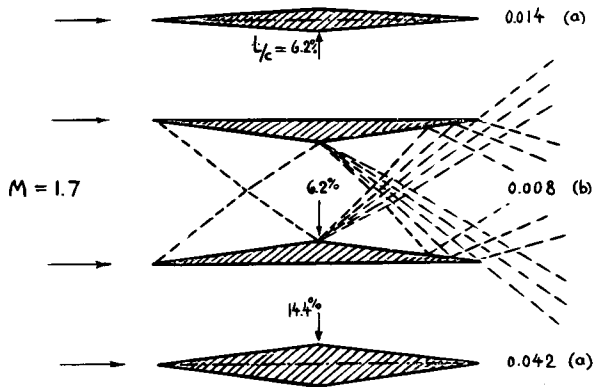


Figure 50. Arrangement and drag of a supersonic type of biplane, designed for $M = 1.7$; (a) wave-drag plus estimated skin-friction drag coefficient, (b) experimental results (80,b,c).

(B) INTERACTION AT SUPERSONIC SPEEDS

Interference and/or interaction at supersonic speeds between the component parts of air-borne vehicles (such as wing, fuselage, tail and possibly other elements) have recently been analyzed and/or reconsidered in a broad and general manner (84). Some examples are listed as follows.

Biplane. As pointed out in (80, a) wave drag due to thickness (at zero lift) can be avoided by arranging two wings in biplane form as shown in figure 50. At a certain Mach number (for which the biplane configuration must specifically be designed) the pair of compression waves originating from the two leading edges, meets the opposite wing surfaces at points where expansion waves of the same intensity are just about to start (80, d). The two types of waves thus cancel each other, at least theoretically. Wind-tunnel tests (80, c) with the arrangement as in figure 50 show a drag reduction from $C_{D_s} = 0.014$ or 0.042 , respectively, to 0.008 , where the coefficients are based upon the wing area or the sum of the areas, respectively. Inasmuch as a skin-friction component is included in these values, drag is not reduced to zero. Depending upon the wing that may be considered to be the equivalent monoplane, the total-drag reduction is between 43 and 81%.

- (77) Publications concerning transonic area-rule:
 - a) Whitcomb, Drag Rise of Wing-Body Combinations, NACA Doct. RM L52H08. This is the original report (1952) presenting the "area rule" derived from experimental results; see also Aeron. Engg. Rev. June 1956 p.42, and NACA T. Rpt 1273 (1956).
 - b) Spreiter, Transonic Area Rule, NACA T. Note 3673.
 - d) A configuration similar to that in figure 48 is tunnel-tested by Osborne in NACA RM L52E14. Subsonic values (\times) from this report are used in the illustration as basis for the test points from (a).
 - e) Lindsey, Flow Pattern, NACA T. Note 3703 (1956).
 - f) Wave drag of bumped and indented bodies is investigated by McLean-Rennemann in NACA T. Note 3744 (1956).
- (78) Experimental wing results on transonic area rule:
 - a) See results in (35) and (38) of Chapter XVII.
 - c) Nelson, 22 Rectangular Wings, NACA T. Note 3501 (1955); see also McDevitt in T. Rpt 1253 (1955).
 - d) Nelson, 38 Cambered Wings, NACA T. Note 3502.
- (79) The author considers postponement and a rate reduction of the drag rise to be the result of area-rule application. The drag-divergence Mach number is obviously increased and the rise of the coefficient above that number is apparently reduced in a manner very similar to that when applying wing sweep. Fuselage "contouring" (see (62,g) in Chapter XV) similar to indentation as in figure 48, although a different approach, seems to lead to the "same" results as the area rule. Successful experiments are reported in J. Aeron. Sci. 1955 p.173, by Hilton.
- (80) Dealing with the supersonic type of biplane:
 - a) Busemann, Lufo 1935 p.210 and 1937 p.55; also in "Foundations of High-Speed Aerodynamics" Dover 1951.
 - b) Walchner, Lufo 1937 p.55; Yb. D. Lufo 1937 p.1,198.
 - c) Ferri, Biplane Experiments, Atti Guidonia No. 37 & 38, 1940; see also Analysis in J. A. Sci. 1957 p.1.
 - d) Reference (84,c) shows that the biplane drag oscillates between a maximum function and zero, as the Mach number is varied (multiple reflection).
- (81) Characteristics of shrouded bodies:
 - a) Ferrari, L'Aerotecnica 1937 p.507.
 - b) Byrd, Shrouded Theory, NACA T. Note 3718 (1956).
 - c) The shroud presents additional viscous drag, of course.
- (82) Friedman, Between Bodies, NACA T. Note 3345 (1954).

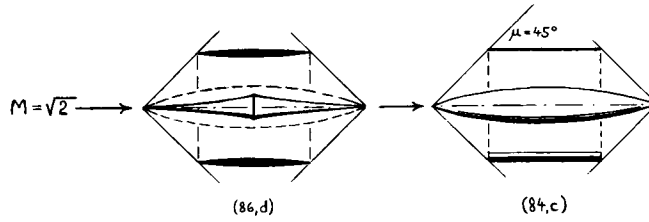


Figure 51. Two examples of shrouded bodies, illustrating supersonic type of interaction.

Shrouded Body. The three-dimensional equivalent of the biplane is a "shrouded" body possibly in the form as in figure 51. The right-hand part of the illustration represents a configuration "free of wave drag". The cylinder (straight on the outside) must be positioned, with respect to the center body, in such a manner that its rims are located on the two Mach or shock cones, respectively, as shown. On the inside, the cylinder must then be given a shape which combines with that of the center body so as to provide complete cancellation of all compression and expansion waves (81, c).

Supersonic Area Rule. The left-hand part of figure 51 is an example for what is called the "supersonic area rule" (84). The ogival body of revolution is the equivalent of the thin "spindle" in the center plus the ring or tube having a 6% thick biconvex section. The "ogival" shape as shown in the illustration, named "SearsHaack" body (50 and 84) provides minimum drag for a given volume. Note that this shape is among others a function of the Mach angle (controlling the angle of the conical points). In a wing-body combination, the fore and after Mach cones (each touching the wing tips) also determine the length on the central body where an indentation similar to that in figure 48 must be applied in order to minimize the displacement- or wave-type interference drag. Theoretical prediction and experimental results (84, c) show, however, that the reduction of drag thus obtained is by no means as spectacular (79) as at or near $M = 1$. — For $M = 1$, where the angle $\mu = 90^\circ$ (and for diameters which are small in comparison to the length of the combination) the *transonic* area rule is automatically obtained from the geometry as shown in figure 51.

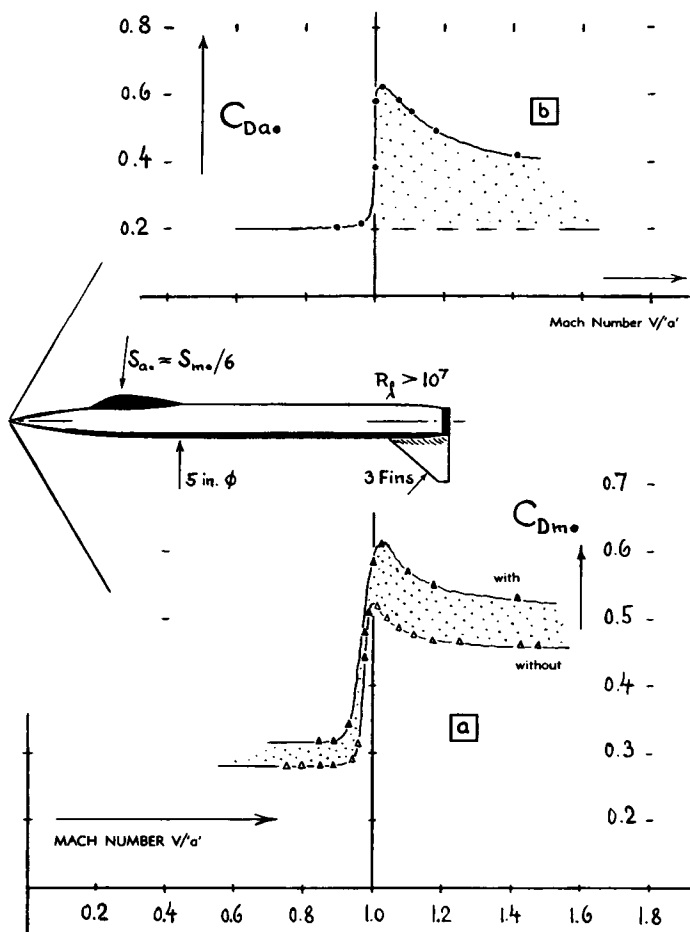


Figure 52. Drag at transonic speeds of and due to a pilot's canopy (88,c); (a) total drag coefficient with and without canopy, (b) drag coefficient (on canopy frontal area) of the canopy including interference with the "fuselage" body.

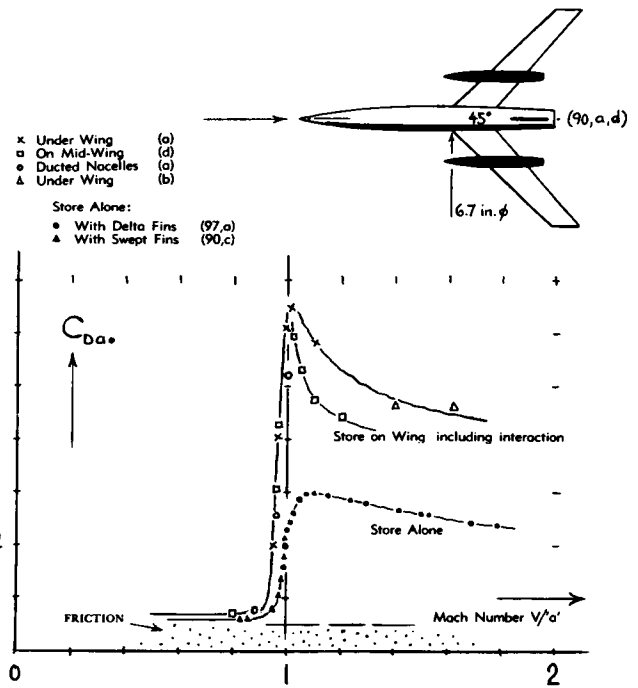


Figure 53. Drag coefficient of and caused by external stores and/or engine nacelles based on their frontal area, all tested (90) on swept wings.

(C) DRAG OF COMPONENT PARTS

Canopy. The transonic drag characteristics of a canopy added to a missile body, are presented in figure 52. Application of the area rule qualitatively explains the magnitude of the added drag. Assuming, for example, that the shape (surface angles) of the added canopy be sufficiently similar to that of the "main" body, it may then be expected that the total wave drag coefficient (on combined area) grows in proportion to the square of the frontal area (see figure 24 near $d/x = 0$). In case of the canopy (figure 52) having a combined frontal area $S_c = 1.16 S_m$ we may thus expect, the drag of the combination to be $1.16^2 = 1.34$ times that of the main body alone. As tested at $M = 1.02$, wave-drag components are approximately as follows:

for main body alone	$C_{Dm} = 0.22$	(0.10)
canopy differential	$= 0.07$	(0.08)
on canopy area	$= 0.40$	(0.25)
for combined wave drag	$= 0.29$	(0.18)
based on total area	$= 0.25$	(0.17)

The experimental result of "0.29" is equal (in this case) to the analytical value of $1.34 \cdot 0.22 = 0.29$. Another canopy investigation (88, a) yields the values as listed above in parentheses. This time, the experimental coefficient (at $M = 1$) of "0.18" is higher than the analytical estimate of $1.10^2 \cdot 0.10 = 0.12$.

Drag may reduce, when placing the canopy away from the maximum thickness of the fuselage body (see also the speculation in this respect on page 15-30 and the experimental result on the "belly" tank on page 8-8).

External Stores. Experimental results on several stores (and/or engine nacelles) are presented in figure 53. While a swept wing of the type as shown, is expected to have drag characteristics similar to those in figure 42, the combination with the pair of bodies installed on the wing panels, produces an additional component, peaked at $M \approx 1$ (92, a). It seems to be this component (also evident in figures 52 and 54) that can be reduced effectively by a redistribution of volume (as explained in connection with figure 48). It is furthermore suggested that not only wave drag is involved in producing the drag peaks, but that boundary-layer and shock-induced separation may also be responsible for a significant part of the drag increment (92, b).

(83) Comments on area rule methods:

- a) "Area" rules are not precisely new inventions. As early as 1944, tests have been conducted on fuselage indentations in conjunction with swept wings (see Frenzl in ZFW 1957).
- b) A recent treatment of the subject is by Vandrey in Zeitschr. FlugWiss. 1957 p.44.

(84) Wing-body configurations (supersonic area rule):

- a) Jones, Wing & Body, NACA T. Rpt 1284 (1956).
- c) Lomax & Heaslet, Wing & Body, J. Aeron. Sci. 1956 p.1061; also "Body Distortions", NACA T. Rpt 1282.
- d) Cramer, Pressure Distribution, J. A. Sci. 1957 p.629.

(85) Experiments on wing-body interference:

- a) Katzen, Cylinder Plus Delta, NACA T. Note 3794.
- b) Estabrooks, Cylinder Versus Parabolic, RM L52K12a.

(86) Supersonic interaction, including lift:

- a) Jones, Minimum Drag, J. A. Sci. 1951 p.75; 1952 p.813.
- b) Nielsen, Cylinder + Wing, NACA TR 1252, TN 3722.
- c) Graham, General Theory, J. Aeron. Sci. 1957 p.142.
- d) Graham (Douglas), General, NACA Tech. Memo 1421.

(88) Drag of airplane canopies at transonic speeds:

- a) Welsh, Canopy on Body, NACA Doct. RM L51A29.
- b) Alexander, Windshield on Body, NACA RM L8E04.
- c) Purser, Pilot's Canopy, NACA Document RM L7L22.

(90) Transonic drag of streamline stores and/or nacelles:

- a) NACA, On Swept Wing, RM L51D26 and L52J22.
- b) Jacobsen, Under Delta Wing, NACA RM L52H29.
- c) Mason, Under Fuselage, NACA Doc. RM L53J22.
- d) Pepper, Smooth Nacelles, NACA Doc. RM L50G17a.

(91) Transonic drag of and due to wing-tip tanks:

- a) English, On Straight Wing, NACA RM L54F29a.
- b) Coe, Ducted on Small AR, NACA Doct. RM A52J21.
- c) Hoffman, Smooth on Swept Wing, NACA RM L51L27.
- d) Spreeman, Smooth on Swept Wing, NACA RM L9J06.

(92) Notes on transonic interference drag:

- a) The peak of the bomb-drag coefficient in figure 38, marked by (X) has a shape similar to those of the stores in figures 53 and 54.

b) A Likely mechanism of transonic interference drag is as follows. Along the wing root (in the corner between wing and body) the boundary layer grows and accumulates more than anywhere else. The compression shock originating from the wing's trailing edge, may then easily cause an extended flow separation. Figure 11 demonstrates that the resultant "base" drag can be very high, in the vicinity of $M = 1$.

c) Transonic interference drag in wing-body combinations is significantly less for cylindrical than for parabolic body shapes. Both (77,a) and (85,b) show that a drag peak (as in several of the illustrations) does not occur in configurations where the wings are attached to the cylindrical part of the fuselage.

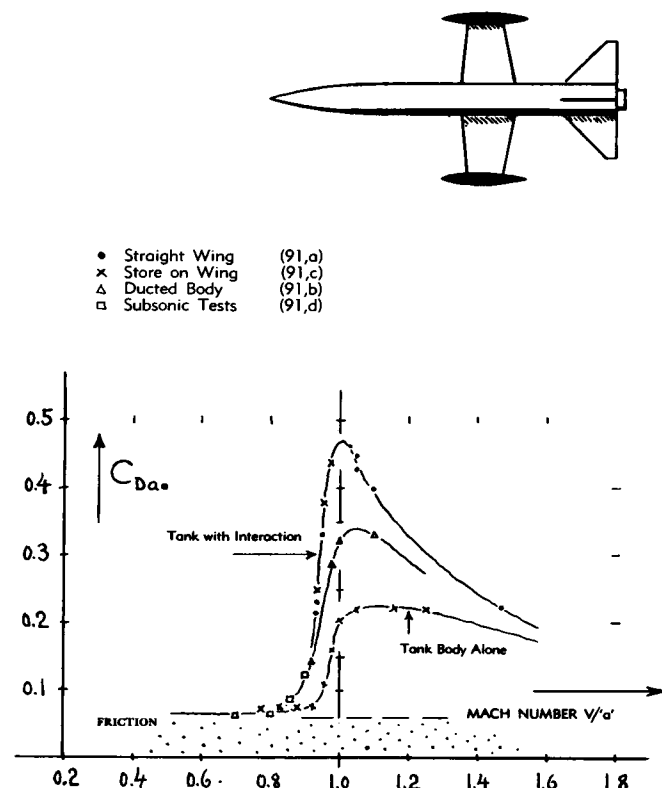


Figure 54. Drag coefficient of and due to wing-tip tanks (91).

Wing-Tip Tanks are an efficient means of carrying outside loads at subsonic speeds (see Chapter XIII). Figure 54 proves, however, that tanks of this type can produce a component of transonic interference drag (92, b) in the order of 100% (or even more) of their basic drag at such speeds, i.e. when flying alone. Figure 54 also demonstrates that the tank drag coefficient is largest in combination with a straight wing, and less in a small-aspect-ratio swept configuration.

(D) INTERNAL FLOW AT TRANSONIC SPEEDS

Mechanism of drag caused by flow through internal systems is treated in Chapter IX. Conditions at transonic and supersonic speeds are different, however, in certain respects, from those in uncompressed fluid flow. Characteristics are as follows.

Open-Nose Inlet. When driving one of the subsonic-type nose-inlet or cowling shapes (such as in figure 47 of Chapter XV, for example) beyond $M = 1$, a detached bow wave originates ahead of the opening. Pressure losses across such an essentially normal shock are known, and they are comparatively small as long as the Mach number does not exceed unity too much. Such an inlet opening might basically be used in an aircraft designed for this speed range. — Figure 55 presents the drag coefficient of a fin-stabilized parabolic body of revolution in three different conditions; (a) as the basic body with solid pointed nose, (b) as ducted body with a mass-flow ratio in the order of 0.8, and (c) as open-nose body *without* internal flow ($w = 0$; blocked duct). — After cutting an unobstructed cylindrical duct into a “streamline” body (exposed to a supersonic fluid flow) the external *wave drag* of that body (102) is *reduced*, simply because the *displacement* of the ducted body is smaller than that of the solid shape. Not counting the drag due to internal losses of momentum, the drag of the configuration can thus be *smaller* than that of the same-size solid body. Certain experimental results (see reference 99) confirm this conclusion qualitatively. Also, figure 55 shows such a drag reduction at Mach numbers between 1.0 and 1.2.

Additive Drag. Drag of a body (fuselage or nacelle) equipped with an internal duct (including inlet and outlet opening) is basically equal to that of the *ducted* body plus an *internal component of drag*, corresponding to the loss of momentum of the stream tube passing through the duct. Another component of drag arises, when reducing the mass flow through the system ($\rho w S_d$) below what is called maximum (with $w = V$). To explain the increment, it is useful first to consider conditions in subsonic (uncompressed) flow. As pointed out in Chapter IX, an inlet opening is usually designed for a certain velocity ratio w/V (where w = inlet velocity). Upon reducing that ratio below the design value, the flow must “spill” over the rim of the inlet. In subsonic (uncompressed) fluid flow, it is theoretically possible that this flow around

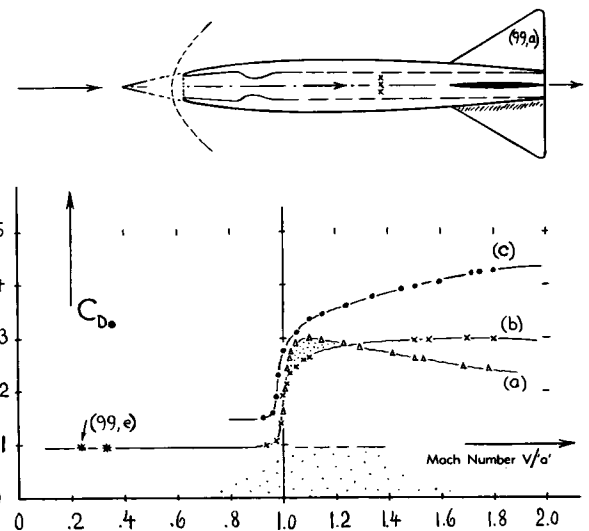


Figure 55. Drag coefficient (99,a) of a fin-stabilized parabolic body; (a) solid and pointed body, (b) ducted body with ≈ 0.8 mass-flow ratio, (c) open-nosed body with zero internal flow (blocked duct).

the rim (or “lip”) takes place without any loss of momentum and without an increase of the external drag. A certain component of the *increased static pressure across the inlet opening* is simply counterbalanced by pressure and suction forces (equivalent to negative drag or to thrust) on the inside, at the rim and on the outside of the cowling. Actually, the flow loses some momentum, because of viscous friction, and it may eventually separate from the outside shape. The resultant additional component of *external drag* (102,f) corresponds to what in supersonic aerodynamics is called the “additive” drag (96). The mechanism at Mach numbers above unity is, of course, different insofar as a detached shock wave is involved, of the form as indicated in figure 55. Behind the shock front, the flow turns sideways, thus “spilling over” to the extent as the quantity $(\rho_{amb} V S_d)$ is larger than the corresponding quantity $(\rho_w V S_d)$ in the duct entrance. Additive drag is thus found to correspond to the mass flow of air spilling from the inlet opening; and it can thus also be called “spillage drag” (106,a). The additive drag is maximum at zero flow ratio (that is, for a blocked duct with open nose) where it corresponds to the stagnation pressure. Based on inlet area, the coefficient is then

$$C_{D_{add}} = "q"/q \quad (60)$$

where “ q ” as in equation 4. In the range of smaller flow ratios, the additive drag coefficient is roughly

$$C_{D_{add}} \approx 1 - "m"/"m"_{max} \quad (61)$$

where “ m ” = mass flow through the duct in slugs/sec, and “ m ”_{max} = flow ratio corresponding to $w = V$.

More accurate (and more complicated) formulas are listed in (96,a). Some negative component of drag due to suction develops, however, in body or cowling shapes which are conical and/or parabolic on the outside rather than cylindrical. Additive drag is, therefore, sometimes found (99) to be less than indicated by theory; and equation 61 may then very well be adequate for engineering purposes, to predict the magnitude of spillage drag in open nose arrangements.

- (95) Transonic mechanism of air inlets:
 - a) Nichols-Pendley, Summary, NACA Doct. RM L52A07.
 - b) Principles, ZFW 1954, 235 & 300; 1955, 165.
 - c) Wyatt, Turbojet Inlets, Aeron. Eng. Review Oct. 1951.
 - d) Connors-Meyers, Design Criteria, NACA T. Note 3589.
 - e) Luskin-Klein, Turbojet Installation Principles, Transactions ASME 1950/51 p.375.
 - f) Stubbs, Supersonic Inlets, SAE J. 1957 p.34.
 - g) Drell, Induction Systems, A. Eng. Review Nov. 1956.
 - h) Watson, Analysis of 6 Systems, NACA RM A53H03.
- (96) Additive or incremental drag of air intakes:
 - a) Sibulkin, Additive Drag, NACA T.Rpt 1187 (1951).
 - b) Klein, Scoop Drag, Douglas Rpt SM-13744 (1950).
- (98) Transonic drag of parabolic bodies of revolution:
 - a) NACA, Store Alone W/out Fins, Doct. RM L50G17a.
 - b) Loving, 4 Streamline Bodies in Tunnel, RM L52J01.
 - c) Pendley, Body In Transonic Tunnel, RM L52H22.
 - d) NACA, Flight Tests, Doct. RM L53J22.
- (99) Experimental characteristics of open-nose intlets:
 - a) Sears and Others, Flight Tests on Normal-Shock Inlets, NACA Doct. RM L50L18 = Tech. Note 3218.
 - b) Continuation of (a) in NACA Tech. Rpt 1281 (1956).
 - c) Brajnikoff, 4 Supersonic Inlets, NACA T.N. 3724.
 - d) Pendley, Subsonic Inlets, NACA Tech. Note 3436.
 - e) Blackaby, Low-Speed Tests, NACA T. Note 3170.
 - f) Sears, Continuation of (a), NACA RM L51E02.
- (100) Experimental characteristics of twin inlets:
 - a) Stroud, Forebody Influence, NACA Doct. RM A51K14.
 - b) Carter, Merlet, Flight Tests, NACA RM L53E05.
 - c) NACA, Side Inlets are further treated in Docts. RM E51G06, E52E02, E52G08, E52G23, E52H20, E53G09.
- (102) Theoretical shape characteristics of ducted bodies:
 - a) Parker, Minimum Drag Bodies, NACA T.Rpt 1213.
 - b) Bennett, Open-Nose Bodies, J. Aer. Sci. 1953 p.720.
 - c) Ferri, Theory, NACA Technical Report 841 (1946).
 - d) Brown-Parker, Calculation, NACA T.Rpt 808 (1945).
 - e) Heaslet, Minimum Drag, NACA T.Rpt 1256 (1956).
 - f) Fradenburgh, Subsonic Inlets, NACA Tech. Rpt 1193.
- (104) Characteristics of conical-nose intlets:
 - a) Ferri, New Type Inlet, NACA T. Rpt 1104 (1951).
 - b) Ferri, Theory and Experimental, NACA T.Rpt 1189.
 - c) Oswatitsch, Diffusion, NACA T.Memo 1140 (1947).
 - d) Pendley, 5 Annular Inlets, NACA RM L53F18a.
 - e) Moekel, Conical Separation, NACA RM E51J08.
 - f) Dailey, Flow Pattern, J. Aer. Sci. 1955 p.733.
 - g) ARC, Inlet Flow Pattern, Report RM 2827.
- (106) Controlled-internal-flow configurations:
 - a) Gorton, Translating Spike, NACA RM E53G10.
 - b) Merlet-Putland, Axial Position, NACA RM L54G21a.
 - c) Beke, Bypass Discharge, NACA RM E52L18a.
 - d) Evvard, Perforated Inlets, NACA T. Note 3767.
 - e) Simon, Scoop Inlet with Ramp, NACA RM E52H29.
- (107) An example for variable-geometry air intakes are those of the Lockheed F-104 "Starfighter". On each side of the fuselage, a half-cone spike is automatically "moving back and forward, to focus the shock wave onto the rim of the intake opening".

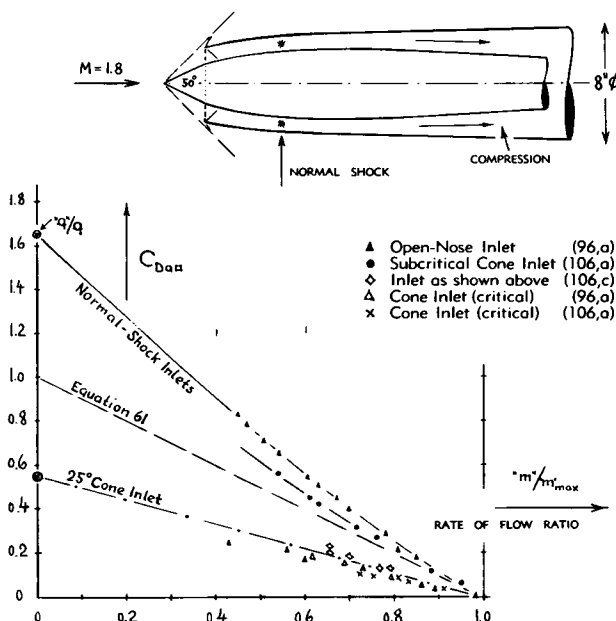


Figure 56. Additive (spilling) drag coefficient (on total inlet area) of various inlet openings.

Oblique-Shock Inlets. Since losses of momentum across oblique shocks are less than those through a normal shock, placement of a conical nose ahead and in the center of the inlet (as shown in figure 56) produces configurations (104) that are more efficient internally (producing higher compression across a second or last normal shock). Operation of this type inlet can be subcritical (with the normal shock ahead of the opening; see reference 104,a) or critical (with the normal shock in the diffuser throat; see reference 104,c) or supercritical (with the last shock in the expanding part of the internal diffuser). It is reported that only the last type is stable (while the subcritical type is prone to produce back and forth oscillations of the normal shock). - Conical-nose (oblique-shock) inlets have also less additive drag. In the range of higher mass flow ratios and/or for critical and possibly supercritical operation, that drag component corresponds to the pressure coefficient " C_{po} " of the conical centerbody as in free flow. The additive drag coefficient (on inlet area *including the cone*) is then approximately

$$C_{D_0} = C_{po}(1 - "m"/"m"_{max}) \quad (64)$$

The graph (figure 56) roughly confirms this equation. However, for subcritical operation and/or at flow ratios approaching zero, higher drag coefficients are obtained, depending upon the location of cone and conical wave in relation to the rim of the inlet (see analysis in reference 96,a). It should also be noted that the drag coefficient as indicated by equation 60, increases as a function of M'number, while that of conical-nose inlets (in critical operation; equation 64) reduces in proportion to the cone-drag coefficient.

Controlled Inlets. The type of inlet as in figure 56 is most efficient (a) with the conical shock wave located at a small distance ahead of the inlet lip, and (b) with the second (or last, and normal) shock located at or slightly aft of the diffuser throat (where velocity and shock loss are the smallest possible). Flow pattern and mass flow ratio required, vary very much, however, as a function of craft speed (Mach number). To retain favorable conditions through a certain M'number range – variable geometry (95) (106) is therefore desirable. So, by moving the center body as in figure 56 (also called "spike") in fore-and-aft direction, both the external pattern (the location of the conical shock with respect to the rim of the inlet) and the internal geometry (the shape of the diffuser) can be changed and/or controlled together in such a manner that optimum internal and external conditions of fluid flow may be approximated; see the example (107).

Optimum Outside Shape. Analytical studies concerning the shape of ducted bodies are listed in (102). These investigations and experimental results in (99) prove that *conical* outside shapes result in somewhat smaller external body drag than parabolic shapes. In fact, theory (see reference 102,b in particular) indicates that *convex* (hollow) cowling shapes may be optimum in regard to drag.

Internal (Momentum) Drag in the form as treated in Chapter IX, is not to be considered as such in jet-type engines. Their thrust results from the differential between entering and "exhausted" momentum, so that the drag corresponding to that of the stream tube "captured" by the inlet, is part of the engine system. However, in cases where air is led into an airplane for purposes other than propulsion, the momentum drag, as in Chapter IX, must be considered.

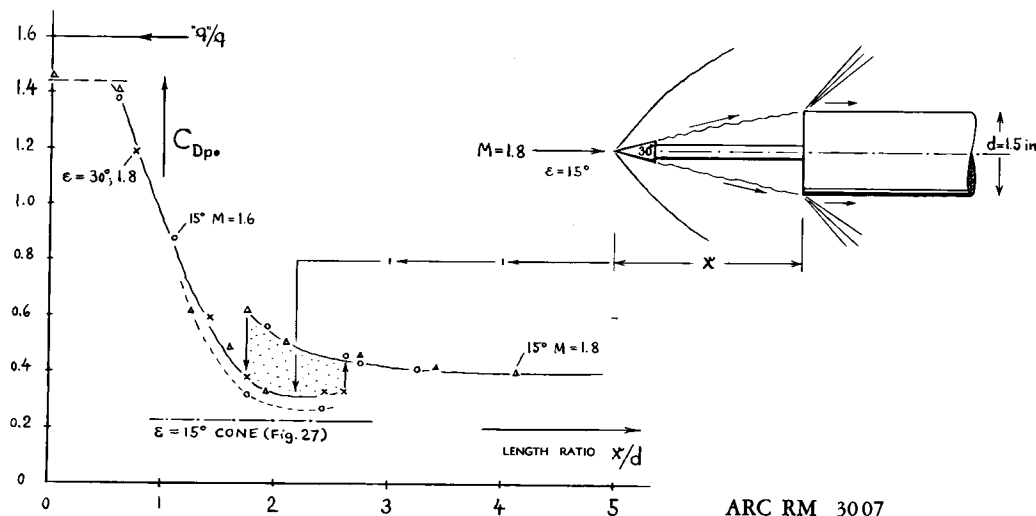


Figure 57. Combination of a blunt-faced cylinder with a cone-pointed "spike", extending ahead by various length ratios x/d . The results demonstrate supersonic interference effects as well as the mechanism of diffusion and external (and/or additive) drag in conical-nose air inlets. Phases as a function of spike length are as follows:

- With the spike protruding to a distance in the order of the cylinder's diameter, the shock wave originating from the conical point, combines with the detached wave in front of the cylinder's blunt face. We thus have a two-shock deceleration (or diffusion) and a drag coefficient (of cylinder face plus conical point) which is noticeably reduced.
- At spike length ratios around $x/d = 2$, an optimum flow pattern is then obtained. The roughly conical (or ogival) separation space behind the conical tip has grown in this case to such a diameter that the "conical" flow as shown in the illustration, passes just outside the edge of the cylinder. As a consequence, there is only one (slightly curved) shock front. Flow pattern and drag coefficient are essentially the same as in a solid forebody having the same shape as cone plus dead air space.
- As the spike is made longer and longer (to and beyond $x/d = 3$) the conical tip assumes the same flow pattern as in free flow (i.e. on a sting, but without interference from the larger cylindrical body). This means that the flow closes in behind the cone's base (likely as in figure 3,b). The interaction with the blunt cylinder is then a matter of separation along the stem of the spike caused by the viscous wake developing along that stem. The graph shows that the influence of the spike upon the flow pattern is still appreciable in this phase; the drag coefficient of the combination is reduced from ≈ 1.4 (without spike) to the level of ≈ 0.4 .

CHAPTER XVII - DRAG IN SUPERSONIC FLOW

In the first edition of this book, this chapter was introduced by saying: "Only a few guided missiles and one or two experimental airplanes have flown at speeds above that of sound — as of today (1951). Theory and experimental information are rapidly progressing, however, in the field of supersonic aerodynamics." Today (6 years later) there are dozens of missile types, some of them "available" as standard military equipment. Several types of airplanes have also been developed, repeatedly flown and timed at speeds up to twice the velocity of sound, in various countries of this earth. One or two of these have been produced in numbers; and they can be flown at supersonic speeds as a matter of routine. Plans are also under way at this time (in England) of developing an airliner carrying some 100 passengers at Mach numbers around 1.5. Characteristics of these aircraft are more transonic, however, than supersonic. Most of the aerodynamic information pertaining to them is presented in Chapter XVI, accordingly. In distinction from that chapter, more "pure" supersonic characteristics are discussed in the text that follows below, such as those of straight wings in particular.

1. ELEMENTS OF SUPERSONIC FLOW

Mach Angle. A body flying at a velocity greater than that of sound, causes a sudden compression of those air particles which are more or less directly encountered by its nose. As indicated by the sketch in figure 1, the corresponding compression is propagated in all directions as a spherical wave, essentially with the sonic velocity "a". At the same time, the body proceeds at its own velocity 'V', however. Seen from the system of the body, a wave with an essentially straight front, therefore, originates from the advancing point of compression, composed of the velocities "a" and V. The angle between the wave and the flight direction is the Mach angle " μ ", named (as the Mach number "M") after the physicist Mach (3):

$$\sin \mu = 'a'/V = 1/M \quad (1)$$

In the three-dimensional case, the wave forms the surface of a cone. Compression waves produced by two-dimensional shapes such as airfoil sections, have the shape of a wedge's surface.

Compression Front. The angle as per equation 1, only applies to the limiting case of vanishingly small compression, as from a mathematical point or from a "leading edge" line, respectively. In physical bodies such as the foil section in figure 14, for example, additional waves originate, however, from the surface between "a" and "b"; and these waves start out at a Mach angle corresponding to local conditions of flow and measured against the sloping surface rather than against the general direction of motion. All these waves subsequently combine; and they end up on a compression or shock front. Because of the magnitude of the pressure changes involved, the shock wave (as distinct from the Mach wave above) has an angle larger than indicated by equation 1. However, as the intensity of the shock decreases toward the outside space, the wave then curves back in such a manner as to approach the Mach angle at some larger distance away from the body, where the compression across the front, approaches zero.

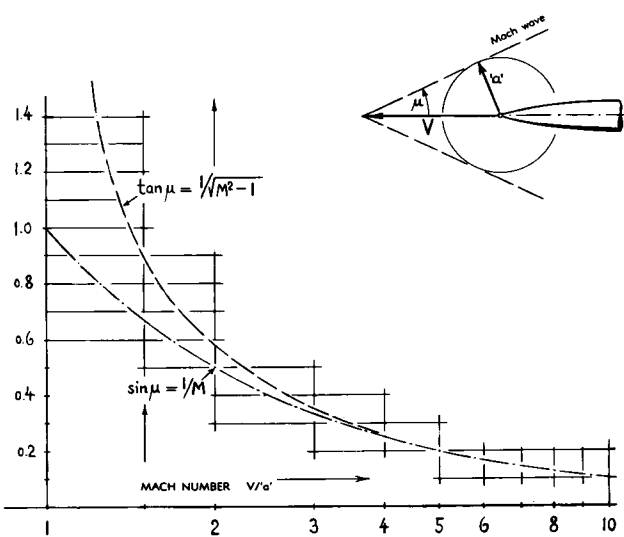


Figure 1. Basic Mach angle functions.

Silent Space. Since any pressure change caused by the approaching body, cannot proceed faster than the speed of sound, all of the space ahead of a compression front originating from the foremost point of an obstacle, is necessarily entirely undisturbed. In other words, that space is silent in respect to any noise produced by the body, as demonstrated by bullets and/or missiles approaching at supersonic speeds. This lack of "warning" in supersonic flow is greatly different from conditions of potential fluid flow at lower speeds (below the critical Mach number as explained in chapter XV).

Expansion. An important characteristic of supersonic flow is its capability of turning around a corner without causing or experiencing separation. The analytical solution of this type of flow is known as "Prandtl-Meyer" expansion (4). The physical mechanism is the combination of a pressure drop, around the corner considered, with the volumetric expansion of the gas upon entering the reduced-pressure space at supersonic velocity. For example, at an initial velocity corresponding to $M = 1$, a fluid flow is *theoretically* capable of turning through a maximum angle of 130° , i.e. for the maximum possible pressure drop (into vacuum) obtained at $M \rightarrow \infty$. For considerably smaller pressure reductions, the expansion mechanism is still so powerful that existing flow separations past bluff shapes and/or sharp leading edges of foil sections *can* be eliminated, reduced or postponed significantly. A number of examples of this type are presented in Chapter XV under headings such as "up-down-up" and "drag dip". The pressure drop corresponding to expansion can also be utilized in the prediction of wave drag originating along tapering afterbodies; and it thus represents part of the supersonic "shock-expansion" theory. Expansion as such takes place without loss or dissipation of momentum or energy. However, the deceleration eventually required to restore the static pressure to the ambient level, usually takes place in form of a compression shock, thus involving wave drag.

Stagnation Temperature. In incompressible fluid flow Bernoulli's principle (see Chapter I) states that the sum of static plus dynamic pressure is constant, as long as no momentum is added to, or diverted from a given stream of fluid. As a consequence, dynamic pressure ($0.5 \rho V^2$) is converted into a *static* pressure differential (the magnitude of which is equal to $0.5 \rho V^2$), obtained at every stagnation point (where $w = 0$). In a compressible fluid, the temperature changes, however, as a function of pressure; and an exchange takes place between kinetic and heat energy. In gasdynamics, constant total energy must, therefore, replace Bernoulli's constant. Upon reducing speed,

part of the kinetic energy of the air particles is then transformed into heat. The increment corresponds to

$$\Delta T/T_{\text{amb}} = 0.5 (k - 1) (V^2 - w^2) / (a')^2 \quad (4)$$

where T_{amb} = ambient absolute temperature and w = local velocity at a certain point within a given flow pattern. For a ratio of $k = C_p/C_v = 1.4$ as in tropospheric and stratospheric altitudes therefore:

$$\Delta T/T_{\text{amb}} = 0.2 M^2 (1 - (w/V)^2) \quad (5)$$

and for the stagnation point (where $w = 0$):

$$\Delta T = 0.2 T_{\text{amb}} M^2 \quad (6)$$

For example, for "normal" air with an absolute temperature $T = 288^\circ\text{C}$, the increment is then

$$\Delta T_{\circ\text{C}} = 57.6 M^2 \quad (7)$$

Thus flying near sea level at $M = 1$ (corresponding to 1120 ft/sec), the *increment* is theoretically expected to be $\approx 58^\circ\text{C}$ or 104°F . Although increments actually obtained are only 90% of the theoretical maximum, operation of man-carrying aircraft under these conditions (for periods of time longer than a few minutes) is already impossible without some means of "*refrigeration*." Considering next a projectile or a guided missile traveling at $M = 2$ (say at 40,000 ft altitude where the absolute temperature may be $T = 238^\circ\text{K}$), the increment of temperature will theoretically be 230°C or 415°F . Temperatures caused by compressibility at supersonic speeds are spectacularly illustrated by the fact that practically all of the many meteors striking the earth's atmosphere (at very high speeds) simply disintegrate (melt and vaporize) as a consequence of the heat generated on their surface by fluid friction.

Entropy. To illustrate the transformation of dynamic energy into heat, as it partly takes place in compressible fluids, an experiment presented in (1,a) is quoted (in somewhat modified form) as follows. Considering the flow of a gas in a pipe of constant diameter, the average velocity is constant (under ordinary conditions). The speed can be increased, however, by introducing heat (by heating the pipe from the outside). The maximum speed thus obtainable is sonic. Computing now velocity as a function of heat flux, one finds that supersonic speeds may only be obtained after subsequently taking out heat, a process which corresponds to that of supersonic expansion (increased cross-sectional area of a stream tube) as shown in figure 1 of Chapter XVI. Assuming next that supersonic flow be established in the pipe considered, the speed can suddenly drop to a well defined subsonic value, by means of a *shock*. Corresponding to the compression taking place across the shock front,

the temperature rises; kinetic energy is converted into heat, a process which is readily possible. By cooling the pipe, we can then restore the original flow at subsonic velocity as considered first in this paragraph. The important parameter in the cycle considered, is the temperature level at which heat is added or taken out, respectively. According to the second law of thermodynamics, mechanical energy must be applied when introducing heat into a system at higher temperature, and/or when taking out heat at lower temperature. As a consequence, any sudden transition from subsonic to supersonic speed, in the pipe flow considered, by means of what we may call an "expansion shock" is not possible. Or, to express it in different terms, the *entropy* increases (a process common in nature) in a compression shock while a sudden expansion in the pipe flow considered, would mean a reduction of entropy (a process which is physically not possible). Every discontinuous compression (identical with a shock) is thus coupled with an *increase of entropy*. Considering an airplane flying at transonic or supersonic speeds, where shock waves are produced, any increase of entropy, means heating the air particles passing through the shock sheets. Corresponding to the heat thus produced by the craft, its drag is necessarily increased. Shocks produced by slender obstacles are comparatively "weak", however. Drag due to growth of entropy can be so small, accordingly, that it may be neglected altogether, within a limited range of supersonic Mach numbers. In fact, linearized supersonic theory (involving only "small perturbations") gives realistic results without taking into account heat transfer as explained above.

2. SKIN-FRICTION IN COMPRESSIVE FLOW

Skin-friction drag can be small at supersonic speeds in comparison to pressure drag. Shapes of wings and bodies have been improved to such a degree, however, that viscous friction can now be said to have the same importance as wave drag.

BL Temperature. Because of the increase of temperature within the boundary layer as explained in the preceding section, skin friction generally tends to decrease as a function of Mach number. The mechanics of this effect can easily be understood by the simple analysis described as follows. Directly at the surface of a flat plate in tangential fluid flow, the velocity is zero. The temperature is consequently increased by a value approaching that as indicated by equation 6. The average density within the boundary layer is reduced, accordingly, in the proportion of $\rho \sim 1/T_{BL}$; thus

$$\rho_{BL}/\rho_{amb} = T_{amb}/T_{BL} = 1/(1 + o M^2)$$

where o = suitable integration constant. Skin friction is also a function of viscosity μ (in sec/ft²); and this type of viscosity (see Chapter I) can be assumed to be roughly

$$\mu_{BL}/\mu_{amb} = T_{BL}/T_{amb} \quad (11)$$

Considering now *laminar* BL flow, skin friction drag is

$$D_f \sim \rho C_f \sim \rho/R^{1/2} \sim \mu^{1/2} \rho / \rho^{1/2} \\ \sim (T_{BL}/T_{amb})^{1/2} (T_{amb}/T_{BL})^{1/2} = 1$$

- (1) Modern information on supersonic fluid flow:
 - a) VonKármán, "Foundations of High-Speed Aerodynamics", Vol.V of "Jet Propulsion and High Speed Aerodynamics" by Summerfield (Princeton University Press), abstracted in Proc.U.S.Cong. Appl.Mech.1951 (ASME 1952).
 - b) See Prandtl's, Liepmann's and Ferri's books as quoted in footnote (1) of Chapter XVI; see also Bonney's "Engineering Supersonic Aerodynamics", McGraw-Hill 1950.
 - c) Certain other texts on gas dynamics are highly "mathematical". About one of them Munk has said: The volume "presents itself to the engineer as an endless and dreamy parade of shadowy and colorless mathematical statements".
 - d) A "complete" compilation of basic gas dynamic equations, and of tables and graphs representing shock wave mechanics, Prandtl-Meyer expansion and cone-wedge pressure forces — is given in NACA T.Rpt 1135 (1953).
- (2) In atmospheric air, up to some 300,000 ft (≈ 90 km) of altitude, the specific heat ratio " γ ", or "k" (as denoted in this book) is $= 1.405 \approx 1.40 = 7/5$. Because of this constancy, we have eliminated "k" from most of the equations and/or parameters used in this chapter and in Chapter XVI.
- (3) Ernst Mach, Austrian physicist 1838 to 1916.
- (4) "Expansion", by Prandtl, Physikalische Zeitschrift 1907 p.23; and by Meyer, Forschungsheft VDI No. 62 (1908); Transl. by Cornell Res.Foundation, also Transl. by British MOS.

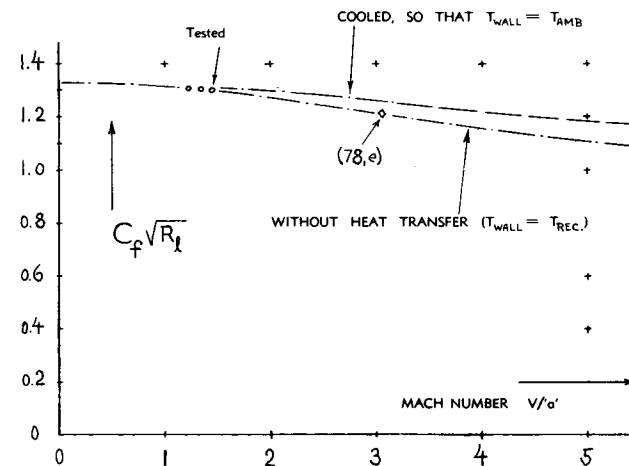
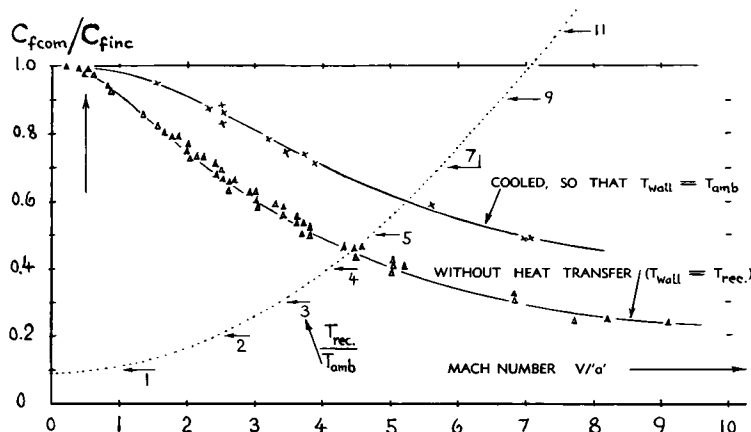


Figure 2. Mean-total *laminar* skin-friction parameter as a function of Mach number (8).



In other words, for laminar BL flow, compressibility and temperature do not affect the magnitude of friction and/or that of the skin-friction drag coefficient (based upon ambient physical properties). Actually, and when making a more refined analysis, some small reduction is found for laminar BL flow. Evaluation of a complete solution (8,f) by mechanical computation (8,g) yields the function plotted in figure 2. Experimental results (obtained to $M \approx 3$) confirm the theoretical prediction very well. Up to $M \approx 5$, laminar friction may be approximated by

$$C_{f_{com}} / C_{f_{inc}} = 1 / \sqrt[4]{1 + 0.045 M^2} \quad (12)$$

Turbulent Friction. As far as turbulent boundary-layer flow is concerned, the reduction of density due to increased temperature (as explained above) is predominant. On the basis of $C_f \sim 1/R^{1/6}$ - (as found in Chapter II) our simple analysis started above, yields for turbulent boundary layer a drag

$$D_f \sim \rho / R^{1/6} \sim \mu^{1/6} \rho^{5/6} \sim (T_{BL} / T_{amb})^{1/6} / (T_{BL} / T_{amb})^{5/6} \\ = (T_{BL} / T_{amb})^{-2/3} \sim 1 / (1 + o M^2)^{2/3} \quad (13)$$

A more accurate analysis is much more complicated. The fact that there are one or two dozens of theoretical treatments available (10) suggests that a strict solution (without the assistance of experimental terms) is not possible. The existing experimental material is presented in figure 3 in the form of the ratio $C_{f_{com}} / C_{f_{inc}}$ taken (12) at constant Reynolds number (with the number based upon surface length "l" or "x"). For the condition of "no heat transfer" (insulated body skin) the results can be expressed by

$$C_{f_{com}} / C_{f_{inc}} = (1 + 0.15 M^2)^{-0.58} \quad (15)$$

For example at $M = 4$, turbulent skin friction is thus reduced to less than one half the uncompressible value (as indicated by the Schoenherr function, for instance, presented in Chapter II). Considering, however, boundary-layer and skin temperature at such a Mach number, some type of cooling (refrigeration)

Figure 3. Turbulent skin-friction (12) drag ratios (local and/or mean-total) as a function of Mach number; (a) without heat transfer ($T_{wall} = T_{rec}$, where the recovery temperature T_{rec} corresponds to 90% of the stagnation-point temperature) and (b) cooled to $T_{wall} = T_{amb}$. Experimental points are selected from (11).

will be absolutely necessary to make any aircraft "operational", when flying at such speeds. A second function for turbulent friction is included in figure 3, accordingly, indicating the friction ratio for the condition of $T_{wall} = T_{amb}$. Skin friction is higher in this case; the reduction as against the value in un-compressed fluid is still appreciable, however.

BL Stability. Considering now a Reynolds number of $R_c = 10^7$, for example, the turbulent skin friction coefficient $C_{f_{inc}} \approx 0.003$ is found to be more than 6 times as high as the laminar value (which is somewhat less than 0.0005 at that R' number). It then becomes evident that the stability of the laminar boundary layer flow and the Reynolds number of BL transition as a function of Mach number, are of great importance, not only for skin friction as such but also for a possible interaction of the BL with shock waves. The first part of this problem is the development of the laminar boundary layer at constant pressure, such as for instance along a plane wall. Analytical investigation (15) indicates that stability and R' number of transition reduce in this case as a function of increasing Mach number, such as shown in figure 4 up to M' numbers between 4 and 5 (16).

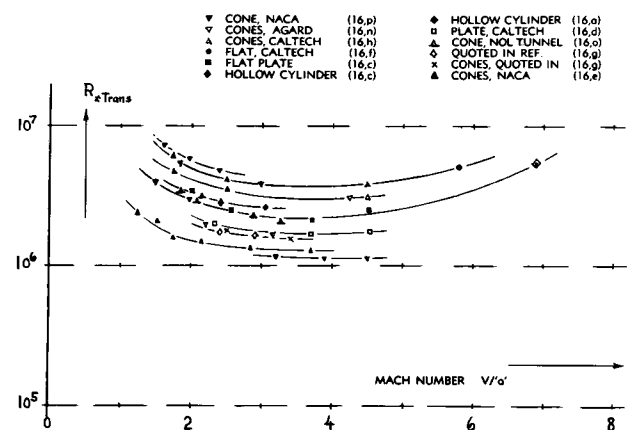


Figure 4. Reynolds number indicating transition in the BL flow along flat plates and straight cones (where pressure is \approx constant) as a function of Mach number.

BIBLIOGRAPHICAL REFERENCES:

- (8) Analysis and experiments on *laminar skin friction*:
- Kármán-Tsien, Basic Analysis, J.A.Sci.1938 p.227.
 - Monaghan, Approximation, ARC RM 2760 (1949).
 - Rubesin, Review of Theory, Trans ASME 1949 p.383.
 - Klunker, Methods of Analysis, NACA Technical Notes 2499 and 2916; see also Technical Note 2891.
 - Moore, Solution, J.Aeron.Sci.1952 p.229 & 288.
 - Young-Jansen, Computations, J.Aeron.Sci.1952 p.229.
 - VanDriest, Crocco Method, NACA T.Note 2597(1952).
 - Kay, Laminar & Turbulent, J.Aeron.Sci.1954 p.117.
 - Maydew, Experimental, NACA Tech.Note 2740.
- (10) Analysis of *turbulent friction* at supersonic speeds:
- Frankl-Voishel, Russian, NACA T.Memo 1053.
 - Wilson, Theory and Experiment, J.Aeron.Sci.1950 p.585.
 - Eckert, J.Aeron.Sci.1950 p.573, 1952 p.23, 1954 p.695.
 - Tucker, Approximation, NACA T.Notes 2045 & 2337.
 - VanDriest, Heat Transfer, J.Aeron.Sci.1951 p.145; see also Cone B'Layer, J.A.Sci.1952 p.55.
 - Cope, Analysis, ARC RM 2840 (1953); also 2613.
 - Coles, Problem of BL, Zts.Ang.Math.Phys. 1954 p.181.
 - NACA, BL Similarity, Tech Notes 2541/2/3 and 2692.
 - An engineering type procedure of calculating laminar and/or turbulent friction as a function of Mach number and/or wall temperature, is given by Eckert in Journal Aeronautical Sciences 1955 p.585.
- (11) Experimental results on *turbulent skin friction*:
- Wilson, Theory and Experiment, J.A.Sci.1950 p.585.
 - Rubesin, Analysis and Experiment, NACA T.Notes 2305 and 2917; also Trans ASME 1949 p.385.
 - Brinich, Experiments NACA T.Notes 2203 and 2742.
 - Chapman-Kester, On Cylinders, NACA T.Note 3097; see also J.Aeron.Sci.1953 p.441.
 - Wegener (NOL), at $M = 7$, J.Aer.Sci. 1953 p.220.
 - Liepmann-Dhawan, in NACA Technical Note 2567.
 - Coles (Caltech), On Flat Plate, J.Aeron.Sci.1952 p.717 and 1954 p.433; also ZAMM 1954.
 - Lobb-Winkler-Persh (NOL) J.Aeron.Sci.1955 p.1.
 - Sommer-Short, Heated Boundary Layer, NACA T.Note 3391 (1955); also J.Aeron.Sci.1956 p.536.
 - Hill, In Hypersonic Flow, J.Aeron.Sci.1956 p.35. This paper shows that thickness of laminar sublayer is increased.
- (12) "Equal Reynolds number" is often based upon momentum thickness. A number based on length "l" or "x" as used in plotting the results in figure 3, is more convenient, however, for practical applications.
- (13) The *minimum critical (instability)* Reynolds number on cones is 3 times (10,e) that on a plane surface (flat plate). Tetervin (NACA T.Note 4078 and J.A.Sci.1957 p.545) has shown, however, that the *transition* number is less.
- (15) Influence of heat flux upon BL stability:
- Van Driest, Cooling Analysis, NACA T.Note 2597 and in J.Aeron.Sci.1952 p.801.
 - Sternberg (Aberdeen), Experimental Verification of (a) on Rocket, J.Aeron.Sci.1952 p.721.
 - Lees, Stability, NACA T.Note 1115 and T.Rpt 876.
 - Low, Heat Flux Analysis, J.Aeron.Sci.1955 p.329.
 - Dunn, Stability Analysis, J.Aeron.Sci.1955 p.455.
 - Czarnecki, Heat on RM-10, NACA T.Rpt 1240.
- (16) Experimental results on *transition* of BL flow:
- Bertram, at $M = 6.9$, NACA T.Note 3546 (1955).
 - NACA, On Flat Plates, T.Notes 2351 and 3473.
 - Brinich, NACA T.Notes 2742, 3509, 3659, 3979.
 - Coles, On Flat Plate, J.Aeron.Sciences 1954 p.433.
 - NACA, On Cones, T.Note 2131, 3020 and 3097.
 - Probstein, Evaluation, IAS Paper 1956.
 - Gazley, Review of Data, J.Aeron.Sci.1953 p.19.
 - Laufer, Tunnel Tests, J.Aeron.Sci.1954 p.497.
 - Fischer, On V-2 in Flight, Trans ASME 1949 p.457.
 - NACA, Summary, in AGARD Memo AG8/M4(1953).
 - Chapman, Base Drag, NACA Tech Note 3869.
 - NACA, Influence of Blunting LE, T.Notes 3653 & 3659.
 - Evvard, Fluctuations, J.Aeron.Sci.1954 p.731.
 - Lange, in J.Aeron.Sci.1953 p.718 and 1955 p.282.

However, upon withdrawing heat from the BL (through the solid surface) i.e. by cooling the boundary layer, stability can be increased very significantly. Such cooling (heat transfer onto the moving body's mass of metal) takes place during the short duration of firing projectile models in a ballistic range or during the initial seconds or possibly minutes after launching a missile such as the "V-2". As a consequence, critical R'numbers (indicating BL transition) have been found under such conditions (15,b) in the order of $R_{x\text{trans}} = (2 \text{ to } 9) 10^7$ (see figure 5) at M'numbers between 1.3 and 2.7. Corresponding transition numbers obtained on a "RM-10" missile model (15,g) when cooled to ambient temperature, are doubled as against the number for natural BL heating; they are then in the order of $2 \cdot 10^7$, at $M = 1.6$. At larger M'numbers, the experimental results plotted in figure 4 seem to indicate a reversal in the variation of the transition R'number. The growth of those numbers above $M \approx 4$ (also proposed in reference 16,f, to be real) may very well be a consequence of hypersonic BL flow conditions within the narrow space between body surface and shock wave.

Cone Flow. The fact that in figure 4 the experimental points obtained on cones are on the highest level, is not accidental. Because of the conical flow pattern, the BL is continuously thinned and thus stabilized. The equivalent flat-plate Reynolds number on conical and/or ogival noses can be between 1/2 and 2/3 of that computed on the basis of the distance "x" from the point, along the surface (10,e). Vice-versa, critical R'numbers can thus be obtained on such body noses which are possibly two times as high as they would be on a flat surface under otherwise equal conditions (13).

Pressure Gradient. As in subsonic aerodynamics, size and magnitude of the pressure gradient along the surface of a solid body, has a very great influence upon stability and transition, respectively, of the BL flow. Contrary to conditions in uncompressed fluid flow, *negative* gradients are necessarily obtained at transonic and supersonic speeds, by means of the Prandtl-Meyer type of expansion around corners, and in particular *past curved shapes*. A 10% thick biconvex foil section, for example, in a flow at $M = 2$, will have a steadily reducing pressure distribution corresponding to a total differential between LE and TE of $\Delta p/q$ of the order of 0.4. Corresponding (but lesser) gradients are found on streamline shapes (such as on the missile bodies in figures 34 through 37 of Chapter XVI). Transition R'numbers are plotted in figure 5, as tested on ogival and/or parabolic body shapes (where a favorable pressure gradient is pre-

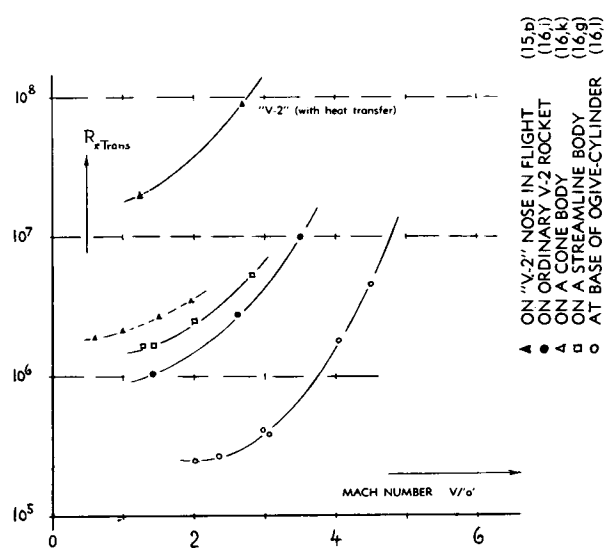


Figure 5. Reynolds number indicating BL transition as found on *ogival* and *parabolic* body shapes (having a negative pressure gradient) as a function of M'number. Note that the V-2 results are obtained on the conical part of that vehicle's nose; *cooling* (rather than a favorable pressure gradient) seems to be responsible for the very high transition R'numbers found in that case.

sent). We see (a) that in contrast to those in figure 4, the critical R'numbers grow steadily as the Mach number is increased; and (b) that levels are reached in this manner far above those in figure 4. The lowest line in figure 5 at supersonic speeds, corresponds to transition tested near the base of ogive-cylinder combinations (16,l) where a favorable pressure gradient is available only part of the way, i.e. past the ogival nose.

Surface Roughness. Basically in the same manner as under subsonic (uncompressed) conditions (described in Chapter II) boundary layers in supersonic fluid flow are also very sensitive against added disturbances such as mechanical *vibrations* (from any type of *machinery* connected with the testing), tunnel *turbulence*, *sound waves* and finally against surface *roughness*. Such factors are evidently responsible for the various levels in figure 4 (and partly for those in figure 5 as well). Boundary-layer transition as a function of *roughness* is treated in Chapter II. At supersonic speeds (corresponding to $M = 3.5$) uniformly distributed roughness has, for example, been investigated in (19,b). On the *cooled* surface (i.e. with $T_{wall} = T_{amb}$) of an ogive-cylinder body, the transition R'number was found to be reduced to $\approx 1/2$ the original value by a grain size " k " roughly four times that required to obtain the same relative reduction

in figure 10 of Chapter II. Experiments with various *single* roughness elements such as in (19,a) and as quoted in (16,f) and in (16,g), show that at M'numbers between 1.5 and 3.5, the "grain" size (height) of these elements required to produce the same relative reduction in transition R'number as in uncompressed fluid flow, is between 3 and 10 times as large as under those conditions. Such results agree very well with the general experience that laminar BL is so often found in supersonic testing at Reynolds numbers where in subsonic aerodynamics, most certainly turbulent flow is to be expected.

Critical Roughness Size. Figure 6 is presented as an example, showing how on a parabolic body of revolution the grain size (in a "sand" strip near the nose extending over a length equal to 3.5% of that of the body) required to produce fully turbulent BL flow, grows considerably as the M'number is increased. It can now be assumed that the "permissible" or "required" roughness size may grow in proportion to the thickness of the boundary layer, and in particular to that of the *sublayer* where finer surface protuberances develop their influence upon BL flow. The thickness of that layer increases in proportion to $1/\theta \sim T$. Applying then equation 6, the roughness size " k " required, can be expected to increase as a function of M'number at the rate of

$$"k" \sim 1 + 0.2 M^2 \quad (17)$$

For example, at $M = 3$, we thus obtain a size " k " that is almost 3 times the value in uncompressed fluid flow (as in figures 10 and 11 of Chapter II). By the same reason, one can also expect that the maximum-*permissible* grain size, in turbulent BL flow (in the definition as given in Chapter V, indicating the beginning of roughness-type flow) should be higher at supersonic speeds, at least in the same ratio as given above in equation 17. The experimental results in figure 6 confirm this argument, at least qualitatively. In one of the two examples presented, the grain size required to produce turbulence, grows to \approx tenfold as the Mach number is increased from 1 to 4. A simple conclusion to be drawn from this result, is the possibility that when increasing " R' " in proportion to " M' ", the boundary layer of this body can be entirely turbulent at $M = 1$; – and it can then become completely laminarized upon approaching $M = 4$. This is indeed a reversal from what is to be expected in uncompressed fluid flow (such as at smaller subsonic Mach numbers).

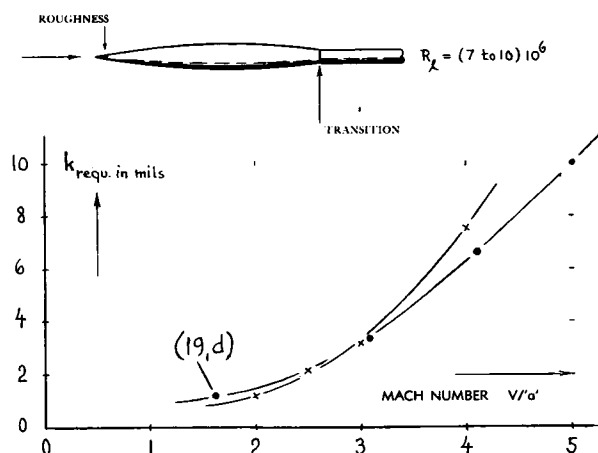


Figure 6. Example for the influence of supersonic compressibility upon boundary-layer stability; roughness grain size (in a narrow strip near the nose of a parabolic body) required (19,c) to produce fully turbulent BL flow — as a function of Mach number.

Drag Due to Roughness. In the case of roughness elements (such as sand grains) uniformly distributed over the surface, it can be argued that above the R' -number at which roughness-type BL flow (as explained in Chapter V) becomes established for a certain grain size, viscosity does no longer affect the drag. Equation 13 may then be rewritten as

$$D_f \sim \varrho \sim (T_{amb}/T_{BL}) \sim 1/(1 + o M^2) \quad (18)$$

A preliminary guess (20,a) is that the exponent in equation 15 be doubled in order to represent drag in

developed roughness flow. This type of boundary-layer-bound drag can thus be expected to decrease as a function of M'number at a rate which is greater than that of the turbulent skin friction coefficient as indicated in figure 3. An experimental result (20,c) confirms this prediction insofar as skin-drag coefficients are indicated at a level which is even below that of the equation. A stabilizing influence of the pressure distribution along the parabolic body used in these tests may have preserved laminar flow, however, over some portion of the forebody — in spite of surface roughness. It is clear, at any rate, that the coefficient for a rough surface cannot reduce to a level below that for smooth (but turbulent) BL flow. Read also footnote (20,e).

Lap Joints, similar to those in figure 10 of Chapter V have been investigated on the cylindrical body of a free-flight model (20,b). Evaluation by means of the principles presented in that chapter, indicates “reduced” drag coefficients “ c_D ” (on the lap joints’ frontal area) roughly 3 times as high as those known for uncompressed flow conditions. It is therefore concluded that the drag produced by these joints is, at least partly, *wave drag*. This conclusion is confirmed insofar as the incremental drag coefficients as tested, reduce from “2” to “1”, as the M'number is increased from 1.2 to 2.1. This reduction roughly corresponds to that of two-dimensional wave drag (equation 30).

3. TRANSONIC DRAG OF STRAIGHT WINGS

The *transonic* characteristics of airfoil sections and/or straight wings are treated in this “supersonic” chapter, rather than in Chapter XVI, for reasons of convenience.

Flow Pattern. In the beginning of Chapter XVI, it is explained that flow conditions in a closed duct (wind tunnel) are critical at and in the vicinity of $M = 1$. Even in free flow (with an unlimited space available) conditions are still critical, particularly past all types of sections in two-dimensional fluid flow. The subject of *transonic* characteristics is also problematic in regard to theoretical analysis, where mostly numerical solutions have only been established so far, for a few selected shapes. Considering a wing flying at a speed approaching $M = 1$, a detached shock wave of vanishingly small intensity originates at an indeterminate distance ahead of that obstacle. Upon increasing the Mach number to and very slightly above unity, the shock wave approaches the wing very rapidly. Slightly subsonic speeds are found behind this wave. A com-

- (17) Influence of pressure gradient upon transition:
 - a) Weil, Biconvex Section, J.Aeron.Sci.1951 p.311.
 - b) Probstein as in footnote (16,f).
 - c) Allen, On Airfoil Sections, NACA T.Note 1255(1947).
 - d) Critical R'number of spheres, figure 10, Chapter XV.
- (19) Influence of surface roughness on transition:
 - a) Brinich, Single R'Elements, NACA T.Note 3267(1954).
 - b) Jedlicka, BL on Ogive Cylinder, NACA T.Note 3342.
 - c) Fallis, Stimulation, J.Aeron.Sci.1955 p.339.
 - d) Results on cone-ogive-cylinder combinations similar to those in (c) are reported by Luther (Caltech) in Journal Aeronautical Sciences 1957 p.579.
- (20) Influence of surface roughness on drag:
 - a) Hoerner, Influence of Compressibility on Drag, German ZWB Rpt UM 7810 (1944); also T.Rpt F-TR-1188-ND, ATI 43187 (USAF Wright Field, 1947).
 - b) Hopko, Rivets and Lap Joints, NACA RM L52F09.
 - c) Jackson, Sand Roughness, NACA RM L52B26.
 - d) Wade, Experimental, UTIA Rpt 34 (1956).
 - e) Liepmann explains in J.Aeron.Sci.1957 p.784 that turbulent friction along rough surfaces corresponds to $C_{f,com} = C_{f,inc} / (1 + 0.18 M^2)$. This function confirms equation 18 very well.

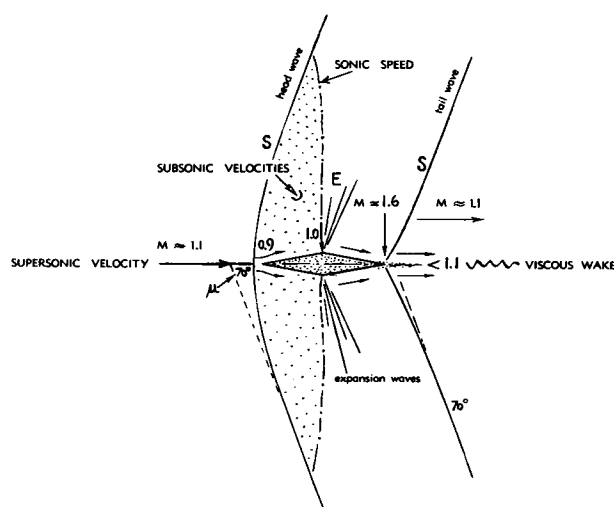


Figure 7. Flow pattern past a two-dimensional double-wedge section at a certain transonic speed. "E" = expansion fan. Note; we cannot show the flow pattern at $M = 1$, inasmuch as it extends to infinity (up and down).

pressible, but first subsonic type of flow pattern then develops along the forebody of the airfoil section, accelerating again and reaching sonic speed at the location where the stream tubes have the narrowest cross section, tentatively as indicated in figure 7. Supersonic expansion takes place there, around the section's shoulder; and the flow is finally restored to ambient pressure across a shock wave originating from the trailing edge of the airfoil section. Within the two fields of subsonic velocities bounded by shock and sonic lines, the air is given the opportunity of turning somewhat sideways (up and down, respectively, in the illustration) in order to "get around" the obstacle, using a bypass, so to speak. As the Mach number at which the wing moves against the air (or vice versa) is further increased above $M = 1$, the boundary line at which sonic velocity is reached, moves toward the leading edge, while the head wave moves in the opposite direction; and we then have a flow pattern different from the one as shown in figure 7. Finally, at a supersonic Mach number, the magnitude of which is a function of airfoil thickness ratio or leading-edge wedge angle (see figure 25 in Chapter XVI), the shock attaches itself to that edge; and at a still very slightly higher M' number, shock front and sonic boundary meet each other, thus starting "pure" supersonic flow.

Similarity Rules. The mixed subsonic-supersonic flow pattern as in figure 7, is not readily susceptible to simple and explicit theoretical treatment. *Similarity rules* have been established, however, for the transonic range of the Mach number. Such rules, based upon physical properties, body dimensions and speed

or speed components, are very useful tools in the analysis, interpolation, extrapolation and correlation of experimental results. There are dozens of similarity "rules" in fluid dynamics, also called "laws" or not given any specific name, usually based upon a certain non-dimensional parameter such as the Reynolds, Froude or Mach number, in particular. Similarity then means that (disregarding the influence of certain *other* parameters) flow conditions (pattern, pressures, forces) in one particular set of dimensions, speed and/or physical constants, are similar (or equal when given in coefficient form) to those in a different combination of parameters, provided that the "similarity number" is the same (see also text in Chapter I on this subject). Such rules are of particular importance in cases where a quantitative solution of a certain problem has not yet been established. A similarity rule is then a welcome expedient of concluding from one specific experimental result upon the characteristics of a series of other combinations of dimensions, speeds and/or physical properties of the fluid involved (29).

Transonic Similarity. Disregarding skin friction and flow separation (if any) and if applied to slender shapes, similarity analysis (28,b and f) predicts for airfoil sections in two-dimensional flow, that

$C_{D_0}(M/\varepsilon)^{2/3}$ is a unique function of

$$(M^2 - 1)/(M^2 \varepsilon)^{2/3} \quad (20)$$

On wedges (in symmetrical flow) the drag coefficient (on projected frontal area) is also equal to $|C_p|$, taking into account the proper sign (as a function of surface inclination, against or away from the oncoming flow). For application to airfoil sections other than wedges, the surface angle " ε " is to be replaced by the thickness ratio (t/c) when using the last equation.

Wedges, with the sharp edge ahead, are a type of body comparatively easy to test. A number of experimental results are available, accordingly, on such *single* wedges. Figure 8,a presents their *forebody* drag coefficient (not including any base drag) in form of the similarity parameters as indicated by equation 20. It should be noted that in double-symmetric double wedges the half vertex angle $\varepsilon = t/c$, where c = chord of the double wedge. Figure 8,b presents the pressure drag coefficient of the *afterbody* of such sections. It is seen that the coefficient of this drag component decreases as a function of M' number, while that of the forebody increases across the transonic Mach-number range. It follows from this mechanism, that for high *subsonic* speeds (and at small supersonic speeds) slightly reduced drag may be obtained by using a double wedge (or other foil shape) whose forebody is shorter than the afterbody, as we have it in practically all subsonic-type airfoil sections.

Transonic Theory. Sharp-shouldered double wedges are one of the special shapes mentioned above where theoretical analysis has been successful. The simplest approach to the subsonic type of flow past the wedge's forebody is as described in Chapter XVI, under the subheading of "two-dimensional plate". Figure 8 shows certain theoretical points for $M = 1$. At this

M' -number, the drag of double wedge sections corresponds theoretically to

$$\begin{aligned} C_{D_1} &\approx 1.25 \quad (t/c)^{2/3} \text{ for the forebody} \\ C_{D_2} &\approx 2.75 \quad (t/c)^{2/3} \text{ for the afterbody} \\ C_{D_3} &\approx 4.00 \quad (t/c)^{2/3} \text{ for the D'wedge} \end{aligned}$$

where $t/c = \tan \varepsilon$ = tangent of half-vertex angle ε . Based

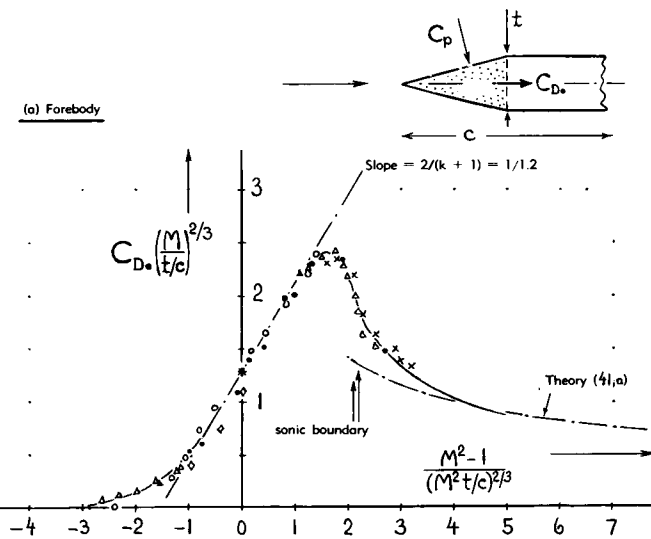
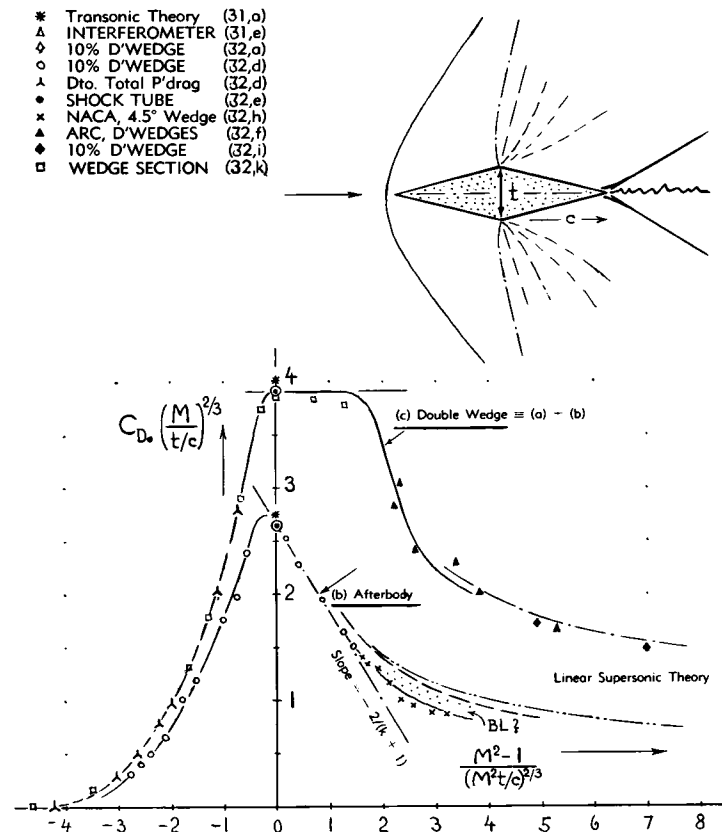


Figure 8. Pressure or wave drag coefficient of wedges, presented in form of transonic similarity parameters.

- (26) Airfoil and wing theory at $M = 1$:
 - a) Guderley, Airfoil Theory at $M = 1$; USAF ATI Tech Data Digest 1947 No.9; AMC Tech Rpt 5783 (1949); also J.Aeron.Sci.1950 p.723 and 1956 p.961.
 - b) Gardner, Transonic Acceleration, J.A.Sci.1950 p.47.
 - c) See also the sources in footnote (60).
 - d) Joshihara, Transonic Wedge, J.Aeron.Sci.1957 p.661.
- (28) Principles of transonic similarity:
 - b) Spreiter, NACA Tech Note 2273 and T.Rpt 1153.
 - c) Bömelburg, Generalization, ZFW 1955 p.313.
 - d) Oswatitsch, numerous papers on transonic similarity, referenced, for example, in (31,g).
 - f) The improved type of correlation (including " M^2 ") in the parameters as in figure 8, is discussed and confirmed in NACA T.Notes 2724, 2887, 3096 and 3225.
- (29) An incompressible example of this sort is the von Kármán-Schoenherr line (in Chapter II). While to this date, a "solution" of turbulent skin-friction drag has not been found, application of a similarity law concerning flow pattern and shear forces in the boundary layer, makes it possible to predict this type of skin friction drag for Reynolds numbers between 10^5 and 10^9 , and evidently to infinity — on the basis of one single correctly tested point, anywhere within that range. Of course, to prove the law, thousands of points have been determined over a period of 50 years; and a debate regarding the proper slope is still going on (see Chapter XI).
- (31) Wedge analysis at transonic speeds:
 - a) Guderley, Wedge at $M = 1$, J.Aeron.Sci.1950 p.723.
 - b) Coles, Wedge at $M \approx 1$, J.Math. and Phys. 1951 p.79.
 - c) Vincenti-Wagoner, NACA T.R. 1095 (TN 2339, 2528).
 - d) Liepmann-Bryson, J.A.Sci.1950 p.745.
 - e) Bryson, Interferometric Tests, NACA T.Rpt 1094.
 - f) Truitt in J.Aeron.Sci.1954 p.860.
 - g) Spreiter, Evaluation of Transonic Similarity, NACA T.Note 2726 or T.Rpt 1153; also J.A.Sci.1954 p.70 & 360.
 - h) Trilling, Transonic Wedge Flow, ZAMP 1953 No. 5.
- (32) Transonic experimental results on wedges:
 - a) Humphreys, 10% D'Wedge, NACA T.Note 3306.
 - b) NACA, Two Double Wedges in T.Rpt 1106.
 - c) See references (31,d,e); and (5) in chapter XV.
 - d) Nelson, Pressure Distribution, NACA RM L52C18.
 - e) Griffith, Shock Tube Results, J.A.Sci.1952 p.249.
 - f) Hilton-Pruden, Force Tests on Double Wedges, ARC RM 2057 and 2197; see also RM 2864.
 - g) Groth-Pack, Wedge Flow Pattern, ARC RM 2321.
 - h) Vincenti, Transonic D'Wedge, NACA T.Note 3225, continuation on Finite-Span Wings in T.Note 3522.
 - i) ARC, 10% Supersonic Sections, RM 2800 (1954).
 - k) Lina, 6% Double Wedge, NACA Doc. RM L9A12; when plotting these results in figure 8,c — an estimated component of skin-friction drag was first subtracted.
 - l) Valensi (NPL), Wedge Pressure, ARC RM 2482.
 - m) Gooderum, Lifting Wedges, NACA Tech Note 3626.



upon wing area ($b c$) the total wave-drag coefficient of symmetrical D'wedges (at zero lift) is

$$C_{DW} \approx 4 (t/c)^{5/3} \quad (21)$$

Figure 10 presents experimental points confirming this function sufficiently well. The ranges above $M = 1$ (31,c) and below $M = 1$ (as in 31,h) have also been investigated analytically. The slope of the reduced drag coefficient against the M'number parameter, as indicated in (31,g), is in the notation as used in figure 8:

$$2/(k + 1) = 0.83 \quad (22)$$

The slope for the wedge's afterbody has the same but negative value. The total drag *parameter* (as in figure 8,c) shows a *constant* value accordingly, within a certain range above $M = 1$. The theoretical functions are well confirmed by experimental results (see figure 8). Within the range of lower supersonic M'numbers, the drag of the *forebody* (mixed flow) is higher than that as indicated by linear supersonic theory (41). Wave drag of the *afterbody* as tested, is slightly less, however, than predicted by any theory. The growth of the boundary layer (as marked in figure 8,b) is evidently responsible for the discrepancy.

Fairing at $M = 1$. The function (equation 21), indicating the peak of transonic wave drag in two-dimensional flow at $M \approx 1$, can be utilized to determine the optimum thickness ratio of a fairing (resulting in minimum drag for a given frontal area). Including skin friction, the total drag coefficient of a double-wedge section is

$$C_{D\bullet} = 2 C_f (c/t) + 4 (t/c)^{2/3} \quad (26)$$

For example, for a skin-friction coefficient of $C_f = 0.002$ (a value which may be "half" way between turbulent and laminar BL conditions) differentiation of the last equation yields an "optimum" length ratio c/t in the order of 50, or an "optimum" thickness ratio in the order of 2%. This value is by far smaller than the corresponding value found in uncompressed fluid flow (which is in the order of $t/c = 25\%$, as shown in Chapter VI).

Drag of 10% D'Wedge. Specific drag coefficients across the transonic range can be evaluated from the general functions in figure 8. Figure 9 presents, as an example, the coefficient of a 10% thick symmetrical D'wedge section plotted against Mach Number. The constant part of the similarity function (see figure 8,c) results in a reduction of the pressure-drag coefficient at the rate of

$$dC_D/dM = - (2/3) C_{D1} \quad (27)$$

where C_{D1} = coefficient at $M = 1$ (the theoretical

magnitude of which is listed above). Tested *total* drag coefficients agree reasonably well with transonic and supersonic theory, after adding an appropriate component for skin-friction.

A *Biconvex or Double-Arc* section (12% thick) has been tested by pressure distribution technique across the transonic range (31,e). Characteristics are similar to those of double wedges (as in figures 8 and 9). Reference (34) presents a solution (based on linearized transonic theory) for the pressure distribution of a symmetrical double-arc section at $M = 1$:

$$C_p / (t/c)^{2/3} = (1/\sqrt{x/c}) - 4\sqrt{x/c} \quad (28)$$

Integration of this function over the chord "c" of a 10% thick section yields drag coefficients

$$\begin{aligned} C_{D\bullet} &= 0.32 \text{ for the forebody} \\ C_{D\bullet} &= 0.52 \text{ for the afterbody} \\ C_{D\bullet} &= 0.84 \text{ total pressure drag} \end{aligned}$$

The total wave (pressure) drag is found to be the \approx same as that of a double-wedge section having the same thickness ratio (as indicated by equation 21). Distribution of the drag between fore and afterbody is somewhat different, however. The forebody pressure drag of the biconvex shape is somewhat smaller than that of the D'wedge, whose components are listed in context with figure 8. Experimental results in figure 9 show that the pressure drag of a double-arc section (33,c) is smaller than that of the D'wedge, at speeds below $M = 1$.

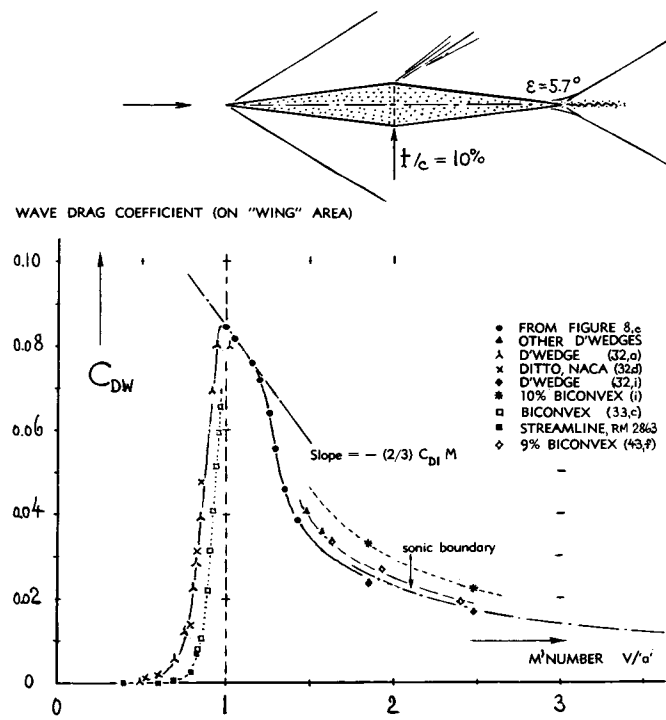


Figure 9. Wave-drag coefficient of 10% thick double-wedge section at transonic Mach numbers.

Round-Nosed Airfoil sections of the conventional subsonic type (extrapolated where necessary to $A = \infty$) have somewhat smaller total wave drag coefficients (at and below $M = 1$) than symmetrical double-wedge sections. Analysis predicts optimum thickness locations between 40 and 50% of the chord in two-dimensional flow (in straight wings) at M'numbers between 1.0 and 1.3. The comparative drag characteristics of D'wedges and of "streamline"-shape sections reverse their order, however, from one end of the transonic regime to the other. This can already be concluded from the results in figure 9, where at $M = 1.95$ and 2.47, the wave drag of a biconvex section is found to be higher than that of a double wedge having the same thickness ratio. Regarding truly "round-nosed" sections see again later.

- * THEORY FOR DOUBLE WEDGE (31,a)
- 65 SERIES EXTRAPOLATED (36,a)
- BICONVEX SECTION (31,e)
- △ DOUBLE WEDGE, FROM FIGURE 9
- + EXTRAPOLATED TO $A = \infty$ FIGURE 13

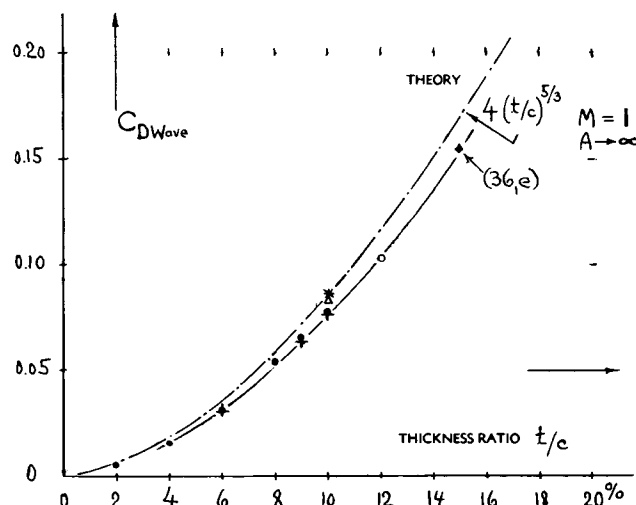


Figure 10. Pressure drag coefficient of symmetrical airfoils at $M = 1$ (in 2-dimensional flow at zero lift).

- (33) Experimental results on biconvex sections:
 a) ARC, RM 1130, 2196 and 2800 (also RM 2057).
 b) Daley-Lord, 6% Sections, NACA T.Note 3424.
 c) In Transonic Tunnel, Michel, ONERA Rpt 65; AGARD Rpt AG17/P7-1954; see in NACA T.Note 3970.
 d) Bryson, Interferometric Tests, NACA T.Rpt 1094.
 e) See also footnotes (43) and (48,e).
 f) NACA, 10% Biconvex Section, Doct. RM A9G18.
 g) Pressure distributions on biconvex foil sections, at $M = 1$, for various thickness locations (tested by Michel, ONERA) are correlated with transonic theory by Spreiter in NACA T.Note 3970 (1957).
- (34) Maeder, Biconvex Section at $M = 1$, J.A.Sc. 1956, 187.
- (35) Transonic tunnel tests on *straight wings*:
 a) Nelson, 22 Rectangular, NACA T.Note 3501.
 b) Nelson, 36 Symmetrical Wings, NACA T.Note 3529.
 c) Nelson, Cambered Wings, NACA T.Note 3502.
 d) Polhamus, Bump Summary, NACA T.Note 3469.
- (36) Transonic *Flight-test* results on *straight wings*:
 a) Mathews-Thompson-Katz, Free Falling Results, NACA Docts. RM L5E03, L6J14, L6J16, L6J30, L6K08C, L7E08, L7K14, L8F24; also Thompson, Proc.Internat. Aeron.Conf.1949 p.582.
 b) Mathews-Thompson, 65-009, NACA T.Rpt. 988.
 c) Kell (RAE), Free Falling Vehicle, ARC RM 2902.
 e) Mellenthin, 0015 on Bump, NACA T.Note 3036.

Finite Wings. The above considerations of *two-dimensional* flow characteristics are somewhat academic, insofar as in aircraft and/or missile wings (where those sections are to be used) the aspect ratio has an important effect upon the magnitude of wave drag at transonic speeds. Upon reducing the A'ratio of a wing from infinite to \approx zero, its flow pattern transforms naturally from a two-dimensional to a three-dimensional one. Pressures and forces at transonic speeds become relaxed, accordingly. Figure 11 presents results primarily of certain groups of wings (having constant thickness ratio each) demonstrating the influence of the aspect ratio at transonic speeds. Reduction of the A'ratio has consequences as follows:

- (a) The subsonic drag divergence M'number is considerably increased (see Chapter XV on this subject).

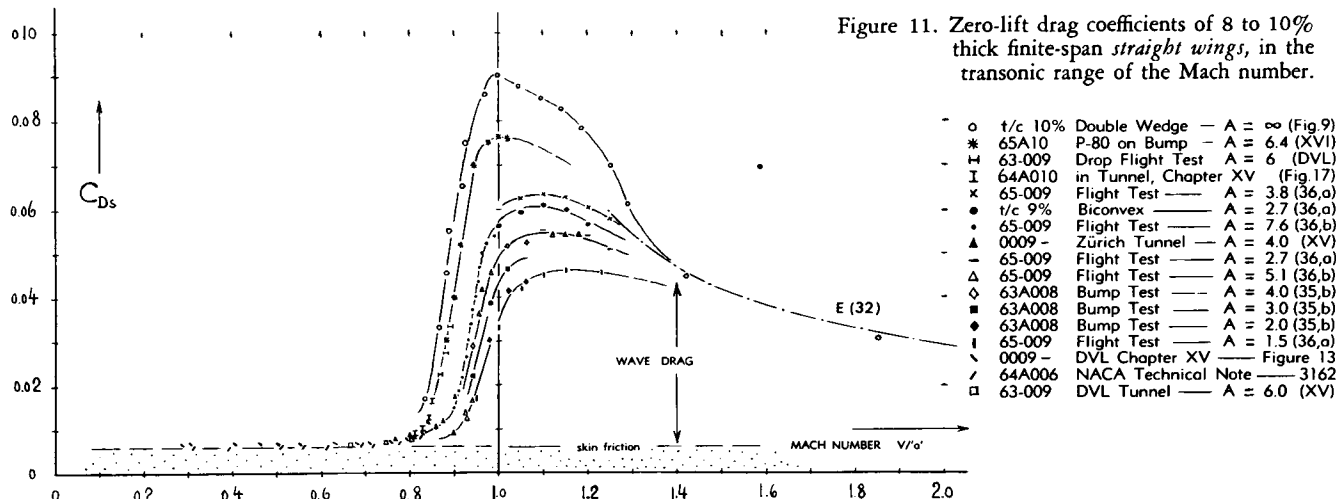


Figure 11. Zero-lift drag coefficients of 8 to 10% thick finite-span *straight wings*, in the transonic range of the Mach number.

- (b) The growth of C_{D_s} at M'numbers above drag divergence (also treated in Chapter XV) is reduced.
- (c) The peak of the drag coefficient (at $M \approx 1$) typical of 2-dimensional characteristics, is completely eliminated as the aspect ratio is reduced below 5 or 4.
- (d) As a consequence of (c), the drag coefficients now exhibit maximum values at M'numbers in the lower supersonic range, rather than at $M \approx 1$.
- (e) The coefficient is also reduced at higher transonic speeds. It is suggested, however, that all wings finally approach a supersonic function similar to that as shown in the graph (figure 11).

Aspect Ratio. The system of transonic similarity relations includes also the A'ratio of wings (38) thus permitting evaluation and correlation of experimental results. Figure 12 shows how pressure or wave drag (at zero lift) decreases, eventually to \approx zero (38,d) as the aspect ratio parameter $A(t/c)^{1/3}$ is reduced. The linear part of the function (below $A(t/c)^{1/3} \approx 1$) results in

$$C_{DW} = 2.3 A(t/c)^2 \quad (29)$$

In the range of larger aspect ratios, of the magnitude as in subsonic-type airplanes (if using them at supersonic speeds) the alleviating effect is less significant. Above $A(t/c)^{1/3} \approx 4$, the experimental results approach an upper limit, the level of which is related to the theoretical and experimental values as in figure 10. Functions similar to that in figure 12 have also been established (35) for values of the M'number parameter $(M^2 - 1)(t/c)^{2/3}$ different from zero (as for $M = 1$ in our illustration). It is suspected, how-

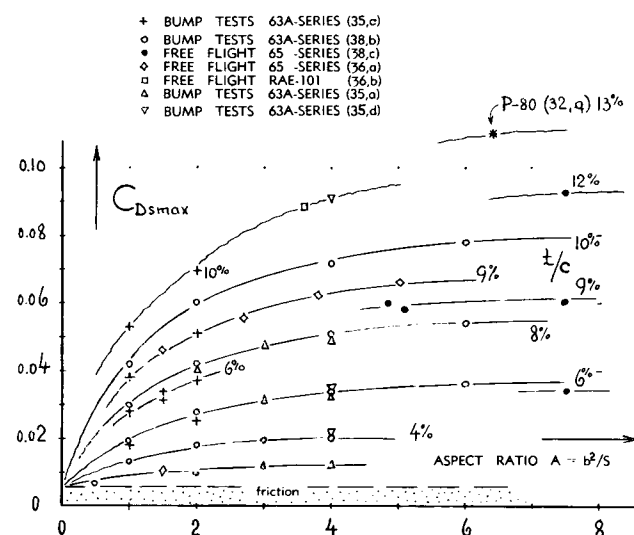


Figure 13. Maximum transonic drag coefficients (at M between 1.0 and 1.2) of wings with symmetrical foil sections (at zero lift) as a function of their aspect ratio.

ever, that more of this type of presentation (although scientifically correct) may not give the engineer the desirable more direct information. We have therefore plotted, in figure 13, transonic maxima of the drag coefficient (at zero lift) directly taken from the experimental material (such as in figure 11) as a function of the wing aspect ratio. For each family of wings with constant foil section each, the coefficient is seen monotonically decreasing along one of the lines, as the aspect ratio is reduced. Qualitatively the same reduction is also obtained by theoretical analysis as in (38,e).

● BUMP TESTS $A = 1$ to 6, 63A-SERIES, $t/c = (4$ to $10)\%$ (38,b)
 ✕ FLIGHT TESTS $A = 1$ to 7, 65-SERIES, $t/c = (6$ to $12)\%$ (38,a)
 △ BUMP TESTS $A = 2$ to 4, 63A-SERIES, $t/c = (4$ to $8)\%$ (35,a)

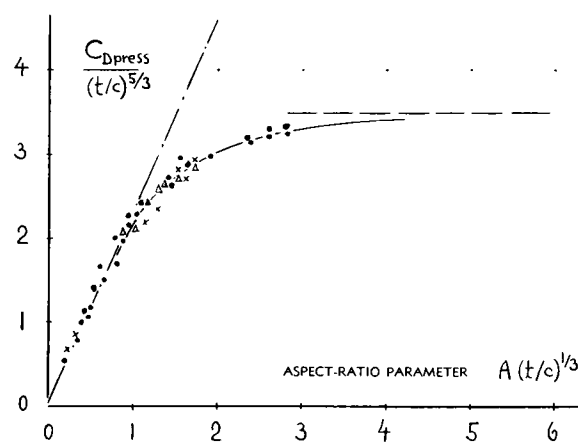


Figure 12. Reduction of pressure or wave drag (at zero lift) of wings at transonic speeds as a function of their aspect ratio, presented in form of similarity parameters.

4. STRAIGHT WINGS IN SUPERSONIC FLOW

Flow Pattern. Figure 14 gives an illustration of flow pattern and pressure distribution of a double-wedge section at zero lift. The drag corresponding to the positive pressure on the forebody is the equivalent of the momentum losses (or momentum transfer) taking place along and across the compression shock wave originating from the leading edge (at "a"). At the corner "b", the flow is then accelerated by means of a Prandtl-Meyer-type expansion to a speed exceeding that of the undisturbed flow. The second component of drag, due to the negative pressure on the D'wedge's afterbody, corresponds to the tail wave (originating from the trailing edge at "c"). Considering very small thickness ratios (equivalent to "small" perturbations) in non-viscous fluid flow, pressure as well as velocity are restored to the respective ambient values when passing through the tail wave. Under realistic conditions, the static pressure also increases to the level of the undisturbed flow, while a *deficiency* of speed, momentum, "total" pressure and/or enthalpy is necessarily left behind the moving wing. This deficiency is not concentrated, however, in form of a wake similar to that corresponding to skin friction. Rather, a loss of speed is spread out sideways (that is, up and down in figure 14) in form of a "shadow".

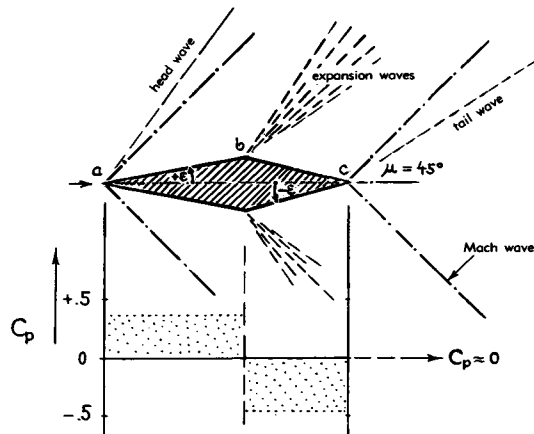


Figure 14. Flow pattern and pressure distribution of a D-wedge airfoil section in supersonic flow (at $M \approx 1.4$).

Thin-Airfoil, Linearized Theory (41) applies under conditions where the perturbation velocities caused by the airfoil's displacement, are small; it neglects heat transfer, assumes infinitely weak and straight shock waves and it disregards viscosity, of course. It then predicts for every element on the surface of slender two-dimensional shapes a pressure coefficient

$$C_p = 2 \epsilon \tan \mu = 2 \epsilon / \sqrt{M^2 - 1} \quad (30)$$

where ϵ = local angle of inclination of the element (considered to be positive when the surface is inclined *against* the oncoming flow) and where μ = Mach angle as in equation 1 or in figure 1. Integrating the pressure function over the surface of the section, the *wave-drag coefficient* (subscript "W") of this and of other symmetrical airfoil shapes, based on frontal area, is found to be

$$C_{DW} = K(t/c) / \sqrt{M^2 - 1} \quad (31)$$

or based on plan-form or "wing" area:

$$C_{DW} = K(t/c)^2 / \sqrt{M^2 - 1} \quad (32)$$

The factor is $K = 1$ for single wedges (moving with the sharp edge ahead, and disregarding base drag); $K = 4$ in case of symmetrical double-wedge sections. As a function of the location of the maximum thickness along the chord, the factor of double-wedge sections, as indicated by linearized theory, is

$$K = (c/x) / (1 - (x/c)) \quad (34)$$

-
- (38) Transonic aspect-ratio correlation:
 a) Spreiter, Similarity Theory, NACA T.Note 2273 (1951).
 b) McDevitt, Similarity Correlation, NACA T.Rpt. 1253; transonic bump results in T.Notes 3501 and 3502.
 c) Danforth, Similarity Correlation, NACA RM L51G20.
 d) Boundary-layer thickness (displacement) becomes apparent in foil thickness ratios of and below 2 or 3%.
 e) Gardner, Accelerating Flight, J.A.Sci.1950 p.47.
- (41) Airfoil theory at supersonic speeds:
 a) Ackeret, Airfoils at Speeds Faster Than Sound, ZFM 1925 p.72; NACA T.Memo 317; also in Vol. 7 of Handbuch der Physik, Berlin 1927.
 b) Busemann, Second-Order Theory, Forschung 1933 p.87 (Brit.RTP Transl.1786); also Handb.Exp.Physik WH VI.
 c) Taylor, Application of (a), ARC RM 1467 (1932).

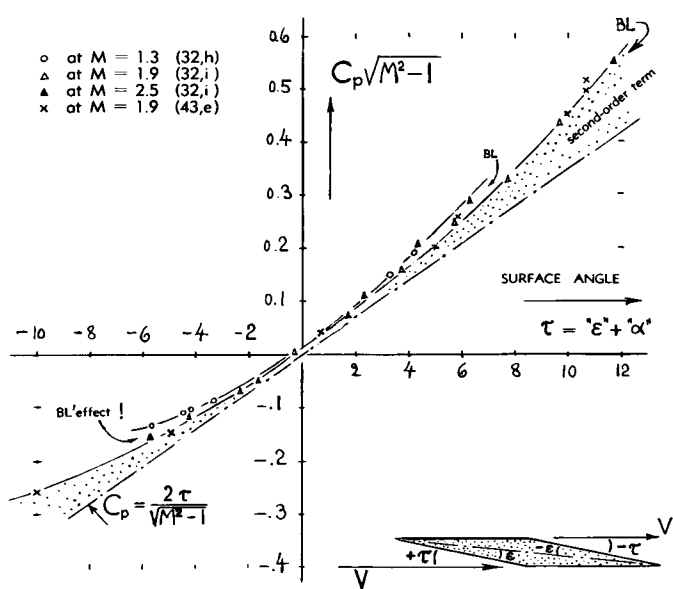


Figure 16. Pressure coefficient on the sloping surfaces of double wedge sections.

Second-Order Theory. Surface pressure coefficients obtained on double wedges, tested at various angles of attack, are plotted in figure 16. In comparison to linearized theory, the graph shows a considerable influence of second-order terms as treated later (see equ. 84) as a hypersonic phenomenon. Forces in the forebody are thus larger than, and those in the afterbody are smaller than indicated by simple theory (equation 30). For double wedges at moderately high supersonic Mach numbers, we can approximate the hypersonic term for practical purposes by

$$\Delta C_p = +1.2 \tau^2; \quad \Delta C_D = \pm 1.2 \tau^2 \quad (35)$$

where $\tau \equiv (t/c)$ in double-symmetrical D-wedges at zero angle of attack.

Afterbody Drag. There is also noticeable (in figure 16) an additional effect due to the presence (displacement) of the boundary layer, particularly at " $\tau = 0$ ", where a component of C_p roughly in the order of 0.01 is found for each of the sections tested. This effect too, is explained later (in the last section of this chapter) as a hypersonic phenomenon. For example, in a 10% thick D-wedge section at zero lift and at $M = 2.5$, the total differential in the pressure-drag forces on fore and afterbody respectively (caused by second-order terms in combination with the BL effect) is thus in the order of $\pm 15\%$. In other words, the forward half of a symmetrical section has a wave drag somewhat higher, and the rear a drag somewhat lower than indicated by equation 30 or 31. As a consequence, the optimum shape of a double wedge section (giving a minimum of wave drag in supersonic flow) is expected to have a thickness location slightly aft of 50% of the chord.

Biconvex Sections. The wave-drag term $C_{DW}/(t/c)^2 = K \tan \mu$ is easily obtained as a multiple of the Mach angle function in figure 1; and it decreases as such in the same manner as that function — when the Mach number is increased. Figure 9 displays characteristics of a 10% thick *double-wedge* section; and equation 32 is seen to represent the supersonic phase of the pressure-drag function of that section.

— The pressure distribution of a slender *biconvex* (or symmetrical *double-arc*) section along the chord "c", corresponds to

$$C_p = 4 (t/c) (1 - 2x/c) / \sqrt{M^2 - 1} \quad (39)$$

Integration of this distribution over the thickness "t" of the section yields the factor K (as in equation 31) equal to $16/3 = 5.3$. This factor is larger than that of the double wedge (see the experimental results in figure 9 at $M = 1.85$ and 2.47). In fact, integration of equation 30 over the thickness of any foil section proves that the double wedge (with constant surface angle " ϵ ") yields the least wave drag coefficient (based upon frontal area).

Round-nosed airfoil sections (not covered by any of the thin-wing theories) have still higher wave-drag coefficients. The drag of one particular such section shown in figure 15, is significantly reduced upon *reversing the direction of flight* (so that the sharp edge is leading), although a noticeable component of drag is then caused by separation from, and suction at the bluff "base". Round-nosed sections exhibit, of course, a detached bow wave and a stagnation point, in a manner similar to that of bluff and/or round bodies. Experimental results (42,c) thus show on the nose of a 65-009 shape, a positive pressure "peak" of appreciable magnitude. The corresponding component of the drag coefficient increases as a function of Mach number, in a manner similar to the stagnation pressure in figure 1 of Chapter XVI. A constant "K" value can, therefore, *not* be expected for this type of streamline sections. If such values are computed for the

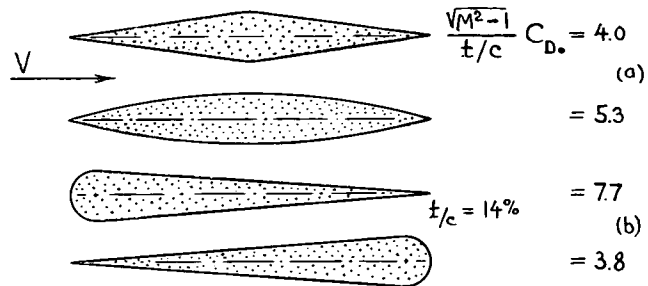


Figure 15. Comparison of the reduced pressure drag coefficients of four types of airfoil sections, at a Mach number of 1.5; (a) as indicated by theory (equation 31,) and (b) as tested (skin friction subtracted).

65-009 section mentioned (tested by pressure plotting) they are, for example, $K \approx 7.5$ at $M = 1.65$ and $K \approx 11$ at $M = 2.4$. Wave drag of round-nosed foil sections is thus significantly larger at super/hypersonic speeds, than that of wedges and/or sharp-nosed other shapes. "K" values have also been estimated for various foil shapes when applied in swept and/or "delta" wings (42). They are approximately:

- $K = 5.5$ for streamline foils with $x/c = 50\%$
- $= 6.0$ in round-nosed foils with $x/c = 30\%$
- $= 6.5$ for a slender elliptical airfoil section

Obviously, these values can only be used in applications where (on account of the three-dimensional "swept" flow pattern) the bow wave is attached to the leading edge.

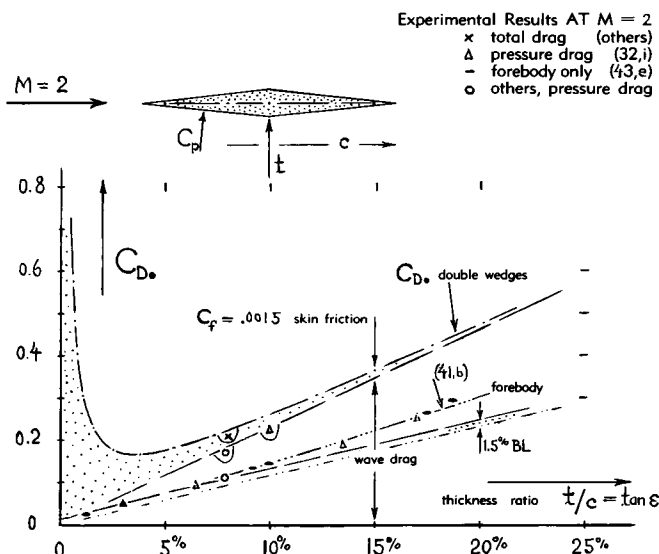


Figure 17. Profile drag coefficient of double-wedge sections, based on frontal area, calculated for $M = 2$.

Optimum Fairing. Combining the wave-drag coefficient as in equation 31 with a skin-friction component of $2 C_f(c/t)$, the drag coefficient C_D is obtained (based on frontal area). For a symmetrical double-wedge shape, this coefficient is plotted in figure 17 for $M = 2$ and on the basis of $C_f = 0.002$. One set of experimental points (43,e) demonstrates again that in the forebody, pressure drag is higher than indicated by linearized theory (see equation 35). In respect to total drag (including skin friction) the graph indicates an optimum thickness ratio (producing a minimum of drag on the given frontal area of a fairing, for example) below 5%, at the particular M -number considered. Using now a single wedge section, similar to the one in figure 15, with a blunt edge aft, drag coefficients almost as low as those of the D'-wedge section are readily obtained for a fairing. This result then leads to the analysis as follows.

Blunt Trailing Edge. To this date, we do not have a simple and explicit solution for the base drag originating at the cut-off or thickened blunt end of a foil section. On the basis of the mechanics of this type of drag explained at length in Chapter XVI, we can very well make an estimate, however, using in particular the "maximum" function ($\Delta P_B / P_{amb}$) in figure 12 of that chapter. We can also approximate the influence of viscous forebody drag through the use of figure 13 in the same chapter. The base drag of a blunted section, flying at supersonic speed, then corresponds to the coefficient (on wing area)

$$C_{D(B)} = (h/c)(B 1.43/M^2)/(1 + E C_f(t/h)^2) \quad (44)$$

This function was evaluated (numerically) for a 10% biconvex section at a Mach number of 1.5. In doing this, the constants "B" and "E" were selected in such

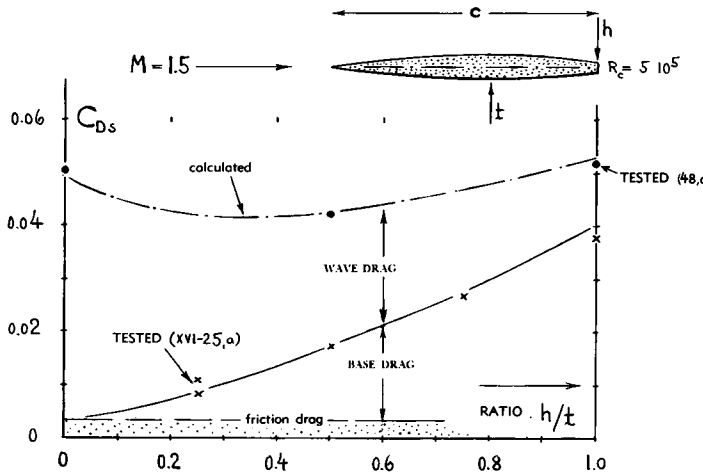


Figure 18. Drag coefficient of a 10% foil section as tested and as determined by computation (see text) as a function of trailing edge thickness ratio, at $M = 1.5$.

- (42) Relative merits of various foil-section shapes:
 - a) Nonweiler, Analysis for Swept Wings, ARC RM 2795.
 - b) Cooper, For "Arrow" Wings, NACA T.Note 3183.
 - c) Rainey, 65-009 Press. Distribution, NACA RM L9L16.
- (43) Investigation of foil sections at supersonic speeds:
 - a) Busemann, Forschung 1933 p.87, as in (41,b).
 - b) Double Wedges, see footnote (32).
 - c) Biconvex sections also in NACA T.Notes 3548 & 3550.
 - d) See also footnotes (33), (42,c) and (48,e).
 - e) Mueller, Spoiler on Wedge, NACA RM L52L31; TN 4180.
 - f) Czarnecki, Biconvex with Flap, NACA RM L50J19.
- (48) Airfoil sections with blunt trailing edges:
 - a) For base pressure see reference (25) in Chap XVI.
 - b) Morrow, Flight Tests, NACA T.Notes 3548 and 3550.
 - c) Chapman, Theoretical Analysis, NACA T.Rpt 1063.
 - d) Chapman, Thick T'edges, NACA (A9H11)T.N. 3503.
 - e) Katzen, 31 Airfoils Tested, NACA RM A54B08a. For thickness between 2 and 6%, this report does not show any drag reduction due to thick TE, at $M = 2$.
 - f) Syvertson, $M = 3$ and 5 , NACA RM A53B02.
 - g) Chapman, Hypersonic Analysis, NACA T.Note 2787.

a manner that tested base-drag values were matched
— The wave-drag coefficient of the type of section as
in figure 18 is approximately

$$C_{DW} = 5 \tan \mu (t/c)^2 (1 - 0.5 (h/t)^{2/3}) \quad (45)$$

The illustration presents the drag coefficient as a function of the TE thickness ratio h/t . The optimum ratio (giving minimum drag under the conditions stated) is found in the vicinity of $h/t = 38\%$. Experimental results (48,d) confirm the analysis. The reduction of drag is not spectacular; the decrement grows, however, as the section thickness ratio is increased. Inasmuch as the base-drag component reduces rapidly as a function of M' number (see figure 11 in Chapter XVI) more favorable results can also be expected at higher Mach numbers. For example, at $M \rightarrow \infty$, where the base drag component is zero, full thickness of the trailing edge (with $h = t$) is bound to be the optimum, then yielding for all slender types of sections a pressure-drag coefficient which may only be as low as 25% of that of the original double-symmetrical shape. The same problem is also treated analytically in (48,c) using *hypersonic* shock-expansion theory. As an example, figure 19 shows results taken from that source, for an 8% thick biconvex foil section. The reduction of pressure drag is modest in the range of Mach numbers below ≈ 3 , where the optimum trailing edge thickness is in the order of 0.4 t . However, significant reductions of drag are obtained at hypersonic M' numbers (approaching $1/M = 0$ in the graph).

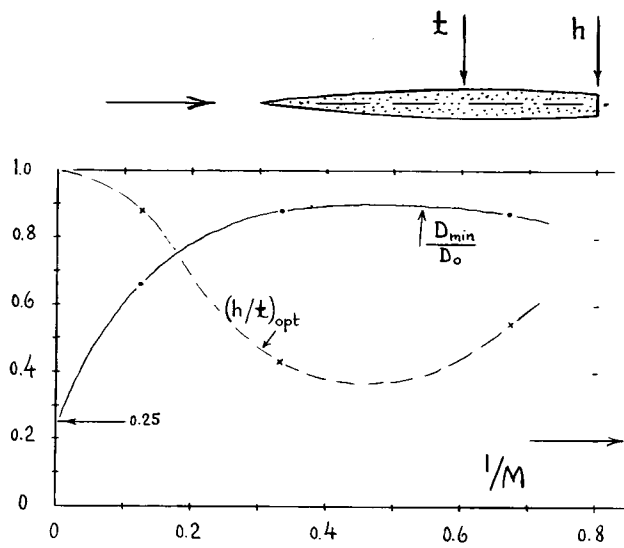


Figure 19. Example (48,g) showing "optimum" characteristics of an 8% thick biconvex foil section (similar to that in figure 18) at supersonic and hypersonic Mach numbers.

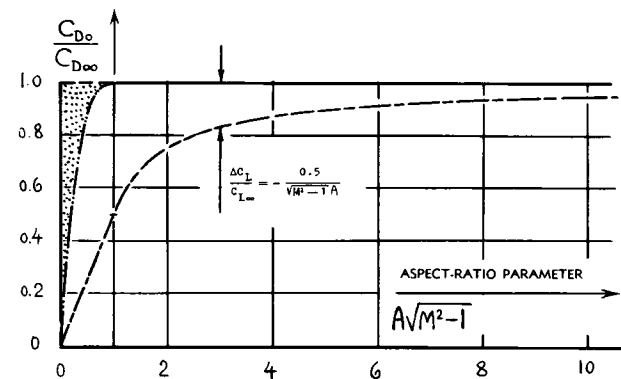
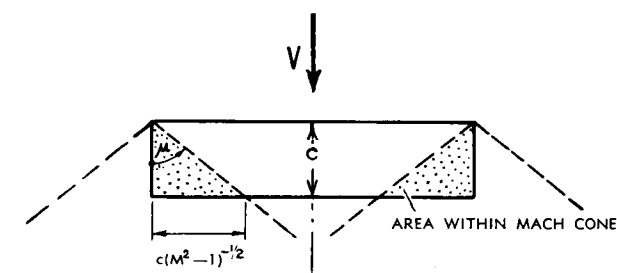


Figure 20. Variation of supersonic wave-drag and lift characteristics of straight rectangular wings, as a function of their "aspect ratio".

Aspect Ratio. Corresponding to the mechanics of supersonic flow, only the triangular portions behind the two Mach lines originating from the front corners of rectangular wings, shaded in figure 20, can have a three-dimensional flow pattern. All other points along the trailing edge, between these limiting Mach lines, cannot "know" that the wing span is limited; no signal is transmitted from the front corners to that portion of the wing. The part of the wing span within each of the two Mach cones is defined by

$$\Delta b = c / \sqrt{M^2 - 1} \quad (48)$$

as marked in figure 20. The term

$$b/\Delta b = A \sqrt{M^2 - 1} \quad (49)$$

is a type of "effective" aspect ratio, accordingly, of such rectangular wings in supersonic flow. As pointed out in (53), the wave drag due to thickness (indicated by equations 31 and 32) is then affected by aspect ratio, only below the limiting value of $A\sqrt{M^2 - 1} = 1$. The corresponding geometrical aspect ratio is comparatively low; at $M = 1.5$, for example, it is approximately $A = 1$. Figure 20 shows how drag due to thickness reduces below the limiting A' ratio parameter, approaching zero as $A \rightarrow 0$. It is suggested, however, that the lateral wing edges (particularly when square) may have some influence upon drag (not covered by wave theory).

5. DRAG OF WINGS DUE TO LIFT

(A) DRAG AT SUPERSONIC SPEEDS

Induced Drag. The mechanism of drag in finite-span lifting wings caused by the downward deflection of an equivalent "stream tube" (as described in Chapter VII) also applies in supersonic fluid flow (52). In the same manner as in thin, sharp and flat plates and/or as in planing bottoms (Chapter XI) consideration of induced drag as such does not lead to any practical results, however, in *supersonic* fluid flow. The induced component appears always intimately coupled with another wave-type component of drag due to lift; and total pressure drag due to lift is a function of the angle of attack rather than of lift. In order to obtain drag as a function of lift, it is necessary to consider lift as a function of the angle of attack, or what we call the "lift angle" $d\alpha/dC_L$, which is then equal to dC_D/dC_L^2 .

(52) *Induced drag at supersonic speeds:*

- a) As explained in Chapter VII, the equivalent mass of fluid deflected by a wing corresponds to a "tube" having a diameter equal to the wing span.
- b) The problem has been studied under supersonic conditions (in NACA Tech Rpts 957 and 983) with respect to the *downwash field* behind the wing. This field is somewhat different from that at subsonic speeds; the induced drag as such is essentially equal to that at subsonic speeds, however.
- c) Physical aspects of lift generation at supersonic speeds are also considered by vonKármán in J.Aeron.Sci.1947 p.383. The trailing vortex pattern is naturally confined to the space within the Mach cone originating from the frontal projection of the wing. *Far behind the wing*, the same pair of vortices will remain as in subsonic (uncompressed) fluid flow.
- (53) Theory of supersonic finite-span wings:
 - a) Schlichting, Finite Aspect Ratio, NACA T.Memo 897, corrected presentation by Taunt-Ward in ARC RM 2421.
 - b) Bonney, *Rectangular Wings with Finite Aspect Ratio*, J.Aeron.Sci.1947 p.110; also in his book (1,b).
 - c) VonKármán, as in footnote (52,c).
 - d) Nielson, AR and Taper, NACA T.Note 1487 (1947).
- (54) Notes on characteristics of finite-span wings:
 - a) The transonic and supersonic mechanics of *slender wings* are derived and expounded in the publications listed in footnotes (70,a) and (74,b) of Chapter XVI.
 - b) The constant of equation 66 is 2, instead of 0.5π as in small-aspect-ratio wings in uncompressed fluid flow.
 - c) By cutting off the *triangular wing tip* portions in figure 20, the added drag due to finite aspect ratio can theoretically be eliminated. Theory does not give any information, however, on the parasitic type of drag possibly originating from the lateral edges of such a plan-form shape.
 - d) The wing-tip wave drag might also be eliminated by *end plates*; see J.Aeron.Sci.1956 p.808 on this subject, and NACA Document RM E53A02 (at $M = 2$).

In Two-Dimensional Flow. Equation 30 can readily be applied to a flat plate inclined against the fluid flow by an angle of attack. The resulting positive pressure on the lower side together with the negative component on the upper side give the lift coefficient

$$C_L = 4 \alpha \tan \mu; \quad dC_L/d\alpha = 4/\sqrt{M^2 - 1} \quad (55)$$

Since the pressure forces are necessarily normal to the surface of the plate considered, the "lift" presents a component in the direction of flow, namely the drag due to lift, the coefficient of which is

$$C_{DL} = C_L \alpha = 4 \alpha^2 \tan \mu \quad (56)$$

After replacing α by C_L (as per equation 55) drag due to lift in two-dimensional supersonic flow corresponds to

$$C_{DL} = 0.25 C_L^2 / \tan \mu = 0.25 C_L^2 \sqrt{M^2 - 1}$$

As in uncompressed fluid flow, the drag due to lift is proportional to the square of the lift. It is always larger than the induced drag (as indicated by lifting-line theory; Chapter VII); and it does not reduce to zero as the aspect ratio is increased to infinity. Since (in supersonic flow) lift and wave drag are but two different components of one and the same pressure forces, they can be predicted from each other. Combining equations 55 and 57, drag due to lift is thus found to be

$$dC_{DL}/dC_L^2 = d\alpha/dC_L = 0.25 \sqrt{M^2 - 1} \quad (58)$$

Some experimental results on airfoils (tested between tunnel walls and/or in higher aspect ratios) are plotted in this form in *figure 22*.

Total Drag. As far as skin friction is concerned, a basic component must be considered in the form of $2 \cdot C_f$ where C_f = coefficient to be determined through application of figure 3 (or possibly of figure 2). "Viscous" effects also reduce lift, so that the drag ratio dC_D/dC_L^2 as in figure 22, is between 10 and 15% higher than predicted by theory. Within the boundaries of linearized supersonic theory, the wave drag due to lift can be added to that caused by thickness. The sum of equations 32 and 57 then presents the total *pressure* drag of straight wings having higher aspect ratios.

Lift (Aspect Ratio). Equation 57 (correct for $A \rightarrow \infty$) may for practical purposes be applied in higher aspect ratios. As pointed out in (53) some flow around the wing tips takes place, however, within the shaded triangular areas as in *figure 20*, from the pressure to the suction side. As a consequence, the pressure differentials due to angle of attack on these wing-tip por-

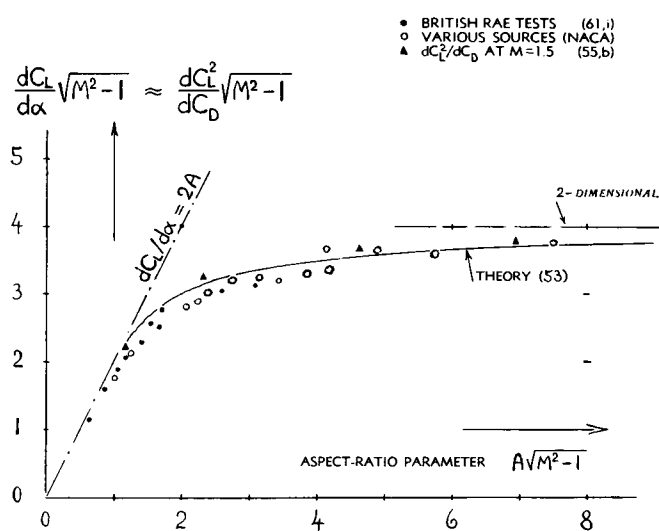


Figure 21. Lift-curve-slope of straight (rectangular) wings at "supersonic" Mach numbers (above shock-wave attachment) as a function of their aspect ratio.

tions, are on the average only half as large as in two-dimensional flow. The lift of the wing is reduced (54,c) accordingly, corresponding to

$$\Delta C_L/C_{L\infty} = -0.5 (A\sqrt{M^2 - 1}) \quad (64)$$

Figure 20 demonstrates that this function is different from that indicating drag due to thickness. — Upon reducing the lift-curve slope, wave drag due to lift (as in the left part of equation 58) is increased; namely in proportion to

$$(dC_D/dC_L^2)/(dC_D/dC_L^2)_\infty = 2/(2 - (1/\sqrt{M^2 - 1}) A)$$

Figure 21 shows (again) that tested lift-curve slopes and/or experimental values of the drag-due-to-lift parameter (dC_L^2/dC_D) are $\approx 10\%$ below the theoretical function.

Slender Wings. Figure 21 also represents the range of small-aspect ratios, below unity and approaching zero (54,a). The lift-curve slope is here simply

$$dC_L/d\alpha = 2 A \quad (66)$$

This function is identical with that for slender wings at subsonic speeds (see Chapter VII) except for the constant (54,b). Drag due to lift is again a component of the normal force, due to lift of slender wings:

$$dC_D/dC_L^2 = 0.5/A \quad (67)$$

— applies to A' -ratios corresponding to $A\sqrt{M^2 - 1} < 1$. The similarity of the graph (figure 21) with (and/or the differences against) that in figure 47 of Chapter XVI (representing "delta" wings) should be noted.

Ring-Shaped Wings (in form of a cylindrical piece of shell) are analyzed and/or tested in (56). As long as the diameter/chord ratio

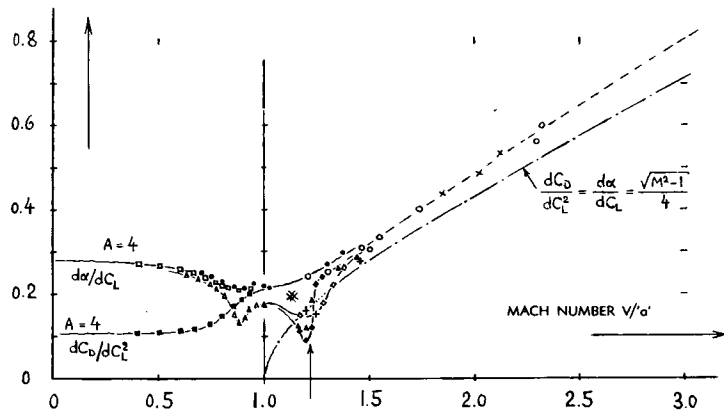
$$d/c > \tan \mu = 1/\sqrt{M^2 - 1} \quad (68)$$

the wave drag due to thickness of such wings may be equal to that of the respective airfoil section as in two-dimensional flow. Analysis (56,a) predicts that the ring's lift corresponds to

$$dC_L/d\alpha = 2/\sqrt{M^2 - 1} \quad (69)$$

where C_L is based upon the developed wing area ($d\pi c$). In this definition, thus the lift-curve slope is $1/2$ that of a wing in two-dimensional flow as indicated by supersonic theory (equation 55). Drag due to lift of the ring foil at truly supersonic Mach numbers is $D_L = \propto L$; thus:

$$dC_D/dC_L^2 = 0.5\sqrt{M^2 - 1} \quad (70)$$



- (a) At Subsonic M-numbers:
 - △ 63A006 on Bump (38,c)
 - 63A008 Cylinder (58,a)
 - Ditto, $A = 4$, Drag = $f(lift)$
- (b) "Lift Angle" Results:
 - 63A006, A' 'ratio = 4 (61,h)
 - ◊ 8% Double Wedge (61,f)
 - + Between Tunnel Walls (58,b)
- (c) Drag-due-to-Lift Results:
 - × Guidonia Sections (55,d)
 - ♦ 8% Double Wedge (61,f)
 - ▲ 6% D-wedge Section (32,f)
 - From Various Other Sources

Figure 22. "Lift angle" and drag due to lift of airfoil sections and of straight wings at transonic and supersonic Mach numbers.

(B) DRAG DUE TO LIFT AT TRANSONIC SPEEDS

Flow Pattern. At transonic speeds (where the bow shock wave is detached) some flow is expected to take place around the leading edge of airfoils. The corresponding suction force not only affects lift and lift-curve slope, it also tends to reduce drag due to lift, particularly in round-nosed sections. Similarity laws such as in (60,c) are again available, suitable to correlate transonic results. In regard to drag, conditions are complicated, however, by presence and interference of the boundary layer. Only a more qualitative presentation can therefore be made in the following paragraphs.

Drag and Lift. Figure 22 gives a general survey on "lift angle" and drag-due-to-lift parameter as a function of Mach number:

- (a) At subsonic speeds, drag due to lift (induced drag) is a function of aspect ratio. The drag parameter is different from the lift-curve slope.
- (b) Approaching $M = 1$, the drag due to lift ratio increases appreciably. Suction around the leading edge is evidently lost in this phase, so that the value of dC_D/dC_L^2 grows until it equals that of $d\alpha/dC_L$, as in flat and sharp plates (see Chapter VII).
- (c) Conditions at and in the vicinity of $M = 1$, will be discussed in the next paragraph (below).
- (d) At certain supersonic Mach numbers (see figure 25 in Chapter XVI) the bow shock wave attaches itself to the leading edge of wedge-type foil sections. At or shortly below these M'numbers, theory (60) predicts a maximum suction force to develop around the L-edge. Figure 22 gives proof that this effect can actually take place (though to a degree appreciably below the theoretically possible). The graph shows, on the other hand, that suction does not develop at any M'number, in a particular round-nosed foil section as tested. In this case, we can then expect that $dC_D/dC_L^2 = d\alpha/dC_L$.
- (e) Finally, at "supersonic" speeds (above $M \approx 1.4$ in figure 22) drag due to lift is as explained in the preceding section of this chapter.

-
- (55) Experimental results on supersonic lift and drag:
 - a) Gooderum, D'Wedges at $M = 1.3$, NACA T.Note 3626.
 - b) Nielsen, Aspect Ratio, NACA Document RM A8E06.
 - c) Vincenti, Comparison, NACA T.Rpt 1033 (1951).
 - d) Ferri, Guidonia Tunnel Results, NACA T.Memo 946.
 - (56) Characteristics of ring-shaped "wings":
 - a) Mirels, Drag and Lift Theory, NACA T.Note 1678.
 - b) Ribner, Journal Aeron.Sciences 1947 p.529.
 - c) Ehlers, With Cylinder Body, J.Aer.Sci.1955 p.239.
 - d) Nordström, Body Interference, ZFW 1956 p.272.
 - e) See also "shrouded" bodies in Chapter XVI, (81).
 - f) See also ring wings in Chapter VII, footnote (28).
 - (58) Wings at high subsonic Mach numbers:
 - a) Allen, Various A'ratios, NACA Doct. RM A53C19. British ARC, "Memos" 7308, 7703, 7705 (1943/44).
 - c) Stivers, 64A-Series Sections, NACA T.Note 3162.
 - (60) Lift analysis at transonic speeds:
 - a) Guderley, at $M = 1$, J.A.Sci.1953 p.757 (Wedge), 1954 p.261 (Plate), 1956 p.961 (A'ratio).
 - b) Vincenti-Wagoner, Transonic, NACA T.Rpt 1180.
 - c) Harder, Similarity, NACA T.Note 2724 (1952).
 - d) Spreiter, Similarity, NACA T.Note 2273(1951).
 - e) Spreiter, Analysis at $M = 1$, NACA T.Note 3970.
 - (61) Experimental results on wings at transonic speeds:
 - a) Vincenti, D'Wedges, NACA T.Note 3225 (1954).
 - b) McDevitt, Similarity Correlation, NACA T.R. 1253.
 - c) Gooderum, Lifting D'Wedges, NACA T.Note 3626.
 - d) Nelson, 36 Wings on Bump, NACA T.Note 3529.
 - e) Mellenthin, 0015 on Bump, NACA T.Note 3036.
 - f) Vincenti, D'Wedge Wing, NACA T.Note 3522.
 - g) Nelson, 38 Cambered Wings, NACA T.Note 3502.
 - h) Sleeman, In Transonic Tunnel, NACA RM L51F14.
 - i) Orman, Wedge, Proc.R.Soc.London A 1951, 1098 p.309.
 - k) See also footnotes (32) (33) (35) (36) (38).
 - (62) Information on the Atlas launch vehicle:
 - a) Atlas-Mercury performance; various NASA publications.
 - b) Fuller, Model Investigation, NASA T N D-1497 (1962).

The Aspect Ratio governs, of course, the drag due to lift at subsonic speeds (below M_{crit}). Its influence at "supersonic" Mach numbers is as shown in, and explained in connection with figure 21. Experimental results on a family of round-nosed wings (61,b) at transonic speeds and at $M = 1$ in particular, are presented in figure 23. Conclusions are as follows:

- (a) At aspect ratios of and below unity, slender-wing theory (54,a) applies again. We see that wings with thin and/or cambered foil sections more or less follow the straight line representing

$$dC_D/dC_L^2 = 1/\pi A \quad (70)$$

which is simply the subsonic type of induced drag (see Chapter VII).

- (b) Where leading-edge suction does not develop, drag due to lift in slender wings is twice as high as the induced drag. This result is identical with that of sharp and flat plates (see again Chapter VII) where $D = L \tan \alpha$. We see in figure 23 that a wing with 63A010 foil section switches from one condition to the other, between $A = 1$ and 2. It is also suggested that wings with sharp leading edges (with double-wedge sections, for example) may not develop much of a thrust due to nose-suction.

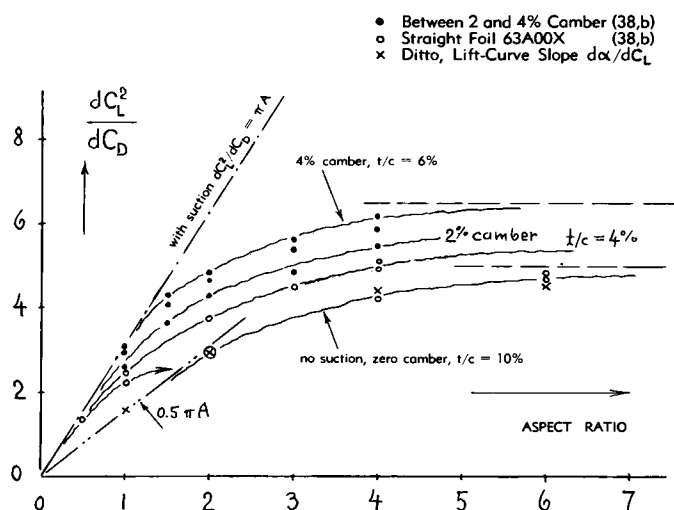


Figure 23. Drag-due-to-lift function of a family of rectangular wings (61,b) at $M \approx 1$. Note that the inverse of (dC_D^2/dC_L^2) is plotted so that the limiting straight-line functions are obtained as in the left side of the graph.

(c) Between small and large aspect ratios, we have a transition in figure 23 similar to that at "supersonic" speeds (figure 21).

(d) Conditions at larger aspect ratios rapidly approach those in two-dimensional flow. *Transonic* theory (60) predicts here that

$$d\alpha/dC_L = (1/3)((k + 1)M^2(t/c)) \quad (72)$$

Under conditions where thrust due to suction around the L-edge does not develop (such as in wings with sharp edges) the drag-due-to-lift parameter may thus be expected to increase at the same rate as the "lift angle" i.e. in proportion to $(t/c)^{1/3}$ and in proportion to $M^{2/3}$.

Foil-Section Camber. On the basis of the last equation, experimental results can be correlated with each other, in regard to thickness ratio (as done indeed in reference 61,b). Presentation as in figure 23 demonstrates more directly the influence of thickness, however; and it also shows that camber has an influence of the same, or of an even larger magnitude than thickness. The horizontal lines shown in the right side of the graph are extrapolated values; they agree by order of magnitude with two-dimensional transonic theory (60).

Practical Approach. Taking into account all the parameters considered in the last paragraphs, drag due to lift at transonic Mach numbers is found to be a complex subject. Inasmuch as this component of drag grows in proportion to the square of the lift, it is of lesser importance, of course, in such designs of airplanes and/or other supersonic vehicles, in which the

lift coefficient is small. If furthermore taking into account the presence of frictional drag (in the wing as well as in the fuselage or body of the configuration considered), we may then very well assume that at lift coefficients of and below 0.1, the total drag coefficient of the vehicle be \approx constant. As a consequence,

$$L/D = C_L/C_D \sim C_L \quad (74)$$

at constant Mach number, and for C_L values below 0.1 or below 0.2 at the most. Assuming next a rough value for dC_D^2/dC_L^2 (as for instance on the basis of figures 22 or 23) we may extend our practical estimate to still higher lift coefficients, and to other Mach numbers.

6. DRAG OF ROCKET VEHICLE

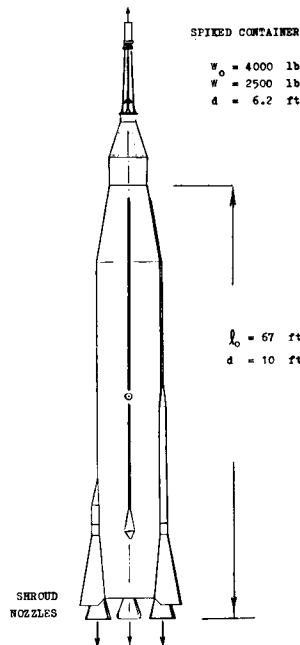
Cone-cylinder configurations are discussed in Chapter XVI. Their drag consists of wave drag originating at the nose, skin friction developing along the cylinder, and of some base drag.

Rocket Vehicles usually consist of a conical nose, of a cylindrical main body, and of certain appendages needed in their operation. A model of the Atlas vehicle shown in figure 24, was tested at $R_L = 7(10)^6$, and at M between 1.5 and 4.6. Without the capsule (but with an essentially conical "payload") drag at $M = 1.9$ is estimated to correspond to the coefficients listed in the illustration. The base area of the two shrouds (needed to keep low the hinge moments of the swivelling rocket nozzles) is about 40% of that of the main body. A component of 0.10 can be attributed to the instruments, actuators and fuel lines on the outside of the vehicle.

Figure 24. Full-scale dimensions of the Atlas D liquid-fuel launch vehicle (62) with a manned Mercury space capsule on top.

$C_{D_0} = 0.12$	WAVE DRAG OF THE NOSE CONE
$C_{D_0} = 0.08$	FOR SKIN FRICTION (0.0027)
$C_{D_0} = 0.20$	BASE DRAG w/o PROPULSION
$C_{D_0} = 0.12$	FOR THE TWO CONICAL SHROUDS
$C_{D_0} = 0.10$	FOR THE VARIOUS APPENDAGES
$C_{D_0} = 0.62$	TOTAL DRAG AS TESTED (62,b)

LIFT-OFF WEIGHT 250,000 lb
LIQUID FUEL WEIGHT 200,000 lb
COMBINED THRUST 360,000 lb



CHAPTER XVIII – DRAG CHARACTERISTICS AT HYPERSONIC SPEEDS

The term "hypersonic" indicates the range of higher supersonic Mach numbers. Hypersonic speeds are usually said to be above $M = 5$. Experimental results have recently become available up to M above 20. There are two types of such results, however. In most of the tests, high temperatures are simply avoided, so that the same gas (air) is involved as at transonic and lower supersonic speeds. In fact, practical applications at or above $M = 5$, may only be possible in the higher layers of the atmosphere, where heating is only a fraction of what it is near sea level. In some other types of hypersonic flow, temperature rises to such extreme levels, however, that the chemical or molecular constitution of the air (gas) changes. Presentation in this chapter leads from supersonic to the "harmless" type of hypersonic results. The so-called real-gas effects are then discussed in a more qualitative manner.

- (5) Theoretical foil characteristics at hypersonic speeds:
 - a) Tsien, Similarity Law, J.Math.Phys.1946 p.247.
 - c) An intelligible explanation of shock- and expansion pressure forces in hypersonic flow is given in (1,b) XVII.
 - d) Eggers, Hypersonic Theory, NACA T.Rpts 1123 and 1249; J.Aeron.Sci.1955 p.231, NACA T.Note 3666(1956).
 - e) Dorrance, Moderate Hypersonic, J.A.Sci.1952 p.598.
 - f) Hamaker, Similarity Law, NACA T.Rpt 1147.
 - h) Flanagan, Review of Theory, J.A.Sci.1953 p.150.
- (6) Hypersonic characteristics of cones and bodies:
 - a) See footnotes (40) and (41) in Chapter XVI.
 - b) VanDyke, Hypersonic Cone Theory, J.A.Sci.1954 p.179 (also 1951 p.499); see also NACA T.Rpt 1194.
 - c) Seiff, 30° 60° 90° Cones, NACA RM A52A14b.
 - d) Eggers, Ogives, NACA T.Rpt 1249 (1955).
 - e) Eggers, Minimum Drag, NACA T.Rpt 1306 (1956).
 - f) Similarity rules for bodies of revolution are basically given in terms of " ϵ " or $\tan \epsilon = d/\ell$. VanDyke (b) has found, however, that at hypersonic speeds, use of the sine function gives best correlation.
 - g) Miele, Minimum Drag Bodies, AIAA Journal 1963 p 168.
- (7) Fin-stabilized free-flight investigations:
 - a) Morrow, Two 6% Thick Sections, NACA TN 3548.
 - b) Lina, Wing With 6% Double Wedge Section, L9A12.
- (8) NACA, wind-tunnel investigation of airfoil sections:
 - a) Syvertson, 6% Biconvex Section, RM A53B02.
 - b) Czarnecki, Circular Arc with TE Flap, RM L50J18 & 19.
 - c) Goin, Various Wings with Blunt T'Edges, RM L53D13.
 - d) Ridyard, With T'Edge Flap at $M = 6.9$, L56B24.

(A) DRAG OF AIRFOIL SECTIONS

Similarity Parameter (5). Hypersonic characteristics of airfoil sections (and of slender bodies of revolution) are classified by the parameter

$$'H' = (\epsilon M) \text{ or } (t/c)M \text{ or } (d/\ell) M \quad (1)$$

We must thus conclude that besides high speed (M) a certain thickness ratio (t/c or d/ℓ) is also necessary to produce "hypersonic" fluid-flow conditions. It can then be postulated that such characteristics will appear in a less slender body at smaller M numbers than in a more slender body. If assuming that "hypersonic" type of flow is established when the similarity parameter above, is equal to unity, a Mach number $M = 10$ is obtained, for example, for a thickness ratio of 10%. This type of definition does no longer hold, however, for bluff and/or blunt bodies such as for example a sphere (having a thickness ratio $d/\ell = 1$). A qualitative condition for hypersonic type of flow may, therefore, said to be the presence of a comparatively narrow space between body surface and forward shock wave. Whether attached (as in slender and pointed shapes) or detached (as in bluff shapes) that bow wave is at hypersonic speeds somehow "wrapped around" the obstacle in a manner related to a Mach angle which is, for example at $M = 10$, approximately equal to $1/M = 0.1 \approx 6^\circ$. These ≈ 6 degrees are also \approx equal to the surface slope of a symmetrical 10% thick double-wedge foil section; and that is the physical meaning of the definition mentioned above, involving a hypersonic similarity parameter equal to unity.

Drag Due to Thickness. Because of the narrowness of the space between shock wave and a foil section's surface, in hypersonic flow, certain second-order terms usually neglected in thin-airfoil supersonic theory, take on a greater or possibly predominant im-

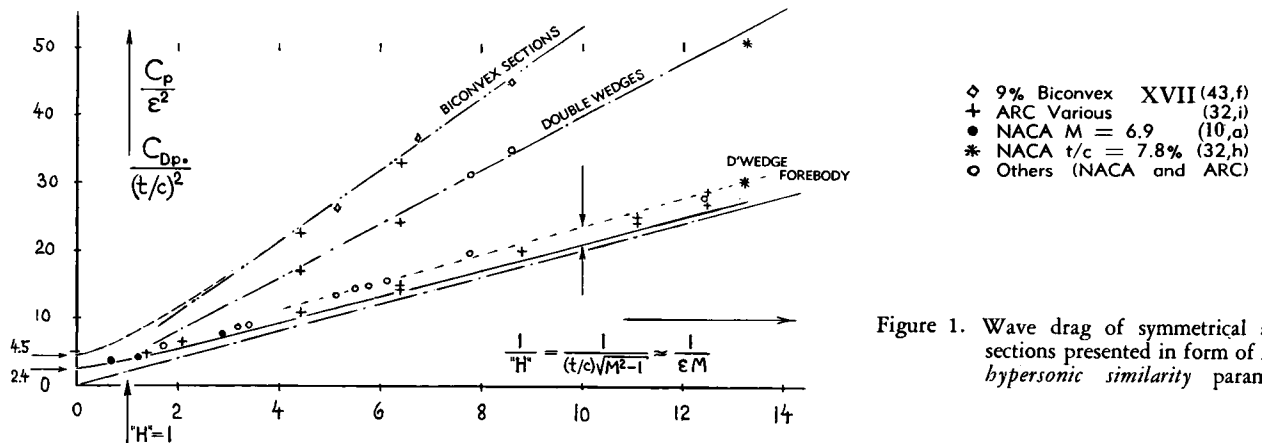


Figure 1. Wave drag of symmetrical airfoil sections presented in form of *super-hypersonic similarity* parameters.

portance. Both the positive pressure aft of the shock wave on the forebody of slender foil sections, and the negative pressure behind a Prandtl-Meyer type of expansion, can be correlated against the similarity parameter as in equation (1). It has been pointed out (6,b) however, that hypersonic pressure or drag coefficients can be combined with supersonic characteristics, when plotting them against the parameter

$$"H" = \varepsilon \sqrt{M^2 - 1} \quad (2)$$

where $\varepsilon \equiv t/c$. In terms of hypersonic similarity, the pressure-drag coefficient of the double wedge as indicated by equation 31 in Chapter XVII, is:

$$C_{Dp} / \varepsilon^2 = 4 / "H" = 4 / (\varepsilon \sqrt{M^2 - 1}) \quad (3)$$

Double Wedges. Experimental pressure results obtained on various double wedges, are plotted in figure 1, against $1/"H"$, so as to make the basic function of the drag coefficient a straight line. Hypersonic theory (5,a,d,e) including higher-order terms, predicts for fore — or afterbody of a double-wedge section:

$$C_p = (2/M)\varepsilon + 1.2\varepsilon^2 + 0.4 M\varepsilon^3 \quad (4)$$

Note that ε is positive in the forebody, and negative in the afterbody. The total pressure drag of *D'wedge* sections then corresponds approximately to

$$C_{Dp} / (t/c)^2 = (4/"H") + 0.8 "H" \quad (5)$$

Using equation (2) with $\varepsilon = t/c$, we obtain

$$C_{Dp} = 4(t/c)/M + 0.8(t/c)^3 M \quad (6)$$

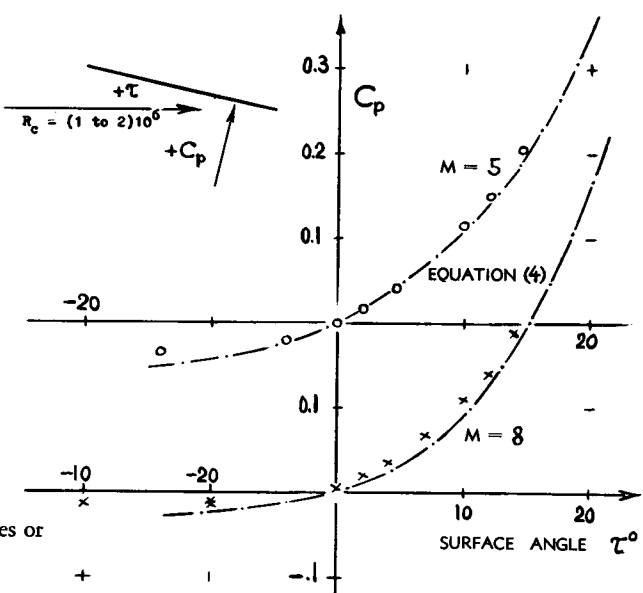
For small thickness ratios, this equation can be written as $C_{Dp} \sim 1/M$. It then follows that wave drag is approximately $D \sim V^2/M \sim V$. This is one of the exceptions where drag is not proportional to the square of the speed.

Figure 2. Pressure coefficient at the surface elements of wedges or flat plates, tested (10,f) at hypersonic speeds.

Afterbody Drag. Equation (4) is plotted in figure 2. This graph is of the same type as that in figure 16, in Chapter XVII. Experimental results obtained on a double-wedge surface confirm the theoretical function very well at $M = 5$. At negative angles (in the afterbody) exceeding some 5° , the presence of the boundary layer evidently reduces the value of the negative pressure coefficient considerably. At $M = 8$, the boundary layer also seems to affect the pressure in the forebody. The displacement due to the layer increases the effective surface angle, particularly between $\tau = 0$ and 10° . With or without boundary layer, figure 2 demonstrates the fact that the pressure-drag coefficient in the forebody of a double wedge increases with a higher power of (t/c) . At the same time, the coefficient reduces in the afterbody. As pointed out in (14) it can be said that above $"H" = 1$, the afterbody pressure corresponding to

$$C_{Dp} / (t/c)^2 \text{ is by } (k + 1) = 2.4 \quad (8)$$

smaller than that of the forebody. As a consequence, the afterbody drag reduces to zero, as $"H" \rightarrow \infty$. This one reduction is of the same nature as that of the base-drag coefficient; see figures 2 and 11 in Chapter XVI.



Single Wedge. As a consequence of what is explained above, a single wedge (with a blunt trailing edge) has less drag at hypersonic speeds than a double-wedge section having the same thickness ratio. For a single wedge, the half-vertex angle is $\tan \epsilon = 0.5 t/c$. The equations above then indicate a forebody drag corresponding to

$$C_{D_0} / (t/c)^2 = (0.5/t) + 0.3 + 0.1 'H'$$

For hypersonic M'numbers (where $\sqrt{M^2 - 1} \approx M$) this equation reduces to

$$C_{D_0} = (t/c)/M + 0.3 (t/c)^2 + 0.05 (t/c)^3 M \quad (11)$$

A Narrow Wedge is shown in figure 3, tested in comparison to a $\frac{3}{4}$ power "conical" body having the same length ratio ℓ/b . If increasing the thickness of the wedge so that it has the same volume as the "cone", the drag coefficients can be expected to be approximately alike. However, if increasing diameter and length of the "cone" (by a factor in the order of 1.4) so that it produces the same lift as the wedge, when at an angle of attack, its drag (in pounds) would approximately be doubled.

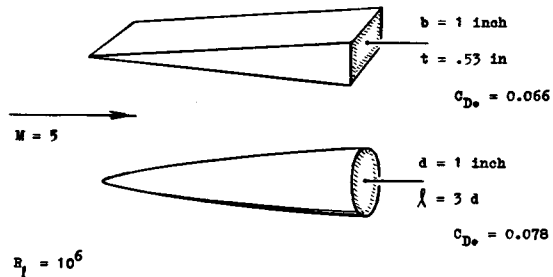


Figure 3. Forebody drag coefficient of a narrow wedge (11) in comparison to that of a cone-like body having a diameter equal to the width (span) of the wedge.

- (9) Magnitude of skin friction at supersonic speeds:
 - a) Jack, Slender Body at $M = 3.1$, NACA RM E51H13.
 - b) Kayser, AGARD Model at $M = 8$, Arnold Center AEDC TN-1960-34; also Mathews, At $M = 10$, TDR-1964-31.
- (10) Lifting wedges and plates at hypersonic M'Numbers:
 - a) Linnell (MIT) in J.Aeron.Sci.1949 p.22; also "Supersonic-Hypersonic Formulas", 1956 p.398.
 - c) McLellan, 5% Wedges at $M = 6.9$, J.Aeron.Sci.1951 p.641; additional results in NACA RM L51D17.
 - d) Tellep-Talbot, Plates, J.Aeron.Sci.1956 p.1099.
 - e) Linnell, Analysis of Lifting Flat Plate in Hypersonic Flow, J.Aeron.Sci.1949 p.22 and 1956 p.398.
 - f) Randall, Pressure, Arnold Center AEDC TN-1960-173.
- (11) Resnikoff, Narrow Wedge Comparison, NACA A54B15.
- (12) Hypersonic characteristics of "ogival" nose bodies:
 - a) Theory of optimum bodies in reference (6).
 - b) Dennis, Family of Shapes, NACA RM A52E22; also (f).
 - c) Jack, Slender Nose Bodies, NACA RM E53J27.
 - d) Kayser, Wing Body at $M = 8$, AEDC TN-1960-34.
 - e) Okuchi, Pressure Distribution, NAVWEPS Rpt 8048.
 - f) Perkins, Slender Noses to $M = 7$, NACA T Rpt 1386.
 - g) Neice, Cones and Ogives, NACA Memo RM A52K07.

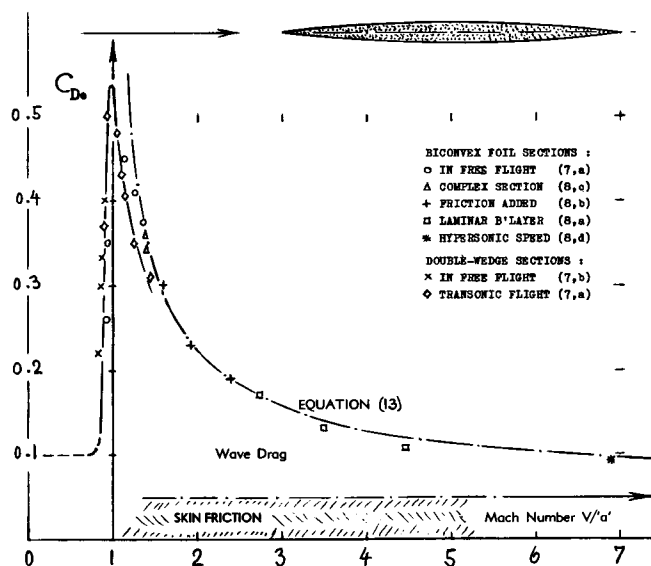


Figure 4. Total drag coefficient of 6% thick double-symmetric sharp-nosed airfoil sections, tested from transonic to hypersonic Mach numbers.

For Double-Arc or biconvex sections, an approximate solution (5,e) indicates the pressure-drag coefficient

$$C_{D_0} \approx 5 (t/c)/M + 2 (t/c)^3 M \quad (13)$$

Experimental results in figure 4 confirm this function, when assuming a reasonable value for the coefficient representing skin friction.

Skin Friction drag can be very small in comparison to supersonic and hypersonic pressure drag. In slender sections, the wetted surface area is large, however, in comparison to the frontal area. Skin friction was measured in (9,a) on a slender ogive-cylinder configuration at $M = 3.1$. Transition from laminar to turbulent boundary-layer flow, takes place at $R_x \approx 4(10)^6$. In laminar condition (around $R_x = 2(10)^6$) the coefficient is in the order of $C_f = 0.001$, while at R' numbers above transition, the coefficient is between $(1.5 \text{ and } 2.0)/1000$. — The variation of the turbulent coefficient with Mach number is presented in figure 3, on page 17-4. The contribution of skin friction to the drag of a slender airfoil section generally corresponds to

$$\Delta C_{D_0} = 2 C_f (c/t) \quad (14)$$

This equation also applies for cones (to be discussed later) if replacing (c/t) by the fineness ratio (ℓ/d) . — The type of skin friction presented in this paragraph, originates at higher Reynolds numbers and in the "harmless" variety of hypersonic flow (where high wall temperatures are avoided). More severe influences of viscosity are discussed later, in connection with "heat" and with "rarefaction".

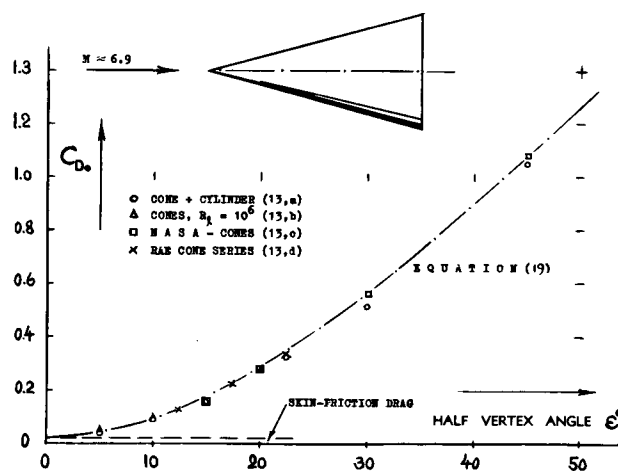
At " $H' \rightarrow \infty$ ". The second-order function as indicated by equation (4), is of practical importance not only at hypersonic speeds, but also within the range of moderately high Mach numbers. This is demonstrated in connection with figure 16 in Chap XVII. Equations (4) through (9) are not complete, however. The permissible limit of their application may be at " $H' = 2$ ". Limiting values for the drag of double-symmetric sections are indicated in figure (1) (at $1/H' = 0$). The pressure drag of a double wedge (equal to that of the forebody) then corresponds to

$$C_{D_0} = 2.4 (t/c)^2 \quad (17)$$

Note that this coefficient increases in proportion to the square of the (t/c) ratio. Drag values of wedges or cones, predicted by inviscid theory for $M \rightarrow \infty$ (or for $1/H' \rightarrow 0$) are completely academic, however. Presence and progressive growth of the boundary layer along the surface of these bodies have a very strong influence upon flow pattern and aerodynamic forces. — As stated in (10,e) the pressure at a flat surface (such as a flat plate) at $M \rightarrow \infty$, corresponds to the coefficient

$$C_p = (k + 1)\tau^2 \quad (18)$$

where τ as in figure 2. For $k = 1.4$ as in ordinary air, this function has the same constant as equation (17). It applies only for positive surface angles, however, while the pressure differential for negative values, such as in the afterbody of a double wedge or at the upper side of a lifting flat plate, is expected to be zero. — When considering the drag of a wedge section, the last equation shows that both the component due to thickness and that due to lift, grow with the square of the surface angle. It is not permissible, therefore, to compute the two and then to add them to each other. Rather, the pressure on each part of the surface has to be determined through the use of equation (18), in order to obtain lift as well as pressure drag.



(B) CONES AND SIMILAR BODIES

Cones (and other three-dimensional slender shapes) follow the same type of hypersonic similarity law as foil sections. Their drag is presented in this form in Chapter XVI (see figure 27 there). As long as the pressure distribution along the surface of a cone (at zero angle of attack) is constant, pressure drag can easily be measured. The formulation derived in Chapter XVI (equation 29) is well confirmed by experimental points (in figure 23, in that chapter) up to $M \approx 8$. We are also in a position to check the equation against experimental results reported (24,b) for a cone with $\epsilon = 9^\circ$, tested in a nitrogen tunnel (in "cold" condition) at Mach numbers between 15 and 19. After extrapolation to zero viscosity, the following comparison is obtained:

$$\begin{aligned} C_{D_0} &= 0.063 && \text{experimental pressure drag} \\ C_{D_0} &= 0.054 && \text{calculated (equation 29)} \end{aligned}$$

Of course, when including some viscosity, forebody drag is increased, particularly for the slender cone considered. — As a function of cone angle, figure 5 presents total drag coefficients tested at Mach numbers almost equal to 7. Since the experimental results are somewhat below the values indicated by equation (29) in Chapter XVI, the following formulation of pressure drag may also be used:

$$C_{D_0} = 2 \sin^2 \epsilon + 0.5 \sin \epsilon / \sqrt{M^2 - 1} \quad (19)$$

Optimum Shapes (Theory). — A large bibliography is available on the subject of three-dimensional bodies moving at hypersonic speeds (6) in essentially inviscid fluid flow. Newton's principle of momentum transfer (see Chapter XIX) has been re-examined (41,b). It is found to apply at $M \rightarrow \infty$, for $k = 1$ or for small values of $(k - 1)/(k + 1)$. In case of a parabolic shape (corresponding to equation (23)) the drag coefficient in axisymmetrical flow is

$$C_{D_0} = (y/x)^2 n^2 (3n - 1) / (2n - 1) \quad (20)$$

For $n = 1$, representing a straight cone, we then obtain $C_{D_0} = 2(y/x)^2 = 2\epsilon^2$ as in hypersonic analysis (Chapter XVI). The optimum shape (giving a minimum C_{D_0}) as found through application of the

Figure 5. Forebody drag coefficients of several series of cones, tested at Reynolds numbers in the order of $R_L = 10^6$.

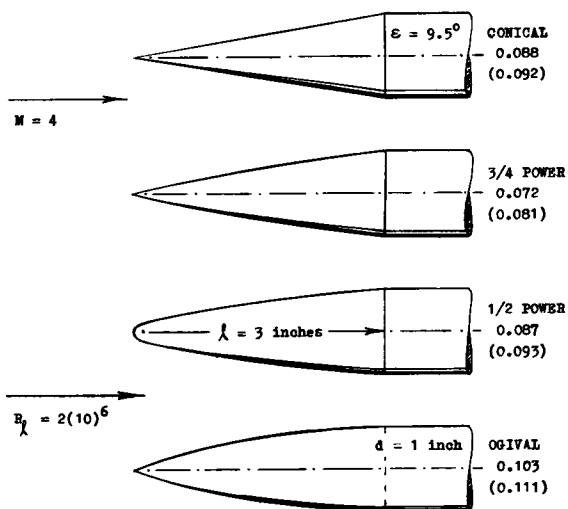


Figure 6. Forebody drag coefficients of a series of "conical" nose shapes, tested (12,b) at Mach numbers between 3 and 5.

Ogives. The drag of an ogival or otherwise curved half-body shape cannot easily be tested by pressure distribution. When measuring by means of a balance, skin friction and base drag are included in the results. Forebody drag coefficients are listed in figure 6 for three shapes differing from that of the cone. Two of these shapes are defined by the function of the radius:

$$r/(d/2) = (x/\lambda)^n \quad (23)$$

where n = exponent, producing the type of curvature. Drag is lowest for the $\frac{3}{4}$ power body. The blunt-nosed $\frac{1}{2}$ power shape does not have higher drag than the cone.

Blunted Cones. When blunting the tip of a slender cone, a shape is obtained, very roughly approaching that of certain parabolic bodies. Total drag coefficients are plotted in figure 7, for a series of blunted cones having a constant fineness ratio $\lambda/d = 3$. At M between 6 and 7, minimum drag is obtained for a bluntness ratio around 10%. Results are also plotted for $M = 3$, and $= 2$. It is seen that the optimum bluntness ratio increases as the Mach number is reduced. For example at $M = 2$, minimum drag is found between 15 and 20% bluntness. At any rate, some bluntness is not only permissible but even desirable. Considering frontal area, the blunt portion evidently contributes less than the conical parts. In a two-dimensional shape, such as a wing section for example, the same type of blunted and/or curved form would not result in forebody wave drag, less than that of a wedge.

- (13) Experimental characteristics of cones:
 - a) Cooper, Series of Cone Cylinders, NACA RM L51J09.
 - b) Ladson, Series of Cones, NASA TN D-1473 (1962).
 - c) Penland, Lifting Cone Cylinders, NASA TN D-840.
 - d) Peckham, Slender Cones, RAE Rpt Aero-2863 (1963).
 - e) Jack, 5 Cone-Cylinder Bodies, NACA RM E52C10.
 - f) See also references (41) in the "supersonic" chapter.
- (14) Reymond, Hypersonic Cone Theory, J.Aeron Sci 1957 p 389.
- (15) Influence of blunting the tip of slender "cones":
 - a) Sommer, Truncated Cones, NACA A52B13; see (12,f).
 - b) Whitfield, Viscosity, AEDC TDR-1963-35 & 1964-1.
 - c) Jack, Cone-Cylinder Bodies, NACA RM E52C10.
 - d) Rounded cones have an advantage over pointed ones in regard to heat transfer at re-entry into the denser layers of the atmosphere; Allen's Wright Brothers Lecture (1957).
- (17) Free-flying configurations at hypersonic speeds:
 - a) James, Fin-Stabilized Body, NACA RM A53D02.
 - b) Ulmann, Ballistic Missiles, NACA RM L54D.
 - c) Bixler, Missile Bodies, Nav Ord Lab T Rpt 1961-96.
- (19) Boundary layer shock interaction:
 - a) Lees, Evaluation, J.Aeron.Sci.1951 p.195.
 - b) GALCIT, BL-Induced Pressure, J.A.Sci.1955 p.165.
 - c) Kuo, Along Plate, J.A.Sci.1956 p.125 and 977.
 - d) Kendall, Experiments, J.Aeron.Sci. 1957 p.47.
 - e) Erickson, Shock Pressure at M to 18, NACA TN 4113.

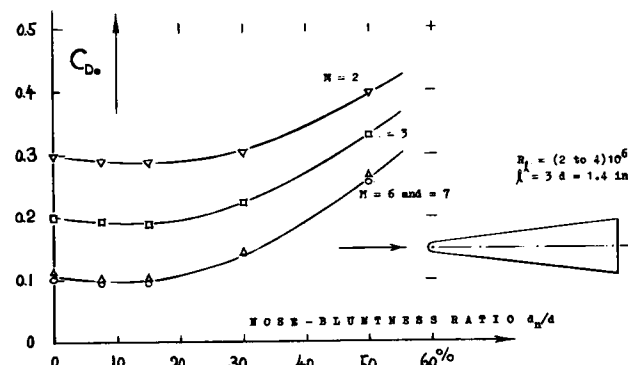


Figure 7. Total drag of a series of cones with $\lambda/d = 3$, tested (15,a) at M between 2 and 7, as a function of nose bluntness.

(C) FREE-FLYING CONFIGURATIONS

Skin Friction. A fin-stabilized body is shown in figure 8, flight-tested at Mach numbers between 0.6 and 10. Since the Reynolds number varies between 1 and 16 millions, skin friction must be assumed to vary accordingly. The value of the drag coefficient due to friction, depends upon the location of boundary-layer transition. A possible assumption is that this transition takes place at the "shoulder" (junction between ogive and cylinder). The fins can be assumed to have laminar flow. For example, at $M = 10$, skin friction drag is then estimated to be as follows:

- Laminar component corresponding to $C_{Df} = 0.0008$, for $R_x = 3(10)^6$, reduced to $2/3$ on account of Mach number (see page 17-3) and corresponding to an area ratio of the ogive and fin surface involved $S_{wet}/S_0 \approx 40$. The result is $C_{Df} = 40(0.0008)2/3 = 0.02$.
- For turbulent flow along the cylindrical portion of the body, the coefficient is $C_{Df} \approx 0.027$, at $R_x = 16(10)^6$. The reduction due to Mach number may be down to 0.3 (see figure 3 on page 17-4). For a wetted area ratio of 24, the turbulent contribution may then be $C_{Df} = 24(0.0027)0.3 \approx 0.02$.

The combined skin-friction component is $C_{Df} = 0.04$, at $M = 10$. — No explanation has been found for the discontinuity of total drag around $M = 6$.

Pressure Drag at $M = 10$. For base drag, figure 2 (on page 16-4) suggests a contribution of $C_{D0} = 0.02$. The wave drag of the ogival nose, may be assumed to be equal to that of a cone with a half-vertex angle $\epsilon = 8^\circ$. On the basis of figure 27 (on page 17-20) a coefficient $C_{D0} \approx 0.05$ is then obtained. The fins have sections which are a combination of a wedge with a slab shape. The base area of the blunt trailing edges is almost $1/2$ of the body's frontal area. The fin drag is assumed to correspond to $C_{Df} = 0.01$ (on body area). Summing up all drag components, we obtain for $M = 10$:

$$\begin{aligned} C_{D0} &= 0.08 && \text{for pressure drag} \\ C_{Df} &= 0.04 && \text{for friction drag} \\ C_{D0} &= 0.12 && \text{for total drag} \\ C_{D0} &= 0.11 && \text{experimental result} \end{aligned}$$

It is seen that the drag of the configuration tested, can reasonably well be estimated.

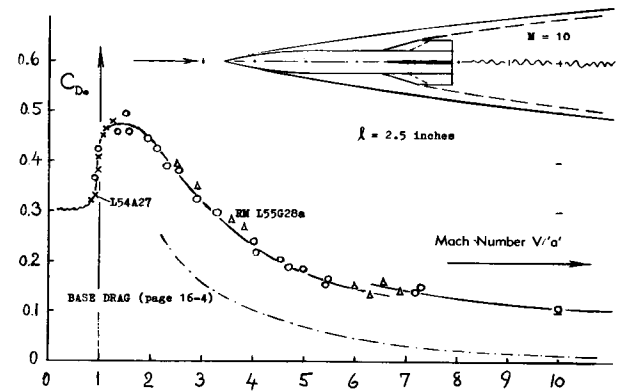


Figure 8. Total drag coefficient of a fin-stabilized body tested in free-flight (17,a) at M/V_a numbers between 0.6 and 10.

A Ballistic Missile is shown in figure 9, tested in a wind tunnel, mounted on a sting. The small fins have a stabilizing area $S_f = 1.9 S_0$, while the larger fins have $S_f = 2.8 S_0$. The difference in total forebody drag is small, however. — The considerably larger drag coefficient of model "C" corresponds to the comparatively blunt nose cone. For $\epsilon = 16^\circ$, figure 27 (on page 16-20) indicates for $(M \sin \epsilon) = 1.1$, a pressure-drag coefficient $C_{D0} = 0.19$. Most of the tested coefficient (0.21) is thus explained.

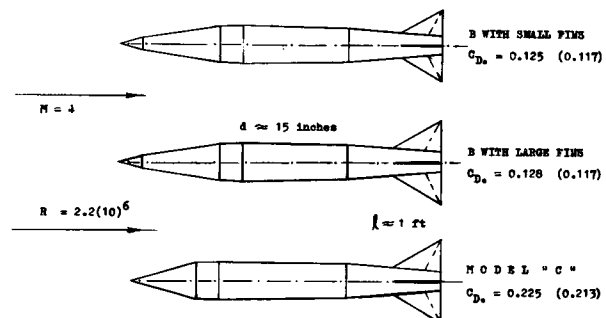


Figure 9. Forebody drag coefficient of a ballistic missile (17,b) shown for three modifications of shape.

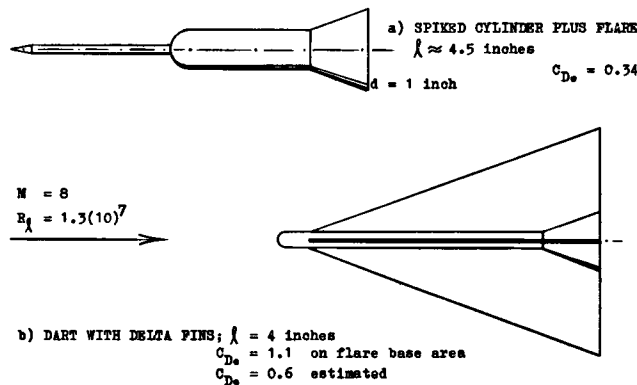


Figure 10. Drag characteristics of two "exotic" missile models, tested (17,c) in free flight, at $M \approx 8$, speed ≈ 6000 ft/sec, in air at about $1/3$ of atmospheric pressure.

Missile Models. A number of "exotic" missile configurations was tested (17,c) at hypersonic Mach numbers between 8 and 15, in free flight along a hypersonic shock tunnel. The length of the models is between 4 and 5 inches. The model scale is stated to be between $1/6$ and $1/8$. The test conditions vary roughly as follows:

air density	between	0.01 and 0.05 lb/ft ³
dynamic pressure	between	0.06 and 1.60 lb/ft ²
stagnation pressure	between	0.14 and 3.30 lb/ft ²
R'number on length	between	2 and $15 \cdot 10^6$

The flow velocity is near 7000 ft/sec; the stagnation temperature in the order of 2000°K. Unfortunately, the angle of attack of the models when tested, was up to 30° . Only two configurations are presented, therefore, in figure 10, with angles in the order of 10° .

(D) VISCOUS EFFECTS IN SLENDER SHAPES

Hypersonic characteristics of slender shapes (wedges and cones) have been considered so far in this chapter, without taking into account the displacement of the boundary layer. Under favorable conditions, this approach gives realistic answers in regard to surface pressure and wave drag. Upon reducing the Reynolds number sufficiently far, presence of and thermodynamic effects within the boundary layer may exert a significant influence, however, upon flow pattern and drag. The principle consequences are:

- a change of shock-wave shape,
- an increase of pressure drag,
- some increase of skin friction.

(a) Characteristics of Two-Dimensional Shapes

BL Displacement. Skin friction as a function of M is presented in figures 2 & 3, Chapter XVII. Considering, however, as an extreme example, a boundary layer at $M = 10$, the recovery temperature near or at the surface of the obstacle producing the BL layer (in the order of 90% of the stagnation temperature as in equ. 6, Chapter XVII) is equal to some 20 times the absolute temperature in the ambient air space. At constant pressure (equal to p_{amb}) the density of the BL sheet closest to the body surface is accordingly reduced to ≈ 0.05 of that in the ambient space; and the average displacement thickness of the boundary layer is increased to several or many times that in uncom-pressed fluid flow. At the end of a flat plate (at the station "x") the displacement thickness of a laminar BL will then have reached the value of

$$\delta_\Delta \approx 0.4 \times M^2 / \sqrt{R_x} \quad (24)$$

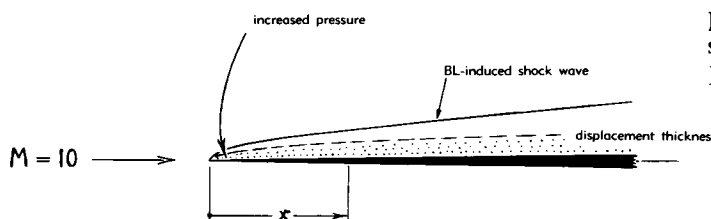


Figure 11. Flow pattern and pressure distribution developing along a thin plate, including boundary layer and BL-induced shock wave.

which is 4% of the plate's length, on one surface of the plate, at $M = 10$ and at $R_x = 10^6$, for example. The BL layer developing along the thin plate as in figure 11 is thus the equivalent of an 8% thick single wedge or more accurately, of a two-dimensional shape roughly equal to the forebody of a 4% thick double-arc or biconvex foil section.

Figure 12. Pressure along sharp-edged plates (in tangential flow) or along slender wedges or cones, induced by presence and displacement of a laminar boundary layer, at hypersonic speeds.

B'Layer-Induced Pressure. Figure 11 shows that a bow wave forms around the boundary layer in a manner similar to that past biconvex, streamline-type or even round-nosed foil sections. As a consequence, there is then a positive pressure as indicated in the illustration, the magnitude of which (19) in laminar tangential fluid flow (along a plane surface), is approximately

$$C_p \approx 0.6 M/\sqrt{R_x} \quad (26)$$

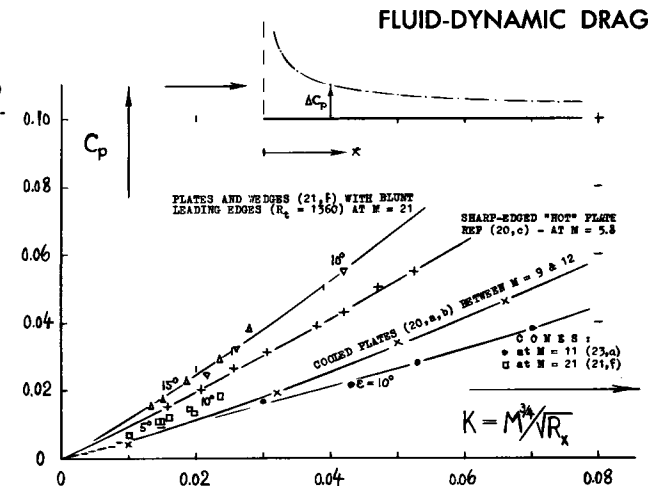
This function not only indicates how pressure at a certain point varies with viscosity. Since the Reynolds number R_x is proportional to the distance x from the leading edge, in downstream direction, the function also expresses the fact that the pressure increment reduces in proportion to $1/\sqrt{x}$. In other words, the pressure due to boundary layer displacement is concentrated near the leading edge — although the evaluation describing $\Delta p \sim \sqrt{1/x}$, breaks down directly at the edge. As indicated by equation (10) on page 16-3, the ambient pressure p_a is related to the dynamic pressure on which the coefficient C_p is based. If expressing the pressure differential discussed, in form of the ratio $(\Delta p/p_a)$ the last equation results in

$$\Delta p/p_a \approx 0.4 M^3/\sqrt{R_x} \quad (27)$$

This is the form in which the analyses in (20) through (25) are presented. It is found, however, that equation (26) gives much better correlation, collapsing results on wedges and cones differing in vertex angle.

B'Layer Viscosity. Equations (26) and (27) are not complete. As shown on page 1-11, the "absolute" viscosity μ increases with the temperature. A factor accounting for this variation has to be added, therefore, in the theoretical analysis of boundary-layer induced pressure. However, temperature and viscosity are a function of the Mach number. As pointed out in (24,a) very good correlation of pressure and drag coefficients is obtained over a considerable range of M' and R' numbers, when using the parameter $K = M^{3/4}/\sqrt{R_x}$. Pressure-differential coefficients in the form of $C_p = \Delta p/q$, are therefore plotted in figure 12, against this parameter.

Heat Transfer. Depending upon the test conditions (as in wind tunnels) the boundary layer directly at the body wall may be hot (when the surface is insulated, thus preventing heat transfer into the body) or it may be cooled (when heat is transferred through the wall). As seen in figure 12, the induced pressure differentials are higher in "hot" condition.



Blunt Leading Edges have a certain pressure drag, to be discussed later. They also increase the induced pressure, along flat plates as presented above. There seems to be a limit of thickness below which the edge does not have any influence upon flow pattern and pressure distribution. This limit is indicated by a Knudsen number (see Chapter XIX) based upon leading-edge thickness, possibly above 0.1. In terms of Reynolds number (also based on thickness) the limit may be below $R_t = 100$. At least, that is what is concluded in (20,b) for Mach numbers between 6 and 12. For results from that source plotted in figure 12, the Reynolds number R_t is only 40, and the Knudsen number is as high as ' K ' = 0.3. Beyond such limits, pressure due to boundary layer can be increased very much, in comparison to that for zero leading-edge thickness. Evaluation of blunt-edged flat plates in (21,f) leads to the following formulation. In comparison to the "hot" function in figure 12, the slope of pressure increments (evidently tested with some heat transfer) can roughly be described by the

$$(\text{slope ratio}) = 0.03 \sqrt{R_t} \quad (28)$$

where $R_t = V t/v$ = Reynolds number based on leading-edge thickness. Another formulation derived (21,b) from experiments is based upon the inviscid wave-drag coefficient of the blunt or rounded edge:

$$C_p = 0.24 C_{D_0}^{2/3} / (x/t)^{2/3} \quad (29)$$

Values for the drag coefficient can be found in the section dealing with "bluff bodies".

Wedge Pressure. Two wedges were tested in helium (21,f) at M between 16 and 24. The pressure differentials induced by the boundary layer are plotted in figure 12. It should be noticed that coefficients evaluated from wedges differing in vertex angle are approximately collapsed. However, the function thus obtained, indicates induced pressures which are much higher than those found on flat plates. Corresponding to a leading-edge Reynolds number of 1300, the wedges are evidently blunt. The high pressure coefficients are explained by equation (28).

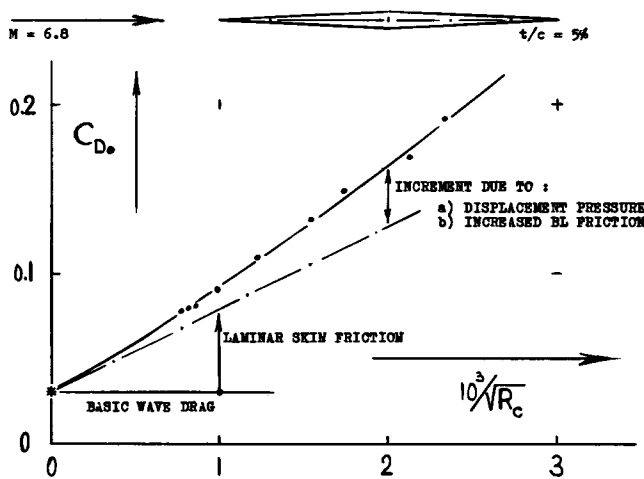


Figure 13. Total drag of a square wing, at zero lift, tested (20,b) at $M = 6.8$, as a function of the R' -number.

Drag of Wing. The zero-lift drag coefficient of a rectangular wing with $A = 1$, and a double-wedge section, is plotted in figure 13 as a function of $(1/\sqrt{R_c})$. The experimental function connects readily with the theoretical point for zero viscosity. Most of the drag increment of the 5% thick section is simply due to laminar skin friction (the coefficient of which is $C_f \sim 1/\sqrt{R_c}$). The additional increment is caused by interference between boundary layer and shock wave. As far as the displacement effect is concerned, it is not clear what takes place along the afterbody where the surface angle is negative.

Wedge Section. The 5% thick single wedge, as illustrated in figure 14, was tested at $M = 6.9$. For $\varepsilon = t/(2c) = 2.5\%$, and for $1/(M\varepsilon) = 5.8$, inviscid theory yields a wave drag coefficient $C_{D_0} \approx 13$ (0.025) ≈ 0.008 . The base drag of this section is estimated (on the basis of the principles presented in Chapter XVI) to correspond to $C_{DB} = 0.5(1.43/M^2) = 0.015$. Skin friction is found (fig. 8/XIX) for $R_c = 10^6$ (as in the test) and for a corresponding $M/\sqrt{R_c} = 6.9/10^3$, in the form of $C_f = 0.01/M = 0.0015$; thus $\Delta C_{D_0} =$

$2(0.0015/0.05) = 0.060$. As the last item, we must now take into account the boundary-layer-induced pressure increment as defined by equation 26. Integration of that pressure over the chord of an airfoil section yields approximately

$$\Delta C_p = 1.2 (M/\sqrt{R_c})$$

For the wedge investigated, a $\Delta C_{D_0} = 0.008$ is thus obtained. Summing up, we then have:

$C_{D_0} = 0.008$ (0.008)	theoretical inviscid wave drag
$= 0.013$ (0.014)	estimated for base drag
$= 0.060$ (0.058)	obtained for skin friction
$= 0.008$ (0.010)	for B'layer-induced pressure
$C_{D_0} = 0.089$ (0.090)	as the total coefficient

The tested coefficients (listed in parentheses) confirm the calculated (and/or estimated) values very well. We realize that (in this particular case) the viscous pressure increment is of the same magnitude as the basic inviscid wave-drag coefficient. If increasing the Mach number further, or upon reducing the R' -number below 10^6 , the "viscous" components are bound to increase appreciably (in the manner as in figure 13). It also appears that the viscous pressure component is only "large" in comparison to the small value of the basic wave drag of the thin section considered.

RECTANGULAR WINGS with $A = 1$



\diamond \square \triangle \times ∇ DELTA WING with DOUBLE WEDGE

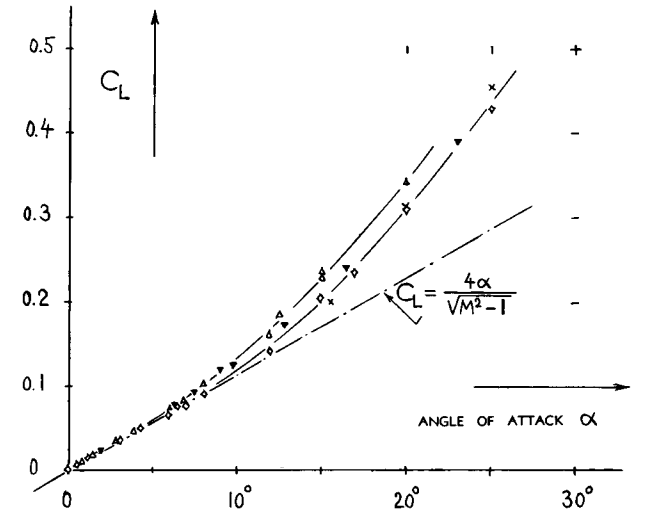


Figure 14. Lifting wings, with $A = 1$, tested (10,a) at a hypersonic speed corresponding to $M = 6.9$.

(20) Boundary-layer induced pressure:

- a) Bertram, BL Displacement, NACA TN 4301 (1958).
- b) Bertram, BL Displacement, NASA TR R-22 (1959).
- c) Kendall, Experimental, J.Aeron Sci 1957 p 47.

(21) Induced pressure due to blunt leading edges:

- a) Bertram, J.A.Sci.1954 p.430, 1956 p.899, 1957 p.627.
- b) Cheng, Blunt-Edge Analysis, J.A.Sci.1956 p.700.
- c) Bogdonoff, at $M = 11$ to 15 , J.A.Sci.1956 p.108.
- d) Hammit (Princeton), in Jet Propulsion 1956 p.241.
- e) Bradfield, Bluntness, J.Aeron.Sci.1954 p.373.
- f) Henderson, At $M = 16$ to 24 , NASA Memo 5-8-59L.

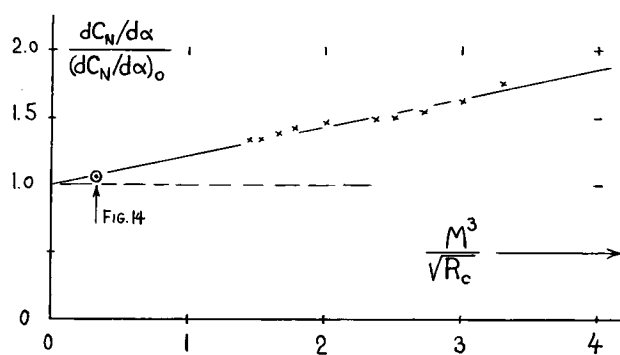


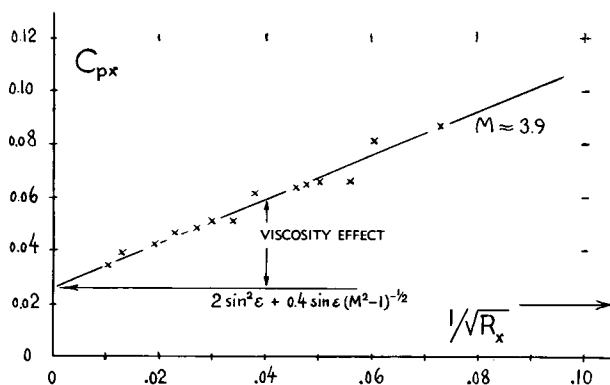
Figure 15. Lift-curve slope of thin and flat rectangular plates, tested (10,d) in rarefied air at $M \approx 3.9$.

Flat Plate Lift. Results of supersonic lifting-wing theory are presented in Chapter XVII. At hypersonic Mach numbers, where $\sqrt{M^2 - 1} \approx M$, linear theory indicating lift-curve slope, reduces to:

$$dC_L/d\alpha \approx (4/M) - (2/AM^2) \quad (30)$$

This solution does not take into account presence and growth of a boundary layer. Figure 14 proves that, at $R_c = 10^6$, lift actually obtained agrees well with theory (at least at angles of attack below 10°). However, normal-force coefficients tested on thin and flat plates at considerably smaller Reynolds numbers (10,d) exhibit lift-curve slopes, which are noticeably higher than indicated by inviscid theory. Figure 15 demonstrates how viscosity, represented by "laminar friction" $\sim (1/\sqrt{R_c})$, increases the lift-curve slope of those plates. The experimental points, obtained at an average $M \approx 3.9$ and at R_c between ≈ 300 and 2000 collapse onto a common single line when plotting the ratio of the tested over the theoretical values (as obtained through application of equation 30) against the parameter $(M^3/\sqrt{R_c})$. It is suggested that practical results (at smaller angles of attack) for larger M 'numbers and/or for smaller R 'numbers can then be found by extrapolation:

$$\Delta(dC_L/d\alpha)/(dC_L/d\alpha)_0 \approx 0.21(M^3/\sqrt{R_c})$$



Wing Drag. Pressure drag corresponding to lift is $D_L = L \tan \alpha$. Hence, in the range of smaller angles of attack:

$$C_{DL} = (dC_L/d\alpha) \alpha^2 = (d\alpha/dC_L) C_L^2 \quad (31)$$

(b) Characteristics of "Conical" Bodies

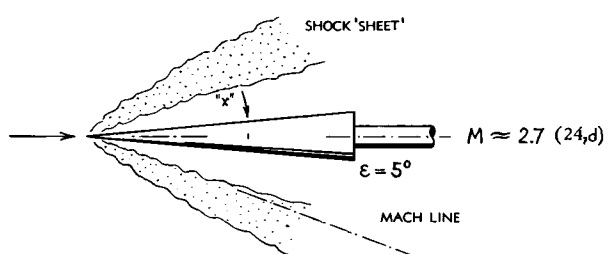
All what is presented above regarding the influence of viscosity on the hypersonic characteristics of plates and wedge sections, also takes place on three-dimensional bodies. To repeat the explanation, we will consider a cone such as in figure 16, at a smaller Reynolds number (where the boundary layer may be comparatively thick) and at a larger (hypersonic) Mach number (where Mach and shock angles are comparatively small). It is then obvious that the boundary layer is "squeezed" within the narrow space between solid surface and shock wave; and it is equally obvious that the B'layer's displacement will force the shock front further outward.

Conical Probes of the type as shown in figure 16 were tested, at $M \approx 3.9$, as a function of Reynolds number. The pressure in the orifice opening at "x" varies approximately as

$$C_{px} = C_{po} + (0.8/\sqrt{R_x}) \quad (32)$$

where $C_{po} = 0.026$ = theoretical cone pressure (as in Chapter XVI) and where R_x = Reynolds number based on distance x (and on ambient flow conditions). In the illustration is the shock flow pattern as reported in (24,d). In distinction to the more or less sharp and concentrated shock waves obtained at higher Reynolds numbers (see Chapter XVI), the sketch in figure 16 displays a very heavy "shock sheet". The intensity of the trailing shock-wave system reduces generally, as the Mach number is increased, until we ultimately arrive at a "one-wave" flow pattern. — Boundary-layer induced pressure increments found on cones with half-vertex angles between 5 and 10° are included in figure 12. It appears that in axi-sym-

Figure 16. Flow pattern of, and static pressure indicated (at "x") by a conical probe (24,c) at $M \approx 3.9$.



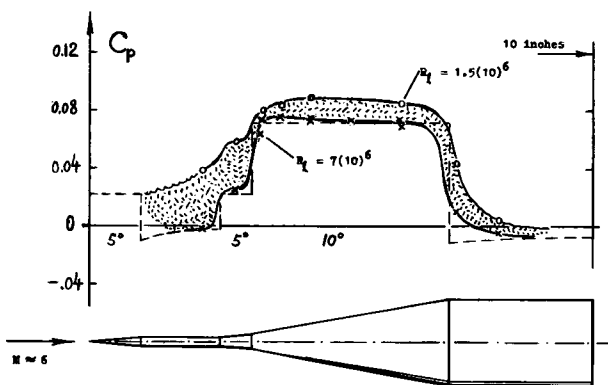


Figure 17. Pressure distribution along a spiked cone-cylinder configuration (26) at two different Reynolds numbers.

metrical flow, the boundary layer spreads out (its thickness reduces) as a function of diameter and circumference of the body (27,c). As a consequence, induced pressure and drag increments seem to be smaller than under two-dimensional conditions.

A Spiked Conical Body was tested (26) at Mach numbers roughly between 3 and 6. At numbers below 4.5, the Reynolds number (on cone length of 4 inches) is about $3(10^6)$. Laminar skin friction is small; and the pressure-drag coefficient $C_{D_0} = 0.078$ agrees with theoretical expectation. In other words, the spike does not seem to have an effect when attached to the tip of the slender cone considered. At $M = 4.2$, the pressure distribution in figure 17, is essentially identical with the theoretical prediction. Results at $M = 6.3$ are different, however. The Reynolds number is $R_L = 0.6(10^6)$ only, in this case; and the boundary layer can be assumed to be thicker than under the condition stated above, at least corresponding to the factor $\sqrt{3}/0.6$. Consequences of viscosity are:

an increase of pressure along spike and "skirt",
an increase of pressure along the main cone,
an increase of pressure drag by 19%.

- (22) Penland, Drag Brakes on Fuselage, NACA RM L55K23.
- (23) Boundary-layer displacement on conical bodies:
 - a) Anderson, Wright-Patt Aeron Res Lab Rpt 1962-387.
 - b) Wagner, Blunted Cones, NASA TN D-2182 (1964).
 - c) Talbot, Viscous Flow, NACA Tech Note 4327 (1958).
- (24) Drag of cones in hypersonic viscous flow:
 - a) Francis, Ford Aeronutronic Div Rpt U-1855 (1962).
 - b) Whitfield, To $M = 19$, AEDC TDR 1963-35 & 1964-1.
 - c) Talbot, Cone Probes, NACA T Note 3219 (1954).
 - d) Stalder, NACA T Note 2244 or T Rpt 1032 (1950).
- (25) Blunt cylinder noses at hypersonic speeds:
 - a) Lees, Hemispherical, J.Aeron Sci 1957 p 195.
 - b) Van Hise, Analytical Study, NASA TR R-78 (1961).
 - c) Wagner, Pressure and Drag, NASA TR R-182 (1963).
 - d) Horstman (Princeton) Wright-Patt ARL Rpt 1963-14.
 - e) Witcofski, Cylindrical Rods, NASA TN D-1266 (1962).
 - f) Inouye, Comparison, NASA TN D-1426 (1962).

The increments of pressure and drag are evidently caused by the displacement of the boundary layer, making the effective cone angles larger than the geometrical ones.

Drag Brakes. An ogive-cylinder configuration is shown in figure 18, with a pair of "panels" which can be deflected from the rear end to serve as brakes. The drag coefficient of the "vehicle" is plotted as a function of the deflection angle. As far as braking is concerned, the flaps investigated, are very effective; total drag can be increased to fourfold, when deflecting the flaps to 30° . To explain the drag, equation (29) or the function plotted in figure 27, both on page 16-20 may be used. In the present case, it is sufficient, however, to apply the first term of these formulations. Thus, based on geometrical brake-flap area:

$$C_{D_B} = C_p (\sin \delta) = 2.1 (\sin^3 \delta) \quad (33)$$

To refer this component to the body's frontal area, a factor of 2.3 has to be used, thus accounting for the size of the brake flaps. The equation then confirms the experimental value of $\Delta C_{D_B} = 0.03$, at $\delta = 10^\circ$, when adding a component of 0.01 for base pressure (see page 16-4). However, at $\delta = 20^\circ$ (where $\Delta C_{D_B} = 0.15$) and at 30° (where $\Delta C_{D_B} = 0.40$) the equation gives values which are too high. It must evidently be considered that the flaps are curved; and that at $\delta = 30^\circ$, for example, the inclination of the flap surfaces near their lateral edges, against the direction of the undisturbed flow, is appreciably less than 30° . There is also a possibility of interference between the boundary layer developing along the body and the deflected brake flaps. Such interference is discussed in several places, in connection with "spikes"; and in Chapter XX in connection with steps in the surface.

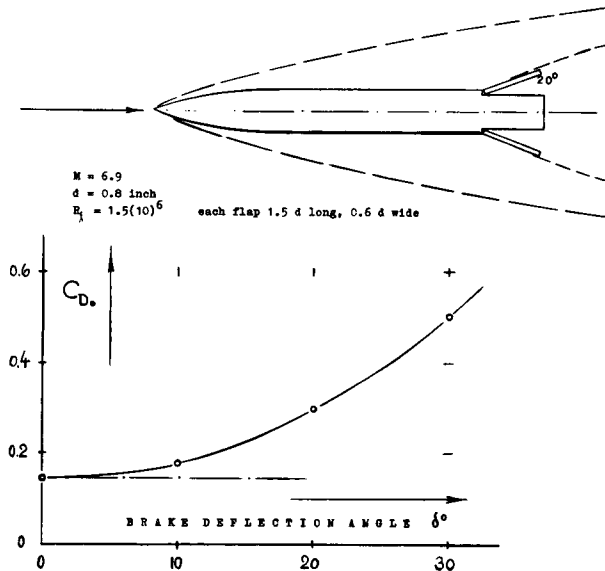


Figure 18. The influence of a pair of brake flaps (22) deflected from the rear of an ogive-cylinder combination.

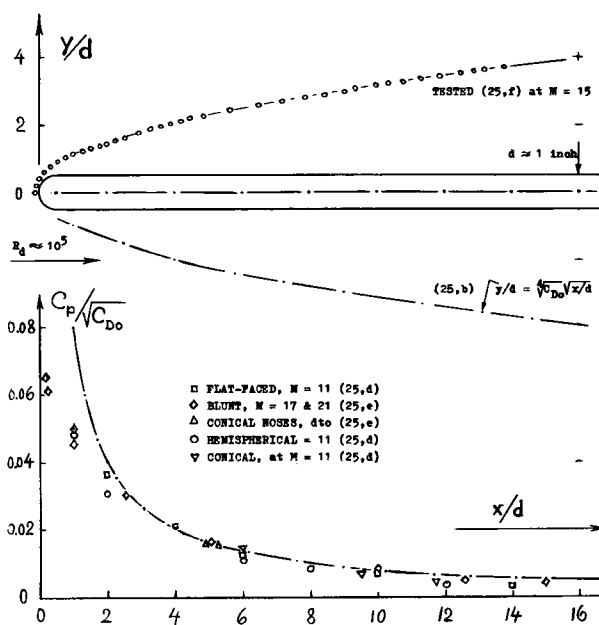


Figure 19. Pressure along the surface of circular cylinders, induced by the wave drag of blunt nose shapes.

Blunt Cylinders have been investigated (25) at low Reynolds numbers, in order to get some information on the influence of nose shape on the drag of conical and similar bodies. The so-called blast-wave analysis considers the flow pattern produced by a blunt nose to be a function of its drag coefficient only. Nose-drag coefficients at higher supersonic speeds can be found later, under "bluff bodies". Roughly, the induced pressure coefficient (along the cylinder surface) varies as

$$C_p = 0.1 \sqrt{C_{D0}} / (x/d) \quad (36)$$

where x = axial distance from the nose point. We have plotted the pressure distribution for three different nose shapes, in figure 19. Directly behind the nose, equation (36) does not apply.

Skin-Friction drag along the surface of a slender body, at hypersonic speeds, is for laminar condition and without heat transfer, given by the coefficient

$$C_f \approx 0.7 f(M) \sqrt{p/p_\infty} / \sqrt{R_x} \quad (37)$$

It thus increases with the induced pressure differential. The function $f(M)$ accounts for the non-linear variation of viscosity with temperature (as mentioned above). Tentatively it may be

$$f(M) = 1 / (M^2 - 1)^{1/16} \quad (38)$$

which gives for small M' numbers correctly $f(M) = 1$. This function agrees approximately with that in figure 2 on page 17-3. For hypersonic M' numbers:

$$f(M) = 1/M^{1/8} \quad (39)$$

Delta Wings. Drag coefficients (based on wing area) are presented in figure 20, for a series of delta wings, tested at zero lift and at $M = 6.8$. In regard to pressure drag it can qualitatively be said that such wings are between two-dimensional sections and conical forebodies. The variation of laminar skin friction in proportion to $1/\sqrt{R_c}$ is evident. In comparison to the function as on page 2-4, there is a drag increment, evidently caused by presence and displacement of the boundary layer.

Total Drag of Cones. Base drag can be assumed to be zero, within the range of hypersonic speeds. The drag of a cone (or that of a conical nose) thus consists of

- the basic pressure or wave drag,
- the basic skin friction drag,
- the increments due to boundary layer.

Cones have been analyzed (24,a) at hypersonic Mach numbers between 10 and 20, and for laminar boundary-layer flow. Since pressure as well as laminar skin friction depend upon the similarity parameter as in figure 12, the following equation was found (24,a) for the total forebody drag of cones in cooled condition (with heat transfer, so that $T_w/T_\infty = 0.1$):

$$C_{D0} = 2 \epsilon^2 + 2.9 K + (0.4/\epsilon^2) K^2 \quad (40)$$

where $K = M^{3/4} / \sqrt{R_x}$. As plotted in figure 21, for cones with a half-vertex angle $\epsilon = 9^\circ$, the function is sufficiently confirmed by total drag coefficients tested at Mach numbers between 10 and 20. One group of points obtained in "hot" condition, shows that drag is higher. At K values below 0.015, the drag coefficient seems to have a tendency of being higher than indicated by the equation. Experimental results at M below 10, have evidently minimum drag coefficients higher than indicated by the first term of equation (40).

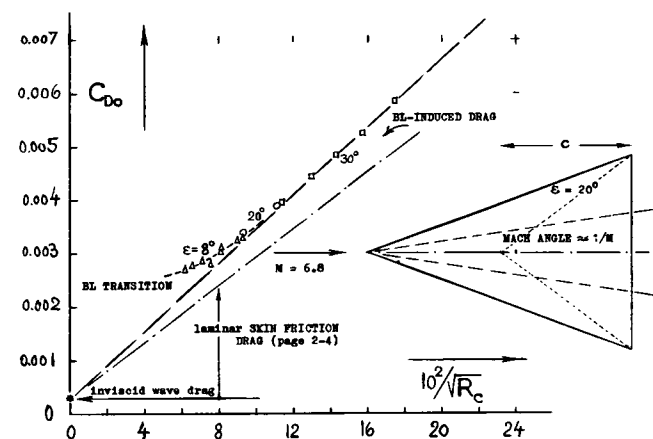


Figure 20. Drag coefficients (on plan-form area) of a family of delta wings (20,b) varying in half-vertex angle ϵ between 8 and 30° , as a function of Reynolds number.

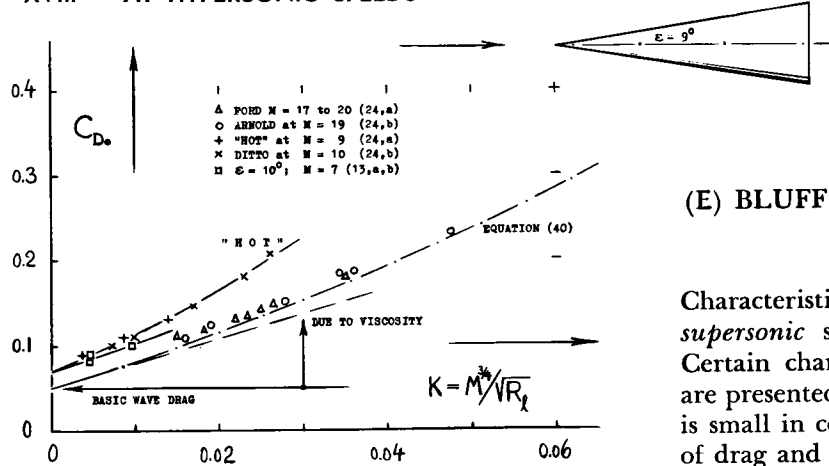


Figure 21. Total forebody drag coefficients of cones, primarily with 9° half-vertex angle, at hypersonic Mach numbers between 10 and 20, primarily in cooled condition, as a function of the viscous similarity parameter "K".

Transition to turbulent boundary-layer flow usually does not take place in model tests at hypersonic speeds. In fact, it has been reported that even with stimulation, transition is not obtained at Reynolds numbers in the order of $R_\ell = 3 \cdot 10^6$. It seems that the negative pressure gradient along the surface, corresponding to equation (26) and possibly a gradient corresponding to the expansion around the "shoulder" of cone-cylinder combinations, has a strong stabilizing effect upon the boundary layer. Transition is reported and discussed in (30). Besides the influence of the pressure gradient as above, practical results are as follows:

- Transition is delayed at higher M' numbers.
- Cooling (heat transfer) delays transition.
- Nose blunting increases transition R' numbers.
- Leading-edge sweep leads to early transition.
- Surface roughness promotes transition.

The transition Reynolds number as found in (30,a) on a hollow cylinder, is in the order of $R_x = 6 \cdot 10^6$, at $M = 6.9$. — As far as roughness is concerned, results in (30,e) indicate that single elements (such as spherical grains) fail to have an effect, as long as their height is less than the boundary-layer thickness.

Turbulent Friction. Under full-scale conditions, transition must eventually be expected. Analysis of turbulent skin friction such as in (27,b) is complex. As an approximation, it is suggested to use the functions in figure 3, on page 17-4.

- (26) Neice, Spiked Cone-Cylinder Body, NACA RM A54C04.
- (27) Information on skin friction at hypersonic speeds:
 - a) See (20,b); also NACA L52A14; NASA R-26 & 123.
 - b) Van Driest, Turbulent Boundary Layer, J.Aeron Sci 1951 p 145.
 - c) Probstein, Laminar Flow, J.Aeron Sci 1956 p 208.
- (28) Drag of delta wings at hypersonic speeds:
 - a) A Series of Delta Wings, see in reference (20,b).
 - b) Bertram, Delta Wings at $M = 6.9$, NACA RM L54G28.
 - c) Bertram, Slab Delta at $M = 7$ to 18, NASA TR R-153.
 - d) Elliptic Cross Section, Minnesota U Rpt ARL 1963-231.
 - e) Goldberg, Delta Plate, NASA TN D-1959 (1963).

(E) BLUFF BODIES AT HYPERSONIC SPEEDS

Characteristics of bluff three-dimensional bodies at supersonic speeds are discussed in Chapter XVI. Certain characteristics typical of hypersonic speeds are presented in this section. As long as skin friction is small in comparison to pressure forces, that type of drag and the influence of Reynolds number can very often be disregarded.

(1) Two-Dimensional Shapes

Blunt Shapes. The maximum pressure, in the stagnation point of the blunt shapes presented in figure 22, is equal to that as indicated by equation 4 in Chapter XVI. At hypersonic Mach numbers (above $M \approx 3$, and in air) that pressure corresponds to

$$C_{p_0} = 1.84 - (0.76/M^2) \quad (41)$$

Out of the narrow and high-pressure space between the solid's face and the detached bow wave, an ex-

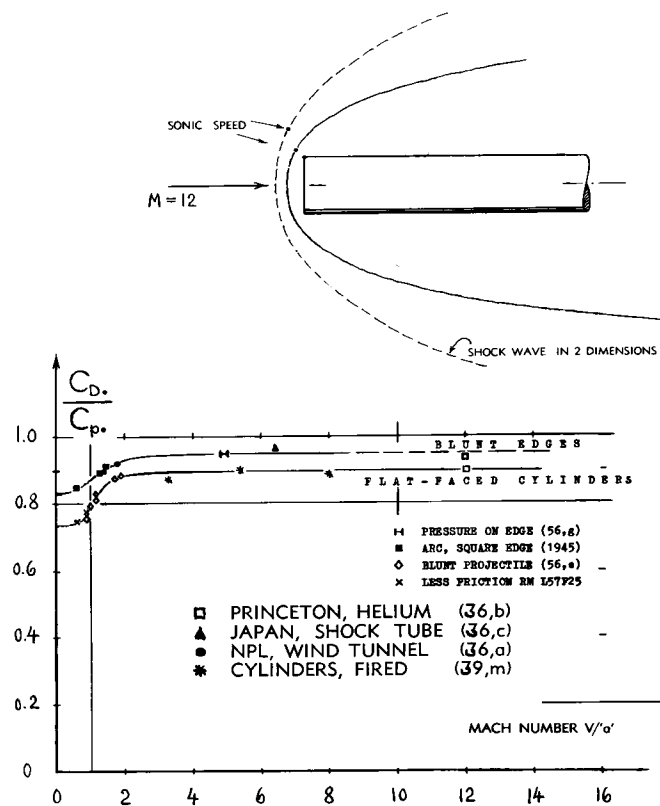


Figure 22. Drag of blunt shapes, at hypersonic Mach numbers.

*p*ansion takes place. Sonic speed is subsequently obtained at the sharp edges or shoulders of such shapes; and the static pressure there is equal to 0.53 of the pressure at the stagnation point. With maximum and minimum pressures thus fixed, the average pressure on the face of blunt shapes can be expected to be a constant fraction of the stagnation pressure $C_{p\infty}$. Pressure drag coefficients of blunt edges and of blunt cylinders in axial flow (some of them previously presented, in figures 14 and 18 of Chapter XVI) are plotted in figure 22, in the form of $C_{D\infty}/C_{p\infty}$. Above $M \approx 5$, they seem to indicate constant values of

$$\begin{aligned} C_{D\infty}/C_{p\infty} &= 0.89 \text{ for the blunt cylinder head} \\ &= 0.94 \text{ for the blunt leading edge} \end{aligned}$$

These values can be considered to be an improved version of the "K" values indicated in Chapter XVI for bluff wedges and cones. For hypersonic conditions, equation 21 of that chapter can be simplified to

$$C_{D\infty}/C_{p\infty} = K - 0.76 (1 - K)/M^2 \quad (42)$$

where "0.76" as in equation 41. For $K = C_{D\infty}/C_{p\infty} = 0.94$ as found empirically for higher Mach numbers, the drag decrement of the two-dimensional blunt shape (in figure 22) is then obtained as $\Delta C_{D\infty}/C_{p\infty} = -0.046/M^2$. This function matches the experimental points down to $M = 2$.

Newtonian-Type Flow (41). The stagnation or impact pressure $C_{p\infty}$ (equation 41) also predominates in producing drag on the forward face of bodies such as spheres (55) or circular cylinders in cross flow. Away from the stagnation point, the surface pressure reduces; and it has empirically been found (41) that under hypersonic conditions, the static pressure *approximately* corresponds to

$$C_p = C_{p\infty} \sin^2 \epsilon \quad (43)$$

where ϵ = local angle of surface inclination against the undisturbed direction of the oncoming fluid stream. In words, the air particles "striking" an obstacle, lose their normal component of momentum. Pressure distributions as indicated by the equation have been named "*modified Newtonian*" thus referring to the mechanics of free-molecule flow (as explained at the end of Chapter XIX).

Circular Cylinder. Application of the Newtonian principle to the two-dimensional shape of a cylinder (at $\alpha = 90^\circ$, in cross flow) yields the drag coefficient

$$C_{D\infty} = C_{p\infty} \int \cos^2 \varphi d(\sin \varphi) = (2/3) C_{p\infty} \quad (44)$$

where φ = angle as in figure 2 of Chapter III. Pres-

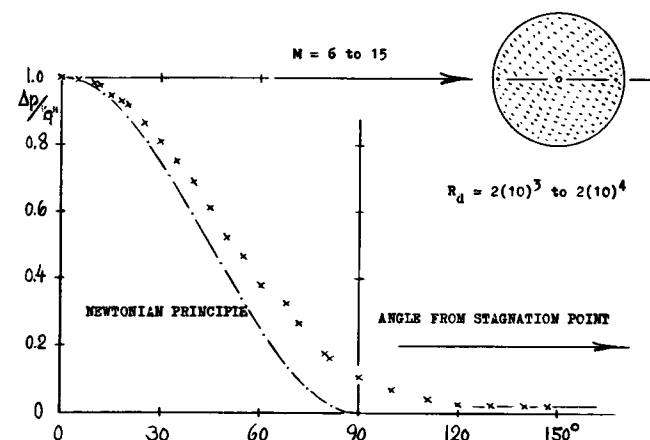


Figure 23. Pressure distribution around circular cylinders in 2-dimensional cross flow, as tested (42,d) at M between 6 and 15, and at R_d between $2(10)^3$ and $2(10)^4$

Similar distributions are found in (28,e) for M between 2 and 10. It should be noted that one of the reasons for the increased pressures tested, is viscosity (at the comparatively small Reynolds numbers listed).

sure distributions as tested at $M \approx 6.9$ and ≈ 5.7 respectively (39,a) show, however, that the pressure coefficient at the sides of the cylinder, at 90° from the stagnation point is somewhat positive, while the Newtonian approximation reduces to zero in those places. In fact, the distribution plotted in figure 23, shows that the pressure is higher than according to the Newtonian theory.

Shoulder Pressure. Behind edge or "shoulder" of bluff shapes (such as the blunt leading edge of the flat plate illustrated in figure 22) the static pressure remains positive for a distance measuring several times their thickness or diameter, respectively. In air (for $k = 1.4$) that pressure is estimated (21) approximately to correspond to

$$C_{pS} = 0.1 - (0.6/M^2) \quad (45)$$

This shoulder pressure is *positive* at hypersonic speeds (above $M \approx 3$); and it approaches $C_p = 0.1$, as M grows to higher values. Further downstream, the static pressure returns to the ambient level.

Centrifugal Effect. Because of centrifugal forces, within the stream developing between shock front and bluff-body face, the static pressure at the solid surface can be slightly less than that directly behind the curved shock sheet. A theoretical analysis of this effect is given in (6,e). Experimental evidence of reduced pressure is occasionally found, particularly on hemispherical heads (54) in the vicinity of $\approx 45^\circ$ away from the stagnation point. It seems, however, that tested decrements (such as mentioned above) fall short of the theoretical prediction.

- LEADING EDGES IN 2 DIMENSIONS:
 ◎ PRESSURE DISTRIBUTION (55,a)
 • N P L, IN WIND TUNNEL (36,a)
 ▲ JAPAN, INTERFEROMETER (36,c)

CIRCULAR CYLINDER HEADS:

- PRESSURE DISTRIBUTION (55,a)
- PRINCETON IN HELIUM (36,b)
- ◊ GALCIT, HYPERSONIC (39,a)
- △ NACA, AS IN FIG. 20, CHAP. XVI
- + NEW MEXICO FIRINGS (35,b)
- N P L, IN WIND TUNNEL (36,a)

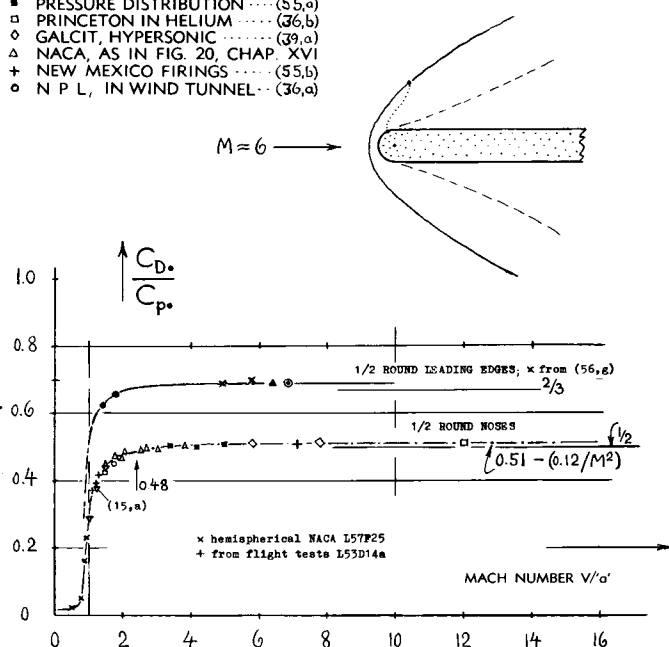


Figure 24. Drag function of round shapes, at hypersonic Mach numbers.

Round Leading Edges. The influence of positive shoulder pressure (equation 45) is also found in two-dimensional shapes, such as on round leading edges and/or at the lateral sides of circular cylinders in cross flow. Some experimental drag coefficients are presented in figure 24. At "hypersonic" Mach numbers (above $M \approx 3$) pressure drag of $1/2$ circular edges is higher than indicated by equation (44) the differential being in the order of $(0.69 - 0.67) = 0.02$. The reason for the increment is the same as in, and the variation against Mach number is similar to that of, hemispherical noses (see later).

Leading Wedge. The round leading edge in figure 24, has less drag ($C_D = 1.25$, at $M = 6$) than the flat-faced edge in figure 22 ($C_D = 1.75$). The pressure distributions of three groups of shapes are reported in (44,a), tested at $M = 6$. Figure 25 shows how the drag reduces when increasing the chordwise length x of the shapes. The coefficient of the blunt wedges connects to the function indicated by equation (11). It must be realized that the flow pattern of blunt shapes differs from that of more slender wedges. For example, at $M = 6$, the critical half-vertex angle is theoretically $\epsilon = 42^\circ$. Above this angle, the wedge (or any similar shape) produces a detached shock front. As found in (44,a) practically full stagnation pressure is obtained (at the vertex line) at angles above $\epsilon = 51^\circ$, for $M = 6$. As a consequence, any Newtonian theory does not correctly describe the pressure distribution around such blunt shapes.

- (30) Boundary layer transition at hypersonic speeds:
 a) Bertram, On Hollow Cylinder, NACA TN 3546 (1956).
 b) Krasnican, In Free Flight, NASA Memo 3-4-59E.
 c) Low, Discussion of Results, NACA RM E56E10.
 d) Bibliography, Lockheed Rpt 1962 (ASTIA AD-296,151).
 e) Holloway, Roughness Elements, NASA TN D-2054.
 f) Mabey, Roughness, RAE TN Aero 2941 (1963).
 g) NACA TN 3048 & 3103; NASA TN D-1220 & 1378.
- (36) Bluff head shapes in hypersonic fluid flow:
 a) Holder, Half Body Shapes, J.Aeron.Sci.1954 p.317.
 b) Vas, At $M \approx 12$, Princeton Engg Rpt 382 (1957).
 c) Takamaki, L'Edges, J.Phys.Soc.Japan 1957 p.550.
- (39) Results on bluff bodies at hypersonic speeds:
 a) GALCIT; Cones Cylinder, J.A.Sci.1956 p.177 & 1054.
 b) Lees, Evaluation, J.Aeron.Sci.1957 p.195.
 c) Li, Stagnation Point, J.A.Sci.1957 p.25.
 e) Soule, Firing Models, NACA T.Note 2120.
 h) Cone — Sphere — Cylinder, J.A.Sci.1952 p.757.
 i) Freeman, Theory, J.Fluid Mech.1956 p.366.
 m) Long, Axial Cylinder at $M = 8$, NAVORD Rpt 4382.
- (41) Newtonian-type hypersonic pressure distribution:
 a) The approach is explained in (39,a,c) & (42,a,c).
 b) Coles, Newtonian Theory, J.Aeron.Sci.1957 p.448.
 c) Tokyo, Cylinder at $M = 2$, J.A.Sci.1956 p.830.
 e) Love, Newtonian Theory, J.Aeron.Sci. 1959 p.314.
 f) Wells, Tables of Body Forces, NASA TR-R-127.
 g) Rainey, Forces and Pressures, NASA TN D-176 (1959).
- (42) Circular cylinders in hypersonic cross flow:
 a) Penland, Cylinder at $M = 6.9$, NACA RM L54A14.
 b) Gowen, f (M and R), NACA Tech.Note 2960 (1953).
 c) Grimminger, Lifting Bodies, J.A.Sci.1950 p.675.
 d) Gregorek, Pressure Distribution, J.AIAA 1963 p.210.
 e) Beckwith, Heat Transfer, NASA TR R-104 (1961).
- (43) This value agrees with higher-order solutions of hypersonic theory; Lees, Hypersonic Similarity J.Aeron.Sci. 1951 p.700.
- (44) Wave drag due to blunt leading edges:
 a) Goldberg, Edge Shapes, NASA TN D-1793 (1963).
 b) Stainback, Delta Wing, NASA TN D-1246 (1962).

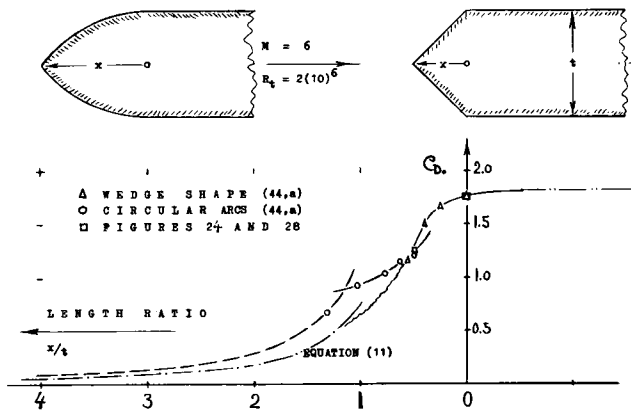
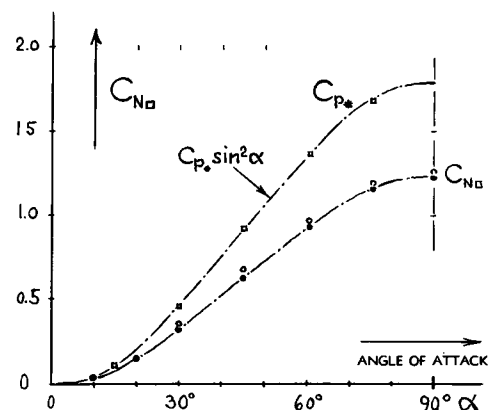
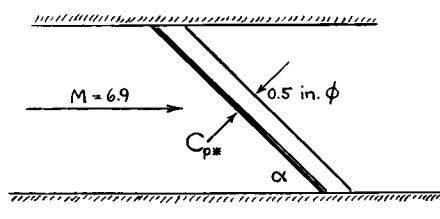


Figure 25. Wave drag at hypersonic speeds due to blunt leading edges (44,a) as a function of their shape and length ratio.

Figure 26. Maximum-pressure and drag coefficient of a circular cylinder, tested (42,a) at $M = 6.9$, as a function of its angle of attack (representing inclination against the fluid flow).



Double Arc. Within the range of higher fineness ratios, a circular arc (or any similar) edge shape, is known to have more drag than a wedge having the same length. At a ratio $x/t = 1.1$ or 1.2 , where the tangent vertex angle of the arc shape exceeds the critical value, the flow pattern changes. In the more blunt condition, the shock wave detaches as described above. Around $x/t = 1$, drag is still appreciably higher than that of a wedge having the same length. It seems, however, that there is a cross-over point (near $x/t = 0.5$) where shape does not affect the drag coefficient. The experimental functions have been extrapolated into the range of hollow shapes, where drag corresponding to full stagnation pressure will eventually be reached.

Leading-Edge Sweep. A delta wing with a half-circular leading edge was tested (44,b) at $M = 5$. For an angle of sweep of 60° , Newtonian theory expects a reduction of pressure at the leading edge corresponding to $\cos^2 60^\circ = 0.25$. The measured maximum pressure increment at the edge was found to be $\Delta p \approx 0.27$ "q". A similar slab-type delta wing (with 70° leading-edge sweep) was tested (28,c) at M between 7 and 18. Evaluation at $M = 7$, yields a maximum pressure coefficient $C_{P*} = 0.24$, while Newtonian theory expects a coefficient of 0.22. Approximately, therefore, pressure and wave drag due to swept edges can be predicted through the use of equation (46).

Inclined Cylinder. Drag of Cylinders in oblique flow panels is explained on the basis of the "cross-flow principle," in Chapter XV. The same method now applied to cylinders inclined against a hypersonic stream of air, is found to be identical with the modified Newtonian principle, applied to such cylinders a second time. Figure 26 shows first, that the maximum or stagnation pressure coefficient varies corresponding to

$$C_p = C_{p*} \sin^2 \alpha \quad (46)$$

where α = angle of attack of the cylinder (42). The normal-force coefficient C_N on cylinder area $S_\Box =$

$d \cdot l$, where l = length in axial direction) is then

$$C_{N\Box} = C_{D*} \sin^2 \alpha \quad (47)$$

where C_{D*} = drag coefficient at $\alpha = 90^\circ$ as in equation (44). The drag coefficient at other angles is simply

$$C_{D\Box} = C_{D*} \sin^3 \alpha \quad (48)$$

and the lift coefficient is

$$C_{L\Box} = C_{D*} \sin^2 \alpha \cos \alpha \quad (49)$$

in the same manner as in uncompressed fluid flow (see figure 18, Chapter III). In addition to the pressure forces considered, there is also a small skin-friction component included in the *balance*-tested points plotted in figure 26, thus placing them slightly above the *pressure*-tested drag function.

Spoiler. Disregarding the range of smaller Reynolds numbers, viscosity may not noticeably affect flow pattern and drag of bluff shapes at supersonic and hypersonic Mach numbers. There is the type of *interference* shown in figure 27, however, between an

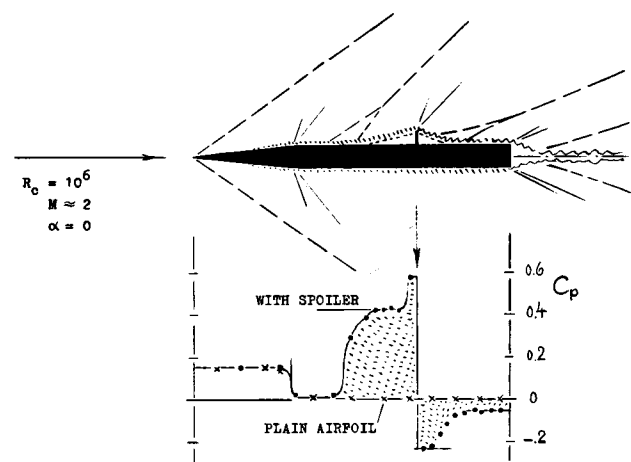


Figure 27. Flow pattern and pressure distribution around a spoiler (45,b) having a height equal to 5% of the chord of the 6% thick wing section shown.

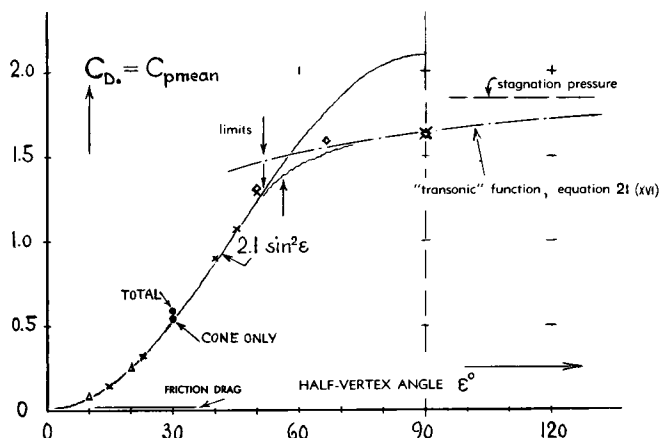
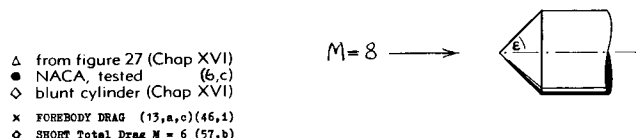


Figure 28. Drag coefficient of *bluff cones*, with half-vertex angles up to 90° , and to 180° (thus representing hollow shapes), tested at and calculated for $M \approx 8$.

obstacle and the boundary layer within which that obstacle is placed. Owing to increasing pressure, the boundary layer separates ahead of the spoiler plate. It then forms a wedge-like "dead" space; and the resulting flow pattern is very similar to that past a wedge. There is a shock wave originating from around the leading edge of the "wedge". An expansion then takes place around the edge of the spoiler into a separated "base" space, where the pressure is negative (below the ambient level). The flow pattern terminates with a recompression shock wave, in the same manner as behind the base of a blunt trailing edge. The pressure differential across the spoiler plate is $\Delta C_p = 0.8$, in the case presented, at $M \approx 2$. It can be expected that this coefficient will vary somewhat when increasing the Mach number. There is a considerable influence of spoiler height; that is, of the ratio of height to boundary-layer thickness. Separation, shock wave angle and resultant pressures are correlated in (45,c). The mechanism is also discussed in Chapter XX, in connection with surface irregularities (steps). — As far as the effectiveness of a spoiler at supersonic speeds is concerned, it can be seen in figure 27 that the lift differential produced (ΔC_L in the order of -0.08) is due to the increase of pressure *ahead* of the obstacle. In subsonic flow, the control effect of a spoiler is always based on the reduction of pressure ("spoiling" of flow and lift) *behind* the plate or flap.

(2) Three-Dimensional Bodies

Bluff Cones. Figure 28 presents experimental and theoretical results at high Mach numbers (in the order of $M = 8$) in regard to the drag coefficient of cones up to and exceeding $\epsilon = 90^\circ$ (where the cones transform into hollow head shapes). In preparing the graph, two theories have successfully been utilized; (a) hypersonic cone theory (as approximated by equ. 29, Chap. XVI); and (b) the "transonic"-type theory presented in Chapter XVI (equ. 21 and figure 19). At half-vertex angles above $\approx 50^\circ$, where detachment of the bow wave is to be expected, a transition takes most likely place to the bluff-body function as indicated. That function is then expected to increase further until it reaches the full value of the stagnation pressure at $\epsilon = 180^\circ$ (which represents a hollow "scoop"-like shape).

Blunted Cone. It has been shown (in figure 7) that slightly blunting the tip of a cone, can reduce its drag. In this respect, shape (b) in figure 30 is evidently too blunt. Also included in the illustration is a flat but thick (slab-type) delta shape (c) having the same half-vertex angle as the cones. Its drag coefficient is almost the same as that of the pointed cone (a).

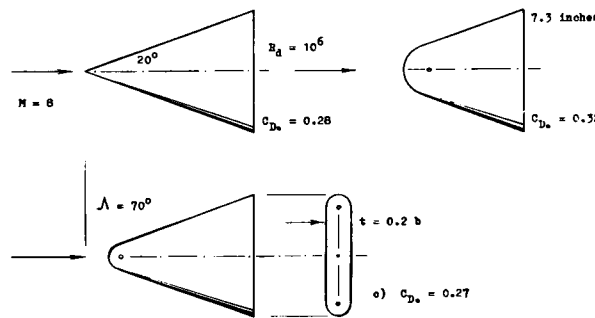


Figure 30. Total-drag coefficients at $M = 8$, of three conical bodies (46,g) showing the influence of shape modifications.

- (45) Boundary-layer separation ahead of obstacles:
 a) Lange, Status of Information, NACA TN 3065 (1954).
 b) Mueller, Spoilers at $M = 1.9$, NACA TN 4180 (1958).
 c) Chapman, Separation, NACA T Rpt 1356 (1958).
 d) Lord, Spoiler Characteristics, NACA RM L56E22.

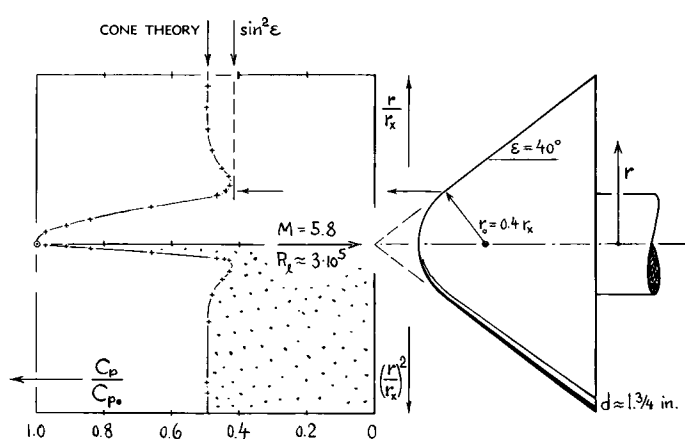


Figure 31. Pressure distribution on the surface of a rounded cone, tested (39,a) at $M = 5.8$.

Rounded Cone. Characteristics of another bluff shape are presented in figure 31. Pressure on the rounded part corresponds to "Newtonian" distribution. This type of pressure continues to a point somewhat aft of the juncture with the conical portion of the shape. Subsequently, some compression takes place, however, raising the pressure to the level as indicated by super-hypersonic cone theory (see Chapter XVI, figure 27). Transition evidently takes place, in this manner, from the detached-bow-wave pattern (where the Newtonian approximation applies) to that of "attached" conical flow (where pressure corresponds to cone theory). Pressure-drag ratios, obtained by integration of experimental distributions, are:

$$\begin{aligned} C_{D_0}/C_{D_0} &= 0.495 \text{ for the pointed cone} \\ &= 0.501 \text{ for the rounded cone} \end{aligned}$$

One reason for the fact that rounding does not increase the drag very much, is the smallness of the area on which pressures, in the order of that at the stagnation point, are found in three-dimensional shapes.

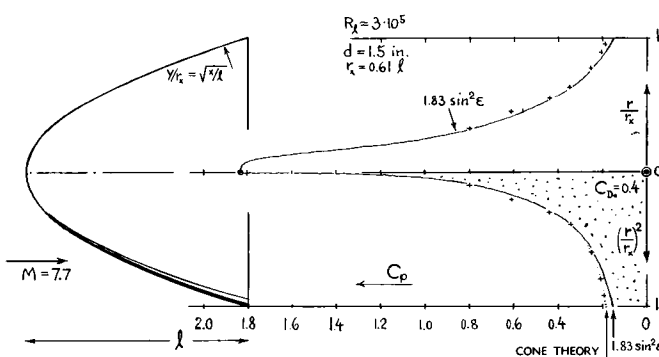


Figure 32. Pressure distribution on the surface of a parabolic body of revolution, tested (46,e) at $M = 7.7$.

Parabolic Nose Shape. The pressure distribution of the three-dimensional solid as in figure 32, is very close to the Newtonian type. Upon approaching the body's shoulder (where the surface angle has reduced to $\epsilon \approx 17^\circ$) one can see, however, that the tested pressure corresponds to cone theory, rather than to the approximation as indicated by equation (43). Here again, we thus realize that a transition takes place from detached to attached shock wave flow. The integrated drag coefficient of the parabolic body is $C_{D_0} = 0.40$. Analysis in (46,e) indicates that this coefficient is approximately 15% higher than that of a pointed cone having the same length ratio $l/d = 0.83$ (or the same diameter ratio $d/l = 1.21$). Between these two shapes, there is an optimum (giving minimum drag on frontal area) expected to be obtained for a parabolic form corresponding to

$$r/r_x = (x/l)^m \quad (52)$$

where $r =$ radius, x indicating maximum radius ($r_x = 0.5 d$) and where "m" is between 0.7 and 0.8.

Newtonian Analysis. A capsule type of re-entry body is presented in figure 33, tested at $M = 9$. Drag at $\alpha = 180^\circ$ corresponds to equation (19). Modified Newtonian theory (listed in parentheses) underestimates the drag in that case appreciably, while at $\alpha = 0$ (where the shape is blunt, but "round") agreement is good. In the vicinity of $\alpha = 70^\circ$ (where lift is zero) the area of the body projected in wind direction, is near a minimum, in the order of $0.6 (d^2/4)$. Since shape (surface angles against wind) is favorable at that angle, the drag coefficient is at a minimum in the order of 0.4. At an angle of attack between 90° (normal to the axis) and 123° (normal to the windward cone surface) shape and flow pattern are similar to that of a circular cylinder. For $C_{D_0} = 1.24$ as for the cylinder, and on the basis of a projected area ratio of 0.56, a capsule coefficient $C_{D_0} = 0.69$ is obtained, which agrees with the experimental value. Another maximum corresponding to $C_{D_0} = 0.9$, is found at $\alpha = 130^\circ$ (where lift is again zero). Newtonian theory predicts the angles of maximum and minimum drag values very well. This theory has, therefore, been used such as in (41,f) to study drag and other forces on many basic shapes of re-entry vehicles. In fact, the Newtonian approach is the only practical one, through which forces on complicated shapes and/or at angles of attack different from zero can reasonably well be predicted.

- (46) Characteristics of bluff, rounded, blunted cones:
 a) Sommer, Truncated Cones to $M \approx 7$, NACA RM A52B13.
 b) NACA, RM A52A14b; also J.Appl.Phys.1950 No. 11.
 c) Bertram, Blunted at $M = 6.9$, J.A.Sci.1956 p.899.
 d) Eggers, Rounded, NACA Tech.Note 3666 (1956).
 e) Kubota, At $M = 7.7$, GALCIT Memo 40 (1957).
 f) Kahl, BRL Rpt (see A.Engg.Review Oct. 1957 p.63).
 g) Merz, At $M = 8$, Arnold Center AEDC TDR-1962-187.
 h) Seiff, Free Flight, NACA RM A52A14b; T Rpt 1222.
 i) Penland, Sharp Cones, NASA TN D-2283 (1964).

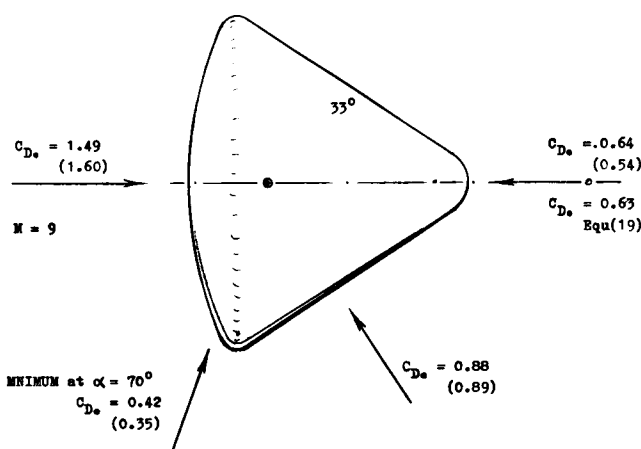


Figure 33. Total drag coefficients of a conical or capsule-type body (50,a) at several angles of attack as indicated. Modified Newtonian values are listed in parentheses.

At Angle of Attack. Almost all of our presentation in this chapter deals with conditions at zero angle of attack (no lift). A number of reports listed under (13) and (46) also contain information on forces of, and/or pressures on cones when at an angle of attack. An analysis of experimental pressure distributions is presented in (13,d), for M roughly between 7 and 8. It is shown that the Newtonian principle of $(\text{pressure}) = f(\text{local angle of attack})$ can be utilized in the interpolation and prediction of pressure distributions. It is thus possible to obtain the pressure around the circumference of a cone when at an angle of attack. It can also be said that approximately the pressure along the windward generator of a certain cone (1) is equal to that of a different cone (2) having a half vertex angle $\varepsilon_2 = (\varepsilon_1 + \alpha)$.

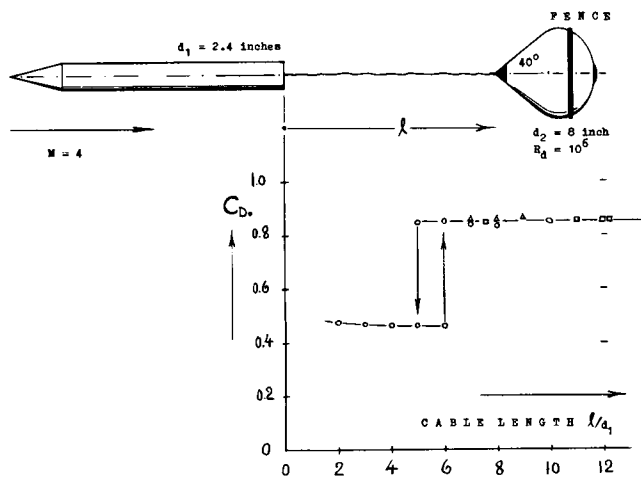


Figure 34. Drag of an inflatable balloon-type device (50,b) when towed behind a cone-cylinder body.

Towed Cones. Parachutes, when used to decelerate and to recover missiles, have limitations as to speed, that is as to structural forces and temperatures. As an alternative, inflatable balloon-type drag devices were, therefore, developed (50,a) by the Goodyear Aircraft Corporation. As seen in figure 34, there is a critical tow-line length, below which the wake from the "payload" interferes very much with the flow pattern of the drag device. Wake plus cable evidently have the same effect as a spike protruding from the face of the towed body. This mechanism is explained in other places in this book; see under "spike". The minimum cable length required, is between 3 and 6 times the diameter of the towing cylinder, at M around 4. However, the interference described, evidently increases with the Mach number. In the configuration shown in figure 35, the drag coefficient obtained at $M = 10$, is only $C_D = 0.5$, for cable-length ratios between 9 and 18. The drag coefficient of the towing body is higher (0.93)

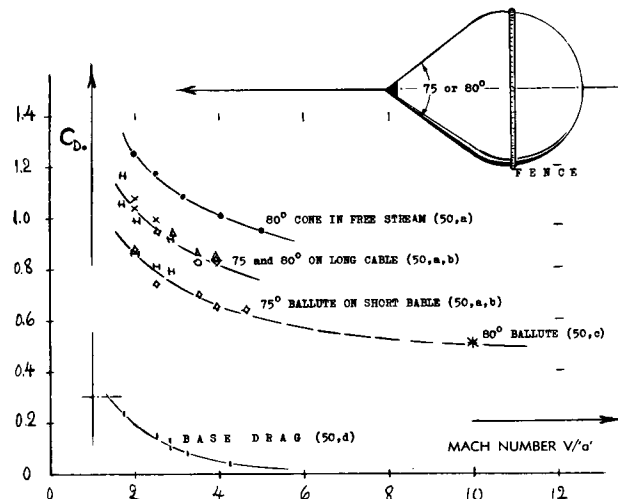


Figure 35. Total drag coefficient of "ballute"-type inflated bodies (50) as a function of Mach number.

than that in figure 34 ($C_D \approx 0.2$). Also considering the area ratio ($S_1/S_2 = 0.04$) in comparison to 0.09 in figure 34, a drag coefficient based on frontal area of the towed body, $\Delta C_D = 0.04 (0.93) = 0.037$ is obtained, while in the configuration at $M = 4$, this coefficient is $\Delta C_D = 0.09 (0.2) = 0.018$. In supersonic flow, not all of the loss of momentum is concentrated in the wake. In fact, the loss due to wave drag is carried sideways along the shock front. At any rate, pressure distribution tests reported in (50,a) at $M = 10$, prove that the coefficient at the conical face of the towed drag body is as low as $C_p = \Delta p/q = 0.11$, while for $\varepsilon = 40^\circ$ it should be $C_p \approx 2 \sin^2 \varepsilon = 0.83$. The maximum pressure recorded is near the "rim" of the cone, in the order of $C_p = 0.5$. In conclusion, at $M = 10$, the wake coming from the towing body is comparatively heavy; and/or it is large enough to cause the spike-type mechanism of separation from the point of the towed body.

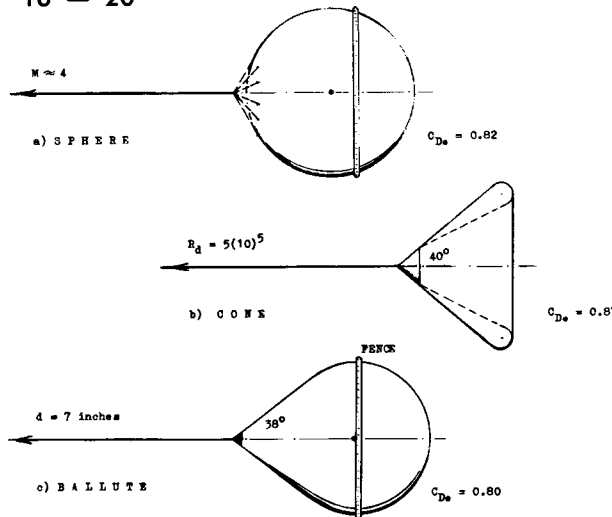


Figure 36. Drag coefficients of several shapes of inflated deceleration devices (50) when towed behind a "payload".

Inflated Shapes. When inflating a rubber-coated balloon-type device, it has the tendency of bulging into a shape similar to that of a sphere. When towing such a device, its forebody tends to assume a more or less conical shape. The result is a so-called ballute. Figure 36 presents drag coefficients of this and of two other shapes. It should be noticed that the drag coefficient of a spherical balloon when towed ($C_{D_0} = 0.82$) is lower than that of the spherical nose in figure 26 ($C_{D_0} = 0.51 (1.81) = 0.92$). Disregarding a small influence of shape, the difference is evidently caused by the wake in which the towed body is placed. Also, using equation (19) a coefficient $C_{D_0} = 0.91$ is found for the 2 times 40° conical device. After adding a value for base drag (as in figure 20, on page 16-16) $C_{D_0} = 0.97$ is obtained, while the tested coefficient is 0.83 (in figure 36).

Spheres. Figure 37 presents the hypersonic pressure distribution around a hemispherical head. If plotted against the square of the radius (representing the frontal area of the sphere) a linear distribution is obtained; and the drag coefficient of the head is then simply

$$C_{D_0} = C_{p_0} \int \cos^2 \varphi d(\sin \varphi) = 0.5 C_{p_0} \quad (53)$$

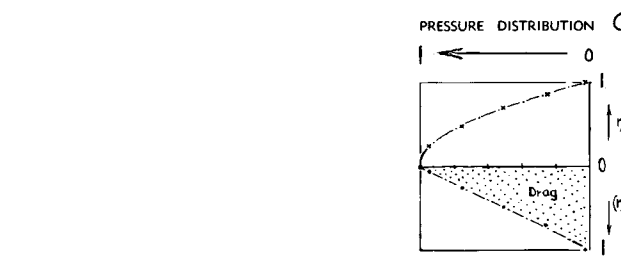


Figure 37. Flow pattern, pressure distribution and drag integration of a hemispherical head, tested (54,c) at $M = 5.7$. There are similar distributions in (15,a) (28,c) (54,h) (56,b) at M between 2 and 19.

Inasmuch as the base pressure coefficient at hypersonic M' -numbers is \approx zero, for most practical purposes, equation (53) also represents the drag of spheres at such speeds (see figure 20 of Chapter XVI).

Flat Disk. Several blunt-based bodies of the type as shown in figure 38, were tested at $\alpha = 180^\circ$, that is with the flat face first. In this case, the particular shape of these bodies such as length and cone angle, may not matter; and the base drag corresponding to the pressure within the "dead" space can be assumed to be independent of the particular shape. In fact, we may consider the flat-faced bodies to be circular disks. Their total drag coefficient is presented in the illustration, as a function of Mach number. Since base drag is included in the tested values, the total drag coefficient increases² as the M' -number is reduced. The face-pressure coefficient can be assumed to be the same as that in figure 22.

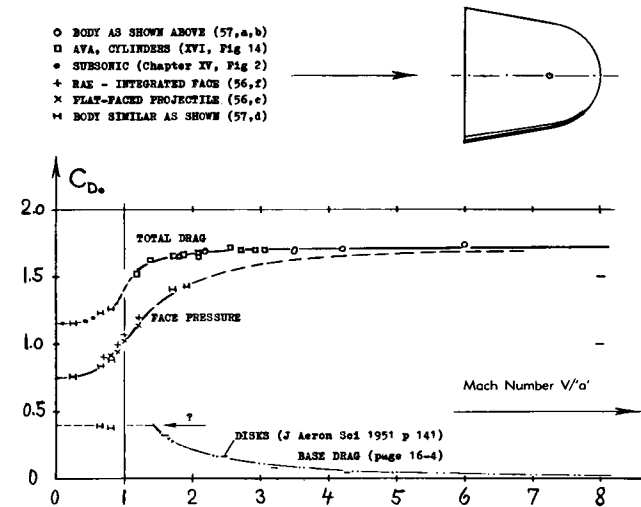
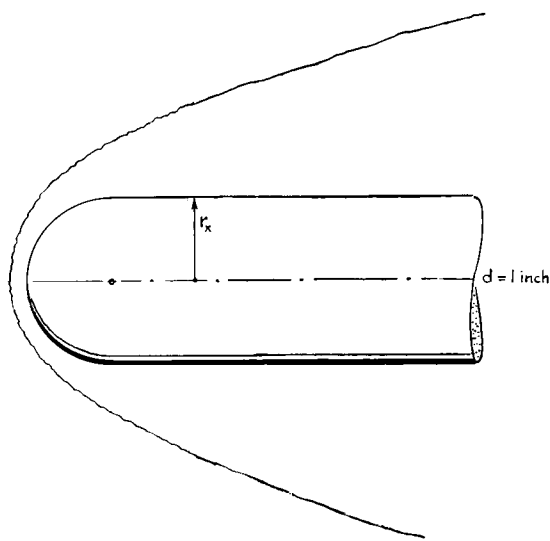


Figure 38. Total drag coefficients (57) of flat-faced short bodies ("disks") as a function of Mach number.



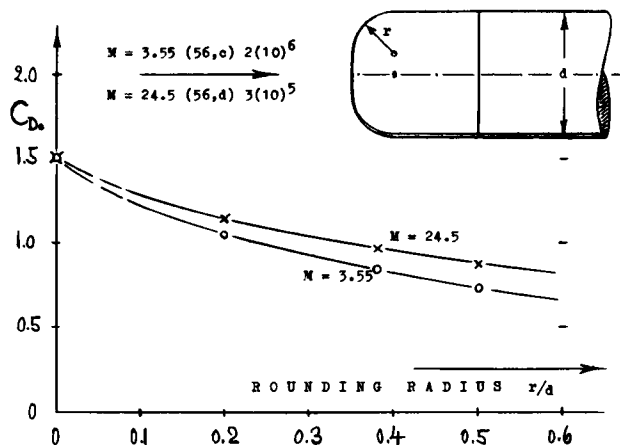


Figure 40. Drag coefficient of a short cylindrical body (56,c) as a function of the rounding radius.

A blunt Cylinder is shown in figure 40. Drag is maximum for a flat face; and it reduces considerably when rounding the rim. A radius $r = 0.5 d$, produces a hemispherical shape; and it reduces the drag coefficient, roughly to half the original value.

Face Pressure. Pressure and velocity distributions are presented in figure 41, for several more or less rounded shapes. For all but the flat face, the modified Newtonian theory gives a fair (or qualitative) description of the distribution. To repeat, pressure (either the differential $(p - p_a)$ or total pressure (the difference being small at hypersonic speeds) varies approximately as

$$\frac{p}{p_*} = \sin^2 \epsilon \quad (55)$$

where p_* = pressure at the stagnation point, and ϵ = surface angle, equal to 90° in a flat face. At the stagnation point, the local velocity "u" is zero. It increases from there approximately according to

$$u = \sqrt{(2/\rho)(p_* - p)} = \sqrt{(2/\rho)p_*(1 - \sin^2 \epsilon)}$$

- (50) Inflatable balloon-type drag devices, at supersonic speeds:
 - a) Alexander, Goodyear, Wright Patt ASD-TDR-1962-702.
 - b) McShera, Drag and Stability, NASA TN D-1601 (1963).
 - c) Kaiser, Ballute at $M = 10$, Arnold AEDC TDR-1962-39.
 - d) Charcenko, Solid Cones, NASA TN D-994 (1961).
 - e) McShera, Influence of Payload Wake, NASA TN D-919.
 - f) The wake characteristics behind ogive-cylinder bodies, to affect the effectiveness of parachutes or other deceleration devices, are reported from subsonic to hypersonic speeds, by Heinrich, Wright Patterson AFSC Rpts ASD-TDR-62-1103 and 1104 (DDC AD-427,736 and 748; 1963).
 - h) Chauvin, Pressure Distribution, NACA RM L52K06.
 - i) Rose, "Hot" at $M \approx 9$, J.Aeron Sci 1958 p 758.
- (54) Hypersonic characteristics of $1/2$ spherical shapes:
 - a) Stalder, Hemisphere with Spike, NACA T.Note 3287.
 - b) NACA, Hemispherical Heads, RM A52B13 & L52K06.
 - c) GALCIT, At Hypersonic Speeds, in J.Aeron.Sci.1956 p.177 and 1054; also in GALCIT Memo 40 (1957).
 - d) Crawford, Hemisphere, NACA T.Note 3706, 1956.
 - g) Stine, Heat on Round Nose, NACA T.Note 3344(1954).
- (55) Spheres tested at hypersonic Mach numbers:
 - a) Clark-Harris, Ballistic Tests, J.A.Sci. 1952 p.385.
 - b) Hodges, Firings, Journal Aeron.Sci. 1957 p.755.
 - c) When plotting these results in figure 24, a small correction was applied for rear-side pressure.
- (56) Drag and/or pressure distribution of blunt bodies:
 - a) Canning, Flat-Faced Ballistic Tests, NACA A57C25.
 - b) Cooper, Face Pressure, NASA Memo 1-3-59L.
 - c) McDearmon, Family of Shapes, NASA TM X-467.
 - d) Witcofski, Same at $M = 24.5$, NASA TN D-2282.
 - e) Spooner, Flat-Faced Shells, NACA RM SL56D27.
 - f) Stanbrook, Blunt Cylinder Transonic, RAE Aero-2876.
 - g) Julius, Blunt Body Shapes, NASA TN D-157 (1959).

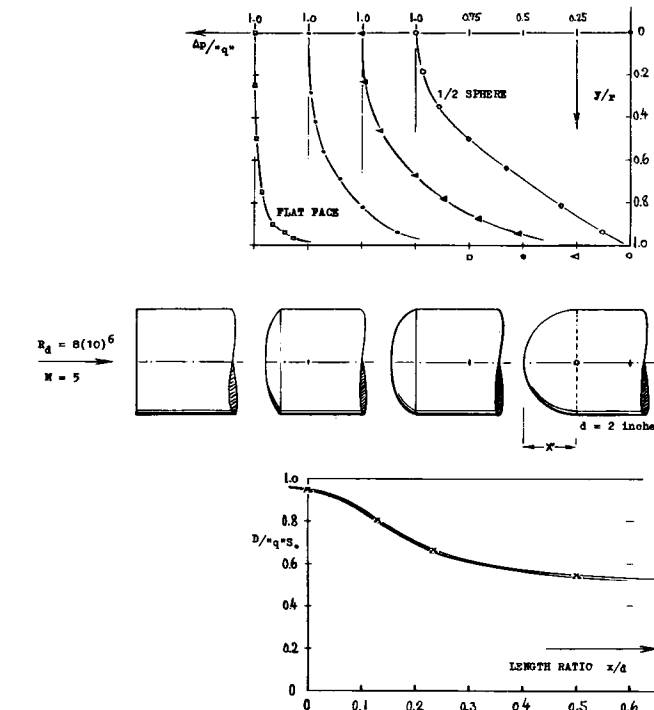


Figure 41. Pressure distribution over the faces of several blunt nose shapes (56,b).

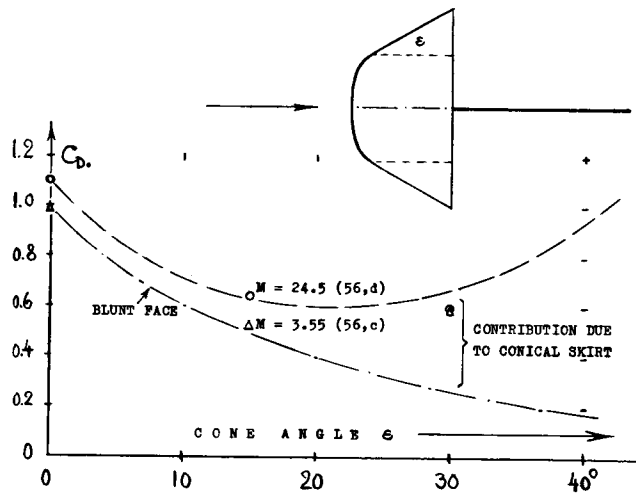


Figure 42. The influence of conical skirts (56,c,d) on the forebody drag of a short and blunt shape.

Conical Skirt. If using a short cylinder such as one of the bodies in figure 40, as a re-entry space vehicle, stability can be increased by adding a conical skirt. Figure 42 shows that the drag coefficient (on increased base area) reduces at first as the skirt angle is increased. However, when referring the drag to the original cylinder area, considerably increased coefficients are obtained. — Drag of the conical portions has been approximated by $C_{Dc} = 2 \sin^2 \epsilon$. Referring this contribution to the combined base area, a theoretical function is obtained in figure 42. The experimental points remain somewhat below this function; and it can be suspected that the boundary layer is responsible for the result. — The skirted bodies in the illustration can also be considered to be blunted cones. The data in figures 6 and 46 are then confirmed, showing an optimum bluntness (where the drag for a given fineness ratio is a minimum).

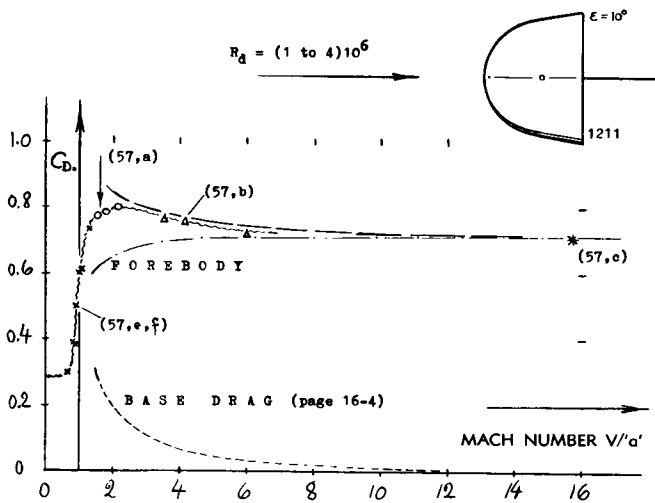


Figure 43. Total drag coefficients of short bodies (57) as a function of the Mach number.

As a Function of Mach Number, figure 43 presents the drag coefficient of a particular round-nosed, but short cone, selected from the large family of shapes reported in (57). Between $M = 4$ and 16 (where a single point is plotted, evaluated from firing tests on a very similar shape) interpolation is obtained:

- by assuming that the wave drag would be proportional to the pressure as in equation (41).
- taking maximum experimental base drag as indicated in figure 2 on page 16-4.

It is then found that the total coefficient is nearly constant between $M = 8$ and 16 (and beyond this Mach number). The increase of the coefficient when reducing M from 6 to 2, is evidently due to base drag.

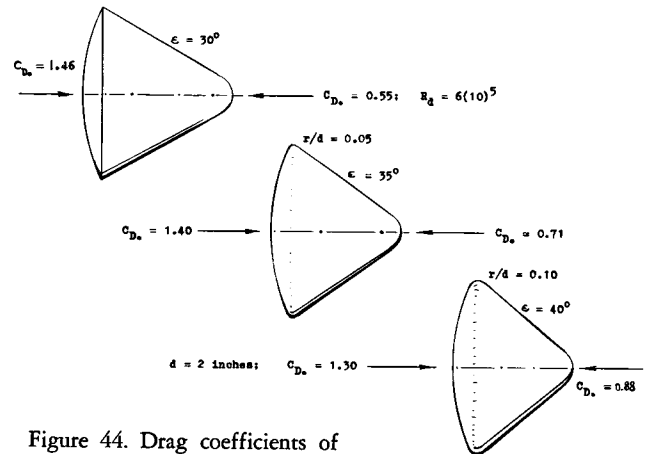


Figure 44. Drag coefficients of various satellite capsules tested (60,d) in helium, at $M = 24.5$, for $\alpha = 0$, and 180° . The drag in cone-first direction can be explained by $C_D = 2.1 \sin^2 \epsilon$.

Satellite Capsule. When developing their manned, re-entering and recoverable satellite vehicles, the Russians as well (in the "Sputniks") as the United States (in the Mercury Program) arrived at a shape of the type as in figure 44. Basically, such capsules are cones. During launching they move point-first, forming the nose of the rocket vehicle. When re-entering, the conical body is steered so that the blunt base meets the atmosphere. Maximum drag is thus provided with a minimum of heat transfer. Of course, a protective and/or ablating shield prevents most of the heat still remaining, from penetrating into the space craft. Another reason for the "conical" shape of satellite capsules, are their aerodynamic stability characteristics. In comparison to a cylindrical body, say of the same length/diameter ratio, the capsules as in figure 44, develop only a fraction of the normal force when at an angle of attack. As a consequence, and since the axial force (drag) is large (when flying blunt-base-first) the lift-curve slope of a "conical" capsule is negative. Longitudinal stability may also be increased by giving the base of the cone a somewhat curved shape.

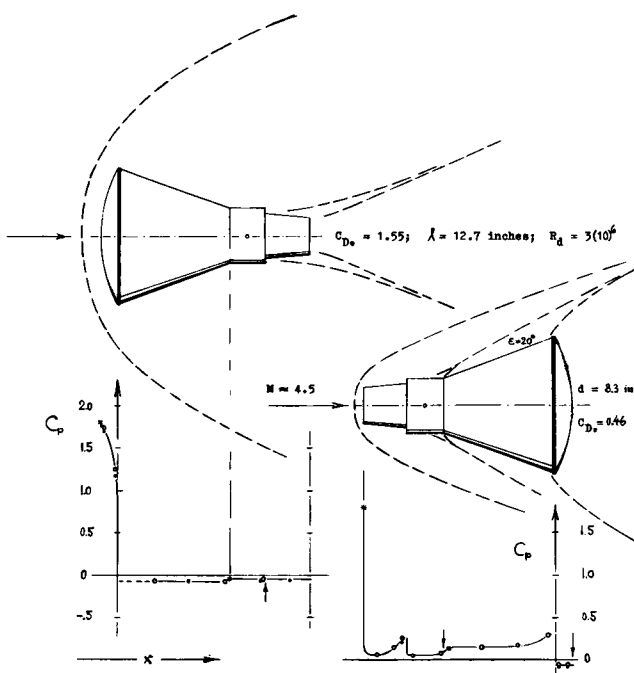


Figure 45. Pressure distribution and drag coefficient of the 1/9 scale model (60,b,c) of the Mercury satellite capsule, both in base-first and in "cone"-first flight direction.

- (57) Family of short bodies at $\alpha = 0$ to 180° :
 - a) Shaw, At $M = 1.6$ to 2.1 , NASA TN D-1781 (1963).
 - b) Keyes, At $M = 3.5$ to 6.0 , NASA TN D-2201 (1964).
 - c) Compton, At $M = 15$, NASA TM X-507 (1961).
 - d) Peterson, Retrorocket Body, NASA TN D-1300 (1962).
 - e) Wehrrend, Stability Transonic, NASA TN D-1202.
 - f) Brooks, Transonic Results, NASA TN D-1926 (1963).
- (60) Characteristics of satellite capsules:
 - a) Ried, Basic Body, NASA TN D-1085 (1963).
 - b) Shaw, Reentry Capsule, NASA TM X-233 (1959).
 - c) Newlander, Mercury Capsule, NASA TM X-336 (1960).
 - d) Johnston, Spacecraft, NASA TN D-1379 (1962).
- (61) Grimwood, Mercury Satellite Program, NASA SP-4001.
- (70) General information on extreme temperatures:
 - b) Dorrance, Aerothermodynamics, A.Eng.Rev. Jan. 1957.
 - c) Donaldson, Proc.U.S.Congr. Appl.Mech.1951 p.757.
 - d) Kurzweg, Hyperballistics, A.Eng.Rev. Dec. 1956.
 - e) Bond, Aerophysics, Aero Digest June 1956 p.21.
 - f) A review on high-temperature phenomena in shock tubes, including a large bibliography is given by Hertzberg in Appl.Mechanics Rev. December 1956.
 - k) Various aspects of aerodynamic heating in aircraft are presented in the July 1955 issue of Trans.ASME.
- (71) Facts and consequences of dissociation:
 - a) Romig, Normal Shocks, J.Aeron.Sci.1956 p.185.
 - b) Kuo, "Viscous" Dissociation, J.A.Sci.1957 p.345.
 - c) Moore, BL in Dissociation, J.A.Sci.1952 p.505.
 - d) Wood, Dissociation, NACA T.Note 3634 (1956).
 - e) Dommett, Air Properties, RAE T.Note GW 429 (1956).
 - f) Lighthill, Thermodynamics, J.Fluid Mech.1957 p.1.
- (72) Examples of high temperatures:
 - in chemistry, below 10^3 °K
 - in plasma jet above 10^4 °K
 - surface of average "star" 10^4 °K
 - meteors in the order of 10^4 °K
 - thermonuclear reactions 10^8 °K
- (74) Influence of temperature on skin friction:
 - a) VonKármán, Heat and Friction, Trans ASME 1939, 705.
 - b) Wilson, Real Laminar Friction, J.Aeron.Sci.1962 p.640.
 - d) Rumsey, On 10° Cone, NASA TN D-745 (1961).
 - e) Centola, Conical Bodies, NASA TN D-1975 (1963).

Pressure Distribution. Typical drag coefficients are listed in figure 44, for $\alpha = 0$ (flying blunt-base-first) and for $\alpha = 180^\circ$ (as during launching). The pressure distributions shown in figure 45, help to understand the origin of drag or axial forces as well as their magnitude. In the base-first attitude, almost all of the drag is due to the pressure at the blunt face. Whatever negative pressure there is along the afterbody, reduces in comparison to the face pressure as the Mach number is increased. — In the reversed direction, at $\alpha = 180^\circ$, there is some positive pressure along the conical portion of the capsule. Using equation (19) this pressure can be predicted or explained. There is some negative base pressure to be expected. As presented on page 16-4, the corresponding drag coefficient is bound to be small at hypersonic Mach numbers.

Short Nose Shape. A series of bodies with a length/diameter ratio of 1, was tested (56,c) at $M = 3.55$, and in (56,d) at $M = 24.5$ in helium. Their shape is given by the function $x \sim r^n$, where $r = \text{radius}$. For $n = 1$, a cone is obtained, and for $n = 2$ a parabolic contour. For higher values of n (up to 10) the exponential shape results in a flat portion around the center of the bodies thus making them blunted. Balance-tested forebody-drag coefficients are plotted in figure 46 as a function of the shape exponent " n ". It is not always desirable to have a high drag coefficient, such as in a re-entering vehicle to be recovered before hitting the ground. For example, in ballistic missiles, lesser drag coefficients might be preferable. The plot, as in figure 46, permits to determine a nose shape possibly having the least drag, for a given fineness ratio. For $l/d = 1$, that shape corresponds to an exponent in the vicinity of 1.5, both at $M = 3.55$ and at 24.5. For $l/d = 0.5$, the exponent giving minimum drag, is in the order of 2.5.

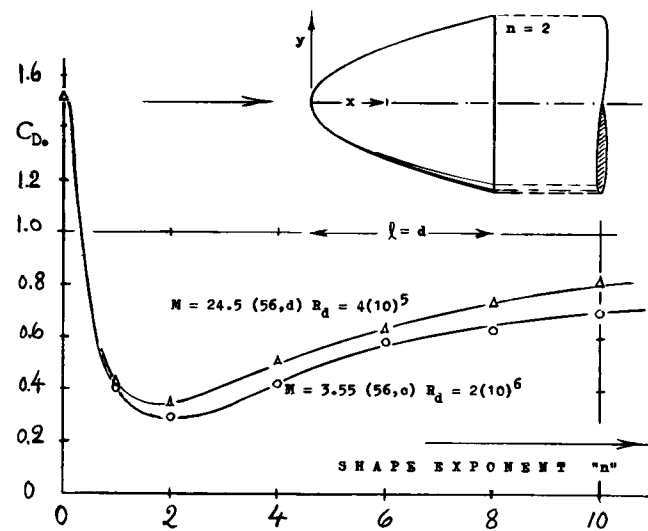


Figure 46. Forebody drag coefficients of a family of "exponential" nose shapes as a function of " n ". It should be noted that the optimum exponent $n = 2$, indicates a $1/2$ power body in the definition as in figure 6.

(F) TEMPERATURE AND HEAT TRANSFER

High Temperatures. It is pointed out in Chapter XVII that the temperature in the stagnation point and in the boundary layer increases significantly as a function of Mach number (see equation 6 in that Chapter). We have plotted in figure 48 the temperatures thus to be expected to prevail within the boundary layer developing along the surface of an *insulated* (non-heat-conducting) solid body. To indicate the severeness of the practical engineering consequences of such heating, facts should be noted as follows:

Limit of human comfort	40 °C	(0.9)
Water boils at sea level	100 °C	(1.4)
Plastics melting at some	150 °C	(1.7)
Light alloys lose strength	200 °C	(1.9)
Titanium loses strength	550 °C	(3.2)
Aluminum melts at some	660 °C	(3.5)
Iron melting at some	1540 °C	(5.3)
Ceramics may be melting at	3000 °C	(7.0)

The values added in parentheses, indicate approximate Mach numbers (based on $T_{amb} = 273^{\circ}\text{K} \equiv 0^{\circ}\text{C}$) where the temperatures as listed, are possibly obtained in steady-state flight (without heat transfer of any type). It is then realized that *continuous* flight of manned aircraft within the denser layers of the atmosphere, can already become critical at $M = 1$.

Radiation. At M between 3 and 4, the theoretical stagnation temperatures may be such that artillery shell and/or missiles carrying a warhead, might explode. The fact that these devices can be pushed to Mach numbers in the order of 5 through tropospheric densities, without heat damage, can partly be explained on the basis of cooling, through heat transfer onto the vehicle's mass of metal. However, the heat balance on the surface of a flying solid is also a function of radiation, away from the hot body. For example, at $z = 40$ km, heat transfer onto a vehicle flying at $M = 4$, is reduced to the order of 1% of that at sea level; see (75,c). Radiation is also of importance near the ground, where the theoretically possible high temperatures (as in figure 48) do not actually come true.

Heat in Hypersonic Tests. High temperatures and corresponding heat damage on wind-tunnel models tested at hypersonic speeds, are avoided by operation at very low temperatures (as for example at -200°C) obtained by expansion of the working gas to very low static pressures (for example at the level of 0.01 atm). Reference (76) proves, however, that metal can be melted in a wind tunnel when using higher pressures and higher ambient temperatures.

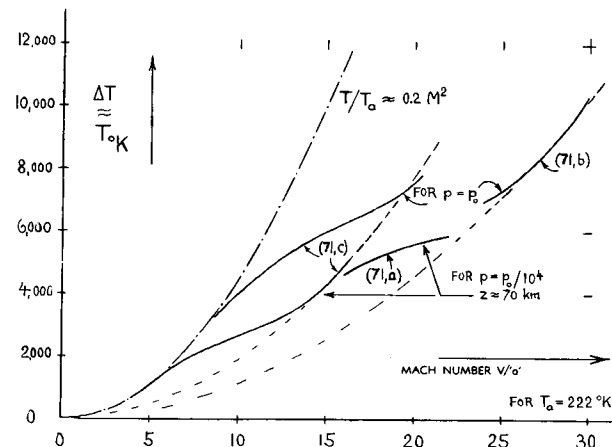


Figure 48. Temperature at a stagnation point and within the boundary layer, indicated by the values $T = \Delta T$, calculated for $T_{amb} = 400^{\circ}\text{R}$. Estimates for the two altitudes are shown, accounting for the heat consumed by dissociation of air molecules as a consequence of high temperature.

Heat Transfer (75). Considering a rocket vehicle flying through the *higher* layers of the atmosphere, possibly at a Mach number of 10, very high temperatures (corresponding to $T/T_{amb} \approx 0.2 \text{ M}^2 = 20$) might be expected to arise in the fluid flow surrounding the object. There are sound reasons, however, why such temperatures are not necessarily found in the solid skin of such a vehicle. Disregarding dissociation (which may reduce the stagnation temperature to 1/2 or even to 1/4) the volume of heat (in distinction to temperature) originating in a stream of rarefied gas, can be very small (74). Whatever amount of heat is produced (75,c) may be readily absorbed by the obstacle's or vehicle's mass of metal. From there it may then be discharged through *radiation* into space. The temperature on and within the skin of a vehicle, moving through the upper layers of the atmosphere, is thus the result of two "equally" strong or "equally" weak types of heat transfer. When proceeding into higher and higher altitudes, *radiation* is soon bound to predominate. This result is also illustrated by the fact (75,a) that the temperature of a body, at rest in *highly rarefied gas*, is expected to be considerably *below* the "kinetic" temperature of the surrounding medium. Finally, when traveling through the "exosphere", the temperature in a solid body is completely determined by radiation, from the sun onto the body and from the body into space. Understanding of these physical reactions, it seems, requires "unlearning" of certain effects to which we are accustomed in our daily sea-level type of atmosphere.

Molecular Changes. The large and sudden increase of pressure and temperature in some volume of gas when going through a strong shock, affects the equilibrium between the various forms of energy stored in the molecules. Molecular "vibration" (between the atoms making up a molecule) begins at temperatures in the order of 600 °K. Dissociation (breakdown of a molecule into atoms or into smaller groups of atoms) of oxygen begins roughly at temperatures of the order of 2000 °K, and that of nitrogen at some 4000 °K. Electronic excitation of the atoms (luminescence) is finally encountered at temperatures above 5000 °K.

Dissociation. At certain temperatures (the levels of which are a function of static pressure) the molecules of oxygen, and later those of nitrogen, making up the mixture that we call "air" — begin to break up. This process of changing from the molecular form of (O_2) or (N_2) into the atomic forms of O and N, is called dissociation. Thermodynamic properties of dissociated air are somehow different from those of ordinary air. The consequences of dissociation (and of certain other physical, chemical and electronic changes) have, therefore, been studied; see references under (71). Figure 48 presents, as one of the results of those studies, the temperature in the stagnation point, in the boundary layer, and possibly in the skin of a solid body exposed to this type of hypersonic flow. Dissociation consumes heat; the stagnation temperature is reduced, accordingly. It is suggested in the graph that after completion of dissociation (first of the oxygen molecules involved) the temperature may continue to rise along a line which is less than half the original function, as for a "perfect" gas. A second "transition" then takes place, on account of nitrogen dissociation; and it is suggested that another, still lower function of $T(M)$ is finally obtained.

The Stagnation Pressure in air is given by equation (4) in the "transonic" chapter. Since the gas behind a shock wave at Mach numbers, say above 10, is no longer ordinary atmospheric air, certain properties are different (70,c). In particular, the ratio of the specific heats is no longer $k = 1.4$, but lower than that. As a consequence, the maximum possible stagnation pressure (at M approaching infinity) is as follows:

$k = 1.66$	such as in helium	" q_x " = 1.76
$k = 1.40$	in atmospheric air	" q_x " = 1.84
$k = 1.20$	possibly at $M = 20$	" q_x " = 1.90
$k = 1.00$	limiting condition	" q_x " = 2.00

Pressure drag coefficients of blunt bodies must be expected to vary accordingly. Reference (71,c) also concludes that after dissociation, the viscosity " μ " is increased almost to 1.5 times the original value (at the same temperature).

Hypersonic Vehicle. When launching one of the Mercury satellites (80) by means of an Atlas rocket (as in figure 24, Chapter XVII) acceleration reaches a maximum of 6 or 7 "g". The maximum dynamic pressure encountered is almost 1000 lb/ft². The maximum speed obtained is in the order of 26,000 ft/sec or 7.8 km/sec, at a cut-off altitude around 500,000 ft, or 160 km. The Mach number in this condition is in the order of 10. The time required for the exit maneuver is about 5 minutes. The maximum temperature on the shingles protecting the conical portion of the capsule was found to be between 400 and 700 °C.

Stanton Number. Heat transfer into a flying body is a function of material and insulation. What we are considering here, is transfer through the boundary layer. Along the surface of slender bodies, heat corresponds to skin friction. The transfer of this heat (Q) through the boundary layer, is proportional to the differential $(\Delta T) = (T_r - T_w)$ where T_r = recovery temperature ≈ 0.9 (stagnation temperature). Transfer is also proportional to surface S (ft²) and time "t" (sec). The result is " h " = $Q / (\Delta T S t)$. This parameter can be made non-dimensional by converting it into the so-called Stanton number:

$$"S" = "h" / (g \rho V c_p) \quad (60)$$

where c_p = specific heat of the air. In turbulent boundary layer this number is approximately

$$"S" = 0.6 C_f \quad (61)$$

where C_f as in figure 3 (Chapter XVII). Transfer through a laminar boundary layer is less than that through a turbulent layer. Very roughly, at R_x between 10^6 and 10^7 , the Stanton number is:

$$"S" = 0.0003 \text{ for laminar condition}$$

$$"S" = 0.0015 \text{ in turbulent B'layer}$$

- (75) Information on heat transfer, theoretical and experimental:
 - a) Stalder, Heat Transfer, NACA T.Rpt 944 (1949).
 - b) Schaf, Chapter IX of "Heat Transfer", Univ.Mich. Press 1953; also experimental in Chapter X.
 - c) Adams, Radiation, Trans ASME 1955 p 735.
 - d) van Driest, Aerodynamic Heating, J.Aero Sci 1956 p 26.
 - e) Centolanzi, Short Bodies, NASA TN D-1975 (1963).
 - f) Conti, Cone to $\alpha = 90^\circ$, NASA TN D-962 (1961).
 - g) Burbank, Flat-Face Cylinder, NASA TM X-19 (1959).
 - h) See also references (42,e) and (56,b).
- (76) McLellan, Aerodynamic Melting, Trans ASME 1955 p.727.
- (77) A gas very suitable for experimentation at high Mach numbers, and not too high Reynolds numbers, is *helium*. See "Analysis of Helium Flow", NACA T.Note 4063 (1957).
- (78) Meteors consisting of iron (rather than "rock") also *burn*.
- (80) NASA, United States Manned Orbital Flights, Special Report 1962; also Rpt SP-6 (1962) and SP-45 (1963).
- (82) General information on meteorites:
 - a) Whipple, Data, Rev Mod Phys 1943 p 256; also "Theory" in Proc Nat Acad Sci Washington 1950 p 687 and 1951 p 19; also "Rockets and Meteors" in Am Meteorolog Soc Bull 1952 p 13; "Meteors", Univ N.M. Press 1952.
 - b) Grimming, Data, J Appl Phys 1948 p 947.
 - c) Hansen, Review (Erosion), NASA TN 3962 (1957).
 - d) Singer, Particles, Jet Prop 1956 p 1071.
- (83) Cosmic Dust, see NASA D-488 and D-1174.

Blunt Bodies. In and around the stagnation point, heat is the consequence of compression (and not of friction). Heat transfer data can be expressed in form of the Stanton number, using speed and air properties as in the undisturbed ambient flow. The resulting numbers for blunt bodies are a function of Mach and Reynolds number. To give an indication of the order of magnitude of heat transfer, rough values are listed in figure 49 for conditions as noted.

- Slender bodies such as cones have roughly the same coefficients as stated above for skin friction.
- At the stagnation point of hemispherical noses, heat transfer is higher than that due to friction.
- In the center of a flat face, transfer is about half of that as in the stagnation point of a sphere.
- In separated spaces (such as behind a cylinder in cross flow) transfer is low by comparison.

Re-Entry of the Mercury satellite "into" the atmosphere takes place with the blunt end first. Deceleration is provided by the face drag corresponding to $C_{D_0} \approx 1.5$ (as in the "blunt-body" section of this chapter). Maximum dynamic pressure is reported (80) to have been 470 lb/ft². On the basis of a frontal area $S_* = 30 \text{ ft}^2$ and a re-entering weight of 2500 lb, a maximum deceleration above 7 "g" is obtained. The time between the firing of the retro-rockets and the deployment of the recovery parachute was about 6 minutes. During this period, the air temperature across the frontal shock wave assumes values between 4000 and 5000° C. However, the temperature within the ablating heat shield protecting the blunt end, was found to be only 1600° C, while that on the conical afterbody is reported to have been about 500° C. For comparison, afterbody temperatures during orbital flight were roughly between 0 and 100° C (in daylight).

Meteorites (82). Typical specimens are believed to travel through space at a speed in the order of 20 km/sec, while the earth is moving along at some 30 km/sec, around the sun. Depending upon the direction of the meteorites, they therefore enter into the atmosphere of the earth with initial relative speeds possibly between 20 and 60 km/sec. Because of the mechanism of heat transfer (explained above) the temperature actually produced within the solid mass of a meteor, is at first very small. This is evidenced by the fact that meteors do *not* light up before reaching altitudes of some 100 km. However, encountering denser layers of the atmosphere, meteorites experience decelerations up to the order of 1 km/sec², corresponding to some 100 "g" units. The heat energy absorbed during this period melts and vaporizes the usually stony material. As a consequence, the original mass reduces to "nothing" upon reaching altitudes, say around 50 km. As a matter of interest, an estimated number of 100 million meteorites enter into our atmosphere per day, with only a very few of these reaching the ground of the earth in what is left of their "solid" state.

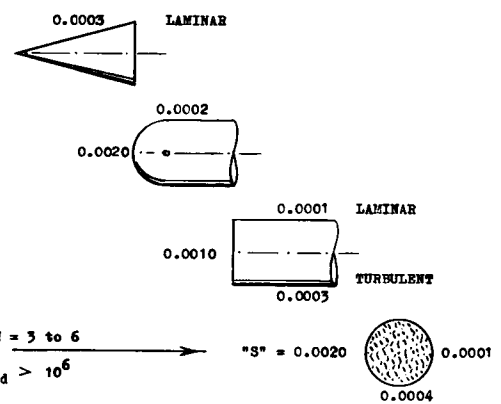


Figure 49. Stanton number values roughly indicating heat transfer (75) at Reynolds numbers above $R_d = 10^6$ and at Mach numbers between 3 and 6.

Drag of a Meteorite. We will consider, as an example, a "stony" meteor, with an assumed diameter of 1 mm, with a volume in the order of 1 mm^3 , and a mass of $3/10^3$ grams which is $3/10^6$ kg, or equal to $W/g \approx 3/10^7 \text{ kp-sec}^2/\text{m}$. We will assume that this meteorite moves at 30 km/sec through the atmosphere, at the time it begins to be visible. At an altitude of 80 km where this "experiment" may take place, the atmospheric density ρ can be assumed to be approximately 10^{-5} kg/m^3 (*Chapter XIX*) or in the order of $1/10^6 \text{ kp-sec}^2/\text{m}^3$. The dynamic pressure under the conditions assumed is then

$$q = 0.5 \rho V^2 = 0.5 (30)^2 10^6 / 10^6 \approx 450 \text{ (kp/m}^2\text{)}$$

On the basis of a drag coefficient $C_{D_0} = 2$ (as in *Chap XIX*) the aerodynamic drag of the meteor may then be estimated to be

$$D = C_{D_0} q S_* = 2 (450)/10^6 = 9/10^4 \text{ (kp)}$$

where $S_* = 1/10^6$ is the frontal area in m^2 . The deceleration corresponds to

$$dV/dt = -9 (10)^7 / 3 (10)^4 = -3000 \text{ (m/sec}^2\text{)} \approx -300 \text{ "g"}$$

where $3/10^7$ = mass as above. The Reynolds number of the meteor considered is tentatively

$$R_d = V d \rho / \mu = 30 (10)^3 10^7 / (10^6 3/10^7) = 100$$

where μ = absolute viscosity, estimated to be $3/10^7$ ($\text{kp-sec}/\text{m}^2$) as in *Chapter I*. The Mach number is in the order of

$$M = 30 (10)^3 / 300 = 100$$

The analysis above, demonstrates that the motion of a meteor can be correlated with its aerodynamic drag.

A "kp" is a kilopond, equal to the force of a kilogram. A "kg" is a kilogram (mass), which can be expressed in ($\text{kp-sec}^2/\text{m}$).

CHAPTER XIX — DRAG AT HIGH SPEEDS AS AFFECTED BY VISCOSITY AND RAREFACTION

The flight of rocket-propelled vehicles (missiles and satellites) leads into the upper layers of the earth's atmosphere. To shoot such devices into extreme altitudes (and possibly to keep them there), comparatively high speeds are required. Such combination of speed and rarefaction leads into conditions where theoretical laws and empirical functions of ordinary gas dynamics do no longer give correct information. The deviations from supersonic and inviscid hypersonic characteristics (as presented in the "supersonic" chapter) grow in particular with the degree of rarefaction. However, certain of the effects encountered at altitude, can basically (and at least theoretically) also be produced by the combination of high speeds with high viscosity. This then is the reason for treating the influence of "viscosity" and that of the atmospheric properties at higher altitudes together in this chapter. In more conventional terms, the chapter deals (a) with the influence of viscosity and heat at super-hypersonic Mach numbers, (b) with the aerophysical properties of, and the gas-dynamic characteristics in the upper layers of the earth's atmosphere. Research, both theoretical and experimental, has only broached so far on certain of the phenomena to be expected at extreme speeds and in particular in rarefied fluid flow. By combining available results on both of these effects, an effort is made to give a conspectus of the aerodynamic characteristics encountered (for example) by a missile or a satellite, when going from subsonic and supersonic speeds through various phases into the field of rarefied and free molecule flow.

(A) REALMS OF FLUID DYNAMICS

Aerodynamic characteristics of a satellite or any similar vehicle, when travelling at extreme altitudes, are radically different from those during the take-off period (when traversing atmospheric layers having densities of the same order as at sea level). The transition from one extreme to the other is continuous, however; and there are physical quantities by which the location between the two extremes can be defined and measured.

Mean-Free Path. To understand the mechanics of rarefied fluid flow, one has to consider motion and time history of the gas molecules involved. In air at sea-level pressure, the number of atoms per unit volume is extremely high, the mean-average velocity of their "oscillating" thermal motions is also high, but the (average or effective) length " λ " of the so-called mean-free path that each molecule travels, statistically, before colliding with another one is very short. To give an illustration, that dimension in sea-level air is of the order of $1/10^4$ mm (which is approximately the microscopic particle size of tobacco smoke). No distinction has to be made, accordingly, between the individual molecules; and the fluid is considered to be a continuum. The path length grows, however, as a function of absolute "kinetic" temperature, and it increases in proportion to $1/p$; thus roughly:

$$\lambda \sim T^{1/2} / p \quad (1)$$

-
- (1) The term "hypersonic", indicates flow conditions at higher supersonic Mach numbers. The type of flow is usually within the continuum phase of ordinary gas dynamics.
 - (2) Mechanics of rarefied fluid flow:
 - a) Zahm, "Superaerodynamics", J.Frankl.Inst.1934 p.153.
 - b) Tsien, "Superaerodynamics", J.Aeron.Sci.1946 p.652.
 - c) Ashley, Free Molecule Theory, J.Aeron.Sci.1949 p.95.
 - d) Patterson, Molecular Flow, Wiley 1956; see also General Survey in Aeron.Engg.Review 1955 (February).
 - e) Principles of *kinetic gas theory* and earlier work in this field are reviewed in (a) and (c).

Since T increases appreciably (at really high altitudes) while p reduces extremely rapidly as a function of altitude, the mean-free path increases at a progressive rate. For example, at an altitude of 100 km (where meteors can be observed, and where $p/p_0 \approx 10^{-6}$) the mean-free path measures approximately 100 mm. At 200 km of altitude (which may be the minimum altitude required for an earth satellite) the path length approaches 1 km.

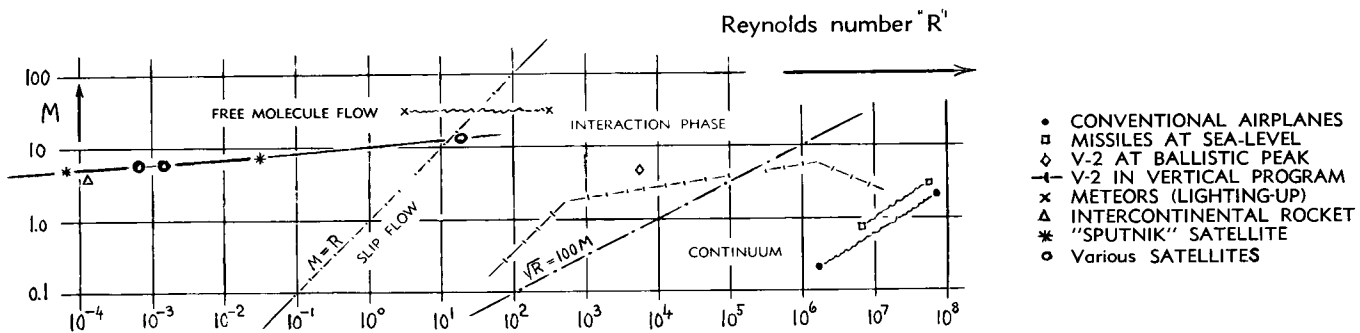


Figure 1. Realms of fluid dynamics, from continuum-type to free-molecule conditions of flow.

Knudsen Number. Assuming now some vehicle ascending through the atmosphere, the mean free path " λ " of the molecules will first grow to a magnitude equal to the dimension " ℓ " of the vehicle. It can then be assumed that the fluid stream is no longer continuous, and that the gas molecules will strike against the moving solid as "individuals". At still higher altitudes, there will be so few (33) molecules (atoms or ions) left in a certain volume of space, that they do no longer interfere with each other, when and after striking the solid body. This then is the phase of "free-molecule flow". The ratio (λ/ℓ) can now be used as a measure, indicating the degree of interference between molecules; and this ratio is called the Knudsen number (51). Since $\lambda \sim v/a$, that number can conveniently be expressed by the more familiar Mach and Reynolds numbers:

$$K = \lambda/\ell = 1.26 \sqrt{k} \cdot v / (a \cdot \ell) \approx 1.5 M/R_\ell \quad (2)$$

The realm of continuum-type fluid dynamics is thus found to be in the range of smaller M'numbers and larger R'numbers. Vice versa, the other extreme (of free molecule flow) is obtained at larger M'numbers and smaller R'numbers.

Rarefaction. Since the speed "V" is part of both the R'number and the M'number, the parameter as per equation 2, is basically independent of speed. Disregarding a smaller influence of temperature, that equation can also approximately be written as K'number $\sim 1/(p \cdot \ell)$. It is then realized that the Knudsen number is a function of the atmospheric pressure "p" and the size of " ℓ " of some vehicle traversing the atmosphere. Considering, however, a solid body of given size, (M/R) can primarily be considered as a measure indicating the degree of rarefaction. This parameter is properly to be used under conditions where the boundary layer is absent, or where the B'layer does not interfere with the flow pattern.

BL Thickness. With regard to skin friction and ordinary consequences of viscosity, within the denser layers of the atmosphere, the boundary layer thickness (rather than length or diameter of the solid body involved) must be considered to be the significant dimension to be used in equation 2. Since (in laminar B'layer flow) the thickness δ varies as $1/\sqrt{R_\ell}$, the parameter $(M/\sqrt{R_\ell})$ is thus obtained (in place of M/R_ℓ). Making similar substitutions as above, we then find that the square of this "number" is approximately

$$(M^2/R_\ell) \sim V / (\ell \rho) \quad (3)$$

Speed "V" is thus part of this parameter; and consequences of rarefaction must be expected to grow as a function of speed or Mach number. The "same" phenomena can also be obtained, however, by reducing " ℓ " and/or " ρ ", which then means reducing the Reynolds number. In view of the interactions taking place in supersonic flow (see later) it is suggested to call $(M/\sqrt{R_\ell})$ or (M^2/R_ℓ) the "viscous interaction parameter".

Phases of Fluid Dynamics. To indicate quantitatively, whether a certain combination of Mach and Reynolds number produces an ordinary continuum-type flow pattern, or Newtonian conditions of fluid flow, or any other phase in the wide field between those extremes — certain educated estimates have been made (2). Based on the Knudsen number (equation 2) or the rarefaction parameter (equation 3) free molecule flow is expected to prevail at $M/R > 10$ or > 1 . For the border line of continuum flow, on the other hand, a value of the "interaction" parameter as per equation 3 is assumed in the order of $M/\sqrt{R_\ell} = 0.01$ (or of $\sqrt{R_\ell}/M = 100$). Figure 1 presents the corresponding two limiting lines. The results of other, specific estimates have also been included in that graph showing, for example, that man-carrying airplanes (including the most advanced types) are completely in the region of continuum flow, that high-altitude rockets may range across the entire space between the two extremes, and that "applications," really within the phase of free-molecule flow, are meteors (see XVIII), man-made satellites (as we can say after October 1957) and intercontinental rockets.

"Interaction". As pointed out later (see figure 24) boundary layer characteristics in free-molecule flow, are completely different from those in continuum flow. Since this and possibly other effects of so-called slip flow were expected to be of primary significance for flow pattern and forces within the whole field of R' and M' numbers in between the extremes (see figure 1) this field was named the regime of *slip flow* (3). It appears, however, that phenomena attributable to "slip", are of importance primarily at subsonic Mach numbers and/or upon closely approaching the regime of free-molecule flow. At supersonic speeds and in the rest of the field between the extremes, other boundary-layer effects, such as thermal displacement and shock interaction, have a much more important influence upon flow pattern and resultant pressures and forces. It is, therefore, suggested to consider, and to name, at least an appropriate part of that field, that of "viscous interaction". Aerodynamic studies in this phase are thus concerned with increased boundary layer thickness (at lower R' -numbers) with higher temperatures (at higher Mach numbers) and as a consequence of both of these parameters, with severe boundary-layer shock-wave *interactions*. The term "interaction" might also be understood to indicate the mutual interference between gas molecules in this phase, in distinction to conditions in free-molecule flow. The term of "slip flow", on the other hand, seems to be appropriate to indicate the *transition* between the "interaction" and "free-molecule" phases, as marked in figure 1.

- (3) Comment on slip phenomenon: Some investigations have originally been carried out on slip as such; see references under (2). It was later realized, however, that "most present developments are not based on slip and temperature jump" (Schaaf, Review in Appl.Mech.Rev.1956 p.413). Indeed, viscous phenomena, in combination with Mach-number effects, appear to be the essence of real fluid flow at high speeds and in higher altitudes.
- (4) We may assume that *airplanes* of the "conventional" type would be able, within the foreseeable future, to travel at $M = 3$ (i.e. at a speed in the order of 2000 mph) at a service altitude, let us say of 80,000 ft. For a wing chord of possibly 15 ft, their Reynolds number will then be of the order of 10^7 , and the parameter $\sqrt{R_t}/M$ will roughly be in the vicinity of 10^3 . Figure 1 readily indicates that a craft under such conditions is still very well within the region of ordinary gas dynamics.
- (5) The various phases of gas-dynamics are demonstrated by Ivey in "Mechanical Analogy", J.Aeron.Sci.1950 p.519.
- (8) Impact pressure in compressible fluid flow:
 - a) See "Barker Effect" in Chapter III.
 - b) Homann, Forschung 1936 No. 1 & 3, NACA TM 1334.
 - c) Macmillan, Pitot Tube, J.R.Aeron.Soc.1954 p.570.
 - d) Kane, Interpretation, NACA T.Note 2210 (1950).
 - e) Sherman, Impact Probe, NACA T.Note 2995 (1953).

(B) VISCOUS EFFECTS AT HIGH SPEEDS

Bluff bodies are treated in Chapters XVI and XVIII without specific reference to viscosity. Pressure forces on such bodies behind a detached, normal-shock-type wave front, are usually so high that skin friction and/or boundary-layer effects are comparatively small and of negligible magnitude. Some experiments carried out on bluff bodies, at very small Reynolds numbers (and at higher Mach numbers) thus reaching into the "interaction" field as in figure 1, are presented as follows.

(1) BLUFF BODIES IN SUPERSONIC FLOW

Stagnation Pressure. The magnitude of the pressure experienced in the open end of a Pitot tube usually corresponds to $(P_{amb} + q)$ in uncompressed fluid flow and to $(P_{amb} + "q")$ in compressible and/or in supersonic streams of air or gas (see Chapter XVI for the definition of "q"). At smaller, or very small Reynolds numbers (see Chapter III) that pressure is larger, however, than corresponding to the stagnation pressure — because of viscous interference from the outside surface surrounding the opening of the Pitot probe. This so-called *Barker effect* can be approximated by

$$\Delta C_p = o/R_d \quad (5)$$

where $R_d = R'$ -number based on the diameter of the tube; and where $o \approx 6$ for open tubes. In supersonic flow, conditions are complicated, of course, by the presence of an essentially normal shock ahead of such an opening. Figure 2 shows, however, that the

ROUND SHAPES:	
\times	SOURCE SHAPE $M = .35$ (8,e)
Δ	DITTO AT $M = 2.5$ (8,e)
\circ	SPHERE AT $M = 0$ (8,b)
PITOT-TYPE TUBES	
$+$	AT M' NUMBER $= .35$ (8,e)
\bullet	AT M' NUMBER ZERO (8,b)
\square	BARKER AT $M = 0$ (8,a)

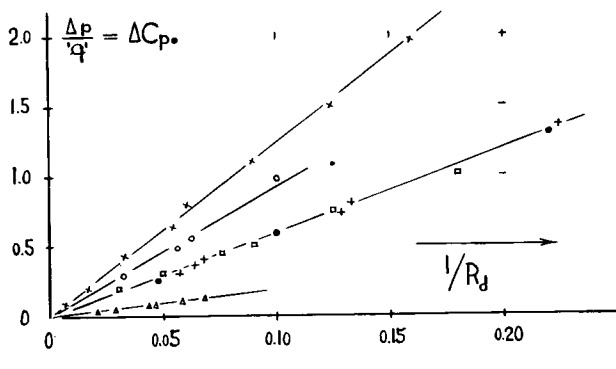


Figure 2. Variation of the pressure indicated in the opening of impact-pressure probes, as a function of $\frac{1}{R_d}$.

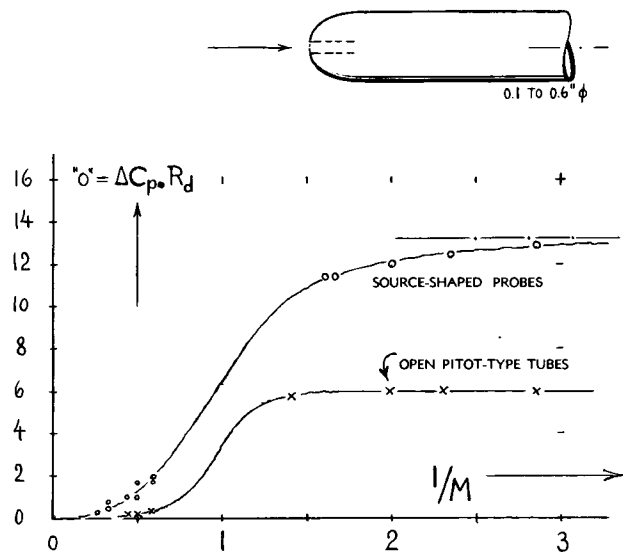


Figure 3. Correlation of the viscous increment of the pressure indicated by stagnation- or impact-pressure probes (8,e) against the Mach number parameter ($1/M$).

same type of pressure rise takes place at Mach numbers between 2 and 4 in the opening of a "source-shaped" pressure probe. For the M' number as stated, and for R_d between 50 and 100, we find that the R and M combination of the probes as tested, is about in the middle of the two boundary lines in figure 1. There is no method available, to this date, of correlating stagnation-pressure results within the "interaction" phase. Inasmuch as skin friction eventually reduces to zero within the free-molecule phase, we expect, however, that the magnitude of ΔC_{p*} decreases as M/R_d is increased. Assuming that equation 5 really holds for all Mach numbers, values of $o = (\Delta C_{p*} R_d)$ are then plotted in figure 3, as a function of $(1/M)$. The lines drawn through the very few experimental points, are heuristic, of course. They give a qualitative indication, however, of the manner in which the viscous-type pressure increment in the vicinity of a stagnation point may vary at high M' numbers and/or at low R' numbers, as a function of these numbers.

Spheres as a Function of R' number. The drag coefficient of spheres as a function of Mach number is presented in Chapters XV (figure 6) and XVI (figure 20). It is stated there that at Reynolds numbers above 10^4 , the magnitude of the coefficient does not noticeably vary with that number. Experimental results from various sources, obtained over a wide range of the Reynolds number, are plotted in figure 4. Conclusions are as follows:

- (a) Variations are not significant between $R_d = 10^3$ and 10^6 , although there is a slight and flat dip in the middle of this range.
- (b) A discontinuity seems to exist between 10^2 and 10^3 . Since this result is found in two different investigations, the step in the drag function may very well be genuine; and it may then have something to do with the wake generation past the sphere's base.

For comparison, an experimental function obtained at $M \rightarrow 0$, has also been plotted in the graph.

At Very Low R' Numbers. Most of the experimental points in figure 4 are in the field of continuum flow; some of them are in the "interaction" phase, however. Viscosity must be expected to have a twofold influence upon supersonic drag; first, simply through friction, and second because of boundary layer displacement. Within the "laminar" phase of the Reynolds number (at R_d between 10^2 and 10^4) both of these effects may approximately be proportional to $1/\sqrt{R_d}$. Thus plotting (12) the sphere drag coefficients (tested at Mach numbers between 2 and 3) as in figure 5, a general (if qualitative) picture is obtained of bluff body characteristics at low Reynolds numbers. Such bodies show first an incremental drag coefficient $\Delta C_{D*} \sim 1/\sqrt{R_d}$; and the total coefficient of the sphere may approximately be:

$$C_{D*} = 0.95 + (5/\sqrt{R_d}) \quad (12)$$

Stokes' solution (12,a) for uncompressed fluid flow (corresponding to $M = 0$) is also shown in figure 4.

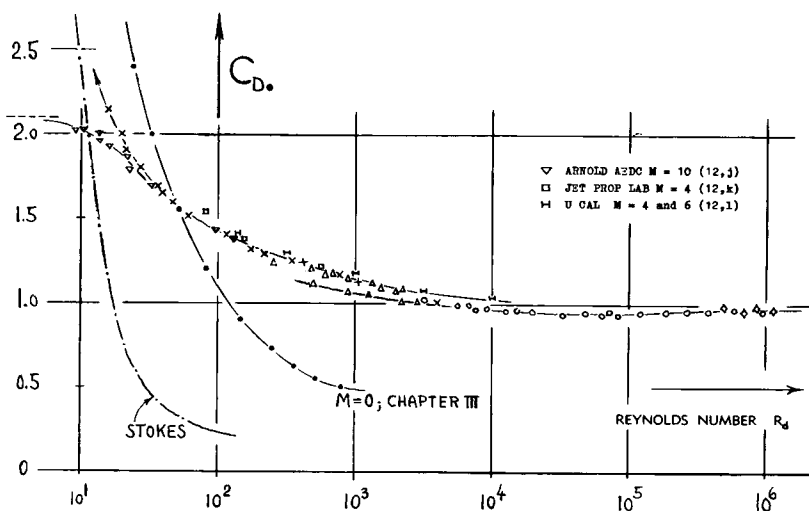


Figure 4. Supersonic drag coefficients of spheres, tested at Reynolds numbers between 10^1 and 10^6 .

The fact that the experimental function, found for M between 2 and 3, approaches Stokes' line, indicates that viscous forces take over more and more. Eventually, the drag coefficient can be expected to cross the viscous function, however, because of the slip phenomenon; and it may finally be expected to end up at the level corresponding to free-molecule flow.

Cylinder. The Knudsen number (as in equation 2) has been used to correlate experimental results on spheres and other bodies obtained between the continuum and the free-molecule phases of flow. Drag coefficients at different Mach numbers do not collapse, however, when using the Knudsen number. We have, therefore, plotted in figure 6, results on circular cylinders in the same manner as those of spheres (in figure 5) as a function of the Reynolds number parameter $1/\sqrt{R_d}$. At $M = 4$, the cylinder's drag coefficient seems to vary as

$$C_{D_0} = 1.2 + 3/\sqrt{R_d} \quad (13)$$

At a Reynolds number in the order of unity, the coefficient assumes the value as in free-molecule flow.

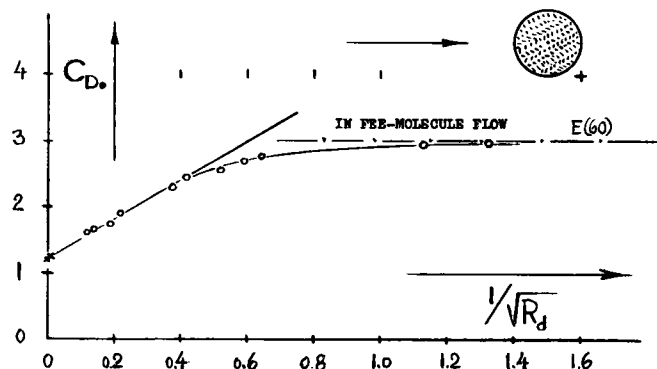


Figure 6. Drag coefficient (60,f) of a circular cylinder (in cross flow) at $M = 4$, as a function of the Reynolds number.

- (11) Spheres at higher Reynolds numbers:
 - a) Hedges, High-Speed Firings, J.A.Sci.1957 p.755.
 - b) Clark-Harris, Ballistic Tests, J.A.Sci.1952 p.385.
- (12) Drag of spheres as a function of R' -number:
 - a) Stokes, Viscous Theory, see Chapter III.
 - c) Characteristics in free molecule flow, see (58).
 - d) Charters and Thomas, J.Aeron.Science 1945 p.468.
 - e) Kane (Berkeley), Experiments, J.Aeron.Sci.1951 p.259; also continuation in J.Aeron.Sci.1951 p.566.
 - g) May-Witt, Free Flight, J.Aeron.Sci.1953 p.635.
 - i) May, in Free Flight, NAVORD Rpt 4392 (1956); see also Journal Applied Physics 1957 p.910.
 - j) Kinslow and Potter, At $M = 10.6$, Arnold Center AEDC TD Rpt 1962-205; see also AIAA J. 1963 p.2467.
 - k) Wegener, At $M = 4$, Jet Prop Lab Rpt 34-160 (1960).
 - l) Aeroesty, Density, U.Cal Berkeley HE-150-192 (1962).
- (14) Base pressure results in rarefied fluid flow:
 - a) Kavanau, Rarefied Supersonic, J.A.Sci.1956 p.193.
 - b) Lehnert, On Spheres, NAVORD Rpt 2774 (1953).
 - c) The correlation in figure 7 against $M/\sqrt{R_d}$ is empirical.
 - d) Ferri, On Bluff Bodies, USAF WADC T.Note 1956-294.
 - e) Linnell, Cone Analysis, J.Aeron.Sci.1957 p.390.
 - f) Penland, Hypersonic Cylinders, NACA RM L54A14.

- WITH LATERAL SUPPORT (12,e)
- IN TUNNEL, ON STING (12,e)
- △ NAVORD FREE FIRINGS (12,i)

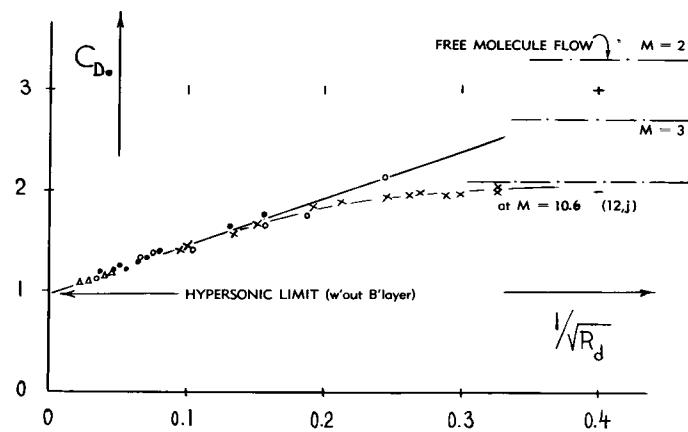


Figure 5. Drag coefficient of spheres, tested at Mach numbers between 2 and 3, as a function of Reynolds number.

Base Pressure. Part of the total drag of spheres (as shown in figure 4) corresponds to a pressure deficiency at their rear side. The corresponding base drag component is investigated in (14,b) at M' -numbers between 1.6 and 5.0, and at R' -numbers (on sphere diameter) between 10^4 and 10^6 . Results are as follows:

- (a) The dip in the total drag coefficient (at $R_d \approx 10^5$ in figure 4) corresponds to a variation of the base drag coefficient,
- (b) The base pressure variation is of the same type as that of the ratio presented in figure 7 of Chapter XVI, between $R_d = 10^5$ and 10^6 .

Zero Base Drag. Figures 6 and 12 in Chapter XVI suggest that the base-drag coefficient behind projectiles and similar body shapes approaches the maximum possible ratio, as M increases to hypersonic values. Since the maximum pressure differential (corresponding to vacuum) approaches zero at the same time, base drag seems to approach zero as $M \rightarrow \infty$. However, tunnel tests on a circular cylinder (in cross flow) as reported in (14,f) display positive values at the rear (base) side, corresponding to $C_{PB} = 0.02$ (or to more) at $M = 6.9$. It is also concluded in (14,d) that the pressure on the afterbody of a bluff double wedge can be positive because of "shoulder pressure" produced by the rise of entropy across the shock front. Analysis of the flow past a cone (14,e) finally produces quantitative results in similarity form. It can thus be concluded that the base pressure differential behind a cone-cylinder configuration turns *positive* upon exceeding the value ' $H' = M \sin \epsilon = 3$ or 4. Extrapolation to $1/H' = 0$, leads to a *negative* base-drag coefficient (on dynamic pressure) between 0.04 and 0.05, at $M \rightarrow \infty$ for cone-cylinder-combinations in axial flow.

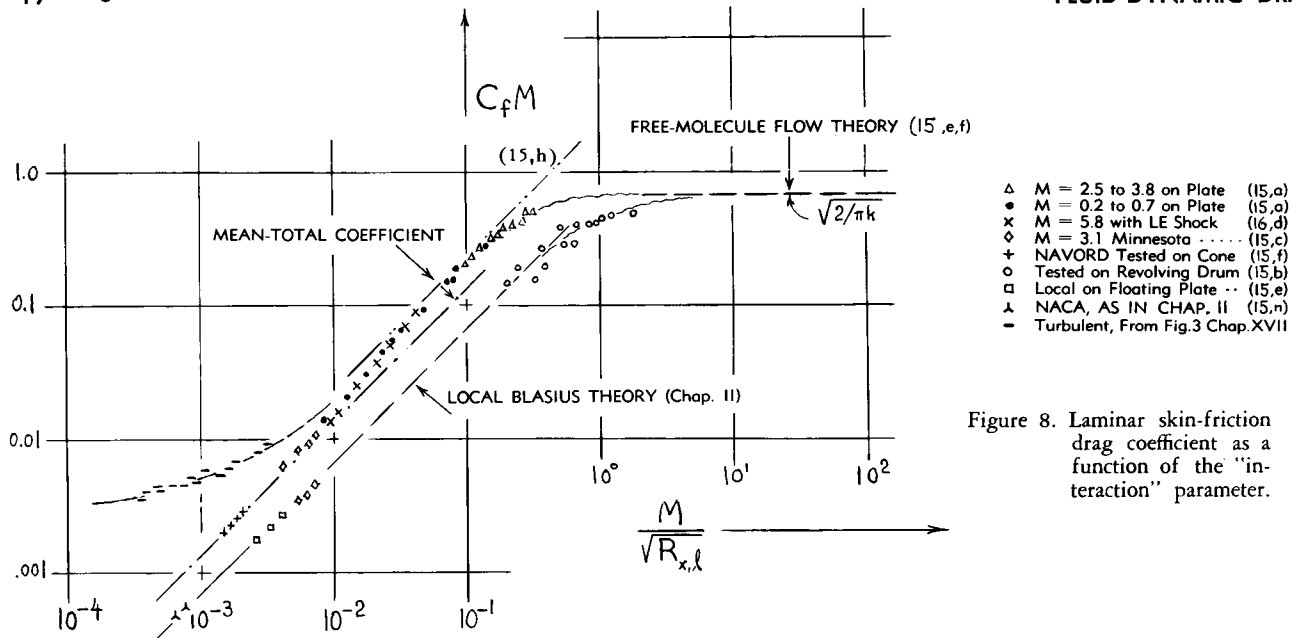


Figure 8. Laminar skin-friction drag coefficient as a function of the "interaction" parameter.

At Low Reynolds Numbers. Figure 7 in Chapter XVI demonstrates several phases through which the base pressure ratio (p_B/p_{amb}) passes, when reducing the Reynolds number. In the vicinity of $R_\lambda = 10^5$, the pressure reaches a maximum (at M' -numbers of 2.5 and 2.8, for which experimental results are shown). Base pressure reduces (and base drag increases) again, however, when decreasing the R' -number below 10^5 . Experimental results (14,a) obtained at Mach numbers between 2 and 4, and at R' -numbers between 10^2 and 10^4 , clearly show that in this phase (to be checked in figure 1) base pressure approaches zero, and base drag approaches the maximum possible level (corresponding to vacuum). The experimental results can be correlated (14,c) with each other in the form as plotted in figure 7 thus presenting the base drag of the configuration tested (and probably that of similar "slender" solids) across the whole range of the R' - and M' -number parameter as used in plotting the graph. Another, more qualitative result of the investigation (14,a) is the fact that the base pressure is no longer uniform across the base area.

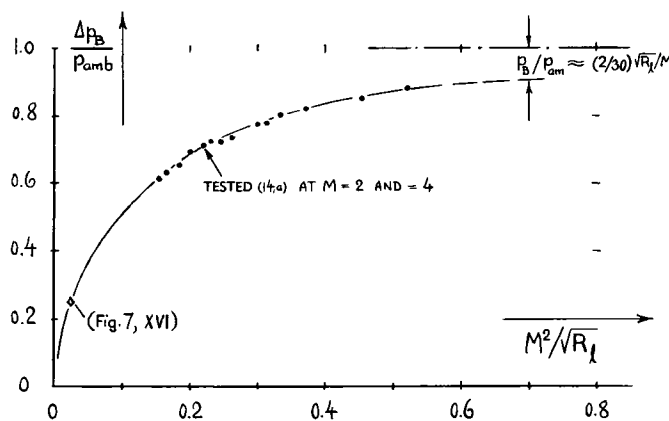


Figure 7. Correlation of base-drag ratio, behind a cylindrical body, in supersonic (at $M > 2$) and viscous flow (below $R_\lambda = 10^5$) against the parameter $(M^2/\sqrt{R_\lambda})$.

(2) VISCOUS EFFECTS IN SLENDER SHAPES

Skin Friction. It should be noted that equation 26 is governed by the "interaction" parameter (as in equation 3). The same dependence is also evident in figure 8, where tested laminar skin-friction coefficients, in the form of $(C_f M)$ are plotted against $(M/\sqrt{R_\lambda})$. Included in that graph (in identical terminology) are also the Blasius functions for laminar skin friction in uncompressed fluid flow (see figures 5 and 6 in Chapter II). Very good correlation is thus found between subsonic and supersonic results. Also shown in the graph (figure 8) is the skin-friction function for free-molecule flow — which in the terminology used, appears as a constant upper limit. We have thus in this illustration, the "complete" story of plane laminar skin friction (of the Blasius type, see page 2-4) from "uncompressed" and/or subsonic to hypersonic speeds and reaching into the field of free-molecule flow, all presented in one graph. In regard to laminar skin friction, the results suggest that simple gas dynamics are applicable to $M/\sqrt{R_\lambda} < 10^{-2}$. We have then a shock-affected phase between 10^{-2} and 10^{-1} (which we can consider to represent the "interaction" phase in figure 1) and a *transitional* (or slip-flow) phase between 10^{-1} and 10^{+1} , above which free molecular flow is finally established. This classification is compatible with that in figure 1.

Turbulent Boundary Layer. Considerable information is available on turbulent flow at supersonic speeds (see Chapter XVII). We have evaluated certain of those results and plotted them (17) in figure 8, in the form of rarefied fluid-flow parameters. Interpretation is as follows. As a function of *Mach number*, the turbulent skin friction coefficient reduces at first considerably (see figure 3, Chapter XVII) while that corresponding to laminar boundary layer flow *essentially* remains constant (as stated in Chapters XV and XVII). Naturally, turbulent friction should not be expected to reduce *below* the level as found for laminar BL flow. The experimental results as plotted in figure 8 suggest that the laminar function represents the limiting condition for the turbulent function. It is thus proposed that at higher Mach numbers and/or at lower R' numbers (that is, above $M/\sqrt{R_f} \approx 10^{-2}$) the distinction between laminar and turbulent BL flow becomes lost (17,b).

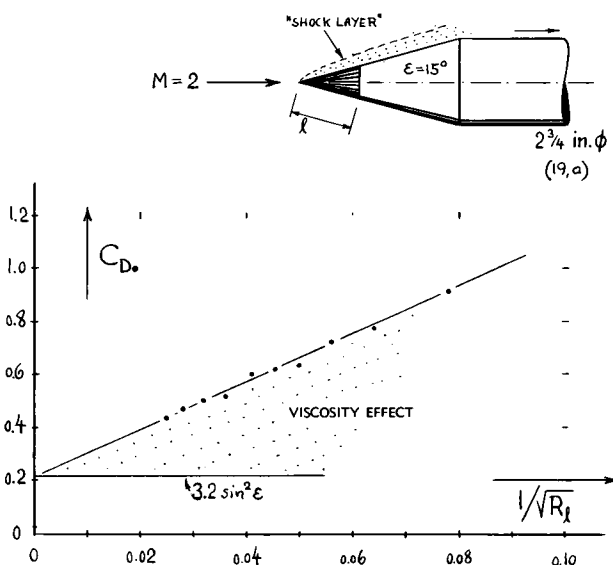


Figure 9. Total drag coefficient of the conical point as shown, at $M = 2$, as a function of Reynolds number.

- (15) Laminar skin friction in rarefied fluid flow:
 - a) Schaaf, Plates Tested, J.Aeron.Sci.1954 p.85.
 - b) Kulthau, Local Friction on Drum, J.Appl.Phys. 1949 p.217 and Proc. 3rd Mid-West Conf. Minneapolis 1953.
 - c) Bradfield (Minnesota), J.Aeron.Sci.1953 p.373.
 - d) NACA, Theories, T.Notes 2244, →2423, 2818.
 - e) Coles, At $M = 2.6$, J.Aeron.Sci.1952 p.717.
 - f) Review by Kaye (MIT) in J.A.Sci.1954 p.117.
 - g) Hill, Hypersonic Friction, J.A.Sci.1956 p.41.
 - h) Lin-Schaaf, Slip Effect, NACA T.Note 2568 (1952).
 - i) For friction at low M' numbers see (2) in Chap.II.
 - j) Klunker, Theory for $M = 1$ to 10, NACA T.Note 2499.
 - n) Dhawan, Local Friction, NACA T.Note 2567 (1951).
 - o) Mirels, Slip Effect, NACA T.Note 2609 (1952).
- (17) Notes on skin-friction in compressible fluid flow:
 - a) Note that the *reduction* of laminar skin friction due to compressibility (temperature) as indicated in figure 2 of Chapter XVII, is comparatively small — so that it can hardly be noticed in the points plotted in figure 8.
 - b) This interpretation of *turbulent* friction results, as in figure 8, is heuristic. It is also suggested that vorticity originating across a boundary-layer induced shock wave — is turbulence, thus possibly rendering a "laminar" layer effectively turbulent.
- (18) The intensity of the trailing shock-wave system reduces generally, as the Mach number is increased — until we ultimately arrive at a "one-wave" flow pattern. Within such a pattern, it is then possible for the positive pressure aft of the oblique shock "sheet" to extend into the base space.
- (19) Cones at high speeds and/or low R' numbers:
 - a) Ipsen, Cones in Rarefied Flow, Jet Prop.1956 p.1076; see also Schaaf, Jet Prop.1956 p.247.
 - b) Talbot, Cone Probes, NACA T.Note 3219 (1954).
 - d) Munson, Tests at $M = 18$, GALCIT Memo 35 (1956).
- (20) Notes concerning drag and flow pattern of cones:
 - a) Additional tests, at $M = 4$, on the same cone as in figure 9, show higher "viscous" increments.
 - b) Cone flow is an example where the physical meaning of the interaction parameter (equation 3) becomes evident. Pressure in and narrowness of the space between shock front and solid surface are increased by Mach number (reduced shock angle) as well as by reduction of the R' number (resulting in larger BL layer displacement).

Cone Drag. Figure 9 presents the drag coefficient of a small cone, tested at various Reynolds numbers. Comparison of the conditions with the R and M plan (figure 1) shows that, at the lowest R' number tested, we are roughly 1/3 up in the "interaction" field. Through extrapolation to $1/\sqrt{R_f} = 0$ (representing zero viscosity, corresponding to $R_f \rightarrow \infty$) a coefficient is obtained as indicated by *inviscid* hypersonic theory ($C_{D_0} = f(\sin^2 \epsilon)$, see Chapter XVI). The graph demonstrates that the "viscous" component of the drag coefficient increases approximately in proportion to $1/\sqrt{R_f}$. That component is made up of two parts, a frictional value (similar to the function in figure 8) and a shock pressure differential (the local magnitude of which may be as in equation (26) p.18 -8. Both of these parts can be expected to increase in proportion to $1/\sqrt{R_f}$. In contrast to the skin friction coefficient, the shock-pressure component also increases in proportion to M (see footnote 20).

(C) AERO-PHYSICAL CONDITIONS
IN THE UPPER ATMOSPHERE

The variation of the physical properties of atmospheric air, as a function of altitude, is presented in Chapter I, including the lower part of the "stratosphere", up to some 70,000 ft or ≈ 20 km of altitude. This is as high as "conventional" type of airplanes (using air to feed their engines) may be designed to operate. Characteristics of the upper atmosphere, extending to tenfold and more of that altitude, are presented as follows.

Dimensions of the Earth (30). The nominal circumference of the earth (at the equator) is 40,000 km (32). Each quadrant thus contributes 10,000 km (which is the basis for the definition of the "meter"). The diameter of the earth is 12,740 km, and the radius is 6,370 km. In fractions of that radius, altitudes are as follows:

height of Mount Everest is above troposphere	0.1%
is extending to some meteors lighting up around	0.2% 1.0%
reached by one-stage rockets	3%
satellites orbiting between	2%
and a maximum corresponding to intercontinental ballistic rockets	25% 10%

These percentages are intended to give a certain scale to the altitudes considered later. For comparison, the moon has a diameter of almost 3500 km (little more than $\frac{1}{4}$ of that of the earth). Its average distance from the earth is $\approx 380,000$ km (equal to ≈ 30 diameters of the earth). Also, to give a general idea

-
- (30) Dealing with the extremely large range of dimensions encountered in the atmosphere (from those of dust to the circumference of the earth) only a metric system seems to be adequate. Dimensions are thus given, in this chapter, primarily in millimeters and kilometers.
 - (31) Determination of dust in space and atmosphere:
 - a) Gazley, "Exosphere", J Aeron Sci 1959 p 770.
 - b) Lagow, Proc 1st Internat Space Sci Symp, Nice 1960.
 - c) Whipple, Dust Cloud, "Nature" 1961 p 127.
 - d) McCracken, Dust From Satellite, NASA TN D-1174.
 - (32) The nautical, geographical sea- or British Admiralty mile (equal to 6080 ft or to ≈ 1.15 statute miles) corresponds to one minute ($= 1/60$ of a degree) on the earth's circumference. That circumference is then equal to $60 \cdot 360 = 21600$ nautical miles; and the radius of the earth is $0.5/\pi$ times the circumference. One "kilometer" is equal to $\approx 5/8$ of a statute mile (which, in turn, is 5280 ft).
 - (33) The terms "empty" and "a few molecules" are relative. Stalder, Heat Transfer, NACA T.Rpt 944 (1949).

of the *altitudes* actually encountered within the different realms as in *figure 1*, the following example is quoted from (36,b). Assuming a vehicle with a length of 100 ft, traveling at speeds corresponding to $M = 10$, the limit of conventional gas dynamics is reached at an altitude of the order of 130 km; beyond this point, the region of "interaction" is obtained; and at approximately 270 km of altitude, the field of free molecule flow is finally entered into. The Reynolds number at this point is $R_f = 1$, at $M = 10$ and for $l = 100$ ft.

Atmospheric Layers. Not only pressure (and temperature) change as a function of altitude. The chemical and electrical properties of the atmosphere vary also very much. In reference to these properties, certain more or less concentric "layers" have been established, or they are postulated and assumed to exist. They are briefly as follows:

- (a) The *troposphere*, extending to some 8 km at the earth's poles, and to some 16 km at the equator, roughly consists of 79% molecular nitrogen and 20% molecular oxygen. Temperature reduces steadily within this layer (see Chapter I).
- (b) The *stratosphere* extends to some 50 km of altitude. Temperature in this layer is at first comparatively constant (on a level below "freezing" 220°K, standardized at -16°C in the temperate zones of the earth).
- (c) Because of ultraviolet radiation from the sun, temperature increases considerably (by some 100°C) between 30 and 50 km of altitude. The formation of ozone (O_3) coincides with the rise in temperature; thus the "ozone layer".
- (d) In the *mesosphere*, between 55 and 85 km, temperature decreases rapidly with altitude to a level of $\approx 150^{\circ}\text{K}$.

The Thermosphere. In aerodynamic respect, all the regions listed so far, contain one and the same type of gas (molecular nitrogen and oxygen) id est without chemical changes (except for the formation of ozone). Under the influence of radiation from the sun, the chemical constitution of the atmosphere begins to "disintegrate" above ≈ 90 km of altitude. As a consequence, the temperature increases rapidly in what is called the *thermosphere* (36,k,1) eventually rising to extremely high values. Generally, it can be said regarding temperature in higher altitudes, that it is not as important as density (for example) and that measured values are comparatively uncertain. Some information is presented in figure 14a.

Number Density. One way of measuring the density of the atmosphere, is to indicate the number "n" of particles per unit of space. If counting the basic particles (of nitrogen and oxygen) the density of air at standard sea level, corresponds to $n = 8 \times (10)^{20}$ protons and/or neutrons per cm^3 . Since more than 99% of the atmospheric weight is concentrated in the combined tropo- and stratospheres, the "layers" listed as follows might be considered to be comparatively "empty" spaces containing "some" gaseous particles. However, the terms "empty" and "a few particles" are relative. It is said in (33) that "a large mean free path should not be construed as an indication that the number of molecules per unit volume is small". For example at 400 km of altitude (which is higher up in the ionosphere), the mean-free path approaches " λ " = 10 km, in comparison to $\approx 10^{-4}$ mm at sea level. The ratio of these two quantities is 10^6 . However, the number "n" of particles (not counting electrons) in one cubic centimeter is still in the order of 10^{10} .

Upper Layers. Another important difference between the upper and lower layers lies in their *chemical* and electrical constitution. Both because of these changes and of rarefaction, fluid-dynamic thinking must be adjusted to principles and standards different from those in conventional gas dynamics.

(e) The *ionosphere* begins, possibly between 80 and 100 km of altitude, with *dissociation*. This process starts first with the oxygen molecules (O_2) breaking them down into atoms (O). The ionosphere consists of approximately 69% nitrogen (N_2) and 31% oxygen (O).

(f) Ionization is a process whereby, under the influence of ultraviolet (and other) solar radiation, one or more electrons are split off from a molecule or an atom. An "ion" can thus be understood to be a positively charged atom or molecule. Ionization first of atomic oxygen and later of nitrogen, follows or takes place at the same time as dissociation, thus giving this region its name. Corresponding to the concentration of ions and electrons, the *ionosphere* contains several layers (particularly the "E" and "F" layers). These layers are of great importance for radio transmission .

(g) Dissociation of nitrogen follows at an altitude in the order of 350 km (where the F2 layer is known to be). Only atomic forms, thus exist above this altitude. Temperature is believed to be in the order of 1000°K , at the F"ledge" (at ≈ 400 km).

(h) According to recent evaluations (36,h,i) of satellite performance, the temperature may reach a fairly constant plateau (at or somewhat below 2000°K) roughly at 400 km of altitude. Whether such a pause (starting an "exosphere") is true or not, the temperature is concluded (36,k,l) to continue (or to resume) "mounting" across the thermosphere.

(i) Because of their very light weight, the elements of *hydrogen* (and of helium) accumulate on top of the nitrogen and oxygen layers listed above. Such accumulation, in form of protons et cetera, is believed to be completed at some 1000 km of altitude.

Radiation Belts. In the vicinity of 3000 km, there is an inner so-called vanAllen belt, concentrated in latitudes near the earth's equator, consisting of charged particles (primarily protons). Another belt, consisting of electrons and other particles (gas from the sun) is found between 13, and 20,000 km. This belt comes down to lesser altitudes near the magnetic poles of the earth.

Interplanetary Space. For fluid-dynamic purposes, we may think of the higher reaches of the thermosphere as of a "vacuum", with a "few" hydrogen atoms, ions, neutrons, protons, and some "more" electrons, scattered within. Such a description also holds for the outer space, say at the orbit of the moon (380,000 km from the earth). The "atmosphere", therefore, does not really have a limit. It is suggested (36,k,l) that it "blends" into that of the interplanetary space at an "altitude" of $\approx 100,000$ km (equal to some 8 earth diameters. The properties in that space, say at a distance from the sun corresponding to the orbit of the earth, is speculated to be as follows:

temperature, at least (35,k,l)	$50,000^\circ\text{K}$
number of H protons (35,l)	$100/\text{cm}^3$
number of electrons, order of	$1000/\text{cm}^3$
mass density of gas, possibly	10^{-19} kg/m^3
dust content, possibly	10^{-19} kg/m^3

For comparison, the number density in interstellar space may correspond to one proton or to 1000 electrons per cm^3 of volume, so that the gas density would be in the order of 10^{-21} kg/m^3 . Some 1850 electrons have the mass of 1 proton. One H proton $\approx 1.7/10^{24}$ gram or $1.7/10^{27}$ kg mass. The reader must be cautioned as to the accuracy of the values listed; their estimate is in continuing flux at this time.

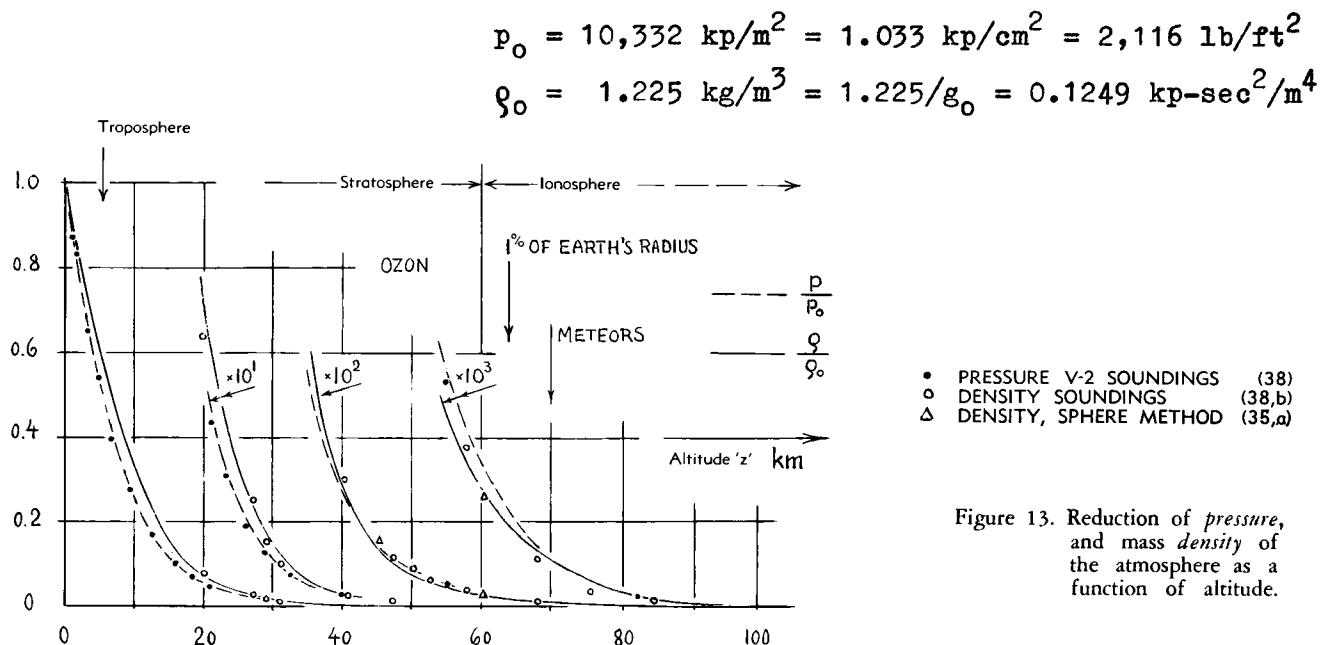


Figure 13. Reduction of pressure, and mass density of the atmosphere as a function of altitude.

Stratospheric Pressure is shown in figure 13, as a function of altitude, with both quantities indicated by linear scales. It is possible, in this manner, to visualize how rapidly the ambient static pressure reduces. Even after plotting the pressure and density ratios in tenfold, hundredfold and in thousandfold scales, each time pressure levels are soon obtained which can no longer be distinguished from "zero". Up to some 60 km of altitude, mass density across the stratosphere can be approximated by the function

$$z (\text{km}) = 17 \log (1/\varsigma) \quad (34)$$

where $\varsigma = \rho/\rho_0$. A number of experimental points (38) confirm the density function.

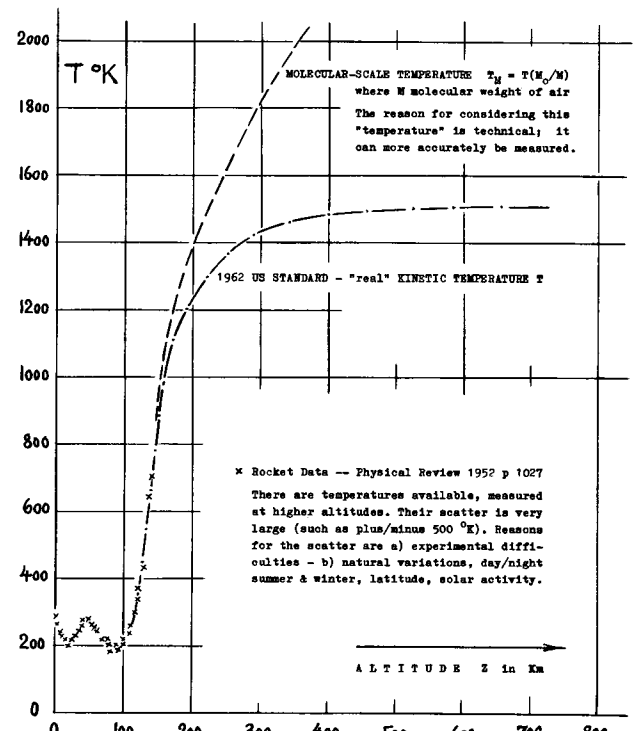


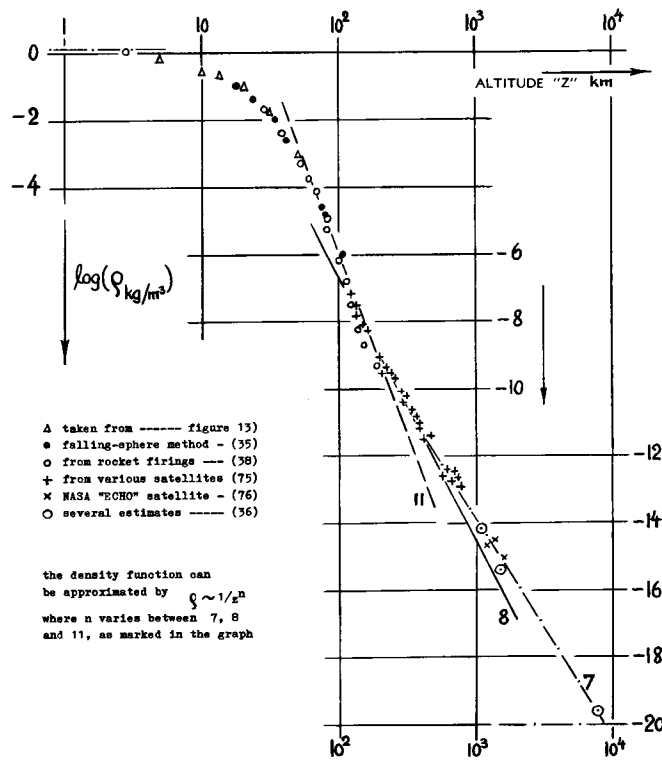
Figure 14a. This graph presents average kinetic temperatures, for altitudes higher up than those in figure 14. It is understood that measuring temperature is very difficult. It is also explained in (36,m) that the quantity T/M is obtained from high altitude soundings, where " M " = molecular weight of the air. Roughly at an altitude of 900 km, the molecular weight is only half of that at sea level. Consequently, the so called molecular-scale temperature is twice as high, at that altitude, as the kinetic temperature. Information for altitudes above 700 km is very uncertain. We know, however, that the kinetic temperature (whatever meaning it may have, in comparison to radiation) eventually rises to extreme values (such as 10,000 and 50,000 °K).

(34) Gravity. The acceleration due to the earth's gravity is at sea level $g_0 = 32.17 \text{ (ft/sec}^2\text{)} = 9.81 \text{ (m/sec}^2\text{)}$. This quantity varies in proportion to $(r + z)^2$ where $(r + z)$ = distance from the earth's center of gravity. As a consequence, acceleration reduces, as a function of the altitude "z", as follows:

$$g_z/g_0 = r^2/(r + z)^2 = (1 + (z/r))^{-2}$$

For example at $z = 0.1 r$ (corresponding to $z = 637 \text{ km}$) gravity acceleration is thus 17 or 18% less than at sea level. Escape velocity from earth in horizontal direction is $V = \sqrt{2gr}$, where r = distance from the earth's center. At sea level that speed is in the order of 11 km/sec ($M \approx 33$). See Malina "Escape by Rocket", J.Aeron.Sci. 1947 p.471.

Figure 15. Atmospheric mass density (in kg mass per cubic meter) as a function of geometric altitude (in km). Values up to some 200 km are derived from rocket soundings (38). Results between 100 and 700 km are derived from satellite observations (37).



Temperature. When calculating Reynolds numbers, the viscosity $\mu = \gamma \rho$ is required. The quantity μ is (for practical purposes) only a function of temperature. The normalized variation of temperature (36,c) is presented in figure 14, in form of a ratio, to some 100 km of altitude. Temperature also determines the speed of sound. The Mach number at a certain speed "V" changes, accordingly, in comparison to that at sea level, as indicated in the graph. As mentioned before, and as indicated in figure 14 by the heavy arrow, the temperature rises considerably at altitudes above 100 km, reaching a level in the order of 2000 °K. Atoms, protons, ions, neutrons as such, do not have a "temperature". The heat which they produce when impinging upon the wall of a container, or the surface of a vehicle, corresponds to their kinetic energy. A so-called "kinetic" temperature of 2000 °K (for example) thus indicates that the particles have a certain mean-average velocity. Because of the unbelievably small gas density, a body traveling through outer space, would never "feel" the extreme temperatures quoted above. Rather, it will be exposed to the heat radiation of the sun, id est on one side; and it will give off heat on the other side. Its equilibrium temperature will thus be similar to that on the surface of the earth, say 270 or 280 °K.

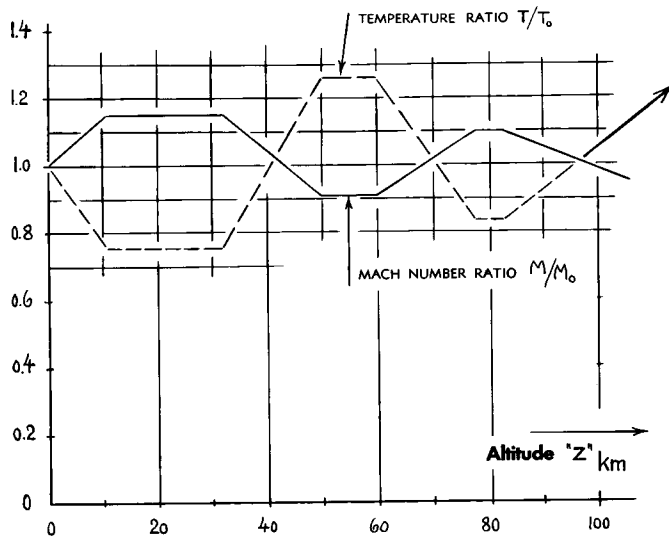


Figure 14. Normalized variation (36) of temperature and M -number in the stratosphere, presented in form of ratios.

Atmospheric Density has been determined by rocket soundings (38) up to altitudes of ≈ 220 km. Since we are nowadays interested in conditions much higher up, extrapolation by theoretical and statistical means is desirable. Such extrapolation has greatly been improved through evaluation of the drag of the many satellites (37) circling the earth since 1957. We have plotted in figure 15, the logarithm of (ρ in kg/m^3) where kg indicates the mass in the metric system (in contradistinction to kilopond "kp", equal to the "old" engineering kilogram which means weight or force). Because of the variations in temperature, composition and atomic qualities within the upper atmosphere, the density function is complex; no explicit formulation is available. The experimental points coincide at first with the stratospheric function (equation 34). Theoretical guidance is available in form of various "models" presented in (36). Statistically we can say that the experimental results in the graph vary as

$$\rho \sim 1/z^n \quad (35)$$

where $n = 11$ between 70 and 150 km,
 $= 8$ between 150 and 800 km.

For example, at $z = 637$ km (where a satellite might orbit) the density is in the order of $\rho = 10^{-13} \text{ kg}/\text{m}^3$. Since at sea level $\rho_0 = 1.23 \text{ kg}/\text{m}^3$, the number also indicates that the density at 637 km, which is 10% of the earth's radius, is $\rho \approx \rho_0/10^{13}$. Using the interplanetary and interstellar values mentioned above, together with the dust content, there might be an ultimate limit to which the density can reduce, possibly at the level of 10^{-20} as indicated in the graph.

"Molecular" Speed. Since in so-called free-molecule aerodynamics the average or "most-probable" particle speed "v" replaces the speed of sound, we will no longer consider temperature within the thermosphere and in interplanetary space. The arithmetic average of the gas-particle velocities as derived and/or estimated by Minzner (36,m) is presented in figure 16. This speed more than doubles between 100 and 200 km of altitude. At 500 km, where a satellite may orbit, the average velocity is in the order of $v = 1.4$ km/sec. For a satellite speed $V = 7.5$ km/sec, the ratio " s " = V/v is then approximately $7.5/1.4 = 5.4$. The variation of the particle speed is much less spectacular than that of pressure and density. The average velocity may, nevertheless, reach and exceed the level of 7 km/sec upon approaching the interplanetary space

- (35) Variations of density (method and/or latitude):
 - a) Bartman-Jones-Peterson, Densities From 17 Inch Falling Spheres, Univ Mich Engg Res Inst Rpts 1954, 1956, 1959.
 - b) Otterman, From 12 ft Sphere, Willow Run Labs Rpt 1960 (Astia AD-242, 757).
 - c) La Gow, Satellites/Rockets, Phys Fluids 1958 p 478.
 - d) Jastrow, Radiation Belt, Astronautics July 1959 p 20.
 - e) Comparison Fort Churchill/New Mexico, see (37,d).
 - f) Peterson, Falling Sphere, NASA CR-29 (1964).
- (36) Physical properties of the atmosphere (analysis):
 - a) "Standard" Atmosphere to 70,000 ft, see Chapter I.
 - b) Roberts, Atmosphere, Aeron.Engg.Review Oct. 1948.
 - c) NACA, Tentative Upper Atmosphere, T.Note 1200.
 - d) Grimmer, Analysis, RAND Rpt R-105 (1948).
 - e) Supersonic Handbook, NAVORD Rpt 1488 (1950).
 - f) ICAO Standard Atmosphere NACA T.Rpt 1235(1954).
 - g) Johnson and Others, Thermal Characteristics at High Speeds (mean free path computed to altitudes of 150 miles) in AMC Wright Field Tech.Rpt 5632 (1957).
 - h) Paetzold, Russian Satellites, Planet Space Sci 1959 p 115.
 - i) Mather (New Delhi), To 1000 km, J Sci Industr Res 1960 p 311.
 - j) Gazley, Exosphere, J Aero Space Sci 1959 p 770.
 - k) Chapman, High Atmosphere, Proc IRE Feb 1959.
 - l) Ratcliffe, "Physics Upper Atmosphere", Academic Press.
 - m) Minzner, US Standard Atmosphere 1962, Superintendent of Documents, U. S. Government Printing Office.
- (37) Densities as derived from satellite drag:
 - a) Sterne, Orbital Evaluation, Smithsonian Contrib Astrophys 1958 p 207.
 - b) Miklinevich, Soviet Satellite, J Am Rock Soc Russian Suppl 30, 1960 p 407.
 - c) Smithsonian Astrophys Observatory Spec Rpts No. 3,7, 12 (1957/58).
 - d) Science Comm Inc (Washington, DC) Rpt Nonr 3071 1960, ASTIA AD-243886.
 - e) Groves, Method and Data, Roy Soc (London) Proc Soc A 1959 p 28.
 - f) Harris, Method and Sputnik I, Science 1958 p 471.
 - g) Schilling, Smithso Spec Rpt 18 (1958), and Planet Space Sci 1959 p 136.
 - h) Champion, Planetary & Space Sciences 1959 p 259.
 - i) Cornford (RAE), From Orbits, IAS Paper 1959-141 (Nature 1959 p 1224).
- (38) Rocket soundings are reported as follows:
 - a) Havens, 160 Kilometers, J.Geophys.Res. March 1952.
 - b) Newell, Altitude Rocket Research, New York; also Upper Air Rockets, in J.Am.Rocket Society 1953 p.7.
 - c) Horowitz, Viking, J Geophys Res 1957 p 57; 1958 p 757; 1959 p 1627 & 2331.
- (39) For example, the speed of light is $\approx 300,000$ km/sec.

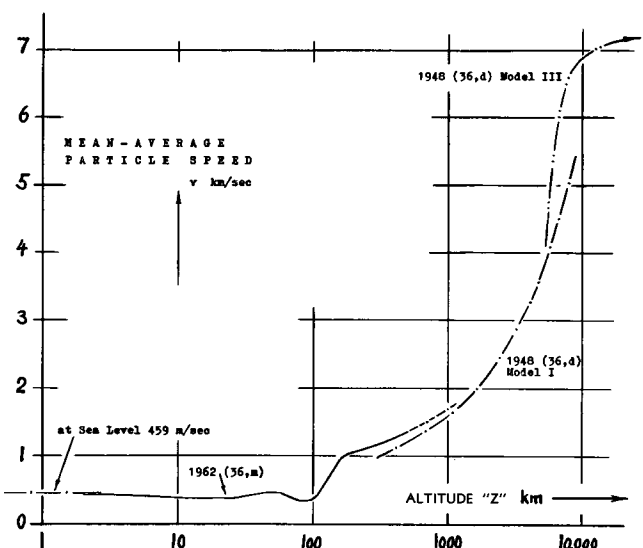


Figure 16. Variation of the arithmetic average of the kinetic gas particle velocity (36,m), as a function of geometric altitude above sea level.

Mean-Free Path. The significance of the length " λ " is explained in the first section of this chapter. The best information on the quantity of " λ ", available at this time, is presented in figure 17. Since $(\lambda n) = \text{constant}$, where $n = \text{number density of particles}$ (protons et cetera), it might be expected that the mean free path grows to the order of 10^6 or 10^7 km in the interplanetary, and to 10^9 or 10^{10} km in the interstellar space.

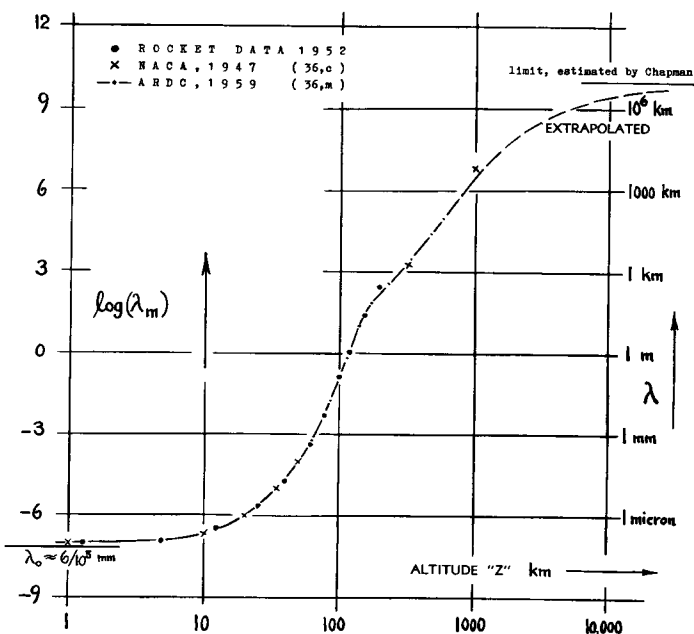


Figure 17. Variation of the mean free path length " λ " as a function of altitude.

(D) DRAG IN FREE MOLECULE FLOW

Figure 8 indicates that, above a certain value of the parameter $M/\sqrt{R_d}$, the skin friction drag coefficient C_f does no longer vary as a function of the Reynolds number. Figure 5 suggests, in a similar manner, that the drag coefficient of the sphere may reach a constant terminal level at a certain value of the parameter $(1/\sqrt{R_d})$. The gas-dynamic phase thus entered into, is that of "free molecule flow" as defined in the first section of this chapter. Some theoretical and a very few experimental results, indicating drag in this type of flow, are presented as follows.

(I) PRINCIPLES OF FREE MOLECULE FLOW

Molecular Speed Ratio. The transmission of sound (equivalent to pressure variations) gradually loses its significance, as altitude is increased and as density is reduced, accordingly. The speed of sound is related, however, to the "most probable" thermal velocity (54) of the gas molecules

$$v = \sqrt{2' R' T g} \quad (40)$$

where 'R' = gas constant and T = absolute temperature. This function differs from that for the speed of sound only in regard to the constant, which is $k = 1.4$ (in air) instead of "2" as in the equation. As a consequence, we find the molecular speed ratio

$$"s" = V/v = \sqrt{k/2} M \approx 0.84 M \quad (41)$$

Using this ratio, in place of the Mach number "M", thus eliminates the specific heat ratio "k". The physical significance of "s" can be visualized by considering, for example, a disk in a stream of gas molecules normal to its surface. As long as "s" is smaller than unity, molecules will then strike, not only against the forward face of the disk, but also to some degree against the rear face, by virtue of their own oscillating thermal velocities indicated by the statistical average "v". However, at $V > v$, the molecules can only strike the forward face of the disk, and "vacuum" is then obtained on the rear surface. The molecular speed thus has a meaning similar to that of the sonic speed; and the ratio (V/v) is applied, accordingly, to classify characteristics such as the drag coefficient, in free molecular flow.

Newton's Theory. Under extreme conditions we may have a not too large solid body, moving through "gas" which is rarefied to such a degree that only a "few" particles (molecules, atoms, protons) may strike against

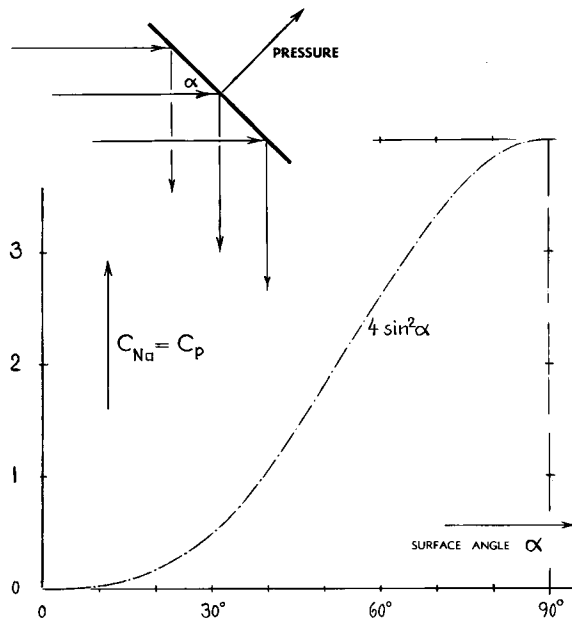


Figure 19. Theoretical pressure coefficient on a surface element in Newtonian flow (i.e. in free molecule flow at "s" → ∞, and for fully elastic "specular" reflection).

it during the time the body travels a distance equal to its length. Assuming now a uniform stream of discrete particles, flying through a space which is otherwise "empty" (vacuum), Newton developed a theory (52) for the dynamic forces originating on an obstacle placed in that stream. The particles striking a surface element "S" of the solid, at the angle 'α' or 'ε', re-bound (possibly similar to balls), without interfering in any noticeable manner with each other. The average pressure originating on the element equals the mass flow of the particles times the change of their *normal* velocity component. This change is $V \sin\alpha$ if assuming an inelastic reflection, and it is equal to $2 V \sin\alpha$, assuming elastic reflection. Consequently:

$$C_P = \Delta p/q = (2 \text{ or } 4) \sin^2 \alpha \quad (44)$$

which is Newton's "sine-square" law, as illustrated in figure 19. The aerodynamic components of the pressure are

$$\begin{aligned} C_D &= (2 \text{ or } 4) \sin^3 \alpha \\ \text{and } C_L &= (2 \text{ or } 4) \sin^2 \alpha \cos \alpha \end{aligned} \quad (45)$$

Drag Bodies. The pressure originating on the rear surface of all solid bodies in a Newtonian type of flow is zero (corresponding to vacuum). A plate placed normal to the stream of particles has consequently a drag coefficient between 2 (inelastic) and 4 (specular); the sphere has theoretically such a coefficient between 1 and 2. The drag coefficient of cones, pyramids, or wedges, pointing upstream, corresponds to their half apex angle ε; a circular cylinder in transversal flow has $C_{D_0} = 8/3 = 2.67$, if assuming elastic reflection. A surface in tangential flow does not experience any force (which we could consider to be skin friction) in this theoretical type of flow.

Newtonian-Type Flow. Newton's drag function (with a constant of "2") was erroneously applied to wind forces on buildings and structures, and thus used by engineers for two centuries (52,b). It has recently been established, however, that equation 44 happens to apply to non-viscous hypersonic fluid flow past cones (52,c) with the constant "2" being correct for $k = 1$; see Chapter XVIII.

Reflection from an obstacle might really be elastic or specular for a very smooth surface and at small angles " ε " or " α ". Newton had already speculated, however, that the reflection may very well not be elastic. He then assumed that, after striking against the solid surface, the molecules would continue in a direction parallel to the surface, thus obtaining the lesser constant (of "2") as in equation 44. However, in distinction to Newton's tacit assumption, molecules are not at rest in relation to the undisturbed gas space; they have their own *thermal* movement, "oscillating" with velocities which are varying in magnitude as well as direction. Although this fact does not make any difference in case of specular reflection (at very high "s" ratios), it does affect forces resulting from inelastic reflection. On the basis of modern kinetic gas theory, reflection can be "diffuse", meaning that the molecules are "adsorbed" for a short time into the "pores" of the surface and subsequently "re-emitted" from that surface, without any reference to their original direction of mass movement. This type of *re-emission* then takes place in so-called Maxwellian velocity distribution (see sketch in figure 20) with the direction of the emission controlled by "Knudsen's cosine law" (51). Diffuse reflection is expected to prevail in round and/or in bluff body shapes, i.e. at higher values of " α ", and from rough surfaces (at all angles). Only this manner of reflection is assumed, accordingly, for the bluff-type body shapes discussed later. In fact, results in figure 8 suggest that "reflection" is diffuse, even at zero surface angle.

- (50) Theoretical information on free molecule flow:
 - a) Heineman, Comm. Pure & Appl. Math. 1948 p.259.
 - b) Ashley, Free Molecule Flow, J.A.Sci. 1949 p.95.
 - c) Stalder, Complete Theory, NACA T.Note 2423 (1951).
 - d) Stalder and Others, Theory and Experiment, NACA Tech.Rpt 1032 (1950) (= T.Note 2244, 1950).
 - e) Sugiura, Disk Rarefied, J.Phys.Soc.Japan 1954 p.244.
- (51) Knudsen, Annalen der Physik 1909 p.75; 1911 p.593; also "Kinetic Energy of Gases", London 1934.
- (52) Newtonian theory of fluid flow:
 - a) Newton, Professor of Mathematics, Queens College, Cambridge-England, 1642-1727; "Principia Mathematica".
 - b) VonKármán, Newton and Aerodynamics, a historical evaluation in Journal Aeron. Sciences 1942 p.521.
 - c) Cole, Hypersonic Application, J.A.Sci. 1957 p.448.
 - d) Carter, Optimum Shapes, J.Aeron.Sci. 1957 p.527.
- (53) Sänger, High-Speed Gas Dynamics, ZWB FB 972 (1938).
- (54) The "most probable" speed must not be confused with the "mean average" velocity $\bar{v} = \sqrt{8} p/\pi q = \sqrt{8/\pi k} a$.
- (55) The temperature difference (heat transfer) between body and gas has a certain bearing upon the forces due to diffuse re-emission. To simplify analysis, no heat transfer is often assumed for this type of flow.

Impinging Momentum. For speeds corresponding to " s " $\gg 1$ and for larger angles " α ", results of theoretical analysis (50,c) can be presented in simple terms. Based upon the area S_a of a flat plate the drag originating in that plate, through diffuse reflection, is then indicated by

$$C_{D\alpha} = 2 \sin\alpha + (\sqrt{\pi} \sin^2\alpha / s) \quad (51)$$

The first term, plotted in figure 20, represents the momentum of the *impinging* molecules. These molecules are, so to speak, shot *into* the surface (where they *remain* for a certain time). The reaction is not a pressure, accordingly, in a direction normal to the surface. Rather, momentum is transferred *in the direction of mass motion*. The result is thus purely a drag force, even though the surface element considered may be at an angle against the oncoming flow. As a consequence, there is also no lift component resulting from the impinging momentum of the gas molecules. The drag coefficient based upon *projected frontal area* of the plate (at angle α) is simply $C_{D\alpha} = 2 \sin\alpha / \sin\alpha = 2$. This result is independent of the angle " α "; and *all* not too slender body shapes are expected to have this coefficient at "s" or M'numbers approaching infinity.

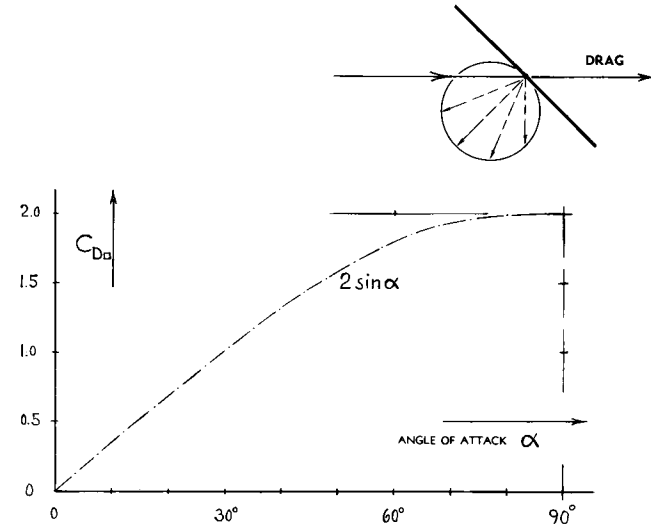


Figure 20. — Drag coefficient on a surface element in free molecule flow (at " $s \rightarrow \infty$ ") expected on the basis of *diffuse re-emission* of the gas molecules.

ReEmission (55). The second term in equation 51 represents the normal or pressure force originating through re-emission of the "trapped" gas molecules from the solid surface. The corresponding coefficient of a flat plate is

$$C_{pr} = C_{N\alpha} = \sqrt{\pi} \sin^2\alpha / s \quad (53)$$

As a "pressure" this force thus has a drag and a lift component. For example, the total drag coefficient of a flat plate (of any shape) at $\alpha = 90^\circ$ to the stream, is approximately

$$C_{D\alpha} = 2 + (\sqrt{\pi} / s) \quad (54)$$

(2) DRAG OF VARIOUS BODY SHAPES

Bluff Cone. Forces on the forward face of cones (at zero angle of attack) correspond to their half vertex angle “ ε ”. For higher “ s ” numbers and for larger cone angles, their drag coefficient (on projected frontal area) as derived from the complete functions in (50,c) is approximately

$$C_{D\bullet} = 2 + (1/s')^2 + (\sqrt{\pi}/s') \quad (56)$$

The first two terms of this equation represent the impinging momentum of the gas molecules, while the third (and further terms) indicate the pressure originating through re-emission. A physical explanation for the existence of the second term is found when considering the momentum corresponding to the thermal motions of the molecules. In comparison to the momentum representing translatory *mass* motion, the component due to thermal motions reduces to zero, as V or “ s ” $\rightarrow \infty$; and it increases vice versa, upon reducing the “ s ” number, as indicated in the equation. Figure 21 presents the drag coefficient of a disk (equal to a cone having $\varepsilon = 90^\circ$). The excess of the complete theoretical function over equation 56 reflects primarily the influence of the cone angle, which does not appear in our simplified formula.

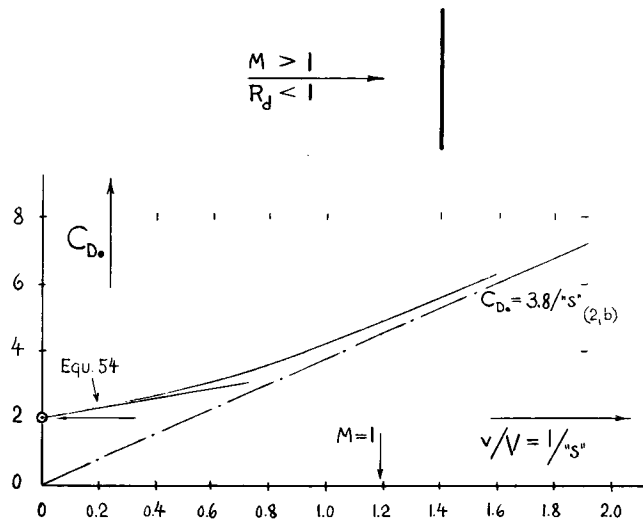


Figure 21. Drag coefficient of flat *plate* in free molecule flow, calculated for diffuse reflection/re-emission through the use of the theoretical functions in (50,c).

The *Sphere* has been investigated (58) theoretically and experimentally in free-molecule flow, at small subsonic Mach numbers. The result is the straight line as in figure 22 corresponding to

$$C_{D\bullet} = 4.2/s'' = 5.0/M \quad (58)$$

Characteristics at supersonic Mach numbers are as in-

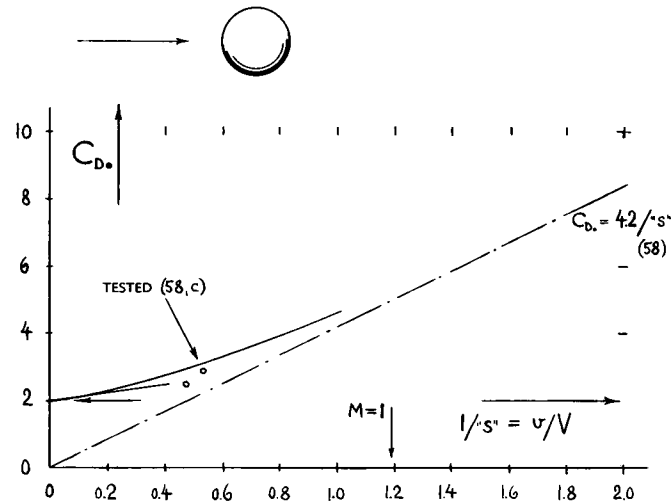


Figure 22. Drag coefficient of the *sphere* in free molecule flow; (a) for small “ s ” ratios (58,a,b); and (b) for “ s ” $\rightarrow \infty$ (58,c).

dicated in the graph. At high “ s ” numbers, the coefficient of the sphere in free molecule flow (62) with diffuse reflection (and re-emission) as described above, is

$$C_{D\bullet} = 2 + (1.4/s') \quad (59)$$

The upper one of the two experimental points (58,c) produced in figure 22, was tested at $M = 2.2$ and at $R_d = 14$. A check in figure 1 indicates that this point corresponds to a location still within the field of interaction and/or slip flow, but near the border line of free-molecule flow.

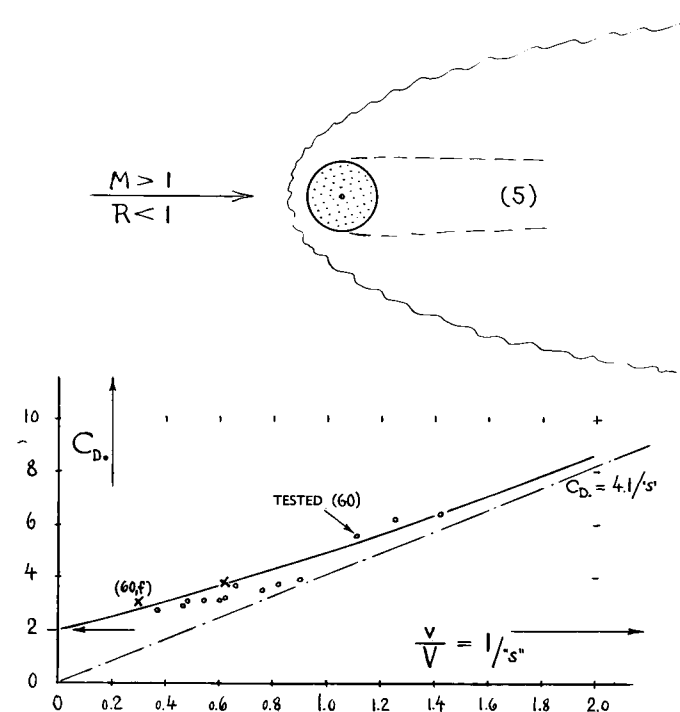


Figure 23. Drag coefficient of circular *cylinders* in free molecule flow; (a) as indicated by theory (50,c) for diffuse reflection; (b) as tested (60) without heat transfer.

Circular Cylinder. Upon integrating the complete drag function (50,c) over the surface of a cylinder in cross flow, its drag coefficient is obtained in the form as plotted in figure 23. At "s" $\ll 1$, the coefficient is expected to end up in the form of $C_{D_0} \sim 1/s$. For "s" numbers above unity (i.e. for $1/s$ as in the graph, below unity) the coefficient is approximately

$$C_{D_0} = 2 + (2.3/s) \quad (60)$$

(31 ?)

Wind-tunnel tests (60) confirm the theoretical prediction fairly well (62). The existing discrepancies (particularly at $1/s \approx 0.8$) are explained by the difficulties of the experiment. The points below $1/s = 1$ do somehow agree with theory assuming *specular reflection*. Whether this is fortuitous or not, is not known to this time.

Slip Flow. The fact that in the continuum type of fluid flow, the velocity directly at a solid surface is zero, is explained by kinetic theory (2,d) by temporary "adsorption" of the gas molecules into the solid surface. The degree of adsorption (or the number of molecules adsorbed) gradually reduces when changing the fluid-dynamic conditions from those of continuum to free molecule flow. A finite mean-average velocity can and does exist, accordingly, adjacent to solid walls at higher values of the viscous interaction parameter $M/\sqrt{R_x}$. The gas molecules (or at least part of those striking against a solid) are then *slipping* over and

along the surface. The resultant wall-velocity ratio w/V is presented, in figure 24, as a function of the "viscous" interaction parameter. The range above $M/\sqrt{R_x} = 10$, where the wall velocity is at and above 90% of the free stream speed, indicates conditions in free-molecule flow where the slip effect eventually becomes complete. The boundary layer then ceases to exist; and the influence of the Reynolds number reduces to zero.

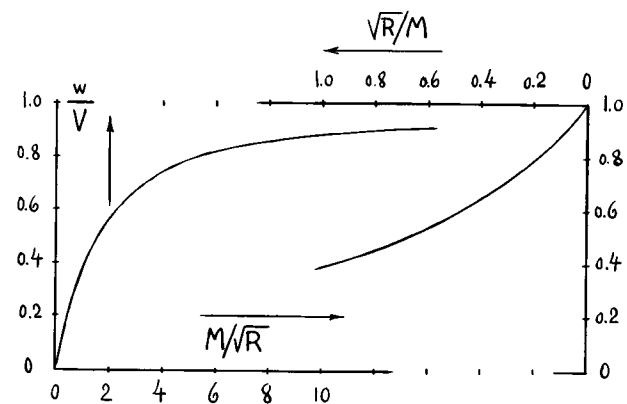


Figure 24. Slip flow velocity (15,0) at solid surface (w/V); starting from continuum-type fluid flow, in the left-hand part of the graph; and in free-molecule flow, in the right hand part.

Shear Force. Specular reflection does not produce any shear forces at all. Molecules impinging "onto" a solid surface (as in the diffuse type of reflection) do produce tangential forces, however. At higher Mach or "s" numbers, and at small angles of attack, the shear force originating along a plane surface in tangential flow (at $\alpha = 0$) then corresponds to

$$C_f = D/qS = C_\tau = \tau/q = 1/(\sqrt{\pi}s) = 0.57/s \approx 0.67/M$$

This coefficient is included in figure 8 in the form of $(C_f M) = 0.67$. A flat plate, for example, wetted on both sides may have a coefficient of $\approx 2/\sqrt{\pi}s$. At M or "s" between 1 and 2, this expression yields a section drag coefficient in the order of $C_{D_S} = 1$. This value is some 100, or even 200 times as high as that due to skin-friction drag in the region of conventional aerodynamics. The nature of this drag must be understood on the basis of the mechanics of diffuse reflection, as presented above.

Slender Cones. Tangential forces (or skin friction) can also be derived from free-molecular cone theory (50,c). For larger "s" numbers, the drag coefficient of slender cones (on projected frontal area) is

$$C_{D_0} = 1/(\sqrt{\pi} e^{H^2}) + 1 + \text{erf}(H) + (\sqrt{\pi}/s) \quad (64)$$

where "erf" = error function (see mathematical ta-

-
- (58) Spheres investigated in free-molecule flow:
 - a) Millikan, Reflection, Phys. Review 1923 p.1 & 217.
 - b) Epstein, Spheres, Physical Review 1924 p.710.
 - c) Kane and Sherman, J. Aeron. Sci. 1951 p.259 and 566.
 - d) Szymanski, Analysis, Arch. Mech. Stosowanej (Polish Periodical, Warsaw) 1956 p.449 and 1957 p.35.
 - (60) Drag characteristics of circular cylinders:
 - a) Stalder, Experiments, NACA T.Rpt 1032 (1950).
 - b) Stalder, Heat Transfer, NACA T.Rpt 1093 (1951).
 - c) To do the experimenters in (a & b) justice, it should be realized under what conditions the results in figure 23 were obtained. Tested was a wire, 3/1000 of an inch in diameter at 'H' between 4 and 185 and at R_d between 0.005 and 0.9. Forces measured were between 1 and 20 milligrams.
 - e) Talbot (Journal Aeron. Sciences 1957 p.458) gives the forces originating on a circular cylinder (such as the body of a rocket) when inclined at an angle " α ".
 - f) Maslach, Transition, U.Cal Berkeley Rpt AS-1963-3.
 - (61) Note that here as in Chapter XVIII, the speed in "H" is the component normal to the solid surface ($V \sin \alpha$).
 - (62) The second terms in equations 59 and 60 reflect the influence of the thermal motions (represented by "v") in relation to the bulk speed "V". The constants in those terms also correspond somehow with the "wetted" area.
 - (64) Sänger-Bredt, Long-Range Ballistic Bomber (in minimum altitude of 50 km), German Doct. ZWB UM 3538 (1944); discussed by Ley in Aeron. Engg. Review Feb. 1951 p.20.

bles) and where $H = ('s' \sin \varepsilon)$ is seen to be essentially equal to the hypersonic similarity parameter (as in Chap. XVIII); see also (61). Considering now that the ratio between frontal and wetted area of a cone is

$$S_0/S_{\text{wet}} = \sin \varepsilon \quad (65)$$

the cone's drag can be indicated by the coefficient (on wetted forebody area)

$$C_f = C_{D_0} \sin \varepsilon = 1/(\sqrt{\pi} e^H s) + \sin \varepsilon + \operatorname{erf}(H) \sin \varepsilon + (\sin \varepsilon \sqrt{\pi}/s) \quad (66)$$

For " ε " = 0 (as in a surface in tangential flow) this function reduces to that of the shear force (above). The drag of a *slender cone*, for diffuse reflection at higher "s" numbers can be approximated by (70):

$$C_{D_0} = 1 + (\sqrt{\pi}/s') \text{ and } C_f = 1/(\sqrt{\pi} \cdot s') \quad (67)$$

The influence of the angle " ε " can best be realized by considering the combined coefficient on wetted area:

$$C_{D_{\text{wet}}} = 1/(\sqrt{\pi} \cdot s') + \sin \varepsilon + (\sqrt{\pi} \sin \varepsilon / s') \quad (68)$$

Optimum Shapes. Under conditions where the reflection of the molecules is *specular*, shape has an appreciable influence on drag in free-molecule flow. Analysis (52,d) indicates in this case, as optimum forebody of a cylindrical solid, a shape between conical and ogival. This type of flow may not be very likely to occur, however. In case of *diffuse* reflection, it is obvious, from equation 51, that at " $s' \rightarrow \infty$ ", the drag coefficient (on frontal area) of any solid body is $C_{D_0} = 2$. If looking for an "optimum" shape under such conditions, the only type that can be suggested, is a form minimizing drag for a given *volume*. That shape would be a long prismatic or cylindrical body with only a small forward face directed against the oncoming gas molecules. Within the range of *finite* "s" numbers, the drag of such a cylinder in axial flow, may be approximated by

$$C_{D_0} = 2, \text{ and } C_f = 0.56/s' \quad (70)$$

Optimum length-diameter ratios can then be determined. Differentiation leads to

$$(\ell/d)_{\text{opt}} = \sqrt{\pi} \cdot s' \quad (71)$$

Approximating the drag of a slender cone by $C_{D_0} = 1$, and by the same C_f function as above, the optimum length ratio is found to be the same as that of the circular cylinder. For example, for " s' " = 5, that ratio is in the order of $\ell/d = 9$.

Magnitude of Lift. The theoretical solution (50,c) can also be applied in the prediction of lift produced in a "flat plate" set at an angle of attack against a stream of atoms. On the basis of "diffuse" reflection, lift is only obtained by way of re-emission; thus approximately:

$$C_L = \sqrt{\pi} \sin \alpha \cos \alpha / s' \quad (74)$$

When evaluating this equation, it is found that lift produced in the free-molecule region of the atmosphere is usually negligibly small, in comparison to the weight of any man-made vehicle suitable to be sent up. This conclusion is illustrated by the behavior of upper-atmosphere rockets which may helplessly tumble through space without sufficient aerodynamic stabilization originating in their fins.

Drag Due to Lift. Drag of the plate considered corresponds to

$$C_D \approx 2 \sin \alpha + 1.13/s' \quad (75)$$

The drag of a wedge section (or that of any similar shape) is indicated by (70):

$$C_D \approx (t/c) + (1.13/s') \quad (76)$$

As long as $\alpha < (t/c)$ of a double wedge, or as long as $\alpha < 0.5 (t/c)$ in a single wedge, the projected frontal area is then not increased over the original area corresponding to thickness. Below this "critical" angle, drag (in "diffuse"-reflection flow) therefore corresponds to the last equation, while above that angle, equation 75 must be applied.

- (69) Magnitude of "electric" drag of satellites:
a) Jastrow, Theory, J.Geophys Res 1957 p 413.
b) Knechtel, Experimental, AIAA J. 1964 p 1148.
- (70) If considering $\operatorname{erf}(H)$ in equation 64 to be zero, that is for small values of ε or α .
- (73) A satellite "falls around the earth", traveling at a speed corresponding to $(V^2 r) = \text{constant}$. The speed required to keep it flying, is $V = \sqrt{g r}$. At sea level, that speed is $\approx 8 \text{ km/sec}$.
- (74) Exchange of energy at high speeds:
a) Roberts, Gas and Solid, Proc Roy Soc (London) A, Vol 129 (1930) No.809, and Vol 135 (1932) No.826.
b) Jastrow, "Electric", Scientific American, Aug 1959.
c) Bryant, Solar Radiation, NASA TN D-1063.
d) King-Hele, Proc Internat SS Symp 1960 p 24.
e) Jacchia, Perturbations, Nature 1959 p 183 & 1662.
f) Shapiro, "Solar Pressure", Science 1960 p 1484.
- (75) Evaluation of satellite performance:
a) King-Hele (RAE), Nature 1959 p 183,527,881; also Anglo-Am Aeron Conf NY City, Oct 1959; also (74,d).
b) Jastrow (NASA), Nature 1959 p 526 & 1662.
- (76) Characteristics of NASA "Echo I" satellite:
a) Bryant, Radiation Pressure, NASA TN D-1124 (1961).
b) Westrick, Orbit, NASA TN D-1366 (1962).
c) Mark, Radiation Press, Aerospace Engg, Apr 1961.
d) Science 1960 p 1484, 1487; J Geophys Res 1960 p 3512.
e) Zadunaisky, Smithsonian Astrophys Rpt 61 (1961).
- (78) Earth and atmosphere are rotating together, at a speed of 0.5 km/sec. Therefore, the ballistic and the aerodynamic speed can differ in a satellite, by plus/minus 5%.

Decay of Satellites. Drag usually means deceleration. The most convenient satellite to be considered, is NASA's balloon type "Echo I" (76). Its inflated diameter is 100 ft ($S_0 \approx 700 \text{ m}^2$) while its mass is or was only $\approx 75/\text{g} \approx 7.6 \text{ kp-sec}^2/\text{m}$. We will assume that this satellite would move in a perfectly circular orbit (near its actual perigee) corresponding to $z = 1000 \text{ km}$, at a speed approaching 8 km/sec. On the basis of $C_D = 2$, and $\rho = 1/10^{14} \text{ kg/m}^3 \approx 1/10^{15} \text{ kp-sec}^2/\text{m}^4$ (see figure 15), its drag (78) will then be in the order of

$$D = 2 (0.5) 7500^2 (700)/10^{15} = 4/10^5 \text{ (kp)}$$

Deceleration might thus be expected to be

$$dV/dt = -D/M = -4/7.6 (10)^5 \approx -5/10^6 (\text{m/sec}^2)$$

Tentatively, the loss of speed in one revolution (with a period 'T' = 100 minutes = 6000 seconds) is then

$$\Delta V = 'T' (dV/dt) = -6000 (5)/10^6 \approx -0.03 (\text{m/sec})$$

It will be seen, however, that the speed actually increases.

Consideration of Energy. To get a satellite up, energy has to be "pumped" into it:

- (a) potential energy to lift its weight W to the altitude z, at the orbital radius $r_0 + z$ (where $r_0 = 6370 \text{ km} = \text{radius of earth}$); correspond'g to:

$$dE_p = 'M'g dz \quad (\text{m-kp})$$

where $g = 7.3 \text{ m/sec}^2$, at $z = 1000 \text{ km}$.

- (b) kinetic energy to accelerate its mass 'M' = W/g to the required equilibrium speed V; thus:

$$E_k = 'M' V^2/2 = W V^2/2 g \quad (\text{m-kp})$$

where roughly $g = 9.81 \approx 10 \text{ m/sec}^2 = \text{acceleration}$, $W = \text{weight at the ground} = 75 \text{ kp}$.

Satellite Speed. To keep a satellite in its orbit, an equilibrium speed is required:

$$V = \sqrt{(gr^2)/r} ; \quad \text{where } (gr^2) = \text{constant} \quad (82)$$

When changing the altitude, either by increasing the energy (through rocket thrust) or by reducing it (through drag) therefore:

$$(V\sqrt{r}) \quad \text{or} \quad (V^2r) = \text{constant} \quad (83)$$

Drag Energy. During one revolution of the satellite, kinetic energy is taken away because of drag:

$$\Delta E = -D V T \quad (\text{m-kp}) \quad (84)$$

where 'T' = period, and 'TV' = circumferential length of the orbit. In the case of "Echo I" as assumed above, the energy "lost" during one revolution is

$$\Delta E = -V D T = -0.32 (6) 10^3 \approx -1800 \text{ (m-kp)}$$

where 'T' $\approx 100 \text{ min} = 6000 \text{ seconds}$. For small differentials, and assuming that the speed might remain constant, the equation under (a) results in a loss of altitude during one orbit, in the order of 33 meters.

Reduction of Period. Considering equation (83), it can be seen that when changing total energy and altitude:

$$(\Delta V/V) \text{ has to be} = -0.5 (\Delta z/r) \quad (86)$$

As the necessary difference between the new and the original orbit, we thus obtain per revolution:

$$\begin{aligned} \Delta V &= -0.5 V (\Delta z/r) \\ &= 0.5 (7500) 33/7.37 (10)^6 = +1.6/100 \quad (\text{m/sec}) \end{aligned}$$

which is extremely small in comparison to $V = 7500 \text{ m/sec}$; $\Delta V/V \approx 2/10^6$. The orbital period reduces in proportion to $1/V$, and in proportion to the reduced radius and/or the circumference of the orbit. Corresponding to the increased speed, the kinetic energy (as under (b) above) is increased. As a consequence, the potential energy has to be reduced further; and the loss of altitude must be expected to be more than the 33 meters tentatively found above.—Actually, orbit of "Echo I" is (or was) not circular; the eccentricity varies between 1 and 8%. The altitude changes between 900 and 2000 km. In an elliptical orbit of this type, the satellite dips into denser altitudes once every time around, while for most of its orbit, drag can be considered to be zero by comparison. As reported in (76,a,b) the average loss of altitude of "Echo I", was 14 m per orbit; the average reduction of the period was $\Delta T = -0.04 \text{ seconds per orbit}$.

A "kp" is a kilopond, equal to the force of a kilogram. A "kg" is a kilogram (mass), which can be expressed in $(\text{kp-sec}^2/\text{m})$.

CHAPTER XX — VARIOUS PRACTICAL RESULTS

When preparing the 1965 edition of "Fluid-Dynamic Drag", a considerable number of "new" results was available. Since this book has widely been accepted among engineers engaged in the practical application of aerodynamics and hydrodynamics, it was decided to add the following chapter. As far as possible, reference is made in each case reported, to the place in the preceding 19 chapters where related and/or theoretical information on the same subject can be found.

A. EXAMPLES OF PRESSURE DRAG

Interesting examples of pressure drag in uncom-pressed flow, or at subsonic speeds, are presented in this section.

Flat Plates, varying in shape, but all exposed to flow normal to their surface, are shown in figure 1. Based upon their projected solid frontal area, their drag coefficient is only slightly larger ($C_{D_0} = 1.2$) than that of the basic square (or round) plate (with $C_{D_0} = 1.17$, as in Chapter III). The second shape (with a solidity ratio $\sigma = 0.4$) approaches two-dimen-sional conditions of flow. Its coefficient is somewhat higher, accordingly.

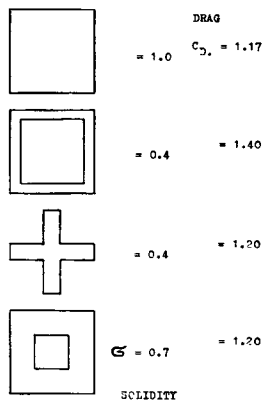


Figure 1. Drag coefficients of thin plates (1,a) varying in shape (with cut-outs) in air flow normal to their surface.

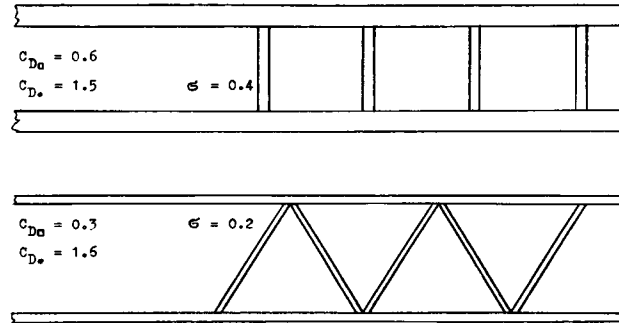


Figure 2. Drag coefficients of two simple lattice beams, tested (1,a) between walls.

Lattice Beams. A considerable volume of information is available in (1,a) regarding the drag (wind resistance) of many types of steel structures, thus supplementing what is presented in Chapter IV. As an example, figure 2 presents the drag of two simple lattice beams as tested in cross flow. While it should be remembered that the drag in two-dimensional flow, id est the drag of long and slender flat plates, corresponds to $C_{D_0} = 1.96$ (see page 3-16) the ele-ments of the beams in figure 2, have only values of 1.5 and 1.6, respectively. It is shown in figure 3, how the drag coefficients vary with the solidity ratio of such beams. As a practical value, $C_{D_0} = 1.5$ seems to be good enough for many or most lattice beams (with solidity ratios between 0.3 and 0.8). At both ends of the graph, the coefficient ends up at the level of $C_{D_0} = 1.96$, as for plates in 2-dimensional flow.

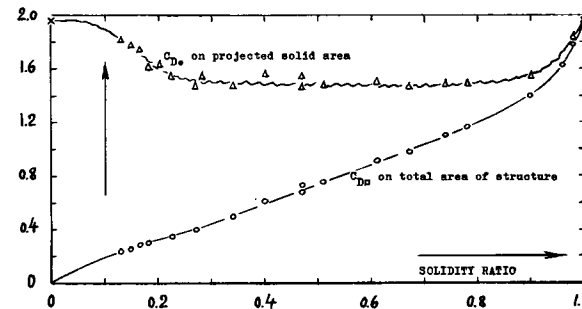


Figure 3. The drag of various lattice beams (such as in figure 2) in two-dimensional flow (1,a) as a function of their geometrical solidity ratio.

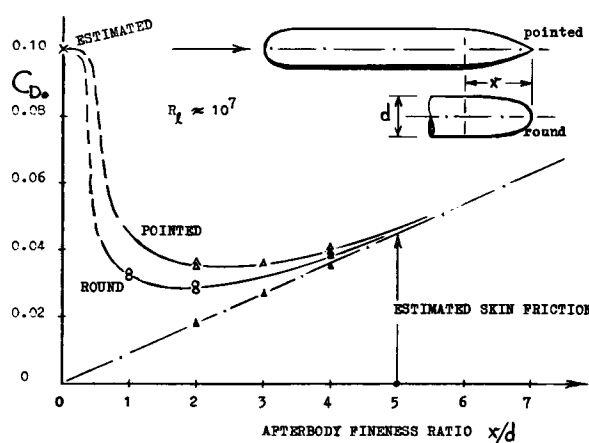


Figure 4. Afterbody drag (1,b) as a function of the length of a tail, when added to the cylindrical shape as shown.

Afterbody. One of the subjects treated in Chapter III, is base drag. The well-known method of eliminating this type of drag, is "streamlining" the afterbody, id est reducing its diameter more or less slowly, ending in a point. There can be practical reasons, however, why such shaping cannot be done. In fact, it might be desirable to keep the main body cylindrical. In this case, base drag can be reduced by boat-tailing, or by some other type of "gently" reducing the diameter, or by adding a tail, shaped as in figure 4. Of course, when adding something to which the flow is intended to keep attached, a certain increment of skin friction must be expected. We see in the graph, how the afterbody drag drops considerably, when adding a tail piece with a length equal to one body diameter. The minimum of the drag is obtained with about $x = 2 d$. When increasing the tail length further, skin friction causes the combined drag to grow again. — One other interesting result in figure 4, is the fact that a rounded tail shape is more favorable than a pointed one, considering equal length.

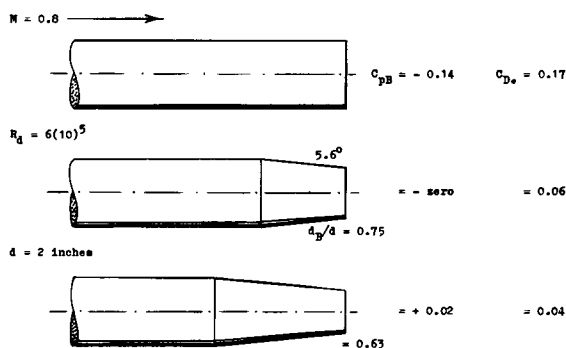


Figure 5. Drag coefficient of boat-tailed afterbodies (1,c).

Boat-Tailing is well known at supersonic speeds. Figure 5 shows that at $M = 0.8$ (which can be considered in this case, to be completely subsonic) a boat tail shape can reduce the pressure or base drag considerably. In fact, the pressure at the remaining small base, is easily reduced to zero. When comparing the drag coefficients listed in the illustration with those in figure 4, it must be considered that no tail length is added when boat-tailing the cylinder tested. No skin-friction component is added, accordingly, although some friction (along the cylinder extending forward into the wind-tunnel nozzle) is included in figure 5.

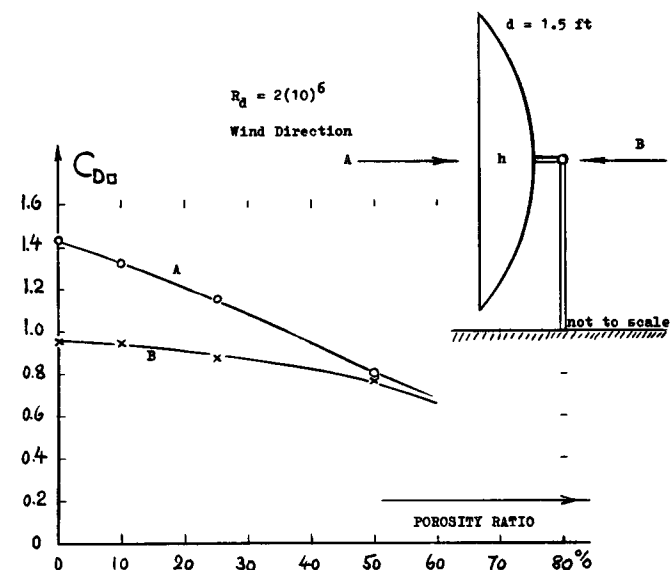


Figure 6. Drag of a parabolic antenna reflector model (2) as a function of its porosity ratio.

Radar Antennas are comparatively large structures, designed to emit and to receive radio waves. Their surface is usually a "screen" rather than solid metal. In the investigation of a systematic series of circular reflectors (2) in a wind tunnel, the porosity of such screens was imitated by drilling many comparatively small holes into sheet metal. Figure 6 demonstrates how the aerodynamic drag reduces, as the porosity ratio is increased from zero to a maximum of 50%. The result is similar to that of parachutes and other devices shown in figure 57 on page 13-24, that is when prohibiting their oscillation. As a matter of interest, we have also plotted the drag coefficient as measured when blowing against the reflector from the convex side (marked "B"). Corresponding to shape, the drag (wind resistance) is then appreciably lower, particularly in the range of small porosity ratios. This difference evidently disappears at ratios above 50%.

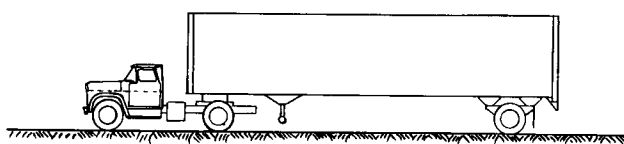


Figure 7. Aerodynamic drag of a 1960 Chevrolet trailer truck, tunnel-tested (3) on a $\frac{1}{8}$ scale model.

Trailer Truck. Total and aerodynamic drag of a truck are reported in figure 12, in Chapter XII. Results of a wind-tunnel investigation (3) are presented in figure 7. The comparatively smooth model has a coefficient (on projected full-scale frontal area of 95 ft^2) of $C_{D_0} = 0.72$ in the condition as shown. Two-thirds of this drag originate in the big and box-like trailer. When changing the forward edges of that trailer (which are 45° chamfered as in the illustration) the following drag variations are obtained:

- +19% when making the edges square
- 24% when rounding the edges (1 ft radius)

General Motors also tried a radical variation, placing the cab over the engine. The resulting drag coefficient was $C_{D_0} = 0.70$. A considerable reduction was obtained when closing the gap between cab and trailer; $C_{D_0} = 0.46$. — As a matter of interest, the engine power required to overcome the aerodynamic drag (corresponding to $C_{D_0} = 0.7$) at a speed of 60 mph, is in the order of 100 HP. About the same power is required to cover the mechanical resistance, on the basis of a vehicle weight in the order of 55,000 lb.

Gun Openings. The drag caused by openings in the fuselage of an airplane, to permit installation and the use of guns, is presented in figure 11, on page 13-3. Figure 8 shows the results of another wind-tunnel investigation (4,a) regarding such openings, suitable for 50 caliber machine guns or 20 mm cannons. The ratio of the projected opening area S_o to the frontal

area of the smooth fuselage body S_b , is $\approx 0.4\%$. The result, in form of a coefficient based upon projected frontal opening area, corresponds to:

- $C_{D_o} = 1.70$ for natural boundary-layer transition
- $C_{D_o} = 0.35$ in turbulent boundary layer
- $C_{D_o} = 0.25$ with fairing attached, as shown

The high value of 1.7, evidently includes some interference with the still laminar boundary layer along the smooth $\frac{1}{4}$ scale fuselage model. This interference is eliminated when fixing transition ahead of the openings.

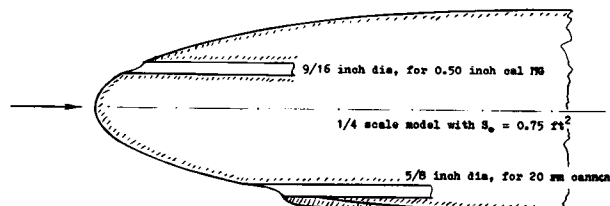


Figure 8. Openings for guns or cannons tested for drag (4,a) in a $\frac{1}{4}$ scale model of a fuselage, having a full-scale frontal area of 12 ft^2 .

A Cooling Duct is shown in figure 9, installed at the lower side of a smooth fuselage body. The internal velocity w , and the drag coefficients are defined for the total frontal area S_o of the cooler core. The external drag (of and caused by the duct on the outside) corresponds to

- $C_{D_o} = 0.033$ for $S_o = 1.5 \text{ ft}^2$, which is 0.9% of S
- $C_{D_o} = 0.040$ for $S_o = 2.5 \text{ ft}^2$, which is 1.5% of S

where S = wing area of the airplane for which fuselage and cooler are intended to be used. The external values listed, are small in comparison to those found in figure 7 on page 9-6. The internal drag (loss of

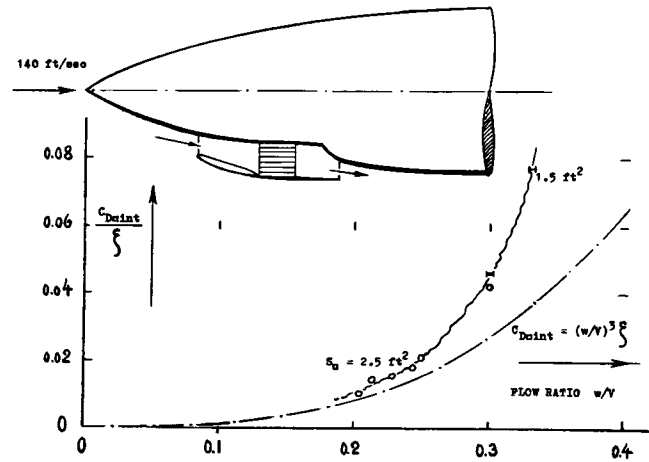


Figure 9. Internal drag (corresponding to the loss of momentum) of a cooling duct, investigated (4,b) in two sizes.

- (1) Information on pressure drag:
 - a) Flachsbart and Winter, Wind Loading on Lattice Structures, "Der Stahlbau" 1934 p 65 & 73, 1936 p 65; Translation by Sandia Corp (Albuquerque, NM) 1955.
 - b) Peterson, Flygtek Forsokanstalt Stockholm Rpt 75 (1957); quoted in "Hansa" 1959 p 19.
 - c) Salmi, Afterbodies and Jets, NACA RM E54I13.
- (2) Fox, Wind Loads on Reflector Antennas, Jet Prop Lab (CIT) Memo CP-3 (1962); also Pressures, in Memo CP-4.
- (3) Flynn and Kyropoulos, Truck Aerodynamics, Paper SAE Internat Congr 1961; see SAE Transactions.
- (4) Drag of airplane component parts:
 - a) Fedziuk, Gun Openings, NACA W Rpt L-502 (1942).
 - b) Nelson, Cooling Duct, NACA W Rpt L-115 (1944).
 - c) Neely, Bomber Modifications, NACA W Rpt L-114.
- (5) Wind Forces Structures, A Soc Civ Engrs Trans 1961, 1124.

momentum of the flow through the duct) approximately corresponds to the coefficient (explained on page 9-5):

$$C_{D_d} = (w/V)^3 \xi \quad (1)$$

where ξ = pressure-loss coefficient of the core installed in the duct. In the tests reported in figure 9, the core coefficient varies between 1.7 and 11. Since the internal drag is expected to grow in proportion to the loss coefficient, we have plotted the ratio (C_{D_d}/ξ). It is seen that this ratio begins increasing in proportion to $(w/V)^3$. In the same manner as found on page 9-4 (in a radiator installation) the internal coefficient increases over and above the values indicated by equation (1) at flow ratios w/V exceeding about 0.2.

A Nacelle of the underslung type as it is often used in twin- or multiple-engine airplanes, is illustrated in figure 10. Aerodynamic characteristics of such nacelles are found on page 13-6. The beneficial effect of a trailing-edge flap is described in connection with figure 16 in that chapter. Such a flap tends to restore the lift defect caused by the presence of an underslung body; and it thus eliminates the induced-drag component corresponding to the dent in the lift distribution. The modification shown in part (b) of figure 10, is not really a trailing-edge "flap". It is an extension of the wing chord, however; and it evidently has the effect of a flap. As tested at C_L in the order of 0.2, the modification has the following effects, expressed in form of coefficients based upon the frontal area of the nacelle:

$$\begin{aligned} \text{lift increased;} & \Delta C_{L_0} = +0.40 \\ \text{drag increased;} & \Delta C_{D_0} = -0.01 \end{aligned}$$

The configurations were also tested with the engine cowl flaps 10° opened. In this condition, the influence of the nacelle modification is somewhat increased, both in regard to the lift- and the drag differential.

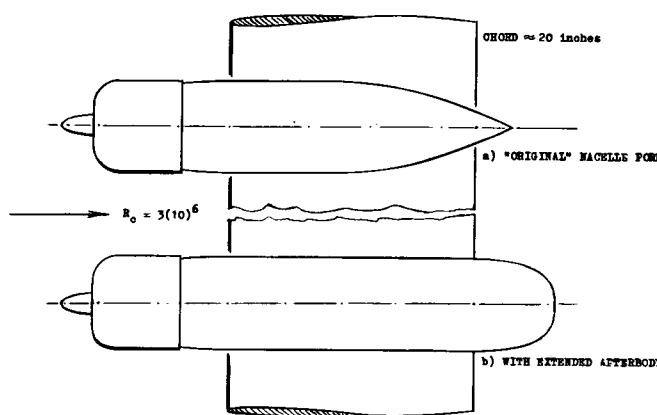


Figure 10. Plan-form shape of an "original" and a "modified" engine nacelle, wind-tunnel tested (4,c) as part of a bomber.

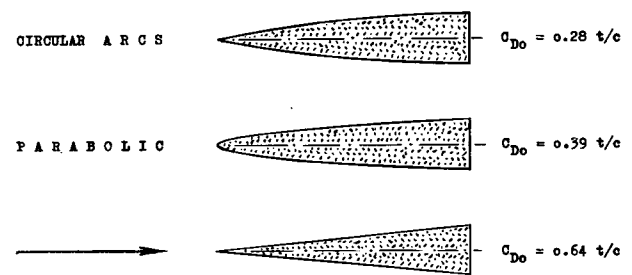


Figure 11. Pressure-drag coefficients of thin base-vented strut sections, at zero cavitation number.

B. HYDRODYNAMIC INFORMATION

Considerable progress has been made during the last years in the field of hydrofoils. A subject particularly important at higher speeds, is ventilation, thereby prohibiting or postponing cavitation.

Base-Vented Hydrofoils have been investigated both by the NASA and at the Naval Ordnance Test Station in California. At zero lift, the pressure drag of thin strut sections with a base or cavity pressure $p_c = p_a$ (so that the cavitation or ventilation number is zero) is indicated by the coefficient (on projected frontal or base area)

$$C_{D_0} = k(t/c) \quad (2)$$

It is shown in figure 11, how the "constant" k depends upon shape. Theoretically, there are sections possible, with maximum thickness somewhat ahead of the base. Their pressure drag can be zero, but these sections would start cavitating at a certain critical speed. A most promising shape is the parabolic one, which will never cavitate. Reliable experimental results of straight sections of this type do not seem to be available. We have plotted the pressure drag coefficient of wedge sections in figure 12, as a function of their thickness ratio. For practical purposes, it is seen that " k " in the last equation is really a constant, if considering thickness ratios below 20%. We will assume that the same linearity applies to parabolic sections.

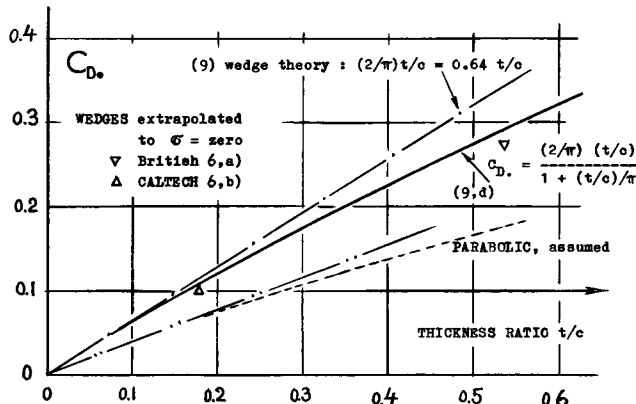


Figure 12. Pressure-drag coefficient of base-vented wedge sections (at zero cavitation number) as a function of their thickness ratio.

The Cavitation Number (as in equation 2, on page 10-5) is not always zero, as assumed in this section, so far. It is shown on page 10-8, how the drag of more or less blunt and sharp-edged bodies increases as a function of the cavitation number, id est in the linear fashion

$$C_{D_0} = C_{D_0} (1 + \sigma) \quad (4)$$

We have plotted experimental results of thin wedges in two-dimensional flow, in figure 13. These wedges have a half-apex angle $\epsilon = 5^\circ$, so that their thickness ratio is

$$t/c = 2 \tan \epsilon = 0.174 = 17.4\%$$

It seems that at cavitation numbers below 0.1, the drag follows equation (4). However, at numbers above 0.2, drag tends to correspond to $C_{D_0} = \sigma$. This would mean that all drag is "base" drag. In fact, " σ " is a base-drag coefficient, by definition (see equation (2) on page 10-5). Actually, pressure along the forebody reduces somewhat, as the cavitation number is increased. As explained in (9,b) drag of thin wedges is reduced, accordingly, corresponding to

$$\Delta C_{D_0} = -0.45 (t/c) \quad (5)$$

After subtracting this differential, an asymptotic line is obtained. When comparing the experimental points with the two theoretical limits, some skin friction must be taken into account. Using methods as in Chapter II, a differential ΔC_{D_0} in the order of 0.02 can be estimated (see the next equation). The agreement then obtained in figure 13 is very satisfactory.

- (6) Testing of base-vented strut sections:
 - a) Cox & Clayden, Wedges, J.Fluid Mech 1958 p 615.
 - b) Waid, Cal Tech Hydro Lab Rpt E-73.6 (1957).
 - c) Parkin, "Flat Plate", Caltech Hydro Lab Rpt 47-6 (1956).
 - d) Drag of a surface-piercing (base-vented) strut is presented in figure 29, on page 10-16.
- (7) Lifting base-vented hydrofoils experimental:
 - a) Johnson, Parabolic Foil, NASA TN D-119 (1959).
 - b) Christopher, Straight Foil, NASA TN D-728 (1961).
 - c) Lang, Nav Ord Test Sta NAVWEPS Rpt 7584 (1960).
 - d) Lang, A = 1, NOTS NAVEWS Rpt 7920 (1962).

Parabolic Sections can also be used as lifting hydrofoils. Their characteristics as such, are reported in (7). All we know at this time regarding the drag at zero lift, of the parabolic type of "strut" sections as in figure 11, is the pressure coefficient at zero cavitation number. To obtain real drag values, it is first necessary to add skin friction.

$$C_{D_0} = 2 C_f (c/t) \quad (6)$$

where $C_f \approx 0.003$ for turbulent boundary-layer flow. For small cavitation- or ventilation numbers, a pressure drag component can then be determined, using the constant as in figure 11, amplified corresponding to equation (4). At higher cavitation numbers, the same method might be applied as explained above for wedges.

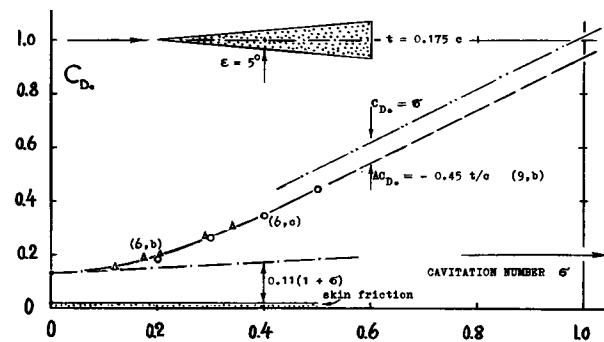


Figure 13. The pressure-drag coefficient of a thin base-vented wedge section, as a function of the cavitation number.

An Optimum Strut section can be found, considering only drag. We have plotted in figure 14, the skin friction component as per equation (6); and we have added the pressure drag, for zero cavitation number, as listed in figure 8. While the minimum total drag of the wedge shape is found in a thickness ratio around 10%, the optimum parabolic strut is 12 or 13% thick. Of course, these thickness ratios reduce, as ventilation number and pressure drag increase.

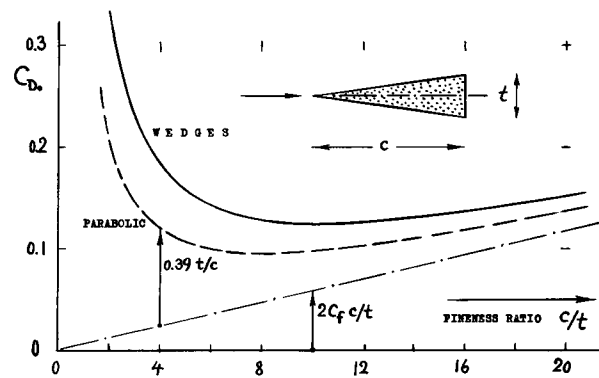


Figure 14. Optimization of strut sections, on the basis of skin-friction plus pressure drag.

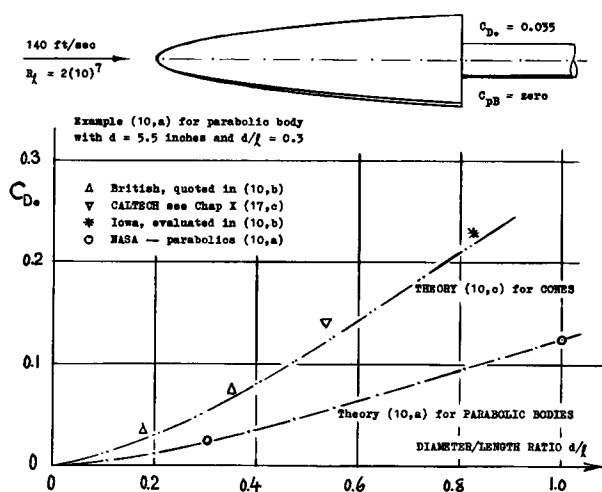


Figure 15. Pressure drag coefficients of base-vented bodies of revolution, at zero cavitation number.

Parabolic Bodies of revolution of the type as in figure 15, can also be driven through water without any cavitation, when ventilating their bases. Theory (10,a) predicts for slender shapes, vented so that the "cavitation" number is zero, the pressure drag coefficient

$$C_{D_0} = ((d/l)^2/16) \ln(16(l/d)^2) \quad (8)$$

This equation is good enough for diameter ratios d/l below 20%. For higher ratios, a more complete formulation is available, plotted in the graph. Theory is confirmed by the pressure-drag coefficients evaluated from testing two bodies, at tank speeds between 135 and 165 ft/sec. Friction drag of the slender body shown in the illustration, corresponds to $C_{D_0} = 0.017$, so that its total drag coefficient is $0.025 + 0.017 = 0.042$.

Approximation. The formulation as in equation (8) is not very simple. And the complete function as in (10,a) is extremely complex. For practical purposes (where other drag components are to be considered, such as skin friction for example) an approximation to the theoretical solution is desirable. We have found that the pressure drag of slender parabolic bodies (of the type as in figure 15) at zero cavitation number, reasonably corresponds to

$$C_{D_0} = 0.14 (d/l)^{1.5} \quad (9)$$

For slender cones (in the same type of flow as the parabolic bodies above) a theoretical solution is quoted in (10,a) taken from a British source (10,c). This solution predicts drag values about twice as high

as those of parabolic halfbodies (as in the last equation). The drag of slender cones can be approximated by

$$C_{D_0} = 0.33 (d/l)^{1.5} \quad (10)$$

The experimental results in figure 15, are all somewhat above this function.

Short Bodies. Drag coefficients extrapolated to zero cavity pressure, are listed in figure 16, for a few bodies with length ratios l/d between 0.5 and 1.0. For cavitation or ventilation numbers different from zero, their coefficient is expected, or it was tested, to vary as indicated by equation (4). The most favorable shape is the parabolic one. The type with the highest drag coefficients, is the conical.

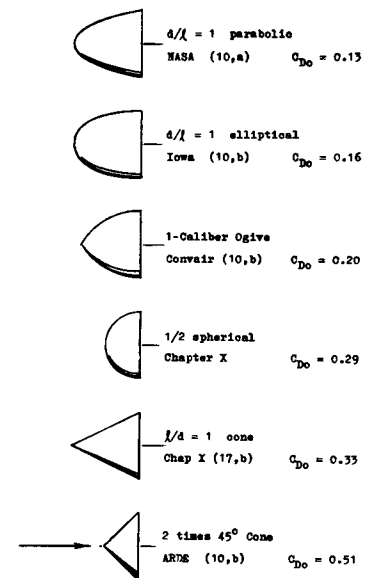


Figure 16. Drag coefficients, extrapolated to zero cavitation number, of several more or less blunt bodies of revolution.

C. RESULTS AT TRANSONIC SPEEDS

The transonic phase of aerodynamics (say between $M = 0.9$ and 1.2) has suffered in the early days of testing from experimental difficulties, particularly in wind tunnels. After perfecting transonic facilities and techniques, reliable results are now readily available. Some of them are presented as follows.

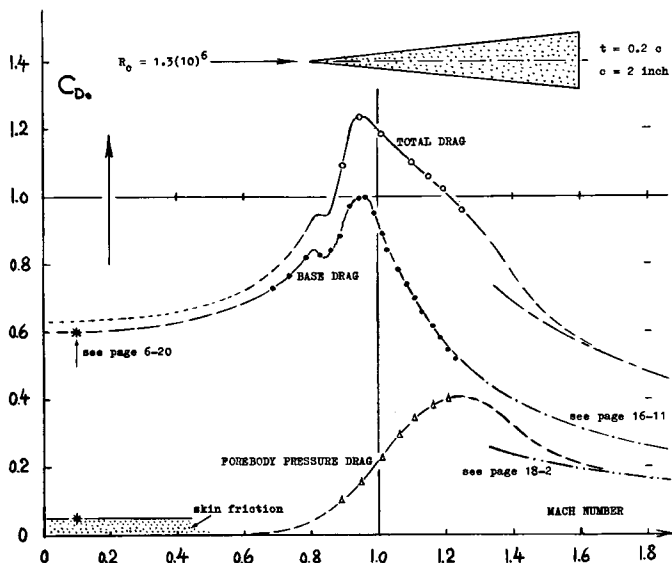


Figure 17. Drag characteristics of a wedge section (12) from subsonic to supersonic speeds.

Single Wedge. The drag components of a 20% thick wedge (tested between tunnel walls) are presented in figure 17. Results have been amplified by estimates for small Mach numbers, of skin friction as well as of base drag (see figure 39 on page 6-20). Pressure drag along the forebody, at first negligibly small in the section considered, grows considerably when approaching and crossing $M = 1$. The base drag shows a dip, slightly above $M = 0.8$. This dip (not found in the "transonic" chapter) might be assumed to be of the same nature as those found in bluff bodies at higher subsonic speeds; see page 15-6. A description of the mechanism is given on page 15-7, under "up-down-up". After passing $M = 1$, the base pressure coefficient decreases, in the manner as in figure 11 on page 16-11.

An Ejection Seat, investigated in (13,a) is shown in figure 18. Comparatively small models of such seats, complete with pilot, are tested in (13,c) at transonic speeds. Drag of a particular configuration is a function of angle of attack and Mach number. Based upon projected frontal area, and at zero angle of attack (measured against the horizontal through the seat) drag coefficients are roughly as follows:

$$\begin{aligned} C_{D_0} &= 0.8 \text{ at } M = 0.7 \\ C_{D_0} &= 1.0 \text{ at } M = 1.0 \\ C_{D_0} &= 1.2 \text{ at } M = 1.3 \end{aligned}$$

The values can greatly be changed, however, by the trimming and stabilizing devices (flaps) which are likely to be needed in the successful use of such seats. Lift (also tested in the references listed) will have a considerable influence upon the trajectory (see page 13-22) obtained after ejection.

Parachutes are used, not only to enable personnel to jump safely from their airplanes, but also as a device suitable to decelerate airplanes when landing, or missiles when returning to the ground. In the latter application, speeds are likely to be supersonic; forces are bound to be comparatively high. For this reason, and to eliminate oscillations (see page 13-26) ribbon-type parachutes (sewed together from strong ribbons,

- (9) Theoretical Analysis of base-vented sections:
 - a) Tulin, Strut Sections, DTMB Rpt 834 (1953).
 - b) Fabula, Cut-Off Edges, NOTS NAVWEPS Rpt 7571.
 - c) Wu, Free Streamline, J.Fluid Mech 1963 p 65.
 - d) Brown, Supercavitation, Davidson Lab Rpt 971.
 - e) Lang, Discussion, NOTS NAVORD Rpt 6606 (1959).
- (10) Characteristics of base-vented bodies:
 - a) Johnson, Parabolic Bodies, NASA R-86 (1961).
 - b) Macagno, Inst Hydraul Res Univ of Iowa (1963).
 - c) Armstrong, Theory, Brit.Arm RD Estab Rpt 21/54.
- (12) Johnston, Drag from Subsonic to Supersonic Speeds of a Wedge Section, NASA Memo 4-30-59L.
- (13) Ejection seats at transonic speeds:
 - a) Byrne, Transonic, MIT Nav Sup'so Lab Rpt 69 (1954).
 - b) Visconti, 1/8 Scale Model, NACA RM L51H08.
 - c) Summers, Pilot-Seat Models, NACA RM A58E02.
- (14) Johnson, Drag Ribbon Parachutes, NASA TM X-448 (1960).

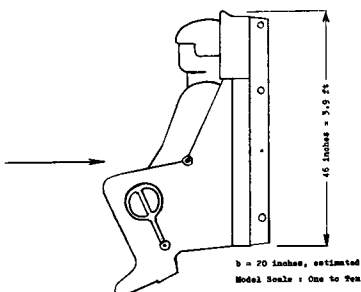


Figure 18. Example of a pilot-ejection seat (13,a) investigated in a high-speed wind tunnel.

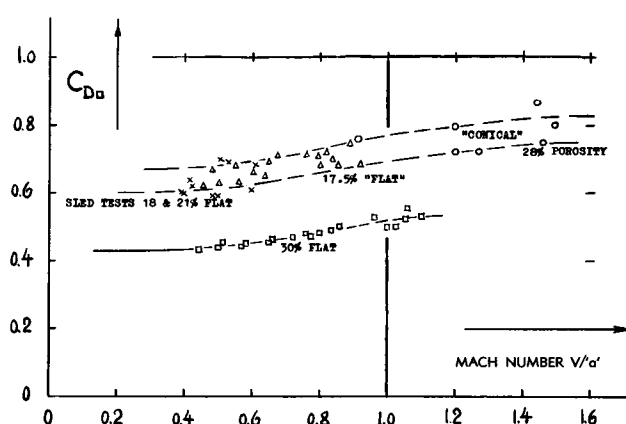


Figure 19. Drag coefficients at transonic speeds of several ribbon-type parachutes (14).

in crosswise fashion) are most suitable. Drag results of full-scale drop tests (15,a) from altitudes between 50, and 70,000 ft, are presented in figure 19. The nominal diameter of the parachutes investigated is 6 ft. The dynamic pressure during deployment at supersonic speeds at high altitude, was between 80 and 200 lb/ft². The weight of the "test vehicle" (that is, the weight carried) was between 1000 and 1500 lb, while maximum load in the parachute was considerably higher. The drag coefficients plotted, vary with the porosity of the canopy, in the manner as described on page 13-23. The coefficients are based upon the "projected" area of the canopy, for which the parachutes are constructed (corresponding to a diameter of 6 ft). The fact that the "conical" design with a porosity of 28%, has drag coefficients approximately of the same magnitude as the "flat" parachute with only 17.5% porosity, must be explained by a difference in the real inflated diameter (which was not measured during the tests reported). As a function of Mach number, the coefficients increase, for example from $C_{D\alpha} = 0.6$ at subsonic, to 0.8 at supersonic speeds.

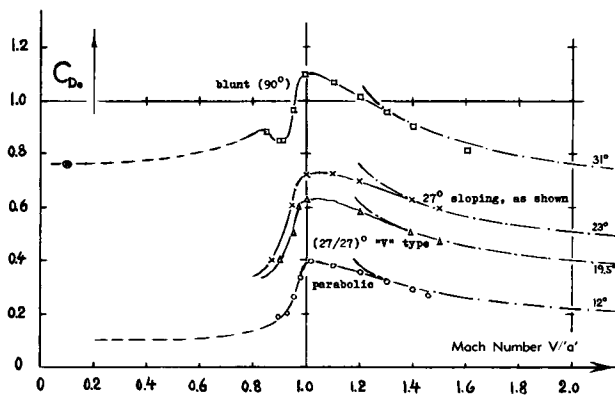


Figure 20. Flight-tested (15,a) drag coefficients (on projected frontal area of the added body) of several canopy shapes, of the type as in figure 21, as a function of Mach number.

Windshield. Results of a basic investigation of a canopy, attached to a cylindrical body, are presented in figures 20 and 21. The drag due to the canopy, in form of a drag coefficient based on projected frontal area of the added body, is least for a smooth "parabolic" shape. When providing a flat, but inclined (sloping) windshield, the drag coefficient increases as a function of the inclination angle. There are also "V" shaped windshields tested in (15,a) that is canopies with a ridge line sloping at an angle ϵ_s as in figure 21, and with a plan form, "V" shaped corresponding to an half-apex angle ϵ_p . The resultant angle of each side of this type, measured against the direction of the undisturbed flow, corresponds to

$$\cot \epsilon = \cot \epsilon_s + \cot \epsilon_p \quad (13)$$

Maximum transonic drag coefficients (at $M \approx 1$) of the canopies tested, are plotted as a function of ϵ , in figure 21.

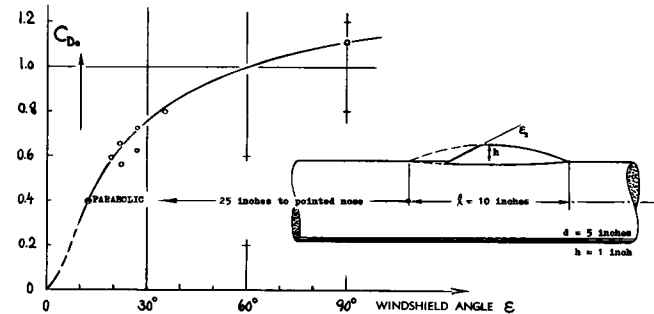


Figure 21. Maximum drag coefficient (at $M = 1$) of the type of canopy shown (15,a) as a function of the slope angle of the windshield.

A Blunt Canopy, with $\epsilon = 90^\circ$ is included in figure 20. Drag at all speeds is, of course, very high for such a bluff windshield. It should be noticed, however, that the drag function is not similar in character to that of a blunt cylinder in axial flow (as on page 16-13). In fact, the drag coefficient reduces as the Mach number is increased above unity. It is suggested that the flow separates ahead of the blunt face of the 90° canopy. The mechanism of this separation seems to be the same as that due to a spike (see pages 16-40 and 20-10). In other words, the surface of the cylindrical body to which the canopy is attached, has the same effect as a spike; and the flow pattern ahead of the windshield is more or less conical. Using equation (19) in Chapter XVIII, the half-apex angle of a cone producing approximately the same drag (at supersonic speeds) as the blunt face of the 90° canopy, is found to be $\epsilon = 31^\circ$. For example at $M = 2$, the drag coefficients are:

$C_{D\alpha} = 0.11$	for the parabolic afterbody
$C_{D\alpha} = 0.79$	for the blunt windshield
$C_{D\alpha} = 0.90$	for the complete canopy

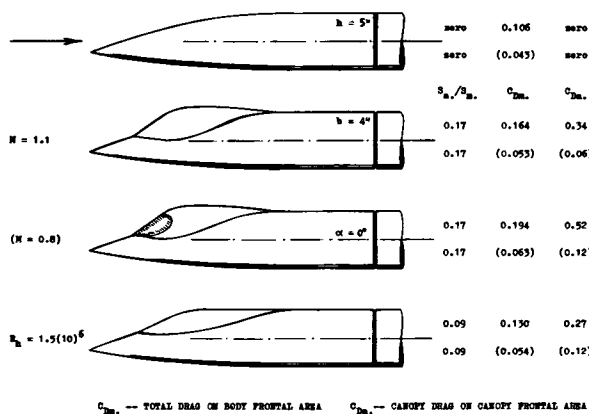


Figure 22. Drag of and due to canopies attached to the nose of a fuselage body (15,b), at $M = 1.1$. Results obtained at $M = 0.8$, are listed in parentheses.

On Fuselage. Results of tunnel tests at $M = 1.1$ (and at $M = 0.8$) on several smooth shapes (no gaps or other surface imperfections) are presented in figure 22. Based upon maximum added area (normal to main-body axis) drag coefficients at $M = 1.1$, are roughly between 0.3 and 0.5. The magnitude of this coefficient depends not only on canopy shape, but also upon location in relation to the fuselage. Corresponding to the transonic area rule (page 16-34) drag increments are low when and if the cross-section distribution of fuselage plus added body is "smooth". By arranging the canopy volume near the nose of the main body (where the area distribution is "hollow") it might even be possible that the combined wave drag be lower than that of the fuselage alone. At any rate, a drag coefficient in the order of $C_{D_{a,c}} = 0.3$, is only half of that reported in figure 52 (in Chapter XVI) for a canopy similar in shape, but located near the cylindrical part of the fuselage body. — Addition of a "V" shaped windshield increases the coefficient in figure 22, to $C_{D_{a,c}} = 0.52$. — As a matter of interest, drag coefficients are also listed (in parentheses) as found for the subsonic Mach number of 0.8. The level of the combined drag coefficient $C_{D_{m,c}}$ is between 0.04 and 0.06, at this M -number. The drag of and due to the canopies corresponds to $C_{D_{a,c}}$ between 0.06 and 0.12, which is considerably smaller than at transonic Mach numbers. The drag-divergence Mach number is about 0.91.

Location. Drag at transonic speeds, of the wing-body configuration shown in figure 23, is reported in (15,c). The maximum drag coefficient (at $M \approx 1.1$) for $C_L = 0.2$, is as follows:

$$\begin{aligned} C_D &= 0.033 && \text{plain, without a canopy} \\ C_D &= 0.033 && \text{with canopy in forward location} \\ C_D &= 0.031 && \text{with canopy in position as shown} \end{aligned}$$

The size of the canopy corresponds to the frontal area ratio (in comparison to that of the fuselage) $S_{a,c}/S_m = 10\%$. "Forward" means that the canopy was moved 1/12 of the wing span. The fact that the addition of the canopy volume does not increase the drag, may be explained on the basis of the transonic area rule (described on page 16-34). However, in rear location, the canopy *reduces* somewhat the drag of the swept-wing configuration (at constant lift coefficient). When expressing the reduction in form of a coefficient based on canopy frontal area, a value $C_{D_c} \approx -0.3$ is found. As explained in the report (15,c) lift at constant angle of attack, is increased when adding the canopy, by $\Delta C_L = 0.03$. The angle of attack required to obtain $C_L = 0.2$, is reduced by $\Delta\alpha = -0.5^\circ$. It thus seems that the efficiency (lift distribution) of the wing is improved when adding the canopy. On the basis of an increased lift-curve slope, a reduction of the induced drag can be estimated. Based on canopy area, the resultant differential is in the order of $\Delta C_{D_c} = -0.1$. This is only a third of the amount stated above. The predominant mechanism responsible for the drag reduction, therefore, seems to be that corresponding to the area rule.

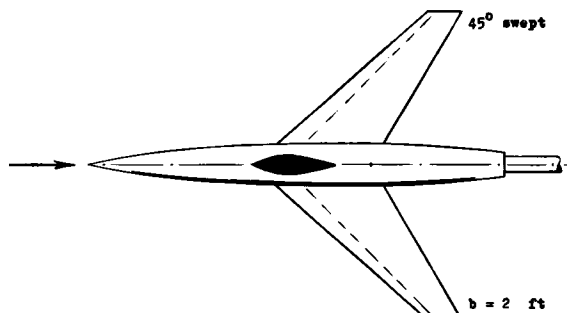


Figure 23. Canopy added to a swept-wing configuration tested (15,c) at transonic speeds.

Drag of canopies and windshields:

- a) Kell, Canopies Tested in Free Flight at Transonic Speeds, ARC RM 3024 (1957).
- b) Cornette, Canopy on Body, NACA RM L55G08.
- c) Robinson, Influence of Canopy Location, NACA RM L54E11.
- d) Robins, As (b) at $M = 1.4$ and 2.0, NACA L55H23.
- e) Cornette, Pressure Distribution, NACA RM L56H22.
- f) Kouyoumjian, Canopies in Free Flight, NACA TN 4405.
- (20) Gacynski, Various Forebody Shapes, NACA RM L53I23a.

(22) Retrorockets on the face of blunt bodies:

- a) Charczenko, Thin Retro-Jet, NASA TN D-751 (1961).
- b) Wasko, From a Sphere, NASA T'Note TN D-1535.
- c) Peterson, 4 Retrorockets, NASA T'Note TN D-1300.

(23) Influence of spikes on the drag of blunt bodies:

- a) Referenced in various places.
- b) Crawford, Spiked Nose, NASA TN D-118 (1959).
- c) Champney, Drag Devices, WADC Rpt 59-324 (1961).
- d) Spooner, Artillery Shell, NACA RM SL56D27.
- e) Wagner, Heat Pressure $M = 19$, NASA TN D-891.

D. NOSE DRAG AT SUPERSONIC SPEEDS

Nose Shape. Forebody drag coefficients are listed in figure 24 for a circular cylinder (in axial flow). Drag is small for a long and pointed nose; it is comparatively high for a hemispherical shape (see figure 20 in Chapter XVI and figure 24 in Chapter XVIII); and drag is maximum for the flat face shown (see figure 22 in Chapter XVIII).

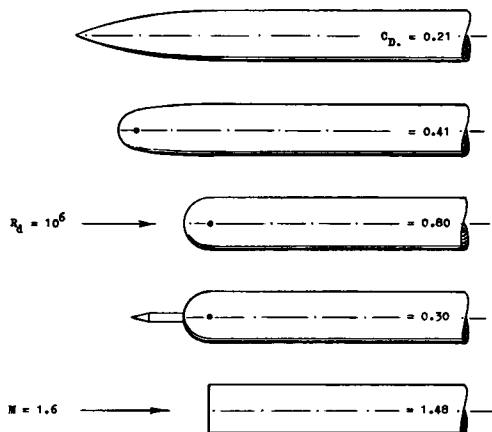


Figure 24. Drag of a forebody varying in shape between blunt and pointed (20). Included is the influence of a spike upon the drag of a hemispherical head.

Spike. A hemispherical head reduces the drag of a flat-faced nose almost to half. The coefficient of either a flat or a round shape can be further reduced when using a so-called spike. The mechanism through which such spikes may affect the drag of blunt body shapes, is described on page 16-40, in figure 57. Two more examples, investigated at $M = 7$ and 8, are presented in figure 25. The drag coefficients plotted (particularly at or near zero spike length) evidently include more than the pressure on the forward face of the blunt bodies shown. The reduction, down to coefficients in the order of $C_{D_0} = 0.2$, is very considerable. Of course, to obtain such results, it is necessary to carry (or to extend during flight, when needed) a spike with a length equal to at least 2 body diameters. In comparison to a long pointed shape having the same drag coefficient, structural advantages (dimensions, weight, cost) of a spiked nose can be considered, provided that the space in the slender body is not needed or useful.

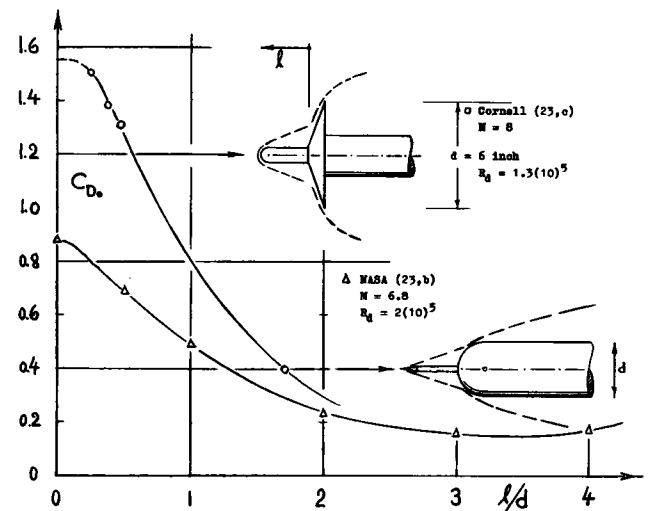


Figure 25. Two spiked bodies, tested (23) at Mach numbers in the order of 7 and 8.

Blunt "Probe". Experimental results concerning spikes are numerous. For example, there is an investigation (23,e) at $M = 19$, showing a reduction of the wave-drag coefficient of a hemispherical nose from 0.9 to below 0.1, for spike length ratios l/d above 3 or 4. As far as transonic conditions are concerned, the example of a flat-faced fin-stabilized shell is shown in figure 26. The addition of a blunt "probe" reduces the drag. Surprisingly, the interference effect is also found at subsonic speeds; at $M = 0.8$, the drag coefficient is reduced from 1.0 to 0.3. At supersonic Mach numbers, the drag coefficient of the flat-faced body continues rising (as in figures 22 and 38, in Chapter XVIII) while that of the spiked shell starts reducing in a manner similar to that of cones (see for example figure 23 in Chapter XVI).

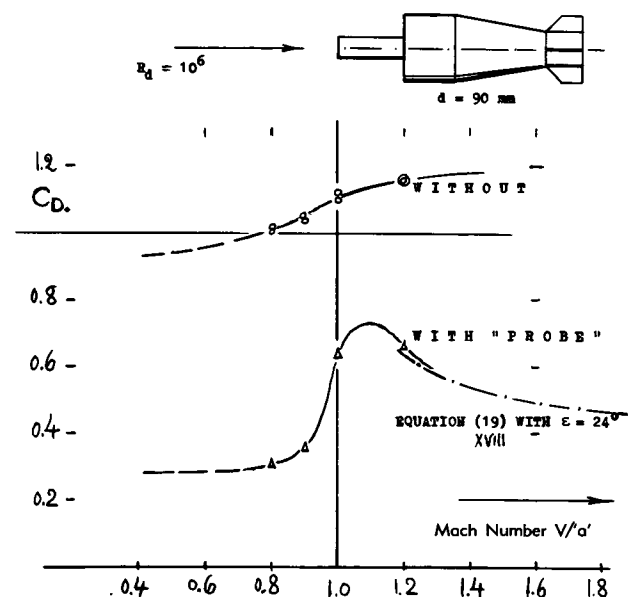


Figure 26. Drag (reduced to zero base contribution) of a blunt artillery shell (23,d) with and without a "probe".

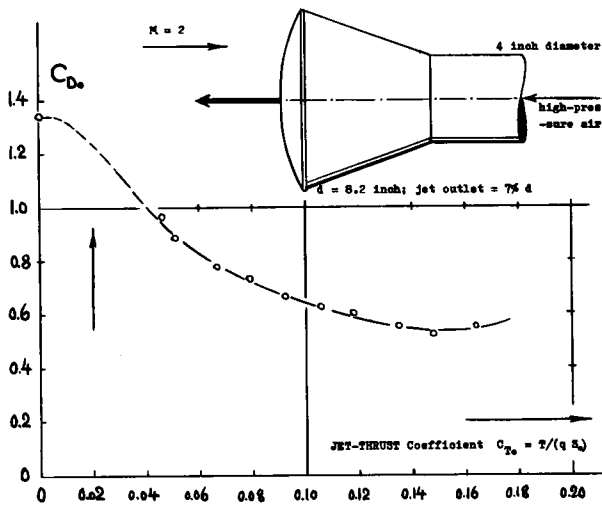


Figure 27. Influence of a thin retro-rocket jet (22,a) issuing from the blunt face of a reentry-type capsule model.

Retro-Rockets are used as a means suitable to decelerate a vehicle. Figure 48 shows the arrangement of a comparatively small jet issuing forward, from the face of a blunt body. At a Mach number of 2, the drag coefficient of this body is $C_{D_0} = 1.6$. As shown in the graph (at zero jet thrust) a coefficient of 1.34 represents the pressure at the face of the body. As a function of jet thrust, the pressure (wave) drag of the body reduces very considerably. A minimum coefficient $C_{D_0} = 0.55$ is obtained with a thrust coefficient (on body frontal area) in the order of 0.15. The retro-jet evidently has the same effect as a spike, described above. Spike or jet can cause the flow to separate from the blunt face of the body. The resultant flow pattern is similar to that around a conical nose. It thus appears that the thin jet described, is a very effective device suitable to reduce pressure (wave) drag at supersonic speeds. It should be remembered, however, that the satellites used in the United States in the "Mercury" program (61) did have retro rockets. Evidently, these rockets were fired at the beginning of re-entry into the atmosphere, before air density and aerodynamic drag assumed any magnitude.

E. NACELLES, LOADS, EXTERNAL STORES

Many airplanes carry more or less "streamline" bodies to house engines, to store extra fuel or as special equipment such as bombs, for example. All these bodies have the fact in common that they are exposed to the air stream, thus increasing the drag of the aircraft. Characteristics of a number of these appendages are presented in the following, as tested at transonic and supersonic speeds. Principle variations are location as well as type of suspension.

Jet Engines are basically ducted bodies. Their drag can be lower than that of a solid body having the same outside diameter. Figure 28 shows the combination of a slender body with a pair of engines, as it might be used in a missile (or possibly in a supersonic airplane). We are prepared for the fact that the drag of two or more bodies when attached to each other, will be larger than the sum of their component values tested separately. However, this is not so in the configuration considered. At a number $M = 2$, drag coefficients based on fuselage cross-sectional area (corresponding to a diameter of 6 inches) are as follows:

$C_{D_0} = 0.113$	for fuselage tested alone
$C_{D_0} = 0.070$	for two isolated engines
$C_{D_0} = 0.017$	estimated, struts with $t/c = 6\%$
$C_{D_0} = 0.200$	sum of the individual parts
$C_{D_0} = 0.151$	for configuration, as tested

According to this account, the complete configuration has only 75% of the drag obtained when summing up the component parts. As explained in (27,b,c,d) the reduction is due to a favorable interference of the pressure fields around the bodies, with each other. This type of interference is called buoyancy. In the present case, it may be assumed that the fuselage reduces the pressure along the forebody of the engines. To account for the differential found above, a pressure reduction corresponding to $\Delta C_p = -0.08$ would be sufficient. The buoyancy effect can also be demonstrated in terms of the drag of and due to the

- (27) Drag of stores or engines mounted on a fuselage body:
 - a) Madden, Body plus Engines, NACA RM E51E29.
 - b) Kremzier, Evaluation of (a), NACA RM E52B21.
 - c) Friedman, Body Wave Drag, NACA RM A51L20.
 - d) Hoffman, Longitudinal Position, NACA RM L54E26.
 - e) Dobson, "Fairey Delta", RAE T'Note Aero-2844 (1962).
- (28) Stores or engine nacelles suspended below the wing:
 - a) Hasel, Swept Wing at $M = 1.6$, NACA RM L51K14a.
 - b) Driver, Same Tanks at $M = 2$, NACA RM L52F03.
 - c) Jacobsen, Series of Stores Under Straight, Delta and Swept Wings at $M = 1.4$ & 2.0 , RM L52-F13, -H29, -J27.
 - d) Foster, Swept-Wing Fighter Model, NACA L56F15a.
 - e) Pepper, Free-Flight Tests, NACA RM L50G17a.

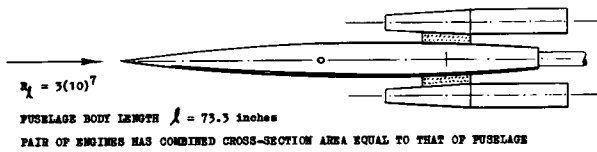


Figure 28. A pair of jet engines attached to an RM-10 fuselage body, tested (27,a,b) At $M = 2$.

engines, as follows. Based upon the sum of their cross-section areas, the drag coefficient of the engines is

$$\begin{aligned} C_{D_0} &= 0.035 && \text{when tested separately} \\ C_{D_0} &= 0.038 && \text{when attached to fuselage} \\ C_{D_0} &= 0.021 && \text{after subtracting strut drag} \end{aligned}$$

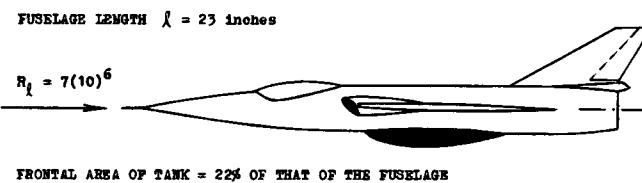


Figure 29. A 1/24 scale model of the Fairey Delta-2 airplane, tested (27,e) with and without a fuel tank under the fuselage, at M-numbers between 1.4 and 2.0.

A Fuel Tank is shown in figure 29, attached to the lower side of the fuselage. The maximum height (or thickness) of this tank is 1.4 ft, full scale, while the width is 2 ft. The drag caused by the tank, at Mach numbers between 1.6 and 1.7, corresponds to a coefficient based on the added frontal area, in the order of $C_{D_0} = 0.32$.

Pylon Suspension. In airplane configurations jet engines are very often suspended below the wing. Since the contribution to drag, of the "strut" supporting the nacelle or store, is included in the coefficient based on frontal area of the added body, the coefficients can be expected to increase with the distance below the wing. On the other hand, close to the wing there is an interference effect, increasing the drag appreciably. As a consequence, drag of wing-pylon-store configurations does not change very much at vertical distances z/d between 1 and 2. A comparison with other types of suspension is presented in figure 30. As shown in part (a) of the illustration, the underslung type has some 10% less drag (eliminating the pylon). It is also shown in part (b) that a nacelle placed around the wing section, has a lower drag coefficient than in underslung position.

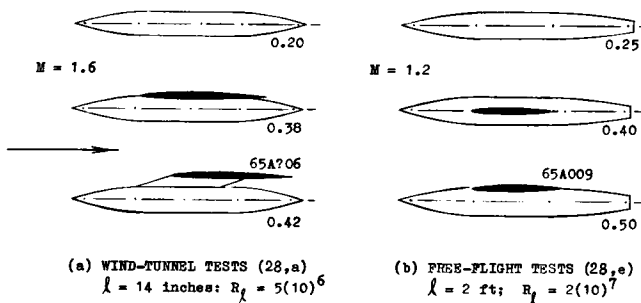


Figure 30. Drag coefficients (on frontal area of body) of and due to stores, tanks or nacelles, at selected supersonic speeds. Comparison between isolated body, placed around swept-wing section, underslung and pylon-supported configurations.

Chordwise Position. Drag of and due to a store (or engine nacelle) also depends upon its longitudinal position in relation to the wing. Typical results of a systematic investigation of mutual interference (29) are presented in figure 31. It should first be noticed that no pylon is present in these tests; wing and store are supported separately in the wind tunnel. Differential drag forces induced by the store upon the wing are at least of the same magnitude as those in the other direction. Mutual interference results in a variation of the drag coefficient (on store frontal area) roughly between 0.1 and 0.4, while the isolated store has a $C_{D_0} = 0.255$.

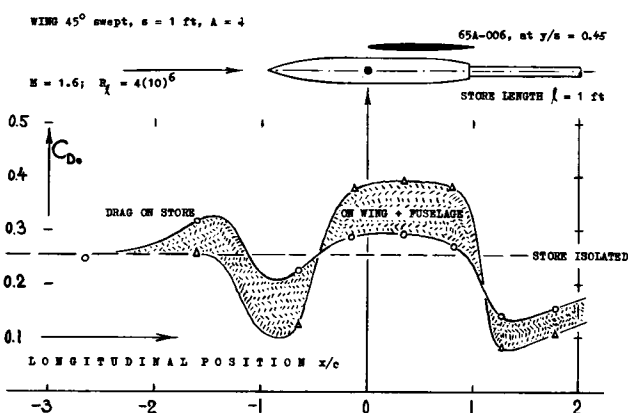


Figure 31. Mutual interference drag between a store body and a swept wing, tested (29) at $M = 1.6$.

Buoyancy. The drag variations in figure 31, can qualitatively be explained (29,a) on the basis of buoyancy; id est, from the consideration of the pressure fields around wing and store body. In particular, pressure is increased along the forebody; while an expansion takes place along the boat-tailed end of the store. These regions of positive, neutral or negative pressure, extend outward between limiting lines corresponding to the Mach angle. This angle is defined on page 17-1; its cotangent is

$$\beta = \cot\mu = \sqrt{M^2 - 1} \quad (16)$$

(a) Considering now in figure 31, the influence of the store upon the wing, it can be said that at $x/c = -0.9$, the nose of the wing is within the negative pressure field around the tail of the store. Between $x/c = -0.1$ and $+0.8$, the rear end of the wing section is in the same negative field. Finally, at and beyond $x/c = +1.2$, the positive pressure field around the forebody of the store, induces some negative drag on the rear of the wing section.

(b) As far as the fuselage (not shown in the illustration) is concerned, the positive pressure produced by its nose, evidently meets the forebody of the store, at x/c around -1.4 . The fuselage also helps to reduce the drag of the store, at x/c above $+1.2$.

(c) Considering the pressure field around the wing section, it must be realized that for 45° sweep, at $M = 1.6$, conditions are not yet "supersonic". As a consequence, there is a positive pressure field ahead of the leading edge. This field evidently acts upon the boat tail of the store, in positions around $x/c = -0.8$. Between $x/c = -0.2$ and $+0.7$, the negative pressure along the rear end of the section, make the pressure on the tail of the store more negative. The same pressure field evidently meets the nose of the body, at and beyond $x/c = +1.2$.

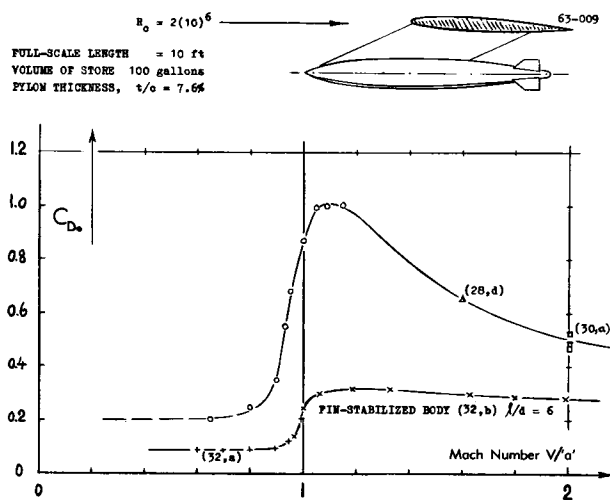


Figure 32. Drag coefficient of and due to an external store carried below the swept wing of the Douglas D-558-II research airplane, tested on a 1/16 scale model by the NACA (30).

Transonic Drag. In addition to what is presented on pages 16-36 and -37, drag characteristics are shown in figure 32, of fin-stabilized stores as a function of the Mach number. At $M = 1.6$, the coefficient of these stores is higher ($C_{D_0} = 0.65$) than that of the pylon-suspended body in figure 30, for two reasons. First, the fins represent additional drag. Included in figure 32, is the coefficient of a free-flying fin-stabilized body, with $C_{D_0} \approx 0.3$. There is an interference effect evident, increasing the drag of and due to the added body by more than 100%. The second reason for the high store-drag coefficients, therefore, is the fact that they are located in an unfavorable position in relation to the wing chord; see figure 31. Speaking now about transonic Mach numbers, the coefficient of the stores in figure 32, reaches a maximum of $C_{D_0} \approx 1.0$, at $M = 1.1$. The interference between store, pylon, wing and fuselage, is evidently very severe around that Mach number. Transonic area-rule considerations can explain the magnitude of the drag increase. It should also be taken into account that all drag increments have been concentrated upon the store bodies, in the evaluation as presented in this section.

F. SURFACE IMPERFECTIONS

Drag due to roughness elements at subsonic speeds, is presented in Chapter V. Results obtained at transonic and supersonic Mach numbers, are as follows.

Body with Rings. Figure 33 presents the drag coefficient of a Sears-Haack body without and with a blunt ring attached. The average drag increment due to the ring corresponds to the pressure coefficients at its faces. The results prove that a downstream fairing is hardly of any use. However, a 10° ramp added to the upstream face, reduces the transonic drag appreciably. If considering the ring to be a surface irregularity, it should be realized that its thickness (height) is comparatively large, while the boundary-layer must be estimated to be comparatively thin (considering an R' -number of the body as high as $3(10)^7$).

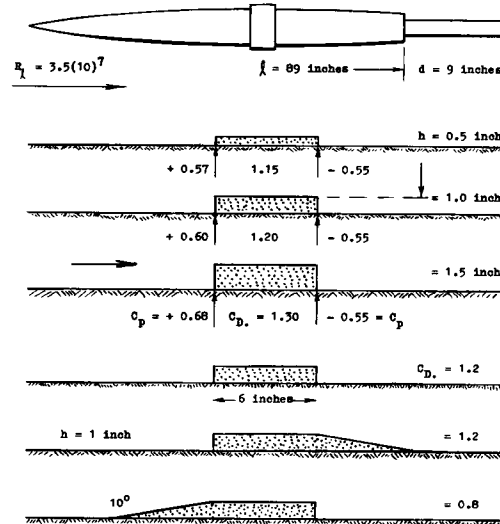


Figure 33. Drag due to a blunt ring tested (35,a) on a slender body of revolution, at transonic speeds, corresponding to M between 1.0 and 1.1.

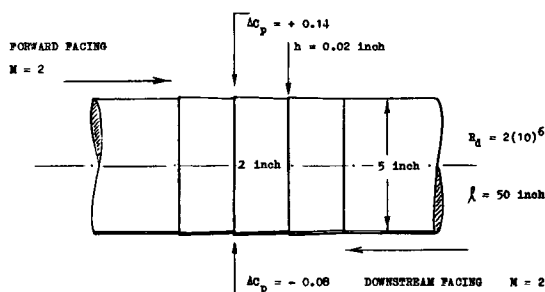


Figure 34. Drag caused by steps representing sheet-metal joints, investigated (35,b) at supersonic speeds, using a slender ogive-cylinder body combination.

Surface Steps. Surface imperfections including steps, are presented in Chapter V, for subsonic conditions. Results at Mach numbers between 1.6 and 2.0, are found in (35,b). Ahead of and behind the steps (respectively) shown in figure 34, the flow (and/or the boundary layer) separates. The static pressures in the separated spaces and on the faces of the steps, represent drag. Typical values are listed in the illustration. The average thickness of the boundary layer developing along the ogive-cylinder body used as a carrier for the surface irregularities investigated, is estimated to be more than 0.2 inches. The height of the steps is thus less than 10% of the BL thickness. The comparatively small magnitude of the pressure differentials reported, seems to reflect these conditions. — The body surface between the steps is sloping at the rate of plus or minus (respectively) $0.02/2 = 0.01$. Using 2-dimensional theory (see page 17-14) the resultant pressure coefficient is $\pm 2(0.01)/\sqrt{M^2 - 1} \approx \pm 0.01$, for $M = 2$ as in figure 34. The value of 0.01 represents the drag coefficient of one of the sloping surfaces, based on the frontal area of one step.

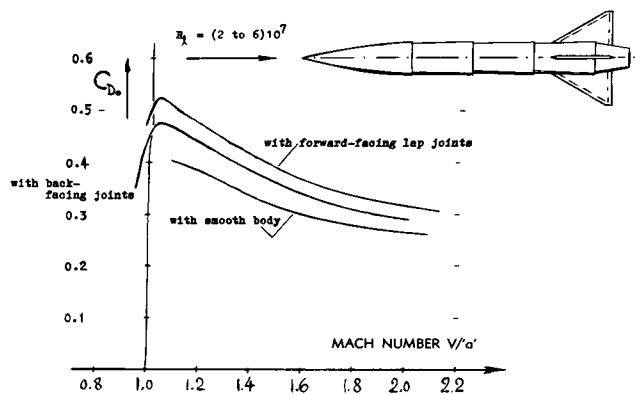


Figure 35. Drag caused by surface steps representing sheetmetal lap joints, tested (35,a) in free flight, at supersonic speeds, using the vehicle as shown.

Lap Joints. Results of a free-flight investigation (35,a) at Mach numbers between 1 and 2, are presented in figure 35. The height of the steps, simulating sheet-metal lap joints, is 0.064 inches, in comparison to a body diameter of 5 inches. The differentials tested (at an average M-number of 1.5) can be reduced to drag coefficients based upon the sum of the step faces used. The result is:

$$\begin{aligned} C_{D_0} &= 0.45 && \text{for the back-facing joints} \\ C_{D_0} &= 0.75 && \text{for the forward-facing steps} \end{aligned}$$

Rivet Heads. A number of 32 "round" rivet heads, each with a height of $3/64$ inches and roughly $1/4$ inch diameter, were also tested (35,a) using the vehicle as in figure 35. Based on the sum of the head areas, drag coefficients derived are as follows:

$$\begin{aligned} C_{D_0} &= 2.00 && \text{based on frontal area} \\ C_{D_0} &= 0.26 && \text{on square of head diameter} \end{aligned}$$

Applying the equation for the drag of a biconvex airfoil section (as in figure 15 on page 17-14) a value in the order of $C_{D_0} = 1.8$ can be estimated. Considering the presence of a boundary layer on the surface of the test vehicle, the value of 2.0 as listed above, thus appears to be high.

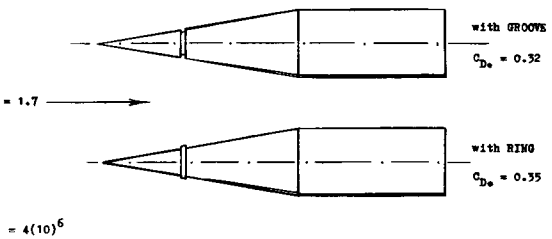


Figure 36. Basic surface irregularities tested (35,c) in free flight, on the cone-cylinder type of projectile shown.

Projectile. Figure 36 shows a simple cone-cylinder type of projectile. In the results derived from firings at $M = 1.7$, listed as follows, dimensions are given as fractions of the caliber (the diameter of the cylindrical part).

- Grooves cut into the conical nose, with a depth up to 0.04 calibers, do not noticeably increase the drag.
- Blunt rings placed around the nose, with a maximum height (thickness) of 0.02 calibers, have drag coefficients (based upon their projected face area) in the order of $C_{D_0} = 0.8$.

G. CHARACTERISTICS OF BASE DRAG

Base drag in uncompressed fluid flow is discussed in Chapter III; and at supersonic speeds in Chapter XVI. Additional information on the subject, primarily at transonic and supersonic Mach numbers, is presented as follows.

Length of Body. Figure 37 presents the pressure coefficient as found at the base of a cone-cylinder body, the length of which was varied between 2 and 5 units. It is explained on pages 3-19, and on 16-5 and -6, how base drag reduces as body length and boundary layer thickness are increased. The same variation can also be obtained when reducing the Reynolds number (thereby increasing frictional drag coefficient and boundary-layer thickness). However, the variation as in figure 37, seems to be comparatively large. The explanation presented in the source (42,c) relies completely upon the local conditions of flow directly ahead of the base. While at afterbody length ratios, say above 5, pressure and Mach number approaching the base of a cylindrical body, are for practical purposes equal to those in the undisturbed flow, the M'number is locally increased at and for some distance behind the rim of the conical nose of the body. At any rate, base drag increases as the length of the afterbody is reduced.

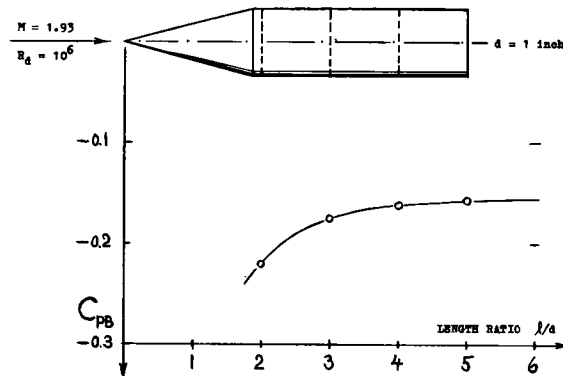


Figure 37. Pressure coefficient at $M \approx 2$, behind the base of a cone-cylinder combination (42,c) the length of which was varied as shown.

Tail Surfaces. Figure 38 shows how the presence of tail surfaces affects the base pressure (or drag) coefficient. At a Mach number of 2, the coefficient is about doubled (from $C_{pb} = -0.2$ to -0.4) when adding the surfaces as shown. A qualitative explanation is as follows. Behind the tail section, the static pressure is reduced (corresponding to an expansion of the flow along the rear half of the foil section, tapering to a sharp trailing edge). According to the principles stated in Chapter XVII (pages 17-13 and 14) the 10% thick biconvex section used, produces (at least theoretically) negative pressures down to $C_p = -0.23$, at $M = 2$. By simple superposition of the negative pressure field upon the boundary of the wake behind the base, the level of the pressure in that area is evidently reduced. Theory also suggests that the tail-surface pressure varies in proportion $1/\sqrt{M^2 - 1}$.

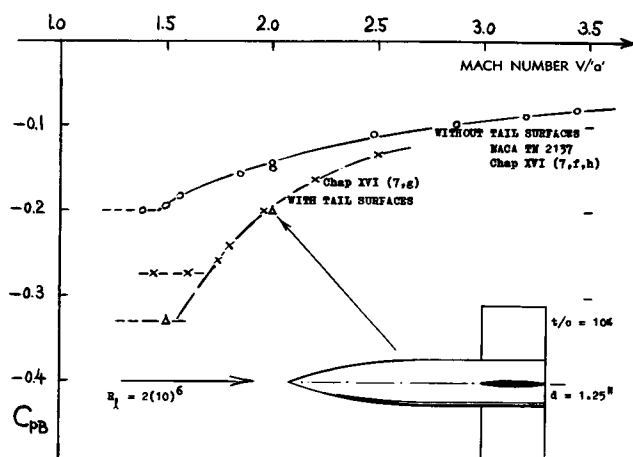


Figure 38. Influence at supersonic speeds of tail surfaces (42,b) upon the base pressure of an ogive-cylinder body.

- (29) Smith (NACA) systematic investigation of store interference on swept-wing configuration, at $M = 1.6$:
 - a) Mutual and Lift Drag Interference, RM L55A13a.
 - b) Lateral Forces and Pitching Moments, RM L55E26a.
 - c) Size and Shape of Store, RM L55H01 and L55L08.
 - d) Store on Delta Wing Configuration, RM L55I27a.
 - e) Swept Wing Configuration at $M = 2$, RM L55K15.
 - (30) Investigation by the NACA of external stores on a model of the Douglas D-558-II research airplane:
 - a) Smith, Characteristics at $M = 2$, RM L54F02.
 - b) Silvers, At High Subsonic Speeds, RM L55D11.
 - c) Kelly, At Transonic Speeds, RM L55I07.
 - (32) Fin-stabilized bodies, tested alone, by NACA:
 - a) Ward, Bombs at Subsonic Speeds, SL57J15a.
 - b) Hart, Various Bodies in Flight, RM L9130.
 - (35) Surface imperfections at supersonic speeds:
 - a) Holdaway, Body with Steps, NACA RM A57E24.
 - b) Czarnecki, Irregularities, NASA TN D-835 (1961).
 - c) Dickinson, Aberdeen Ball Res Lab Rpt 1284 (1960).
 - d) Hopko, In Free Flight, NACA RM L54I21.
 - (42) Base drag experiments at supersonic speeds:
 - a) Scott, Base With Jets, NASA Memo 3-10-59L.
 - b) Spahr, Tail Surfaces, NACA TN 2360 (1951).
 - c) Love, Body Length, NACA TN 3819 (1957).
 - d) Reller, Various Bodies, NACA TN 3393 (1955).
- Also Blaylock, Reflector Antenna, JPL Rpt CP-6 (1964).

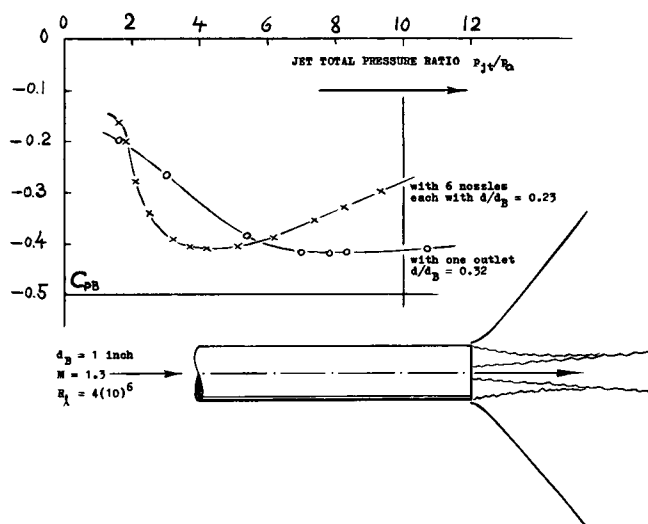


Figure 39. Base pressure (measured between body rim and jet or jets) as affected (42,a) by presence and strength of one or more jets issuing from the base.

Rocket Nozzles are usually protruding from the blunt base of the "vehicle" which they are intended to propel. As long as their diameter (or the sum of their outlet areas) is small in comparison to the dimensions of the base, the exiting high-speed jet flow is likely to make the base pressure more negative, by way of mixing and suction. As shown in figure 39, a single jet can thus increase the magnitude of the base pressure from $C_{PB} = -0.2$ to -0.4 . The same increment occurs in a multiple arrangement. The magnitude of base drag, as distinct from pressure, reduces, however, possibly to zero, as the outlet-area ratio (corresponding to diameter as well as number of nozzles used) is increased. In other words, vehicle efficiency is increased, when filling the space behind the base with jet flow. When this is not possible by any reason, it might be advisable to give the body a suitable boat-tail shape.

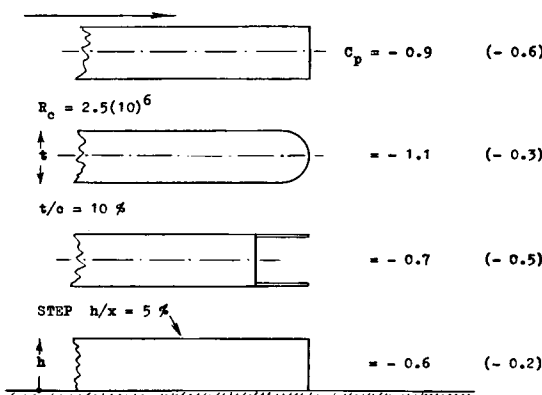


Figure 40. Pressure coefficient behind the blunt trailing edge of a two-dimensional section, tested (44) at $M = 1.0$. The values in parentheses are for the subsonic number $M = 0.4$.

Trailing Edge. Pressure was measured in the middle of the blunt trailing edge of a two-dimensional section (having a sharp leading edge). As listed in figure 40, at subsonic speeds (at $M = 0.4$) the magnitude of the base pressure coefficient is considerably reduced when rounding the edge. However, at transonic speeds, such rounding produces very high pressure values; $C_{P\min} = -1.1$. The formation of a vortex street is evidently favored by the round edge. On the other hand, when making the trailing edge "hollow", the strength of the vortex street seems to be reduced; the minimum pressure (at $M \approx 1.0$) corresponds to $C_{PB} = -0.7$. There is also shown in figure 40, a backward-facing step. The value of the base pressure is low; the surface of the plate on which the step is placed, evidently makes the lateral motions of a vortex street impossible.

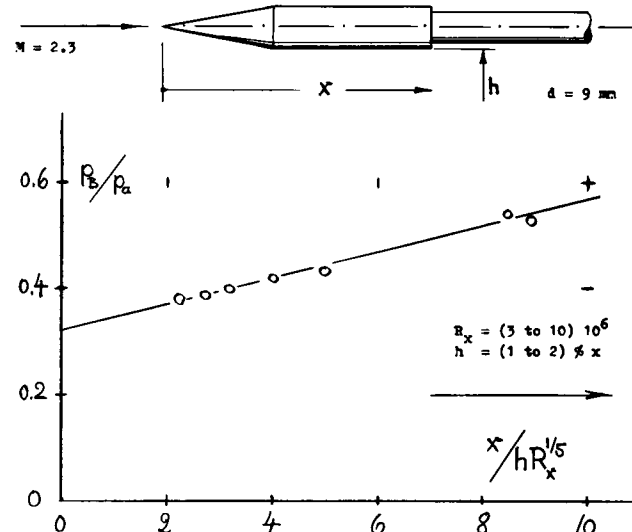


Figure 41. Pressure behind a step in the surface of the body shown, tested (46) in the presence of turbulent boundary layer.

Step Pressure. In supersonic wind-tunnel tests, the boundary layer can be laminar almost up to $R_x = 10^7$. Many investigations, therefore, apply to conditions which may not always be correct in full scale. Backward-facing steps in the surface of a cone-cylinder body were tested (46) at $M = 2.3$. It can now be speculated that the pressure behind a step be a function of (h/δ) . It can also be assumed that the turbulent boundary layer thickness δ be proportional to $(x/R_x^{1/5})$ where x = length of the surface to the step. We have plotted in figure 41, the absolute base-pressure ratio as tested, against the parameter $(x/hR_x^{1/5})$. The result is a tentatively straight-line function. The minimum pressure is $P_b = 0.09 P_a$ where P_a = ambient pressure as in equation (10) on page 16-3. The minimum can be expected when no viscosity is involved. As x increases, or as R_x decreases, the boundary layer grows, thus reducing mixing and suction past the base of the step.

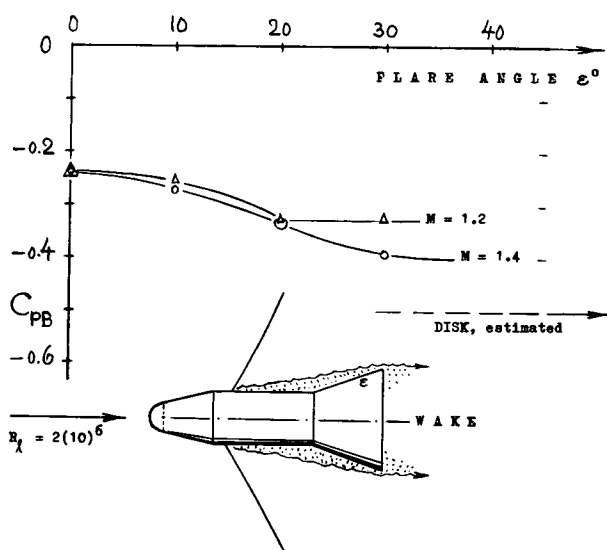


Figure 42. Pressure coefficient at the base of a flared body (43) as a function of the "skirt" angle.

Flared Base. The pressure behind the base of a body also depends upon the angle at which the forebody ends. A flared body is shown in figure 42. Pressure coefficients are listed in the illustration for a Mach number between 1.0 and 1.1, where base drag is maximum. Base pressure grows more negative as the flare angle is increased. In fact, we might speculate that at $\epsilon = 90^\circ$, the pressure is similar to that behind a flat disk (see figure 18, in Chapter XVI). However, between $\epsilon = 20$ and 30 degrees, the flow separates ahead of the conical "skirt". The effective angle and the magnitude of the base pressure coefficient are reduced, accordingly.

Boattail. The drag characteristics of a family of boattailed bodies are reported in (45). An evaluation of this source is presented in figure 32 (on page 16-23). As far as base pressure (rather than drag contribution) is concerned, figure 43 shows how the coefficient varies with the boattail angle. Since base diameter and area vary with the flare angle, two explanations are possible:

- We can say that early recompression (behind the base) is favored as the boat-tail angle is increased.
- When reducing the base diameter, the thickness of the boundary layer arriving at the rim of the base, is considerably increased. According to the principles shown in figure 37 (on page 3-19) and figure 13 (on page 16-12) the magnitude of the negative base pressure can be expected to reduce.

We may assume that those two mechanisms combine with each other, thus affecting the base pressure as shown in figure 43. In fact, at $S_B / S_0 = 0.1$, the pressure coefficient evidently crosses the zero axis. Positive pressure can thus be predicted for the end of a pointed afterbody (when the base area is zero).

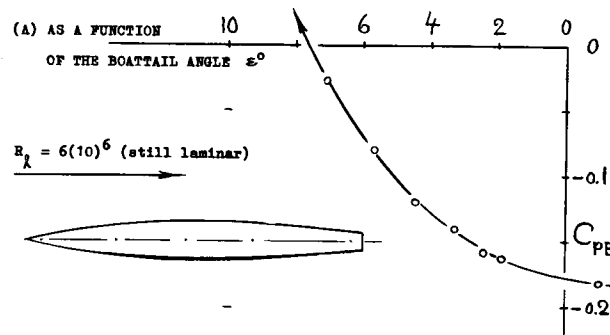
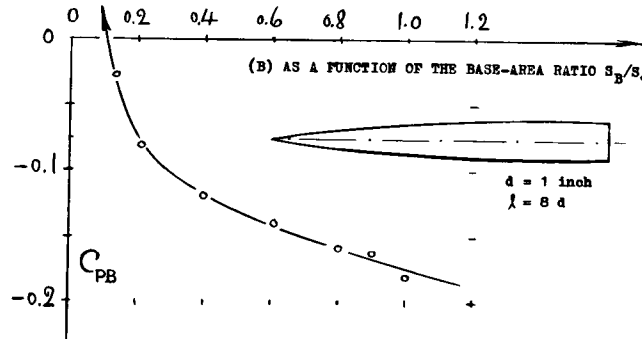


Figure 43. Pressure coefficient at the base of a family of boattailed bodies (45) at $M = 1.9$, as a function of tail angle and base-area ratio.



- (43) Wakefield, Flared Bodies, NASA TM X-106 (1959).
- (44) Nash, 2-Dimensional Base Flow, NPL Aero Rpt 1070 (1963).
- (45) Brown and Goodwin (NACA), Family of Boat-Tail Bodies:
 - a) Pressure at M between 1.6 and 2.4, T'Note 3054 (1953).
 - b) All Drag Components, Tech Note 3708 (1956).
- (46) Rom, Step in BL, Israel Inst of Tech TAE Rpt 31 (1963).

A Pointed Tail can be considered to be the extreme of a boat-tailed body; but it is a shape about which theoretical as well as experimental information at supersonic speeds, is not readily available. Results of a wind-tunnel investigation are reproduced, however, in figure 44. Directly behind the shoulder, an expansion takes place, indicated by a drop of the pressure coefficient, almost to $C_p = -0.16$. On the basis of simple 2-dimensional theory (page 17-14) one might expect:

$$C_p = 2 (\sin \epsilon) / \sqrt{M^2 - 1} \quad (20)$$

With $\sin \epsilon = -0.174$, and for $\sqrt{M^2 - 1} = 1.65$, this equation indicates a $C_p = -0.21$, which is a value somewhat more negative than the minimum stated above. The boundary layer at the end of the cylindrical forebody (the length of which is not reported) can be made responsible for the difference. — Shortly behind the shoulder, a *recompression* begins. In fact, the pressure rises so much, that at the pointed end of the tail, a positive pressure corresponding to $C_p = +0.06$ is obtained. This compression is evidently a consequence of the 3-dimensional flow pattern. The integrated drag coefficient of the tail in figure 44, is $C_{D_0} = 0.094$. This value is less than the base drag of the blunt cylinder (without the tail). It seems, however, that the efficiency of the long tail (considering weight, cost and space required) is not very good; and that is evidently the practical reason why such tails are "never" used in supersonic applications.

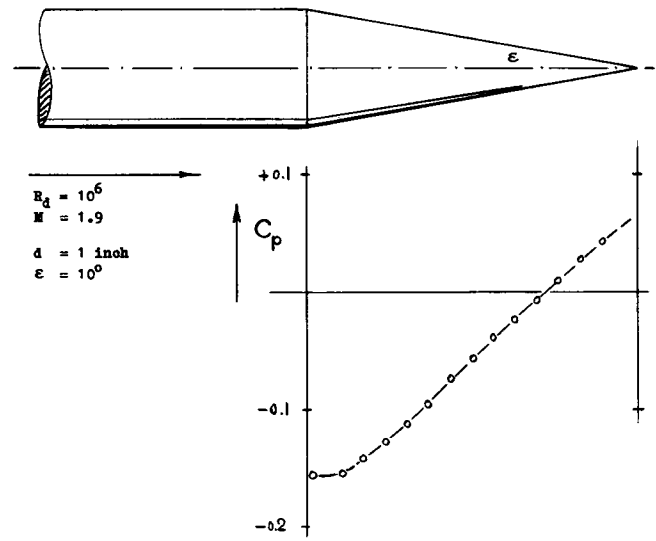


Figure 44. Pressure distribution, showing recompression taking place along a pointed tail cone (42,c).

NOTE:

In writing this book, two dimensionless coefficients have extensively been used:

$$C_{D_0} = D / (q S_0)$$

where $q = 0.5 \rho V^2$, and S_0 = projected frontal area, as listed under "symbols" on page 1-2.

$$C_p = \Delta p / (q S_0)$$

where $\Delta p = (p - p_a)$ and p_a = ambient pressure (in the undisturbed flow).

ALPHABETICAL SUBJECT INDEX

- Ackeret, supersonic airfoil theory 17-13
 Aerodynamic efficiency of aircraft 14-11
 Aerophysical characteristics (atmosphere) 19-8
 Afterbody pressure and drag characteristics:
 boat-tailed bodies (three-dimensional) 16-22
 on double cones at transonic speeds 16-24
 second order supersonic theory 17-14, 18-2
 Airfoil sections, aerodynamic characteristics:
 sections with thick trailing edges 3-21
 systematic section families (classification) 6-8
 sections with boundary-layer control 2-14
 foil section in reversed flow 6-20 and 15-4
 foil sections in compressible fluid flow 15-10
 foil section with surface roughness 15-12
 influence of section camber 15-19 and 17-20
 0015 section at transonic speeds 15-39
 airfoil sections at sonic speed ($M = 1$) 17-8
 airfoils at supersonic Mach numbers 17-13
 foil sections in rarefied fluid flow 19-17
 laminar profiles, see under "laminarization"
 Airships, aerodynamic characteristics:
 drag of bare hull shapes (figure 23) 6-17
 performance of complete airships 14-1
 Airplanes, aerodynamic drag analysis:
 Me-109 example – full scale analysis 14-3
 statistical collection of data 14-9
 complete models in tunnels 14-11 and 15-34
 sailplane drag and lift characteristics 14-13
 interference drag against Mach number 15-35
 Antenna devices, used on airplanes:
 cable-type antenna ("wire") 4-5
 sheet-metal rods used as antennas 15-8
 Area rules (in compressible fluid flow):
 principle of fuselage contouring 15-38
 canopy location on fuselage 15-30
 transonic area rule 16-34
 Armament components:
 gun turret (interference effect) 8-9
 gun openings (portholes) 13-3
 tail turret on fuselage 13-3
 Aspect ratio characteristics:
 effective aspect ratio of wings 7-3
 small and zero aspect ratios 7-17
 of hydrofoils (in water) 10-12 and 11-31
 of planing plates in water 11-20
 slender wings at transonic speeds 16-33
 relaxation at transonic speeds 15-41 and 17-11
 influence at supersonic speeds 17-17
 Atmospheric properties (pressure, density):
 in the troposphere (standardized values) 1-11
 in the upper layers (aerophysics properties) 19-10
 Automobiles, specific characteristics:
 lift and induced drag of automobiles 12-3
 racing cars (example) 12-16
 Barker effect (viscosity) 3-1 and 19-3
 Base-drag characteristics:
 base drag at subsonic speeds 3-18
 airfoils with trailing edges 3-21 and 17-16
 base drag of railroad trains 12-13
 at transonic and supersonic speeds 16-4
 base pressure in rarefied fluid flow 19-5
 Biconvex foil sections 17-10 and 17-14
 Biplane Characteristics:
 in uncompressed fluid flow (lifting) 7-12
 biplane at supersonic Mach numbers 16-35
 Birds, lift and drag characteristics 7-22
 Bluff-body shape characteristics:
 in uncompressed fluid flow 3-9 and 4-2
 influence of rounding radius 3-13
 in compressible fluid flow (subsonic) 15-3
 at transonic and supersonic speeds 16-14
 bluff bodies in hypersonic fluid flow 18-17
 body shapes in free molecule flow 19-15
 Blunt rear ends (of 3-dimensional bodies):
 as applied in automobiles 12-4
 on boat-tailed bodies 16-22
 Blunt shapes, drag characteristics of:
 blunt leading edges (figure 22) 3-12
 cylinder in axial flow (figure 23) 3-13
 cylinders at transonic speeds (figure 14) 16-13
 blunt L'edges at hypersonic speeds 18-15
 Blunt trailing edges:
 in uncompressed fluid flow 3-21
 in compressible fluid flow 15-7 and 15-16
 at supersonic speeds 17-15
 Boat-tail characteristics (3-dimensional bodies):
 in uncompressed fluid flow 3-20
 at supersonic speeds 16-22
 Boats (smaller craft in water):
 performance of motorboats 11-16
 drag of submarines 11-17
 planing characteristics 11-24
 characteristics of racing boats 11-25
 principles of hydrofoil boats 11-30

Bodies (three-dimensional) characteristics of:	
drag of streamline bodies	6-16 and 15-25
parabolic body shapes	16-24 and 18-18
simple bodies in free molecule flow	19-15
see also "bluff bodies" and "streamline bodies"	
Bombs (as external loads):	
drag and interference at subsonic speeds	13-18
drag in compressible fluid flow	15-31
characteristics at transonic speeds	16-26
Boundary layer characteristics:	
various thickness definitions of B'layer	2-2
presence of laminar sublayer	2-3
stability & transition of B'layer	2-8 and 17-4
laminarization	2-11, 6-6, 15-10 and 17-5
boundary layer on laminar foil sections	2-14
B'layer originating along the ground	4-2
dynamic pressure in boundary layer	5-6 and 8-3
stability, f (compressibility)	15-9 and 17-4
transition on cones at supersonic speeds	17-5
boundary-layer shock-wave interaction	18-7
slip effect in rarefied fluid flow	19-16
Boundary-layer control:	
B'layer suction on rear of sphere	3-27
B'layer control through slots and slats	6-14
B'layer bleed-off in radiators	9-4
Cables (stranded wires)	4-5 and 13-20
Canopies on fuselages, drag of and due to:	
drag in uncompressed fluid flow	13-2
drag in compressible fluid flow	15-8
interference drag (location)	15-30
application of transonic area rule	16-36
Caps and Cups, drag of	3-17
Cavitation (in water flow):	
general principles of cavitation	10-4
drag of cavitating conical shapes	10-7
Centrifugal effect at hypersonic speeds	18-14
Circular cylinders, characteristics of:	
pressure distribution around cylinders	3-3
drag in uncompressed fluid flow (figure 12)	3-9
cylinders with surface roughness	3-10
cylinders in axial flow	3-12, 15-4, 16-13 and 19-17
rotating pair of cylinders	3-25
cylinder with B'layer suction control	3-27
rotating cylinders (lifting)	7-11
cylinders in water (with guide vanes)	10-3
fairings around cylinders	10-3 and 13-19
drag in compressible fluid flow	15-6
at transonic and supersonic speeds	16-16
cylinders in free molecule flow	18-18
Circulation (lift) around sections	7-2 and 7-11
Cockpits, open type on fuselages	13-1
Configurations (wing plus body):	
in uncompressed fluid flow (interference)	8-15
complete airplane configurations	14-8 and 15-33
in compressible fluid flow (interference)	15-28
transonic area rule applied to	16-34
Cone characteristics:	
cones in uncompressed fluid flow	3-17
cones in water (cavitating)	10-7
in transonic/supersonic flow (figure 23)	16-18
cones in hypersonic flow	18-10 and 19-7
bluff cones at hypersonic speeds	18-17
cone drag in free molecule flow	19-16
Control surfaces	5-14 and 13-13
Cowlings, around engines:	
cowlings around radiators	9-6
around radial engines	13-7
in compressible flow (critical M'number)	15-32
supersonic-type cowlings (additive drag)	16-38
Cosine principle, see under "cross flow"	
Creeping motion, at low R'number	2-1 and 3-1
Critical Mach numbers:	
of airfoil sections (drag divergence)	15-15
of swept wings (leading edge)	15-22 and 16-30
of cones and wedges (shock attachment)	16-19
Critical Reynolds number:	
of the boundary layer (transition)	2-8
of rivet heads (drag coefficient)	5-9
of airfoil sections (transition)	6-2
of round shapes in water (figure 1)	10-1
critical number of sphere	3-7, 10-1 and 15-9
in supersonic fluid flow (temperature)	17-4
Critical roughness grain size	5-2
Critical speed (in regard to cavitation)	10-5
Cross-flow (cosine) principle:	
circular cylinder in uncompressed flow	3-11
application in zero-aspect ratio wings	7-18
inclined shaft (in water)	10-16
application in swept wings	15-20
inclined cylinder at hypersonic speed	18-16
Cylindrical elements:	
round smoke stacks (vortex street)	4-4
cables (stranded wires)	4-5
surface-piercing cylinder (in water)	10-15
inclined cylinder (cross flow)	10-16 and 18-16
fairings around cylinders	13-19
supersonic fairings around cylinders	16-17
see also under "circular cylinder"	
Deceleration tests on vehicles:	
on automobiles (on road)	12-1
on airships (full scale)	14-2
Delta wing characteristics:	
definition of delta wings	16-31
drag at transonic speeds	16-30
Density of air and water	1-10
Density in upper atmosphere	19-11
Diffuser efficiency	9-4, 9-17 and 16-38
Dihedral of wings, influence of:	
in airplane wings (at low speeds)	7-9
in hydrofoils (surface-piercing)	11-29
Dirt and mud on wing surface	5-12

- Disks, drag characteristics of:
 at very small Reynolds numbers 3-1
 as a function of Reynolds number 3-15
 used in interference method 8-4
 disks in water (sea anchors) 10-3
 drag when cavitating in water 10-6
 in free molecule flow (theoretical) 19-15
 Dissociation of air molecules 18-25
- Dive-brake flaps, aerodynamic characteristics:
 in uncompressed fluid flow 3-18, 13-11 and 13-28
 brakes in compressible fluid flow 15-32
- Double-arc airfoil sections 17-10 and 17-14
- Double spinner (air inlet) 9-18
- Double-wedge sections, characteristics of:
 double wedges in transonic fluid flow 17-9
 D-wedges in supersonic fluid flow 17-14 and 18-2
 in free molecule flow (drag and lift) 19-17
- Downwash behind wings:
 induced drag as a consequence of 7-2
 drag of horizontal tail in downwash 7-15
- Drag area (definition of) 1-8
- Drag coefficient (definition) 1-9
- Drag divergence (as a function of Mach number):
 in airfoil sections (Mach number) 15-17
 swept wings ("cosine" & "cross flow") 15-22
 drag above drag divergence (drag rise) 15-38
 see also "critical M'number" and "transonic"
- Drop-test technique:
 parachutes tested by 13-24
 on wing-body configurations 16-2
 applied to bombs 16-26
- Ducted systems (internal flow):
 mechanics of radiator systems 9-3
 mechanics of ventilation systems 9-14
 internal flow at supersonic speeds 16-38
- Dust, drag and sinking speed 3-2
- Dynamic pressure:
 definition of dynamic pressure 1-10
 viscous interference on 3-1 and 19-3
 stagnation pressure 15-2, 16-3 and 17-2
- Earth, some characteristics of 19-8
- Edges, shape and interference of:
 viscous effect of longitudinal edges 2-8
 drag due to sheet-metal edges 5-10
 lateral wing edges (flow pattern) 6-4
- Effective characteristics:
 dynamic pressure (in boundary layer) 5-6
 effective aspect ratio of wings 7-5
 effective thickness in cavitating flow 10-6
 thickness ratio (in compressive flow) 15-15
- Efficiency in transportation:
 of automobiles (rolling resistance) 12-7
 of railroad trains (including traction) 12-14
 of airplanes (against viscous drag) 14-9
- Ejection seats (catapulted) 13-22
- Elevator (horizontal tail) drag due to 13-12
- Ellipsoids (as bluff shapes) 3-12
- Elliptical cylinders in cross flow 3-11
- "E" method (performance) 7-5 and 14-12
- End plates, attached to wings:
 on airplane wings (at subsonic speeds) 7-9
 on hydrofoils (in water) 11-27
 in supersonic fluid flow (footnote) 17-17
- Engine installations, aerodynamics of:
 engine cowlings (shape of) 9-7 and 13-8
 drag of jet engine installations 9-9
 imperfections due to installation of 14-5
 cowlings in compressible fluid flow 15-32
 inlets at transonic/supersonic speeds 16-38
- Entropy (as a part of gas dynamics) 17-2
- Expansion (from supersonic speeds):
 boundary-layer re-attachment due to 15-7
 expansion around airfoil-section noses 15-18
- Prandtl-Meyer expansion theory 17-2
- laminarization due to expansion 17-2 and 17-5
- External loads (on airplanes):
 drag of wing-tip tanks 7-7 and 13-17
 drag of external stores (tanks) 8-8 and 13-16
 drag of bombs attached to airplanes 13-17
- Fabrics, aerodynamic characteristics of:
 principles of porosity and permeability 3-23
 drag of flags (fluttering in wind) 3-25
 in parachutes and tow targets 13-24 and 13-27
- Fairings placed around bluff bodies:
 basic drag coefficients of fairings 6-9
 blisters (optimum shape) on wall 8-4
 around circular cylinders 10-3 and 13-19
 fairings around airplane wheels 13-14
 movable gun-barrel fairings 13-20
 fairings in compressible fluid flow 15-12
 3-dimensional at supersonic speeds 16-17
 optimum at sonic/supersonic speeds 17-10 & 15
- Fillets along strut and wing junctions 8-12
- Fish (swimming in water) drag of 10-1
- Flags (fluttering in wind) drag of 3-25
- Flaps (landing flaps on wings):
 drag due to lift of flapped wings 6-14
 induced drag, due to flaps 7-8
- Flettner rotor (lifting) 7-12
- Floats on water-based airplanes:
 aerodynamic drag of floats 13-9
 planing characteristics of floats 11-25
- Flow pattern (specific types of):
 wing tips (vortex pattern) 7-5
 pair of disks (interference) 8-1
 fuselage with obstacle attached 8-4
 horizontal tail at end of fuselage 8-14
 automobiles (over ground) 12-1
 D-wedge section at transonic speed 17-8
- Flying boat hulls 11-24 and 13-9
- Foil sections, see "airfoils" and "hydrofoils"
- Forebody (negative drag) 3-12

Formation flying (induced drag)	7-15
Friction (on wetted surface area):	
of airship hulls	6-16 and 14-1
as found on boats and ships	11-3
Froude number:	
similarity law (water surface)	1-10
applied to boats and ships	11-2 and 11-12
Full-Scale experimental results:	
of airships, resistance	14-1
analysis of Me-109 fighter	14-7
performance of sailplanes	14-13
fighter airplanes at higher speeds	15-34
Fuselages, characteristics of:	
induced drag of fuselages	8-18
engine-air intakes in fuselage	9-18
with canopies and windshields	13-2
full-scale analysis (Me-109)	14-5
Gaps in surface, drag due to:	
in plane surfaces (walls)	5-7
sheet-metal discontinuities	5-10
in control surfaces	5-13
Gas-dynamic functions (basic)	17-2
Glide-path control of wing	8-15
Grains, see under "roughness" and "sand"	
Grids (screens) characteristics of	3-23
Ground effect (interference):	
on buildings (boundary layer)	4-2
on wings (induced drag)	7-13
automobiles over road	12-1
Guide vanes (influence of):	
bluff body with guide vanes	3-26
attached to cylinders (in water)	10-3
Guns (armament) drag due to:	
gun turrets on fuselage	8-9 and 13-3
portholes for guns in fuselage	13-3
gun-barrel fairings (movable)	13-20
Half-body characteristics:	
in axial flow (heads)	3-12 and 16-14
bodies attached to walls	8-3
Heat, affecting aerodynamics, see "temperature"	
Hemispherical head or nose shapes:	
in uncompressed fluid flow	3-12
at hypersonic speeds	18-20
Holes in wetted surface, drag of	5-10
Horizontal tail (interference)	13-14
Houses (buildings) wind loads	4-2
Human body (drag and lift)	3-13
Hydrofoil boats	11-26 and 11-30
Hydrofoils (operating in water):	
characteristics in cavitating flow	10-9
induced and wave drag of hydrofoils	11-26
Hypersonic drag characteristics:	
hypersonic similarity principles	18-1
bluff body shapes in hypersonic flow	18-13
Ice formation on wings	5-12
Image method (testing vehicles)	12-1
Impact pressure (stagnation)	15-2 and 16-3
Inclined circular cylinders (oblique flow):	
in uncompressed fluid flow	3-11
in hypersonic fluid flow	18-16
Induced drag characteristics:	
due to wing flaps (lift distribution)	7-8
induced drag of swept wings	7-8
drag due to wing twist	7-7 and 15-33
in biplane configurations	7-12
ground effect on induced drag	7-13
due to body interference	8-13 and 8-18
in a sailboat (water-wave drag)	11-18
of hydrofoils (in water)	11-26
of automobiles (lifting)	12-3
in compressible fluid flow	15-33
at supersonic speeds	17-17
Inlet openings, aerodynamic characteristics:	
intakes for radiators and engines	9-4 and 9-9
scoops for reciprocating engines	9-13
intakes for ventilation air	9-14
marine-type inlets (for condenser water)	9-16
for engines in compressive flow	15-32
inlets at supersonic speeds	16-38
Interference drag, characteristics of:	
pairs of cylinders and struts	8-1
on streamline bodies (fuselages)	8-6
on struts, when attached to "walls"	8-10
on tail assembly (in corners)	8-12
on wing sections due to protuberances	8-13
induced interference drag	8-14 and 8-18
in wing-body configurations	8-15
interference method (plates)	8-19
interference on motor vehicles	12-15
compressibility effect (general)	15-29
Internal drag (momentum loss in ducts):	
principles of internal drag	9-2
internal drag in radiator systems	9-3
in engine installations	9-8
momentum loss at transonic speeds	16-38
Internal pressure:	
in buildings (due to wind)	4-3
in radiators (due to stagnation)	9-3
Ionization of atmospheric air	19-9
Irregularities of and in wetted surfaces:	
drag of sheet-metal joints	5-7
rivet heads, protruding from surface	5-8
gaps and holes (in sheet metal surface)	5-10
Junctions between various elements:	
between strut and wall	8-10
between pairs of struts	8-13
between wing and fuselage	8-16
Knudsen number (in rarefied gases)	19-2

- Laminar-flow foil sections:
 principles (pressure gradient) 2-10
 influence of surface roughness 2-10, 2-13 and 6-7
 laminarization through suction 2-14
 dirt and mud on wings 5-12
 thickness location (gradient) 6-6
 in compressible fluid flow 15-13
- Laminarization through pressure gradient:
 in uncompressed fluid flow 2-10 and 6-6
 on streamline bodies 6-18 and 15-10
 in compressive flow 15-7, 15-10 and 15-14
 on spheres through compressibility 15-9
 at supersonic speeds 17-4
- Landing flaps, parasitic drag due to 6-13
- Landing gears (of airplanes) 13-14
- Leaks, drag due to 9-5 and 13-5
- Lift, special types of drag due to:
 parasitic drag of foil sections 6-11
 due to lift of flat plates 7-3
 of lifting rotating cylinders 7-11
 of streamline bodies (vortex pattern) 7-20
 interference effects on induced drag 8-17
 originating in ducted systems 9-10
 of automobiles (over ground) 12-3
 in supersonic fluid flow 17-17
 of wings at hypersonic speeds 18-10
 see also under "induced drag"
- Locomotives, aerodynamic drag 12-11
- Loss coefficient (momentum):
 of screens (pervious sheets) 3-23
 in ducted systems (also in diffusers) 9-1
- Mach number and Mach angle 15-1 and 17-1
- Magnus effect (on circular cylinders) 7-11
- Maximum speed results:
 of airplanes at subsonic speeds 14-8
 at higher Mach numbers 15-38
- Maximum transonic D'coefficients 16-32 & 17-12
- Me-109 and Me-262 performance 14-3 and 14-9
- Mean free path (in gases) 19-1
- Meteors, characteristics (vaporizing) 18-26
- Momentum (concept and application):
 basic consideration (exchange of) 1-7
 momentum in boundary layer 2-3
- Motor vehicles (see "automobiles") 12-8
- Motorboats, hydrodynamics of 11-16
- Motorcycles, aerodynamic drag 12-9
- Nacelles (housing engines), drag due to:
 interference drag 8-15, 13-6 and 15-30
 induced drag, caused by 8-18 and 13-6
 nacelles with radial engines 13-7
 in compressible fluid flow 15-29 and 16-36
- Newton and Newtonian type of flow:
 hypersonic cone flow 18-4
 inclined circular cylinder 18-16
 Newton's drag theory 19-13
- Notation, general 1-2
- Oblique flow, characteristics in:
 inclined circular cylinders 3-11 and 18-16
 swept wings (cross-flow principle) 15-20
 see "Newtonian flow", "cross flow principle"
- Openings in surface, see "inlets", "outlets", "holes"
- Optimum dimensions and shapes:
 section-thickness ratio 6-5, 15-13, 17-10 & 17-15
 optimum lift coefficient of wings 6-11
 optimum fineness ratio of bodies 6-18
 optimum radius of fillets 8-12
 optimum speed of autos and trains 12-8 & 12-14
 optimum shape of nacelles 13-5
 optimum bodies in free molecule flow 19-17
- Outlets (for air) characteristics:
 drag due to outlet openings 9-2
 in ventilation systems 9-16
- Paint, grain sizes (roughness) 5-3 and 10-2
- Parabolic body shapes (pressure distribution):
 at transonic speeds 16-23
 at hypersonic speeds 18-18
- Parachutes, aerodynamic characteristics:
 porosity and permeability 3-24 and 13-23
 gliding and oscillating parachutes 13-24
 aeroelasticity effects in canopies 13-26
- Performance of airplanes:
 take-off (flap deflection) 7-8
 formation flying of airplanes 7-15
 range of airplanes (drop tanks) 13-17
 "e" method, drag due to lift 14-12
 climb performance 14-14
- Permeability and porosity:
 of screens and grids 3-24
 in parachute canopies 13-23
- Permissible roughness grain size:
 in air f(speed) (figure 3) 5-2
 in water f(speed) (figure 3) 10-2
- Planing along surface of water:
 planing principles 11-19
 planing-type boats and seaplanes 11-23
- Plates in fluid flow normal to surface:
 influence of "aspect ratio" 3-15
 drag of perforated disk 3-16
 rear-side pressure 3-16 and 16-15
 interference between 2 plates 8-1
 in compressible fluid flow 15-3
 in free molecule flow (theory) 19-13
- Porosity (permeability) 3-24 and 13-23
- Prandtl, theoretical information:
 lifting-line wing theory 7-2
 compressibility rule (Prandtl factor) 15-2
 Prandtl-Meyer expansion 17-2
- Pressure, various types (definitions) 1-4
- Pressure drag (from distribution):
 at low Reynolds numbers (viscosity) 3-1
 of the sphere (rear-side pressure) 3-10
 in cavitating water flow 10-7

Pressure distribution:	
laminar profiles (pressure gradient)	2-11
of circular cylinder (figure 2)	3-3
distribution around sphere (figure 9)	3-7
peaked pressure distributions	10-7 and 15-18
distribution around automobiles (lift)	12-3
biconvex section at $M = 1$	17-10
of double wedge at supersonic speeds	17-13
Pressure gradient (along surface):	
interference mechanism (B'layer)	8-6
Prandtl-Meyer supersonic expansion	17-5
see "laminarization" "interference" "separation"	
Profile drag, see "airfoil section drag"	
Projectiles (at transonic speeds)	16-22
Propellers, influence on drag:	
double spinner (air inlet)	9-18
due to asymmetric engine power	13-13
drag of stopped propellers	13-21
lift and induced drag due to thrust	14-14
Protuberances on wetted surface:	
drag due to (general)	5-7
concentration and slope of $C_f(R)$	5-4 and 11-4
protuberances on automobiles	12-16
Pylon-suspended stores or nacelles	13-16
Radial engines, drag due to:	
cowlings for radial engines	9-7
engine in nose of fuselage	13-4
Radiators, drag caused by:	
built into airplane wing or fuselage	9-6
lift due to, and induced drag	9-10
influence of heating and compressibility	9-11
radiator flow in automobiles	12-6
Radius of fillets, optimum	8-12
Railroad vehicles, aerodynamic drag:	
drag of locomotives	12-11
drag of railroad trains	12-12
Re-attachment of boundary layer:	
at subsonic speeds	15-7 and 15-18
see also "expansion" and "pressure gradient"	
Recompression in transonic fluid flow:	
without shock (local flow field)	15-17
through normal shock	16-2
in air inlets (intake openings)	16-38
Rectangular wing characteristics:	
in uncompressed fluid flow	7-6
at supersonic speeds (theory)	17-16
Resistance (synonymous with drag):	
of displacement vessels (in water)	11-3
rolling resistance of automobiles	12-7
traction resistance of RR vehicles	12-14
Reversal theorem of pointed wings	16-31
Reynolds number, at low values of:	
bluff bodies at low R'numbers	3-1
drag of elliptical sections	3-11
drag of airfoil sections	6-4
drag as a function of lift	6-10
streamline-body characteristics	6-16
Reynolds number, influence of:	
critical Reynolds number of sphere	3-7
R'number in airfoil sections	6-3
influence of R'number on base drag	16-7
on sphere at supersonic speeds	19-4
Ring-shaped wings, lift and drag:	
in uncompressed fluid flow	7-13
theory at supersonic speeds	17-18
Rivet heads on sheet-metal skin	5-8
Rocket vehicles (V-2)	18-2
Rolling resistance of automobiles	12-7
Rotating (axial) bodies (figure 24)	3-13
Rotating circular cylinders:	
pair of cylinders (B'layer control)	3-25
Flettner rotor (lifting)	7-11
Rotor (lifting blades)	7-22
Roughness of wetted surface, drag due to:	
permissible grain size	5-1 and 10-2
concentration and $C_f(R)$ slope	5-4 and 11-10
influence in water (general)	10-2
due to fouling (ships in water)	11-5
in compressible fluid flow	15-10
on streamline bodies (figure 36)	15-27
at supersonic Mach numbers	17-6
Round airfoil noses:	
at transonic Mach numbers	17-11
at supersonic/hypersonic speeds	17-14
Round bodies, characteristics of:	
pressure distribution	3-3 and 3-7
critical Reynolds number of	3-7 and 3-10
drag of round head shapes	3-12 and 18-20
drag of bodies at supersonic speeds	16-16
bodies at hypersonic speeds	18-18
see also "circular", "cylinders" and "spheres"	
Rounded body shapes, drag of:	
influence of rounding radius (figure 23)	3-13
spheroidal head shapes	16-17
rounded leading edges	16-17 and 18-15
Sail boats, hydrodynamics of	11-18
Sailplane (glider) characteristics	14-13
Sand-type surface roughness	5-4 and 10-2
Satellites (general conditions)	19-18
Scoop intakes (air or water)	9-14
Seaplane characteristics:	
planing (in water) on floats	11-24
aerodynamic drag of seaplanes	13-9
Separation of flow (boundary layer):	
basic mechanism of separation	3-3
vortex system behind bluff bodies	3-5
separation from boat tails	16-23
Sharp leading edges, flow around:	
in uncompressed fluid flow	6-13
at supersonic speeds	17-13
Sheet-metal surface characteristics:	
drag caused by sheet-metal joints	5-7 and 17-7
holes and gaps in surface	5-10
structural imperfections	14-4

- Ship resistance in water:**
- Schoenherr line (skin friction) 2-5 and 11-10
 - drag of barges (bluff shapes) 11-5
 - wind resistance of ships 11-8
 - influence of surface roughness 11-9
 - full-scale-model correlation 11-9
 - resistance in sea waves 11-11 and 11-14
 - general resistance statistics 11-16
- Shoulder pressure (hypersonic) 18-14
- Similarity, various rules:**
- subsonic (Prandtl) similarity 15-2
 - transonic similarity functions 16-20 and 17-8
 - transonic area rule 16-34
 - similarity rules in general 1-9
 - hypersonic similarity 18-1
- Ski runner, wind resistance of 3-14
- Skis, drag and lift characteristics:**
- hydrodynamic characteristics 11-25 and 11-32
 - aerodynamic characteristics of skis 13-16
- Skin-friction characteristics:**
- laminar and turbulent skin friction 2-4
 - Schoenherr line (turbulent) 2-5 and 11-10
 - local friction or shear-drag coefficient 2-6
 - friction in compressible fluid flow 15-9
 - at supersonic M numbers (figure 3) 17-4
 - in rarefied fluid flow (slipping) 19-6
 - see "laminarization", "B'layer", "transition"
- Slip flow characteristics 19-3 and 19-6
- Slotted devices (slots, slats):**
- wing leading edge slots and/or slats 6-14
 - slotted flaps at trailing edge 6-14
- Smoke stacks (vortex street)** 4-4
- Speed of sound** 1-11, 15-1 and 19-11
- Sphere, pressure on and drag of:**
- pressure distribution (figure 9) 3-7
 - rear-side pressure 3-10 and 16-16
 - drag with boundary-layer suction 3-26
 - spherical structure in wind 4-7
 - drag and lift of rotating sphere (ball) 7-20
 - critical Reynolds number in water 10-8
 - drag in compressible fluid flow 15-6
 - spheres in supersonic fluid flow 16-16
 - spheres at hypersonic speeds 18-20
 - influence of low Reynolds number 19-4
 - drag in free molecule flow 19-15
- Split flaps (attached to wings)** 6-14
- Splitter plate (vortex street)** 3-7
- Spoiler (lateral control) drag of** 13-12
- Spray (in water)** 10-13 and 11-25
- Stagnation pressure** 15-2 and 19-3
- Stagnation temperature** 15-3 and 18-24
- Steps on floats & flying-boat hulls 11-24 and 13-9
- Stimulation of turbulence 6-16 and 11-2
- Stokes analysis of viscous drag 3-1
- Stores (tanks) externally mounted** 13-16
- Streamline bodies, drag of:**
- interference drag on bodies 13-16
 - in compressible fluid flow 15-31
 - drag at transonic speeds 16-24
- Streamline bodies, specific characteristics:**
- drag as a function of Reynolds number 6-16
 - lift of streamline bodies 7-19
 - pressure distribution of bodies 15-24
 - bodies with surface roughness 15-27
- Streetcar (land-borne vehicle) 12-10
- Strouhal number (vortex frequency) 3-5
- Structures (exposed to wind):**
- buildings and houses 4-3
 - smoke stacks (vortex street) 4-4
 - bridges and masts 4-6
- Strut-section characteristics:**
- in uncompressed fluid flow 6-10
 - interference in junctions 8-11
 - in water (surface-piercing) 10-14
 - in compressible fluid flow 15-7 and 15-12
 - inclined struts (analysis) 15-21
- Submarines (in water) 11-17
- Surface-piercing effects (in water):**
- in struts (ventilation) 10-16
 - in hydrofoil systems (lift and drag) 11-28
- Surface-roughness characteristics:**
- paint and grain sizes 5-3 and 10-2
 - fouling (on ships in water) 11-4
 - roughness at supersonic speeds 17-6
 - see also "roughness" and "protuberances"
- Swept wings, characteristics of:**
- induced drag of swept wings 7-8
 - cosine or cross-flow principle 15-20
 - definition of sweep 15-20
 - drag divergence of swept wings 15-22
 - in compressible fluid flow 15-23
 - "sheared" and "yawed" wings 15-24
 - swept-wing configurations 15-38
 - transonic drag of swept wings 15-42
- Tail surfaces (on airplanes)** 7-14 and 13-13
- Tail wheels (at end of fuselage)** 13-15
- Tandem-wing arrangements** 7-14
- Tanks (external), characteristics of:**
- wing-tip tanks 7-7 and 16-37
 - interference effects of tanks 8-8
 - underslung-type tanks 13-16
- Taper ratio of straight wings** 7-6
- Temperature, values and influence of:**
- in the atmosphere 1-11 and 19-11
 - stagnation temperature 15-3 and 18-24
 - influence on skin friction 15-9 and 17-3
 - dissociation due to temperature 18-25
- Thickness ratio of airfoil sections:**
- influence on section drag 6-5
 - optimum thickness ratios 6-5, 17-10 and 17-15
- Thrust, influence on lift and drag** 14-14
- Tip tanks (on wings)** 7-7, 13-17 and 16-37
- Tip vortex, flow pattern of** 7-5
- Torpedo, running in water** 10-4
- Tow targets, drag of** 13-27

Townend ring (engine cowling)	3-26
Trailing edge, influence on drag:	
base drag, blunt edges	6-20, 16-11 and 17-16
optimum width (in 3-dimensional body)	8-5
Transition of boundary layer flow:	
as a function of pressure gradient 2-11 and 17-5	
as a function of surface roughness	5-1
Transonic drag characteristics:	
wing characteristics above D'divergence	15-39
airplanes at transonic speeds 15-39 and 16-34	
base drag at transonic speeds	16-5
transonic testing techniques	16-2
drag of cones at transonic speeds	16-19
triangular (delta) wings	16-30
drag of streamline bodies	16-24
transonic area rule	16-34
flow pattern around airfoil section	17-8
transonic wing similarity	17-8 and 17-12
Triangular (delta) wings, transonic	16-30
Turbulence, influence of:	
stimulation of turbulence 2-16, 6-16, 19 and 11-2	
B'layer turbulence on sphere	3-7 and 15-9
wind-tunnel turbulence factors	6-2
Ventilation (in water, similar to cavitation):	
ventilation and cavitation (distinction)	10-14
along surface-piercing solids	11-29 and 11-31
Ventilation (in air), drag due to:	
inlet openings (scoops) for ventilation	9-14
outlet openings for air	9-16
ventilation devices for RR vehicles	12-12
Viscosity properties of air and water	1-11
Viscosity and its influence upon:	
stagnation pressure	3-1 and 19-3
base pressure	16-7 and 19-6
supersonic wedge pressures	18-3
spheres at supersonic speeds	19-5
pressure and drag of slender cones	19-7
lift-curve slope at hypersonic speeds	18-9
"V" shape (dihedral), influence of:	
in airplane wings	7-9
in hydrofoils (surface-piercing)	11-29
Vortex generation and vortex characteristics:	
vorticity (and "rotation")	1-6
vortices originating at wing tips	7-4
vortex core cavitation (in water)	10-6
Vortex street (double-row vortex trail):	
vortex frequency in street	3-6
oscillations due to vortex street	4-5
alternating lift due to	3-5

Wake characteristics:	
viscous wake behind fuselage	8-14
see also "vortex street" (and "interference")	
Water, fluid flow characteristics in:	
turbulence in water (general)	10-1
surface-piercing solids	10-15
see also "wave resistance" and "cavitation"	
Wave drag in compressible fluid flow:	
wings at transonic speeds	17-7
flow pattern past D'wedge	17-8 and 17-13
wave drag due to lift	17-20
Wave resistance (in water):	
wave and spray drag	10-13
resistance of ship hulls	11-11 and 11-18
of submerged bodies (submarines)	11-18
of hydrofoils near surface	11-26
Waviness of wetted surface	5-8
Wedge-section characteristics:	
bluff wedges in uncompressed flow	3-18
characteristics of single wedge in water	10-7
in compressible fluid flow	15-4
at transonic speeds	17-8
at hypersonic speeds (figure 1)	18-2
wedges in free molecule flow	19-17
Wetted-area utilization:	
coefficients on wetted area	6-16 and 14-10
compressible interference analysis	15-36
aerodynamic efficiency of airplanes	14-7
Wheels as part of vehicles:	
on land-borne vehicles	12-7 and 12-14
as part of aircraft landing gears	13-14
Wind characteristics near ground	4-2
Wind socks (made of fabric)	13-27
Windshields, see "canopies" and "fuselages"	
Wing-tip characteristics:	
parasite drag originating at tips	6-4 and 7-21
flow pattern around wing tips	6-20 and 7-5
fuel tanks at wing tips	7-7, 13-17 and 16-37
Wings (drag of, non-lifting):	
ring-shaped wings	7-13 and 17-18
wings at transonic speeds	15-41 and 17-18
straight wings at supersonic speeds	17-13
triangular and delta wings	16-30
swept-wing characteristics	16-28
Wings (lifting) characteristics of:	
influence of flaps on drag	6-14 and 7-8
influence of planform on induced drag	7-4
influence of wing twist on induced drag	7-7
influence of angle of sweep on drag	7-8
biplane characteristics	7-12
influence of dihedral on lift and drag	7-9
ground effect on induced angle	7-13
wings in tandem arrangement	7-14
glide-path control (induced drag)	8-15
triangular and delta wings	16-33
lifting wings at supersonic speeds	17-17
lift in free molecule flow	19-17
Wires, see "circular cylinders" and "cables"	
"W" wings (type of sweep, also "M" shape)	15-24

When proofreading the 1965 edition, the following notes were added.

Pressure can be absolute (measured against vacuum) or a differential measured from the atmospheric or ambient level. Dynamic pressure $q = 0.5 \rho V^2$, represents such a differential, while "total" or Pitot pressure is the absolute pressure at a stagnation point. Stagnation or impact pressure can be meant to be absolute or to be the increment against the ambient pressure. We have the coefficient of the incremental stagnation pressure in compressible fluid flow, and particularly in supersonic flow, denoted by "q" in equation (4) on page 16-3. The same pressure is also used in Chapter XVIII (for example on page 18-14) where it is represented by C_p .

Fieseler "Stork". For those who doubt that this airplane was the first operational STOL (page 0-6) it is mentioned that some 1500 airplanes of this type were built and used during World War II. Imitations have appeared after that war, both in the United States, and by Dornier.

Vortex Street (page 3-6). The C_p in equations (14) and (17) is meant to indicate the pressure at the rear side (base) of the bodies considered.

Cones. The "new" experimental data in figure 34 (on page 3-18) indicated by (►) were evaluated from reference (50,f) in Chapter XVIII.

Streamline Bodies (p 6-16, also 3-1). Finned ellipsoidal bodies have been tested down to Reynolds numbers below 10^3 by Robertson (Illinois), J.ASpace Sci 1962 p 842. Results confirm the estimated function as in figure 22 (on page 6-16).

The Wing Tip shape No. 5, discussed on page 7-5, has been adopted by some designers. It is referred to as the "Hoerner Wing Tip"; and it is commercially available (without any monetary advantage to the author) as an accessory for Cessna airplanes.

The Critical Reynolds Number of spheres as discussed on page 10-1, has a comparison in the fact that the transition R'number of the boundary layer at supersonic speeds varies with the so-called unit R'number ("R" = V/w in ft or any other linear dimension). See in this respect: Potter and Whitfield, Arnold AEDC TN-1958-77 (J. Aerospace Sci 1959 p 186) and TR-1960-5; also J. Fluid Mech 1962 p 501.

Elastic Surface. When properly designed and "tuned", an elastic coating can dampen boundary-layer oscillations, and postpone transition from laminar to turbulent flow, to higher speeds (such as possibly in fish, page 10-1 and reference 1). Investigations by Kramer; see J. ASpace Sci 1957 No. 6; A Soc Naval Eng J. 1960 p 25, 1961 p 103, 1962 p 341.

Hydrofoil Boats, as mentioned on page 11-30. The most advanced type is "Patrol Craft Hydrofoil" (PCH) built in 1963 by Boeing for the U.S. Navy. Designed after the experimental 5 l-ton boat "Sea Legs" (by Gibbs & Cox, 1957) the PCH has fully submerged, automatically controlled foils.

displacement weight	$\Delta = 108$ ltons
hull length, overall	$l = 116$ ft
design speed	$V = 45$ kts
2 gas turbines, continuous	$P = 6200$ HP

See Lacey (BuShips) in "Hovering Craft and Hydrofoil", April 1964.

Radial Engines. On p 9-11, "liquid" is meant to indicate the cylinder temperature.

Automobiles. The world speed record (see page 12-16) is now held by Breedlove, on a jet-engine powered car sponsored by Shell and Goodyear, designed by aircraft engineers, at around 400 mph. A new attempt is being undertaken at the time of printing this text.

The Area Rule as presented on page 16-34 (see reference 77) has subsonic equivalents; such as the underslung fuel tank on page 8-8, or many examples of interference (in Chapter VIII). At supersonic Mach numbers, area considerations (explained by "longitudinal buoyancy") are found in Chapter XX in connection with external stores.

Skin Friction. At the time where this edition is being printed, the author is preparing a report for NASA on "Skin Friction From Subsonic to Supersonic Speeds". The information on pages 17-3 and -4, will thus be amplified. The report might be available from the Defense Documentation Center in 1965 (Contract Number NAS1-3181).

Spikes are mentioned in various places; see page 16-27 (reference 53,b,f), pages 18-7 and -11 reference (17,c); page 16-40 (evaluated from ARC,RM 3007, 1952/57); and in Chapter XX (figures 25 and 26). A movable inlet cone as on page 16-39 produces the same mechanism as a spike. Also, any blunt obstacle placed on a wall (such as "imperfections" in Chapter XX, or the blunt windshield in figures 20 and 21 in that chapter) causes separation similar to that around a spike. The same effect should be involved at subsonic speeds, such as in figure 8 on page 8-4, for example. Also the tow line in figure 34 on page 18-19 (plus towing body) has a spike effect.

Meteorites. On page 18-26 the drag coefficient is assumed to be $C_{D_0} = 2$. During deceleration, not only mass and frontal area reduce, but drag coefficient and shape also change (disregarding the influence of extreme temperatures and their consequences in terms of gas properties).

Interplanetary Gas Properties. On page 19-11 density in the order of $\rho = 10^{-20}$ kg mass per m^3 is suggested as a lower "limit". There are other estimates such as ρ between 10^{-18} and 10^{-19} proposed by Koelle, and quoted by KD Wood in "Aerospace Vehicle Design, Volume I Aircraft Design", published 1963.

Rarefied Fluid Flow. In addition to the experimental results in Chapter XIX, the following references were found:

- a) Maslach, Cylinder Drag, UCal Berkeley Rpt AS-1963-3; DDC AD-414,998; also Physics of Fluids 1963 p 315.
- b) Bloxsom, Bodies in Hypersonic Flow, Journal Aero-Space Sciences 1962 p 1429.
- c) Kinslow, Spheres in Hypervelocity, AIAA Journal 1963 p 2467.
- d) Shien-Pu Tang, Cylinder, UCal Berkeley Rpt AS-1964-3, DDC AD-431,774.

Reference. On page 16-11, in (24,b) it should read: Sept 1956 p 59.

Index. Subjects in Chapter XX are not included in the Index.

A French Edition of "Fluid-Dynamic Drag" will be published by Gauthier-Villars in Paris. English-language readers are notified herewith that the present edition is much more enlarged than the French edition.
